frontiers | Research Topics

Women in chemistry 2022

Edited by
Anna Maria Maria Papini, Chen Liao, Cosima Damiana Calvano, Daniela Iacopino, Debbie C. Crans, Dönüs Tuncel, Federica Sabuzi, Francesca Maria Toma, Gabriela Oksdath-Mansilla, Ganna Gryn'ova, Giusy Lofrano, Hoda A. Ahmed, Hongli Wen, Houjuan Zhu, Irene Fahim, Jie Shen, Joana Cardoso Costa, Jyotirmayee Mohanty, Karen Martinez, Lara Massai, Lorraine Christine Nagle, Lucia Caporaso, Luisa Margarida Martins, Maela Manzoli, Margherita Brindisi, Maria Chiara Arno, Marie Erard, Nicole J. Jaffrezic-Renault, Ottavia Giuffrè, Pinar Sen, Qiong Sun, Rachelle J. Bienstock, Rajni Verma, Reshma Rani, Rosalia Maria Cigala, Sarah Pike, Sarish Rehman, Srabanti Ghosh, Sudipta Roy, Vânia André, Viktorya Aviyente and Weiwei Han

Published in
Frontiers in Chemistry



FRONTIERS EBOOK COPYRIGHT STATEMENT

The copyright in the text of individual articles in this ebook is the property of their respective authors or their respective institutions or funders. The copyright in graphics and images within each article may be subject to copyright of other parties. In both cases this is subject to a license granted to Frontiers.

The compilation of articles constituting this ebook is the property of Frontiers.

Each article within this ebook, and the ebook itself, are published under the most recent version of the Creative Commons CC-BY licence. The version current at the date of publication of this ebook is CC-BY 4.0. If the CC-BY licence is updated, the licence granted by Frontiers is automatically updated to the new version.

When exercising any right under the CC-BY licence, Frontiers must be attributed as the original publisher of the article or ebook, as applicable.

Authors have the responsibility of ensuring that any graphics or other materials which are the property of others may be included in the CC-BY licence, but this should be checked before relying on the CC-BY licence to reproduce those materials. Any copyright notices relating to those materials must be complied with.

Copyright and source acknowledgement notices may not be removed and must be displayed in any copy, derivative work or partial copy which includes the elements in question.

All copyright, and all rights therein, are protected by national and international copyright laws. The above represents a summary only. For further information please read Frontiers' Conditions for Website Use and Copyright Statement, and the applicable CC-BY licence.

ISSN 1664-8714
ISBN 978-2-8325-3524-0
DOI 10.3389/978-2-8325-3524-0

About Frontiers

Frontiers is more than just an open access publisher of scholarly articles: it is a pioneering approach to the world of academia, radically improving the way scholarly research is managed. The grand vision of Frontiers is a world where all people have an equal opportunity to seek, share and generate knowledge. Frontiers provides immediate and permanent online open access to all its publications, but this alone is not enough to realize our grand goals.

Frontiers journal series

The Frontiers journal series is a multi-tier and interdisciplinary set of open-access, online journals, promising a paradigm shift from the current review, selection and dissemination processes in academic publishing. All Frontiers journals are driven by researchers for researchers; therefore, they constitute a service to the scholarly community. At the same time, the *Frontiers journal series* operates on a revolutionary invention, the tiered publishing system, initially addressing specific communities of scholars, and gradually climbing up to broader public understanding, thus serving the interests of the lay society, too.

Dedication to quality

Each Frontiers article is a landmark of the highest quality, thanks to genuinely collaborative interactions between authors and review editors, who include some of the world's best academicians. Research must be certified by peers before entering a stream of knowledge that may eventually reach the public - and shape society; therefore, Frontiers only applies the most rigorous and unbiased reviews. Frontiers revolutionizes research publishing by freely delivering the most outstanding research, evaluated with no bias from both the academic and social point of view. By applying the most advanced information technologies, Frontiers is catapulting scholarly publishing into a new generation.

What are Frontiers Research Topics?

Frontiers Research Topics are very popular trademarks of the *Frontiers journals series*: they are collections of at least ten articles, all centered on a particular subject. With their unique mix of varied contributions from Original Research to Review Articles, Frontiers Research Topics unify the most influential researchers, the latest key findings and historical advances in a hot research area.

Find out more on how to host your own Frontiers Research Topic or contribute to one as an author by contacting the Frontiers editorial office: frontiersin.org/about/contact

Women in chemistry 2022

Topic editors
Anna Maria Maria Papini — University of Florence, Italy
Chen Liao — Argonne National Laboratory (DOE), United States
Cosima Damiana Calvano — University of Bari Aldo Moro, Italy
Daniela Iacopino — University College Cork, Ireland
Debbie C. Crans — Colorado State University, United States
Dönüs Tuncel — Bilkent University, Türkiye
Federica Sabuzi — University of Rome Tor Vergata, Italy
Francesca Maria Toma — Berkeley Lab (DOE), United States
Gabriela Oksdath-Mansilla — Universidad Nacional de Córdoba, Argentina
Ganna Gryn'ova — Heidelberg University, Germany
Giusy Lofrano — University of Salerno, Italy
Hoda A. Ahmed — Cairo University, Egypt
Hongli Wen — Guangdong University of Technology, China
Houjuan Zhu — Institute of Materials Research and Engineering (A*STAR), Singapore
Irene Fahim — Nile University, Egypt
Jie Shen — Hangzhou City University, China
Joana Cardoso Costa — University of Coimbra, Portugal
Jyotirmayee Mohanty — Bhabha Atomic Research Centre (BARC), India
Karen Martinez — University of Copenhagen, Denmark
Lara Massai — University of Florence, Italy
Lorraine Christine Nagle — University College Cork, Ireland
Lucia Caporaso — University of Salerno, Italy
Luisa Margarida Martins — Universidade de Lisboa, Portugal
Maela Manzoli — University of Turin, Italy
Margherita Brindisi — University of Naples Federico II, Italy
Maria Chiara Arno — University of Birmingham, United Kingdom
Marie Erard — Université Paris-Saclay, France
Nicole J. Jaffrezic-Renault — Université Claude Bernard Lyon 1, France
Ottavia Giuffrè — University of Messina, Italy
Pinar Sen — Rhodes University, South Africa
Qiong Sun — Qingdao University of Science and Technology, China
Rachelle J. Bienstock — RJB Computational Modeling LLC, United States
Rajni Verma — Seoul National University, Republic of Korea
Reshma Rani — Jubilant Life Sciences, India
Rosalia Maria Cigala — University of Messina, Italy
Sarah Pike — University of Birmingham, United Kingdom
Sarish Rehman — McGill University, Canada
Srabanti Ghosh — Central Glass and Ceramic Research Institute (CSIR), India
Sudipta Roy — University of Strathclyde, United Kingdom
Vânia André — University of Lisbon, Portugal
Viktorya Aviyente — Boğaziçi University, Türkiye
Weiwei Han — Jilin University, China

Citation

Papini, A. M. M., Liao, C., Calvano, C. D., Iacopino, D., Crans, D. C., Tuncel, D., Sabuzi, F., Toma, F. M., Oksdath-Mansilla, G., Gryn'ova, G., Lofrano, G., Ahmed, H. A., Wen, H., Zhu, H., Fahim, I., Shen, J., Costa, J. C., Mohanty, J., Martinez, K., Massai, L., Nagle, L. C., Caporaso, L., Martins, L. M., Manzoli, M., Brindisi, M., Arno, M. C., Erard, M., Jaffrezic-Renault, N. J., Giuffrè, O., Sen, P., Sun, Q., Bienstock, R. J., Verma, R., Rani, R., Cigala, R. M., Pike, S., Rehman, S., Ghosh, S., Roy, S., André, V., Aviyente, V., Han, W., eds. (2023). *Women in chemistry 2022*. Lausanne: Frontiers Media SA. doi: 10.3389/978-2-8325-3524-0

Table of contents

07 Editorial: Women in chemistry 2022
Irene S. Fahim, Vânia André, Jyotirmayee Mohanty, Rosalia Maria Cigala, Srabanti Ghosh, Luísa M. D. R. S. Martins, Weiwei Han, Anna Maria Papini, Joana Costa, Maela Manzoli, Ottavia Giuffrè, Reshma Rani, Sarish Rehman, Debbie C. Crans, Gabriela Oksdath-Mansilla and Federica Sabuzi

13 Solvent-Induced Selectivity of Isoprene From Bio-Derived Prenol
Jotheeswari Kothandaraman, Lelia Cosimbescu and Marie S. Swita

23 Methylene Blue as a Photo-Redox Catalyst: The Development Synthesis of Tetrahydrobenzo[*b*]pyran Scaffolds via a Single-Electron Transfer/Energy Transfer
Farzaneh Mohamadpour

33 Determination of trace levels of organic fining agents in wines: Latest and relevant findings
David Bongiorno, Giuseppe Avellone, Anna Napoli, Fabio Mazzotti, Daniela Piazzese, Valentina Censi and Serena Indelicato

40 Fatty Acids/Tetraphenylethylene Conjugates: Hybrid AIEgens for the Preparation of Peptide-Based Supramolecular Gels
Elisa Impresari, Alberto Bossi, Edoardo Mario Lumina, Marco Aldo Ortenzi, Josine Marie Kothuis, Graziella Cappelletti, Daniela Maggioni, Michael S. Christodoulou, Raffaella Bucci and Sara Pellegrino

54 Toward practical issues: Identification and mitigation of the impurity effect in glyme solvents on the reversibility of Mg plating/stripping in Mg batteries
Zhenzhen Yang, Mengxi Yang, Nathan T. Hahn, Justin Connell, Ira Bloom, Chen Liao, Brian J. Ingram and Lynn Trahey

68 Thioester deprotection using a biomimetic NCL approach
Valentina Villamil, Cecilia Saiz and Graciela Mahler

80 Structure-activity assessment of flavonoids as modulators of copper transport
Vanessa J. Lee and Marie C. Heffern

95 Overcoming the rise in local deposit resistance during electrophoretic deposition *via* suspension replenishing
Prabal Tiwari, Noah D. Ferson, David P. Arnold and Jennifer S. Andrew

106 A holistic carrier-bound immobilization approach for unspecific peroxygenase
Piera De Santis, Noémi Petrovai, Lars-Erik Meyer, Markus Hobisch and Selin Kara

116 Spectral denoising based on Hilbert–Huang transform combined with F-test
Xihui Bian, Mengxuan Ling, Yuanyuan Chu, Peng Liu and Xiaoyao Tan

125 Electrodeposited Fe on Cu foam as advanced fenton reagent for catalytic mineralization of methyl orange
Modestas Vainoris, Aliona Nicolenco, Natalia Tsyntsaru, Elizabeth Podlaha-Murphy, Francisco Alcaide and Henrikas Cesiulis

135 Urea-based anticancer agents. Exploring 100-years of research with an eye to the future
Roberta Listro, Giacomo Rossino, Federica Piaggi, Falilat Folasade Sonekan, Daniela Rossi, Pasquale Linciano and Simona Collina

163 G-quadruplexes formation within the promoter of TEAD4 oncogene and their interaction with Vimentin
Marta Cozzaglio, Silvia Ceschi, Elisabetta Groaz, Mattia Sturlese and Claudia Sissi

174 Triggering cell death in cancers using self-illuminating nanocomposites
Tijana Rajh, Tamara Koritarov, Ben Blaiszik, Syeda Fatima Z. Rizvi, Vani Konda and Marc Bissonnette

190 Current strategies for ligand bioconjugation to poly(acrylamide) gels for 2D cell culture: Balancing chemo-selectivity, biofunctionality, and user-friendliness
Alexis Wolfel, Minye Jin and Julieta I. Paez

199 Bioplastics: A new analytical challenge
Valentina Censi, Filippo Saiano, David Bongiorno, Serena Indelicato, Anna Napoli and Daniela Piazzese

207 Property-governed performance of platinum-modified titania photocatalysts
Kunlei Wang and Ewa Kowalska

223 A macrocyclic molecule with multiple antioxidative activities protects the lens from oxidative damage
Jinmin Zhang, Yu Yu, Magy A. Mekhail, Hongli Wu and Kayla N. Green

236 Supramolecular association studied by Fluorescence correlation spectroscopy
Mercedes Novo and Wajih Al-Soufi

243 Identification and characterization of alternative sites and molecular probes for SARS-CoV-2 target proteins
Suhasini M. Iyengar, Kelly K. Barnsley, Hoang Yen Vu, Ian Jef A. Bongalonta, Alyssa S. Herrod, Jasmine A. Scott and Mary Jo Ondrechen

258 Conformational switch and multiple supramolecular structures of a newly identified self-assembling protein-mimetic peptide from *Pseudomonas aeruginosa* YeaZ protein
Elettra Fasola, Giulia Alboreggia, Stefano Pieraccini, Francesco Oliva, Fatima Ezzahra Agharbaoui, Michela Bollati, Giovanni Bertoni, Sandro Recchia, Marcello Marelli, Umberto Piarulli, Sara Pellegrino and Silvia Gazzola

271 Rational design of potent ultrashort antimicrobial peptides with programmable assembly into nanostructured hydrogels
Priscila Cardoso, Samuel Appiah Danso, Andrew Hung, Chaitali Dekiwadia, Nimish Pradhan, Jamie Strachan, Brody McDonald, Kate Firipis, Jacinta F. White, Arturo Aburto-Medina, Charlotte E. Conn and Céline Valéry

288 Mining the Protein Data Bank to inspire fragment library design
Julia Revillo Imbernon, Luca Chiesa and Esther Kellenberger

299 Biostimulants derived from organic urban wastes and biomasses: An innovative approach
Alessia Giordana, Mery Malandrino, Alfonso Zambon, Gigliola Lusvardi, Lorenza Operti and Giuseppina Cerrato

308 Promising anticancer agents based on 8-hydroxyquinoline hydrazone copper(II) complexes
Nádia Ribeiro, Ipek Bulut, Baris Sergi, Vivien Pósa, Gabriella Spengler, Giuseppe Sciortino, Vânia André, Liliana P. Ferreira, Tarita Biver, Valeria Ugone, Eugenio Garribba, João Costa-Pessoa, Éva A. Enyedy, Ceyda Acilan and Isabel Correia

325 Atomic scale insight into the decomposition of nanocrystalline zinc hydroxynitrate toward ZnO using Mn^{2+} paramagnetic probes
Ioana D. Vlaicu, Mariana Stefan, Cristian Radu, Daniela C. Culita, Dana Radu and Daniela Ghica

335 Population analysis and the effects of Gaussian basis set quality and quantum mechanical approach: main group through heavy element species
Sasha C. North, Kameron R. Jorgensen, Jason Pricetolstoy and Angela K. Wilson

frontiers | Frontiers in Chemistry

TYPE Editorial
PUBLISHED 06 October 2023
DOI 10.3389/fchem.2023.1230005

Check for updates

OPEN ACCESS

EDITED AND REVIEWED BY
Steve Suib,
University of Connecticut, United States

*CORRESPONDENCE
Debbie C. Crans,
debbie.crans@colostate.edu

RECEIVED 27 May 2023
ACCEPTED 27 September 2023
PUBLISHED 06 October 2023

CITATION
Fahim IS, André V, Mohanty J, Cigala RM, Ghosh S, Martins LMDRS, Han W, Papini AM, Costa J, Manzoli M, Giuffrè O, Rani R, Rehman S, Crans DC, Oksdath-Mansilla G and Sabuzi F (2023), Editorial: Women in chemistry 2022. *Front. Chem.* 11:1230005. doi: 10.3389/fchem.2023.1230005

COPYRIGHT
© 2023 Fahim, André, Mohanty, Cigala, Ghosh, Martins, Han, Papini, Costa, Manzoli, Giuffrè, Rani, Rehman, Crans, Oksdath-Mansilla and Sabuzi. This is an open-access article distributed under the terms of the Creative Commons Attribution License (CC BY). The use, distribution or reproduction in other forums is permitted, provided the original author(s) and the copyright owner(s) are credited and that the original publication in this journal is cited, in accordance with accepted academic practice. No use, distribution or reproduction is permitted which does not comply with these terms.

Editorial: Women in chemistry 2022

Irene S. Fahim[1], Vânia André[2,3], Jyotirmayee Mohanty[4,5], Rosalia Maria Cigala[6], Srabanti Ghosh[7], Luísa M. D. R. S. Martins[8], Weiwei Han[9], Anna Maria Papini[10], Joana Costa[11], Maela Manzoli[12], Ottavia Giuffrè[6], Reshma Rani[13], Sarish Rehman[14], Debbie C. Crans[15]*, Gabriela Oksdath-Mansilla[16] and Federica Sabuzi[17]

[1]Industrial Engineering Program, Director Smart Engineering Systems Research Center, Nile University, Giza, Egypt, [2]Centro de Química Estrutural, Institute of Molecular Sciences, Instituto Superior Técnico, Universidade de Lisboa, Lisbon, Portugal, [3]Associação Do Instituto Superior Técnico para a Investigação e Desenvolvimento, Lisbon, Portugal, [4]Bhabha Atomic Research Centre, Trombay, India, [5]Homi Bhabha National Institute, Training School Complex, Mumbai, India, [6]Department of Chemical, Biological, Pharmaceutical and Environmental Sciences, University of Messina, Messina, Italy, [7]Energy Materials and Devices Division, CSIR—Central Glass and Ceramic Research Institute, Kolkata, India, [8]Centro de Química Estrutural, Institute of Molecular Sciences, Departamento de Engenharia Química, Instituto Superior Técnico, Universidade de Lisboa, Lisbon, Portugal, [9]Key Laboratory for Molecular Enzymology and Engineering of Ministry of Education, School of Life Sciences, Jilin University, Changchun, China, [10]Interdepartmental Research Unit of Peptide and Protein Chemistry and Biology, Department of Chemistry "Ugo Schiff", University of Florence, Sesto Fiorentino, Italy, [11]Centre for Functional Ecology, Associate Laboratory TERRA, Department of Life Sciences, University of Coimbra, Coimbra, Portugal, [12]Department of Drug Science and Technology and NIS Centre, University of Turin, Turin, Italy, [13]Drug Discovery Chemistry, Jubilant Biosys, Noida, Uttar Pradesh, India, [14]Department of Chemistry, McGill University, Montreal, QC, Canada, [15]Department of Chemistry, Colorado State University, Fort Collins, CO, United States, [16]Instituto de Investigaciones en Físico-Química de Córdoba (INFIQC-CONICET), Departamento de Química Orgánica, Facultad de Ciencias Químicas, Universidad Nacional de Córdoba, Ciudad Universitaria, Córdoba, Argentina, [17]Department of Chemical Science and Technologies University of Rome Tor Vergata, Roma, Italy

KEYWORDS

bioplastics, photocatalyst, waste valorization, oxidative stress, anticancer agents, antimicrobial peptide, luminescent material, hydrogel

Editorial on the Research Topic
Women in chemistry 2022

Introduction

A wide plethora of research exists on women in STEM education, but research by female chemists in educational and employment settings is scarce, especially in the Middle East and North Africa region. Most current industries use computer-driven machinery, and rising levels of automation and automated control systems that are driven by machines have altered shop floor procedures. The necessary qualifications and skills for chemistry jobs have changed as a result.

Chemistry education in Egypt is advancing. At least 15 STEM high schools operated by the Education Ministry have been established since 2011. In 2017, 43% of Egypt's university STEM students were women which is higher than the percentage in the UK and all over the

globe. The percentage increased to reach almost 47% in 2018/2019 as was reported in the Higher education bulletin from CAPMAS. The percentage of female graduates by field is shown in the 2021 UNESCO scientific report using data from 2018: agriculture 49.4%, engineering 20.9%, health & welfare 56%, natural sciences 64.2%, and ICT 36.8%. According to UNESCO data, in 2018 only 46% of Egypt's total number of scientific researchers were women. This percentage exceeds the average percentage of female researchers in the Arab World which accounts for around 43% and that of EU which accounts for 34%.

Women must engage in all fields in order for societies to advance and stay up with the times. However, in some fields, such as the male-dominated field of Mechanical and Electrical Engineering, there is very little female representation, so we are striving to raise awareness among youth in society.

This editorial plays a small part in this by documenting women's work in chemistry with all of its qualitative ramifications, highlighting successful research stories, and focusing on advancing and sustaining the presence in public and private sector institutions to emphasize the significance of women working in this profession and empowering them in the field of Chemistry.

Diverse international representation of researchers have contributed to this Research Topic in the 2022 edition and all the manuscripts were published after a thorough peer review process. The following is a summary of the areas and contributions in each of these manuscripts organized in terms of broad research topics.

Analytical chemistry

This section includes 2 articles involving some areas of Analytical Chemistry, as bioplastic analysis and food products. Censi et al. reported on bioplastics, defined as materials obtained from biomass sources and recycled food waste. They can be divided into biodegradable, bio-based, or both. This minireview described the different methods for bioplastic qualitative analysis, such as fluorescence, Nuclear Magnetic Resonance (NMR), Fourier-Transform Infrared Spectroscopy (FTIR), UV-VIS spectrophotometry, Differential Scanning Calorimetry (DSC), Thermogravimetric Analysis (TGA) and for bioplastic quantitative analysis, such as Gas Chromatography (GC), High-Performance Liquid Chromatography (HPLC), TGA associated with Mass Spectrometry (TGA-MS). The processes of biopolymer degradation were also examined considering the advantages and disadvantages of each method, and their potential environmental impact.

The determination of trace levels of organic fining agents in wines was reported by Bongiorno et al. Fining agents were commonly added to wines to reduce or remove some undesirable compounds, such as proteins, phenols, and tannins. The residues of fining agents should not be present in the final product, any trace residues must be quantified using detection methods. Among them there are immunochemical assays such as Enzyme-Linked Immunosorbent Assay (ELISA), for the detection of exogenous protein residues; Mass Spectrometry (MS) based methods for the determination of contaminants, antioxidants, polymers, surfactants, and proteins; biosensors for the detection of food allergens as lysozyme, ovalbumin, caseins, lactoglobulin.

Photocatalysis and photochemistry

Research advances in photocatalysis towards sustainable technology for converting solar energy into fuels, mainly through the solar-driven conversion of water and CO_2 into fuels and chemicals.Many important photocatalytic reactions, i.e., Water splitting, hydrogen evolution, oxygen reduction, CO_2 reduction, and organic reaction, have been explored. Mainly the photocatalyst has been considered a significant player, and a wide range of photocatalyst materials, from oxides, perovskites, (oxy) halides, organic semiconductors (graphitic carbon nitrides, conjugated polymers, porous polymers, covalent organic framework, etc.), porous materials, and 2D materials for photocatalytic fuel production. Traditional metal oxides are widely utilized photocatalysts but are limited with poor efficiency and absorb light in the short wavelength range. In recent years, significant progress has been achieved in improving the performance of oxide semiconductors by increasing the exposed active areas. A series of new visible light active photocatalysts such as TiO_2, $BiVO_4$, WO_3, Fe_2O_3, Cu_2O, spinel oxides, perovskites, etc.,.have been developed through the integration of binary or ternary structured photocatalyst loaded with co-catalysts which lower photoexcited charge carriers recombination and achieve high catalytic efficiency and photo-stability. The photocatalytic performance is essentially dependent on the electronic structure of photocatalysts, and the conversion efficiency could be enhanced via rational catalyst design, such as introducing vacancies and constructing a heterointerface. In spite of significant progress in materials development, the current status of the photocatalysts is limited to practical applications from laboratory-scale to industrial-scale. Moreover, various photoreactor systems have been developed for low-cost solar fuel production, which is promising for realizing the commercialization of such technologies. This Research Topic features one review and one original research paper on this Research Topic.

The first article focuses on the synthesis of Catalyst: The Development Synthesis of Tetrahydrobenzo [b]pyran Scaffolds via a Single-Electron Transfer/Energy Transfer Farzaneh Mohamadpour. The authors report on methylene blue (MB+)-derived photo-excited state functions was employed in an aqueous solution as single-electron transfer (SET) and energy transfer catalysts. The formation of malononitrile, and dimedone, a radical tandem Knoevenagel–Michael cyclocondensation reaction of tetrahydrobenzo [b] pyran scaffolds, were developed. A gram-scale cyclization is possible, implying that the technology may be applied in industries.

The review by Wang and Kowalska is focused on the use Property-governed performance of platinum-modified titania photocatalysts. The preparation of platinum deposited on the surface of titania has been shown to improve photocatalytic performance both under UV and visible light. Interestingly, the property governed activity for Pt/TiO_2 photocatalysts such as platinum content, platinum properties (size, aggregation/uniform

distribution, oxidation state), titania properties (size, crystallinity, specific surface area, polymorphic form, defect density, morphology, surface characteristics) and the contact between platinum and titania have been considered an highlighted.

Chemical biology

In this study, Lee and Heffern investigated the interface between the biological activity of flavonoids and their interaction with copper ions as potential therapeutic targets. Flavonoids are small polyphenolic molecules that are widely distributed in plant products, are known to have beneficial health effects and exhibit complex behaviour in biological systems. Copper contributes to the proper functioning of biological systems and its deregulation is associated with several metabolic diseases. Spectroscopic techniques were used to study the binding of flavonoids to Cu(II) and their radical scavenging activities. The authors identified important structural groups involved in this interaction related to ring substitution. The biological effects of flavonoids on copper transport were also evaluated and shown to be influenced by their hydrophobicity. In conclusion, relevant aspects of the influence of flavonoids on copper transport have been elucidated, contributing to new dietary recommendations and potential therapeutic development.

Zhang et al. showed that the potential drug molecule $^{OH}Py_2N_2$ is the first example of a low molecular weight, macrocyclic small molecule capable of activating cellular mechanisms of protection against oxidative stress. The results reported clearly show that there are multiple pathways that $^{OH}Py_2N_2$ may impact to promote natural mechanisms within cells that protect against chronic oxidative stress in the eye. The work is a paradigmatic example of the contribution of chemical biology, combining the organic and inorganic design of small molecules with studies aimed at elucidating their potential to impact eye disease. Only such a multidisciplinary approach will, soon, be able to characterise the structural components of the $^{OH}Py_2N_2$ molecule responsible for the activation of these pathways and hopefully lead to the identification of non-surgical therapeutic options whose benefits outweigh the risks of cataract surgery complications that may still occur, especially in patients of advanced age.

Electrochemistry

This Research Topic features two original research papers on the Electrochemistry section. The first one is entitled "Toward practical Research Topic: Identification and mitigation of the impurity effect in glyme solvents on the reversibility of Mg plating/stripping in Mg batteries," which addresses the challenges associated with the reversible electrochemical plating and stripping of magnesium in magnesium batteries. The authors focus on ether glyme solutions containing the MgTFSI2 salt, which are commonly used electrolytes for achieving reversible behavior of Mg electrodes. The study systematically identifies impurities in these systems and investigates their effects on the Mg deposition-dissolution processes. This study evaluates various mitigation methods to eliminate impurities and discusses their beneficial effects on improved reactivity. Ultimately, the authors propose a conditioning protocol that can be easily implemented and safer for practical applications of MgTFSI2/glyme electrolytes containing impurities. In this article, the authors emphasize the significance of glymes as solvents and MgTFSI2 as a promising salt for Mg batteries, which makes a significant contribution to the field of Mg batteries by addressing the impurity effect in glyme solvents and providing practical strategies for their mitigation. The systematic identification of impurities, evaluation of mitigation methods, and proposal of a conditioning protocol demonstrate the author's thorough research and understanding of the subject matter. This study's findings can potentially facilitate the development of practical and efficient electrolyte systems for Mg batteries.

The second paper submitted to this section is entitled: Electrodeposited Fe on Cu foam as advanced Fenton reagent for catalytic mineralization of methyl orange," which addresses the significant Research Topic of textile dye pollution in water and proposes an innovative solution using Fe/Cu catalysts in heterogeneous Fenton's reaction. This study uses environmentally friendly electrodeposition techniques to explore the degradation of methyl orange, a model azo dye, in aqueous solutions. In this work, the authors have discussed the advantages of bimetallic Fenton reagents, specifically Fe/Cu catalysts, regarding their catalytic efficiency and stability. They also explain how immobilizing iron species onto porous templates like metal foam can enhance the catalyst's activity. The use of metal foam as a substrate is justified based on its durability, ductility, and highly effective surface area. This study offers valuable insights into using Fe/Cu catalysts on copper foam as an effective solution for the degradation of textile dyes in wastewater. The research findings, experimental approach, and the environmentally friendly nature of the proposed method make it a significant contribution to the field of wastewater treatment.

Green and sustainable chemistry

Gender inequality, the fifth sustainable development goal outlined by the United Nations is considered as a significant hindrance to sustainable development and without fully addressing it, reaching the other goals will be much more difficult. Within this context, women play a pivotal role in contributing to improve economic, social, and environmental Research Topic crucial for achieving a sustainable future. Green chemistry is a continuously evolving frontier, which embraces the development of chemical processes and environment-friendly products alternative to hazardous substances to prevent pollution. The extensive use of crude oil raised the need for more sustainable feedstock for energy and materials, which has to meet the growing demand for goods. The design of sustainable chemical processes reduces waste and demand on diminishing resources. In this frame, waste lignocellulosic biomass represents a sustainable alternative feedstock to fossil resources for fuels and chemicals. Indeed this frame, it is possible to obtain innovative materials starting from wastes, for example, humic and fulvic acids formulate nanohybrids with silica obtained from rice husks can be used for agricultural applications and circular processes involving urban waste valorization (Giordana et al.). Another possibility is to employ

added value molecules from renewable resources to optimize the production of chemicals usually obtained from fossil resources: isoprene can be prepared under mild conditions by selective catalytic conversion of prenol, which is an allylic alcohol that can be synthesised from renewable sources using metabolically engineered *Escherichia coli* (Kothandaraman et al.). Moreover, through the practice of green and sustainable chemistry, processes that use smaller amounts of energy can be conceived. Practical Mg-ion batteries require highly reversible Mg deposition and large current density, therefore both identification and removal of impurity in glyme solvents are crucial to achieve reversible Mg electrochemistry. Yang et al. were able to reach this goal, employing a facile conditioning protocol to further improve the performance of MgTFSI2/Gx electrolytes.

Inorganic chemistry

Among the most relevant and active Inorganic Chemistry research areas, the search for biological activity of coordination compounds is a mature, yet constantly growing field. In particular, there is an urgent need for the development of new classes of compounds due to acquired resistance or limitations of the currently approved drugs against cancer.

In this Research Topic, we highlight the ability of coordination compounds such as hydrazone copper (II) complexes to behave as antiproliferative agents. Correia and co-workers managed to synthesise new copper (II) complexes bearing benzohydrazide-hydrazone derivatives of 8-hydroxy-2-quinolinecarbaldehyde and evaluate their behaviour in malignant melanoma (A-375) and lung (A-549) cancer cells. All the new compounds appeared to be potent on cancer cells, albeit with varying efficiencies in cell lines of different origins. Globally this group of complexes is more active against the melanoma cells (A-375), than in lung (A-549) cancer cells, but in both cases the IC_{50} values are in the low μM range.

Medicinal and pharmaceutical chemistry

The primary goal of a medicinal chemist is to discover hit compounds and then hit to lead optimization with ideal selectivity towards the targets such as enzymes, proteins, receptors, DNA, and RNA which play a crucial role in disease pathways. Based on the structure and function of a suitable target, hit molecules can be designed with chosen potency, selectivity, and optimal ADME/T parameters. To date, a wide class of small molecules including natural products/their metabolites and synthetic molecules have been designed or discovered which play a crucial role in various therapeutic areas.

Natural polyphenolic small molecules such as flavonoids possess antioxidant as well as prooxidant properties. Lee et al. reported that flavonoids might affect copper transport and offer new therapeutic development. Listro et al. reviewed urea-based molecules as anticancer agents and highlighted the relevance of the urea moiety in the medicinal chemistry scenario of anticancer drugs. Ribeiro et al. synthesized Cu-complexes with hydroxyquinoline hydrazones and tested them for anticancer activities in melanoma and lung adenocarcinoma cell lines. These Cu-complexes exhibit promising anticancer activities in the low micromolar range and induce oxidative and DNA damage. Small molecules have the potential to interact with nucleic acid secondary structures such as G-quadruplexes (G4s) offering a new direction in the development of therapeutics. Besides small molecules, macrocyclic molecule, and protein-mimetic peptides (PMPs) are reported to display significant pharmacological properties that have potential in therapeutics development. Despite of Research Topic of large compounds, still there is a large chemical gap to discover new small chemical molecules with improved potency, efficacy and selectivity, and target identification. Due to the highly heterogeneous nature of various disease phenotypes and the complex mechanism of action of small molecules in biological systems, the combination approach of potential clinical candidates with existing drugs might be a suitable therapeutic application.

Nanoscience

The aim of the Research Topic: Women in Chemistry 2022 is to highlight the significant contributions from women researchers. The study by Vlaicu et al. of the Research Topic "*Atomic scale insight into the decomposition of nanocrystalline zinc hydroxynitrate toward ZnO using Mn^{2+} paramagnetic probes*" guides to the right selection of the most appropriate zinc hydroxynitrate synthesis method. Promising compound that exhibits a range of particular properties: anion-exchange, intercalation capacity and biocompatibility, becoming useful for a wide variety of applications in fields from nanotechnology to healthcare and agriculture. The study represents a model for the right choice of synthesis for specific applications and in the development of new green, cost-effective synthesis routes for Mn^{2+} doped nano-ZnO.

Another important study collected on this Research Topic by Cardoso et al. is represented by "*Rational design of potent ultrashort antimicrobial peptides with programmable assembly into nanostructured hydrogels*". The always important question of the microbial resistance to common antibiotics is threatening to cause the next pandemic crisis and in this special section, the authors reported a study on the bi-functional rational design of Fmoc-peptides as both antimicrobial and hydrogelator substances for the fast, adaptable, and cost-efficient antimicrobial peptide design with programmable physicochemical properties.

The last contribution to the Nanoscience section of this Research Topic is represented by the original research by Tiwari et al., entitled "*Overcoming the rise in local deposit resistance during electrophoretic deposition via suspension replenishing*". A promising method is represented by Electrophoretic deposition for the scalable assembly of colloidally stable nanomaterials into thick films and arrays. The study highlights an important effect, namely, that the growth of the ion-depletion region plays the most significant role in the increase of the deposit resistance, demonstrating also a method to maintain constant deposit resistance in Electrophoretic deposition by periodic replenishing of suspension, improving its scalability.

Organic chemistry

Following the celebration of International Women's Day 2022, the UNESCO International Day of Women and Girls in Science,

Frontiers in Chemistry is proud to offer this platform to promote the work of women scientists, across all branches of Organic Chemistry.

At present, less than 30% of researchers worldwide are women. Long-standing biases and gender stereotypes are discouraging girls and women away from science-related fields, and STEM research in particular. Organic Chemistry is no exception to this. Science and gender equality are, however, essential to ensure sustainable development as highlighted by UNESCO. In order to change traditional mindsets, gender equality must be promoted, stereotypes defeated, and girls and women should be encouraged to pursue STEM careers.

This Research Topic has the aim of bringing into the spotlight the contributions of female researchers in all areas of Organic Chemistry. The works presented here include applications in synthesis, and modification of immobilization techniques and hydrogels and demonstrate the diversity of research performed in Organic Chemistry.

The work by Villamil et al. describes advances in thiol-thioester chemistry. The team explored the use of 2-aminothiols for the deprotection of thiols bearing an acyl group. The best results were obtained using cysteamine or L-cysteine in an aqueous buffer pH 8 at room temperature for 30 min. This process demonstrates that this deprotection can take place under very mild conditions and can yield inhibitors of a wide-range of metallo-β-Lactamases.

The work by Santis et al. describes the immobilization of an enzyme that catalyzes the regio- and stereospecific hydroxylation of non-activated C–H bonds at the only expense of H_2O_2. The team investigated both covalent and ionic immobilization and metal affinity binding and was found to lead to high immobilization yields and result in significantly greater stability for a peroxygenase.

The review by Wolfel et al. discusses current strategies for ligand bioconjugation to poly (acrylamide) gels with respect to chemo-selectivity and site-specificity of attachment as well as preservation of ligand's functionality. These biomaterials have many advantages such as convenient synthesis, desirable mechanical properties within physiological range of native soft tissues, the potential to be functionalized with ligands to support the culture of living cells, and their optical transparency making them compatible with microscopy investigations. The review focuses on the application of materials for cell culture studies including specific functions of these hydrogels, and how user-friendly they are compared to the chemoselectivity the hydrogels exhibit.

Supramolecular chemistry

Supramolecular chemistry enables the design and synthesis of multiple compounds and functional materials, leading to advancements in interdisciplinary fields such as chemistry, physics, materials science, biology, drug delivery, and nanotechnology. The papers published in this section are an example of the multidisciplinarity of the field, focusing on the dynamics and structural characterization of supramolecular complexes, peptide-based aggregates and fluorescent gels.

Novo and Al-Soufi described the evaluation of thermodynamic parameters, dynamics of supramolecular association and structural information of supramolecular complexes by fluorescence correlation spectroscopy (FCS). FCS is very useful for studying the dynamics in supramolecular host-guest complexes, when the relaxation time of the complex formation is faster than the observation time (fast-exchange dynamics), in opposition to the slow-exchange regime, which is vital for the understanding of supramolecular complexes and their function.

Fasola et al. identified a protein mimetic peptide (PMP) from *Pseudomonas aeruginosa* YeaZ protein. This PMP has the ability to switch to different secondary structural elements (α-helix, β-sheet), and to form different aggregate types (helical nanofibers, 2D-sheets and hydrogel) by changing external conditions such as concentration, hydrophobicity and temperature. PMP is a promising candidate for the generation of improved biocompatible and responsive materials from a single building block.

Impresari et al. developed different AIEgen-based luminescent hybrid supramolecular structures comprising of tetraphenylethylene scaffold and fatty acids of different chain lengths in water. The presence of longer alkyl chains facilitates the formation of stable emissive aggregates. N-terminus capping agents were used in the development of cell-viable peptides that self-assembled into luminescent fibrillary materials, which were able to form supramolecular gels in aqueous solution. Considering the widespread importance of luminescent materials, these fluorescent gels can be used as suitable substrates for *in vitro* models and bio-imaging studies.

This section further aims to encourage more women to pursue careers in this field.

Theoretical and computational chemistry

In the continually evolving landscape of scientific research, it's undeniable that women have made remarkable strides, particularly in the field of Chemistry. Beyond their invaluable contributions, women continue to challenge the *status quo*, driving innovation, and inspiring future generations of researchers. We recognize and salute these brilliant minds, focusing on four recent theoretical and computational chemistry contributions span across diverse Research Topic, fragment library design, spectral denoising, SARS-CoV-2 target proteins study and encapsulating population analysis.

Our journey begins with the work of Imbernon et al., who effectively harnessed the wealth of data in the Protein Data Bank to inspire fragment library design for drug discovery. The team identified fragments with multiple binding sites and modes, unravelling the potential of these multi-targeting fragments to provide frequent hits in screening, thus redefining modern medicinal chemistry.

Switching gears, Iyengar et al. took a profound leap into the fight against COVID-19. Using their expertise in computational chemistry, the team investigated alternative target sites for molecular probe design on three SARS-CoV-2 proteins, uncovering key interactions that contribute to the viral proteins' function. These findings have the potential to revolutionize our approach to battling such an unpredictable and lethal virus.

Continuing on a biomedical front, Bian et al. and her colleagues unravel the usage of spectral denoising in improving data analysis.

The team developed a novel spectral denoising method utilizing the Hilbert–Huang transform and F-test, resulting in superior results to conventional methods. This advancement is critical in modern science, with potential applications spanning from chemical investigations to medical diagnostics.

Lastly, we delve into the field of population analysis with the contribution from North et al. In their notable work, they examined the impact of basis sets and quantum methodology choices on population analysis. The results shed light on the significant variations in atomic charges based on adopted approaches, thereby highlighting the importance of careful method selection in population analysis studies.

Collectively, these works underscore the diversity of applications for computational and theoretical chemistry, from drug discovery and molecular probe design to enhanced data analysis methods.

In light of their achievements, we emphasize the growing importance and need for diversity in the scientific community. We hope that highlighting these contributions by women will inspire future generations of scientists, underscoring that gender should never be a barrier to innovation and discovery. As we move forward, let's continue to celebrate and encourage more women in Chemistry, the echoes of their impact reverberating within the scientific community and beyond.

Conclusion

We have included some highlights from various research activities in the field of chemistry. We anticipate that this will be a useful reference tool for students and researchers working in various areas of chemistry who are conducting chemical studies of novel systems with potential applications. This Research Topic discusses current and promising trends in chemical, biological, theoretical and computational chemistry for a sustainable and green future. The authors present contributions with original research articles, mini and full reviews, and papers on related Research Topics in this Research Topic. Electrochemical, inorganic and supermolecular chemistry are covered in the Research Topic. Researchers can refine their studies in the search by using the information provided here. Moreover, this outstanding Research Topic of manuscripts emphasises the ongoing and powerful role that nanoscience plays in our understanding of complex processes. The contributions made by the development and application of novel chemistry research tools are numerous. The work described in the manuscripts also demonstrates an acceleration in the translation of research diagnostics, and potential applications in chemistry. The reader is expected to enjoy and value the contributions of Women in Chemistry. We would like to thank all authors, reviewers, and Editorial Board members for their significant contributions to the implementation of this special Research Topic.

Author contributions

All authors listed have made a substantial, direct, and intellectual contribution to the work and approved it for publication.

Conflict of interest

The authors declare that the research was conducted in the absence of any commercial or financial relationships that could be construed as a potential conflict of interest.

Publisher's note

All claims expressed in this article are solely those of the authors and do not necessarily represent those of their affiliated organizations, or those of the publisher, the editors and the reviewers. Any product that may be evaluated in this article, or claim that may be made by its manufacturer, is not guaranteed or endorsed by the publisher.

frontiers | Frontiers in Chemistry

ORIGINAL RESEARCH
published: 17 May 2022
doi: 10.3389/fchem.2022.879129

Solvent-Induced Selectivity of Isoprene From Bio-Derived Prenol

Jotheeswari Kothandaraman[†], *Lelia Cosimbescu*[*†] *and Marie S. Swita*

Pacific Northwest National Laboratory, Richland, WA, United States

In this work we demonstrate the selective catalytic conversion of prenol, which is an allylic alcohol that can be prepared from renewable resources to isoprene. The catalyst is an inexpensive molybdenum complex (Molyvan L) designed and used as an additive for lubricants. Isoprene is generated under relatively mild reaction parameters at 130–150°C, for 2 h, under vapor pressure conditions that do not exceed 50 psi. Two cases were studied: one in which Molyvan L was dissolved in a base oil at 1% concentration (weight/weight) and then mixed with a solvent and prenol and the other in which neat Molyvan L was introduced in the reaction and the base oil was replaced with the solvent and prenol. We investigated the selectivity of the reaction using the following solvents in both cases: dodecane, dodecanol, isododecane, octane, blendstock for oxygenate blending (BOB3), a fuel surrogate, a polyalphaolefin (PAO4), and methoxy polyethylene glycol (methoxy PEG350). Although conversion of prenol was above 94% in all experiments, isoprene was formed with various degrees of efficiency alongside a prenol isomeric alcohol, diprenyl ether and mixed ether via intramolecular and intermolecular dehydration reactions. Dodecane appeared to have the highest level of selectivity initially in base oil so we studied the effect of various dodecane-like solvents on isoprene yield and product profile. Surprisingly, octane (similar to dodecane) and isododecane (branched alkane) generated insignificant amounts of byproducts, essentially providing the highly desired isoprene with a very high selectivity. Branching of the solvent does not appear to have an effect on selectivity. Another advantage of this catalyst is the low loadings required to effect the transformation; that is, 0.25% (weight/volume) in the cases using neat Molyvan L and 0.5% (weight/volume) in the cases using Molyvan L dissolved in the base oil. Provided that prenol can be produced in large scale from bioresources, this work would enable the sustainable production of isoprene, in good yield, and with very high selectivity.

Keywords: prenol, isoprene, selective catalysis, bio-derived, sustainability

OPEN ACCESS

Edited by:
Maela Manzoli,
University of Turin, Italy

Reviewed by:
Zhi Li,
ShanghaiTech University, China
Aida Luz Villa,
Universidad de Antioquia, Colombia

***Correspondence:**
Lelia Cosimbescu
lelia.cosimbescu@pnnl.gov

[†]These authors have contributed equally to this work and share first authorship

Specialty section:
This article was submitted to Green and Sustainable Chemistry, a section of the journal Frontiers in Chemistry

Received: *18 February 2022*
Accepted: *26 April 2022*
Published: *17 May 2022*

Citation:
Kothandaraman J, Cosimbescu L and Swita MS (2022) Solvent-Induced Selectivity of Isoprene From Bio-Derived Prenol. Front. Chem. 10:879129. doi: 10.3389/fchem.2022.879129

1 INTRODUCTION

Isoprene, an unsaturated hydrocarbon, is an important monomer used in the production of synthetic rubber (approximately 95% of isoprene produced is used for this purpose). It also is an important platform chemical used for a wide range of applications, such as fragrances, medicines, and pesticides. Currently, isoprene is mostly produced from fossil sources as a byproduct of the thermal cracking of oil or naphtha. About 800,000 metric tons are produced annually. With a strong industrial demand for isoprene, its sustainable production from raw materials derived from renewable sources is highly desired. (Ezinkwo et al., 2013).

Prenol (3-methyl-2-buten-1-ol) has been identified as an interesting and unusual oxygenated biofuel blendstock for use in spark ignition engines primarily because it exhibits a novel "octane

hyperboosting" effect when blended with gasoline mixtures (Monroe et al., 2019). Because of its unique positioning of olefinic and alcohol functional groups, when blended with gasoline the research octane number (RON) of the mixture exceeds the performance of the individual pure components. This is in contrast with the well-known synergistic blending of oxygenates into gasoline, in which the measured RON never surpasses the RON of best performing component. In addition to reducing NO_x and soot production during combustion, which is typical of most alcohol-based fuels, prenol has low water miscibility, good energy density, high octane sensitivity, and low Reid vapor pressure. With the current trend of decarbonizing the transportation sector, including fuels and bio-derived oxygenates blending into fuels, there is even a greater incentive to produce prenol from biorenewable resources. Currently prenol is produced industrially as an intermediate for the generation of citral using petroleum-derived chemicals via a two-step process that first involves reacting isobutene and formaldehyde to form isoprenol and then isomerization of the isoprenol to prenol. (Bonrath and Netscher, 2005; Parker et al., 2016). Prenol is not naturally abundant, however, because of its promising fuel performance, researchers have studied its synthesis from renewable sources using metabolically engineered *Escherichia coli*. (Chou and Keasling, 2012; Zheng et al., 2013; George et al., 2015; Gupta and Phulara, 2015; Liang et al., 2021). With recent developments in biosynthetic approaches, prenol production of more than 2 g/L has been demonstrated, thus showing its potential as a next generation biofuel. (Zheng et al., 2013; Clomburg et al., 2019).

Previously, while studying the reactivity of prenol in the presence of Molyvan L (a molybdenum additive used as a friction modifier), we identified the major products of the reaction: 2-methylbut-3-en-2-ol, ethers, and isoprene (2-methyl-1,3-butadiene) (Cosimbescu et al., 2022). These moieties were produced via isomerization of prenol, intermolecular and intramolecular dehydrations, respectively, albeit with no selectivity to any specific product. Producing isoprene from bio-derived prenol by selective intramolecular dehydration is an attractive alternative route to the conventional petroleum-derived process. Bioproduction of isoprene has been gaining much attention recently, (Yang et al., 2012; Wang et al., 2017; Li et al., 2018; Li et al., 2019; Janke et al., 2020), and inspired by the body of work, we wanted to leverage our early results with prenol/Molyvan L catalyst and explore the potential of producing isoprene by selective intramolecular dehydration of 2-methylbut-3-en-2-ol, a tertiary isomeric alcohol of prenol that forms *in situ* in presence of Molyvan L.

In this work, we investigated conditions for the selective catalytic production of isoprene from prenol using Molyvan L as an inexpensive homogenous catalyst. Previous work published by us and by other research teams has shown that the selective production of isoprene from prenol is challenging under relatively mild conditions (<150°C) and often results in a mixture of products, such as ethers, ketones, and isomers of prenol in the presence of both homogenous and heterogeneous catalysts (Marton et al., 1989; Bianchini et al., 2001; Todd and Bielawski, 2013; Cosimbescu et al., 2022). Notably, Taylor and Shenk reported selective production of isoprene from prenol isomeric alcohol under harsh conditions (300°C) (Taylor and Shenk, 2002). However, in their study, the alcohol was prepared in 50% yield by the reduction of its butyne precursor, 2-methylbut-3-yne-2-ol, with a large excess of copper zinc dust. Several other products also were formed, presumably making isolation of the alcohol difficult. In contrast, our process is not only energy efficient (occurring at a lower temperature, low catalyst loadings, short reaction times), but can use "green" prenol produced from biomass. We have identified that the solvent plays a key role in controlling the selectivity of the product distribution <150°C. Furthermore, the optimized reaction conditions that provide high selectivity also would enable the separation of isoprene from the reaction mixture via distillation, as the minor products formed have much higher boiling points. To the best of our knowledge, this work is the first report of selective, catalytic, and high yielding production of isoprene directly from prenol under relatively mild reaction conditions and short reaction times.

2 MATERIALS AND METHODS

2.1 Reagents

Prenol and isododecane (2,2,4,6,6-pentamethylheptane) were purchased from TCI America and used without further purification. Octane, methoxy PEG350 and dodecane were purchased from Aldrich and used as received. The blendstock for oxygenate blending (BOB3) was obtained from a commercial refiner and was used as received. BOB3 is a winter-blend, premium unadditized gasoline, with the lowest amount of butane among all available BOBs and therefore has the lowest vapor pressure. A detailed hydrocarbon analysis was conducted at Intertek Laboratory in accordance with ASTM D2699 to provide the BOB3 composition and carbon typing. The hydrocarbon group types in terms of total mass percent were as follows: paraffins—6.8225; isoparaffins—44.9437; olefins—8.5925; naphthenes—13.7524; aromatics—22.5572; c14+—0.7997; unknowns—2.5320. The fuel surrogate blend was prepared in house from the following components: isooctane (55%), heptane (15%), xylene (25%), 1-hexene (5%), and it is designed to mimic a gasoline fuel but with much fewer components. All components were reagent grade and purchased from Fisher.

Polyalphaolefin 4 (PAO4, provided by Exxon Mobil) was the base oil for Molyvan L additive/catalyst. PAO4 is a Group IV lubricant base stock with a kinematic viscosity around 4cSt at 100°C. Molyvan L [molybdenum di (2-ethylhexyl) phosphorodithioate] was obtained from Vanderbilt Chemicals LLC and was provided as a concentrated oil solution (75% w/w). We further diluted the received lubricant additive in PAO4 to obtain a 1% (w/w) solution. In the "neat" experiments, we used the molybdenum-based catalyst as received, in concentrated form.

2.2 Experimental Procedure

A 50 ml pressure vessel rated up to 1,000 psig from McMaster Carr was loaded with either: 5 ml prenol, 5 ml solvent (octane, dodecane isododecane, methoxy PEG 350, BOB3, fuel surrogate,

or PAO4) and 10 ml of 1% Molyvan solution in PAO4; or 5 ml prenol, 15 ml of solvent as defined above, and 55–60 mg neat Molyvan L as the Mo catalyst. The reaction mixtures were premixed in a 20 ml scintillation vial to ensure homogeneity and take an aliquot that served as a baseline for the reaction. As such, the initial concentration of prenol was kept the same in both configurations, at 25% (v/v). The internal temperature was monitored via a handheld Omega thermometer attached to a type K thermocouple. A pressure gauge (McMaster Carr - part number: 9767T21) was attached to the side of the reaction vessel to monitor vapor pressures, typically between 40–50 psig. An external Omega type K thermocouple, attached to an over-temperature controller offset at 250°C, was kept inside the vessel heating mantle to prevent overheating. The mixtures were stirred at a temperature ~150°C for 2 h, then chilled in ice as to prevent the loss of volatiles, particularly isoprene and placed in freezer.

2.3 Analysis

2.3.1 Gas Chromatography *via* Flame Ionization Detection

Original (fresh, 0 h) and heated samples (2 h) were analyzed via GC-FID to quantify used prenol and generate conversions, as well as qualitatively compare the magnitude of isoprene peak from each reaction condition. Samples were analyzed using an Agilent 7,890 gas chromatograph equipped with a flame ionizing detector. The column was a DB5-MS 30 m × 250 µm x 1.0 µm film thickness with a carrier gas of helium flowing at 2.0 ml/min. The oven temperature was initially held for 1.0 min at 40°C and then ramped up at 10°C/min to a final temperature of 325°C, where it was held for 10 min. The injection volume of each neat sample was 1 µl and the inlet was heated to 260°C. Each sample was integrated using Agilent Data Analysis software. A baseline drop was used for integration to determine each peak area of compounds of interest. Using the peak areas, specific samples were compared to their respective originals at the beginning of the experiment. Chromatograms from each sample set (before and after heating) were overlaid to qualitatively inspect for area differences indicative of chemical changes with heating. All GC-FID overlays can be found in the SI.

2.4 Spectral Characterization

NMR spectra were obtained using a Bruker Avance NEO or Varian 500 MHz NMR Spectrometer console scanned at 500 MHz (^{1}H). The chemical shifts are reported in delta (δ) units, parts per million (ppm) downfield from tetramethylsilane (TMS), Samples were prepared in deuterated chloroform containing dimethylterephthalate (DMTP) as an internal standard.

3 RESULTS AND DISCUSSION

A simple process set-up comprised of a 50 ml pressure vessel rated up to 1,000 psig was loaded with either 5 ml prenol, 5 ml solvent (octane, dodecane, isododecane, methoxy PEG350, BOB3, fuel surrogate, or PAO4) and 10 ml of 1% Molyvan L solution in PAO4 (data shown in **Supplementary Table S1**) or 5 ml prenol, 15 ml of solvent as defined above, and 55–60 mg neat Molyvan L as the molybdenum catalyst (data shown in **Supplementary Table S2**).

The reaction mixtures were premixed in a 20 ml scintillation vial to achieve homogeneity, and an aliquot of the mixture served as a baseline for the reaction. As such, the initial concentration of prenol was kept constant in both experiments, at 25% (volume/volume). Original ("fresh", unheated, 0 h) and heated (2 h) samples were analyzed *via* gas chromatography-flame ionization detection (GC-FID) to quantify the percent of prenol used and generate conversions and to qualitatively compare the magnitude of isoprene peak from each reaction condition. The reaction profile was similar to others previously run, with four major products identified via GC-FID (**Figure 1**). Other minor unidentified species also were present, totaling no more than 10% of the total products.

After the prescribed reaction time (2 h after reaching near 150°C), the reactor was chilled in ice to minimize the loss of the most volatile component, isoprene, and the mixture was transferred to a vial and then stored in a freezer until testing. The set-up has several metal hardware attachments (i.e., an inner temperature probe, a pressure gauge, and a rupture disk) of substantial volume where product(s) can condense and escape the final mixture, thus skewing the analytical results. The upper part of the set-up was not cooled, providing opportunities for product loss, particularly isoprene. The two configurations are referred to as 1% Molyvan L base oil solution and neat Molyvan L. These distinctively different conditions were implemented to probe for the highest conversion of prenol to products and for selectivity towards isoprene. Initial studies explored only lubricant containing systems and dodecane provided a promising result, that is why the study was continued in lubricant solvent-systems and expanded to systems without lubricant. The qualitative abundance data is shown in **Figure 2** and **Figure 4**.

The solvents screened are not typical organic solvents; rather, they are fuel-related solvents from which this research originated. As mentioned, it was discovered serendipitously that dodecane provided enhanced selectivity with a 1% Molyvan L base oil solution (**Figure 2**). While all solvent media tested provided near quantitative conversions of prenol, only few generated high amounts of isoprene. Dodecanol, which is slightly more polar than dodecane, was tested also, and although it yielded a substantial amount of isoprene, it also participated in dehydration reactions with itself and prenol and generated extra major byproducts aside from those shown in **Figure 2**. Therefore, the apparent enhanced selectivity for isoprene in this case is not real, as the graph ignores those byproducts only formed with dodecanol. Fuel surrogate and BOB3 generated large amounts of isoprene, as it qualitatively appears to be the largest product, but not selectively. We also investigated the methoxy PEG350 as a polar solvent, but we encountered challenges in assessing reaction efficiency towards isoprene formation because the solvent and products partition between the base oil and polar phases. A large amount of the isomeric alcohol was found in the

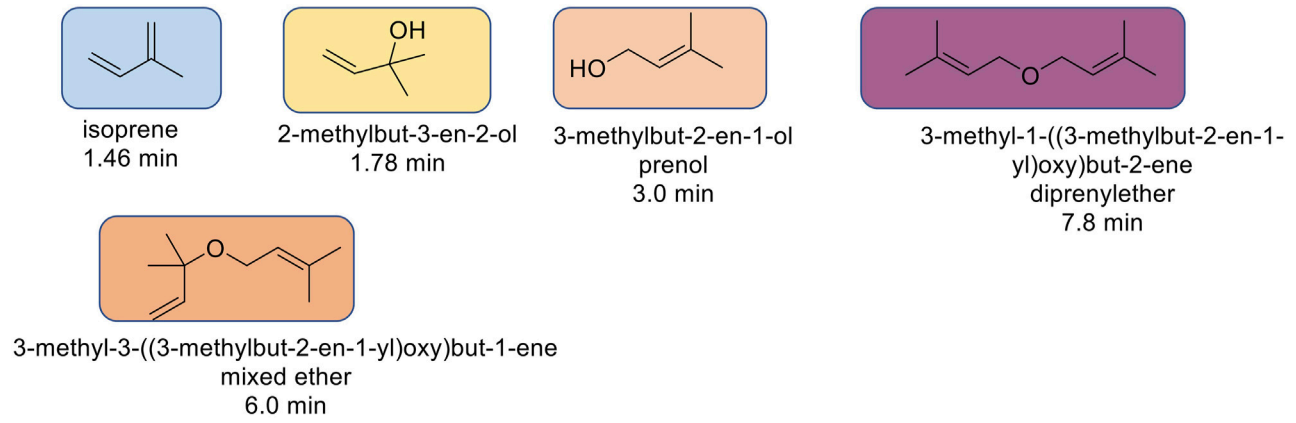


FIGURE 1 | Structures of major products and their corresponding GC-FID retention times.

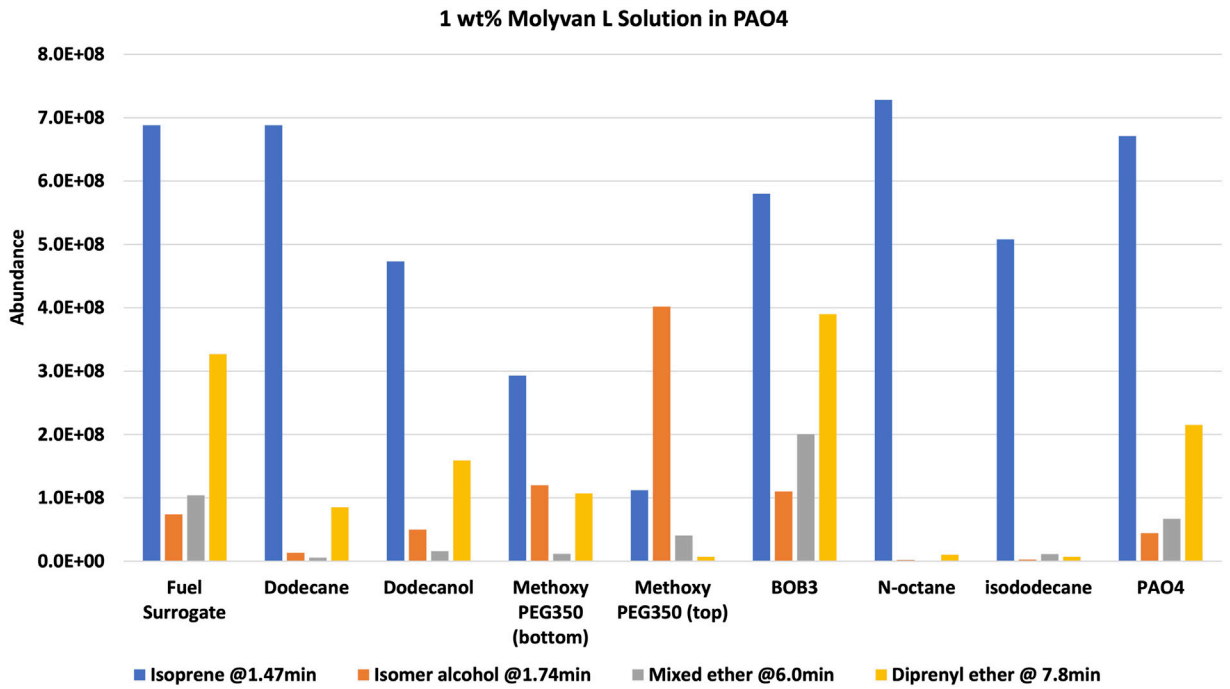


FIGURE 2 | ***1 wt% Molyvan L*** solution in PAO4. Reaction composition: 5 ml solvent, 5 ml prenol, 10 ml Molyvan L solution.

bottom layer (aqueous, polar), so this reaction also did not provide the desired selectivity. Encouraged by the enhanced selectivity of dodecane, other high boiling-point solvents (required to minimize the vapor pressure of the system) such as octane and isododecane were explored. We were surprised to discover that both solvents provided very high selectivity towards the desired product with minimal formation of side products. The GC-FID of octane is shown as an example in **Figure 3**.

Although isododecane is expensive and is not a realistic solvent for a prospective industrial process, we chose it to study the effect of branching on selectivity. Both linear and branched systems have exhibited similar selectivity, showing the reaction profile is independent of solvent branching. In one example, PAO4 (a branched solvent system) was used as the solvent as well as the molybdenum catalyst medium to study its selectivity (**Figure 2**). Notably, PAO4 showed enhanced reactivity, as significant amounts (about 5% based on conversion of prenol compared to trace amounts for other solvent conditions) of isoprene and byproducts were formed in the "fresh" unheated sample even though it was placed in the freezer immediately after mixing.

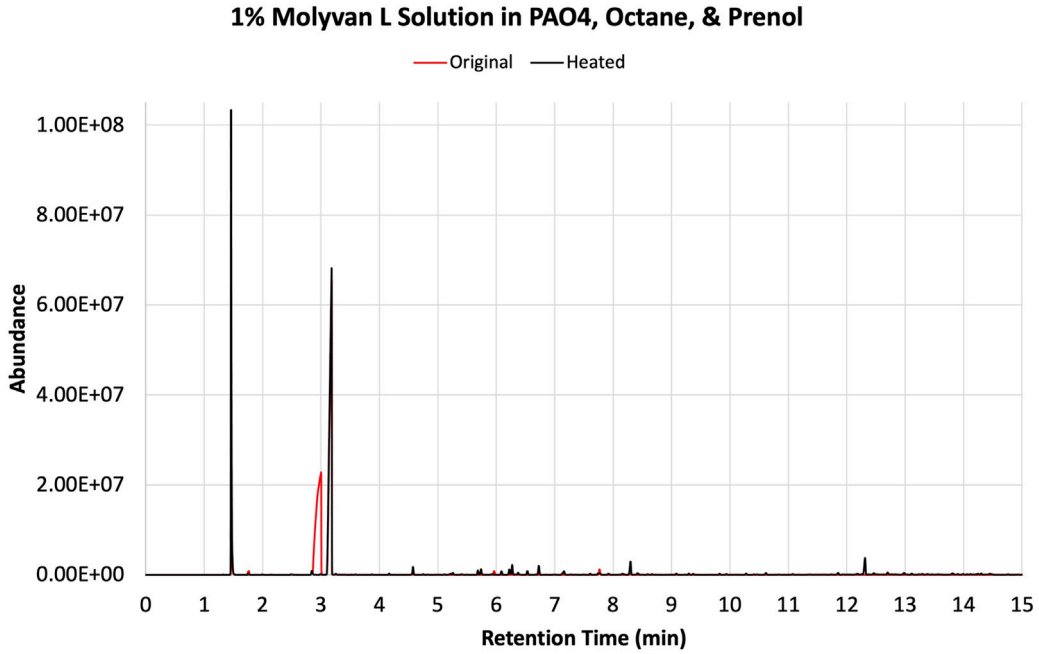


FIGURE 3 | GC-FID traces of prenol, octane, and 1% Molyvan L base oil mixture before (red) and after (black) heating in a closed vessel.

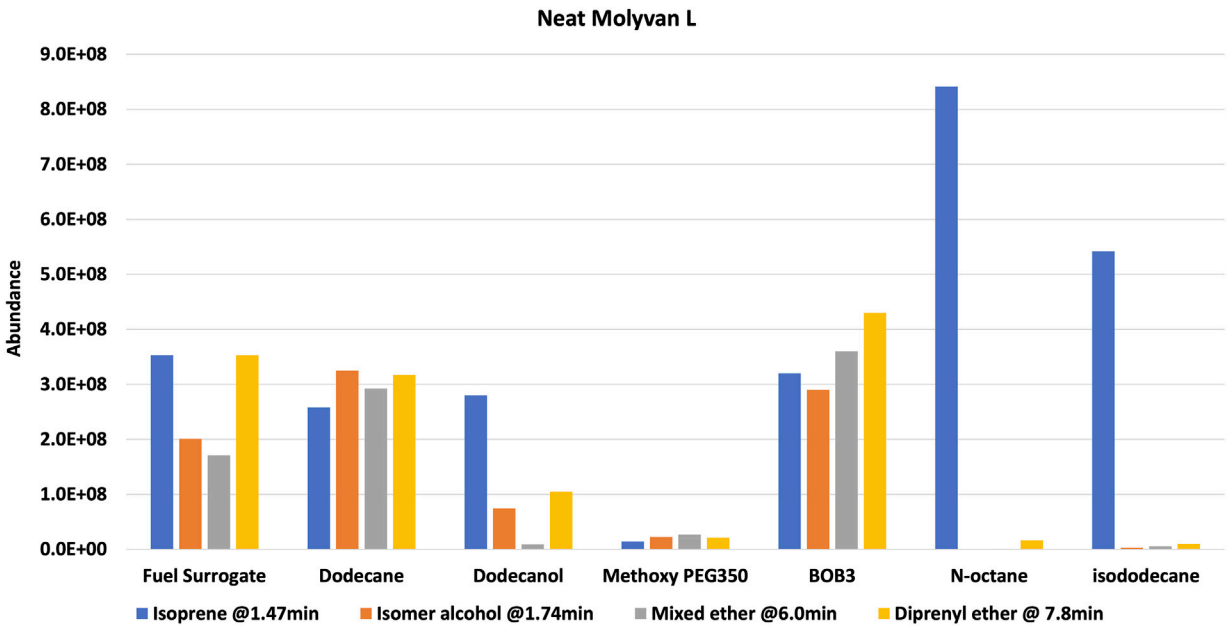


FIGURE 4 | ***Neat Molyvan L*** (75% in neutral oil). Reaction composition: 5 ml prenol, 15 ml solvent, Molyvan L (~55–60 mg).

Experiments were repeated with neat catalyst without a base oil, PAO4 (**Figure 4**). Overall, for this case, conversions and selectivity for isoprene appear slightly lower than those in the case in which a base oil was included (compare **Supplementary Tables S1, S2**). This is particularly true for the initially tested solvents (i.e., dodecane, fuel surrogate, BOB3, and methoxy PEG350). This is most evident in the case of dodecane, which yields much lower amounts of isoprene than the base oil containing counterpart (entries two in **Supplementary Tables S1, S2**). On closer examination of the data, the catalyst

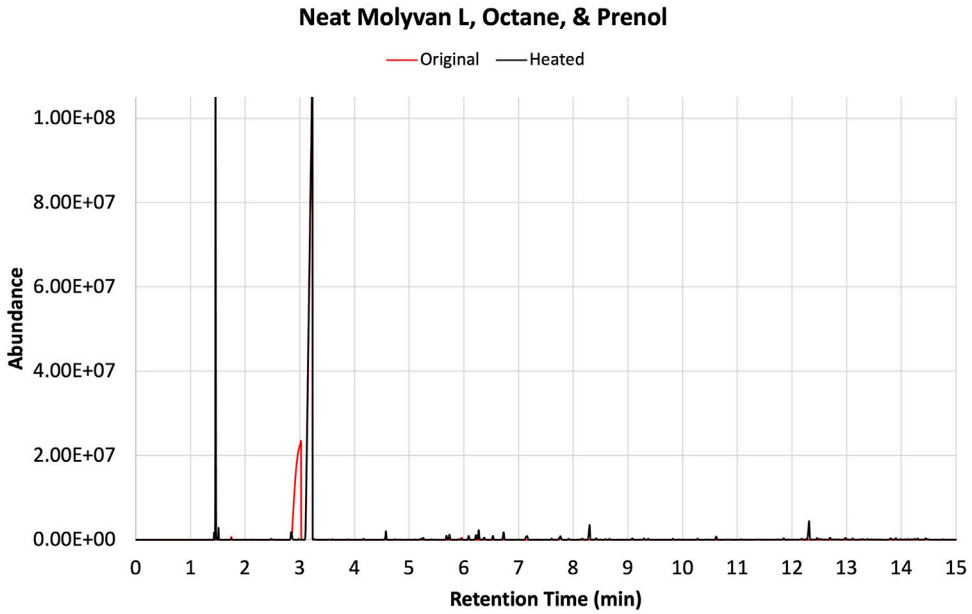


FIGURE 5 | GC-FID traces of prenol, octane, and neat Molyvan L mixture before (red) and after (black) heating in a closed vessel.

concentration in the overall *neat* mixture was about half of that used in the lubricant mixture. The lower conversions could be attributed to this discrepancy; however, the product profile and isoprene selectivity are unlikely to be affected by the lower catalyst amounts. In contrast, octane and isododecane (**Figure 4**) show remarkable selectivity even when neat Molyvan L was used. The octane product profile is shown as an example in **Figure 5**.

Notably, these solvents promoted enhanced reactivities even at cold temperatures (freezing and room temperatures), as a significant amount of isoprene was formed in the "fresh" samples. It is important to note that although BOB3 was included as a (co)solvent in the testing matrix, even if it provided a stellar selectivity for isoprene, it would not be a useful or practical solvent system, as isoprene could not be isolated due to the complex make-up of this fuel blend and the presence of many light fractions that would co-distill with isoprene. In contrast, all other mixtures could be easily subjected to distillation to isolate the lowest boiling point fraction, isoprene. In all examples from **Figures 2**, **4** a GC-FID peak area discrepancy from the prenol consumed and the major products formed suggests mass losses. About 10% of the mixtures are made up of unidentified species that are present in much smaller amounts than the byproducts of interest. All things considered, there still appears to be ~20–25% area loss from prenol to products, albeit GC-FID is not a quantitative technique. Isoprene is the lightest fraction of the reaction mixture at 1.47 min and therefore is the most likely component to escape the mixture during transfers, transport, and analysis. Although 2-methylbut-3-en-2-ol (the isomer of prenol) appears close in retention time to isoprene at 1.76 min, its boiling point is substantially higher than isoprene, at 99 versus 34°C. To confirm our suspicions, an experiment mimicking the 1 wt% Molyvan L solution in PAO4 conditions was conducted, in which 10 ml of PAO4, 5 ml of octane, and 2.7 ml of isoprene were heated at ~145–150°C for 2 h. Aliquots before and after heating were analyzed by ^{1}HNMR to quantify losses during heating (**Supplementary Figures S18, S19**). Isoprene quantification before and after heating against an internal standard (dimethylterephthalate) revealed a 12% loss as a result of heating alone, not accounting for equal losses during transfers and weighing (2.03 mmol isoprene per gram of solution before heating versus 1.78 mmol of isoprene per gram of solution after heating).

To quantitatively evaluate the amount of isoprene in the final mixtures, albeit after storage in the freezer for several weeks, we conducted ^{1}HNMR analysis using the procedure described below. First, an aliquot (~0.2 g) from the reaction mixture was combined with a $CDCl_3$ solution (~0.6 g) containing a known amount of internal standard (dimethylterephthalate). This internal standard has well resolved singlet peaks (8.1 and 3.9 ppm) against the isoprene signature peaks (6.48–6.42 ppm) and away from other olefinic byproducts. A weight measurement is more accurate than a volume measurement and it enables integration of proton peaks of these constituents and therefore quantification of the amount of isoprene present in the mixture. The two selected experiments for this study were those with octane solvent that gave the largest selectivity. Details of this procedure are found in the SI. The yields of isoprene from entries six in **Supplementary Tables S1, S2** derived both from ^{1}HNMR and GC-FID analyses are shown in **Table 1**.

The stacked ^{1}HNMR results of the two reaction mixtures demonstrate the similarity of the mixtures, the absence of isomeric alcohol that appears at 5.9 ppm, but presence of other olefinic species that partly overlap with the isoprene peaks at ~5 ppm (**Figure 6**).

TABLE 1 | Yields of isoprene from entry six of **Supplementary Tables S1, S2** derived both from ^{1}HNMR and GC-FID analyses.

Experiment	Yield From ^{1}HNMR (%)	Apparent Yield From GC-FID (%)
Octane (1 wt% Molyvan L in base oil, entry 6 in **Supplementary Table S1**)	54	44
Octane (neat Molyvan L, entry 6 in **Supplementary Table S2**)	69	52

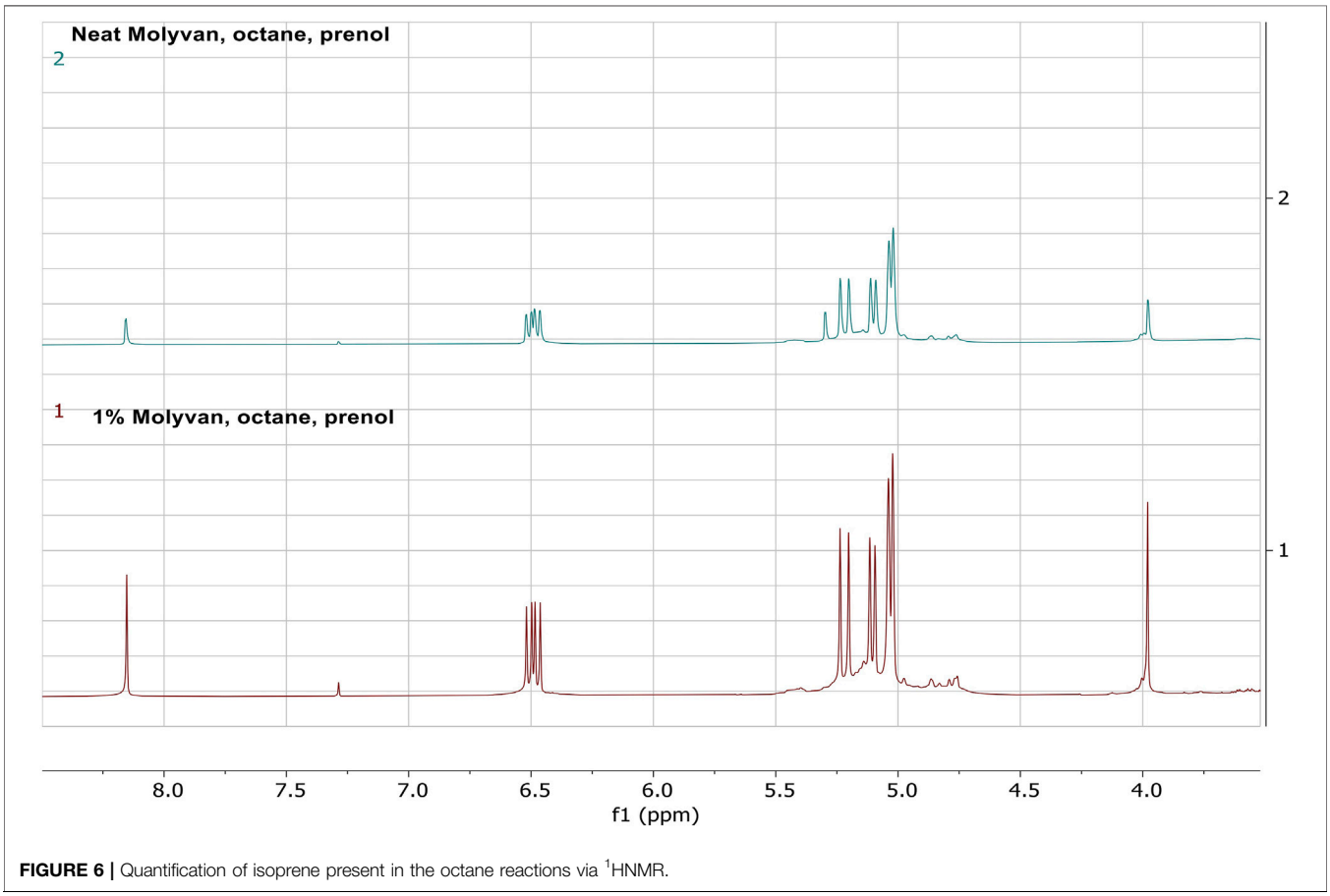


FIGURE 6 | Quantification of isoprene present in the octane reactions via ^{1}HNMR.

Previous attempts by others to synthesize isoprene or ethers from prenol resulted in low yields and poor selectivity. For example, Bielawski et al. studied a graphite oxide activated zeolite catalyst at 150°C for selective dehydration of different alcohols, including prenol, to corresponding alkenes (Todd and Bielawski, 2013). Although some alcohols formed olefins with good conversion and selectivity, prenol or the isomeric alcohol formed isoprene with poor yields and selectivity. Similarly, while attempting to form carbonyl compounds by isomerization of allylic alcohols at 100°C, Bianchini et al. reported that prenol formed a range of products including isoprene but with poor yields and selectivity (Bianchini et al., 2001). The reaction mechanism and the conditions controlling the selectivity of dehydration of prenol or the isomeric alcohol is of fundamental interest. As mentioned earlier, we serendipitously identified that by simply choosing the right solvent, isoprene can be selectively formed from prenol (isomerization followed by elimination), thus suppressing ether formation (substitution). Strong protic or Lewis acid catalysts have been reported to be active for allylic rearrangements and dehydration reactions (Overman et al., 1978; Moser, 1989; Larsen et al., 1997; Jacob et al., 1998; Matthias Kiefer et al., 1998; Korstanje et al., 2012). Molyvan-L, a strong Lewis acid catalyst, is likely to catalyze an allylic rearrangement of prenol to a more stable and substituted tertiary alcohol (i.e., the isomeric alcohol), (Belgacem et al., 1992; Jacob et al., 1998; Matthias Kiefer et al., 1998; Fronczek et al., 2002), which then can undergo intramolecular dehydration to form isoprene (**Figure 7**). A reaction mechanism for isoprene formation from *in situ* formed isomeric alcohol has been proposed based on previously reported oxo complexes (Korstanje et al., 2012; Korstanje et al., 2013). The Lewis acidic Molyvan-L coordinates with the isomeric alcohol to

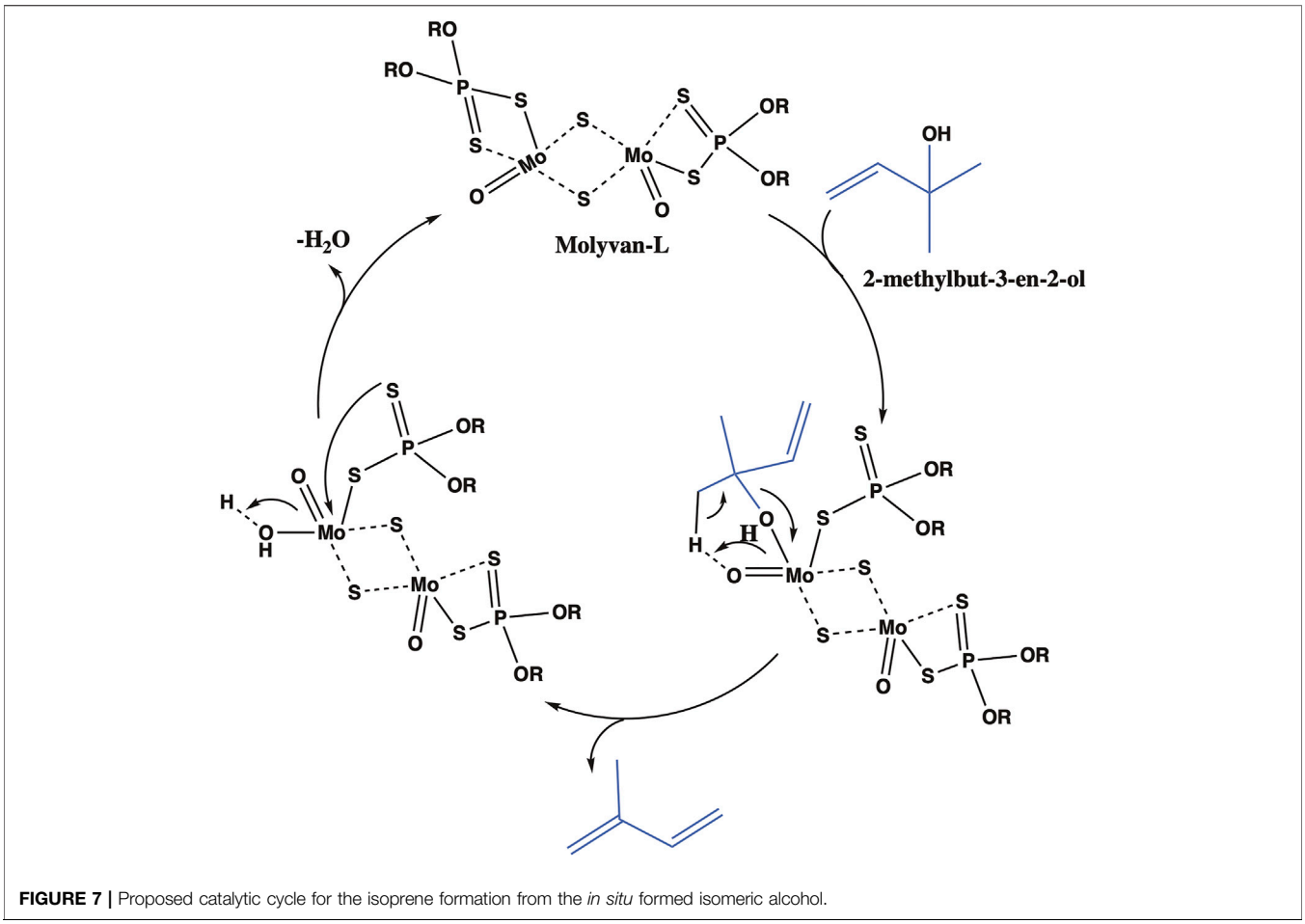


FIGURE 7 | Proposed catalytic cycle for the isoprene formation from the *in situ* formed isomeric alcohol.

form molybdenum-alkoxy species, which then expels isoprene to form a hydroxy molybdenum species. Upon expulsion of water, the original Molyvan-L catalyst is regenerated for subsequent catalysis.

As shown in many entries in **Supplementary Tables S1, S2**, the strong Lewis acidic Molyvan-L also can coordinate with multiple alcohols and catalyze the intermolecular dehydration of prenol to ethers but to a significantly lesser extent in octane and isododecane solvents. Notably, that significant reactivity difference is observed even between two simple straight chain alkanes, dodecane (entry two in **Supplementary Table S2**) and octane (entry six in **Supplementary Table S2**). The difference in the boiling point and vapor pressure between these solvents could influence the product distribution. At a reaction temperature of 150°C, in the case of octane (boiling point 125.6°C), the prenol isomer alcohol concentration in the condensed phase is expected to be higher as opposed to dodecane (boiling point 216.2°C), which could influence the subsequent product distribution. At this point, it is not very clear how the solvent affects the selectivity to one product over the other. *In situ* reactivity studies could shed light on the reaction mechanism. In addition to the aforementioned direct formation of isoprene from prenol via isomer alcohol dehydration, isoprene formation from elimination of ethers could not be excluded (Al-Faze et al., 2021).

Overall, the process is expected to be easily scalable, provided the reaction is run in a vessel capable of sustaining the vapor pressure of the reaction medium. A qualitative analysis of the most selective process, octane with or without PAO4, appears amenable for scale-up. The reagents are inexpensive or recyclable. Molyvan L was used at 0.25% (weight/volume) concentration in the neat reaction condition, and reaction optimization may lower that amount further. PAO4 is a commodity chemical and costs about $1/pound. N-octane is not inexpensive; however, more work may reveal that 99% reagent grade is not necessary to achieve high reactivity, and a lower grade solvent may be sufficient. The octane should be recoverable in the isoprene isolation process, via fractional distillation, or after isoprene removal, or the remaining mixture could be recycled back through another reaction cycle. There are many adjustments that could be made to optimize the process, reduce energy requirements, and improve cost. We have only laid the foundation for future opportunities.

4 CONCLUSION

We have reported herein a simple, efficient, and selective synthesis of isoprene from prenol in the presence of a

commercially available molybdenum catalyst. We serendipitously found that the choice of solvent plays a key role in suppressing the formation of side products such as ethers. Among the solvents tested, the use of simple long chain alkanes such as octane but also highly branched alkanes such as isododecane resulted in high conversion and selectivity to isoprene. In the case of octane, the highest yield was obtained with neat Molyvan L, in the absence of PAO4, at 69% yield (and quantitative conversion of prenol). Selectivity is very high at ~90% based on results from our GC-FID analysis. Discerning the reaction mechanism could provide additional insights and understanding of the catalytic cycle and help to optimize the production of isoprene under mild conditions.

DATA AVAILABILITY STATEMENT

The original contributions presented in the study are included in the article/**Supplementary Material**, further inquiries can be directed to the corresponding author.

AUTHOR CONTRIBUTIONS

LC proposed the original concept and methodology and interpreted data. JK proposed molybdenum-based catalytic mechanisms and conducted ^{1}HNMR analyses. MS conducted GC-FID analyses. All authors contributed to the writing of the manuscript.

FUNDING

The research was supported by the U.S. Department of Energy's Office of Energy Efficiency and Renewable Energy and Bioenergy Technologies Office. The views expressed in the article do not necessarily represent the views of the Department of Energy or the United States Government.

ACKNOWLEDGMENTS

The authors gratefully acknowledge the support and guidance of Kevin Stork of the Department of Energy and Dr. Daniel Gaspar of Pacific Northwest National Laboratory (PNNL). The authors are also grateful to Cortland Johnson of PNNL for improving the TOC image.

SUPPLEMENTARY MATERIAL

The Supplementary Material for this article can be found online at: https://www.frontiersin.org/articles/10.3389/fchem.2022.879129/full#supplementary-material

REFERENCES

Al-Faze, R., Kozhevnikova, E. F., and Kozhevnikov, I. V. (2021). Diethyl Ether Conversion to Ethene and Ethanol Catalyzed by Heteropoly Acids. *ACS Omega* 6 (13), 9310–9318. doi:10.1021/acsomega.1c00958

Belgacem, J., Kress, J., and Osborn, J. A. (1992). On the Allylic Rearrangements in Metal Oxo Complexes: Mechanistic and Catalytic Studies on MoO_2(allyloxo)$_2$(CH_3CN)$_2$ and Analogous Complexes. *J. Am. Chem. Soc.* 114 (4), 1501–1502. doi:10.1021/ja00030a067

Bianchini, C., Meli, A., and Oberhauser, W. (2001). Isomerization of Allylic Alcohols to Carbonyl Compounds by Aqueous-Biphase Rhodium Catalysis. *New J. Chem.* 25 (1), 11–12. doi:10.1039/b001478h

Bonrath, W., and Netscher, T. (2005). Catalytic Processes in Vitamins Synthesis and Production. *Appl. Catal. A General* 280 (1), 55–73. doi:10.1016/j.apcata.2004.08.028

Chou, H. H., and Keasling, J. D. (2012). Synthetic Pathway for Production of Five-Carbon Alcohols from Isopentenyl Diphosphate. *Appl. Environ. Microbiol.* 78 (22), 7849–7855. doi:10.1128/AEM.01175-12

Clomburg, J. M., Qian, S., Tan, Z., Cheong, S., and Gonzalez, R. (2019). The Isoprenoid Alcohol Pathway, a Synthetic Route for Isoprenoid Biosynthesis. *Proc. Natl. Acad. Sci. U.S.A.* 116 (26), 12810–12815. doi:10.1073/pnas.1821004116

Cosimbescu, L., Campbell, K. B., Kothandaraman, J., Malhotra, D., and Swita, M. S. (2022). Investigations of Prenol Reactions Catalyzed by Zinc and Molybdenum Complexes. *Fuel* 307, 121857. doi:10.1016/j.fuel.2021.121857

Ezinkwo, G. O., Tretjakov, V. F., Talyshinky, R. M., Ilolov, A. M., and Mutombo, T. A. (2013). Overview of the Catalytic Production of Isoprene from Different Raw Materials; Prospects of Isoprene Production from Bio-Ethanol. *Catal. Sustain. Energy* 1, e0006. doi:10.2478/cse-2013-0006

Fronczek, F. R., Luck, R. L., and Wang, G. (2002). Synthesis, Characterization and Reactivity of $MoCl_2(O)(O_2)(OPR_3)_2$, OPR_3=$OPMePh_2$, $OPPh_3$; an Isomerization Catalyst for Some Allylic Alcohols. *Inorg. Chem. Commun.* 5 (6), 384–387. doi:10.1016/s1387-7003(02)00410-0

George, K. W., Thompson, M. G., Kang, A., Baidoo, E., Wang, G., Chan, L. J. G., et al. (2015). Metabolic Engineering for the High-Yield Production of Isoprenoid-Based C5 Alcohols in E. coli. *Sci. Rep.* 5, 11128. doi:10.1038/srep11128

Gupta, P., and Phulara, S. C. (2015). Metabolic Engineering for Isoprenoid-Based Biofuel Production. *J. Appl. Microbiol.* 119 (3), 605–619. doi:10.1111/jam.12871

Jacob, J., Espenson, J. H., Jensen, J. H., and Gordon, M. S. (1998). 1,3-transposition of Allylic Alcohols Catalyzed by Methyltrioxorhenium. *Organometallics* 17 (9), 1835–1840. doi:10.1021/om971115n

Janke, C., Gaida, S., and Jennewein, S. (2020). The Production of Isoprene from Cellulose Using Recombinant Clostridium Cellulolyticum Strains Expressing Isoprene Synthase. *Microbiologyopen* 9 (4), e1008. doi:10.1002/mbo3.1008

Kiefer, M., Siegel, W., Therre, J, Pahl, M., Werner, A., and Schäfer-Lüderssen, U. (1998). *Continuous Method for the Preparation of Dimethylvinylcarbinol by Isomerisation of Prenol*. EP0941979B1.

Korstanje, T. J., de Waard, E. F., Jastrzebski, J. T. B. H., and Klein Gebbink, R. J. M. (2012). Rhenium-Catalyzed Dehydration of Nonbenzylic and Terpene Alcohols to Olefins. *ACS Catal.* 2 (10), 2173–2181. doi:10.1021/cs300455w

Korstanje, T. J., Folkertsma, E., Lutz, M., Jastrzebski, J. T. B. H., and Klein Gebbink, R. J. M. (2013). Synthesis, Characterization, and Catalytic Behavior of Dioxomolybdenum Complexes Bearing AcAc-Type Ligands. *Eur. J. Inorg. Chem.* 2013 (12), 2195–2204. doi:10.1002/ejic.201201350

Larsen, G., Lotero, E., Petkovic, L. M., and Shobe, D. S. (1997). Alcohol Dehydration Reactions over Tungstated Zirconia Catalysts. *J. Catal.* 169(1), 67–75. doi:10.1006/jcat.1997.1698

Li, M., Chen, H., Liu, C., Guo, J., Xu, X., Zhang, H., et al. (2019). Improvement of Isoprene Production in Escherichia coli by Rational Optimization of RBSs and Key Enzymes Screening. *Microb. Cell Fact.* 18 (1), 4. doi:10.1186/s12934-018-1051-3

Li, M., Nian, R., Xian, M., and Zhang, H. (2018). Metabolic Engineering for the Production of Isoprene and Isopentenol by Escherichia Coli. *Appl. Microbiol. Biotechnol.* 102 (18), 7725–7738. doi:10.1007/s00253-018-9200-5

Liang, H., Ma, X., Ning, W., Liu, Y., Sinskey, A. J., Stephanopoulos, G., et al. (2021). Constructing an Ethanol Utilization Pathway in Escherichia coli to Produce

Acetyl-CoA Derived Compounds. *Metab. Eng.* 65, 223–231. doi:10.1016/j.ymben.2020.11.010

Marton, D., Slaviero, P., and Tagliavini, G. (1989). Organotins as Etherification Catalysts. III. Etherifications and Hydro-Hydroxy-Eliminations Promoted by Butyltin Trichloride. *Tetrahedron* 45 (22), 7099–7108. doi:10.1016/s0040-4020(01)89178-x

Monroe, E., Gladden, J., Albrecht, K. O., Bays, J. T., McCormick, R., Davis, R. W., et al. (2019). Discovery of Novel Octane Hyperboosting Phenomenon in Prenol Biofuel/gasoline Blends. *Fuel* 239, 1143–1148. doi:10.1016/j.fuel.2018.11.046

Moser, W. (1989). Silicon-rich H-ZSM-5 Catalyzed Conversion of Aqueous Ethanol to Ethylene. *J. Catal.* 117 (1), 19–32. doi:10.1016/0021-9517(89)90217-0

Overman, L. E., Campbell, C. B., and Knoll, F. M. (1978). Mild Procedures for Interconverting Allylic Oxygen Functionality. Cyclization-Induced [3,3] Sigmatropic Rearrangement of Allylic Carbamates. *J. Am. Chem. Soc.* 100(15), 4822–4834. doi:10.1021/ja00483a032

Parker, G. L., Smith, L. K., and Baxendale, I. R. (2016). Development of the Industrial Synthesis of Vitamin A. *Tetrahedron* 72 (13), 1645–1652. doi:10.1016/j.tet.2016.02.029

Taylor, H. S., and Shenk, W. J. (2002). The Conversion of Acetone to Isoprene. *J. Am. Chem. Soc.* 63 (10), 2756–2757. doi:10.1021/ja01855a073

Todd, A. D., and Bielawski, C. W. (2013). Graphite Oxide Activated Zeolite NaY: Applications in Alcohol Dehydration. *Catal. Sci. Technol.* 3 (1), 135–139. doi:10.1039/c2cy20474f

Wang, S., Wang, Z., Wang, Y., Nie, Q., Yi, X., Ge, W., et al. (2017). Production of Isoprene, One of the High-Density Fuel Precursors, from Peanut Hull Using the High-Efficient Lignin-Removal Pretreatment Method. *Biotechnol. Biofuels* 10, 297. doi:10.1186/s13068-017-0988-5

Yang, J., Zhao, G., Sun, Y., Zheng, Y., Jiang, X., Liu, W., et al. (2012). Bio-isoprene Production Using Exogenous MVA Pathway and Isoprene Synthase in Escherichia coli. *Bioresour. Technol.* 104, 642–647. doi:10.1016/j.biortech.2011.10.042

Zheng, Y., Liu, Q., Li, L., Qin, W., Yang, J., Zhang, H., et al. (2013). Metabolic Engineering of Escherichia coli for High-Specificity Production of Isoprenol and Prenol as Next Generation of Biofuels. *Biotechnol. Biofuels* 6, 57. doi:10.1186/1754-6834-6-57

Conflict of Interest: The authors declare that the research was conducted in the absence of any commercial or financial relationships that could be construed as a potential conflict of interest.

Publisher's Note: All claims expressed in this article are solely those of the authors and do not necessarily represent those of their affiliated organizations, or those of the publisher, the editors and the reviewers. Any product that may be evaluated in this article, or claim that may be made by its manufacturer, is not guaranteed or endorsed by the publisher.

Copyright © 2022 Kothandaraman, Cosimbescu and Swita. This is an open-access article distributed under the terms of the Creative Commons Attribution License (CC BY). The use, distribution or reproduction in other forums is permitted, provided the original author(s) and the copyright owner(s) are credited and that the original publication in this journal is cited, in accordance with accepted academic practice. No use, distribution or reproduction is permitted which does not comply with these terms.

frontiers | Frontiers in Chemistry

ORIGINAL RESEARCH
published: 18 July 2022
doi: 10.3389/fchem.2022.934781

Methylene Blue as a Photo-Redox Catalyst: The Development Synthesis of Tetrahydrobenzo[*b*]pyran Scaffolds via a Single-Electron Transfer/Energy Transfer

Farzaneh Mohamadpour *

School of Engineering, Apadana Institute of Higher Education, Shiraz, Iran

In a green tandem reaction using aldehyde derivatives, malononitrile, and dimedone, a radical tandem Knoevenagel–Michael cyclocondensation reaction of tetrahydrobenzo[*b*]pyran scaffolds was developed. Using visible light as a sustainable energy source, methylene blue (MB^+)-derived photo-excited state functions were employed in an aqueous solution as single-electron transfer (SET) and energy transfer catalysts. The range of yields is quite uniform (81–98%, average 92.18%), and the range of reaction time is very fast (2–7 min, average 3.7 min), and the point mentioned in the discussion is that the procedure tolerates a range of donating and withdrawing groups, while still giving very excellent yields. The reaction is fairly insensitive to the nature of the substituents. Research conducted in this project aims to develop a non-metallic cationic dye that is both inexpensive and widely available for more widespread use. In addition to energy efficiency and environmental friendliness, methylene blue also offers an excellent atom economy, time-saving features, and ease of use. As a result, a wide range of long-term chemical and environmental properties can be obtained. The turnover number and turnover frequency of tetrahydrobenzo[*b*]pyran scaffolds have been computed. Surprisingly, gram-scale cyclization is a possibility, implying that the technology may be applied in industries.

Keywords: methylene blue (MB^+), photo-redox catalyst, renewable energy source, tetrahydrobenzo[b]pyran scaffolds, aqueous solvent, photochemical synthesis

OPEN ACCESS

Edited by:
Luisa Margarida Martins, Universidade de Lisboa, Portugal

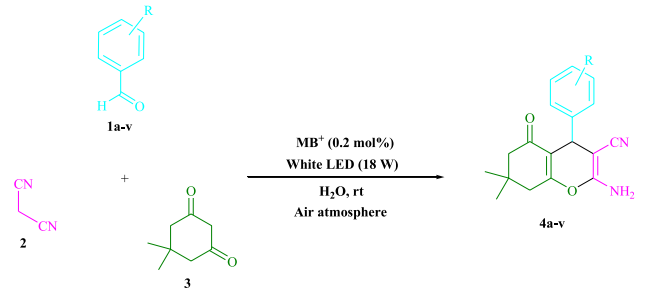
Reviewed by:
Ganesh Chandra Nandi, National Institute of Technology, Tiruchirappalli, India
Mozhgan Afshari, Islamic Azad University, Shoushtar Branch, Iran

***Correspondence:**
Farzaneh Mohamadpour
mohamadpour.f.7@gmail.com

Specialty section:
This article was submitted to Photocatalysis and Photochemistry, a section of the journal Frontiers in Chemistry

Received: *03 May 2022*
Accepted: *01 June 2022*
Published: *18 July 2022*

Citation:
Mohamadpour F (2022) Methylene Blue as a Photo-Redox Catalyst: The Development Synthesis of Tetrahydrobenzo[b]pyran Scaffolds via a Single-Electron Transfer/Energy Transfer. Front. Chem. 10:934781. doi: 10.3389/fchem.2022.934781



Graphical Abstract |

1 INTRODUCTION

Photoredox catalysts have recently played an increasingly important role in the organic synthesis by forming C–C and C–heteroatom bonds via single electron transfer (SET) and photo-induced electron transfer (PET). From small-scale to large-scale, they are required for a variety of treatments. Technological advances have led to the development of flow reactors (Politano and Oksdath-Mansilla, 2018) using visible light and dual photosensitized electrochemical reactions (Verschueren and De Borggraeve, 2019), resulting in a more inexpensive, green, and efficient method of reaction. It took until much later for MB^{+}'s staining properties to be recognized. Methylene blue belongs to the thiazine dye family and is a cationic dye. Several medical procedures involve the use of methylene blue. It possesses anti-malarial effects and has been demonstrated to be effective in the treatment of methemoglobinemia (Wainwright and Crossley, 2002; Clifton and Leikin, 2003; Tardivo et al., 2005). MB^{+} has a $\tau_f \sim 1.0$ ns singlet lifetime, a 664 nm absorbance, and a molar absorbance (ε = 94,000) (Romero et al., 2016). With a triplet lifespan of $\tau_f \sim 32$ μs(Pitre et al., 2016), the triplet $^3MB^{+*}$ is a significantly more stable excited state (Patel et al., 2021). The photocatalytic cycles of methylene blue are depicted in **Figure 1** (Patel et al., 2021). When the dye in the ground state is bombarded with visible light to produce the high-energy excited state of the dye (Dye*), the photoredox cycle begins. Two distinct pathways from the dye in the excited state (Dye*) are used to demonstrate the visible light photoredox catalysis. The Dye* reductive property can be used in the presence of a sacrificial electron acceptor. In other words, as an electron donor, Dye* leads to the radical cation species of Dye. Dye* acts as an electron acceptor in the presence of a sacrificial electron donor (Miyabe, 2017).

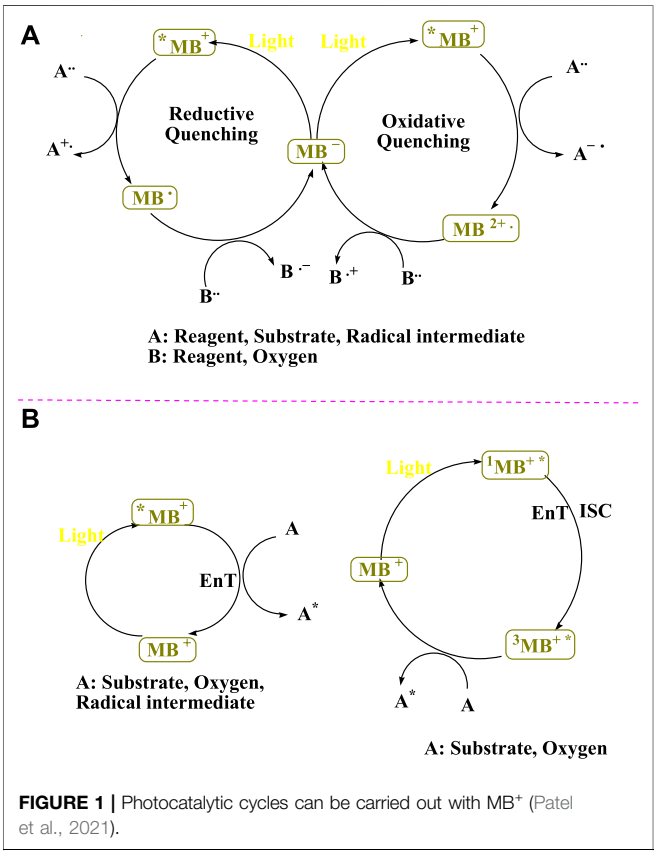


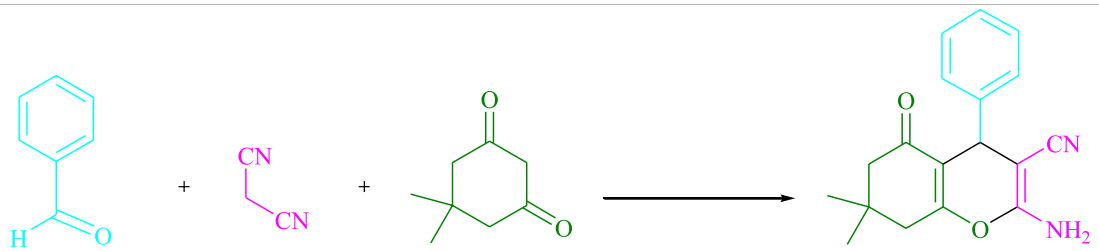
FIGURE 1 | Photocatalytic cycles can be carried out with MB^{+} (Patel et al., 2021).

Furthermore, green chemists believe that visible light irradiation is a reliable technique for environmentally friendly organic chemical syntheses since it has large energy reserves, low prices, and renewable energy sources (Mohamadpour, 2021a; Mohamadpour, 2021b).

Because of their biological and pharmacological action, the structures that makeup pyran derivatives have aroused the curiosity of biochemists and synthetic organic chemists (**Figure 2**) such as Chk1 kinase inhibitory activity (Foloppe et al., 2006), analgesic properties (Kuo et al., 1984), anticancer (Wang et al., 2000), vasodilatory (Ahluwalia et al., 1997), spamolytic (Ellis, 1977), antihypertensive, hepatoprotective, cardiotonic (Heber et al., 1993), vasodilator (Coates, 1990), anti-leukemic (Fokialakis et al., 2002; Beagley et al., 2003), emetic (Cannon et al., 1975), anti-anaphylactic (Biot et al., 1997), diuretic (Hafez et al., 1987), and anti-alzheimer activities (Bayer et al., 2006).

Several methods for synthesizing tetrahydrobenzo[*b*]pyran scaffolds with MCRs in the presence of various catalysts have been published. For example, $CaHPO_4$ (Bodaghifard et al., 2016), SiO_2NPs (Banerjee et al., 2011), ethylenediamine diacetate (Zhou et al., 2017), silica-bonded N-propylpiperazine sodium n-propionate (Niknam et al., 2013), I_2 (Bhosale et al., 2007), $NH_4Al(SO_4)_2.12H_2O$

TABLE 1 | Optimization of various photocatalysts[a].



Entry	Photocatalyst	Solvent (3 ml)	Time (min)	Isolated yields (%)
1	—	H_2O	20	64
2	Methylene blue (0.1 mol%)	H_2O	3	81
3	**Methylene blue (0.2 mol%)**	**H_2O**	**3**	**97**
4	Methylene blue (0.5 mol%)	H_2O	3	97
5	Riboflavin (0.2 mol%)	H_2O	3	61
6	Acenaphthenequinone (0.2 mol%)	H_2O	3	46
7	Phenanthrenequinone (0.2 mol%)	H_2O	3	43
8	Erythrosin B (0.2 mol%)	H_2O	3	48
9	9*H*-Xanthen-9-one (0.2 mol%)	H_2O	3	49
10	Xanthene (0.2 mol%)	H_2O	3	47
11	Rhodamine B (0.2 mol%)	H_2O	3	63
12	Rose bengal (0.2 mol%)	H_2O	3	56
13	Fluorescein (0.2 mol%)	H_2O	3	67

[a]*Reaction conditions: malononitrile (1 mmol), benzaldehyde (1 mmol), and dimedone (1 mmol) in H_2O, as well as a white LED (18 W) and a variety of photocatalysts, were utilized at room temperature.*

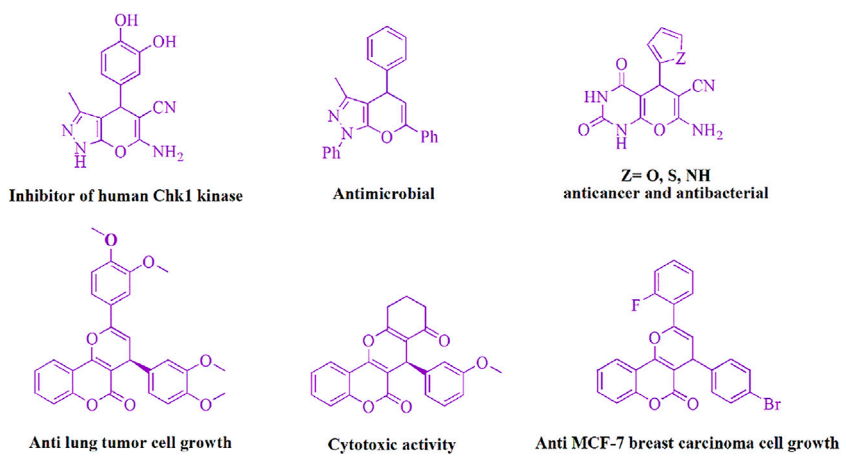


FIGURE 2 | Pyran motifs can be found in a variety of medicinally important compounds.

(Mohammadi et al., 2017), $NH_4H_2PO_4/Al_2O_3$ (Maleki and Sedigh Ashrafi, 2014), ACoPc-MNPs (Zolfigol et al., 2016), ZnO NPs (Banerjee and Saha, 2013), Fe_3O_4@SiO_2-imid-PMA (Esmaeilpour et al., 2015), $NiFe_2O_4$@SiO_2–$H_3PW_{12}O_{40}$ (Maleki et al., 2016), theophylline (Mohamadpour, 2021c), triethanolamine (Rahnamaf et al., 2020), sodium alginate (Mohamadpour, 2022a), Fe_3O_4@SiO_2@TiO_2 (Khazaei et al., 2015), $MgFe_2O_4$ nanoparticles (Eshtehardian et al., 2020), trichloroisocyanuric acid (Hojati et al., 2018), Na2 eosin Y (Mohamadpour, 2021d), DABCO (Tahmassebi et al., 2011), and Pd nanoparticles (Saha and Pal, 2012). There are limitations on metal catalysts such as, expensive reagents, severe reaction conditions, monotonous yields, environmental hazards, workup processes, and long reaction times associated with these methods. A homogenous catalyst is also difficult to separate from a reaction mixture. Our goal was to investigate photocatalysts (Mohamadpour, 2021e; Mohamadpour, 2021f) in green environments in order to synthesize heterocyclic compounds that had previously been explored. This research also shows the use of MB^+ (Mohamadpour, 2022b; Mohamadpour, 2022c) as a metal-free dye photo-redox catalyzer that is low-cost and widely available.

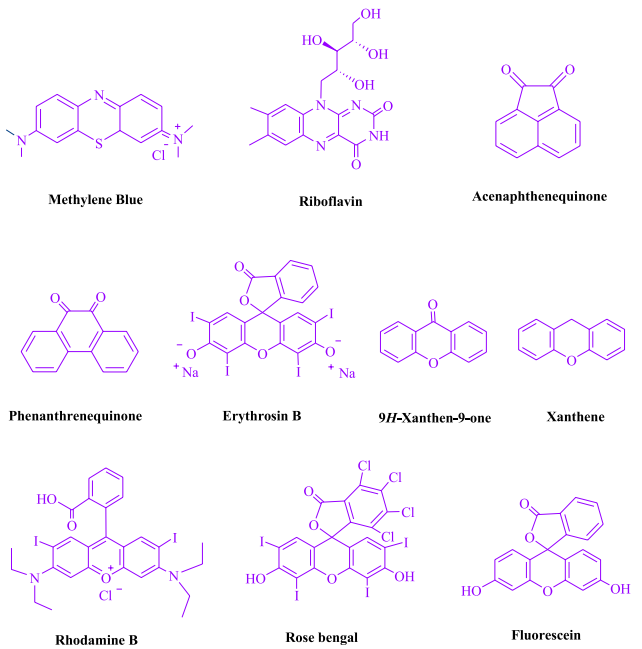


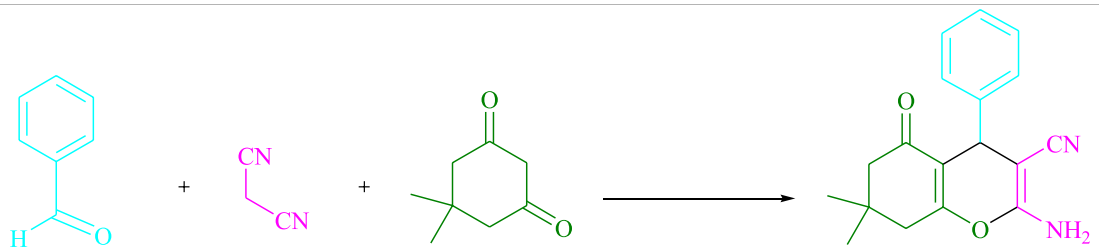
FIGURE 3 | Structures of various photocatalysts.

Visible light assists Knoevenagel–Michael cyclocondensation process of aldehyde derivatives, malononitrile, and dimedone in an aqueous solvent at room temperature and in an air environment. This was a successful one-pot reaction that was completed in a timely, cost-effective, and simple manner.

2 RESULTS AND DISCUSSION

To begin, LED irradiation was used to study the reaction of benzaldehyde, malononitrile, and dimedone in H_2O (3 ml) at room temperature. In 3 ml H_2O for 20 min, there was a 64% yield of **4a** without photocatalysts. As a way of improving the reaction, methylene blue, riboflavin, acenaphthenequinone, phenanthrenequinone, erythrosin B, 9*H*-xanthen-9-one, xanthene, rhodamine B, rose Bengal, and fluorescein (**Figure 3**) were examined in the same settings. This reaction proceeded with 43–97% yields and produced the acceptable matching product **4a** (**Table 1**). Methylene blue, according to the data, performed better in such a response. Using 0.2 mol% MB^+, the yield was raised to 97% (**Table 1**, entry 3). The CH_2Cl_2, DMSO, toluene, THF, and DMF all resulted in decreased yields. When the reaction is carried out in EtOAc, EtOH, MeOH, H_2O/EtOH (1:1), CH_3CN, or solvent-free conditions, the reaction rate and yield increase. With a high yield and rate, the reaction took place in H_2O. Using the same conditions as entry 12, a yield of 97% was obtained. In **Table 2**, the impact of white light on the yield was examined using a variety of light sources. Testing without the light source resulted in a small amount of **4a**. The effective synthesis of product **4a** requires visible light and MB^+, according to the findings. Changes in the intensity of white LEDs were also used to find the improved settings (10, 12, 18, and 20 W).

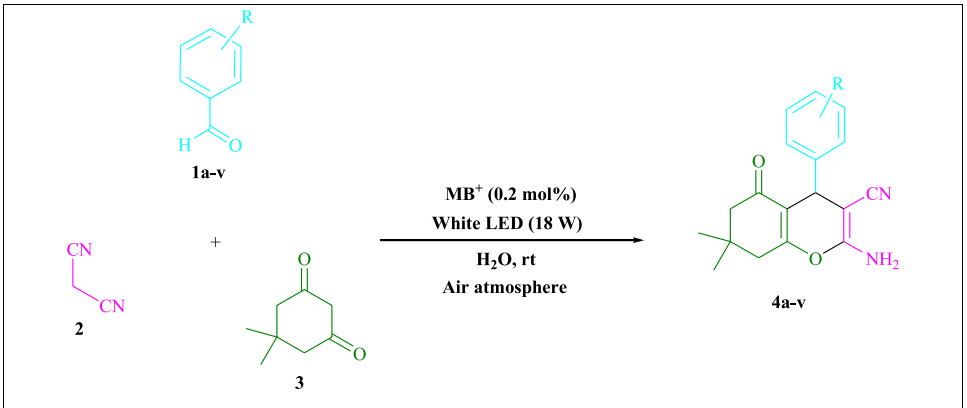
TABLE 2 | Optimization of the solvents and visible light[a].

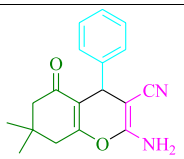


Entry	Light source	Solvent (3 ml)	Time (min)	Isolated yields (%)
1	—	H_2O	15	trace
2	Blue light (18 W)	H_2O	3	90
3	Green light (18 W)	H_2O	3	86
4	White light (10 W)	H_2O	3	83
5	White light (12 W)	H_2O	3	91
6	White light (20 W)	H_2O	3	97
7	White light (18 W)	EtOAc	3	71
8	White light (18 W)	EtOH	3	76
9	White light (18 W)	—	8	74
10	White light (18 W)	MeOH	6	67
11	White light (18 W)	H_2O/EtOH (1:1)	3	88
12	**White light (18 W)**	**H_2O**	**3**	**97**
13	White light (18 W)	CH_3CN	3	68
14	White light (18 W)	CH_2Cl_2	20	33
15	White light (18 W)	DMSO	25	35
16	White light (18 W)	toluene	25	28
17	White light (18 W)	THF	15	18
18	White light (18 W)	DMF	15	24

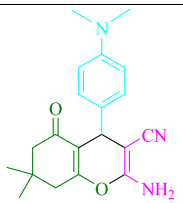
[a]*Reaction conditions: at room temperature, malononitrile (1 mmol), benzaldehyde (1 mmol), and dimedone (1 mmol) were added to MB^+ (0.2 mol %).*

TABLE 3 | Synthesis of tetrahydrobenzo[*b*]pyran scaffolds.

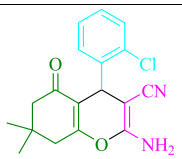




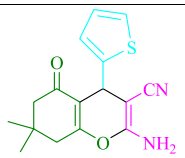
4a (3 min, 97%)
Mp. 227-229 °C
Lit. 226-228 °C[Bodaghifard et al., 2016]



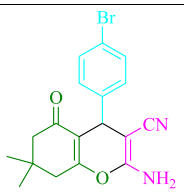
4b (3 min, 93%)
Mp. 211-213 °C
Lit. 208-210 °C[Zhou et al., 2017]



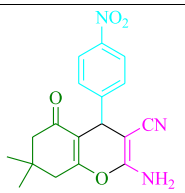
4c (3 min, 88%)
Mp. 215-217 °C
Lit. 214-216 °C[Zhou et al., 2017]



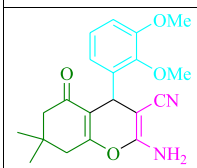
4d (2 min, 96%)
Mp. 206-208 °C
Lit. 208-210 °C[Maleki et al., 2016]



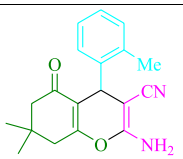
4e (5 min, 85%)
Mp. 203-205 °C
Lit. 204-206 °C[Bodaghifard et al., 2016]



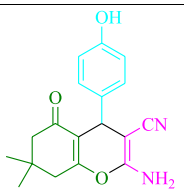
4f (3 min, 98%)
Mp. 181-183 °C
Lit. 180-181 °C[Zhou et al., 2017]



4g (5 min, 95%)
Mp. 216-218 °C
Lit. 217-219 °C[Banerjee et al., 2011]



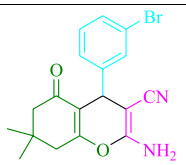
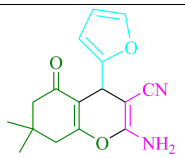
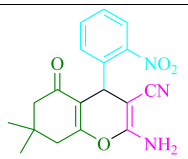
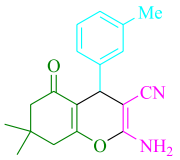
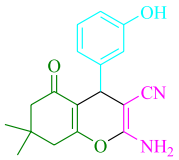
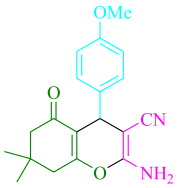
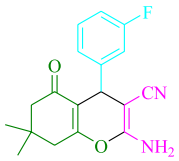
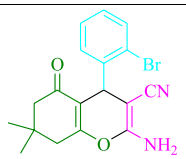
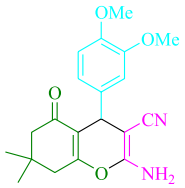
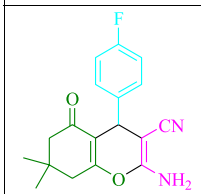
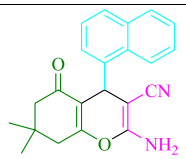
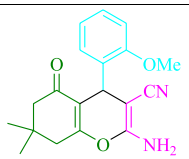
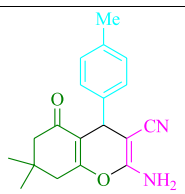
4h (2 min, 98%)
Mp. 210-212 °C
Lit. 211-212 °C[Maleki et al., 2016]

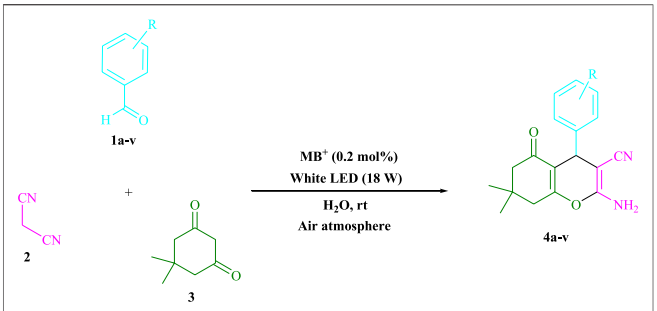


4i (7 min, 84%)
Mp. 211-213 °C
Lit. 210-212 °C[Zolfigol et al., 2016]

(Continued on following page)

TABLE 3 | (*Continued*) Synthesis of tetrahydrobenzo[*b*]pyran scaffolds.

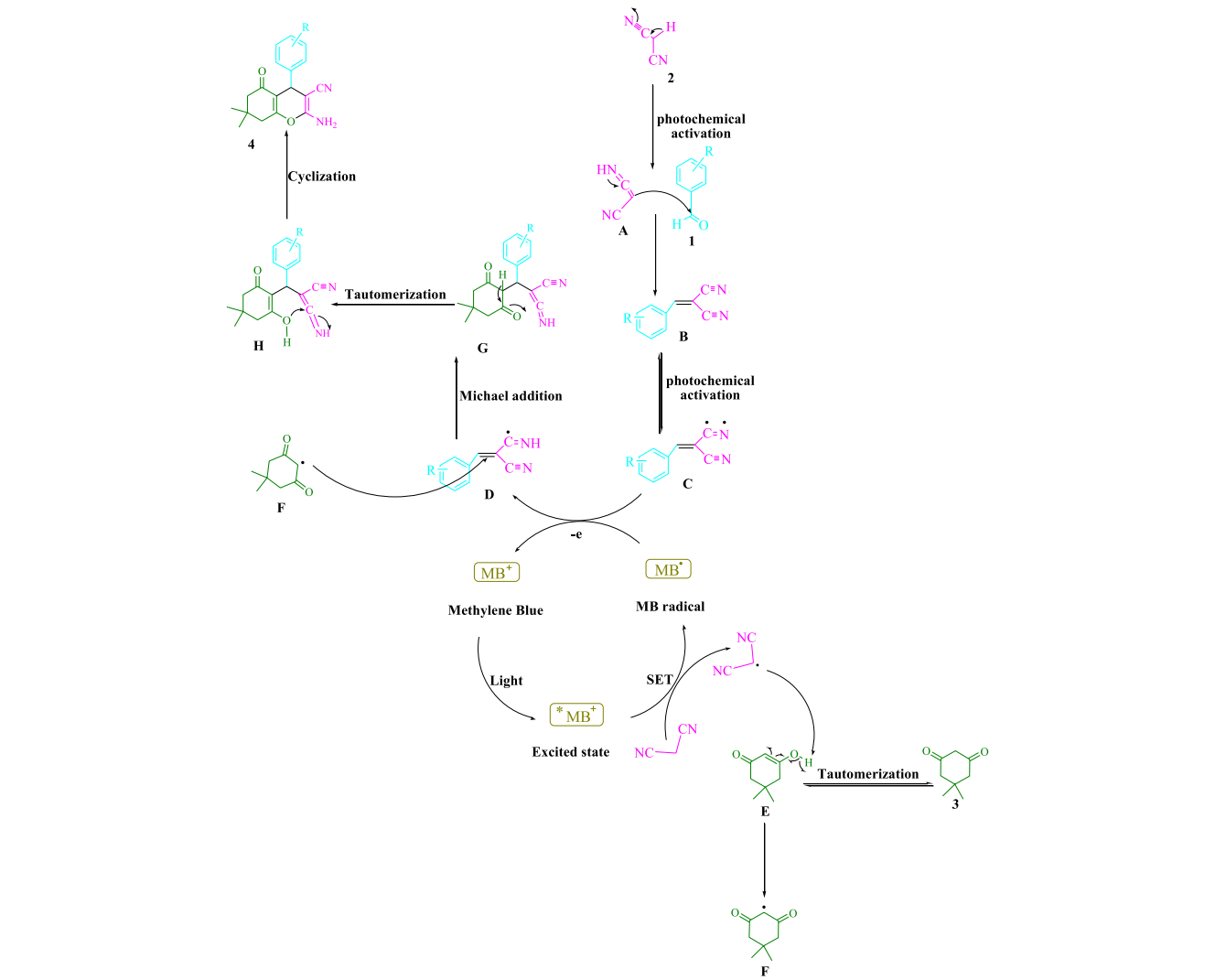
 **4j** (5 min, 82%) Mp. 230-232 °C Lit. 228-230 °C[Banerjee et al., 2011]	 **4k** (2 min, 97%) Mp. 217-219 °C Lit. 216-217 °C[Maleki et al., 2016]	 **4l** (2 min, 96%) Mp. 225-227 °C Lit. 223-226 °C[Bodaghifard et al., 2016]
 **4m** (3 min, 95%) Mp. 196-198 °C Lit. 198-200 °C[Niknam et al., 2013]	 **4n** (7 min, 81%) Mp. 227-229 °C Lit. 226-228 °C[Zolfigol et al., 2016]	 **4o** (4 min, 95%) Mp. 204-206 °C Lit. 202-205 °C[Bodaghifard et al., 2016]
 **4p** (2 min, 95%) Mp. 209-211 °C Lit. 210-212 °C[Khazaei et al., 2015]	 **4q** (5 min, 87%) Mp. 151-153 °C Lit. 150-152 °C[Khazaei et al., 2015]	 **4r** (5 min, 92%) Mp. 225-227 °C Lit. 227-229 °C[Banerjee and Saha, 2013]
 **4s** (3 min, 98%) Mp. 196-198 °C Lit. 198-200 °C[Niknam et al., 2013]	 **4t** (6 min, 88%) Mp. 215-217 °C Lit. 215-218 °C[Khazaei et al., 2015]	 **4u** (3 min, 91%) Mp. 208-210 °C Lit. 211-212 °C[Maleki et al., 2016]
 **4v** (3 min, 97%) Mp. 223-225 °C Lit. 221-223 °C[Niknam et al., 2013]		



SCHEME 1 | Synthesis of tetrahydrobenzo[*b*]pyran scaffolds.

TABLE 4 | Calculated turnover number (TON) and turnover frequency (TOF).

Entry	Product	TON	TOF	Entry	Product	TON	TOF
1	**4a**	485	161.6	12	**4l**	480	240
2	**4b**	465	155	13	**4m**	475	158.3
3	**4c**	440	146.6	14	**4n**	405	57.8
4	**4d**	480	240	15	**4o**	475	118.7
5	**4e**	425	85	16	**4p**	475	237.5
6	**4f**	490	163.3	17	**4q**	435	87
7	**4g**	475	95	18	**4r**	460	92
8	**4h**	490	245	19	**4s**	490	163.3
9	**4i**	420	60	20	**4t**	440	73.3
10	**4j**	410	82	21	**4u**	455	151.6
11	**4k**	485	242.5	22	**4v**	485	161.6



SCHEME 2 | There has been a mechanistic approach presented for synthesizing tetrahydrobenzo[*b*]pyran scaffolds.

TABLE 5 | Comparing the catalytic characteristics of different catalysts described in the text for the production of catalyst **4a**[a].

Entry	Catalyst	Conditions	Time/yield (%)	Reference
1	$CaHPO_4$	H_2O/EtOH, 80°C	120 min/91	Bodaghifard et al. (2016)
2	SiO_2 NPs	EtOH, rt	25 min/94	Banerjee et al. (2011)
3	Silica-bonded N-propylpiperazine sodium n-propionate	H_2O/EtOH, Reflux	25 min/90	Niknam et al. (2013)
4	I_2	DMSO, 120°C	3.2 h/92	Bhosale et al. (2007)
5	$NH_4Al(SO_4)_2.12H_2O$	EtOH, 80°C	120 min/92	Mohammadi et al. (2017)
6	$NH_4H_2PO_4/Al_2O_3$	EtOH, Reflux	15 min/86	Maleki and Ashrafi, (2014)
7	$Fe_3O_4@SiO_2$-imid-PMA	H_2O, Reflux	20 min/94	Esmaeilpour et al. (2015)
8	Theophylline	H_2O/EtOH, rt	10 min/89	Mohamadpour, (2021c)
9	Trichloroisocyanuric acid	EtOH, 80 °C	10 min/90	Rahnamaf et al. (2020)
10	**MB^+**	**visible light irradiation, H_2O, rt**	**3 min/97**	**This work**

[a]*Based on the benzaldehyde, malononitrile, and dimedone three-component synthesis.*

White LED (18 W) was found to be the best choice according to the researchers (**Table 2**, entry 12). **Table 3** and **Scheme 1** show that a wide variety of substrates were evaluated under ideal conditions. In **Table 3**, it appears that the benzaldehyde substituent had no influence on the outcome of the reaction. Within the reaction conditions, polar and halides were allowed. The current reaction conditions permit both electron-donating and electron-withdrawing reactions to proceed successfully. *Ortho*-, *meta*-, and *para*-substituted aromatic aldehydes have a very high yield. Various aldehydes, such as the heavier naphthaldehyde, result in a completed product with negligible yield loss. Heterocyclic aldehydes followed a similar pattern in terms of reactivity.

Likewise, **Table 4** displays the turnover number (TON) and turnover frequency (TOF). A higher TON and TOF numerical value mean less catalyst is utilized, and a higher yield, and the catalyst becomes more efficient with increasing value.

The chosen strategy is depicted in **Scheme 2**. It is possible to tautomerize malononitrile (**2**) by exposing it to visible light (**A**). After that, the aldehydes (**1**) and (**A**) are joined to generate arylidenemalononitrile (**B**), which is photochemically activated to yield a radical intermediate (**C**). More energy can be utilized to accelerate this reaction, altering visible light. According to recent studies (Patel et al., 2021), visible light energy is utilized by this widely available cationic dye to create catalytic approaches that use single-electron transfer (SET) as well as energy transfer (EnT). To boost the visible-light–induced $*MB^+$, a SET approach is used to produce the malononitrile radical. The energy transfer (EnT) activity between the radical adduct (**C**) and the MB radical produces the intermediate (**D**) and ground-state MB. The intermediate (**F**) is formed when the malononitrile radical takes a hydrogen atom from (**E**). The intermediates (**F**) and (**D**) combine as a Michael acceptor to generate (**G**), which then undergo intramolecular cyclization and tautomerization to give rise to the final product (**4**).

A comparison of the catalytic ability of several catalysts described in the literature is presented in **Table 5** for the synthesis of tetrahydrobenzo[*b*]pyran scaffolds. In the presence of visible light, it could possess a number of useful properties, such as the need for a small amount of photocatalyst, a rapid reaction time, aqueous solvents, and the absence of byproducts. The atom–economic protocol is exceedingly successful at multigram scales and has significant industrial implications. Their efficiency and purity set them apart from other materials.

3 EXPERIMENT

3.1 General

A 9100 electro–thermal apparatus was used to determine the melting points of all compounds. A Bruker (DRX-400 and DRX-300) instrument was also used to record the nuclear magnetic resonance (1HNMR) spectra using CDCl3 as the solvent.

3.1.1 Preparation of Tetrahydrobenzo[b]pyran Scaffolds in General (4a–v)

Methylene blue (0.2 mol%) was mixed with dimedone (**3**, 1.0 mmol), malononitrile (**2**, 1.0 mmol), and aldehydes (**1**, 1.0 mmol) in H_2O (3 ml) and agitated at room temperature under white LED (18 W) irradiation. The reaction, which used *n*-hexane/ethyl acetate (3:1) as the eluent, was monitored using TLC. As a result of the reaction, the resultant substance was screened and rinsed with water, and the crude solid was crystallized from ethanol in order to yield the pure chemical without further purification. If we could make the aforementioned compounds using gram scale methods, we would be able to scale up to the level of pharmaceutical process development. 50 mmol of m-tolualdehyde, malononitrile, and dimedone were used in one experiment. The large-scale reaction ran well, requiring only 3 min to complete, and the product was recovered using typical filtration processes. The ^{1}HNMR spectrum of this material suggests that it is spectroscopically pure. After comparing the spectroscopic data, the products were categorized (^{1}HNMR). The ^{1}HNMR spectra files are provided in the **Supplementary Material**.

4 CONCLUSION

According to the findings, using a single-electron transfer (SET)/energy transfer (EnT), a radical tandem Knoevenagel–Michael cyclocondensation process of aldehyde derivatives, malononitrile, and dimedone can be used to generate metal-free tetrahydrobenzo[*b*]pyran scaffolds. In an aqueous solution and an air atmosphere at room temperature, visible light is used as a renewable energy source. Green protocol advantages include the

use of minimal amounts of photocatalyst, excellent yields, a reaction side that is highly efficient, safe conditions for the reaction, and a speedy procedure without the use of toxic chemicals or solvents. The purification process did not require chromatography. A model substrate reaction at the multigram scale demonstrates that this reaction can be scaled up without compromising the outcome. Due to these advantages, this technology offers significant benefits for industrial applications and for environmental concerns.

DATA AVAILABILITY STATEMENT

The datasets presented in this study can be found in online repositories. The names of the repository/repositories and accession number(s) can be found in the article/ **Supplementary Material**.

AUTHOR CONTRIBUTIONS

The author confirms being the sole contributor of this work and has approved it for publication.

ACKNOWLEDGMENTS

We gratefully acknowledge financial support from the Research Council of the Apadana Institute of Higher Education.

SUPPLEMENTARY MATERIAL

The Supplementary Material for this article can be found online at: https://www.frontiersin.org/articles/10.3389/fchem.2022.934781/full#supplementary-material

REFERENCES

Adbel Aziz Hafez, E., Abdel Aziz Hafez, E., Hilmy Elnagdi, M., Ghani Ali Elagamey, A., and Mohamed Abdel Aziz El-Taweel, F. (1987). Nitriles in Heterocyclic Synthesis: Novel Synthesis of Benzo[c]coumarin and of Benzo[c] pyrano[3,2-C]quinoline Derivatives. *Heterocycles* 26, 903–907. doi:10.3987/R-1987-04-086310.3987/r-1987-04-0903

Ahluwalia, V. K., Dahiya, A., and Garg, V. K. (1997). Reaction of 5-Amino-4-Formyl-3-Methyl (Or Phenyl)-1-Phenyl-1h-Pyrazoles with Active Methylene Compounds: Synthesis of Fused Heterocyclic Rings. *Indian J. Biochem. Biophysics* 36, 88.

Banerjee, S., Horn, A., Khatri, H., and Sereda, G. (2011). A Green One-Pot Multicomponent Synthesis of 4H-Pyrans and Polysubstituted Aniline Derivatives of Biological, Pharmacological, and Optical Applications Using Silica Nanoparticles as Reusable Catalyst. *Tetrahedron Lett.* 52, 1878–1881. doi:10.1016/j.tetlet.2011.02.031

Banerjee, S., and Saha, A. (2013). Free-ZnO Nanoparticles: a Mild, Efficient and Reusable Catalyst for the One-Pot Multicomponent Synthesis of Tetrahydrobenzo[b]pyran and Dihydropyrimidone Derivatives. *New J. Chem.* 37, 4170–4176. doi:10.1039/C3NJ00723E

Bayer, T. A., Schäfer, S., Breyhan, H., Wirths, O., Treiber, C., and Multhaup, G. (2006). A Vicious Circle: Role of Oxidative Stress, Intraneuronal Aβ and Cu in Alzheimer's Disease. *Clin. Neuropathol.* 25, 163.

Beagley, P., Blackie, M. A. L., Chibale, K., Clarkson, C., Meijboom, R., Moss, J. R., et al. (2003). Synthesis and Antiplasmodial Activity *In Vitro* of New Ferrocene-Chloroquine Analogues. *Dalton Trans.* 0, 3046–3051. doi:10.1039/B303335J

Bhosale, R. S., Magar, C. V., Solanke, K. S., Mane, S. B., Choudhary, S. S., and Pawar, R. P. (2007). Molecular Iodine: An Efficient Catalyst for the Synthesis of Tetrahydrobenzo[b]pyrans. *Synth. Commun.* 37, 4353–4357. doi:10.1080/00397910701578578

Biot, C., Glorian, G., Maciejewski, L. A., Brocard, J. S., Domarle, O., Blampain, G., et al. (1997). Synthesis and Antimalarial Activity *In Vitro* and *In Vivo* of a New Ferrocene–Chloroquine Analogue. *J. Med. Chem.* 40, 3715–3718. doi:10.1021/jm970401y

Bodaghifard, M. A., Solimannejad, M., Asadbegi, S., and Dolatabadifarahani, S. (2016). Mild and Green Synthesis of Tetrahydrobenzopyran, Pyranopyrimidinone and Polyhydroquinoline Derivatives and DFT Study on Product Structures, *Res. Chem. Intermed.* 42, 1165–1179. doi:10.1007/s11164-015-2079-1

Cannon, J. G., Khonje, P. R., and Long, J. P. (1975). Centrally Acting Emetics. 9. Hofmann and Emde Degradation Products of Nuciferine. *J. Med. Chem.* 18, 110–112. doi:10.1021/jm00235a026

Clifton, J., II, and Leikin, J. B. (2003). Methylene Blue. *Am. J. Ther.* 10, 289–291. doi:10.1097/00045391-200307000-00009

Coates, W. J. (1990). Pyrimidopyrimidine Derivatives. *Eur. Pat. 351058, Chem. Abstr.* 113, 40711.

Ellis, G. P. (1977). "The Chemistry of Heterocyclic Compounds," in *Chromenes, Chromenes, and Chromenes, Weissberger*. Editor E. C. Taylor (New York: John Wiley), 13.

Eshtehardian, B., Rouhani, M., and Mirjafary, Z. (2020). Green Protocol for Synthesis of $MgFe_2O_4$ Nanoparticles and Study of Their Activity as an Efficient Catalyst for the Synthesis of Chromene and Pyran Derivatives under Ultrasound Irradiation. *J. Iran. Chem. Soc.*17, 469. doi:10.1007/s13738-019-01783-3–

Esmaeilpour, M., Javidi, J., Dehghani, F., and Nowroozi Dodeji, F. (2015). A Green One-Pot Three-Component Synthesis of Tetrahydrobenzo[b]pyran and 3,4-dihydropyrano[c]chromene Derivatives Using a Fe_3O_4@SiO_2-Imid-PMAn Magnetic Nanocatalyst under Ultrasonic Irradiation or Reflux Conditions. *RSC Adv.* 5, 26625–26633. doi:10.1039/C5RA01021G

Fokialakis, N., Magiatis, P., Chinou, I., Mitaku, S., and Tillequin, F. (2002). Megistoquinones I and II, Two Quinoline Alkaloids with Antibacterial Activity from the Bark of Sarcomelicope Megistophylla. *Chem. Pharm. Bull.* 50, 413–414. doi:10.1248/cpb.50.413

Foloppe, N., Fisher, L. M., Howes, R., Potter, A., Robertson, A. G. S., and Surgenor, A. E. (2006). Identification of Chemically Diverse Chk1 Inhibitors by Receptor-Based Virtual Screening. *Bioorg. Med. Chem.* 14, 4792–4802. doi:10.1016/j.bmc.2006.03.021

Heber, D., Heers, C., and Ravens, U. (1993). Positive Inotropic Activity of 5-Amino-6-Cyano-1,3-Dimethyl-1,2,3,4-Tetrahydropyrido[2,3-D]pyrim Idine-2,4-Dione in Cardiac Muscle from guinea-pig and Man. Part 6: Compounds with Positive Inotropic Activity. *Pharmazie* 48, 537.

Hojati, S. F., MoeiniEghbali, N., Mohamadi, S., and Ghorbani, T. (2018). Trichloroisocyanuric Acid as a Highly Efficient Catalyst for the Synthesis of Tetrahydrobenzo[b]pyran Derivatives. *Org. Prep. Proced. Int.* 50, 408–415. doi:10.1080/00304948.2018.1468982

Khazaei, A., Gholami, F., Khakyzadeh, V., Moosavi-Zare, A. R., and Afsar, J. (2015). Magnetic Core-Shell Titanium Dioxide Nanoparticles as an Efficient Catalyst for Domino Knoevenagel-Michael-Cyclocondensation Reaction of Malononitrile, Various Aldehydes and Dimedone. *RSC Adv.* 5, 14305–14310. doi:10.1039/C4RA16300A

Kuo, S. C., Huang, L. J., and Nakamura, H. (1984). Studies on Heterocyclic Compounds. 6. Synthesis and Analgesic and Antiinflammatory Activities of 3,4-Dimethylpyrano[2,3-C]pyrazol-6-One Derivatives. *J. Med. Chem.* 27, 539–544. doi:10.1021/jm00370a020

Maleki, B., and Ashrafi, S. S. (2014). Nano α-Al_2O_3 Supported Ammonium Dihydrogen Phosphate ($NH_4H_2PO_4$/Al_2O_3): Preparation, Characterization and its Application as a Novel and Heterogeneous Catalyst for the One-Pot Synthesis of Tetrahydrobenzo[b]pyran and Pyrano[2,3-C]pyrazole Derivatives. *RSC Adv.* 4, 42873–42891. doi:10.1039/C4RA07813F

Maleki, B., Eshghi, H., Barghamadi, M., Nasiri, N., Khojastehnezhad, A., Sedigh Ashrafi, S., et al. (2016). Silica-coated Magnetic $NiFe_2O_4$ Nanoparticles-Supported H3PW12O40; Synthesis, Preparation, and Application as an Efficient, Magnetic, Green Catalyst for One-Pot Synthesis of Tetrahydrobenzo[b]pyran and Pyrano[2,3-C]pyrazole Derivatives. *Res. Chem. Intermed.* 42, 3071–3093. doi:10.1007/s11164-015-2198-8

Miyabe, H. (2017). "Organic Reactions Promoted by Metal-free Organic Dyes under Visible Light Irradiation," in *Visible-Light Photocatalysis of Carbon-Based Materials* (IntechOpen).

Mohamadpour, F. (2021e). A New Role for Photoexcited Na_2 Eosin Y as Direct Hydrogen Atom Transfer (HAT) Photocatalyst in Photochemical Synthesis of Dihydropyrano[2,3-C]pyrazole Scaffolds Promoted by Visible Light Irradiation under Air Atmosphere. *J. Photochem. Photobiol. A Chem.* 418 (2021e), 113428. doi:10.1016/j.jphotochem.2021.113428

Mohamadpour, F. (2021b). Catalyst-free and Solvent-free Visible Light Irradiation-Assisted Knoevenagel-Michael Cyclocondensation of Aryl Aldehydes, Malononitrile, and Resorcinol at Room Temperature. *Monatsh Chem.* 152, 507–512. doi:10.1007/s00706-021-02763-1

Mohamadpour, F. (2021a). Catalyst-free, Visible Light Irradiation Promoted Synthesis of Spiroacenaphthylenes and 1*H*-Pyrazolo[1,2-*B*]phthalazine-5,10-Diones in Aqueous Ethyl Lactate. *J. Photochem. Photobiol. A Chem.* 407, 113041. doi:10.1016/j.jphotochem.2020.113041

Mohamadpour, F. (2022a). Green Approach for Metal-free One-Pot Synthesis of Tetrahydrobenzo[*b*]pyrans with Sodium Alginate as a Reusable Bifunctional Biopolymeric Catalyst. *Organic Preparations. Proc. Int.* doi:10.1080/00304948.2022.2037369

Mohamadpour, F. (2021f). New Role for Photoexcited Organic Dye, Na2 Eosin Y via the Direct Hydrogen Atom Transfer (HAT) Process in Photochemical Visible-Light-Induced Synthesis of Spiroacenaphthylenes and 1H-Pyrazolo [1,2-B]phthalazine-5,10-Diones under Air Atmosphere. *Dyes Pigments* 194 (2021f), 109628. doi:10.1016/j.dyepig.2021.109628

Mohamadpour, F. (2021d). Photoexcited Na2 Eosin Y as Direct Hydrogen Atom Transfer (HAT) Photocatalyst Promoted Photochemical Metal-free Synthesis of Tetrahydrobenzo[b]pyran Scaffolds via Visible Light-Mediated under Air Atmosphere. *J. Taiwan Inst. Chem. Eng.* 129, 52–63. doi:10.1016/j.jtice.2021.09.017

Mohamadpour, F. (2021c). Synthesis of Pyran-Annulated Heterocyclic Systems Catalyzed by Theophylline as a Green and Bio-Based Catalyst. *Polycycl. Aromat. Compd.* 41, 160. doi:10.1080/10406638.2019.1575246

Mohamadpour, F. (2022c). The Development of Friedländer Heteroannulation through a Single Electron Transfer and Energy Transfer Pathway Using Methylene Blue (MB^+). *Sci. Rep.* 12. doi:10.1038/s41598-022-11349-8

Mohamadpour, F. (2022b). The Development of Imin-Based Tandem Michael-Mannich Cyclocondensation Through a Single-Electron Transfer (SET)/energy Transfer (EnT) Pathway in the Use of Methylene Blue (MB^+) as a Photo-Redox Catalyst. *RSC Adv.* 12 (2022b), 10701–10710. doi:10.1039/D2RA01190E

Mohammadi, A. A., Asghariganjeh, M. R., and Hadadzahmatkesh, A. (2017). Synthesis of Tetrahydrobenzo[b]pyran under Catalysis of $NH_4Al(SO_4)_2{\cdot}12H_2O$ (Alum). *Arabian J. Chem.* 10, S2213–S2216. doi:10.1016/j.arabjc.2013.07.055

Niknam, K., Borazjani, N., Rashidian, R., and Jamali, A. (2013). Silica-bonded N-Propylpiperazine Sodium N-Propionate as Recyclable Catalyst for Synthesis of 4H-Pyran Derivatives. *Chin. J. Catal.* 34, 2245–2254. doi:10.1016/S1872-2067(12)60693-7

Patel, R. I., Sharma, A., Sharma, S., and Sharma, A. (2021). Visible Light-Mediated Applications of Methylene Blue in Organic Synthesis. *Org. Chem. Front.* 8 (2021), 1694–1718. doi:10.1039/D0QO01182G

Pitre, S. P., McTiernan, C. D., and Scaiano, J. C. (2016). Understanding the Kinetics and Spectroscopy of Photoredox Catalysis and Transition-metal-free Alternatives. *Acc. Chem. Res.* 49, 1320–1330. doi:10.1021/acs.accounts.6b00012

Politano, F., and Oksdath-Mansilla, G. (2018). Light on the Horizon: Current Research and Future Perspectives in Flow Photochemistry. *Org. Process Res. Dev.* 22, 1045–1062. doi:10.1021/acs.oprd.8b00213

Rahnamafa, R., Moradi, L., and Khoobi, M. (2020). Rapid and Green Synthesis of 4H-Benzo[b]pyrans Using Triethanolamine as an Efficient Homogeneous Catalyst under Ambient Conditions. *Res. Chem. Intermed.* 46, 2109–2116. doi:10.1007/s11164-020-04081-3

Romero, N. A., Nicewicz, D. A., Lu, L. Q., and Xiao, W. J. (2016). Organic Photoredox Catalysis. *Chem. Rev.* 116, 10075–10166. doi:10.1021/acs.chemrev.6b00057

Saha, M., and Pal, A. K. (2012). Palladium (0) Nanoparticles: a Novel and Reusable Catalyst for the Synthesis of Various Pyran Derivatives, *Anp* 01, 61. doi:10.4236/anp.2012.13009

Tahmassebi, D., Bryson, J. A., and Binz, S. I. (2011). 1,4-Diazabicyclo[2.2.2]octane as an Efficient Catalyst for a Clean, One-Pot Synthesis of Tetrahydrobenzo[b]pyran Derivatives via Multicomponent Reaction in Aqueous Media. *Synth. Commun.* 41, 2701–2711. doi:10.1080/00397911.2010.515345

Tardivo, J. P., Del Giglio, A., De Oliveira, C. S., Gabrielli, D. S., Junqueira, H. C., Tada, D. B., et al. (2005). Methylene Blue in Photodynamic Therapy: From Basic Mechanisms to Clinical Applications. *Photodiagnosis Photodyn. Ther.* 2, 175–191. doi:10.1016/S1572-1000(05)00097-9

Verschueren, R. H., and De Borggraeve, W. M. (2019). Electrochemistry and Photoredox Catalysis: A Comparative Evaluation in Organic Synthesis. *Molecules* 24, 2122–2160. doi:10.3390/molecules24112122

Wainwright, M., and Crossley, K. B. (2002). Methylene Blue - a Therapeutic Dye for All Seasons? *J. Chemother.* 14, 431–443. doi:10.1179/joc.2002.14.5.431

Wang, J.-L., Liu, D., Zhang, Z.-J., Shan, S., Han, X., Srinivasula, S. M., et al. (2000). Structure-based Discovery of an Organic Compound that Binds Bcl-2 Protein and Induces Apoptosis of Tumor Cells. *Proc. Natl. Acad. Sci. U.S.A.* 97, 7124–7129. doi:10.1073/pnas.97.13.7124

Zhou, Z., Zhang, Y., and Hu, X. (2017). Efficient One-Pot Synthesis of Tetrahydrobenzo[b]pyrans by Ethylenediamine Diacetate-Catalyzed Multicomponent Reaction under Solvent-free Conditions, *Polycycl. Aromat. Compd.* 37, 39. doi:10.1080/10406638.2015.1088042

Zolfigol, M. A., Safaiee, M., and Bahrami-Nejad, N. (2016). Dendrimeric Magnetic Nanoparticle Cores with Co-phthalocyanine Tags and Their Application in the Synthesis of Tetrahydrobenzo[b]pyran Derivatives. *New J. Chem.* 40, 5071–5079. doi:10.1039/C6NJ00243A

Conflict of Interest: The author declares that the research was conducted in the absence of any commercial or financial relationships that could be construed as a potential conflict of interest.

Publisher's Note: All claims expressed in this article are solely those of the authors and do not necessarily represent those of their affiliated organizations, or those of the publisher, the editors, and the reviewers. Any product that may be evaluated in this article, or claim that may be made by its manufacturer, is not guaranteed or endorsed by the publisher.

Copyright © 2022 Mohamadpour. This is an open-access article distributed under the terms of the Creative Commons Attribution License (CC BY). The use, distribution or reproduction in other forums is permitted, provided the original author(s) and the copyright owner(s) are credited and that the original publication in this journal is cited, in accordance with accepted academic practice. No use, distribution or reproduction is permitted which does not comply with these terms.

frontiers | Frontiers in Chemistry

TYPE Mini Review
PUBLISHED 05 August 2022
DOI 10.3389/fchem.2022.944021

Check for updates

OPEN ACCESS

EDITED BY
Cosima Damiana Calvano,
University of Bari Aldo Moro, Italy

REVIEWED BY
Simone Vincenzi,
University of Padua, Italy

*CORRESPONDENCE
Serena Indelicato,
serena.indelicato@unipa.it

SPECIALTY SECTION
This article was submitted to Analytical Chemistry,
a section of the journal
Frontiers in Chemistry

RECEIVED 14 May 2022
ACCEPTED 30 June 2022
PUBLISHED 05 August 2022

CITATION
Bongiorno D, Avellone G, Napoli A, Mazzotti F, Piazzese D, Censi V and Indelicato S (2022), Determination of trace levels of organic fining agents in wines: Latest and relevant findings. *Front. Chem.* 10:944021.
doi: 10.3389/fchem.2022.944021

COPYRIGHT
© 2022 Bongiorno, Avellone, Napoli, Mazzotti, Piazzese, Censi and Indelicato. This is an open-access article distributed under the terms of the Creative Commons Attribution License (CC BY). The use, distribution or reproduction in other forums is permitted, provided the original author(s) and the copyright owner(s) are credited and that the original publication in this journal is cited, in accordance with accepted academic practice. No use, distribution or reproduction is permitted which does not comply with these terms.

Determination of trace levels of organic fining agents in wines: Latest and relevant findings

David Bongiorno[1], Giuseppe Avellone[1], Anna Napoli[2], Fabio Mazzotti[2], Daniela Piazzese[3], Valentina Censi[3] and Serena Indelicato[1]*

[1]Dipartimento Scienze e Tecnologie Biologiche Chimiche e Farmaceutiche (STEBICEF)—Università degli Studi di Palermo—via Archirafi, Palermo, Italy, [2]Dipartimento di Chimica e Tecnologie Chimiche, Università della Calabria Arcavacata di Rende, Calabria, Italy, [3]Dipartmento di Scienze della Terra e del Mare—Università degli Studi di Palermo—via Archirafi, Palermo, Italy

The production of red wine plays a key role in the local and international economies of several nations. During the winemaking process, to clarify the final product, before bottling, and to remove undesired substances (proteins, phenols, and tannins), fining agents are commonly added to wines. These substances have different origins (animal and vegetable proteins or mineral compounds), and they show a potential risk for the health of allergic subjects. For these reasons, the residues of fining agents, constituted by exogenous proteins based on gluten, egg, and milk proteins, should not be present in the final product and their trace residues should be quantified with accuracy. In the last decade, several analytical approaches have been developed for their quantitative determination using different sample treatment protocols and analytical techniques. These methods are based on liquid chromatography coupled with mass spectrometry or enzyme-linked immunosorbent assays (ELISAs). Recently, biosensors have been proposed as a potential alternative to immunoassay approaches, allowing rapid, cheap, and simple multi-residue detection. This short review aimed to report the most recent and relevant findings in the field.

KEYWORDS

fining agents, wine, mass spectrometry, ELISA: enzyme-linked immunosorbent assay, biosensors, allergens

Introduction

In winemaking, the term “fining” indicates a clarification step that implies the addition of substances (fining agents) deemed to reduce or remove some undesirable compounds that could give rise to unpleasing precipitates. The fining process also modifies the wines’ organoleptic characteristics, reduces astringency, and improves color and flavor. Fining agents are removed according to good manufacturing practices, but these substances are considered “processing aids” and should not be present in the final product. According to the FDA (2013), fining agents could not be reported on the wine label, if removed during the winemaking. But the permanence of

"exogenous" compounds in the final products must be evaluated, taking into account their origin (animal or vegetable proteins, mineral compounds) and mostly their potential consequence on the health of the consumer. As aforesaid, the arsenal of fining agents at disposal of the winemaker is quite ample, but the best results often require the adoption of synergistic action of many clarifiers. Among the non-proteic organic compounds used in beverage fining, polyvinylpolypyrrolidone (PVPP), reported as generally recognized as safe (GRAS) and approved for many uses by the FDA, is particularly useful as it is capable of removing flavans and phenols (Ronnau et al., 2000; Adachi et al., 2003; Yoshida et al., 2008). PVPP, by removing phenols, also lowers the bitterness and prevents oxidative browning in white wines. As a collateral effect, PVPP depletes resveratrol (Threlfall et al., 1999) and quercetin (Laborde et al., 2006) commonly associated with the healthy effect of moderate wine consumption (Castellari et al., 1998). The adoption of proteic clarifiers, while preserving most of the healthy substances, can represent a risk for hypersensitive consumers, even if the literature seems to indicate the inconsistency of an allergological risk. Indeed, while proteinaceous fining agents are used to obtain the tannin precipitation, the formation of soluble complexes between tannins and proteins takes place. These complexes can remain in the solution even in correctly processed fined wines. According to Maury et al. (2019), in a study involving the preparation of a model wine, fined with radio-labeled proteins (gelatin or wheat gluten protein), their residue amounted from 24% to 58% of the initial fining proteins added. Finally, the use of animal proteins could also entail ethical or religious concerns, such as vegetarianism or veganism, or religious faith. For this reason, since 31 May 2009, the EU Directive 2007/68/EC established that all wines must declare on the label if proteic allergens have been used during wine production. Similar regulations on the use of eggs, milk, and fish derivatives (isinglass) as clarifiers of wines and stabilizers have also been enacted in other countries such as the United States, New Zealand, and Australia. However, showing these warnings on the label could reduce the attractiveness of the product and potentially damage the perception of its quality.

Classification of protein-based fining agents used in winemaking

Several fining agents are of proteic nature (Marangon et al., 2019), and we can find animal or plant proteins. The former are frequently obtained from collagen (i.e., bovine and porcine gelatin) (Hrazdina et al., 1969; Oberholster et al., 2013), fish gelatin and isinglass (Sanborn et al., 2010), milk (caseinates) (Weber et al., 2009), and white egg (ovalbumin). Among plant proteins, we consider those derived from cereals (Simonato et al., 2009; Iturmendi et al., 2010; Simonato et al., 2011; Simonato et al., 2013), legumes (Granato et al., 2018), grape seeds, potatoes (Gambuti et al., 2012; Gambuti et al., 2016), and seaweeds (Noriega-Domínguez et al., 2010).

Since 2000, several food production protocols have been modified due to the spread of bovine spongiform encephalopathy. Winemaking was no exception, and some of the fining agents of animal origin (bovine proteins) have been abandoned. Consequently, among clarifying agents, porcine gelatin remained the most commonly used protein (Sarni-Manchado et al., 1999; Maury et al., 2001; Smith et al., 2015).

The gelatin (from pig and fish) at low pH gives rise to colloidal particles that, being positively charged, interact with negatively charged particles, originating sediments. Among the fish gelatins, isinglass is very pure gelatin, prepared from the air bladders or, more recently, from other fish tissues (Rizzi et al., 2016).

On the other hand, caseins, which are phosphoproteins obtained from milk, contain sequences of hydrophilic and hydrophobic amino acids, which confer an amphiphilic nature to these fining agents. At the pH of the wine, caseins in association with sodium or potassium form insoluble micelles, which leads to coagulation and sedimentation of the interacting substances (Weber et al., 2007a). In addition, caseins lead to the formation of insoluble complexes with phenolic compounds from grapes and allow removing the excess tannin in over-oaked white wines (Weber et al., 2009; Cosme et al., 2012).

Egg proteins are largely used as clarifying agents due to their ability to bind and reduce tannin content (Cosme et al., 2007; Rizzi et al., 2016). As fish gelatins, they are positively charged and form aggregates with the negatively charged particles of wines. The lysozyme, another egg protein, shows antimicrobial activity against Gram-positive bacteria and, thus, is used as a stabilizer for better control of the fermentation process and against wine spoilage (Weber et al., 2007a). As an alternative to animal proteins, those derived from legumes (pea, lentils, and soy), wheat gluten, and oenological yeast protein extracts (Gaspar et al., 2019) can be used for fining purposes (Marangon et al., 2019).

This notwithstanding, some of them still represent a potential risk to the health of allergic subjects, and therefore have to be traced in the final product. Simonato et al. (2009; 2013) reported that Patatin P (Gambuti et al., 2012) and maize zeins could be used as fining agents. Patatin P, which belongs to glycoproteins, is obtained from a potato aqueous by-product, and it could represent a vegetable-based clarifying agent, with the same properties of animal protein used in winemaking. Maize zeins, extracted from the "corn gluten," plays a good role as a processing aid in winemaking and has the advantage of not requiring a label declaration (European Commission. Directive 2003/89/EC; European Commission. Directive 2007/68/EC).

Cosme et al. (2012) and Kang et al. (2018) investigated a possible application of rice proteins as clarifying agents with properties similar to caseinates for white and rosè wines and gelatin for red wines.

More recently, grape seed proteins have been tested as clarifiers (Vincenzi et al., 2013; Gazzola et al., 2017). These substances overcome the allergological risk related to the use of exogenous proteins during winemaking because the grape seed proteins are considered endogenous components of wine. Finally, Pino Ramos et al. (2022) have studied the fining ability of quinoa proteins as an alternative to animal proteins (i.e., gelatin).

Analytical approaches for identifying exogenous protein in wines

The lack of stringent regulation related to the use of fining agents for the winemaking process and the possibility of adopting proteic clarifiers determines the possible persistence of exogenous proteins in the final product. Therefore, to evaluate their presence and to overcome allergological or food ethics problems, sensitive and accurate detection methods have been developed. Indeed, in the last decade, immunochemical assays, mass spectrometry (MS)-based analytical determinations, and biosensors have been applied to inform allergic consumers about the potential presence of allergens.

Immunochemical assays

The enzyme-linked immunosorbent test (ELISA) represents a useful tool for the detection of exogenous protein residues in wine. It is characterized by easy execution, low cost, rapidity, and good sensitivity. ELISA tests are capable of detecting contamination of egg white, casein, and gluten, and are also useful for identifying and quantifying gelatins. The drawbacks in ELISAs come from the complexity of matrix composition, which can inhibit the immuno-enzymatic reaction (Koestel et al., 2016).

In addition, due to the absorption on the membrane surfaces, and the low pH value of wine and the content of tannins, the ability to interact with proteins in some epitopes could change, causing alterations, impairing sensitivity, or leading to false negatives or to partial responses (Kaul et al., 2007).

Weber et al. (2007a) reported LOD values, in the order of 0.005 μg/ml for the fish gelatin and lysozyme assays, that were complying with the Organisation Internationale de la Vigne et du Vin (OIV, Paris, France requests (values ≤ 0.25 μg/ml)), but not satisfying for other clarifying agents. Deckwart et al. (2014), using an indirect ELISA approach for investigating wine samples, obtained LOD values of caseins in the order of 0.2 μg/ml for red wines, while for white wines, the values ranged from 0.01 μg/ml to 0.1 μg/ml. Different sample pretreatments, based on immunochemical assays, have been proposed to determine various types of exogenous proteins in several commercial wines. Weber et al. (2007b) analyzed four white wines made in Germany, and after a dilution in the ratio of 1:10 in phosphate-buffered saline solution, it was possible to detect lysozyme residues in all of them. Egg albumin was found in just one wine that was refined with a high dosage of dried egg white (20 g/hl). Rolland et al. (2008) tested 153 commercial Australian wines, using a different sample pretreatment for white or red wine. The former was dialyzed (3.5 kDa cutoff) in SnakeSkin pleated dialysis tubing; the latter was simply diluted 1:4 in ethanol; no residual milk or egg proteins were found. Restani et al. (2012) analyzed 63 commercial wines (all filtered through membranes having a pore size of 1 μm) and 16 experimental wines treated with milk proteins (filtered through membranes having a pore size of 3 μm) using both ELISA and immunoblotting techniques, incubating the membranes with specific anti-caseinate antibodies. The authors did not find any detectable protein residue in the wines. Uberti et al. (2014), adopting the same pretreatment approach as Restani et al. (2012), investigated 78 commercial red wines from Australia, New Zealand, and Europe, reporting the oenological practices adopted and the corresponding level of egg white protein residues. The authors did not find egg proteins (LOD 0.0564 μg/ml), despite the wide range of doses (3–10 g/hl) used for refining. Simonato et al. (2011) precipitated wine proteins by means of the KDS method, originally proposed by Vincenzi et al. (2005), which involves protein complexation with dodecyl sulfate, followed by a precipitation step of complexes as potassium salts. They reported that wheat protein residues were detectable only in wines treated with massive gluten amounts (>50 g/hl), far higher than those usually employed in winemaking protocols. Zeleňáková et al. (2021) reported the identification of cow milk allergen in 17 wine samples (vintage 2014–2017) originating from Slovenia. The LOD was 0.24 μg/ml and the LOQ was 1.30 μg/ml. The sample treatment was very quick and easy: the extraction buffer solution (10 ml) was added to 1.00 ml of wine; the sample, maintained under continuous shaking for 5 min, was centrifuged; and the supernatant was sampled for the ELISA test. The findings showed the casein concentrations ranged from 1.634 to 16.715 μg/ml for white wines and from 21.473 to 67.22 μg/ml for red ones.

MS-based methods

As reported elsewhere (Monaci et al., 2010; Maury et al., 2019), the drawbacks of immunochemical assays are mostly related to the formation of soluble protein–tannin complexes, which are not removed by filtration and potentially not recognized by ELISA antibodies. MS-based approaches are far less selective but extremely sensitive, and make it possible to determine an ample collection of molecules ranging from contaminants, antioxidants, polymers, surfactants, and proteins (Indelicato et al., 2016a; Di Donna et al., 2017; Aiello et al., 2020; Bongiorno et al., 2021). MS allows the detection at trace levels of fining agent residues while their identification is

independent of the structure of allergens (Kaul et al., 2007; Kirsch et al., 2009; Picariello et al., 2011).

Tolin et al. (2012a), Tolin et al. (2012b), based on the same analytical approach as Simonato et al. (2011), scrutinized several commercial wines to ascertain the presence of animal protein residues. The nano-liquid chromatography (LC) tandem mass spectrometry (MS/MS) analytical strategy allowed the determination of ovalbumin and caseins at levels of about 100 ng/L and 60 ng/L of wine, respectively. Using this approach, the authors overcome the limitations of classical immunological methods, gaining sensitivity and eliminating the problems affecting immunoassays that rely on the labile tertiary structure of proteins (Kaul et al., 2007) for protein recognition and reactivity.

Monaci et al. (2013) developed an interesting approach based on isotopically labeled peptides of ovalbumin and α S1–casein to determine egg proteins and caseinates in white wine samples. This approach allowed to fairly estimate and take into account tryptic digestion yields in the analytical procedure. Good LODs were also achieved, ranging between 0.4 and 1.1 μg/ml (depending on the peptide considered as a marker of the fining agent). In order to reduce the analysis costs, Losito et al. (2013) proposed an approach for the determination of caseinate residues in refined white wines using LC coupled with a 3D ion trap mass spectrometer. The optimization of an appropriate wine volume and a protein extraction/digestion protocol, followed by MS/MS analysis performed on an ion trap instrument, provided a good sensitivity (LOD lower than 0.25 μg/ml) complying with the request of OIV, which represents the reference value in the current European legislation.

Another research aspect being pursued is the continuous refinement of the wine sample pretreatment. With this goal, Mattarozzi et al. (2014) proposed an LC-MS/MS method for the simultaneous determination of α-, β-casein, and ovalbumin in commercial red wine after a thorough evaluation of different sample treatments. According to the authors, among the most widely adopted strategies involving the use of denaturing agents, protein precipitation, cutoff filters, or size exclusion purification cartridges, the size exclusion-based procedure provided the best performance in terms of both accuracy (recovery) and precision. The validated LC-MS/MS method has proven sensitive enough to identify and quantify allergens in red wine protein extracts at trace levels, with LODs and LOQs values ranging from 0.01 to 0.8 μg/ml and from 0.03 to 2 μg/ml, respectively. De Angelis et al. (2017) succeeded in the upgrade of an analytical workflow based on the use of pre-enrichment columns. The sample clean-up was based on either size exclusion columns (SEC) or cut-off filters (UF), followed by selective peptide enrichment on a 1-cm-long C-18 trap column. It was found that the SEC-based procedure provided faster analyses, but the lengthier UF was the most sensitive approach, resulting in LODs and LOQs of 0.036 and 0.12 μg/ml for egg and 0.050 and 0.17 μg/ml for milk, respectively. Pilolli et al. (2014) evaluated two MS-based approaches: LC- high resolution (HR) MS and LC-MS/MS. These two approaches usually have different applications (Di Stefano et al., 2012; Indelicato et al., 2016b), but have proven to be equally well-suited for quantification and screening purposes. As can be foreseen, the main advantage of HR-MS lies in the open possibility of retrospective analysis. On the other hand, the MS/MS method was more sensitive to analytes and less sensitive to matrix. The same authors developed a new approach based on the integration of mass spectrometry and immunoassay (MSIA) (Pilolli et al., 2017) to detect egg allergens. Polyclonal antibodies raised against native ovalbumin were immobilized onto MSIA-customized disposable tips. The protocol implied a 1:4 dilution of the wine sample, an automated purification/enrichment step on MSIA, followed by tryptic digestion and LC-MS/MS determination. LOD and LOQ values obtained were 0.01 and 0.03 μg/ml, respectively.

The development of LC-MS/MS methods for the detection of caseins, albumin, and lysozyme in wines brought more refined approaches capable of increasing sensitivity and reducing analysis time, as reported by Rodrigues Spinelli et al. (2021). The authors claimed recovery values ranging from 90.7% to 108.6% introducing a pH adjustment, the use of cellulose ester membranes, precipitation with organic solvents, and a final concentration/clean-up. The LOQ values ranged from 0.01 to 0.25 μg/ml. Pig gelatin and egg white proteins have been determined in 5-year aged Nebbiolo-based red wine by Restani et al. (2014) and Dal Bello et al. (2021). Biomarker peptides were detected and quantified by a nano LC-HR-MS method.

Yang et al. (2021) have recently developed an LC-MS/MS method to quantify ovalbumin, ovotransferrin, β–lactoglobulin, and 4 caseins (α S1-, α S2-, β-, and κ–casein). The authors optimized the clean-up procedure for wine samples using an extraction treatment by a PVPP solution, trypsin digestion of proteins followed by peptide purification on HLB SPE cartridges to remove buffers, digest reagents, other matrix components, and interfering peptides. This article reported a standard addition strategy to quantify the wine allergens. The LODs for egg allergens were 0.1 μg/ml and for milk allergens 0.003–0.015 μg/ml, showing high sensitivity, simple clean-up procedure, and a reduction of costs for this approach.

Since MS approaches become increasingly customary, it has started to appear in literature articles dealing with the investigation of a large number of wine samples to detect and quantify exogenous protein residues. Jessy Pavón-Pérez et al. (2019) analyzed white and red wines from four different grape varieties produced by 14 Chilean wineries. This approach to determining casein and ovalbumin is based on ultrafiltration membranes, protein precipitation with organic solvents, followed by a fast (7 h) enzymatic digestion. The LOD and LOQ achieved

using an LC-MS/MS approach ranged from 4.70 to 8.50 μg/L and 10 to 20 μg/L, respectively.

Biosensors

Since the ELISA approach is somewhat doubtful as far as it concerns false negatives or positives (Lacorn et al., 2011), and the MS approach requires pricey instrumentation and more specialized operators, it was reasonable to expect the development of simpler and still reliable approaches to determine protein residues in wines. Up to date, several electrochemical biosensors have been proposed for the detection of food allergens (lysozyme, ovalbumin, caseins, and lactoglobulin) (Vasilescu et al., 2016), but only a few of them have been tested on wines (Ocaña et al., 2015; Mihai et al., 2015; Pilolli et al., 2015; Wessels and Paschke-Kratzin, 2016; Titoiu et al., 2019). The recent availability of several aptamer sequences, specifically synthesized for lysozyme capture, prompted the development of several sensors for the detection of lysozyme in wines (Mihai et al., 2015; Ocaña et al., 2015; Titoiu et al., 2019). Aptamers are short oligonucleotide or peptide sequences that are more stable with respect to antibodies, with the further advantage of reduced production costs. The LOD values for such biosensors range from few ppt to ppm levels (Vasilescu et al., 2016). On the other hand, Pilolli et al. (2015) and Pilolli and Monaci (2016) worked on the development of a surface plasmon resonance (SPR)-based biosensor to detect egg-related fining allergens. The same group refined the approach (2016) in order to increase the sensitivity while still maintaining the speed and easy sample handling of the sensor-based instrumentation. Indeed, wine samples were subjected to a very short pretreatment by PVP/SEC purification steps that allowed reaching a LOD of up to 0.2 μg/ml. Recently, Baldo et al. (2021) and Rodrigues Spinelli et al. (2021) described the combination of a disposable electrochemical device with magnetic beads, delivering an ultrasensitive detection of the egg allergen ovalbumin in wines. The approach leads to a LOD of 0.2 fg/ml within a wide linear range of concentration from 0.01 to 10 pg/ml (European Commission, 2003; European Commission, 2007).

Conclusion

The determination of protein residues in wines remains a strong topic in the current research. While early applications relied on the more economical ELISA approach, in recent years, HPLC/MS has gained new ground due to a lower risk of false positives and substantial sensitivity improvements. These improvements, however, do not come cheap since the quantitative determination of protein residues in wines is complicated by several steps of sample treatment, analyte recoveries, and ionization efficiency of the peptides quantified. Thus, in order to reduce costs and improve determination time, recently, some sensor-based applications have started to appear. In wines, their application is actually limited to lysozyme and ovalbumin detection, but it is foreseeable that their wide-spread use will obtain reliable results at very reasonable costs since their development is rapidly gaining momentum.

Author contributions

SI and DB: topic choice, paper definition, literature selection, manuscript editing, and supervision. DP, AN, GA, FM and VC: literature selection and manuscript editing.

Conflict of interest

The authors declare that the research was conducted in the absence of any commercial or financial relationships that could be construed as a potential conflict of interest.

Publisher's note

All claims expressed in this article are solely those of the authors and do not necessarily represent those of their affiliated organizations, or those of the publisher, the editors, and the reviewers. Any product that may be evaluated in this article, or claim that may be made by its manufacturer, is not guaranteed or endorsed by the publisher.

References

Adachi, A., Fukunaga, A., Hayashi, K., Kunisada, M., and Horikawa, T. (2003). Anaphylaxis to polyvinylpyrrolidone after vaginal application of povidone-iodine. *Contact Dermat.* 48, 133–136. doi:10.1034/j.1600-0536.2003.00050.x

Aiello, D., Siciliano, C., Mazzotti, F., Di Donna, L., Risoluti, R., Napoli, A., et al. (2020). Protein extraction, enrichment and MALDI MS and MS/MS analysis from bitter orange leaves (*Citrus aurantium*). *Molecules* 25, 1485. doi:10.3390/molecules25071485

Baldo, T. A., dos Anjos Proença, C., da Silva Felix, F., Freitas, T. A., Sakata, S. K., Angnes, L., et al. (2021). Disposable electrochemical microfluidic device for ultrasensitive detection of egg allergen in wine samples. *Talanta* 232, 122447. doi:10.1016/j.talanta.2021.122447

Bongiorno, D., Di Stefano, V., Indelicato, S., Avellone, G., and Ceraulo, L. (2021). Bio-phenols determination in olive oils: Recent mass spectrometry approaches. *Mass Spectrom. Rev.*, e21744. doi:10.1002/mas.21744

Castellari, M., Spinabelli, U., Riponi, C., and Amati, A. (1998). Influence of some technological practices on the quantity of resveratrol in wine. *Eur. Food Res. Technol.* 206, 151–155. doi:10.1007/s002170050232

Cosme, F., Capao, I., Filipe-Ribeiro, L., Bennett, R. N., and Mendes-Faia, A. (2012). Evaluating potential alternatives to potassium caseinate for white wine fining: Effects on physicochemical and sensory characteristics. *LWT - Food Sci. Technol.* 46, 382–387. doi:10.1016/j.lwt.2011.12.016

Cosme, F., Ricardo-da-Silva, J. M., and Laureano, O. (2007). Protein fining agents: Characterization and red wine fining assays. *Ital. J. Food Sci.* 19, 39–56.

Dal Bello, F., Lamberti, C., Giribaldi, M., Garino, C., Locatelli, M., Gastaldi, D., et al. (2021). Multi-target detection of egg-white and pig gelatin fining agents in Nebbiolo-based aged red wine by means of nanoHPLC-HRMS. *Food Chem. x.* 345, 128822. doi:10.1016/j.foodchem.2020.128822

De Angelis, E., Pilolli, R., and Monaci, L. (2017). Coupling SPE on-line pre-enrichment with HPLC and MS/MS for thesensitive detection of multiple allergens in wine. *Food control.*. 73, 814–820. doi:10.1016/j.foodcont.2016.09.031

Deckwart, M., Carstens, C., Webber-Witt, M., Schafer, V., Eichhorn, L., Kang, S., et al. (2014). Development of a sensitive ELISA for the detection of casein-containing fining agents in red and white wines. *J. Agric. Food Chem.* 62, 6803–6812. doi:10.1021/jf5006098

Di Donna, L., Taverna, D., Indelicato, S., Napoli, A., Sindona, G., Mazzotti, F., et al. (2017). Rapid assay of resveratrol in red wine by paper spray tandem mass spectrometry and isotope dilution. *Food Chem. x.* 229, 354–357. doi:10.1016/j.foodchem.2017.02.098

Di Stefano, V., Avellone, G., Bongiorno, D., Cunsolo, V., Muccilli, V., Sforza, S., et al. (2012). Applications of liquid chromatography-mass spectrometry for food analysis. *J. Chromatogr. A* 12 (1259), 74–85. doi:10.1016/j.chroma.2012.04.023

European Commission (2003). Directive 2003/89/EC of the European Parliament and of the Council of 10 November 2003 amending Directive 2000/13/EC as regards indication of the ingredients present in foodstuffs. *Off. J. Eur. Union* 308, 15–18.

European Commission (20072007). Directive 2007/68/EC of 27 november 2007 amending annex IIIa of the directive2001/13/EC of the European parliament and of the council as regards certain food ingredients. *Off. J. Eur. Union* 310, 15–18.

Gambuti, A., Rinaldi, A., and Moio, L. (2012). Use of patatin, a protein extracted from potato, as alternative to animal proteins in fining of red wine. *Eur. Food Res. Technol.* 235, 753–765. doi:10.1007/s00217-012-1791-y

Gambuti, A., Rinaldi, A., Romano, R., Manzo, N., and Moio, L. (2016). Performance of a protein extracted from potatoes for fining of white mustsfining of white musts. *Food Chem. x.* 190, 237–243. doi:10.1016/j.foodchem.2015.05.067

Gaspar, L. M., Machado, A., Coutinho, R., Sousa, S., Santos, R., Xavier, A., et al. (2019). Development of potential yeast protein extracts for red wine clarification and stabilization. *Front. Microbiol.* 10, 2310. doi:10.3389/fmicb.2019.02310

Gazzola, D., Vincenzi, S., Marangon, M., Pasini, G., and Curioni, A. (2017). Grape seed extract: The first protein-based fining agent endogenous to grapesfirst protein-based fining agent endogenous to grapes. *Aust. J. Grape Wine Res.* 23, 215–225. doi:10.1111/ajgw.12268

Granato, T. M., Ferranti, P., Iametti, S., and Bonomi, F. (2018). Affinity and selectivity of plant proteins for red wine components relevant to color and aroma traitsffinity and selectivity of plant proteins for red wine components relevant to color and aroma traits. *Food Chem. x.* 256, 235–243. doi:10.1016/j.foodchem.2018.02.085

Hrazdina, G., Van Buren, J. P., and Robinson, W. B. (1969). Influence of molecular size of gelatin on reaction with tannic acid. *Am. J. Enol. Vitic.* 20, 66–68.

Indelicato, S., Bongiorno, D., Ceraulo, L., Calabrese, V., Piazzese, D., Napoli, A., et al. (2016a). Electrospray ion mobility mass spectrometry of positively and negatively charged (1*R*, 2*S*)-dodecyl(2-hydroxy-1-methyl-2-phenylethyl) dimethylammonium bromide aggregates. *Rapid Commun. Mass Spectrom.* 30, 230–238. doi:10.1002/rcm.7422

Indelicato, S., Bongiorno, D., Turco Liveri, V., Calabrese, V., Indelicato, S., Piazzese, D., et al. (2016b). Collision induced fragmentations of multiply charged sodium bis(2-ethylhexyl)-sulfosuccinate aggregates in gas phase: Neutral loss versus charge separation. *Int. J. Mass Spectrom.* 409, 29–37. doi:10.1016/j.ijms.2016.09.014

Iturmendi, N., Durán, D., and Marín-Arroyo, M. R. (2010). Fining of red wines with gluten or yeast extract protein. *Int. J. Food Sci. Technol.* 45, 200–207. doi:10.1111/j.1365-2621.2009.02121.x

Kang, W., Niimi, J., and Bastian, S. E. P. (2018). Reduction of red wine astringency perception using vegetable protein fining agentsfining agents. *Am. J. Enol. Vitic.* 69, 22–31. doi:10.5344/ajev.2017.17054

Kaul, S., Luttkopf, D., Kastner, B., Vogel, L., Holtz, G., Vieths, S., et al. (2007). Mediator release assays based on human or murine immunoglobulin E in allergen standardization. *Clin. Exp. Allergy* 37, 141–150. doi:10.1111/j.1365-2222.2006.02618.x

Kirsch, S., Fourdrilis, S., Dobson, R., Scippo, M. L., Maghuin-Rogister, G., De Pauw, E., et al. (2009). Quantitative methods for food allergens: A review. *Anal. Bioanal. Chem.* 395, 57–67. doi:10.1007/s00216-009-2869-7

Koestel, C., Simonin, C., Belcher, S., and Rösti, J. (2016). Implementation of an Enzyme Linked Immunosorbent Assay for the quantification of allergenic egg residues in red wines using commercially available antibodies. *J. Food Sci.* 81 (8), 2099–2106. doi:10.1111/1750-3841.13378

Laborde, B., Moine-Ledoux, V., Richard, T., Saucier, C., Dubourdieu, D., Monti, J. P., et al. (2006). PVPP-Polyphenol complexes: A molecular approach. *J. Agric. Food Chem.* 54, 4383–4389. doi:10.1021/jf060427a

Lacorn, M., Gossewein, C., and Immer, U. (2011). Determination of residual egg white proteins in red wines during and after fining. *Am. J. Enol. Vitic.* 62, 382–385. doi:10.5344/ajev.2011.10037

Losito, I., Introna, B., Monaci, L., Minella, S., and Palmisano, F. (2013). Development of a method for the quantification of caseinate traces in italian commercial white wines based on liquid chromatography–electrospray ionization–ion trap–mass spectrometry. *J. Agric. Food Chem.* 61, 12436–12444. doi:10.1021/jf4034909

Marangon, M., Vincenzi, S., and Curioni, A. (2019). Wine fining with plant proteins. *Molecules* 24 (11), 2186. doi:10.3390/molecules24112186

Mattarozzi, M., Milioli, M., Bignardi, C., Elviri, L., Corradini, C., Careri, M., et al. (2014). Investigation of different sample pre-treatment routes for liquid chromatography–tandem mass spectrometry detection of caseins and ovalbumin in fortified red winefied red wine. *Food control.*. 38, 82–87. doi:10.1016/j.foodcont.2013.10.015

Maury, C., Sarni-Manchado, P., and Cheynier, V. (2019). Highlighting protein fining residues in a model red wine. *Food Chem. x.* 279, 272–278. doi:10.1016/j.foodchem.2018.11.141

Maury, C., Sarni-Manchado, P., Lefebvre, S., Cheynier, V., and Moutounet, M. (2001). Influence of fining with different molecular weight gelatins on proanthocyanidin composition and perception of wines. *Am. J. Enol. Vitic.* 52, 140–145.

Mihai, I., Vezeanu, A., Polonschii, C., Albu, C., Radu, G. L., Vasilescu, A., et al. (2015). Label-free detection of lysozyme in wines using an aptamer based biosensor and SPR detection. *Sensors Actuators B Chem.* 206, 198–204. doi:10.1016/j.snb.2014.09.050

Monaci, L., Losito, I., De Angelis, E., Pilolli, R., and Visconti, A. (2013). Multi-allergen quantification of fining-related egg and milk proteins in white wines by high-resolution mass spectrometryfication of fining-related egg and milk proteins in white wines by high-resolution mass spectrometry. *Rapid Commun. Mass Spectrom.* 27, 2009–2018. doi:10.1002/rcm.6662

Monaci, L., Losito, I., Palmisano, F., and Visconti, A. (2010). Identification of allergenic milk proteins markers in fined white wines by capillary liquid chromatography-electrospray ionization-tandem mass spectrometry. *J. Chromatogr. A* 1217, 4300–4305. doi:10.1016/j.chroma.2010.04.035

Noriega-Domínguez, M. J., Durán, D. S., Vírseda, P., and Marín-Arroyo, M. R. (2010). Non-animal proteins as clarifying agents for red wines. *OENO One* 44, 179. doi:10.20870/oeno-one.2010.44.3.1472

Oberholster, A., Carstens, L. M., and du Toit, W. J. (2013). Investigation of the effect of gelatine, egg albumin and cross-flow microfiltration on the phenolic composition of Pinotage wineffect of gelatine, egg albumin and cross-flow microfiltration on the phenolic composition of Pinotage wine. *Food Chem. x.* 138, 1275–1281. doi:10.1016/j.foodchem.2012.09.128

Ocaña, C., Hayat, A., Mishra, R., Vasilescu, A., del Valle, M., and Marty, J. L. (2015). A novel electrochemicalaptamer–antibody sandwich assay for lysozyme detection. *Analyst* 140, 4148–4153. doi:10.1039/C5AN00243E

Pavón-Pérez, J., Henriquez-Aedo, K., and Aranda, M. (2019). Mass spectrometry determination of fining-related allergen proteins in Chilean wines. *Food Anal. Methods* 12, 827–837. doi:10.1007/s12161-018-01416-0

Picariello, G., Mamone, G., Addeo, F., and Ferranti, P. (2011). The frontiers of mass spectrometry-based techniques in food allergenomics. *J. Chromatogr. A* 1218, 7386–7398. doi:10.1016/j.chroma.2011.06.033

Pilolli, R., Chaudhari, R., Palmisano, F., and Monaci, L. (2017). Development of a mass spectrometry immunoassay for unambiguous detection of egg allergen traces in wines. *Anal. Bioanal. Chem.* 409, 1581–1589. doi:10.1007/s00216-016-0099-3

Pilolli, R., De Angelis, E., Godula, M., Visconti, A., and Monaci, L. (2014). Orbitrap™ monostage MS versus hybrid linear ion trap MS: Application to multi-allergen screening in wine. *J. Mass Spectrom.* 49, 1254–1263. doi:10.1002/jms.3453

Pilolli, R., and Monaci, L. (2016). Challenging the limit of detection for egg allergen detection in red wines by surface plasmon resonance biosensor. *Food Anal. Methods* 9, 2754–2761. doi:10.1007/s12161-016-0464-z

Pilolli, R., Visconti, A., and Monaci, L. (2015). Rapid and label-free detection of egg allergen traces in wines by surface plasmon resonance biosensor. *Anal. Bioanal. Chem.* 407, 3787–3797. doi:10.1007/s00216-015-8607-4

PinoRamos, L. L., PeñaMartínez, P. A., and Laurie, V. F. (2022). Quinoa protein extract: An effective alternative for the fining of wine phenolics. *J. Sci. Food Agric.*. doi:10.1002/jsfa.11982

Restani, P., Uberti, F., Tarantino, C., Ballabio, C., Gombac, F., Bastiani, E., et al. (2014). Collaborative interlaboratory studies for the validation of ELISA methods for the detection of allergenic fining agents used in wine according to the criteria of OIV resolution 427 – 2010 modified by OIV – comex 502 – 2012. *Food Anal. Methods* 7, 706–712. doi:10.1007/s12161-013-9741-2

Restani, P., Uberti, F., Tarantino, C., Ballabio, C., Gombac, F., Bastiani, E., et al. (2012). Validation by a collaborative interlaboratory study of an ELISA method for the detection of caseinate used as a fining agent in wine. *Food Anal. Methods* 5, 480–486. doi:10.1007/s12161-011-9270-9

Rizzi, C., Mainente, F., Pasini, G., and Simonato, B. (2016). Hidden exogenous proteins in wine: Problems, methods of detection and related legislation – a review. *Czech J. Food Sci.* 34, 93–104. doi:10.17221/357/2015-CJFS

Rodrigues Spinelli, F., Drehmerab, A. P., Valentin, L., Nascimento, S., Baptistã, M., Vanderlinde, R., et al. (2021). Development of a sample preparation approach for the analysis of fining agents in wines by liquid chromatography with tandem mass spectrometry. *Food Chem. x.* 350, 129198. doi:10.1016/j.foodchem.2021.129198

Rolland, J. M., Apostolou, E., De Leon, M. P., Stockley, C. S., and O' Hehir, R. E. (2008). Specific and sensitive enzyme-linked immunosorbent assays for analysis of residual allergenic food proteins in commercial bottled wine fined with egg white, milk, and nongrape-derived tannins. *J. Agric. Food Chem.* 56, 349–354. doi:10.1021/jf073330c

Ronnau, A. C., Wulferink, M., Gleichmann, E., Unver, E., Ruzicka, T., Krutmann, J., et al. (2000). Anaphylaxis to polyvinylpyrrolidone in an analgesic preparation. *Br. J. Dermatol.* 143, 1055–1058. doi:10.1046/j.1365-2133.2000.03843.x

Sanborn, M., Edwards, C. G., and Ross, C. F. (2010). Impact of fining on chemical and sensory properties of Washington State Chardonnay and Gewürztraminer wines. *Am. J. Enol. Vitic.* 61, 31–41.

Sarni-Manchado, P., Deleris, A., Avallone, S., Cheynier, V., and Moutounet, M. (1999). Analysis and characterization of wine condensed tannins precipitated by proteins used as fining agent in enology. *Am. J. Enol. Vitic.* 50, 81–86.

Simonato, B., Mainente, F., Selvatico, E., Violoni, M., and Pasini, G. (2013). Assessment of the fining efficiency of zeins extracted from commercial corn gluten and sensory analysis of the treated wine. *LWT - Food Sci. Technol.* 54, 549–556. doi:10.1016/j.lwt.2013.06.029

Simonato, B., Mainente, F., Suglia, I., Curioni, A., and Pasini, G. (2009). Evaluation of fining efficiency of corn zeins in red wine: A preliminary study. *Ital. J. Food Sci.* 21, 97–105.

Simonato, B., Mainente, F., Tolin, S., and Pasini, G. (2011). Immunochemical and mass spectrometry detection of residual proteins in gluten fined red wine. *J. Agric. Food Chem.* 59, 3101–3110. doi:10.1021/jf104490z

Smith, P. A., McRae, J. M., and Bindon, K. A. (2015). Impact of winemaking practices on the concentration and composition of tannins in red wine. *Aust. J. Grape Wine Res.* 21, 601–614. doi:10.1111/ajgw.12188

Threlfall, R. T., Morri, s. J. R., and Mauromoustakos, A. (1999). Effects of fining agents on trans-resveratrol concentration in wine. *Aust. J. Grape Wine Res.* 5, 22–26. doi:10.1111/j.1755-0238.1999.tb00147.x

Titoiu, A. M., Porumb, R., Fanjul-Bolado, P., Epure, P., Zamfir, M., and Vasilescu, A. (2019). Detection of allergenic lysozyme during winemaking with an electrochemical aptasensor. *Electroanalysis* 31, 2262–2273. doi:10.1002/elan.201900333

Tolin, S., Pasini, G., Curioni, A., Arrigoni, G., Masi, A., Mainente, F., et al. (2012b). Mass spectrometry detection of egg proteins in red wines treated with egg white. *Food control.*. 23, 87–94. doi:10.1016/j.foodcont.2011.06.016

Tolin, S., Pasini, G., Simonato, B., Mainente, F., and Arrigoni, G. (2012a). Analysis of commercial wines by LC-MS/MS reveals the presence of residual milk and egg white allergens. *Food control.*. 28, 321–326. doi:10.1016/j.foodcont.2012.05.015

Uberti, F., Danzi, R., Stockley, C., Peñas, E., Ballabio, C., Di Lorenzo, C., et al. (2014). Immunochemical investigation of allergenic residues in experimental and commercially-available wines fined with egg white proteinsfined with egg white proteins. *Food Chem. x.* 159, 343–352. doi:10.1016/j.foodchem.2014.03.025

Vasilescu, A., Nunes, G., Hayat, A., Latif, U., and Marty, J. L. (2016). Electrochemical affinity biosensors based on disposable screen-printed electrodes for detection of food allergens. *Sensors* 16 (11), 1863. doi:10.3390/s16111863

Vincenzi, S., Dinnella, C., Recchia, A., Monteleone, E., Gazzola, D., Pasini, G., et al. (2013). Grape seed proteins: A new fining agent for astringency reduction in red wine. *Aust. J. Grape Wine Res.* 19, 153–160. doi:10.1111/ajgw.12030

Vincenzi, S., Mosconi, S., Zoccatelli, G., Dalla Pellegrina, C., Veneri, G., Chignola, R., et al. (2005). Development of a new procedure for protein recovery and quantification in wine. *Am. J. Enol. Vitic.* 56, 182–187.

Weber, P., Steinhart, H., and Paschke, A. (2007b). Allergenic potential of fining agent residues in German wines related to their dosage and an ordinary bentonite treatment. *Agro Food Ind. Hi Tech.* 18, 22–24.

Weber, P., Steinhart, H., and Paschke, A. (2009). Determination of the bovine food allergen casein in white wines by quantitative indirect ELISA, SDS-PAGE, Western blot and immunostaining. *J. Agric. Food Chem.* 57, 8399–8405. doi:10.1021/jf9013982

Weber, P., Steinhart, H., and Paschke, A. (2007a). Investigation of the allergenic potential of wines fined with various proteinogenic fining agents by ELISA. *J. Agric. Food Chem.* 55, 3127–3133. doi:10.1021/jf063436s

Wessels, H., and Paschke-Kratzin, A. (2016). New SPR-based methods for analysis of allergenic agents used in wine treatment. in Proceedings of the BIO Web of Conferences, 39th World Congress of Vine and Wine, Brazil, Bento Gonçalves, 24-28 October 2016 EDP Sciences, 598

Yang, Y., Yang, Y., Zhang, J., Yao, K., Liu, J., Shao, B., et al. (2021). Combination of polyvinylpolypyrrolidone extraction and standard addition strategy for the accurate determination of multiple allergen residues in red wine by UPLC-MS/MS. *J. Chromatogr. B* 1179, 122849. doi:10.1016/j.jchromb.2021.122849

Yoshida, K., Sakurai, Y., Kawahara, S., Takeda, T., Ishikawa, T., Murakami, T., et al. (2008). Anaphylaxis to polyvinylpyrrolidone in povidone-iodine for impetigo contagiosum in a boy with atopic dermatitis. *Int. Arch. Allergy Immunol.* 146, 169–173. doi:10.1159/000113522

Zeleňáková, L., Fikselová, M., Žiarovská, J., Kolesárová, A., and Jurčaga, L. (2021). Identification of cow milk allergen in the products of grape processing. *J. Microbiol. Biotechnol. Food Sci.* 8, 1098–1102. doi:10.15414/jmbfs.2019.8.4.1098-1102

frontiers | Frontiers in Chemistry

ORIGINAL RESEARCH
published: 08 August 2022
doi: 10.3389/fchem.2022.927563

Fatty Acids/Tetraphenylethylene Conjugates: Hybrid AIEgens for the Preparation of Peptide-Based Supramolecular Gels

*Elisa Impresari[1], Alberto Bossi[2,3], Edoardo Mario Lumina[1], Marco Aldo Ortenzi[4], Josine Marie Kothuis[5], Graziella Cappelletti[5], Daniela Maggioni[6], Michael S. Christodoulou[7], Raffaella Bucci[1] and Sara Pellegrino[1]**

[1]DISFARM, Dipartimento Di Scienze Farmaceutiche, Sezione Chimica Generale e Organica "A. Marchesini", Università degli Studi di Milano, Milan, Italy, [2]Istituto di Scienze e Tecnologie Chimiche "G.Natta", Consiglio Nazionale delle Ricerche (CNR-SCITEC), Milan, Italy, [3]SmartMatLab Center, Milan, Italy, [4]CRC Materiali Polimerici "LaMPo", Dipartimento di Chimica, Università degli Studi di Milano, Milan, Italy, [5]Department of Biosciences, Università degli Studi di Milano, Milan, Italy, [6]Dipartimento di Chimica, Università degli Studi di Milano, Milan, Italy, [7]Department of Food, Environmental and Nutritional Sciences (DeFENS), Università degli Studi di Milano, Milan, Italy

OPEN ACCESS

Edited by:
Maria Chiara Arno,
University of Birmingham,
United Kingdom

Reviewed by:
Yujie Xie,
Shanghai University, China
Laura Macdougall,
University of Colorado Boulder,
United States

***Correspondence:**
Sara Pellegrino
sara.pellegrino@unimi.it

Specialty section:
This article was submitted to Supramolecular Chemistry, a section of the journal Frontiers in Chemistry

Received: 24 April 2022
Accepted: 22 June 2022
Published: 08 August 2022

Citation:
Impresari E, Bossi A, Lumina EM, Ortenzi MA, Kothuis JM, Cappelletti G, Maggioni D, Christodoulou MS, Bucci R and Pellegrino S (2022) Fatty Acids/Tetraphenylethylene Conjugates: Hybrid AIEgens for the Preparation of Peptide-Based Supramolecular Gels. Front. Chem. 10:927563. doi: 10.3389/fchem.2022.927563

Aggregation-induced emissive materials are gaining particular attention in the last decades due to their wide application in different fields, from optical devices to biomedicine. In this work, compounds having these kinds of properties, composed of tetraphenylethylene scaffold combined with fatty acids of different lengths, were synthesized and characterized. These molecules were found able to self-assemble into different supramolecular emissive structures depending on the chemical composition and water content. Furthermore, they were used as *N-terminus* capping agents in the development of peptide-based materials. The functionalization of a 5-mer laminin-derived peptide led to the obtainment of luminescent fibrillary materials that were not cytotoxic and were able to form supramolecular gels in aqueous environment.

Keywords: aggregation-induced emission (AIE), peptide materials, luminescent materials, self-assembly, supramolecular gel

1 INTRODUCTION

Luminescent materials are employed nowadays for technological applications in different fields, such as light-emitting devices, OLEDs, chemical sensing, and bio-imaging (Zhu et al., 2017; Liu Y. et al., 2018; Huang et al., 2020; Meng et al., 2020; Zeng et al., 2020; Zhou et al., 2020; Kalva et al., 2021; Chen et al., 2022; Niu et al., 2022). Fluorescent gels combine the elastic and mechanic features of gels with the additional property of being light emitting, paving the way to advanced applications. As an example, an injectable, photoluminescent hydrogel for the delivery of stem cells into heart and skeletal muscle tissues (Niu et al., 2019) has been recently developed. In this context, supramolecular fluorescent gels are gaining particular interest nowadays as they can address some of the major drawbacks of polymeric ones, e.g., difficult synthesis, process scalability, fluorescence emission, and toxicity (Li et al., 2019). The use of small-molecule emissive gelators has thus been started to be exploited in different applications, as biomedicine (Lim et al., 2019; Rajasekar and Lavanya, 2022) and photoelectronics (Cheng et al., 2020; Cao et al., 2021).

Commonly, organic fluorescent materials are built with conventional π conjugated chromophores, such as fluorescein and rhodamine, that in the solid-state, as well as in

concentrated solutions, could form strong π–π stacking interactions. Such aggregates, upon photoexcitation, tend to decay via non-radiative pathways resulting in strong luminescence quenching, often named "aggregation-caused quenching" (ACQ) (Thomas et al., 2007; Huang et al., 2019). This phenomenon practically hampers the use of many chromophores, where intermolecular interaction may occur such as in sensing materials, thus limiting their practical use (Yuan et al., 2010). In 2001, Luo et al. observed that, in some materials, the aggregation plays a constructive role instead of a destructive one in the fluorescence process and coined the term "aggregation-induced emission" (AIE) for this phenomenon (Luo et al., 2001; Hong et al., 2009). Unlike conventional ACQ dyes, AIE luminogens (AIEgens) show negligible or extremely weak emission in dilute solution, while they brightly emit in the solid or aggregate state. Nowadays, numerous AIEgens have been synthesized and widely investigated due to their intrinsic tendency to aggregate and turn on their emission (Martínez-Ávila et al., 2009; Zhang et al., 2014; Arribat et al., 2019; Xu et al., 2020; Meti et al., 2021; Gialelis et al., 2022). AIEgens could indeed be used despite their amount, preventing the use of sophisticated instruments thanks to their high signal-to-noise ratios. Furthermore, the formation of a few emissive aggregates can be readily visualized, improving sensitivity and speed in applications (Liu et al., 2010; Kwok et al., 2015). Tetraphenylethylene (TPE) is the prototype AIEgens due to its easy synthesis and a wide range of possibilities to modify the scaffold (Feng H.T. et al., 2018; Liu Q et al., 2018; Yang et al., 2018; García-González et al., 2021; Ma et al., 2021; Saraswathi and Joseph, 2022). Although some debate still exists, both restriction of intramolecular rotation and intramolecular π–π stacking interactions have been generally recognized as the mechanism of the TPE intense bluish emission (Chen et al., 2019). Substituents present on the TPE phenyl rings can affect its emission properties (Ceballos et al., 2017). It has been reported that para-substituents exert a strong influence on the TPE emission (Yang et al., 2018), as examples, diethylamino TPE shows a yellow emission, while a pyrene derivative emits a white light (Feng X. et al., 2018). On the other hand, the introduction of self-assembling moieties can influence TPE aggregation ability into ordered and well-defined morphologies leading to a wide variety of micro- and nano-architectures (Salimimarand et al., 2017; Talloj et al., 2020; Zhang et al., 2022).

In this work, we developed hybrid compounds combining TPE and fatty acids (FAs). FAs are amphiphilic molecules able to self-assemble into aggregates of various shapes and sizes (Kindt et al., 2020; Singh et al., 2021; Vicente-García and Colomer, 2021). Fluorescent FA derivatives have been found in several applications as direct probes for membranes and liposomes, in the preparation of fluorescent phospholipids, and as biosensors (Muroski et al., 2017; Tokunaga et al., 2017; Gu et al., 2018; Laguerre and Schultz, 2018). Their combination with TPE could lead to hybrid compounds combining the AIE features of TPE and the surfactant properties of FAs. Here, starting from amino-TPE, the functionalization with FAs of different lengths was carried out through amide coupling. The emission properties and the self-assembly tendencies of the obtained compounds were studied by fluorescence, DLS, and electron microscopy. Finally, we investigated the exploitation of the head carboxylic group, for the conjugation of biomolecules such as peptides. In particular, the obtained compounds were used as N-*terminus* capping agents in the development of peptide-based materials. Peptides are indeed able to organize themselves into ordered structures and are widely exploited in the development of smart materials (Clerici et al., 2016; Fuertes et al., 2017; Gagni et al., 2019; Banerjee and Hamley, 2020; Locarno et al., 2020; Vaghi et al., 2020; Varanko et al., 2020; Bucci et al., 2021a; Bucci et al., 2021b; Surís-Valls et al., 2022) and supramolecular gels (Makam and Gazit, 2018; Jain and Roy, 2020; Tsutsumi et al., 2021; Kurbasic et al., 2022). Ultra-short peptides derived from natural proteins, such as amyloidogenic ones, have been investigated, the phenylalanine dipeptide being the most exploited motif (Diaferia et al., 2019; Bucci et al., 2020; Gil et al., 2020; Ji et al., 2021; Criado-Gonzalez et al., 2022). Here, we selected the IKVAV sequence derived from laminin glycoprotein, one of the major components of the basement membrane (Patel et al., 2019), to be functionalized with the developed FA/TPEs conjugates. The laminin 5-mer peptide, once conjugated to highly hydrophobic moieties, is indeed able to induce the amyloid-like fibril formation and it has been used for the preparation of polymeric hydrogels and in the design of bioactive scaffolds (Sahab Negah et al., 2018; Jain and Roy, 2019; Firipis et al., 2021; Yin et al., 2021). Its functionalization with FA/TPEs led to luminescent morphologically different architectures that have been able to form supramolecular gels in an aqueous environment.

2 MATERIALS AND METHODS

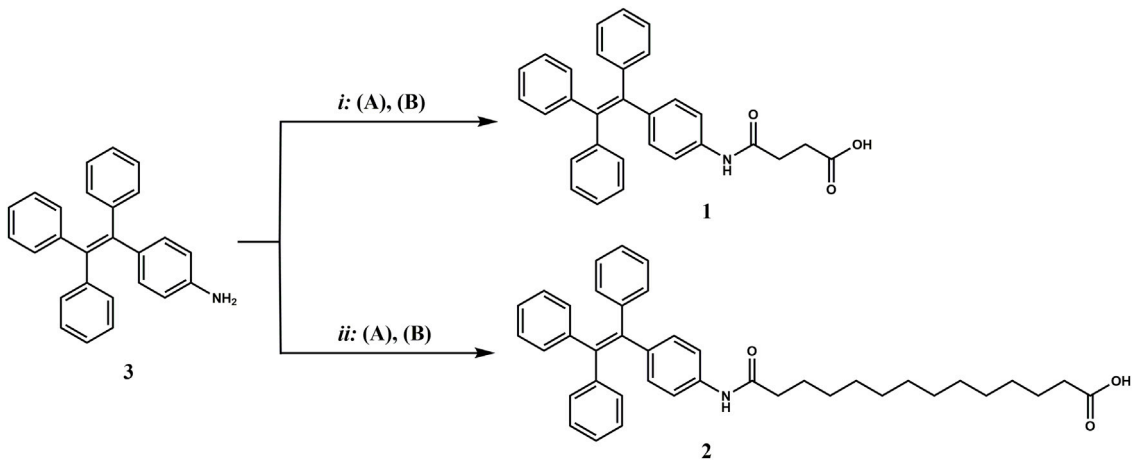
The solvents were purchased from common commercial sources and used without additional purification. Zinc, titanium (IV) tetrachloride, succinic anhydride, tetradecanedioic acid, TFA, Dulbecco's modified Eagle's medium (DMEM)—low glucose, 2-propanol, Triton X-100, 3-(4,5-dimethylthiazol-2-yl)-2,5-diphenyl tetrazolium bromide (MTT), non-essential amino acids, hydrochloric acid (HCl) and TIPS were purchased from Sigma-Aldrich (Taufkirchen, Germany). Benzophenone was purchased from Merck KGaA (Darmstadt, Germany). 4-Aminobenzophenone, EDC hydrochloride, all the Fmoc-amino acids, HBTU, and HATU were purchased from Fluorochem (Hadfield, United Kingdom). Rink amide AM resin (100–200 mesh, 0.7 mmol/g) was purchased from Novabiochem (Läufelfingen, Switzerland). DIEA was purchased from Iris Biotech GmbH (Marktredwitz, Germany). Dimethyl sulfoxide (DMSO) was purchased from PanReac AppliChem ITW Reagents (Darmstadt, Germany). Penicillin/streptomycin, L-glutamine, and fetal bovine serum were purchased from EuroClone (Pero, Italy).

The peptides were prepared by solid-phase peptide synthesis (SPPS) using the Fmoc/t-Bu strategy on Rink Amide AM resin (100–200 mesh, 0.7 mmol/g). The two peptides were manually synthesized using as coupling systems HBTU/DIEA for the natural amino acids and HATU/DIEA for the two fluorescent

TABLE 1 | Sequence and chemical characteristics of compounds **4** and **5**.

Compound	Sequence	RP-HPLC purity (%)	R_t	m/z cld.	m/z fnd.
4	**1**-IKVAV-NH_2	99.4	11.4 min[a]	957.56	957.66
5	**2**-IKVAV-NH_2	99.1	13.9 min[b]	1097.71	1098.64

[a]*Gradient elution for compound* ***4****: 40%–100% of B in A over 20 min at a flowrate of 0.8 ml/min. A: 0.1% TFA in 100% H_2O; B: 0.1% TFA in 100% CH_3CN.*
[b]*Gradient elution for compound* ***5****: 50%–100% of B in A over 20 min at a flowrate of 0.8 ml/min. A: 0.1% TFA in 100% H_2O; B: 0.1% TFA in 100% CH_3CN.*



SCHEME 1 | Synthesis of the FA/AIE conjugates, compounds **1** and **2**, starting from compound **3**, 4-amino-TPE. *i*: **(A)** succinic anhydride, compound **3**, DIEA in dioxane, reflux, 2 h; **(B)** room temperature (rt), overnight (o.n.).; *ii*: **(A)** tetradecanedioic acid, EDC hydrochloride in DCM, 0°C, 30 min; **(B)** compound **3**, DIEA in DCM, rt, o.n.

hybrid compounds. Once removed from the resin, compounds **4** and **5** were characterized by ESI-MS and NMR techniques and analyzed by RP-HPLC (see **Table 1** and SI for the experimental procedure).

NMR spectroscopic experiments were carried out either on a 400 MHz Bruker Advance Neo spectrometer (400 and 100 MHz for ^{1}H and ^{13}C, respectively) or a 500 MHz Bruker BioSpin GmbH (500 and 125 MHz for ^{1}H and ^{13}C, respectively). Chemical shifts are given in ppm relative to the DMSO-d_6 internal standard, and coupling constants (*J*) are reported in hertz (Hz).

Mass spectra were acquired on a Fison MD800 spectrometer and electrospray ion trap on a Finnigan LCQ Fleet spectrometer from Thermo Scientific.

The purity of compounds **4** and **5** was analyzed by analytical RP-HPLC (Jasco LC-NetII/ADC series, equipped with an RP-HPLC Pump PU-4180 and a PDA Detector MD-4010), using a Gemini-NX C18 column from Phenomenex (5 µm, 150 × 4.6 mm). The solvent system used was 0.1% TFA in 100% H_2O (A) and 0.1% TFA in 100% CH_3CN (B), the flow rate 0.8 ml/min, column at 30°C, λ 220 nm.

FT-IR spectroscopy measurements were made on a Perkin Elmer Spotlight 400 FT-IR spectrophotometer equipped with a diamond crystal attenuated total reflectance (ATR) accessory. All the sample were analyzed at room temperature in the solid state. A total of 32 scans were performed for all measurements with a resolution of 4 cm^{-1} in the 4,000–650 cm^{-1} spectral region.

CD spectra were measured on a Jasco J-820 spectropolarimeter with a 0.1 cm quartz cuvette. The spectra were recorded from 190 to 250 nm with a 0.2 nm step and a 2 s collection time per step, taking four averages and using a sensitivity of 100 mdeg and a scanning speed of 50 nm/min. The spectrum of the solvent was subtracted to eliminate interference from cell, solvent, and optical equipment. The CD spectra were plotted as the mean residue ellipticity θ (degree*cm^2*$dmol^{-1}$) versus wavelength λ (nm). Noise-reduction was obtained using a Fourier-transform filter program. The stock solutions of peptides **4** and **5** were prepared in TFE (1 mM, 1 ml) and diluted to 50 µM with different TFE/water mixtures in order to analyze the following conditions: A) 100% TFE, B) 7.5:2.5, C) 1:1, D) 3:7, E) 2:8, F) 1:9, and G) 0.5:9.5 TFE/water mixtures.

TEM samples were prepared by solvent evaporation on a holey carbon grid sample and were observed under a transmission electron microscope L120C (ThermoFisher, United States) operating at 120 KV. Images were acquired by a Ceta camera 4kx4k.

SEM samples were prepared by solvent evaporation on a silicon wafer, both at room temperature and at 60°C, while the gels were transferred as such. All the samples were sputter-coated with gold for 10 s at 0.016 mA Ar plasma (Scancoat six

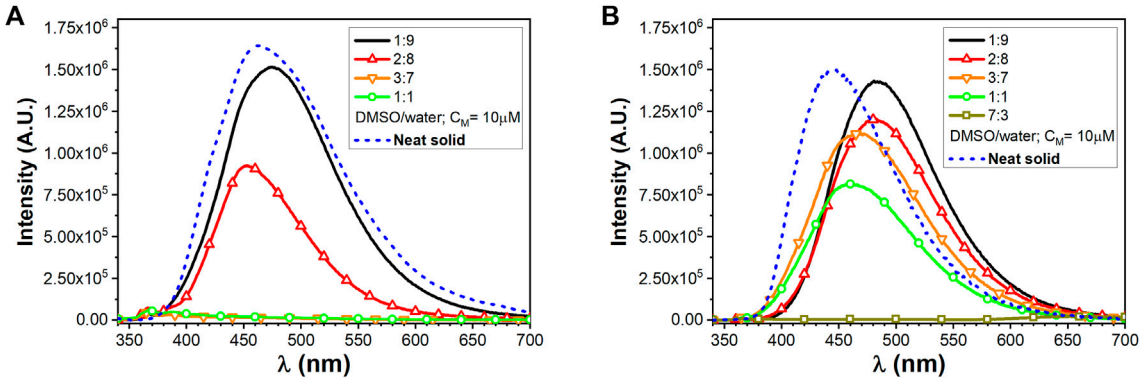


FIGURE 1 | Emission spectra of TPE/FA conjugates, **(A)** for compound **1** and **(B)** for compound **2**, at different DMSO/water ratios (C_M = 10 μM) and in the presence of TFA together with solid-state neat emission.

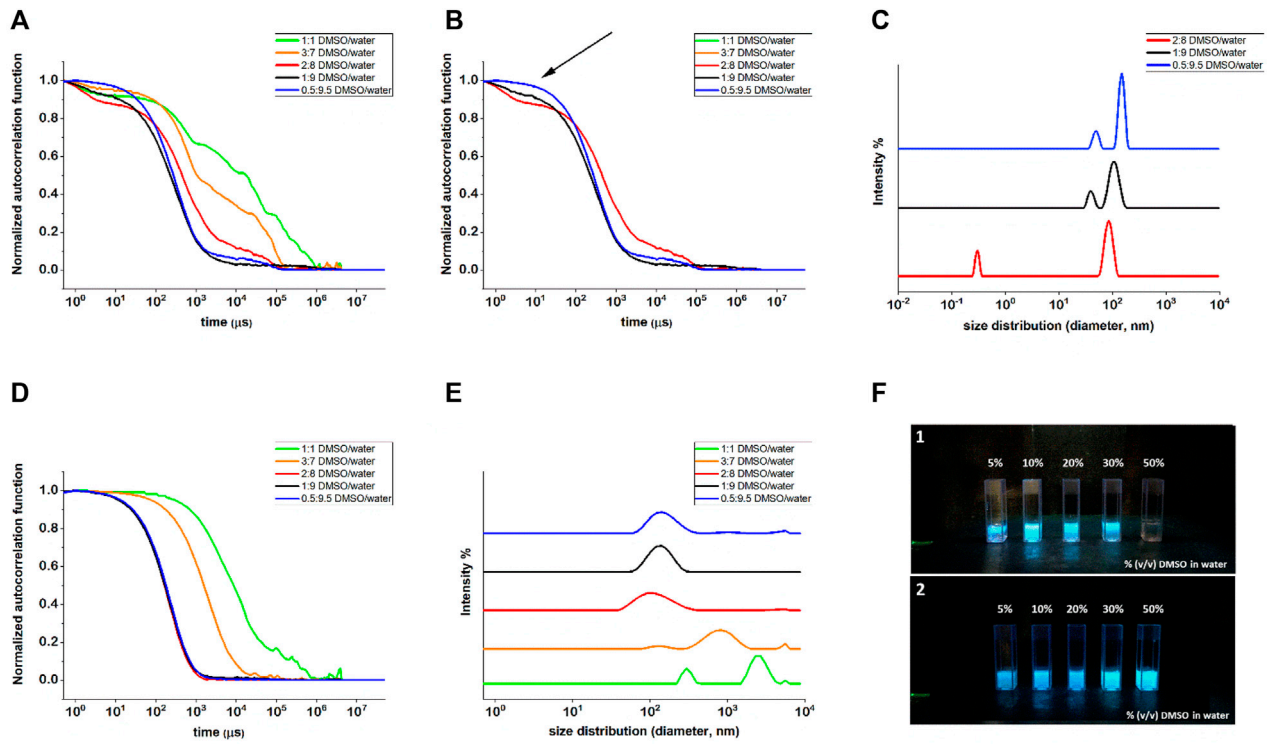


FIGURE 2 | DLS measurements of compounds **1 (A–C)** and **2 (D,E)** in different DMSO/water mixtures. **(A)** Normalized autocorrelation functions of all the DMSO/water ratios, highlighting the noisy profiles of 1:1 and 3:7 DMSO/water ratios, whose fitting was not achievable; **(B)** normalized autocorrelation functions of compound **1** for 2:8, 1:9 and 0.5:9.5 DMSO/water ratios, where the arrow indicates the presence of 1:9 and 2:8 of small components that were not properly fitted by NNLS fitting; **(C)** intensity weighted size distribution for compound **1** in 2:8, 1:9, and 0.5:9.5 DMSO/water ratios. **(D)** Normalized autocorrelation functions for compound **2** and **(E)** intensity weighted size distribution for all the DMSO/water ratios for compound **2**. **(F)** Images of compounds **1** (F1 panel) and **2** (F2 panel) suspensions in water with increasing DMSO percentages. The pictures were taken under a UV light illumination (λ_{ex} = 365 nm).

sputter coater) for SEM imaging using an SEM-EDS JSM-IT500 LV (JEOL Spa) operating at high vacuum, which provided the direct visualization of the self-assembled aggregated structures.

For the gel formation, 6 mg of compound **4** or **5** was dissolved in 500 μL of acetonitrile, using alternate ultrasonic bath and vortex until a clear solution was obtained. Then, for compound **4**, 500 μL of a 0.1 M $NaHPO_4$ aqueous buffer

(pH = 8.4) was added to the solution. After having obtained a clear solution with the aid of an ultrasonic bath and vortex, the sample was left to self-assemble in gel at r.t. overnight. On the contrary, the solution of compound **5** in acetonitrile was diluted with 500 μL of 0.1% (v/v) TFA in water, alternating ultrasonic bath and vortex until a clear solution was obtained. Then, the sample was heated at 65°C for 45 min and cooled down to r.t. for 3 min.

The confocal images were acquired on a Nikon spinning disk confocal microscope, equipped with the CSI-W1 confocal scanner unit. The samples were excited with the 405 nm laser.

UV–vis absorption spectra were obtained on a Shimadzu UV–vis–NIR 3600 spectrophotometer in a 1 cm path length quartz cell. Photoluminescence quantum yields were measured with a C11347 Quantaurus-QY absolute photoluminescence quantum yield spectrometer (Hamamatsu Photonics), equipped with a 150 W xenon lamp, an integrating sphere, and a multi-channel detector steady-state spectrofluorometer (Edinburg Instrument Ltd.). Continuous excitation for the steady-state measurements was provided by a 450 W xenon arc lamp, and the excitation wavelength was set at 325 nm. Photoluminescence lifetime measurements were determined by the time-correlated single-photon counting (TCSPC) method, and they were performed using an Edinburg Pulsed Diode PLED-375 (Edinburg Instrument Ltd.), with a central wavelength of 375 nm. Photoluminescence experiments at room temperature were carried out in various solvent solutions at several concentrations, in the range of $1–2x10^{-5}$ mol/L in dichloromethane (DCM), dimethylsulfoxide (DMSO)/water mixtures. In all experiments, 10–20 μL of a mother solution 0.26 mM of trifluoroacetic acid (TFA) in DMSO was added to avoid carboxylic acid dissociation or amine-ammonium equilibrium. The acid did not influence the luminescence of the aggregates but rather speed up the aggregation and stabilizes the aggregates.

Lifetime was fitted with a multiexponential decay curves, and the average lifetime was calculated according to $\tau_{av}\frac{\sum_{n=1}^{m}\alpha_n\tau_n^2}{\sum_{n=1}^{m}\alpha_n\tau_n}$, m is the *nth* component of the fitted decay; a is the pre-exponential value of the *nth* component.

For PL measurements, a trace amount of trifluoroacetic acid was added to the measured solution to avoid carboxylic acid dissociation or amine-ammonium equilibrium.

The dynamic light scattering (DLS) measurements were performed using a Malvern Zetasizer Nano instrument (Malvern Panalytical, Ltd.) at 25°C, equipped with a 633 nm solid-state He–Ne laser at a scattering angle of 173°. Analyses were carried out on 50 μM samples dispersed in DMSO/water mixtures by using viscosity and refractive index data reported in LeBel and Goring (1962) after the samples were aged for 24–48 h at rt. The size measurements were averaged from at least three repeated measurements.

Rheological tests were conducted at 25°C using an Anton Paar MCR 302 Rheometer (Anton Paar GmbH), operating in a 25 mm parallel geometry with a 1 mm distance gap. The frequency sweep measurements were performed at 0.8% strain from 0.1 to 100 rad/s at 25°C.

Human neuroblastoma SK-N-SH cells (kindly provided by prof. Adriana Bellucci, University of Brescia, Italy) were grown in complete medium composed of DMEM low glucose, supplemented with 10% fetal bovine serum, 1% penicillin/streptomycin, 1% L-glutamine, and 1% non-essential amino acids. Cells were maintained at 37°C under a humidified atmosphere of 5% CO_2.

The cell viability was tested by MTT (3-(4,5-dimethylthiazol-2-yl)-2,5-diphenyl tetrazolium bromide) assay. Neuroblastoma cells were seeded into a 48-well plate (15000 cells/well) in complete medium. After 24 h, cells were treated with different concentrations (0.001–100 μM) of the compound of interest or with vehicle (1% DMSO). Treated and untreated cells were incubated for 24 h at 37°C under a humidified atmosphere of 5% CO_2. Next, 30 μL of MTT (5 mg/ml) was added to the cells and incubated for 3 h at 37°C under a humidified atmosphere of 5% CO_2. Afterward, formazan crystals were solubilized with acidified (0.1M HCl) isopropanol containing 10% Triton X-100. The optical density (OD) was determined at a wavelength of 570 nm using an Infinite 200Pro Tecan plate reader (Tecan Group Ltd.). Compounds were tested in triplicate. The cell viability was expressed as the percentage (%) of *viable cells* relative to the vehicle (100%). All experimental data were shown as mean ± SD. Data were analyzed by a one-way non-parametric ANOVA Kruskal–Wallis test with Dunnett's correction for multiple comparison using Prism Software. The statistical significance was set at $p < 0.05$.

3 RESULTS AND DISCUSSION

3.1 Synthesis of the FA/TPE Conjugates and Their Characterization

3.1.1 Synthesis

Compounds **1** and **2**, functionalized with succinic and tetradecanedioic acids, respectively, were synthesized starting from 4-amino-TPE (**Scheme 1**, compound **3**) obtained following a general protocol (reported in the SI). In the case of the shorter FA/TPE conjugate, the reaction was carried out in basic conditions, using DIEA as base in the presence of a slight excess of succinic anhydride in dioxane, to yield compound **1** in 65.27% (see the SI for procedure details; **Supplementary Figure S1**). Regarding the synthesis of the longer conjugate, compound **2**, the coupling reaction between compound **3** and tetradecanedioic acid was performed using EDC as a coupling reagent added in substoichiometric ratio, in order to activate only a carboxyl group. The desired product **2** was obtained in a 31.95% yield (see the SI for procedure details; **Supplementary Figure S2**).

3.1.2 Fluorescence Spectroscopy

The photophysical properties of the synthesized AIEgens have been studied in dilute solutions, neat solid state, and as aggregate forms obtained from solvent/water mixtures, adding trifluoroacetic acid (TFA) mixture to avoid issues of carboxylic acid dissociation/amine-ammonium equilibrium.

In dilute solutions, the UV–vis absorptions of compounds **1** and **2** in dichloromethane (DCM) and dimethyl sulfoxide

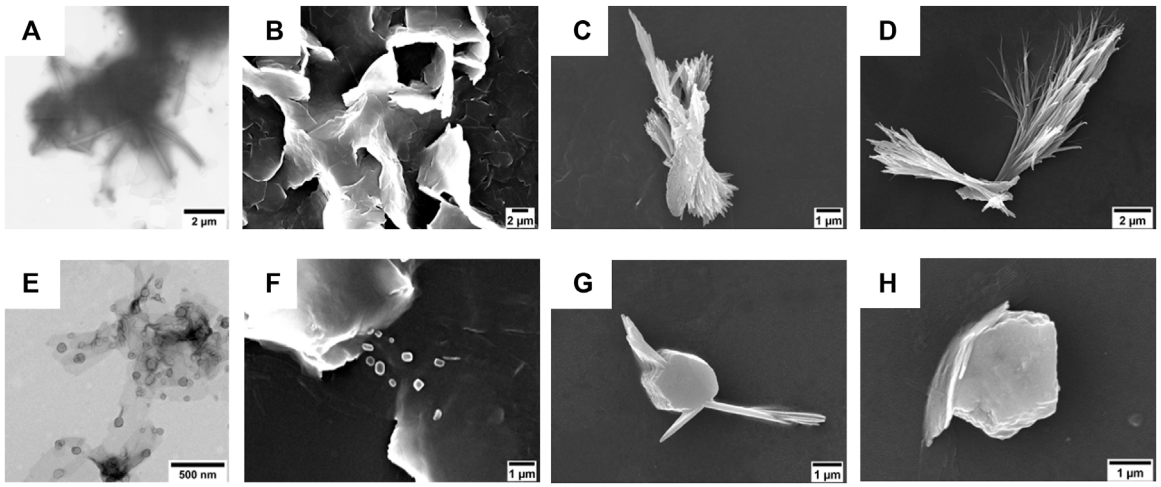


FIGURE 3 | (A,E) TEM micrographs of **(A)** compound **1** (50 μM) and **(E)** compound **2** (50 μM). The scale bars are 1 μm **(A)** and 500 nm **(E)**. **(B–D)** SEM micrographs of compound **1** (50 μM) after its self-assembly in **(B)** 5% (v/v), **(C)** 10% (v/v), and **(D)** 20% (v/v) DMSO in water. Scale bars are 2 μm **(B,C)** and 1 μm **(D)**. **(F–H)** SEM micrographs of compound **2** (50 μM) after its self-assembly in **(F)** 5% (v/v), **(G)** 10% (v/v), and **(H)** 20% (v/v) DMSO in water. Scale bar is 1 μm.

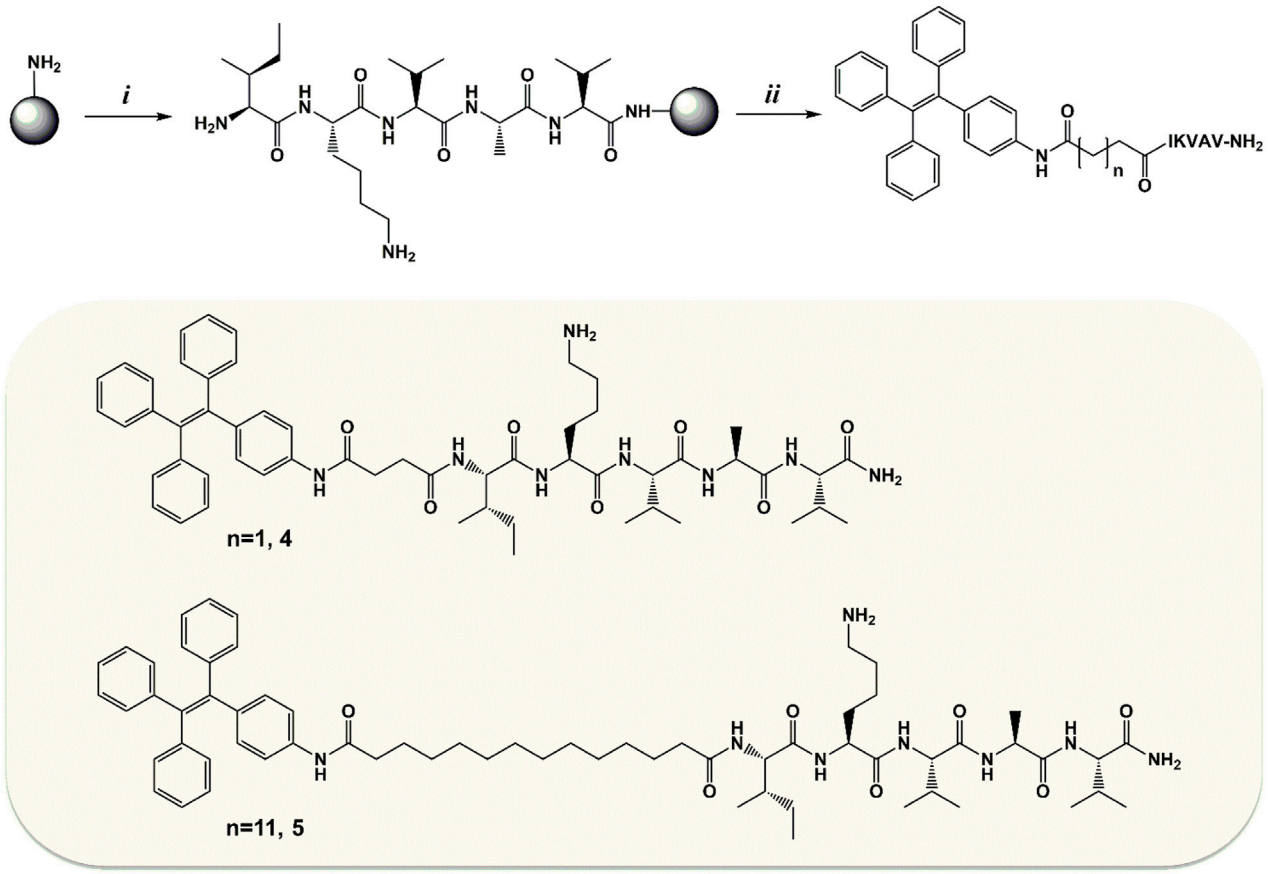
(DMSO) show the presence of a high energy band around 250 nm and a second one around 320 nm characterized by a molar absorptivity of ca. $1.5 \times 10^4\ M^{-1}cm^{-1}$, typical of a π–π*-type transition of the conjugated TPE scaffold (Bolzoni et al., 2013) (**Supplementary Figures S7A, S8A** in the SI). As observed in **Supplementary Figures S7B, S8B** in the SI, no appreciable optical variation can be observed with/without a small amount of TFA, implying that the protonation state of carboxylic acid function did not affect the TPE absorption features. As expected, no emission can be detected in the diluted solution arising from the TPE excitation. On the contrary, intense photoluminescence emissions can be detected upon molecular aggregations. The photophysical properties of the self-assembled **1** and **2** homostructures were evaluated by a modified solvent displacement technique used to self-assemble other aromatic peptides (Reches and Gazit, 2003; Yuran et al., 2012; Bonetti et al., 2015; Bucci et al., 2017; Bucci et al., 2020). To trigger the self-assembly, a stock solution of compounds **1** and **2** in DMSO (1 mM) was diluted with different DMSO/water mixtures (containing a small amount of TFA) to a final concentration of 10 μM and characterized after an incubation of 5–10 min. The aggregates of compound **1** at a 2:8 DMSO/water ratio have to be aged up to 40 min to get a stable luminescence. **Figure 1** shows the emission properties of the aggregates together with the emission of the pure neat solid sample of the two compounds. The solid microcrystalline sample of **1** behaves like an AIEgen and shows a broad bluish emission with a maximum at 465 nm (FWHM 5500 cm^{-1}) and a quantum yield of emission (QY) of 0.25. The spectrum from the 1:9 DMSO/water mixture clearly provides a similar bluish emission centered at 474 nm and displays a QY = 0.25. Increasing the amount of the DMSO content until reaching a 2:8 DMSO/water ratio, the emission undergoes a slight shift toward the blue (λ_{max} = 453 nm) and a slightly decreased QY (0.21). On the contrary, by just increasing the DMSO to 30% (3:7 DMSO/water mixture), no emission is detectable.

The microcrystalline solid sample of **2**, featuring a longer alkyl chain as a substituent of the TPE core, shows emission with a maximum at 445 nm (FWHM 4900 cm^{-1}) and a QY of 0.1. It is worth noting that, in contrast to **1**, the emission from the 1:9 DMSO/water mixture clearly provides a similar bluish-green emission centered at 485 nm while displaying the highest QY of 0.52. The 2:8 DMSO/water mixture displays a similar emission although the QY drops to 0.44. The full photophysical parameters for compounds **1** and **2** are, respectively, reported in **Supplementary Tables S3, S4** in the SI. Clearly, the presence of the longer alkyl chain in **2** results in a more pronounced tendency to form stable and efficient emissive aggregates even at lower water content.

3.1.3 Dynamic Light Scattering Analyses

Dynamic light scattering measurements were taken into account to get insights into the self-assembly tendency of compounds **1** and **2** as a function of the different DMSO/water ratios. Compound **1** showed a very poor scattering power when dissolved in 1:1 and 3:7 DMSO/water mixtures, and only when the water content was increased to reach a 2:8 DMSO/water ratio, the correlation function showed to be stable over several acquirements, suggesting that some aggregates were starting to form (**Figure 2A**).

Nevertheless, the fitting of the correlograms was poor, such that no reliable size distribution could be achieved. By further increasing the water content and passing from 1:9 to 0.5:9.5 DMSO/water ratio, the very first part of the correlogram changed, becoming less evident the starting flex (indicated with an arrow in **Figure 2B**) compatible with a very small component of the mixture. Good fittings of the curves were obtained only for the last two solvent ratios (1:9 and 0.5:9.5) that eventually led to the size distribution reported in **Figure 2C**) with two peaks,



SCHEME 2 | Synthesis of compounds **4** and **5**. *i*: the 5-mer sequence of laminin (IKVAV-NH_2) was synthesized manually by SPPS using the Fmoc/t-Bu strategy and Rink Amide AM resin (100–200 mesh, loading 0.7 mmol/g) as solid support. *ii*: the on-resin coupling with the TPE/FA conjugate (**2** for compound **4** or **3** for compound **5**) was performed o.n. at rt in DMF using as coupling system 3:2.5:4 equivalents of TPE/FA conjugate/HATU/DIEA. Once the Kaiser test confirmed the successful conjugation, the peptidyl-bound resin underwent cleavage, giving compound **4** or **5**.

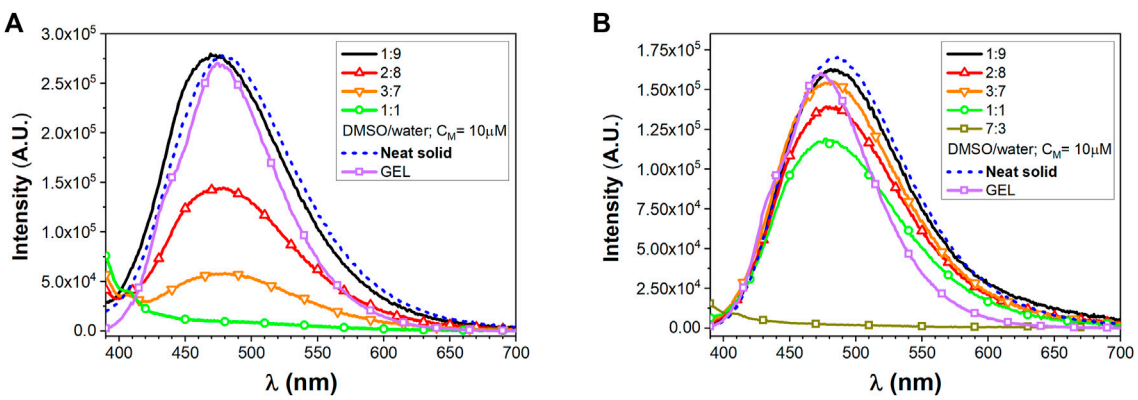


FIGURE 4 | Emission spectra of peptide conjugates, **(A)** for compound 4 and **(B)** for compound 5, at different DMSO/water ratios (C_M = 10 μM) and in the presence of TFA together with solid-state neat emission and GEL emission.

compatible with non-isotropic objects, as revealed by the TEM analysis for this molecule (see **Figure 3A**). Even compound **2** improved its scattering capacity when the non-solvent amount increased: while for 1:1 and 3:7 DMSO/water ratios, the correlograms were poor and the size distribution showed two populations possibly related to the undissolved solid material,

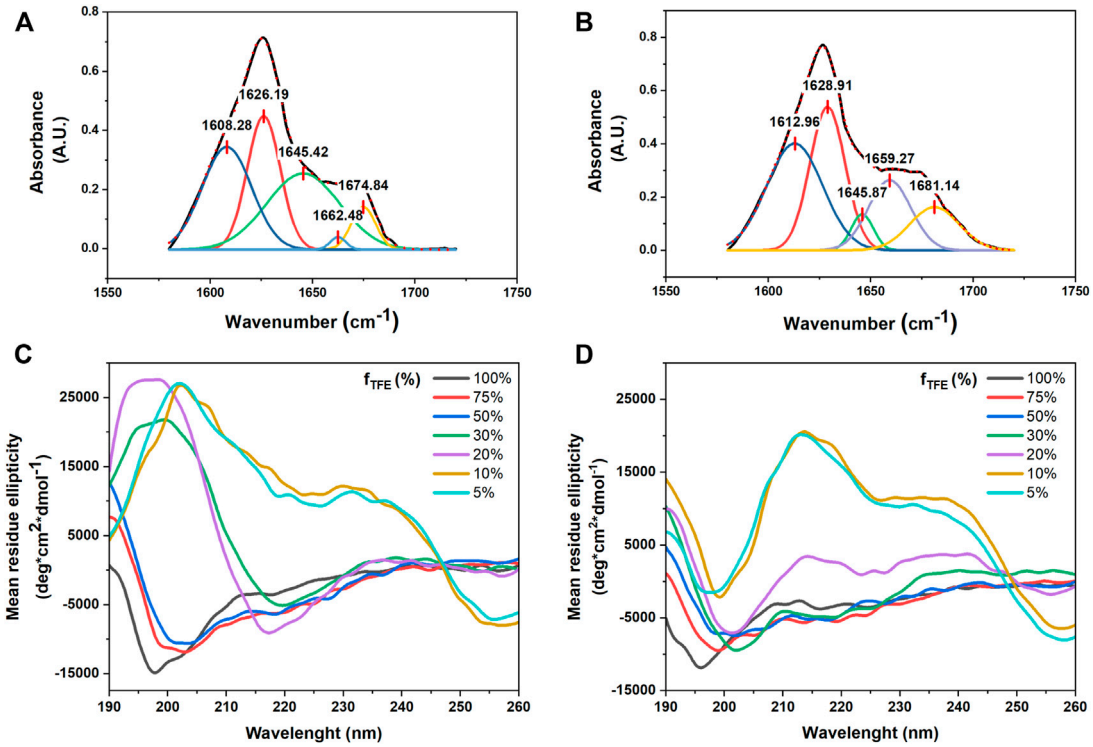


FIGURE 5 | Selected region of ATR-FTIR spectra for compounds **4** and **5**: deconvoluted amide I peaks for compounds **4 (A)** and **5 (B)** in powder form. Both compounds are characterized by a mixture of conformations, with a predominant unordered structure for compound **4**, while compound **5** displays a higher propensity for the β-sheet conformation. CD signatures of **(C)** compounds **4** and **(D) 5**. All samples were prepared in various TFE–water mixtures at a concentration of 50 μM. The CD signal was converted to the mean residue ellipticity, which normalizes for peptide length and concentration.

starting from the DMSO/water ratio 2:8 on, the correlograms became stable and repeatable (**Figure 2D**). These findings suggested the formation of stable and regular self-assembled structures, and their fitting led to size distribution by intensity with one population only, centered at 140 ± 44 nm (**Figure 2E**, the upper traces). The obtained value of hydrodynamic diameter was in agreement with the TEM results (see **Figure 3B**). Moreover, the behavior of the two compounds seen by DLS nicely agrees with the fluorescence spectroscopy results, suggesting that for compound **2** the aggregates start to massively form in mixtures with a minor water content, as it can be macroscopically observed in the pictures of the different DMSO/water mixtures (**Figure 2F**).

3.1.4 Electron Microscopy Analyses

The morphologies of the aggregates were investigated by TEM and SEM. In particular, the TEM analysis conducted on the suspensions of compounds **1** and **2** in 5% (v/v) DMSO in water showed the presence of tubular and lamellar structures for the shortest FA/TPE conjugate (**Figure 3A**) and the formation of spherical assemblies for the longest one (**Figure 3E**).

On the other hand, SEM investigations revealed that the obtainment of stable morphologies is strictly dependent on water concentration (**Figures 3B–D,F–H**).

In the case of compound **1**, at lower DMSO percentages, the formation of lamellar structure is evident (**Figures 3B,C**). This is probably due to the strong π–π interactions among the hydrophobic TPE moieties leading to a coalescence of the nanotubular assemblies into plates (Salimimarand et al., 2017). By increasing the DMSO amount (**Figure 3D**), it is indeed possible to observe the bundle of nanofibers characterized by an 85 nm inner diameter (**Supplementary Figure S12D**). The coalescence was also observed upon heating at 60°C (see **Supplementary Figure S12** in the SI).

The elongation of the alkyl chain on compound **2** leads to a different *scenario* in which the presence of both globular and fibrillar structures is evident. In particular, the formation of bigger agglomerates was observed by increasing the amount of DMSO (**Figures 3G,H**). This change in the morphology could be ascribed to the longer hydrophobic chain that, being more flexible, could favor a more compact, globular shape.

The self-assembly behavior of both FA/TPE conjugates was ascertained by confocal microscopy (**Supplementary Figure S16**). The confocal images of the colloidal suspensions (10% (v/v) DMSO in water) confirmed the presence of spherical aggregates of fibers for compound **1** and bigger globular agglomerates for compound **2**.

3.2 FA/TPE Peptides: Synthesis and Characterization

3.2.1 Synthesis

Compounds **1** and **2** were then used as N-*terminus* capping agents for ultra-short peptides. In particular, the IKVAV

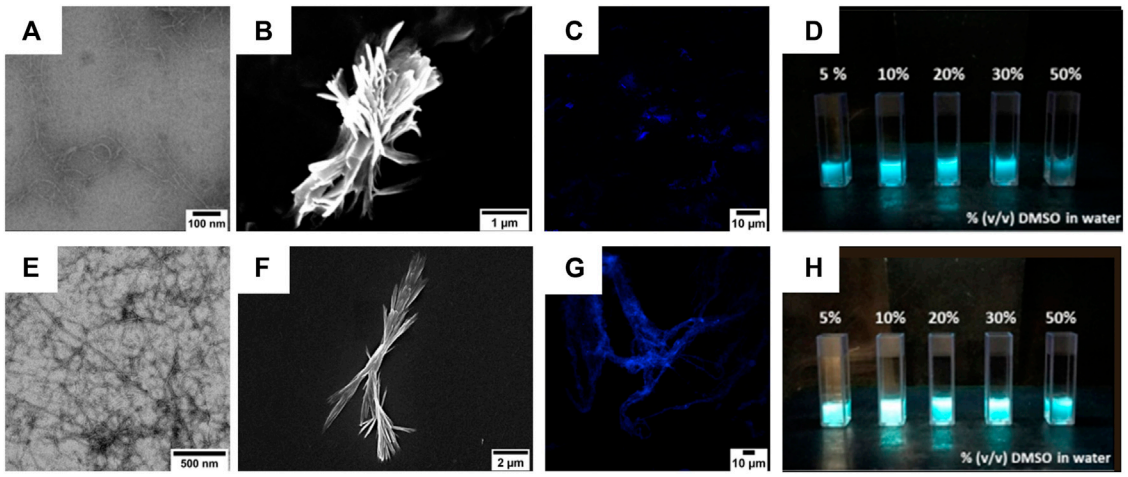


FIGURE 6 | (A,B) TEM **(A)** and SEM **(B)** micrographs of compound **4** (50 µM) after its self-assembly in 1:9 (v/v) DMSO/water mixture. Scale bars are 100 nm **(A)** and 1 µm **(B)**. **(E,F)** TEM **(E)** and SEM **(F)** micrographs of compound **5** (50 µM) after its self-assembly in 1:9 (v/v) DMSO/water mixture. Scale bars are 200 nm **(E)** and 2 µm **(F)**. **(C,G)** Confocal images of compounds **4 (C)** and **5 (G)** after their self-assembly in a 1:9 (v/v) DMSO/water mixture. Scale bars are 10 µm. **(D,H)** Images of compounds **4 (D)** and **5 (H)** suspensions in water with increasing DMSO percentages. The pictures were taken under UV light illumination (λ_{ex} = 365 nm).

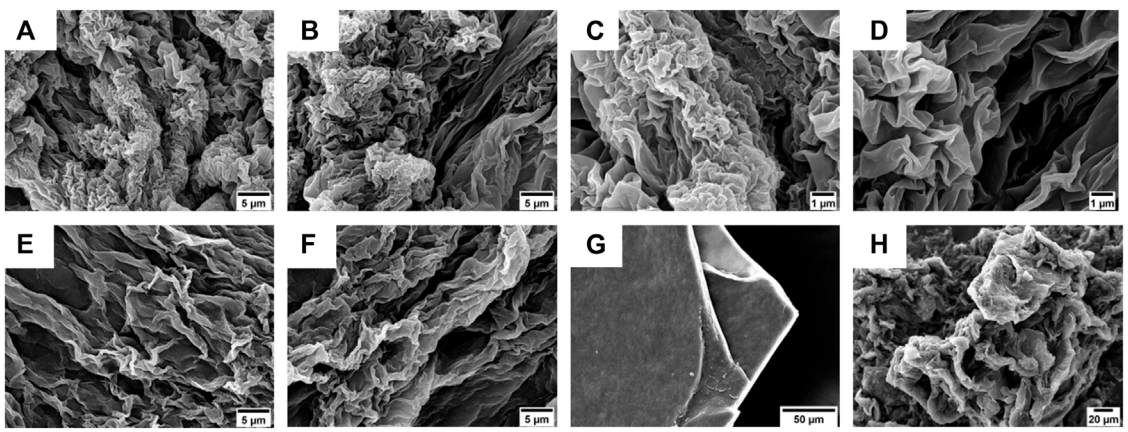


FIGURE 7 | (A–D) SEM micrographs of the gel obtained from compound **4** (0.6% w/t) in 50% (v/v) CH_3CN in 0.1 M $NaHPO_4$ in water. Scale bars are 5 µm **(A,B)** and 1 µm **(C,D)**. **(E,F)** SEM micrographs of the gel obtained from compound **5** (0.6% w/t) in 50% (v/v) CH_3CN in 0.1% TFA in water. Scale bar is 5 µm. **(G,H)** SEM micrographs of xerogel obtained from compounds **4 (G)** and **5 (H)** after slow evaporation at rt. Scale bars are, respectively, 50 µm **(G)** and 20 µm **(H)**.

sequence from laminin was selected. This sequence is able to induce fibril formation in water environment, and it has been used for the functionalization of polymeric hydrogels (Perera et al., 2019; Yin et al., 2021). Here, we wanted to investigate the effect of FA/TPE hybrids on IKVAV self–assembly. Our aim was to obtain new AIE peptide-based nanomaterials, through the combination of the luminogen feature of TPE, the self-assembly propensity of FAs, and the amyloidogenic 5-mer laminin sequence. Furthermore, the gelation ability of the so-obtained hybrid compounds was also investigated. To this aim, compounds **4** and **5** were synthesized by solid-phase peptide synthesis (SPPS) using the Fmoc/t-Bu strategy (**Scheme 2**).

3.2.2 Fluorescence Spectroscopy

As already discussed for precursors **1** and **2**, the new peptide conjugates have been investigated in solution and as aggregates, again in the presence of a trace amount of TFA. Absorption studies on compounds **4** and **5** were performed only in DMSO, since they are only partially soluble in DCM. As reported in **Supplementary Figures S9A, S10A** in the SI, the absorptions closely resemble those of the parent compounds **1** and **2** and they are correlated to the presence of the TPE chromophore. Derivatives **4** and **5** show a residual luminescence peaking at 365 nm in diluted DMSO solution, possibly ascribed to the TPE moiety (**Figure 4**). Intense photoluminescence emissions can be instead detected upon molecular aggregation. The photophysical

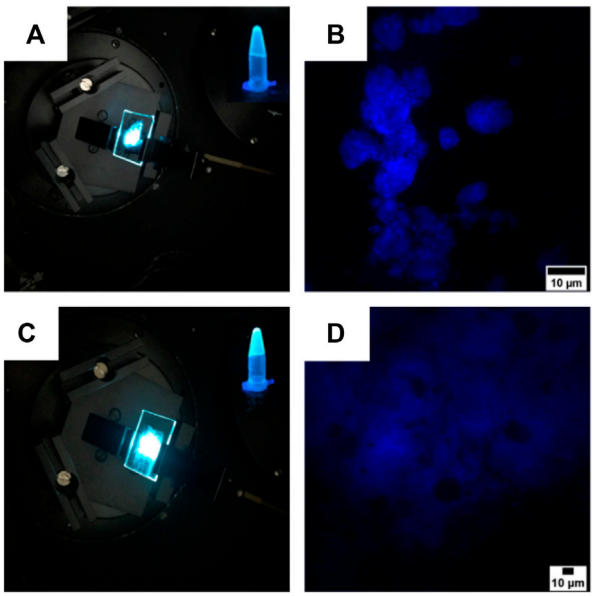


FIGURE 8 | (A,C) Images of the gels obtained from compounds **4 (A)** and **5 (C)** spread on two coverslips with the superimposing photographs of the compounds in the gel state. The pictures of the cover slips were taken under a laser illumination (λ_{ex} = 325 nm), while the two superimposed photographs were taken under a UV light illumination (λ_{ex} = 365 nm). **(B,D)** Confocal images of the gels obtained from compounds **4 (B)** and **5 (D)**. Scale bars are 10 μm.

properties of the self-assembled **4** and **5** homostructures were evaluated similarly to their parent systems **1** and **2**.

Derivatives **4** and **5** show a residual luminescence peaking at 365 nm in the diluted DMSO solution, possibly ascribed to the TPE moiety (**Figure 4**). Intense photoluminescence emissions can be instead detected upon molecular aggregation. The photophysical properties of the self-assembled **4** and **5** homostructures were evaluated similarly to their parent systems **1** and **2**.

The solid microcrystalline sample of **4** shows a broad bluish emission with a maximum at 479 nm (FWHM 4500 cm^{-1}) and a QY of 0.38. The spectrum from the 1:9 DMSO/water mixture clearly provides a similar bluish emission centered at 470 nm, displaying a QY = 0.14. Increasing the amount of DMSO content as in a 2:8 DMSO/water mixture led to a reduction of the tendency to aggregate resulting in poorly emissive system with a QY of only 0.055.

The solid microcrystalline sample of **5**, featuring a longer alkyl chain as a substituent of the TPE core, shows emission with maximum at 484 nm (FWHM 4400 cm^{-1}) and a QY of 0.42. The luminescence of the 1:9 and 2:8 DMSO/water mixtures provides a bluish-green aggregate emission centered at 482 nm displaying a high QY = 0.62–0.65.

3.2.3 Secondary Structure Analysis

The secondary structure of the synthesized FA/TPE peptides **4** and **5** was investigated by both ATR-IR and CD experiments (**Figure 5**). In the ATR-IR spectrum of compound **4** (**Figure 5A**), the deconvolution and the fitting of the amide I band showed a major peak in the amide I region at 1645.42 cm^{-1}, indicating an unordered conformation. In the same region, the spectrum of compound **5** (**Figure 5B**) exhibited two major peaks at 1612.96 and 1628.91 cm^{-1}, which correspond to a β-sheet conformation (Litvinov et al., 2012).

CD spectra of compounds **4** and **5** in different TFE/water mixtures (**Figures 5C,D**) showed that the secondary structure of the two peptides dramatically changed by increasing the percentage of water. The CD signatures of compounds **4** and **5** in 100% TFE showed a large negative band at from 190 to around 210 nm and small negative peaks at around 220 nm, which correspond to an unordered structure. By increasing the percentage of water until 50% (v/v), the CD signatures showed a positive peak at 190 nm, while the large negative band shifted to

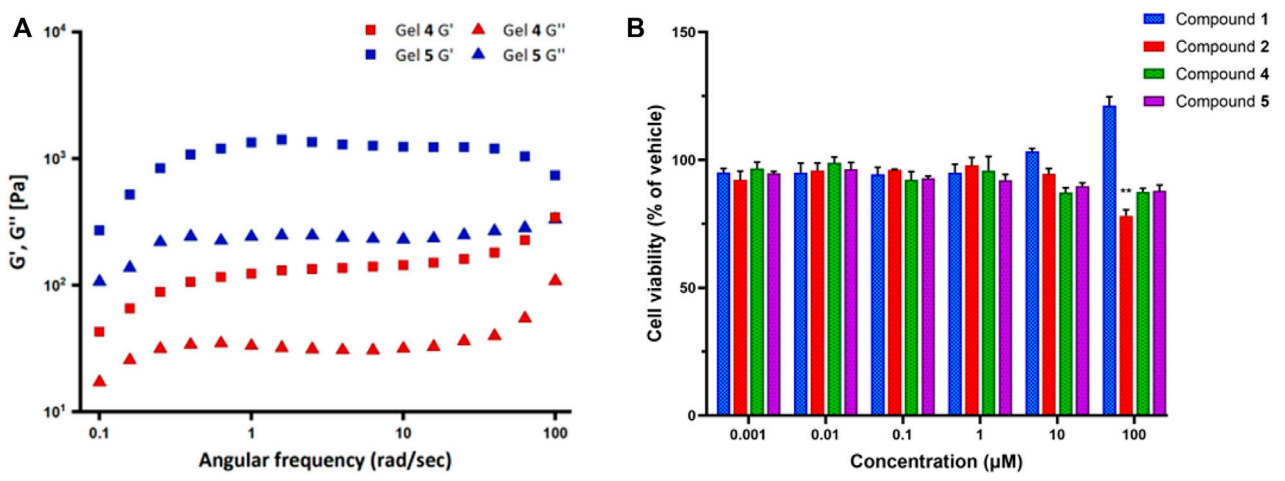


FIGURE 9 | (A) Frequency sweep experiments for the gels synthesized from compounds **4** (Gel **4**) and **5** (Gel **5**). G′ is the storage modulus and G″ is the loss modulus. **(B)** The effect of compounds **1**, **2**, **4**, and **5** on cell viability by MTT assay. SK-N-SH neuroblastoma cells were treated with compound solutions ranging from 0.001 to 100 μM for 24 h. Data represent the mean ± SD of triplicate measurements. $^{**}p < 0.01$ compound **2** versus vehicle.

around 200 nm with small negative peaks at around 220 nm, suggesting a partial helical tendency for both the compounds. The CD signature of the two compounds in 20% (v/v) and 30% (v/v) TFE in water showed two opposite behaviors: while compound **4** showed an intense positive peak at 195 nm and a large intense negative band at around 220 nm, which correspond to a β-sheet conformation, compound **5** in 30% (v/v) was characterized by a positive peak at 190 nm and three negative peaks at 202, 219, and 225 nm, whereas in 20% (v/v), it revealed two slight Cotton effect bands approximately at 215 and 230 nm, which were due to the aromatic π–π effects of TPE. In addition, at the lowest concentration of TFE in water (20% (v/v), 10% (v/v), and 5% (v/v) for compound **4** and the latter two for compound **5**), the CD signatures showed a bisignated Cotton effect signal, approximately at 210 and 230 nm for compound **4** and approximately at 220 and 240 nm for compound **5**, indicating strong π–π stacking of TPE chromophores in water (Chu et al., 2018).

The tendency to self-assemble compounds **4** and **5** was also ascertained by the DLS investigation. The DLS measurements were carried out on the two compounds dissolved in 50 μM 0.5: 0.95 DMSO/water mixture, after being aged for 48 h. The results showed a good scattering level, indicating the presence of some relevant nanostructures in suspension. The two species showed similar intensity-weighted size distribution profiles, presenting two peaks centered at 204 ± 27 nm and 996 ± 171 nm in the case of compound **4** and 359 ± 54 nm and 1230 ± 238 nm for compound **5** (**Supplementary Figure S11**). The double distribution is due to the non-isotropic shape of the self-assembled structures.

3.2.4 Electron Microscopy Analyses

TEM and SEM analyses of nanocolloidal suspension of compound **4** in 10% (v/v) DMSO in water showed the formation of fiber-like aggregates (**Figures 6A,B**). A similar behavior was also observed for compound **5** (**Figures 6C,D**). In particular, both TEM and SEM images showed the formation of belts that could assemble into fibers, suggesting that the amyloid tendency of the peptide sequence prevails on the FA and TPE contributions to self-assembly.

The colloidal suspensions (10% (v/v) DMSO in water) were also visualized by confocal microscopy, showing that compound **4** preferred self-assembling into short and fractal fiber aggregates, whereas compound **5** adopted a large and symmetric fiber network.

3.2.5 Gel Formation and Evaluation

Inspired from the previous results obtained by Jain *et al.* on laminin-derived lipophilic conjugates (Jain and Roy, 2019; Jain and Roy, 2020), compounds **4** and **5** were tested for gelation in various conditions, by varying: *i*) the pH of the organic/water mixtures, *ii*) the concentration of the gelators, and *iii*) the trigger for gelation (e.g., heating, sonication) (results not shown). The optimal conditions were 6 mM (0.6% w/t) in 50% (v/v) CH_3CN in 0.1 M $NaHPO_4$ in water (pH = 8.4) for compound **4**, while for compound **5** 5 mM (0.6% w/t) 50% (v/v) CH_3CN in 0.1% TFA in water. The gelation of **4** was obtained at room temperature (rt) using alternate vortexing and sonication, allowing the solution undisturbed overnight (o.n.) to self-assemble in gel, while compound **5** required to be heated at 65°C for 30 min, after which the peptide self-assembled immediately in gel. The gel from compound **4** showed a flower-like fractal architectures when analyzed by SEM (**Figures 7A–D**).

On the other hand, the gel obtained using compound **5** as a gelator showed the presence of more extended lamellar structures (**Figures 7E,F**).

To better understand the morphology responsible for gel formation, we also analyzed the xerogel obtained from gels **4** and **5** after slowly evaporation at rt (**Figures 7G,H**). For compound **4**, lamellar multilayers were observed, while for **5,** a more disordered structure were present.

Gel formation also results in a luminescent material (**Figures 8A,C**), which was studied in analogy to the characterization already described for compounds **4** and **5**. The fluorescence traces are reported in **Figure 6**. Compound **4** displays an emission centered at 476 nm (FWHM 4050 cm^{-1}) and a QY of 0.26. Compound **5** displays a bluish emission with a maximum at 475 nm (FWHM 3950 cm^{-1}) and a QY of 0.38. For both compounds, the luminescence band and efficiency closely resemble those measured in the DMSO/water mixture as well as those obtained from the neat solids.

Confocal microscopy confirmed the architectures revealed by SEM, as the gel of compound **4** self-assembled into flower-like aggregates (**Figure 8B**), while the gel synthesized from compound **5** adopted a more flexible structure characterized by the presence of hollows (**Figure 8D**).

Therefore, we tested the viscoelastic properties of the synthesized gels using oscillatory rheometry (**Figure 9A**). The frequency sweep experiments were performed from 0.1 to 100 rad/s with a strain of 0.8%.

The results showed that for both compounds **4** and **5**, the storage modulus (G′) is higher than the loss modulus (G″), thus indicating that both the gels have a predominant elastic feature over the viscous one. Moreover, both moduli have some dependence over frequency. Overall, compound **5** moduli are always far higher than those of compound **4**, G′ being approximately 1300 Pa versus 130 Pa in the 1–10 rad/s range. Such values, especially in the case of compound **5**, indicate that the gel is relatively stiff. At high frequencies, behaviors are different: G′ and G″ of compound **4** tend to increase, whereas compound **5** G′ decreases; therefore, at about 100 rad/s, the difference in the values of loss and elastic modulus between the two gels is lower than in the rest of the frequency range.

3.2.6 Cytotoxicity

Finally, the cell viability of the FA/TPE hybrid compounds **1** and **2** and the conjugated peptides **4** and **5** were assessed by 3-(4,5-dimethylthiazol-2-yl)-2,5-diphenyltetrazolium bromide (MTT) assay. Neuroblastoma SK-N-SH cell line was used as the human neuronal model system. These cells are extensively used for both basic and applied research in biomedicine, including neurotoxicity (Cheung et al., 2009) and neurodegeneration (Xicoy et al., 2017). The cells were cultured for 24 h and then exposed to vehicle (1% DMSO) or the compound solutions in the concentration range from 0.001 to 100 μM for 1 day. The experimental results revealed that the viability of SK-N-SH cells significantly decreased upon treatment with

100 μM of compounds **2** (78.1%, respectively; $p = 0.0047$) when compared to vehicle (**Figure 9B**). Although the treatment of SK-N-SH cells with 10 and 100 μM of compound **1** demonstrated a slight increase in the cell viability, no significant changes were observed after treatment with compounds **1**, **4,** and **5** compared to vehicle.

4 CONCLUSION

In this work, hybrid molecules combining the AIE properties of TPE and the surfactant ability of fatty acids were synthesized and characterized. Starting from 4-amino-TPE, the functionalization with FAs of different lengths was performed through amide coupling. The emission properties and the self-assembly tendencies of the obtained compounds were studied by fluorescence, DLS, and electron microscopy (EM). Our results showed that the presence of a longer alkyl chain results in a more pronounced tendency to form stable and efficient emissive aggregates. The obtained compounds were then used as *N*-terminus capping agents in the development of peptide-based materials. In particular, the exploitation of the free carboxylic group led to the functionalization of the 5-mer laminin-derived IKVAV peptide. The conjugates self-assembled into luminescent fibrillary materials that were able to form supramolecular gels in the aqueous environment. Gels showed interesting rheological features, with a marked prevalence of elastic over loss modulus, thus indicating that they can be considered relatively stiff, especially in the case of compound **5**. Thus, the definition of compounds with the potential to supply a suitable substrate for *in vitro* models is relevant for a wide range of studies and applications.

DATA AVAILABILITY STATEMENT

The original contributions presented in the study are included in the article/**Supplementary Material**; further inquiries can be directed to the corresponding author.

AUTHOR CONTRIBUTIONS

SP and MC conceived the research; EI and EL synthesized compounds 1 and 2, EI synthesized the peptides, characterized them, performed IR and CD conformational analyses, and conducted the gelation studies; AB performed fluorescence studies; MO performed gelation studies; JK and GC performed cytotoxicity investigations; DM, EI, and RB performed DLS experiments; SP, EI, and RB interpreted the data; SP and EI wrote the article. All authors reviewed the article.

FUNDING

This work was funded by the University of Milano: PSR 2020 Line 3, Seal of Excellence (SEED), IceFree project.

ACKNOWLEDGMENTS

The authors thank Andrea Mazzola and Ruben Favero for their contribution in the synthesis of the TPE derivatives and Donatella Nava and Lucia Feni of the University of Milan for the NMR analyses and their valuable contribution in the interpretation of the spectra. AB thanks M. Penconi and D. Marinotto of the CNR-SCITEC for the valuable and useful discussions. SP and EI thank Nadia Santo and Laura Madaschi of the Uni^{TECH} NOLIMITS, Imaging facility of the University of Milan, for the implementation of both TEM and confocal images and Stefania Crespi, University of Milan, for her valuable work on the SEM images.

SUPPLEMENTARY MATERIAL

The Supplementary Material for this article can be found online at: https://www.frontiersin.org/articles/10.3389/fchem.2022.927563/full#supplementary-material

REFERENCES

Arribat, M., Rémond, E., Richeter, S., Gerbier, P., Clément, S., and Cavelier, F. (2019). Silole Amino Acids with Aggregation-Induced Emission Features Synthesized by Hydrosilylation. *Eur. J. Org. Chem.* 2019 (12), 2275–2281. doi:10.1002/ejoc.201801869

Banerjee, A., and Hamley, I. W. (2020). Introduction to Peptide Soft Materials. *Soft Matter* 16 (44), 9998–10000. doi:10.1039/D0SM90212H

Bolzoni, A., Viglianti, L., Bossi, A., Mussini, P. R., Cauteruccio, S., Baldoli, C., et al. (2013). Synthesis, Photophysics, and Electrochemistry of Tetra(2-Thienyl) ethylene (TTE) Derivatives. *Eur. J. Org. Chem.* 2013 (33), 7489–7499. doi:10.1002/ejoc.201300745

Bonetti, A., Pellegrino, S., Das, P., Yuran, S., Bucci, R., Ferri, N., et al. (2015). Dipeptide Nanotubes Containing Unnatural Fluorine-Substituted β2,3-Diarylamino Acid and L-Alanine as Candidates for Biomedical Applications. *Org. Lett.* 17 (18), 4468–4471. doi:10.1021/acs.orglett.5b02132

Bucci, R., Bossi, A., Erba, E., Vaghi, F., Saha, A., Yuran, S., et al. (2020). Nucleobase Morpholino β Amino Acids as Molecular Chimeras for the Preparation of Photoluminescent Materials from Ribonucleosides. *Sci. Rep.* 10 (1), 19331. doi:10.1038/s41598-020-76297-7

Bucci, R., Das, P., Iannuzzi, F., Feligioni, M., Gandolfi, R., Gelmi, M. L., et al. (2017). Self-assembly of an Amphipathic ααβ-tripeptide into Cationic Spherical Particles for Intracellular Delivery. *Org. Biomol. Chem.* 15 (32), 6773–6779. doi:10.1039/C7OB01693J

Bucci, R., Foschi, F., Loro, C., Erba, E., Gelmi, M. L., and Pellegrino, S. (2021a). Fishing in the Toolbox of Cyclic Turn Mimics: a Literature Overview of the Last Decade. *Eur. J. Org. Chem.* 2021 (20), 2887–2900. doi:10.1002/ejoc.202100244

Bucci, R., Georgilis, E., Bittner, A. M., Gelmi, M. L., and Clerici, F. (2021b). Peptide-Based Electrospun Fibers: Current Status and Emerging Developments. *Nanomaterials* 11, 1262. doi:10.3390/nano11051262

Cao, X., Gao, A., Hou, J.-t., and Yi, T. (2021). Fluorescent Supramolecular Self-Assembly Gels and Their Application as Sensors: A Review. *Coord. Chem. Rev.* 434, 213792. doi:10.1016/j.ccr.2021.213792

Ceballos, S. A., Gil, S., and Costero, A. M. (2017). Influence of Side Chain Characteristics on the Aggregation-Induced Emission (AIE) Properties of Tetrasubstituted Tetraphenylethylene (TPE). *RSC Adv.* 7 (23), 14279–14282. doi:10.1039/C7RA01024A

Chen, H., Liu, H., Xiong, Y., He, J., Zhao, Z., and Tang, B. Z. (2022). New Aggregation-Induced Delayed Fluorescent Materials for Efficient OLEDs with High Stabilities of Emission Color and Efficiency. *Mat. Chem. Front.* 6 (7), 924–932. doi:10.1039/D1QM01625C

Chen, Y., Lam, J. W. Y., Kwok, R. T. K., Liu, B., and Tang, B. Z. (2019). Aggregation-induced Emission: Fundamental Understanding and Future Developments. *Mat. Horiz.* 6 (3), 428–433. doi:10.1039/C8MH01331D

Cheng, Q., Hao, A., and Xing, P. (2020). Stimulus-responsive Luminescent Hydrogels: Design and Applications. *Adv. Colloid Interface Sci.* 286, 102301. doi:10.1016/j.cis.2020.102301

Cheung, Y.-T., Lau, W. K.-W., Yu, M.-S., Lai, C. S.-W., Yeung, S.-C., So, K.-F., et al. (2009). Effects of All-Trans-Retinoic Acid on Human SH-Sy5y Neuroblastoma as *In Vitro* Model in Neurotoxicity Research. *NeuroToxicology* 30 (1), 127–135. doi:10.1016/j.neuro.2008.11.001

Chu, N.-T., Chakravarthy, R. D., Shih, N.-C., Lin, Y.-H., Liu, Y.-C., Lin, J.-H., et al. (2018). Fluorescent Supramolecular Hydrogels Self-Assembled from Tetraphenylethene (TPE)/single Amino Acid Conjugates. *RSC Adv.* 8 (37), 20922–20927. doi:10.1039/C8RA02296H

Clerici, F., Erba, E., Gelmi, M. L., and Pellegrino, S. (2016). Non-standard Amino Acids and Peptides: From Self-Assembly to Nanomaterials. *Tetrahedron Lett.* 57 (50), 5540–5550. doi:10.1016/j.tetlet.2016.11.022

Criado-Gonzalez, M., Espinosa-Cano, E., Rojo, L., Boulmedais, F., Aguilar, M. R., and Hernández, R. (2022). Injectable Tripeptide/Polymer Nanoparticles Supramolecular Hydrogel: A Candidate for the Treatment of Inflammatory Pathologies. *ACS Appl. Mat. Interfaces* 14 (8), 10068–10080. doi:10.1021/acsami.1c22993

Diaferia, C., Roviello, V., Morelli, G., and Accardo, A. (2019). Self-Assembly of PEGylated Diphenylalanines into Photoluminescent Fibrillary Aggregates. *ChemPhysChem* 20 (21), 2774–2782. doi:10.1002/cphc.201900884

Feng H.T., H.-T., Yuan, Y.-X., Xiong, J.-B., Zheng, Y.-S., and Tang, B. Z. (2018). Macrocycles and Cages Based on Tetraphenylethylene with Aggregation-Induced Emission Effect. *Chem. Soc. Rev.* 47 (19), 7452–7476. doi:10.1039/C8CS00444G

Feng, X., Qi, C., Feng, H.-T., Zhao, Z., Sung, H. H. Y., Williams, I. D., et al. (2018). Dual Fluorescence of Tetraphenylethylene-Substituted Pyrenes with Aggregation-Induced Emission Characteristics for White-Light Emission. *Chem. Sci.* 9 (25), 5679–5687. doi:10.1039/C8SC01709C

Firipis, K., Boyd-Moss, M., Long, B., Dekiwadia, C., Hoskin, W., Pirogova, E., et al. (2021). Tuneable Hybrid Hydrogels via Complementary Self-Assembly of a Bioactive Peptide with a Robust Polysaccharide. *ACS Biomater. Sci. Eng.* 7 (7), 3340–3350. doi:10.1021/acsbiomaterials.1c00675

Fuertes, A., Juanes, M., Granja, J. R., and Montenegro, J. (2017). Supramolecular Functional Assemblies: Dynamic Membrane Transporters and Peptide Nanotubular Composites. *Chem. Commun.* 53 (56), 7861–7871. doi:10.1039/C7CC02997G

Gagni, P., Romanato, A., Bergamaschi, G., Bettotti, P., Vanna, R., Piotto, C., et al. (2019). A Self-Assembling Peptide Hydrogel for Ultrarapid 3D Bioassays. *Nanoscale Adv.* 1 (2), 490–497. doi:10.1039/C8NA00158H

García-González, M. C., Navarro-Huerta, A., Rodríguez-Muñoz, F. C., Vera-Alvízar, E. G., Vera Ramírez, M. A., Rodríguez-Hernández, J., et al. (2021). The Design of Dihalogenated TPE Monoboronate Complexes as Mechanofluorochromic Crystals. *CrystEngComm* 23 (34), 5908–5917. doi:10.1039/D1CE00442E

Gialelis, T. L., Owyong, T. C., Ding, S., Li, W., Yu, M., O'Brien-Simpson, N. M., et al. (2022). Development and Application of Diels-Alder Adducts Displaying AIE Properties. *Cell. Rep. Phys. Sci.* 3 (2), 100766. doi:10.1016/j.xcrp.2022.100766

Gil, A. M., Casanovas, J., Mayans, E., Jiménez, A. I., Puiggalí, J., and Alemán, C. (2020). Heterochirality Restricts the Self-Assembly of Phenylalanine Dipeptides Capped with Highly Aromatic Groups. *J. Phys. Chem. B* 124 (28), 5913–5918. doi:10.1021/acs.jpcb.0c04513

Gu, Y., Lin, D., Fei, X., Wang, C., Yang, Q., Tang, Y., et al. (2018). A Novel Fluorescent Long-Chain Fatty Acid-Substituted Dye: Labeling and Biodegrading ofMicrothrix Parvicella. *RSC Adv.* 8 (62), 35855–35862. doi:10.1039/C8RA06986G

Hong, Y., Lam, J. W. Y., and Tang, B. Z. (2009). Aggregation-induced Emission: Phenomenon, Mechanism and Applications. *Chem. Commun.* (29), 4332–4353. doi:10.1039/B904665H

Huang, S., Gao, T., Bi, A., Cao, X., Feng, B., Liu, M., et al. (2020). Revealing Aggregation-Induced Emission Effect of Imidazolium Derivatives and Application for Detection of Hg2+. *Dyes Pigments* 172, 107830. doi:10.1016/j.dyepig.2019.107830

Huang, Y., Xing, J., Gong, Q., Chen, L.-C., Liu, G., Yao, C., et al. (2019). Reducing Aggregation Caused Quenching Effect through Co-assembly of PAH Chromophores and Molecular Barriers. *Nat. Commun.* 10 (1), 169. doi:10.1038/s41467-018-08092-y

Jain, R., and Roy, S. (2019). Designing a Bioactive Scaffold from Coassembled Collagen-Laminin Short Peptide Hydrogels for Controlling Cell Behaviour. *RSC Adv.* 9 (66), 38745–38759. doi:10.1039/C9RA07454F

Jain, R., and Roy, S. (2020). Tuning the Gelation Behavior of Short Laminin Derived Peptides via Solvent Mediated Self-Assembly. *Mater. Sci. Eng. C* 108, 110483. doi:10.1016/j.msec.2019.110483

Ji, W., Tang, Y., Makam, P., Yao, Y., Jiao, R., Cai, K., et al. (2021). Expanding the Structural Diversity and Functional Scope of Diphenylalanine-Based Peptide Architectures by Hierarchical Coassembly. *J. Am. Chem. Soc.* 143 (42), 17633–17645. doi:10.1021/jacs.1c07915

Kalva, N., Uthaman, S., Jang, E. H., Augustine, R., Jeon, S. H., Huh, K. M., et al. (2021). Aggregation-induced Emission-Active Hyperbranched Polymer-Based Nanoparticles and Their Biological Imaging Applications. *Dyes Pigments* 186, 108975. doi:10.1016/j.dyepig.2020.108975

Kindt, J. T., Szostak, J. W., and Wang, A. (2020). Bulk Self-Assembly of Giant, Unilamellar Vesicles. *ACS Nano* 14 (11), 14627–14634. doi:10.1021/acsnano.0c03125

Kurbasic, M., Garcia, A. M., Viada, S., and Marchesan, S. (2022). Heterochiral Tetrapeptide Self-assembly into Hydrogel Biomaterials for Hydrolase Mimicry. *J. Pep Sci.* 28 (1), e3304. doi:10.1002/psc.3304

Kwok, R. T. K., Leung, C. W. T., Lam, J. W. Y., and Tang, B. Z. (2015). Biosensing by Luminogens with Aggregation-Induced Emission Characteristics. *Chem. Soc. Rev.* 44 (13), 4228–4238. doi:10.1039/c4cs00325j

Laguerre, A., and Schultz, C. (2018). Novel Lipid Tools and Probes for Biological Investigations. *Curr. Opin. Cell. Biol.* 53, 97–104. doi:10.1016/j.ceb.2018.06.013

LeBel, R. G., and Goring, D. A. I. (1962). Density, Viscosity, Refractive Index, and Hygroscopicity of Mixtures of Water and Dimethyl Sulfoxide. *J. Chem. Eng. Data* 7 (1), 100–101. doi:10.1021/je60012a032

Li, Y., Young, D. J., and Loh, X. J. (2019). Fluorescent Gels: a Review of Synthesis, Properties, Applications and Challenges. *Mat. Chem. Front.* 3 (8), 1489–1502. doi:10.1039/C9QM00127A

Lim, J. Y. C., Lin, Q., Xue, K., and Loh, X. J. (2019). Recent Advances in Supramolecular Hydrogels for Biomedical Applications. *Mater. Today Adv.* 3, 100021. doi:10.1016/j.mtadv.2019.100021

Litvinov, R. I., Faizullin, D. A., Zuev, Y. F., and Weisel, J. W. (2012). The α-Helix to β-Sheet Transition in Stretched and Compressed Hydrated Fibrin Clots. *Biophysical J.* 103 (5), 1020–1027. doi:10.1016/j.bpj.2012.07.046

Liu, Q., Xia, Q., Wang, S., Li, B. S., and Tang, B. Z. (2018). *In Situ* visualizable Self-Assembly, Aggregation-Induced Emission and Circularly Polarized Luminescence of Tetraphenylethene and Alanine-Based Chiral Polytriazole. *J. Mat. Chem. C* 6 (17), 4807–4816. doi:10.1039/C8TC00838H

Liu, Y., Li, C., Ren, Z., Yan, S., and Bryce, M. R. (2018). All-organic Thermally Activated Delayed Fluorescence Materials for Organic Light-Emitting Diodes. *Nat. Rev. Mater* 3 (4), 18020. doi:10.1038/natrevmats.2018.20

Liu, Y., Yu, Y., Lam, J. W. Y., Hong, Y., Faisal, M., Yuan, W. Z., et al. (2010). Simple Biosensor with High Selectivity and Sensitivity: Thiol-specific Biomolecular Probing and Intracellular Imaging by AIE Fluorogen on a TLC Plate through a Thiol-Ene Click Mechanism. *Chem. Eur. J.* 16 (28), 8433–8438. doi:10.1002/chem.200902505

Locarno, S., Argentiere, S., Ruffoni, A., Maggioni, D., Soave, R., Bucci, R., et al. (2020). Self-assembled Hydrophobic Ala-Aib Peptide Encapsulating Curcumin: a Convenient System for Water Insoluble Drugs. *RSC Adv.* 10 (17), 9964–9975. doi:10.1039/C9RA10981A

Luo, J., Xie, Z., Lam, J. W. Y., Cheng, L., Tang, B. Z., Chen, H., et al. (2001). Aggregation-induced Emission of 1-Methyl-1,2,3,4,5-Pentaphenylsilole. *Chem. Commun.* (18), 1740–1741. doi:10.1039/B105159H

Ma, H., Wang, L., Liang, Y., Cui, Z., Fu, P., Liu, M., et al. (2021). Novel Tetraphenylethylene (TPE)-functionalized Nitroxide/alkoxyamine for Nitroxide-Mediated Homogeneous and Heterogeneous Polymerizations. *Polym. Chem.* 12 (4), 526–533. doi:10.1039/D0PY01369B

Makam, P., and Gazit, E. (2018). Minimalistic Peptide Supramolecular Co-assembly: Expanding the Conformational Space for Nanotechnology. *Chem. Soc. Rev.* 47 (10), 3406–3420. doi:10.1039/C7CS00827A

Martínez-Ávila, O., Hijazi, K., Marradi, M., Clavel, C., Campion, C., Kelly, C., et al. (2009). GoldManno-Glyconanoparticles: Multivalent Systems to Block HIV-1

Gp120 Binding to the Lectin DC-SIGN. *Chem. Eur. J.* 15 (38), 9874–9888. doi:10.1002/chem.200900923

Meng, L., Jiang, S., Song, M., Yan, F., Zhang, W., Xu, B., et al. (2020). TICT-based Near-Infrared Ratiometric Organic Fluorescent Thermometer for Intracellular Temperature Sensing. *ACS Appl. Mat. Interfaces* 12 (24), 26842–26851. doi:10.1021/acsami.0c03714

Meti, P., Yang, J.-W., and Gong, Y.-D. (2021). Aggregation Induced Emission Properties of Cruciform-type Conjugated Pyrazine Molecules with Four Pendent Donor Groups. *Dyes Pigments* 192, 109419. doi:10.1016/j.dyepig.2021.109419

Muroski, M. E., Miska, J., Chang, A. L., Zhang, P., Rashidi, A., Moore, H., et al. (2017). Fatty Acid Uptake in T Cell Subsets Using a Quantum Dot Fatty Acid Conjugate. *Sci. Rep.* 7 (1), 5790. doi:10.1038/s41598-017-05556-x

Niu, H., Li, X., Li, H., Fan, Z., Ma, J., and Guan, J. (2019). Thermosensitive, Fast Gelling, Photoluminescent, Highly Flexible, and Degradable Hydrogels for Stem Cell Delivery. *Acta Biomater.* 83, 96–108. doi:10.1016/j.actbio.2018.10.038

Niu, X., Zhang, H., Wu, X., Zhu, S., Feng, H., and Liu, W. (2022). A Novel "Turn-On" Fluorescent Sensor Based on Tetraphenylethylene-Planarized Bis-Schiff Base for Dual-State TFA Detection. *J. Mol. Struct.* 1259, 132754. doi:10.1016/j.molstruc.2022.132754

Patel, R., Santhosh, M., Dash, J. K., Karpoormath, R., Jha, A., Kwak, J., et al. (2019). Ile-Lys-Val-ala-Val (IKVAV) Peptide for Neuronal Tissue Engineering. *Polym. Adv. Technol.* 30 (1), 4–12. doi:10.1002/pat.4442

Perera, T. H., Howell, S. M., and Smith Callahan, L. A. (2019). Manipulation of Extracellular Matrix Remodeling and Neurite Extension by Mouse Embryonic Stem Cells Using IKVAV and LRE Peptide Tethering in Hyaluronic Acid Matrices. *Biomacromolecules* 20 (8), 3009–3020. doi:10.1021/acs.biomac.9b00578

Rajasekar, M., and Lavanya, M. (2022). Gel Scaffolds and Emerging Applications in Biomedicine. *RSC Adv.* 12 (25), 15925–15949. doi:10.1039/D2RA00924B

Reches, M., and Gazit, E. (2003). Casting Metal Nanowires within Discrete Self-Assembled Peptide Nanotubes. *Science* 300 (5619), 625–627. doi:10.1126/science.1082387

Sahab Negah, S., Khooei, A., Samini, F., and Gorji, A. (2018). Laminin-derived Ile-Lys-Val-Ala-Val: a Promising Bioactive Peptide in Neural Tissue Engineering in Traumatic Brain Injury. *Cell. Tissue Res.* 371 (2), 223–236. doi:10.1007/s00441-017-2717-6

Salimimarand, M., La, D. D., Kobaisi, M. A., and Bhosale, S. V. (2017). Flower-like Superstructures of AIE-Active Tetraphenylethylene through Solvophobic Controlled Self-Assembly. *Sci. Rep.* 7 (1), 42898. doi:10.1038/srep42898

Saraswathi, S. K., and Joseph, J. (2022). Thymine-Induced Dynamic Switching of Self-Assembled Nanofibers in Diaminotriazine-Functionalized Tetraphenylethylene Derivatives: Implications for One-Dimensional Molecular Devices. *ACS Appl. Nano Mat.* 5 (2), 3018–3027. doi:10.1021/acsanm.2c00310

Singh, A. K., Italiya, K. S., Narisepalli, S., Chitkara, D., and Mittal, A. (2021). Role of Chain Length and Degree of Unsaturation of Fatty Acids in the Physicochemical and Pharmacological Behavior of Drug-Fatty Acid Conjugates in Diabetes. *J. Med. Chem.* 64 (19), 14217–14229. doi:10.1021/acs.jmedchem.1c00391

Surís-Valls, R., Hogervorst, T. P., Schoenmakers, S. M. C., Hendrix, M. M. R. M., Milroy, L., and Voets, I. K. (2022). Inhibition of Ice Recrystallization by Nanotube-Forming Cyclic Peptides. *Biomacromolecules* 23 (2), 520–529. doi:10.1021/acs.biomac.1c01267

Talloj, S. K., Mohammed, M., and Lin, H.-C. (2020). Construction of Self-Assembled Nanostructure-Based Tetraphenylethylene Dipeptides: Supramolecular Nanobelts as Biomimetic Hydrogels for Cell Adhesion and Proliferation. *J. Mat. Chem. B* 8 (33), 7483–7493. doi:10.1039/D0TB01147A

Thomas, S. W., Joly, G. D., and Swager, T. M. (2007). Chemical Sensors Based on Amplifying Fluorescent Conjugated Polymers. *Chem. Rev.* 107 (4), 1339–1386. doi:10.1021/cr0501339

Tokunaga, T., Watanabe, B., Sato, S., Kawamoto, J., and Kurihara, T. (2017). Synthesis and Functional Assessment of a Novel Fatty Acid Probe, ω-Ethynyl Eicosapentaenoic Acid Analog, to Analyze the *In Vivo* Behavior of Eicosapentaenoic Acid. *Bioconjugate Chem.* 28 (8), 2077–2085. doi:10.1021/acs.bioconjchem.7b00235

Tsutsumi, H., Tanaka, K., Chia, J. Y., and Mihara, H. (2021). Short Self-assembling Peptides with a Urea Bond: A New Type of Supramolecular Peptide Hydrogel Materials. *Peptide Sci.* 113 (2), e24214. doi:10.1002/pep2.24214

Vaghi, F., Bucci, R., Clerici, F., Contini, A., and Gelmi, M. L. (2020). Non-natural 3-Arylmorpholino-β-Amino Acid as a PPII Helix Inducer. *Org. Lett.* 22 (15), 6197–6202. doi:10.1021/acs.orglett.0c02331

Varanko, A., Saha, S., and Chilkoti, A. (2020). Recent Trends in Protein and Peptide-Based Biomaterials for Advanced Drug Delivery. *Adv. Drug Deliv. Rev.* 156, 133–187. doi:10.1016/j.addr.2020.08.008

Vicente-García, C., and Colomer, I. (2021). New Antimicrobial Self-Assembling Short Lipopeptides. *Org. Biomol. Chem.* 19 (31), 6797–6803. doi:10.1039/D1OB01227D

Xicoy, H., Wieringa, B., and Martens, G. J. M. (2017). The SH-Sy5y Cell Line in Parkinson's Disease Research: a Systematic Review. *Mol. Neurodegener.* 12 (1), 10. doi:10.1186/s13024-017-0149-0

Xu, S., Duan, Y., and Liu, B. (2020). Precise Molecular Design for High-Performance Luminogens with Aggregation-Induced Emission. *Adv. Mater.* 32 (1), 1903530. doi:10.1002/adma.201903530

Yang, Z., Chi, Z., Mao, Z., Zhang, Y., Liu, S., Zhao, J., et al. (2018). Recent Advances in Mechano-Responsive Luminescence of Tetraphenylethylene Derivatives with Aggregation-Induced Emission Properties. *Mat. Chem. Front.* 2 (5), 861–890. doi:10.1039/C8QM00062J

Yin, Y., Wang, W., Shao, Q., Li, B., Yu, D., Zhou, X., et al. (2021). Pentapeptide IKVAV-Engineered Hydrogels for Neural Stem Cell Attachment. *Biomater. Sci.* 9 (8), 2887–2892. doi:10.1039/D0BM01454K

Yuan, W. Z., Lu, P., Chen, S., Lam, J. W. Y., Wang, Z., Liu, Y., et al. (2010). Changing the Behavior of Chromophores from Aggregation-Caused Quenching to Aggregation-Induced Emission: Development of Highly Efficient Light Emitters in the Solid State. *Adv. Mat.* 22 (19), 2159–2163. doi:10.1002/adma.200904056

Yuran, S., Razvag, Y., and Reches, M. (2012). Coassembly of Aromatic Dipeptides into Biomolecular Necklaces. *ACS Nano* 6 (11), 9559–9566. doi:10.1021/nn302983e

Zeng, J., Guo, J., Liu, H., Zhao, Z., and Tang, B. Z. (2020). A Multifunctional Bipolar Luminogen with Delayed Fluorescence for High-Performance Monochromatic and Color-Stable Warm-White OLEDs. *Adv. Funct. Mat.* 30 (17), 2000019. doi:10.1002/adfm.202000019

Zhang, L., Li, Y., Mu, G., Yang, L., Ren, C., Wang, Z., et al. (2022). Structure of Self-Assembled Peptide Determines the Activity of Aggregation-Induced Emission Luminogen-Peptide Conjugate for Detecting Alkaline Phosphatase. *Anal. Chem.* 94 (4), 2236–2243. doi:10.1021/acs.analchem.1c04936

Zhang, X., Zhang, X., Tao, L., Chi, Z., Xu, J., and Wei, Y. (2014). Aggregation Induced Emission-Based Fluorescent Nanoparticles: Fabrication Methodologies and Biomedical Applications. *J. Mat. Chem. B* 2 (28), 4398–4414. doi:10.1039/C4TB00291A

Zhou, J., Jangili, P., Son, S., Ji, M. S., Won, M., and Kim, J. S. (2020). Fluorescent Diagnostic Probes in Neurodegenerative Diseases. *Adv. Mat.* 32 (51), 2001945. doi:10.1002/adma.202001945

Zhu, X., Su, Q., Feng, W., and Li, F. (2017). Anti-Stokes Shift Luminescent Materials for Bio-Applications. *Chem. Soc. Rev.* 46 (4), 1025–1039. doi:10.1039/C6CS00415F

Conflict of Interest: The authors declare that the research was conducted in the absence of any commercial or financial relationships that could be construed as a potential conflict of interest.

Publisher's Note: All claims expressed in this article are solely those of the authors and do not necessarily represent those of their affiliated organizations, or those of the publisher, the editors, and the reviewers. Any product that may be evaluated in this article, or claim that may be made by its manufacturer, is not guaranteed or endorsed by the publisher.

Copyright © 2022 Impresari, Bossi, Lumina, Ortenzi, Kothuis, Cappelletti, Maggioni, Christodoulou, Bucci and Pellegrino. This is an open-access article distributed under the terms of the Creative Commons Attribution License (CC BY). The use, distribution or reproduction in other forums is permitted, provided the original author(s) and the copyright owner(s) are credited and that the original publication in this journal is cited, in accordance with accepted academic practice. No use, distribution or reproduction is permitted which does not comply with these terms.

frontiers | Frontiers in Chemistry

TYPE Original Research
PUBLISHED 12 August 2022
DOI 10.3389/fchem.2022.966332

Check for updates

OPEN ACCESS

EDITED BY
Faiz Ullah Shah,
Luleå University of Technology, Sweden

REVIEWED BY
Jennifer L. Schaefer,
University of Notre Dame, United States
Liubin Wang,
Hebei University, China

*CORRESPONDENCE
Zhenzhen Yang,
yangzhzh@anl.gov
Lynn Trahey,
Trahey@anl.gov

SPECIALTY SECTION
This article was submitted to Green and Sustainable Chemistry, a section of the journal Frontiers in Chemistry

RECEIVED 10 June 2022
ACCEPTED 11 July 2022
PUBLISHED 12 August 2022

CITATION
Yang Z, Yang M, Hahn NT, Connell J, Bloom I, Liao C, Ingram BJ and Trahey L (2022), Toward practical issues: Identification and mitigation of the impurity effect in glyme solvents on the reversibility of Mg plating/stripping in Mg batteries.
Front. Chem. 10:966332.
doi: 10.3389/fchem.2022.966332

COPYRIGHT
© 2022 Yang, Yang, Hahn, Connell, Bloom, Liao, Ingram and Trahey. This is an open-access article distributed under the terms of the Creative Commons Attribution License (CC BY). The use, distribution or reproduction in other forums is permitted, provided the original author(s) and the copyright owner(s) are credited and that the original publication in this journal is cited, in accordance with accepted academic practice. No use, distribution or reproduction is permitted which does not comply with these terms.

Toward practical issues: Identification and mitigation of the impurity effect in glyme solvents on the reversibility of Mg plating/stripping in Mg batteries

Zhenzhen Yang[1,2]*, Mengxi Yang[1], Nathan T. Hahn[2,3], Justin Connell[2,4], Ira Bloom[1], Chen Liao[1,2], Brian J. Ingram[1,2] and Lynn Trahey[2]*

[1]Chemical Sciences and Engineering Division, Argonne National Laboratory, Lemont, IL, United States, [2]Joint Center for Energy Storage Research, Argonne National Laboratory, Lemont, IL, United States, [3]Material, Physical, and Chemical Sciences Center, Sandia National Laboratories, Albuquerque, NM, United States, [4]Materials Science Division, Argonne National Laboratory, Lemont, IL, United States

Reversible electrochemical magnesium plating/stripping processes are important for the development of high-energy-density Mg batteries based on Mg anodes. Ether glyme solutions such as monoglyme (G1), diglyme (G2), and triglyme (G3) with the $MgTFSI_2$ salt are one of the conventional and commonly used electrolytes that can obtain the reversible behavior of Mg electrodes. However, the electrolyte cathodic efficiency is argued to be limited due to the enormous parasitic reductive decomposition and passivation, which is governed by impurities. In this work, a systematic identification of the impurities in these systems and their effect on the Mg deposition–dissolution processes is reported. The mitigation methods generally used for eliminating impurities are evaluated, and their beneficial effects on the improved reactivity are also discussed. By comparing the performances, we proposed a necessary conditioning protocol that can be easy to handle and much safer toward the practical application of $MgTFSI_2$/glyme electrolytes containing impurities.

KEYWORDS

reversibility, Mg plating/stripping, glyme solvent, Mg $(TFSI)_2$, impurity effect

1 Introduction

Multivalent energy storage technologies based on Mg, Zn, or Ca are attracting increasing attention due to their high volumetric capacities (i.e., 3,832 mA h/cm^3 Mg vs. 2,062 mA h/cm^3 Li and 1,136 mAh/cm^3 Na) and low cost due to their natural abundancy (Yoo et al., 2013; Muldoon et al., 2014). Significant efforts have been devoted in the search for an optimal combination of electrodes/electrolyte materials since Aurbach reported the first rechargeable Mg battery prototype (Aurbach et al., 2000; Aurbach et al., 2007). However, the development of useful electrolytes, exhibiting a wide

electrochemical window with suitable compatibility with anode and cathode materials, is still very limited. Years of fundamental studies have shown that the electrolyte properties such as conductivity, viscosity, solvation structure, and chemical stability greatly affect the electrochemical performance (Deivanayagam et al., 2019; Leon et al., 2022) and are highly dependent on the exact formulation and a complex interaction between solvents and salts. With these constraints, only a few solvents meeting the requirements are currently practical in terms of their ability to dissociate Mg (or Zn and Ca) salts and show reversible metal plating and stripping processes (Bitenc et al., 2019; Deivanayagam et al., 2019). Among them, ethereal solvents such as glymes are perhaps most commonly employed due to low viscosity, high chemical stability, and relatively low vapor pressure for multivalent systems. For example, magnesium bis-(trifluoromethanesulfonyl) imide [Mg $(TFSI)_2$] salt (Shterenberg et al., 2015) or magnesium carba-closo-dodecaborate [Mg $(HCB_{11}H_{11})_2$] in glyme solvents has been intensively explored as promising candidates for Mg batteries (McArthur et al., 2017; Hahn et al., 2018; Fisher et al., 2019).

Despite these attractive characteristics, these electrolytes exhibited poor Coulombic efficiency for Mg deposition and stripping (Connell et al., 2016; Sa et al., 2016). The origin of their poor electrochemical performance is still debated due to conflicting experimental observations and theoretical explanations of the Mg anode passivation mechanisms. Recent studies have suggested that the presence of trace levels of chemical impurities from solvents and anions can affect the material properties substantially (Connell et al., 2016; Kang et al., 2019). Even at very low concentrations, the impurities in the glyme system play an important role in determining the degree of reversibility of magnesium deposition/stripping. For example, it was reported that trace levels of H_2O ($\leq$ 3 ppm) have a profound impact on the reversibility of Mg deposition and stability at the electrode/electrolyte interface, as well as passivation behaviors (Connell et al., 2016). However, detailed investigations of other chemical impurities in addition to water have not been reported yet. Generally, impurities in solvents used for formulation can come from synthesis/manufacturing processes, degradation, storage conditions, or chance contamination. Similarly, impurities from raw materials can react with various chemicals or the atmosphere to form other substances, like reactive intermediates or degradation products during electrolyte preparation and storage, which have the potential to affect the performance as well.

Currently, $MgTFSI_2$ is one of the few simple salts known that can be dissolved in many organic solvents and show high anodic stability, so it is the most commonly used ether-soluble salt for Mg batteries (Ha et al., 2014; Shterenberg et al., 2015). Herein, as a benchmarking system and commercially available material, we specifically focus on the details of $MgTFSI_2$ in glycol dimethyl ether solutions (Gx) including monoglyme (G1), diglyme (G2), and triglyme (G3). We systematically identified the impurities present in these systems and their effect on electrochemical performance. Mitigation strategies to remove the impurities and improve the activity are assessed, including ordinary purification methods, adding electrolyte additives, and electrochemical conditioning. Each mitigation method is investigated to elucidate why performance is amended. Finally, we propose a facile conditioning process based on electrochemical galvanostatic cycling, which is the necessity step in practical use to maximize the Coulombic efficiency of Mg deposition–dissolution. We believe that the impurity issues are not limited to $MgTFSI_2$/Gx but are generic to most electrolyte systems for the Mg battery, so this work will provide an effective approach to optimize and achieve the advanced performance for more practical electrolyte systems.

2 Results and discussion

2.1 Identification of impurities and performance with as-received Gx solvents

Glymes usually are synthesized by several common methods at large scales using ethylene epoxide and alcohols with Lewis acid catalyzed at high temperature and pressure (Tang and Zhao, 2014). The common materials and routes to prepare glymes are shown in Supplementary Figure S1. The most common impurity expected in the "as-received" Gx is small amounts of water. Most glymes are completely miscible with water and alcohols so that its presence is inevitable. Therefore, the Karl Fischer titration was employed to determine the water content in the "as-received" Gx solvent, and the results are given in Figure 1A. It is clear that the water content increases from G1 to G3 as the chain increases in the glyme chemistry, which is indicative of the added chemical steps or larger alcohols needed to go from one to another. Moreover, the polarity including dipole moments and dielectric constants increases with the ethylene oxide chain length (Tang and Zhao, 2014); thus, higher polarity may also contribute to the higher measures of water content from G1 to G3.

Because of their manufacturing process, some other organic impurities such as diethyl ether and hydrocarbons could be found in glymes as well. Gas chromatography-mass spectrometry (GC-MS) is ideally suited for the determination of the trace organic impurities due to its excellent sensitivity. The total ion current chromatograms (TICs) obtained from GC for the "as-received" Gx are given in Figure 1B. Due to trace amounts of impurities, the chromatograms were magnified to reveal the small impurity peaks in glymes (the large peaks are due to the solvent itself). It shows the raw material from the supplier contained impurity peaks primarily located in the 1–6 min region. The peaks were assigned to the most probable candidates from the NIST library, as provided in Table 1. We hypothesize that these impurities could be the residues of

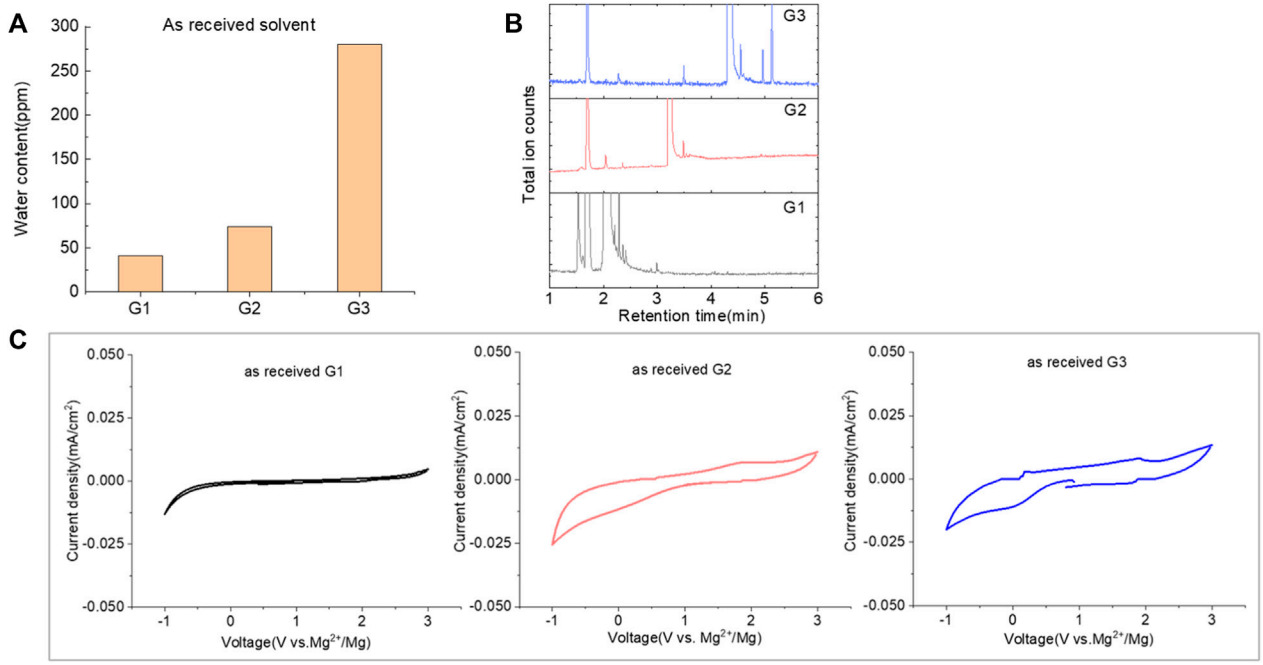


FIGURE 1
(A) Water content in the as-received solvents from G1 to G3 by Karl Fischer titration. **(B)** Chromatograms (total ion count) of the as-received solvents in G1, G2, and G3 by GC-MS. **(C)** Cyclic voltammogram of the freshly prepared electrolyte using "as-received" G1, G2, and G3 with 0.5 M $MgTFIS_2$ on a Pt electrode. Scan rate: 25 mV/s.

unconverted starting reactants such as propylene oxide and alcohols, or from the intermediates such as 2-ethoxyethanol (see Supplementary Figure S1), or the result of the instability of glymes at high temperatures possibly arising in an industrial plant during production, purification, and even packing. The increase of impurities with the chain length can probably be explained by the increasing boiling point with the chain length of the glymes, which complicates their purification as it requires higher temperatures in the purification process so that additional decomposition processes may occur. As a result, any such common products that may be produced in the synthesis would be hard to monitor in the commercial solvents. In fact, it is difficult to remove all the impurity substances effectively and fully at a large scale by manufacturing processes unless proper care is taken in every step involved with the increased cost.

Figure 1C shows the first CV result from the freshly prepared solution based on the "as-received" G1, G2, and G3 containing 0.5 M $MgTFSI_2$ using a Pt working electrode. A reductive process occurs at an onset higher than 0 V, and no oxidative current is obtained in positive scan in the CV curve. This small reductive current is attributed to irreversible processes such as the formation of a passivation film on the electrode surface, rather than Mg deposition. Not surprisingly, the "as-received" solvent cannot support any reversible Mg deposition/stripping, regardless of the solvent used.

2.2 Improved performance: Solvent purification processing

The purity of glymes is confirmed to be critical to enable the efficient Mg electrochemical activity. Typical purification treatments to remove impurities from hydrophilic solvents are adsorption with molecular sieves (MS) and distillation. As noted in Figure 2A, the storage of the "wet" glymes over 3-Å molecular sieves for 48 h readily provided "dry" solvent with moisture content in the 10–20 ppm range. Distilling over Na/K can reduce the water content < 10 ppm. We evaluated the relative effects of absorption and distillation purification methods on Mg deposition/stripping in $MgTFSI_2$-Gx solutions, as shown in Figure 2B. Compared to the electrochemical activity from "as-received" Gx solvents, both methods show evidence of increased Columbic efficiency (CE) and current density upon Mg deposition and dissolution; however, the distillation purification approach results in significantly enhanced performance. This suggests a "relatively clean" solvent was obtained by distillation and confirms that water impurity plays a critical role in controlling the nature of Mg deposition/stripping, consistent with previous reporting (Connell et al., 2016).

Also it should be noted that regardless of the solvent, the onset plating voltage in the distilled solution tends to be more

10.3389/fchem.2022.966332

TABLE 1 Impurity identification in the as-received solvents by GC-MS.

Solvent	RT (min)	Possible compound
G1 monoglyme	1.70	Propylene oxide
	2.29	ethanol, 2 -ethoxy
	2.42	2-Methyl-1-butanol
	2.99	3-Methoxy-1,2-propanediol
G2 diglyme	1.70	Propylene oxide
	2.04	Methoxyethanol
	2.36	ethanol, 2-(ethenyloxy)-
	3.48	1-hexanol
	3.55	4-methoxy butanoic acid
G3 triglyme	1.70	Propylene oxide
	2.3	2-(2-Methoxyethoxy)ethanol
	3.38	1-hexanol
	4.57	tetraglyme
	4.97	4-Methoxybutanoic acid
	5.15	butyl diglyme

positive (−0.2 V vs. Mg^{2+}/Mg) compared to that in the dried solution (−0.5 V vs. Mg^{2+}/Mg), indicating that the beginning of plating requires a higher overpotential activation for the dried solution due to more passivation at the electrode interface from impurities. This general phenomenon does not occur on the opposite polarization. The subsequent Mg stripping voltage starts

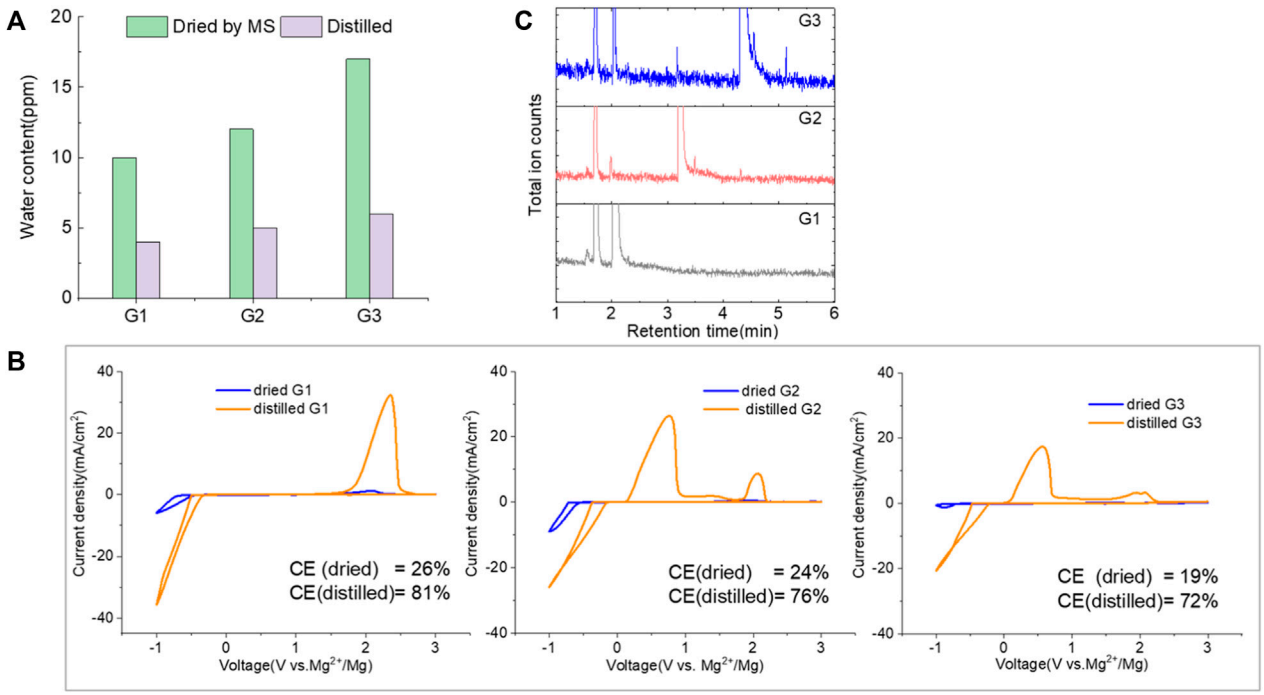


FIGURE 2
(A) Water content in the solvents dried by molecular sieve, distilled over Na/K measured *via* Karl Fischer titration. **(B)** Cyclic voltammograms (CVs) for the electrolytes with 0.5 M $MgTFSI_2$ in pretreated G1, G2, and G3 dried by molecular sieves and distillation methods. Pt was used as the working electrode and a scan rate of 25 mV s^{-1}. **(C)** Chromatograms (total ion count) of the distilled solvents in G1, G2, and G3 by GC-MS.

from ~2.0 V for all the dried solutions. However, a single oxidation peak appears at 2.0 V for distilled G1, and a large oxidation peak occurs at ~0.4 V with a smaller peak near 2.0 V for distilled G2 and G3. This overpotential decrease probably suggests that the reaction products formed from the side reaction between Mg^0 and the electrolyte components (e.g., SEI) make the dissolution of Mg^0 easier in distilled G2 and G3 than that in distilled G1. The difference in the interfacial properties with different solvents inspired us to further explore and understand the fundamental mechanism for these behavior changes and will be the subject of a separate report.

We noted that a trend was found using both approaches that the performance decreases in the order of G1>G2>G3. The preferred solvation structures formed in G1–G3 affect the performance, which has been discussed in the literature (Seguin et al., 2019). Although with pretreatments, more impurities still existing in the glymes with longer chains are also partially responsible for the performance difference. Despite containing similar water contents, the distinct difference in the performance between distilled G2 and G3 suggests that other organic impurities contribute to CE. The GC-MS measurement in Figure 2C reveals that the signals of some small alcohol impurities such as 2-ethoxyethanol and 1-butanol are present in the as-received G1 solvent and disappear after distillation; however, larger alcohols are not completely removed by distillation in G2 and G3. The role of organic impurities on the performance is discussed in Section 2.4.

By evaluating the performance, we demonstrated that most of the moisture along with some small organic impurities can be successfully removed from "as-received" solvents by the Na/K distillation process. Therefore, this method is employed to ensure solvent purity and provide better performance at the laboratory scale. Nevertheless, there is a risk associated with this aggressive purification method utilizing reactive Na/K of personal injury and incurred liability (Michaels, 2000). To mitigate this risk, alternative purification approaches including the use of molecular sieves and calcium hydride (CaH_2), which are convenient and often the drying agent of choices in the purification of laboratory solvents, can rapidly provide relatively dry glymes suitable for the Mg battery. Mg deposition/stripping efficiency (data for CaH_2 drying are shown in Supplementary Figure S2), however, is lower than that from Na/K distillation (~20% vs. ~70%), suggesting that the drying agent composition plays a role in removing impurities.

2.3 Improved performance: Incorporating supporting additives and co-salt

Mitigating the impurity issues and enhancing performance can be achieved through alternative paths. Adding reductive scavengers, such as Mg metal powders, Bu_2Mg, $CrCl_3$, and $AlCl_3$ in THF-based solutions, is an effective way to remove the interfering impurities, yet these methods rely on the use of flammable Mg powder or toxic $CrCl_3$, which are not practical for commercial manufacturing (Ha et al., 2016; Deivanayagam et al., 2019; He et al., 2019). Recently, $Mg(BH_4)_2$ has been proposed as an effective water scavenging species in Mg $(TFSI)_2$/tetraglyme electrolyte (Ma et al., 2017). Thus, $MgTFSI_2$/G2 electrolytes were prepared with 10 mM $Mg(BH_4)_2$. The resulting CVs are presented in Figure 3. For as-received G2, the CV matches the data in Figure 1C, and no improvement is evident after $Mg(BH_4)_2$ addition. The performance in dried solvent (MS) exhibits reversible behavior with improved CE from 24% to 38%. The CE of distilled G2 systems is enhanced from 76% to 83% upon Mg $(BH_4)_2$ addition. The trend indicates that supporting additives like $Mg(BH_4)_2$ are optimized in extrinsically dried or distilled solvents to minimize the water content. The exact water content cannot be easily determined in the solutions by the Karl Fischer analysis due to the interference from the residual BH_4^- (Ma et al., 2017). More recently, Wang et al. (2020) have reported that adding 0.1 M Mg $(BH_4)_2$ improves the performance in $MgTFSI_2$/G2 and revealed that the mechanism was due to the preferred adsorption of BH_4^- anions on the Mg metal surface. But considering the much higher amount they used, it would be the same strategy as we discussed as follows as a co-salt system rather than as the supporting additive.

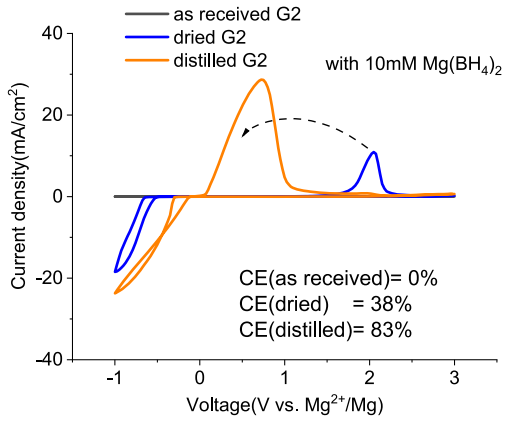


FIGURE 3
First cyclic voltammograms (CVs) for the electrolytes with 0.5 M $MgTFIS_2$ and 10 mM Mg $(BH_4)_2$ in G2 from as-received solvents, dried by molecular sieves, and distilled. Pt was used as the working electrode, and the scan rate was 25 mV s^{-1}.

Inspired by the electrolyte composition and a better reversibility in the magnesium–aluminum–chloride complex (MACC), the reintroduction of chlorides, such as $MgCl_2$, is another successful method to boost the $MgTFSI_2$/Gx performance and is widely employed by the community (Barile et al., 2014; Pan et al., 2016; Sa et al., 2016). However, these "additions" are far from being similar to the addition of a small amount of supporting additives adopted earlier because it requires a substantial quantity of $MgCl_2$ to combat the negative effects of impurities and support magnesium deposition at high efficiency (Connell et al., 2016; Connell et al., 2020). In this work, 0.25 M $MgCl_2$ was added to 0.25 M $MgTFSI_2$/Gx (1:1 ratio for Cl: TFSI), resulting in a total Mg^{2+} concentration of 0.5 M to compare the $MgCl_2$ effect on the electrolyte performance. Figure 4 (A–C) displays the results of the first CV, a Pt working electrode in solutions of "as-received," "dried," and "distilled" Gx based on 0.25 M $MgCl_2$ and 0.25 M $MgTFSI_2$. As expected, adding $MgCl_2$ to the $MgTFSI_2$/Gx solutions increases the overall electrochemical properties in terms of current density and CE (Figures 4D vs. Figures 1C and 2B) for all solvents with different treatments. Compared to the results in Figure 2C, the onset potential for the stripping peak is also greatly reduced with the addition of $MgCl_2$. For example, in G1 solution, it shifts from ~2V to 0.5 V during positive scanning, implying less passivated Mg formed in the cathodic scan. With the presence of more impurity residues in the "as-received," however, the improvement in CE was limited even with the addition of $MgCl_2$. The mixed co-salt $MgCl_2$/$MgTFSI_2$ in dried and distilled solvents restores the CE. Again, the results suggest any beneficial effect that Cl^- has can be maximized in the "clean" electrolyte with much lower concentration of impurity residues.

The twofold advantages of $MgCl_2$ are responsible for the enhanced reversible Mg cycling behavior: the dramatic changes in the solvation structure in the bulk electrolyte (i.e., formation of Mg_xCl_y complex cationic species and an interplay between TFSI and Cl coordination) and interface speciation upon the addition of $MgCl_2$ to the electrolyte (Connell et al., 2016). The changes in bulk electrolyte characteristics with $MgCl_2$ including ionic conductivity, ionic speciation, and anion association strength are reported elsewhere and not discussed in this work (Sa et al., 2016; Salama et al., 2017; Connell et al., 2020). Herein, we investigated the influence of $MgCl_2$ on surface chemistry because the interface formation on the Mg electrode is highly susceptible to impurities and can be significantly changed by Cl^-. To verify the beneficial role of $MgCl_2$ on the formation of the surface layer, Mg electrodes cycled in dried $MgTFSI_2$/G2 with and without $MgCl_2$ electrolytes are characterized by XPS. Figure 5A displays the high-resolution spectra of Mg2p, Cl2p, S2p, C1s, O1s, and F1s on the Mg surface with the detailed analysis of the composition of the surface layer by carefully fitting the XPS spectra. It is immediately evident that with $MgCl_2$, the electrode has a smaller amount of MgO/Mg $(OH)_2$, resulting in more

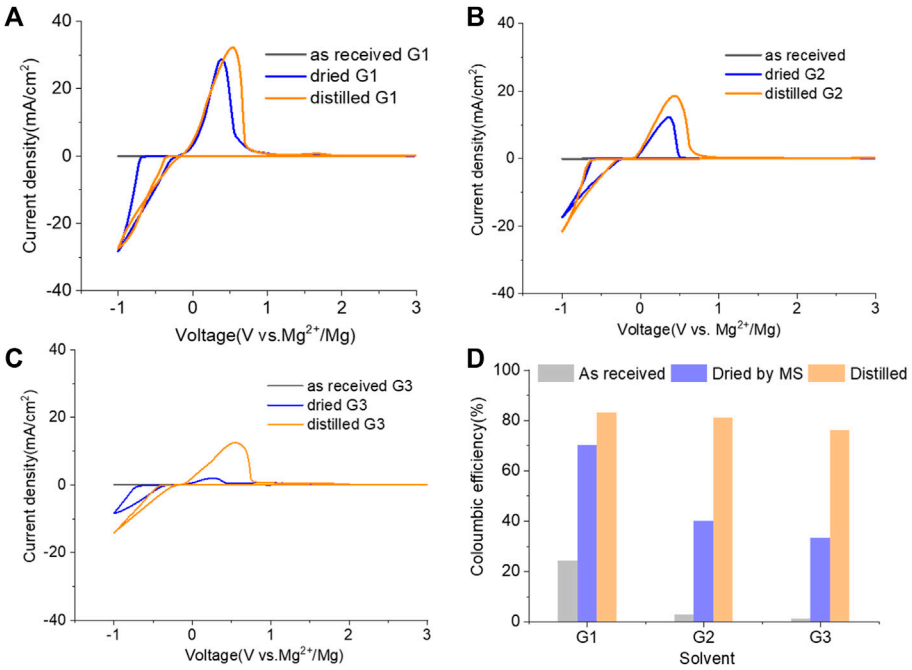


FIGURE 4
Cyclic voltammograms (CVs) for the electrolytes in **(A)** G1, **(B)** G2, **(C)** G3, and **(D)** Coulombic efficiency for each solvent (dried by molecular sieves, distilled) containing 0.25 M $MgTFIS_2$ and 0.25 M $MgCl_2$. Pt was used as the working electrode, and the scan rate was 25 mV s^{-1}.

accessibility of the underlying active metallic Mg, estimated by a much higher Mg^0 peak at 49.4 eV in Mg2p spectrum. The active species of $Mg_xCl_y^-$ cation in addition to TFSI-coordinated Mg^{2+} in the solution can precede the electron transfer and be involved on the interface, causing Mg–Cl bonding to be present in the Cl2p region around 200 eV on the surface layer. Similar results using Pt as a working electrode have been reported in the previous work (Connell et al., 2016). The presence of O = SO, Mg_xS in the S2p region, and $-CF_x$, MgF_2 peaks in the F 1s region suggest the decomposition of $TFSI^-$ in both electrolytes. The instability of $TFSI^-$ and its reduction on the Mg anode are also observed in the following section after extensive cycling (i.e., "conditioning"). The carbon spectra in each electrolyte feature a major peak at 286 eV and a smaller peak at 288 eV, which is the characteristic of C–O–C and O–C = O, respectively, attributed to the decomposition of G2. However, the atomic percentage of surface composition (at% summarized in Figure 5B) is dominated by higher carbon and a lower content of F with $MgCl_2$. It appears that TFSI decomposition is less extensive but rather solvent decomposition is more in the case of mixed $MgCl_2$/$MgTFSI_2$-electrolyte than the pure TFSI solution. It reveals that chloride addition affects the reaction of both the TFSI anion and the solvent during surface layer formation. Although with a certain level of impurities in the dried electrolyte, Cl^- can competitively react/more strongly bind to the Mg surface and depress the overall coverage by MgO/Mg $(OH)_2$ from impurities, as well as inhibit TFSI from decomposition to some extent.

2.4 Improved performance: Electrolytic conditioning

It was shown that even rigorously cleaned $MgTFSI_2$/glyme solutions are limited to a Coulombic efficiency of ~70% for Mg deposition/dissolution during the first cycle. The strategies with adding reducing agents are significant advancements toward the implementation of the $MgTFSI_2$/Gx electrolyte, but the practical CE values have not been obtained. To further improve the performance, earlier reports focused on electrochemical conditioning by extensive repeated CV cycling between −1.2 and 2.8 V at a slow scan rate for 200–500 cycles (Barile et al., 2014). Nevertheless, to the community, the term "conditioning" does not have a formal definition, and in many cases, it simply implies "cycling until it works better." Consequently, the disadvantage of the traditional conditioning methods using the potential-controlled cycling is the lack of quantifiable evaluation for optimized performance. Hereafter, we proposed a facile conditioning protocol for practical applications, modified based on the galvanostatic cycling suggested by a previous report (Shterenberg et al., 2015). Our conditioning

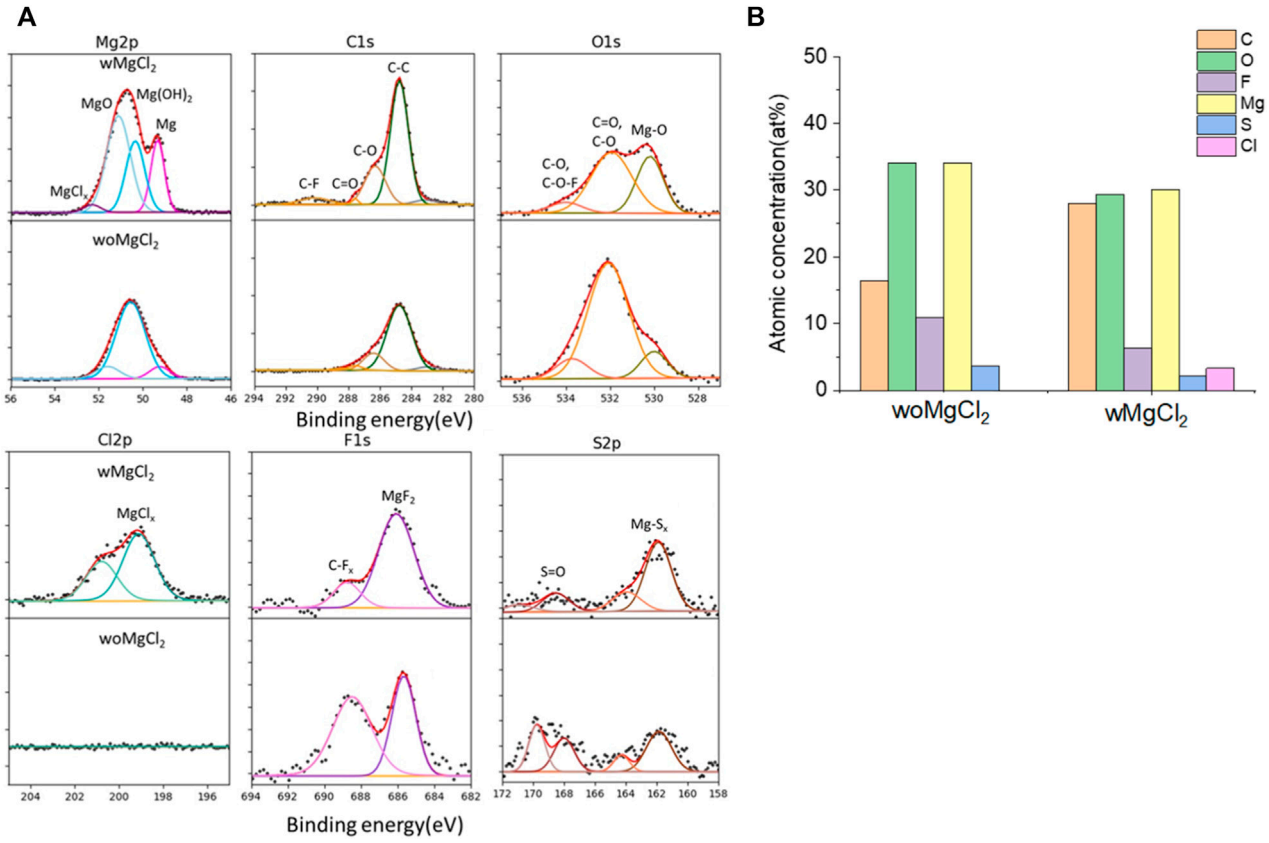


FIGURE 5
(A) High-resolution XPS spectra of Mg 2p, C1s, O1s, Cl 2p, F 1s, and S 2p on the surface layer of the cycled Mg electrode with/without $MgCl_2$ in $MgTFSI_2$/G2 dried solutions. **(B)** Atomic percentage (at%) of the SEI on Mg electrodes cycled with/without 0.25 M $MgCl_2$ in $MgTFSI_2$-G2 electrolytes.

method within an electrochemical cell (Figure 9 shown in experimental) entails attaching the WE lead to one Mg rod; the CE/RE leads to the second Mg rod and cycling Mg^{2+} back and forth between the rods at a fixed current while changing the direction of flow every 1,000 s. Typical current levels in our cells are 0.1–1 mA depending on the electrolyte status and electrode surface area. The overall charge per volume required to attain the optimized electrochemical response can be as little as 5 C/ml (1 C = 1 mA × 1,000 s) or as much as 20–30 C/ml, depending on the electrolyte purity, shelf life, etc. The CV response on a third Pt electrode is verified periodically (i.e., every 5–10 C/ml) to assess the progress. Supplementary Figure S3 illustrates the two-electrode electrolysis conditioning process using "as-received" G2 as an example. A large current of 1 mA was used in the first step to start conditioning for 10 ks, as shown in Supplementary Figure S3A. CV measurement was carried out, and CE was calculated to check if there is any improvement, as shown in Supplementary Figure S3B. The cell polarization decreases gradually, indicated by voltage vs. time profiles in Supplementary Figure S3A, demonstrating that conditioning is still working. After 1 mA conditioning, a slower conditioning process was applied using lower current, e.g., 0.5 mA or less, as the electrolyte becomes cleaner. In theory, as the impurities become more dilute and the flux of impurities to the surface is decreased, they cannot diffuse toward the Mg surfaces as quickly, so a lower current/longer time conditioning protocol might be needed toward the end. Supplementary Figure S3B shows the changes in the CV measurement of the electrolyte throughout a typical conditioning process. A reductive feature (~−0.5 V) ascribed to Mg deposition and a corresponding small stripping peak (0.5 V) appear after passing 10 C/ml in the first conditioning step. This deposition and stripping feature evolve in character in the following condition cycles using lower currents. The current density increases significantly, and CE also improves from 25% to 81% for the "as-received" solution after passing 30 C/ml in the electrolyte. The conditioning process is stopped at this point because we found that the CE cannot be improved any further as conditioning continues. CE in fact decreases if overdose of conditioning is applied.

Figure 6 demonstrates the CVs of Mg plating/stripping in the solutions, which contain "as-received," "dried," and "distilled" G1, G2, and G3 solvents using the same electrolytes from Figure 4

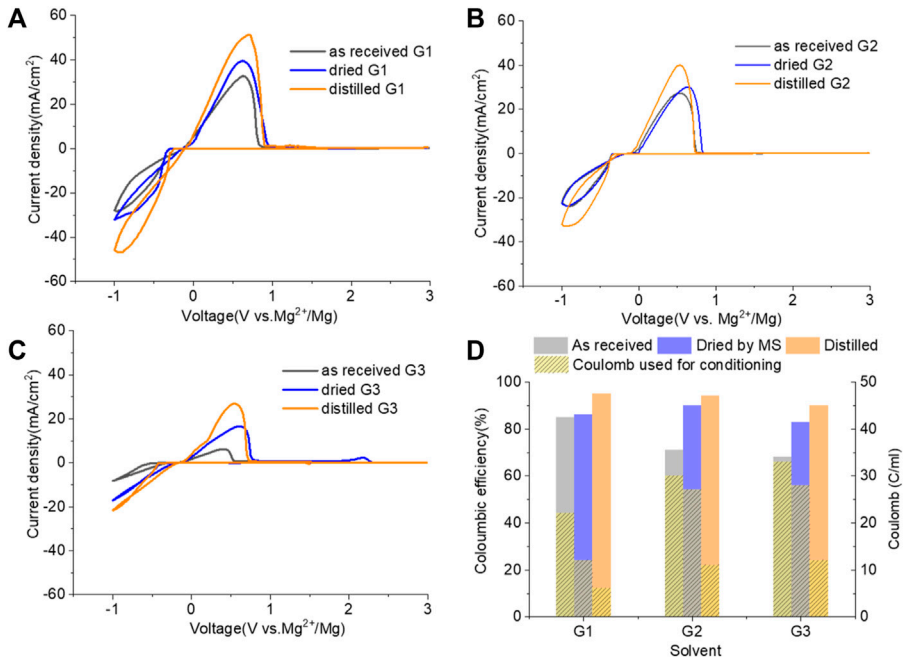


FIGURE 6
Cyclic voltammograms (CVs) for the electrolytes in **(A)** G,1 **(B)** G2, and **(C)** G3 (as received, dried by molecular sieves, and distilled) containing 0.25 M $MgTFIS_2$ and 0.25 M $MgCl_2$ after conditioning. Pt was used as the working electrode, and the scan rate was 25 mV s^{-1}. **(D)** Columbic efficiency from CV in each used solvent after conditioning. The filled pattern indicates the total charge used for conditioning to eliminate impurities and optimize the reversibility of Mg deposition/stripping.

after the conditioning process. CE of each testing solution and the total charge used for conditioning to eliminate impurity residues and optimize the efficiency are provided in Figure 6D. After conditioning, the CE (and the current density) improves but decreases in the order of G1 > G2 > G3. On the other hand, the conditioning cycles and total charge used for conditioning particularly in "as-received" and "dried" solutions increase in the order of G1< G2 < G3. Lower CE is obtained in G2 and G3 even using the similar amount of charge during the conditioning process. This again implies that more impurities are present in the longer chain Gx.

It is critical to initiate testing with highly pure materials to minimize the conditioning requirements. We found that in most cases for $MgTFSI_2$/Gx systems, conditioning is required, nonetheless, to maximize Mg deposition/stripping efficiency and obtain relatively constant electrochemical results. One possibility for the observed low CE is the ubiquity, solubility, and proclivity of H_2O to physisorb on reaction container surfaces. Although the "conditioning-free" electrolytes with additives such as heptamethyldisilazane (HpMS) can scavenge water, the CE was still below 70% due to trace water left (Kang et al., 2019). As such, achieving anhydrous conditions is always questionable and challenging. The fundamental question "How dry is dry?" proves to be difficult to answer if an accurate determination of a trace water contaminant lower than the ppm level (<3 ppm) is required.

Another possibility is some protic organic contaminants (R-OH) such as ethyl glycol, as discussed in Section 2.2, are not readily removed, even by rigorous distillation processes. Electrolytic conditioning can break down these protic residual molecules, evidenced from GC-MS data before and after the conditioning process in distilled $MgTFSI_2$/G2 solutions as a case study, as shown in Figure 7A. We observed that the signals for longer alcohols such as methoxyethanol and propanol disappear after conditioning. To confirm the inhibitory effect of organic impurities, we intentionally added 500 ppm methoxyethanol to conditioned $MgTFSI_2$/G2 solutions. Figure 7B shows that the resultant CE decreases from 88% to ~57%, and the plating/stripping current density decreases significantly. Both are restored upon performing a subsequent conditioning process. These results further exemplify that the organic impurities in addition to water in the glyme solvent inhibit the performance and suggest the necessity of conditioning, which can aid to remove these species.

Additionally, in addition to impurities in the as-received solvents, process-related detrimental substances may form in the prepared electrolyte, which could be treated as impurities as well.

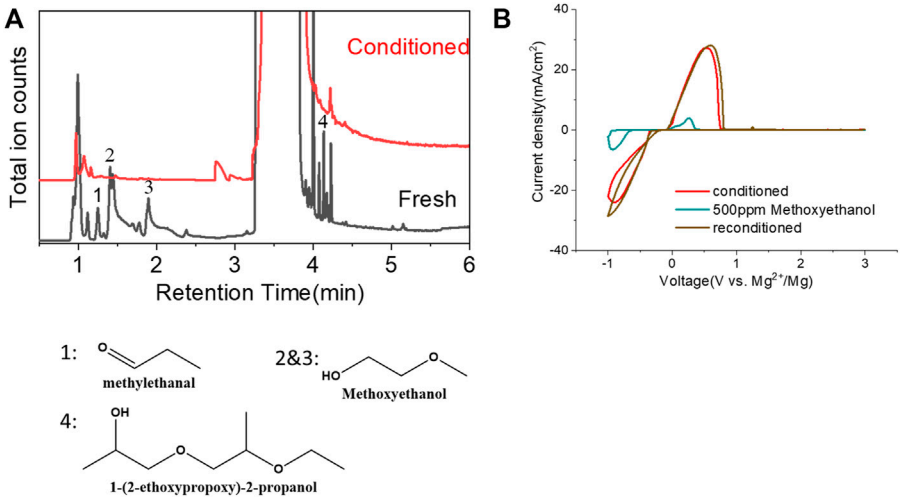


FIGURE 7
(A) Chromatograms (total ion count) of the distilled solvents G2 for the fresh electrolyte and conditioned electrolyte by GC-MS. **(B)** CV measurement before and after intentionally adding 500 ppm methoxyethanol in the conditioned solution. The performance is restored to the conditioned values after performing conditioning again. Scan rate: 25 mV/s.

A previous study from Barile et al. (2014) identified the presence of high molecular weight species in the freshly synthesized MACC electrolyte. These oligomers formed due to ring-opening polymerization of THF during electrolyte formulation can impede the performance, but they were removed by the conditioning process to improve the performance. Unlike in MACC, the ESI-MS data in Supplementary Figure S4 confirm that no oligomeric species is present in the as-prepared $MgTFSI_2$/G2 (distilled) solution, indicating no such ring-open polymerization for an acyclic ether solvent. Table 2 summarizes the major cation speciation as identified from the ESI-MS for both freshly prepared and conditioned solutions. Both spectra show Mg $(G2)_2^{2+}$ and Mg (TFSI) $(G2)^+$ species as the two most intense peaks. However, their relative ratio increases from 0.6:1 in the fresh electrolyte to ~4.9:1 in the conditioned electrolyte. This suggests that after conditioning, most Mg^{2+} are solvated by two G2 molecules only without forming contact Mg–TFSI ion pairs, or some TFSI anions are released from the Mg (TFSI) $(G2)^+$ structure during cycling. This preferred structure can facilitate fast ion exchange, which might be responsible for the highly reversible magnesium plating and a better Coulombic efficiency in the conditioned solution. On the other hand, four new species are recognized only from the conditioned electrolyte (see Table 2 for the possible structure), although their concentrations are much lower. They contain nitrogen and fluorine that are liberated from $TFSI^-$, indicating the decomposition of the salt itself. This observation is consistent with the results revealed by our XPS and EDS data on the black mass deposited onto the Mg electrode in Supplementary Figure S5 and the other literature (Yoo et al., 2017). TFSI anions or [Mg $(TFSI)]^+$ ion pairs could be easily attacked by the free nucleophilic OH^- from water/alcohol impurities or by simply releasing from the Mg $(OH)_2$ surface, resulting in bond breaking of C–S of TFSI (Yu et al., 2017). It is likely that gains in CE by conditioning/continuous cycling may come at the expense of the decomposition of $MgTFSI_2$, particularly with the presence of impurities. Thus, the instability of $MgTFSI_2$ itself at the Mg anode/electrolyte interface is another important factor that limits the electrochemical performance (to reach CE > 95%). Other relatively stable salts such as magnesium tetra (hexafluoroisopropyl)borate (Mg $[B(hfip)_4]_2$ and magnesium tetrakis (perfluoro-tert-butoxy)aluminate (Mg $[TPFA]_2$), or co-salt magnesium triflate [Mg $(OTf)_2$] with $MgCl_2$ in glymes, are now being developed to overcome this limitation (Deivanayagam et al., 2019; Lau et al., 2019; Dlugatch et al., 2021; Ren et al., 2021).

TABLE 2 Mass spectra speciation of the major cation species probed by ESI-MS for freshly prepared and conditioned 0.5 M Mg $(TFSI)_2$/G2 solutions.

Solution	m/z	Compound/empirical formula	Ratio (%)
Fresh	142	Mg $(G2)_2^{2+}$	37.2
	438	Mg (TFSI) $(G2)^+$	62.8
Conditioned	142	Mg $(G2)_2^{2+}$	80.6
	184	Mg $(G2)_2(CF_3)^{2+}$	1.6
	220	Mg $(G2)_2(C_6H_{14}O_3N)^{2+}$	0.3
	438	Mg (TFSI) $(G2)^+$	16.3
	618	Mg (TFSI) $(G2)_2(CH_3ON)^+$	1.0
	947	Mg_3 $(TFSI)_2$ $(G2)_2F_3^+$	0.2

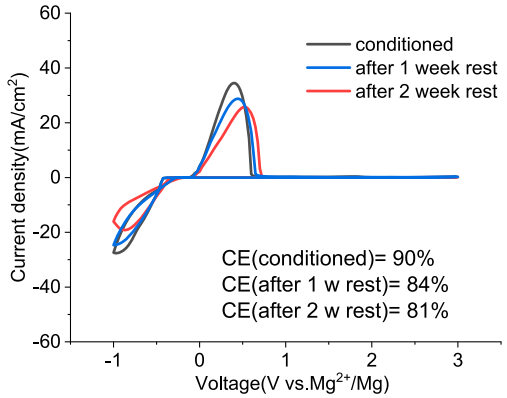


FIGURE 8
Cyclic voltammograms of the conditioned $MgTFSI_2/MgCl_2$ in dried G2 and after resting for 1 week and 2 weeks at OCP.

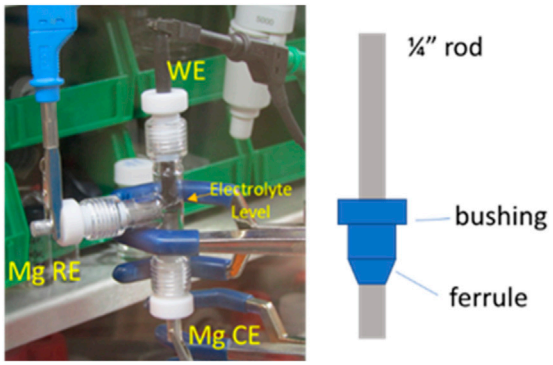


FIGURE 9
Photograph of an assembled three-electrode cell in the glovebox. It is mounted in a standard three-prong lab clamp.

The purity of the salt also affects the Mg plating/stripping efficiency. Mg $(TFSI)_2$ salt is highly hygroscopic and forms a crystalline hexahydrate with residue water, making it extremely hard to eliminate the water completely from the salt (Ma et al., 2017). It is difficult to determine the water content in the salt and efficacy of electrochemical conditioning to remove it from salt. Drying salts at an elevated temperature (140–180°C) appears to be insufficient, and other synthesis/purification techniques, such as recrystallization of commercial salts, should be considered in the future.

As such, we propose that electrochemical conditioning is necessary for the $MgTFSI_2$/glyme electrolytes prior to battery operation. This charge (Q)-controlled electrolytic conditioning protocol we developed to remove impurities is controllable, quantitative, and repeatable from batch to batch. Also, this process is practical, requires no special synthesis/purification apparatus in the glovebox, and provides a safe method to implement in the lab that does not make use of highly reactive materials such as Na and K. We suggest this protocol as a solution to many users to accurately assess the electrolyte performance based on the $MgTFSI_2$/Gx system.

2.5 Aging and storage

We investigated the stability of the conditioned electrolyte under resting conditions in a sealed cell stored in an inert atmosphere for extended times. Figure 8 compares the CV of the solution containing $MgCl_2/MgTFSI_2$ in dried G2 after 1 or 2 weeks at OCP. The overpotential after 1 week resting remains the same as the conditioned but increases slightly after 2 weeks of resting. The CE decreases by ~5% after every week of storage. The results indicate that the aging of $MgCl_2/MgTFSI_2$ in G2 is not as severe as the MACC in THF, which undergoes ongoing THF ring-opening polymerization (Barile et al., 2014); however, we observed that this stability is dependent on the storage environment. For example, the glovebox atmosphere should be maintained at < 1 ppm O_2 and H_2O.

3 Conclusion

This study presents the identification of impurity in glyme solvents, which have been extensively used in Mg batteries. GC-MS shows that in addition to water, other protic organic contaminants (R-OH) like butanol affect the reversibility of Mg cycling significantly. Purifying methods to remove impurities including molecule sieve drying, Na/K distillation, additive addition, and hybrid salt were evaluated and compared. We conclude that the removal of impurity is vital to achieving reversible Mg electrochemistry. We proposed a facile conditioning protocol to further improve the performance of $MgTFSI_2$/Gx electrolytes by galvanostatic cycling at different currents. The conditioned electrolyte after Q-controlled electrochemical conditioning demonstrates highly reversible Mg deposition and a large current density, characteristics that are necessary for practical Mg-ion batteries. GC-MS data reveal that residual water during the electrolyte preparation and some organic impurities can be effectively eliminated by a conditioning process. ESI-MS data show that the speciation favoring Mg complexes such as $Mg(G2)_2^{2+}$ enables much more reversible Mg deposition from the conditioned solution. New decomposition species are also formed during cycling because of the instability of $MgTFSI_2$ itself. This work also illustrates that glyme solvents may undergo subtle aging processes during storage.

4 Experimental and methods

4.1 Chemicals

All chemicals were purchased from Sigma Aldrich, unless otherwise stated. Monoethylene glycol dimethyl ether (G1, 99.5%), diethylene glycol dimethyl ether (G2, 99.5%), and triethylene glycol dimethyl ether (G3, 99%) were received and stored in an argon-filled glovebox. The solvents used as-is, that is, without any treatment, for electrolyte formulations were called "as-received" in the following text. Solvents were dried prior to use over molecular sieve (alumina 3 Å) for 48 h in the glovebox in a stationary mode and named "dried by MS" in the text. For comparison, all the solvents were purified by vacuum distillation (25 cm Vigreux column) over liquid Na/K alloy; in the main text, they are referred to as "distilled solvent." Although this method provides solvents in a purified, dry form, the use of such highly reactive agents can be quite dangerous for both the novice and the experienced researcher. Extreme caution and PPE (hood, blast shields, face shield, and protective and fire-resistant clothing) should always be used. Considering the danger and laborious work introduced by using metallic Na/K, purification by calcium hydride was also tried in this work to evaluate its feasibility in practice; the solvent was referred to as "dried by CaH_2." Typically, fresh ground CaH_2 (~10 g) was added to 1 L of solvent in a side-arm Schlenk flask, and the solvent was allowed to stir over CaH_2 overnight. Once finished, all the solvents were stored in an inert atmosphere (i.e., glovebox). The water content in these samples was determined by Karl Fischer titration (Mettler-Toledo).

Mg $(TFSI)_2$ (99.5%, solvionic) and $MgCl_2$ (99.9%) were vacuum-dried at 150°C for 24 h before use. The electrolytes contained different mixtures were stirred at room temperature for 1 day to make uniform solutions. All electrolytes were prepared in a wet-chemical glovebox and then were transferred into another glovebox, which was equipped with electrochemistry testing apparatus using a sealed mason jar without exposure to air.

4.2 Gas chromatography—mass spectrometry measurement

The impurities in the solvents were identified using the Clarus 600/560D gas chromatograph with a mass spectrometer detector. An autosampler (Perkin Elmer) was used to make the sample injections. The inlet was equipped with a split/splitless injector and a nonpolar Supelco SLB™-5 ms (30 m × 0.25 mm I.D. × 0.25 μm) film capillary column. A constant helium flow rate of 1.0 ml/min was used as the carrier gas. An inlet temperature was set at 220°C, and the oven temperature was programmed to heat from 50 to 250°C at 20°C/min. The final oven temperature was held for 5 min to allow all the compounds to elute. The overall measurement time was 15 min. The mass ranges from 15 to 300 m/z, and the event time was 0.1 s in a scan mode. The mass spectrometer was run in the electron impact ionization (EI) mode. The temperature of the ion source was set to 180 C, and the filament was operated at a voltage of 70 V. Data were processed by TurboMass™ software with the commercial searchable libraries (NIST) for automatic peak detection and spectral deconvolution.

4.3 Electrochemistry

Cyclic voltammograms of each electrolyte were carried out using a customized three-electrode glass T-cell (ACE Glass), as shown in Figure 9. The bushing and ferrule were made of polytetrafluoroethylene (PTFE) to resist organic solvents. All glassware and sealing parts were dried in an oven at 120°C overnight before transferring into the glovebox. A Pt disk was cleaned by immersing it in 1 M HNO_3 before testing and was used as the working electrode (2 mm in diameter, CH instruments, Austin, TX). Mg rods, polished in the glovebox to expose fresh metal surface, were used as the counter and reference electrodes (99.9% purity). To ensure the consistency and comparison of the electrochemistry activity between different electrolytes, 1.5 ml of solution was introduced in the cell to keep the same electrolyte level. The distance between each electrode was fixed for every experiment. Cyclic voltammetry (CV) was performed using a Gamry electrochemical workstation in the glovebox.

4.4 Liquid chromatography–electrospray ionization–mass spectrometry (LC-ESI-MS)

Mass spectrometry measurements were taken using an Agilent Technologies 1260 Infinity liquid chromatograph equipped with an Agilent 6120 Quadrupole ESI mass spectrometer. A direct infusion method with sample *via* airtight Hamilton syringes was used to minimize exposure to an ambient atmosphere. The detector capillary voltage was 3000 V, the drying gas (N2) flow rate was 12 L/min, the nebulizer pressure was 35 psig, the drying gas temperature was 350°C, and the fragmentor voltage was 70 V. The spectrometer measured a range of m/z values from 150 to 2,000.

4.5 X-ray photoelectron spectroscopy

A PHI VersaProbe II was used for XPS measurements of Mg electrodes after cycling. This system was attached to an Ar-atmosphere glovebox, and the samples were transferred to the XPS through a glovebox without exposure to air. A 100-W X-ray beam was focused to a 100 μm diameter. A high-resolution spectrum for each individual element was taken with a 23.5 eV pass energy over 30 scans. Spectra were calibrated against a C–C 284.8 eV carbon peak.

Data availability statement

The original contributions presented in the study are included in the article/Supplementary Material; further inquiries can be directed to the corresponding authors.

Author contributions

ZY: conceptualization, investigation, data curation, formal analysis, validation writing— original draft, and writing— review and editing. MY: investigation. NH, JC, IB, and CL: investigation and review and editing. BI and LT: supervision and review and editing.

Acknowledgements

This work was supported as part of the Joint Center for Energy Storage Research, an Energy Innovation Hub funded by the U.S. Department of Energy, Office of Science, Basic Energy Sciences. The submitted manuscript has been created by UChicago Argonne, LLC, Operator of Argonne National Laboratory ("Argonne"). Argonne, a U.S. Department of Energy Office of Science laboratory, is being operated under the contract no. DE-AC02-06CH11357. Sandia National Laboratories is a multimission laboratory managed and operated by the National Technology and Engineering Solutions of Sandia, LLC, a wholly owned subsidiary of Honeywell International Inc., for the U.S. Department of Energy's National Nuclear Security Administration under the contract DE-NA0003525. This article describes the objective technical results and analysis. Any subjective views or opinions that might be expressed in the article do not necessarily represent the views of the U.S. Department of Energy or the United States Government.

Conflict of interest

The authors declare that the research was conducted in the absence of any commercial or financial relationships that could be construed as a potential conflict of interest.

Publisher's note

All claims expressed in this article are solely those of the authors and do not necessarily represent those of their affiliated organizations, or those of the publisher, the editors, and the reviewers. Any product that may be evaluated in this article, or claim that may be made by its manufacturer, is not guaranteed or endorsed by the publisher.

Supplementary material

The Supplementary Material for this article can be found online at: https://www.frontiersin.org/articles/10.3389/fchem.2022.966332/full#supplementary-material

References

Aurbach, D., Lu, Z., Schechter, A., Gofer, Y., Gizbar, H., Turgeman, R., et al. (2000). Prototype systems for rechargeable magnesium batteries. *Nature* 407, 724–727. doi:10.1038/35037553

Aurbach, D., Suresh, G. S., Levi, E., Mitelman, A., Mizrahi, O., Chusid, O., et al. (2007). Progress in rechargeable magnesium battery Technology. *Adv. Mater.* 19, 4260–4267. doi:10.1002/adma.200701495

Barile, C. J., Barile, E. C., Zavadil, K. R., Nuzzo, R. G., and Gewirth, A. A. (2014). Electrolytic conditioning of a magnesium aluminum chloride complex for reversible magnesium deposition. *J. Phys. Chem. C* 118, 27623–27630. doi:10.1021/jp506951b

Bitenc, J., Pirnat, K., Žagar, E., Randon-Vitanova, A., and Dominko, R. (2019). Effect of salts on the electrochemical performance of Mg metal–organic battery. *J. Power Sources* 430, 90–94. doi:10.1016/j.jpowsour.2019.04.114

Connell, J. G., Genorio, B., Lopes, P. P., Strmcnik, D., Stamenkovic, V. R., Markovic, N. M., et al. (2016). Tuning the reversibility of Mg anodes via controlled surface passivation by H_2O/Cl^- in organic electrolytes. *Chem. Mater.* 28, 8268–8277. doi:10.1021/acs.chemmater.6b03227

Connell, J. G., Zorko, M., Agarwal, G., Yang, M., Liao, C., Assary, R. S., et al. (2020). Anion association strength as a unifying descriptor for the reversibility of divalent metal deposition in nonaqueous electrolytes. *ACS Appl. Mater. Interfaces* 12, 36137–36147. doi:10.1021/acsami.0c09404

Deivanayagam, R., Ingram, B. J., and Shahbazian-Yassar, R. (2019). Progress in development of electrolytes for magnesium batteries. *Energy Storage Mater.* 21, 136–153. doi:10.1016/j.ensm.2019.05.028

Dlugatch, B., Mohankumar, M., Attias, R., Krishna, B. M., Elias, Y., Gofer, Y., et al. (2021). Evaluation of $Mg[B(HFIP)_4]_2$-Based electrolyte solutions for rechargeable Mg batteries. *ACS Appl. Mater. Interfaces* 13, 54894–54905. doi:10.1021/acsami.1c13419

Fisher, S. P., Tomich, A. W., Guo, J., and Lavallo, V. (2019). Teaching an old dog new tricks: new directions in fundamental and applied closo-carborane anion chemistry. *Chem. Commun.* 55, 1684–1701. doi:10.1039/c8cc09663e

Ha, S.-Y., Lee, Y.-W., Woo, S. W., Koo, B., Kim, J.-S., Cho, J., et al. (2014). Magnesium(II) bis(trifluoromethane sulfonyl) imide-based electrolytes with wide electrochemical windows for rechargeable magnesium batteries. *ACS Appl. Mater. Interfaces* 6, 4063–4073. doi:10.1021/am405619v

Ha, J. H., Adams, B., Cho, J.-H., Duffort, V., Kim, J. H., Chung, K. Y., et al. (2016). A conditioning-free magnesium chloride complex electrolyte for rechargeable magnesium batteries. *J. Mater. Chem. A* 4, 7160–7164. doi:10.1039/c6ta01684g

Hahn, N. T., Seguin, T. J., Lau, K.-C., Liao, C., Ingram, B. J., Persson, K. A., et al. (2018). Enhanced stability of the carba-closo-dodecaborate anion for high-voltage battery electrolytes through rational design. *J. Am. Chem. Soc.* 140, 11076–11084. doi:10.1021/jacs.8b05967

He, Y., Li, Q., Yang, L., Yang, C., and Xu, D. (2019). Electrochemical-conditioning-free and water-resistant hybrid $AlCl_3/MgCl_2/Mg(TFSI)_2$ electrolytes for rechargeable magnesium batteries. *Angew. Chem. Int. Ed.* 58, 7615–7619. doi:10.1002/anie.201812824

Kang, S.-J., Kim, H., Hwang, S., Jo, M., Jang, M., Park, C., et al. (2019). Electrolyte additive enabling conditioning-free electrolytes for magnesium batteries. *ACS Appl. Mater. Interfaces* 11, 517–524. doi:10.1021/acsami.8b13588

Lau, K.-C., Seguin, T. J., Carino, E. V., Hahn, N. T., Connell, J. G., Ingram, B. J., et al. (2019). Widening electrochemical window of Mg salt by weakly coordinating perfluoroalkoxyaluminate anion for Mg battery electrolyte. *J. Electrochem. Soc.* 166, A1510–A1519. doi:10.1149/2.0751908jes

Leon, N. J., He, M., and Liao, C. (2022). Solvation, rational design, and interfaces: Development of divalent electrolytes. *Front. Energy Res.* 9. doi:10.3389/fenrg.2021.802398

Ma, Z., Kar, M., Xiao, C., Forsyth, M., and MacFarlane, D. R. (2017). Electrochemical cycling of Mg in $Mg[TFSI]_2$/tetraglyme electrolytes. *Electrochem. Commun.* 78, 29–32. doi:10.1016/j.elecom.2017.03.018

McArthur, S. G., Jay, R., Geng, L., Guo, J., and Lavallo, V. (2017). Below the 12-vertex: 10-vertex carborane anions as non-corrosive, halide free, electrolytes for rechargeable Mg batteries. *Chem. Commun.* 53, 4453–4456. doi:10.1039/c7cc01570d

Michaels, D. (2000). *Multiple injury accident resulting from the sodium-potassium explosion in building 9201-5 at the Y-12 plan*. National Chemical Safety Program: Office of Oversight Environment, Safety and Health Available at: https://ncsp.tamu.edu/reports/DOE/oversight/9912y12.pdf.

Muldoon, J., Bucur, C. B., and Gregory, T. (2014). Quest for nonaqueous multivalent secondary batteries: Magnesium and beyond. *Chem. Rev.* 114, 11683–11720. doi:10.1021/cr500049y

Pan, B., Huang, J., He, M., Brombosz, S. M., Vaughey, J. T., Zhang, L., et al. (2016). The role of $MgCl_2$ as a Lewis base in $ROMgCl–MgCl_2$ electrolytes for magnesium-ion batteries. *ChemSusChem* 9, 595–599. doi:10.1002/cssc.201501557

Ren, W., Wu, D., NuLi, Y., Zhang, D., Yang, Y., Wang, Y., et al. (2021). An efficient bulky Mg[B(Otfe)4]2 electrolyte and its derivatively general design strategy for rechargeable magnesium batteries. *ACS Energy Lett.* 6, 3212–3220. doi:10.1021/acsenergylett.1c01411

Sa, N., Pan, B., Saha-Shah, A., Hubaud, A. A., Vaughey, J. T., Baker, L. A., et al. (2016). Role of chloride for a simple, non-grignard Mg electrolyte in ether-based solvents. *ACS Appl. Mater. Interfaces* 8, 16002–16008. doi:10.1021/acsami.6b03193

Salama, M., Shterenberg, I., Shimon, J. W. L., Keinan-Adamsky, K., Afri, M., Gofer, Y., et al. (2017). Structural analysis of magnesium chloride complexes in dimethoxyethane solutions in the context of Mg batteries Research. *J. Phys. Chem. C* 121, 24909–24918. doi:10.1021/acs.jpcc.7b05452

Seguin, T. J., Hahn, N. T., Zavadil, K. R., and Persson, K. A. (2019). Elucidating non-aqueous solvent stability and associated decomposition mechanisms for Mg energy storage applications from first-principles. *Front. Chem.* 7, 175. doi:10.3389/fchem.2019.00175

Shterenberg, I., Salama, M., Yoo, H. D., Gofer, Y., Park, J.-B., Sun, Y.-K., et al. (2015). Evaluation of $(CF_3SO_2)_2N^-$(TFSI) based electrolyte solutions for Mg batteries. *J. Electrochem. Soc.* 162, A7118–A7128. doi:10.1149/2.0161513jes

Tang, S., and Zhao, H. (2014). Glymes as versatile solvents for chemical reactions and processes: from the laboratory to industry. *RSC Adv.* 4, 11251–11287. doi:10.1039/c3ra47191h

Wang, H., Feng, X., Chen, Y., Liu, Y.-S., Han, K. S., Zhou, M., et al. (2020). Reversible electrochemical interface of Mg metal and conventional electrolyte enabled by intermediate adsorption. *ACS Energy Lett.* 5, 200–206. doi:10.1021/acsenergylett.9b02211

Yoo, H. D., Shterenberg, I., Gofer, Y., Gershinsky, G., Pour, N., Aurbach, D., et al. (2013). Mg rechargeable batteries: an on-going challenge. *Energy Environ. Sci.* 6, 2265. doi:10.1039/c3ee40871j

Yoo, H. D., Han, S.-D., Bolotin, I. L., Nolis, G. M., Bayliss, R. D., Burrell, A. K., et al. (2017). Degradation mechanisms of magnesium metal anodes in electrolytes based on $(CF_3SO_2)_2N^-$ at high current densities. *Langmuir* 33, 9398–9406. doi:10.1021/acs.langmuir.7b01051

Yu, Y., Baskin, A., Valero-Vidal, C., Hahn, N. T., Liu, Q., Zavadil, K. R., et al. (2017). Instability at the electrode/electrolyte interface induced by hard cation chelation and nucleophilic attack. *Chem. Mater.* 29, 8504–8512. doi:10.1021/acs.chemmater.7b03404

frontiers | Frontiers in Chemistry

TYPE Original Research
PUBLISHED 22 August 2022
DOI 10.3389/fchem.2022.934376

Check for updates

OPEN ACCESS

EDITED BY
Thierry Brigaud,
CY Cergy Paris Université, France

REVIEWED BY
William Brittain,
Durham University, United Kingdom
Gosuke Hayashi,
Nagoya University, Japan

*CORRESPONDENCE
Graciela Mahler,
gmahler@fq.edu.uy

SPECIALTY SECTION
This article was submitted to Organic Chemistry,
a section of the journal
Frontiers in Chemistry

RECEIVED 02 May 2022
ACCEPTED 06 July 2022
PUBLISHED 22 August 2022

CITATION
Villamil V, Saiz C and Mahler G (2022), Thioester deprotection using a biomimetic NCL approach.
Front. Chem. 10:934376.
doi: 10.3389/fchem.2022.934376

COPYRIGHT
© 2022 Villamil, Saiz and Mahler. This is an open-access article distributed under the terms of the Creative Commons Attribution License (CC BY). The use, distribution or reproduction in other forums is permitted, provided the original author(s) and the copyright owner(s) are credited and that the original publication in this journal is cited, in accordance with accepted academic practice. No use, distribution or reproduction is permitted which does not comply with these terms.

Thioester deprotection using a biomimetic NCL approach

Valentina Villamil[1,2], Cecilia Saiz[1] and Graciela Mahler[1]*

[1]Laboratorio de Química Farmacéutica (DQO), Facultad de Química, Universidad de la República, Montevideo, Uruguay, [2]Graduate Program in Chemistry, Facultad de Química, Universidad de la República (UdelaR), Montevideo, Uruguay

The reversibility of the thiol-thioester linkage has been broadly employed in many fields of biochemistry (lipid synthesis) and chemistry (dynamic combinatorial chemistry and material science). When the transthioesterification is followed by a S-to-N acyl transfer to give an amide bond, it is called Native Chemical Ligation (NCL), a high-yield chemoselective process used for peptide synthesis. Recently, we described thioglycolic acid (TGA) as a useful reagent for thioester deprotection both in solution and anchored to a solid-support under mild conditions. Inspired by NCL, in this work, we extended this approach and explored the use of 2-aminothiols for the deprotection of thiols bearing an acyl group. The best results were obtained using cysteamine or L-cysteine in an aqueous buffer pH 8 at room temperature for 30 min. The described approach was useful for S-acetyl, S-butyryl, and S-benzoyl heterocycles deprotection with yields up to 84%. Employing this methodology, we prepared six new analogs **2** of mercaptomethyl bisthiazolidine **1**, a useful inhibitor of a wide-range of Metallo-β-Lactamases (MBLs). Compared with the previous methodologies (TGA polymer supported and TGA in solution), the biomimetic deprotection herein described presents better performance with higher yields, shorter reaction times, less time-consuming operations, easier setup, and lower costs.

KEYWORDS

thioester deprotection, transthioesterification, native chemical ligation, bisthiazolidine, thiol

Introduction

The thiol-thioester exchange occurs smoothly in neutral aqueous media at room temperature and is a highly chemoselective process. Due to these ideal features, this exchange reaction is found in many natural processes, including energy metabolism, mitosis, and autophagy (Pietrocola et al., 2015). Moreover, the abundance of thioester-mediated processes in nature has led to speculation regarding the role of these derivatives in the origin of life (Chandru et al., 2016; Vallee et al., 2017).

Besides the importance of the thiol-thioester exchange in biochemical processes, the reversibility of this linkage has been broadly used in the field of dynamic combinatorial chemistry (Mondal and Hirsch, 2015) and, more recently, applied in material science (Worrell et al., 2018).

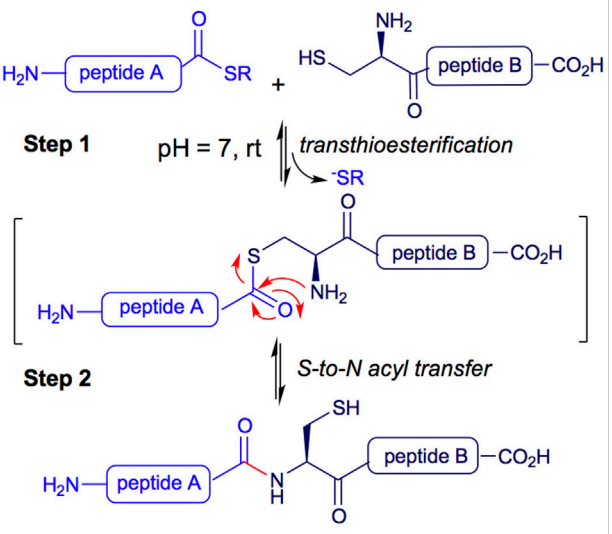


FIGURE 1
Native chemical ligation peptide synthesis.

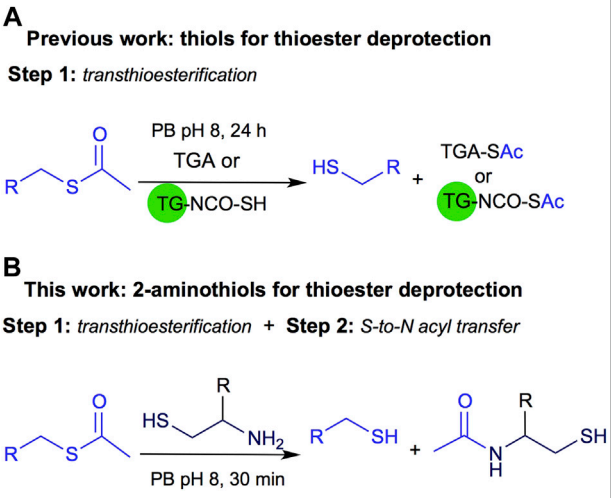


FIGURE 2
(A) Previous work on thioester deprotection using Method A polymer supported TGA (TG-NCO-SH) or Method B TGA in solution. **(B)** This work uses 2-aminothiols for thioacetyl deprotection.

In particular, Native Chemical Ligation (NCL) is a methodology used for peptide synthesis. It is a high-yielding chemoselective process, successfully applied to peptide and protein synthesis, chemical modification of proteins, protein-protein ligation, and the development of probes and molecular machines (Dawson et al., 1994; Gui et al., 2016; Burke et al., 2017). The NCL process begins with a reversible transthioesterification between two peptides. The mercapto group of an N-terminal cysteine residue of a peptide B attacks the C-terminal thioester of a second unprotected peptide A in an aqueous buffer at pH 7.0 (see Figure 1, Step 1). A second step consists of an S-to-N acyl transfer, leading to the formation of an amide bond between both peptides A and B (Figure 1, Step 2) (Serra et al., 2020).

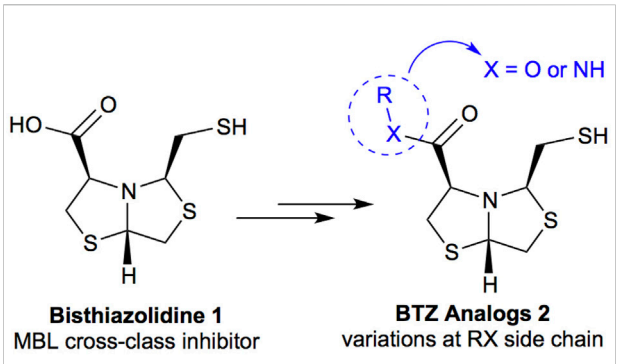


FIGURE 3
Bisthiazolidines **1** and BTZ analogs **2** with variations at RX.

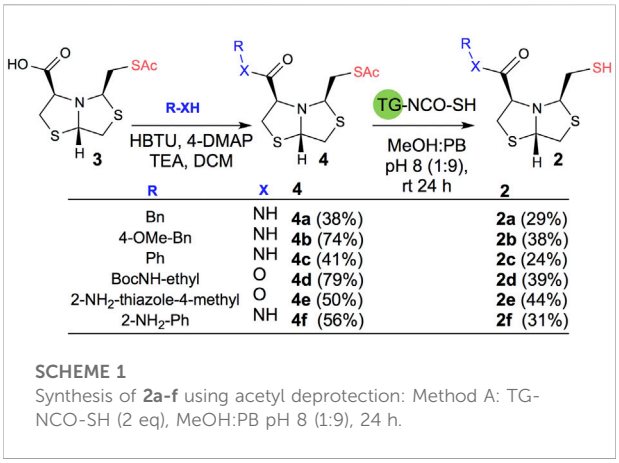
Recently, we described another application of this reversible process applied to thiol deprotection in solution under mild conditions. This methodology is a valuable tool, especially when the substrate does not support harsh conditions like strong basic media. The deprotection is carried out using thioglycolic acid anchored to a solid support like TentaGel® resin (TG-NCO-SH, Method A) or in solution (Method B), Figure 2A (Villamil et al., 2021). Both homogeneous and heterogeneous approaches were conveniently carried out at room temperature, in aqueous buffer at pH 8, and the methods were useful for thioacetyl deprotection of several substrates, affording the free thiol after 24 h of reaction.

Bisthiazolidines **1** (BTZ) are cross-class metallo-β-lactamases (MBLs) inhibitors active *in vitro* and against MBL-expressing bacterial pathogens, Figure 3. These compounds were designed as penicillin analogs and behaved as competitive inhibitors of MBLs from all subclasses, with K_i values in the micromolar range. BTZ were effective against NDM-1, VIM-2, L1, and IMP-1, all MBLs of clinical importance (Mojica et al., 2015; González et al., 2016; Hinchliffe et al., 2016).

Previous studies showed that the mercaptomethyl group present in **1** is essential for MBL inhibition (Hinchliffe et al., 2016). With this in mind, we aimed to prepare new bisthiazolidine analogs **2** with variations on the carboxylic acid (R) in order to improve the inhibition activity. The synthetic route proposed includes thiol deprotection as the key step, see Figure 3.

Inspired by the NCL approach, in this work we propose to use 2-aminothiols for the deprotection of the thioacetyl derivatives as shown in Figure 2B. Although NCL is widely used in several fields of organic chemistry, to the best of our knowledge, it has not been explored for thioester deprotection in solution.

10.3389/fchem.2022.934376



SCHEME 1
Synthesis of **2a-f** using acetyl deprotection: Method A: TG-NCO-SH (2 eq), MeOH:PB pH 8 (1:9), 24 h.

Results and Discussion

In order to prepare new BTZ analogs **2**, first we synthesized S-acetylated bisthiazolidine **3** as previously described (Villamil et al., 2021). Then, amides **4a-c**, **4f,** and esters **4d-e** were obtained starting from **3** and the corresponding amine or alcohol (R-XH), using HBTU as a coupling agent in DCM with yields ranging from 38 to 79%, see Scheme 1.

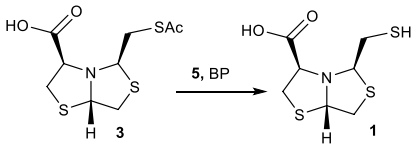
Based on our previous results, we performed the deprotection of thioacetylated compounds **4a-f** using TGA anchored to a TentaGel® resin (TG-NCO-SH), Method A. In this reaction, a transthioesterification process occurs between the thioester and the thiol. The mercaptomethyl derivatives **2a-f** were obtained after chromatographic column purification with yields ranging from 24 to 44%, as shown in Scheme 1.

Inspired by the Native Chemical Ligation (NCL) mechanism, where a transthioesterification reaction is followed by a 1-5 S,N-acyl transfer to form an amide and shift the equilibrium toward the product (Figure 1; Agouridas et al., 2019) and the report for the use of cysteamine (Cym) in acetonitrile under reflux for the conversion of simple and unfunctionalized thioesters into thiols (Endo et al., 1974), we envisioned that 2-aminothiols **5a-c** could be useful for the deprotection of acyl thioesters, as shown in Figure 2B.

In order to rapidly evaluate several sets of reaction conditions, we used reaction miniaturization, a concept developed by High Throughput Experimentation (HTE) to find the best reagents and conditions for a desired product. HTE is a tool that allows to perform a large number of experiments in parallel. The advantages of the reaction miniaturization studies is that they require a few milligrams of reagents (microscale) and shorter manipulation times compared to traditional experimentation (Wong and Cernak, 2018; Mennen et al., 2019).

Experimental and computational studies support the notion of the thiolate as the effective nucleophilic species in NCL (Wang et al., 2011; Diemer et al., 2022). In this sense, the aminothiols **5a-c** to be screened were selected basically based on the pKa value of the thiol, dismissing other possible ionic species (Maguire et al., 2020).

TABLE 1 Optimization of thioester deprotection using different 2-aminothiols 5a-c for the deprotection of 3.



	pH	Time (h)	HPLC 1 yield (%)[a]		
			L-CysOEt 5a	L-Cys 5b	Cym 5c
1	7	0.5	nd	64	69
2		1	nd	80	79
3		2	76	90	84
4	8	0.25	nd	62	62
5		0.5	68	83	89
6		1	nd	78	73
7		2	90	nd	nd

[a]Yields were determined using a validated HPLC technique in which BTZ **1** was used as external standard.

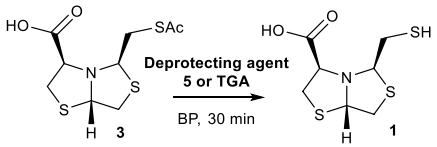
We reasoned that L-Cysteine ethyl ester (L-CysOEt, **5a**) bearing a thiol with a pKa = 6.5 could be first explored since it is close to neutral pH (Friedman et al., 1965). According to the Henderson-Hasselbach equation, the ratio of the L-CysOEt species SH/S^- is 1/2.5 in H_2O at pH 7.30 (Henderson, 1908). A different aspect to consider is that thiolates are susceptible to oxidation (leading to disulfide species), a process that is accelerated when the pH of the solution is close to or above the thiol pKa.

Taking these considerations into account, the deprotection reaction of **3** was screened in aqueous buffers pH range from 5 to 8, aminothiol **5a** equivalents from 1 to 10 and the time from 0.5 to 6 h, see Supplementary Table S1. Aliquots were taken at different times and diluted for HPLC analysis. Overall, the best conditions for **3** deprotection were achieved using 2 eq L-CysOEt at pH 8, during 2 h to give **1** in 90% yield (see Supplementary Table S1). Since the thiol–thioester exchange is an equilibrium (Bongiardina et al., 2021), an excess of the deprotecting agent **5a** is required to shift the equilibrium toward the desired product. The reactions performed at pH 5 and 6 provided the less favorable yields, even when using more equivalents of 2-aminothiol or longer reaction times.

Based on these results, we extended the screening of 2-aminothiols including L-Cysteine (L-Cys, **5b**) and Cysteamine (Cym, **5c**) for the deprotection of thioacetyl bisthiazolidine **3**. These 2-aminothiols bear a thiol pKa value of 8.3 and

10.3389/fchem.2022.934376

TABLE 2 Deprotection of thioester 3 under optimized conditions MeOH:BP (1:9), pH 8, rt, 30 min, aminothiol 5 (2 eq) or TGA (2 eq).



Entry	Deprotecting agent (2 eq)	1 Yield (%)[a]
1	L-CysOEt **5a**	65
2	L-Cys **5b**	75
3	Cym **5c**	78
4	TGA[b]	56[b]

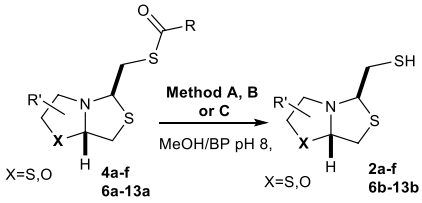
[a]Yields correspond to purified compounds by column chromatography on flash SiO_2.
[b] values were obtained from reference (Villamil et al., 2021).

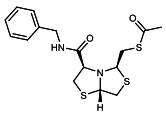
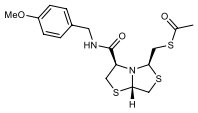
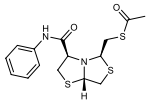
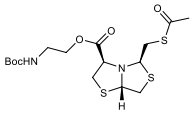
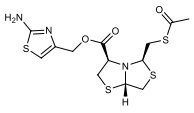
8.2 respectively (Pitman and Morris, 1979). Thus, to ensure a significant amount of thiolate, the reaction was performed at pH 7 (Table 1 entry 1–3) and pH 8 (Table 1, entry 4–7), and the reaction time was screened from 0.25 to 2 h using 2 equivalents of **5b/c**.

Both 2-aminothiols, L-Cys **5b** and Cym **5c,** gave similar yields compared to L-Cys-OEt **5a**. Overall, Cym **5c** was the best deprotecting agent, using 2 equivalents at pH 8 after only 30 min, affording **1** in 89% HPLC yield, Table 1, entry 5.

The HTE allowed us to find the best reaction conditions by running several experiments simultaneously rather than carrying out single ones, reducing the cost and time of the experiments. Overall, we performed 23 reactions in aqueous media, using less than 30 mg of compound **3** to find the optimal conditions for the deprotection reaction. This example shows the potential of the

TABLE 3 Thiol deprotection yield (%) using Method A, B and C of different substituted BTZ. Method A: TG-NCO-SH (2 eq) MeOH:BP pH 8 (1:9), 24 h; Method B: TGA (2 eq), MeOH:PB pH 8 (1:9), 0.5 or 24 h; Method C: Cym (2 eq), MeOH:PB pH 8 (1:9)0.5 h.

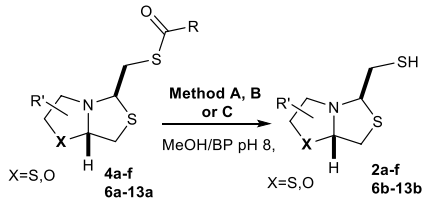


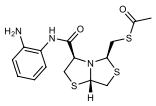
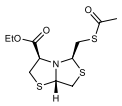
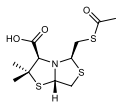
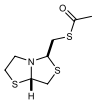
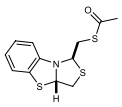
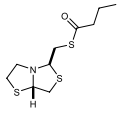
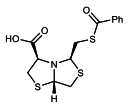
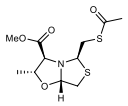
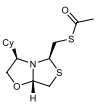
Entry	Starting Material		Method, Yield %, (time h)			
			Product	A, (24 h)	B, (0.5 or 24 h)	C, (0.5 h)
1		4a	2a	29	15 (0.5)	64
2		4b	2b	38	10 (0.5)	50
3		4c	2c	24	10 (0.5)	58
4		4d	2d	39	28 (0.5)	70
5		4e	2e	44	24 (0.5)	68

(Continued on following page)

10.3389/fchem.2022.934376

TABLE 3 (*Continued*) Thiol deprotection yield (%) using Method A, B and C of different substituted BTZ. Method A: TG-NCO-SH (2 eq) MeOH:BP pH 8 (1:9), 24 h; Method B: TGA (2 eq), MeOH:PB pH 8 (1:9), 0.5 or 24 h; Method C: Cym (2 eq), MeOH:PB pH 8 (1:9)0.5 h.



Entry	Starting Material		Method, Yield %, (time h)			
			Product	A, (24 h)	B, (0.5 or 24 h)	C, (0.5 h)
6		4f	2f	31	20 (0.5)	78
7		6a	6b	6,610	56 (24)*	59
8		7a	7b	9,210	71 (24)*	84
9		8a	8b	7,910	77 (24)*	80
10		9a	9b	6,610	51 (24)*	59
11		10a	8b	6,110	58 (24)*	51
12		11a	1	7,610	75 (24)*	78
13		12a	12b	6,810	69 (24)*	80
14		13a	13b	6,510	53 (24)*	61

Yields correspond to purified compounds by column chromatography on flash SiO_2.

*: value extracted from (Villamil et al., 2021)..

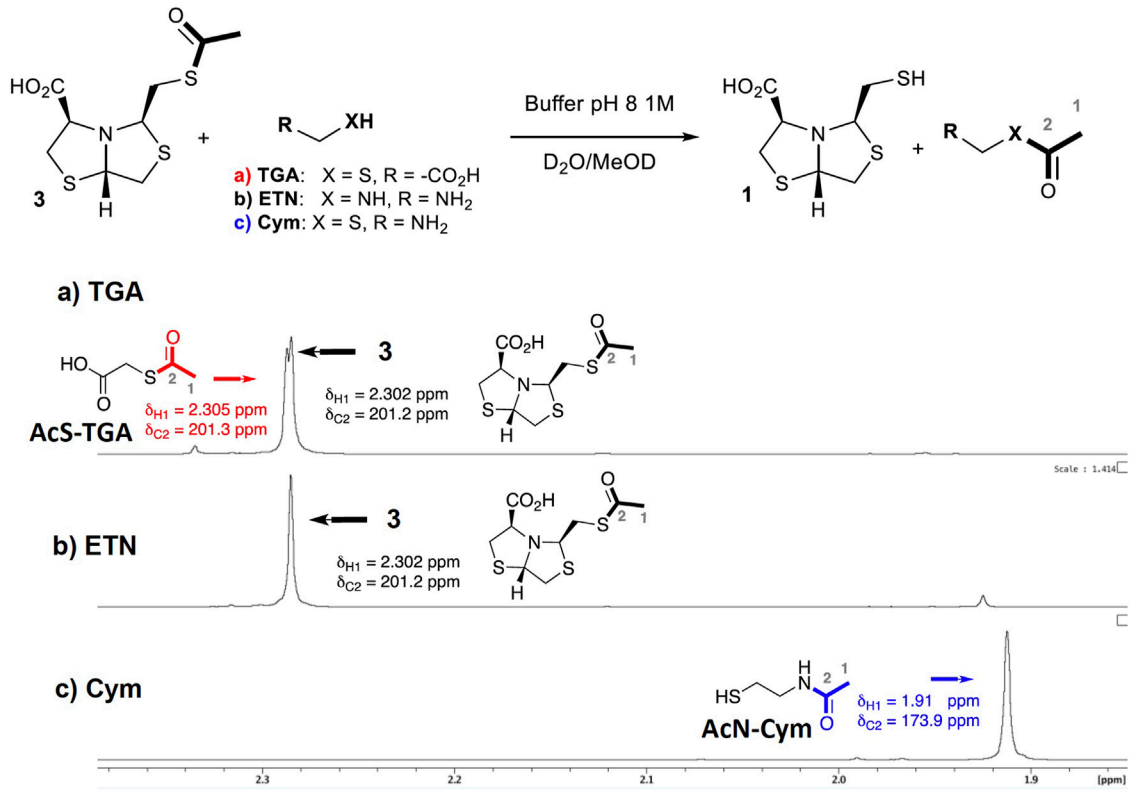


FIGURE 4
Comparison of ^{1}H-NMR spectra for the deprotection reaction of **3** using different additives. Reaction of **3** (0.04 mmol) in D_2O, PB [1 M] at pH 8, and MeOD-d4 (10%) at 27°C after 40 min: **(A)** TGA (0.08 mmol); **(B)** ethylenediamine (0.08 mmol); **(C)** Cym **5c** (0.08 mmol). The ^{13}C chemical shift of C2 atoms was obtained from ^{1}H,^{13}C-HMBC correlations to the respective acetyl protons.

reaction miniaturization tool, mainly due to waste reduction and shorter time-consuming operations.

Reaction scale-up for the deprotection of thioacetyl 3

Once the best reaction conditions were established, the reaction was scaled-up for deprotection of **3** using 2-aminothiols L-CysOEt **5a**, L-Cys **5b**, and Cym **5c** at pH 8 for 30 min. The isolated yields of **1** were 65%, 75%, and 78%, respectively, see Table 2, entries 1, 2, and 3. These results correlate well with the yields determined by HPLC at 68%, 83%, and 89%, respectively (Table 1), validating the results obtained by HTE. The three 2-aminothiols employed afford the free thiols in better yields than previously described TGA in solution (56% yield after 30 min), Table 2. The yield values for TGA in solution was obtained in a previous work (Villamil et al., 2021).

Deprotection of thioacetyl bicycles **4a-f** using the optimized conditions (Method C: Cym **5c** pH 8, 30 min at rt) led to analogs **2a-f** in yields ranging from 50 to 78%, Table 3. The average yield was 65%, remarkably higher than those obtained using the TGA solid-supported approach (Method A, average yield of 34%). In addition, the reaction time decreased from 24 h to 30 min. This aspect is crucial since products **2a-f**, containing a free thiol, are easily oxidized in aqueous buffer. 2-aminothiols **5** allowed to set up reactions in shorter reaction times compared with TGA, affording better yields, probably by avoiding product oxidation.

In order to highlight the best performance of Cym regarding TGA in solution, we carried out the deprotection reaction of the new derivatives **4a-f** using method B (TGA in solution) after 30 min instead of 24 h, to compare the yields with method C (Cym in solution). The average yields were methods B and C, was 18% and 65%, respectively, significantly higher when using Cym, Table 3. The yield values for methods A and B (24 h) were obtained in a previous work (Villamil et al., 2021).

Reaction scope

To extend the methodology scope, different S-acyl bisthiazolidines **6a-11a**, and S-acetyl oxazolidines **12a** and **13a** were assayed using Cym **5c** (Method C) and compared with our

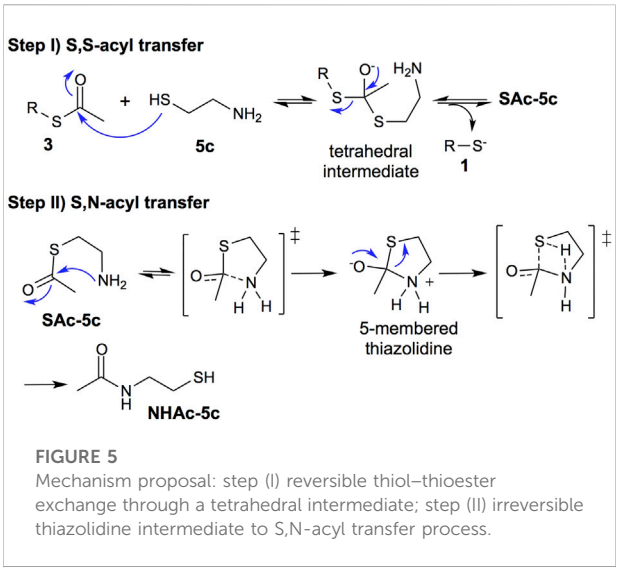


FIGURE 5
Mechanism proposal: step (I) reversible thiol–thioester exchange through a tetrahedral intermediate; step (II) irreversible thiazolidine intermediate to S,N-acyl transfer process.

previous results using TGA solid-supported and TGA in solution (Method A and B, respectively) (Villamil et al., 2021), see Table 3.

Method C smoothly deprotected S-acetyl bisthiazolidines/oxazolidines **6a**-**9a**, **12a,** and **13a** with yields ranging from 59 to 84%, Table 3, entries 7–10, 13, and 14. In addition, different acyl side chains like propyl thioester **10a** and benzoyl thioester **11a** were deprotected in moderate to good yields, 51 and 78%, respectively, in Table 3, entries 11 and 12.

Altogether, the results obtained with our previous approaches (Methods A and B) led to slightly lower average yields compared to Method C (56, 64, and 67%, respectively) and shorter reaction times, 24 h vs 30 min. In addition, regarding method A, Cym is a common reagent in organic laboratories and is less expensive than Tentagel® resin.

Overall, Method C herein reported provides better yields in a shorter time with a lower-cost reagent and easier setup.

Mechanistic insights

As described in NCL, the presence of a 2-aminothiol enables an intramolecular *S*-to-*N*-acyl migration, releasing the thiol and displacing the equilibrium toward the products (Wang et al., 2011). This fact suggests that when using Cym for thioester deprotection, an analogous process is occurring. In order to confirm the deprotection mechanism, NMR experiments were performed. Three sets of conditions were assayed in PB pH 8 using different deprotecting agents: 1) thioglycolic acid (TGA, 2 eq); 2) ethylenediamine (ETN, 2 eq); and 3) Cysteamine **5c** (2 eq).

In the first experiment, when using TGA for thiol deprotection, after 40 min of reaction, 50% of the deprotection product was observed and thioacetylated TGA could be detected, Figure 4A.

Transthioesterification is the main deprotection mechanism in these conditions. A complete deprotection was observed after 9 h of incubation, Supplementary Figure S1.

On the other hand, when ethylenediamine (ETN) is used, the deprotection reaction is not observed by ^{1}H NMR after 40 min, Figure 4B. This result indicates that only an amine group is not able to deprotect the thiol.

Finally, when Cym **5c** is used as a deprotecting agent, a complete thiol deprotection is observed after 40 min of incubation. Only N-acetylated cysteamine and free-thiol **1** were found in the ^{1}H-NMR spectra, while S-acetylated cysteamine was not detected, see Figure 4C. The ^{1}H-NMR spectra at t = 40 min comparison of experiments 1) and c) shows that the reaction rate is faster for c), observing a complete deprotection of **3**.

Based on the obtained results and the numerous studies of the NCL mechanism (Barnett and Jencks, 1969; Wang et al., 2011), we propose, as a first step, a reversible S,S-acyl transfer involving an anionic concerted S_N2 displacement mechanism with the formation of a tetrahedral intermediate, Figure 5, Step I (Barnett and Jencks, 1969). This is a common intermediate for the deprotection of thioesters using 2-aminothiols or thiols lacking the amino group.

The second step involves the *S,N*-acyl transfer, which could proceed by an *5-endo-trig* cyclization to form a thiazolidine intermediate, an irreversible step faster than the thiol–thioester exchange (Figure 5, step II).

In summary, the thiol-thioester exchange step is reversible, whereas the S,N-acyl transfer is irreversible, displacing the thiol-thioester exchange equilibrium toward the product **1** and N-acetylated cysteamine (NHAc-**5c**), increasing the deprotection reaction rate.

Conclusion

In summary, we found that 2-aminothiols are suitable deprotecting agents for acyl thioester groups under aqueous mild conditions, mimicking a NCL approach. The reversibility of thiol–thioester exchange and the high efficacy of the intramolecular S,N-acyl migration process are driving forces to increase the reaction rate, affording shorter reaction times. In addition to this, the mild experimental conditions, near neutral pH, disfavor oxidation processes or bisthiazolidine-ring opening, increasing the deprotection reaction yields.

The new Cym deprotection methodology allowed us to prepare six new analogs of BTZ **1** with different substitutions at carboxylic acid (**2a-f**) to further be evaluated as MBL inhibitors.

The biomimetic deprotection herein described presents better performance than previous reported methodologies (TGA polymer supported and TGA in solution), with higher

yields, less time-consuming operation, shorter reaction times, easier setup, and lower costs. We envision that these conditions could provide a simple and practical method for labile thioester hydrolysis.

Experimental section

General Methods. All reactions were carried out in dry, freshly distilled solvents under anhydrous conditions unless otherwise stated. Reactions were monitored by analytical thin layer chromatography (TLC) on 0.25 mm silica gel coated plastic sheets (SIL G/UV 254). Flash chromatography on Silica gel 60 (40 μm average particle diameter) was used to purify the crude reaction mixtures. Yields are reported for chromatographic and spectroscopically (^{1}H and ^{13}C NMR) pure compounds unless otherwise stated. ^{1}H and ^{13}C NMR spectra were recorded on a Bruker Avance 400 instrument at 400 and 100 MHz, respectively. Chemical shifts (δ) are expressed in ppm downfield from TMS as an internal standard unless otherwise stated. Multiplicities are indicated as s (singlet), d (doublet), t (triplet), q (quartet), m (multiplet), b (broad). Assignments of ^{1}H and ^{13}C NMR peaks were made based on a combination of COSY, HSQC, and HMBC spectra. Electrospray ESI high-resolution mass spectra (HRMS) were recorded on a MicroTOF-Q spectrometer from Bruker Daltronics. Optical rotation was measured using a Jasco p-2000 polarimeter with a 2.0 ml cell, optical path length of 100 mm and sodium lamp (λ = 589 nm) at room temperature. The concentration c is given as g/100 ml.

HPLC Equipment and Method Validation. The liquid chromatography analysis was performed using Waters HPLC equipment, with binary pumps (Waters 1,525) and a photodiode array detector (Waters 2,996), with a loop injection of 20 μL (Rheodyne 1727). A reverse phase C18 separation column was used (Kinetex NUCLEOSIL® C18, 150 mm × 4 mm, 5 μm) with detection at λ = 205 nm for all compounds at 37°C. The eluent consisted of TFA 0.003 M (mobile phase A) and MeCN (mobile phase B) at a flow rate of 1.2 ml/min. The injection volume was 20 μl. Initial conditions 70/30 (mobile phase A/mobile phase B) changed in 2 min–55/45, maintained for 3.5 min, and changed in 0.1 min–5/95, maintained for 2.4 min. Data and chromatograms were collected and analyzed using the Empower System program by Waters Corporation, 2002. System linearity was verified in the concentration range: 0.01, 0.041, 0.102, 0.163, 0.203, and 0.244 mg/ml, prepared from a stock solution of BTZ **1**, 1 mM in MeOH. Linearity was established from the calibration curve using least squares linear regression analysis and a correlation coefficient (R^2) value of 0.9991 was found. A standard of 0.203 mg/ml was injected five times to evaluate the precision system, and a % RSD value of 1.0% was found.

Synthetic procedures

Compounds **1**, (González et al., 2016; Hinchliffe et al., 2016), **3**, (Villam il et al., 2021), **6–13** (Saiz et al., 2014; Villamil et al., 2021) were prepared according to previous reports.

Method A: General method for deprotection using TG-NCO-SH

A solution of **4a** (0.0167 g, 0.0454 mmol) in MeOH (0.5 ml) and degassed BP pH 8 1M (1.0 ml) was added to the polymer-supported deprotecting agent (TG-NCO-SH, 0.222 g, 0.0908 mmol) prepared as previously described (Villamil et al., 2021) and stirred for 24 h at room temperature under a nitrogen atmosphere. Then, the polymer was filtered and washed with MeOH. The organic layer was dried over Na_2SO_4, filtered and evaporated. The mixture was poured into a NaCl saturated solution and extracted with EtOAc (3 × 30 ml). The combined organic layers were dried, filtered, and concentrated to dryness. The crude was purified by column chromatography on flash SiO_2 (CH_2Cl_2/nHex 3:1) to yield **2a** (0.0043 g, 29%) as a colorless oil.

Method B: As previously described

(Villamil et al., 2021)

Method C: General method for deprotection using Cym

In a two-necked flask, **4a** (0.04 g, 0.11 mmol) was dissolved in MeOH (2 ml) and BP pH 8 1M (18 ml) and cysteamine hydrochloride **5c** (0.026 g, 0.22 mmol) was added. The reaction mixture was stirred for 30 min at room temperature, then poured into a NaCl saturated aqueous solution (30 ml) and extracted with EtOAc (3 × 30 ml). The combined organic layers were dried, filtered, and concentrated to dryness. The crude was purified by column chromatography on flash SiO_2 (CH_2Cl_2/nHex 3:1) to yield **2a** (0.023 g, 64%) as a colorless oil.

Optimization of the deprotection conditions of 3 using L-Cys-OEt 5a

Compound **3** was incubated into separate 2 ml Eppendorf® tubes at different pH and L-Cys-OEt **5a** concentrations, as described: **3** (100 μL of a solution of 42 mM in MeOH) was added to aqueous buffer 1M (pH 5, 6, 7 or 8, final volume 1 ml) and L-Cys-OEt **5a** (10, 20, 60 or 100 μl of a solution 420 mM in MeOH, corresponding to 1, 2, 6 or 10 equivalents) was added. The reaction solution was kept at 25°C and at suitable time intervals, aliquots of 100 μl were taken and acetonitrile (400 μl) was added. Then, the solution was vortexed, filtered, and chromatographed (Supplementary Table S1).

Optimization of the deprotection conditions of **3** using L-Cys **5b** and Cym **5c** was carried out using the same methodology as described for L-Cys-OEt **5a** (Table 1).

10.3389/fchem.2022.934376

Representative procedure for deprotection of 3 using L-Cys-OEt 5a in preparative scale

(Table 2) In a two-necked flask, compound **3** was dissolved (0.05 g, 0.18 mmol) in MeOH (1 ml) and added BP at pH 8 1M (19 ml) and L-Cys-OEt **5a** hydrochloride (0.067 g, 0.36 mmol). The reaction mixture was stirred for 30 min at room temperature. It was poured into HCl 5% and extracted with EtOAc (3 × 30 ml). The combined organic extracts were dried, filtered, and concentrated to dryness, and the crude was purified by column chromatography on flash SiO_2 (nHex/EtOAc/AcOH 7:3:0.01) to yield **1** (0.028 g, 65%).

Deprotection of **3** using thiols **5b**, **5c,** and TGA was carried out using the same methods as described for **5a** (Table 2).

Representative procedure for the synthesis of thioacetylated BTZ 4a-f

S-(((3R,5R,7aS)-3-(benzylcarbamoyl)tetrahydro-2H-thiazolo [4,3-b]thiazol-5-yl)methyl) ethanethioate (4a)

Into a two-necked flask under nitrogen atmosphere, **3** (0.1 , 0.36 mmol) was dissolved in dry CH_2Cl_2 (8 ml) and cooled in an ice bath. To the mixture was added HBTU (0.163 g, 0.43 mmol), DIPEA (0.139 g, 1.08 mmol), 4-DMAP (0.005 g, 0.036 mmol) and benzylamine (0.043 g, 0.4 mmol) and warmed to room temperature with stirring for 2 h. Then it was poured into a NaCl saturated aqueous solution (30 ml) and extracted with CH_2Cl_2 (3 × 30 ml). The combined organic layers were dried, filtered, and concentrated *in vacuo* to dryness. The crude product was purified by column chromatography on flash SiO_2 (*n*Hex/EtOAc 3:1) to yield **4a** (0.051 g, 38%) as a white solid: MP = 61–65°C $[\alpha]_D^{20}$ -54.9 (*c* = 0.91 in CH_2Cl_2); ^{1}H NMR (400 MHz, $CDCl_3$) δ 7.51 (br, 1H, NH), 7.37–7.28 (m, 5H, ArH), 4.94 (dd, *J* = 5.8, 4.1 Hz, 1H, CH), 4.53 (dd, *J* = 14.9, 6.3 Hz, 1H, CH-H), 4.44 (dd, *J* = 14.9, 5.7 Hz, 1H, CH-H), 4.33 (dd, *J* = 8.1, 5.2 Hz, 1H, CH), 4.09 (dd, *J* = 7.1, 2.9 Hz, 1H, CH), 3.55 (dd, *J* = 11.9, 5.8 Hz, 1H, CH-H), 3.52 (dd, *J* = 11.5, 2.5 Hz, 1H, CH-H), 3.27 (dd, *J* = 11.1, 7.1 Hz, 1H, CH-H), 3.19 (dd, *J* = 14.0, 5.2 Hz, 1H, CH-H), 3.13 (dd, *J* = 14.0, 8.1 Hz, 1H, CH-H), 3.09 (dd, *J* = 11.9, 4.0 Hz, 1H, CH-H), 2.14 (s, 3H, CH_3); ^{13}C{^{1}H} NMR (100 MHz, $CDCl_3$) δ 195.1, 170.3, 138.2, 128.9, 127.8, 127.7, 73.3, 72.8, 72.0, 43.6, 39.7, 37.8, 33.6, 30.6, HRMS (ESI/Q-TOF) m/z: $[M + Na]^+$ Calcd for $C_{16}H_{20}N_2O_2NaS_3$ 391.0585, found 391.0585.

S-(((3R,5R,7aS)-3-((4-methoxybenzyl) carbamoyl)tetrahydro-2H-thiazolo [4,3-b] thiazol-5-yl)methyl) ethanethioate (4b)

Prepared in an analogous route as described for **4a,** starting from **3** (0.12 g, 0.43 mmol) and 4-methoxybenzylamine (0.065 g, 0.47 mmol), purified by column chromatography on flash silica gel (*n*Hex/EtOAc 2:1) to yield **4b** (0.127 g, 74%) as a colorless oil $[\alpha]_D^{20}$ −73.6 (*c* = 1.96 in CH_2Cl_2); ^{1}H NMR (400 MHz, $CDCl_3$) δ 7.43 (t, *J* = 5.9 Hz, 1H, ArH), 7.22 (dt, *J* = 4.9, 2.9 Hz, 2H, ArH), 6.88 (dt, *J* = 5.0, 3.0 Hz, 2H, ArH), 4.92 (dd, *J* = 5.8, 4.1 Hz, 1H, CH), 4.46 (dd, *J* = 14.6, 6.3 Hz, 1H, CH-H), 4.36 (dd, *J* = 14.6, 5.6 Hz, 1H, CH-H), 4.31 (dd, *J* = 7.9, 5.4 Hz, 1H, CH), 4.07 (dd, *J* = 7.1, 2.9 Hz, 1H, CH), 3.80 (s, 3H, CH_3), 3.54 (dd, *J* = 11.9, 5.8 Hz, 1H, CH-H), 3.50 (dd, *J* = 11.1, 2.9 Hz, 1H, CH-H), 3.26 (dd, *J* = 11.1, 7.1 Hz, 1H, CH-H), 3.17 (dd, *J* = 13.6, 5.0 Hz, 1H, CH-H), 3.12 (dd, *J* = 13.7, 7.5 Hz, 1H, CH-H), 3.08 (dd, *J* = 11.9, 4.1 Hz, 1H CH-H), 2.17 (s, 3H, CH_3); ^{13}C{^{1}H} NMR (100 MHz, $CDCl_3$) δ 195.1, 170.1, 159.2, 130.3, 129.2, 114.2, 73.3, 72.7, 71.9, 55.4, 43.1, 39.6, 37.8, 33.6, 30.6. HRMS (ESI/Q-TOF) m/z: $[M + Na]^+$ Calcd for $C_{17}H_{22}N_2O_3NaS_3$ 421.0690, found 421.0687.

S-(((3R,5R,7aS)-3-(phenylcarbamoyl)tetrahydro-2H-thiazolo [4,3-b]thiazol-5-yl) methyl) ethanethioate (4c)

Prepared in an analogous route as described for **4a,** starting from **3** (0.15 g, 0.54 mmol) and aniline (0.055 g, 0.59 mmol), purified by column chromatography on flash SiO_2 (*n*Hex/EtOAc 5:2) to yield **4c** (0.077 g, 41%) as a colorless oil $[\alpha]_D^{20}$ −177.5 (*c* = 1.84 in CH_2Cl_2); ^{1}H NMR (400 MHz, $CDCl_3$) δ 9.03 (br, 1H, NH), 7.65 (d, *J* = 7.7 Hz, 2H, ArH), 7.35 (t, *J* = 7.9 Hz, 2H, ArH), 7.13 (t, *J* = 7.4 Hz, 1H, ArH), 5.03 (dd, *J* = 5.7, 4.6 Hz, 1H, CH), 4.42 (dd, *J* = 9.0, 4.2 Hz, 1H, CH), 4.12 (dd, *J* = 7.2, 3.1 Hz, 1H, CH), 3.63 (dd, *J* = 11.9, 5.9 Hz, 1H, CH-H), 3.54 (dd, *J* = 11.2, 3.0 Hz, 1H, CH-H), 3.33 (dd, *J* = 14.4, 3.9 Hz, 1H CH-H), 3.32 (dd, *J* = 11.7, 7.9 Hz, 1H, CH-H), 3.20 (dd, *J* = 14.1, 9.1 Hz, 1H, CH-H), 3.12 (dd, *J* = 11.9, 4.3 Hz, 1H, CH-H), 2.25 (s, 3H, CH_3); ^{13}C{^{1}H} NMR (100 MHz, $CDCl_3$) δ 195.3, 168.3, 137.6, 129.2, 124.7, 119.7, 73.2, 73.1, 71.9, 39.8, 37.8, 33.5, 30.8; HRMS (ESI/Q-TOF) m/z: $[M + Na]^+$ Calcd for $C_{15}H_{18}N_2O_2NaS_3$ 377.0428, found 377.0428.

S-((acetylthio)methyl)tetra hydro-2H-thiazolo [4,3-b]thiazole-3-carboxylate (4d)

Prepared in an analogous route as described for **4a** starting from **3** (0.1 g, 0.36 mmol) and N-boc-ethanolamine (0.069 g, 0.43 mmol), purified by column chromatography on flash SiO_2 (*n*Hex/EtOAc 7:3) to yield **4d** (0.12 g, 79%) as a white powder: MP = 65–71°C $[\alpha]_D^{20}$ -74.0 (*c* = 3.25 in CH_2Cl_2); ^{1}H NMR (400 MHz, $CDCl_3$) δ 5.15 (dd, *J* = 5.3, 3.4 Hz, 1H, CH), 5.05 (br, 1H, NH), 4.31 (t, *J* = 6.7 Hz, 1H, CH), 4.25–4.22 (m, 3H, CH, CH_2), 3.58, (dd, *J* = 11.9, 5.4 Hz, 1H, CH-H), 3.45–3.43 (m, 2H, CH_2), 3.34–3.26 (m, 3H, CH_2, CH-H), 3.10 (dd, *J* = 11.6, 3.7 Hz, 1H, CH-H), 3.08 (dd, *J* = 13.9, 7.4 Hz, 1H, CH-H), 2.36 (s, 3H, CH_3), 1.45 (s, 9H, $(CH_3)_3$); ^{13}C{^{1}H} NMR (100 MHz, $CDCl_3$) δ 195.8, 170.5, 155.9, 79.7, 74.1, 71.6, 70.0, 64.9, 39.6, 38.4, 37.7, 34.3, 30.7, 28,5; HRMS (ESI/Q-TOF) m/z: $[M + Na]^+$ Calcd for $C_{16}H_{26}N_2O_5NaS_3$ 445.0902, found 445.0906.

(3R,5R,7aS)-(2-aminothiazol-5-yl)methyl 5-((acetylthio) methyl)tetrahydro-2H-thiazolo [4,3-b]thiazole-3-carboxylate (4e)

Prepared in an analogous route as described for **4a** starting from **3** (0.2 g, 0.7 mmol) and (2-aminothiazol-4-yl)methanol (0.1 g, 0.77 mmol), purified by column chromatography on flash silica gel (nHex/EtOAc 2:3) to yield **4e** (0.137 g, 50%) as a colorless oil $[\alpha]_D^{20}$ −33.8 (*c* = 2.3 in CH_2Cl_2); ^{1}H NMR (400 MHz, $CDCl_3$) δ 6.51 (s, 1H, H (4)-thiazol), 5.64 (br, 2H, NH_2), 5.18 (dd, *J* = 5.3, 3.3 Hz, 1H, CH), 5.06 (d, *J* = 12.6 Hz, 1H, CH-H), 5.02 (d, *J* = 12.6 Hz, 1H, CH-H), 4.29 (t, *J* = 6.8 Hz, 1H, CH), 4.28 (dd, *J* = 6.5, 5.0 Hz, 1H, CH), 3.58 (dd, *J* = 11.9, 5.4 Hz, 1H, CH-H), 3.34–3.24 (m, 3H, CH-H, CH_2), 3.12–3.06 (m, 2H, CH_2), 2.34 (s, 3H, CH_3); ^{13}C{^{1}H} NMR (100 MHz, $CDCl_3$) δ 195.7, 170.3, 168.7, 146.1, 107.6, 74.1, 71.5, 69.9, 62.7, 38.5, 37.7, 34.5, 30.7; HRMS (ESI/Q-TOF) m/z: $[M + Na]^+$ Calcd for $C_{13}H_{17}N_3O_3NaS_4$ 414.0050, found 414.0041.

S-(((3R,5R,7aS)-3-((2-aminophenyl)carbamoyl) tetrahydro-2H-thiazolo[4,3-b] thiazol-5-yl) methyl) ethanethioate (4f)

Prepared in an analogous route as described for **4a** starting from **3** (0.15 g, 0.54 mmol) and *o*-phenylenediamine (0.203 g, 1.88 mmol), purified by column chromatography on flash SiO_2 (CH_2Cl_2/EtOAc 9:1) to yield **4f** (0.111 g, 56%) as a colorless oil: $[\alpha]_D^{20}$ −100.7 (*c* = 4.5 in CH_2Cl_2); ^{1}H NMR (400 MHz, $CDCl_3$) δ 8.87 (br, 1H, NH), 7.23 (d, *J* = 7.8 Hz, 1H, ArH), 7.06 (t, *J* = 7.6 Hz, 1H, ArH), 6.80 (t, *J* = 7.5 Hz, 2H, ArH), 5.07 (t, *J* = 5.0 Hz, 1H, CH), 4.43 (dd, *J* = 8.1, 5.1 Hz, 1H, CH), 4.16 (dd, *J* = 7.0, 2.4 Hz, 1H, CH), 3.90 (br, 2H, NH_2), 3.57 (dd, *J* = 11.9, 5.9 Hz, 1H, CH-H), 3.51 (dd, *J* = 11.3, 2.3 Hz, 1H, CH-H), 3.30–3.18 (m, 3H, CH_2, CH-H), 3.09 (dd, *J* = 11.9, 4.1 Hz, 1H, CH-H), 2.26 (s, 3H, CH_3); ^{13}C{^{1}H} NMR (100 MHz, $CDCl_3$) δ 195.4, 169.1, 140.8, 127.5, 125.4, 123.4, 119.4, 117.9, 73.2, 72.9, 72.0, 39.7, 37.7, 33.6, 30.7; HRMS (ESI/Q-TOF) m/z: $[M + Na]^+$ Calcd for $C_{15}H_{19}N_3O_2NaS_3$ 392.0537, found 392.0540.

Synthesis of analogs 2a-g

(3R,5R,7aS)-N-benzyl-5-(mercaptomethyl) tetrahydro-2H-thiazolo [4,3-b]thiazole-3-carboxamide (2a)

Yield: Method A (29%): Method C (64%)

^{1}H NMR (400 MHz, $CDCl_3$) δ 7.77 (br, 1H, NH), 7.36–7.28 (m, 5H, ArH), 4.88 (dd, *J* = 5.8, 5.0 Hz, 1H, CH), 4.49 (qd, *J* = 14.8, 6.0 Hz, 2H, CH_2), 4.31 (dd, *J* = 8.1, 5.3 Hz, 1H, CH), 4.07 (dd, *J* = 7.3, 3.7 Hz, 1H, CH), 3.49 (dd, *J* = 11.0, 3.9 Hz, 1H, CH-H), 3.46 (dd, *J* = 11.6, 5.7 Hz, 1H, CH-H), 3.34 (dd, *J* = 11.2, 7.3 Hz, 1H, CH-H), 3.06 (dd, *J* = 11.8, 4.8 Hz, 1H, CH-H), 2.77 (ddd, *J* = 13.4, 8.1, 5.3 Hz, 1H, CH-H), 2.69 (dd, *J* = 13.9, 8.4 Hz, 1H, CH-H), 1.55 (t, *J* = 8.4 Hz, 1H, SH); ^{13}C{^{1}H} NMR (100 MHz, $CDCl_3$) δ 170.3, 138.2, 128.9, 127.9, 127.7, 74.9, 72.9, 72.1, 43.6, 39.5, 33.8, 33.3; HRMS (ESI/Q-TOF) m/z $[M + Na]^+$ Calcd for $C_{14}H_{18}N_2ONaS_3$ 349.0479, found 349.0478; $[\alpha]_D^{20}$ -80.0 (*c* = 0.66 in CH_2Cl_2).

(3R,5R,7aS)-5-(mercaptomethyl)-N-(4-methoxybenzyl) tetrahydro-2H-thiazolo [4,3-b] thiazole-3-carboxamide (2b)

Prepared in an analogous route as described for **2a** starting from **4b** (0.0181 g, 0.0454 mmol), purified by column chromatography on flash SiO_2 (nHex/EtOAc 3:1) to yield **2b** (Method A: 38%, Method C: 50%) as a colorless oil $[\alpha]_D^{20}$ -108.5 (*c* = 1.0 in CH_2Cl_2); ^{1}H NMR (400 MHz, $CDCl_3$) δ 7.69 (br, 1H, NH), 7.23–7.19 (m, 2H, ArH), 6.88–6.85 (m, 2H, ArH), 4.86 (dd, *J* = 5.8, 4.9 Hz, 1H, CH), 4.47–4.36 (m, 2H, CH_2), 4.29 (dd, *J* = 8.1, 5.3 Hz, 1H, CH), 4.05 (dd, *J* = 7.3, 3.8 Hz, 1H, CH), 3.80 (s, 3H, CH_3), 3.46 (dd, *J* = 11.2, 3.8 Hz, 1H, CH-H), 3.44 (dd, *J* = 11.8, 6.0 Hz, 1H, CH-H), 3.32 (dd, *J* = 11.2, 7.3 Hz, 1H, CH-H), 3.05 (dd, *J* = 11.8, 4.8 Hz, 1H, CH-H), 2.76 (ddd, *J* = 13.6, 8.1, 5.3 Hz, 1H, CH-H), 2.68 (dt, *J* = 14.0, 8.4 Hz, 1H, CH-H), 1.56 (t, *J* = 8.4 Hz, 1H, SH); ^{13}C{^{1}H} NMR (100 MHz, CDCl3) δ 170.2, 159.2, 130.3, 129.2, 114.3, 74.9, 72.8, 72.1, 55.4, 43.0, 39.5, 33.8, 33.3; HRMS (ESI/Q-TOF) m/z: $[M + Na]^+$ Calcd for $C_{15}H_{20}N_2O_2NaS_3$ 379.0585, found 379.0591.

(3R,5R,7aS)-5-(mercaptomethyl)-N-phenyltetrahydro-2H-thiazolo [4,3-b]thiazole-3-carboxamide (2c)

Prepared in an analogous route as described for **2a** starting from **4c** (0.0161 g, 0.0454 mmol), purified by column chromatography on flash SiO_2 (nHex/EtOAc 3:1) to yield **2c** (Method A: 24%, Method C: 58%) as a colorless oil $[\alpha]_D^{20}$ −116.6 (*c* = 0.25 in CH_2Cl_2); ^{1}H NMR (400 MHz, $CDCl_3$) δ 9.44 (br, 1H, NH), 7.65 (dd, *J* = 8.5, 1.0 Hz, 2H, ArH), 7.36–7.31 (m, 2H, ArH), 7.15–7.11 (m, 1H, ArH), 4.99 (dd, *J* = 5.9, 5.2 Hz, 1H, CH), 4.43 (dd, *J* = 8.4, 4.7 Hz, 1H, CH), 4.11 (dd, *J* = 7.5, 3.5 Hz, 1H, CH), 3.57 (dd, *J* = 11.5, 3.7 Hz, 1H, CH-H), 3.54 (dd, *J* = 12.0, 5.9 Hz, 1H, CH-H), 3.38 (dd, *J* = 11.4, 7.5 Hz, 1H, CH-H), 3.12 (dd, *J* = 11.8, 5.0 Hz, 1H, CH-H), 2.96 (ddd, *J* = 14.0, 7.8, 4.7 Hz, 1H, CH-H), 2.84 (dd, *J* = 14.1, 8.5 Hz, 1H, CH-H), 1.82 (t, *J* = 8.2 Hz, 1H, SH); ^{13}C{^{1}H} NMR (100 MHz, $CDCl_3$) δ 168.6, 137.7, 129.2, 124.7, 119.8, 74.6, 72.8, 72.4, 39.5, 33.6, 33.3. HRMS (ESI/Q-TOF) m/z: $[M + Na]^+$ Calcd for $C_{13}H_{16}N_2ONaS_3$ 335.0322, found 335.0321.

(3R,5R,7aS)-2-((tert-butoxycarbonyl)amino) ethyl 5-(mercaptomethyl)tetrahydro-2H-thiazolo [4,3-b]thiazole-3-carboxylate (2d)

Prepared in an analogous route as described for **2a** starting from **4d** (0.0192 g, 0.0454 mmol), purified by column chromatography on flash SiO_2 (nHex/EtOAc 8:2) to yield **2d** (Method A: 39%, Method C: 70%) as a colorless oil $[\alpha]_D^{20}$ −35.9 (*c* = 2.13 in CH_2Cl_2); ^{1}H NMR (400 MHz, $CDCl_3$) δ 5.08 (dd, *J* = 5.3, 3.8 Hz, 1H, CH), 4.83 (br, 1H, NH), 4.31 (dd, *J* = 7.8, 5.9 Hz, 1H, CH), 4.25 (dd, *J* = 6.6, 4.8 Hz, 1H, CH), 4.24 (t, *J* = 5.3 Hz, 2H, CH_2), 3.54 (dd, *J* = 12.0, 5.4 Hz, 1H, CH-H), 3.43 (t, *J* = 4.9 Hz, 2H, CH_2), 3.34 (dd, *J* = 11.0, 4.9 Hz, 1H, CH-H), 3.27 (dd, *J* = 11.0, 6.6 Hz, 1H, CH-H), 3.09 (dd, *J* = 11.9, 3.8 Hz, 1H, CH-H), 2.88 (dt, *J* = 13.6, 7.5 Hz, 1H, CH-H), 2.64 (ddd, *J* = 13.6, 9.6,

5.9 Hz, 1H, CH-H), 1.97 (dd, *J* = 9.6, 7.2 Hz, 1H, SH), 1.45 (s, 9H, $(CH_3)_3$); $^{13}C\{^1H\}$ NMR (100 MHz, $CDCl_3$) δ 170.6, 155.9, 79.9, 75.0, 73.5, 70.6, 64.8, 39.7, 39.3, 34.3, 33.9, 28.5; HRMS (ESI/Q-TOF) m/z: $[M + Na]^+$ Calcd for $C_{14}H_{24}N_2O_4NaS_3$ 403.0796, found 403.0796.

(3R,5R,7aS)-(2-aminothiazol-4-yl)methyl 5-(mercaptomethyl) tetrahydro-2H-thiazolo [4,3-b]thiazole-3-carboxylate (2e)

Prepared in an analogous route as described for **2a** starting from **4e** (0.0178 g, 0.0454 mmol), purified by column chromatography on flash SiO_2 (nHex/EtOAc 2:3) to yield **2e** (Method A: 44%, Method C: 68%) as a colorless oil $[\alpha]_D^{20}$ −33.4 (*c* = 1.63 in CH_2Cl_2); ^1H NMR (400 MHz, $CDCl_3$) δ 6.52 (s, 1H, H (4)-thiazole), 5.38 (br, 2H, NH_2), 5.09 (dd, *J* = 5.2, 4.1 Hz, 1H, CH), 5.06 (d, *J* = 12.6 Hz, 1H, CH-H), 5.03 (d, *J* = 12.6 Hz, 1H, CH-H), 4.32 (dd, *J* = 7.2, 6.4 Hz, 1H, CH), 4.26 (dd, *J* = 6.6, 5.3 Hz, 1H, CH), 3.52 (dd, *J* = 11.9, 5.4 Hz, 1H, CH-H), 3.35 (dd, *J* = 11.0, 5.2 Hz, 1H, CH-H), 3.28 (dd, *J* = 11.0, 6.7 Hz, 1H, CH-H), 3.07 (dd, *J* = 11.9, 4.0 Hz, 1H, CH-H), 2.87 (dt, *J* = 13.7, 7.4 Hz, 1H, CH-H), 2.62 (ddd, *J* = 13.6, 9.4, 6.3 Hz, 1H, CH-H), 1.97 (dd, *J* = 9.4, 7.6 Hz, 1H, SH); $^{13}C\{^1H\}$ NMR (100 MHz, $CDCl_3$) δ 170.4, 168.5, 146.2, 108.0, 75.2, 73.5, 70.4, 62.8, 39.2, 34.3, 33.8; HRMS (ESI/Q-TOF) m/z: $[M + Na]^+$ Calcd for $C_{11}H_{15}N_3O_2NaS_4$ 371.9945, found 371.9945.

(3R,5R,7aS)-N-(2-aminophenyl)-5-(mercaptomethyl) tetrahydro-2H-thiazolo [4,3-b]thiazole-3-carboxamide (2f)

Prepared in an analogous route as described for **2a** starting from **4f** (0.0168 g, 0.0454 mmol), purified by column chromatography on flash SiO_2 (CH_2Cl_2/EtOAc 9:1) to yield **2f** (Method A: 31%, Method C: 78%) as a colorless oil $[\alpha]_D^{20}$ -68.3 (*c* = 1.85 in CH_2Cl_2); ^1H NMR (400 MHz, $CDCl_3$) δ 9.19 (br, 1H, NH), 7.29 (dd, *J* = 8.2, 1.3 Hz, 1H, ArH), 7.08 (td, *J* = 7.8, 1.4 Hz, 1H, ArH), 6.84–6.80 (m, 2H, ArH), 5.06 (dd, *J* = 5.6, 4.7 Hz, 1H, CH), 4.45 (dd, *J* = 8.2, 5.0 Hz, 1H, CH), 4.24 (dd, *J* = 7.2, 2.7 Hz, 1H, CH), 3.60 (dd, *J* = 11.3, 2.7 Hz, 1H, CH-H), 3.55 (dd, *J* = 12.0, 5.9 Hz, 1H, CH-H), 3.35 (dd, *J* = 11.3, 7.2 Hz, 1H, CH-H), 3.13 (dd, *J* = 11.9, 4.5 Hz, 1H, CH-H), 2.97–2.80 (m, 2H, CH_2), 1.84 (t, *J* = 8.2 Hz, 1H, SH); $^{13}C\{^1H\}$ NMR (100 MHz, $CDCl_3$) δ 169.1, 140.4, 127.5, 125.1, 123.9, 119.8, 118.3, 75.0, 73.2, 73.1, 39.6, 33.7, 33.5, HRMS (ESI/Q-TOF) m/z: $[M + Na]^+$ Calcd for $C_{13}H_{17}N_3ONaS_3$ 350.0431, found 350.0430.

Deprotection of **6–13** was carried out using the same approach as described for **4a**, Method C).

Data availability statement

The raw data supporting the conclusion of this article will be made available by the authors, without undue reservation.

Author contributions

Conceived and designed the experiments: VV, CS, and GM. Performed the experiments: VV and CS. Analyzed the data: VV, CS, and GM. Contributed reagents/materials/analysis tools: CS and GM. Contributed to the writing of the manuscript: VV, CS, and GM.

Funding

This work was supported by the National Institute of Allergy and Infectious Diseases of the National Institutes of Health (NIH) to GM under Award Number R01AI100560. This study was also supported in part by funds from the Comisión Sectorial de Investigación Científica (CSIC)-Grupos from UdelaR. VV is the recipient of a fellowship from CSIC-UdelaR.

Acknowledgments

We would like to thank Horacio Pezaroglo and Gonzalo Hernández for running the NMR spectra. The Chemistry Department of the UdelaR is thankful to the CSIC for supporting acquisition of the HPLC-MS.

Conflict of interest

The authors declare that the research was conducted in the absence of any commercial or financial relationships that could be construed as a potential conflict of interest.

Publisher's note

All claims expressed in this article are solely those of the authors and do not necessarily represent those of their affiliated organizations, or those of the publisher, the editors, and the reviewers. Any product that may be evaluated in this article, or claim that may be made by its manufacturer, is not guaranteed or endorsed by the publisher.

Supplementary material

The Supplementary Material for this article can be found online at: https://www.frontiersin.org/articles/10.3389/fchem.2022.934376/full#supplementary-material

References

Agouridas, V., Mahdi, O. E., Diemer, V., Cargoët, M., Monbaliu, J. C. M., Melnyk, O., et al. (2019). Native chemical ligation and extended methods: Mechanisms, catalysis, scope, and limitations. *Chem. Rev.* 119 (12), 7328–7443. doi:10.1021/acs.chemrev.8b00712

Barnett, R. E., and Jencks, W. P. (1969). Diffusion-controlled proton transfer in intramolecular thiol ester aminolysis and thiazoline hydrolysis. *J. Am. Chem. Soc.* 91 (9), 2358–2369. doi:10.1021/ja01037a029

Bongiardina, N. J., Long, K. F., Podgórski, M., and Bowman, C. N. (2021). Substituted thiols in dynamic thiol–thioester reactions. *Macromolecules* 54 (18), 8341–8351. doi:10.1021/acs.macromol.1c00649

Burke, H. M., McSweeney, L., and Scanlan, E. M. (2017). Exploring chemoselective S-to-N acyl transfer reactions in synthesis and chemical biology. *Nat. Commun.* 8, 15655. doi:10.1038/ncomms15655

Chandru, K., Gilbert, A., Butch, C., Aono, M., and Cleaves, H. J. (2016). The abiotic chemistry of thiolated acetate derivatives and the origin of life. *Sci. Rep.* 6, 1–11. doi:10.1038/srep29883

Dawson, P. E., Muir, T. W., Clark-Lewis, I., and Kent, S. B. (1994). Synthesis of proteins by native chemical ligation. *Science* 266 (5186), 776–779. doi:10.1126/science.7973629

Diemer, V., Firstova, O., Agouridas, V., and Melnyk, O. (2022). Pedal to the metal: The homogeneous catalysis of the native chemical ligation reaction. *Chemistry* 28 (16), e202104229. doi:10.1002/chem.202104229

Endo, T., Oda, K., and Mukaiyama, T. (1974). Facile conversion of thiolesters into thiols using cysteamine. *Chem. Lett.* 3, 443–444. doi:10.1246/cl.1974.443

Friedman, M., Cavins, J. F., and Wall, J. S. (1965). Relative nucleophilic reactivities of amino groups and mercaptide ions in addition reactions with α, β-unsaturated Compounds[1, 2]. *J. Am. Chem. Soc.* 87 (16), 3672–3682. doi:10.1021/ja01094a025

González, M. M., Kosmopoulou, M., Mojica, M. F., Castillo, V., Hinchliffe, P., PettinatiBrem, J., et al. (2016). Bisthiazolidines: A substrate-mimicking scaffold as an inhibitor of the NDM-1 carbapenemase. *ACS Infect. Dis.* 1, 544–554. doi:10.1021/acsinfecdis.5b00046

Gui, Y., Qiu, L., Li, Y., Li, H., and Dong, S. (2016). Internal activation of peptidyl prolyl thioesters in native chemical ligation. *J. Am. Chem. Soc.* 138 (14), 4890–4899. doi:10.1021/jacs.6b01202

Henderson, L. (1908). Concerning the relationship between the strength of acids and their capacity to preserve neutrality. *Am. J. Physiology-Legacy Content* 21 (4), 465. doi:10.1152/ajplegacy.1908.21.4.465-s

Hinchliffe, P., González, M. M., Mojica, M. F., Gonzalez, J. M., Castillo, V., Saiz, C., et al. (2016). Cross-class metallo-β-lactamase inhibition by bisthiazolidines reveals multiple binding modes. *Proc. Natl. Acad. Sci. U. S. A.* 113, E3745–E3754. doi:10.1073/pnas.1601368113

Maguire, O. R., Zhu, J., Brittain, W. D., Hudson, A. S., Cobb, S. L., O'Donoghue, A. C., et al. (2020). N-Terminal speciation for native chemical ligation. *Chem. Commun.* 56 (45), 6114–6117. doi:10.1039/d0cc01604g

Mennen, S. M., Alhambra, C., Allen, C. L., Barberis, M., Berritt, S., Brandt, T. A., et al. (2019). The evolution of high-throughput experimentation in pharmaceutical development and perspectives on the future. *Org. Process Res. Dev.* 23, 1213–1242. doi:10.1021/acs.oprd.9b00140

Mojica, M. F., Mahler, G., Bethel, C. R., Taracila, M. A., Kosmopoulou, M., Papp-Wallace, K. M., et al. (2015). Exploring the role of residue 228 in substrate and inhibitor recognition by VIM metallo-β-lactamases. *Biochemistry* 54, 3183–3196. doi:10.1021/acs.biochem.5b00106

Mondal, M., and Hirsch, A. K. (2015). Dynamic combinatorial chemistry: A tool to facilitate the identification of inhibitors for protein targets. *Chem. Soc. Rev.* 44 (8), 2455–2488. doi:10.1039/c4cs00493k

Pietrocola, F., Galluzzi, L., Bravo-San, J. M., Madeo, P. F., and Kroemer, G. (2015). Acetyl coenzyme A: A central metabolite and second messenger. *Cell Metab.* 21 (6), 805–821. doi:10.1016/j.cmet.2015.05.014

Pitman, I., and Morris, I. Aust. (1979). Covalent additions of glutathione, cysteine, homocysteine, cysteamine and thioglycolic acid to quinazoline cation. *Aust. J. Chem.* 32 (7), 1567. doi:10.1071/ch9791567

Saiz, C., Castillo, V., Fontán, P., Bonilla, M., Salinas, G., Rodríguez-Haralambides, A., et al. (2014). Discovering Echinococcus granulosus thioredoxin glutathione reductase inhibitors through site-specific dynamic combinatorial chemistry. *Mol. Divers.* 18 (1), 1–12. doi:10.1007/s11030-013-9485-3

Serra, G., Posada, L., and Hojo, H. (2020). On-resin synthesis of cyclic peptides via tandem N-to-S acyl migration and intramolecular thiol additive-free native chemical ligation. *Chem. Commun.* 56 (6), 956–959. doi:10.1039/c9cc07783a

Vallee, Y., Shalayel, I., Ly, K. D., Rao, K. R., De Paëpe, G., Märker, K., et al. (2017). At the very beginning of life on earth: The thiol-rich peptide (TRP) world hypothesis. *Int. J. Dev. Biol.Dev. Biol.* 61, 471–478. doi:10.1387/ijdb.170028yv

Villamil, V., Saiz, C., and Mahler, G. (2021). A new procedure for thioester deprotection using thioglycolic acid in both homogeneous and heterogeneous phase. *Tetrahedron* 94, 132335. doi:10.1016/j.tet.2021.132335

Wang, C., Guo, Q. X., and Fu, Y. (2011). Theoretical analysis of the detailed mechanism of native chemical ligation reactions. *Chem. Asian J.* 6 (5), 1241–1251. doi:10.1002/asia.201000760

Wong, H., and Cernak, T. (2018). Reaction miniaturization in eco-friendly solvents. *Curr. Opin. Green Sustain. Chem.* 11, 91–98. doi:10.1016/j.cogsc.2018.06.001

Worrell, B. T., Mavila, S., Wang, C., Kontour, T. M., Lim, C. H., McBride, M. K., et al. (2018). A user's guide to the thiol-thioester exchange in organic media: Scope, limitations, and applications in material science. *Polym. Chem.* 9 (36), 4523–4534. doi:10.1039/c8py01031e

frontiers | Frontiers in Chemistry

TYPE Original Research
PUBLISHED 23 August 2022
DOI 10.3389/fchem.2022.972198

Check for updates

OPEN ACCESS

EDITED BY
Debbie C. Crans,
Colorado State University, United States

REVIEWED BY
Marian Valko,
Slovak University of Technology in Bratislava, Slovakia
Gloria Mazzone,
University of Calabria, Italy

*CORRESPONDENCE
Marie C. Heffern,
mcheffern@ucdavis.edu

SPECIALTY SECTION
This article was submitted to Chemical Biology,
a section of the journal
Frontiers in Chemistry

RECEIVED 17 June 2022
ACCEPTED 11 July 2022
PUBLISHED 23 August 2022

CITATION
Lee VJ and Heffern MC (2022), Structure-activity assessment of flavonoids as modulators of copper transport.
Front. Chem. 10:972198.
doi: 10.3389/fchem.2022.972198

COPYRIGHT
© 2022 Lee and Heffern. This is an open-access article distributed under the terms of the Creative Commons Attribution License (CC BY). The use, distribution or reproduction in other forums is permitted, provided the original author(s) and the copyright owner(s) are credited and that the original publication in this journal is cited, in accordance with accepted academic practice. No use, distribution or reproduction is permitted which does not comply with these terms.

Structure-activity assessment of flavonoids as modulators of copper transport

Vanessa J. Lee and Marie C. Heffern*

Department of Chemistry, University of California, Davis, Davis, CA, United States

Flavonoids are polyphenolic small molecules that are abundant in plant products and are largely recognized for their beneficial health effects. Possessing both antioxidant and prooxidant properties, flavonoids have complex behavior in biological systems. The presented work investigates the intersection between the biological activity of flavonoids and their interactions with copper ions. Copper is required for the proper functioning of biological systems. As such, dysregulation of copper is associated with metabolic disease states such as diabetes and Wilson's disease. There is evidence that flavonoids bind copper ions, but the biological implications of their interactions remain unclear. Better understanding these interactions will provide insight into the mechanisms of flavonoids' biological behavior and can inform potential therapeutic targets. We employed a variety of spectroscopic techniques to study flavonoid-Cu(II) binding and radical scavenging activities. We identified structural moieties important in flavonoid-copper interactions which relate to ring substitution but not the traditional structural subclassifications. The biological effects of the investigated flavonoids specifically on copper trafficking were assessed in knockout yeast models as well as in human hepatocytes. The copper modulating abilities of strong copper-binding flavonoids were largely influenced by the relative hydrophobicities. Combined, these spectroscopic and biological data help elucidate the intricate nature of flavonoids in affecting copper transport and open avenues to inform dietary recommendations and therapeutic development.

Abbreviations: 3-HF, 3-hydroxyflavone 3-hydroxy-2-phenylchromen-4-one; Bio A, Biochanin A 5,7-dihydroxy-3-(4-methoxyphenyl)chromen-4-one; Cat, (±)-catechin (2S,3R)-2-(3,4-dihydroxyphenyl)-3,4-dihydro-2H-chromene-3,5,7-triol; Chrys, Chrysin 5,7-dihydroxy-2-phenylchromen-4-one; Cyan, Cyanidin 2-(3,4-dihydroxyphenyl)chromenylium-3,5,7-triol; EC, (-)-epicatechin (2*R*, 3*R*)-2-(3,4-dihydroxyphenyl)-3,4-dihydro-2*H*-chromene-3,5,7-triol; ECG, (-)-epicatechin gallate [(2R,3R)-2-(3,4-dihydroxyphenyl)-5,7-dihydroxy-3,4-dihydro-2H-chromen-3-yl] 3,4,5-trihydroxybenzoate; EGC, (-)-epigallocatechin (2R,3R)-2-(3,4,5-trihydroxyphenyl)-3,4-dihydro-2H-chromene-3,5,7-triol; EGCG, (-)-epigallocatechin gallate [(2R,3R)-5,7-dihydroxy-2-(3,4,5-trihydroxyphenyl)-3,4-dihydro-2H-chromen-3-yl] 3,4,5-trihydroxybenzoate; Gen, Genistein 5,7-dihydroxy-3-(4-hydroxyphenyl)chromen-4-one; Hdin, Hesperidin (2S)-5-hydroxy-2-(3-hydroxy-4-methoxyphenyl)-7-[(2S,3R,4S,5S,6R)-3,4,5-trihydroxy-6-[[(2R,3R,4R,5R,6S)-3,4,5-trihydroxy-6-methyloxan-2-yl]oxymethyl]oxan-2-yl]oxy-2,3-dihydrochromen-4-one; Htin, Hesperetin (2S)-5,7-dihydroxy-2-(3-hydroxy-4-methoxyphenyl)-2,3-dihydrochromen-4-one; Kae, Kaempferol 3,5,7-trihydroxy-2-(4-hydroxyphenyl)chromen-4-one; Lut, Luteolin 2-(3,4-dihydroxyphenyl)-5,7-dihydroxychromen-4-one; Ngenin, Naringenin (2S)-5,7-dihydroxy-2-(4-hydroxyphenyl)-2,3-dihydrochromen-4-one; Ngin, Naringin (2S)-7-[(2S,3R,4S,5S,6R)-4,5-dihydroxy-6-(hydroxymethyl)-3-[(2S,3R,4R,5R,6S)-3,4,5-trihydroxy-6-methyloxan-2-yl]oxyoxan-2-yl]oxy-5-hydroxy-2-(4-hydroxyphenyl)-2,3-dihydrochromen-4-one; QT, Quercetin 2-(3,4-dihydroxyphenyl)-3,5,7-trihydroxychromen-4-one; Rut, Rutin 2-(3,4-dihydroxyphenyl)-5,7-dihydroxy-3-[(2S,3R,4S,5S,6R)-3,4,5-trihydroxy-6-[[(2R,3R,4R,5R,6S)-3,4,5-trihydroxy-6-methyloxan-2-yl]oxymethyl]oxan-2-yl]oxychromen-4-one.

KEYWORDS

flavonoids, copper trafficking, antioxidant activity, ionophore, chelator

1 Introduction

Flavonoids are a class of small phenolic secondary plant metabolites. Ubiquitous in the plant kingdom, flavonoids are recognized as micronutrients that are biologically active in mammalian systems (Datta et al., 2004). Flavonoids are widely studied for their health benefits which include anti-inflammatory and anti-cancer properties (Dai et al., 2017). However, the mechanisms of their biological activity remain unclear due to flavonoids' complex activity as both anti- and pro-oxidants. Flavonoids share a core structure containing two benzene rings connected by a heterocyclic pyran ring (Figure 1). Derivatization of this core structure differentiates flavonoids into subclasses based on oxidation and substitution of the heterocyclic C-ring (Table 1). Modest structural differences correspond to changes in biological effects with variations in hydroxyl group positions relating to differing antioxidant activity (Rice-Evans et al., 1996). Often, flavonoids are studied by subclasses with the assumption that molecules within subclasses behave similarly.

Interactions of flavonoids with metal ions are a source of both anti- and pro-oxidant activity (Perron et al., 2011). Flavonoids have been shown to perform Fenton-type reactions in the presence of Fe(III) and Cu(II) ions (Fang et al., 2020). Furthermore, coordination to metal ions affects the oxidative activity of flavonoids. There is evidence that flavonoids interact with metal ions including Fe(III), Zn(II), and Cu(II) with varying reports on the potential biological effects (Weber 1988; Escandar and Sala 1991; Fernandez et al., 2002; Ren et al., 2008; Pekal et al., 2011; Říha et al., 2014; Anderson, Larson, and Berreau 2016; Cherrak et al., 2016).

While copper is an essential trace metal micronutrient, its dysregulation and mislocalization is correlated with a host of pathologies including Wilson's disease, neurodegeneration, and some cancers (Baldari et al., 2020). The causal relationship between these pathologies and copper dysregulation is still undetermined, but redirecting copper trafficking, either by removal or altering the localization of the metal ion, is emerging as a viable therapeutic strategy (Hunsaker and Franz 2019). For instance, copper chelation therapies have shown encouraging effects in reducing morbidity in Wilson's disease patients and restricting tumor angiogenesis (Baldari et al., 2020). By in large, the focus on copper-modulating agents have been on synthetic chelators and ionophores, with less attention paid to natural products such as flavonoids. Investigating the copper-modulating properties of flavonoids may not only facilitate rational design but may also inform on nutrition-based effects

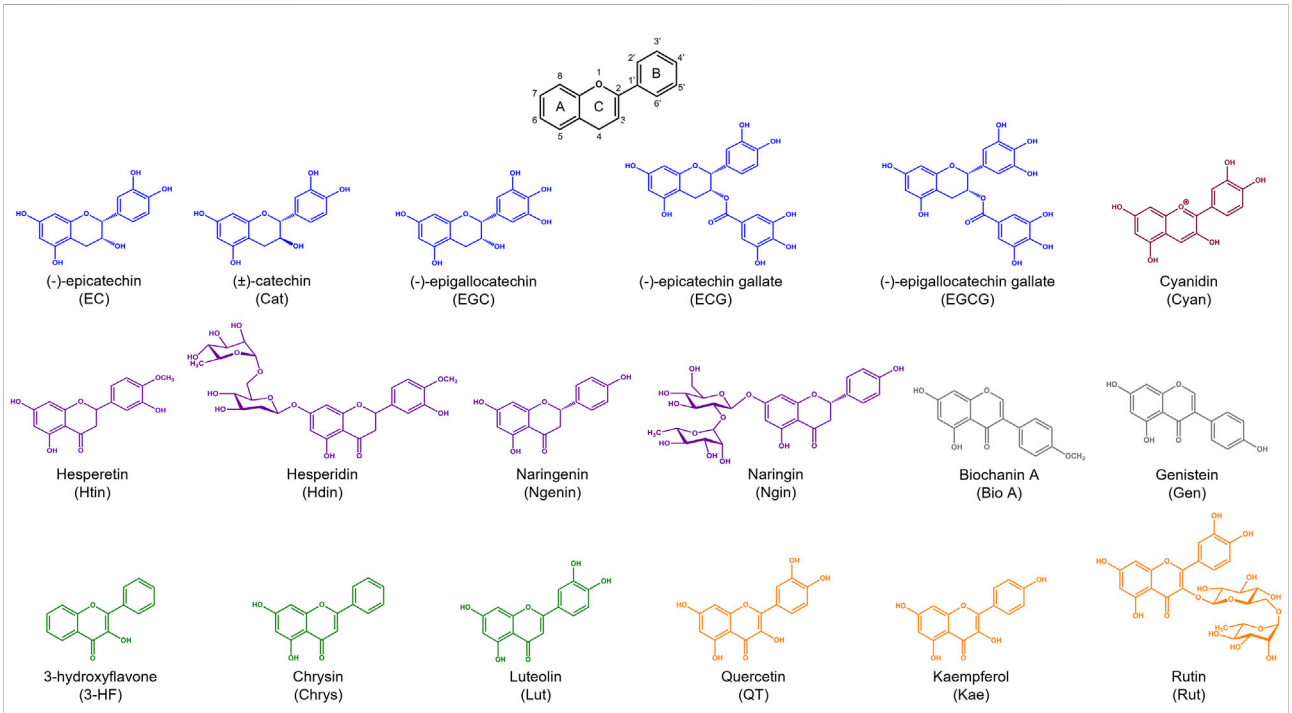
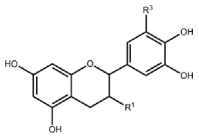
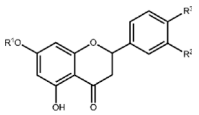
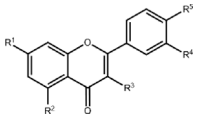
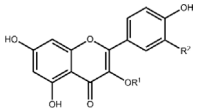
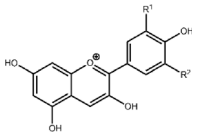
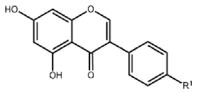


FIGURE 1
The core structure shared by flavonoids is composed of two benzene rings (rings A and B) connected by a heterocyclic pyran ring (ring C). Flavonoid subclasses include flavonols (blue), flavanones (purple), flavones (green), flavonols (orange), anthocyanins (maroon), and isoflavones (grey).

TABLE 1 Structures and subclasses of flavonoids.

Subclass	Structure	Flavonoids	Substitutions
Flavan-3-ols		Epicatechin (EC)	R^1 = OH, R^2 = H
		Catechin (Cat)	R^1 = OH, R^2 = H
		Epigallocatechin (EGC)	R^1 = OH, R^2 = OH
		Epicatechin gallate (ECG)	R^1 = gallate, R^2 = H
		Epigallocatechin gallate (EGCG)	R^1 = gallate, R^2 = OH
Flavanones		Hesperetin (Htin)	R^1 = H, R^2 = OH, R^3 = OCH_3
		Hesperidin (Hdin)	R^1 = glucoside, R^2 = OH, R^3 = OCH_3
		Naringenin (Ngenin)	R^1 = H, R^2 = H, R^3 = OH
		Naringin (Ngin)	R^1 = glycoside, R^2 = H, R^3 = OH
Flavones		Luteolin (Lut)	R^1 = OH, R^2 = OH, R^3 = H, R^4 = OH, R^5 = OH
		Chrysin (Chrys)	R^1 = OH, R^2 = OH, R^3 = H, R^4 = H, R^5 = H
		3-hydroxyflavone (3-HF)	R^1 = H, R^2 = H, R^3 = OH, R^4 = H, R^5 = H
Flavonols		Quercetin (QT)	R^1 = H, R^2 = OH
		Kaempferol (Kae)	R^1 = H, R^2 = H
		Rutin (Rut)	R^1 = rutinoside, R^2 = OH
Anthocyanins		Cyanidin (Cyan)	R^1 = H, R^2 = OH
Isoflavones		Biochanin A (Bio A)	R^1 = OCH_3
		Genistein (Gen)	R^1 = OH

of such plant-derived products. As flavonoids display metal chelating properties, their health benefits may in part be due to their ability to affect copper trafficking (Říha et al., 2014).

Indeed, some flavonoids reportedly protect against symptoms of copper-dysregulation associated pathologies (Cremonini et al., 2018), but the structure/function relationship between how their chelating abilities relate to their potential therapeutic actions in these scenarios requires further elucidation. To this end, this work sought to elucidate the relationship between flavonoid-copper interactions and their ability to affect copper trafficking in cell-based models. A library of 18 flavonoids was compiled composed of flavonoids that are bioavailable through food consumption and recognized for their health benefits. The Cu(II)-binding properties of the 18 flavonoids spanning the subclasses (Table 1) were directly compared spectroscopically, and their impact on Cu(II)-associated redox activity was assessed with *in vitro* assays. Flavonoids with appreciable Cu(II)-binding abilities were assessed for their ability to alter copper trafficking in cell-based eukaryotic models. Taken together, this study offers a deeper understanding of how specific structural features of flavonoids may relate to their potential therapeutic activity in copper-associated disorders.

2 Materials and methods

All chemicals were used as purchased without further purification. (-)-Epicatechin (EC), (-)-epicatechin gallate (ECG), quercetin (QT), 3-hydroxyflavone (3-HF), hesperetin, ACES, tricine, and bathocuproine disulfonic acid disodium salt (BCS) were obtained from Sigma-Aldrich (St. Louis, MO). Catechin (Cat), luteolin (Lut), (-)-epigallocatechin (EGC), and biochanin A were purchased from VWR (Radnor, PA). (-)-Epigallocatechin gallate (EGCG), chrysin, naringenin, naringin, hesperidin, rutin, kaempferol, cyanidin, genistein, hematoxylin, coumarin-3-carboxylic acid (CCA), ascorbic acid, ethylenediaminetetraacetic acid (EDTA), tris(hydroxymethyl-d_3)amino-d_2-methane (deuterated Tris, Tris-d_{11}), MOPS, BisTris, and all solvents were obtained from Fisher Scientific (Waltham, MA).

2.1 Determination of binding ratio and binding affinity

All UV-Vis studies were performed on a Shimadzu UV-1900i at 30°C or 37°C using quartz cuvettes (Starna) with a pathlength of 1 cm. Milli-Q water was the reference for all studies, and the spectrum of the buffer was subtracted, and the spectra were normalized after data collection.

50 μM solutions of flavonoids were prepared in 50 mM buffer (pH 7.4). $CuSO_4$, dissolved in Milli-Q water, was titrated into the solution in ratios ranging from 10–250 μM.

2.2 Identification of binding location

2.2.1 ^{1}H Studies

Spectra were recorded on a Bruker 400 MHz NMR spectrometer with Topspin 3.2 running IconNMR 50 mM solutions of flavonoids were prepared in DMSO-d_6 and 12.5 mM solutions of $CuSO_4$ were prepared in MeOD. Samples were prepared of flavonoids alone at a final concentration of 12.5 mM flavonoid and with 0.25 equivalents of $CuSO_4$ dissolved in 50:50 DMSO-d_6:MeOD.

2.3 DPPH radical scavenging of flavonoids

The radical scavenging abilities of flavonoids were studied using the DPPH$^\bullet$ assay as previously described (Xie and Schaich 2014; Zhao et al., 2020). In short, 50 μM 2,2-diphenyl-1-picrylhydrazyl free radical (DPPH) in ethanol was added to preincubated solutions of 50 μM flavonoid, or ascorbic acid as the positive control, with and without 50 μM $CuSO_4$ or $ZnCl_2$ in a 96-well plate. Time dependent absorbance measurements were recorded at 515 nm over the course of 60 min using a Spectramax i3x microplate reader (Molecular Devices, San Jose, CA). The radical scavenging ability was calculated using the following equation:

$$DPPH\ scavenging\ \% = \left[1 - \left(A_{sample} - A_{flav}\right)/A_{DPPH}\right] \times 100\% \quad (1)$$

where A_{sample} is the absorbance of the flavonoid and DPPH, A_{flav} is the absorbance of the flavonoid alone, and A_{DPPH} is the absorbance of DPPH alone at the end of the 1-h measurement.

2.4 Measurement of $^\bullet$OH in solution

The amount of $^\bullet$OH in solution was measured as previously described (Hu et al., 2016). A solution of 2.5 mM CCA and 500 μM ascorbic acid was prepared in 10 mM phosphate buffer, pH 7.4. 50 μl of the CCA/ascorbic acid solution was added to 200 μl of pre-incubated flavonoid/$CuSO_4$ solutions at the described concentrations. Time-dependent fluorescence intensity measurements were recorded with excitation at 388 nm and emission at 450 nm over the course of 90 min using a Spectramax i3x microplate reader (Molecular Devices, San Jose, CA).

2.5 Assessment of copper transport in yeast

Saccharomyces cerevisiae strains used in this study are listed in Supplementary Table S2. Yeast cells were cultured in YPD (1% yeast extract, 2% peptone, 2% glucose) and YPGE (1% yeast extract, 2% peptone, 3% glycerol, 2% ethanol) media. Growth in liquid YPD media was monitored at 600 nm. For qualitative observations, spot plate assays were performed on YPD and YPGE plates supplemented with the indicated flavonoids and copper. 10-fold serial dilutions of overnight YPD cultures were spotted on YPGE agar plates supplemented with 25 μM flavonoids or 5 μM CuSO4 and incubated at 37°C for the indicated time.

2.6 HepG2 cell culture and stimulations

HepG2 cells were maintained in 4.5 g/L DMEM media supplemented with 10% fetal bovine serum, 1% sodium pyruvate, 1% glutamine, 1% Penicillin-Strepomycin. Cells were incubated at 37°C with 5% CO_2 in complete media until 70% confluence. HepG2 cells were plated at 300,000 cells/well in 6-well plates and allowed to grow for 24 h. Stimulations of 20 μM flavonoid with and without 50 μM CuSO4 were added to the wells and incubated for 24 h.

2.7 Cell viability

Cell viability was measured using the MTS assay (Promega, Madison, WI). HepG2 cells were plated at 10,000 cells/well in a 96-well plate and allowed to grow for 24 h. Wells were stimulated with 20 μM flavonoid with and without 50 μM CuSO4. After 24 h, media was removed, and cells were washed with DPBS to remove excess flavonoid. 20 μl of MTS reagent was added to each well and incubated for 1 h. Absorbance at 490 nm was measured.

2.8 Intracellular copper measurements

After stimulations, HepG2 cells were washed with cold 50 mM EDTA in HEPES buffer to remove any copper on the cell surface followed by washes with HEPES buffer. Cells were resuspended in 50 μl HEPES buffer and added to 250 ml 70% nitric acid. Samples were boiled for 1 h at 95°C then allowed to

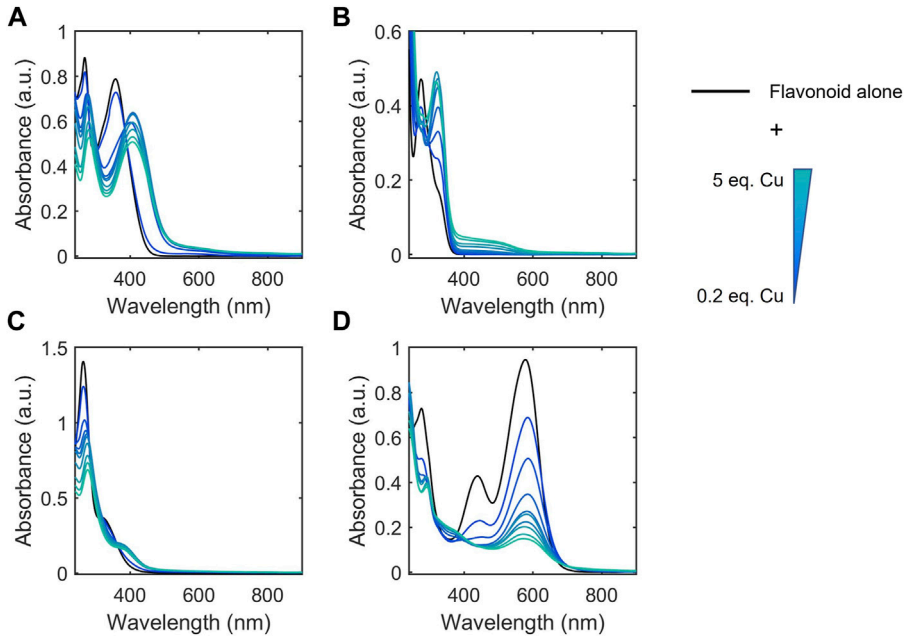


FIGURE 2
Electronic absorption spectra of representative flavonoids **(A)** luteolin, **(B)** EGCG, **(C)** biochanin A, and **(D)** cyanidin (black) in 50 mM MOPS buffer (pH 7.4) titrated with $CuSO_4$. Flavonoids were prepared at 50 μM and $CuSO_4$ was titrated into the solution from 0.2 to 5 molar equivalences. Flavonoids typically have two distinct absorption bands: a strong absorbance between 270 and 295 nm (Band II) and a weak Band I absorbance that appears as a shoulder at slightly longer wavelengths. Changes in the intensities and shifts in the lambda max wavelengths of these bands, indicate interactions of Cu(II) with the flavonoids. Electronic absorption spectra of the remaining flavonoids tested are shown in Supplementary Figure S1.

sit at room temperature for 24 h. Samples were diluted to 5 ml with nanopure water. Metal analysis was performed using a Perking Elmer 5300 DV optical emission ICP with auto sampler. Measured copper levels were normalized to the control sample.

2.9 Western blot analysis

After stimulations, HepG2 cells were washed with DPBS and lysed with 60 μl RIPA buffer. Whole cell lysates were centrifuged at 15,000 rpm at 4°C for 1 h. The supernatant was collected and stored at −20°C. Protein quantification was determined using the BCA assay. 20 μg of protein sample was loaded into 15-well SDS-PAGE gels and transferred to polyvinylidene difluoride (PVDF) membranes. PVDF membranes were incubated at 4°C overnight with primary antibodies. Primary antibodies used were anti-CCS (1:2000, sc-55561, Santa Cruz Biotechnology, anti-mouse), and anti-α-tubulin (1:10,000, MA1-80017, ThermoFisher, anti-rat). Primary antibodies were removed, and the membranes were washed with tris buffered saline with Tween (TBST). Membranes were then incubated in secondary antibodies at room temperature for 1 h. Secondary antibodies used were anti-mouse IgG AlexaFluor800 (A32789, 1:5000 Invitrogen) and anti-rat IgG (A21428, 1:5000 Invitrogen), AlexaFluor647, and a horseradish peroxidase-conjugated secondary antibody. Blot images were recorded on a BioRad ChemiDoc imaging system and processed in ImageLab.

3 Results and discussion

3.1 Spectroscopic characterization of flavonoid-copper binding interactions in solution

A breadth of techniques have been applied to probe aspects of flavonoid-metal interactions including computational methods, electrochemical studies, and various spectroscopies (Korotkova et al., 2012; Samsonowicz and Regulska 2017; Xu et al., 2020). However, reports have used varying experimental conditions including solvents, buffers, and pH conditions, yielding contradicting parameters for flavonoid-metal interactions (Samsonowicz and Regulska 2017). Thus, to allow connections to be made between structural features and biological function, we applied a universal approach that would allow us to comparatively study our selected library of flavonoids across the subclasses. The conjugated structure of flavonoids lends itself

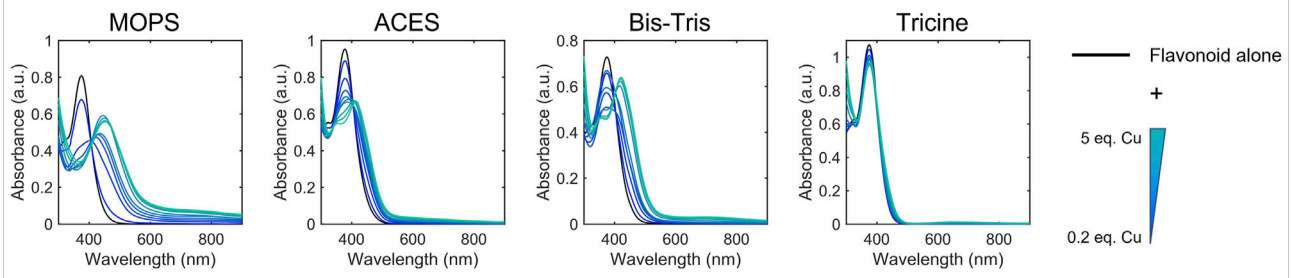


FIGURE 3
Representative electronic absorbance spectra of QT and $CuSO_4$ in various 50 mM buffers (pH 7.4) for determining binding affinity ranges. $CuSO_4$ was titrated into a 50 μM solution of QT from 0.2 to 5 equivalences. Spectral changes correspond to binding between QT and Cu(II) which indicates that QT has a stronger binding affinity than the corresponding buffer. Conversely, the lack of spectral changes upon Cu(II) addition in tricine buffer indicates that the binding affinity between tricine and Cu(II) is stronger than that of QT and Cu(II). These experiments allow us to estimate the binding affinity of QT and Cu(II) to be between that of BisTris-Cu(II) (5.3 μM) and tricine-Cu(II) (50 nM). Electronic absorption spectra of the remaining flavonoids tested are shown in Supplementary Figure S1.

TABLE 2 Binding affinity ranges of flavonoids with Cu(II).

Binding affinity ranges			
100 μM	**17.4 μM**	**5.3 μM**	**50 nM**
EC, cat, EGC, hesperetin, Hesperidin, naringenin, naringin, chrysin, biochanin A, genistein	Rutin	ECG, EGCG, 3-HF, Luteolin, QT, Kaempferol, Cyanidin	

to analysis by absorption spectroscopy. There are two major peaks in UV-Vis spectra for flavonoids. Band I corresponds to absorbance by the B ring while Band II appears at lower wavelengths due to absorbance by the A ring (Figure 2A). (Kumar and Pandey 2013) Flavanols and flavanones do not have conjugation between the A and B rings. This lack of conjugation is reflected in the presence of a strong absorbance between 270 and 295 nm (Band II) and a weak Band I absorbance that appears as a shoulder at slightly longer wavelengths (Figure 2B). (Rice-Evans et al., 1996)

Cu(II) binding near or at sites of conjugation yields spectral changes to these bands, which indicate metal-flavonoid interactions. We used these spectral changes to monitor metal binding in the presence of Cu(II)-binding buffers to categorize the flavonoids based on approximate apparent binding affinity ranges. Flavonoids were classified into Cu(II) binding affinities based on their ability to compete for Cu(II) binding with 50 mM MOPS (K_d = 100 μM), ACES (K_d = 17.4 μM), BisTris (K_d = 5.3 μM), and Tricine (K_d = 50 nM) (Figure 3; Table 2). (Kandegedara and Rorabacher 1999; Atp 1979; Azab and El-Nady 1994; Azab et al., 2001; Fernandez et al., 2002) Spectra were recorded for the flavonoids alone in each of the buffers as well as after Cu(II) addition. Changes in the spectra upon Cu(II) addition indicate that the flavonoids have a greater affinity for Cu(II) than the buffer and therefore interact in solution. If the buffer has a greater binding affinity for Cu(II) than the flavonoid, no spectral changes are observed. All flavonoids tested showed binding in 50 mM MOPS, indicating K_d < 100 μM. While binding affinity ranges showed some correlation to flavonoid subclasses, some exceptions arise based on the type of functional group and position. The flavanones and isoflavones were all relatively weak binders with K_d >17.4 μM. While flavanols with -OH modifications at the C-3 position also showed relatively weak binding affinities with K_d >17.4 μM, the presence of a gallate modification at the C-3 position in epicatechin gallate (ECG) and epigallocatechin gallate (EGCG) increases the K_d of the flavanols to 5.3 μM–50 nM. This indicates that a gallate moiety on the C-ring can endow stronger Cu(II)-binding ability to this subclass, while, surprisingly, a catechol on the B-ring does not. Interestingly, the anthocyanin, cyanidin, which differs from epigallocatechin (EGC) by the introduction of conjugation between the A and C rings, shows a strong binding affinity, suggesting that such conjugation may contribute to the electron donating abilities of the flavonoid. Among the flavones, luteolin and 3-hydroxyflavone (3-HF) were strong binders with K_d between 5.3 μM and 50 nM whereas chrysin showed weak binding (K_d > 17.4 μM). Luteolin and chrysin only differ by

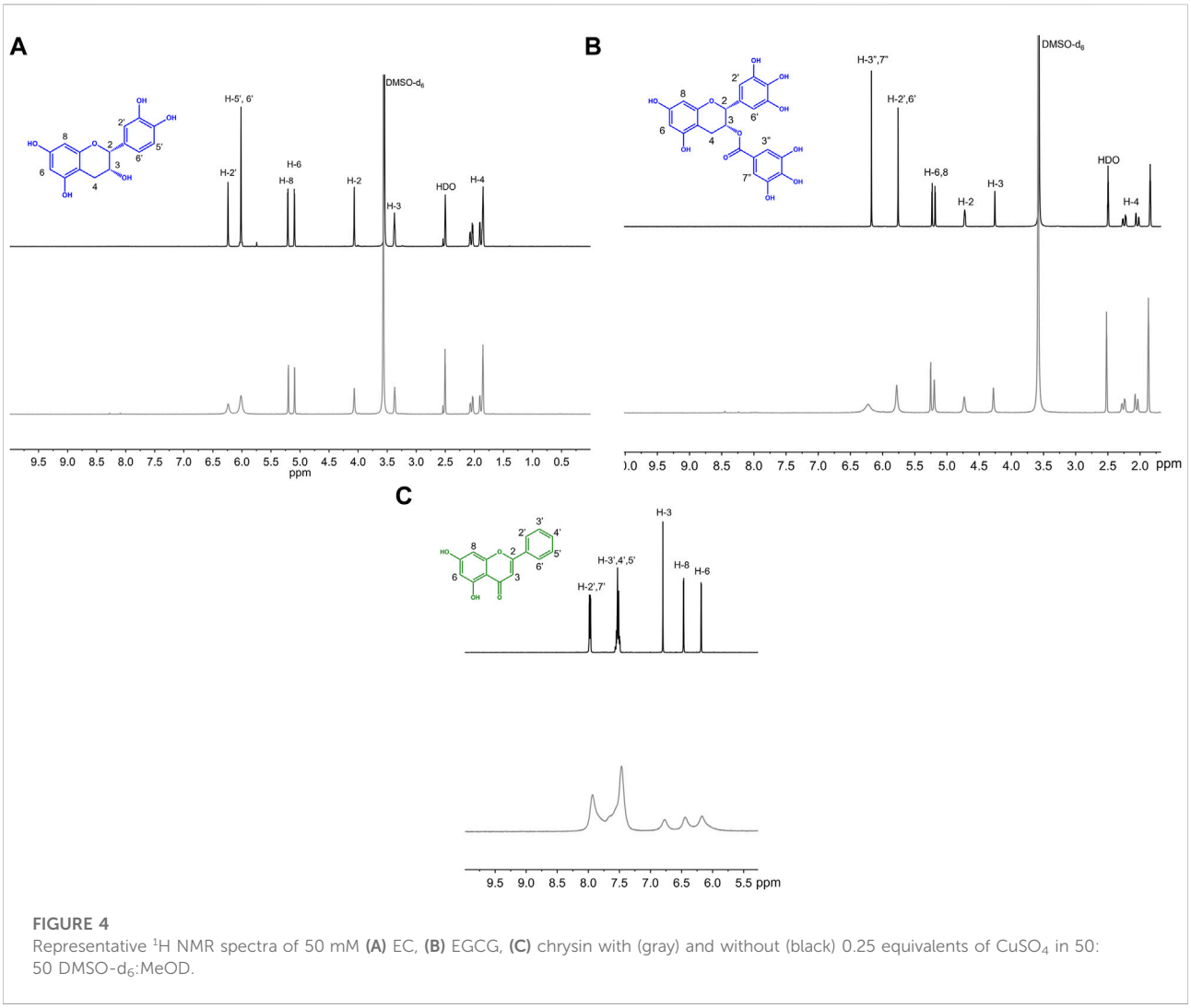


FIGURE 4
Representative ^{1}H NMR spectra of 50 mM **(A)** EC, **(B)** EGCG, **(C)** chrysin with (gray) and without (black) 0.25 equivalents of $CuSO_4$ in 50: 50 DMSO-d_6:MeOD.

the presence of a catechol moiety on the B-ring of the former, suggesting that Cu(II)-binding to luteolin likely occurs at this site. While the catechol moiety is absent in 3-HF, this flavone differs from chrysin by the presence of an -OH group in the C-3 position of the C-ring, suggesting that this functional group, likely in cooperation with the ketone at the C-4 position, coordinates to Cu(II). Of the flavonols, both quercetin (QT) and kaempferol are strong binders with K_d in the 5.3 μM–50 nM range. However, the C-3 O-rutinoside analogue of QT, rutin, showed reduced binding affinity (K_d in the 17.4–5.3 μM range), suggesting that this sugar modification disrupts Cu(II)-binding. The determined binding affinity ranges of QT and rutin support previously modeled binding affinities (Zhang et al., 2018).

To help further understand the contributions of specific structural features, we used the changes in absorption spectra to identify the location of Cu(II) interaction. Cu(II) interactions with the flavanols and flavanones increase the Band II absorbance, and flavanol-Cu(II) interactions also produce a bathochromic shift in Band I absorbance. These spectral shifts are attributed to changes in the conjugation on the B-ring where Cu(II) is hypothesized to interact. Flavonols and flavones likely interact with Cu(II) at the C-ring carbonyl which is supported by a bathochromic shift in Band I upon introduction of the metal ion in solution. Similar to the flavanones, the isoflavones show a large Band II absorbance and a smaller Band I absorbance that appears as a shoulder (Figure 2C). Cu(II) interactions cause a bathochromic shift in Band I absorbance likely due to interactions with the hydroxy group on the A-ring. Finally, the spectrum of cyanidin likewise shows a bathochromic shift in Band I upon addition of Cu(II) as well as significant decreases in absorbance (Figure 2D). These interaction locations were confirmed by ^{1}H-NMR: as Cu(II) is paramagnetic, coordination will cause faster relaxation of nuclei within electronic proximity, resulting in observed broadening in

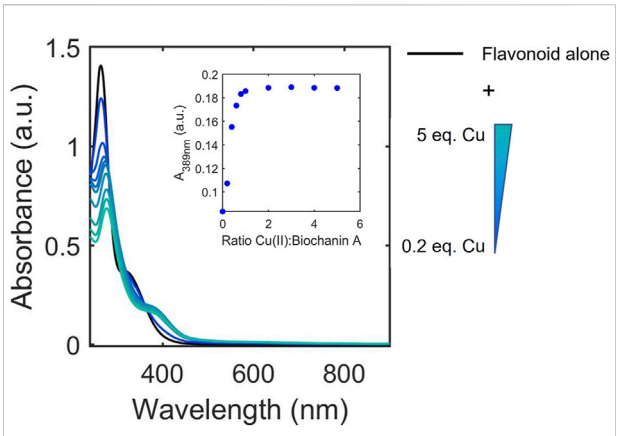


FIGURE 5
Representative electronic absorbance spectra of biochanin A upon addition of 0.2–5 equivalences of copper in 50 mM MOPS buffer (pH 7.4) for the determination of binding ratios. The inset shows absorbance at 389 nm where spectral changes occur due to Cu(II) binding to biochanin A. The changes in absorbance at 389 nm plateau at 1 equivalence of Cu(II) which indicates a 1:1 binding ratio between biochanin A and Cu(II).

the spectra. This property can be exploited to confirm the site of interaction on the flavonoid molecules. The addition of 0.25 equivalents of Cu(II) to epicatechin (EC) results in broadening of the downfield peaks which correspond to the B-ring protons (Figure 4A). (Davis et al., 1996) The localized broadening confirms the interaction of Cu(II) ions at the diol on the B-ring. The spectra of EGCG also present localized broadening around the most downfield protons (Figure 4B). The most downfield peak corresponds to the protons on the gallate group indicating that rather than interacting at the B-ring, Cu(II) ions interact at the gallate moiety (Delius et al., 2017). This confirms that it is indeed the interaction of Cu(II) with the gallate group that contributes to the stronger binding observed in the binding affinity estimation. It does appear that there is some interaction with the hydroxy groups on the B-ring evidenced by the large decrease in intensity of the peak at 5.8 ppm corresponding to the B-ring protons. Study of the flavanols is made easier by a saturated C-ring which results in no conjugation between the A- and B-rings and therefore more localized broadening. When conjugation is present throughout the molecule, introduction of paramagnetic Cu(II) to the flavonoid solutions results in universal broadening in the ^{1}H-NMR spectra. Interpretation of spectra is more difficult with broadening across all peaks, but changes in intensity of peaks provide insight into the location of interaction. The spectrum of chrysin and Cu(II) shows broadening throughout the spectrum but has a significantly larger decrease in peak intensity of the peaks corresponding to the A- and C-ring protons (Figure 4C). (Ansari 2008) This confirms the expected interaction of Cu(II) with the 4-carbonyl of the C-ring and the 5-OH on the A-ring. These results are supported by the UV-Vis interactions observed as well as previously reported crystal structures and computational studies (Bukhari et al., 2009; Pekal et al., 2011; Říha et al., 2014).

The UV-Vis titrations were also examined to determine whether binding affinity classifications were associated with ligand-to-metal stoichiometries. Although the method of continuous variation (Job's plot) has been applied to study some flavonoid/metal complexes, this method primarily works for interactions with large dissociation constants (Ulatowski et al., 2016). Thus, to allow for broader analysis of the flavonoid library, we opted to apply the mole ratio plot analysis using the characteristic absorbance of the Cu(II)-flavonoid complexes to approximate and compare binding stoichiometries of flavonoids to Cu(II) under buffered aqueous conditions at physiological pH. To achieve this, we monitored the equivalents of Cu(II) at which the intensities of the absorbance of flavonoid-Cu(II) peaks plateau, indicating stable species formation (Figure 5). Consistent with literature, the binding ratios vary between 1:2, 1:1, and 2:1 copper-to-flavonoid (Table 3). In the same way gallate modifications affects binding affinity, flavanols with gallate groups have altered binding ratios (1:1 copper-to-flavonoid) compared to their ungallated counterparts, which typically have 2:1 copper-to-flavonoid binding ratios. Additionally, as observed with the binding affinities, the O-rutinoside modification on rutin alters the binding ratio relative to its unmodified counterpart, QT, with the former having a 1:1 binding ratio in contrast to the 2:1 ratio of the latter. The 2:1 ratio of QT suggests the presence of two binding sites for Cu(II) likely occurring at the B-ring diol as well as the 4-carbonyl on the C-ring and either the 5-OH of the A-ring or the 3-OH on the C-ring. The glycone on rutin likely disrupts interactions around the 4-carbonyl allowing for binding to occur only at the B-ring. However, beyond these two observations, the binding ratios do not seem to have dependence on or correlation to structural subclass or binding affinities.

3.1.1 Flavonoids impart antioxidant activity through multiple mechanisms

Flavonoids are well-known to exhibit antioxidant activity, with reactive oxygen species (ROS) scavenging being one of the most common hypothesized mechanisms. The flavonoid library was classified by their antioxidant activity with the 2,2-diphenyl-1-picryl-hydrazyl-hydrate (DPPH) free radical assay (Campos et al., 2009; Xie and Schaich 2014; María Pilar de et al., 2019). The stable DPPH free radical is purple in solution, and its reduction by an antioxidation discolors the solution, allowing loss of absorbance at its λ_{max} = 515 nm to be used to assess antioxidant activity. Ascorbic acid was used as a positive control and scavenged 97% of DPPH in solution (Figure 6A). The antioxidant capacity of the flavonoids alone were tested in the absence of Cu(II) using endpoint reads of the DPPH

TABLE 3 Binding ratios of flavonoids to Cu(II) ions in solution. Ratios were determined by titrating $CuSO_4$ into a 50 μM solution of flavonoid and monitoring the absorbance values of peaks that correspond to flavonoid-Cu(II) complexes.

Binding ratios (Cu:flavonoid)		
1:2	**1:1**	**2:1**
EC, Cat, hesperidin, naringin, 3-HF, luteolin, chrysin, kaempferol	EGC, ECG, EGCG, hesperetin, naringenin, rutin, cyanidin. biochanin A, genistein	QT

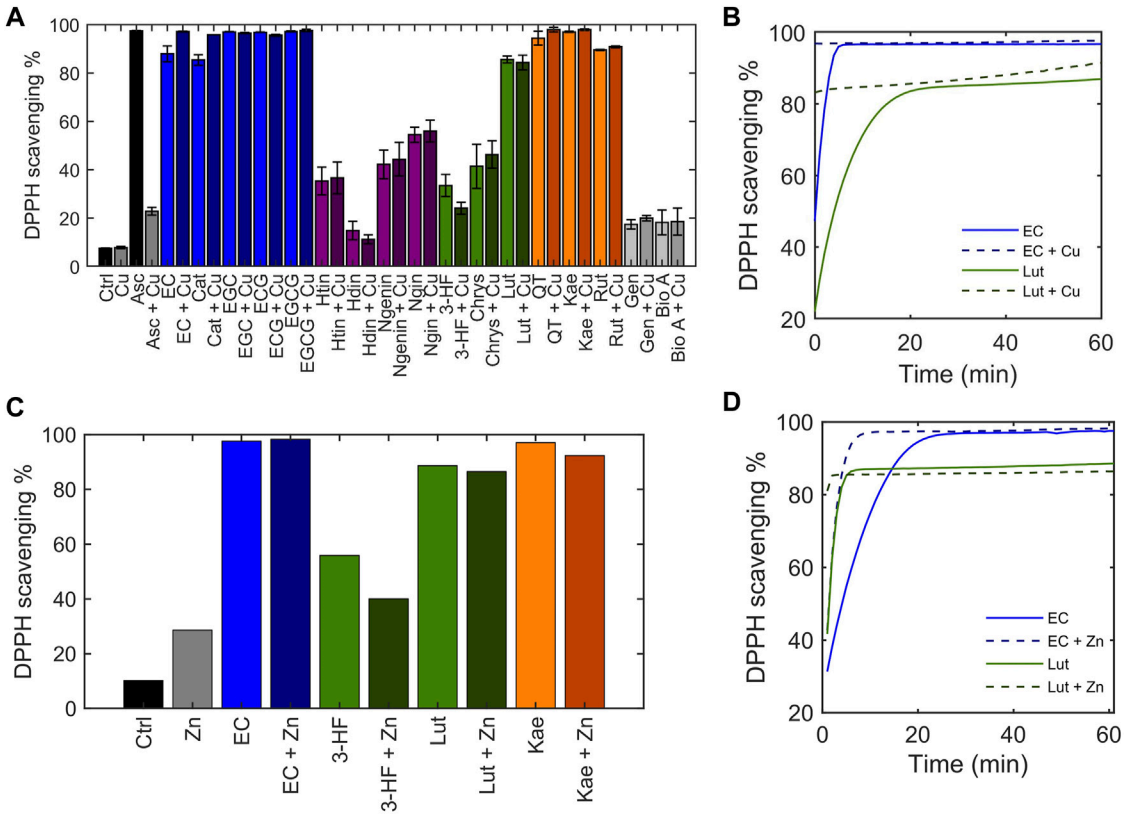


FIGURE 6
Determination of the ability of flavonoids to scavenge the DPPH radical, depicted as DPPH scavenging %. 50 μM flavonoid or ascorbic acid was incubated with 50 μM $CuSO_4$ before addition of 50 μM DPPH●. **(A)** The DPPH scavenging % was determined using the 515 nm absorbance of DPPH at the end of a 1-h reaction. **(B)** Time-dependent scavenging activity of representative flavonoids EC and luteolin in the presence of 50 μM $CuSO_4$ measured over the course of 1 hour. **(C)** End-point DPPH scavenging % of flavonoids in the presence of 50 μM $ZnCl_2$ after a 1-h reaction. **(D)** Time-dependent DPPH scavenging activity of representative flavonoids EC and luteolin in the presence of 50 μM $ZnCl_2$ measured over 1 hour.

free radical signal. The flavanols tested, all of which contain o-catechol groups in the B-ring were able to scavenge over 80% of DPPH in solution whereas the flavanones, which are similar to the flavanols but do not contain the B-ring *o*-catechol, did not exhibit DPPH radical scavenging abilities. Similarly, the flavones and isoflavones tested were unable to scavenge DPPH radical in solution except for luteolin. Of importance to note is that luteolin has an *o*-catechol group on its B-ring which the non-scavenging flavonoids lack. These results are consistent with previous studies and indicate the importance of the *o*-catechol group in antioxidant activity (Manuela Silva et al., 2002). An exception is kaempferol, which lacks the *o*-catechol group but exhibits radical scavenging abilities, suggesting that the hydroxy group on the B-ring may participate in antioxidant activity.

Little differences were observed in the endpoint reads of the DPPH assay when Cu(II) was added. While the DPPH reads at

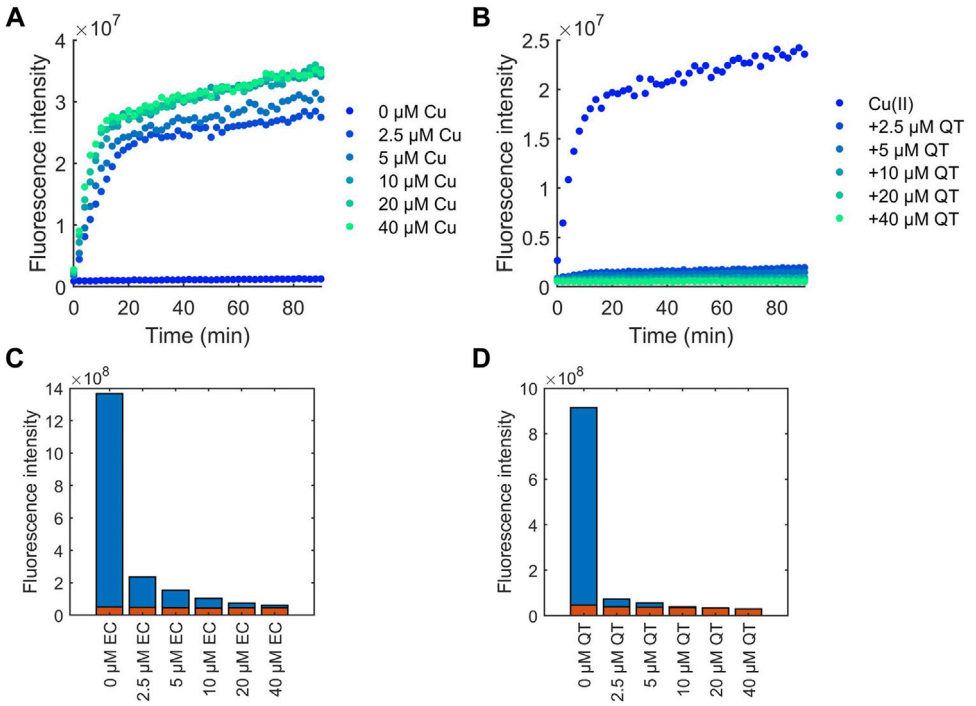


FIGURE 7
CCA fluorescence intensity measurements for determining the effects of flavonoids on the time-dependent generation of $^{\bullet}$OH. Flavonoid effects were compared to **(A)** Cu(II) addition alone, with **(B)** QT shown as an example. 2.5 mM CCA and 50 μM ascorbic acid were used for all experiments. The calculated area under the curve over the course of 90 min was measured for flavonoid solutions. **(C)** EC and **(D)** QT effects are shown as representative plots in the presence (blue) and absence (red) of Cu(II).

endpoint allow for general classification of the antioxidant capacity of the flavonoids, solvent effects, particularly those that may associate with the radical, have been shown to influence endpoint quantitation (Xie and Schaich 2014). A more accurate comparison on antioxidant activity can be made by monitoring scavenging kinetics. Thus, to thoroughly understand the scavenging kinetics of flavonoids in comparison to their Cu(II)-bound forms, absorbance measurements were recorded over time, beginning immediately after addition of DPPH to solution. For all flavonoids that exhibit DPPH radical scavenging properties based on endpoint reads, the presence of Cu(II) increased the kinetics of the scavenging reaction (representative plots of EC and luteolin shown in Figure 6B). It has been suggested that rather than the antioxidant activity occurring from redox reactions with the Cu(II) center, coordination of Cu(II) at the hydroxy groups on the B-ring stabilizes a semiquinone radical intermediate facilitating the DPPH radical scavenging mechanism (Bukhari et al., 2009). To test this hypothesis, Zn(II) was substituted for Cu(II). Zn(II), like Cu(II), behaves as a Lewis acid, but it is redox-inactive. The scavenging activities of flavonoids in the presence of Zn(II) show similar trends as in the presence of Cu(II) (Figures 6C,D). The rate of scavenging was increased in the presence of Zn(II) which supports the hypothesis that the increased antioxidant activity with Cu(II) addition is due to its interaction with the B-ring hydroxy groups as a Lewis acid rather than metal-centered redox activity. The DPPH assay demonstrates that flavonoids' radical scavenging abilities are affected by Cu(II) but are not correlated with the strength of copper interaction.

Another mechanism by which flavonoids potentially possess antioxidant activity is by chelating redox-active Cu(II) ions thereby preventing production of ROS produced via Fenton-like chemistry (Hu et al., 2016). To assess this, coumarin-3-carboxylic (3-CCA) was used as a probe to examine the protection of flavonoids against Cu(II)-induced production of $^{\bullet}$OH (Hu et al., 2016). Ascorbic acid and copper undergo a redox cycling reaction which produces $^{\bullet}$OH. 3-CCA reacts with $^{\bullet}$OH to form 7-hydroxy-3-carboxycoumarinic acid which fluoresces with excitation at 388 nm and emission at 450 nm. The fluorescence intensity can be monitored to observe production of $^{\bullet}$OH in solution. As expected, the concentration of Cu(II) ions in solution was positively correlated to the amount of $^{\bullet}$OH detected (Figure 7A). Introduction of all flavonoids to solution decreased detected $^{\bullet}$OH, with increasing amounts of flavonoids decreasing $^{\bullet}$OH production (Figures 7B; Supplementary Figure S2). In contrast to the flavonoid

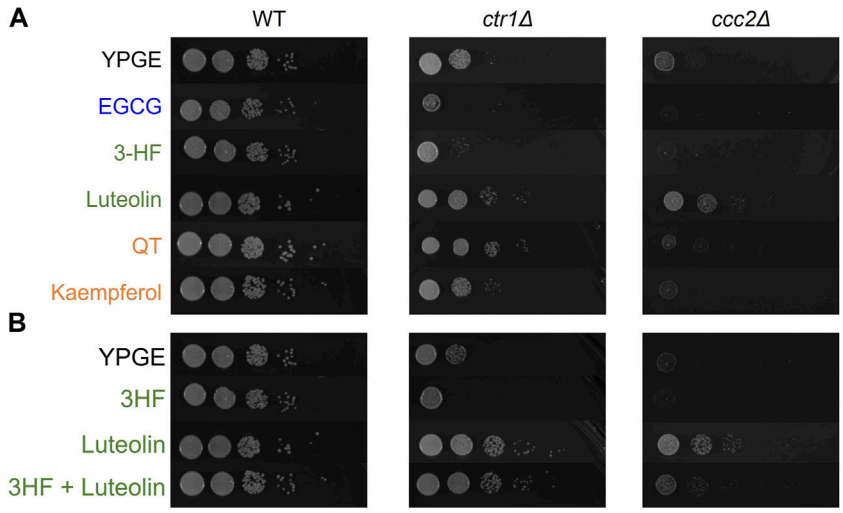


FIGURE 8
Serially diluted *S. cerevisiae* strains were spotted on the noted YPGE plates and incubated at 37°C for 4 days before imaging. **(A)** YPGE agar plates were prepared with 25 μM of the noted flavonoid. **(B)** Mixed ligand plates were prepared with 25 μM of each noted flavonoid. Treatment with mixed ligands exhibit changes suggestive of competition between ligands.

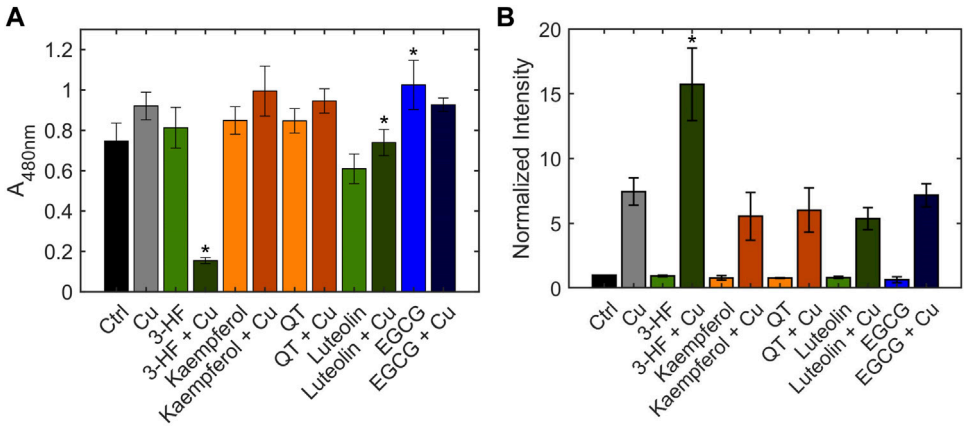


FIGURE 9
(A) Cell viability of HepG2 cells in the presence and absence of flavonoids and Cu(II), measured using the MTS assay. HepG2 cells were stimulated with 20 μM flavonoid with or without 50 μM $CuSO_4$. The MTS reagent was added after 24 h. After 1 h incubation with the reagent, absorbance was measured at 490 nm. **(B)** Quantification of total cellular copper of HepG2 cells in the presence and absence of flavonoids and Cu(II), measured by ICP-OES. HepG2 cells were stimulated with 20 μM flavonoid with or without 50 μM $CuSO_4$ for 24 h. Error bars represent SD, $n = 3$. *$p < 0.05$ versus the vehicle control.

effects on DPPH scavenging, the protective effects of the flavonoids against Cu(II)-induced production of ROS correlates to their binding affinities. For example, at 4-fold excess, EC is unable to reduce production of $^{\bullet}$OH to baseline levels (Figure 7C), whereas QT was able to stop $^{\bullet}$OH generation at 1 equivalent (Figure 7D).

Flavonoids are often touted and have been extensively studied for their antioxidant effects. Due to their known interactions with copper ions, it has been hypothesized that some of their antioxidant activity is a result of those interactions (Fernandez et al., 2002; Ren et al., 2008; Pekal et al., 2011; Cherrak et al., 2016). The discrepancies between the CCA and DPPH assays indicate that while copper interactions do have an effect on the antioxidant activity of flavonoids, the mechanism by which copper has its influence varies based on the flavonoid. While copper

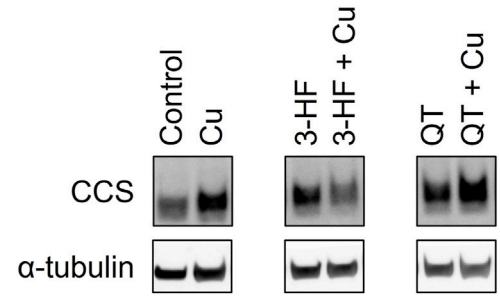


FIGURE 10
Western blot analysis of the CCS protein in lysates of HepG2 cells in the presence and absence of the flavonoids 3-HF or QT and Cu(II). HepG2 cells were stimulated with 20 μM flavonoid with and without 50 μM $CuSO_4$ and incubated for 24 h. Cell lysates were collected, and Western blot analysis was performed using antibodies specific for CCS with α-tubulin as a control. Western blot images for the remaining assessed flavonoids are shown in Supplementary Figure S5.

binding affinity generally correlates with $^{\bullet}$OH levels from Cu(II)-induced Fenton-like chemistry as measured with the CCA assay, these trends do not apply to general free radical scavenging as measured with the DPPH assay. It is important to note that the ability to protect against $^{\bullet}$OH generation is not directly correlated to structure of the flavonoids, but rather to the binding affinities of the flavonoids to Cu(II). Stronger binders, like QT and kaempferol, can prevent $^{\bullet}$OH production, whereas weaker binders, like EC, cannot eliminate $^{\bullet}$OH generation. Both the CCA and DPPH assays demonstrate that antioxidant activity of flavonoids is not delineated by subclass but rather functional group location and identity.

3.2 Understanding the bioactivity of flavonoids

3.2.1 Effects of flavonoids on copper trafficking in yeast

Having gained an understanding of the structural features important to flavonoid-copper interactions in solution, we extended investigations to probe how the flavonoids' appreciable interactions with Cu(II) in buffered solutions influence copper trafficking in cell-based models. The ability of these flavonoids to transport copper was probed in *Saccharomyces cerevisiae* (*S. cerevisiae*) as a model eukaryotic organism (Soma et al., 2018). Two knockout strains of *S. Cerevisiae*, *ctr1Δ* and *ccc2Δ*, were treated with various flavonoids to observe differences in growth. The *ctr1* gene encodes a high-affinity copper transporter localized at the plasma membrane, and its knockdown restricts copper import from the extracellular space into the cytosol (Wu et al., 2009). The *ccc2* gene encodes a copper-transporting ATPase hypothesized to translocate copper from the cytosol to extracytosolic compartments, and its knockdown has been shown to induce a functional copper deficiency (Yuan et al., 1995). Under aerobic growth conditions (e.g. YPGE media), compared to its wild-type (WT) counterpart, the knockout strains show impaired growth that is rescued with copper supplementation (Supplementary Figure S3). We posited that copper-binding flavonoids could affect copper bioavailability to the knockdown strains, which could be monitored by differences in yeast growth. Specifically, we investigated the activity of 3-HF, luteolin, QT, and kaempferol, as these represent strong binders with a common ring conjugation structure. Growth rescue of *ctr1Δ* cells would suggest that copper is being imported by the flavonoid while rescue of *ccc2Δ* cells would indicate that the flavonoid can improve intracellular copper availability to extracytosolic compartments. To assess growth with a large dynamic range of detection, a spot assay was performed, where yeast were plated on agar in a 1:10 dilution series of four dilutions. Interestingly, despite the similarities of the flavonoids with respect to solution-based binding affinities and ring structures, they showed notable differences in effects on growth rescue of the knockouts (Figure 8).

In both knockout strains, 3-HF further restricts growth, which may indicate chelation of extracellular copper without transport into the cell. Conversely, luteolin treatment exhibits growth rescue effects on both *ctr1Δ* and *ccc2Δ* suggesting that it can transport copper into the cell and affect its intracellular availability. The differences in the behavior of these two may be attributed in their relative hydrophobicities. *S. cerevisiae* have cell walls that are hydrophilic (Klis et al., 2002). The relatively higher hydrophobicity of 3-HF (reported log p = 4.17 (Pogodaeva et al., 2012)) may explain its inability to transport copper into yeast cells in contrast to the more hydrophilic luteolin [reported log p = 0.7 (Quintieri et al., 2008)] (Supplementary Table S1). The simultaneous treatment with both 3-HF and luteolin result in a combined effect, with growth rescue that is less than luteolin but similar to copper supplementation alone suggesting that the two flavonoids may compete in their effects (Figure 8B). This may point to the possibility of modulation of copper ionophoric effects based on flavonoid content. Kaempferol and QT have reported log p values that are similar to one another but are in between those of luteolin and 3-HF (log p = 1.87 (Sreelakshmi et al., 2017) and 1.82 (Rothwell et al., 2005) respectively). Interestingly, while kaempferol shows only modest to no growth rescue of the *ctr1Δ* and *ccc2Δ*, QT shows a strong growth rescue of the *ctr1Δ* strain comparable to that of luteolin. This may be in part due to the ability of QT to complex Cu(II) at a 2:1 ratio of copper-to-flavonoid, allowing for translocation of higher concentrations of copper into the cell. The growth rescue by both luteolin and QT of the *ctr1Δ* strain may also point to the importance of the catechol in the B-ring in facilitating copper import. However, in the *ccc2Δ* strain, no growth rescue is observed by QT, suggesting that while QT may facilitate copper import, it does not have a beneficial impact on extracytosolic copper availability.

Additionally, we tested the effects of EGCG on the growth of the knockout strains, as EGCG is a well-reported copper modulator in cell-based assays. In both strains, EGCG exhibited potent inhibition on cell growth, suggesting that it may serve as an extracellular Cu(II) chelator to withhold the metal ion from the organism.

3.2.2 Effects of flavonoids on copper trafficking in human hepatocytes

The inability of 3-HF to improve copper availability to the yeast knockout strains was a surprising observation, given that recent work reported that this particular flavonoid acts as a potent copper ionophore in mammalian cancer cell lines. In this context, Dai et al. posited that the delivery of copper by 3-HF could cause a redox imbalance in the cell, leading to copper-induced cell death (Dai et al., 2017), or "cuproptosis" (Oliveri 2022). We thus assessed the same flavonoids in HepG2 cells, a human hepatocarcinoma cell line sensitive to cuproptosis. Cell viability was measured using the MTS assay in which an MTS tetrazolium compound is reduced by the mitochondria of viable cells to produce a colored formazan complex whose absorbance is monitored. Consistent with the previous report, our results show that in the presence of supplemented copper, 3-HF significantly reduces cell viability (Figure 9A), and this effect correlates with increased intracellular copper levels, as measured by ICP-OES (Figure 9B). Conversely to yeast cells, HepG2 cells have a hydrophobic cell membrane, which may explain the differential effects in copper import between the two systems. The effect of 3-HF on copper metabolism is further validated by changes to the expression of the copper chaperone for superoxide dismutase (CCS), a reported marker for cytosolic copper deficiency (Bertinato and L'Abbé 2003). Interestingly, supplemental copper increases CCS expression, while the addition of 3-HF with supplemental copper decreases expression (Figure 10). Although CCS expression has been shown to increase in the presence of copper chelators and copper-deficient conditions, its response to acute treatment of supplemental copper remains unclear. While this complicates the interpretation of the CCS expression data, the difference between supplemented copper with and without 3-HF remain apparent, suggesting that the flavonoid modulates copper by different mechanisms than treatment with Cu(II) salt alone.

While none of the other flavonoids tested significantly altered intracellular copper levels relative to the no-flavonoid controls, luteolin and EGCG treatments signficantly affected cell viability. Previous work has shown that while EGCG shows antioxidant properties, its copper complex conversely functions as a pro-oxidant (Azam et al., 2004). These contrasting effects may be reflected in the cell viability data where EGCG improves cell viability over the control whereas the presence of Cu(II) reduces this effect. This may suggest the differences in cell viability with EGCG may be due to affecting the reactive oxygen species balance in the cell rather than by copper-modulating mechanisms. Luteolin, on the other hand, reduces cell viability, and this effect is attenuated by Cu(II) addition. Given the relative hydrophilicity of luteolin, it is possible that the flavonoid alters reactive oxygen species balance in the extracellular environment, but further studies are required to assess this effect. However, as both EGCG and luteolin treatments show no significant changes in either intracellular copper levels or CCS levels, their impact on cell viability may be independent of copper modulation. In contrast, while QT shows no changes in intracellular copper levels nor cell viability, the flavonoid induces a notable increase in expression in CCS in the presence of Cu(II). This may suggest that while QT does not affect copper import, it may modulate intracellular copper distribution and availability.

The cell-based assays demonstrate that despite similar behaviors of the flavonoids in solution, these are not necessarily predictive of their *biological* behavior. Moreover, even among eukaryotic systems, the structural features of the flavonoids may lend to differences in interactions in components such as membrane environments.

4 Conclusion

In this work, we focused on characterizing and assessing the ability of flavonoids to serve as modulators of copper trafficking. Structure-based characterization of flavonoid-Cu(II) interactions in buffered aqueous solutions showed wide diversity in the binding affinities and ratios that correspond more closely to specific functional group modifications and locations rather than the traditional subclassification of flavonoids by ring structures. Binding affinities correlated to protective effects against $^{\bullet}$OH generation but not necessarily general scavenging activity. We further assessed how structural factors may affect the ability of flavonoids with appreciable Cu(II) affinity to traffic the metal in biological contexts. In yeast models, we found that hydrophobicities trend with the transport of copper into the cells. The more hydrophilic flavonoids, luteolin and QT, can cross the yeast cell wall and rescue growth of strains with copper trafficking proteins knocked out. However, a different trend was observed in mammalian HepG2 cells, which have relatively hydrophobic cell membranes, with the most pronounced copper transport effects exhibited by 3-HF. 3-HF increased intracellular copper levels and subsequently induced cuproptosis. While the exact mechanisms of 3-HF transport require further elucidation, decreased CCS protein expression suggests that 3-HF affects cellular copper trafficking mechanisms. Though 3-HF had the most marked effect on copper trafficking markers, treatment with QT also demonstrated effects on CCS expression suggesting potential modulation of intracellular localization. Taken together, our studies demonstrate an approach for linking the structure of natural products to their potential functions as copper modulators. Future work should take

into account organism-specific copper modulation as well as the heightened importance of functional group substitution and hydrophobicities rather than traditional subclassifications. The data offers insight to guiding principles for identifying such agents within the flavonoid structural family, which can both inform nutritional recommendations as well as therapeutic agent design for impacting copper-associated disorders.

Data availability statement

The raw data supporting the conclusions of this article will be made available by the authors, without undue reservation.

Author contributions

VL and MH designed research; VL performed research; VL and MH analyzed data; VL and MH wrote the manuscript with input from all authors.

Funding

This work was supported by the National Science Foundation (NSF CAREER 2048265). We also thank the Hartwell Foundation for their generous support for MH as a Hartwell Individual Biomedical Investigator, as well as the UC Davis CAMPOS Program and the University of California's Presidential Postdoctoral Fellowship Program for their support of MH as a CAMPOS Faculty Fellow and former UC President's Postdoctoral Fellow, respectively.

Acknowledgments

We would like to thank Dr. Wenbo Yang for training and assistance on the ICP-OES instrument at Rausser College of Natural Resources at UC Berkeley. We would like to thank Professor Vishal Gohil and Dr. Mohammad Zulkifli for their conversations and support regarding yeast culture. We would like to thank Kylie Uyeda and Nathaniel Harder for their support and advice.

Conflict of interest

The authors declare that the research was conducted in the absence of any commercial or financial relationships that could be construed as a potential conflict of interest.

Publisher's note

All claims expressed in this article are solely those of the authors and do not necessarily represent those of their affiliated organizations, or those of the publisher, the editors and the reviewers. Any product that may be evaluated in this article, or claim that may be made by its manufacturer, is not guaranteed or endorsed by the publisher.

Supplementary material

The Supplementary Material for this article can be found online at: https://www.frontiersin.org/articles/10.3389/fchem.2022.972198/full#supplementary-material

References

Anderson, S. N., Larson, M. T., and Berreau, L. M. (2016). Solution or solid-it doesn't matter: Visible light-induced CO release reactivity of zinc flavonolato complexes. *Dalton Trans.* 45 (37), 14570–14580. doi:10.1039/c6dt01709f

Ansari, A. A. (2008). DFT and 1H NMR molecular spectroscopic studies on biologically anti-oxidant active paramagnetic lanthanide(III)-Chrysin complexes. *Main. Group Chem.* 7 (1), 43–56. doi:10.1080/10241220801912637

Atp, A. (1979). Metal ion/buffer interactions. *Eur. J. Biochem.* 530, 523–530.

Azab, H. A., and El-Nady, A. M. (1994). Ternary complexes in solution. Comparison of the coordination tendency of some biologically important zwitterionic buffers toward the binary complexes of Cu(II) and adenosine 5′-Mono-5′-Di-and 5′-triphosphate. *Monatsh. Chem.* 125 (8–9), 849–858. doi:10.1007/BF00812698

Azab, H. A., Orabi, A. S., and Enas, T. (2001). Role of biologically important zwitterionic buffer secondary ligands on the stability of the mixed-ligand complexes of divalent metal ions and adenosine 5′-Mono-5′-Di-and 5′-triphosphate. *J. Chem. Eng. Data* 46 (2), 346–354. doi:10.1021/je0001779

Azam, S., Hadi, N., Khan, N. U., and Hadi, S. M. (2004). Prooxidant property of green tea polyphenols epicatechin and epigallocatechin-3-gallate: Implications for anticancer properties. *Toxicol. Vitro* 18 (5), 555–561. doi:10.1016/j.tiv.2003.12.012

Baldari, Silvia, Di Rocco, G., and Toietta, G. (2020). Current biomedical use of copper chelation therapy. *Int. J. Mol. Sci.* 21 (3), 1069. doi:10.3390/ijms21031069

Bertinato, J., and L'Abbé, M. R. (2003). Copper modulates the degradation of copper chaperone for Cu, Zn superoxide dismutase by the 26 S proteosome. *J. Biol. Chem.* 278 (37), 35071–35078. doi:10.1074/jbc.M302242200

Bukhari, S. B., Memon, S., Mahroof-Tahir, M., and Bhanger, M. I. (2009). Synthesis, characterization and antioxidant activity copper-quercetin complex. *Spectrochimica Acta Part A Mol. Biomol. Spectrosc.* 71 (5), 1901–1906. doi:10.1016/j.saa.2008.07.030

Campos, C., Guzmán, R., López-Fernández, E., and Casado, Á. (2009). Evaluation of the copper(II) reduction assay using bathocuproinedisulfonic acid disodium salt for the total antioxidant capacity assessment: The CUPRAC-BCS assay. *Anal. Biochem.* 392 (1), 37–44. doi:10.1016/j.ab.2009.05.024

Cherrak, S. A., Mokhtari-Soulimane, N., Berroukeche, F., Bensenane, B., Cherbonnel, A., Merzouk, H., et al. (2016). *In vitro* antioxidant versus metal ion chelating properties of flavonoids: A structure-activity investigation. *PLoS ONE* 11 (10), e0165575. doi:10.1371/journal.pone.0165575

Cremonini, E., Wang, Z., Ahmed, B., Adamo, A. M., Daveri, E., Mills, D. A., et al. (2018). (-)-Epicatechin protects the intestinal barrier from high fat diet-induced permeabilization: Implications for steatosis and insulin resistance. *Redox Biol.* 14 (2017), 588–599. doi:10.1016/j.redox.2017.11.002

Dai, F., Wen, J. Y., Yu, T. D., Zhen Bao, X., Zhuang Li, X., and Zhou, B. (2017). Structural basis, chemical driving forces and biological implications of flavones as

Cu(II) ionophores. *Free Radic. Biol. Med.* 108, 554–563. doi:10.1016/j.freeradbiomed.2017.04.023

Datta, N., Singanusong, R., Chen, S. S., Yao, L. H., Jiang, Y. M., Shi, J., et al. (2004). Flavonoids in food and their health benefits. *Plant Foods Hum. Nutr.* 59, 113–122. doi:10.1007/s11130-004-0049-7

Davis, A. L., Ya, C., Davies, A. P., and Lewis, J. R. (1996). 1H and 13C NMR assignments of some green tea polyphenols. *Magn. Reson. Chem.* 34 (11), 887–890. doi:10.1002/(SICI)1097-458X(199611)34:11<887::AID-OMR995>3.0.CO;2-U

Delius, J., Frank, O., and Hofmann, T. (2017). Label-free quantitative 1H NMR spectroscopy to study low-affinity ligand–protein interactions in solution: A contribution to the mechanism of polyphenol-mediated astringency. *PLoS ONE* 12 (9), e0184487. doi:10.1371/journal.pone.0184487

Escandar, G. M., and Sala, L. F. (1991). Complexing behavior of rutin and quercetin. *Can. J. Chem.* 69 (12), 1994–2001. doi:10.1139/v91-288

Fang, X., Gao, W., Yang, Z., Gao, Z., and Li, H. (2020). Dual anti-/prooxidant behaviors of flavonoids pertaining to Cu(II)-Catalyzed tyrosine nitration of the insulin receptor Kinase domain in an antidiabetic study. *J. Agric. Food Chem.* 68 (22), 6202–6211. doi:10.1021/acs.jafc.0c01676

Fernandez, M. T., Mira, M. L., Helena Florêncio, M., and Jennings, K. R. (2002). Iron and copper chelation by flavonoids: An electrospray mass spectrometry study. *J. Inorg. Biochem.* 92 (2), 105–111. doi:10.1016/S0162-0134(02)00511-1

Hu, X., Zhang, Q., Wang, W., Yuan, Z., Zhu, X., Chen, B., et al. (2016). Tripeptide GGH as the inhibitor of copper-amyloid-β-mediated redox reaction and toxicity. *ACS Chem. Neurosci.* 7 (9), 1255–1263. doi:10.1021/acschemneuro.6b00145

Hunsaker, E. W., and Franz, K. J. (2019). Emerging opportunities to manipulate metal trafficking for therapeutic benefit. *Inorg. Chem.* 1, 13528–13545. doi:10.1021/acs.inorgchem.9b01029

Kandegedara, A., and Rorabacher, D. B. (1999). Noncomplexing tertiary amines as 'better' buffers covering the range of PH 3-11. Temperature dependence of their acid dissociation constants. *Anal. Chem.* 71 (15), 3140–3144. doi:10.1021/ac9902594

Klis, Frans M., Mol, P., Hellingwerf, K., and Brul, S. (2002). Pieternella mol, klaas hellingwerf, and stanley BrulDynamics of cell wall structure in Saccharomyces cerevisiae. *FEMS Microbiol. Rev.* 26 (3), 239–256. doi:10.1111/j.1574-6976.2002.tb00613.x

Korotkova, E. I., Voronova, O. A., and Dorozhko, E. V. (2012). Study of antioxidant properties of flavonoids by voltammetry. *J. Solid State Electrochem.* 16 (7), 2435–2440. doi:10.1007/s10008-012-1707-6

Kumar, S., and Pandey, A. K. (2013). Chemistry and biological activities of flavonoids: An overview. *Sci. World J.* 2013, 162750. Availble at: http://www.pubmedcentral.nih.gov/articlerender.fcgi?artid=3891543&tool=pmcentrez&rendertype=abstract. doi:10.1155/2013/162750

Manuela Silva, M., Santos, M. R., Caroco, G., Rocha, R., Goncalo, J., Mira, L., et al. (2002). Structure-antioxidant activity relationships of flavonoids: A Re-examination. *Free Radic. Res.* 36 (11), 1219–1227. doi:10.1080/1071576021000016472

María Pilar de, T., Yolanda Cavero, R., Isabel Calvo, M., and Vizmanos, J. L. W. (2019). A simple and a reliable method to quantify antioxidant activity *in vivo*. *Antioxidants* 8 (5), 142. doi:10.3390/antiox8050142

Oliveri, V. (2022). Selective targeting of cancer cells by copper ionophores: An overview. *Front. Mol. Biosci.* 9, 841814. doi:10.3389/fmolb.2022.841814

Pękal, A., Biesaga, M., and Pyrzynska, K. (2011). Interaction of quercetin with copper ions: Complexation, oxidation and reactivity towards radicals. *BioMetals* 24 (1), 41–49. doi:10.1007/s10534-010-9372-7

Perron, N. R., García, C. R., Pinzón, J. R., Chaur, M. N., Brumaghim, J. L., and Brumaghim, J. L. (2011). Antioxidant and prooxidant effects of polyphenol compounds on copper-mediated DNA damage. *J. Inorg. Biochem.* 105 (5), 745–753. doi:10.1016/j.jinorgbio.2011.02.009

Pogodaeva, N. N., Medvedeva, S. A., Sukhov, B. G., and Larina, L. I. (2012). Spectroscopic study of the reaction of a natural arabinogalactan Polysaccharide with 3-hydroxyflavones in aqueous solutions. *Chem. Nat. Compd.* 48 (5), 723–727. doi:10.1007/s10600-012-0368-0

Quintieri, L., Palatini, P., Nassi, A., Ruzza, P., and Floreani, M. (2008). Flavonoids Diosmetin and luteolin Inhibit Midazolam metabolism by human liver Microsomes and recombinant CYP 3A4 and CYP3A5 Enzymes. *Biochem. Pharmacol.* 75 (6), 1426–1437. doi:10.1016/j.bcp.2007.11.012

Ren, J., Meng, S., Lekka, C. E., and Kaxiras, E. (2008). Complexation of flavonoids with iron: Structure and optical signatures. *J. Phys. Chem. B* 112 (6), 1845–1850. doi:10.1021/jp076881e

Rice-Evans, C. A., Miller, N. J., and George, P. (1996). Structure-antioxidant activity relationships of flavonoids and phenolic acids. *Free Radic. Biol. Med.* 20 (7), 933–956. doi:10.1016/0891-5849(95)02227-9

Říha, M., Jana, K., Filipský, T., Macáková, K., Rocha, L., Bovicelli, P., et al. (2014). *In vitro* evaluation of copper-chelating properties of flavonoids. *RSC Adv.* 4 (62), 32628–32638. doi:10.1039/c4ra04575k

Rothwell, J. A., Day, A. J., and Morgan, M. R. A. (2005). Experimental determination of octanol-water partition Coefficients of quercetin and related flavonoids. *J. Agric. Food Chem.* 53 (11), 4355–4360. doi:10.1021/jf0483669

Samsonowicz, M., and Regulska, E. (2017). Spectroscopic study of molecular structure, antioxidant activity and biological effects of metal hydroxyflavonol complexes. *Spectrochimica Acta Part A Mol. Biomol. Spectrosc.* 173, 757–771. doi:10.1016/j.saa.2016.10.031

Soma, S., Latimer, A. J., Chun, H., Vicary, A. C., Timbalia, S. A., Boulet, A., et al. (2018). Elesclomol restores mitochondrial function in genetic models of copper deficiency. *Proc. Natl. Acad. Sci. U. S. A.* 115 (32), 8161–8166. doi:10.1073/pnas.1806296115

Sreelakshmi, V., Raj, N., and Abraham, A. (2017). Evaluation of the drug-like properties of kaempferol, Chrysophanol and Emodin and their interactions with EGFR tyrosine Kinase - an *in silico* approach. *Nat. Product. Commun.* 12 (6), 915–920. doi:10.1177/1934578x1701200621

Ulatowski, F., Dabrowa, K., Bałakier, T., and Jurczak, J. (2016). Recognizing the limited applicability of job plots in studying host-guest interactions in supramolecular chemistry. *J. Org. Chem.* 81 (5), 1746–1756. doi:10.1021/acs.joc.5b02909

Weber, G. (1988). HPLC with electrochemical detection of metal-flavonoid-complexes isolated from food. *Chromatographia* 26 (1), 133–138. doi:10.1007/BF02268137

Wu, X., Sinani, D., Kim, H., and Lee, J. (2009). Copper transport activity of yeast Ctr1 is down-regulated via its C terminus in response to excess copper. *J. Biol. Chem.* 284 (7), 4112–4122. doi:10.1074/jbc.M807909200

Xie, J., and Schaich, K. M. (2014). Re-evaluation of the 2, 2-diphenyl-1-picrylhydrazyl free radical (DPPH) assay for antioxidant activity. *J. Agric. Food Chem.* 62 (19), 4251–4260. doi:10.1021/jf500180u

Xu, Y., Yang, J., Lu, Y., Qian, L.-L., Yin Yang, Z., Min Han, R., et al. (2020). Copper(II) coordination and translocation in luteolin and effect on radical scavenging. *J. Phys. Chem. B* 124 (2), 380–388. doi:10.1021/acs.jpcb.9b10531

Yuan, D. S., Stearman, R., Dancis, A., Dunn, T., Beeler, T., Klausner, R. D., et al. (1995). The menkes/wilson disease gene homologue in yeast provides copper to a ceruloplasmin-like oxidase required for iron uptake. *Proc. Natl. Acad. Sci. U. S. A.* 92 (7), 2632–2636. doi:10.1073/pnas.92.7.2632

Zhang, L., Liu, Y., Wang, Y., Xu, M., and Hu, X. (2018). UV–Vis spectroscopy combined with chemometric study on the interactions of three dietary flavonoids with copper ions. *Food Chem.* 263, 208–215. doi:10.1016/j.foodchem.2018.05.009

Zhao, B., Wang, X., Liu, H., Lv, C., and Lu, J. (2020). Structural characterization and antioxidant activity of oligosaccharides from panax ginseng C. A. Meyer. *Int. J. Biol. Macromol.* 150, 737–745. doi:10.1016/j.ijbiomac.2020.02.016

frontiers | Frontiers in Chemistry

TYPE Original Research
PUBLISHED 26 August 2022
DOI 10.3389/fchem.2022.970407

Check for updates

OPEN ACCESS

EDITED BY
Rajni Verma,
The University of Melbourne, Australia

REVIEWED BY
Gayani Pathiraja,
University of North Carolina at Greensboro, United States
Aminul Islam,
Jashore University of Science and Technology, Bangladesh

*CORRESPONDENCE
Jennifer S. Andrew,
jandrew@mse.ufl.edu

SPECIALTY SECTION
This article was submitted to Nanoscience, a section of the journal Frontiers in Chemistry

RECEIVED 15 June 2022
ACCEPTED 22 July 2022
PUBLISHED 26 August 2022

CITATION
Tiwari P, Ferson ND, Arnold DP and Andrew JS (2022), Overcoming the rise in local deposit resistance during electrophoretic deposition via suspension replenishing. *Front. Chem.* 10:970407. doi: 10.3389/fchem.2022.970407

COPYRIGHT
© 2022 Tiwari, Ferson, Arnold and Andrew. This is an open-access article distributed under the terms of the Creative Commons Attribution License (CC BY). The use, distribution or reproduction in other forums is permitted, provided the original author(s) and the copyright owner(s) are credited and that the original publication in this journal is cited, in accordance with accepted academic practice. No use, distribution or reproduction is permitted which does not comply with these terms.

Overcoming the rise in local deposit resistance during electrophoretic deposition *via* suspension replenishing

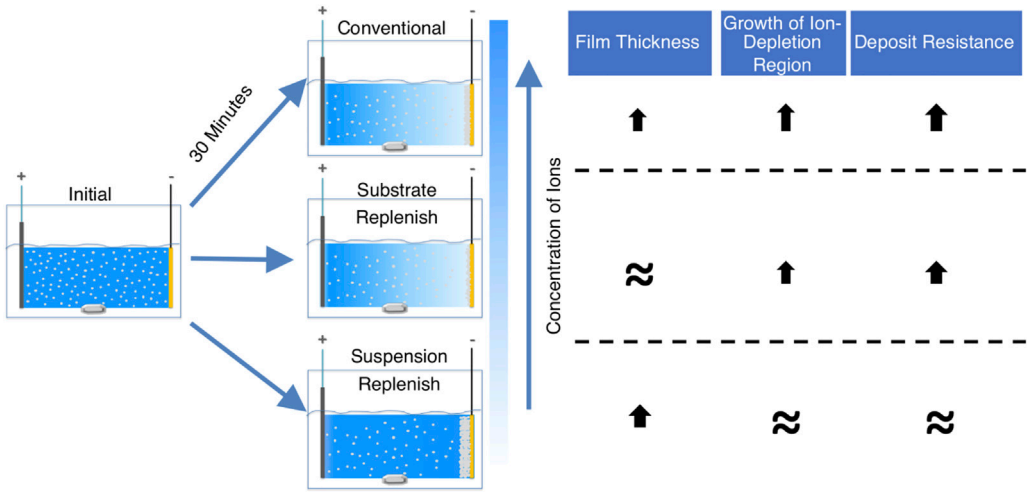
Prabal Tiwari[1], Noah D. Ferson[1], David P. Arnold[2] and Jennifer S. Andrew[1]*

[1]Department of Materials Science and Engineering, University of Florida, Gainesville, FL, United States, [2]Department of Electrical and Computer Engineering, University of Florida, Gainesville, FL, United States

Nanomaterials have unique properties, functionalities, and excellent performance, and as a result have gained significant interest across disciplines and industries. However, currently, there is a lack of techniques that can assemble as-synthesized nanomaterials in a scalable manner. Electrophoretic deposition (EPD) is a promising method for the scalable assembly of colloidally stable nanomaterials into thick films and arrays. In EPD, an electric field is used to assemble charged colloidal particles onto an oppositely charged substrate. However, in constant voltage EPD the deposition rate decreases with increasing deposition time, which has been attributed in part to the fact that the electric field in the suspension decreases with time. This decreasing electric field has been attributed to two probable causes, (i) increased resistance of the particle film and/or (ii) the growth of an ion-depletion region at the substrate. Here, to increase EPD yield and scalability we sought to distinguish between these two effects and found that the growth of the ion-depletion region plays the most significant role in the increase of the deposit resistance. Here, we also demonstrate a method to maintain constant deposit resistance in EPD by periodic replenishing of suspension, thereby improving EPD's scalability.

KEYWORDS

electrophoretic deposition kinetics, colloidal processing, scalable nanomanufacturing, materials assembly, alumina



Graphical Abstract

Highlights

1) Suspension replenishment enables constant deposit resistance with time.
2) Ion-depletion causes a decrease in the electric field during electrophoretic deposition.
3) Film formation plays an insignificant role in increasing deposit resistance.
4) Electric field can be maintained constant *via* ion-replenishing.

1 Introduction

The growth of nanotechnology is contingent upon further advancements in nanomanufacturing technologies (Philp and Fraser Stoddart, 1996; Whitesides and Grzybowski, 2002; Gates et al., 2005; Biswas et al., 2012; Bauer et al., 2018). Nanomanufacturing techniques can be broadly classified into top-down and bottom-up approaches or some combination of the two (Philp and Fraser Stoddart, 1996; Whitesides and Grzybowski, 2002; Gates et al., 2005; Merkel et al., 2010; Biswas et al., 2012; Pascall et al., 2014; Vogel et al., 2015; Jesse et al., 2016; Liu et al., 2016; Isaacoff and Brown, 2017; Fu et al., 2018; Yin et al., 2020). Top-down approaches involve cutting down macro-sized materials into nanomaterials with the help of external stimuli. Some examples of top-down approaches are lithography, molding, and milling. On the other hand, bottom-up approaches involve the assembly of atoms/molecules/colloidal particles into a larger nanostructure driven by interaction forces between them and/or external stimuli. Some examples of bottom-up approaches are atomic layer deposition, sol-gel nanofabrication, self-assembly, vapor deposition, Langmuir-Blodgett assembly, electric-field-assisted assembly, and capillary-force-assisted assembly. Both top-down and bottom-up approaches have benefits and limitations of their own. Top-down approaches have the advantage of precision and repeatability (Biswas et al., 2012; Jesse et al., 2016). However, they suffer from high capital and operating costs, low scalability, and diffraction limits of the electromagnetic wave being used which limits the feature size in lithography (Gates et al., 2005; Merkel et al., 2010; Biswas et al., 2012; Fu et al., 2018). Bottom-up approaches, on the other hand, have the advantage of high scalability, relatively low cost, the ability to fabricate structures upon non-planar substrates, and compatibility with organic materials (Philp and Fraser Stoddart, 1996; Whitesides and Grzybowski, 2002; Biswas et al., 2012; Vogel et al., 2015; Isaacoff and Brown, 2017; Yin et al., 2020). However, bottom-up approaches suffer from limited repeatability and a lack of control over the process. Thus, improvements and innovations in both top-down and bottom-up approaches are required to develop the next generation of nanomanufacturing technologies.

One promising bottom-up technique that is gaining attention in research labs and industry because of its scalability, cost-effectiveness, tunability, simple setup, and versatility in depositing a wide range of materials over many substrate shapes is electrophoretic deposition (EPD) (Besra and Liu, 2007; Dickerson and Boccaccini, 2011; Kalinina and Pikalova, 2019; Sikkema et al., 2020; Atiq Ur Rehman et al., 2021). EPD assembles charged colloidal particles onto an oppositely charged substrate under the application of an externally applied electric field. Due to its advantages, EPD has been used to form 2-D and 3-D assemblies of various classes of materials such as metals, ceramics, organics, and biomaterials onto planar, non-planar, and patterned substrates (Sarkar and Nicholson, 1996; Van der Biest and Vandeperre, 1999; Biest and Vandeperre, 2002; Zhitomirsky, 2002; Sarkar et al., 2004; Besra and Liu, 2007;

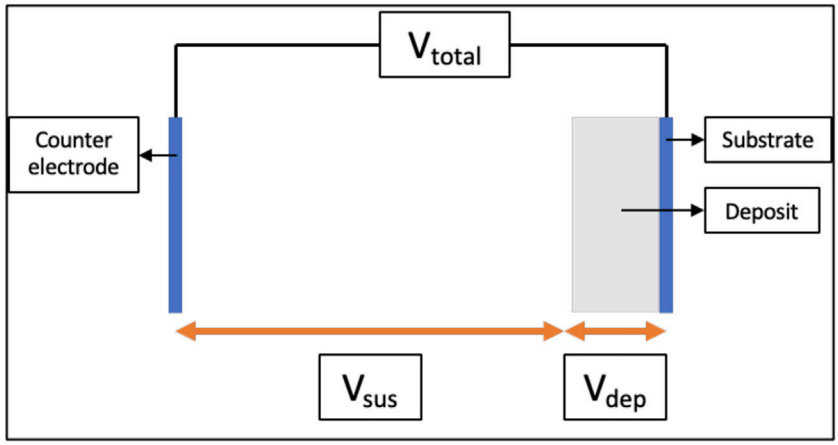


FIGURE 1
Schematic showing voltages across a typical electrophoretic deposition cell used in constant-voltage mode.

Corni et al., 2008; Novak and König, 2009; Boccaccini et al., 2010b, 2010a; Boccaccini and Dickerson, 2013; Chavez-Valdez et al., 2013; Guo et al., 2015; Diba et al., 2016; Ma et al., 2018; Kalinina and Pikalova, 2019; Obregón et al., 2019; Hu et al., 2020; Lim et al., 2021). However, the underlying mechanisms and kinetics of EPD are still not well-understood (Dickerson and Boccaccini, 2011; Fuseini and Zaghloul, 2022).

Although the first-documented observation of electrophoresis was done by the French chemist Gautherot in 1801, it took more than a century before a theoretical framework for the kinetics of EPD were established by Hamaker in 1940 (Hamaker, 1940; Besra and Liu, 2007). According to Hamaker's equation (Equation 1), EPD yield (m) depends on a sticking parameter (*f*) which is the ratio of the number of particles that adhere to the substrate and become part of the deposit to the total number of particles reaching the substrate, particle concentration (C_s), electrophoretic mobility of the particle being deposited (μ), area of the substrate (A), effective electric field in the suspension (E), and time (t):

$$m = fC_s\mu AEt \quad (1)$$

Later it was observed that some of these factors do not necessarily remain constant but can decrease as a function of time, which can lead to a plateau in EPD yield (Sarkar and Nicholson, 1996; Anné et al., 2004; van der Biest et al., 2004; Wang et al., 2004; Stappers et al., 2008; Ferrari and Moreno, 2010). The particle concentration in the suspension decreases as particles deposit on the substrate, or as they settle out of the suspension. The electrophoretic mobility of the particles has also been shown to decrease during EPD due to a shift in the pH of the suspension (Kershner et al., 2004; Tiwari et al., 2020). Finally, the effective electric field in the suspension has been observed to decrease in the suspension during constant-voltage EPD (Zhang et al., 1994; Sarkar and Nicholson, 1996). The factors responsible for causing a decrease in particle concentration and particle electrophoretic mobility are well-understood and can be controlled (Sarkar and Nicholson, 1996; Besra and Liu, 2007; Tiwari et al., 2020). However, there is currently no consensus on the factor(s) that cause the decrease in electric field in the suspension (De and Nicholson, 2004; Kershner et al., 2004; Besra et al., 2010; Mishra et al., 2010; MISHRA et al., 2013; Tiwari et al., 2020).

In constant-voltage EPD, the total applied voltage difference (V_{total}) between the substrate and the counter-electrode is maintained constant using a power supply as shown with the help of a schematic in Figure 1. The V_{total} in the EPD cell is distributed as the sum of the voltage drop across the suspension (V_{sus}) and the voltage drop across the deposit (V_{dep}). The corresponding electric fields in the suspension (E_{sus}) and the deposit (E_{dep}) are not necessarily the same, or constant with time. In current literature, an increase in V_{dep} and corresponding E_{dep} with time has been observed (Sarkar and Nicholson, 1996; Negishi et al., 2005; van Tassel and Randall, 2006b; Stappers et al., 2008). This increase in V_{dep} was widely attributed to the rise in local deposit resistance (R_{dep}) during EPD, which will be discussed in-depth in the next section. Consequently, there is a decrease in V_{sus}, and in the corresponding E_{sus} (Negishi et al., 2004, 2005). Therefore, to understand and be able to better control the electric field on the deposit as well in the suspension, it is vital to understand the root cause behind the rise in local deposit resistance as a function of time.

There have been different explanations put forward to justify the increase in local deposit resistance during EPD (Boccaccini and Dickerson, 2013). Some researchers suggested that the increase in deposit resistance is caused because the thickness of the deposit is increasing with time (Sarkar and Nicholson,

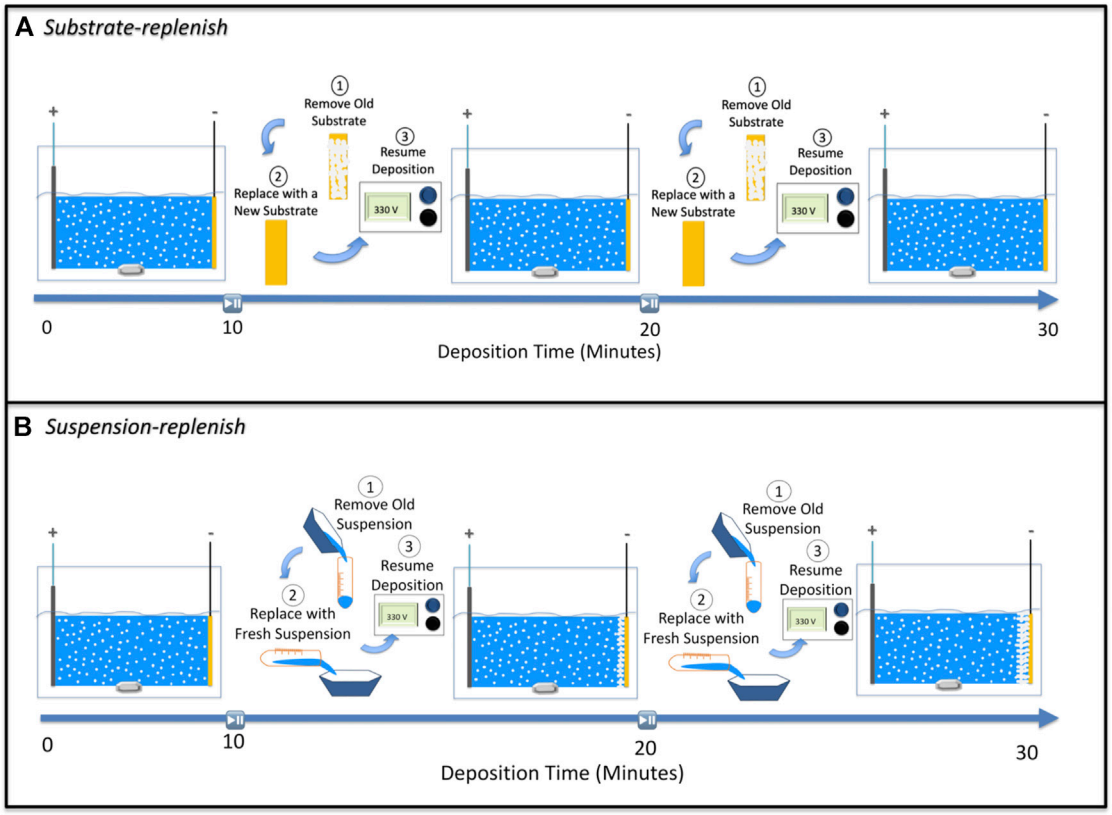


FIGURE 2
Schematic showing steps involved in **(A)** substrate-replenish electrophoretic deposition and **(B)** suspension-replenish electrophoretic deposition.

1996). The hypothesis for this justification is that the resistivity of the deposit is higher than that of the suspension, and hence, an increase in deposit thickness leads to an increase in deposit resistance (Sarkar and Nicholson, 1996). However, further studies contradicted this claim by showing that the resistance of the deposit remains the same before and after the deposition, suggesting there must be another factor causing the rise in deposit resistance during EPD (Argirusis et al., 2006; Stappers et al., 2008; Schneider et al., 2010).

Further theoretical and experimental studies pointed to the electrochemical consumption of ions on the deposit electrode as the reason for the rise in deposit resistance during EPD (van Tassel and Randall, 2006b; Stappers et al., 2008; Hu et al., 2019). In a series of papers, Tassel et al. put forward a theory to explain the formation and stabilization of an 'ion-depleted conduction region' on the deposit electrode during constant-current EPD (De and Nicholson, 2004; van Tassel and Randall, 2006a, 2006b, 2007a, 2007b, 2007c). They showed that during EPD, a high resistivity 'ion-depleted conduction region' forms and grows due to the consumption of ions on the deposit electrode. In a typical electrochemical cell, this region will not be stable because of the immediate onset of convection currents that supply ions to this region. However, they argued that in an EPD cell, this region is stabilized against convection due to the buffering action of particles i.e., adsorption/desorption equilibria of ions from the particle surface present in the ion-depleted region. Thus, this region is confined to the deposited particle layer. The conduction of ionic current through this high resistivity 'ion-depleted conduction region' can proceed even above the equilibrium limit current and leads to a very high R_{dep} and E_{dep}. On the other hand, in constant-voltage EPD, the electrochemical consumption of ions on the deposit electrode will also lead to the formation and growth of a stable ion-depleted conduction region. The only difference is that the current cannot exceed the equilibrium limit current in constant-voltage EPD. To study the role of the ion-depleted region on deposit resistance during constant-voltage EPD, Stappers et al. measured the deposit impedance as a function of time in a constant-voltage EPD *via* impedance spectroscopy (Stappers et al., 2008). They reported that the deposit impedance increases as deposition proceeds but returned to the original value after the deposition was stopped. Moreover, when they paused the

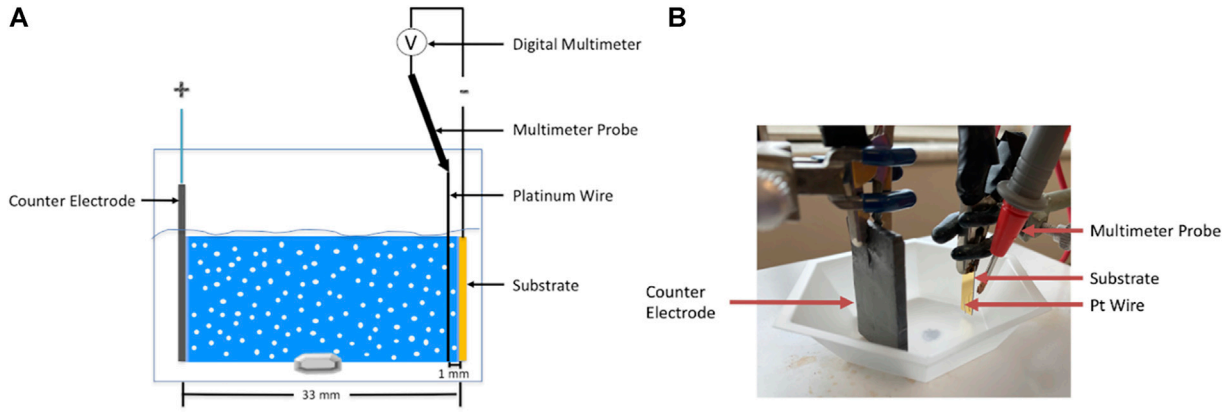


FIGURE 3
(A) Schematic and **(B)** the corresponding photograph of the electrophoretic deposition setup.

deposition and replaced the particle suspension with the supernatant solution (without particles) and then resumed the deposition, the deposit impedance continued to increase. These two observations suggest that the deposit impedance is a function of the electrochemical depletion of ions on the deposit electrode rather than the growth of high-resistivity particle film. However, they were unable to maintain a constant deposit impedance and hence constant electric field, likely because they are merely recirculating the suspension from a reservoir where the ionic concentration was being depleted with time.

We hypothesized that instead of recirculating the suspension as per the study by Stappers et al., replenishing the suspension using a suspension-replenish EPD approach (Figure 2B) it would be possible to hinder the growth of the ion-depletion region and maintain constant deposit resistance as it will keep the ionic concentration constant during EPD. To confirm our hypothesis, in this study, we isolated and compared the individual effects of the growing deposit and the growing ion-depletion region on the increase in deposit resistance during constant-voltage EPD of alumina particles. We accomplished this by developing two modified EPD approaches (details provided in the experimental section), where either the substrate (along with the deposited film) or the suspension was replenished (Figure 2). Substrate-replenish EPD (Figure 2A) allowed us to periodically restart the growth of the deposit onto a fresh substrate while allowing the ion-depletion region to grow unhindered. On the other hand, suspension-replenish EPD (Figure 2B) allowed us to periodically restart the growth of the ion-depletion region by replenishing the ions and particles in the suspension while letting the deposit grow unhindered. We found that the growth of the ion-depletion region and not the deposit growth causes the increase in deposit resistance. We also found that the deposit resistance remained nearly constant during the suspension-replenish EPD. Thus, confirming our hypothesis that the growth of the ion-depletion region can be hindered, and deposit resistance can be kept constant *via* replenishment of ions using suspension-replenish EPD, which then helps maintain a near-constant electric field in the suspension.

For future work, improvements to suspension-replenish EPD can be achieved using a continuous-flow setup with automatic adjustments based on a live feedback mechanism to maintain constant particle concentration, pH, and conductivity in the EPD cell. Moreover, when measuring the electric field during EPD, one must be aware that the presence of the mulitmeter probe has the potential to impact the experiment. To overcome these challenges, computational tools can be utilized. Simulations of EPD experiments at varying scales will further help us visualize and understand the local and bulk electrochemical changes occurring during EPD.

2 Experimental details

2.1 Suspension preparation and characterization

α-alumina nanoparticles (> 99% purity, 80 nm diameter, 3.97 g/cm^3 density) were purchased from US Research Nanomaterials, Inc., USA. A positively charged suspension of 0.25 volume % α-alumina nanoparticles was prepared in ethanol (200 proof ethanol, Acros Organics) by using hydrochloric acid (Technical HCl, Fischer Chemical) as the dispersing agent. The suspension was sonicated using an ultrasonicator (Branson SFX 550 probe ultra-sonicator). Effective pH (pHe) measurements were made using the ASTM D6423-19 standard protocol using a Thermo Scientific 5107 BNMD No-Cal pH/Automated Temperature Compensation combination electrode connected to a Thermo Scientific Orion Star A111 bench-top pH meter

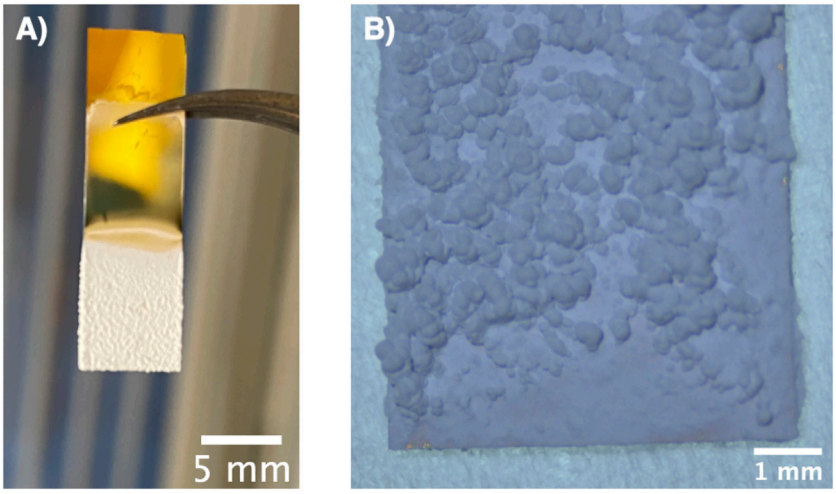


FIGURE 4
(A) Photograph and **(B)** optical micrograph of a typical α-alumina nanoparticles film deposited *via* electrophoretic deposition.

(Fuel and Engines, 1999). pHe measurements were recorded after 30 s of immersion in a stirred suspension. A Malvern Panalytical Zetasizer was used to measure the electrophoretic mobility and zeta potential of the nanoparticles in suspension. The Hückel model was used to calculate the zeta potential from particle mobility (Hunter, 2001). The suspension, with a pHe of 1.70 +/- 0.04 obtained by mixing 0.4 ml of 0.02 M HCL in ethanol solution with 19.6 ml of ethanol having particle mobility and zeta potential of 0.74 +/- 0.07 μm cm/V.s and 53.90 +/- 4.79 mV respectively, was used as the starting suspension for all depositions.

2.2 Electrophoretic depositions

Figure 3 shows a schematic and a corresponding photograph of the electrophoretic deposition setup that was used to perform the deposition of alumina nanoparticles using an applied electric field of 100 V/cm. Here, a hexagonal weighing boat was used to contain 20 ml of suspension. A magnetic stir rod and plate were used to stir the suspension during deposition. The electric field was applied by connecting a counter electrode (graphite) and a substrate placed 33 mm apart in the suspension to the positive and negative terminals of the power supply, respectively. To fabricate the substrate, a 10 nm titanium adhesion layer was sputtered onto a 100 4-inch prime-grade silicon wafer followed by sputtering of 100 nm gold layer using a KJL CMS-18 sputtering instrument. The wafer was then diced into 6 mm (width) × 20 mm (height) substrates using an ADT 7100 dicing saw. To image the EPD films, a cross-section of the film was prepared using an FEI Helios Nanolab 600 dual-beam focused ion beam (FIB)/Scanning Electron Microscope (SEM) using methods described elsewhere (Langford and Petford-Long, 2001). Imaging of the cross-section was performed using the same instrument; the cross-section was tilted 45° relative to the electron beam and dynamic focus was used to keep the entire cross-section in focus.

2.2.1 Substrate replenish electrophoretic deposition

In this substrate replenish EPD approach, we ran 30-min depositions starting with a fresh suspension of alumina nanoparticles at 100 V/cm while pausing the deposition at 10-min and 20-min time points to remove the substrate covered with deposit and to introduce a fresh substrate (without any deposit). The old suspension was collected in a centrifuge tube whilst the substrate is being replenished. After the substrate was replaced, the old suspension was reintroduced into the EPD boat followed by resumption of deposition (Figure 2A).

2.2.2 Suspension replenish electrophoretic deposition

In this suspension replenish EPD approach, we performed 30-min depositions starting with a fresh suspension of alumina nanoparticles at 100 V/cm while pausing the deposition at 10-min and 20-min time points to remove the old suspension and introduce a fresh suspension followed by resumption of the deposition (Figure 2B).

2.3 Deposit resistance measurement

The deposit resistance was calculated *via* Ohm's law using the voltage difference measured between the substrate (deposit

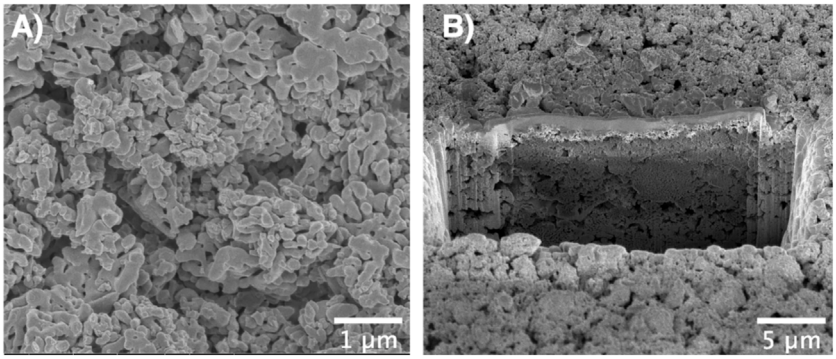


FIGURE 5
(A) Top-view SEM image and **(B)** Cross-sectional SEM image of the film prepared *via* FIB showing the porous structure of the EPD film.

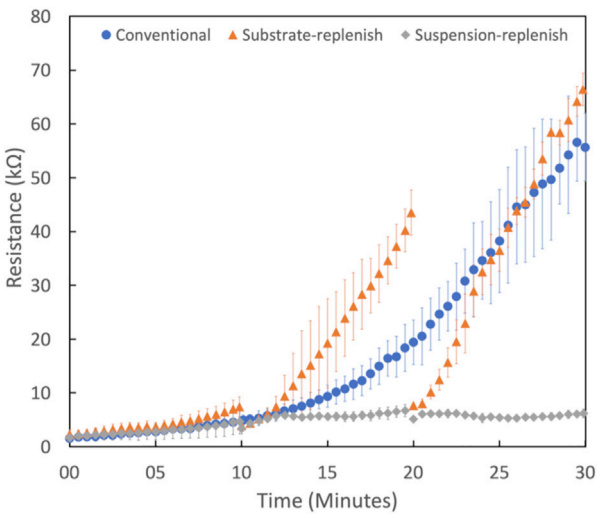


FIGURE 6
Deposit resistance as a function of time for conventional electrophoretic deposition (●) substrate-replenish electrophoretic deposition (▲) suspension-replenish electrophoretic deposition (◆) of alumina nanoparticles performed at 100 V/cm in constant-voltage mode. For each type of deposition, three replicate runs were performed to calculate the average and SD in deposit resistance plotted here.

electrode) and a Pt wire (0.1 mm diameter) submerged at a distance of 1 mm parallel to the center of the substrate and the current value that was recorded from the power supply. A Siglent SDM 3055 digital multimeter and multimeter probe were used to measure the voltage difference as shown with the help of a schematic in Figure 3. The Pt wire was electrically connected to the multimeter probe with copper (Cu) tape. A distance of 1 mm was chosen as it allowed us to keep the Pt wire as close to the substrate as possible without disrupting the film growth since our films did not grow thicker than 1 mm. The voltage readings were automatically recorded using the Easy DMM software (Siglent).

3 Results and discussion

3.1 Deposit resistance during conventional electrophoretic deposition

Figure 4 shows a photograph and an optical micrograph of a typical film obtained *via* electrophoretic deposition of α-alumina nanoparticles. Here, full coverage of the submerged part of the substrate with the particles is seen. The porous structure of the films is evident from the SEM images of the top view (Figure 5A) as well as the cross-sectional view (Figure 5B) of the film. Due to edge effects i.e., the concentration of electric field on the substrate edges, the film thickness was highest at the edges as evident in Figure 4A (Pascall et al., 2013). It was also observed that the film roughness increased with time, which could be attributed to the decreasing stability of the suspension as the pHe of the suspension shifts towards the isoelectric point of alumina with time (Tiwari et al., 2020). The decrease in suspension stability leads to the agglomeration of particles in the suspension, which these agglomerates then deposit onto the substrate and increase film roughness Joung and Buie, 2011.

To measure how the deposit resistance changes during conventional electrophoretic deposition, we performed 30-min depositions of the positively charged alumina nanoparticles with an applied electric field of 100 V/cm. Figure 6 shows that the deposit resistance increases exponentially during conventional EPD. This increase can be attributed to the growing thickness of the film of deposited alumina nanoparticles since it has a higher resistivity than the suspension it is replacing (Sarkar and Nicholson, 1996). Secondly, it could be caused due to the formation and growth of a high resistivity ion-depletion region on the substrate. This region is formed because of the depletion of H_3O^+ or H_2EtO^+ ions as they

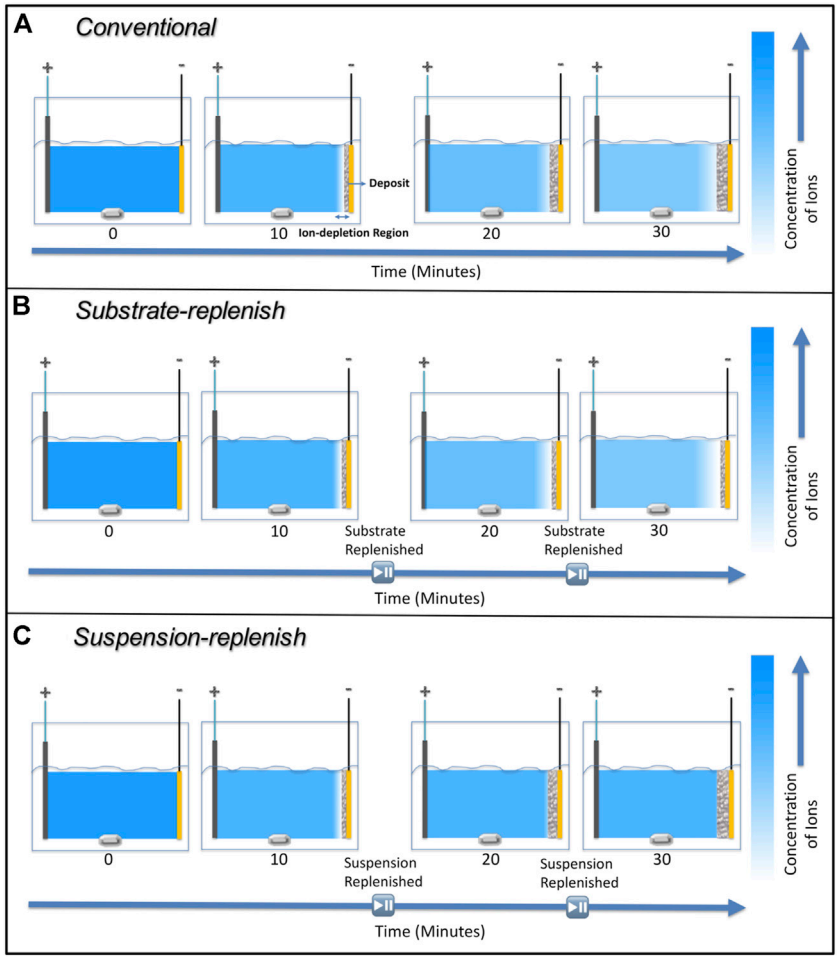


FIGURE 7
Schematic showing the ion-depletion region and deposit growth on the substrate during **(A)** conventional electrophoretic deposition, **(B)** substrate-replenish electrophoretic deposition, and **(C)** suspension-replenish electrophoretic deposition.

undergo electrochemical reactions to form H_2 gas on the substrate (De and Nicholson, 2004; van Tassel and Randall, 2007a). This region is not present on the counter electrode because the primary reactions there result in the generation of ions (H_2EtO^+ or H_3O^+) while the depletion of Cl^- ions as they undergo electrochemical conversion into Cl_2 is negligible (van Tassel and Randall, 2007b). Therefore, both deposit and ion-depletion regions grow unhindered for the entire duration of the deposition in conventional EPD as shown with the help of a schematic in Figure 7A.

3.2 Deposit resistance during substrate-replenish electrophoretic deposition

To isolate the effect of the ion-depletion region growth on the deposit resistance, we performed substrate-replenish EPD (Figure 2A). In this modified EPD approach, we ran 30-min depositions starting with a fresh suspension of alumina nanoparticles at 100 V/cm while pausing the deposition at 10-min and 20-min time points to remove the substrate and introduce a fresh substrate followed by resumption of the deposition. Here, the ion-depletion region is growing for the entire 30-min duration of the experiment, while the deposit growth is restarted every 10 min *via* substrate-replenishment, shown schematically in Figure 7B. Figure 6 shows that the deposit resistance in substrate-replenish EPD increases exponentially from 0 to 10 min and then drops sharply to nearly the original value at 10 min, followed by an exponential rise from 10 to 20 min and drop to nearly the original value at 20 min, and finally an exponential rise from 20 to 30 min. The increase in deposit resistance during substrate-replenish EPD is quite similar to that in conventional EPD (Figure 6) suggesting that the deposit resistance is mainly a function of the ion-depletion region growth.

Note, that there are two minor differences between the deposit resistance increase in conventional and substrate-replenish EPD.

First, the rate of the exponential rise in deposit resistance from 10 to 30 min in substrate-replenish EPD is greater than that in conventional EPD, which we attributed to the faster electrochemical depletion of ions in the substrate replenish EPD because of the greater conductive surface area provided by periodic replacement of substrate covered by deposit film with fresh substrates having no deposit on them to begin with. Secondly, the return of deposit resistance deposit to the baseline resistance at 10- and 20-min time-points is attributed to the temporary removal of the ion-depletion region as the suspension is homogenized upon collection in the centrifuge tube.

3.3 Deposit resistance during suspension-replenish electrophoretic deposition

Finally, to isolate the effect of the growing deposit on the deposit resistance, we performed suspension-replenish EPD (Figure 2B). In this modified EPD approach, we ran 30-min depositions starting with a fresh suspension of alumina nanoparticles at 100 V/cm while pausing the deposition at 10-min and 20-min time points to remove the old suspension and introduce a fresh suspension followed by resumption of the deposition. In this approach, the deposit is growing for the entire 30 min while the ion-depletion region growth is restarted every 10 min with suspension-replenishment as shown with the help of a schematic in Figure 7C. Figure 6 shows that in suspension-replenish EPD, deposit resistance remains nearly constant with time relative to the conventional and substrate-replenish EPD. These results further confirm that the deposit resistance is primarily a function of the growth of the ion-depletion region and not due to the deposit growth. This also proves our hypothesis that the deposit resistance increase can be mitigated by minimizing the growth of the ion-depletion region *via* the replenishment of ions.

In summary, deposit resistance increases by a factor of only 3.7x during suspension-replenish EPD compared to 36x and 29x in conventional and substrate-replenish EPD, respectively. Therefore, it can be concluded that the growth of the ion-depletion region and not the deposit growth is the main driver for the increase in deposit resistance during EPD in agreement with recent studies (Argirusis et al., 2006; Stappers et al., 2008; Schneider et al., 2010). This also confirms our hypothesis that the deposit resistance and hence electric field can be maintained nearly constant by hindering the growth of the ion-depletion region *via* ion replenishment using a novel suspension replenish EPD approach which can help improve EPD yield.

4 Conclusion

In this work, we isolated the individual effects of the growth of the ion-depletion region and deposit growth on the local deposit resistance increase during electrophoretic deposition. We found that the main cause for the increase in deposit resistance is the ion-depletion region which forms and grows due to the electrochemical depletion of ions on the substrate. On the other hand, the effect of deposit growth on the increase in deposit resistance was found to be minimal. We also showed that deposit resistance, which is known to be the cause behind the decrease in electric field in the suspension during constant-voltage EPD can be maintained nearly constant *via* ion-replenishment using a new suspension-replenish EPD. While in Stappers et al.'s study, deposit resistance increased with time, which is most likely due to the fact they were recirculating instead of replenishing the suspension (Stappers et al., 2008). Thus, by using a suspension replenish approach the electric field in the suspension can be maintained constant improving EPD yield. Thereby, enabling a route to manufacture nanomaterials-based products and devices in an efficient and scalable manner.

Data availability statement

The original contributions presented in the study are included in the article/supplementary material, further inquiries can be directed to the corresponding author.

Author contributions

PT, carried out the majority of the experiments outlined in the manuscript, NF also contributed to the experimental efforts. PT, DA, and JA conceived of the ideas, and JA was in charge of overall planning. PT drafted the manuscript with support from NF, DA, and JA.

Acknowledgments

We would like to acknowledge the National Science Foundation for providing the funds for this work through the Scalable Nanomanufacturing Program, Award No. CMMI-1727930. We would also like to acknowledge the Research Service Center at the University of Florida for providing the characterization facility and tools, and Dr. Nicholas Rudawski for helping with the preparation of the cross-section of our deposit using Focused-Ion Beam (FIB) and subsequent imaging using Scanning Electron Microscope (SEM).

Conflict of interest

The authors declare that the research was conducted in the absence of any commercial or financial relationships that could be construed as a potential conflict of interest.

Publisher's note

All claims expressed in this article are solely those of the authors and do not necessarily represent those of their affiliated organizations, or those of the publisher, the editors and the reviewers. Any product that may be evaluated in this article, or claim that may be made by its manufacturer, is not guaranteed or endorsed by the publisher.

References

Anné, G., Vanmeensel, K., Vleugels, J., and van der Biest, O. (2004). Influence of the suspension composition on the electric field and deposition rate during electrophoretic deposition. *Colloids Surfaces A Physicochem. Eng. Aspects* 245, 35–39. doi:10.1016/j.colsurfa.2004.07.001

Argirusis, C., Damjanović, T., and Schneider, O. (2006). An impedance study of the electrophoretic deposition from yttrium silicate suspensions. *J. Mat. Sci.* 41, 8059–8067. doi:10.1007/s10853-006-0417-9

Atiq Ur Rehman, M., Chen, Q., Braem, A., Shaffer, M. S. P., and Boccaccini, A. R. (2021). Electrophoretic deposition of carbon nanotubes: recent progress and remaining challenges. *Int. Mater. Rev.* 66, 533–562. doi:10.1080/09506608.2020.1831299

Bauer, M. J., Wen, X., Tiwari, P., Arnold, D. P., and Andrew, J. S. (2018). Magnetic field sensors using arrays of electrospun magnetoelectric Janus nanowires. *Microsyst. Nanoeng.* 4, 37. doi:10.1038/s41378-018-0038-x

Besra, L., and Liu, M. (2007). A review on fundamentals and applications of electrophoretic deposition (EPD). *Prog. Mat. Sci.* 52, 1–61. doi:10.1016/j.pmatsci.2006.07.001

Besra, L., Uchikoshi, T., Suzuki, T. S., and Sakka, Y. (2010). Experimental verification of pH localization mechanism of particle consolidation at the electrode/solution interface and its application to pulsed DC electrophoretic deposition (EPD). *J. Eur. Ceram. Soc.* 30, 1187–1193. doi:10.1016/j.jeurceramsoc.2009.07.004

Biest, O. O. Van Der, and Vandeperre, L. J. (2002). Electrophoretic deposition. *Membr. Technol.* 2002, 13. doi:10.1016/S0958-2118(02)80166-5

Biswas, A., Bayer, I. S., Biris, A. S., Wang, T., Dervishi, E., and Faupel, F. (2012). Advances in top-down and bottom-up surface nanofabrication: techniques, applications & future prospects. *Adv. Colloid Interface Sci.* 170, 2–27. doi:10.1016/j.cis.2011.11.001

Boccaccini, A. R., Cho, J., Subhani, T., Kaya, C., and Kaya, F. (2010a). Electrophoretic deposition of carbon nanotube-ceramic nanocomposites. *J. Eur. Ceram. Soc.* 30, 1115–1129. doi:10.1016/j.jeurceramsoc.2009.03.016

Boccaccini, A. R., and Dickerson, J. H. (2013). Electrophoretic deposition: fundamentals and applications. *J. Phys. Chem. B* 117, 1501. doi:10.1021/jp211212y

Boccaccini, A. R., Keim, S., Ma, R., Li, Y., and Zhitomirsky, I. (2010b). Electrophoretic deposition of biomaterials. *J. R. Soc. Interface* 7, S581–S613. doi:10.1098/rsif.2010.0156.focus

Chavez-Valdez, A., Shaffer, M. S. P., and Boccaccini, A. R. (2013). Applications of graphene electrophoretic deposition. A review. *J. Phys. Chem. B* 117, 1502–1515. doi:10.1021/jp3064917

Corni, I., Ryan, M. P., and Boccaccini, A. R. (2008). Electrophoretic deposition: From traditional ceramics to nanotechnology. *J. Eur. Ceram. Soc.* 28, 1353–1367. doi:10.1016/j.jeurceramsoc.2007.12.011

De, D., and Nicholson, P. S. (2004). Role of ionic depletion in deposition during electrophoretic deposition. *J. Am. Ceram. Soc.* 82, 3031–3036. doi:10.1111/j.1151-2916.1999.tb02198.x

Diba, M., Fam, D. W. H., Boccaccini, A. R., and Shaffer, M. S. P. (2016). Electrophoretic deposition of graphene-related materials: A review of the fundamentals. *Prog. Mater. Sci.* 82, 83–117. doi:10.1016/j.pmatsci.2016.03.002

Dickerson, J. H., and Boccaccini, A. R. (2011). *Electrophoretic deposition of nanomaterials*. Germany: Springer.

Ferrari, B., and Moreno, R. (2010). EPD kinetics: A review. *J. Eur. Ceram. Soc.* 30, 1069–1078. doi:10.1016/j.jeurceramsoc.2009.08.022

Fu, X., Cai, J., Zhang, X., Li, W. di, Ge, H., and Hu, Y. (2018). Top-down fabrication of shape-controlled, monodisperse nanoparticles for biomedical applications. *Adv. Drug Deliv. Rev.* 132, 169–187. doi:10.1016/j.addr.2018.07.006

Fuel, E., and Engines, A. S. (1999). Standard test method for determination of pHe of ethanol , denatured fuel ethanol , and fuel ethanol (ASTM D6423 – 14). *Readings*, 4–6. doi:10.1520/D6423-14.2

Fuseini, M., and Zaghloul, M. M. Y. (2022). Statistical and qualitative analyses of the kinetic models using electrophoretic deposition of polyaniline. *J. Industrial Eng. Chem.* 113, 475–487. doi:10.1016/j.jiec.2022.06.023

Gates, B. D., Xu, Q., Stewart, M., Ryan, D., Willson, C. G., and Whitesides, G. M. (2005). New approaches to nanofabrication: Molding, printing, and other techniques. *Chem. Rev.* 105, 1171–1196. doi:10.1021/cr0300760

Guo, X., Li, X., Li, H., Zhang, D., Lai, C., and Li, W. (2015). A comprehensive investigation on the electrophoretic deposition (EPD) of Nano-Al/Ni energetic composite coatings for the combustion application. *Surf. Coatings Technol.* 265, 83–91. doi:10.1016/j.surfcoat.2015.01.056

Hamaker, H. C. (1940). Formation of a deposit by electrophoresis. *Trans. Faraday Soc.* 35, 279–287. doi:10.1039/tf9403500279

Hu, S., Li, W., Finklea, H., and Liu, X. (2020). A review of electrophoretic deposition of metal oxides and its application in solid oxide fuel cells. *Adv. Colloid Interface Sci.* 276, 102102. doi:10.1016/j.cis.2020.102102

Hu, S., Li, W. W., Li, W. W., Zhang, N., Qi, H., Finklea, H., et al. (2019). A study on the electrophoretic deposition of gadolinium doped ceria on polypyrrole coated yttrium stabilized zirconia. *J. Colloid Interface Sci.* 555, 115–123. doi:10.1016/j.jcis.2019.07.094

Hunter, R. J. (2001). *Foundations of colloid science*. United Kingdom: Oxford University Press.

Isaacoff, B. P., and Brown, K. A. (2017). Progress in top-down control of bottom-up assembly. *Nano Lett.* 17, 6508–6510. doi:10.1021/acs.nanolett.7b04479

Jesse, S., Borisevich, A. Y., Fowlkes, J. D., Lupini, A. R., Rack, P. D., Unocic, R. R., et al. (2016). Directing matter: Toward atomic-scale 3D nanofabrication. *ACS Nano* 10, 5600–5618. doi:10.1021/acsnano.6b02489

Joung, Y. S., and Buie, C. R. (2011). Electrophoretic deposition of unstable colloidal suspensions for superhydrophobic surfaces. *Langmuir* 27, 4156–4163. doi:10.1021/la200286t

Kalinina, E. G., and Pikalova, E. Y. (2019). New trends in the development of electrophoretic deposition method in the solid oxide fuel cell technology: Theoretical approaches, experimental solutions and development prospects. *Russ. Chem. Rev.* 88, 1179–1219. doi:10.1070/rcr4889

Kershner, R. J., Bullard, J. W., and Cima, M. J. (2004). The role of electrochemical reactions during electrophoretic particle deposition. *J. Colloid Interface Sci.* 278, 146–154. doi:10.1016/j.jcis.2004.05.017

Langford, R. M., and Petford-Long, A. K. (2001). Preparation of transmission electron microscopy cross-section specimens using focused ion beam milling. *J. Vac. Sci. Technol. A Vac. Surfaces, Films* 19, 2186–2193. doi:10.1116/1.1378072

Lim, D., Noh, S., and Song, Y. (2021). Programmable nanoparticle patterning by droplet electrophoretic deposition. *J. Mater. Res. Technol.* 14, 3150–3160. doi:10.1016/j.jmrt.2021.08.068

Liu, N., Wang, F., Liu, L., Yu, H., Xie, S., Wang, J., et al. (2016). Rapidly patterning micro/nano devices by directly assembling ions and nanomaterials. *Sci. Rep.* 6, 32106–32110. doi:10.1038/srep32106

Ma, Y., Han, J., Wang, M., Chen, X., and Jia, S. (2018). Electrophoretic deposition of graphene-based materials: A review of materials and their applications. *J. Materiomics* 4, 108–120. doi:10.1016/j.jmat.2018.02.004

Merkel, T. J., Herlihy, K. P., Nunes, J., Orgel, R. M., Rolland, J. P., and Desimone, J. M. (2010). Scalable, shape-specific, top-down fabrication methods for the synthesis of engineered colloidal particles. *Langmuir* 26, 13086–13096. doi:10.1021/la903890h

Mishra, M., Bhattacharjee, S., Besra, L., Sharma, H. S., Uchikoshi, T., and Sakka, Y. (2010). Effect of pH localization on microstructure evolution of deposits during aqueous electrophoretic deposition (EPD). *J. Eur. Ceram. Soc.* 30, 2467–2473. doi:10.1016/j.jeurceramsoc.2010.04.034

Mishra, M., Sakka, Y., Uchikoshi, T., and Besra, L. (2013). pH localization: a case study during electrophoretic deposition of ternary MAX phase carbide-Ti3SiC2. *J. Ceram. Soc. Jpn.* 121, 348–354. doi:10.2109/jcersj2.121.348

Negishi, H., Yamaji, K., Imura, T., Kitamoto, D., Ikegami, T., and Yanagishita, H. (2005). Electrophoretic deposition mechanism of YSZ/n-Propanol suspension. *J. Electrochem. Soc.* 152, J16. doi:10.1149/1.1845301

Negishi, H., Yamaji, K., Sakai, N., Horita, T., Yanagishita, H., and Yokokawa, H. (2004). Electrophoretic deposition of YSZ powders for solid oxide fuel cells. *J. Mater. Sci.* 39, 833–838. doi:10.1023/B:JMSC.0000012911.86185.13

Novak, S., and König, K. (2009). Fabrication of alumina parts by electrophoretic deposition from ethanol and aqueous suspensions. *Ceram. Int.* 35, 2823–2829. doi:10.1016/j.ceramint.2009.03.033

Obregón, S., Amor, G., and Vázquez, A. (2019). Electrophoretic deposition of photocatalytic materials. *Adv. Colloid Interface Sci.* 269, 236–255. doi:10.1016/j.cis.2019.05.003

Pascall, A. J., Qian, F., Wang, G., Worsley, M. A., Li, Y., and Kuntz, J. D. (2014). Light-directed electrophoretic deposition: A new additive manufacturing technique for arbitrarily patterned 3D composites. *Adv. Mat.* 26, 2252–2256. doi:10.1002/adma.201304953

Pascall, A. J., Sullivan, K. T., and Kuntz, J. D. (2013). Morphology of electrophoretically deposited films on electrode strips. *J. Phys. Chem. B* 117, 1702–1707. doi:10.1021/jp306447n

Philp, D., and Fraser Stoddart, J. (1996). Self-Assembly in natural and unnatural systems. *Angew. Chem. Int. Ed. Engl.* 35, 1154–1196. doi:10.1002/anie.199611541

Sarkar, P., De, D., and Rho, H. (2004). Synthesis and microstructural manipulation of ceramics by electrophoretic deposition. *J. Mater. Sci.* 39, 819–823. doi:10.1023/B:JMSC.0000012909.46419.0e

Sarkar, P., and Nicholson, P. S. (1996). Electrophoretic deposition (EPD): Mechanisms, kinetics, and application to ceramics. *J. Am. Ceram. Soc.* 79, 1987–2002. doi:10.1111/j.1151-2916.1996.tb08929.x

Schneider, O., Große-Brauckmann, J., and Argirusis, C. (2010). Impedance study of the electrophoretic deposition of yttrium silicate from a polymeric precursor sol. *J. Eur. Ceram. Soc.* 30, 1089–1096. doi:10.1016/j.jeurceramsoc.2009.07.020

Sikkema, R., Baker, K., and Zhitomirsky, I. (2020). Electrophoretic deposition of polymers and proteins for biomedical applications. *Adv. Colloid Interface Sci.* 284, 102272. doi:10.1016/j.cis.2020.102272

Stappers, L., Zhang, L., van der Biest, O., and Fransaer, J. (2008). The effect of electrolyte conductivity on electrophoretic deposition. *J. Colloid Interface Sci.* 328, 436–446. doi:10.1016/j.jcis.2008.09.022

Tiwari, P., Ferson, N. D., and Andrew, J. S. (2020). Elucidating the role of electrophoretic mobility for increasing yield in the electrophoretic deposition of nanomaterials. *J. Colloid Interface Sci.* 570, 109–115. doi:10.1016/j.jcis.2020.02.103

Van der Biest, O. O., and Vandeperre, L. J. (1999). Electrophoretic deposition of materials. *Annu. Rev. Mat. Sci.* 29, 327–352. doi:10.1146/annurev.matsci.29.1.327

van der Biest, O., Put, S., Anné, G., and Vleugels, J. (2004). Electrophoretic deposition for coatings and free standing objects. *J. Mater. Sci.* 39, 779–785. doi:10.1023/B:JMSC.0000012905.62256.39

van Tassel, J. J., and Randall, C. A. (2007a). Ionic gradients at an electrode above the equilibrium limit current. 1. Concentration and charge gradients in an immobile electrolyte. *J. Phys. Chem. C* 111, 3341–3348. doi:10.1021/jp064804y

van Tassel, J. J., and Randall, C. A. (2007b). Ionic gradients at an electrode above the equilibrium limit current. 2. Transition to convection. *J. Phys. Chem. C* 111, 3349–3357. doi:10.1021/jp064805q

van Tassel, J. J., and Randall, C. A. (2007c). Ionic gradients at an electrode above the equilibrium limit current. 3. Stabilization of ion depleted conduction by a nanoporous alumina layer during electrophoretic deposition. *J. Phys. Chem. C* 111, 3358–3365. doi:10.1021/jp064807a

van Tassel, J. J., and Randall, C. A. (2006a). Mechanisms of electrophoretic deposition. *Key Eng. Mater.* 314, 167–174. doi:10.4028/0-87849-998-9.167

van Tassel, J. J., and Randall, C. A. (2006b). Role of ion depletion in the electrophoretic deposition of alumina powder from ethanol with increasing quantities of HCl. *J. Mat. Sci.* 41, 8031–8046. doi:10.1007/s10853-006-0770-8

Vogel, N., Retsch, M., Fustin, C. A., del Campo, A., and Jonas, U. (2015). Advances in colloidal assembly: The design of structure and hierarchy in two and three dimensions. *Chem. Rev.* 115, 6265–6311. doi:10.1021/cr400081d

Wang, Y. C., Leu, I. C., and Hon, M. H. (2004). Kinetics of electrophoretic deposition for nanocrystalline zinc oxide coatings. *J. Am. Ceram. Soc.* 87, 84–88. doi:10.1111/j.1551-2916.2004.00084.x

Whitesides, G. M., and Grzybowski, B. (2002). Self-assembly at all scales. *Science* 295, 2418–2421. doi:10.1126/science.1070821

Yin, J., Huang, Y., Hameed, S., Zhou, R., Xie, L., and Ying, Y. (2020). Large scale assembly of nanomaterials: Mechanisms and applications. *Nanoscale* 12, 17571–17589. doi:10.1039/d0nr04156d

Zhang, Z., Huang, Y., and Jiang, Z. (1994). Electrophoretic deposition forming of SiC-tzp composites in a nonaqueous sol media. *J. Am. Ceram. Soc.* 77, 1946–1949. doi:10.1111/j.1151-2916.1994.tb07075.x

Zhitomirsky, I. (2002). Cathodic electrodeposition of ceramic and organoceramic materials. Fundamental aspects. *Adv. Colloid Interface Sci.* 97, 279–317. doi:10.1016/S0001-8686(01)00068-9

frontiers | Frontiers in Chemistry

TYPE Original Research
PUBLISHED 30 August 2022
DOI 10.3389/fchem.2022.985997

Check for updates

OPEN ACCESS

EDITED BY
Gabriela Oksdath-Mansilla,
Universidad Nacional de Córdoba,
Argentina

REVIEWED BY
Roger Sheldon,
University of the Witwatersrand, South Africa
Francesca Paradisi,
University of Bern, Switzerland

*CORRESPONDENCE
Selin Kara,
selin.kara@bce.au.dk

SPECIALTY SECTION
This article was submitted to Organic Chemistry,
a section of the journal
Frontiers in Chemistry

RECEIVED 04 July 2022
ACCEPTED 01 August 2022
PUBLISHED 30 August 2022

CITATION
De Santis P, Petrovai N, Meyer L-E, Hobisch M and Kara S (2022), A holistic carrier-bound immobilization approach for unspecific peroxygenase.
Front. Chem. 10:985997.
doi: 10.3389/fchem.2022.985997

COPYRIGHT
© 2022 De Santis, Petrovai, Meyer, Hobisch and Kara. This is an open-access article distributed under the terms of the Creative Commons Attribution License (CC BY). The use, distribution or reproduction in other forums is permitted, provided the original author(s) and the copyright owner(s) are credited and that the original publication in this journal is cited, in accordance with accepted academic practice. No use, distribution or reproduction is permitted which does not comply with these terms.

A holistic carrier-bound immobilization approach for unspecific peroxygenase

Piera De Santis[1], Noémi Petrovai[1], Lars-Erik Meyer[1], Markus Hobisch[1] and Selin Kara[1,2]*

[1]Biocatalysis and Bioprocessing Group, Department of Biological and Chemical Engineering, Aarhus University, Aarhus, Denmark, [2]Institute of Technical Chemistry, Leibniz University Hannover, Hannover, Germany

Unspecific peroxygenases (UPOs) are among the most studied enzymes in the last decade and their well-deserved fame owes to the enzyme's ability of catalyzing the regio- and stereospecific hydroxylation of non-activated C–H bonds at the only expense of H_2O_2. This leads to more direct routes for the synthesis of different chiral compounds as well as to easier oxyfunctionalization of complex molecules. Unfortunately, due to the high sensitivity towards the process conditions, UPOs' application at industrial level has been hampered until now. However, this challenge can be overcome by enzyme immobilization, a valid strategy that has been proven to give several benefits. Within this article, we present three different immobilization procedures suitable for UPOs and two of them led to very promising results. The immobilized enzyme, indeed, shows longer stability and increased robustness to reaction conditions. The immobilized enzyme half-life time is 15-fold higher than for the free *Aae*UPO PaDa-I and no enzyme deactivation occurred when incubated in organic media for 120 h. Moreover, *Aae*UPO PaDa-I is proved to be recycled and reused up to 7 times when immobilized.

KEYWORDS

biocatalysis, unspecific peroxygenase, immobilization techniques, enzyme stability, process intensification

Introduction

During the past 2 decades, biocatalysis has become a valid and extensively used approach for chemical synthesis. On the one hand, this strategy helps to overcome the weaknesses of some traditional chemical processes, while on the other hand, it enables the development of more environmentally friendly processes (Wu et al., 2021). In addition, protein and process engineering, computer modeling and computational studies have paved the way for the industrial use of enzymes nowadays. One of the main benefits of using enzymes as catalysts is related to their high stereo- and regio-selectivity, which is particularly useful in the case of selective oxidation and oxyfunctionalization of non-activated C–H, C–C-, or C=C-bonds (Hobisch et al., 2021). In fact, from the organic chemistry perspective, site-specific oxyfunctionalization reactions are difficult to obtain since they rely on a fragile equilibrium between reactivity and selectivity, which,

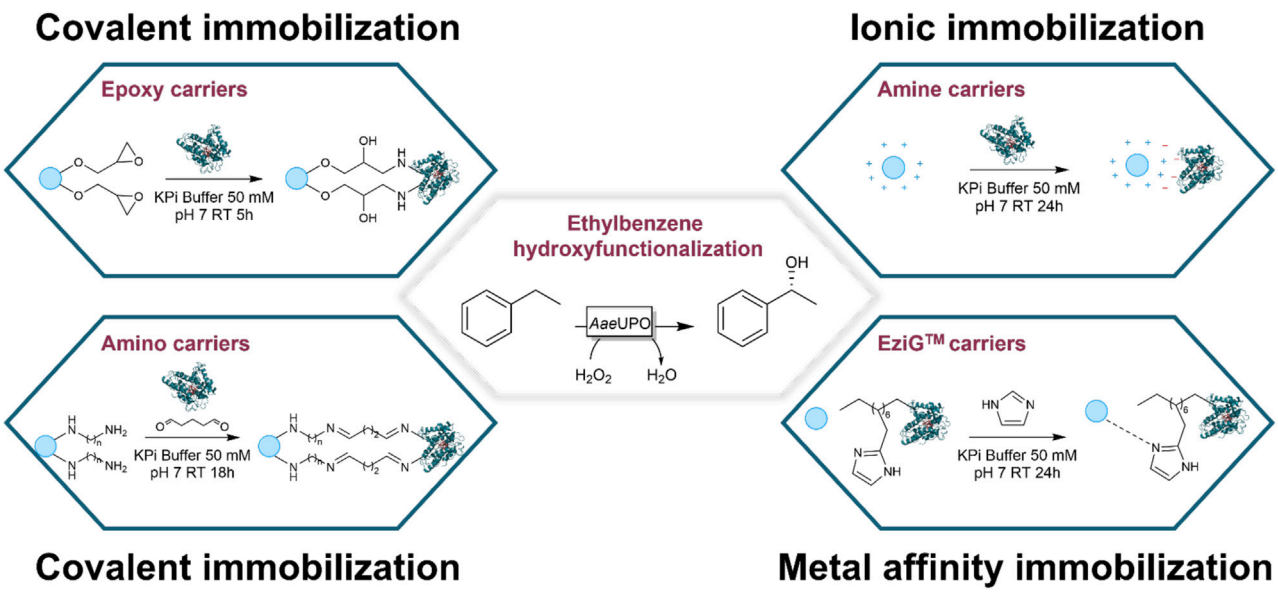


FIGURE 1
Schematic representation of the covalent, ionic, and metal affinity-binding immobilization techniques investigated in this study. The ethylbenzene hydroxy functionalization to (*R*)-1-phenylethanol is the model reaction chosen as proof-of-concept of immobilized enzyme applicability.

conversely, can be easily reached with enzymes. Therefore, biocatalysis opens the way to the selective oxyfunctionalization of organic molecules which plays a key role in the industrial scenario. In fact, these reactions are essential for the synthesis of building blocks, fine chemicals, functionalized polymers, and pharmaceutical compounds (Chanysheva et al., 2018; Grogan 2021).

Among the different enzyme families able to catalyze these crucial reactions, unspecific peroxygenases (UPOs) drew attention due to their interesting characteristics. Even though UPOs are heme-thiolate enzymes like the well-known P450 monooxygenases, they are independent from the use of expensive electron donors like nicotinamide adenine dinucleotide phosphate (NADPH) and auxiliary flavoproteins. In fact, UPOs only rely on hydrogen peroxide (H_2O_2) as cosubstrate and oxidant agent, solving the crucial problem of cofactor recycling (Molina-Espeja et al., 2015). Furthermore, as highlighted by Ramirez-Escudero et al., UPOs do not only show the catalytic activity of P450s, the classical heme-peroxidase, but also a chloroperoxidative one from *Caldariomyces fumago* (Ramirez-Escudero et al., 2018; Hofrichter et al., 2020). This hybrid activity earned them a position as the first member of a subclass of oxidoreductases (EC.1.11.2.1) (Ramirez-Escudero et al., 2018). In addition, UPOs have a vast selection of transformations and a wide substrate scope that ensures their adoption to produce several fine chemicals. Unspecific peroxygenases from *Agrocybe aegerita*, in particular, is one of the most studied UPOs (Hofrichter and Ullrich 2014; Dong et al., 2018).

The bottleneck of UPOs' application on industrial scale is nowadays due to the high cost of the heme-enzymes. Therefore, beside the improvement of the enzyme turnover number, which on the one hand was achieved *via* protein engineering (Molina-Espeja et al., 2014), and on the other hand by choosing the proper strategy for the *in situ* provision of the cosubstrate (Burek et al., 2019), another economically feasible approach to the use of UPOs is related to the enzyme recovery and recycling. The enzyme immobilization is the foremost strategy to do that (Figure 1).

As highlighted by Boudrant and coworkers, enzyme immobilization can represent the optimal solution to overcome different issues related to the use of biocatalysts (Boudrant et al., 2020). In fact, in this manner, is possible to improve the enzyme stability towards different organic solvents also at extreme values of pH and temperature (Sheldon, Basso et al., 2021). Higher biocatalyst loading into the reactors can be achieved, and, as aforementioned, this technique allows enzyme recyclability and simplified downstream processing (Thompson et al., 2019a). In addition, it also enables the use of enzymes in continuous processing (De Santis et al. 2020). Briefly, the enzyme immobilization leads to the development of a biocatalyst that can sustain the industrial requirements (higher stability and therewith higher overall productivity), and at the same time can be easily isolated and recovered from the reaction system.

This study offers an in-dept analysis of different carrier-bound immobilization methods to boost the use of UPOs at technical scales. In details, the experiments were performed with *Aae*UPO PaDa-I, a laboratory-evolved variant of UPO from

Agrocybe aegerita benefitting from nine mutations including four in the signal peptide and five in the mature protein. Therewith, the secretion into the media and the stability in terms of temperature and cosolvents presence were significantly increased (Molina-Espeja et al., 2014; Molina-Espeja et al., 2015). So far, PaDa-I is the most promising mutant variant of UPOs.

We aimed to determine the most appropriate carrier bound immobilization protocol for the biocatalyst. The optimum (carrier) candidate should retain as much enzyme as possible and, at the same time, avoid any loss of its activity. Additionally, different parameters and carrier characteristics therefore need to be considered. As far as the latter is concerned, the size and the diameter of the pores play a crucial role. Parameters like (i) protein loading, (ii) immobilized enzyme activity, and (iii) immobilization yield and (iv) activity yield were used to evaluate the immobilization procedures (Liese and Hilterhaus 2013; Boudrant et al., 2020; Guisan et al., 2020).

Materials and methods

General information. All solvents, reactants, and starting materials were received from commercial suppliers in the highest available purity (Sigma Aldrich, VWR, Carl Roth, Thermo Fisher) and used as received. Carriers for covalent immobilization (Lifetech™ ECR8285, ECR8215F, ECR8304F, ECR8404F, ECR8409F, ECR8315F, ECR8415F) as well as carriers for ionic immobilization (Lifetech™ ECR1508, ECR1604) were received from Purolite Life Sciences Ltd. (Llantrisant, United Kingdom) and treated as described below. Carriers for affinity immobilization of purified his-tagged enzyme (EziG™ Amber, Coral, and Opal) were received from EnginZyme A.B. (Solna, Sweden) and treated as described below. Potassium phosphate buffer (KPi buffer) was always freshly prepared in the lab for the experiments. All experiments were carried out under atmospheric conditions if not stated otherwise. For shaking and incubation of the carriers, a roller mixer from IKA (Staufen, Germany) was used. For photometric measurements, a temperature-controlled Cary 60 UV/Vis spectrophotometer from Agilent technologies (Santa Clara, California, United States) was used.

The mutant variant *Aae*UPO PaDa-I was used in the covalent and ionic immobilization procedures; conversely, the his-tagged PaDa-I was adopted for the experiments with the EziG™ carriers. Both the enzymes were produced *via* fermentation as described by Hobisch et al. (Hobisch and Kara 2021). The his-tagged PaDa-I was used as both crude preparation and purified enzyme; the purification was performed *via* immobilized-metal affinity chromatography (IMAC) with the Ni-NTA purification system and performed as described by the producer (see Supporting Information) (Fisher Scientific Thermo, 2015).

Covalent immobilization procedure. 1 g of each epoxy carrier (Lifetech™ ECR8285 and ECR8215F) was incubated in 2.5 mL of 50 mM KPi buffer (pH 7) on a roller mixer for 5 min followed by vacuum filtration for 5 min. This washing procedure was performed a total of three times. Subsequently, the supports were incubated in 3.0 ml of a PaDa-I dilution in 50 mM KPi buffer (pH 7, 0.27 mg_{enzyme} mL^{-1}) for 5 h at room temperature under careful mixing and then for 14 h at 4°C. Finally, the carriers were vacuum filtered. The filtrate was washed again with 2.5 mL of 50 mM KPi buffer (pH 7) by mixing for 5 min and then decanting. This procedure was repeated one last time, and finally the support-immobilized PaDa-I was stored at 4 °C (Purolite Life Sciences 2015). All the three supernatants were stored at 4 °C for the further analyses (see below).

Amino carriers (Lifetech™ ECR8304F, ECR8404F, ECR8409F, ECR8315F and ECR8415F) were treated as described above but preactivated for 1 hour by adding 2.5 mL of a 25% (v/v) glutaraldehyde solution with stirring followed by filtration and washing (Purolite Life Sciences 2015).

Ionic immobilization procedure. 0.5 g of each amine carrier (Lifetech™ ECR1508 and ECR1604) was equilibrated with 2.5 mL of deionized water for 5 min on a roller mixer and then vacuum filtrated for 5 min. Afterwards, the resin was incubated in 1.7 mL of a PaDa-I dilution in 50 mM KPi buffer (pH 7, 0.24 mg_{enzyme} mL^{-1}) for 24 h at room temperature under gentle mixing. Eventually, the carriers were vacuum filtered. The filtrate was washed again with 2.5 mL of 50 mM KPi buffer (pH 7) by mixing for 5 min and then decanting. This procedure was repeated one last time, and finally the support-immobilized PaDa-I was stored at 4 °C (Purolite Life Sciences 2015). All the three supernatants were stored at 4 °C for further analysis (see below).

Metal affinity binding immobilization procedure. 0.5 g of each carrier (EziG™ Amber, Coral, and Opal) was incubated with 2.9 mL of a PaDa-I dilution in 50 mM KPi buffer (pH 7, 1.4 mg_{enzyme} mL^{-1}) for 24 h at room temperature under careful mixing. Finally, the carriers were vacuum filtered. The filtrate was washed again with 2.5 mL of 50 mM KPi buffer (pH 7) by mixing for 5 min and then decanting. This procedure was repeated one last time, and finally the support-immobilized PaDa-I was stored at 4 °C (Bormann et al., 2020). All the three supernatants were stored at 4 °C for the further analyses (see below).

Assessment of the enzyme immobilization. Bicinchoninic acid protein assay (Pierce™ 660 nm) was performed on all the wash fractions from the immobilization procedures (see above) to evaluate the mass of leached protein during the immobilization protocol. A calibration curve was obtained by measuring the absorbance of a dilution series of bovine serum albumin (BSA) in triplicates. By determining the concentration of the free PaDa-I in the wash fractions after the immobilization, the protein loading and immobilization yield were calculated (Eqss 1, 2, respectively) (Antharavally et al., 2009).

10.3389/fchem.2022.985997

$$\textit{Protein loading (PL)}\left(\frac{mg_{immo.\ enzyme}}{g_{wet\ carrier}}\right) = \frac{m_{enzyme\ used\ initially} - m_{wash/filtrate\ \ fractions}}{m_{wet\ carrier}} \quad (1)$$

$$\textit{Immobilization yield (\%)} = \frac{m_{enzyme\ offered}\left(mg_{enzyme}\right) - m_{enzyme\ supernatants}\left(mg_{enzyme}\right)}{m_{enzyme\ offered}\left(mg_{enzyme}\right)} \times 100 \quad (2)$$

To evaluate the immobilized enzyme's activity, instead, a standard activity assay was performed on the immobilized enzyme as well as on the liquid fractions collected during the immobilization procedure. This assay is based on the absorbance of oxidized form of 2,2′-azino-bis(3-ethylbenzothiazoline-6-sulfonic acid) (ABTS) at 405 nm.

To investigate the liquid fraction, the PaDa-I-catalyzed oxidation of 990 µL 0.3 mM ABTS with 10 µL enzyme sample and 1.75 µL 3.5% (v/v) H_2O_2 was photometrically tracked over time and evaluated in triplicates in the time interval from 0.05 to 0.2 min; the measurements were performed in triplicates and the volumetric activity was calculated (Eq. 3) (Kadnikova and Kosti´ 2002).

$$Activity_{vol.}\left(\frac{U}{mL}\right) = \frac{\Delta Abs_{405\ nm} \times DF \times V}{\varepsilon_{405\ nm}^{ABTS^{+\bullet}} \times v \times d} \quad (3)$$

$\Delta Abs_{405\ nm}$ (min^{-1}) = measured absorbance at 405 nm over time; DF (1) = dilution factor; d (cm) = light path; V (mL) = sample volume; v (mL) = enzyme volume in the sample; $\varepsilon_{405\ nm}^{ABTS^{+\bullet}}$ = molar extinction coefficient, 36.8 mM^{-1} cm^{-1} (Burek et al., 2019)

To investigate the immobilized enzyme, 10 mL of 0.3 mM ABTS, 1–10 mg of immobilized enzyme and 17.5 µL of 3.5% (v/v) H_2O_2 were stirred at 250 rpm at 25 °C. From the time of addition of the hydrogen peroxide, five samples (0.5 mL each) were taken every 30 s. The experiments were performed in triplicates and the activity was calculated Eq. 4.

$$Activity_{immo.}\left(\frac{U}{g_{wet\ carrier}}\right) = \frac{\Delta Abs_{405\ nm} \times DF \times V}{\varepsilon_{405\ nm}^{ABTS^{+\bullet}} \times m_{wet\ carrier} \times d} \quad (4)$$

By correlating the volumetric activity and the protein loading, the specific activity and the immobilization yield can be calculated Eqs 5, 6, respectively).

$$Activity_{spec.}\left(\frac{U}{mg_{immo.\ enzyme}}\right) = \frac{A_{immo}}{PL} \quad (5)$$

$$\textit{Activity yield (\%)} = \frac{Activity_{spec.}\left(Umg^{-1}_{immo.\ enzyme}\right) \times m_{immo.\ enzyme}\left(mg_{enzyme}\right)}{m_{enzyme\ offered}\left(mg_{enzyme}\right) \times Activity_{spec.}\left(Umg^{-1}_{free\ enzyme}\right)} \times 100 \quad (6)$$

Results and discussion

Three different immobilization techniques were investigated, each of which was based on a different type of interaction between the carrier and the enzyme (covalent, ionic, and metal affinity interactions, Figure 1). The first one relied on the formation of a covalent bond between the carrier functional groups and the enzyme amino acids. Two different carrier families were studied within the covalent binding technique: the epoxy and the amino supports, both supplied by Purolite Life Sciences (Llantrisant, United Kingdom).

As epoxy carriers, Lifetech™ ECR8285 and Lifetech™ ECR8215F were chosen and both resins are composed of polymethacrylate material functionalized with epoxy groups enabling a multipoint covalent attachment of the enzyme on the carrier surface. The differences between the two resins are their particle size and pore diameter (see Supporting Information). The formation of a covalent bond is here based on the interaction between nucleophilic amino acids (mainly lysines) and the epoxy group, which leads to the opening of the epoxydic ring (Figure 1) (Mateo et al., 2007). Because of the type of interaction, pH plays an important role for the success of the immobilization procedure. It is therefore important to emphasize that it is likely that an alkaline pH (instead of the neutral pH here applied) would have favored the nucleophilic attack and led to a higher immobilization yield. Unfortunately, this condition is not suitable for UPOs since activity is negatively affected by basic conditions (Molina-Espeja et al., 2014).

As amino carriers, Lifetech™ ECR8304F, ECR8404F, ECR8409F, ECR8315F and ECR8415F were selected. The differences between the five resins are their particle size, pore diameter, and the amino-spacer length (see Supporting Information). In contrast to the epoxy carrier case, the covalent bond is here obtained through a simple carbonyl-amine condensation reaction (see Figure 1). The resins need to be activated before via glutaraldehyde addition. Then, the activated carrier can bind the enzyme linking the second terminal aldehydes of glutaraldehyde and one of the amino groups of *Aae*UPO PaDa-I.

When it comes to the enzyme immobilization on amino carriers, not only different supports but also different enzyme-to-carrier ratios were investigated. Moreover, also the storage stability was determined up to 30 days after the immobilization.

For the characterization of the free and immobilized biocatalyst, the well-accepted assay system oxidizing ABTS to its single radical specie ($ABTS^{\bullet+}$) was used to determine enzyme activity (Kadnikova and Kosti´ 2002). Conversely, the protein loading was calculated according to the Pierce™ protein concentration assay. Both epoxy and amino supports showed a similar trend: higher protein loadings and activities were observed when supports with larger pore diameters were used. Moreover, comparison of the amino carriers also shows that shorter spacer lengths lead to higher protein loading and activity (Table 1).

TABLE 1 Screening results obtained for the covalent immobilization of *Aae*UPO PaDa-I.

Carriers[a]	Protein loading ($mg_{protein}/g_{carrier}$)	Immobilization yield (%)	Specific activity (U/mg)[b]	Activity yield (%)	Pore diameter (Å)	Spacer length[c]
Epoxy carriers						
ECR8285	0.250 ± 0.004	54	4.7	0.44	400–600	-
ECR8215F	0.484 ± 0.004	54	44 ± 4	4	1200–1800	-
Amino carriers						
ECR8304F	0.670 ± 0.007	57	2	0.2	300–600	Short spacer
ECR8404F	0.40 ± 0.09	32	n.d.[d]	n.d	300–600	Long spacer
ECR8409F	0.43 ± 0.01	35	n.d	n.d	600–1200	Long spacer
ECR8315F	0.616 ± 0.006	55	27.5 ± 0.5	3	1200–1800	Short spacer
ECR8415F	0.45 ± 0.05	28	21 ± 5	1	1200–1800	Long spacer

[a]All the here evaluated carriers are part of the Lifetech™.
ECR, resins supplied by Purolite Ltd. The resins are characterized by a common specific particle size of 150–300 μm, except for ECR8285 whom shows a particle size of 250–1000 μm.
[b]per mg of enzyme immobilized.
[c]Short spacer: C2, long spacer: C6.
[d]Not detected.

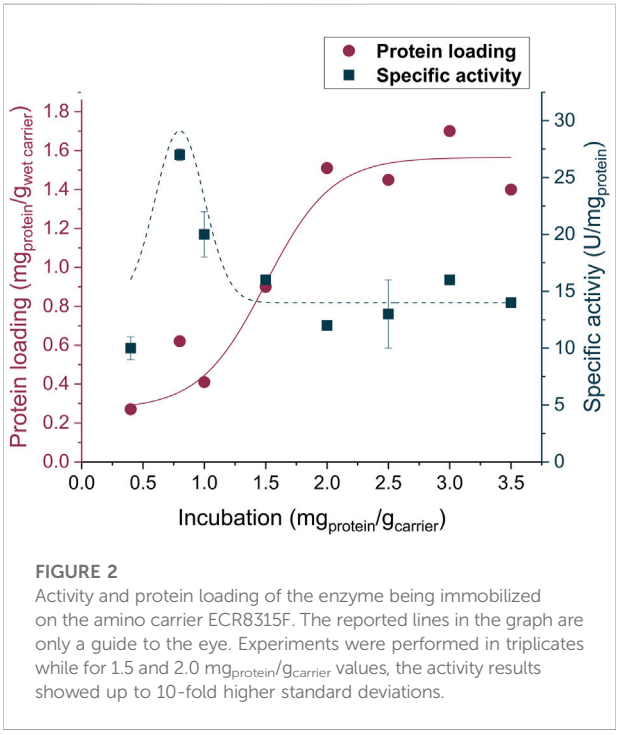


FIGURE 2
Activity and protein loading of the enzyme being immobilized on the amino carrier ECR8315F. The reported lines in the graph are only a guide to the eye. Experiments were performed in triplicates while for 1.5 and 2.0 $mg_{protein}/g_{carrier}$ values, the activity results showed up to 10-fold higher standard deviations.

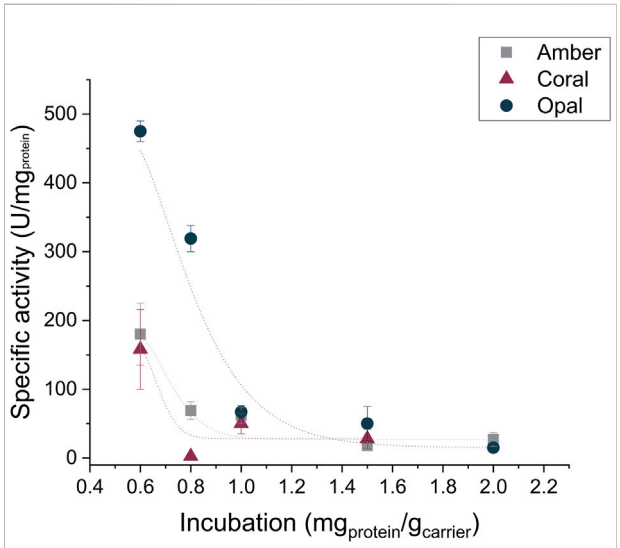


FIGURE 3
Activity of the enzyme being immobilized on the Amber, Coral, and Opal EziG™ carriers incubated at different protein-to-carrier ratios. The reported lines in the graph are only a guide to the eye.

Among the supports evaluated for covalent immobilization, Lifetech™ ECR8315F led to the highest protein loading and enzyme activity. Therefore, the immobilization procedure was further optimized for this carrier. Different enzyme-to-carrier ratios were evaluated (from 0.4 to 3.5 $mg_{protein}/g_{carrier}$) and, as highlighted in Figure 2, the 0.8 $mg_{protein}\ g_{carrier}^{-1}$ showed the right balance between a high protein loading and a satisfactory activity. It is worth noticing that by increasing the enzyme-to-carrier ratio, even if there is an increment in the protein loading, the enzyme activity tends to fluctuate or even decrease. This phenomenon might be attributed to the formation of multilayers on the carrier surface.

Additionally, the long-term process stability of immobilized *Aae*UPO PaDa-I was determined over 30 days and up to 60% of the enzyme activity was retained. Within the ionic immobilization strategy, two different resins from Purolite Life Sciences were evaluated (Lifetech™ ECR1508 and ECR1604) (see Supporting Information). Here, the carriers differ according to their functional group, a tertiary, and a quaternary amine (Table 2), and the enzyme is retained due to ionic interactions

TABLE 2 Screening results obtained for the ionic immobilization of *Aae*UPO PaDa-I.

Carriers[a]	Protein loading ($mg_{protein}/g_{carrier}$)	Immobilization yield (%)	Specific activity (U/mg)[b]	Activity yield (%)
ECR1508	0.658 ± 0.002	38	9 ± 1	1
ECR1604	0.833 ± 0.003	61	7 ± 3	1

[a]All the here evaluated carriers are part of the Lifetech™ supplied by Purolite Ltd. The resins are characterized by a common specific particle size of 150–300 μm.
[b]Per mg of enzyme immobilized.

TABLE 3 Screening results obtained for the affinity immobilization of purified his-tagged *Aae*UPO PaDa-I.

Carriers[a] (optimum ratio)	Protein loading ($mg_{protein}/g_{carrier}$)	Immobilization yield (%)	Specific activity (U/mg)[b]	Activity yield (%)	Pore diameter (Å)
Amber (0.8)	0.37 ± 0.01	46	69 ± 13	11	300
Coral (1.0)	0.27 ± 0.03	45	50 ± 16	5	300
Opal (1.2)	0.76 ± 0.02	92	67 ± 9	55	500

[a]All the evaluated carriers are part of the EziG™ carriers supplied by EnginZyme A.B.; for each carrier, only the data related to the optimum enzyme-to-carrier ratio are reported in the table. The Amber one is a controlled pore glass material coated with a semi-hydrophobic polymer, the Coral is covered by a hydrophobic polymer, while the Opal carrier is made only of glass. In all cases, the particle size is 75–125 μm.
[b]Per mg of enzyme immobilized.

being established with the carrier's and enzyme's surface charge. Therefore, parameters like the isoelectric point of the enzyme, the optimal pH, and the ionic strength of the immobilization buffer must be carefully selected.

When *Aae*UPO PaDa-I is immobilized on Lifetech™ ECR1604 (quaternary amine), we observed a slightly higher protein loading (20%) compared to the enzyme being immobilized on Lifetech™ ECR1508 (tertiary amine). We hypothesize that the interaction between the negatively charged enzyme and the–NR_3^+ functional group is stronger compared to the–NR_2 moiety. Conversely, the immobilized enzyme observes a similar activity when immobilized on both carriers (Table 2). Furthermore, the activity was measured 4 weeks after the immobilization and remained steady.

As regards the metal affinity immobilization technique, we investigated the three porous carriers from EnginZyme A.B. (Solna, Sweden): EziG™ Amber, Coral, and Opal. These three carriers are made of a controlled-pore glass material covered by an organic polymer leading to hydrophobic, semi-hydrophobic, or hydrophilic resins (see Supporting Information). Additionally, Fe^{3+} ions are linked to the carrier surface. For the enzyme immobilization to occur, the cations interact with the lone pair of electrons of a histidine group (Cassimjee et al., 2018); therefore, his-tagged PaDa-I was used for the following immobilization investigations. When applied to purified his-tagged PaDa-I, we observed a significantly higher specific activity for immobilized enzyme on the Opal EziG™ carrier although the protein loading is similar for all carriers (Figure 3, Table 3).

Again, we evaluated different enzyme-to-carrier ratios to reach the optimal protein loading without compromising the enzyme activity and found an optimal ratio at 0.8 $mg_{PaDa\text{-}I}$ $g_{carrier}^{-1}$ for EziG™ Amber and 1.0 $mg_{PaDa\text{-}I}$ $g_{carrier}^{-1}$ EziG™ Coral. Eventually, the highest specific activity was reached when the purified his tagged PaDa-I was immobilized on EziG™ Opal carrier with a final enzyme-to-carrier ratio of 1.2 $mg_{PaDa\text{-}I}$ $g_{carrier}^{-1}$ (Supplementary Figure 3SI; Supplementary Tables S7–9). Moreover, the activity of the immobilized enzyme retained up to 1 month.

Further experiments were devoted to the proof-of-concept of our model reaction system, the hydroxy functionalization of ethylbenzene to the enantiopure (*R*)-1-phenylethanol. In this case, the covalently immobilized PaDa-I (Lifetech™ ECR8315F) was adopted and different parameters like (i) the amount of immobilized enzyme, (ii) the shaking intensity and (iii) the reaction temperature were optimized (see Supporting Information). These experiments were crucial to prove not only the applicability of the developed immobilization procedure to the model reaction, but also that the covalent enzyme immobilization do not affect either the regio- or the enantioselectivity properties of the enzyme. However, it cannot be omitted that also the (*R*)-1-phenylethanol overoxidation to acetophenone occurred as a side-reaction; when the optimum conditions are applied, a target product selectivity of 74% is achieved. Yet this datum was not an unforeseen phenomenon; in fact, even if the kinetics parameter regulating the alcohol overoxidation

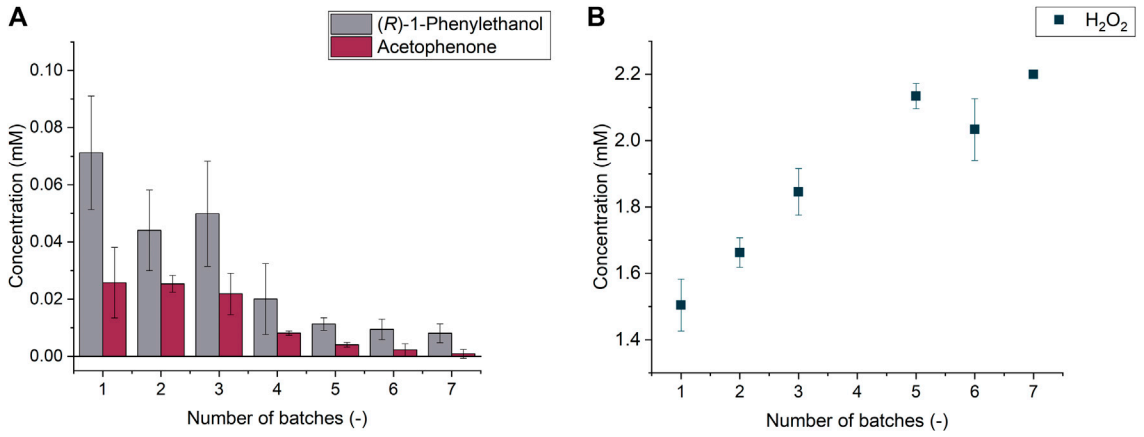


FIGURE 4
(*R*)-1-phenylethanol and acetophenone formation through the repeated batches **(A)** hydrogen peroxide concentration determined at the end of each batch **(B)**.

are still under debate, the ketone formation is a well-known side rection of UPOs catalysis (Kluge et al., 2012).

The optimized conditions laid the foundation for additional experiments about the enzyme recyclability (see Supporting Information). Repetitive batch experiments were indeed successfully conducted and demonstrated that the covalently immobilized enzyme can be recycle up to 7 times, with a loss of product formation of 89% after six batches (see Figure 4).

Before concluding this chapter, it is worth observing that the aforementioned procedures are only part of the numerous available immobilization techniques. Unexpectedly, despite the countless advantages of enzymatic immobilization as well as the big appeal UPOs have captured since their discovery in 2004, only few research about the combination of these two core topics have been published so far. For instance, one of the first published UPOs carrier bound immobilization procedures, involved the recombinant unspecific peroxygenase from *Agrocybe aegerita* (*rAae*UPO) on Relizyme™, which is a polymethacrylate resin functionalized with hexamethylenamino groups (Fernandez-Fueyo et al., 2016). Similar to the aforementioned study, also Fernandez-Fueyo and coworkers evaluated the enzyme immobilization efficiency via protein concentration assay of the supernatant and via ABTS activity assay. When comparing their results with the ones shown before (Table 1) a similar behavior can be noted: the loss of enzyme performance (in both cases around 20-fold) is well-balanced by the increase in the enzyme stability. Recently, the same enzyme was chosen by Carballares and coworkers to investigate the effect of the pH in ion exchange immobilization procedures on cationic supports; after an in-depth analysis, different activity assays proved that the best results are achieved with MANAE agarose (Carballares et al., 2021). As it also emerges from the experiments conducted (see Table 2), high immobilization yield value can be achieved via ionic immobilization. However, the pH control necessary to perform this immobilization can negatively affect the enzyme activity. In fact, as proved by Carballares et al., albeit the ionic immobilization performed at pH 9 led to an immobilization yield of almost 100%, it also caused a decrease in enzyme activity and stability; according to these results they concluded that, to take the most advantage from the immobilization procedure, the *rAae*UPO needs to be immobilized at pH 5. Turning back to the covalent immobilization, Molina-Espeja et al. proved the feasibility of directed unique-point covalent immobilization (DUCI) strategy by synthetizing and immobilizing a new PaDa-I-Cys variant, through the formation of a single disulfide bridge between the just introduced cysteine and the carrier (Molina-Espeja et al., 2019). The main advantage of this immobilization procedure is the strict control on enzyme orientation exercised by the activated carrier. One of the two carrier materials studied for the directed unique-point enzyme immobilization, is a polymethacrylate epoxy activated carrier which led to results comparable to the ones presented for the Lifetech™ ECR8215F (see Table 1). Moreover, the authors used fluorescence confocal microscopy to visualize the enzyme bound to the epoxy-carrier and, since only a negligible amount of the non-modified PaDa-I was linked to the carriers, to prove the selectivity of the immobilization procedure.

Carrier-free immobilization strategies can also represent a valid alternative; carrier-free methods generally show advantages like high volumetric activity and stability against unnatural condition. According to authors' knowledge, so far Poraj Kobielska and coworkers have demonstrated the feasibility of unspecific peroxygenase encapsulation in polyvinylalcohol/polyethylenglycol gel

beads (Poraj-Kobielska et al., 2015) and Kara and coworkers in alginate beads (Hobisch et al., 2020).

Eventually, it is also worth to mention the positive effect that *in-silico* analysis can have in the development of an immobilization procedure. These can indeed act as guidelines helping us to shortlist the countless procedures, to point out the optimal conditions and to foresee the immobilized enzyme behavior. A tool like molecular docking, for example, can help better understanding the protein domains involved in the anchoring phase and predict the effect on the enzyme active site (Holyavka et al., 2016). Similarly, software like Swiss Pdb Viewer and Maestro identify the amino acid residues on the enzyme surface and provide information about their special position. Both were indeed used by Sakibaev and coworkers to determine the distance between the active center of the enzyme and the potential sites for binding, an important parameter to predict the effect of the immobilization procedure on the enzyme activity (Sakibaev et al., 2019). An alternative is represented by algorithms such as LIGRe (ligand interacting group reactivity) that determines the amino acids reactivity at a given pH highlighting the regions of the enzyme prone to interact with the carrier functional group (Torres-Salas, del Monte-Martinez et al., 2011). Moreover, microscopes such as scanning electron microscope (SEM) and fluorescence confocal microscopy are often used to display the enzyme distribution throughout the carrier pores and to predict substrate/product diffusion limitation problems within the support, respectively (Molina-Espeja et al., 2019; Ahmad et al., 2020).

Conclusion

Among the different immobilization strategies investigated, metal affinity binding using the Opal EziG™ support, proved to be the most suitable method for *Aae*UPO PaDa-I. The optimized condition led to an immobilization yield of 92% and to an activity yield of 55%; moreover, the 75% of enzyme activity was kept up to 30 days. However, it is worth noting that these promising results were obtained using purified PaDa-I, which consists of an extra cost that negatively affect the labour and overhead (L&O) costs (Thompson et al., 2019b). Comparing only the results of the crude enzyme extract immobilization procedures, covalent immobilization with the amino carrier Lifetech™ ECR8315F is found to be the optimum. When immobilized on this carrier, the enzyme has an immobilization yield of 55% and an activity yield of 2%. Moreover, even if 40% of enzyme activity is lost after 30 days, the half-life time of the immobilized enzyme is 15-fold higher than for the free PaDa-I. Eventually, the covalently immobilized enzyme was adopted as catalyst in the ethylbenzene hydroxy-functionalization reaction (proof-of-concept) and to validate the hypothesis of enzyme recyclability (until 7 times). According to Thompson *et al.*, the obtained results respect industrial requirements like high enzyme loading (>10wt%) and partially satisfy requirements such as high retained activity (>50%) and enzyme recyclability (Thompson et al., 2019a). Moreover, an upscale from 1 to 10 g immobilization performed with the Lifetech™ ECR8315F carrier with no negative consequences, reveals its potential use on larger scales, e.g. in flow, and foreshadows that the system is robust enough for further increase. Considering this very promising results, future experiments will be devoted to further improve immobilization and reaction conditions in order to continue reducing the gap between the enzyme properties and the industrial requirements.

Data availability statement

The original contributions presented in the study are included in the article/Supplementary Material further inquiries can be directed to the corresponding author.

Author contributions

SK conceptualized the project. PD designed and planned the experiments. PD, L-EM, and MH cloned the genes and expressed and purified the enzymes. PD performed and analyzed the immobilization experiments. PD and NP tested and analyzed the model reaction. PD wrote the original draft and was responsible for validation, data curation, and visualization. PD, L-EM, MH, and SK reviewed and edited the final draft. All authors agreed with the final version of the submitted manuscript. SK coordinated the project and allocated the funding.

Funding

This project has received funding from the European Union's Horizon 2020 research and innovation program under the Marie Skłodowska-Curie grant agreement No 764920. SK gratefully acknowledges the Independent Research Fund Denmark (PHOTOX-*f* project, grant No 9063-00031B) for the grant funding in the framework of Sapere Aude DFF-Starting Grant.

Acknowledgments

Prof. Dr. Miguel Alcalde (CSIC, Spain) and Prof. Dr.-Ing. Dirk Holtmann (Technische Hochschule Mittelhessen, Germany) are gratefully acknowledged for supplying the plasmids for the PaDa-I variant. The authors are also grateful to Dr. Karim Engelmark Cassimjee from EnginZyme A.B. (Solna, Sweden), Dr. Simona Serban and Dr. Alessandra Basso from Purolite Ltd. (Unit D, Llantrisant CF728LF, United Kingdom) for providing free immobilization carrier samples.

Conflict of interest

The authors declare that the research was conducted in the absence of any commercial or financial relationships that could be construed as a potential conflict of interest.

Publisher's note

All claims expressed in this article are solely those of the authors and do not necessarily represent those of their affiliated organizations, or those of the publisher, the editors and the reviewers. Any product that may be evaluated in this article, or claim that may be made by its manufacturer, is not guaranteed or endorsed by the publisher.

Supplementary Material

The Supplementary Material for this article can be found online at: https://www.frontiersin.org/articles/10.3389/fchem.2022.985997/full#supplementary-material

References

Ahmad, M., Ali, B., Khan, S., Akhtar, N., Kahn, M. F., and Panda, B. P. (2020). Immobilization of β-glucuronidase: Biocatalysis of glycyrrhizin to 18β-glycyrrhetinic acid and *in-silico* lead finding. *J. Chin. Pharm. Sci.* 29 (5), 333–340.

Antharavally, B. S., Mallia, K. A., Rangaraj, P., Bell, P., and Bell, P. A. (2009). Quantitation of proteins using a dye-metal-based colorimetric protein assay. *Anal. Biochem.* 385 (2), 342–345. doi:10.1016/j.ab.2008.11.024

Bormann, S., Burek, B. O., Ulber, R., and Holtmann, D. (2020). Immobilization of unspecific peroxygenase expressed in Pichia pastoris by metal affinity binding. *Mol. Catal.* 492. doi:10.1016/j.mcat.2020.110999

Boudrant, J., Fernandez-Lafuente, J. M. R., and Fernandez-Lafuente, R. (2020). Parameters necessary to define an immobilized enzyme preparation. *Process Biochem.* 90, 66–80. doi:10.1016/j.procbio.2019.11.026

Burek, B. O., Bormann, S., Hollmann, F., Holtmann, J. Z. D., and Holtmann, D. (2019). Hydrogen peroxide driven biocatalysis. *Green Chem.* 21 (12), 3232–3249. doi:10.1039/c9gc00633h

Carballares, D., Morellon-Sterling, R., Xu, X., Hollmann, F., and Fernandez-Lafuente, R. (2021). Immobilization of the peroxygenase from Agrocybe aegerita. The effect of the immobilization pH on the features of an ionically exchanged dimeric peroxygenase. *Catalysts* 11 (5). doi:10.3390/catal11050560

Cassimjee, K. E. F., and Hans-Jurgen, G. (2018). *EziG: A universal platform for enzyme immobilisation*. Cambridge: Royal Society of Chemistry, 345–362.

Chanysheva, A. R., Zorin, E. N., and Zorin, V. V. (2018). Enantioselective bioreduction of acetophenone into (R)- and (S)-1-Phenylethanols. *Russ. J. Gen. Chem.* 87 (13), 3259–3262. doi:10.1134/s1070363217130229

De Santis, P., Meyer, L.-E., and Kara, S. (2020). The rise of continuous flow biocatalysis – fundamentals, very recent developments and future perspectives. *React. Chem. Eng*

Dong, J., Fernández-Fueyo, E., Hollmann, F., Paul, C. E., Pesic, M., Schmidt, S., et al. (2018). Biocatalytic oxidation reactions: A chemist's perspective. *Angew. Chem. Int. Ed.* 57 (30), 9238–9261. doi:10.1002/anie.201800343

Fernández-Fueyo, E., Ni, Y., Gomez Baraibar, A. G., Alcalde, M., van Langen, L. M., and Hollmann, F. (2016). Towards preparative peroxygenase-catalyzed oxyfunctionalization reactions in organic media. *J. Mol. Catal. B Enzym.* 134, 347–352. doi:10.1016/j.molcatb.2016.09.013

Fisher Scientific, Thermo (2015). *Ni-Nta purification system*. Life Technologies Corporation. Available at: https://tools.thermofisher.com/content/sfs/manuals/ninta_system_man.pdf.

Grogan, G. (2021). Hemoprotein catalyzed oxygenations: P450s, UPOs, and progress toward scalable reactions. *JACS Au* 1 (9), 1312–1329. doi:10.1021/jacsau.1c00251

Guisan, J. M., Bolivar, J. M., Lopez-Gallego, F., and Rocha-Martín, J. (2020). *Immobilization of enzymes and cells-methods and protocols*. Springer Science+Business Media.

Hobisch, M., Holtmann, D., Gomez de Santos, P., Alcalde, M., Kara, F., and Kara, S. (2021). Recent developments in the use of peroxygenases - exploring their high potential in selective oxyfunctionalisations. *Biotechnol. Adv.* 51, 107615. doi:10.1016/j.biotechadv.2020.107615

Hobisch, M., and Kara, S. (2021). *Automated feeding and fermentation phase transitions for the production of unspecific peroxygenase by Pichia pastoris*.

Hofrichter, M., Kellner, H., Herzog, R., Karich, A., Liers, C., Scheibner, K., et al. (2020). *Fungal peroxygenases: A phylogenetically old superfamily of heme enzymes with promiscuity for oxygen transfer reactions*.

Hofrichter, M., and Ullrich, R. (2014). Oxidations catalyzed by fungal peroxygenases. *Curr. Opin. Chem. Biol.* 19, 116–125. doi:10.1016/j.cbpa.2014.01.015

Holyavka, M. G., Kondratyev, M. S., Samchenko, A. A., Kabanov, A. V., Artyukhov, V. M., and Artyukhov, V. G. (2016). *In silico* design of high-affinity ligands for the immobilization of inulinase. *Comput. Biol. Med.* 71, 198–204. doi:10.1016/j.compbiomed.2016.02.015

Kadnikova, E. N., and Kosti´, N. M. (2002). Oxidation of ABTS by hydrogen peroxide catalyzed by horseradish peroxidase encapsulated into sol–gel glass. Effects of glass matrix on reactivity. *J. Mol. Catal. B Enzym.* 18 (1-3), 39–48. doi:10.1016/s1381-1177(02)00057-7

Kluge, M., Ullrich, R., Hofrichter, K., and Hofrichter, M. (2012). Stereoselective benzylic hydroxylation of alkylbenzenes and epoxidation of styrene derivatives catalyzed by the peroxygenase of Agrocybe aegerita. *Green Chem.* 14 (2), 440–446. doi:10.1039/c1gc16173c

Liese, A., and Hilterhaus, L. (2013). Evaluation of immobilized enzymes for industrial applications. *Chem. Soc. Rev.* 42 (15), 6236–6249. doi:10.1039/c3cs35511j

Mateo, C., Grazu, V., Palomo, J. M., Lopez-Gallego, F., Fernandez-Lafuente, R., and Guisan, J. M. (2007). Immobilization of enzymes on heterofunctional epoxy supports. *Nat. Protoc.* 2 (5), 1022–1033. doi:10.1038/nprot.2007.133

Molina-Espeja, P., Garcia-Ruiz, E., Gonzalez-Perez, D., Ullrich, R., Alcalde, M., and Alcalde, M. (2014). Directed evolution of unspecific peroxygenase from Agrocybe aegerita. *Appl. Environ. Microbiol.* 80 (11), 3496–3507. doi:10.1128/aem.00490-14

Molina-Espeja, P., Ma, S., Mate, D. M., Alcalde, R., and Alcalde, M. (2015). Tandem-yeast expression system for engineering and producing unspecific peroxygenase. *Enzyme Microb. Technol.* 73-74, 29–33. doi:10.1016/j.enzmictec.2015.03.004

Molina-Espeja, P., Santos-Moriano, P., García-Ruiz, E., Ballesteros, A., Alcalde, F. J., and Alcalde, M. (2019). Structure-guided immobilization of an evolved unspecific peroxygenase. *Int. J. Mol. Sci.* 20 (7). doi:10.3390/ijms20071627

Poraj-Kobielska, M., Peter, S., Leonhardt, S., Ullrich, R., Hofrichter, K., and Hofrichter, M. (2015). Immobilization of unspecific peroxygenases (EC 1.11.2.1) in PVA/PEG gel and hollow fiber modules. *Biochem. Eng. J.* 98, 144–150. doi:10.1016/j.bej.2015.02.037

Purolite Life Sciences (2015). *Lifetech™ ECR enzyme immobilization procedures*. Retrieved 29-08-2020, 2020, Available at: https://www.puro-lite.com/dam/jcr:3c5b978b-3829-4f92-8654-390863042f09/Lifetech%20ECR%20immobi-lisation%20procedures.pdf.

Ramirez-Escudero, M., Molina-Espeja, P., Gomez de Santos, P., Hofrichter, M., Sanz-Aparicio, J., and Alcalde, M. (2018). Structural insights into the substrate promiscuity of a laboratory-evolved peroxygenase. *ACS Chem. Biol.* 13 (12), 3259–3268. doi:10.1021/acschembio.8b00500

Sakibaev, F. A., Holyavka, M. G., Artyukhov, S. M., and Artyukhov, V. G. (2019). An in silico search for the sites of potential binding with charged and hydrophobic carriers in the molecules of endoinulinase from Aspergillus ficuum and exoinulinase from Aspergillus awamori. *Biophysics* 64 (3), 323–330. doi:10.1134/s0006350919030199

Sheldon, R. A., Brady, A. D., and Brady, D. (2021). New frontiers in enzyme immobilisation: Robust biocatalysts for a circular bio-based economy. *Chem. Soc. Rev.* 50 (10), 5850–5862. doi:10.1039/d1cs00015b

Thompson, M. P., Derrington, S. R., Heath, R. S., Porter, J. L., Mangas-Sanchez, J., Devine, P. N., et al. (2019a). A generic platform for the immobilisation of engineered biocatalysts. *Tetrahedron* 75 (3), 327–334. doi:10.1016/j.tet.2018.12.004

Thompson, M. P., Peñafiel, I., Turner, S. C., and Turner, N. J. (2019b). Biocatalysis using immobilized enzymes in continuous flow for the synthesis of fine chemicals. *Org. Process Res. Dev.* 23 (1), 9–18. doi:10.1021/acs.oprd.8b00305

Torres-Salas, P., del Monte-Martinez, A., Cutiño-Avila, B., Rodriguez-Colinas, B., Alcalde, M., Plou, A. O., et al. (2011). Immobilized biocatalysts: Novel approaches and tools for binding enzymes to supports. *Adv. Mat.* 23 (44), 5275–5282. doi:10.1002/adma.201101821

Wu, S., Snajdrova, R., Moore, J. C., Bornscheuer, K., and Bornscheuer, U. T. (2021). Biocatalysis: Enzymatic synthesis for industrial applications. *Angew. Chem. Int. Ed.* 60 (1), 88–119. doi:10.1002/anie.202006648

frontiers | Frontiers in Chemistry

TYPE Original Research
PUBLISHED 30 August 2022
DOI 10.3389/fchem.2022.949461

Check for updates

OPEN ACCESS

EDITED BY
Ganna Gryn'ova,
Heidelberg University, Germany

REVIEWED BY
Wensheng Cai,
Nankai University, China
Terry J. Frankcombe,
University of New South Wales, Australia
Michele Ceotto,
University of Milan, Italy

*CORRESPONDENCE
Xihui Bian,
bianxihui@163.com

SPECIALTY SECTION
This article was submitted to Theoretical and Computational Chemistry, a section of the journal Frontiers in Chemistry

RECEIVED 21 May 2022
ACCEPTED 01 August 2022
PUBLISHED 30 August 2022

CITATION
Bian X, Ling M, Chu Y, Liu P and Tan X (2022), Spectral denoising based on Hilbert–Huang transform combined with F-test.
Front. Chem. 10:949461.
doi: 10.3389/fchem.2022.949461

COPYRIGHT
© 2022 Bian, Ling, Chu, Liu and Tan. This is an open-access article distributed under the terms of the Creative Commons Attribution License (CC BY). The use, distribution or reproduction in other forums is permitted, provided the original author(s) and the copyright owner(s) are credited and that the original publication in this journal is cited, in accordance with accepted academic practice. No use, distribution or reproduction is permitted which does not comply with these terms.

Spectral denoising based on Hilbert–Huang transform combined with F-test

Xihui Bian[1,2,3]*, Mengxuan Ling[1,2,3], Yuanyuan Chu[1], Peng Liu[1] and Xiaoyao Tan[1]

[1]Key Laboratory of Separation Membranes and Membrane Processes, School of Chemical Engineering and Technology, Tiangong University, Tianjin, China, [2]Key Lab of Process Analysis and Control of Sichuan Universities, Yibin University, Sichuan, China, [3]State Key Laboratory of Plateau Ecology and Agriculture, Qinghai University, Xining, China

Due to the influence of uncontrollable factors such as the environment and instruments, noise is unavoidable in a spectral signal, which may affect the spectral resolution and analysis result. In the present work, a novel spectral denoising method is developed based on the Hilbert–Huang transform (HHT) and F-test. In this approach, the original spectral signal is first decomposed by empirical mode decomposition (EMD). A series of intrinsic mode functions (IMFs) and a residual (**r**) are obtained. Then, the Hilbert transform (HT) is performed on each IMF and **r** to calculate their instantaneous frequencies. The mean and standard deviation of instantaneous frequencies are calculated to further illustrate the IMF frequency information. Third, the F-test is used to determine the cut-off point between noise frequency components and non-noise ones. Finally, the denoising signal is reconstructed by adding the IMF components after the cut-off point. Artificially chemical noised signal, X-ray diffraction (XRD) spectrum, and X-ray photoelectron spectrum (XPS) are used to validate the performance of the method in terms of the signal-to-noise ratio (SNR). The results show that the method provides superior denoising capabilities compared with Savitzky–Golay (SG) smoothing.

KEYWORDS

denoising, Hilbert–Huang transform, empirical mode decomposition, x-ray diffraction, x-ray photoelectron spectrum, f-test

Introduction

As a fast, non-destructive analytical technique, spectral analysis plays an increasingly important role in the fields of traditional Chinese medicine (TCM) (Ma et al., 2020), food (Bian et al., 2017; Amendola et al., 2020), bio-medicine (Wu et al., 2021; Yang et al., 2022), and the environment (Sipponen and Osterberg, 2019), etc. However, spectra often contain noise from instruments and operational errors. Instrumental noise mainly includes dark noise caused by the thermal effect, photon noise caused by the photon hitting detector, and electronic noise caused by the A/D converter and circuit board error. In addition, non-standard experimental operations can also produce noise (Mishra et al., 2020). The noise could obscure some useful information in the spectra, which results in low

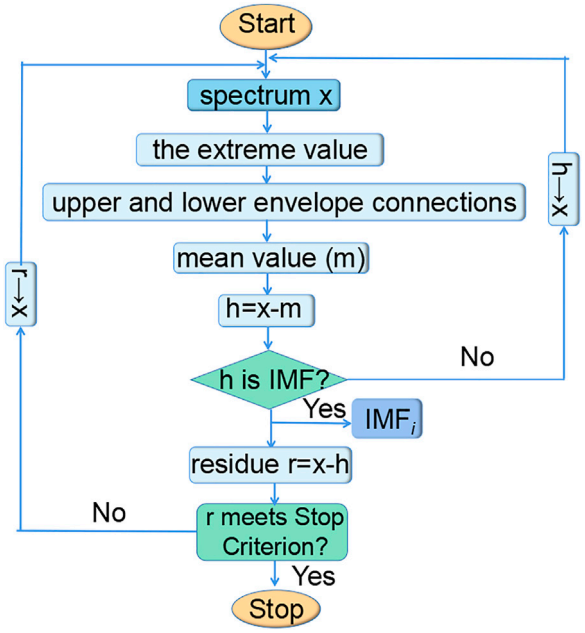


FIGURE 1
Sifting process of EMD.

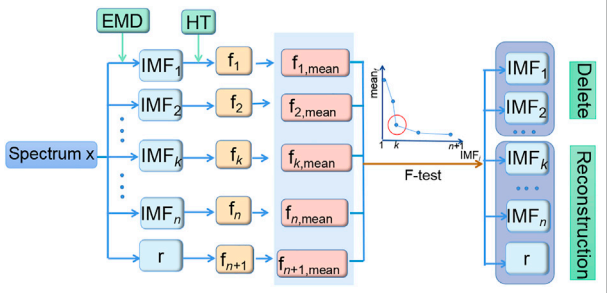


FIGURE 2
Flowchart of the spectral denoising method based on Hilbert–Huang transform combined with the F-test.

resolution and prediction accuracy. Therefore, it is essential to remove noise from the spectra without unduly reducing the underlying information (Chen et al., 2004).

The commonly used spectral signal denoising methods are Savitzky–Golay (SG) smoothing (Savitzky and Golay, 1964) and wavelet transformation (WT) (Shao et al., 2002). SG smoothing is a filtering method based on local polynomial least square fitting in the time domain, also known as convolution smoothing, which has been developed from the moving average method (Zhang et al., 2019). The SG smoothing is a weighted average method that emphasizes the role of the center point (Chu X. L. et al., 2022). A symmetric window of $i = 2\omega+1$ is used, where i and ω are the points of the moving window (i.e., window size) and half window width, respectively. The smoothed value at wavelength k is

$$x_{k,\text{smooth}} = \bar{x}_k = \frac{1}{H}\sum_{i=-\omega}^{+\omega} x_{k+i}h_i, \quad (1)$$

where h_i is the smoothing coefficient, which can be obtained by polynomial fitting based on the least square. H is the normalized factor $H = \sum_{i=-\omega}^{+\omega} h_i$. Most of the noise and interference of abnormal points can be removed by SG smoothing. Moreover, the peak shift of the spectrum is overcome without delays. However, SG smoothing is only performed once for noise removal, which cannot remove noise completely from the spectrum with in-homogeneous frequency. Compared with SG smoothing, WT is more refined and efficient because it decomposes the original spectra into details and approximations with different frequencies step by step (Shao et al., 2019). Many wavelet functions such as Haar, Daubechies, Symlets, and Coiflets have been developed for WT (Fan et al., 2017). In recent decades, WT has become quite a useful tool for signal processing in analytical chemistry (Bian et al., 2011). However, abundant wavelet functions and decomposition scales also make it difficult to select the parameters for WT (Chen et al., 2011).

To overcome the drawbacks of WT, Huang et al. (1998) introduced the Hilbert–Huang transform (HHT), which includes empirical mode decomposition (EMD) and Hilbert transform (HT). EMD can decompose any complex signal into a finite number of intrinsic modal function components (IMFs) and a residual (Bian et al., 2016). Compared with WT, the decomposition of EMD does not require any predefined basis function, which is adaptive and can be applied to any signal (Wang et al., 2018; Yao et al., 2019). Then, HT is performed on each IMF, and their corresponding instantaneous frequencies can be obtained (Peng et al., 2005). HHT denoising has been successfully used in fault diagnosis (Jin et al., 2015; Fan et al., 2022), speech recognition (Krishna and Ramaswamy, 2017), biomedical signal (Lin and Zhu, 2012; Chen et al., 2021), geophysics (Tang et al., 2015; Chen et al., 2017), and so on. However, spectral denoising by HHT is seldom used in analytical chemistry. Moreover, previous studies have determined the cut-off point between noise and useful signal by observing IMF components. However, it is difficult to distinguish. Therefore, it is crucial to determine the cut-off point between high and low frequencies.

In this research, an effective method based on HHT and F-test is proposed to eliminate the noise from the noisy spectral signal. Initially, EMD is introduced to decompose the original spectrum. A series of IMFs from high to low frequencies are obtained. Then, HT is applied to each IMF to obtain instantaneous frequencies. The mean instantaneous frequency combined with the F-test is used to determine the cut-off point between noise components and non-noise ones. Artificially

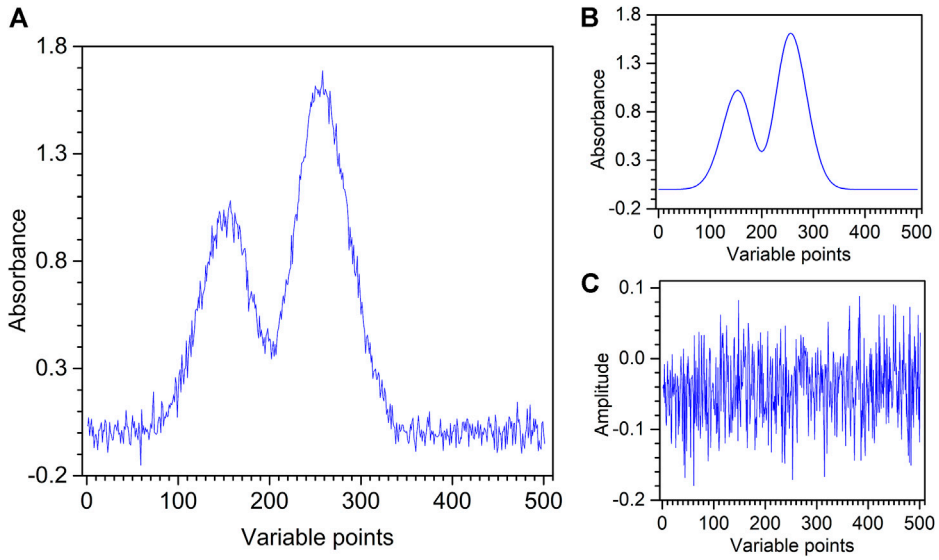


FIGURE 3
Artificially chemical noised signal **(A)** with its pure signal **(B)** and noise **(C)**.

chemical noised signal, X-ray diffraction (XRD) spectrum, and X-ray photoelectron spectrum (XPS) were used to verify the effectiveness and feasibility of the proposed method. The performance of the method is evaluated by the SNR and compared with SG smoothing.

Theory and algorithm

Empirical mode decomposition

EMD is a new adaptive spectral decomposition method. Through a sifting process, EMD can decompose spectra into a certain number of IMFs and a residual. With the increase in IMF orders, the degree of oscillation becomes lower and lower (Bian et al., 2017). The flow chart of the sifting process of EMD is shown in Figure 1.

First, in the sifting process for the spectrum, all local maxima and minima of the original spectrum **x** are connected to form upper and lower envelopes by cubic spline lines, respectively. Then, the mean values **m** of the two envelopes are computed by the simple average. Subsequently, component **h** is computed by which the difference between the original spectrum **x** and mean values **m** can be found. Whether **h** is an IMF by definition is determined. It is worth noting that the IMFs satisfy two conditions. One is that in the whole data set, the number of extreme and zero-crossings must either be the same or different at most by one. The other is that at any point, the mean value of the upper and lower envelopes is zero (Sun et al., 2006). If **h**

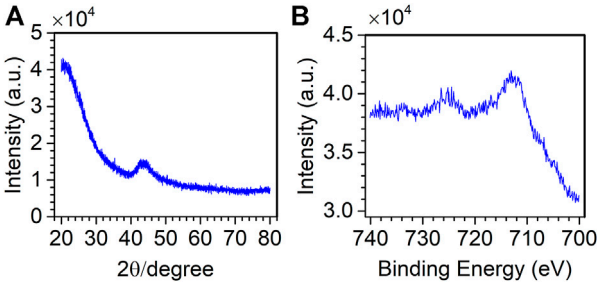


FIGURE 4
XRD spectrum of the Fe/SCN catalyst **(A)** and the XPS spectrum of the FeNiOS-NS catalyst **(B)**.

does not meet the IMF definition, **h**, as a new cycle performs the abovementioned operations until an IMF is obtained. After determining an IMF component, the component **h** is subtracted from the spectrum **x** to get the residual **r**, and whether the residual **r** becomes a monotone function is judged. Finally, the sifting process ends till the residue contains no more than one extreme.

Instantaneous frequency calculation based on Hilbert transform

Although the oscillations decrease with the increase of IMF orders, it is difficult to know the frequency value of the IMF itself.

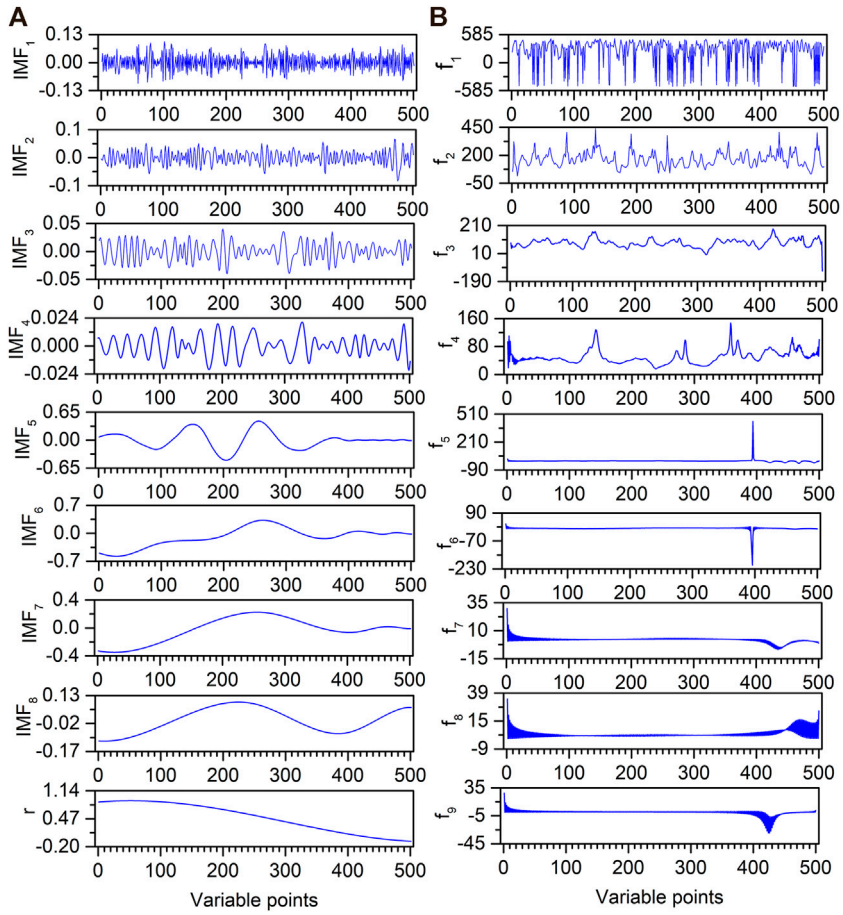


FIGURE 5
EMD decomposition results **(A)** and their corresponding instantaneous frequencies **(B)** for artificially chemical noised signal.

HT is introduced to calculate the instantaneous frequency of each IMF (Li et al., 2016).

For a signal $x(\tau)$, its Hilbert transform $H(t)$ is defined as

$$H(t) = \frac{1}{\pi} P \int_{-\infty}^{+\infty} \frac{x(\tau)}{t-\tau} d(\tau). \quad (2)$$

Eq. 2 defines HT as the convolution of $x(\tau)$ with $1/t$. Therefore, HT emphasizes the local properties of $x(\tau)$. Then, P indicates the Cauchy principal value of the singular integral to avoid singularities at $t = \tau$, $t = \pm \infty$; this transform exists for all functions of class L^P (Le Van Quyen. et al., 2001).

With this definition, $x(\tau)$ and $H(t)$ form the complex conjugate pair, and an analytic signal, $Z(t)$, is obtained,

$$Z(t) = x(t) + iH(t) = a(t)e^{i\theta(t)} \quad (3)$$

in which,

$$a(t) = \left[x^2(t) + H^2(t)\right]^{\frac{1}{2}}, \quad (4)$$

$$\theta(t) = \arctan\left(\frac{H(t)}{x(t)}\right), \quad (5)$$

where $a(t)$ is the instantaneous amplitude of $x(\tau)$, which can reflect the change of energy of $x(\tau)$ with t. $\theta(t)$ is the instantaneous phase of $x(\tau)$, and the instantaneous frequency $\omega(t)$ of signal $x(\tau)$ can be obtained as follows,

$$\omega(t) = \frac{d\theta(t)}{d(t)}. \quad (6)$$

The proposed denoising method

A novel method is proposed for spectral denoising based on EMD and HT. EMD is used to decompose the original spectrum into mono-component IMFs with different frequencies. HT is combined with F-test to determine the cut-off point of IMFs between noise components and non-noise ones. The denoising

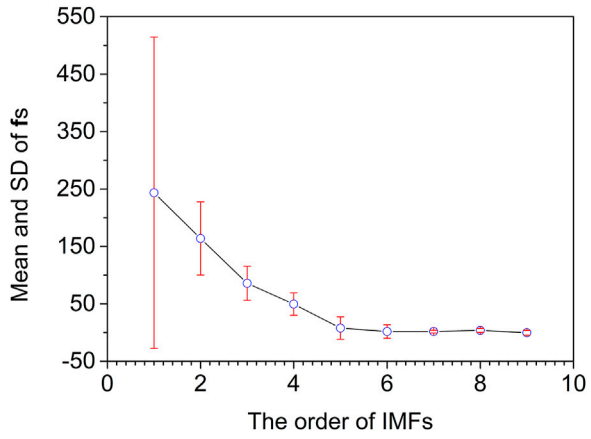


FIGURE 6
Mean and standard deviation of instantaneous frequencies for artificially chemical noised signal.

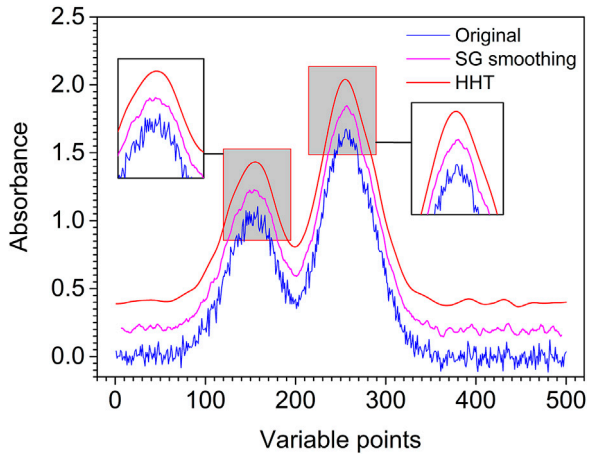


FIGURE 7
Original (blue line), SG smoothing (pink line), and HHT denoising (red line) artificially chemical noised signal.

process of the method is shown in Figure 2. The corresponding MATLAB code and datasets can be downloaded from the website https://github.com/bianxihui/chemometrics-matlab-HHT-with-F-test. The details could be described as follows.

1) The original spectrum **x** is decomposed into a finite and often small number of frequency components containing n IMFs and a residue **r** by EMD. The low-order IMFs correspond to the high-frequency components and vice versa.
2) HT is applied to each IMF component and **r** to calculate their corresponding instantaneous frequency f_1 f_2 … f_n f_{n+1} by using Eqs 2 and 5, 6. Meanwhile, mean and standard deviations of f_1 f_2 … f_n f_{n+1} are obtained.
3) The cut-off point k is judged by Eq. 7,

$$F_k = \frac{(SD_k)^2}{(SD_{k+1})^2}, \tag{7}$$

where SD_k and SD_{k+1} are the standard deviation of f_{n+1}, f_n … f_2 f_1, and F_k is the ratio of $(SD_k)^2$ to $(SD_{k+1})^2$. The significant difference of F_k is determined by the F-test with a 99.95% confidence interval. The degrees of freedom are set to 2 and 4, respectively. Furthermore, the F-test is being applied to distinguish a significant difference between the kth and (k+1)-th SD of **fs**. When F_k has a significant difference, k is judged as the cut-off point.

4) IMF_1, IMF_2, and IMF_k are the noising components that are deleted. The denoising spectrum is reconstructed by summing IMF_{k+1}, IMF_{k+2}, IMF_n, and **r**.

Experimental

The artificially chemical noised signal, XRD spectrum, and XPS spectrum are used to evaluate the performance of the proposed method. The artificially chemical noised signal is shown in Figure 3A, which is composed of 501 variables recorded in the range of 1–501, with a digitization interval of 1. It contains an artificially chemical signal with random noise in which the pure artificially chemical signal y_1 is produced by the Gaussian function represented by Eq. 8, as shown in Figure 3B.

$$y_1 = 2\exp\left[-\left(\frac{x-2}{2}+4\right)\right]|\cos x - 1.2|. \tag{8}$$

The noise signal y_2 is added by Eq. 9.

$$y_2 = 0.05 \times \mathrm{randn}(p), \tag{9}$$

where p represents the number of variables of an artificially chemical signal, that is, 501 values are generated. Moreover, randn generates values from a normal distribution with mean 1 and standard deviation 1, as shown in Figure 3C. The artificially chemical noised signal $y = y_1+y_2$.

The spectrum from the study by Wang *et al.* is measured on an X-ray diffractometer (D/MAX-RB, Japan) for catalyst materials (Fe/SCN) (Wang et al., 2021; Chu Y. Y et al., 2022). The diffraction angle range is 20–80°, the interval is 0.02°, and there are 3,001 variables.

The spectrum from the study by Chu *et al.* is measured on an X-ray photoelectron spectrometer (PHI 5700) for catalyst materials (FeNiOS-NS) (Chu Y. Y. et al., 2022). The binding energy is 700.08–740.08 eV, the interval is 0.1 eV, and there are 400 variables.

Figure 4 shows the original spectrum of XRD and XPS. By visual inspection, in Figure 4A, the spectral noise distribution is

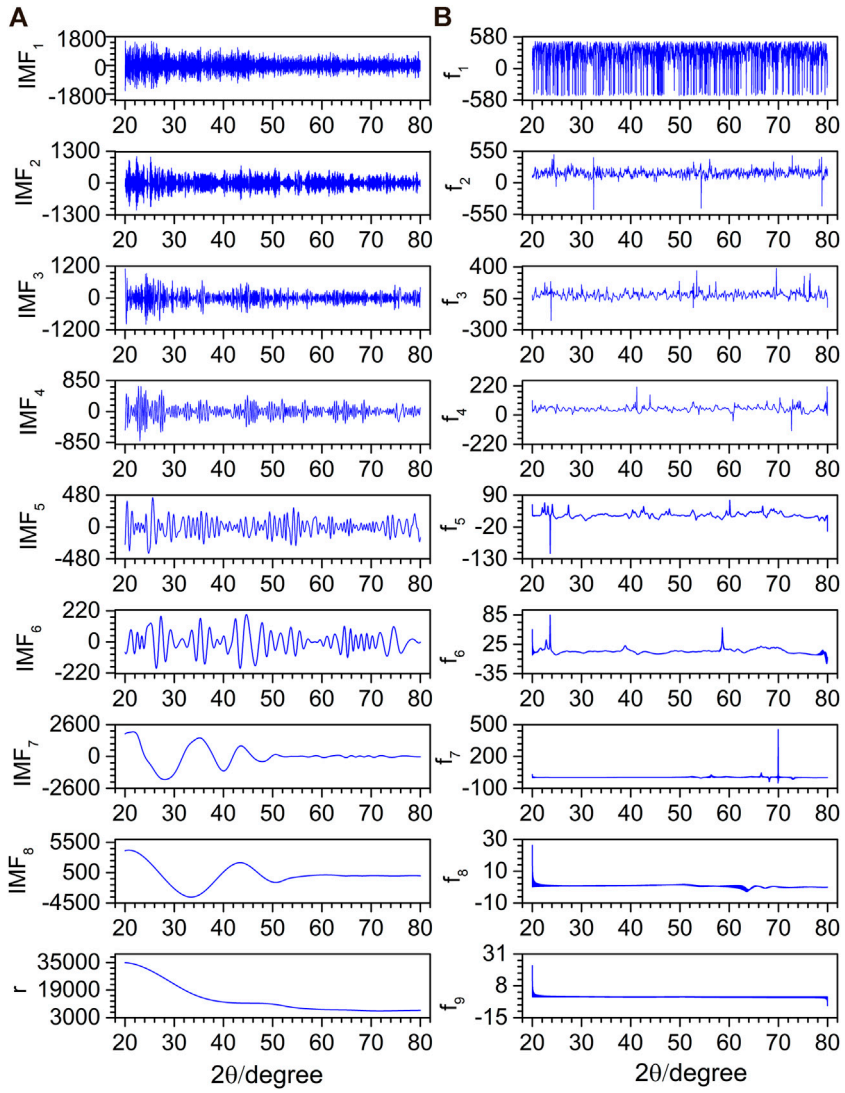


FIGURE 8
EMD decomposition results **(A)** and their corresponding instantaneous frequencies **(B)** for the XRD spectrum.

uniform, and the peak appears at the diffraction angle of 40–50 degrees. In Figure 4B, the spectrum contains sharp noise, which covers the peaks. Therefore, it is necessary to remove the useless noise and retain the useful peaks.

Results and discussion

Denoising of the artificially chemical noised signal

Based on the self-adaption and frequency decomposition superiorities, EMD is introduced to decompose the original artificially chemical noised signal. Figure 5A shows the decomposition result of EMD for an artificially chemical noised signal. The original spectrum is decomposed into eight IMFs (IMF_1–IMF_8) and an **r**. It is clear that the oscillation frequency decreases as the order of IMF becomes larger. By visual inspection, IMF_1–IMF_4 are obvious noise components with little information, while an **r** is the low-frequency components, which are extremely slow. However, it is difficult to determine whether IMF_5 is a noise component or not.

Different IMF components have different frequencies, and HT can be used to calculate their instantaneous frequencies. The HT results for IMFs of artificially chemical noised signals are shown in Figure 5B. The f_1 contains a large number of peaks. With the increase of the f order, the number of peaks gradually decreases. Although the total variation range of the instantaneous frequency

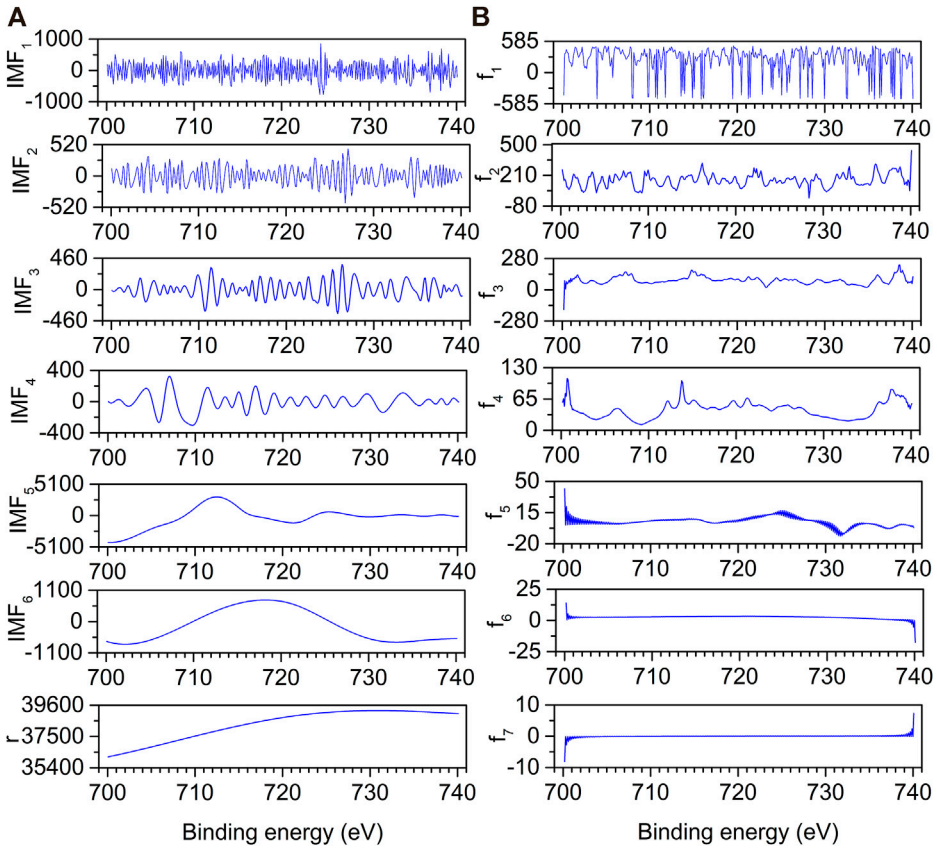


FIGURE 9
EMD decomposition results **(A)** and their corresponding instantaneous frequencies **(B)** for XPS spectrum.

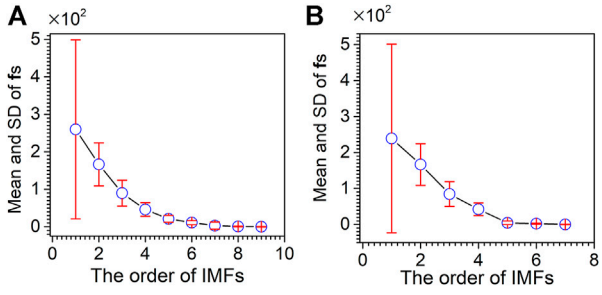


FIGURE 10
Mean and standard deviation of instantaneous frequencies for the XRD spectrum **(A)** and XPS spectrum **(B)**.

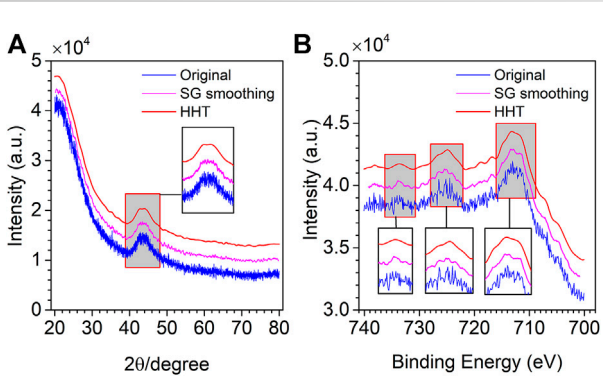


FIGURE 11
Original (blue line), SG smoothing (pink line) and HHT denoising (red line) XRD spectrum **(A)** and XPS spectrum **(B)**.

becomes smaller with the increase of the f order, the instantaneous frequency value for each variable is different for the same f order. Thus, the mean instantaneous frequencies of f_{n+1}, f_n, ... f_1 are calculated to observe the trends in frequencies. Meanwhile, the standard deviations of f_{n+1}, f_n, ... f_1 are further calculated for evaluating the noising degree of IMFs. As shown in Figure 6, the mean and standard deviation of f_1–f_4 are much higher than those of f_5–f_9. Furthermore, the mean of f_5–f_9 tends to be flat, and the

standard deviation of f_5–f_9 is relatively low. Subsequently, IMF_4 is judged as the cut-off point by the F-test. Therefore IMF_1–IMF_4 are deleted as noise, and IMF_5–IMF_8 and an **r** are reconstituted as useful signals.

To better evaluate the performance of the proposed method, SG smoothing applied to the artificially chemical noised signal denoising is compared with that of the proposed method, and SG smoothing window size is selected as 13. The comparison between the proposed method and the SG smoothing denoising results are shown in Figure 7. It is obvious from the figure that the spectrum is smoother and the peaks are more obvious after denoising by the proposed method. In order to illustrate quantitatively the superiority of the proposed method, the SNR of the two methods is calculated, where the SNR of the proposed method and SG smoothing is 22.59 and 21.60, respectively. It can be seen that compared with SG smoothing denoising, the SNR of the proposed method of denoising is improved and the denoising effect is more ideal.

Denoising of the experimental spectrum

To compare and verify the denoising effect of the proposed denoising method on the actual spectrum, noisy XRD and XPS spectra were selected for denoising. Figure 8A depicts the decomposition result of EMD for an XRD spectrum. The original spectrum is decomposed into eight IMFs (IMF_1–IMF_8) and an **r**. It is difficult to determine whether IMF_5 and IMF_6 are noise components or not by visual inspection. The instantaneous frequency of each IMF is obtained by HT, as shown in Figure 8B. With the increase of the f order, the number of peaks gradually decreases. Figure 9A depicts the EMD results of an XPS spectrum which is decomposed into six IMFs (IMF_1–IMF_6) and an **r**. The corresponding frequencies fs are calculated in Figure 9B. Similarly, whether IMF_4 is a noise component or not, cannot be determined.

The mean and standard deviation of the f order for XRD and XPS spectra are calculated. As shown in Figure 10A, for the XRD spectrum, with the increase of IMF orders, the mean instantaneous frequency of f first decreases and then approaches being flat. The change in the standard deviation of f is directly proportional to the mean instantaneous frequency. The IMF with a large mean instantaneous frequency has a large standard deviation. Five is determined as the cut-off point by the F-test for the XRD spectrum. IMF_6–IMF_8 and an **r** are reconstructed as the denoising XRD spectrum. As shown in Figure 10B, for the XPS spectrum, the variation of the mean and standard deviation of fs is similar to that of the XRD spectrum. Four is determined as the cut-off point by the F-test for the XPS spectrum. IMF_5, IMF_6, and an **r** are reconstructed as the denoising XPS spectra.

The SG smoothing is also applied to noisy XRD and XPS spectra. 21 and 17 are selected as the window size for the two spectra. Figures 11A,B show the denoising results of XRD and XPS spectra by SG smoothing and the proposed method. It is clear from Figure 11A that SG smoothing cannot remove the noise completely, and some noise is still left in the spectrum. In contrast to SG smoothing, the method proposed in this research not only makes the spectrum exceedingly smooth after denoising, but useful information is also retained. From Figure 11B, XPS spectral noise is also not completely removed by SG smoothing, especially at the three peaks. However, most of the noise is removed by the proposed method while retaining useful information.

Conclusion

A novel denoising method is proposed based on HHT combined with the F-test. EMD is applied to adaptively decompose the spectrum without setting parameters. Then, HT is performed on IMFs to calculate the instantaneous frequencies. In addition, mean instantaneous frequencies are combined with the F-test as the criterion for distinguishing noise components and non-noise ones. It is concluded that the proposed denoising method is valid by noise removal for the artificially chemical noised signal, XRD, and XPS spectra. Moreover, compared with SG smoothing, the proposed method shows superiority both in observation and the SNR.

Data availability statement

The raw data supporting the conclusions of this article will be made available by the authors, without undue reservation.

Author contributions

XB: project administration, supervision, validation, writing—review and editing, and funding acquisition. ML: methodology, software, visualization, and writing—original draft. YC: investigation, data curation, and validation. PL: supervision, resources, and writing—review, and editing. XT: funding acquisition, resources, and supervision.

Funding

This study is supported by the Key Lab of Process Analysis and Control of Sichuan Universities (No. 2020001) and the Opening Foundation of State Key Laboratory of Plateau Ecology and Agriculture (No. 2021-KF-07).

Conflict of interest

The authors declare that the research was conducted in the absence of any commercial or financial relationships that could be construed as a potential conflict of interest.

Publisher's note

All claims expressed in this article are solely those of the authors and do not necessarily represent those of their affiliated organizations, or those of the publisher, the editors, and the reviewers. Any product that may be evaluated in this article, or claim that may be made by its manufacturer, is not guaranteed, or endorsed by the publisher.

References

Amendola, L., Firmani, P., Bucci, R., Marini, F., and Biancolillo, A. (2020). Authentication of sorrento walnuts by NIR spectroscopy coupled with different chemometric classification strategies. *Appl. Sci. (Basel).* 10 (11), 4003. doi:10.3390/app10114003

Bian, X. H., Chen, D., Cai, W. S., Grant, E., and Shao, X. G. (2011). Rapid determination of metabolites in bio-fluid samples by Raman spectroscopy and optimum combinations of chemometric methods. *Chin. J. Chem.* 29 (11), 2525–2532. doi:10.1002/cjoc.201180425

Bian, X. H., Li, S. J., Lin, L. G., Tan, X. Y., Fan, Q. J., and Li, M. (2016). High and low frequency unfolded partial least squares regression based on empirical mode decomposition for quantitative analysis of fuel oil samples. *Anal. Chim. Acta* 925, 16–22. doi:10.1016/j.aca.2016.04.029

Bian, X. H., Zhang, C. X., Liu, P., Wei, J. F., Tan, X. Y., Lin, L. G., et al. (2017). Rapid identification of milk samples by high and low frequency unfolded partial least squares discriminant analysis combined with near infrared spectroscopy. *Chemom. Intell. Lab. Syst.* 170, 96–101. doi:10.1016/j.chemolab.2017.09.004

Chen, D., Cai, W. S., Shao, X. G., and Su, Q. (2004). A background and noise elimination method for quantitative calibration of near infrared spectra. *Anal. Chim. Acta* 511 (1), 37–45. doi:10.1016/j.aca.2004.01.042

Chen, D., Chen, Z. W., and Grant, E. (2011). Adaptive wavelet transform suppresses background and noise for quantitative analysis by Raman spectrometry. *Anal. Bioanal. Chem.* 400 (2), 625–634. doi:10.1007/s00216-011-4761-5

Chen, L. L., Wang, C. Y., Chen, J. J., Xiang, Z. J., and Hu, X. (2021). Voice disorder identification by using Hilbert-Huang transform (HHT) and K nearest neighbor (KNN). *J. Voice* 35 (6), 932.e1–932.e11. doi:10.1016/j.jvoice.2020.03.009

Chen, Y. K., Zhou, Y. T., Chen, W., Zu, S. H., Huang, W. L., and Zhang, D. (2017). Empirical low-rank approximation for seismic noise attenuation. *IEEE Trans. Geosci. Remote Sens.* 55 (8), 4696–4711. doi:10.1109/TGRS.2017.2698342

Chu, X. L., Huang, Y., Yun, Y. H., and Bian, X. H. (2022). "*Spectral preprocessing methods" in chemometric methods in analytical spectroscopy technology.*. Springer, Singapore Press, 111–168.

Chu, Y. Y., Zhang, X. X., Deng, B. H., Wang, K. X., and Tan, X. Y. (2022). A facile method to synthesize 3D nanosheets of Fe/S doped α-Ni$(OH)_2$ as an electrocatalyst for improved oxygen evolution reaction. *Nanotechnology* 33 (40), 405605. doi:10.1088/1361-6528/ac5aeb

Fan, M. L., Cai, W. S., and Shao, X. G. (2017). Investigating the structural change in protein aqueous solution using temperature-dependent near-infrared spectroscopy and continuous wavelet transform. *Appl. Spectrosc.* 71, 472–479. doi:10.1177/0003702816664103

Fan, M., Xia, J. L., Meng, X. Y., and Zhang, K. (2022). Single-phase grounding fault types identification based on multi-feature transformation and fusion. *Sensors* 22 (9), 3521. doi:10.3390/s22093521

Huang, N. E., Sheng, Z., Long, S. R., Wu, M. L. C., Shih, H. H., Zheng, Q. N., et al. (1998). The empirical mode decomposition and the Hilbert spectrum for nonlinear and non-stationary time series analysis. *P. Roy. Soc. A-Math Phy.* 454, 903–995. doi:10.1098/rspa.1998.0193

Jin, S., Kim, J. S., and Lee, S. K. (2015). Sensitive method for detecting tooth faults in gearboxes based on wavelet denoising and empirical mode decomposition. *J. Mech. Sci. Technol.* 29 (8), 3165–3173. doi:10.1007/s12206-015-0715-8

Krishna, P. K. M., and Ramaswamy, K. (2017). Single channel speech separation based on empirical mode decomposition and Hilbert transform. *IET signal Process.* 11 (5), 579–586. doi:10.1049/iet-spr.2016.0450

Le Van Quyen, M, Foucher, J., Lachaux, J. P., Rodriguez, E., Lutz, A., Martinerie, J., et al. (2001). Comparison of Hilbert transform and wavelet methods for the analysis of neuronal synchrony. *J. Neurosci. Methods* 111 (2), 83–98. doi:10.1016/S0165-0270(01)00372-7

Li, H., Xue, G. Q., Zhao, P., Zhong, H. S., and Khan, M. Y. (2016). The hilbert-huang transform based denoising method for the TEM response of a PRBS source signal. *Pure Appl. Geophys.* 173 (8), 2777–2789. doi:10.1007/s00024-016-1308-x

Lin, C. F., and Zhu, J. D. (2012). Hilbert-huang transformation-based time-frequency analysis methods in biomedical signal applications. *Proc. Inst. Mech. Eng. H.* 226 (H3), 208–216. doi:10.1177/0954411911434246

Ma, L. J., Liu, D. H., Du, C. Z., Lin, L., Zhu, J. Y., Huang, X. G., et al. (2020). Novel NIR modeling design and assignment in process quality contral of honeysuckle flower by QbD. *Spectrochimica Acta Part A Mol. Biomol. Spectrosc.* 242, 118740. doi:10.1016/j.saa.2020.118740

Mishra, P., Biancolillo, A., Roger, J. M., Marini, F., and Rutledge, D. N. (2020). New data preprocessing trends based on ensemble of multiple preprocessing techniques. *TrAC Trends Anal. Chem.* 132, 116045. doi:10.1016/j.trac.2020.116045

Peng, Z. K., Tse, P. W., and Chu, F. L. (2005). An improved Hilbert-Huang transform and its application in vibration signal analysis. *J. Sound. Vib.* 286 (1-2), 187–205. doi:10.1016/j.jsv.2004.10.005

Savitzky, A., and Golay, M. J. E. (1964). Smoothing and differentiation of data by simplified least squares procedures. *Anal. Chem.* 36, 1627–1639. doi:10.1021/ac60214a047

Shao, L. M., Lin, X. Q., and Shao, X. G. (2002). A wavelet transform and its application to spectroscopic analysis. *Appl. Spectrosc. Rev.* 37 (4), 429–450. doi:10.1081/ASR-120016391

Shao, X. G., Cui, X. Y., Wang, M., and Cai, W. S. (2019). High order derivative to investigate the complexity of the near infrared spectra of aqueous solutions. *Spectrochimica Acta Part A Mol. Biomol. Spectrosc.* 213, 83–89. doi:10.1016/j.saa.2019.01.059

Sipponen, M. H., and Osterberg, M. (2019). Aqueous ammonia pre-treatment of wheat straw: process optimization and broad spectrum dye adsorption on nitrogen-containing lignin. *Front. Chem.* 7, 545. doi:10.3389/fchem.2019.00545

Sun, Z. Q., Zhou, J. M., and Zhou, P. (2006). Application of Hilbert-Huang transform to denoising in vortex flowmeter. *J. Cent. South Univ. Technol.* 13 (5), 501–505. doi:10.1007/s11771-006-0076-7

Tang, J. T., Ren, Z. Y., Zhou, C., Zhang, L. C., Yuan, Y., and Xiao, X. (2015). Frequency-domain electromagnetic methods for exploration of the shallow subsurface: a review. *Chin. J. Geophys-Ch* 58 (8), 2681–2705. doi:10.6038/cjg20150807

Wang, K. X., Chu, Y. Y., Zhang, X. X., Zhao, R. C., and Tan, X. Y. (2021). Facile method to synthesize a high-activity S-doped Fe/SNC single-atom catalyst by metal-organic frameworks for oxygen reduction reaction in acidic medium. *Energy Fuels* 35 (24), 20243–20249. doi:10.1021/acs.energyfuels.1c03198

Wang, R. K., Sun, S. G., Guo, X. H., and Yan, D. (2018). EMD threshold denoising algorithm based on variance estimation. *Circuits Syst. Signal Process.* 37 (12), 5369–5388. doi:10.1007/s00034-018-0819-3

Wu, X. Y., Bian, X. H., Lin, E., Wang, H. T., Guo, Y. G., and Tan, X. Y. (2020). Weighted multiscale support vector regression for fast quantification of vegetable oils in edible blend oil by ultraviolet-visible spectroscopy. *Food Chem.* 342, 128245. doi:10.1016/j.foodchem.2020.128245

Wu, Z. X., Jiang, D. J., Hsieh, C. W., Chen, G. Y., Liao, B., Cao, D. S., et al. (2021). Hyperbolic relational graph convolution networks plus: a simple but highly efficient QSAR-modeling method. *Brief. Bioinform.* 22 (5), bbab112. doi:10.1093/bib/bbab112

Yang, X., Wu, Z. Y., Ou, Q. H., Qian, K., Jiang, L. Q., Yang, W. Y., et al. (2022). Diagnosis of lung cancer by FTIR spectroscopy combined with Raman spectroscopy based on data fusion and wavelet transform. *Front. Chem.* 10, 810837. doi:10.3389/fchem.2022.810837

Yao, Z. J., Liu, X. J., Yang, W. J., Wang, C. C., and Chang, S. P. (2019). A coarse-to-fine denoising method for dynamic calibration signals of pressure sensor based on adaptive mode decompositions. *Measurement* 163, 107935–171321. doi:10.1016/j.measurement.2020.107935

Zhang, G. W., Peng, S. L., Cao, S. Y., Zhao, J., Xie, Q., Han, Q. J., et al. (2019). A fast progressive spectrum denoising combined with partial least squares algorithm and its application in online Fourier transform infrared quantitative analysis. *Anal. Chim. Acta.* 1074, 62–68. doi:10.1016/j.aca.2019.04.055

frontiers | Frontiers in Chemistry

TYPE Original Research
PUBLISHED 15 September 2022
DOI 10.3389/fchem.2022.977980

Check for updates

OPEN ACCESS

EDITED BY
Lorraine Christine Nagle,
University College Cork, Ireland

REVIEWED BY
Buzuayehu Abebe,
Adama Science and Technology University, Ethiopia
Wei Wei,
Jiangsu University, China

*CORRESPONDENCE
Aliona Nicolenco,
alionanicolenco@gmail.com
Henrikas Cesiulis,
henrikas.cesiulis@chf.vu.lt

SPECIALTY SECTION
This article was submitted to Electrochemistry, a section of the journal Frontiers in Chemistry

RECEIVED 25 June 2022
ACCEPTED 25 August 2022
PUBLISHED 15 September 2022

CITATION
Vainoris M, Nicolenco A, Tsyntsaru N, Podlaha-Murphy E, Alcaide F and Cesiulis H (2022), Electrodeposited Fe on Cu foam as advanced fenton reagent for catalytic mineralization of methyl orange.
Front. Chem. 10:977980.
doi: 10.3389/fchem.2022.977980

COPYRIGHT
© 2022 Vainoris, Nicolenco, Tsyntsaru, Podlaha-Murphy, Alcaide and Cesiulis. This is an open-access article distributed under the terms of the Creative Commons Attribution License (CC BY). The use, distribution or reproduction in other forums is permitted, provided the original author(s) and the copyright owner(s) are credited and that the original publication in this journal is cited, in accordance with accepted academic practice. No use, distribution or reproduction is permitted which does not comply with these terms.

Electrodeposited Fe on Cu foam as advanced fenton reagent for catalytic mineralization of methyl orange

Modestas Vainoris[1], Aliona Nicolenco[2,3]*, Natalia Tsyntsaru[1,2], Elizabeth Podlaha-Murphy[4], Francisco Alcaide[5] and Henrikas Cesiulis[1]*

[1]Faculty of Chemistry and Geosciences, Vilnius University, Vilnius, Lithuania, [2]Institute of Applied Physics of ASM, Chisinau, Moldova, [3]Departament de Física, Universitat Autònoma de Barcelona, Bellaterra, Spain, [4]Department of Chemical and Biomolecular Engineering Clarkson University, Potsdam, NY, United States, [5]CIDETEC, Basque Research and Technology Alliance (BRTA), Donostia-San Sebastián, Spain

In many countries, the textile industry remains the major contributor to environmental pollution. Untreated textile dyes discharged into water negatively impact the performance of aquatic organisms and may cause a variety of serious problems to their predators. Effective wastewater treatment is a key to reducing environmental and human health risks. In this work, the Fe/Cu catalysts were used in heterogeneous Fenton's reaction for the degradation of high concentrations of methyl orange (model azo dye) in aqueous solutions. For the first time, the catalysts were prepared onto commercial copper foams by potentiostatic electrodeposition of iron using an environmentally friendly electrolyte. The influence of electrodeposition conditions, H_2O_2 concentration, dye concentration and temperature on the model dye degradation was investigated. It was revealed that both the surface area and the catalyst loading play the major role in the effective dye degradation. The experimental results involving spectrophotometric measurements coupled with total carbon and nitrogen quantification suggest that a solution containing up to 100 mg/L of methyl orange can be successfully decolorized within 90 s at 50°C using porous Fe/Cu catalyst in the presence of hydrogen peroxide that largely surpasses the current state-of-the-art performance. Already within the first 10°min, ~ 30% of total methyl orange concentration is fully mineralized. The described process represents a cost-efficient and environmentally friendly way to treat azo dyes in aqueous solutions.

KEYWORDS

heterogeneous fenton reaction, electrodeposition, Fe/Cu catalyst, methyl orange, enviromentally friendly

Introduction

The production volume in the textile industry is increasing each year, which generates huge amounts of effluent containing dyes and other pollutants. Textile wastewater must be treated to remove or decrease the concentration of pollutants to the acceptable levels before its reuse or discharging into the environment (Holkar et al., 2016). This is especially the case of widely used azo dyes which contain one or more nitrogen-to-nitrogen double bonds (-N=N-) (Li et al., 2015; Sha et al., 2016), and 60–70% of dye groups and are fairly stable (Ananthashankar et al., 2013). Over the years various physical (coagulation, adsorption, reverse osmosis), chemical (ozonation and chlorination), and anaerobic biodegradation techniques have been developed to remove organic pollutants, including the azo dyes (Vandevivere et al., 1998; Murali et al., 2013). Usually, these techniques require expensive equipment, and do not fully mineralize all the pollutants but rather convert them into other organic compounds. In addition, the cleaning process may cause undesirable effects, e.g., chlorine gas evolution or precipitates, when chlorination is used as a water remediation procedure (Dutta et al., 2001; Tak and Kumar, 2017).

In recent years, advanced oxidation processes (AOPs) as a way to mineralize various organic dyes in waste water, and due to their high efficiency AOPs have drawn considerable attention. Also, decolorization dyes based on Fenton processes are of great interest (Miklos et al., 2018). Generally, this process involves a generation of the most reactive oxidizing agent in water treatment, namely reactive hydroxyl radicals, which non-selectively and rapidly react with numerous species. Since hydroxyl radicals have a very short lifetime, they are only produced *in-situ* through different chemical reactions processes. Fe(II) is the most frequently used because it can activate H_2O_2 and produce hydroxyl radicals in water (Deng and Zhao, 2015). In the Fenton process, H_2O_2 reacts with Fe^{2+} to generate strong reactive species.

The reactive species produced are traditionally recognized as hydroxyl radicals, though other substances such as ferryl-ions (also products of this reaction) (Deng and Zhao, 2015). In addition to Fe^{2+} ions, the oxidizing solution may contain other metal ions, e.g., Cu^{+}, Cr^{3+}, Co^{2+}, Ti^{3+}, W^{6+}, Mo^{n+}, etc., that can catalyze similar (Fenton-like) reactions (Wang et al., 2016; Zhang et al., 2018; Séverin et al., 2020). Remarkably, bimetallic Fenton reagents demonstrate a higher catalytic efficiency compared to the homogeneous Fe(II)-based catalysts. The activity of the catalyst can be greatly enhanced by combining Cu and Fe, where Cu can strongly accelerate the reduction cycle of Fe^{3+} to Fe^{2+} (Fe^{2+} has higher reaction rate when breaking down hydrogen peroxide) through exposed metal active sites and increase the accumulation of •OH oxidants in the system (Rossi et al., 2014). Heterogeneous Fe/Cu catalysts demonstrated great activity at various concentrations of organic matter as well as stability with multiples uses (Rossi et al., 2014; Wang Y. et al., 2015; Zhang et al., 2017).

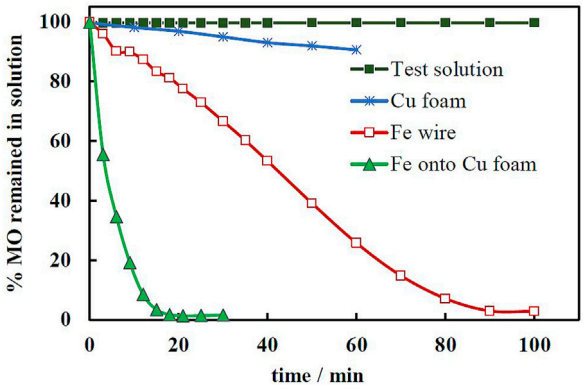


FIGURE 1
Preliminary evaluation of the catalytic activity of plane and 3D surface catalysts for degradation of MO. The geometrical area was 1 cm^2 on all used substrates. The catalysts were electrodeposited at -1.5 V and q = 150 C. The test solution contained 100 mg/L of MO, 20 g/L Na_2SO_4 and 25 μL of H_2O_2.

Sludge management is an important factor that greatly affects the total treatment costs. One of the ways to reduce the amount of generated sludge is to use heterogeneous Fenton instead of homogeneous reaction, because the heterogeneous reaction has lower activation energy than the homogenous one (Karthikeyan et al., 2011), and higher removal efficiency (Fontecha-Cámara et al., 2011; Zárate-Guzmán et al., 2019). The overview of main advantages and disadvantages of different Fenton processes were discussed in details in (Xu et al., 2020). Moreover, the efficiency of the Fenton process can be manipulated by applying photo degradation and using various iron oxidation states for active hydroxyl radical's generation (Devi et al., 2010).

Surface texturization is an energy-efficient approach to achieve high degree of organics breakdown. Highly active catalysts can be prepared by immobilizing (or depositing) iron species into porous templates, e.g., zeolites, activated carbon, etc., or using various nanoparticles (Fontecha-Cámara et al., 2011; Wang J. et al., 2015; Litter, 2017). However, these templates could clump up in real wastewater forming larger clusters.

Metal foam as a substrate for catalyst looks attractive because it has durability, ductility, light specific weight. In addition, such 3D porous materials have numerous applications in electrochemical technologies. Therefore, in this work, we fabricated an advanced Fe/Cu-foam catalyst for Fenton's reaction, where a thin Fe coating was electrodeposited onto highly porous metallic copper foam. From the catalytic point of view, the importance has an "effective area" of catalyst in the reaction media, that in our case it is a solution. In order to estimate this parameter in the solution, the capacity of double electric layer (DEL) was chosen as an indicator of the effective surface area. DEL is thin enough in the moderately concentrated

solutions (tens of nanometers), and replicates all surface irregularities that are higher than the thickness of DEL. The peculiarities of mass-transport, charge transfer and charging of DEL on the foam electrode were described in (Vainoris et al., 2020). The fabricated Fe/Cu-foam catalyst seems an attractive substrate for catalysts as the effective surface area of the foam is from 7 to 14 times bigger than the geometrical area of the smooth surface (Vainoris et al., 2020). Moreover, our preliminary results on the evaluation of the catalytic activity of plane surface (copper wire) vs. foam (Figure 1) confirm the effectiveness of the 3D substrate (taken into account that the geometrical area was the same). Therefore, in this paper we will be dealing with the foam substrate only.

In addition, the environmental issues were taken into account in this study, therefore for the electrodeposition process, i.e., an Fe(III)-based citrate-glycolate electrolyte (Mažeika et al., 2021) was used to ensure the stability of the bath over long periods of time and a high deposition rate. The activity of obtained catalysts was assessed using an aqueous solution of model nitro-dye, i.e., methyl orange (MO), investigating the rate of decolorization and degree of mineralization. The effects of various parameters that may influence the rate of Fenton-like heterogeneous reaction such as operating temperature, concentrations of dye and hydrogen peroxide were evaluated.

Materials and methods

Materials and sample preparation

All the chemicals were of analytical grade and were used without further purification (Carl Roth, Karlsruhe, Germany). Solutions have been prepared using deionized water (DI). Cu foam electrodes served as working electrodes were purchased from Alfa Aesar. The porosity of these electrodes is ~90–91%. Electrochemical depositions have been performed and controlled using programmable potentiostat/galvanostat AUTOLAB PGSTAT 128N (Metrohm, Utrecht, Netherlands); the software used for controlling the hardware was Nova 1.11.2. All electrodepositions have been performed using a standard three-electrode cell, where Cu foam acted as a working electrode, circular platinized titanium mesh (Alfa Aesar, Ward Hill, MA, United States) was used as a counter electrode, and Ag/AgCl/KClsat (Sigma-Aldrich, St. Louis, MO, SA) was used as a reference electrode. All values of potentials are indicated in the text against this reference electrode. The distance between the counter and working electrode was fixed at 2.5 cm, and the distance between working and reference electrodes was fixed at 1.5 cm. The geometric size of working porous electrodes was 1 cm × 1 cm.

Prior measurements working electrodes have been washed and degreased using acetone, ethanol, and water in the ultrasonic bath. The native copper oxide layer has been removed by dipping copper foam into 2 M H_2SO_4 solution for 10 s and afterward rinsed with DI water. Electrodeposition of iron was carried out using a Fe(III)-based solution to avoid bath stability issues: 0.1 M $Fe_2(SO4)_3$, 0.3 M citric acid, and 1 M glycolic acid (Nicolenco et al., 2018). The pH of solutions was adjusted to 6.5 by sodium hydroxide and measured using a pH-meter ProLine Plus (Prosence B.V, Oosterhout, Netherlands). The electrodeposition was carried out at a constant temperature of 60°C (±0.5°C) and under constant stirring using a magnetic stirring bar at 600 rpm. Three distinct potentials have been chosen for electrodeposition: 1.5, −1.7, and −1.9 V with five corresponding amounts of charge for each potential applied: 150, 300, 450, 900, and 1350 C. All the depositions were replicated at least 8 times.

Catalytic activity

MO aqueous solution was used to evaluate the catalytic activity of the modified foams. The test solution contained 40, 70, or 100 mg/L of MO and 20 g/L Na_2SO_4. The pH was adjusted to pH 3 (±0.1) using 95% H_2SO_4 solution. The temperature of the dye solution was kept at chosen value (30, 40, or 50°C) and constant stirring was applied using a magnetic stirring bar at 600 rpm. All the experiments were carried out in 100 ml cell. Hydrogen peroxide was added to the beaker with MO solution 1 min before the experiment, allowing the full distribution of it.

The modified copper foams were immersed into the dye solution for 10 min unless stated otherwise. The decolorization of the solution was tracked every minute by extracting 2 ml of solution and measuring the light absorption in 320–620 nm range (scan step 2 nm) using a spectrophotometer (T60 UV-Visible Spectrophotometer, PG Instruments Limited, United Kingdom). After the measurement, the aliquot was poured back into the beaker. The current efficiency was determined gravimetrically by tracking the weight of copper before deposition and after deposition of Fe.

The total organic content (TOC) and total nitrogen (TN) were determined using the TOC-VCSN Shimadzu analyzer (with TNM-1 block for nitrogen determination). The analysis was carried out after removing iron from the test solution by increasing pH to 9.8 using a 7 M NaOH solution. The formed iron oxides and hydroxides have been removed via centrifuge, and the supernatant was used for TOC and TN analysis.

Characterization

The morphology of Fe-covered copper foams was investigated using a scanning electron microscope (SEM, Hitachi's Tabletop Microscope TM-3000, Tokyo, Japan), equipped with an EDX module.

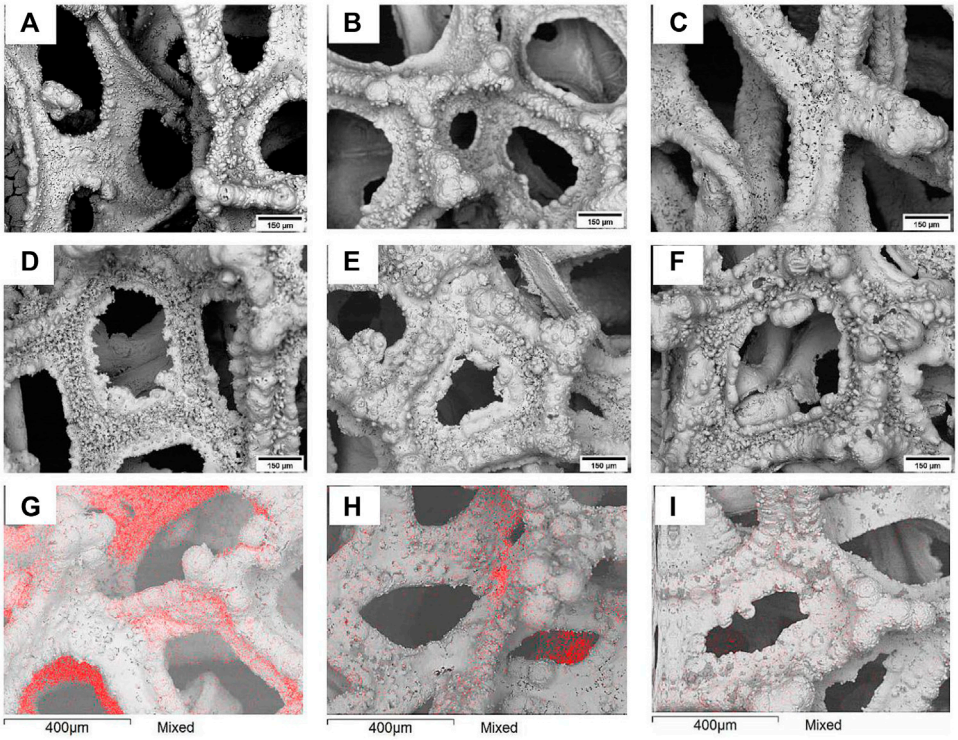


FIGURE 2
SEM images of electrochemically deposited copper under different conditions: top row q = 450 C **(A)** −1.5 V, **(B)** −1.7 V **(C)** −1.9 V; middle row—E = −1.9 V **(D)** q = 150 C, **(E)** q = 900 C, **(F)** q = 1350 C; bottom row—SEM/EDS map analysis, where the red color on the images indicates the Cu distribution at **(G)** 150 C, **(H)** 300 C, **(I)** 450 **(C)**.

Results and discussion

Electrochemical iron deposition onto copper foam

Electrodeposition onto 3D substrates is generally challenging due to the complicated mass transport of charged species through the channels of the substrate. To obtain a good quality, the electrodeposition of Fe coating onto the Cu foam was performed under strict control of temperature and stirring. Three specific potential values were selected. For each one five distinct amounts of coulombs were let through the electrochemical cell. Figure 1 shows the surface morphology of obtained Fe/Cu catalysts.

With increasing the cathodic potential, Fe deposits become dendritic (see Figures 2A–C). It is worth mentioning that due to the complex shape of the copper foams all substrates exhibited a certain degree of edge effect, i.e., quicker growth and formation of an almost foam-like structure was observed at the edges of the foam substrate. Remarkably, such unevenly structured Fe deposits could provide more active sites for the Fenton reaction catalysis comparing to the flat surfaces. With increase in deposition time (i.e., charge passed, see Figures 2D–F), uneven bumps are developed on the surface, which could increase the surface area and enhance the activity of heterogeneous catalyst. Furthermore, the EDS map analysis (Figures 2G–I) reveals open copper parts at short electrodeposition time (60% of copper and 40% of iron), which are losing their visibility under prolonged time (increased charged passed).

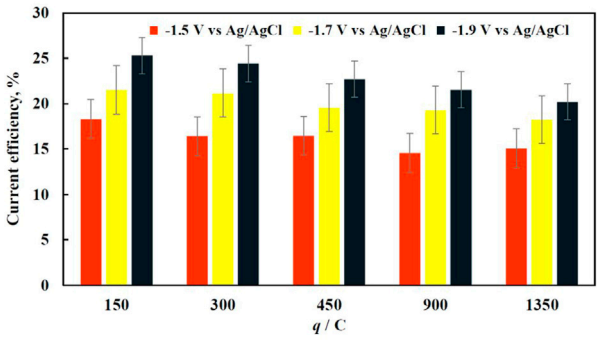


FIGURE 3
The dependence of current efficiency for iron deposition on the amount of charge passed through the electrochemical cell at various applied potentials (marked on the graph).

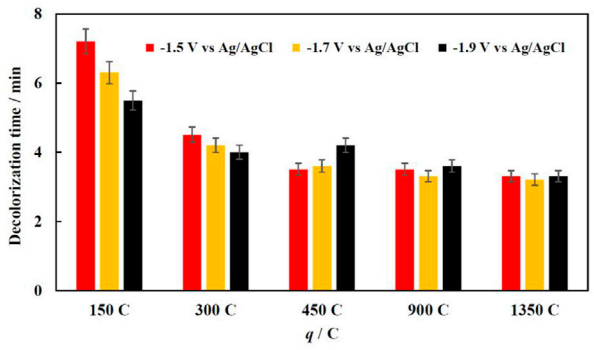


FIGURE 4
Effect of electrodeposition conditions (potential applied and charge passed) on decolorization time of 70 mg/L MO solution at 30°C.

As it is seen in Figure 3, the current efficiency of the deposition did not exceed 30% regardless the potential applied. This is mainly caused by abundant hydrogen evolution reaction that accompanies iron electrodeposition and adsorption of organic matter on the working electrode that blocks the active surface of the electrode. At lower cathodic potentials, the current density is quite low, hence the rate of iron electrodeposition is quite slow and the surface coverage is not uniform probably due to electrocrystallization limits. With the increase in applied cathodic potential, there is a noticeable increase in the current efficiency, which is most likely caused by the interplay of partial current of side reactions and iron electrodeposition.

As the deposition time increases, the current efficiency drops regardless of the applied potential (Figure 3) probably due to the vigorous mixing that breaks apart the fragile dendrite-like structure. Nevertheless, the drop is relatively small, i.e., ~3%. However, the decrease of current efficiency under longer deposition time becomes more significant at higher potentials. The morphology of iron deposits at −1.9 V vs. Ag/AgCl becomes foam-like (foam formation on the copper foam), and the moving electrolyte solution inside of the copper foams pores destroys this less mechanically stable structure. The drop in the current efficiency, when comparing the shortest and longest deposition times, becomes around 5% and is significant since the overall deposition efficiency reaches its maximum at approximately 25%.

The effect of Fe electrodeposition potential on fenton reaction rate

To evaluate the effects of both the amount of deposited iron and eventual changes in morphology on the heterogenous Fenton reaction rate, the catalysts were electrochemically deposited under three distinct potentials with five different amounts of charge passed from 150 to 1300 C. The evaluation of catalytic activity was performed at 30°C tracking the average decolorization time in 70 mg/L MO solution in the presence of 90 µL of H_2O_2.

The mechanism of MO degradation involves the cleavage of–N=N- bond with the formation of sulfanil ion and an aromatic amine and causes the disappearance of a characteristic color of the solution. The reaction process further through several steps that lead to full degradation of MO (Han et al., 2015). The obtained results are shown in Figure 4.

When 150 or 300 C are passed for Fe electrodeposition (thinner Fe film deposited and the smaller fraction of coverage Cu substrate by Fe), the decolorization time depends on both the potential and amount of passed charge. When Fe was deposited at higher potentials, the obtained Fe surface has more bumps and an almost foam-like structure (Figure 2), and in turn has more active sites. When a certain amount of iron is deposited on the copper foam, the Fenton reaction occurs at high enough rate, because the iron coating corrodes quickly in acidic media in the presence of H_2O_2 and forms enough Fe^{2+} ions, which later catalytically breakdown hydrogen peroxide into hydroxyl radicals, which in turn degrade organic dyes. The sequence of reactions occurs that within the modified Fenton process in the presence of Fe powder was proposed in (Gomathi Devi et al., 2009).

Further increasing the deposition time and amount of electrodeposited iron on the foam surface did not affect effect on the discoloration rate. The thick iron layer also prevents Cu to participate in a Fenton-like reaction, thus increasing the efficiency of the reaction by replenishing Fe^{2+} ions. However, increasing the amount of iron on the foam could reduce the mineralization efficiency, because of possible side reactions, which consume the ferrous ions and reduce the overall oxidation capacity.

The effect of charge passed for Fe electrodeposition (*q*) at various MO concentrations

The effect of the amount of charge applied for Fe electrodeposition onto Cu foam on MO decolorization time was investigated at three concentrations of MO, i.e., 40, 70, and 100 mg/L, because these concentrations are close enough to those being found in the real wastewater (Yaseen and Scholz, 2019). The layers of Fe were electrodeposited at −1.9 V, because the best performance even at small *q* was obtained (for comparison see Figure 4). The other parameters were kept as 40°C and 90 µL of H_2O_2. The acquired dependences of decolorization time on charge amount passed for catalyst formation are shown in Figure 5.

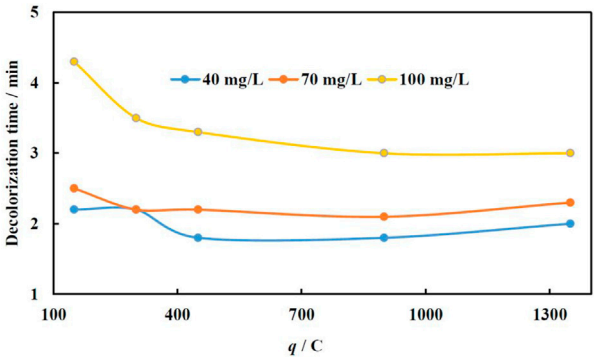


FIGURE 5
Dependence of decolorization time on MO concentration and catalyst deposition conditions (charge passed), at 40°C, 90 μL H_2O_2. Fe was electrodeposited at −1.9 V.

The catalysts with a relatively low Fe load (less amount of q used for electroforming) and therefore higher fraction of exposed Cu substrate demonstrate a lower catalytic efficiency as compared to a catalyst with a higher load of Fe (higher amount of q used for electroforming). The same results were obtained for the catalysts with high Fe loading, i.e., produced at 1350 C, where the Cu substrate is fully covered, and no exposed regions are in contact with the solution.

Effect of hydrogen peroxide concentration on fenton reaction rate

The mechanism of the Fenton reaction is quite complicated. Both heterogeneous and homogeneous reactions can occur simultaneously, and interdependencies exist between concentrations of organic matter, iron ions, and hydrogen peroxide. To determine the optimal H_2O_2 concentration, three concentrations of MO were chosen, and the catalyst with an excessive amount of iron (deposited at −1.9 V and q = 450 C) was used. The experiments were conducted at 30 and 40°C.

Figure 6 shows the variation of decolorization time as a function of the total H_2O_2 volume added to the MO solution. The fastest discoloration rate at lowest added H_2O_2 volumes was achieved for a solution containing the lowest concentration of MO, i.e., 40 mg/L. The results imply that the solution became transparent in less than 2 min after adding 50 μL of H_2O_2 (0.6 mm). Remarkably, when increasing MO concentration up to 100 mg/L, the optimal ratio between MO and hydrogen peroxide concentrations remains the same. Thus, for a 70 mg/L MO solution the optimal concentration of peroxide is 90 μL (1.1 mm), and for 100 mg/L MO—120 μL (or 1.2 mm of H_2O_2), that gives a factor of f = 0.8. This coefficient has been applied in all following experiments with variable concentration of MO in the solution. Note, that using a too low concentration of peroxide results either in a partial decolorization of the solution or a slower decolorization and only a partial mineralization. A large surplus of H_2O_2 does not increase the rate of discoloration. It is probably due to the complexity of the Fenton reaction (Gomathi Devi et al., 2009), where the initial concentration of organic compounds is directly responsible for decolorization time, and the rate-determining step of dye decolorization is the dye reaction with •OH radicals (Eq. 1):

$$\bullet OH + Dye \rightarrow Oxidised\ dye + H_2O \quad (1)$$

It is surmised that under surplus of H_2O_2 the concentration of •OH radicals in the solution are kept high enough, and does not influence the decolorization rate of MO at relatively small concentrations of one (40–70 mg/L), whereas at a higher

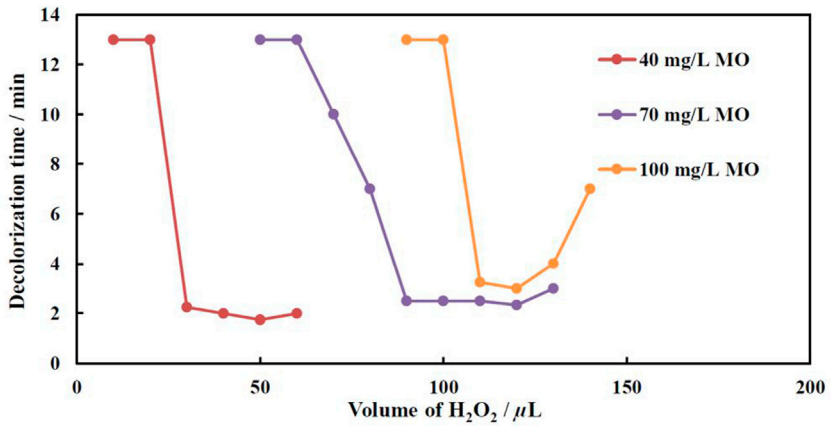


FIGURE 6
Effect of H_2O_2 concentration on decolorization time at various MO concentrations at 40°C. The catalyst was electrodeposited at −1.9 V, q = 450 C.

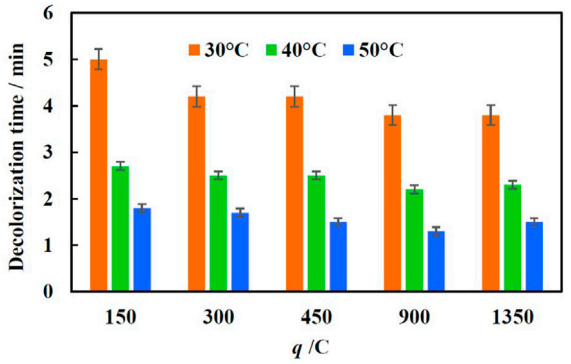


FIGURE 7
Dependence of decolorization time of 70 mg/L of MO solution (H_2O_2 conc.—90 μL) on temperature and amount of electric charge applied for iron deposition conditions.

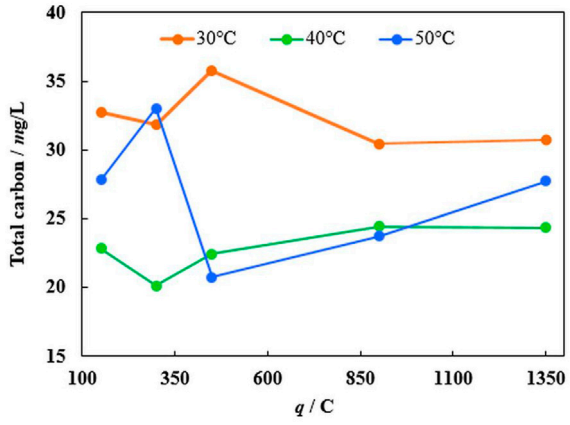


FIGURE 8
The dependence of total carbon amount after 10 min of degradation with immersed catalyst (obtained at −1.9 V) at various temperatures and iron loadings (charge passed).

concentration of MO (100 mg/L) the consumption rate of •OH radicals became higher than the generation of one's rate under reactions (Eqs. 2–5) (Gomathi Devi et al., 2009):

$$Fe^0 + H_2O_2 \rightarrow Fe^{2+}_{ads} \quad (2)$$

$$Fe^{2+}_{ads} + H_2O_2 \rightarrow Fe^{3+} + 2\bullet OH \quad (3)$$

$$Fe^0 + H_2O_2 \rightarrow Fe^{2+} + 2OH^- \quad (4)$$

$$Fe^{2+} + H_2O_2 \rightarrow Fe^{3+} + \bullet OH + OH^- \quad (5)$$

In addition, under excess of H_2O_2, the occurring passivation of iron results in the formation of thin passive layers (Namkung et al., 2005). Therefore, the reactions (2–4) are impeded, and the overall rate of dye oxidation reaction 1) decreases, i.e. decolorization time increases.

Temperature effects on mineralization efficiency

Usually, the temperature of effluents from the textile wet processing is in the range of 30–60°C (Yaseen and Scholz, 2019). In order to simulate real effluents and investigate the effect of temperature on the degradations rate of MO, the catalysts were tested at three temperatures: 30, 40, and 50°C. Decolorization time was tracked at chosen temperatures in the 70 mg/L MO solution, using Fe/Cu catalyst electrodeposited at −1.9 V and 90 μL of H_2O_2. Figure 7 shows that the decolorization time difference between 30° and 50°C is almost 3 min and it is almost independent of the amount of iron on the copper foam. At 30°C the maximum efficiency is reached using catalysts obtained when 450 C and −1.9 V was applied for Fe layer electrodeposition. With further increase in temperature to 40 and 50°C, even a lower amount of iron on the copper foam is enough to reach minimal values of decolorization time, and there

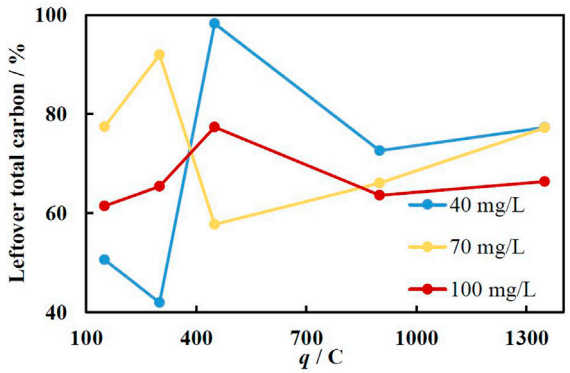


FIGURE 9
The dependence of total carbon amount in the solution on the current charge passed for Fe deposition (at −1.9 V) at various initial MO concentrations at 50°C. Immersion time 10 min.

is no big change with the increase of charge passed. This further proves that under such conditions the overall reaction rate is being controlled by the iron corrosion rate. Since with the increase in temperature the corrosion rate increases as well. This implies that homogeneous Fenton's reaction may occur in the bulk of the solution.

The mineralization efficiency has been investigated to further evaluate the efficiency of the catalyst. The total amount of carbon in the solution has been determined by using catalysed oxidation of all organic matter at high temperatures. From Figure 8, the total MO degradation rate into carbon dioxide and water does not follow the same tendencies as decolorization time dependence on the temperature. Even though with increasing

TABLE 1 Comparison of various Fenton catalysts for the degradation of MO.

Type of catalyst	Catalyst amount	Solution volume (ml)	MO conc	Temperature	H_2O_2 conc	pH	Decolorization time	Ref
Ultrasonically dispersed nano metallic particles	50 mg/L	100	20 mg/L	-	50 mM	2.5	5 min	Singh et al. (2017)
Iron powder dispersed in solution along with UV illumination	10 mg	200	10 ppm		10 ppm	3.0	16 min	Gomathi Devi et al. (2009)
Homogeneous Fenton reaction	Fe^{2+} 0.2 mm		540 µm	Room temperature	3 mM	2.9	15 min	Youssef et al. (2016)
Hollow Co. nanoparticles	0.5 g/L	10	100 mg/L	Room temperature		2.5	4min	Sha et al. (2016)
Electro-Fenton-like process	2.14 mM Fe (II) I—2.1 A	500	106 mg/L			3.0	30 min	Taylor et al. (2013)
Zeolites modified with Fe-Mn/MCM41	1 g/L		100 mg/L	Room temperature	5 mmol/L	3.0	120 min	Zhang et al. (2018)
Tungsten oxide nanoparticles	50 mg	100		65 °C	2.5 ml	3.0	89.7% in 3h	Séverin et al. (2020)
Cu/Fe nanoribbons	14.5 mg		50 mg/L	Room temperature	0.1 g/L	3.0	20 min	Zhang et al. (2017)
Fe/Cu foam		100	100 mg/L	50°C	1.2 mm	3.0	1.5 min	This work

temperature the first degradation step, namely decolorization, occurs faster and the side reactions rates increase as well. However, the iron corrosion rate changes with the temperature, which likely controls the overall MO degradation rate.

Even though working at elevated temperatures may not be desirable, in practice this allows to digest higher concentration of pollutants. The results presented in Figure 9 demonstrate that only after 10 min at 50°C up to 50% of all organic matter was fully mineralized using Fe/Cu catalysts obtained at 150 and 300 C. At higher amounts of deposited iron, the leaching rate is too quick, and the H_2O_2 is likely used for water splitting and other side reactions. In the solution containing 70 mg/L of MO, the mineralization was quite weak at low catalysts loading, but from 450 C and upwards was around 25–35%. This is likely because the amount of iron on the Cu foam was not sufficient to achieve the reaction at its highest rate when the Fe loading was relatively low. The best results were obtained using 100 mg/L concentrations of MO, where the mineralization achieved in 10 min was around 25–40% and almost did not depend on the catalyst loading. This implies, that the iron ions were leached almost at the optimal rate. It is also worth mentioning that after all Fe layer is leached to the solution, the Cu foam substrate can be reused by electrodepositing a fresh portion of the catalyst.

Furthermore, various heterogeneous Fenton catalysts were compared, and the results are shown in Table 1. It can be noted that the effectiveness of catalysts is greatly dependent on the experimental conditions used, particularly the catalyst loading, dye, and H_2O_2 concertation. The Fe/Cu catalyst prepared in this work shows a relatively high efficiency compared with hollow Co. nanoparticles (Sha et al., 2016). With simple synthesis and ease of use, this catalyst shows great promise for upscaling and using it on an industrial scale.

Conclusion

The effective heterogeneous catalytic system containing Fe^0 electrodeposited onto Cu foam was investigated in the Fenton process involving the methyl orange (MO) degradation. The influence of iron deposition conditions, H_2O_2 concentration and temperature on catalytic degradation of MO were investigated using various concentrations of MO in the solution. The optimal conditions for Fe layers deposition on Cu foam which provide the catalyst with a highest activity in Fenton process are: deposition potential −1.9 V vs Ag/AgCl at amount of charge >300 C and the geometric size of electrode 1 cm × 1 cm. This procedure allowed to achieve a full decolorization at a concentration of MO of 100 mg/L in up to 90 s depending on the temperature.

Moreover, the total mineralization efficiency is cca 30–40% already within the first 10 min after the catalyst immersion into the MO dye solution. The described catalytic process allows to effectively mineralize large amounts of MO within several minutes and represents an environmentally friendly and cost-effective alternative to other Fenton catalysts described in the literature.

Data availability statement

The raw data supporting the conclusions of this article will be made available by the authors, without undue reservation.

Author contributions

The electrodeposition of the coatings, structural characterization and catalytic measurements were performed by MV in collaboration with AN and NT, under the supervision of NT, HC, EP-M, and FA; writing-original draft preparation by MV and AN; all the authors contributed to the writing-review and editing.

Funding

The research was supported by the EU's Horizon 2020 research and innovation program under the MSCA grant agreement Nr. 778357 project SMARTELECTRODES and partially from the ANCD project Nr. 20.80009.5007.18.

Conflict of interest

The authors declare that the research was conducted in the absence of any commercial or financial relationships that could be construed as a potential conflict of interest.

Publisher's note

All claims expressed in this article are solely those of the authors and do not necessarily represent those of their affiliated organizations, or those of the publisher, the editors and the reviewers. Any product that may be evaluated in this article, or claim that may be made by its manufacturer, is not guaranteed or endorsed by the publisher.

References

Ananthashankar, R., Ghaly, A., Alhattab, M., and Ramakrishnan, V. (2013). Production, characterization and treatment of textile effluents: A critical review. *Chem. Eng. Process Technol.* 05, 1–18. doi:10.4172/2157-7048.1000182

Deng, Y., and Zhao, R. (2015). Advanced oxidation processes (AOPs) in wastewater treatment. *Curr. Pollut. Rep.* 1, 167–176. doi:10.1007/s40726-015-0015-z

Devi, L. G., Kumar, S. G., Raju, K. S. A., and Rajashekhar, K. E. (2010). Photo-Fenton and photo-Fenton-like processes for the degradation of methyl orange in aqueous medium. *Influ. Oxid. States Iron* 64, 378–385. doi:10.2478/s11696-010-0011-0

Dutta, K., Mukhopadhyay, S., Bhattacharjee, S., and Chaudhuri, B. (2001). Chemical oxidation of methylene blue using a Fenton-like reaction. *J. Hazard. Mat.* 84, 57–71. doi:10.1016/S0304-3894(01)00202-3

Fontecha-Cámara, M. A., Álvarez-Merino, M. A., Carrasco-Marín, F., López-Ramón, M. V., and Moreno-Castilla, C. (2011). Heterogeneous and homogeneous Fenton processes using activated carbon for the removal of the herbicide amitrole from water. *Appl. Catal. B Environ.* 101, 425–430. doi:10.1016/j.apcatb.2010.10.012

Gomathi Devi, L., Girish Kumar, S., Mohan Reddy, K., and Munikrishnappa, C. (2009). Photo degradation of methyl orange an azo dye by advanced Fenton process using zero valent metallic iron: Influence of various reaction parameters and its degradation mechanism. *J. Hazard. Mater.* 164, 459–467. doi:10.1016/j.jhazmat.2008.08.017

Han, L., Xue, S., Zhao, S., Yan, J., Qian, L., and Chen, M. (2015). Biochar supported nanoscale iron particles for the efficient removal of methyl orange dye in aqueous solutions. *PLoS ONE* 10 (7), e0132067. doi:10.1371/journal.pone.0132067

Holkar, C. R., Jadhav, A. J., Pinjari, D. V., Mahamuni, N. M., and Pandit, A. B. (2016). A critical review on textile wastewater treatments: Possible approaches. *J. Environ. Manage.* 182, 351–366. doi:10.1016/j.jenvman.2016.07.090

Karthikeyan, S., Titus, A., Gnanamani, A., Mandal, A. B., and Sekaran, G. (2011). Treatment of textile wastewater by homogeneous and heterogeneous Fenton oxidation processes. *Desalination* 281, 438–445. doi:10.1016/j.desal.2011.08.019

Li, P., Song, Y., Wang, S., Tao, Z., Yu, S., and Liu, Y. (2015). Enhanced decolorization of methyl orange using zero-valent copper nanoparticles under assistance of hydrodynamic cavitation. *Ultrason. Sonochem.* 22, 132–138. doi:10.1016/j.ultsonch.2014.05.025

Litter, M. I. (2017). An overview on heterogeneous Fenton and photoFenton reactions using zerovalent iron materials. *J. Adv. Oxid. Technol.* 20 , 20160164. doi:10.1515/jaots-2016-0164

Mažeika, K., Reklaitis, J., Nicolenco, A., Vainoris, M., Tsyntsaru, N., and Cesiulis, H. (2021). Magnetic state instability of disordered electrodeposited nanogranular Fe films. *J. Magnetism Magnetic Mater.* 540, 168433. doi:10.1016/j.jmmm.2021.168433

Miklos, D. B., Remy, Ch., Jekel, M., Linden, K. G., Drewes, J. E., and Hubner, U. (2018). Evaluation of advanced oxidation processes for water and wastewater treatment – a critical review. *Water Res.* 139, 118–131. doi:10.1016/j.watres.2018.03.042

Murali, V., Ong, S. A., Ho, L. N., and Wong, Y. S. (2013). Decolorization of methyl orange using up flow anaerobic sludge blanket (UASB) reactor-An investigation of co-substrate and dye degradation kinetics. *Desalin. Water Treat.* 51, 7621–7630. doi:10.1080/19443994.2013.782255

Namkung, K. C., Burgess, A. E., and Bremner, D. H. (2005). A fenton-like oxidation process using corrosion of iron metal sheet surfaces in the presence of hydrogen peroxide: A batch process study using model pollutants. *Environ. Technol.* 26 (3), 341–352. doi:10.1080/09593332608618564

Nicolenco, A., Tsyntsaru, N., Fornell, J., Pellicer, E., Reklaitis, J., Baltrunas, D., et al. (2018). Mapping of magnetic and mechanical properties of Fe-W alloys electrodeposited from Fe(III)-based glycolate-citrate bath. *Mat. Des.* 139, 429–438. doi:10.1016/j.matdes.2017.11.011

Rossi, A. F., Martins, R. C., and Quinta-Ferreira, R. M. (2014). Composition effect of iron-copper composite catalysts in the Fenton heterogeneous process efficiency and cooxidation synergy assessment. *Ind. Eng. Chem. Res.* 53, 15369–15373. doi:10.1021/ie501193x

Séverin, N. E., Aimé, S. E., Donourou, D., Diby, B. O., and Jocelin, M. Y. (2020). Catalytic activity of using tungsten oxide with hydrogen peroxide for methyl orange degradation. *Afr. J. Pure Appl. Chem.* 14, 69–80. doi:10.5897/ajpac2019.0827

Sha, Y., Mathew, I., Cui, Q., Clay, M., Gao, F., Zhang, X. J., et al. (2016). Rapid degradation of azo dye methyl orange using hollow cobalt nanoparticles. *Chemosphere* 144, 1530–1535. doi:10.1016/j.chemosphere.2015.10.040

Singh, J., Chang, Y., Koduru, J. R., Yang, J., and Singh, D. P. (2017). Rapid Fenton-like degradation of methyl orange by ultrasonically dispersed nano-metallic particles. *Environ. Eng. Res.* 22, 245–254. doi:10.4491/eer.2016.138

Tak, S., and Kumar, A. (2017). Chlorination disinfection by-products and comparative cost analysis of chlorination and UV disinfection in sewage treatment plants: Indian scenario. *Environ. Sci. Pollut. Res.* 24, 26269–26278. doi:10.1007/s11356-017-0568-z

Taylor, P., He, W., Yan, X., Ma, H., Yu, J., Wang, J., et al. Desalination and water treatment degradation of methyl orange by electro-Fenton-like process in the presence of chloride ion. *Desalin. Water Treat.*, (2013);51 37–41. doi:10.1080/19443994.2013.792133

Vainoris, M., Cesiulis, H., and Tsyntsaru, N. (2020). Metal foam electrode as a cathode for copper electrowinning. *Coatings* 10, 822–829. doi:10.3390/coatings10090822

Vandevivere, P. C., Bianchi, R., and Verstraete, W. (1998). Review: Treatment and reuse of wastewater from the textile wet-processing industry: Review of emerging technologies. *J. Chem. Technol. Biotechnol.* 72, 289–302. doi:10.1002/(sici)1097-4660(199808)72:4<289::aid-jctb905>3.0.co;2-#

Wang, J., Liu, C., Tong, L., Li, J., Luo, R., Qi, J., et al. (2015). Iron-copper bimetallic nanoparticles supported on hollow mesoporous silica spheres: An effective heterogeneous Fenton catalyst for orange II degradation. *RSC Adv.* 5, 69593–69605. doi:10.1039/c5ra10826h

Wang, N., Zheng, T., Zhang, G., and Wang, P. (2016). A review on Fenton-like processes for organic wastewater treatment. *J. Environ. Chem. Eng.* 4, 762–787. doi:10.1016/j.jece.2015.12.016

Wang, Y., Zhao, H., and Zhao, G. (2015). Iron-copper bimetallic nanoparticles embedded within ordered mesoporous carbon as effective and stable heterogeneous Fenton catalyst for the degradation of organic contaminants. *Appl. Catal. B Environ.* 164, 396–406. doi:10.1016/j.apcatb.2014.09.047

Xu, M., Wu, C., and Zhou, Y. (2020). "Advancements in the Fenton process for wastewater treatment," in *From the edited volume advanced oxidation Processes*. Editor C. Bustillo-Lecompte (London, UK: IntechOpen). doi:10.5772/intechopen.90256

Yaseen, D. A., and Scholz, M. (2019). *Textile dye wastewater characteristics and constituents of synthetic effluents: A critical review*. Berlin Heidelberg: Springer. doi:10.1007/s13762-018-2130-z

Youssef, N. A., Shaban, S. A., Ibrahim, F. A., and Mahmoud, A. S. (2016). Degradation of methyl orange using Fenton catalytic reaction. *Egypt. J. Petroleum* 25, 317–321. doi:10.1016/j.ejpe.2015.07.017

Zárate-Guzmán, A. I., González-Gutiérrez, L. V., Godínez, L. A., Medel-Reyes, A., Carrasco-Marín, F., and Romero-Cano, L. A. (2019). Towards understanding of heterogeneous Fenton reaction using carbon-Fe catalysts coupled to *in-situ* H_2O_2 electro-generation as clean technology for wastewater treatment. *Chemosphere* 224, 698–706. doi:10.1016/j.chemosphere.2019.02.101

Zhang, H., Feng, Y., Cheng, Y., Baró, M. D., Altube, A., García-Lecina, E., et al. (2017). Nanoporous Fe-based alloy prepared by selective dissolution: An effective Fenton catalyst for water remediation. *ACS Omega* 2, 653–662. doi:10.1021/acsomega.7b00043

Zhang, X., Dong, J., Hao, Z., Cai, W., and Wang, F. (2018). Fe – Mn/MCM 41 : Preparation, characterization, and catalytic activity for methyl orange in the process of heterogeneous Fenton reaction. *Trans. Tianjin Univ.* 24, 361–369. doi:10.1007/s12209-018-0122-1

frontiers | Frontiers in Chemistry

TYPE Review
PUBLISHED 15 September 2022
DOI 10.3389/fchem.2022.995351

Check for updates

OPEN ACCESS

EDITED BY
Margherita Brindisi,
University of Naples Federico II, Italy

REVIEWED BY
Clemens Zwergel,
Sapienza University of Rome, Italy
Assem Barakat,
King Saud University, Saudi Arabia

*CORRESPONDENCE
Simona Collina,
simona.collina@unipv.it

SPECIALTY SECTION
This article was submitted to Medicinal and Pharmaceutical Chemistry, a section of the journal Frontiers in Chemistry

RECEIVED 15 July 2022
ACCEPTED 24 August 2022
PUBLISHED 15 September 2022

CITATION
Listro R, Rossino G, Piaggi F, Sonekan FF, Rossi D, Linciano P and Collina S (2022), Urea-based anticancer agents. Exploring 100-years of research with an eye to the future.
Front. Chem. 10:995351.
doi: 10.3389/fchem.2022.995351

COPYRIGHT
© 2022 Listro, Rossino, Piaggi, Sonekan, Rossi, Linciano and Collina. This is an open-access article distributed under the terms of the Creative Commons Attribution License (CC BY). The use, distribution or reproduction in other forums is permitted, provided the original author(s) and the copyright owner(s) are credited and that the original publication in this journal is cited, in accordance with accepted academic practice. No use, distribution or reproduction is permitted which does not comply with these terms.

Urea-based anticancer agents. Exploring 100-years of research with an eye to the future

Roberta Listro[1], Giacomo Rossino[1], Federica Piaggi[1], Falilat Folasade Sonekan[1,2], Daniela Rossi[1], Pasquale Linciano[1] and Simona Collina[1]*

[1]Department of Drug Sciences, University of Pavia, Pavia, Italy, [2]School of Pharmacy and Pharmaceutical Sciences, Panoz Institute, Trinity College Dublin, University of Dublin, Dublin, Ireland

Suramin was the first urea-based drug to be approved in clinic, and in the following century a number of milestone drugs based on this scaffold were developed. Indeed, urea soon became a privileged scaffold in medicinal chemistry for its capability to establish a peculiar network of drug–target interactions, for its physicochemical properties that are useful for tuning the druggability of the new chemical entities, and for its structural and synthetic versatility that opened the door to numerous drug design possibilities. In this review, we highlight the relevance of the urea moiety in the medicinal chemistry scenario of anticancer drugs with a special focus on the kinase inhibitors for which this scaffold represented and still represents a pivotal pharmacophoric feature. A general outlook on the approved drugs, recent patents, and current research in this field is herein provided, and the role of the urea moiety in the drug discovery process is discussed form a medicinal chemistry standpoint. We believe that the present review can benefit both academia and pharmaceutical companies' medicinal chemists to prompt research towards new urea derivatives as anticancer agents.

KEYWORDS

urea, anticancer drug, suramin, kinase inhibitors, patent survey, medicinal chemistry

Introduction

Suramin: The first urea-based drug. From trypanocidal to putative anticancer drug

This year marks the 100th anniversary of the introduction of suramin–the first chemotherapeutic agent developed in a medicinal chemistry project–to clinics (Wiedemar et al., 2020). Paul Elrich was the first to report the activity of dye or dye derivatives (such as trypan blue or trypan red) against tropical infections (Wainwright, 2010). To avoid skin staining as a side effect, and therefore looking for colorless derivatives, Oskar Dressel, Richard Kothe, and Bernhard Heymann at Bayer replaced the azo moieties present in trypan dyes with amido and ureyl linkers. These structural modifications preserved the conjugation between the aromatic rings but did not confer a peculiar coloration to the

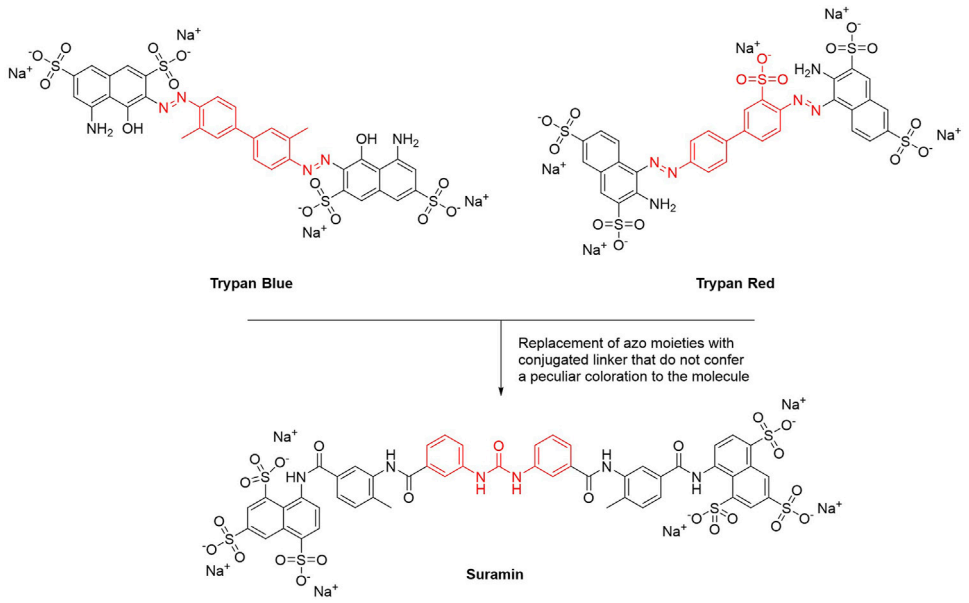


FIGURE 1
Chemical structures of suramin. The main structural modification that led to the discovery of suramin is highlighted in red.

molecule. All urea derivatives showed higher antitrypanosomatidic activities compared to the original dyes. Particularly, suramin (molecule 205 in the original work) was the best-in-class compound and in 1922 it entered in therapy for the treatment of Human African Trypanosomiasis (HAT) (Figure 1) (Wainwright, 2010).

Despite its poor bioavailability and its intrinsic toxicity, suramin is still widely used to treat HAT (Steverding, 2010), and through the years, its use has been extended to other pathological conditions, including other parasitic infections (such as leishmaniasis and malaria) and viral infections (such as HIV, chikungunya, Ebola, dengue, Rift Valley fever and Zika), although with limited effects (Henß et al., 2016; Kuo et al., 2016; Tan et al., 2017). Starting from 1940s, suramin has been evaluated as an anticancer agent. At first, the capability of suramin in reducing the tumor mass in mice engrafted with lymphosarcoma was studied. Later, its potential anticancer activity was assessed in clinical trials against diverse neoplastic diseases such as melanoma, breast, prostate, bladder, brain, and lung tumors. None of these trials proved the efficacy of suramin as an anticancer agent in monotherapy (Parveen et al., 2022). Conversely, suramin was shown to be an effective chemosensitizer in *in vivo* models by enhancing the efficacy of other anticancer drugs such as cyclophosphamide, adriamycin, mitomycin C, taxol and carboplatin in mice (Osswald and Youssef, 1979). However, in a Phase I clinical study concluded in 2003, the association of nontoxic doses of suramin with taxol or carboplatin did not overcome drug resistance in patients with drug-resistant non-small cell lung cancer (Villalona-Calero et al., 2003). Several combination of suramin with anticancer agents endowed with different mechanisms of action have been proposed, namely protein kinases (Hensey et al., 1989), nucleic acid polymerases, fibroblast growth factor receptors (FGFR), heparanase (Nakajima et al., 1991), serine and cysteine proteases (Cadène et al., 1997), caspase (Eichhorst et al., 2004), telomerase histone- and sirtuin histone deacetylases (Trapp et al., 2007), methyltransferases (Feng et al., 2010), RNA-binding protein (i.e. HuR) (Kakuguchi et al., 2018), and many others. The association of suramin with estramustine and docetaxel showed promising results in hormone-refractory prostate cancer patients, though additional trials are necessary to warrant the clinical use of suramin in combinatorial antineoplastic therapies.

Along the years, several suramin derivatives have been developed to enhance its anticancer activity. Firsching et al. (1995) were the first to investigate the antiproliferative and angiostatic activity of a series of nineteen suramin derivatives (**1**, Figure 2) against 5 different human cell lines (HT29, MCF7, SW13, PC3, and T47D). The structure activity relationship (SAR), mainly delineated on the HT29 activity, suggested that the number and position of the sulfonic groups do not affect the activity of the molecules (HT29 IC_{50} = 43–390 μM) indicating the effect of other functional groups, and in particular of the urea moiety, its antiproliferative activity. Indeed, the symmetry of the molecule around the urea moiety seemed to be mandatory for the anticancer activity, as the asymmetrical and truncated suramin derivatives were ineffective against the tumor cell lines that were investigated. Moreover, the replacement of the urea bridge with a

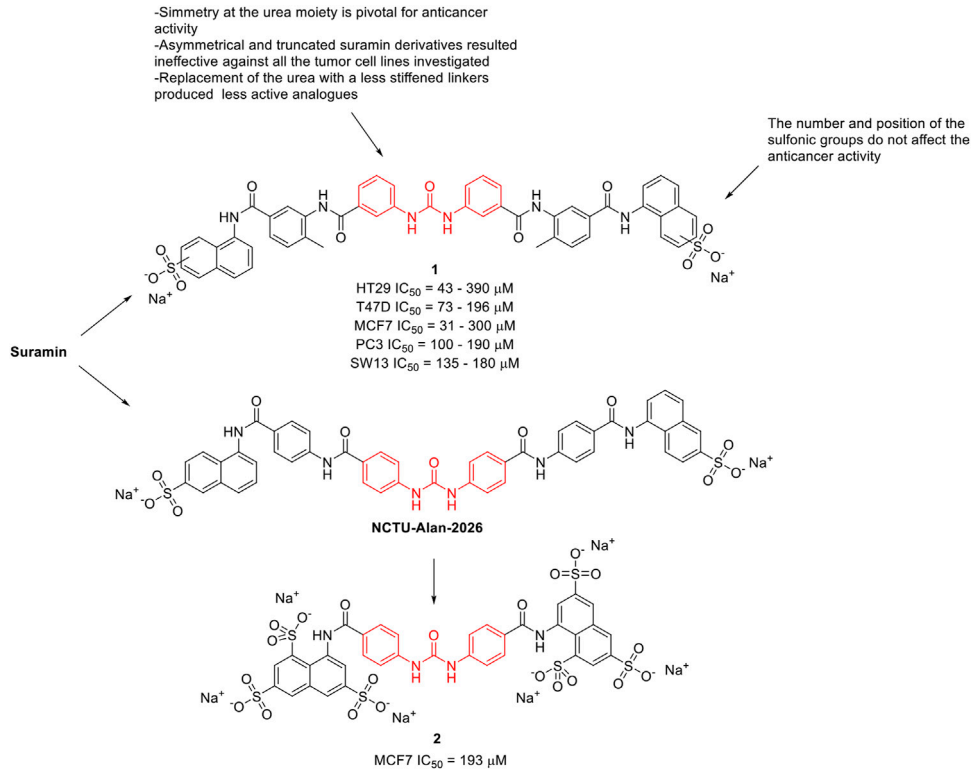


FIGURE 2
Chemical structures and SAR highlights of the suramin's derivatives with proved anticancer activity.

less stiffened linker—succinic acid diamide—produced the least active of the suramin analogues (IC_{50} > 500 μM against almost all the selected cell lines). This trend was almost maintained against the other investigated cancer cell lines (T47D IC_{50} = 73–196 μM, MCF7 IC_{50} = 31–300 μM, PC3 IC_{50} = 100–190 μM, and SW13 IC_{50} = 135–180 μM). This evidence suggested the importance of the urea central unit for antiproliferative action (Firsching et al., 1995).

McCain et al. (2004) investigated the effect of suramin and 45 other congeners as inhibitors of protein-tyrosine phosphatases (PTPs), including Cdc25A. Cdc25A is considered an oncogene and it is overexpressed in breast, head and neck tumors. Several suramin derivatives resulted potent (IC_{50} < 5 μM) and specific (at least 20–30-fold specificity) Cdc25A inhibitors with respect to the other human PTPs tested. SAR profiles revealed that it was the core structure rather than the terminating functionality to affect the inhibitory properties of the molecules. It also appears that both halves of the symmetrical suramin core structure and urea moiety are required for high affinity binding to all PTPs studied. In 2020, Parveen et al. (2020) reported the antiproliferative activity of NCTU-Alan-2026 (Figure 2), a suramin analogue. The mechanism underlying NCTU-Alan-2026's anti-mitogenic activity is mediated by the capability of the molecule to effectively interact with the heparan sulfate binding site of FGF1, thus blocking the interaction between FGF1 and FGF1R2 which ultimately results in anti-proliferative activity. The same authors designed and synthesized a new series of congeners and assessed the anti-proliferative activity in breast cancer MCF7 cell lines, with compound **2** (Figure 2) showing an IC_{50} of 193 μM. Although they were slightly less active than suramin (MCF7 IC_{50} = 153 μM), these derivatives showed a better safety profile, thus encouraging further *in vivo* investigation (Parveen et al., 2020). The binding of these compounds at FGF1 was confirmed by NMR spectroscopy.

Urea-based anticancer drugs

Suramin is the first ever drug containing a urea moiety to be introduced to clinics. Since then, urea soon became a privileged scaffold in medicinal chemistry, as proved by the presence of this moiety in several drugs and bioactive compounds endowed with a broad range of therapeutic and pharmacological properties. Querying the ChemBL, over 90,000 synthetic compounds possessing the urea scaffold in their structure were retrieved (Gaulton et al., 2012). Over the last 20 years there has been an increasing interest of the pharmaceutical community in the

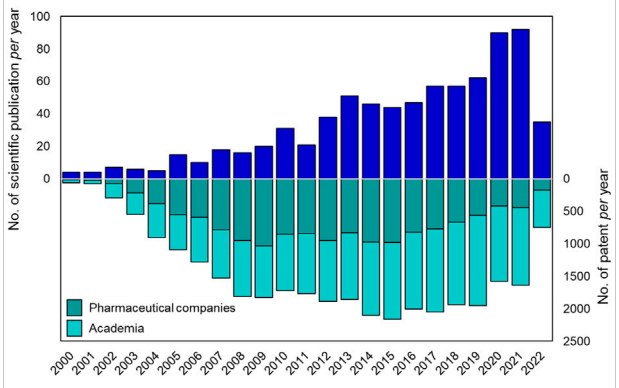


FIGURE 3
Number of publications (reviews and articles) and patents *per* year (from 2000 to 2021) reported in literature about urea-based compounds as anticancer agents. Source Scopus and Espacenet (last web access on 14 July 2022).

design and development of novel urea-based anticancer compounds as testified by the exponential growth in the number of documents published *per* year from the years 2000–2022 (Figure 3).

Recently, several comprehensive reviews have been published about the physicochemical properties of urea, the traditional and breakthrough synthetic methodology of this functional group, and the exploitation of this moiety in modern drug discovery and medicinal chemistry (Ghosh and Brindisi, 2020; Catalano et al., 2021; Liang et al., 2021; Siddig et al., 2021).

Herein, we will give a comprehensive overview on the urea derivatives developed as anticancer agents, highlighting the relevance of the urea functionality from a medicinal chemistry standpoint, and providing the up-to-date information (according to FDA's and EMA's websites and to AdisInsight repository, last access on 16 August 2022) about their therapeutic use, and the highest clinical phase reached. We will provide a dissertation about urea-based anticancer drugs characterized by different mechanisms of action (Figures 4, 5), followed by a special focus on the kinase inhibitors approved for clinical use or currently in clinical trials. Lastly, a patent survey as well as an outlook on the future directions of the research in this field will also be drawn.

Hydroxycarbamide

Hydroxycarbamide (HU, Figure 5) is an antimetabolite discovered in 1928, but its effectiveness as an anticancer drug was demonstrated in clinical trials in the 1960s by Bristol-Myers Squibb. In 1967, HU was launched worldwide for the treatment of diverse tumors such as primary brain cancer, renal cell carcinoma, head and neck cancers, melanoma, and breast cancer. Starting from 1980s, HU was further approved for the treatment of chronic myeloproliferative disorders (MPDs) and chronic myeloid leukemia (CML) (Spivak and Hasselbalch, 2011). HU is a selective and potent inhibitor of ribonucleotide reductase (IC_{50} = 87 μM) by selectively quenching the tyrosyl free radical. This induces the inhibition of DNA synthesis as HU starves the DNA polymerase at the replication forks for dNTPs (Koç et al., 2004). The non-specificity of its mechanism of action makes HU to be an effective cytostatic anticancer drug in a wide variety of cells with a high turnover. Moreover, the depletion of the deoxyribonucleotide pool induced by HU, enhances the anticancer activity of pyrimidine and purine antimetabolites. Several studies demonstrated the potential of HU in sensitizing tumors to other chemotherapeutic agents (Spivak and Hasselbalch, 2011).

Alkylating agents

Nitrosoureas are an old class of alkylating anticancer drugs, characterized by the N-nitroso-urea scaffold from which their

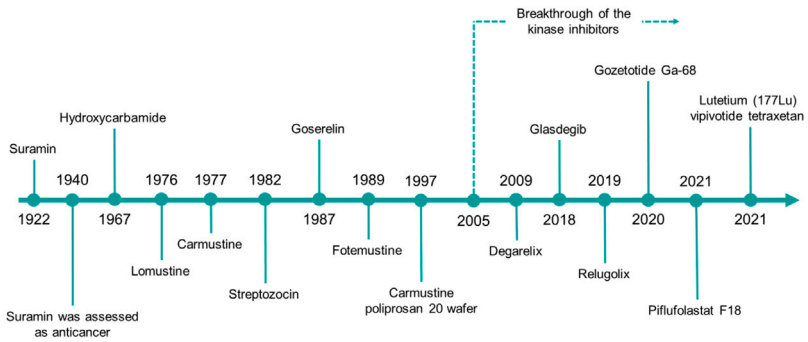


FIGURE 4
The timeline reports the year of the first approval in clinics of the urea-based anticancer drugs from 1922 to date.

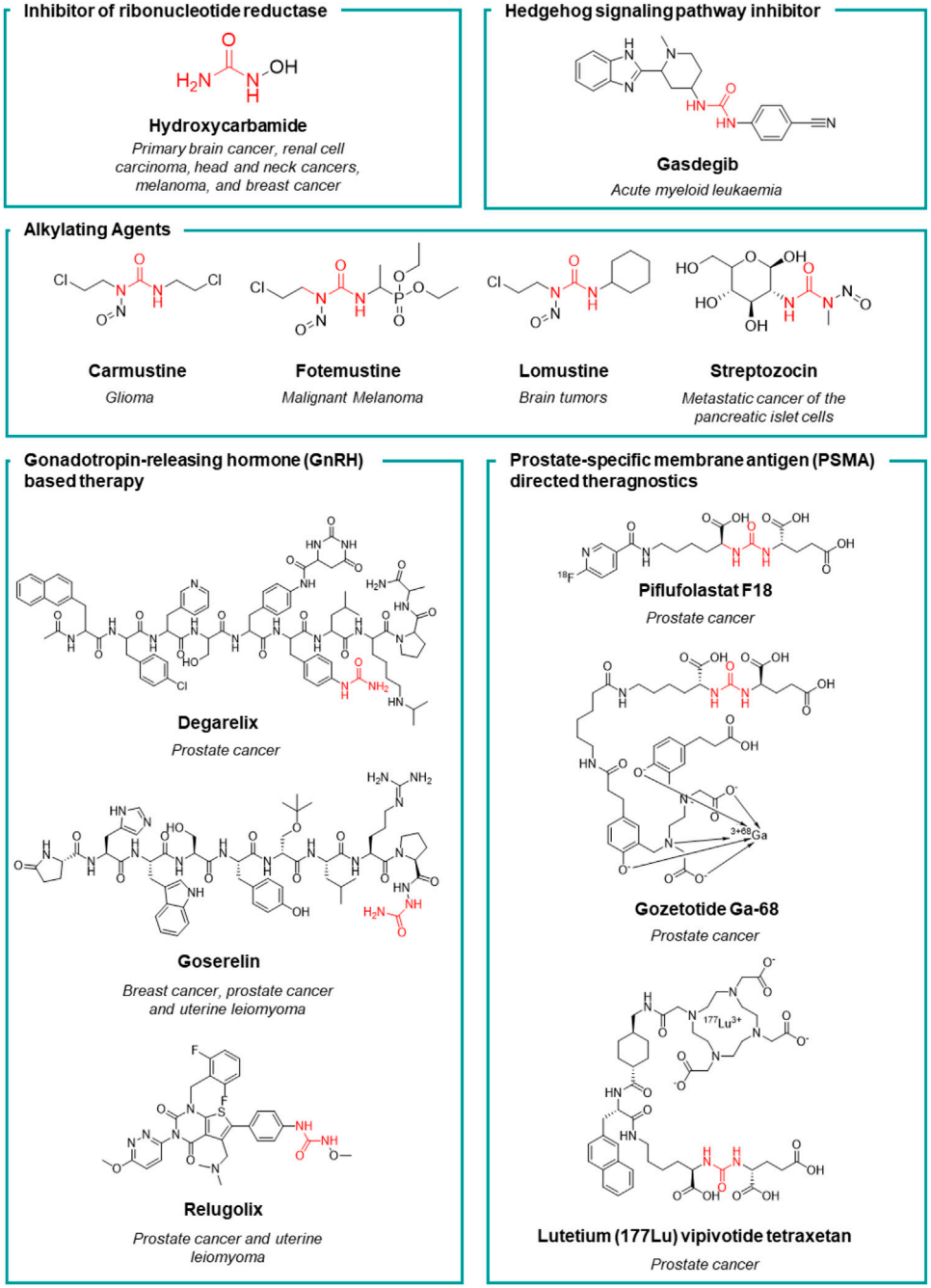


FIGURE 5
Chemical structure and main therapeutic use of the urea-based anticancer drugs (not active as kinase inhibitors) herein discussed.

peculiar mechanism of action arises (Gnewuch and Sosnovsky, 1997). The N-nitroso-urea undergoes spontaneous degradation producing highly reactive alkylating species that generate DNA crosslinking, thus blocking DNA replication and transcription (Colvin et al., 1976; Kohn, 1977; Tong and Ludlum, 1978). Moreover, the reactive species may react with the nucleophilic residues of the DNA repairing enzymes causing their irreversible inactivation. Carmustine, lomustine, fotemustine and streptozocin are the main representative and still clinical used nitrosoureas (Figure 5) (Avendaño and Menéndez, 2015). **Lomustine**, was the first nitrosourea discovered and it was subsequently launched in 1976. Thanks to its high

lipophilicity, it is able to cross the BBB by diffusion and for this reason it is mainly used for the treatment of brain tumors or as a second-line treatment for Hodgkin's lymphoma. Lomustine inhibits the growth of U87 and temozolamide-U87 cell lines with an IC_{50} of 55 and 86 μM, respectively. Lomustine reduces the level of expression of the DNA repair protein O6-alkylguanine-DNA alkyltransferase (Yamamuro et al., 2021). Despite its congeners, lomustine is the sole nitrosourea that is administered orally. Lomustine is still approved in the EU but not in the United States. **Carmustine** was launched the following year (in 1977) and it is still used to treat several types of brain cancer including glioma, glioblastoma multiforme (U87 IC_{50} = 18.2 μM), medulloblastoma and astrocytoma, multiple myeloma, and lymphoma (Hodgkin's and non-Hodgkin's) (Avendaño and Menéndez, 2015; Kumar et al., 2020). **Streptozocin** is a natural anticancer antibiotic isolated from a strain of *Streptomyces achromogens*. From a chemical standpoint it is a glycosylated nitrosourea and it was approved by the United States FDA in 1982 (Vavra et al., 1960 Bhuyan, 1970). The presence of the glucopyranoside sugar portion (in both anomeric forms) gives the structure good solubility in water in comparison to other lipophilic antineoplastic nitrosoureas. The sugar moiety makes the molecule selective for Langerhans cells as it exploits the glucose transporters to concentrate the compound in the β cells of the pancreas (Hosokawa et al., 2001). For this reason, it is mainly used for the treatment of metastatic cancer of pancreatic islet cells (Brentjens and Saltz, 2001). Lastly, **fotemustine** was developed by Servier and was launched for the first time in France in 1989. It has since been made available to other countries in the EU and worldwide, but not in the United States. Fotemustine alkylates guanine by forming chloroethyl adducts at the O6 of guanine, resulting in N1-guanine and N3-cytosine cross linkages, inhibition of DNA synthesis, cell cycle arrest, and finally apoptosis (Hayes et al., 1997). This agent is high lipophilic and crosses the blood-brain barrier and for this reason, it is employed for the treatment of disseminated malignant melanoma (IC_{50} = 173.326 and 125 μM against A375, MABe and RPMI-7591 cell lines, respectively), including cerebral metastases (Moarbess et al., 2008; Menaa, 2013).

Gonadotropin-releasing hormone based therapy

Degarelix (Figure 5) is an injectable gonadotropin-releasing hormone (GnRH) receptor peptide antagonist launched in Europe in 2009 by Ferring Pharmaceuticals for the treatment of prostate cancer. Prostate cancer is known to be hormone-sensitive and responds to anti-androgen treatments (Chuu et al., 2011). Degarelix inhibits gonadal testosterone synthesis in men, and estrogen synthesis in women. It was developed within a medicinal chemistry program aimed at the amelioration of the pharmacodynamic and pharmacokinetic properties of the gonadotropin secretion antagonists cetrorelix (Bajusz et al., 2009) and ganirelix (Nestor et al., 1992). Despite their potency, these two peptides suffer from the stimulation of the release of histamine and relative short acting activity. Moreover, all the previously reported GnRH antagonists have poor water solubility and form gels at low concentration thus preventing the development of formulations that would last more than a month. To improve the solubility and the receptor binding ability of these peptides, functional groups that are able to form H-bonds such as the urea moiety (or cyclic congeners) have been introduced onto the side chain of specific amino acids. Degarelix was the most potent (GnRH IC_{50} = 3 nM) derivative, with very long-acting activity, higher solubility and without propension to form hydrogels, thanks to the presence of the urea moiety. It stabilizes a favorable peptide secondary structure that is less amenable to forming gels. Lastly, the chemistry of urea unlocked the synthesis of this peptide on solid support (Jiang et al., 2001). The improved pharmacodynamic and pharmacokinetic properties allowed for once monthly administration of the drug. Degarelix has been launched in the United States, EU, and other countries worldwide, for the treatment of prostate cancer. A single dose of degarelix, followed by a monthly maintenance dose, causes a rapid decrease in LH and FSH concentrations and, consequently, testosterone (Van Poppel, 2010). Serum concentrations of dihydrotestosterone (DHT) decrease in the same way as those of testosterone. The monthly maintenance dose allows for the suppression of testosterone to be sustained in 97% of patients for at least 1 year, well below medical castration levels (Persson et al., 2009).

Goserelin (Figure 5) is a synthetic analogue of the luteinizing hormone-releasing hormone (LHRH), developed by AstraZeneca. It has been launched in over 100 countries for the treatment of prostate cancer, early breast cancer, uterine hemorrhage, and endometriosis. Goserelin was discovered in 1987 when Dutta et al. synthesized a series of LHRH analogues containing an aza-aminoacid in position 6, 9, or 10 of the endogenous peptides. The introduction of an aza residue in the peptide was beneficial for obtaining derivatives with a higher affinity for the receptor site (GnRH IC_{50} = 2 nM) and for enhancing the stability towards enzymatic degradation, thus improving the pharmacokinetic profile (Dutta et al., 1978). Unlike degarelix, LHRH agonists induce a prolonged blockage of the production of androgen and estrogen hormones thus inducing a drastic reduction in the level of testosterone and estradiol after a month of therapy. An effect comparable to chemical castration is achieved after 4 weeks. As a side effect, such synthetic hormones may often stimulate the growth of prostate cancer in men, and breast cancer in women during the first 2 weeks of therapy, thus compromising the efficacy of the treatment (Nasser, 2022).

Relugolix (Figure 5) is a gonadotropin-releasing hormone (GnRH) receptor antagonist that prevents the secretion of GnRH (GnRH IC_{50} = 0.33 nM) (Huirne and Lambalk, 2001). This results in a reduction of the gonadotropins luteinizing hormone (LH) and follicle-stimulating hormone (FSH) levels, leading to the suppression of estrogen production in women and testosterone production in men. Low levels of estrogen and testosterone can help control of the growth of sex hormone-based tumors such as uterine leiomyoma in woman and prostate cancer in men. The research in this field led to the development of relugolix by Takeda. It was marketed in 2020 in the United States for the treatment of advanced prostate cancer (Shore et al., 2020). Relugolix was moreover registered also in Japan, for uterine leiomyoma (2019) and it was also approved this year in the European Union for the treatment of advanced hormone-sensitive prostate cancer. In addition, Myovant Sciences proved the beneficial effect of the co-administration of estradiol, norethisterone and relugolix for the treatment of heavy menstrual bleeding associated with uterine fibroids (uterine leiomyoma) (Ali et al., 2022). This drug association aims to optimize estradiol levels to achieve the long-term benefit of relugolix, while mitigating the side effects from a low-estrogen state. It is already available in the United States, and it has been approved in the EU for uterine leiomyoma.

Hedgehog signal transduction inhibitors

Glasdegib (Figure 5), discovered by Pfizer, is the only drug currently approved for the treatment of acute myeloid leukemia (AML) and it represents the first and only Hedgehog pathway inhibitor approved for human use (Goldsmith et al., 2019; Thompson and Donald, 2020). This drug inhibits a transmembrane protein involved in hedgehog signal transduction (Fukushima et al., 2016). The Hedgehog signaling pathway plays an essential role in embryogenesis (Pak and Segal, 2016). Glasdegib was registered in 2018 by FDA for the treatment of AML in adult patients who are 75 years or older or have comorbidities that preclude the use of intensive induction chemotherapy (Goldsmith et al., 2019; Thompson and Donald, 2020).

Prostate-specific membrane antigen directed drugs

Prostate-specifc membrane antigen (PSMA) inhibitors have been recently introduced in clinic as radiotracers or theragnostic agents. PSMA, also known as folate hydrolase I (FOLH1) and glutamate carboxypeptidase II (GCPII), is a 750-aminoacid type II transmembrane glycoprotein which is 1000-fold overexpressed on the surface of prostate cancer cells. This difference in expression of PSMA between normal and cancerous cells accounts for the high selectivity of these inhibitors (Evans et al., 2016). The discovery of these high affinity PSMA ligands, took place by Kozikowski et al. Starting from the structure of the N-Acetyl-L-aspartyl-L-glutamate (NAAG) peptide, which is one of the substrates of GCPII, the authors developed a first series of 4,4′-phosphinicobis-butane-1,3-dicarboxylic acids as potent GCPII inhibitor (IC_{50} = 21.7 nM). With the aim to develop a chemically accessible second series of congeners for a swift SAR study, the authors replaced the phosphinic moiety present in the first generation of PSMA ligands with the urea moiety (Figure 6). The urea was chosen to mimic a planar peptide bond between the two amino acids and to improve the resistance to enzymatic hydrolysis (Kozikowski et al., 2001). According to the results achieved, the glu-ureido-glu moiety first, and the glu-ureido-lys moiety then, began to become a common scaffold in the design of the PSMA ligands and of the corresponding radioactive-nuclide derivatives (Figure 6).

N-[N-[(S)-1,3-dicarboxypropyl] carbamoyl]-(S)-[^{11}C]methyl-L-cysteine ([^{11}C]DCMC) was the first reported radiolabeled inhibitor. However, the short half-life of carbon-11 forced the medicinal chemist to consider a different radioisotope, such as [^{125}I] or [^{18}F]. In particular, [^{18}F] is a β+ emitting radionuclide that enables positron emission tomography. [^{18}F]DCFBC (N-[N-[(S)-1,3- dicarboxypropyl]carbamoyl]-(S)-4-[^{18}F]fluorobenzyl-Lcysteine) was initially synthesized as a proof of concept for the exploitation of fluorine-18 for clinical translation. Although [^{18}F] DCFBC was suitable for the visualization of PSMA positive prostate cancer in mice, it is characterized by a long blood residence, which reduces the tumor-to-background ratio (Rowe et al., 2015). Conversely, the pyridyl derivative [^{18}F] DCFPyL (2-(3-{1-carboxy-5-[(6-[^{18}F]fluoro-pyridine-3-carbonyl)-amino]-pentyl}-ureido)-pentanedioic acid) showed a higher binding affinity for PSMA and tumor uptake, and lower blood persistence than [^{18}F]DCFBC, with an overall suitable profile for use in humans (Chen et al., 2011). It was further developed by Progenics Pharmaceuticals under the name of **Piflufolastat F18** (Figure 5) and it is available in the United States for the identification of suspected metastasis or recurrence of prostate cancer. The candidate is under regulatory review in the EU. The extensive SAR around the glu-ureido scaffold, supported by the crystallographic structures resolved for four PSMA inhibitors, validated the urea as a worthy surrogate of the peptide bond. From X-ray structures, the glu-urea-lys moiety fits within the GCPII S1' pocket with the same orientation for all the four derivatives, with the urea interacting with the active-site Zn_1^{2+} ion and the side chains of Tyr552 and His553 (Barinka et al., 2008). Banerjee et al. designed a series of PSMA inhibitors based on the glu-urea-lys peptidomimetic that chelate ^{68}Ga as radiotracers (Banerjee et al., 2010). [^{68}Ga]PSMA-11 (also known as **Gozetotide Ga-68,** Figure 5) was the best-in-class derivative and was further developed by RadioMedix as a tomographic imaging enhancer radiopharmaceutical for the diagnosis of prostate cancer, adenoid cystic carcinoma, renal cell carcinoma,

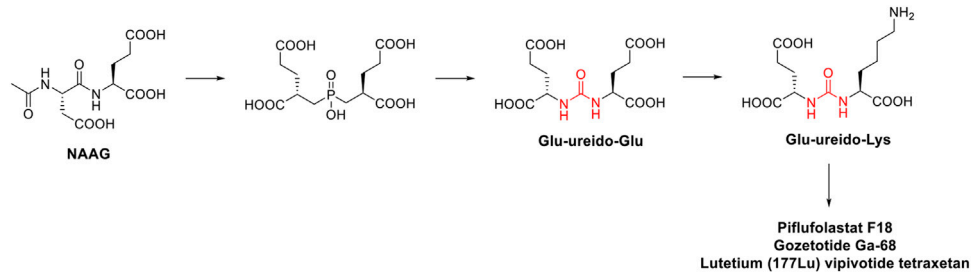


FIGURE 6
Medicinal chemistry rationale that was leading to the development of piflufolastat F18, gozetotide Ga-68 and lutetium (177Lu) vipivotide tetraxetan starting from NAAG.

solid tumours, thyroid cancer, liver cancer and ovarian cancer, using positron emission tomography–computed tomography (PET-CT). Gallium (^{68}Ga) gozetotide is approved in the United States for the diagnosis of prostate cancer and it is undergoing registration in several countries worldwide. However, Gallium (^{68}Ga) gozetotide was not suitable for radiolabeling with therapeutic radiometals. To fix this issue, Benešová et al. reported the synthesis of 177Lu-PSMA-617, where the chelator was conjugated to the Glu-urea-Lys by a naphthalic spacer (Benešová et al., 2015). The naphthalic spacer introduced to reach the accessory hydrophobic pocket in the S1 pocket was detected through the analysis of the GCPII-PSMA inhibitor crystallographic structures. The naphthyl function improved the tumor-targeting and the pharmacokinetics of this PSMA inhibitor. 177Lu-PSMA-617 is characterized by a high binding affinity and internalization, together with a prolonged tumor uptake and rapid kidney clearance making it suitable for endoradiotherapy (ERT) (Pastorino et al., 2020). At the target site, the decay of Lutenium-177 releases a β-particle that causes the focused death of the cancer cell. 177Lu-PSMA-617 was further developed by Advanced Accelerator Applications (a subsidiary of Novartis) with the name of **lutetium (177Lu) vipivotide tetraxetan** (Figure 5). It is approved in the United States for the treatment of (PSMA)-positive metastatic castration-resistant prostate cancer. Preregistration is ongoing in EU.

Kinase inhibitors

In the late 1990s, the discovery of the key role of the kinase-regulated biochemistry pathway in the genesis, sustainment and proliferation of cancer was a breakthrough for new, effective, and selective anticancer therapeutic strategies. Some kinases, such as EGFR (Ayati et al., 2020; Sabbah et al., 2020), VEGFR (Shibuya, 2011; Modi and Kulkarni, 2019; Wang et al., 2020), RAF kinases (Holderfield et al., 2014; Karoulia et al., 2017), PKC (Rui et al., 2017; Linciano et al., 2022), and Aurora kinases (Bavetsias and Linardopoulos, 2015; Yan et al., 2016), just to cite a few, are amplified in various cancer types and their dysregulation is associated with poor prognosis in cancers. Accordingly, the development of drugs targeting several kinases resulted in the winning pharmaceutical option (Kannaiyan and Mahadevan, 2018; Cohen et al., 2021). The approval of the first urea-based oral multikinase inhibitor for the treatment of cancer in humans (Sorafenib) in 2005 represented a milestone in this field. To ameliorate the pharmacodynamic and pharmacokinetic properties of sorafenib and to widen its activity against other tumors, several medicinal chemistry campaigns have been accomplished, leading to the discovery of over 60 kinase inhibitor anticancer drugs (Ayala-Aguilera et al., 2022). From a medicinal chemistry standpoint, the urea moiety played a pivotal role in the design of these kinase inhibitors, and it is present as a central scaffold in 10 kinase inhibitors over 66 approved drugs (Ayala-Aguilera et al., 2022). The urea-based kinase inhibitors are reported in Figure 7 and will be discussed in the following.

Sorafenib was discovered within a drug discovery campaign targeting the Ras–Raf–MEK–ERK oncogenic pathway (Wilhelm et al., 2006). The assessment of a library of 200,000 compounds against Raf1 (or c-Raf) kinase led to the identification of the 3-thienyl urea **3**, which exhibited a c-Raf IC_{50} of 17 μM and was therefore selected for further improvement (Figure 8) (Riedl, 2001; Smith et al., 2001). Nevertheless, the first SAR study around the 3-thienyl urea did not result in a significant improvement in the potency of the original hit compound. To quickly extend the SAR, both Bayer and Onyx Pharmaceuticals synthesized a new library of almost 1000 bis aryl ureas that were prepared using a parallel synthesis approach. The 3-amino-isoxazole **4** exhibited a c-Raf kinase IC_{50} of 1.1 μM (Figure 8) (Smith et al., 2001). The subsequent replacement of the distal aromatic ring with bioisosteres, while preserving the central urea moiety, led to **5.** It was selected as lead compound due to its druggability, its activity in HCT116 proliferation assays and its ability to decrease the phosphorylation of MEK and ERK. Further

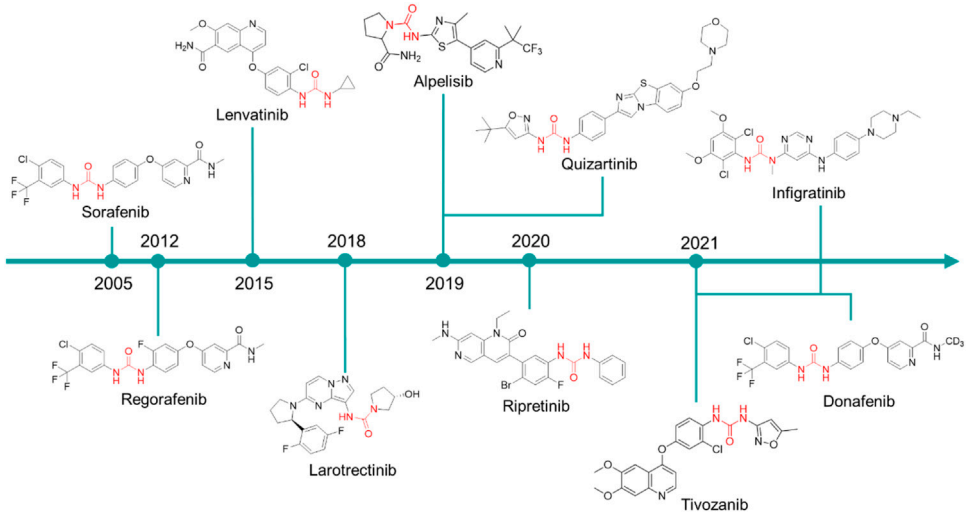


FIGURE 7
Chemical structure of the kinase inhibitors based on aryl-urea moiety approved for clinical use in humans from 2005 to 2021.

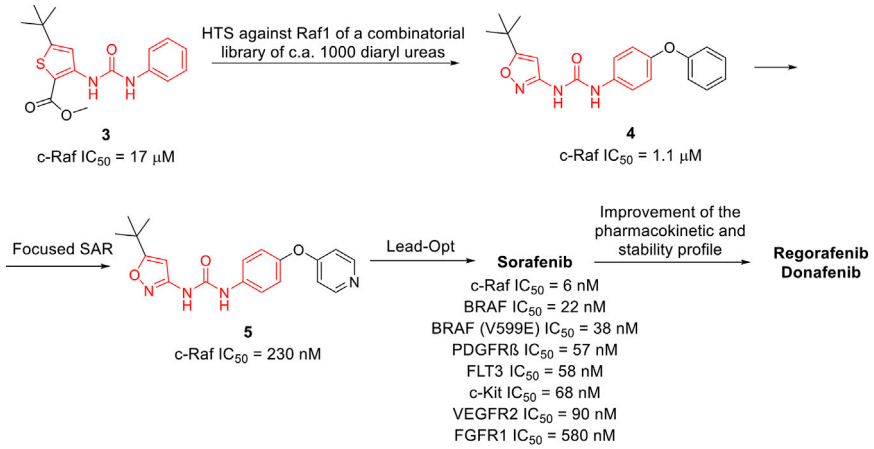


FIGURE 8
Key steps in the optimization process of sorafenib starting from the first identify diarylurea.

preclinical studies demonstrated the efficacy of **5** in inhibiting the growth of HCT116 xenografts, thus providing the first proof of concept for the inhibition of c-Raf kinase, a suitable anticancer therapeutic strategy (Figure 8). Further lead optimization studies confirmed the key role of the urea moiety in the Raf1 kinase inhibition. The modification of both the heterocyclic moiety and the distal pyridine ring of compound **5** led to the identification of **sorafenib** (c-Raf IC_{50} = 6 nM), which has been shown to be effective in both preclinical and clinical studies against several forms of human cancer (Lowinger et al., 2002). Further studies showed the capability of sorafenib to inhibit other intracellular (c-Raf, BRAF and mutant BRAF) and cell surface kinases (KIT, FLT-3, VEGFR-2, VEGFR-3, and PDGFR-ß) (Wilhelm et al., 2004).

The importance of the urea moiety in sorafenib and its congeners was rationalized in 2004, thanks to the X-ray crystallographic structure of BRAF in complex with sorafenib (Wan et al., 2004). As it can be observed in PDB ID: 1UWH, the distal pyridyl ring of sorafenib binds within the ATP binding pocket and interacts with Trp530, Phe582 and Phe594. The

aliphatic side chains of Lys482, Leu513, and Thr528 contact the central phenyl ring of the inhibitor, whereas the trifluoromethyl phenyl ring is buried into a hydrophobic pocket delineated by helices C and E and the N-terminal portion of the kinase. The urea group that plays a pivotal role in c-Raf inhibition forms two hydrogen bonds; the first is established between the nitrogens of the urea and the carboxylate side chain of the catalytic Glu500, whereas the second involves the carbonyl moiety and the peptidic nitrogen of Asp593. These observations provided a clear rationale for the importance of the urea moiety in the design of effective c-Raf inhibitors (Wan et al., 2004).

Regorafenib is a fluorinated analogue of sorafenib (Wilhelm et al., 2011) with a comparable pharmacodynamic profile and an enhanced clinical performance, mainly related to the presence of the fluorine atom at the central aromatic ring. In 2012, it was approved the treatment of metastatic colorectal cancer (Dhillon, 2018) and in 2017 its use was extended to advanced hepatocarcinoma (Heo and Syed, 2018).

Donafenib is a modified form of sorafenib with a trideuterated N-methyl group at the distal pycolinamide moiety. The introduction of the deuterium atoms was guided by the necessity to potentially enhance the stability of sorafenib, thus improving the pharmacokinetic profile. *In vitro* studies demonstrated that donafenib and sorafenib have similar antiproliferative potency in multiple human cancer cell lines. Preclinical, Phase Ia and Ib studies have demonstrated good efficacy and safety profiles for donafenib (Bi et al., 2017; Li et al., 2020). Donafenib is approved in China for the treatment of hepatocellular carcinoma. Other clinical investigations for biliary cancer, acute myeloid leukaemia, thyroid cancer, gastric cancer, gastrointestinal cancer, esophageal cancer, nasopharyngeal cancer, colorectal cancer, cervical cancer and non-small cell lung cancer are underway in China.

Lenvatinib is another oral multikinase inhibitor successor of sorafenib. It is a type IIA inhibitor of VEGFR2 (IC_{50} = 4 nM), although Okomoto et al. recently suggested a re-classification of lenvatinib as a type V inhibitor (Okamoto et al., 2015). Lenvatinib is also an inhibitor of VEGFR1 (IC_{50} = 22 nM) and VEGFR3 (IC_{50} = 5.2 nM) and other pro-angiogenic and pro-oncogenic receptor tyrosine kinases, including FGFR 1 (IC_{50} = 46 nM), PDGFR α and β (IC_{50} = 51 and 39 nM, respectively), and KIT (IC_{50} = 100 nM). In 2015, it was approved for the treatment of non-radioiodine responsive thyroid cancer and in 2016 (Hamidi et al., 2022), for advanced renal cell carcinoma in combination with everolimus (Motzer et al., 2015, 2021). It is currently in clinical trials for the treatment of hepatocellular carcinoma. Lenvatinib differs from regorafenib and sorafenib as the diaryl-urea core scaffold has been replaced with an N-aryl-N-cyclopropyl urea. Notwithstanding this difference, the crystallographic structure of lenvatinib with VEGFR-2 demonstrated an overall comparable binding mode to sorafenib with BRAF (PDB ID: 3WZE) (Okamoto et al., 2015). Both drugs bind at the ATP-binding site of the receptor by exploiting the urea core scaffold which occupies a nearly identical position. The urea is involved in a network of H-bonds with the main-chain nitrogen of Asp1046 and the carboxylate in the sidechain of Glu885 as already observed in the binding mode of sorafenib at VEGFR-2. Notwithstanding the binding mode interests the ATP-binding site on VEGFR2 as well as the neighboring nonconservative allosteric region, the VEGFR2 structure complexed with sorafenib is in a DFG-out conformation, whereas VEGFR2 complexed with lenvatinib is in a DFG-in conformation. This different behavior might justify the longer residence time observed for lenvatinib than sorafenib (Okamoto et al., 2015).

Tivozanib is a potent pan-VEGFR tyrosine kinase inhibitor developed by Kirin Brewery, Co., Ltd. It showed picomolar activity against all three VEGFR isoforms (VEGFR-2 IC_{50} = 0.16 nM, VEGFR-l IC_{50} = 0.21 nM, and VEGFR-3 IC_{50} = 0.24 nM) (Nakamura et al., 2006). Additionally, it has nanomolar activity for cKIT and PDGFR at 1.63 and 1.72 nM, respectively. The sole information regarding the discovery of tivozanib is only reported in patent no. US2003087907A1 (Kubo et al., 2002). The medicinal chemistry aspect of this study is not available. Tivozanib was approved in 2017 by the EMA and in 2021 by FDA as a first-line therapy for the treatment of relapsed or refractory advanced renal cell carcinoma (Salgia et al., 2020).

Ripretinib is a novel type II tyrosine switch control inhibitor being developed by Deciphera Pharmaceuticals for the treatment of KIT or platelet derived growth factor receptor A (PDGFRA)-driven cancers, including gastrointestinal stromal tumor. Ripretinib inhibits KIT and PDGFRA kinases, including other kinases such as PDGFRB, TIE2, VEGFR2 and BRAF (Okamoto et al., 2015). Ripretinib is a type II "switch-control" kinase inhibitor that forces the activation loop (or activation "switch") into an inactive conformation (Smith et al., 2019). This innovative mechanism of action for ripretinib and congeners was confirmed by the recently resolved X-ray crystal structure of KIT1 kinase in complex with the ripretinib chloro analog DP-2976 (PDB ID: 3WZE). The carbonyl of the pyrimidone ring and the urea moiety in particular is involved in a dense network of H-bonds with the key amino acids Lys623, Asp640, and Glu810. These hydrogen bonds contribute to the switch of the kinase activation loop into the inactive type II state. Moreover, the pyridone ring forms additional hydrophobic interactions to further maintain the activation loop in its inactive state. The observed binding mode rationalized the peculiar mechanism of action of ripretinib. The sole information regarding the discovery of ripretinib is only reported in patent no. US8461179B1 (Flynn et al., 2012). The medicinal chemistry aspect of this study is not available. It was approved for medical use by the FDA in May 2020 and by the EMA in November 2021 for the treatment of patients with advanced gastrointestinal stromal tumors after previous therapy with kinase inhibitors.

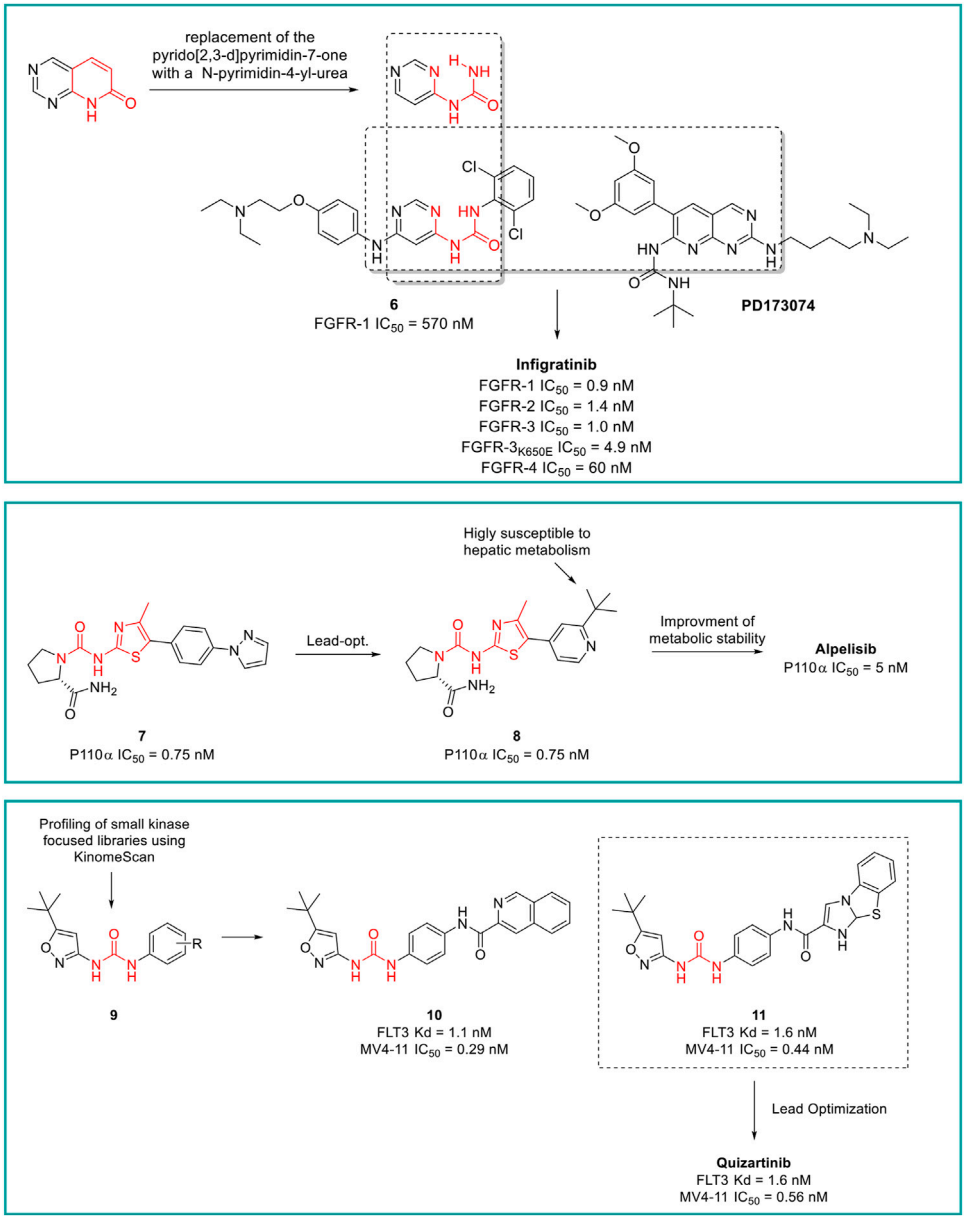


FIGURE 9
Key steps in the design of infigratinib, alpelisib and quizartinib.

Infigratinib is a pan-fibroblast growth factor receptor (FGFR) kinase 1-4 inhibitor, developed by Novartis. Aimed at the identification of potent and selective FGFR inhibitors, Guagnano et al. adopted a nonconventional strategy by replacing the pyrido [2,3-d]pyrimidin-7- one core structure of a well-known class of protein kinase inhibitors with a N-pyrimidin-4- yl-urea motif able to form pseudo six-membered rings by intramolecular hydrogen bonding, as depicted in Figure 9 (Guagnano et al., 2011). The first designed prototype compound **6** showed a submicromolar activity against FGFR1 (IC_{50} = 570 nM) (Furet et al., 2008). In a lead optimization process, the key structural motives of another FGFR1 inhibitor (**PD173074,** (Barvian et al., 2000)) were implemented in the chemical structure of **6**. Indeed, as depicted from the crystallographic structure of FGFR1 in complex with **6**, the two C (3) and C (5) methoxy groups on the aromatic ring of **PD173074** optimally fill the ATP hydrophobic pocket of the kinase (Mohammadi, 1998). A series of 3,5-dimethoxy-phenyl pyrimidinyl urea derivatives were prepared, with Infigratinib being the most potent and

selective compound of these derivatives. It showed low/sub nanomolar activity against FGFR1/2/3/4 and high selectivity over a panel of 76 protein kinases. The achieved binary FGFR1-infigratinib complex validated the rationale behind the design of this new class of FGFR inhibitors. Infigratinib also possessed a suitable pharmacokinetic profile in rodents to support further *in vivo* investigation. It inhibited the proliferation of bladder cancer cells overexpressing wild-type FGFR3 and demonstrated significant anticancer activity in RT112 bladder cancer xenografts (Guagnano et al., 2011). In clinical trials, Infigratinib was assessed for the treatment of head and neck cancer, breast cancer, urogenital cancer, bladder cancer, glioblastoma, achondroplasia, gastric cancer, esophageal cancer, and solid tumors. It is available for the treatment of cholangiocarcinoma in the United States and is under regulatory review for the treatment of previously treated unresectable locally advanced or metastatic cholangiocarcinoma with a fibroblast growth factor receptor 2 (FGFR2) fusion or other rearrangement in the EU.

Alpelisib is an orally bioavailable phosphatidylinositol 3-kinase (PI3K) inhibitor that was developed by Novartis Oncology and assessed for the treatment of diverse solid tumors such as breast cancer, ovarian cancer, and head and neck cancer. Alpelisib is a selective inhibitor of PIK3 in the PI3K/AKT kinase signaling pathway (Yang et al., 2019). This signaling pathway is associated with cancerogenesis and its dysregulation may contribute to tumor resistance. Alpelisib was developed by the same team of medicinal chemists that in the same years discovered infigratinib. Furet et al., reported that the 2-aminothiazole scaffold was a suitable template for the design of selective PI3K inhibitors (Figure 9) (Furet et al., 2013). The first selective PI3Kα prototype (**7**) was obtained by appending a proline residue to the amino group in position 2 of the thiazole using a ureidic linker (Bruce et al., 2012). Through a structure-based approach, the molecule was properly modified to maximize the binding at the ATP pocket of PI3Ka without altering the ureido-thiazole core scaffold as the thiazole nitrogen and the 2-NH group formed key bidentate H-bonds with key amino acids of the kinase. All the designed derivatives showed low nanomolar inhibitor activity against PI3Ka, with compound **8** being the most interesting candidate. Unfortunately, metabolic studies on rat hepatic microsomes revealed a rapid metabolism of the compound, mainly at the t-butyl side chain. To fix this issue, one methyl group of the t-butyl radical was substituted with a CF_3 which significantly improved the metabolic stability and reduced *in vivo* clearance, resulting in the identification of alpelisib. The crystallographic structure of alpelisib in complex with PI3Ka supported the medicinal chemistry rationale as the capability of the compound to establish a couple of H-bonds between the ureidic-thiazole and the side chain of Gln859 was experimentally observed (Furet et al., 2013). Alpelisib displayed a selectivity for p110a 50-fold higher than 442 other kinases, no inhibition of the CYP450 cytochrome and an excellent oral bioavailability in mice, rats and dogs. The proved anticancer activity of alpelisib in PI3Ka driven tumors in animal xenograft models and overall good tolerability supported the further clinical investigation (Furet et al., 2013). Interestingly, the combination of alpelisib and fulvestrant demonstrated increased antitumour activity in comparison to either treatment alone (André et al., 2021) and was registered in Australia and the EU in 2020 and marketed in the United States, Netherlands, Finland, UK and Canada in 2021.

Larotrectinib is a first-in-class, highly selective TRK inhibitor (Federman and McDermott, 2019). It was developed within a joint collaboration between Bayer and Loxo Oncology (a subsidiary of Eli Lilly), for the treatment of adult and pediatric patients with solid tumors (i.e., non-Hodgkin lymphoma, histiocytic disorders and primary CNS cancers) harboring neurotrophic receptor tyrosine kinase (NTRK) gene fusions (Yang et al., 2022). The sole information regarding the discovery of Larotrectinib is only reported in patent no. US8461179B1 (Flynn et al., 2012). The medicinal chemistry aspect of this study is not available. Larotrectinib binds at the ATP binding site of the TRK kinase family resulting in a potent inhibition of TRKA, TRKB and TRKC with IC_{50} values of 6.5, 8.1 and 10.6 nM, respectively, and in a highly selective manner over a panel of kinase and non-receptors (Federman and McDermott, 2019). TRK is mutated in a variety of cancer cell types and these mutations play an important role in tumor cell growth and survival and in drug resistance. Interestingly, larotrectinib showed nanomolar inhibitor activity against the most prevalent TRKA mutations ($TRKA^{G595R}$ IC_{50} = 109.4 nM, $TRKA^{G667C}$ IC_{50} = 32.2 nM, and $TRKA^{F589L}$ IC_{50} = 43.1 nM). Larotrectinib was launched in 2018 in the United States for the treatment of NTRK gene fusions-based solid tumors and in the following years it was registered in the EU and other countries worldwide for the same therapeutic indication.

Quizartinib is an FLT3 kinase inhibitor developed by Daiichi Sankyo Company (previously Ambit Biosciences) and Astellas Pharma, for the treatment of acute myeloid leukaemia (AML) and myelodysplastic syndromes. FLT3 kinase is mutated in approximately one-third of patients with AML, and these patients are less responsive to traditional therapies. From a medicinal chemistry standpoint, quizartinib was developed starting from a high-throughput screening (HTS) of small libraries of compounds using the KinomeScan™ technology (proprietary of Daiichi Sankyo Company). Patel et al. fished out some urea derivatives with general structure **9** as potent FLT3 inhibitors (Figure 9). The aim of the SAR study was to explore the influence of diverse substituents on the aromatic ring on the FLT3 inhibitory activity, leading to the development of a series of derivatives with nanomolar IC_{50} values. Compounds **10** and **11** (Figure 9) were the most potent and selective FLT3 inhibitors (FLT3 IC_{50} of 1.1 and 1.6 nM, respectively) of the series with sub nanomolar IC_{50} in counteracting the MV4-

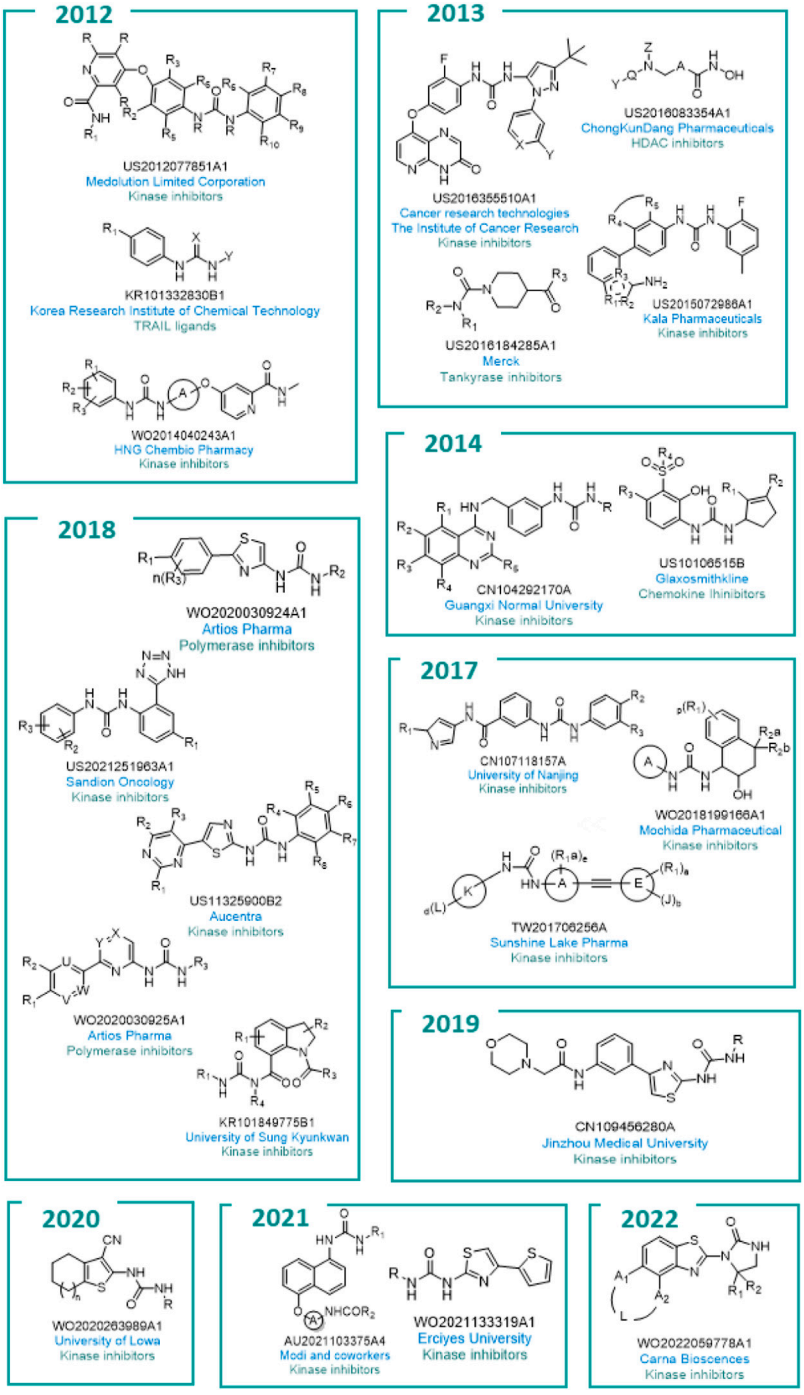


FIGURE 10
General structures of the different patented compounds.

11 cell lines proliferation and excellent pharmacokinetic properties and efficacy in a human tumor xenograft model in mice (Patel et al., 2009). Unfortunately, these two compounds suffer from very low aqueous solubility, especially at higher doses, which compromises the further development. Attributing their improper physicochemical properties to the presence of the amide moiety between the central aromatic ring and the distal heterocycles, Chao et al., in a lead-optimization program, removed the carboxamide and introduced diverse groups known to improve water solubility on the distal ring.



FIGURE 11
The location of academia (green) and companies (blue) which patented urea-based anticancer drugs worldwide.

The introduced substitutions on the main structure of **11** did not affect its potency and selectivity against FLT3 or its antiproliferative activity against MV4-11. Compound **12** was outstanding due to its superior pharmacodynamic (both *in vitro* and *in vivo*), pharmacokinetic and toxicological profile and was advanced into Phase II clinical trials for the treatment of acute myeloid leukemia, with the common name of quizartinib (Figure 9) (Chao et al., 2009). Quizartinib was marketed in Japan in 2019 and obtained pre-registration status in the United States and EU. However, the FDA and EMA express doubts on the approval of this drug due to the lack of a significant benefit-to-risk ratio (Garcia-Horton and Yee, 2020).

The patent landscape

Urea-based compounds with potential anticancer applications have increased in number, as clearly demonstrated by the trend in the literature (Figure 3). A similar trend was observed for patent applications, highlighting the importance of this chemical scaffold in drug development at both industrial and academic level. In the last 20 years, more than 30 thousand patents regarding new potential anticancer agents have been published and among them, 890 patents are focused on urea derivatives as anticancer drugs.

In this section, patents filled in last 10 years are analyzed and discussed.

All the general chemical structures of the urea-based molecules protected are reported in Figure 10.

Companies from all over the world in countries such as the UK, China, Japan, Denmark, Germany, and Australia are active in this field. This includes bigger industries such as GlaxoSmithKline and Merck as well as smaller companies such as Mochida Pharmaceutical and Aucentra (Figure 11).

Of note, since the exploitation of kinases as worthy anticancer targets is quite recent, and due to the discovery of new kinases involved in cancerogenesis, it is not surprising that the scientific world has focused its efforts on this hot topic. As a result, sixteen of the twenty-two patents cover the discovery of kinases inhibitors and ten are owned by Pharma companies.

In 2022, Carna Biosciences registered patent no. WO2022059778A1 (Cyclic urea derivatives) regarding the identification of selective dual-specificity tyrosine-regulated kinases (DYRK) inhibitors (Sawa et al., 2022). DYRK is a type of bispecific protein kinase that phosphorylates tyrosine, serine, and threonine. Five isoforms, namely DYRK1A, DYRK1B, DYRK2, DYRK3, and DYRK4, were identified to date (Boni et al., 2020). Particularly, inhibitors of DYRK1A are of interest for the treatment of EGFR-dependent cancer through the suppression of the cancer cells growing in EGFR-dependent tumors. The development of these derivatives is ongoing.

Scandion Oncology protected with patent no. US2021251963A1 (Urea derivatives for use in the treatment of subjects with elevated expression and/or activity of SRPK1) the discovery of new urea-based Serine/arginine-rich protein-specific kinase 1 (SRPK1) inhibitors as anticancer agents (Brünner and Jan 2021). SRPK1 is involved in the regulation of several mRNA processing pathways including alternative splicing, and overexpression of SRPK1 has been reported in multiple cancers including prostate, breast, lung, and glioma. Endovion (or NS 3728, SCO-101) was shown to be the most promising compound and is in Phase II clinical trials for colorectal tumor and in Phase I clinical trials for pancreatic and breast cancers.

Aucentra therapeutic registered patent no. US11325900B2 (5-(pyrimidin-4-yl)thiazol-2-yl urea derivatives as therapeutic agents) this year, regarding the discovery of urea derivatives as inhibitors of cyclin-dependent kinases (CDKs) (Wang et al., 2018). Of interest for its peculiar involvement in the physiopathology of cancer is isoform CDK8. CDK8 has specifically been reported to be an oncogene connected to colorectal cancer, activating β-catenin-mediated transcription that drives colon tumorigenesis. AU2-85 was presented as the most promising compound with proved anticancer efficacy and safety profiles in animal models. Currently, AU2-85 (or being a new chemical entity, it was renamed sunaciclib) is at the late stage of preclinical studies with a Phase I study planned for 2023.

Mochida Pharmaceutical registered patent no. WO2018199166A1 (Novel tetrahydronaphthyl urea derivatives) in 2017 (Saitoh et al., 2018). The company protected several urea derivatives represented by the general formula in Figure 10 as Tropomyosin receptor kinase A receptor (TrkA) inhibitors. TrkA is involved in several conditions such as pain, neurodegeneration, infection and particularly cancer. No information about clinical studies for the molecules of the present patent are reported at the moment.

In 2017, Sunshine Lake Pharma registered patent no. TW201706256A (Substituted urea derivatives and pharmaceutical uses thereof which provides substituted urea derivatives, and its stereoisomer, geometric isomer, tautomer, nitroxide, hydrate, solvate, metabolism product, ester, and pharmaceutically accepted salt or its prodrug), which was subsequently extended in Europe with accession no. US10065934B2 (Substituted urea derivatives and pharmaceutical uses thereof). In these patents, a deep investigation of the synthetic procedures for the preparation of urea derivatives as FLT3 inhibitors is reported (Cheng et al., 2017, 2018). FLT3 plays an important role in the proliferation and differentiation of hematopoietic stem cells. Overexpression of this receptor is found in AML (acute myeloid leukemia). The anticancer activity against MV4-11 cell lines expressing FLT3/ITD mutation was proved. None of the reported molecules are actually in clinical trials.

Three Pharmaceutical companies focused their efforts on the modulation of VEGFR. Kala Pharmaceuticals, HNG Chembio Pharmacy and Medolution Limited Corporation have patents nos. US2015072986A1 (Urea derivatives and uses thereof) (Kim et al., 2013), WO2014040243A1 (N-substituted phenyl-N′-substituted heterocyclic urea compound and application thereof as anticancer medicament) (Zhang et al., 2012), and US2012077851A1 (Urea derivatives as kinase inhibitors) (Zhang, 2012). HNG Chembio Pharmacy registered the design and synthesis of N-substituted heterocyclic urea derivatives with VEGFR-2 kinase inhibitor activity and the medical application as anticancer thereof. Medolution Limited Corporation protected a series of deuterated derivatives of sorafenib and regorafenib as multitarget kinase inhibitors for the treatment of VEGFR, PDGFR and/or RAF mediated cancer diseases (Zhang, 2012). Lastly, Kala Pharmaceuticals reported the synthesis of three different series of urea with potent and selective inhibitory activity against VEGFR. The most promising candidates are under preclinical studies for the treatment of cancer and ocular diseases (Kim et al., 2013).

In a public-private partnership, Cancer Research Technologies and the Institute of Cancer Research registered patent no. US2016355510A1 (1-(5-tert-butyl-2-aryl-pyrazol-3-yl)-3-[2-fluoro-4-[(3-oxo-4h-pyrido [2,3-b]pyrazin-8-yl)oxy] phenyl]urea derivatives as Raf inhibitors for the treatment of cancer) in 2013 (Springer et al., 2013). The advantages of targeting the inhibition of RAF as a cancer therapy were reported. RAF is a key downstream target for the RAS Guanine-nucleotide binding/GTPase proteins and also mediates the activation of the MAP kinase cascade consisting of RAF-MEK-ERK. RAF genes encode protein kinases that are thought to play important regulatory roles in signal transduction processes that regulate cell proliferation. The *in vitro* activity of the protected molecules, in terms of RAF inhibition was evaluated, along with the *in vivo* anticancer activity of the most interesting compounds.

Besides pharmaceutical companies, academia is also active in this field. In 2021, Modi S.J., Tiwari A and Kulkarni V.M. registered patent no. AU2021103375A4 (A rational Drug Design based identification of orally bioavailable 1,5-disubstituted naphthalene compounds as potent VEGFR-2 inhibitors) where three urea derivatives originating from different modification on sorafenib and regorafenib were reported as VEGFR-2 inhibitors (Modi et al., 2021). The most promising compound reduceed the cell viability of cancer cell line MCF-7 (breast adenocarcinoma), MDA-MB-231 (breast adenocarcinoma) and Hep G2 (hepatocellular carcinoma) and also suppressed the binding of VEGFR-2 on the surface of VEGF. The *in vivo* oral toxicity and pharmacokinetic properties were also investigated using Wistar rats.

Three academic patents focus on the discovery of inhibitors of a specific class of kinases named protein kinase enzyme activated by mitogen (MAPK). MAPK plays a key role in the signal transduction pathways of the p38 mitogen-activated protein kinase (p38MAPK) enzyme (Koul et al., 2013). Significant therapeutical results were attributed to p38MAPK inhibitors for the treatment of cancer, neuropathic pain, and periodontal diseases (Asih et al., 2020). The University of Nanjing registered patent no. CN107118157A (Design and synthesis of diphenyl urea derivative antitumor compounds containing pyrazol frameworks) in 2017, where the synthetic methods for the preparation of diphenyl urea derivatives with a pyrazol moiety and their effectiveness as antitumor agents against $BRAF^{V600E}$ associated cancers were broadly investigated and protected (Zhu et al., 2017). Moreover, the abnormal activation of the downstream MEK-ERK signaling pathway which is crucial for tumor growth, proliferation, invasion, and

metastasis was reported. With the same aim, the teams from the University of Iowa registered patent no. WO2020263989A1 (JNK inhibitors as anticancer agents) in 2020 (Salem and Elsaid, 2020). Herein, a series of ureas, benzamides and benzylamides derivatives were reported as c-Jun N-terminal kinase (JNK) inhibitors. JNKs are involved in several physiopathological processes, including inflammation, morphogenesis, and cell proliferation, differentiation, survival, and death. Persistent activation of JNKs is implicated in cancer development and progression. One of the main pathways controlled by JNK relies on the phosphorylation of the transcription factor p53. JNK is also implicated in the MAPK signaling cascade involved in cardiac hypertrophy. The urea derivatives were tested on A549 (lung carcinoma) cell lines using the MTS assay and showed promising activity. Lastly, in patent no. WO2021133319A1 of Erciyes University (Synthesis of urea derivatives which have p38 mapk inhibition and anticancer efficacy), which was registered in 2021, the inventors reported a series of urea-based compounds as effective inhibitors of MAPK (Dogan et al., 2021). Twenty-three urea derivatives were synthesized and their anticancer activity was evaluated through *in vitro* enzymatic inhibition assays. A real-time cell analyzer (xCelligence) system was adopted and performed on the most interesting compounds to monitor the cellular proliferation and inhibition of p38MAPK. Three urea derivatives were shown to be promising anticancer agents for further *in vivo* investigation.

Regarding the discovery of multi kinases inhibitors, of note is patent no. CN109456280A (4-Phenylthiazole-2-amine derivative containing urea structure, and preparation method and application thereof) that was registered in 2019 by Jinzhou Medical University. 4-phenylthiazole-2-amine ureas as anticancer agents were identified and protected (Cai et al., 2019). These compounds are multi kinase inhibitors that act on VEGFR, PDGFR-β, Kit, RET, Raf and Aurora, and showed promising antiproliferative activity against hepatic cancer cell lines with a comparable effect to sorafenib. University of Sung Kyunkwan registered patent no. KR101849775B1 in 2018 (N-N-aroylureas derivatives preparation method thereof and pharmaceutical compositions for the prevention and treatment of cancer containing the same as an active ingredient) (Kim and Sik, 2018). The inventors protected the discovery of novel N-aryl urea derivatives with anticancer activity against diverse human cancer cell lines characterized by an overexpression of different kinases, along with the development of a pharmaceutical composition for preventing and treating prostate and breast cancer. Lastly, in 2014, Guangxi Normal University registered patent no. CN104292170A (Quinazolinyl-aryl urea derivatives with antitumor function and application thereof) (JIANIAN et al., 2014). The synthetic procedure for the preparation of a series of congeners of sorafenib and gefitinib with quinazolinyl-aryl urea was reported. The compounds were assessed for *in vitro* kinase inhibitor activity and anticancer activity against several human cell lines.

Besides the exploitation of the urea moiety for the design of kinase inhibitors, this versatile scaffold inspired the development of anticancer small molecules that act on diverse targets involved in the physiopathology of cancer. In 2018, Artios Pharma Company registered two patents regarding urea derivatives as polymerase inhibitors. In patent no. WO2020030924A1 (Thiazoleureas as anticancer agents) the reported compounds were directed against RoIQ polymerase. RoIQ is a multifunctional enzyme that is comprised of an N-terminal helicase domain and a C-terminal low-fidelity DNA polymerase domain (Blencowe et al., 2020b). Both domains showed mechanistic functions in Microhomology-mediated end-joining (MMEJ). In general, RoIQ has been shown to be essential for the survival of homologous recombination-defective (HRD) cells and is up-regulated in HRD tumor cell lines. Accordingly, RoIQ is a valuable target for preventing or treating cancers such as breast cancer, ovarian cancer, prostate cancer, and pancreatic tumor retaining BRCA1 deficiency. In patent no. WO2020030925A1 (Heterocyclic substituted ureas, for use against cancer), Polq polymerase was selected as the target for a new series of heterocyclic urea derivatives (Blencowe et al., 2020a). PolQ is involved in the MMEJ mechanism, such as with the RoIQ enzyme. Inhibition of this enzyme might be exploited for preventing and treating tumor diseases, such as BRCA1 and BRCA2 deficient tumors, including breast, ovarian, prostate, and pancreatic cancer. The most interesting candidates in both patents are actually in Phase I or II for the treatment of metastatic solid tumors.

ChongKunDang Pharmaceuticals registered patent no. US2016083354A1 in 2013 (Novel compounds for selective histone deacetylase inhibitors, and pharmaceutical composition comprising the same) by which the identification of new compounds with histone deacetylase (HDAC) inhibitory activity was protected (Lee Changsik et al., 2013). Through the targeting of HDAC, the histone (protein) acetylation and chromatin structure were affected, inducing a complex transcriptional reprogramming exemplified by reactivation of tumor suppressor genes and repression of oncogenes. This target is particularly involved in several pathologies such as malignant tumors. Using Velcade as positive control, three compounds showed promising activity against multiple myeloma as pan HDAC inhibitors. Compound CKD-581 (or recently baptized as Alteminostat) is under Phase I studies for the treatment of lymphoma and multiple myeloma.

Lastly, among the others, the name of two important big pharmaceutical companies stand out. Glaxosmithkline reported in patent no. US10106515B2 (1-(cyclopent-2-en-1-yl)-3-(2-hydroxy-3-(arylsulfonyl)phenyl)urea derivatives as CXCR2 inhibitors) the exploitation of small molecule urea derivatives as anticancer agents targeting CXCR2. Indeed, chemokines regulate a broad spectrum of cellular functions and exert their actions by binding to chemokine receptors which are G protein-coupled receptors. CXCR2 is expressed

TABLE 1 Summary of cited patents.

Patent number	Patent applicant	Filing date	Mechanism of action	Development stage
KR101332830B1	Korea Research Institute	2012	TRAIL ligands	Preclinical phase
US2012077851A1	Medolution Limited Corporation	2012	Multi Kinases Inhibitors	Preclinical phase
WO2014040243A1	HNG Chembio Pharmacy	2012	VEGFR-2	Preclinical phase
US2016355510A1	Institute of Cancer Research	2013	RAF Inhibitors	Preclinical phase
US2016083354A1	ChongKunDang Pharmaceuticals	2013	HDAC Inhibitors	Phase 1
US2015072986A1	Kala Pharmaceuticals	2013	VEGFR Inhibitors	Preclinical phase
CN104292170A	Guangxi Normal University	2014	Multi Kinases Inhibitors	Preclinical phase
US10106515B2	Glaxosmithkline	2014	CXCR2 Inhibitors	Preclinical phase
CN107118157A	University of Nanjing	2017	MEK-ERK Inhibitors	Preclinical phase
W O 2018199166A1	Mochida Pharmaceutical	2017	TrkA Inhibitors	Preclinical phase
TW201706256A	Sunshine Lake Pharma	2017	FLT3 Inhibitors	Preclinical phase
WO2020030924A1	Artios Pharma Company	2018	RoIQ polymerase Inhibitors	Phase 1
WO2020030925A1	Artios Pharma Company	2018	PolQ polymerase Inhibitors	Phase 2
US11325900B2	Aucentra therapeutic	2018	CDKs Inhibitors	Phase 1
US2021251963A1	Scandion Oncology	2018	SRPK1 Inhibitors	Phase 1 and 2
CN109456280A	Jinzhou Medical University	2019	Multi Kinases Inhibitors	Preclinical phase
WO2020263989A1	University of Iowa	2020	JNK Inhibitors	Preclinical phase
WO2021133319A1	Erciyes University	2021	MAPK Inhibitors	Preclinical phase
AU2021103375A4	Modi S.J. and coworkers	2021	VEGFR1 Inhibitors	Preclinical phase
WO2022059778A1	Carna Biosciences	2022	DYRK Inhibitors	Preclinical
EP21201359	University of Pavia and University of Milano Bicocca	2022	Undisclosed	Preclinical

on a variety of cells including neutrophils, keratinocytes, mast cells, eosinophils, macrophages, endothelial cells, and neurons, including sensory neurons. CXCR2 dysregulations are involved in carcinogenesis (Korbecki et al., 2022). The development of a medical system to improve drug-like properties was additionally reported.

Merck, however, exploited tankyrases as innovative targets for cancer diseases. In 2013, patent no. US2016184285A1 (Piperidine urea derivatives) was registered, which protected the synthesis and anticancer activity of new urea derivatives targeting Tankyrases 1 and 2 (TANKs) (Buchstaller and Dieter, 2013). The piperidine urea derivatives were assessed in an *in vitro* assay, for autoparsylation, measurement of cellular inhibition of Tankyrase through Axin 2 level, and ELISA Assay Biochemical Activity Testing of TNSK 1 and 2 studies. Korea Research Institute of Chemical Technology registered patent no. KR101332830B1 in 2012 (A Cancer sensitizer comprising phenylurea derivatives or salts thereof) which describes the development of phenyl urea derivatives as modulators of the tumor necrosis factor-related apoptosis (TRAIL) (Kim Seong, 2013). TRAIL belongs to the tumor necrosis factor (TNF) protein family, whose activation selectively induces the death of cancer cells by the formation of the death-inducing pathway complex, DISC and the autocatalytic activation of caspase 3. The urea derivatives reported in the patent have the capability to promote the expression of death receptors (DRs) and to effectively suppress the expression of anti-apoptotic proteins in a cancer cell line with TRAIL resistance.

Lastly, in 2022 the University of Pavia and University of Milano Bicocca filled the patent application no. EP21201359 (Substituted vinyl piperazine-piperidine urea derivatives as anticancer agents) (Collina et al., 2022).

A summary of the analyzed patents is reported in Table 1.

All the innovations discussed so far represent remarkable contributions to stimulate the development of new anticancer treatments. The numerous examples retrieved from the recent patent landscape prove the extensive exploitation of the urea moiety as a privileged scaffold in the design and development of new chemical anticancer entities by both pharmaceutical companies and academic research groups.

Future perspective and outlook on novel compounds

As extensively reviewed above, many important antitumor agents contain a urea moiety, and the importance of this structural motif is further demonstrated by the large number of recent patents in this field. If we consider the unique properties of ureas, it is not surprising that this scaffold is regarded as a useful and versatile moiety from a medicinal chemistry standpoint. As described by the many examples reported in

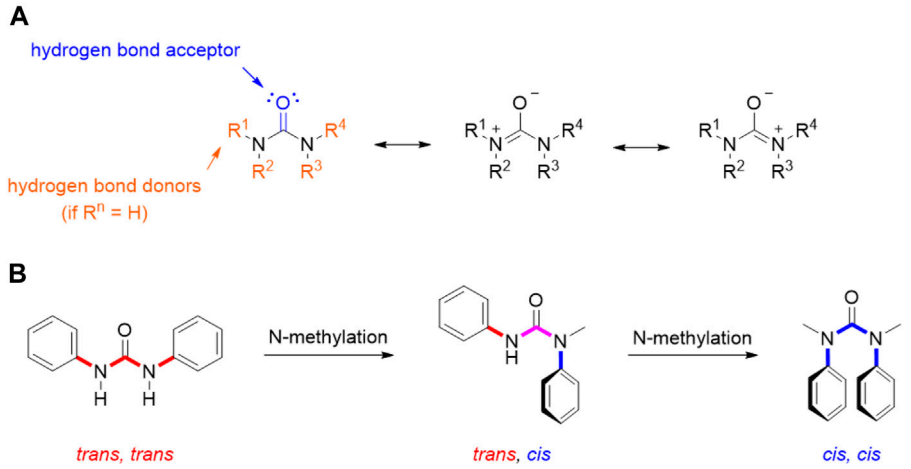


FIGURE 12
Resonance structure for urea moiety **(A)**; conformations of N,N′-diphenyl urea, N-methyl-N,N′- diphenyl urea, and N,N′-dimethyl-N,N′-diphenyl urea **(B)**.

this review, the urea group can serve both as hydrogen bond acceptor and as hydrogen bond donor: the carbonyl group is a nucleophile and a hydrogen bond acceptor endowed with the possibility to engage two hydrogen bonds, whereas the two nitrogens, depending on the degree of substitution, can donate up to four hydrogens (in urea itself). Moreover, the three possible resonance structures of the urea generate a stronger negative dipole on the carbonyl and a positive dipole on the nitrogen than other carbonyl derivatives (Figure 12). This partial separation of charges contributes to the reinforcement of the H-bonds that this functional group is able to entangle with the biological targets.

This also entails some conformational restriction which affects the three-dimensional structure of urea derivatives. In fact, several studies have been conducted in order to determine their prevalent conformation in solution and solid state. Ganis P. and co-workers examined the structure of N,N′-diphenyl-N, N′-diethylurea through X-ray diffraction, demonstrating a non-planar distortion of approximately 30° of amide groups and a bond length of 1.37 Å for the C-N bonds (Ganis et al., 1970). Furthermore, the N-substitution on the urea moiety plays a key role in its conformation (Figure 12). Indeed, in the solid state, N,N′-diphenylureas assume a *trans, trans* conformation, which can be shifted to *cis, cis* by subsequent N-methylation (Figure 3). This conformation is characterized by the stabilizing π-π stacking interactions of the aromatic moieties. A dynamic state is shown in solution, even though the *trans, trans* isomer remains predominant. The possibility to switch the most populated conformation by applying simple structural modifications (e.g., N-methylation) is of great importance for tuning drug-target interactions as it can be exploited to rationally design conformationally constrained urea derivatives that better adapt, for example, to the binding pocket of a target protein, enhancing activity and/or selectivity (Lortie et al., 2003). The physicochemical properties of the urea functionality are of paramount importance in the drug design and development process, since they determine key parameters such as solubility, permeability, metabolism, and bioavailability.

Thanks to the hydrogen bond donor and acceptor features of the urea group, this moiety improves aqueous solubility and permeability. Urea derivatives were successfully employed as hydrotropic agents, i.e. compounds used to improve a drug's solubility in pharmaceutical formulations (Cui, 2013; Herbig and Evers, 2013).

However, it is possible that ureidic compounds are not soluble in water and/or organic solvents. To overcome this problem with a medicinal chemistry approach, different strategies can be adopted: 1) modulation of hydrogen bonds; 2) disruption of planarity; 3) formation of a transient pseudo-ring structure. Regarding the modulation of the hydrogen bond, the introduction of electron donating and electron withdrawing groups on the nitrogen atoms allows for the modification of the inter- and intramolecular hydrogen bonds. Particularly, the nature of aliphatic moieties as nitrogen substituents establishes self-association of the molecules to promote the solubility in non-polar solvents (Lortie et al., 2003). Disrupting the planarity of the urea moiety reduces crystal packing energy and enhances water solubility. This can be achieved by introducing N-substituents to produce asymmetrical compounds (Ishikawa and Hashimoto, 2011). An additional method to disrupt planarity is the insertion of *ortho*-substituents on the N-aryl group of aryl ureas. A strategy that increases both solubility and permeability is the development of a transient pseudo-ring structure that

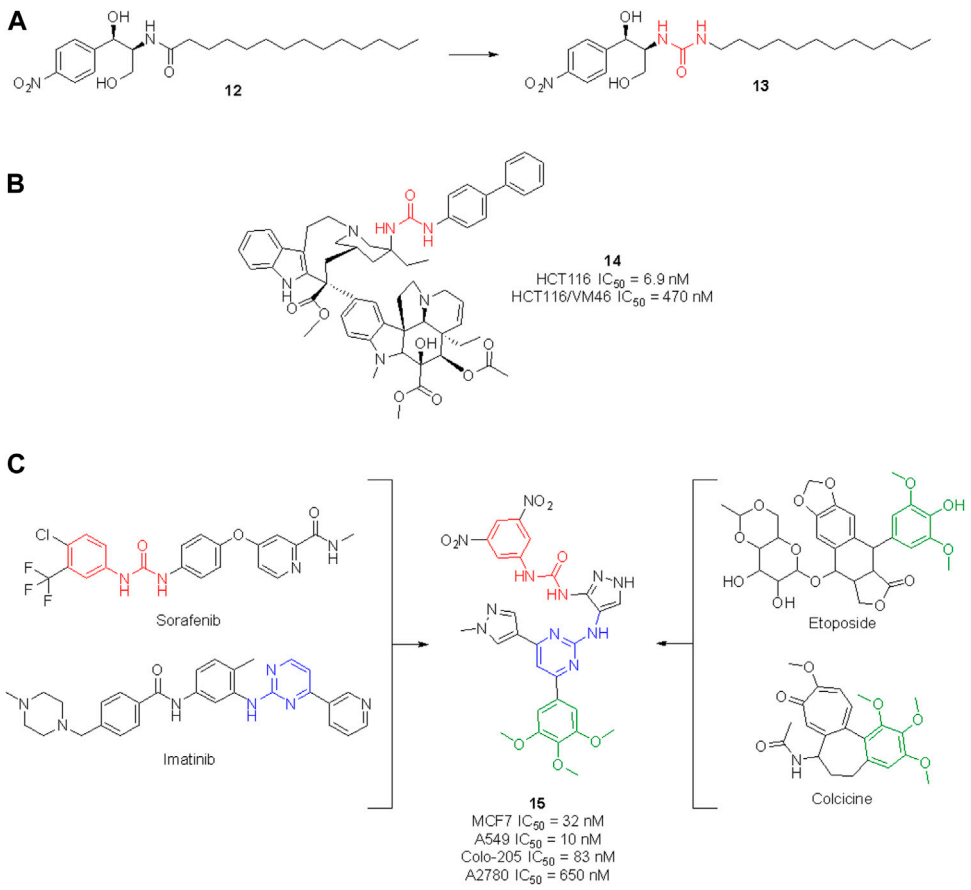


FIGURE 13
Development of new urea-containing ceramide analogs with anti-tumor activity **(A)**; structure of the vinblastine ureidic derivative **(B)**; design of a highly potent anticancer agent by merging the pharmacophoric elements of sorafenib, imatinib, colchicine and etoposide **(C)**.

involves intramolecular hydrogen bonds. In fact, the presence of a hydrogen bond acceptor near the urea moiety may lead the molecule towards a balance between closed (which increases permeability through lipophilic membranes via the reduction of exposed HBD) and open conformation (allowing the interaction of polar groups and solvent) (Alex et al., 2011). An example of this strategy can be found in the aforementioned FGFR inhibitor infigratinib, in which the stable pseudo-ring conformation mimics the pyrido [2,3-d]pyrimidin-7-one core of other known tyrosine kinase inhibitors (Guagnano et al., 2011). Furthermore, lipophilicity is of crucial importance for drugs targeting the central nervous system, as these should cross the blood-brain barrier by passive diffusion. Therefore, the modulation of the lipophilicity/hydrophilicity balance, exploiting the equilibrium between the open and close conformation and/or through the modification of N-substituents are other features accounting for the versatility of urea derivatives in medicinal chemistry.

The urea moiety has also been used as a bioisostere of amides (Kumari et al., 2020). For example, the ceramide analog **12**, which is endowed with potent cytotoxic activity against human colon cancer cells, underwent structural modifications and bioisosteric replacements to draw SAR considerations and identify novel anticancer agents (Figure 13). By substituting the amide group with a urea functionality, compound **13** was obtained, which emerged for its superior efficacy and broader activity toward other cancers (i.e., human renal, lung and prostate cancers as well as human leukemia) (Lim et al., 2003).

The high potential of the urea group to tweak the pharmacological profile of lead compounds encouraged further research in this field, and nowadays several medicinal chemistry research programs are taking advantage of this functionality to design novel molecules with an enhanced therapeutic effect. In the search for effective anticancer agents, natural products (NPs) have always been a major source of inspiration as privileged scaffolds endowed with enriched biological relevance (Martino et al., 2017, 2018;

Khalifa et al., 2019; Malacrida et al., 2021; Varghese and Dalvi, 2021). Although the urea moiety is uncommon among secondary metabolites–i.e., compounds that are produced by living organisms to mediate ecological interactions–it can be added as a decoration or bioisotere on NP scaffolds. The vinblastine derivative **14** (Figure 13) represents a remarkable example of how the urea motif can be exploited to design semisynthetic NP derivatives with improved pharmacodynamic and/or pharmacokinetic profile in respect to the parent natural product. Vinblastine is a vinca alkaloid isolated from *Catharanthus roseus* used for the treatment of Hodgkin's lymphoma, renal cell carcinoma, breast cancer, small cell lung cancer and colon cancer. Its mechanism of action involves the inhibition of microtubule assembly (Martino et al., 2017, 2018; Khalifa et al., 2019; Malacrida et al., 2021; Varghese and Dalvi, 2021). Leggans et al. reported a series of C20′ urea-based vinblastine derivatives and congeners with superior potency and activity against vinblastine-resistant tumor cell lines (Leggans et al., 2013). An extensive SAR revealed the importance of the urea moiety at C20′ over bioisosteric replacement with a thiourea, carbamate or amide. Interestingly, the introduction of a sterically demanding substituent on the second ureic nitrogen significatively contributed to the anticancer potency of these derivatives. These results contradicted the previous observation, i.e., that modification at C20′ of vinblastine might result in detrimental activity, opening instead new perspectives for the improvement of the anticancer activity of vinblastine derivatives. In particular, compound **14** showed a potency 10-times higher than vinblastine and promising cell inhibitory activity against the HCT116 (human colon cancer) and HCT116/VM46 (resistant human colon cancer) cancer cell lines (Leggans et al., 2013).

The growing interest of academia in this field is confirmed by the high number of very recent publications (i.e., within the last 2 years) concerning the discovery of novel antitumor agents containing the urea moiety.

For example, Cherukumalli at al. recently reported a series of new urea derivatives based on the pyrimidine-pyrazole core scaffold. These compounds were designed by combining the key pharmacophoric moieties of sorafenib, imatinib, colchicine and etoposide, as reported in Figure 13. The ten compounds were assessed for antiproliferative activity against several cancer cell lines (MCF-7, A549, Colon-205 and A2780) with IC_{50} values in the low/sub micromolar range. Compound **15** emerged for its excellent cytotoxicity activity, especially in comparison with etoposide. Molecular docking studies suggested that the anticancer activity could be derived from the inhibition of tubulin binding protein, human Abl tyrosine kinase and DNA topoisomerase. However, no experimental IC_{50} against these targets have been reported yet (Cherukumalli et al., 2022). Comparison of computational data with experimental results would allow for the development of an accurate SAR profile that assesses the role of the urea moiety of **15** in the interaction with the target(s).

Gömeç et al. have very recently reported the synthesis of five diaryl urea-compounds with the aim to prove their anticancer properties against colon adenocarcinoma (Figure 14). Compound **16** showed promising anticancer activity against HT-29 cell lines with an estimated IC_{50} of 20 μM, with no cytotoxicity on healthy L929 fibroblast cell lines at the same dose. With a second aim to identify the putative target of **16**, docking calculations were performed against 34 key targets known to be involved in colon cancer. Briefly, **16** potentially being able to bind to Hsp90 revealed the importance of the urea moiety to effectively interact with the target. The urea forms three H-bonds with Gly97 and Lys58 involving the NH and the carbonyl, respectively (Gömeç et al., 2022). In a following study, the same authors reported the anticancer investigation of another set of diphenyl ureas. The designed compounds were predicted to target the estrogen receptor and were assessed for antiproliferative activity against the estrogen receptor (+) breast cancer cell line MCF-7. **17** was the most potent compound of the series with an estimated MCF-7 IC_{50} around 20 μM, but no cytotoxicity in healthy fibroblast cells (Gömeç et al., 2022).

Ganapathi et al., by replacing the phthalimide moiety of apremilast—which is considered a pharmacophore for PDE4 activity - with the aryl urea moiety, reported the design of a series of new sulfonylurea derivatives with anticancer activity. These compounds were tested against human breast (MCF-7), liver (HEPG2) and colon (HCT) cancer cell lines by SRB assay, using doxorubicin as a positive control. Compounds **18** and **19** were the most promising derivatives (Ganapathi et al., 2021).

Recent clinical evidence suggested the potential use of chloroquine (CQ) for the treatment of hepatocellular carcinoma (HCC) by exploiting the capability of this drug in blocking the autophagy. This occurred with a combination of CQ with sorafenib and only at high doses of CQ. Therefore, with the aim to design a dual molecule that can efficiently inhibit autophagy and induce cytotoxicity at the same time, Jin et al. synthesized a series of cinchona alkaloid derivatives with amide, squaramide, thiourea, and urea functional groups. Compound **20** was the most interesting derivative with sub-micromolar IC_{50} against diverse HCC cell lines (Figure 14). Moreover, it was proven to down-regulate Akt activation, reduce the antiapoptotic protein Bcl-xl expression and increase the activated caspase-3 in HCC cells and the expression of LC3-II and p62. The inhibition of autophagosome-lysosome fusion and suppression of the Akt/mTOR/S6k pathway in HCC cells was evaluated (Jin et al., 2021). Hence, this further supports the viability of the introduction of the urea moiety on NP scaffolds to identify new anticancer agents.

Li et al. (2020) synthesized a set of sorafenib derivatives by replacing the pyridine distal ring with a quinoxaline scaffold. The compounds were directly assessed for anticancer activity against

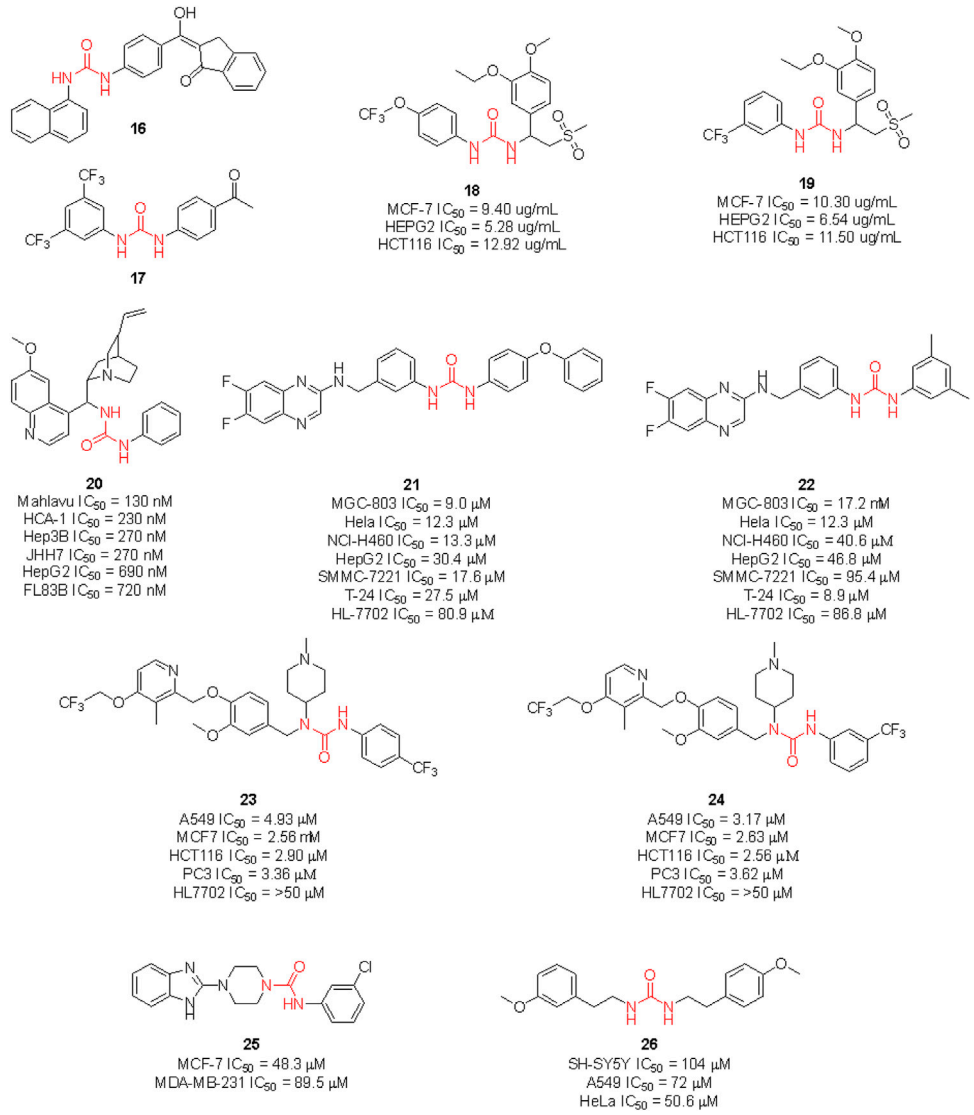


FIGURE 14
Urea-containing anticancer agents discovered in medicinal chemistry research programs within the last 2 years.

six human tumor cell lines, namely MGC-80 (gastric mucinous adenocarcinoma), HeLa (epithelioid cervix carcinoma), NCI-H460 (cell lung cancer), SMMC-7721 (human papillomavirus-related endocervical adenocarcinoma), HepG2 (hepatocellular carcinoma) and T-24 (transitional cell carcinoma). Compounds **21** and **22** were the most interesting candidates with anticancer activity higher than 5-fluorouracil, cisplatin, and sorafenib against MGC-803 cell lines. Lower cytotoxicity on healthy HL-7702 cell lines was observed at the assessed doses. Although the molecules were designed as sorafenib derivatives, no inhibitor activity against kinases was reported.

Hou et al. reported another series of sorafenib derivatives by combining the diaryl urea core scaffold with the pyridyl moiety of proton pump inhibitors. Lansoprazole, indeed, was revealed to exert modest anticancer activity (Hou et al., 2021). The anticancer activity of the designed hybrid molecules was evaluated against non-small cell lung cancer (A549), breast cancer (MCF-7), colon cancer (HCT116) and prostate cancer (PC-3) cell lines. The best antiproliferative activities (IC_{50} < 5 μM), and low toxicity against healthy human liver normal HL7702 cell lines were observed for compounds **23** and **24**. Also in this case, no inhibitor activity against kinases was reported.

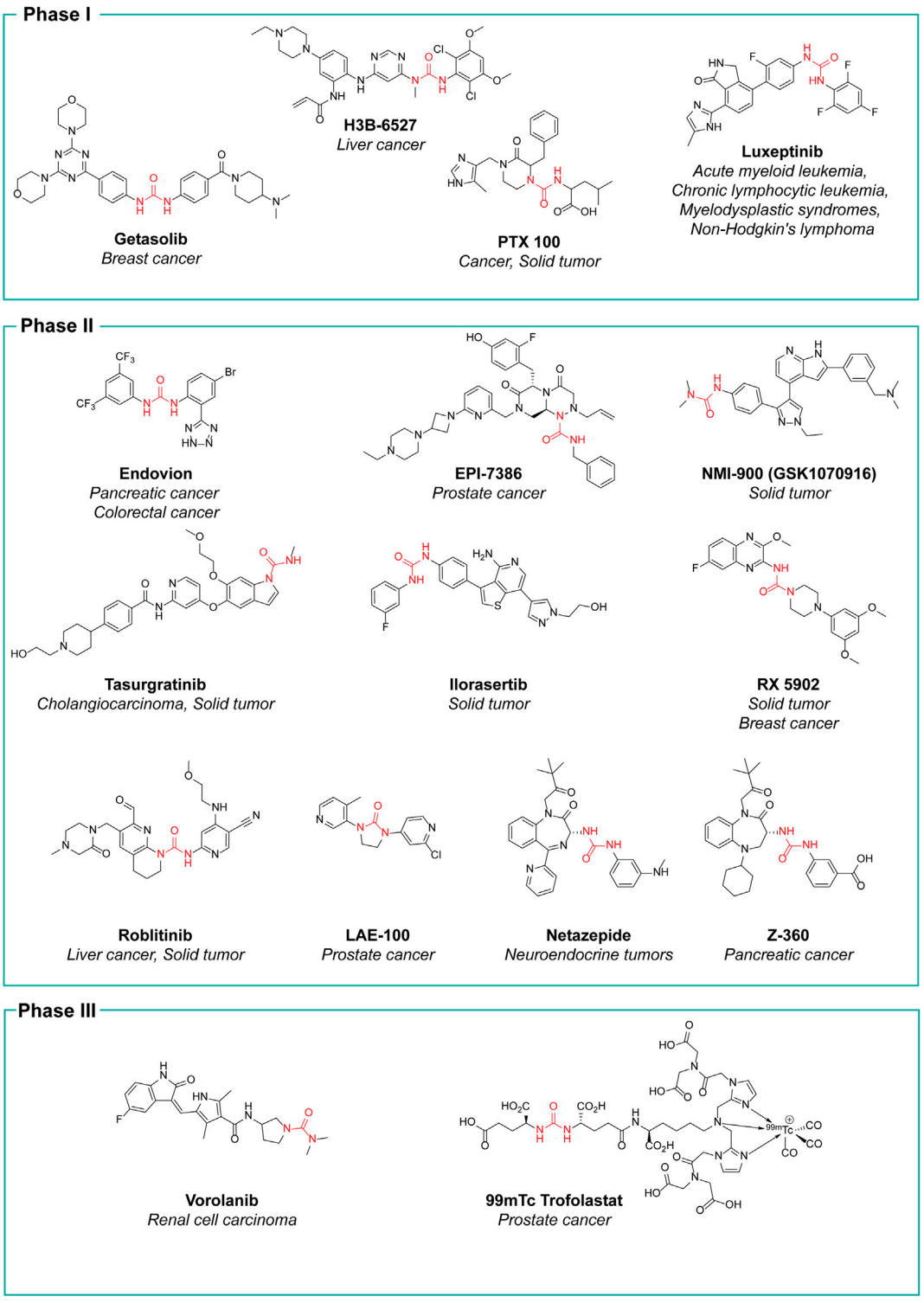


FIGURE 15
Urea-containing compounds currently under clinical evaluation as anticancer agents. For each drug candidate, the highest phase of clinical trials that has been attained is indicated, along with the specific therapeutic indication.

TABLE 2 Clinical trial progression and therapeutic indication for the new chemical entities.

Type of cancers	NCT number	Candidate	Phase 1 Phase 2 Phase 3
Breast cancer	NCT03911973 and NCT04238715	Gedatolisib and Tasurgratinib	
	NCT02003092, NCT01173913	RX5902, Docetaxel/Ritonavir	
Prostate cancer	NCT04421222, NCT01173913 NCT04060394	EPI 7386, Docetaxel/Ritonavir and LAE 001	
Pancreatic cancer	NCT03511222 and NCT00288925	Vorofonib and 1360	
Solid Tumor	NCT03900442 and NCT03511222	PTX 100 and Vorolanib	
	NCT04238715, NCT02325739, NCT02003092, NCT01173913 and NCT02478320	Tasurgratinib, Roblitinib, RX5902, Docetaxel/Ritonavir and Ilorasertib	
Liver cancer	NCT02834780	H38 6527	
	NCT02325739	Roblitinib	
Acute myeloid leukemia	NCT03893682	Luxeptinib	
Non-small cell lung cancer	NCT03511222	Vorofanib	
Chronic lymphocytic leukemia, Myelodysplastic syndromes, Non-Hodgkin's lymphoma	NCT03893682	Luxeptinib	
Cholangiocarcinoma	NCT04238715	Tasurgratinib	
Malignant melanoma, Small cell lung cancer, Malignant thymoma	NCT03511222	Vorolanib	
Renal cell carcinoma	NCT03511222	Vorolanib	
Cervical intraepithelial neoplasia	NCT04276688	Lopinavir/Ritonavir	
Neuroendocrine tumor	NCT01298999	Netazepide	

The above described glasdegib is an example of an already approved drug based on urea and benzimidazole scaffold. Looking for new promising anticancer compounds, Siddig et al. (2021) synthesized and assessed a series of novel thiourea-/urea-benzimidazole derivatives for cytotoxicity against MCF-7 and MDA-MB-321 human breast cancer cell lines. **25** was the most promising compound with IC_{50} of 48.3 and 89.5 μM against MCF-7 and MDA-MB-231 cells, respectively.

Lastly, Özgeriş et al. reported the synthesis of the unsymmetrical urea **26** and investigated its activity as an antibacterial, anticancer and antioxidant agent. Whilst **26** did not show antimicrobial activity, remarkable activity against SH-SY5Y (IC_{50} = 104 μM), A549 (IC_{50} = 72 μM), and especially against the HeLa cells (IC_{50} = 50.6 μM), was observed (Özgeriş et al., 2022).

The examples reported above are evidence that urea is an important and versatile moiety of the medicinal chemist's toolbox: it can be exploited to engage key drug-target interaction (thus enhancing potency and/or selectivity) and to improve the pharmacokinetic profile of a given molecule, modulating water solubility, lipophilicity and metabolic stability. Moreover, it can be used as a bioisostere and to structurally modify natural products.

The research in the field is expected to increase, not only with the discovery of new hit compounds, but also by virtue of the numerous urea derivatives currently under clinical trials for the treatment of different types of cancer. New molecular entities that have not already been presented throughout this review, but are now under advanced evaluation are reported in Figure 15, along with their clinical study phase and therapeutic indication (source AdisInsight, last access on 14 July 2022).

Despite the significant advantages and the high versatility of the urea functionality, it must be noted that in some cases, urea derivatives can still present problematic or sub-optimal

pharmacokinetic properties which cannot be overcome by structural modifications. In these cases, an approach based on pharmaceutical technology can be adopted. Even old active ingredients can have a new life thanks to innovative formulations that enhance their bioavailability and/or safety.

For example, the aforementioned carmustine can lead to severe side effects upon systemic administration, due to its high reactivity. To overcome this issue, in 1997, 20 years after the first approval, Arbor Pharmaceuticals developed and led the carmustine polifeprosan 20 wafer to the market for the treatment of glioma. The authorization was extended in Europe in 2008. This pharmaceutical specialty is a sustained-release biodegradable wafer implant that delivers the chemotherapeutic drug directly to the site of a brain cancer during the surgery, thus minimizing the drug-exposure to other areas of the body (Della Puppa et al., 2011). Very recently, a biosimilar of goserelin formulated as a monthly or trimonthly subcutaneous implant has been developed by Alvogen for the treatment of cancer, female infertility, uterine leiomyoma and endometriosis. An extended-release (XR) microsphere formulation of goserelin is being developed by Luye Pharma Group, utilizing its long-acting and extended-release technology platform for the development of the product. This goserelin formulation was preregistered for prostate cancer in China in 2021 and is in Phase III clinical trials for breast cancer.

A summary of the compounds in clinical trials is reported in Table 2.

Conclusion

In this review, we deeply discussed the key role played by urea moiety in the development of anticancer agents, outlying its presence in several approved antitumor drugs as well as in novel hits and drug candidates. The specific physico-chemical properties of urea moiety, and the possibility to modulate different targets by properly selecting the nitrogen substituents opens many possibilities in drug design. The urea functionality may be fundamental not only for drug-target interactions but also for improving the pharmacokinetic profile of a drug candidate. The present review is expected to provide useful insights in the design of urea-based compounds and would inspire the medicinal chemists for the development of clinically viable candidates. as well as new formulations for old urea-based drugs. Developing innovative pharmaceutical platforms is indeed a winning strategy to improve the pharmacological profile of already marketed drugs, also to bypass developability issues related to the urea moiety, when it is essential for the biological activity. Despite numerous advances, scientists are still trying to develop novel drugs that are useful in clinical oncology and able to overcome resistance to chemotherapy, which is mainly due to protein mutations, i.e., kinases or stress oxidation machinery dysregulation. As extensively herein discussed, urea derivatives can be a powerful tool for the discovery of new, effective therapeutics and hopefully inspire future research toward the development of viable strategies to fight cancer.

Author contributions

All authors listed have made a substantial, direct, and intellectual contribution to the work and approved it for publication.

Conflict of interest

The authors declare that the research was conducted in the absence of any commercial or financial relationships that could be construed as a potential conflict of interest.

Publisher's note

All claims expressed in this article are solely those of the authors and do not necessarily represent those of their affiliated organizations, or those of the publisher, the editors and the reviewers. Any product that may be evaluated in this article, or claim that may be made by its manufacturer, is not guaranteed or endorsed by the publisher.

References

Alex, A., Millan, D. S., Perez, M., Wakenhut, F., and Whitlock, G. A. (2011). Intramolecular hydrogen bonding to improve membrane permeability and absorption in beyond rule of five chemical space. *Medchemcomm* 2, 669. doi:10.1039/c1md00093d

Ali, M., Chen, H.-Y., Chiang, Y.-F., Badary, O. A., Hsia, S.-M., and Al-Hendy, A. (2022). An evaluation of relugolix/estradiol/norethindrone acetate for the treatment of heavy menstrual bleeding associated with uterine fibroids in premenopausal women. *Expert Opin. Pharmacother.* 23, 421–429. doi:10.1080/14656566.2022.2030705

André, F., Ciruelos, E. M., Juric, D., Loibl, S., Campone, M., Mayer, I. A., et al. (2021). Alpelisib plus fulvestrant for PIK3CA-mutated, hormone receptor-positive, human epidermal growth factor receptor-2–negative advanced breast cancer: Final overall survival results from SOLAR-1. *Ann. Oncol.* 32, 208–217. doi:10.1016/j.annonc.2020.11.011

Asih, P. R., Prikas, E., Stefanoska, K., Tan, A. R. P., Ahel, H. I., and Ittner, A. (2020). Functions of p38 MAP kinases in the central nervous system. *Front. Mol. Neurosci.* 13, 570586. doi:10.3389/fnmol.2020.570586

Avendaño, C., and Menéndez, J. C. (2015). "DNA alkylating agents," in *Medicinal chemistry of anticancer drugs* (Netherlands: Elsevier), 197–241. doi:10.1016/B978-0-444-62649-3.00005-3

Ayala-Aguilera, C. C., Valero, T., Lorente-Macías, Á., Baillache, D. J., Croke, S., and Unciti-Broceta, A. (2022). Small molecule kinase inhibitor drugs (1995–2021): Medical indication, pharmacology, and synthesis. *J. Med. Chem.* 65, 1047–1131. doi:10.1021/acs.jmedchem.1c00963

Ayati, A., Moghimi, S., Salarinejad, S., Safavi, M., Pouramiri, B., and Foroumadi, A. (2020). A review on progression of epidermal growth factor receptor (EGFR) inhibitors as an efficient approach in cancer targeted therapy. *Bioorg. Chem.* 99, 103811. doi:10.1016/j.bioorg.2020.103811

Bajusz, S., Csernus, V. J., Janaky, T., Bokser, L., Fekete, M., and Schally, A. V. (2009). New antagonists of LHRH II. Inhibition and potentiation of LHRH by closely related analogues. *Int. J. Pept. Protein Res.* 32, 425–435. doi:10.1111/j.1399-3011.1988.tb01373.x

Banerjee, S. R., Pullambhatla, M., Byun, Y., Nimmagadda, S., Green, G., Fox, J. J., et al. (2010). 68 Ga-labeled inhibitors of prostate-specific membrane antigen (PSMA) for imaging prostate cancer. *J. Med. Chem.* 53, 5333–5341. doi:10.1021/jm100623e

Barinka, C., Byun, Y., Dusich, C. L., Banerjee, S. R., Chen, Y., Castanares, M., et al. (2008). Interactions between human glutamate carboxypeptidase II and urea-based inhibitors: Structural characterization. *J. Med. Chem.* 51, 7737–7743. doi:10.1021/jm800765e

Barvian, M., Boschelli, D. H., Cossrow, J., Dobrusin, E., Fattaey, A., Fritsch, A., et al. (2000). Pyrido [2 , 3- d] pyrimidin-7-one inhibitors of cyclin-dependent kinases. *J. Med. Chem.* 43, 4606–4616. doi:10.1021/jm000271k

Bavetsias, V., and Linardopoulos, S. (2015). Aurora kinase inhibitors: Current status and outlook. *Front. Oncol.* 5, 278. doi:10.3389/fonc.2015.00278

Benešová, M., Schäfer, M., Bauder-Wüst, U., Afshar-Oromieh, A., Kratochwil, C., Mier, W., et al. (2015). Preclinical evaluation of a tailor-made DOTA-conjugated PSMA inhibitor with optimized linker moiety for imaging and endoradiotherapy of prostate cancer. *J. Nucl. Med.* 56, 914–920. doi:10.2967/jnumed.114.147413

Bhuyan, B. K. (1970). The action of streptozotocin on mammalian cells. *Cancer Res.* 30, 2017–2023.

Bi, F., Qiu, M., Chai, X., Niu, J., Ding, Y., Bai, Y., et al. (2017). A multicenter phase II study of donafenib in patients with advanced hepatocellular carcinoma. *J. Clin. Oncol.* 35, e15682. doi:10.1200/JCO.2017.35.15_suppl.e15682

Blencowe, P., Mark, C., Andrew, C., Tennyson, E., Robert, H., Ellen, M., et al. (2020a). Heterocyclic substituted ureas, for use against cancer. WO2020030925A1.

Blencowe, P., Mark, C., Tennyson, E., Ellen, M., Hollie, M., and Laurent, R. (2020b).Thiazoleureas as anticancer agents. WO2020030924A1.

Boni, J., Rubio-Perez, C., López-Bigas, N., Fillat, C., and de la Luna, S. (2020). The DYRK family of kinases in cancer: Molecular functions and therapeutic opportunities. *Cancers (Basel)* 12, 2106–2126. doi:10.3390/cancers12082106

Brentjens, R., and Saltz, L. (2001). Islet cell tumors of the pancreas: The medical oncologist's perspective. *Surg. Clin. North Am.* 81, 527–542. doi:10.1016/S0039-6109(05)70141-9

Bruce, I., Akhlaq, M., Bloomfield, G. C., Budd, E., Cox, B., Cuenoud, B., et al. (2012). Development of isoform selective PI3-kinase inhibitors as pharmacological tools for elucidating the PI3K pathway. *Bioorg. Med. Chem. Lett.* 22, 5445–5450. doi:10.1016/j.bmcl.2012.07.042

Brünner, N. A., and Jan, S. (2021). Urea derivatives for use in the treatment of subjects with elevated expression and/or activity of SRPK1. US2021251963A1.

Buchstaller, H.-P., and Dieter, D. (2013). Piperidine urea derivatives.

Cadène, M., Duranton, J., North, A., Tahar, S.-M., Chignard, M., and Bieth, J. G. (1997). Inhibition of neutrophil serine proteinases by suramin. *J. Biol. Chem.* 272, 9950–9955. doi:10.1074/jbc.272.15.9950

Cai, D., Bo, H., Chungang, F., and Yunhong, J. (2019). 4-Phenylthiazole-2-amine derivative containing urea structure, and preparation method and application thereof. CN109456280A.

Catalano, A., Iacopetta, D., Sinicropi, M. S., and Franchini, C. (2021). Diarylureas as antitumor agents. *Appl. Sci. (Basel).* 11, 374. doi:10.3390/app11010374

Chao, Q., Sprankle, K. G., Grotzfeld, R. M., Lai, A. G., Carter, T. A., Velasco, A. M., et al. (2009). Identification of N-(5-tert-butyl-isoxazol-3-yl)-N′-{4-[7-(2- morpholin-4-yl-ethoxy)imidazo-[2, 1-b] [1, 3]benzothiazol-2-yl]phenyl}urea dihydrochloride (AC220), a uniquely potent, selective, and efficacious FMS-like tyrosine kinase-3 (FLT3) inhibitor. *J. Med. Chem.* 52, 7808–7816. doi:10.1021/jm9007533

Chen, Y., Pullambhatla, M., Foss, C. A., Byun, Y., Nimmagadda, S., Senthamizhchelvan, S., et al. (2011). 2-(3-{1-Carboxy-5-[(6-[18F]Fluoro-Pyridine-3-Carbonyl)-Amino]-Pentyl}-Ureido)-Pentanedioic acid, [18F]DCFPyL, a PSMA-based PET imaging agent for prostate cancer. *Clin. Cancer Res.* 17, 7645–7653. doi:10.1158/1078-0432.CCR-11-1357

Cheng, C., Ying-Jun, Z., Bing, L., Bo-Hua, L., Yu, C., and Zhi-Xin, C. (2018). Substituted urea derivatives and pharmaceutical uses thereof. US10065934B2.

Cheng, C., Ying-Jun, Z., Bing, L., Bo-Hua, L., Yu, C., and Zhi-Xin, C. (2017). *Substituted urea derivatives and pharmaceutical uses thereof which provides substituted urea derivatives, and its stereoisomer, geometric isomer, tautomer, nitroxide, hydrate, solvate, metabolism product, ester, and pharmaceutically accepted salt or its p*. TW201706256A.

Chuu, C.-P., Kokontis, J. M., Hiipakka, R. A., Fukuchi, J., Lin, H.-P., Lin, C.-Y., et al. (2011). Androgens as therapy for androgen receptor-positive castration-resistant prostate cancer. *J. Biomed. Sci.* 18, 63. doi:10.1186/1423-0127-18-63

Cohen, P., Cross, D., and Jänne, P. A. (2021). Kinase drug discovery 20 years after imatinib: Progress and future directions. *Nat. Rev. Drug Discov.* 20, 551–569. doi:10.1038/s41573-021-00195-4

Collina, S., Daniela, R., Pasquale, L., Giacomo, R., Roberta, L., Guido, C., et al. (2022). *Substituted vinyl piperazine-piperidine urea derivatives as anticancer agents*. EP21201359.

Colvin, M., Brundrett, R. B., Cowens, W., Jardine, I., and Ludlum, D. B. (1976). A chemical basis for the antitumor activity of chloroethylnitrosoureas. *Biochem. Pharmacol.* 25, 695–699. doi:10.1016/0006-2952(76)90246-X

Cui, Y. (2013). Hydrotropic solubilization by urea derivatives: A molecular dynamics simulation study. *J. Pharm. (Cairo).* 2013, 1–15. –15. doi:10.1155/2013/791370

Della Puppa, A., Rossetto, M., Ciccarino, P., Denaro, L., Rotilio, A., D'Avella, D., et al. (2011). Carmustine wafer implantation when surgical cavity is communicating with cerebral ventricles: Technical considerations on a clinical series. *World Neurosurg. x.* 76, 156–159. doi:10.1016/j.wneu.2010.10.024

Dhillon, S. (2018). Regorafenib: A review in metastatic colorectal cancer. *Drugs* 78, 1133–1144. doi:10.1007/s40265-018-0938-y

Dogan, S. D., Betul, A. M., Kubra, K. A. A., and Ruveyde, K. (2021). *Synthesis of urea derivatives which have p38 mapk inhibition and anticancer efficacy*. WO2021133319A1.

Dutta, A. S., Furr, B. J. A., Giles, M. B., and Valcaccia, B. (1978). Synthesis and biological activity of highly active .alpha.-aza analogs of luliberin. *J. Med. Chem.* 21, 1018–1024. doi:10.1021/jm00208a004

Eichhorst, S. T., Krueger, A., Müerköster, S., Fas, S. C., Golks, A., Gruetzner, U., et al. (2004). Suramin inhibits death receptor–induced apoptosis *in vitro* and fulminant apoptotic liver damage in mice. *Nat. Med.* 10, 602–609. doi:10.1038/nm1049

Evans, J. C., Malhotra, M., Cryan, J. F., and O'Driscoll, C. M. (2016). The therapeutic and diagnostic potential of the prostate specific membrane antigen/glutamate carboxypeptidase II (PSMA/GCPII) in cancer and neurological disease. *Br. J. Pharmacol.* 173, 3041–3079. doi:10.1111/bph.13576

Federman, N., and McDermott, R. (2019). Larotrectinib, a highly selective tropomyosin receptor kinase (TRK) inhibitor for the treatment of TRK fusion cancer. *Expert Rev. Clin. Pharmacol.* 12, 931–939. doi:10.1080/17512433.2019.1661775

Feng, Y., Li, M., Wang, B., and Zheng, Y. G. (2010). Discovery and mechanistic study of a class of protein arginine methylation inhibitors. *J. Med. Chem.* 53, 6028–6039. doi:10.1021/jm100416n

Firsching, A., Nickel, P., Allolio, B., and Mora, P. (1995). Antiproliferative and angiostatic activity of suramin analogues. *Cancer Res.* 55, 4957–4961.

Flynn, D. L., Kaufman, M. D., and Petillo, P. A. (2012). *Dihydronaphthyridines and related compounds useful as kinase inhibitors for the treatment of proliferative diseases*. US8461179B1.

Fukushima, N., Minami, Y., Kakiuchi, S., Kuwatsuka, Y., Hayakawa, F., Jamieson, C., et al. (2016). Small-molecule Hedgehog inhibitor attenuates the leukemia-initiation potential of acute myeloid leukemia cells. *Cancer Sci.* 107, 1422–1429. doi:10.1111/cas.13019

Furet, P., Caravatti, G., Guagnano, V., Lang, M., Meyer, T., and Schoepfer, J. (2008). Entry into a new class of protein kinase inhibitors by pseudo ring design. *Bioorg. Med. Chem. Lett.* 18, 897–900. doi:10.1016/j.bmcl.2007.12.041

Furet, P., Guagnano, V., Fairhurst, R. A., Imbach-Weese, P., Bruce, I., Knapp, M., et al. (2013). Discovery of NVP-BYL719 a potent and selective phosphatidylinositol-3 kinase alpha inhibitor selected for clinical evaluation. *Bioorg. Med. Chem. Lett.* 23, 3741–3748. doi:10.1016/j.bmcl.2013.05.007

Ganis, P., Avitabile, G., Benedetti, E., Pedone, C., and Goodman, M. (1970). Crystal and molecular structure of N, N′-Diethyl- N, N′-Diphenylurea. *Proc. Natl. Acad. Sci. U. S. A.* 67, 426–433. doi:10.1073/pnas.67.1.426

Garcia-Horton, A., and Yee, K. W. (2020). Quizartinib for the treatment of acute myeloid leukemia. *Expert Opin. Pharmacother.* 21, 2077–2090. doi:10.1080/14656566.2020.1801637

Gaulton, A., Bellis, L. J., Bento, A. P., Chambers, J., Davies, M., Hersey, A., et al. (2012). ChEMBL: A large-scale bioactivity database for drug discovery. *Nucleic Acids Res.* 40, D1100–D1107. doi:10.1093/nar/gkr777

Ghosh, A. K., and Brindisi, M. (2020). Urea derivatives in modern drug discovery and medicinal chemistry. *J. Med. Chem.* 63, 2751–2788. doi:10.1021/acs.jmedchem.9b01541

Gnewuch, C. T., and Sosnovsky, G. (1997). A critical appraisal of the evolution of N -nitrosoureas as anticancer drugs. *Chem. Rev.* 97, 829–1014. doi:10.1021/cr941192h

Goldsmith, S. R., Lovell, A. R., and Schroeder, M. A. (2019). Glasdegib for the treatment of adult patients with newly diagnosed acute myeloid leukemia or high-grade myelodysplastic syndrome who are elderly or otherwise unfit for standard induction chemotherapy. *Drugs Today (Barc).* 55, 545. doi:10.1358/dot.2019.55.9.3020160

Gömeç, M., Yulak, F., Gezegen, H., Özkaraca, M., Sayin, K., and Ataseven, H. (2022). Synthesis of diaryl urea derivatives and evaluation of their antiproliferative activities in colon adenocarcinoma. *J. Mol. Struct.* 1254. doi:10.1016/j.molstruc.2021.132318

Guagnano, V., Furet, P., Spanka, C., Bordas, V., Le Douget, M., Stamm, C., et al. (2011). Discovery of 3-(2, 6-Dichloro-3, 5-dimethoxy-phenyl)-1-{6-[4-(4-ethyl- piperazin-1-yl)-phenylamino]-pyrimidin-4-yl}-1-methyl-urea (NVP-BGJ398), A potent and selective inhibitor of the fibroblast growth factor receptor family of receptor tyrosine kinase. *J. Med. Chem.* 54, 7066–7083. doi:10.1021/jm2006222

Hamidi, S., Boucher, A., Lemieux, B., Rondeau, G., Lebœuf, R., Ste-Marie, L.-G., et al. (2022). Lenvatinib therapy for advanced thyroid cancer: Real-life data on safety, efficacy, and some rare side effects. *J. Endocr. Soc.* 6, bvac048. doi:10.1210/jendso/bvac048

Hayes, M. T., Bartley, J., Parsons, P. G., Eaglesham, G. K., and Prakash, A. S. (1997). Mechanism of action of fotemustine, a new chloroethylnitrosourea anticancer agent: Evidence for the formation of two DNA-reactive intermediates contributing to cytotoxicity. *Biochemistry* 36, 10646–10654. doi:10.1021/bi970791q

Hensey, C. E., Boscoboinik, D., and Azzi, A. (1989). Suramin, an anti-cancer drug, inhibits protein kinase C and induces differentiation in neuroblastoma cell clone NB2A. *FEBS Lett.* 258, 156–158. doi:10.1016/0014-5793(89)81639-4

Henß, L., Beck, S., Weidner, T., Biedenkopf, N., Sliva, K., Weber, C., et al. (2016). Suramin is a potent inhibitor of Chikungunya and Ebola virus cell entry. *Virol. J.* 13, 149. doi:10.1186/s12985-016-0607-2

Heo, Y.-A., and Syed, Y. Y. (2018). Regorafenib: A review in hepatocellular carcinoma. *Drugs* 78, 951–958. doi:10.1007/s40265-018-0932-4

Herbig, M. E., and Evers, D.-H. (2013). Correlation of hydrotropic solubilization by urea with logD of drug molecules and utilization of this effect for topical formulations. *Eur. J. Pharm. Biopharm.* 85, 158–160. doi:10.1016/j.ejpb.2013.06.022

Holderfield, M., Nagel, T. E., and Stuart, D. D. (2014). Mechanism and consequences of RAF kinase activation by small-molecule inhibitors. *Br. J. Cancer* 111, 640–645. doi:10.1038/bjc.2014.139

Hosokawa, M., Dolci, W., and Thorens, B. (2001). Differential sensitivity of GLUT1- and GLUT2-expressing β cells to streptozotocin. *Biochem. Biophys. Res. Commun.* 289, 1114–1117. doi:10.1006/bbrc.2001.6145

Hou, S., Liang, S., Zhang, C., Han, Y., Liang, J., Hu, H., et al. (2021). Design, synthesis and anticancer activity of a new series of n-aryl-n′-[4-(Pyridin-2-ylmethoxy)benzyl]urea derivatives. *Molecules* 26, 3496. doi:10.3390/molecules26123496

Huirne, J. A., and Lambalk, C. B. (2001). Gonadotropin-releasing-hormone-receptor antagonists. *Lancet* 358, 1793–1803. doi:10.1016/S0140-6736(01)06797-6

Ishikawa, M., and Hashimoto, Y. (2011). Improvement in aqueous solubility in small molecule drug discovery programs by disruption of molecular planarity and symmetry. *J. Med. Chem.* 54, 1539–1554. doi:10.1021/jm101356p

Jiang, G., Stalewski, J., Galyean, R., Dykert, J., Schteingart, C., Broqua, P., et al. (2001). GnRH antagonists: A new generation of long acting analogues incorporating p-Ureido-phenylalanines at positions 5 and 6. *J. Med. Chem.* 44, 453–467. doi:10.1021/jm0003900

Jianian, C., Xianfu, W., Guangji, Z., Xiaobo, F., Xingcan, S., Dewen, W., et al. (2014). *Quinazolinyl-aryl urea derivatives with antitumor function and application thereof*. CN104292170A.

Jin, P.-R., Ta, Y.-N. N., Chen, I.-T., Yu, Y.-N., Hsieh, H. T., Nguyen, V.-A. T., et al. (2021). Cinchona Alkaloid-Inspired Urea-Containing Autophagy Inhibitor Shows Single-Agent Anticancer Efficacy. *J. Med. Chem.* 64, 14513–14525. doi:10.1021/acs.jmedchem.1c01036

Kakuguchi, W., Nomura, T., Kitamura, T., Otsuguro, S., Matsushita, K., Sakaitani, M., et al. (2018). Suramin, screened from an approved drug library, inhibits HuR functions and attenuates malignant phenotype of oral cancer cells. *Cancer Med.* 7, 6269–6280. doi:10.1002/cam4.1877

Kannaiyan, R., and Mahadevan, D. (2018). A comprehensive review of protein kinase inhibitors for cancer therapy. *Expert Rev. Anticancer Ther.* 18, 1249–1270. doi:10.1080/14737140.2018.1527688

Karoulia, Z., Gavathiotis, E., and Poulikakos, P. I. (2017). New perspectives for targeting RAF kinase in human cancer. *Nat. Rev. Cancer* 17, 676–691. doi:10.1038/nrc.2017.79

Khalifa, S. A. M., Elias, N., Farag, M. A., Chen, L., Saeed, A., Hegazy, M.-E. F., et al. (2019). Marine Natural Products: A Source of Novel Anticancer Drugs. *Mar. Drugs* 17, 491. doi:10.3390/md17090491

Kim, J., Nguyen, M. N., Enlow, E., Ong, W. Z., Nowak, P. W., and Feutrill, J. T. (2013). *Urea derivatives and uses thereof*. WO/2014/201127.

Kim, I. S., and Sik, K. H. (2018). *N-N-aroylureas derivatives preparation method thereof and pharmaceutical compositions for the prevention and treatment of cancer containing the same as an active ingredient*. KR101849775B1.

Kim Seong, H. (2013). *A Cancer sensitizer comprising phenylurea derivatives or salts thereof*. KR101332830B1.

Koç, A., Wheeler, L. J., Mathews, C. K., and Merrill, G. F. (2004). Hydroxyurea arrests DNA replication by a mechanism that preserves basal dNTP pools. *J. Biol. Chem.* 279, 223–230. doi:10.1074/jbc.M303952200

Kohn, K. (1977). Interstrand cross-linking of DNA by 1, 3-bis(2-chloroethyl)-1-nitrosourea and other 1-(2-haloethyl)-1-nitrosoureas. *Cancer Res.* 37, 1450–1454.

Korbecki, J., Kupnicka, P., Chlubek, M., Gorący, J., Gutowska, I., and Baranowska-Bosiacka, I. (2022). CXCR2 receptor: Regulation of expression, signal transduction, and involvement in cancer. *Int. J. Mol. Sci.* 23, 2168. doi:10.3390/ijms23042168

Koul, H. K., Pal, M., and Koul, S. (2013). Role of p38 MAP kinase signal transduction in solid tumors. *Genes Cancer* 4, 342–359. doi:10.1177/1947601913507951

Kozikowski, A. P., Nan, F., Conti, P., Zhang, J., Ramadan, E., Bzdega, T., et al. (2001). Design of remarkably simple, yet potent urea-based inhibitors of glutamate carboxypeptidase II (NAALADase). *J. Med. Chem.* 44, 298–301. doi:10.1021/jm000406m

Kubo, K., Sakai, T., Nagao, R., Fujiwara, Y., Isoe, T., and Hasegawa, K. (2002). *Quinoline derivative having azolyl group and quinazoline derivative*. US20030087907A1.

Kumar, N., Lal, N., Nemaysh, V., and Luthra, P. M. (2020). Design, synthesis, DNA binding studies and evaluation of anticancer potential of novel substituted biscarbazole derivatives against human glioma U87 MG cell line. *Bioorg. Chem.* 100, 103911. doi:10.1016/j.bioorg.2020.103911

Kumari, S., Carmona, A. V., Tiwari, A. K., and Trippier, P. C. (2020). Amide bond bioisosteres: Strategies, synthesis, and successes. *J. Med. Chem.* 63, 12290–12358. doi:10.1021/acs.jmedchem.0c00530

Kuo, S.-C., Wang, Y.-M., Ho, Y.-J., Chang, T.-Y., Lai, Z.-Z., Tsui, P.-Y., et al. (2016). Suramin treatment reduces chikungunya pathogenesis in mice. *Antivir. Res.* 134, 89–96. doi:10.1016/j.antiviral.2016.07.025

Lee, C., Hyun-Mo, Y., Hojin, C., Dohoon, K., Soyoung, K., Nina, H., et al. (2013). *Novel compounds for selective histone deacetylase inhibitors, and pharmaceutical composition comprising the same*. US2016083354A1.

Leggans, E. K., Duncan, K. K., Barker, T. J., Schleicher, K. D., and Boger, D. L. (2013). A remarkable series of vinblastine analogues displaying enhanced activity and an unprecedented tubulin binding steric tolerance: C20′ urea derivatives. *J. Med. Chem.* 56, 628–639. doi:10.1021/jm3015684

Li, X., Qiu, M., Wang, S., Zhu, H., Feng, B., and Zheng, L. (2020). A Phase I dose-escalation, pharmacokinetics and food-effect study of oral donafenib in patients with advanced solid tumours. *Cancer Chemother. Pharmacol.* 85, 593–604. doi:10.1007/s00280-020-04031-1

Liang, X., Yang, Q., Wu, P., He, C., Yin, L., Xu, F., et al. (2021). The synthesis review of the approved tyrosine kinase inhibitors for anticancer therapy in 2015–2020. *Bioorg. Chem.* 113, 105011. doi:10.1016/j.bioorg.2021.105011

Lim, S., Ryu, J. H., Lm, C., and Yim, C. B. (2003). Synthesis and cytotoxicity of new 3-alkyl-1-(1-methyl-2-phenylethyl)ureas related to ceramide. *Arch. Pharm. Res.* 26, 270–274. doi:10.1007/BF02976954

Linciano, P., Nasti, R., Listro, R., Amadio, M., Pascale, A., Potenza, D., et al. (2022). Chiral 2-phenyl-3-hydroxypropyl esters as PKC-alpha modulators: HPLC enantioseparation, NMR absolute configuration assignment, and molecular docking studies. *Chirality* 34, 498–513. doi:10.1002/chir.23406

Lortie, F., Boileau, S., and Bouteiller, L. (2003). N, N-disubstituted ureas: Influence of substituents on the formation of supramolecular polymers. *Chem. Eur. J.* 9, 3008–3014. doi:10.1002/chem.200304801

Lowinger, T., Riedl, B., Dumas, J., and Smith, R. (2002). Design and discovery of small molecules targeting raf-1 kinase. *Curr. Pharm. Des.* 8, 2269–2278. doi:10.2174/1381612023393125

Malacrida, A., Cavalloro, V., Martino, E., Costa, G., Ambrosio, F. A., Alcaro, S., et al. (2021). Anti-multiple myeloma potential of secondary metabolites from Hibiscus sabdariffa—Part 2. *Molecules* 26, 6596. doi:10.3390/molecules26216596

Martino, E., Casamassima, G., Castiglione, S., Cellupica, E., Pantalone, S., Papagni, F., et al. (2018). Vinca alkaloids and analogues as anti-cancer agents: Looking back, peering ahead. *Bioorg. Med. Chem. Lett.* 28, 2816–2826. doi:10.1016/j.bmcl.2018.06.044

Martino, E., Della Volpe, S., Terribile, E., Benetti, E., Sakaj, M., Centamore, A., et al. (2017). The long story of camptothecin: From traditional medicine to drugs. *Bioorg. Med. Chem. Lett.* 27, 701–707. doi:10.1016/j.bmcl.2016.12.085

McCain, D. F., Wu, L., Nickel, P., Kassack, M. U., Kreimeyer, A., Gagliardi, A., et al. (2004). Suramin derivatives as inhibitors and activators of protein-tyrosine phosphatases. *J. Biol. Chem.* 279, 14713–14725. doi:10.1074/jbc.M312488200

Menaa, F. (2013). Latest approved therapies for metastatic melanoma: What comes next? *J. Skin. Cancer* 2013, 1–10. doi:10.1155/2013/735282

Moarbess, G., Deleuze-Masquefa, C., Bonnard, V., Gayraud-Paniagua, S., Vidal, J. R., Bressolle, F., et al. (2008). *In vitro* and *in vivo* anti-tumoral activities of imidazo[1, 2-a]quinoxaline, imidazo[1, 5-a]quinoxaline, and pyrazolo[1, 5-a]quinoxaline derivatives. *Bioorg. Med. Chem.* 16 (13), 6601–6610. doi:10.1016/j.bmc.2008.05.022

Modi, S. J., Anshuly, T., and Madhvarao, K. V. (2021). *A rational Drug Design based identification of orally bioavailable 1,5-disubstituted naphthalene compounds as potent VEGFR-2 inhibitors*. AU2021103375A4.

Modi, S. J., and Kulkarni, V. M. (2019). Vascular endothelial growth factor receptor (VEGFR-2)/KDR inhibitors: Medicinal chemistry perspective. *Med. Drug Discov.* 2, 100009. doi:10.1016/j.medidd.2019.100009

Mohammadi, M. (1998). Crystal structure of an angiogenesis inhibitor bound to the FGF receptor tyrosine kinase domain. *EMBO J.* 17, 5896–5904. doi:10.1093/emboj/17.20.5896

Motzer, R., Alekseev, B., Rha, S.-Y., Porta, C., Eto, M., Powles, T., et al. (2021). Lenvatinib plus pembrolizumab or everolimus for advanced renal cell carcinoma. *N. Engl. J. Med.* 384, 1289–1300. doi:10.1056/NEJMoa2035716

Motzer, R. J., Hutson, T. E., Glen, H., Michaelson, M. D., Molina, A., Eisen, T., et al. (2015). Lenvatinib, everolimus, and the combination in patients with metastatic renal cell carcinoma: A randomised, phase 2, open-label, multicentre trial. *Lancet Oncol.* 16, 1473–1482. doi:10.1016/S1470-2045(15)00290-9

Nakajima, M., DeChavigny, A., Johnson, C. E., Hamada, J. I., Stein, C. A., and Nicolson, G. L. (1991). Suramin: A potent inhibitor of melanoma heparanase and invasion. *J. Biol. Chem.* 266, 9661–9666. doi:10.1016/s0021-9258(18)92871-1

Nakamura, K., Taguchi, E., Miura, T., Yamamoto, A., Takahashi, K., Bichat, F., et al. (2006). KRN951, a highly potent inhibitor of vascular endothelial growth factor receptor tyrosine kinases, has antitumor activities and affects functional vascular properties. *Cancer Res.* 66, 9134–9142. doi:10.1158/0008-5472.CAN-05-4290

Nasser, N. J. (2022). Androgen flare after LHRH initiation is the side effect that makes most of the beneficial effect when it coincides with radiation therapy for prostate cancer. *Cancers (Basel).* 14, 1959. doi:10.3390/cancers14081959

Nestor, J. J., Tahilramani, R., Ho, T. L., Goodpasture, J. C., Vickery, B. H., and Ferrandon, P. (1992). Potent gonadotropin releasing hormone antagonists with low histamine-releasing activity. *J. Med. Chem.* 35, 3942–3948. doi:10.1021/jm00099a023

Okamoto, K., Ikemori-kawada, M., Jestel, A., Funahashi, Y., Matsushima, T., Tsuruoka, A., et al. (2015). Distinct binding mode of multikinase inhibitor lenvatinib revealed by biochemical characterization. *ACS Med. Chem. Lett.* 6, 89–94. doi:10.1021/ml500394m

Osswald, H., and Youssef, M. (1979). Suramin enhancement of the chemotherapeutic actions of cyclophosphamide or adriamycin of intramuscularly-implanted Ehrlich carcinoma. *Cancer Lett.* 6, 337–343. doi:10.1016/S0304-3835(79)80091-9

Özgeriş, F. B., Kaci, F. N., Özgeriş, B., and Görmez, A. (2022). The synthesis of unsymmetrical urea from substituted phenethylamine and the investigation of its antibacterial, anticancer, and antioxidant properties. *Biointerface Res. Appl. Chem.* 12, 7052–7063. doi:10.33263/BRIAC125.70527063

Pak, E., and Segal, R. A. (2016). Hedgehog signal transduction: Key players, oncogenic drivers, and cancer therapy. *Dev. Cell* 38, 333–344. doi:10.1016/j.devcel.2016.07.026

Parveen, N., Lin, Y.-L., Khan, M. I., Chou, R.-H., Sun, C.-M., and Yu, C. (2020). Suramin derivatives play an important role in blocking the interaction between FGF1 and FGFRD2 to inhibit cell proliferation. *Eur. J. Med. Chem.* 206, 112656. doi:10.1016/j.ejmech.2020.112656

Parveen, N., Lin, Y. L., Chou, R. H., Sun, C. M., and Yu, C. (2022). Synthesis of novel suramin analogs with anti-proliferative activity via FGF1 and FGFRD2 blockade. *Front. Chem.* 9, 764200–764220. doi:10.3389/fchem.2021.764200

Pastorino, S., Riondato, M., Uccelli, L., Giovacchini, G., Giovannini, E., Duce, V., et al. (2020). Toward the discovery and development of PSMA targeted inhibitors for nuclear medicine applications. *Curr. Radiopharm.* 13, 63–79. doi:10.2174/1874471012666190729151540

Patel, H. K., Grotzfeld, R. M., Lai, A. G., Mehta, S. A., Milanov, Z. V., Chao, Q., et al. (2009). Arylcarboxyamino-substituted diaryl ureas as potent and selective FLT3 inhibitors. *Bioorg. Med. Chem. Lett.* 19, 5182–5185. doi:10.1016/j.bmcl.2009.07.024

Persson, B.-E., Kold Olesen, T., and Jensen, J.-K. (2009). Degarelix: A new approach for the treatment of prostate cancer. *Neuroendocrinology* 90, 235–244. doi:10.1159/000228832

Riedl, B., Lowinger, T.B, Bankston, D., Barbosa, J., Brittelli, D.R., Carlson, R., et al. (2001). Potent Raf kinase inhibitors from the diphenylurea class Structure activity relationships. *Proc. Am. Assoc. Cancer Res. Annu. Meet.* 42, 923.

Rowe, S. P., Gage, K. L., Faraj, S. F., Macura, K. J., Cornish, T. C., Gonzalez-Roibon, N., et al. (2015). 18 F-DCFBC PET/CT for PSMA-based detection and characterization of primary prostate cancer. *J. Nucl. Med.* 56, 1003–1010. doi:10.2967/jnumed.115.154336

Rui, M., Nasti, R., Bignardi, E., Della Volpe, S., Rossino, G., Rossi, D., et al. (2017). PKC in regenerative therapy: New insights for old targets. *Pharmaceuticals* 10, 46. doi:10.3390/ph10020046

Sabbah, D. A., Hajjo, R., and Sweidan, K. (2020). Review on epidermal growth factor receptor (EGFR) structure, signaling pathways, interactions, and recent updates of EGFR inhibitors. *Curr. Top. Med. Chem.* 20, 815–834. doi:10.2174/1568026620666200303123102

Saitoh, F., Hiroshi, N., Yuji, K., and Tsutomu, S. (2018). *Novel tetrahydronaphthyl urea derivatives*. WO2018199166A1.

Salem, A. K., and Elsaid, A. S. A. M. (2020). *JNK inhibitors as anticancer agents*. WO2020263989A1.

Salgia, N. J., Zengin, Z. B., and Pal, S. K. (2020). Tivozanib in renal cell carcinoma: A new approach to previously treated disease. *Ther. Adv. Med. Oncol.* 12, 175883592092381. doi:10.1177/1758835920923818

Sawa, A., Hideki, N., Kawahata, R., Sawa, W., Iwata, M., Nagao, Y., et al. (2022). *Cyclic urea derivatives*. WO2022059778A1.

Shibuya, M. (2011). Vascular endothelial growth factor (vegf) and its receptor (VEGFR) signaling in angiogenesis: A crucial target for anti- and pro-angiogenic therapies. *Genes Cancer* 2, 1097–1105. doi:10.1177/1947601911423031

Shore, N. D., Saad, F., Cookson, M. S., George, D. J., Saltzstein, D. R., Tutrone, R., et al. (2020). Oral relugolix for androgen-deprivation therapy in advanced prostate cancer. *N. Engl. J. Med.* 382, 2187–2196. doi:10.1056/NEJMoa2004325

Siddig, L. A., Khasawneh, M. A., Samadi, A., Saadeh, H., Abutaha, N., and Wadaan, M. A. (2021). Synthesis of novel thiourea-/urea-benzimidazole derivatives as anticancer agents. *Open Chem.* 19, 1062–1073. doi:10.1515/chem-2021-0093

Smith, B. D., Kaufman, M. D., Lu, W. P., Gupta, A., Leary, C. B., Wise, S. C., et al. (2019). Ripretinib (DCC-2618)Is a switch control kinase inhibitor of a broad spectrum of oncogenic and drug-resistant KIT and PDGFRA variants. *Cancer Cell* 35, 738–751.e9. e9. doi:10.1016/j.ccell.2019.04.006

Smith, R. A., Barbosa, J., Blum, C. L., Bobko, M. A., Caringal, Y. V., Dally, R., et al. (2001). Discovery of heterocyclic ureas as a new class of raf kinase inhibitors: Identification of a second generation lead by a combinatorial chemistry approach. *Bioorg. Med. Chem. Lett.* 11, 2775–2778. doi:10.1016/S0960-894X(01)00571-6

Spivak, J. L., and Hasselbalch, H. (2011). Hydroxycarbamide: A user's guide for chronic myeloproliferative disorders. *Expert Rev. Anticancer Ther.* 11, 403–414. doi:10.1586/era.11.10

Springer, C. J., Alfonso, M. R., Romina, G., Dan, N.-D., and Ion, N.-D. (2013). *1-(5-tert-butyl-2-aryl-pyrazol-3-yl)-3-[2-fluoro-4-[(3-oxo-4h-pyrido[2,3-b]pyrazin-8-yl)oxy]phenyl]urea derivatives as Raf inhibitors for the treatment of cancer*. US2016355510A1.

Steverding, D. (2010). The development of drugs for treatment of sleeping sickness: A historical review. *Parasit. Vectors* 3, 15. doi:10.1186/1756-3305-3-15

Tan, C. W., Sam, I.-C., Chong, W. L., Lee, V. S., and Chan, Y. F. (2017). Polysulfonate suramin inhibits Zika virus infection. *Antivir. Res.* 143, 186–194. doi:10.1016/j.antiviral.2017.04.017

Thompson, L., and Donald, C. M. (2020). Glasdegib: A novel hedgehog pathway inhibitor for acute myeloid leukemia. *J. Adv. Pract. Oncol.* 11, 196–200. doi:10.6004/jadpro.2020.11.2.8

Tong, W. P., and Ludlum, D. B. (1978). Mechanism of action of the nitrosoureas—1. *Biochem. Pharmacol.* 27, 77–81. doi:10.1016/0006-2952(78)90259-9

Trapp, J., Meier, R., Hongwiset, D., Kassack, M. U., Sippl, W., and Jung, M. (2007). Structure–activity studies on suramin analogues as inhibitors of NAD+-Dependent histone deacetylases (sirtuins). *ChemMedChem* 2, 1419–1431. doi:10.1002/cmdc.200700003

Van Poppel, H. (2010). Evaluation of degarelix in the management of prostate cancer. *Cancer Manag. Res.* 39–52. doi:10.2147/CMAR.S8841

Varghese, R., and Dalvi, Y. B. (2021). Natural products as anticancer agents. *Curr. Drug Targets* 22, 1272–1287. doi:10.2174/1389450121999201230204526

Vavra, J. J., Deboer, C., Dietz, A., Hanka, L. J., and Sokolski, W. T. (1960). Streptozotocin, a new antibacterial antibiotic. *Antibiot. Annu.* 7, 230–235.

Villalona-Calero, M. A., Wientjes, M. G., Otterson, G. A., Kanter, S., Young, D., Murgo, A. J., et al. (2003). Phase I study of low-dose suramin as a chemosensitizer in patients with advanced non-small cell lung cancer. *Clin. Cancer Res.* 9, 3303–3311. Available at: http://www.ncbi.nlm.nih.gov/pubmed/12960116.

Wainwright, M. (2010). Dyes, trypanosomiasis and DNA: A historical and critical review. *Biotech. Histochem.* 85, 341–354. doi:10.3109/10520290903297528

Wan, P. T. C., Garnett, M. J., Roe, S. M., Lee, S., Niculescu-Duvaz, D., Good, V. M., et al. (2004). Mechanism of activation of the RAF-ERK signaling pathway by oncogenic mutations of B-RAF. *Cell* 116, 855–867. doi:10.1016/S0092-8674(04)00215-6

Wang, S., Stephen, P., and Mingfeng, Y. (2018). *5-(pyrimidin-4-yl)thiazol-2-yl urea derivatives as therapeutic agents*. US11325900B2.

Wang, X., Bove, A. M., Simone, G., and Ma, B. (2020). Molecular bases of VEGFR-2-mediated physiological function and pathological role. *Front. Cell Dev. Biol.* 8, 599281. doi:10.3389/fcell.2020.599281

Wiedemar, N., Hauser, D. A., and Mäser, P. (2020). 100 years of suramin. *Antimicrob. Agents Chemother.* 64, e01168–19. doi:10.1128/AAC.01168-19

Wilhelm, S., Carter, C., Lynch, M., Lowinger, T., Dumas, J., Smith, R. A., et al. (2006). Discovery and development of sorafenib: A multikinase inhibitor for treating cancer. *Nat. Rev. Drug Discov.* 5, 835–844. doi:10.1038/nrd2130

Wilhelm, S. M., Carter, C., Tang, L., Wilkie, D., McNabola, A., Rong, H., et al. (2004). BAY 43-9006 exhibits broad spectrum oral antitumor activity and targets the RAF/MEK/ERK pathway and receptor tyrosine kinases involved in tumor progression and angiogenesis. *Cancer Res.* 64, 7099–7109. doi:10.1158/0008-5472.CAN-04-1443

Wilhelm, S. M., Dumas, J., Adnane, L., Lynch, M., Carter, C. A., Schütz, G., et al. (2011). Regorafenib (bay 73-4506): A new oral multikinase inhibitor of angiogenic, stromal and oncogenic receptor tyrosine kinases with potent preclinical antitumor activity. *Int. J. Cancer* 129, 245–255. doi:10.1002/ijc.25864

Yamamuro, S., Takahashi, M., Satomi, K., Sasaki, N., Kobayashi, T., Uchida, E., et al. (2021). Lomustine and nimustine exert efficient antitumor effects against glioblastoma models with acquired temozolomide resistance. *Cancer Sci.* 112 (11), 4736–4747. doi:10.1111/cas.15141

Yan, M., Wang, C., He, B., Yang, M., Tong, M., Long, Z., et al. (2016). Aurora-A kinase: A potent oncogene and target for cancer therapy. *Med. Res. Rev.* 36, 1036–1079. doi:10.1002/med.21399

Yang, J. C. H., Brose, M. S., Castro, G., Kim, E. S., Lassen, U. N., Leyvraz, S., et al. (2022). Rationale and design of ON-TRK: A novel prospective non-interventional study in patients with TRK fusion cancer treated with larotrectinib. *BMC Cancer* 22, 625. doi:10.1186/s12885-022-09687-x

Yang, J., Nie, J., Ma, X., Wei, Y., Peng, Y., and Wei, X. (2019). Targeting PI3K in cancer: Mechanisms and advances in clinical trials. *Mol. Cancer* 18, 26. doi:10.1186/s12943-019-0954-x

Zhang, D. (2012). *Urea derivatives as kinase inhibitors*. US2012077851A1.

Zhang, S., Shuqiang, S., and Yuting, T. (2012). *N-substituted phenyl-N'-substituted heterocyclic urea compound and application thereof as anticancer medicament*. WO2014040243A1.

Zhu, H., Zefeng, W., Pengfei, W., and Lu, S. (2017). *Design and synthesis of diphenyl urea derivative antitumor compounds containing pyrazol framework*. CN107118157A.

frontiers | Frontiers in Chemistry

TYPE Original Research
PUBLISHED 15 September 2022
DOI 10.3389/fchem.2022.1008075

Check for updates

OPEN ACCESS

EDITED BY
Margherita Brindisi,
University of Naples Federico II, Italy

REVIEWED BY
Mateus Webba Da Silva,
Ulster University, United Kingdom
Nunzia Iaccarino,
University of Naples Federico II, Italy

*CORRESPONDENCE
Claudia Sissi,
claudia.sissi@unipd.it

SPECIALTY SECTION
This article was submitted to Medicinal and Pharmaceutical Chemistry, a section of the journal Frontiers in Chemistry

RECEIVED 31 July 2022
ACCEPTED 24 August 2022
PUBLISHED 15 September 2022

CITATION
Cozzaglio M, Ceschi S, Groaz E, Sturlese M and Sissi C (2022), G-quadruplexes formation within the promoter of TEAD4 oncogene and their interaction with Vimentin.
Front. Chem. 10:1008075.
doi: 10.3389/fchem.2022.1008075

COPYRIGHT
© 2022 Cozzaglio, Ceschi, Groaz, Sturlese and Sissi. This is an open-access article distributed under the terms of the Creative Commons Attribution License (CC BY). The use, distribution or reproduction in other forums is permitted, provided the original author(s) and the copyright owner(s) are credited and that the original publication in this journal is cited, in accordance with accepted academic practice. No use, distribution or reproduction is permitted which does not comply with these terms.

G-quadruplexes formation within the promoter of TEAD4 oncogene and their interaction with Vimentin

Marta Cozzaglio[1], Silvia Ceschi[1], Elisabetta Groaz[1,2], Mattia Sturlese[1] and Claudia Sissi[1]*

[1]Department of Pharmaceutical and Pharmacological Sciences, University of Padova, Padova, Italy, [2]KU Leuven, Rega Institute for Medical Research, KU Leuven, Medicinal Chemistry, Leuven, Belgium

G-quadruplexes (G4s) are nucleic acid secondary structures detected within human chromosomes, that cluster at gene promoters and enhancers. This suggests that G4s may play specific roles in the regulation of gene expression. Within a distinct subgroup of G-rich domains, the formation of two or more adjacent G4 units (G4-repeats) is feasible. Recently it was shown that Vimentin, a protein highly expressed within mesenchymal cells, selectively recognizes these arrangements. Putative G4-repeats have been searched within the human gene proximal promoters by the bioinformatics tool QPARSE and they resulted to be enriched at genes related to epithelial-to-mesenchymal transition (EMT). This suggested that Vimentin binding at these sites might be relevant for the maintenance of the mesenchymal phenotype. Among all the identified sequences, in the present study we selected the one located within the promoter of the TEAD4 oncogene. TEAD4 codifies for a transcriptional enhancer factor, TEAD4, that actively promotes EMT, supporting, cell proliferation and migration. Moreover, in colorectal cancer cells TEAD4 directly enhances the expression of Vimentin. Thus, the possible interaction of Vimentin with TEAD4 promoter could highlight a positive feedback loop between these two factors, associated to important tumor metastasis related events. Here, we exploited spectroscopic and electrophoretic measurements under different conditions to address the folding behavior of the selected sequence. This allowed us to validate the folding of TEAD4 promoter into a G4-repeat able to interact with Vimentin.

KEYWORDS

G-quadruplex, TEAD4, Vimentin, G4-repeats, EMT

1 Introduction

Starting from 1953, when Watson and Crick identified the B-form of the DNA (Watson et al., 1974), up to our days, it has been clarified that DNA is a very plastic molecule, that can fold into a variety of secondary structures (Bochman et al., 2012). G-quadruplex (G4) is a non-canonical DNA secondary structure, which corresponds to a

tetrahelical arrangement that can form at guanine-rich tracts. Here, four guanine residues interact through Hoogsteen hydrogen bonds and give rise to planar arrays, called G-tetrads, that interact with each other through π-π stacking. This structural core is further stabilized by monovalent cations that are coordinated in the center of the tetrads (Largy et al., 2016). The four strands of the G4 may belong to just one (monomolecular arrangement) or different (bi- or tetra-molecular arrangements) DNA filaments. In both instances, the strands can pair with variable relative orientations, based on which G-quadruplexes can be classified into parallel, antiparallel, or hybrid.

To fold into a monomeric G4 structure, a DNA filament must contain four runs of at least two consecutive guanines, each of them separated by no less than one nucleotide. Based on these sequence requirements, several algorithms have been designed to identify those regions potentially capable of forming G4 structures within the genome (Todd 2005). These sites, defined as PQS (potential G4 forming sequences) are enriched mainly at telomeres, gene promoters, ribosomal DNA, recombination sites and 5′-UTR regions (Rigo et al., 2017). In living cells, the presence of G4s at these sites has been experimentally confirmed thanks to the development of antibodies and fluorescent probes capable of selectively recognizing these structures (Schaffitzel et al., 2001). These analyses associated multiple physiological roles of G4s to their genomic location. In particular, the enrichment in PQS around the TSS (transcription starting site) of various oncogenes suggested an important role of G4 structures in the regulation of their expression (Eddy and Maizels 2006). This was further confirmed by the ability of G4 selective ligands to influence the expression of their target genes (Balasubramanian 2011).

More recently, the interest was attracted by those sites where multiple PQS are located in close positions along the genome since this clustering was not the simple result of a statistical enrichment of guanines at these sites (Berselli et al., 2019). Noteworthy, this PQS distribution can support the folding of multiple G-quadruplex units within a single short DNA fragment, giving rise to the so-called G4-repeats. The first *in vitro* structural studies of G4-repeats were based on the human telomeric sequence and later on they were extended to oncogene promoters such as hTERT, ILPR, KRAS, c-KIT and c-MYC (Monsen et al., 2021), (Monsen et al., 2020), (Schonhoft et al., 2009), (Marquevielle et al., 2020), (Rigo and Sissi 2017), (Monsen et al., 2022).

Recently, it has been observed that Vimentin, an intermediate filament (IF) protein, is able to interact selectively with G4-repeats. This complex involves only the tetrameric form of the protein that is found within the nucleus as a soluble nuclear fraction (Ceschi et al., 2022). Although an architectural role has long been considered the main function of Vimentin, it is well recognized that it also participates to various signaling cascades and it can act as a transcriptional regulator within metastatic cancer cells (Mergui et al., 2010), (Jang et al., 2021). In particular, Vimentin expression is highly reactivated during epithelial to mesenchymal transition (EMT), a process that occurs during both physiological tissue development/regeneration and pathological cancer progression towards metastasis. Noteworthy, a bioinformatic search for G4-repeats at proximal gene promoters, followed by GO analysis, highlighted an intriguing correlation between the functions of Vimentin and those of the genes containing putative Vimentin binding sites at their promoters (Ceschi et al., 2022).

Among all the genes identified as potentially able to accommodate a G4-repeat at their proximal promoter, we were interested in TEAD4. This gene, located at chromosome 12, codifies for a transcriptional enhancer factor (TEAD4) that interacts with YAP/TAZ and other transcription factors to regulate different cellular processes. Among them, TEAD4 plays an important role in cancer, being actively involved in the regulation of metastatic behavior and cancer stem cell dynamics (Barry. 2021) (Chen et al., 2020). Remarkably, it has been shown that in colorectal cancer cells TEAD4 promotes EMT in a YAP independent manner, regulating the expression of Vimentin (Liu et al., 2016).

In the present study, we evaluated the structural features of the G4-repeat putatively occurring at the TEAD4 proximal promoter and we addressed its interaction with Vimentin. These data will help to clarify whether the recruitment of Vimentin at G4-repeats might represent a mechanism through which the regulation of different EMT-related genes such as TEAD4 is achieved.

2 Materials and methods

2.1 Oligonucleotides

Oligonucleotides were purchased from Eurogentec (Liége, Belgium) as RP-HPLC purified products. Oligonucleotides were dissolved in milliQ H_2O to prepare 100 μM stock solutions. Before use, each sample was heated at 95°C for 7 min in the required buffer and then slowly cooled down at room temperature to equilibrate the system. The DNA sequences used in this work are listed in Table 1.

The ability of tested oligonucleotides to form intramolecular hairpins was predicted by the use of the IDT OligoAnalyzer tool (https://eu.idtdna.com/calc/analyzer). Setting parameters were 150 mM Na^+ and 2 μM oligo concentration.

2.2 Circular dichroism

Circular dichroism spectra were recorded on a Jasco J-810 spectropolarimeter equipped with a Peltier temperature controller using 1 cm pathlength quartz cuvette. CD spectra

TABLE 1 DNA sequences herein studied.

Sequence name	Sequence reported in the 5′-3′ direction
TEAD4-full	CGGGCGGGCGAGGGGCCGGGCCGCCGGGGCGGGGCGGGGCCGGGC
TEAD4-full-2TT	CGGGCGGGCGAGGGGCCGGGTTGTTGGGGCGGGGCGGGGCCGGGC
TEAD4-far	CGGGGCGGGGCGGGGCCGGGC
TEAD4-near	CGGGCGGGCGAGGGGCCGGGC
Marker 22 nts	GGATGTGAGTGTGAGTGTGAGG
Marker 44 nts	GGATGTGAGTGTGAGTGTGAGGGGATGTGAGTGTGAGTGTGAGG

were recorded from 230 to 330 nm. DNA samples were used at 2–4 μM final concentration in 5 mM Tris, pH 7.5. The salt concentration and the temperature used for the experiments varied according to the purpose of the assays.

For CD kinetic experiments, spectra were acquired immediately after the manual addition of the selected cation into the cuvette from a stock solution, with the following parameters: scanning speed 200 nm/min; interval scan of 60 s, bandwidth of 2 nm; data interval of 0.5 nm; response of 1 s.

For CD melting experiments, spectra were acquired between 95 and 25°C every 2°C. Each spectrum represents the average of 2 scans acquired with the following parameters: scanning speed 100 nm/min; band width of 2 nm; data interval of 0.5 nm; response of 2 s. Spectra were reported as molar ellipticity ([θ]). To analyze the variation of signals at single wavelength each data point was subtracted of the starting CD value contribution and the difference was normalized between 0 and 1 (relative molar ellipticity).

2.3 Thermal differential spectra (TDS)

Thermal differential spectra were obtained by subtracting the oligonucleotide UV-spectrum acquired at 25°C from the one recorded at 95°C. Experiments were performed using 2–4 μM oligonucleotide solution in 5 mM Tris pH 7.5, 150 mM KCl.

2.4 Expression and purification of vimentin

The genomic sequence that corresponds to full-length human Vimentin (residues Met1-Glu466) was inserted into the pET21a + vector by Genescript. The plasmid was used to transform competent *E. Coli* BL21 (DE3) cells. Bacteria were grown at 37°C in LB media until an OD_{600} of 0.7 was reached. At this point, the expression of Vimentin was induced by adding 1 mM isopropyl-β-D-thiogalactopyranoside (IPTG). Vimentin was purified as previously described (Herrmann et al., 2004). Briefly, cells were collected by centrifugation at 7000 g for 20 min at 4°C, resuspended in 10 mM Tris, 2 mM PMSF, 10 mM $MgCl_2$, pH 7.5. After resuspension, the cells were sonicated and up to 0.2% Triton X-100 and 50 g/ml DNase I were added. The inclusion bodies were harvested by centrifugation, and then resuspended in the corresponding washing buffer (10 mM Tris, 1 mM EDTA, 1 mM DTT, 2 mM PMSF, 1.5 M KCl, pH 7.5). After centrifugation, this procedure was repeated with the same buffer without KCl. Finally, the pellets were washed with 10 mM Tris, 0.1 mM EDTA, pH 7.5. After the last washing step, inclusion bodies were resuspended in a denaturing buffer (9.5 M urea in 10 mM Tris, pH 7.5). The solubilized IF proteins were collected by centrifugation at 60,000 g for 1 h at 20°C. Vimentin was purified from the supernatant by two steps of exchange chromatography, using first an anionic (Q Sepharose FF, Cytiva) then a cationic (SP Sepharose FF, Cytiva) column. The buffer used for the exchange chromatography was 10 mM Tris, 500 mM NaCl, 1 mM DTT, pH 7.5. Purified Vimentin was stored at −80°C.

2.5 Protein sample preparation

The day before use, Vimentin was renatured following the protocol developed by Herrmann and others to avoid polymerization into filaments (Herrmann et al., 2004). The protein was dialyzed at room temperature against dialysis buffer (5 mM Tris, 1 mM EDTA, 0.1 mM EGTA, 1 mM dithiothreitol, pH 8.4) containing a progressively reduced urea concentration (6, 4, 2, and 1 M urea). Dialysis against a large volume of buffer with 1M urea proceeded overnight at 4°C. The next day, dialysis was continued against tetramer buffer (5 mM Tris, pH 8.4) for 1 h at room temperature. After dialysis, the protein concentration was determined by measuring the absorption at 280 nm with ε = 24,900 $cm^{-1}M^{-1}$.

2.6 Polyacrylamide gel electrophoresis

For each sample, a solution of oligonucleotide (2–4 μM strand concentration) in 5 mM Tris, pH 7.5 was heated at 95°C for 7 min and allowed to cool down to room

temperature overnight. Afterwards, variable concentrations of KCl (0, 10 and 150 mM) were added to the samples and they were led to equilibrate overnight at room temperature. The samples were then loaded on a native 15% polyacrylamide (19: 1 acrylamide: bis-acrylamide) gel in 1 × TBE (89 mM Tris, 89 mM boric acid, 0.02M EDTA) implemented with 20 mM KCl. The gel was stained with Sybr Green II and the resolved bands were visualized on an image acquisition system (Geliance 600 Imaging system, Perkin-Elmer).

2.7 Electrophoretic mobility shift assays

Electrophoretic mobility shift assays (EMSA) were performed on 1.5% agarose gels in 1 × TBE buffer and 10 mM KCl. Each reaction sample contained 500 nM DNA and 8 μM Vimentin, in 5 mM Tris, 150 mM KCl, pH 8.4. Vimentin was added to oligonucleotide solutions and incubation was performed for 1 h at room temperature. Immediately before loading, 3 μl of gel loading buffer (50% glycerol, 50% water) were added to the samples. Electrophoresis proceeded for 2 h at 6 V/cm at 4°C. Gels were stained with Sybr Green II to visualize nucleic acids and with Coomassie Brilliant Blue G250 for protein detection. Gel images were acquired with a Geliance 600 apparatus.

3 Results

3.1 Rational selection of a sequence that potentially folds into a G4-repeat

In a previous study (Ceschi et al., 2022) the Q-PARSE bioinformatics tool was used to search sequences containing two contiguous G4-forming elements in the region covering 100 nucleotides upstream the transcription starting site of human genes. The search was extended to both, the forward and reverse strands. The searched pattern comprised islands of 3–4 guanines with connecting loops of maximum 5 nucleotides. The software provided an output of 1477 genes that contain at least one putative double G4-repeat. Among the retrieved sequences, we chose to characterize a sequence, TEAD4-full (Table 1), located 31 nucleotides upstream the TSS of the TEAD4 oncogene.

Besides the functional roles of the protein encoded by this gene, the selected sequence represented an attracting system thanks to its guanines number and distribution. The study of any G4-repeat system might be very complex due to the potential coexistence of multiple structural equilibria (Monsen et al., 2022). However, it was possible to subdivide TEAD4-full into two shorter domains, each of them comprising 4 runs of at least 3 guanines (thus each of them putatively able to fold into a stable G4), separated by a short linker (Figure 1). Thus, we took

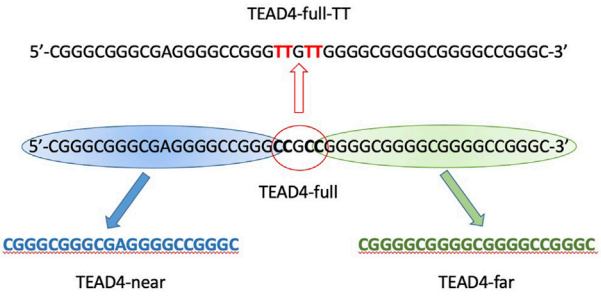


FIGURE 1
Schematic representation of TEAD4 studied sequences.

advantage of this base composition of TEAD4-full and we started its characterization by analyzing the conformational features of the two short sequences located at the 5′- and 3′-end, addressed as TEAD4-near and TEAD4-far, respectively.

3.2 TEAD4-near folds prevalently into an antiparallel G-quadruplex structure

To address the conformational features of the selected sequences, we performed CD spectroscopy that allows to follow the folding process of oligonucleotides and provides useful insights into the topology of the nucleic acid arrangements in solution. Since it is known that G-quadruplex formation is promoted by the presence of some cations, in particular potassium, we started our analyses by monitoring the modifications of the CD spectrum of TEAD4-near in 5 mM Tris, pH 7.5 upon addition of 10 and 150 mM KCl (Largy et al., 2016). Under both conditions, we observed an increase in molar ellipticity at 290 nm and a decrease at 260 nm that occurred in the same time scale at the two tested KCl concentrations (Figure 2).

The shape of the CD spectrum is known to be different for a G4 of parallel or antiparallel topology (Balagurumoorthy et al., 1992). Parallel G4s typically show a positive signal at 265 nm and a negative one at 240 nm, whereas antiparallel quadruplexes exhibit a positive signal at 290 nm and a negative one around 260 nm. Thus, the CD spectra of TEAD4-near suggested that the addition of potassium drove the formation an antiparallel G4. The presence of a G4 structure was further confirmed by the UV thermal differential spectrum (TDS) (Supplementary Figure S1A), that exhibited the characteristic pattern associated to this non-canonical structure, with two positive peaks at 240 and 277 nm, a shoulder at 255 nm and a negative minimum at 296 nm (Mergny 2005).

The melting and annealing profiles of TEAD4-near were acquired at the physiologically relevant KCl concentration (150 mM) and they were perfectly reversible (Figure 3). The

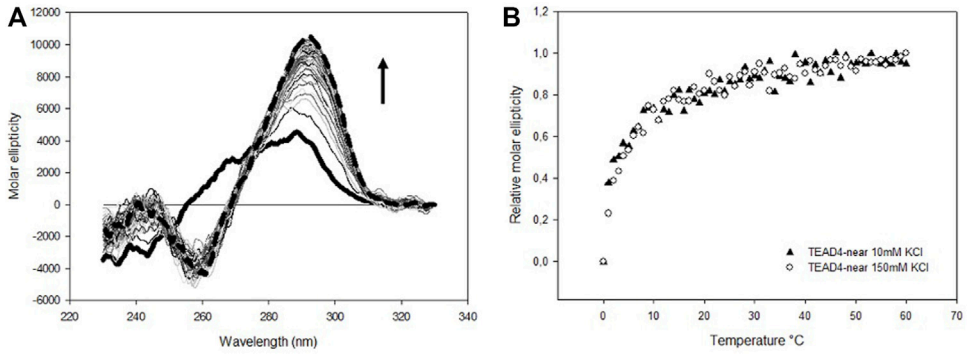


FIGURE 2
(A) Time dependent variation of CD spectra of 4 μM TEAD4-near in 5 mM Tris pH 7.5, upon addition of 150 mM KCl recorded at 25°C. Solid and dashed lines correspond to the oligonucleotide in the absence of metal ion and after 1 h incubation, respectively. **(B)** Time dependent relative variation of molar ellipticity at 290 nm of 4 μM TEAD4-near in 5 mM Tris pH 7.5, upon addition of 10 or 150 mM KCl.

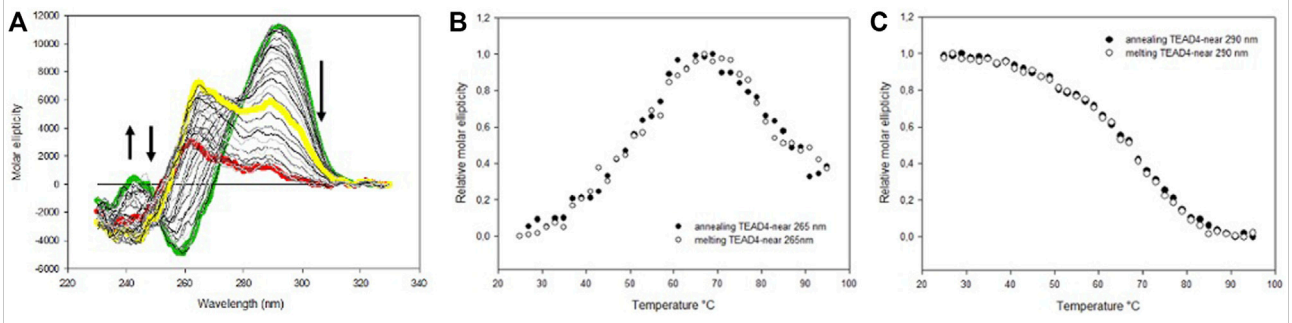


FIGURE 3
(A) CD spectra of 4 μM TEAD4-near in 5 mM Tris pH 7.5, 150 mM KCl, acquired at increasing temperatures. The green, yellow and red lines correspond to spectra acquired at 25, 70 and 95°C, respectively. **(B)** and **(C)** Variation of the relative molar ellipticity at 265 and 290 nm, respectively, recorded during the annealing and the melting of 4 μM TEAD4-near in 5 mM Tris pH 7.5, 150 mM KCl.

melting profile showed a progressive reduction of the CD signal at 290 nm. This decrease was paired with an increment of the signal at 265 nm that reached the maximal intensity at about 70°C and that was lost at higher temperatures (Figure 3A). This transition can be attributed to an intermediate state occurring along the folding/unfolding of the antiparallel G4 but which presence was negligible at physiological temperature.

To verify whether some of the detected species might correspond to intermolecular arrangements, native polyacrylamide gel electrophoresis (PAGE) experiments were performed. TEAD4-near samples were analyzed before and after an annealing step carried out in the presence of KCl. All of them run as a single band with an electrophoretic mobility higher compared to the one of an unfolded 22-nts scrambled oligonucleotide (Supplementary Figure S2A), thus confirming that TEAD4-near folds only into intramolecular structures under our experimental conditions.

3.3 The folding of TEAD4-far comprises parallel and antiparallel G4 components

Consistently with the above described experimental approach, we started the characterization of TEAD4-far structural equilibria by monitoring in time the CD spectra modifications upon addition of increasing KCl concentrations up to 150 mM (Figure 4A). At all tested conditions, the CD spectra of TEAD4-far progressively evolved towards the formation of two main positive peaks located at 290 and 265 nm that, as supported by TDS, were associated to its folding into G4 (Supplementary Figure S1B).

CD spectra with maxima at both 265 and 290 nm are typical of G4 with hybrid topology (Balagurumoorthy et al., 1992). Alternatively, they can be observed when a sequence in solution distributes between parallel and antiparallel conformations. Here, by comparing the molar ellipticity of the oligonucleotide solutions after 1 h of incubation, it emerged that their relative intensities were a

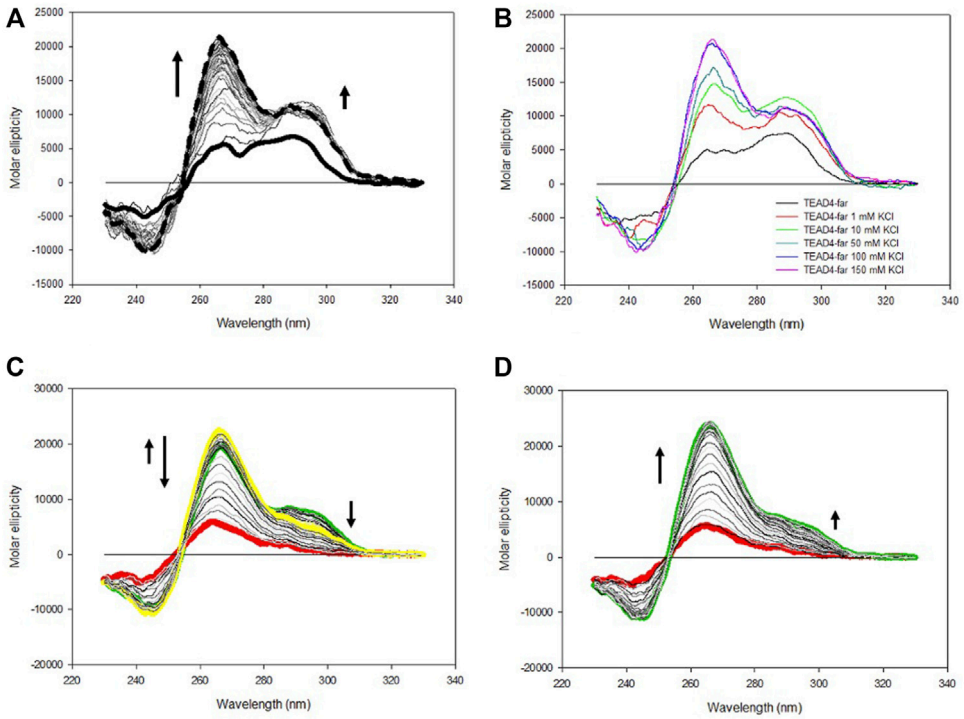


FIGURE 4
(A) Time dependent variation of CD spectra of 4 μM TEAD4-far in 5 mM Tris, pH 7.5 upon addition of 150 mM KCl at 25°C. Solid and dashed lines correspond to the oligonucleotide in the absence of metal ion and after 1 h incubation, respectively. **(B)** CD spectra of 4 μM TEAD4-far in 5 mM Tris pH 7.5 in the absence and presence of 1–150 mM KCl acquired after 1 h at 25°C. **(C)** and **(D)** CD spectra of 4 μM TEAD4-far in 5 mM Tris pH 7.5, 150 mM KCl, acquired during melting **(C)** or annealing **(D)** at 20°C/h. The green, yellow and red lines correspond to spectra acquired at 25, 65 and 95°C, respectively.

function of the metal ion concentration (Figure 4B). As far it concerns the peak at 265 nm, it reached the maximum of molar ellipticity at 100 mM KCl. Conversely, the intensity of the peak at 290 nm increased moving from 1 to 10 mM KCl while further increments of the metal ion concentration reduced it to converge towards a constant value of molar ellipticity. The differential response at these two wavelengths was further highlighted by comparing the folding kinetic of the oligonucleotide at these two wavelengths, the variation of the signal at 265 nm being much slower than the one occurring at 290 nm at all tested KCl concentrations (Supplementary Figure S3). These data indicated a competition between two distinct oligonucleotide arrangements that leads to their different relative abundance as a function of KCl concentration. At high KCl concentration parallel G4 arrangement was favored. Interestingly, melting/annealing profiles acquired in 10 mM KCl nicely overlapped (Supplementary Figure S4). Conversely, in 150 mM KCl, by heating of the solution up to 65°C, a modest but significant rearrangement occurred, which corresponded to an increase of the molar ellipticity at 265 nm associated to a reduction of the signal intensity at 290 nm (Figures 4C,D). Noteworthy, this species was the one preserved at r.t. after the annealing.

Overall, data suggested that TEAD4-far distributes between a kinetically favored antiparallel structure and a thermodynamic favored parallel conformation, the annealing shifting the system towards the last one at physiologically relevant KCl concentrations. PAGE experiments confirmed that none of them is related to intermolecular folded structures (Supplementary Figure S2B).

3.4 TEAD4-full folds into an extended parallel G4

Based on the above presented results, it was unexpected to observe that the addition of KCl up to 150 mM to TEAD4-full produced only modest changes of the dichroic signal. They comprised a fast increment at 290 nm that was paired with a very slow rearrangement at lower wavelengths that occurred on the time scale of hours (Figures 5A; Supplementary Figure S5). This chiroptical profile markedly changed as a function of potassium concentration when we analyzed the annealed oligonucleotide solutions (Figure 5B) with a positive band centered at 265 nm progressively emerging above 50 mM

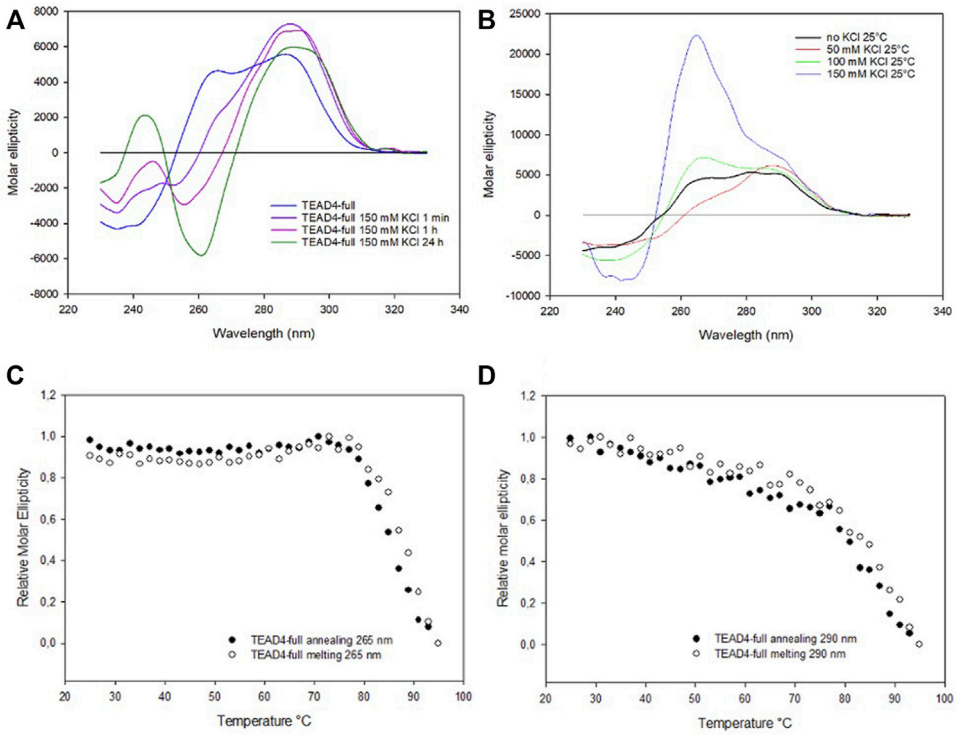


FIGURE 5
(A) CD spectra of 2 μM TEAD4-full in 5 mM Tris, pH 7.5, in the absence of KCl and 1 min, 1 h and 24 h after the addition of 150 mM KCl at 25°C. **(B)** CD spectra of 2 μM TEAD4-full in 5 mM Tris after annealing in presence of 50, 100 or 150 mM KCl. **(C)** and **(D)** Relative variation of the molar ellipticity recorded at 265 and 290 nm, respectively, during annealing and melting of 2 μM TEAD4-full in 5 mM Tris pH 7.5, 150 mM KCl at 20°C/h.

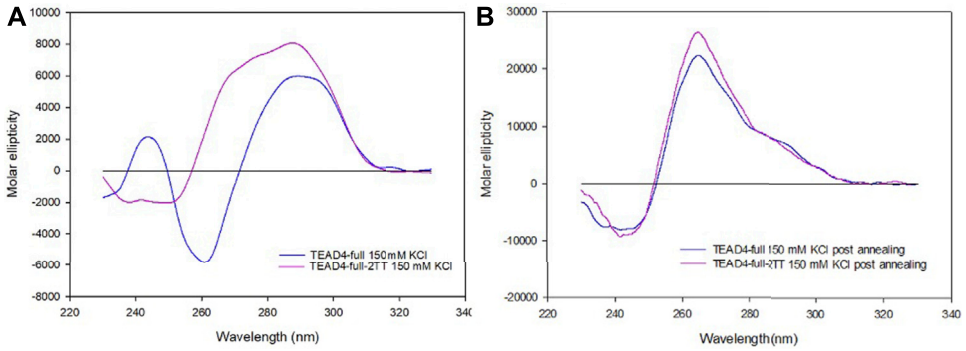


FIGURE 6
CD spectra of 2 μM TEAD4-full and TEAD4-full-2TT in 5 mM Tris, pH 7.5, 150 mM KCl acquired 24 h after addition of the salt at 25°C **(A)** or after annealing **(B)**.

KCl. In particular, at 150 mM KCl, this contribution was largely dominant. UV thermal differential scans confirmed that it corresponded to TEAD4-full preferentially folded into G4, since the negative signal at 296 nm, characteristic of the G4 structure, was remarkably more intense when compared to the one acquired before the annealing step (Supplementary Figure S1C–D). These data supported the preferential formation of a parallel G4 at physiological KCl concentration.

10.3389/fchem.2022.1008075

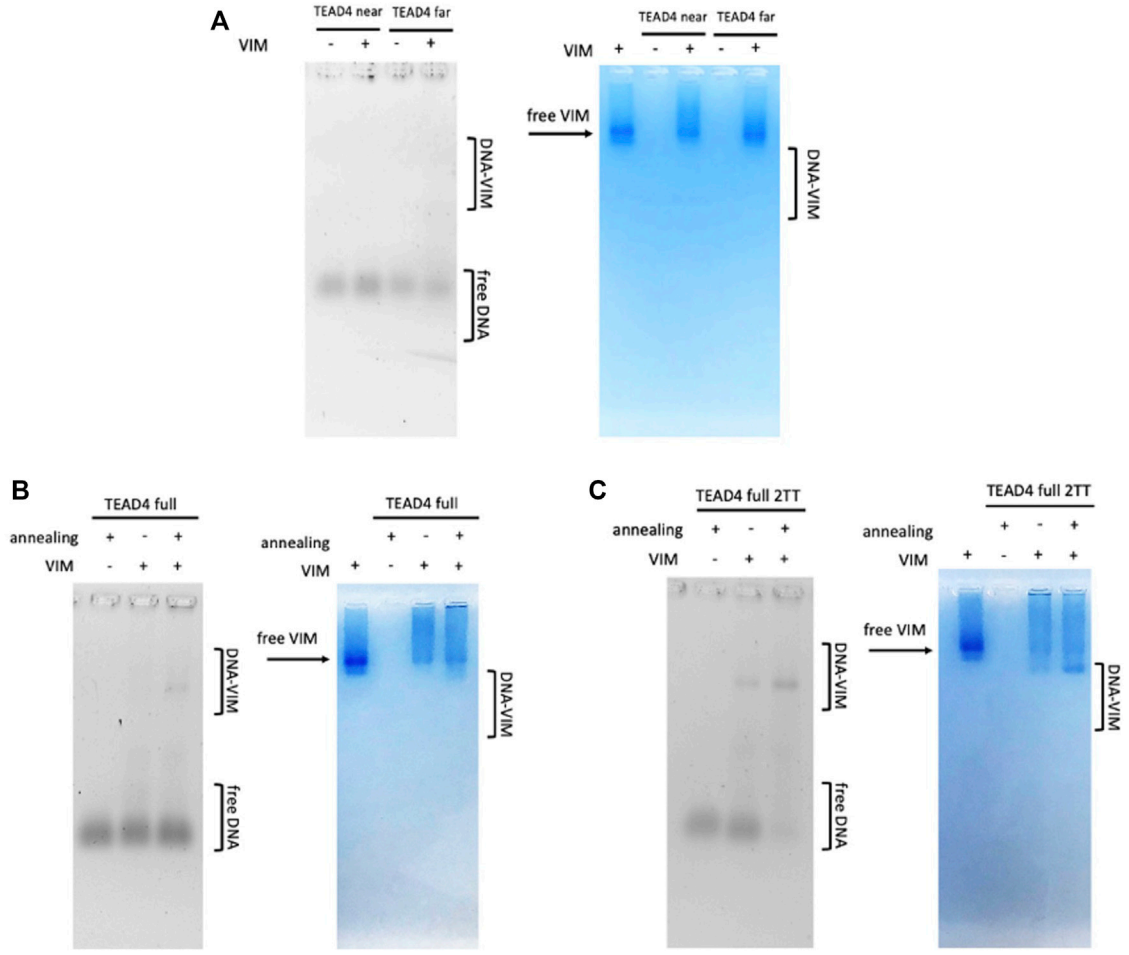


FIGURE 7
EMSA of tested oligonucleotides (500 nM) incubated with 8 μM Vimentin in 5 mM Tris, pH 8.4, 150 mM KCl, stained with Sybr Green II (on the left) and Coomassie Brilliant Blue G250 (on the right) Panel **(A)** TEAD4-near and TEAD4-far; Panel **(B)** TEAD4-full before and after annealing in presence of KCl; Panel **(C)** TEAD4-full-2TT before and after annealing in presence of KCl.

Worth of note, once annealed, at all tested salt concentrations the system was at the thermodynamic equilibrium and, subsequent melting/annealing cycles were fully reversible (Figure 6). Their profiles further supported that at the lower tested KCl concentration the presence of multiple components was preserved (Supplementary Figure S6). Also for this sequence, PAGE confirmed the conserved presence of only intramolecular structures (Supplementary Figure S2C).

According to these data, it is possible to propose that the addition of metal ion to TEAD4-full stabilized an intramolecular arrangement that prevents the formation of the G4-repeat, the thermal denaturation of this starting arrangement(s) allowing the formation of the more thermodynamic stable parallel G4. Based on the intensity of the signal, it appeared that at physiological conditions it covered both the two G4 domains. This is compatible with the formation of a G4-repeat.

3.5 The mutated TEAD4-full-2TT adopts a parallel G4 conformation

The described structural folding landscape of TEAD4-full is complex. To better describe it, we designed a sequence with a reduced propensity to adopt G4-competing structures. By analyzing the TEAD4-full sequence with the IDT OligoAnalizer prediction tool, we retrieved several hairpin structures, as expected for a sequence with such a remarkable high GC content. Noteworthy, the most stable hairpins involved constantly the central four cytosines paired with different guanines that, based on our data on the short TEAD4 domains, should be involved in G-tetrads formation (Supplementary Figure S7). To validate the potential impact of these secondary structures on the G4 formation, we considered to reduce them by converting the central cytosines into thymines

(Figure 1). Thus, we characterized the mutated sequence TEAD4-full-2TT reported in Table 1.

The CD spectra of TEAD4-full-2TT after the addition of 150 mM KCl showed a weak peak at 290 nm similar to the one of TEAD4-full. However, differently from the wild-type sequence, it comprised also a weak shoulder at 265 nm, likely due to the presence of a small fraction of parallel G4 (Figure 6A). The annealing of this solution readily drove a strong increment of this component, comparable to TEAD-full although slightly more intense (Figure 6B). These data indicated that the introduced mutations did not fully prevent the formation of potentially G4-repeat competing structures, but they reduced them thus making more efficient the structural rearrangement towards the thermodynamically favored parallel G4-repeat.

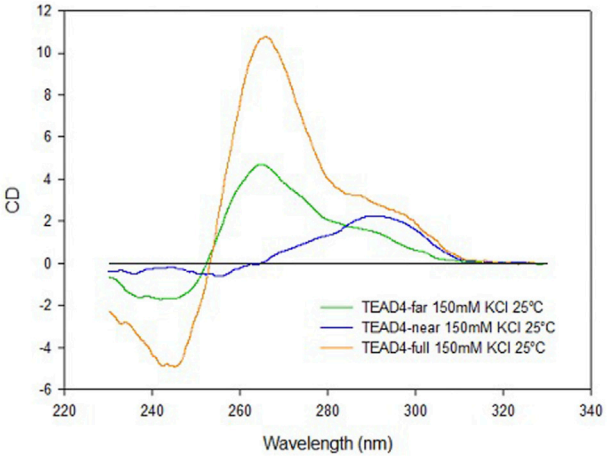


FIGURE 8
CD spectra of TEAD4-full, TEAD4-far and TEAD4-near in 5 mM Tris, pH 7.5, after annealing in presence of 150 mM KCl.

3.6 The G4-repeats of TEAD4-full and TEAD4-full-2TT are recognized by Vimentin

To address the binding of Vimentin to TEAD4, we performed electrophoretic mobility shift assays with the purified recombinant human protein. Binding reactions were carried out at pH 8.4 to avoid Vimentin polymerization into filaments (Herrmann et al., 2004). Due to the complex folding landscape of the herein tested sequences, oligonucleotides were either equilibrated or annealed in 150 mM KCl to promote G-quadruplex formation before protein addition.

As expected from the high selectivity of Vimentin for G4-repeats, no protein-DNA complexes were observed when Vimentin was incubated with the isolated TEAD4-near and TEAD4-far (Figure 7A). Conversely, as shown in Figure 7B, Vimentin interacted with TEAD4-full. Remarkably, the complex formation occurred only when the oligonucleotide was previously annealed in 150 mM KCl. This result further confirmed that the parallel G4 arrangement induced in these conditions actually corresponds to a G4-repeat.

It was interesting to observe that Vimentin did bind to TEAD4-full-2TT either before and after the annealing. In the first case, the interaction was weak, while no free DNA was observed when Vimentin was added to the previously annealed TEAD4-full-2TT (Figure 7C). The higher affinity of the protein for this full-length mutated sequence further indicated that the selected mutations efficiently reduced the formation of structural motives that compete with the complete folding of TEAD4-full into a G4-repeat.

4 Discussion

TEAD4 is an oncogene with important roles in cancer, including epithelial-to-mesenchymal transition (EMT), metastasis, chemotherapeutic drug resistance and, consistently, it represents a valuable target for anticancer treatment (Chen et al., 2020). The presence of a long G-rich domain within its promoter is attractive since its potential conversion into non-canonical DNA arrangements may lead to unique sites of intervention to modulate its functions. This will potentially drive towards a better description of TEAD4 functional roles and eventually to novel therapeutic tools. As a starting point, it was demanding to explore the conformational profile of this G-reach domain.

The combined data obtained by CD and UV spectroscopic analyses at physiologically relevant KCl concentration, showed that at the identified long G-rich site, two short DNA domains can individually fold into different G4 structures. TEAD4-far folds into a combination of parallel and antiparallel intramolecular G4s, the antiparallel ones being kinetically favored, while the parallel ones being more thermodynamically stable and, remarkably, being largely dependent on KCl concentration. In principle, TEAD4-near can be addressed as less polymorphic since in solution it mainly folds into an intramolecular antiparallel G4. However, along the folding pathway, a parallel contribution was also detected. Although at physiological temperature its presence is negligible *in vitro*, we cannot rule out its occurrence to a significant extent in the complex nuclear environment.

As supported by the interaction of TEAD4-full with Vimentin, the full-length G-rich domain folds into a repeat formed by two G4 modules. However, the folding behavior of the full-length sequence TEAD4-full, did not correspond to the sum of its two domains as clearly emerged by comparing their chiroptical contributions (Figure 8). In particular, it appears that TEAD4-near, being prevalently folded into an antiparallel G4,

does not contribute to the relevant parallel G4 content (as derived from the positive band at 265 nm) of the full length TEAD4-full. This issue can be addressed based on literature data. Indeed, conformational rearrangements occurring when multiple G4 modules are arranged into a continuous array have been already highlighted, first of all for the telomeres, that can accommodate several nearby G4s with the same sequence composition but with a combination of distinct topologies (Monsen et al., 2021) (Carrino et al., 2021). More recent evidences pointed that at gene promoters, contiguous G4s are expected to evolve towards a conserved preferential parallel conformation (Schonhoft et al., 2009) (Monsen et al., 2022). It has been proposed that this can be the result of a favorable contribution deriving from G4-G4 stacking interaction, easily occurring between two parallel G4s but hindered with the antiparallel ones. In our model, as above mentioned, TEAD4-near can undergo an antiparallel to parallel transition, thus it is not at odd to consider that the last is preferred when it is flanked by the TEAD4-far.

The parallel G4-repeat of TEAD4-full is expected to be much more stable in comparison to the two isolated G4 units. However, we observed how its folding is impaired before the annealing at high KCl concentration. Here, as supported by the characterization of the mutated TEAD4-full-2TT sequence, we related this to the possible competition between G4-repeats and alternative intramolecular pairings. Again, this evidence does not rule out the formation of the G4-repeat in the intracellular environment where the complex composition can influence the relative stabilities of the folded species. Moreover, we should consider that in the cell, the herein studied sequence is inserted within a long frame of dsDNA. While as previously reported (Buglione et al., 2021) this template well supports G4-repeat formation, it might elicit alternative folding.

Finally, the herein reported interaction of our tested sequences with Vimentin, is valuable not only from a structural point of view. Indeed, in colorectal cancer cells, TEAD4 binds the promoter of Vimentin to induce its expression and the level of these two proteins are correlated to drive EMT, ultimately increasing the migration of tumor cells and the tumor metastasis (Liu et al., 2016). Our result, by supporting a direct interaction of Vimentin with TEAD4 promoter can foresee the occurrence of a positive feedback between these two factors, that could be associated to important tumor related pathways.

In conclusion, the herein described binding interaction between Vimentin and TEAD4-full can be considered as a new target: it paves the way to the identification of novel mechanisms worth to be exploited to realize safer and more efficient treatments for oncological patients.

Data availability statement

The original contributions presented in the study are included in the article/Supplementary Material, further inquiries can be directed to the corresponding author.

Author contributions

MC, SC and CS contributed to conception and design of the study. MC was involved in all experimental settings and performed all data analyses, EG contributed to sequences selection and design, MS contributed to protein production and purification selection, SC supervised protein-DNA studies, MC wrote the first draft of the manuscript, SC and CS cured manuscript writing, review and editing. All authors contributed to manuscript revision, read, and approved the submitted version.

Funding

The research leading to these results has received funding from AIRC under IG 2021–ID. 26474 project–P.I. Claudia Sissi. The PhD fellowship of MC was founded by Cariparo.

Conflict of interest

The authors declare that the research was conducted in the absence of any commercial or financial relationships that could be construed as a potential conflict of interest.

Publisher's note

All claims expressed in this article are solely those of the authors and do not necessarily represent those of their affiliated organizations, or those of the publisher, the editors and the reviewers. Any product that may be evaluated in this article, or claim that may be made by its manufacturer, is not guaranteed or endorsed by the publisher.

Supplementary material

The Supplementary Material for this article can be found online at: https://www.frontiersin.org/articles/10.3389/fchem.2022.1008075/full#supplementary-material

References

Balagurumoorthy, P., Brahmachari, S. K., Mohanty, D., Bansal, M., and Sasisekharan, V. (1992). Hairpin and parallel quartet structures for telomeric sequences. *Nucleic Acids Res.* 20 (15), 4061–4067. doi:10.1093/nar/20.15.4061

Balasubramanian, S. (2011). Targeting G-quadruplexes in gene promoters: A novel anticancer strategy? *DRUG Discov.* 15, 261–275. doi:10.1038/nrd3428

Barry, E R., Simov, V., Valtingojer, I., and Venier, O. (2021). Vladimir simov, Iris valtingojer, and olivier VenierRecent therapeutic approaches to modulate the hippo pathway in oncology and regenerative medicine. *Cells* 10 (10), 2715. doi:10.3390/cells10102715

Berselli, M., Lavezzo, E., and Toppo, S. (2019). Qparse: Searching for long-looped or multimeric G-quadruplexes potentially distinctive and druggable. *Bioinformatics* 36, btz569. doi:10.1093/bioinformatics/btz569

Bochman, M. L., Paeschke, K., and Zakian, V. A. (2012). DNA secondary structures: Stability and function of G-quadruplex structures. *Nat. Rev. Genet.* 13 (11), 770–780. doi:10.1038/nrg3296

Buglione, E., Salerno, D., Cassina, V., Vesco, G., Nardo, L., Dacasto, M., et al. (2021). Nanomechanics of G-quadruplexes within the promoter of the *KIT* oncogene. *Nucleic Acids Res.* 49 (8), 4564–4573. doi:10.1093/nar/gkab079

Carrino, S., Hennecker, C. D., Murrieta, A. C., and Anthony, M. (2021). Frustrated folding of guanine quadruplexes in telomeric DNA. *Nucleic Acids Res.* 49 (6), 3063–3076. doi:10.1093/nar/gkab140

Ceschi, S., Berselli, M., Cozzaglio, M., Giantin, M., Toppo, S., Spolaore, B., et al. (2022). Vimentin binds to G-quadruplex repeats found at telomeres and gene promoters. *Nucleic Acids Res.* 50, 1370–1381. 81. doi:10.1093/nar/gkab1274

Chen, M., Huang, B., Zhu, L., Chen, K., Liu, M., and Zhong, C. (2020). Structural and functional overview of TEAD4 in cancer biology. *Onco. Targets. Ther.* 13, 9865–9874. doi:10.2147/OTT.S266649

Eddy, J., and Maizels, N. (2006). Gene function correlates with potential for G4 DNA formation in the human genome. *Nucleic Acids Res.* 34 (14), 3887–3896. doi:10.1093/nar/gkl529

Herrmann, H., Kreplak, L., and Aebi, U. (2004). Isolation, characterization, and *in vitro* assembly of intermediate filaments. *Methods Cell Biol.* 78, 3–24. doi:10.1016/S0091-679X(04)78001-2

Jang, H-R., Shin, S-B., Kim, C-H., Won, J-Y., Xu, R., Kim, D. E., et al. (2021). PLK1/Vimentin signaling facilitates immune escape by recruiting smad2/3 to PD-L1 promoter in metastatic lung adenocarcinoma. *Cell Death Differ.* 28 (9), 2745–2764. doi:10.1038/s41418-021-00781-4

Largy, E., Mergny, J., and Gabelica, V. (2016). "Role of alkali metal ions in G-quadruplex nucleic acid structure and stability," in *The alkali metal ions: Their role for life*. Editors Astrid Sigel, Helmut Sigel, K. Roland, and O. Sigel (Cham: Springer International Publishing). doi:10.1007/978-3-319-21756-7_7

Liu, Y., Wang, G., Yang, Y., Mei, Z., Liang, Z., Cui, A., et al. (2016). Increased TEAD4 expression and nuclear localization in colorectal cancer promote epithelial–mesenchymal transition and metastasis in a YAP-independent manner. *Oncogene* 35 (21), 2789–2800. doi:10.1038/onc.2015.342

Marquevielle, J., Robert, C., Lagrabette, O., Wahid, M., Bourdoncle, A., Xodo, L. E., et al. (2020). Structure of two G-quadruplexes in equilibrium in the KRAS promoter. *Nucleic Acids Res.* 48 (16), 9336–9345. doi:10.1093/nar/gkaa387

Mergny, J.-L. (2005). Thermal difference spectra: A specific signature for nucleic acid structures. *Nucleic Acids Res.* 33 (16), e138. doi:10.1093/nar/gni134

Mergui, X., Puiffe, M. L., Valteau-Couanet, D., Lipinski, M., Jean, B., and Amor-Guéret, M. (2010). P21Waf1 expression is regulated by nuclear intermediate filament Vimentin in neuroblastoma. *BMC Cancer* 10 (1), 473. doi:10.1186/1471-2407-10-473

Monsen, R. C., Lynn, D., Dean, W. L., Gray, R. D., Sabo, T. M., Srinivas, Cy, et al. (2020). The HTERT core promoter forms three parallel G-quadruplexes. *Nucleic Acids Res.* 48 (10), 5720–5734. doi:10.1093/nar/gkaa107

Monsen, R. C., Lynn, W. L. D., Gray, R. D., Srinivas, C., Jesse, B., Chaires, J. B., et al. (2022). Long promoter sequences form higher-order G-quadruplexes: An integrative structural biology study of *c-myc* , *k-ras* and *c-kit* promoter sequences. *Nucleic Acids Res.* 50 (7), 4127–4147. doi:10.1093/nar/gkac182

Monsen, R. C., Srinivas, C., Dean, W. L., Chaires, J. B., and John, O. T. (2021). The solution structures of higher-order human telomere G-quadruplex multimers. *Nucleic Acids Res.* 49 (3), 1749–1768. doi:10.1093/nar/gkaa1285

Rigo, R., Palumbo, M., and Sissi, C. (2017). G-quadruplexes in human promoters: A challenge for therapeutic applications. *Biochimica Biophysica Acta (BBA) - General Subj.* 1861 (5), 1399–1413. doi:10.1016/j.bbagen.2016.12.024

Rigo, R., and Sissi, C. (2017). Characterization of G4–G4 crosstalk in the *c-KIT* promoter region. *Biochemistry* 56 (33), 4309–4312. doi:10.1021/acs.biochem.7b00660

Schaffitzel, C., Berger, I., Postberg, J., Hanes, J., Lipps, H. J., and Pluckthun, A. (2001). *In vitro* generated antibodies specific for telomeric guanine-quadruplex DNA react with stylonychia lemnae macronuclei. *Proc. Natl. Acad. Sci. U. S. A.* 98 (15), 8572–8577. doi:10.1073/pnas.141229498

Schonhoft, J. D., Bajracharya, R., Dhakal, S., Yu, Z., Mao, H., and Basu, S. (2009). Direct experimental evidence for quadruplex–quadruplex interaction within the human ILPR. *Nucleic Acids Res.* 37 (10), 3310–3320. doi:10.1093/nar/gkp181

Todd, A. K. (2005). Highly prevalent putative quadruplex sequence motifs in human DNA. *Nucleic Acids Res.* 33 (9), 2901–2907. doi:10.1093/nar/gki553

Watson, J. D., and Crick, F. H. (1974). Molecular structure of nucleic acids: A structure for deoxyribose nucleic acid. *Nature* 248 (5451), 765. doi:10.1038/248765a0

frontiers | Frontiers in Chemistry

TYPE Original Research
PUBLISHED 15 September 2022
DOI 10.3389/fchem.2022.962161

Check for updates

OPEN ACCESS

EDITED BY
Li Yuhan,
Chongqing Technology and Business University, China

REVIEWED BY
Leli Zeng,
Seventh Affiliated Hospital, Sun Yat-sen University, China
Vladimir Mulens-Arias,
Pompeu Fabra University, Spain
Clemente Guadalupe Alvarado Beltrán,
Autonomous University of Sinaloa, Mexico

*CORRESPONDENCE
Tijana Rajh,
tijana.rajh@asu.edu

SPECIALTY SECTION
This article was submitted to Photocatalysis and Photochemistry, a section of the journal Frontiers in Chemistry

RECEIVED 06 June 2022
ACCEPTED 22 August 2022
PUBLISHED 15 September 2022

CITATION
Rajh T, Koritarov T, Blaiszik B, Rizvi SFZ, Konda V and Bissonnette M (2022), Triggering cell death in cancers using self-illuminating nanocomposites. *Front. Chem.* 10:962161. doi: 10.3389/fchem.2022.962161

COPYRIGHT
© 2022 Rajh, Koritarov, Blaiszik, Rizvi, Konda and Bissonnette. This is an open-access article distributed under the terms of the Creative Commons Attribution License (CC BY). The use, distribution or reproduction in other forums is permitted, provided the original author(s) and the copyright owner(s) are credited and that the original publication in this journal is cited, in accordance with accepted academic practice. No use, distribution or reproduction is permitted which does not comply with these terms.

Triggering cell death in cancers using self-illuminating nanocomposites

Tijana Rajh[1,2]*, Tamara Koritarov[1], Ben Blaiszik[1], Syeda Fatima Z. Rizvi[1], Vani Konda[3] and Marc Bissonnette[3]

[1]Center for Nanoscale Materials, Argonne National Laboratory, Argonne, IL, United States, [2]School of Molecular Sciences, Arizona State University, Tempe, AZ, United States, [3]Department of Medicine, The University of Chicago Medicine, Chicago, IL, United States

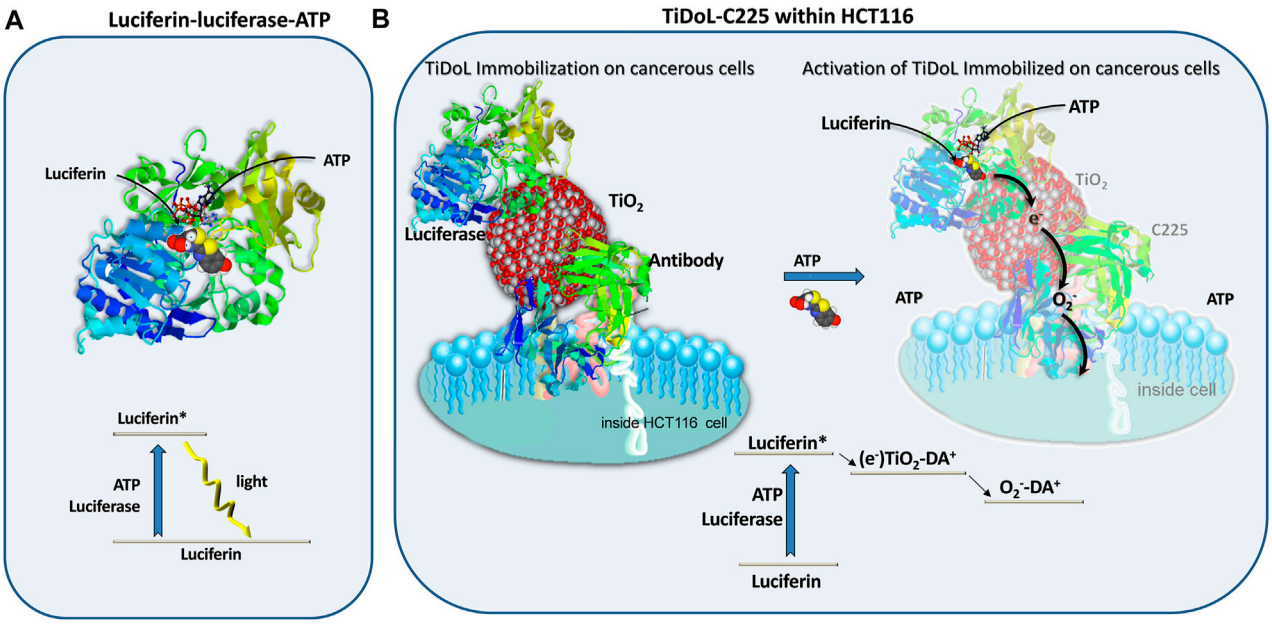
Bioinspired photocatalysis has resulted in efficient solutions for many areas of science and technology spanning from solar cells to medicine. Here we show a new bioinspired semiconductor nanocomposite (nanoTiO_2-DOPA-luciferase, TiDoL) capable of converting light energy within cancerous tissues into chemical species that are highly disruptive to cell metabolism and lead to cell death. This localized activity of semiconductor nanocomposites is triggered by cancer-generated activators. Adenosine triphosphate (ATP) is produced in excess in cancer tissues only and activates nearby immobilized TiDoL composites, thereby eliminating its off-target toxicity. The interaction of TiDoL with cancerous cells was probed *in situ* and in real-time to establish a detailed mechanism of nanoparticle activation, triggering of the apoptotic signaling cascade, and finally, cancer cell death. Activation of TiDoL with non-cancerous cells did not result in cell toxicity. Exploring the activation of antibody-targeted semiconductor conjugates using ATP is a step toward a universal approach to single-cell-targeted medical therapies with more precision, efficacy, and potentially fewer side effects.

KEYWORDS

TiO_2, nanocomposites, luciferase, bioluminescence, extracellular ATP, cancer, apoptosis, real-time confocal microscopy

1 Introduction

Recent progress in advanced medical therapies is focused on targeted therapies with a single-cell level resolution. They hold the promise of reducing off-target drug effects by directing therapeutic agents exclusively to localized diseased tissue (O'Brien et al., 2007; Li, 2014; Petros and DeSimone, 2010; Yang et al., 2018; Schmidt et al., 2020; Jan et al., 2021; Briolay et al., 2021). Several factors are important for cell-targeted therapies among which prevention of the premature release of toxic remedies is one of the most important ones. Several drug delivery systems activated by heat, magnetic fields, ultrasound, or light are being explored (Mura et al., 2013; Briolay et al., 2021; Han and Choi, 2021). Another attractive approach to localized therapies is the use of molecules that are produced by the disease itself as triggers that activate the therapy (LaVan et al., 2003). So far, this approach has been used indirectly for carriers that rely on pH change across the liposome bilayer



SCHEME 1
Silent features of firefly luciferase catalyzed excitation and luminescence of luciferin in the presence of ATP **(A)** and modification of the excitation mechanism to power membrane-immobilized semiconductor particles in tumors *in situ* resulting in radical species such as superoxide radicals ($O_2^{-}\cdot$) capable of initiating the apoptotic signaling cascade within a neighboring cancerous cell **(B)**.

(Maurer-Spurej et al., 1999; Lei et al., 2017) or pathophysiological abnormalities of the vascular system in tumors (EPR effect) (Allen and Cullis, 2004; Lei et al., 2017) that passively accumulate and retain the drug at diseased targets. We take a new approach that takes advantage of the active release of ATP in the extracellular environment of tumors (Stagg and Smyth, 2010; Vultaggio-Poma et al., 2020). One of the most prominent metabolic alterations in cancer cells is the increase in aerobic glycolysis and the dependency on the glycolytic pathway for ATP generation, known as the Warburg effect (Pelicano et al., 2006). Many cancers produce a significant amount of ATP through a glycolic Warburg pathway and maintain high levels of ATP through avid consumption of glucose even during the execution of apoptosis (Oberdanner et al., 2002; Kim and Dang, 2006; Vultaggio-Poma et al., 2020). This highly energetic molecule is accumulated in the tumor interstitium, while it is basically undetectable in healthy tissues (Pellegatti et al., 2008). The excess ATP was previously used for imaging cancers deep in the tissues or to induce luminescence of quantum dots (Kim et al., 2015).

TiO_2 nanoparticles exhibit exceptional photoreactivity (Rajh et al., 2014) and can be functionalized to bind multiple biomolecules to an individual particle (Endres et al., 2007) and initiate photochemical reactions within the cell environment (Paunesku et al., 2003). Their surface modification with enediol molecules extends their light absorption to the visible and near-infrared region of the light spectrum, overcoming the biggest obstacle to the use of TiO_2 nanoparticles for applications in phototherapy (Supplementary Figure S1) (Rajh et al., 2002). It was shown that enediol-modified TiO_2 nanoparticles are highly active under visible light (Liu et al., 2006; Tachan et al., 2014) and have the ability to create reactive radical species upon illumination with visible light (Dimitrijevic et al., 2009). However, the small penetration depth of light in the body still limits the use of semiconductors in photodynamic therapy, restricting the targets to the skin and the lining of a lumen.

In this study, we describe a different approach; instead of delivering the light to the tumor, we take advantage of the presence of the highly energetic molecular source ATP in the extracellular space of the cancerous tissue to create superoxide radicals ($O_2^{-}\cdot$) capable of initiating the apoptotic signaling cascade (Chauhan et al., 2003; Dimitrijevic et al., 2009). Just like ATP activates luciferase-mediated luciferin emission of light (Scheme 1A), a mechanism used by fireflies to create their own light, ATP can power TiO_2 nanocomposites and directly generate electrons capable of a further generation of superoxide radicals $O_2^{-}\cdot$ (Scheme 1B). Superoxide is rather unreactive and its diffusion distance ranges from 0.5 to a few μm, largely controlled by the concentration of superoxide dismutase and nitric oxide radicals (compared to <2 nm for OH· radicals and <250 nm of singlet oxygen) (Panus et al., 1993; Mikkelsen

and Wardman, 2003). As excess ATP is local to tumor regions, photocatalytically produced superoxide radicals are formed within the tumor microenvironment and can diffuse to adjacent cell mitochondria and induce an apoptotic cell-signaling cascade (Chauhan et al., 2003).

In this work, we show that the sensitization of TiO_2 with luciferase enables ATP activation of TiO_2 nanoparticles and mediates an apoptotic cascade within HCT 116 colon cancerous cells. The elevated level of extracellular ATP within the tumor microenvironment is responsible for the localization of composite activity and formation of superoxide radicals within the tumor regions. We demonstrate that nanocomposites do not show any activity within noncancerous immortalized cells YAMC (young adult mouse colonocytes). We explore the strategy for enhancing nanocomposites' retention within the extracellular space, by coupling luciferase-TiO_2 nanocomposites (TiDoL) to the C225 antibody capable of recognizing and binding to receptors uniquely expressed on the HCT 116 surface. Antibody-immobilized nanocomposites confine the formation of radical species to the surface of HCT 116 cells and enhance the efficiency of interaction between superoxide radicals $O_2^{-}\cdot$ and nearby cancerous cells. In this way, the release of superoxide radicals becomes doubly regulated by 1) the level of ATP production in cancerous cells, and 2) the positioning of TiO_2 nanoparticles near cancerous cells using cell-specific antibodies, limiting their activity exclusively to cancerous tissues and therefore mitigating non-systemic toxicity.

2 Materials and methods

2.1 TiO_2 sample preparation

Five nm TiO_2 nanoparticles in water were prepared by the drop-wise addition of $TiCl_4$ to cooled water under vigorous steering as described previously (Rajh et al., 1996). Nanoparticles were deposited on ITO-coated glass slides *via* electrophoretic deposition (EPD) in aqueous solution at a voltage of 20 V and ca. 5 μA current. After deposition, the TiO_2-coated electrodes were sintered at 400°C for 1 h. Following the sintering process, a lead wire was attached to the sample and conduction between the wire and ITO was achieved by the addition of conductive silver paint. The surface of the TiO_2 nanoparticle films was modified by ~12 h of immersion in 10 mg/ml DOPAC solution in 10 mM MES buffer solution at pH 6.1 in the dark. Following functionalization, the carboxyl group of the surface-tethered Dopac was activated by reaction with 50 mM 1-Ethyl-3-[3-dimethylaminopropyl] carbodiimide (EDC) and 44 mM N-hydroxysulfosuccinimide (sulfo-NHS) in MES buffer at pH 6.1 for 2 h. Any remnant EDC-sulfo-NHS was quenched by reaction with excess mercaptoethanol and washed further with MES buffer. After washing, varying amounts of a luciferase enzyme were added to a vial containing the electrodes and MES buffer and allowed to react overnight in a dark refrigerator at 4°C. TiO_2 nanoparticles in phosphate buffer (10 mM PBS, pH 7) were prepared by rapid transition of positive particle charge at pH 3 to negative particle charge at pH 9 by injection of 1M LiOH to TiO_2 solution and subsequent dialysis against 10 mM PBS.

2.2 Chemically induced electrochemical testing

Current measurements were performed on the electrodes in a solution of 10 mM MES buffer (pH 6.1) and 5 mM hydroquinone purged with Ar. No bias voltage was applied, and the reference electrode was Ag/AgCl. The current was allowed to stabilize for 30 s before the luciferin and ATP substrate were injected. For a control film of TiO_2 modified with Dopac, only a nominal change in current was detected when the luciferin-ATP substrate was injected. Experiments were replicated two times.

2.3 Monitoring light emission from functionalized TiO_2 nanoparticles

Light emission from the functionalized TiO_2 nanoparticles in the solution and nanoparticle films was monitored using a Horiba Nanolog Spectrofluorometer. No light emission was observed for any control sample (TiO_2 and TiO_2-Dopac nanoparticles) in the spectrofluorometer after treatment with 100 μl of luciferin/ATP substrate. However, when functionalized TiO_2-DOPAC-luciferase films were treated with 100 μl of luciferin/ATP, an emitted light was observed. The decay kinetics and the emission spectrum were both monitored. Experiments were replicated two times.

2.4 Synthesis of self-illuminating nanoconjugates

We synthesized self-illuminating semiconductor nanoconjugates of titanium dioxide—Dopac—luciferase (TiDoL) by covalent linking of luciferase (*Photinus pyralis* (*firefly*)) with an equimolar particle concentration of 5 nm-TiO_2 nanoparticles through a conductive 3,4-Dihydroxyphenylacetic acid (Dopac) linker. To link negatively charged TiO_2 nanoparticles (in 10 mM phosphate buffered saline, PBS, pH 7) to luciferin that also has an overall negative charge (formal negative charge of −7.0), a small negatively charged linker Dopac (20 fold excess) was first incubated with luciferin to position negatively the charged carboxyl group in the positive pockets of luciferin (Supplementary Figure S2, five large positive pockets, mainly

composed of amino group terminated arginine and lysine) followed by EDS/sulfo-NHS conjugation of Dopac to amino groups of luciferase. TiO_2 nanoparticles were then incubated with (comprehensively washed) Dopac-modified luciferase. Due to their high degree of surface curvature, bare TiO_2 nanoparticles have surface atoms in a distorted crystalline environment and under-coordinated geometry (Rajh et al., 1999). These under-coordinated sites at the surface of small TiO_2 nanoparticles exhibit high reactivity toward bidentate coordination with oxygen-containing ligands enabling their seamless coupling to small molecules such as Dopac. Bidentate binding of Dopac to under-coordinated sites results in reconstruction of the surface atoms of TiO_2 nanoparticles to thermodynamically stable octahedral geometry. This, in turn, introduces new electronic states in the mid-gap region of TiO_2 nanoparticles that originate from Dopac HOMO and lead to enhanced optical properties of the nanoconjugate in the visible region of the spectrum (Rajh et al., 2002; Rego and Batista, 2003). As a result, only successful coupling of bare TiO_2 nanoparticles to DOPAC-modified luciferase will result in the electronic interaction manifested by the appearance of the visible absorption band (Paunesku et al., 2003; Rajh et al., 2004) of the nanoconjugate (TiO_2–Dopac–Luciferase, TiDoL). The appearance of visible absorption and the coupling were monitored by UV absorption spectroscopy and the measurements of zeta potential and electrophoretic mobility using laser Doppler micro-electrophoresis (Supplementary Figure S1; Supplementary Table S1). Detailed linking procedures are as follows:

2.4.1 TiO_2 functionalization/TiDoL

A total of 10 µl of 10 mg/ml Dopac (Sigma-Aldrich, St. Louis, MO, United States) was added to the 250 µl of stock 8.33 µM luciferase (Sigma-Aldrich, St. Louis, MO, United States) under nitrogen and incubated for 30 min. Then 20 µl of already mixed 0.5 ml of 10 mg/ml 1-Ethyl-3-[3-dimethylaminopropyl] carbodiimide hydrochloride (EDC) (Sigma-Aldrich, St. Louis, MO, United States), and 0.5 ml of 10 mg/ml N-Hydroxysuccinimide (NHS) (Sigma-Aldrich, St. Louis, MO, United States) solution was added to the luciferase solution under nitrogen and incubated for 2 h at room temperature under nitrogen. Then, the solution was washed four times with phosphate-buffered saline (PBS) (Sigma-Aldrich, St. Louis, MO, United States) using a centrifuge purification system. After the last wash, the solution was concentrated at 100 µL, and 200 µl of 10 µ of 5 nm TiO_2 was added. A faint yellow color appeared upon the addition of TiO_2 as a result of the formation of a charge transfer complex between TiO_2 and Dopac linked to luciferase confirming a successful coupling reaction. When the equimolar concentration of Dopac was used for modification of luciferase, only partially conjugated TiDoL was obtained as observed by UV/vis absorption spectroscopy. This preparation leads to a final concentration of 6.2 µM TiDoL with an excess of 3.3 µM luciferase. This TiDoL solution was used both as synthesized and with the addition of 25 µl of Dopac to enhance the absorption of luciferase-mediated luciferin emission.

2.4.2 Functionalization of TiDoL with C225 antibody/TiDoL-C225

TiDoL was further modified with an antibody such as C225. For that purpose, 10 µl of 10 mg/ml Dopac (Sigma-Aldrich, St. Louis, MO, United States) was added to 125 µl of 13.3 µM of an anti-EGFR monoclonal antibody, C225 (2 mg/ml Cetuximab/Erbitux, Eli Lilly, New York, NY, United States) under nitrogen. Then 20 µl of already mixed 0.5 ml of 10 mg/ml EDC and 0.5 ml of 10 mg/ml NHS solution was added under a nitrogen atmosphere. The solution was incubated for 2 h at room temperature under nitrogen. Then, the solution was washed four times with PBS using centrifuge purification. After the final wash, the final volume was adjusted to 125 and 300 µl of 6.2 µM TiDoL was added (or TiO_2 for preparation of TiO_2-C225). This preparation makes a final TiDoL-C225 solution with a concentration of 4.15 µM with a 0.28 µM concentration of free C225, which is approximately 5% excess.

2.4.3 Functionalization of TiDoL and TiDoLC225 with alizarin

TiDoL and TiDoL-C225 were modified with alizarine for monitoring nanocomposite fluorescence. A total of 25 µl of TiDoL (TiDoL-C225) was incubated with 372.5 µl of PBS and 2.5 µl of 6 mM alizarine. Pale pink color of the solution was developed after sonication for 5 min.

2.5 Particle characterization

The *Zetasizer* (Malvern Zetasizer Nano-ZS, Malvern, United Kingdom) was used to measure the size, zeta potential (surface charge), and mobility of TiO_2 and TiDoL samples (Supplementary Table S1). Samples were placed in an optical cell equipped with gold electrodes. Dynamic light scattering was measured in the cell using a 633 nm light laser cell with an applied potential and zeta potential, mobility, conductivity, and the size of nanoconjugates were obtained.

2.6 Cell culture

The HCT116 human colon cancer cell line with an overexpression of epidermal growth factor (EGF) receptors (ATCC, 2013) was grown in McCoy's 5a Medium Modified (Gibco, Grand Island, NY, United States), with fetal bovine serum (Gibco, Grand Island, NY, United States) added to a final concentration of 10%, and penicillin–streptomycin (Sigma-Aldrich, St. Louis, MO, United States) added to a final concentration of 5% ay 37°C. The young adult mouse

colonocyte (YAMC) cell line (provided by the University of Chicago Medical Center, Chicago IL, United States, 2015) was derived from the *Immortomouse*, a transgenic animal containing a temperature-sensitive T Ag under the control of an IFN-γ-dependent promoter. YAMC cells proliferate under permissive conditions of 33°C in the presence of 5 U/ml IFN-γ (PeproTech). YAMC cells were cultured in RPMI 1640 containing 5% FBS, 2 mM l-glutamine, penicillin/streptomycin, 5 U/ml IFN-γ, and N-2 supplement (Invitrogen Life Technologies). CT 26 fibroblast cells (ATCC, 2014) were grown in the same media with 10% FBS at 37°C. Cells were cultured under nonpermissive conditions for at least 24 h before experiments, and for the duration of experimentation. The cells were subcultured when they are grown at 70–90% confluence. An optical upright microscope (VWR VistaVision, Radnor, PA, United States) equipped with a camera (Carl Zeiss AxioCam CM1, Oberkochen, Germany) was used to examine the cell cultures and monitor the progress daily. A randomized block design is used for *in vitro* and *in situ* experiments. The cells were divided into eight or four identical blocks, and experimental procedures on each block were assigned randomly.

2.6.1 Cell staining

Every cellular dye was applied with a specific staining protocol described by the manufacturer. The cellular dyes were added to the growth medium incubated and washed with a growth medium and HBSS. Cell membranes of human colorectal cancer cells, including the HCT116 cell line, express multiple glycoprotein ligands (Tomlinson et al., 2000; Nagano et al., 2011) allowing the use of WGA for sensitive imaging of cytoplasmic membranes in HCT116 cell line (Chazotte, 2011; Wang et al., 2012). In addition, fluorescent *WGA* was also used to *stain* the Golgi apparatus (Allen et al., 1989; Chazotte, 2011) as cisternae at the trans face of Golgi membrane stacks participate in glycosylation of proteins that also bind WGA (Elmouelhi et al., 2008). Therefore, WGA (Invitrogen, Grand Island, NY, United States) was used for staining the cell membrane and Golgi apparatus in a fluorescent green color (Alexa 488). Mitotracker red (Invitrogen, Grand Island, NY, United States), a cationic red-fluorescent dye, binds negatively charged mitochondria in live cells and was used for labeling mitochondria with red fluorescence. It possesses a reactive chloromethyl group that forms a covalent bond with free thiols in proteins and peptides, retaining labeling thiol-containing proteins even after mitochondrial depolarization. Mitosox Red (Invitrogen, Grand Island, NY, United States) was a cellular stain that was used to image the superoxide radicals within the cell environment. The nucleus of the cellular cultures was stained with Hoechst (Invitrogen, Grand Island, NY, United States). Hoechst fluorescence is significantly enhanced in condensed chromatin and is used for motoring pyknotic nuclei. Alizarin was used to monitor TiO_2 nanoparticles within the cell environment. The Zeiss LSM 510 Meta confocal microscope (Carl Zeiss, Oberkochen, Germany) was used to image colocalization in stained cell cultures. All experiments were replicated three times and 200 cells were examined for statistics.

2.7 Real-time monitoring of the activity of self-illuminating TiDoL nanoparticles within the cell environment

HCT116 colon cancer cells were grown in 4-well or 8-well plates. For 8-well plates, the final volume of the solution containing all reactants and cell culture media, Hanks Balanced Salts Solution (HBSS), or PBS were 300 µl, and for 4-well plates, the amounts were doubled to a final volume of 600 µl. TiDoL nanoconjugates and controls (luciferase, TiO_2—Dopac, and unconjugated TiO_2—Dopac mixed with luciferase, all in the same 600 nM concentration) were incubated with cells in the presence of ATP (20 µM). The Zeiss LSM 510 Meta confocal microscope (Carl Zeiss, Oberkochen, Germany) was used to visualize cell culture changes in real-time. After 20 min of incubation, an aliquot of luciferin (15 µM final concentration) was injected into the well and the response of the cells to the addition of luciferin was monitored using the transmission mode of a confocal microscope with minimal light exposure that does not perturb the cells in the absence of luciferin injection (Figure 2A, time 0 min). The movement of the cells was recorded for 5 min before injection and 1 h after injection. The injections were repeated until budding of the cells was observed. The movies were made by taking time series photographs with the confocal microscope and enabled continuous monitoring of the effects of luciferin therapy on the cellular level. For investigating the effects of the presence of the antibody, TiDoL-C225 nanoconjugates and controls (luciferase, C225-Dopac and C225-TiO2-Dopac, all in the same 400 nM concentration) were incubated with cells in the presence of ATP (20 µM). Experiments were replicated three times and 200 cells were examined for statistics.

2.8 *In vivo* study of the TiDoL/TiDoL-C225 xenograft model in nude mice

An *in vivo* study with nude mice was carried out in the animal facility at the University of Chicago. All the studies were conducted in compliance with the Institutional Animal Care and Use Committee's requirements for the care and use of laboratory animals in research. A total of 16 nu/nu mice (6 weeks old, male) were implanted with HCT116 cells [3 × 10 (Jan et al., 2021) cells per flank] to induce xenograft tumors. TiDoL, TiDoL-C225, or C225 alone were injected into the tumors at 4 weeks (1.75 µg/g TiDoL, 50 µl injection and 1.25 µg/g TiDoL-C225, 50 µl injection). Half the mice in each group (allocation of animals

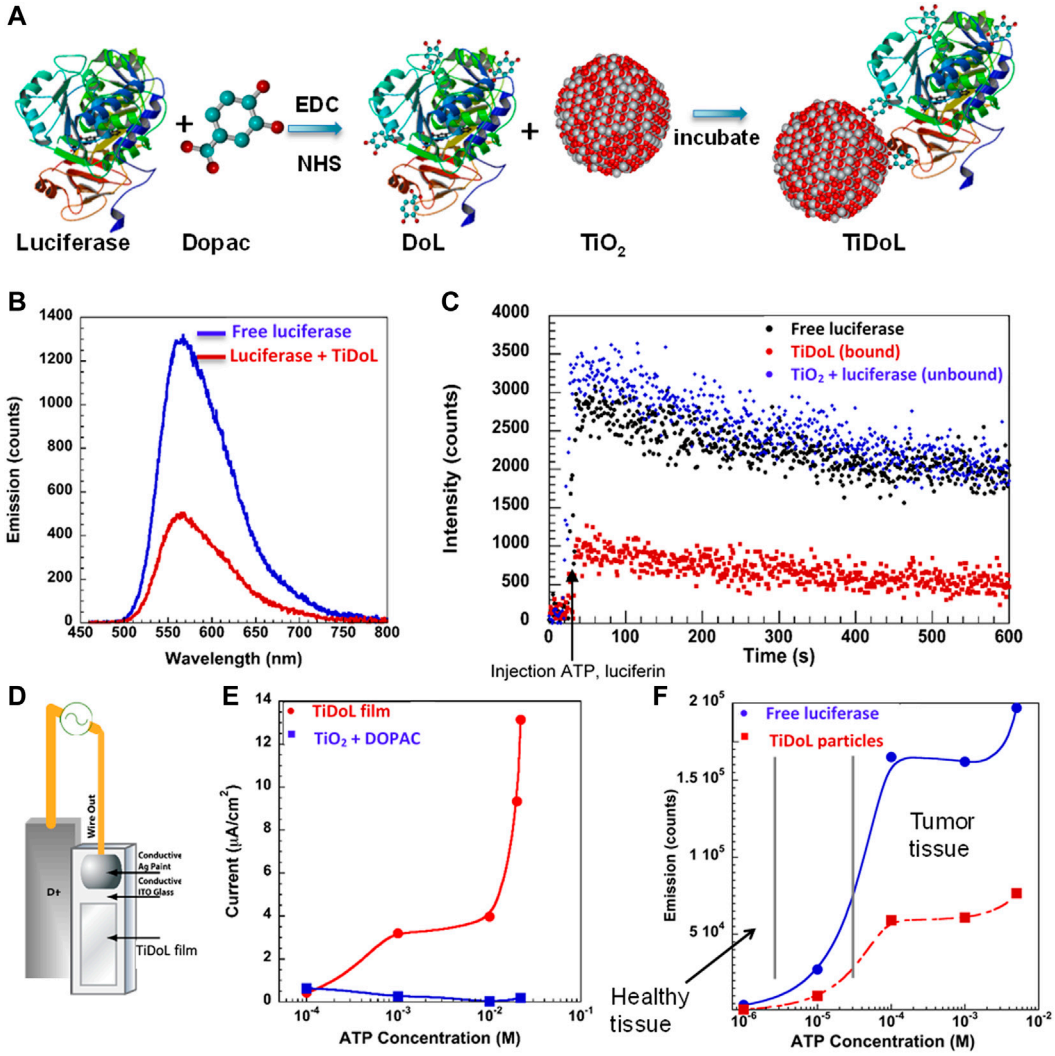


FIGURE 1
(A) Synthesis of self-powering TiDoL nanoparticles. In the first step, 3,4 dihydroxyphenylacetic acid (Dopac) was incubated with luciferase and subsequently reacted using EDC/NHS chemistry. Dopac-labeled luciferase (DoL) was then incubated with 5 nm TiO_2 nanoparticles to result in luciferase covalently linked to TiO_2 nanoparticles *via* a conductive linker (TiDoL). **(B)** Emission of free luciferase activated by luciferin in solution (blue) is quenched by TiDoL nanoparticles (red). **(C)** Kinetics of light emission of free luciferase (10 nM) and luciferin (40 μM) in solution (black); free luciferase and luciferin in the presence of, but not conjugated to, an equimolar concentration of TiO_2-Dopac (10 nM particles) (blue); and TiDoL nanoparticles (10 nM) and luciferin (40 μM) in solution (red). **(D)** Schematics of experimental luciferin induced current measurement setup in conjunction with **(E)** current generated by the luciferase-mediated conversion of luciferin in TiDoL films as a function of ATP concentration. Current measurements were performed on the electrodes in a solution of 10 mM MES buffer (pH 6.1) and 5 mM hydroquinone purged with Ar. **(F)** Bioluminescence emitted by the luciferase-mediated catalysis of luciferin at various concentrations of ATP. Minimal bioluminescence is emitted at ATP concentrations found in healthy tissue (low micromolar levels) for both unconjugated luciferase (blue) and luciferase that has been conjugated to TiO_2-Dopac nanoparticles (red). Significant bioluminescence and bioluminescence quenching by TiDoL nanoparticles are detected at ATP concentrations present in tumor tissue (low millimolar levels).

to the group was random) received IV luciferin × 2 (intraperitoneally, 15 mg/ml in PBS, 10 μl/g of body weight) and the remainder received vehicle. The tumors were measured every 2–3 days for 4 weeks. The tumor volume was calculated using expression volume = (length × width) (Li, 2014)/2 (mm^3). All animals were included in the analysis. Tumor volumes were plotted and fitted to an exponential function of growth using OriginLab. The average values of tumor volumes (Mean) and standard deviations (SD) were obtained using OriginLab and computed by the following expressions:

$$\text{Mean} = \sum_{i=0}^{n} x_i \quad \text{SD} = \sqrt{\sum_{i=1}^{n} \frac{(x_i - \bar{x})^2}{d}} \quad \text{where } d = n - 1 \cdot$$

In the graphs presented in Figure 5, the values were presented as mean (average) values and error bars as standard deviations. Standard deviation values were similar for each group. Histology was performed on tumors surgically removed from sacrificed mice 26 days after treatment, fixed in 3.7% formaldehyde, and embedded in paraffin blocks. Slices were stained with H&E under standard conditions and evaluated for pathological markers by transmission optical and laser confocal microscopy using white light and two color laser excitation (560 and 633 nm light), respectively (Zeiss LSM 510 Meta confocal microscope).

2.9 Statistical analysis

In vivo experiments' data were presented as the average of six tumor measurements and each experiment was carried out at least by duplicates. *In vivo* data were expressed as means ± S.D. (standard deviation). Statistical analysis was performed by using Student's *t*-test employing six independent data points. The criterion for statistical significance was $p < 0.05$. We used Excel (T.TEST function) for the determination of the *p*-value.

3 Results and discussion

3.1 Preparation of adenosine triphosphate-powered nanocomposites

We synthesized self-illuminated semiconductor nanoconjugates (TiDoL) by covalent linking of *Photinus pyralis* (firefly) luciferase with 5 nm TiO_2 nanoparticles through a conductive 3,4-Dihydroxyphenylacetic acid (Dopac) linker (Figure 1A). To link negatively charged TiO_2 nanoparticles (formal negative charge of −7.0 mV, Supplementary Table S1) to luciferase that has an overall negative charge (−5.82 mV), small molecule linker Dopac was first incubated with luciferase to position the negatively charged carboxyl group within the positive pockets of the protein (Supplementary Figure S2, five large positive pockets, mainly composed of amino group-terminated arginine and lysine). Following incubation, EDS/sulfo-NHS conjugation was used to couple the Dopac carboxyl group to an amino group of luciferase. TiO_2 nanoparticles were then added and incubated with Dopac-modified luciferase. Due to their high degree of surface curvature, bare 5 nm TiO_2 nanoparticles have surface atoms in under-coordinated geometry (Rajh et al., 1999). These under-coordinated sites at the surface of small TiO_2 nanoparticles exhibit high reactivity toward bidentate coordination with oxygen-containing ligands enabling their coupling to small molecules such as Dopac. Bidentate binding of Dopac to under-coordinated sites results in the reconstruction of the surface atoms of TiO_2 nanoparticles to thermodynamically stable octahedral geometry (Rajh et al., 2002; Rajh et al., 2014). This, in turn, introduces new electronic states in the mid-gap region of TiO_2 nanoparticles, creating a hybrid nanoparticle with Dopac HOMO and TiO_2 LUMO, leading to enhanced optical properties of the nanoconjugate in the visible region of the spectrum (Rajh et al., 2002; Rego and Batista, 2003). As a result, only successful coupling of bare TiO_2 nanoparticles to Dopac-modified luciferase will result in the electronic interaction manifested by the appearance of the visible absorption band (Paunesku et al., 2003; Rajh et al., 2004) of the nanoconjugate (TiO_2–Dopac–Luciferase, TiDoL). Therefore, nanocomposite coupling was monitored by the appearance of visible absorption at 550 nm (Supplementary Figures S1B,C) and the change in the zeta potential and electrophoretic mobility by laser Doppler micro-electrophoresis.

The formation of the TiDoL complex affected the intensity and, to a smaller extent, the kinetics of luciferase bioluminescence (Figures 1B,C). When the TiDoL nanoparticles were activated with ATP and luciferin, the luminescence was reduced to 60–65% compared to free luciferase, independent of the ATP concentration (Supplementary Figure S3). The decay kinetics of both quenched and unquenched samples were similar; however, somewhat faster kinetics of a sub-millisecond fraction of the luminescence decay was observed, while subsecond decay was unaffected. Interestingly, we did not observe luminescence quenching of unconjugated free luciferase in the presence of TiO_2-Dopac nanoparticles, probably due to the low probability of interaction between free luciferase and TiO_2-Dopac nanoparticles in diluted solutions (10 nM). This finding suggests that the quenching is a result of a strongly distance-dependent interaction, such as energy or electron transfer, and occurs only when luciferase activation is confined to the nanoparticle surface. Independent of the quenching mechanism, both energy and electron transfer results in a charge separation with holes localized on the surface modifier and electrons in TiO_2 nanoparticles (Rajh et al., 2002). We investigated the charge separation by monitoring electron formation in TiO_2 nanoparticles. For this purpose, we constructed an electrochemical cell with a TiDoL working electrode and Pt counter electrode (Figure 1D). We measured the current produced after injection of luciferin and ATP solutions. Immediately after the injection, we observed the rise of the current (Supplementary Figure S4), with the current intensity dependent on ATP and luciferin concentration in a dose-dependent manner (Figure 1E), echoing the dependence of TiDoL photoluminescence on ATP and luciferin concentrations (Figure 1F). The range of ATP concentrations varied from low micro-molar levels (ATP concentration in healthy tissues) to millimolar concentration (ATP concentration in tumor tissues). Once ATP concentration reached the ATP levels found in tumor

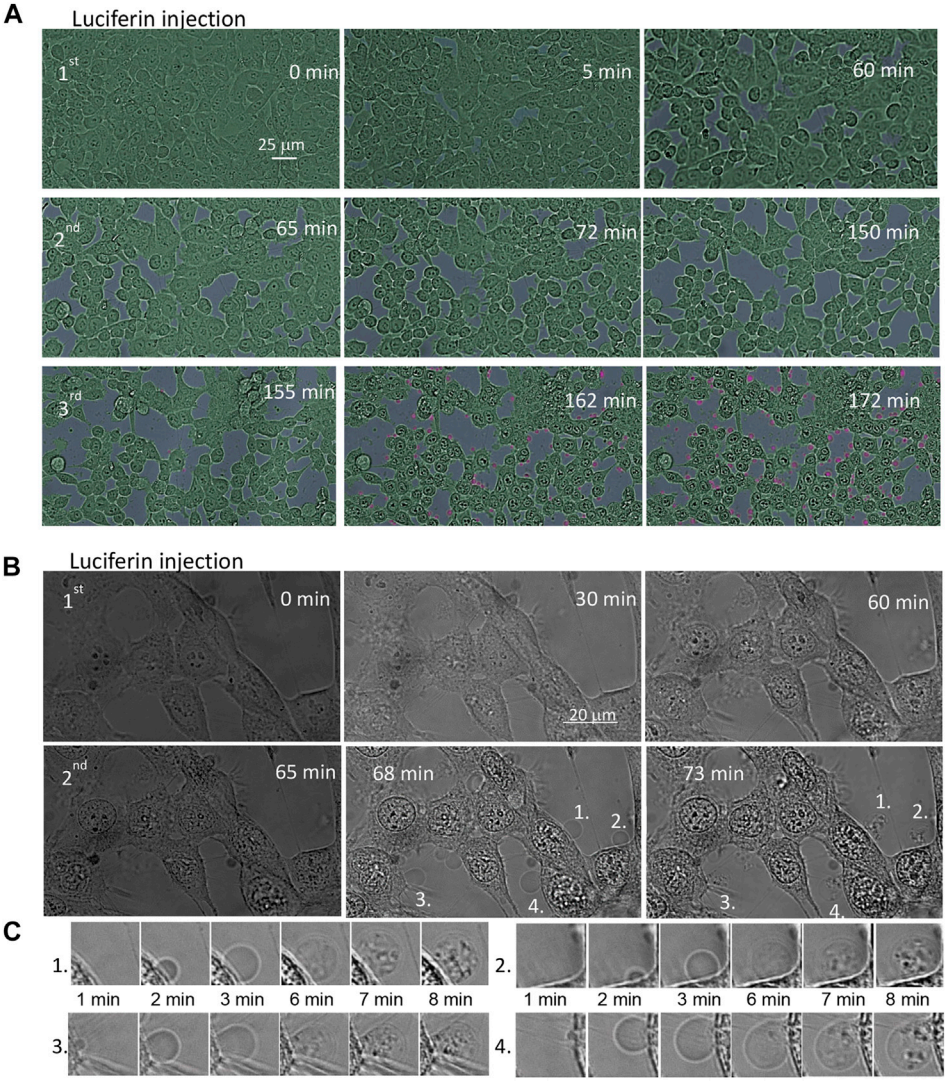


FIGURE 2
Time course of the morphological changes of the HCT116 colon cancer cell line treated with 150 nM TiDoL in the presence of ATP (20 μM). After 20 min of incubation, an aliquot of luciferin (15 μM final concentration) was injected to the well and the response of the cells was monitored using the transmission mode of a confocal microscope. Cells incubated **(A)** in the McCoy culture media (absorption ≤600 nm); three aliquots of luciferin were added (45 μM final concentration) at 60 min intervals to induce cell shrinking (cell interspace shaded in gray) and budding (shaded in pink). Magnification ×40. For clarity, cells were shaded in green and extracellular space in gray. Cells incubated **(B)** in Hanks' Balanced Salt Solution (absorption ≤300 nm); two aliquots of luciferin were sufficient to cause cell budding. Magnification ×126. **(C)** Time course of formation, growth, and transfer of cell material to the apoptotic bodies after the second luciferin injection.

tissues, we observed a significant electric current which was accompanied by a production of superoxide radicals $O_2^{-}\cdot$ that was detected by dihydrorhodamine (DHR) 123 fluorescence (Dimitrijevic et al., 2009). The fluorescence of DHR 123 was suppressed in the presence of a millimolar concentration of p-benzo-quinone (an $O_2^{-}\cdot$ scavenger), confirming that superoxide radicals are the major reactive oxygen species (ROS) formed upon luciferin activation of TiDoL. The concentration of $O_2^{-}\cdot$ was found to be 0.5–5 μM depending on the luciferin and ATP concentration.

3.2 Real-time monitoring of the interaction of TiDoL with HCT116 cells

The dynamic processes of self-illuminating TiDoL nanoparticles within the cell environment *in vitro* were monitored by *in situ* confocal microscopy. This technique is particularly advantageous because it enables the direct correlation of variations in the sample morphology with the sample perturbation (same sample before and after stimuli). Figure 2A and Supplementary Movie S1 show the evolution of

10.3389/fchem.2022.962161

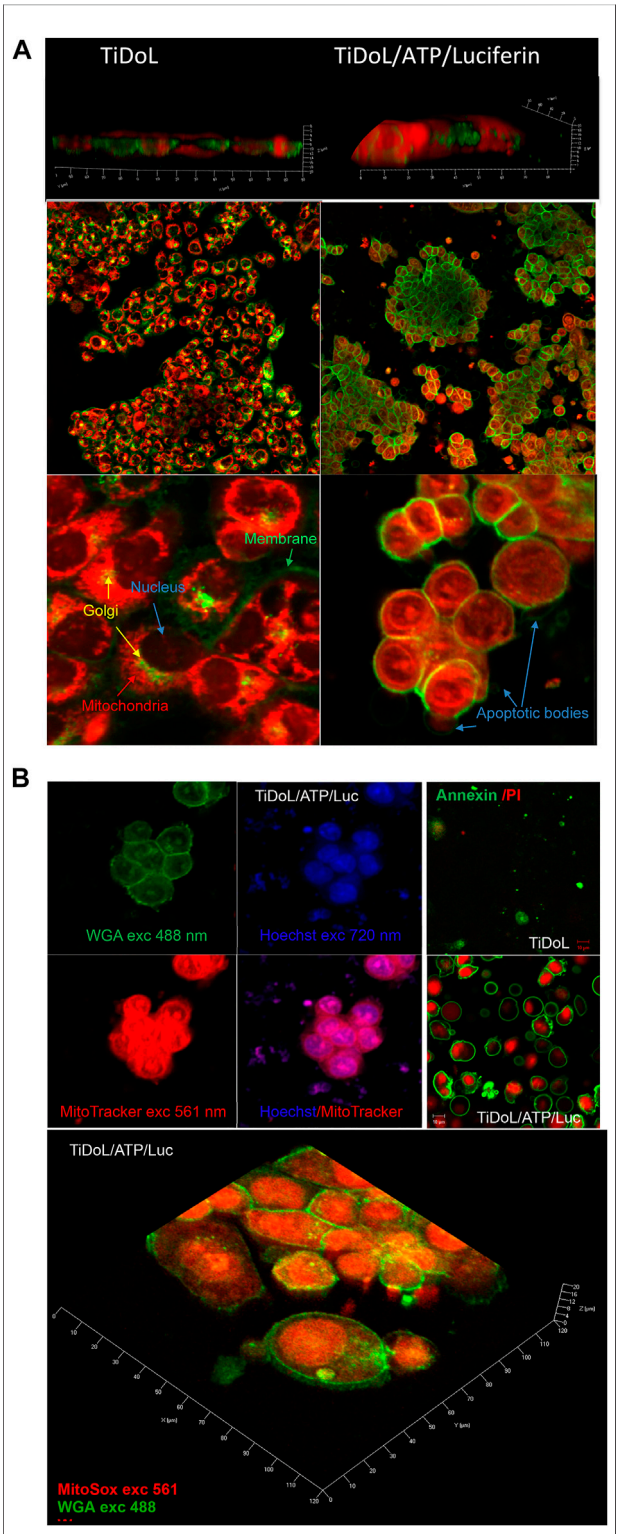


FIGURE 3
(A) Morphological changes in HCT116 cells upon treatment with TiDoL/ATP/luciferin observed staining of the membrane and trans-Golgi with WGA labeled with green Alexa Fluor® 488 and mitochondria staining using MitoTracker Red 12 h after treatment. The left panel depicts viable cells imaged in HBSS after treatment with 150 nM TiDoL, and the right panel depicts cells (*Continued*)

FIGURE 3 (Continued)
treated with 150 nM TiDoL in the presence of 20 μM ATP and two aliquots of 15 μM luciferin added in the intervals of 30 min. Top panels were observed under ×20 magnification, while the bottom panels were observed under ×100 magnification. **(B)** Top left: HCT116 cells after treatment with TiDoL/ATP/luciferin observed by staining the membrane with WGA (green), thiol-containing peptides with MitoTracker (red), and ds DNA with Hoechst 33,342 (blue) 12 h after treatment. Top right: Annexin-FITC and propidium iodide staining before and after treatment with luciferin. Bottom: 3D images of treated cells stained with MitoSox Red for obtaining the distribution of superoxide radicals within treated cells. For comparison, superoxide was below the detection limit in the viable cells.

the cell morphology upon injection of ATP and luciferin to HCT116 colon cancer cells incubated with TiDoL in cell culture media (light absorption $\lambda \leq 600$ nm) at different times after injection of luciferin. Shortly after the first injection (5 min), cell rounding, shrinking, and the appearance of an enlarged intercellular spacing are observed. Cell shrinking continues till it was 85% of the initial surface coverage 50 min after injection (15% intercellular spacing shaded in gray), and after that time, no additional changes were visible. Cell shrinking accompanied by slow detachment from the well support (manifested as a change of the focus plane) is indicative of cell death (Mills et al., 1999). Cells, however, remain with an intact plasma membrane, indicative of the typical morphology of apoptosis. Injection of the second aliquot of luciferin again accelerates changes in cell morphology. Cells shrink further to 60% of their initial surface coverage 85 min after injection of the second dose of luciferin (40% intercellular spacing shaded in gray) and blebbing of the cells is observed throughout the well (Supplementary Movie S1). Despite the decrease in volume, cells remain contained within an intact membrane and are interconnected with stretched actin across large empty intercellular spacing. It is important to note that the addition of supplemental ATP did not induce further changes in cell morphology. Injection of the third aliquot of luciferin rapidly causes even more drastic changes, and after injection, the nuclear membrane starts darkening and nuclear chromatin starts condensing, enhancing the contrast of the image. Concomitantly, cells start forming apoptotic bodies or apoptosomes. The formation of these membrane-enclosed apoptotic bodies is a critical aspect of TiDoL-induced cell death as apoptotic bodies are phagocyted and digested by nearby resident cells (Mills et al., 1999).

This sequence of events was even faster and more clearly observed when cells are exposed to TiDoL/ATP/luciferin in a buffer solution that does not attenuate 560 nm light, suggesting that the energy transfer from luciferase-activated luciferin is a primary mechanism of TiDoL activation (Figure 2B). Subsequent injection of an aliquot of luciferin leads to quick appearance (3 min) of apoptotic bodies, enhanced contrasting of the cell features, and reorganization of the cell chromatin. We observe

packaging of cellular contents into membrane-enclosed apoptotic bodies (Lynch et al., 2017) (Figure 2C). These apoptotic bodies encapsulate the cell material and can be recognized, engulfed, and ingested by macrophages *in vivo,* enabling the clearance of apoptotic cells in the early stage of phagocytosis (Park et al., 2009; Akers et al., 2013). It is important to note that apoptotic processes were not limited to the imaging area. Post-treatment imaging of the cells in the distant areas that were not exposed to imaging light showed the same signs of apoptosis at near 100% efficiency (Supplementary Figure S5), confirming that the radicals formed in the entire sample as a result of the interaction of luciferin and ATP-powered TiDoL are responsible for inducing cell apoptosis.

3.3 *Ex situ* study of the interaction of TiDoL with HCT116 cells using staining

To further understand the process of cell death in colorectal cancerous HCT116 cells *in vitro* induced by the TiDoL/ATP/luciferin system, we investigated their activity *ex situ* using cell staining methods. The HCT116 cells were incubated with TiDoL (or controls with concentrations used for *in situ* measurements, Supplementary Table S2 and Supplementary Figure S6) and activated by two sequential aliquots of luciferin 30 min apart in the CO_2 incubator. Subsequently, live cells were washed and stained using fluorescent wheat germ agglutinin (WGA, labeled with green Alexa Fluor® 488) and MitoTracker® Red. WGA is a lectin that binds glycopeptides, and profuse binding of WGA to the membrane of HCT116 cells demonstrates strong glycosylation of their surface receptors. MitoTracker® is a positively charged dye that labels mitochondria within live cells utilizing their membrane potential.

However, it is chemically reactive, linking to thiol groups in the mitochondria. The dye becomes permanently bound to the thiol-containing proteins in the mitochondria.

Figure 3A shows stained HCT116 cells incubated with TiDoL before (left) and after treatment with luciferin (right). Two images show significant morphological changes after luciferin treatment. All the cells incubated with TiDoL only (left) remain unchanged and have well-defined cytoplasmic membranes (green), Golgi apparatus (yellow), and polarized mitochondria (red). The 3D images also show that cells are spread and adhered to the support (Supplementary Figure S7). After treatment with luciferin, the cells lose their morphological features, shrink laterally, and thicken. However, they still retain strong and intact cytoplasmic membranes (right). The Golgi apparatus disappears, the nuclear membrane becomes permeable, and thiol-containing proteins from mitochondria labeled with MitoTracker become uniformly distributed throughout the cytoplasmic and nuclear regions. There is, however, an indication of the existence of the nuclear membrane of enlarged nuclei (Supplementary Figure S8, faint WGA circle inside the cell membrane outline). Importantly, similar to our findings by *in situ* imaging, new enclosed pressurized membrane vesicles suggestive of apoptotic bodies are also observed, with cells exchanging their content with apoptotic bodies, including thiol-containing peptides and proteins.

Further study of the apoptotic pathway was investigated by imaging the nuclei using Hoechst 33,342 stain, a dye often used to distinguish condensed pyknotic nuclei in apoptotic cells (Manchukonda et al., 2013; Rajh et al., 2014). Figure 3B shows images of the cells by laser excitation using 488 and 561 nm and two-photon excitation using 720 nm light. The image obtained using WGA and MitoTracker depicts the intact membrane and depolarized mitochondria with protein contents throughout both the cytoplasmic and nuclear regions, while two-photon imaging using Hoechst shows pyknotic nuclei, typical of apoptotic cell death. Nuclear chromatin condensation and chromosomal DNA fragmentation are well-described as key features in apoptosis (Manchukonda et al., 2013; Pawłowska et al., 2020). Chromatin condensation is microscopically visible after staining with blue-fluorescent Hoechst 33,342 dye and dense chromatin aggregates typically near the nuclear membrane are observed. Condensed chromatin is the result of a specific DNA fragmentation in the nuclei *via* cleavage by endogenous endonucleases and appears as pyknotic nuclei. The large nuclei and scant cytoplasm observed in two-photon measurements are also indicative of apoptosis (Elmore, 2007). The presence of DNA can also be observed in apoptotic bodies colocalized with thiol-containing proteins outside the cell compartment. MitoSox red staining also indicates enhanced oxidative stress (superoxide was below the detection limit in the viable cells) (Oropesa-Avila et al., 2014). High fluorescence of oxidized MitoSox dye was detected in the nuclear region of TiDoL/luciferin-treated cells and in apoptotic bodies which can be attributed to the higher intensity of the Mitosox red fluorescence when bound to double-stranded DNA rather than to the higher concentrations of superoxide radicals in these cell regions. The detected concentration of $O_2^{-}\cdot$ in these regions was 60% larger than the one in non-treated control cells. Considering that $O_2^{-}\cdot$ steady-state concentrations are estimated to be on the nanomolar level in control cells (Radi, 2018), the $O_2^{-}\cdot$levels in TiDoL-luciferin-treated cells exceed μM levels.

The apoptotic mechanism of cell death was also confirmed using Annexin/propidium iodide apoptosis assay (Figure 3B). Annexin V is a cell protein that binds phosphatidylserines, membrane phospholipids that are held on the inner layer of the cell membrane, and Annexin V does not attach to viable cells. During the early stage of apoptosis, the phosphatidylserines become exposed on the outer layer of the cell membrane, and Annexin V labels phosphatidylserine sites on the membrane surface. At this stage, the cell membrane remains intact and propidium iodide cannot enter to cell interior. At later stages of apoptosis, the membrane becomes somewhat permeable and in addition to annexin binding (green luminescence) propidium

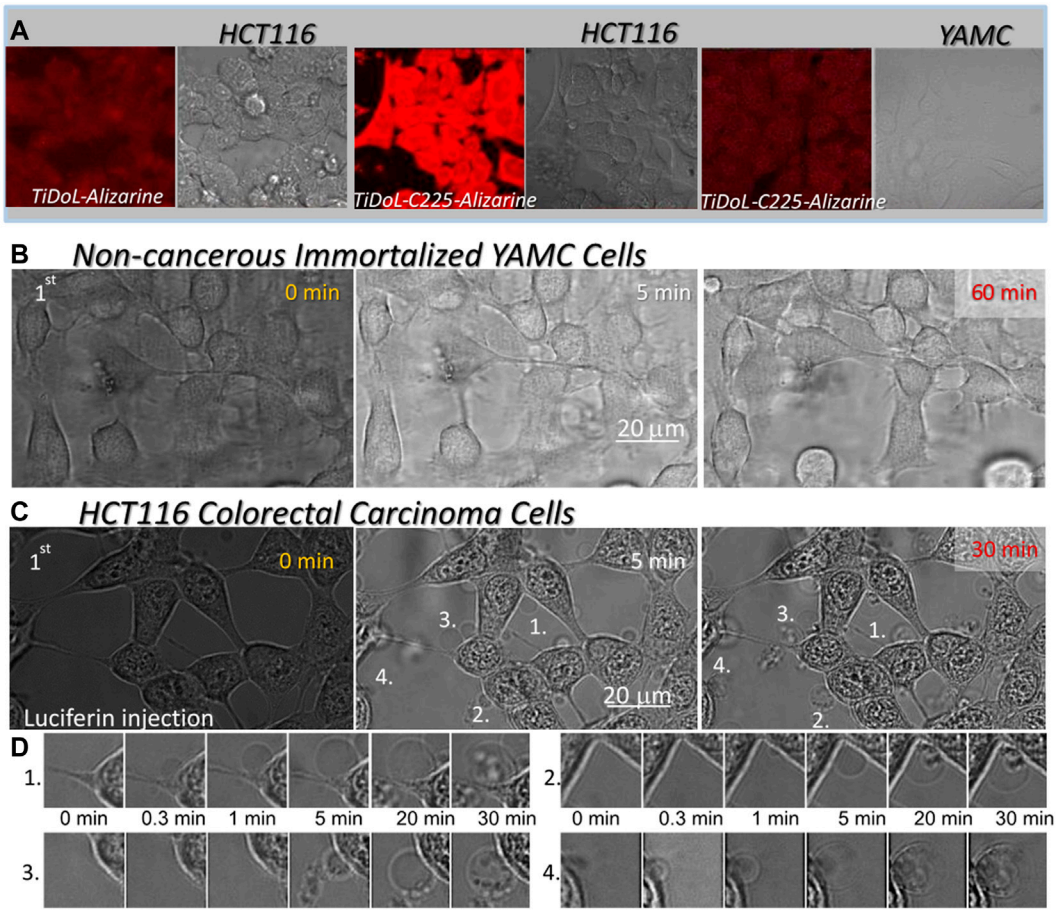


FIGURE 4
(A) Adsorption of nanoconjugates w/o the C225 antibody on HCT116 cells and EGFR(-) immortalized young adult mouse colon (YAMC) cells. Nanocomposites are visualized by imaging fluorescence of alizarin bound to TiO_2 nanoparticles (red) using laser excitation 560 nm and cells (gray) are imaged in the transmission mode. Magnification ×40. **(B)** Time course of the morphological changes of the YAMC colon cell line treated with 150 nM TiDoL-C225. Magnification ×126. **(C)** Time course of the morphological changes of the HCT116 colon cancer cell line treated with 150 nM TiDoL-C225All conditions are the same as in Figure 2B and budding of the cells starts 30 s after first luciferin injections. Magnification ×126. **(D)** Time course of formation, growth, and transfer of cell material to the apoptotic bodies after the first luciferin injection.

iodide penetrates the cell interior and shows red luminescence of the cell interior. In ATP and luciferin-treated cells containing TiDoL, we observe cells in both early and later stages of apoptosis and pressurized apoptotic bodies with phosphatidylserines exposed on their outer membrane surface (green circles). Some of the apoptotic bodies detach from the treated cells and become apo-extracellular vesicles with phosphatidylserines exposed on their outer membrane surface.

Morphological changes confirm the apoptotic pathway of cell death upon ATP initiated *in vitro* treatment of the cancer cells using TiDoL nanoparticles. This is a critical finding, as programmed cell death is characterized by the degradation of cell components within apoptotic cells while their plasma membrane remains intact. It is reported that apoptosis is a physiologically advantageous way of cell death because apoptotic cells can be removed by phagocytosis and digested by nearby resident cells before they lose their outer permeability barrier, thus preventing the induction of inflammatory responses to dying cells and potentially harmful secondary effects (Oropesa-Avila et al., 2014).

3.4 Functionalization of TiDoL with anti-EGFR antibody C225

Selectivity of TiDoL nanoparticles toward cancer cells and their efficiency toward programmed cell death were further enhanced by the functionalization of TiDoL nanoparticles with monoclonal antibody C225 that increases retention of the nanocomposites in tumor regions (Scott et al., 2012). C225

(or Cetuximab®) is a chimeric monoclonal antibody directed against the epidermal growth factor (EGFR) and binds to the extracellular domain of the EGFR. It prevents dimerization of the receptor, resulting in anti-proliferative effects and hinders EGFR-dependent primary tumor growth and metastasis (Liao and Carpenter, 2009). The EGFR is overexpressed on the cell membranes of various solid tumors and is highly expressed on the surface of the HCT116 cell line (EGFR+). C225 have been used successfully as a therapeutic agent in treating metastatic colorectal and head and neck cancers by targeting specific EGFR + cells (Scott et al., 2012). Combining this antibody therapy with photocatalytic nanoparticles can induce correlated activities of photoinduced and antibody therapies of photocatalytic nanoparticles, enhancing the rate and efficiency of targeted therapy (Xu et al., 2007; Rozhkova et al., 2009; Elvira et al., 2012). To visualize antibody-facilitated adsorption (retention) of TiDoL-C225 composites within the cells that express EGFR, we modified nanoconjugates with alizarin, an enediol dye that changes the absorption and fluorescence of TiO2 nanoparticles (Supplementary Figure S1) (Rajh et al., 2002). Figure 4A clearly shows enhanced retention of TiDoL-C225 nanocomposites on the surface of EGFR + colorectal cancerous HCT116 cells (center) while their retention (adsorption) in conditionally immortalized young adult mouse colonocyte (YAMC) cells that do not express EGFR (EGFR(−)) is negligible under the same conditions (right). Likewise, retention of TiDoL nanoconjugates in the absence of the C225 antibody on HC116 cells (EGFR(+)) was negligible as shown by the faint red fluorescence of alizarin-TiDoL (left). Similar poor adherence of TiDoL-C225 was observed for EGFR(−) non-transformed fibroblast CT26 cells (Supplementary Figure S11). These results suggest weak retention and poor activation of TiDoL-C225 within the healthy tissue compared to the one when TiDoL-C225 is integrated with cancerous EGFR(+) cells. Indeed, Figure 4B shows the time sequence of morphological changes associated with the activation of TiDoL-C225 within immortalized YAMC cells (EGFR(−)) that show minor changes even 60 min after activation with luciferin. The composite does not induce morphological changes in YAMC cells even after 3 doses of luciferin. Similar results were obtained for CT26 EGFR-non-transformed fibroblast cells (Supplementary Figures S10).

Indeed, the activation of TiDoL-C225 within HCT116 cells (EGFR+) resulted in the rapid development of the signs of the final stages of apoptotic death (Figure 4C; Supplementary Movie S2). Cell budding was accompanied by darkening of the nuclear membrane and enhancement of the image contrast as a result of chromatin rearrangement. Due to this rapid budding, the cells do not have time to go through the significant shrinking phase; however, they still show strong and intact cytoplasmic membranes that extend to apoptotic bodies (Figure 4D). Cells start to transfer their content to the apoptotic bodies much later compared to the same process in treatment with TiDoL conjugate in the absence of C225 (Figure 2C). Importantly, TiDoL-C225 nanocomposites induced cell death at a concentration as low as 5 nM (0.5 μg/ml TiO_2) compared to 20 nM TiDoL under the same conditions. Antibodies provide specificity to the nanoparticles, increasing their retention within targeted cells that express cognate antigens on the membrane surface. Hence, composites are activated in close proximity to biological targets of interest, enhancing the efficiency of nanocomposites during therapy.

3.5 *In vivo* study of the interaction of TiDoL and TiDoL-C225 with tumors

To demonstrate the applicability of our approach *in vivo,* we administrated a single dose of 50 μl TiDoL (6 μM), TiDoL-C225 (4 μM), and appropriate controls into nude mice bearing the aggressive HCT116 xenograft tumor model. Luciferin was administrated intraperitoneally, one dose 1 h and the other 48 h after TiDoL treatment. We observed significant differences in cancer growth between the tumors with and without luciferin administration in TiDoL-treated nude mice (Figure 5). While those tumors that did not receive luciferin continued exponential growth (Elmouelhi et al., 2008), the progress of luciferin-treated tumors slows down, and 26 days after the treatment, becomes three times smaller on average compared to those that did not receive luciferin. Each point shown in Figure 5A, left is an average of six tumor measurements, and their statistical significance was determined using Student's *t*-test. For the data obtained for the 26th day after TiDoL injection, statistical significance was $p = 0.0068$. Cell growth of all tumors was fitted with a polynomial (parabolic) function and it was found that cell growth in control tumors is dominated by a fast quadratic term, while those administered with luciferin and nanoconjugates show slow linear growth. These findings suggest that upon activation of TiDoL in the tumors with luciferin, a process that competes with cell growth is initiated, limiting the exponential proliferation rate of the tumor.

Administration of targeted TiDoL nanoconjugates modified with the C225 antibody also resulted in limiting the growth of the tumor when treated with luciferin. It was observed that 26 days after treatment, the tumors show three times smaller size on average compared to those treated with antibody C225 only. Each point shown in Figure 5B is an average of six tumor measurements and their statistical significance for data obtained 26 days after injection was $p = 0.0083$. The treatment of the tumor with TiDoL-C225 nanoconjugates only, without administration of luciferin, also slows down the growth rate of the tumor on average in agreement with a previously observed enhanced toxicity of

10.3389/fchem.2022.962161

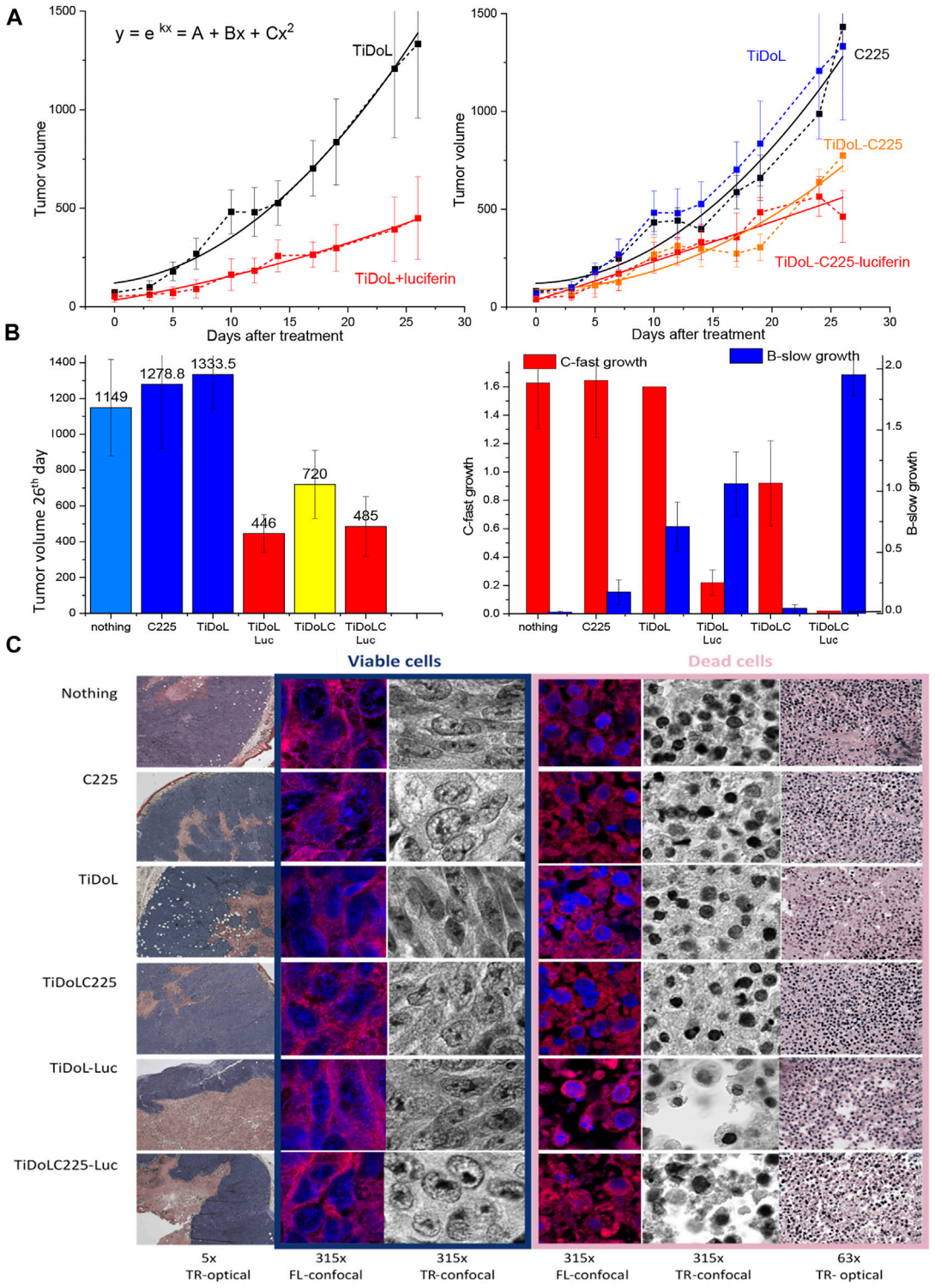


FIGURE 5
In vivo study of tumor growth in nude mice (HCT116 xenografts). **(A)** Evolution of tumors treated with TiDoL (left) and TiDoLC225 (right) w/o activation with luciferin. Each point is an average of six measurements. Statistical significance was determined using Student's *t*-test as $p < 0.0068$ for TiDoL and $p < 0.0083$ for TiDoL-C225. Data are fitted with quadratic polynomial dependence as an approximation of exponential growth. **(B)** Color-coded histogram of tumor sizes 26 days after the treatment of nude mice in conjunction with the histogram of the linear (blue) and quadratic (red) coefficient of tumor growth obtained from data fitting. **(C)** Transmission optical (TR-optical) and laser confocal fluorescence (FL-confocal) and optical (TR-confocal) images of H&E-stained tumor slices obtained by sectioning the tumors 26 days after the treatment at different magnifications.

C225 when conjugated to nanoparticles (Qian et al., 2014). However, the addition of luciferin further slows down the growth rate mechanism fostering linear growth of tumors, and luciferin-treated tumors grow to 30% of the size measured in the controls (Figure 5A, right). Histologic analysis of non-activated control H&E-stained tumors 26 days after the treatment shows that tumors have large areas of growing viable cells and smaller necrosis areas confined to the center of the tumor (Figure 5C), typically attributed to fast-growing tumors outgrowing their blood supply (Lotze and Demarco, 2004). H&E-stained tumors treated by TiDoL and TiDoL-C225 activated with luciferin, however, show large dead cells and denuded areas. Large, denuded areas in TiDoL-C225/luciferin-activated tumors suggest macrophage-assisted clearance of dead cells. These areas are surrounded by a thin belt of viable growing cancerous cells. High magnification (×315) shows faint hematoxylin-stained DNA/RNA in growing cells distributed throughout the nuclei and condensed in a highly stained nucleolus. Dead tumor areas, however, show much smaller pyknotic nuclei in condensed cells. These cells exhibit large denuded areas that in the case of TiDoL-treated tumors are very clean, while in TiDoL-C225-treated tumors show residual debris adjacent to denuded tumor areas. Some of the debris contains DNA/RNA, while others contain mainly proteins stained by eosin. These results suggest that while large tumors in the control group continue to grow, the tumors treated and activated with luciferin show reduced tumor size with cancer cell removal competing with new tumor growth, suggesting the need for tuning of nanoconjugate pharmacology for obtaining optimal efficiency.

4 Conclusion

To summarize, we have developed a composite that takes advantage of the high ATP levels in a tumor microenvironment and uses photodynamic therapy for cancer treatment without using an external light source. The self-illuminating nanoparticle technology enhances existing antibody platforms to an on-demand targeted therapy confined to the regions of tumor activity. The employment of ATP-powered self-illuminating nanoparticles provides a new universal approach that uses the product of disease to target diseased tissues solely. We show that, although not optimized pharmacologically, this technology kills close to 100% of cancerous cells *in vitro* and shows a significant decrease in the tumor size *in vivo* to 30% of their original size in experimental colon cancer models. Herein, we deployed this technology against a colon cancer cell line; however, our additional work shows that the same approach is valid for a very different A172 glioblastoma brain tumor cell line when an anti-IL13 was used as an anchoring antibody instead of C225. This method minimizes the probability of the off-target release of radical species in a double lock-in approach (Augulis and Zigmantas, 2011) and enhances the potency of cell-locked *in situ* nanoparticle delivery of reactive species produced in close proximity to biological targets.

Data availability statement

The original contributions presented in the study are included in the article/Supplementary Material; further inquiries can be directed to the corresponding author.

Ethics statement

The studies involving animals were reviewed and approved by the University of Chicago Institutional Animal Care and Use Committee.

Author contributions

TR prepared and characterized nanoconjugates. BB performed luciferin/luciferase quenching and electrochemical measurements. TK and SR prepared cell cultures and performed cell staining. TR, TK, and SR performed *in vitro* real-time and *ex situ* measurements. VK and MB performed measurements *in vivo*. TR directed the research and performed data analysis.

Funding

Use of the Center for Nanoscale Materials, Office of Science user facility, was supported by the U.S. Department of Energy, Office of Science, Office of Basic Energy Sciences, under contract No. DE-AC02-06CH11357. This work is supported by Laboratory Directed Research and Development (LDRD) funding from Argonne National Laboratory, provided by the Director, Office of Science, of the U.S. Department of Energy under Contract No. DE-AC02-06CH11357.

Acknowledgments

The authors want to thank Harry Christopher Fry for providing luciferase electrostatic distribution images, Chunxing She for performing decay kinetics measurements and Matthew Massich for obtaining measurements on A172 glioblastoma cells.

Conflict of interest

The authors declare that the research was conducted in the absence of any commercial or financial relationships that could be construed as a potential conflict of interest.

Publisher's note

All claims expressed in this article are solely those of the authors and do not necessarily represent those of their affiliated organizations, or those of the publisher, the editors, and the reviewers. Any product that may be evaluated in this article, or claim that may be made by its manufacturer, is not guaranteed or endorsed by the publisher.

Supplementary material

The Supplementary Material for this article can be found online at: https://www.frontiersin.org/articles/10.3389/fchem.2022.962161/full#supplementary-material

SUPPLEMENTARY MOVIE S1
TiDoL within HCT116 cell culture.

SUPPLEMENTARY MOVIE S2
TiDoLC225 within HCT116 cell culture.

SUPPLEMENTARY VIDEO S1
Self-illuminating TiDoL nanocomposites within HCT116 colorectal carcinoma cells. Video spanning 30 min before and 180 min after activation of TiDoL with luciferin (three aliquots) injected into the TiDoL–McCoy media solution, depicting morphological changes of HCT116 cells upon activation of TiDoL. Morphological changes were recorded 60 min after each luciferin injection, one frame every 20 s. Cell shrinking, detachment from the support, and cell blebbing are observed after the first luciferin injection. Injection of the second aliquot of luciferin again accelerates changes in cell morphology. Cells shrink to 60% of their initial surface coverage 85 min after injection of the second dose of luciferin. Blebbing of the cells is observed throughout the well (Supplementary Video S1). Despite the decrease in the cell volume, cells remain contained within an intact membrane and are interconnected with stretched actin across large empty intercellular spacing. The movie also shows that the addition of supplemental ATP did not induce further changes in the cell morphology. Injection of the third aliquot rapidly causes even more drastic changes, and 7 min after injection, cells start forming apoptotic bodies with concomitant reorganization and condensing of nuclear chromatin, enhancing the contrast of the image. Magnification ×40. The last section of the video depicts magnified cell budding (×126) of the cells in HBSS after the second luciferin injection.

SUPPLEMENTARY VIDEO S2
Self-illuminating TiDoL linked to Cetuximab (TiDoL-C225) within colorectal carcinoma HCT116 cells and conditionally immortalized young adult mouse coloncytes (YAMC). HCT116: Video spanning 30 min before and 180 min after activation of TiDoL-C225 with luciferin (three aliquots) injected into the TiDoL-C225-HBSS solution, depicting morphological changes of HCT116 cells upon activation of TiDoL-C225 immobilized on the cell surface (Figure 4C). Morphological changes were recorded 60 min after each luciferin injection, one frame every 20 s. As soon as 20 s after luciferin injection, the cells show the final stages of apoptotic death. Cell budding is accompanied by the darkening of the nuclear membrane and enhancement of the image contrast as a result of chromatin rearrangement. Due to this rapid budding, the cells do not have time to go through the significant shrinking phase; however, they still show strong and intact cytoplasmic membranes that extend to apoptotic bodies. Cells start transferring their content into the apoptotic bodies 20 min after cell budding, which is a much longer timeframe compared to the same process in treatment with TiDoL conjugate in the absence of C225 (that occurred 5 min after cell budding, Supplementary Video S1). This difference indicates the decoupling of signaling cascades involved in the budding and transferring of cell material to the apoptotic bodies. Magnification ×126. YAMC: Video spanning 30 min before and 180 min after activation of TiDoL-C225 with luciferin (three aliquots) injected into the TiDoL-C225-HBSS solution, depicting morphological changes of YAMC cells upon activation of TiDoL-C225. TiDoL-C225 is only nonspecifically weakly adsorbed on the YAMC cell surface (Figure 4B) as they do not express EGFR. Morphological changes were recorded 60 min after each luciferin injection, one frame every 20 s. No significant changes were observed upon all three luciferin injections. Magnification ×126.

References

Akers, J. C., Gonda, D., Kim, R., Carter, B. S., and Chen, C. C. (2013). Biogenesis of extracellular vesicles (EV): Exosomes, microvesicles, retrovirus-like vesicles, and apoptotic bodies. *J. Neurooncol.* 113 (1), 1–11. doi:10.1007/s11060-013-1084-8

Allen, R. D., Schroeder, C. C., and Fok, A. K. (1989). Intracellular binding of wheat-germ agglutinin by Golgi complexes, phagosomes, and lysosomes of paramecium-multimicronucleatum. *J. Histochem. Cytochem.* 37 (2), 195–202. doi:10.1177/37.2.2911005

Allen, T. M., and Cullis, P. R. (2004). Drug delivery systems: Entering the mainstream. *Science* 303 (5665), 1818–1822. doi:10.1126/science.1095833

Augulis, R., and Zigmantas, D. (2011). Two-dimensional electronic spectroscopy with double modulation lock-in detection: Enhancement of sensitivity and noise resistance. *Opt. Express* 19 (14), 13126–13133. doi:10.1364/oe.19.013126

Briolay, T., Petithomme, T., Fouet, M., Nguyen-Pham, N., Blanquart, C., and Boisgerault, N. (2021). Delivery of cancer therapies by synthetic and bio-inspired nanovectors. *Mol. Cancer* 20 (1), 55. doi:10.1186/s12943-021-01346-2

Chauhan, D., Li, G. L., Sattler, M., Podar, K., Mitsiades, C., Mitsiades, N., et al. (2003). Superoxide-dependent and -independent mitochondrial signaling during apoptosis in multiple myeloma cells. *Oncogene* 22 (40), 6296–6300. doi:10.1038/sj.onc.1206734

Chazotte, B. (2011). Labeling membrane glycoproteins or glycolipids with fluorescent wheat germ agglutinin. *Cold Spring Harb. Protoc.* 2011 (5), pdb.prot5623. doi:10.1101/pdb.prot5623)

Dimitrijevic, N. M., Rozhkova, E., and Rajh, T. (2009). Dynamics of localized charges in dopamine-modified TiO2 and their effect on the formation of reactive oxygen species. *J. Am. Chem. Soc.* 131 (8), 2893–2899. doi:10.1021/ja807654k

Elmore, S. (2007). Apoptosis: A review of programmed cell death. *Toxicol. Pathol.* 35 (4), 495–516. doi:10.1080/01926230701320337

Elmouelhi, N., and Yarema, K. J. (2008). "Building on what nature gave us: Engineering cell glycosylation pathway," in *Biotechnology and bioengineering*. Editor W. G. Flynne (Hauppauge, NY: Nova Science Publishers Inc.), 37–74.

Elvira, G., Moreno, B., del Valle, I., Garcia-Sanz, J. A., Canillas, M., Chinarro, E., et al. (2012). Targeting neural stem cells with Titanium Dioxide nanoparticles coupled to specific monoclonal antibodies. *J. Biomater. Appl.* 26 (8), 1069–1089. doi:10.1177/0885328210393294

Endres, P. J., Paunesku, T., Vogt, S., Meade, T. J., and Woloschak, G. E. (2007). DNA-TiO2 nanoconjugates labeled with magnetic resonance contrast agents. *J. Am. Chem. Soc.* 129 (51), 15760–15761. doi:10.1021/ja0772389

Han, H. S., and Choi, K. Y. (2021). Advances in nanomaterial-mediated photothermal cancer therapies: Toward clinical applications. *Biomedicines* 9 (3), 305. doi:10.3390/biomedicines9030305

Jan, M., Sperling, A. S., and Ebert, B. L. (2021). Cancer therapies based on targeted protein degradation — Lessons learned with lenalidomide. *Nat. Rev. Clin. Oncol.* 18 (7), 401–417. doi:10.1038/s41571-021-00479-z

Kim, J.-W., and Dang, C. V. (2006). Cancer's molecular sweet tooth and the Warburg effect. *Cancer Res.* 66 (18), 8927–8930. doi:10.1158/0008-5472.can-06-1501

Kim, Y. R., Kim, S., Choi, J. W., Choi, S. Y., Lee, S.-H., Kim, H., et al. (2015). Bioluminescence-activated deep-tissue photodynamic therapy of cancer. *Theranostics* 5 (8), 805–817. doi:10.7150/thno.11520

LaVan, D. A., McGuire, T., and Langer, R. (2003). Small-scale systems for *in vivo* drug delivery. *Nat. Biotechnol.* 21 (10), 1184–1191. doi:10.1038/nbt876

Lei, Q., Wang, S.-B., Hu, J.-J., Lin, Y.-X., Zhu, C.-H., Rong, L., et al. (2017). Stimuli-Responsive "cluster bomb" for programmed tumor therapy. *ACS Nano* 11 (7), 7201–7214. doi:10.1021/acsnano.7b03088

Li, C. (2014). A targeted approach to cancer imaging and therapy. *Nat. Mat.* 13 (2), 110–115. doi:10.1038/nmat3877

Liao, H. J., and Carpenter, G. (2009). Cetuximab/C225-induced intracellular trafficking of epidermal growth factor receptor. *Cancer Res.* 69 (15), 6179–6183. doi:10.1158/0008-5472.can-09-0049

Liu, J., Saponjic, Z., Dimitrijevic, N. M., Luo, S., Preuss, D., and Rajh, T. (2006). "Hybrid TiO(2) nanoparticles: An approach for developing site specific DNA cleavage," in *Colloidal quantum dots for biomedical applications*. Editors M. Osinski, K. Yamamoto, and T. M. Jovin (Bellingham, WA: SPIE), 6096.

Lotze, M. T., and Demarco, R. A. (2004). Dying dangerously: Necrotic cell death and chronic inflammation promote tumor growth. *Discov. Med.* 4 (24), 448–456.

Lynch, C., Panagopoulou, M., and Gregory, C. D. (2017). Extracellular vesicles arising from apoptotic cells in tumors: Roles in cancer pathogenesis and potential clinical applications. *Front. Immunol.* 8, 1174. doi:10.3389/fimmu.2017.01174

Manchukonda, N. K., Naik, P. K., Santoshi, S., Lopus, M., Joseph, S., Sridhar, B., et al. (2013). Rational design, Synthesis, and biological evaluation of third generation α-noscapine analogues as potent tubulin binding anti-cancer agents. *Plos One* 8 (10), e77970. doi:10.1371/journal.pone.0077970

Maurer-Spurej, E., Wong, K. F., Maurer, N., Fenske, D. B., and Cullis, P. R. (1999). Factors influencing uptake and retention of amino-containing drugs in large unilamellar vesicles exhibiting transmembrane pH gradients. *Biochimica Biophysica Acta - Biomembr.* 1416 (1-2), 1–10. doi:10.1016/s0005-2736(98)00204-1

Mikkelsen, R. B., and Wardman, P. (2003). Biological chemistry of reactive oxygen and nitrogen and radiation-induced signal transduction mechanisms. *Oncogene* 22 (37), 5734–5754. doi:10.1038/sj.onc.1206663

Mills, J. C., Stone, N. L., and Pittman, R. N. (1999). Extranuclear apoptosis: The role of the cytoplasm in the execution phase. *J. Cell Biol.* 146 (4), 703–708. doi:10.1083/jcb.146.4.703

Mura, S., Nicolas, J., and Couvreur, P. (2013). Stimuli-responsive nanocarriers for drug delivery. *Nat. Mat.* 12 (11), 991–1003. doi:10.1038/nmat3776

Nagano, K., Shinkawa, T., Kato, K., Inomata, N., Yabuki, N., and Haramura, M. (2011). Distinct cell surface proteome profiling by biotin labeling and glycoprotein capturing. *J. Proteomics* 74 (10), 1985–1993. doi:10.1016/j.jprot.2011.05.019

O'Brien, C. A., Pollett, A., Gallinger, S., and Dick, J. E. (2007). A human colon cancer cell capable of initiating tumour growth in immunodeficient mice. *Nature* 445 (7123), 106–110. doi:10.1038/nature05372

Oberdanner, C. B., Kiesslich, T., Krammer, B., and Plaetzer, K. (2002). Glucose is required to maintain high ATP-levels for the energy-utilizing steps during PDT-induced apoptosis. *Photochem. Photobiol.* 76 (6), 695–703. doi:10.1562/0031-8655(2002)0760695girtmh2.0.co2

Oropesa-Avila, M., Andrade-Talavera, Y., Garrido-Maraver, J., Cordero, M. D., de la Mata, M., Cotan, D., et al. (2014). Stabilization of apoptotic cells: Generation of zombie cells. *Cell Death Dis.* 5, e1369. doi:10.1038/cddis.2014.332

Panus, P. C., Radi, R., Chumley, P. H., Lillard, R. H., and Freeman, B. A. (1993). Detection of H2O2 release from vascular endothelial cells. *Free Radic. Biol. Med.* 14 (2), 217–223. doi:10.1016/0891-5849(93)90013-k

Park, S.-Y., Jung, M.-Y., Lee, S.-J., Kang, K.-B., Gratchev, A., Riabov, V., et al. (2009). Stabilin-1 mediates phosphatidylserine-dependent clearance of cell corpses in alternatively activated macrophages. *J. Cell Sci.* 122 (18), 3365–3373. doi:10.1242/jcs.049569

Paunesku, T., Rajh, T., Wiederrecht, G., Maser, J., Vogt, S., Stojicevic, N., et al. (2003). Biology of TiO2-oligonucleotide nanocomposites. *Nat. Mat.* 2 (5), 343–346. doi:10.1038/nmat875

Pawłowska, M., Kwaśniewska, A., Mazerska, Z., and Augustin, E. (2020). Enhanced activity of P4503A4 and UGT1A10 induced by acridinone derivatives C-1305 and C-1311 in MCF-7 and HCT116 cancer cells: Consequences for the drugs' cytotoxicity, metabolism and cellular response. *Int. J. Mol. Sci.* 21 (11), 3954. doi:10.3390/ijms21113954

Pelicano, H., Martin, D. S., Xu, R. H., and Huang, P. (2006). Glycolysis inhibition for anticancer treatment. *Oncogene* 25 (34), 4633–4646. doi:10.1038/sj.onc.1209597

Pellegatti, P., Raffaghello, L., Bianchi, G., Piccardi, F., Pistoia, V., and Di Virgilio, F. (2008). Increased level of extracellular ATP at tumor sites: *In vivo* imaging with plasma membrane luciferase. *Plos One* 3 (7), e2599. doi:10.1371/journal.pone.0002599

Petros, R. A., and DeSimone, J. M. (2010). Strategies in the design of nanoparticles for therapeutic applications. *Nat. Rev. Drug Discov.* 9 (8), 615–627. doi:10.1038/nrd2591

Qian, Y., Qiu, M., Wu, Q., Tian, Y., Zhang, Y., Gu, N., et al. (2014). Enhanced cytotoxic activity of cetuximab in EGFR-positive lung cancer by conjugating with gold nanoparticles. *Sci. Rep.* 4 (1), 7490. doi:10.1038/srep07490

Radi, R. (2018). Oxygen radicals, nitric oxide, and peroxynitrite: Redox pathways in molecular medicine. *Proc. Natl. Acad. Sci. U. S. A.* 115 (23), 5839–5848. doi:10.1073/pnas.1804932115

Rajh, T., Chen, L. X., Lukas, K., Liu, T., Thurnauer, M. C., and Tiede, D. M. (2002). Surface restructuring of nanoparticles: An efficient route for ligand-metal oxide crosstalk. *J. Phys. Chem. B* 106 (41), 10543–10552. doi:10.1021/jp021235v

Rajh, T., Saponjic, Z., Liu, J., Dimitrijevic, N. M., Scherer, N. F., Vega-Arroyo, M., et al. (2004). Charge Transfer Across the Nanocrystalline-DNA Interface: Probing DNA Recognition. *Nano Lett.* 4 (6), 1017–1023. doi:10.1021/nl049684p

Rajh, T., Dimitrijevic, N. M., Bissonnette, M., Koritarov, T., and Konda, V. (2014). Titanium Dioxide in the service of the biomedical revolution. *Chem. Rev.* 114 (19), 10177–10216. doi:10.1021/cr500029g

Rajh, T., Nedeljkovic, J. M., Chen, L. X., Poluektov, O., and Thurnauer, M. C. (1999). Improving optical and charge separation properties of nanocrystalline TiO2 by surface modification with vitamin C. *J. Phys. Chem. B* 103 (18), 3515–3519. doi:10.1021/jp9901904

Rajh, T., Ostafin, A. E., Micic, O. I., Tiede, D. M., and Thurnauer, M. C. (1996). Surface modification of small particle TiO2 colloids with cysteine for enhanced photochemical reduction: An EPR study. *J. Phys. Chem.* 100 (11), 4538–4545. doi:10.1021/jp952002p

Rego, L. G. C., and Batista, V. S. (2003). Quantum dynamics simulations of interfacial electron transfer in sensitized TiO2 semiconductors. *J. Am. Chem. Soc.* 125 (26), 7989–7997. doi:10.1021/ja0346330

Rozhkova, E. A., Ulasov, I., Lai, B., Dimitrijevic, N. M., Lesniak, M. S., and Rajh, T. (2009). A high-performance nanobio photocatalyst for targeted brain cancer therapy. *Nano Lett.* 9 (9), 3337–3342. doi:10.1021/nl901610f

Schmidt, C. K., Medina-Sánchez, M., Edmondson, R. J., and Schmidt, O. G. (2020). Engineering microrobots for targeted cancer therapies from a medical perspective. *Nat. Commun.* 11 (1), 5618. doi:10.1038/s41467-020-19322-7

Scott, A. M., Wolchok, J. D., and Old, L. J. (2012). Antibody therapy of cancer. *Nat. Rev. Cancer* 12 (4), 278–287. doi:10.1038/nrc3236

Stagg, J., and Smyth, M. J. (2010). Extracellular adenosine triphosphate and adenosine in cancer. *Oncogene* 29 (39), 5346–5358. doi:10.1038/onc.2010.292

Tachan, Z., Hod, I., and Zaban, A. (2014). The TiO2-catechol complex: Coupling type II sensitization with efficient catalysis of water oxidation. *Adv. Energy Mat.* 4 (6), 1301249. doi:10.1002/aenm.201301249

Tomlinson, J., Wang, J. L., Barsky, S. H., Lee, M. C., Bischoff, J., and Nguyen, M. (2000). Human colon cancer cells express multiple glycoprotein ligands for E-selectin. *Int. J. Oncol.* 16 (2), 347–353. doi:10.3892/ijo.16.2.347

Vultaggio-Poma, V., Sarti, A. C., and Di Virgilio, F. (2020). Extracellular ATP: A feasible target for cancer therapy. *Cells* 9 (11), 2496. doi:10.3390/cells9112496

Wang, W., Yang, Y., Wang, S., Nagaraj, V. J., Liu, Q., Wu, J., et al. (2012). Label-free measuring and mapping of binding kinetics of membrane proteins in single living cells. *Nat. Chem.* 4 (10), 846–853. doi:10.1038/nchem.1434

Xu, J., Sun, Y., Huang, J., Chen, C., Liu, G., Jiang, Y., et al. (2007). Photokilling cancer cells using highly cell-specific antibody-TiO2 bioconjugates and electroporation. *Bioelectrochemistry* 71 (2), 217–222. doi:10.1016/j.bioelechem.2007.06.001

Yang, G. B., Xu, L. G., Xu, J., Zhang, R., Song, G. S., Chao, Y., et al. (2018). Smart nanoreactors for pH-responsive tumor homing, mitochondria-targeting, and enhanced photodynamic-immunotherapy of cancer. *Nano Lett.* 18 (4), 2475–2484. doi:10.1021/acs.nanolett.8b00040

frontiers | Frontiers in Chemistry

TYPE Mini Review
PUBLISHED 20 September 2022
DOI 10.3389/fchem.2022.1012443

Check for updates

OPEN ACCESS

EDITED BY
Gabriela Oksdath-Mansilla,
Universidad Nacional de Córdoba,
Argentina

REVIEWED BY
Miguel Angel Aleman Garcia,
Eindhoven University of Technology,
Netherlands
Lydia Maria Bouchet,
Consejo Nacional de Investigaciones
Científicas y Técnicas (CONICET),
Argentina

*CORRESPONDENCE
Julieta I. Paez,
j.i.paez@utwente.nl

†These authors have contributed equally to this work and share first authorship

SPECIALTY SECTION
This article was submitted to Organic Chemistry,
a section of the journal
Frontiers in Chemistry

RECEIVED 05 August 2022
ACCEPTED 30 August 2022
PUBLISHED 20 September 2022

CITATION
Wolfel A, Jin M and Paez JI (2022), Current strategies for ligand bioconjugation to poly(acrylamide) gels for 2D cell culture: Balancing chemo-selectivity, biofunctionality, and user-friendliness.
Front. Chem. 10:1012443.
doi: 10.3389/fchem.2022.1012443

COPYRIGHT
© 2022 Wolfel, Jin and Paez. This is an open-access article distributed under the terms of the Creative Commons Attribution License (CC BY). The use, distribution or reproduction in other forums is permitted, provided the original author(s) and the copyright owner(s) are credited and that the original publication in this journal is cited, in accordance with accepted academic practice. No use, distribution or reproduction is permitted which does not comply with these terms.

Current strategies for ligand bioconjugation to poly(acrylamide) gels for 2D cell culture: Balancing chemo-selectivity, biofunctionality, and user-friendliness

Alexis Wolfel†, Minye Jin† and Julieta I. Paez*

Developmental Bioengineering, University of Twente, Enschede, Netherlands

Hydrogel biomaterials in combination with living cells are applied in cell biology, tissue engineering and regenerative medicine. In particular, poly(acrylamide) (PAM) hydrogels are frequently used in cell biology laboratories as soft substrates for 2D cell culture. These biomaterials present advantages such as the straightforward synthesis, regulable mechanical properties within physiological range of native soft tissues, the possibility to be biofunctionalized with ligands to support the culture of living cells, and their optical transparency that makes them compatible with microscopy methods. Due to the chemical inertness and protein repellant properties of PAM hydrogels, these materials alone do not support the adhesion of cells. Therefore, biofunctionalization of PAM gels is necessary to confer them bioactivity and to promote cell-material interactions. Herein, the current chemical strategies for the bioconjugation of ligands to PAM gels are reviewed. Different aspects of the existing bioconjugation methods such as chemo-selectivity and site-specificity of attachment, preservation of ligand's functionality after binding, user-friendliness and cost are presented and compared. This work aims at guiding users in the choice of a strategy to biofunctionalize PAM gels with desired biochemical properties.

Abbreviations: AA, Acrylic acid; AM, acrylamide; bis-AA, *N,N′*-methylenebisacrylamide; ECM, extracellular matrix; EDC, 1-ethyl-3-(3-dimethylaminopropyl)carbodiimide; FRP, free radical polymerization; HEA, hydroxyethyl acrylate; hMSCs, human mesenchymal stem cells; HUVECs, human umbilical vein endothelial cells; Ile-Lys-Val-Ala-Val (IKVAV), laminin-mimetic peptide; MS, methylsulfonyl; NHS, *N*-hydroxysuccinimide; NHS-AE, acrylic acid N-hydroxysuccinimide ester; PAM, poly(acrylamide); PBS, phosphate-buffered saline; PEMA, poly(ethylene-*alt*-maleic anhydride); Arg-Gly-Asp (RGD), cell-adhesive peptide; r.t., room temperature; *N*-hydroxy-sulfosuccinimide, (sulfo-NHS); sulfosuccinimidyl 6-(4′-azido-2′-nitrophenylamino)hexanoate (sulfo-SANPAH), *N,N,N′,N′*-tetramethylethane-1,2-diamine (TEMED).

KEYWORDS

hydrogels, bioconjugation, 2D cell culture, chemical reactivity, free radical polymerization, poly(acrylamide) gel, chemo-selectivity, biochemical properties

1 Introduction

Hydrogels are crosslinked polymeric networks that can uptake and retain large amounts of aqueous fluids. This high water swelling ratio, their softness, and the possibility to regulate their biophysical and biochemical properties have made hydrogels the preferred biomaterials to mimic the extracellular matrix (ECM) that supports living cells in their native microenvironment. Therefore, hydrogels with regulated properties are extensively used as supporting materials in cell biology, tissue engineering and regenerative medicine applications.

Poly(acrylamide) (PAM) hydrogels are synthetic matrices widely used as substrates for 2D cell culture. These reductionistic *in vitro* models allow to investigate how cells sense and respond to variations in this synthetic microenvironment. For instance, the effects of hydrogel's elasticity and/or biochemical cues on cell adhesion, spreading, migration, differentiation and protein expression have been reported. (Pelham and Wang, 1997; Heras-Bautista

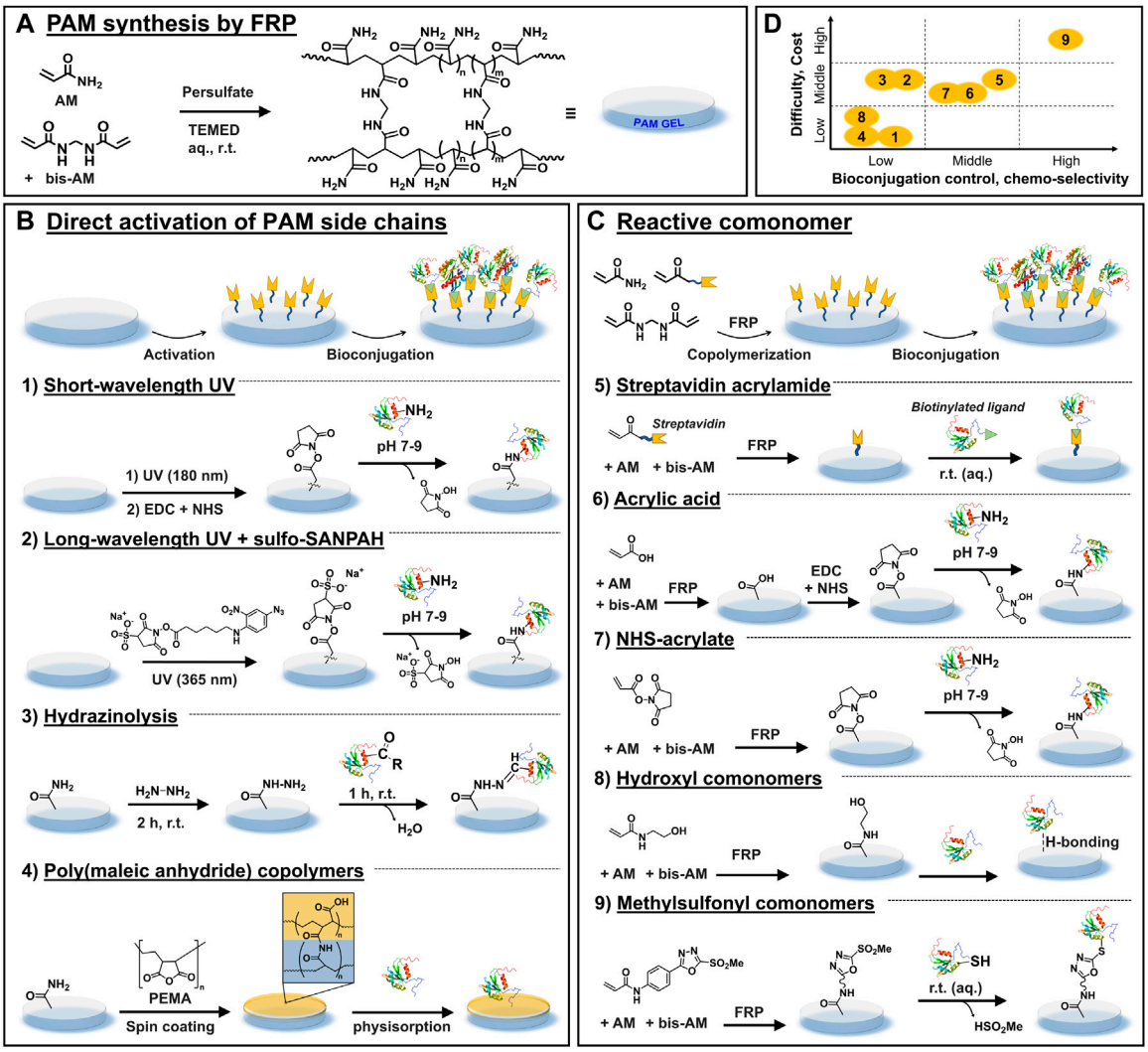


FIGURE 1
Most used chemical strategies for PAM gels biofunctionalization. **(A)** General scheme depicting the synthesis of PAM gels *via* FRP. **(B)** Chemical strategies based on the direct activation of the side chains of PAM after FRP, which is followed by ligand bioconjugation. **(C)** Chemical strategies whereby reactive comonomers are incorporated during FRP, followed by a bioconjugation step. **(D)** Overall qualitative comparison of the different chemical strategies in view of their experimental difficulty and cost vs. control of bioconjugation process and chemo-selectivity.

et al., 2019) PAM hydrogels present important advantages that explain their extended use in cell biology laboratories in the last 25 years. PAM is simple to synthesize and cost-effective, its mechanical properties (e.g., elasticity) can be easily regulated within the physiological range of native soft tissues, and its optical transparency makes it compatible with microscopy methods.

PAM hydrogels are typically synthesized by the acrylic-based free radical polymerization (FRP) of acrylamide (AM) and the crosslinker bis-acrylamide (bis-AM), using persulfate and TEMED as redox initiators (Figure 1A). For comfortable handling during cell culture and imaging, PAM is frequently prepared as thin film (thickness < 100 μm) and covalently attached to conventional microscopy glass coverslips, (Pelham and Wang, 1997), although attachment of thicker film gels to plastic multiwell culture plates is gaining momentum towards high-throughput studies. (Díaz-Bello et al., 2019).

For robust experimentation and reproducible outcome during culture of adherent cells on PAM gels, precise tailoring of mechanical and biochemical features of PAM substrates is desirable. Mechanically tunable PAM gels (for example, with regulable elasticity characterized by the Young's modulus E in the range of 0.1–100 kPa) can be obtained by adjusting the bis-AM crosslinker concentration and/or the total content of acrylamide monomers in the precursor solution, (Denisin and Pruitt, 2016), and numerous standard protocols can be found in the literature. (Tse and Engler, 2010; Paez et al., 2018) In contrast, precise modulation of the biochemical properties (e.g., cell-adhesiveness to promote cell-material interactions) remains challenging because biofunctionalization of these materials is not straightforward. The reason is that PAM hydrogels are intrinsically protein repellent and chemically inert, with the lateral amide groups being poorly reactive under mild aqueous conditions. Mild conditions are required to preserve the integrity and bioactivity of bound ligands post-functionalization. Thus, various chemical strategies to enable the controlled bioconjugation of ligands to PAM gels have been developed. These strategies can be summarized in two main groups: those that target the direct "activation" of the side chains of PAM after FRP, followed by ligand bioconjugation (Figure 1B); and those based on the incorporation of reactive monomers during FRP followed by bioconjugation Figure 1C).

In this mini review, the most used chemical strategies developed for controlled biofunctionalization of PAM gels for cell culture are presented and compared. Commercial PAM hydrogels have become available; thus they are also introduced. Advantages and limitations of the diverse approaches are discussed, especially in terms of chemo-selectivity and site-specificity of binding, preservation of ligand's functionality after conjugation, user-friendliness and cost (wherever known).[1] The aim of this work is to guide users in the choice of a strategy to fabricate PAM gels with tailored biochemical properties for 2D cell culture.

2 Chemical strategies for poly(acrylamide) gels biofunctionalization

2.1 Direct activation of poly(acrylamide) side chains

After gel fabrication, PAM chains are (photo)chemically activated, generally under harsh conditions, to introduce reactive groups that are later used as anchoring groups for biofunctionalization. In a second step, the bioligand is covalently coupled to activated PAM gels (Figure 1B).

2.1.1 Short-wavelength UV irradiation

PAM hydrogels are photochemically activated by short wavelength UV light irradiation (λ = 180 nm, 2–4 min) that forms ozone as well as peroxides and other reactive species on the PAM chains. (Tseng et al., 2011) The substrates are then incubated in EDC/NHS solution for chemical activation (in 10 mM MES buffer, pH 5.5, 15 min, r. t.), followed by incubation with biomolecules that present amine groups, such as fibronectin or fibrinogen (in 10 mM HEPES, pH 8.5, 1 h, r. t.) (Figure 1.B1). (Tseng et al., 2012) A photomask can be used to create ligand micropatterns with good spatial resolution.

This method is simple and has been reported to enable biofunctionalization of PAM hydrogels in a reproducible and homogeneous fashion. However, this procedure uses harsh photoirradiation conditions that might alter the mechanical strength of modified vs. bare PAM gels. Finally, the lack of chemo-selectivity might lead to poor control of the ligand loading and functionality.

2.1.2 Long-wavelength UV irradiation and sulfo-SANPAH

This is one of the most used strategies for PAM hydrogel bioconjugation with amine-bearing ligands. It is mediated by the commercial reagent sulfo-SANPAH, a photoactivatable heterobifunctional molecule. (Pelham and Wang, 1997) The PAM gel is incubated in a solution of sulfo-SANPAH and exposed to longer-wavelength UV light (λ = 330–365 nm, r. t., at variable exposure times and intensity) (Figure 1.B2). Upon

1 The listed reagents' prices correspond to the cheapest alternative that is offered by an European provider, to the best of the author's knowledge at the time of writing.

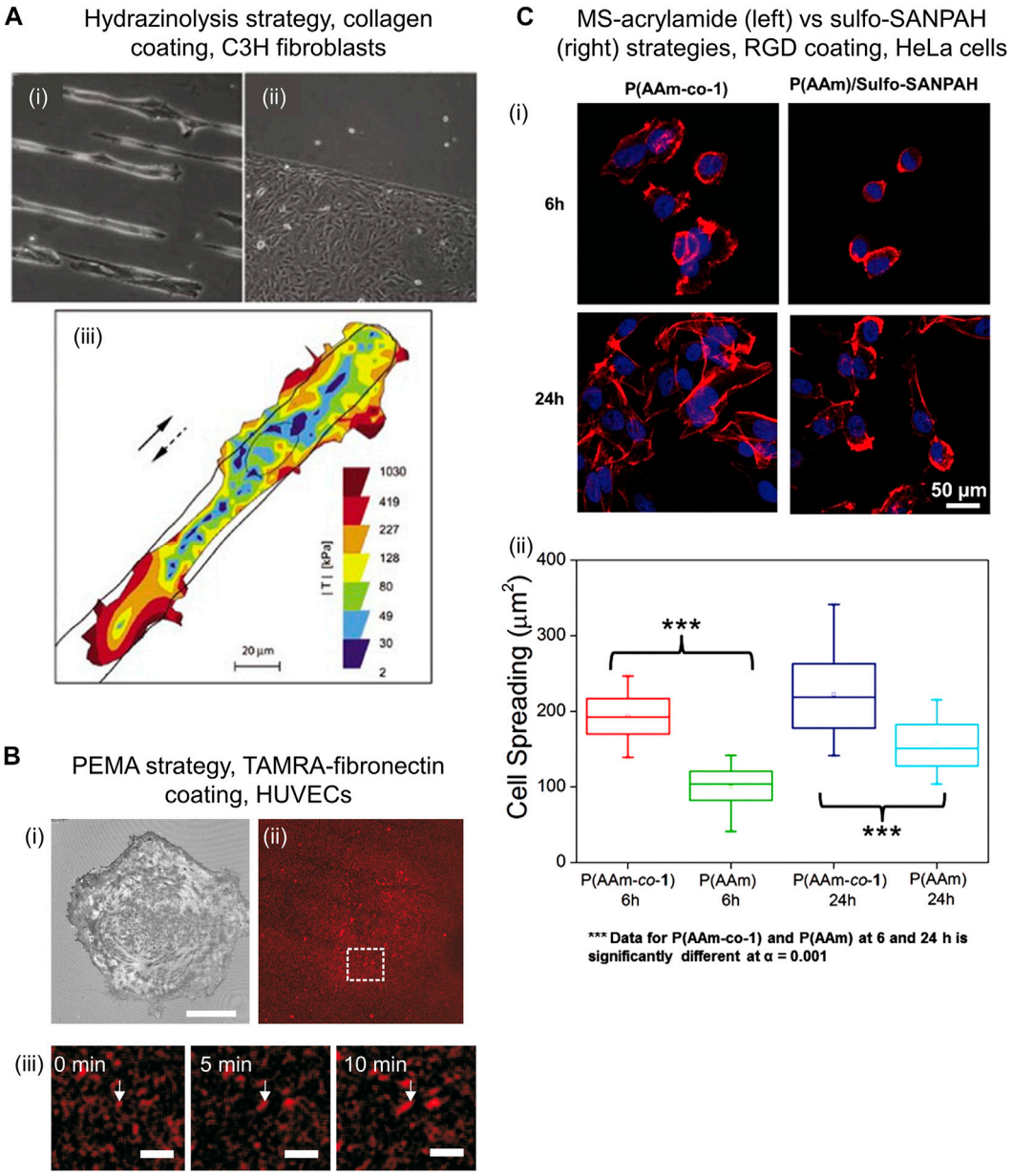


FIGURE 2
Examples of cells cultured on PAM hydrogels that were biofunctionalized through diverse chemical strategies. **(A)** Bright field images of C3H fibroblasts on PAM gels patterned with collagen I using hydrazinolysis strategy on 15 µm stripes (i) and bottom half part of the image (ii). Cells kept viable after 3 days of seeding. Traction map of C3H fibroblast while moving along a 25 µm wide stripe of collagen I (full and dashed arrows indicate original and reversed direction, respectively) (iii). Reproduced with permission from Ref. (Damljanovic et al., 2005). Copyright 2005 Future Science Ltd. **(B)** Reflection interference contrast microscopy image showing adhered HUVECs after 30 min seeding (i) on PAM gels functionalized with TAMRA-fibronectin (ii) *via* PEMA strategy. (Pompe et al., 2011) Scale bar: 30 µm. *In situ* analysis of fibronectin fibrillogenesis shows growing fibronectin fibers over time, indicated by white arrows (iii). Scale bar: 5 µm. Reprinted from Ref. (Pompe et al., 2011). Copyright 2011, with permission from Elsevier Ltd. **(C)** Confocal fluorescence images showing Hela cells after seeding for 6 and 24 h on PAM gels functionalized with RGD peptide *via* MS-acrylamide (left panel) vs. sulfo-SANPAH (right panel) strategies (i). Cell spreading area on PAM-MS gels was significantly larger than on sulfo-SANPAH gels, demonstrating effective and chemo-specific ligand immobilization (ii). Reproduced with permission from Ref. (Farrukh et al., 2016). Copyright 2016 John Wiley and Sons, Inc.

light illumination, sulfo-SANPAH forms highly reactive nitrene groups that bind nonspecifically to the PAM chains and introduce sulfo-succinimidyl groups. Typically, after two rounds of the activation step, the resulting hydrogel is immediately incubated in a solution of ligand (r.t., incubation times from 2 to 16 h). Note that the bioligand

immobilization must be performed immediately after the sulfo-SANPAH step to avoid the inactivation of sulfo-succinimidyl groups *via* hydrolysis. Using this strategy, different ECM proteins such as collagen I were bound to PAM gels to mediate cell adhesion, for example, to study the traction forces generated during cell migration (Dembo and Wang, 1999) or to assess the relationship between energy expenditure during cell spreading and cellular mechanoresponse. (Xie et al., 2021)

In comparison to the short-wavelength irradiation strategy shown above, sulfo-SANPAH strategy is milder and renders higher efficiency of bioconjugation, while it keeps the simplicity of NHS ester/amine coupling. However, sulfo-SANPAH is very pricy (~350 € per 50 mg) and has short shelf life. There is a lack of consensus on the experimental conditions for the photo-illumination step, e.g., in terms of light intensity and irradiation time. Consequently, highly variable irradiation doses can be found in the literature, which is reflected in high variability in the efficiency of bioconjugation. Additionally, poor site-selectivity of the NHS ester/amine binding has been suggested to cause poor binding efficiency and impaired ligand's bioactivity, leading to inconsistent results in cell response. (Farrukh et al., 2016)

2.1.3 Hydrazinolysis

The amide groups of PAM chains are chemically converted to hydrazide groups by reaction with hydrazine (2 h, r. t.), followed by treatment of the gel with acetic acid (1 h, r. t.). The formed hydrazide groups are subsequently coupled to aldehyde or ketone groups located in biomolecules, forming hydrazone bonds. (Timofeev et al., 1996) Aldehyde or ketone bearing biomolecules can be prepared by reaction with an oxidizing agent such as sodium periodate, and then covalently bound to PAM-hydrazide gels (1 h, r. t.) (Lee et al., 2016) (Figure 1.B3). Following this procedure, various ECM proteins including collagen I, collagen IV, fibronectin and laminin were efficiently conjugated to PAM-hydrazide gels and enabled micropatterning for mechano-transduction assays (see Figure 2A). (Damljanovic et al., 2005) Furthermore, fibronectin-coated gels were used to study the influence of interfacial geometry on cancer stem cell tumorigenicity. (Lee et al., 2016)

This simple procedure has been reported to facilitate uniform, reproducible and efficient protein conjugation on PAM surface using inexpensive commercial chemicals. Additionally, the PAM-hydrazide hydrogels can be produced in big batches and are stable for 2 months. (Timofeev et al., 1996) However, some limitations can be mentioned. The oxidation of biomolecules prior to conjugation typically generates multiple aldehyde or ketone groups in the structure. Low control of site-selectivity might decrease ligand's functionality and hamper precise control over loading. Moreover, hydrazone bonds are reversible and prone to hydrolysis under physiological conditions, therefore, biofunctionalized gels are only stable for about 2 days (Timofeev et al., 1996). This is inconvenient for longer-term cell cultures.

2.1.4 Poly(maleic anhydride) copolymers

PAM hydrogels are spin-coated with a thin layer of commercially available poly (maleic anhydride) copolymers, such as poly (ethylene-*alt*-maleic anhydride) (PEMA), and incubated overnight (in PBS, pH 7.4). The anhydride groups of PEMA react chemically with amide groups of PAM hydrogel *via* covalent imide bond formation that leads to the attachment of a PEMA monolayer onto PAM. (Müller et al., 2018) Subsequently, PAM-PEMA gels are incubated in ligand solution, such as fibronectin (in PBS, pH 7.4., r. t., 1 h) and rinsed (Figure 1.B4). The PEMA layer promotes the binding of biomolecules *via* physical adsorption. (Müller et al., 2018) (Pompe et al., 2011) Through this approach, PAM gels biofunctionalized with fibronectin have been used to study the mechano-transduction mechanisms of HUVECs. (Müller et al., 2019) Similar gels were used to evaluate cellular traction force and fibronectin reorganization on adhered HUVECs. (Pompe et al., 2011) It was found that the cellular traction force correlated with the mobility of fibronectin during cell-driven fibronectin fibrillogenesis (Figure 2B).

An advantage of this approach is that a stable PEMA layer on PAM surface can be achieved using the inexpensive PEMA (~70 € per 100 g) in a relatively simple procedure. Spin-coating ensures a thin and uniform layer but could also be a limitation in scaling up production. The lack of specificity and the instability of the ligand binding to the PEMA layer could be a disadvantage for those applications requiring fine control of ligand loading. However, reversible physical interaction between the bioligands and the PEMA layer is advantageous for mechano-transduction studies that require mobility of the adhesive ligands on top of PAM substrates. (Pompe et al., 2011)

2.2 Copolymerization with functionalized acrylic comonomers

Acrylic comonomers that present an additional functional group are copolymerized with AM and bis-AM to synthesize hydrogels with pendant functional groups. After polymerization, such groups are used to immobilize bioligands through covalent or non-covalent interactions (Figure 1C). In principle, by designing the right comonomer, any bioconjugation chemistry could be adapted to the synthesis of functional PAM copolymer hydrogels. Ideally, the comonomer should present decent water solubility and chemical compatibility with FRP conditions (i.e., not inhibiting PAM polymerization), be available from commercial sources or easy to synthesize, as well as cost-effective. Additionally, the introduction of this comonomer should not impair desirable PAM hydrogel properties for cell

culture (i.e., transparency, controlled mechanical and swelling properties).

2.2.1 Streptavidin acrylamide

Streptavidin-acrylamide (streptavidin-AM) is commercially available (~370 € per 1 mg). After copolymerization, the PAM-streptavidin gels are functionalized with biotinylated ligands *via* non-covalent, strong supramolecular interactions between streptavidin and biotin (Figure 1.C5). Conveniently, this reaction occurs in aqueous media and at r. t. By this means, ligands such as laminin, fibronectin, and laminin-mimetic peptide IKVAV have been attached and micropatterned onto gels surface to allow cell attachment. (Hynd et al., 2007) Neural cells showed successful adhesion and a long-term viability on laminin and fibronectin-functionalized substrates.

The advantages of this approach are its simplicity, the use of well-established and user-friendly supramolecular chemistry to bind the ligands, and the compatibility with microcontact printing. Diverse biotinylated ligands can be attached, for which there is good availability of commercial options. In addition, the formed hydrogels are highly hydrophilic and nondegradable. However, the streptavidin-AM comonomer and the biotinylated ligands are expensive, and other PAM functionalization alternatives may be more suitable when micropatterning is not needed. In addition, the (to our knowledge) lack of material characterization on PAM-streptavidin hydrogels may restrain its utilization towards further cell studies.

2.2.2 Acrylic acid

Acrylic acid (AA) is commercially available and cost-effective (~40 € per 1 L). After copolymerization, carboxylic acids of PAM-AA gels are activated with EDC/NHS to form NHS esters, followed by covalent coupling with amine-ligands (Figure 1.C6). The bioconjugation step carries out under mild reaction conditions (1 h, r. t., near-neutral pH) in high yields and the formed amide bond is very stable. Since many biomolecules have free primary amine groups, this strategy offers wide versatility in the type of ligands to immobilize. For example, RGD peptide (Farrukh et al., 2017a), poly-D-lysine (Farrukh et al., 2017b), and laminin mimetic IKVAV peptides (Farrukh et al., 2018) have been successfully bioconjugated to PAM-AA hydrogels. Commercial availability, excellent water solubility and low cost are the most important advantages of this strategy, while potential limitations are the poor site-selectivity of coupling and alteration of various gel's properties, as explained below.

First, the site-selectivity of the NHS ester/amine cannot be controlled, thus any amine group that is sufficiently exposed in the ligand might bind. Many biomolecules have multiple amine groups, and some can play a structural role in their bioactivity. Therefore, their immobilization through NHS ester/amine coupling can lead to impaired functionality when the amine group locates in the active sequence, such as Lys in IKVAV (Farrukh et al., 2018). A possibility to ameliorate this limitation is to add more conjugation steps mediated by biotin/streptavidin supramolecular interactions. For example, after PAM-AA synthesis and functionalization with biotin-PEG-amine *via* NHS ester/amine coupling, the biotin groups can mediate supramolecular binding of streptavidin followed by attachment of site-controlled biotinylated ligands (e.g., produced recombinantly). Using this strategy, hydrogels micropatterned with biotinylated anti-CD3 antibodies by microcontact printing, at tunable ligand density and variable gel stiffness were used to study the interplay of receptors and forces in T cell activation. (Zhang et al., 2021) Although it involves more coupling steps and the use of biotinylated ligands that need to be specially synthesized, this strategy can increase the site-specificity control of the bound molecule.

Second, the carboxylic groups in PAM-AA gels are negatively charged under physiological conditions. This effect increases the water swelling ratio that in turn can significantly modify several hydrogel's properties such as stiffness, zeta-potential, and pore size; consequently impacting cell behavior. For example, 18 mol % content of AA duplicates the swelling capacity of the gels in comparison to bare PAM, which increases the stress relaxation of the material and affects adhesion and differentiation of cultured hMSCs. (Prouvé et al., 2021) A possible way to control excessive swelling is the use of longer-chain carboxylic acid-functionalized comonomers. (Heras-Bautista et al., 2019; Norris et al., 2021)

2.2.3 NHS-acrylate

Acrylic acid *N*-hydroxysuccinimide ester (NHS-AE) (~40 € per 1 g) is commercially available and used to prepared PAM-NHS gels for immobilization of amine-ligands. In relation to PAM-AA gels, PAM-NHS gels skip the AA activation step and can be directly used for NHS ester/amine bioconjugation (Figure 1.C7). On the flipside, NHS-AE presents low water solubility and also inhibits PAM polymerization at concentration >16 mol %, which affects the mechanical strength of resulting gels. (Kumai et al., 2021) Due to solubility issues, NHS-AE is typically dissolved in toluene and incorporated to the AM and bis-AM aqueous mixture before polymerization. Different reported protocols have either localized NHS groups at the surface (Schnaar et al., 1978) or promoted homogeneous incorporation of the monomer along the PAM-NHS gel. (Kumai et al., 2021) Presumably, a differentiated localization of NHS monomers along the gel alters its properties, as well as functionalization efficiency and cell-behavior. MCF7 and MCF10A epithelial cells were seeded on PAM-NHS gels coated with collagen-I and compared with PAM gels functionalized *via* sulfo-SANPAH strategy. No noticeable differences in cell adhesion or morphology were observed between both gels. (Kumai et al., 2021)

Despite the relative simplicity of this approach, NHS groups can hydrolyze over time, thus the ligands must be bioconjugated immediately after copolymerization. Furthermore, the hydrolysis

of NHS groups results in charged carboxylic groups that can change hydrogel properties as explained above.

2.2.4 Hydroxyethyl acrylate

Hydroxylated comonomers endow PAM gels with -OH moieties that are used to immobilize ligands by hydrogen bonding interactions (Figure 1.C8). Diverse ligands can be attached since most biomolecules can participate in hydrogen bonding. However, the immobilization is not chemo-selective and generally is chemically weak, offering little control over ligand loading and stability. Note that hydrogen bonding interactions can be unstable to washing steps, or to changes in temperature or ionic strength. These aspects might be important for studies that require control over ligand density.

Furthermore, hydroxyethyl acrylate (HEA) is inexpensive (~60 € per 1 L). PAM-HEA hydrogels have been modified with fibronectin and laminin (Grevesse et al., 2014) and used to study how substrate area confinement affects collective migration of cells (Mohammed et al., 2019).

2.2.5 Methylsulfonyl acrylamides

Comonomers bearing a methylsulfonyl (MS) group enable the chemo-specific covalent coupling of thiol-containing bioligands under physiological conditions (1 h, PBS, r. t.) (Figure 1.C9). In general, bioconjugating ligands through thiols renders higher site-selectivity compared to amine coupling since free thiols are much less naturally abundant in biomolecules. MS monomers were copolymerized at 2 mol% with AM and bis-AM by usual protocols. The swelling, porosity, and low protein adsorption of PAM-MS gels were comparable to that of PAM gels. (Farrukh et al., 2016) Biofunctionalization with thiol-containing bioligands was quantitative, reproducible and stable; and retention of ligand's bioactivity allowed specific recognition by cells.

The performance of PAM-MS gels for bioconjugation has been compared with that of sulfo-SANPAH gels. (Farrukh et al., 2016) When both substrates were incubated in a bioligand solution of equal concentration, the immobilized ligand density on PAM-MS gels was three times higher compared to sulfo-SANPAH gels. Furthermore, PAM-MS gels only reacted with thiol-containing ligands while sulfo-SANPAH gels reacted with amino and thiol containing ligands demonstrating lower chemo-selectivity of the latter. Compared with PAM-MS gels, sulfo-SANPAH gels showed decreased concentration of bound RGD peptide, which impacted cell behavior by slowing down spreading kinetics and by decreasing final spreading area (Figure 2C). This evidences that selective ligand coupling is an important factor to achieve conclusive studies over cell-materials interactions.

Selective dual functionalization of PAM gels has been reported combining methylsulfonyl/thiol coupling with NHS ester/amine coupling (Farrukh et al., 2017a; Paez et al., 2018). PAM gels were copolymerized with AA and MS comonomers. PAM-AA-MS gels enabled the orthogonal immobilization of polylysine and IKVAV peptide. Neuronal cells cultured on gels *via* sequential bifunctionalization exhibited higher maturation at comparable culture times than when both ligands were incubated simultaneously (Farrukh et al., 2017a).

These reports have shown that functionalization of PAM gels with chemo-selective and quantitative coupling chemistries can impact retention of ligand biofunctionality and cell behavior. However, MS acrylamides are not commercially available, and their synthesis requires 4-5 steps, which reduces the user-friendliness of this approach for biology laboratories without synthetic capability.

2.3 Commercial poly(acrylamide) hydrogels

Commercial PAM hydrogels have become available. PAM gels with different biochemical and biophysical properties and in diverse culture plate configurations are commercialized under the brand Softwell® by Matrigen. (Matrigen, 2022) Collagen-modified and "easy coat" gels with controlled stiffness from E = 0.1–100 kPa are available. "Easy coat" gels contain quinone groups that can be used for covalent biofunctionalization by reacting with amine, thiols or other strong nucleophiles present in a ligand. Therefore, this approach presents poor chemo-selectivity and low control on site-specificity of binding.

The advantage of this strategy is the fast and user-friendly functionalization of the gels with biomolecules; thus, these substrates might be convenient for certain cell studies. However, as frequently occurring with commercial systems, the exact chemical composition of the gels, ligand density, or the chemistry applied for ligand immobilization (e.g., collagen) are undisclosed. The lack of information in composition, poor control over bioligand density and unsure retention of ligand's functionality may lead to inconclusive results on cell culture results. Another limitation is the high cost of these substrates (typically >50 € per culture plate).

3 Discussion and perspectives

In this mini review, diverse strategies for biofunctionalization of PAM hydrogels were introduced in the context of these biomaterials' usage for 2D cell culture. New users should select a convenient strategy after consideration of the advantages and disadvantages of each strategy, the existing capabilities in the laboratory and, most importantly, specific user's needs in view of the biological question under investigation. The showcased methodologies present various levels of complexity, costs and requirement for

especial equipment. Additionally, these strategies enable different degree of control over the loading density on the gels, as well as over stability and preserved bioactivity of the attached ligand. An overall qualitative comparison is presented in Figure 1D.

Two main approaches were distinguished: those based on the direct activation of the side chains of PAM after FRP, and those where reactive comonomers are incorporated during FRP. In general, PAM direct activation strategies are based on the use of commercial reagents, use relatively simple (although often harsh) modification conditions without the need of highly specialized equipment (being thus more user-friendly). Unfortunately, they often offer limited control on the ligand loading, lower preservation of bioactivity and variable stability of the coating over time.

Within strategies mediated by introduction of comonomers during FRP, the use of AA and MS-acrylamide comonomers are generally more chemically controlled, the latter being more chemo-specific and site-selective, ensuring good control of ligand loading and good preservation of ligand's activity. However, MS-acrylamide strategy is more labour intensive and prohibitive for cell culture laboratories without organic synthesis infrastructure and expertise. Interestingly, we noticed that copolymerization strategies often do not report how the mechanical properties of the resulting functional PAM gels compare to pristine PAM gels. This could be a point of attention for future developments, to demonstrate to which extent a new methodology offers the possibility to independently tune mechanical from biochemical properties.

Although out of the scope of this article, specific needs such as patterning of PAM or high throughput handling could be other aspects to consider. Several methodologies allow ligand patterning using various chemical strategies as shown in previous sections. (Daliri et al., 2021) Noteworthy, the introduction of photolabile comonomers into PAM has recently been exploited to dynamically and locally tune the mechanical (Norris et al., 2021) and cell-adhesive (Missirlis et al., 2022) properties of light-responsive PAM gels. In contrast, the realization of truly high throughput PAM systems is still in its infancy. Commercially available PAM gels might provide an answer to this need in the long term; unfortunately, they are currently limited in their ligand options and are expensive. It is expected that more synthetic and fabrication efforts in the future will result in more robust, reproducible and high throughput solutions for biofunctionalized PAM hydrogels.

Author contributions

AW: investigation, visualization, writing–original draft; MJ: investigation, visualization, writing–original draft; JP: conceptualization, investigation, supervision, writing–review and editing, funding acquisition. All authors have approved the final version.

Acknowledgments

The authors thank financial support from the Deutsche Forschungsgemeinschaft (DFG, project no. 422041745) awarded to JP.

Conflict of interest

The authors declare that the research was conducted in the absence of any commercial or financial relationships that could be construed as a potential conflict of interest.

Publisher's note

All claims expressed in this article are solely those of the authors and do not necessarily represent those of their affiliated organizations, or those of the publisher, the editors and the reviewers. Any product that may be evaluated in this article, or claim that may be made by its manufacturer, is not guaranteed or endorsed by the publisher.

References

Daliri, K., Pfannkuche, K., and Garipcan, B. (2021). Effects of physicochemical properties of polyacrylamide (PAA) and (polydimethylsiloxane) PDMS on cardiac cell behavior. *Soft Matter* 17 (5), 1156–1172. doi:10.1039/d0sm01986k

Damljanovic, V., Lagerholm, B. C., and Jacobson, K. (2005). Bulk and micropatterned conjugation of extracellular matrix proteins to characterized polyacrylamide substrates for cell mechanotransduction assays. *BioTechniques* 39 (6), 847–851. doi:10.2144/000112026

Dembo, M., and Wang, Y-L. (1999). Stresses at the cell-to-substrate interface during locomotion of fibroblasts. *Biophysical J.* 76 (4), 2307–2316. doi:10.1016/s0006-3495(99)77386-8

Denisin, A. K., and Pruitt, B. L. (2016). Tuning the range of polyacrylamide gel stiffness for mechanobiology applications. *ACS Appl. Mat. Interfaces* 8 (34), 21893–21902. doi:10.1021/acsami.5b09344

Díaz-Bello, B., Monroy-Romero, A. X., Pérez-Calixto, D., Zamarrón-Hernández, D., Serna-Marquez, N., Vázquez-Victorio, G., et al. (2019). Method for the direct fabrication of polyacrylamide hydrogels with controlled stiffness in polystyrene multiwell plates for mechanobiology assays. *ACS Biomater. Sci. Eng.* 5 (9), 4219–4227. doi:10.1021/acsbiomaterials.9b00988

Farrukh, A., Fan, W., Zhao, S., Salierno, M., Paez, J. I., and del Campo, A. (2018). Photoactivatable Adhesive ligands for light-guided neuronal growth. *ChemBioChem* 19, 1271–1279. doi:10.1002/cbic.201800118

Farrukh, A., Ortega, F., Fan, W., Marichal, N., Paez, J. I., Berninger, B., et al. (2017). Bifunctional hydrogels containing the laminin motif IKVAV promote neurogenesis. *Stem Cell Rep.* 9 (5), 1432–1440. doi:10.1016/j.stemcr.2017.09.002

Farrukh, A., Paez, J. I., Salierno, M., and del Campo, A. (2016). Bioconjugating thiols to poly(acrylamide) gels for cell culture using methylsulfonyl Co-monomers. *Angew. Chem. Int. Ed. Engl.* 55 (6), 2132–2136. doi:10.1002/ange.201509986

Farrukh, A., Paez, J. I., Salierno, M., Fan, W., Berninger, B., and del Campo, A. (2017). Bifunctional poly(acrylamide) hydrogels through orthogonal coupling chemistries. *Biomacromolecules* 18 (3), 906–913. doi:10.1021/acs.biomac.6b01784

Grevesse, T., Versaevel, M., and Gabriele, S. (2014). Preparation of hydroxy-PAAm hydrogels for decoupling the effects of mechanotransduction cues. *J. Vis. Exp.* 90, e51010. doi:10.3791/51010

Heras-Bautista, C. O., Mikhael, N., Lam, J., Shinde, V., Katsen-Globa, A., Dieluweit, S., et al. (2019). Cardiomyocytes facing fibrotic conditions re-express extracellular matrix transcripts. *Acta Biomater.* 89, 180–192. doi:10.1016/j.actbio.2019.03.017

Hynd, M. R., Frampton, J. P., Dowell-Mesfin, N., Turner, J. N., and Shain, W. (2007). Directed cell growth on protein-functionalized hydrogel surfaces. *J. Neurosci. Methods* 162 (1), 255–263. doi:10.1016/j.jneumeth.2007.01.024

Kumai, J., Sasagawa, S., Horie, M., and Yui, Y. (2021). A novel method for polyacrylamide gel preparation using N-hydroxysuccinimide-acrylamide ester to study cell-extracellular matrix mechanical interactions. *Front. Mat.* 8 (20), 637278. doi:10.3389/fmats.2021.637278

Lee, J., Abdeen, A. A., Wycislo, K. L., Fan, T. M., and Kilian, K. A. (2016). Interfacial geometry dictates cancer cell tumorigenicity. *Nat. Mat.* 15 (8), 856–862. doi:10.1038/nmat4610

Matrigen 2022, Matrigen, https://store.matrigen.com/; [accessed August 2022].

Missirlis, D., Baños, M., Lussier, F., and Spatz, J. P. (2022). Facile and versatile method for micropatterning poly(acrylamide) hydrogels using photocleavable comonomers. *ACS Appl. Mat. Interfaces* 14 (3), 3643–3652. doi:10.1021/acsami.1c17901

Mohammed, D., Charras, G., Vercruysse, E., Versaevel, M., Lantoine, J., Alaimo, L., et al. (2019). Substrate area confinement is a key determinant of cell velocity in collective migration. *Nat. Phys.* 15 (8), 858–866. doi:10.1038/s41567-019-0543-3

Müller, A., Müller, S., Nasufovic, V., Arndt, H-D., and Pompe, T. (2019). Actin stress fiber dynamics in laterally confined cells. *Integr. Biol.* 11 (5), 175–185. doi:10.1093/intbio/zyz016

Müller, C., Ansorge, M., Espig, M., Zschoche, S., Schiller, J., and Pompe, T. (2018). Covalent binding of maleic anhydride copolymer monolayers to polyacrylamide hydrogels. *Macromol. Chem. Phys.* 219 (17), 1800206. doi:10.1002/macp.201800206

Norris, S. C. P., Soto, J., Kasko, A. M., and Li, S. (2021). Photodegradable polyacrylamide gels for dynamic control of cell functions. *ACS Appl. Mat. Interfaces* 13 (5), 5929–5944. doi:10.1021/acsami.0c19627

Paez, J. I., Farrukh, A., Ustahüseyin, O., and del Campo, A. (2018). "Biofunctionalization of poly(acrylamide) gels," in *Biomaterials for tissue engineering: Methods and protocols*. Editor K. Chawla (New York, NY: Springer New York), 101–114.

Pelham, R. J., and Wang, Y-I. (1997). Cell locomotion and focal adhesions are regulated by substrate flexibility. *Proc. Natl. Acad. Sci. U. S. A.* 94 (25), 13661–13665. doi:10.1073/pnas.94.25.13661

Pompe, T., Kaufmann, M., Kasimir, M., Johne, S., Glorius, S., Renner, L., et al. (2011). Friction-controlled traction force in cell adhesion. *Biophys. J.* 101 (8), 1863–1870. doi:10.1016/j.bpj.2011.08.027

Prouvé, E., Drouin, B., Chevallier, P., Rémy, M., Durrieu, M-C., and Laroche, G. (2021). Evaluating poly(acrylamide-co-acrylic acid) hydrogels stress relaxation to direct the osteogenic differentiation of mesenchymal stem cells. *Macromol. Biosci.* 21 (6), 2100069. doi:10.1002/mabi.202100069

Schnaar, R. L., Weigel, P. H., Kuhlenschmidt, M. S., Lee, Y. C., and Roseman, S. (1978). Adhesion of chicken hepatocytes to polyacrylamide gels derivatized with N-acetylglucosamine. *J. Biol. Chem.* 253 (21), 7940–7951. doi:10.1016/s0021-9258(17)34462-9

Timofeev, E., Kochetkova, S. V., Mirzabekov, A. D., and Florentiev, V. L. (1996). Regioselective immobilization of short oligonucleotides to acrylic copolymer gels. *Nucleic Acids Res.* 24 (16), 3142–3148. doi:10.1093/nar/24.16.3142

Tse, J. R., and Engler, A. J. (2010). Preparation of hydrogel substrates with tunable mechanical properties. *Curr. Protoc. Cell Biol.* 47 (1), Unit 10.16. doi:10.1002/0471143030.cb1016s47

Tseng, Q., Duchemin-Pelletier, E., Deshiere, A., Balland, M., Guillou, H., and Filhol, O. (2012). Spatial organization of the extracellular matrix regulates cell–cell junction positioning. *Proc. Natl. Acad. Sci. U. S. A.* 109 (5), 1506–1511.et al.

Tseng, Q., Wang, I., Duchemin-Pelletier, E., Azioune, A., Carpi, N., Gao, J., et al. (2011). A new micropatterning method of soft substrates reveals that different tumorigenic signals can promote or reduce cell contraction levels. *Lab. Chip* 11 (13), 2231–2240. doi:10.1039/c0lc00641f

Xie, J., Bao, M., Hu, X., Koopman, W. J. H., and Huck, W. T. S. (2021). Energy expenditure during cell spreading influences the cellular response to matrix stiffness. *Biomaterials* 267, 120494. doi:10.1016/j.biomaterials.2020.120494

Zhang, J., Zhao, R., Li, B., Farrukh, A., Hoth, M., Qu, B., et al. (2021). Micropatterned soft hydrogels to study the interplay of receptors and forces in T cell activation. *Acta Biomater.* 119, 234–246. doi:10.1016/j.actbio.2020.10.028

frontiers | Frontiers in Chemistry

TYPE Mini Review
PUBLISHED 23 September 2022
DOI 10.3389/fchem.2022.971792

Check for updates

OPEN ACCESS

EDITED BY
Cosima Damiana Calvano,
University of Bari Aldo Moro, Italy

REVIEWED BY
Martin Koller,
University of Graz, Austria

*CORRESPONDENCE
Daniela Piazzese,
daniela.piazzese@unipa.it

SPECIALTY SECTION
This article was submitted to Analytical Chemistry,
a section of the journal
Frontiers in Chemistry

RECEIVED 17 June 2022
ACCEPTED 08 September 2022
PUBLISHED 23 September 2022

CITATION
Censi V, Saiano F, Bongiorno D, Indelicato S, Napoli A and Piazzese D (2022), Bioplastics: A new analytical challenge.
Front. Chem. 10:971792.
doi: 10.3389/fchem.2022.971792

COPYRIGHT
© 2022 Censi, Saiano, Bongiorno, Indelicato, Napoli and Piazzese. This is an open-access article distributed under the terms of the Creative Commons Attribution License (CC BY). The use, distribution or reproduction in other forums is permitted, provided the original author(s) and the copyright owner(s) are credited and that the original publication in this journal is cited, in accordance with accepted academic practice. No use, distribution or reproduction is permitted which does not comply with these terms.

Bioplastics: A new analytical challenge

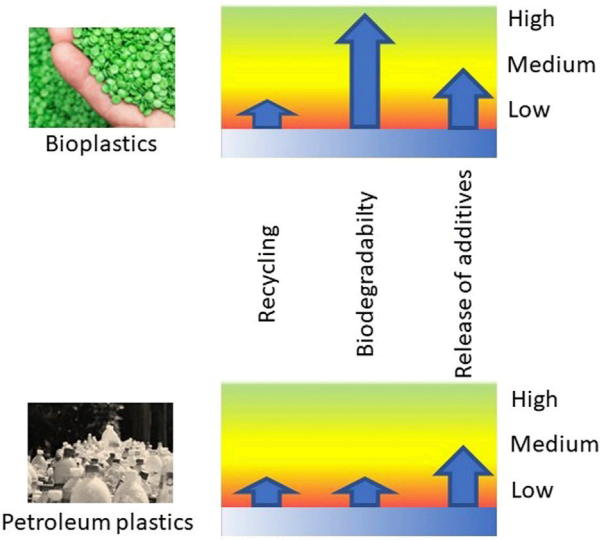
Valentina Censi[1], Filippo Saiano[2], David Bongiorno[3], Serena Indelicato[3], Anna Napoli[4] and Daniela Piazzese[1]*

[1]Department of Earth and Marine Sciences, University of Palermo, Palermo, Italy, [2]Department Agricultural Food and Forestry Sciences, University of Palermo, Palermo, Italy, [3]Department of Biological, Chemical and Pharmaceutical Science and Technology (STEBICEF), University of Palermo, Palermo, Italy, [4]Department of Chemistry and Chemical Technologies, University of Calabria, Arcavacata di Rende (CS), Italy

Even though petroleum-based plastics are advantageous in complying with the performance requirements in many applications, these are related, throughout their life cycle, to several environmental problems, including greenhouse gas emissions and persistence in marine and terrestrial environments. Therefore, the preservation of natural resources and climate change is considered worldwide, the main reason for which is necessary to reduce consumption and dependence on fossil-based materials. Biopolymers (PLA, PHAs, etc.) are examples of plastics whose use is grown exponentially over the years because of the improvements of their physical and mechanical properties using additives of various nature and depending on the scope of application. This review aims to discuss various ways of biopolymer degradation, to evaluate if they represent a new Frontier in eco-sustainability or rather a re-proposal of old problems. Related to this topic, we also have focussed our attention on the different methods for the quantitative analysis of bioplastics, or their degradation by-products, comparing and evaluating the advantages and disadvantages of each technique.

KEYWORDS

bio-plastics, bio-polymers determination, analytical, methods, mass spectrometry, bioplastic degradation



GRAPHICAL ABSTRACT

1 Introduction

Plastics are light, strong durable, and inexpensive synthetic or semi-synthetic organic polymers. Their characteristics justify the very large exploitation in a wide spectrum of human activities explaining why plastics represent an essential element in modern life. About 99% of plastics are made starting from non-renewable resources such as charcoal, petroleum, and natural gas. Accordingly, about 20% of the overall petroleum consumption could be related to the plastics industry (Kasavan 2021). In Europe, plastics are mainly exploited in the packaging (~40%), construction field (~20%), textile industry (~15%), automotive (~10%), and goods (~10%). Considering all these applications, the use of plastics could grow in the next future (World Economic Forum 2016; Gu 2017).

Even if the use of plastics has several benefits, their environmental occurrence is currently a very dangerous issue (Millican 2021) due to the progressive abrasion until the particulate formation. This is usually classified according to dimensions as nano-plastics (ø < 10–4 mm), microplastics (ø < 5 mm), mesoplastics (5 < ø < 25 mm) and macroplastics (ø > 25 mm). Proper management of plastic wastes would be hoped since the abrasion of these solids provides large amounts of plastic particles dangerous for organisms and humans (Filho 2019; Zhao 2021). This mainly occurs in marine systems where plastic wastes are accumulated at the end of their environmental path. Here, the characteristics of durability and resistance of plastics become a great problem in non-correct plastic disposal (Rosenboom 2022; Filho 2021). For these reasons, the critical review work was carried out by selecting data and information mainly related to the degradation process of biopolymers and their potential environmental impact. The knowledge of these materials in the production phase has now reached very good levels of completeness, as evidenced by the huge of information already present in the literature. The analytical-environmental challenge remains open, as highlighted by the insufficient information available for the assessment of the sustainability of biopolymers and their degradation products.

2 Bioplastics

As often reported in the literature, the term "bioplastics" define materials produced from biomass sources (vegetable fats and oils, corn starch, straw, woodchips, sawdust, etc.) and recycled food waste, which can be divided into biodegradable, bio-based, or both. Biodegradable bioplastics are degraded in aqueous fluids under the effects of bacterial activity. These processes lead, as the last step, to CO_2 and H_2O formation in aerobic degradation and CO_2 and CH_4 formation in anaerobic degradation. Bio-based bioplastics in whole or in part result from biomass-based syntheses (Di Bartolo 2021; Naser 2021). Some examples of bioplastics are poly (3-hydroxybutyrate) (PHB), poly (ε-caprolactone) (PCL), poly (butylene succinate) (PBS), poly (lactic acid) (PLA), and poly (ethylene succinate) (PES) (Atiwesh 2021, Roohi 2018). According to their versatility and their capacity to satisfy international standards of certification of composting (Naser 2021) and marine biodegradation (Meereboer 2020), respectively, poly-hydroxy-alkenoates (PHAs) and poly (lactic acid) (PLA) are among the most widespread biopolymers and together with

polypropylene show the highest relative growth rate in their industrial production (Naser 2021).

Poly-hydroxy-alkanoates (PHAs) are non-toxic biocompatible aliphatic bio-polyesters, from microbial fermentation of renewable sources (Venkatachalam 2020; Suzuki 2021). PHAs can be produced from raw materials in wastewater treatment plants, landfills, composting facilities, and farms (Atiwesh 2021). PHAs can also come from wood chips, grass, and green wastes rather than from the more expensive edible crop biomass. PHAs are flexible and crystalline with similar thermoplastic and mechanical properties to synthetic plastics (Akinmulewo 2019). PHAs' properties can change according to the arrangement of different monomers forming the polymer structure, or working on bacterial colonies, fermentation, or substratum. In this way, differing PHA well suited for packaging, fibers, and medical implants were developed differently combining polyesters groups and radical chains.

PHAs can be classified according to the polymer length: long (more than 14 C atoms), medium (between 6 and 14 C atoms), and short chain (between 3 and 5 C atoms) (Albuquerque 2018; Muniyandi 2020).

Poly (3-hydroxybutyrate) (PHB) is the most studied among PHA. It represents the C stock of several bacterial colonies produced through bacterial fermentation from CH_4, which is first oxidized to methanol, via the methane monooxygenase enzyme catalytic pathway, in the second step methanol is transformed into formaldehyde by methanol dehydrogenase (Atiwesh 2021). PHB shows a linear structure as a sequence of CH_3 and CH_2, followed by an ester -COOR group that results in physical-chemical (thermoplasticity, hydrophobicity) and mechanic properties (crystallinity grade and fragility). Commercial PHB shows similar properties to polypropylene (PP) coming from fossil fuels, showing significant stiffness, fragility, a crystallinity grade between 60 and 80%, a fusion temperature close to 180°C, and both an amorphous and a crystalline phase (Suzuki 2021). PHB can be a virgin polymer or with copolymers and additives in blends with better thermoplastic properties, such as the poly (3-hydroxybutyrate-*co*-3-hydroxyvalerate) [P (3HB-*co*-HV)] (McAdam 2020). Poly (lactic acid) (PLA) is both a bio-based and biodegradable thermoplastic polymer belonging to the aliphatic poly-esters class resulting from α-hydroxy acids. It is synthesized from lactic acid through bacterial fermentation of renewable plant-based sources or polymerizing the cyclic lactide dimer after a ring-opening reaction (Ring-Opening Polymerization, ROP) (Masutani 2014). PLA, for commercial purposes, is among the most promising bioplastics due to its mechanical properties, processability, renewability, and non-toxicity (Atiwesh 2021). PLA has larger durability than most biodegradable polymers, with larger transparency and mechanical strength. These properties and their widespread exploitation in several fields make ever-growing worldwide PLA production (Jiménez 2019).

2.1 Physico-chemical characterization

The structural and physicochemical properties of the bioplastics both in solid and solution phases have been extensively studied employing varying analytical approaches intended to characterize their chemical-physical features from several points of view. Thermal techniques such as Thermogravimetric analysis - TGA, and Differential Scanning Calorimetry–DSC, have been used to determine the material properties temperature-dependent in the bulk (Vahabi 2019). Spectroscopic techniques such as FT-IR, UV-Vis, and Fluorescence, are mostly used to highlight variations in the building blocks of the polymer structure (Han 2016). Spectrometric approaches such as NMR and mass-spectrometry are widely used for the qualitative and quantitative determination of several classes of substances including low molecular weight pollutants, high molecular weight polymers up to supramolecular aggregates (Banerjee 2012; Indelicato 2016; Biale 2021; Krawczyk-Walach 2021) Therefore, all these analytical approaches can be very informative in synergy when it comes to evaluating a material undergoing various stresses or degradative processes (Kumar 2017; Akdoğan 2018; Falkenstain 2021; Ghasemlou 2022).

2.2 Benefits and drawbacks

The main benefit of bioplastic exploitation comes from its production from renewable sources. However, biomass production requires suitable spaces, large water consumption, and intensive farming finalized to increase production. Accordingly, bioplastic production can involve the use of pesticides in crops and chemicals during the transformation processes that could be avoided by resorting to eco-friendly syntheses (Arikan 2015). On the other hand, bioplastics are biodegradable without any filler addition, which is often used for increasing their mechanical properties (Iwata 2015; Abe 2021; Van Roijen 2022). Despite the growing request for bioplastics, some handicaps to their larger exploitation come from their expensive production and recycling (Chen 2014; Coppola 2021; Nandakumar 2021; Shah 2021). A cost reduction could be provided from the PHA extraction from cells through halogenated solvents such as $CHCl_3$ and CH_2Cl_2. But these are toxic chemicals that would be largely used for avoiding too viscous polymeric solutions. Further industrial methods for PHA recovery were attempted but a limited PHA yield was obtained (Yang 2015).

3 Degradation process

The study of the degradation process is useful for assessing the environmental impact of bioplastic waste and finding an appropriate measure for implementing waste legislation and policies (Nandakumar 2021; Ghasemlou 2022).

Biodegradation is the process by which materials can be decomposed by microorganisms and used as a food source. The final products of the biodegradation process are CO_2 and H_2O, as also biomass and methane. However, although the material is biodegradable, it may not be in all circumstances or conditions. Several factors influence the biodegradation process, which adds up to microbial density and environmental conditions (i.e., temperature, humidity). These factors are polymer composition, molecular weight, crystallinity, pH, chemical structure, morphology, hydrophilicity, and breakdown products, but the relative extent of their effects is unclear (Meereboer 2020).

The first stage involves the enzymatic or chemical hydrolysis of the polymer chain and the consequent formation of degradation products whose size allows for microorganisms' encapsulation. It follows the decomposition and bio assimilation of the fragmented polymers up to their conversion into carbon dioxide, nitrogen oxide, methane, and water. For this reason, several international methods for assessing the biodegradability of plastics are based on the quantification of carbon dioxide production or the biochemical oxygen demand during the decomposition process (Suzuki 2021).

The abiotic or chemical degradation of bioplastics involves various techniques: pyrolysis, hydrolysis, alcoholysis, and glycolysis. Pyrolysis is a process of thermal cracking, in which the polymer, by heating in an inert environment, is converted into organic vapors, carbons, and gases. In the second stage, these by-products are converted into oil through a condensation process.

The processes of hydrolysis, alcoholysis, and glycolysis are techniques of depolymerization in which the polymer chain is broken down by the action of the water, alcohol, or glycol respectively (Lamberti 2020). The material is hydrolyzed through mechanisms of mass or surface erosion. Surface erosion occurs when the rate of hydrolysis exceeds the rate of diffusion of water in the mass (Piemonte 2013). This mechanism represents the main degradation process for hydrophobic and semi-crystalline polymers and for polymers that exhibit a very rapid hydrolysis rate (Meereboer 2020). The hydrolysis mechanism can change from surface to mass erosion when the material reaches a threshold thickness. Conversely, if the diffusion of water is fast to the rate of hydrolysis, degradation occurs through the entire mass of the polymer leading to a homogeneous erosion. The rate of hydrolysis is affected by several external factors, for example, an increase in temperature promotes the rate of hydrolysis, and therefore a change in the pH value. Alcoholisys occurs when there is a transesterification reaction in which the alcohol group cleaves the external bonds, and the polymer chain splits into its monomers or oligomers. The glycolysis of polyesters involves the insertion of glycol in the polymer chains, breaking the external bonds and replacing them with hydroxyl terminals (Lamberti 2020).

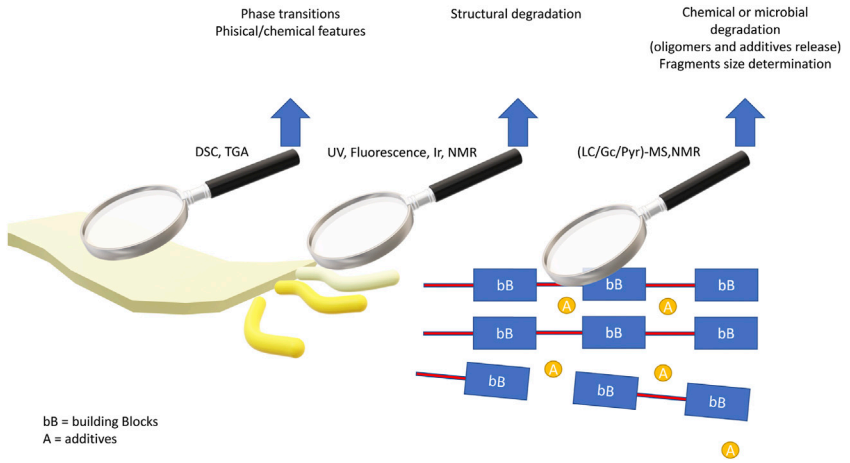
The reason for the large commercial spread of biodegradable bioplastics lies in their easy degradation, which would allow, under natural conditions, in soil, water, and sediment, to rapidly reduce the amount of plastic waste eventually improperly disposed of. The factor limiting the degree of degradation of most bioplastics is the surface of the polymer both in the case of chemical or enzymatic degradation. As already mentioned, the polymer surface is a fundamental aspect in the study of the degradation processes. Biotic (enzymatic) degradation occurs on the surface due to the enzymes' large size which prevents their permeation in the inner polymer structure. Enzymatic hydrolysis of biopolymers is a two-step process: degradation begins with the adsorption of enzymes on the polymer's surface-active sites. The second step is a hydrolytic cleavage of polymer chain bonds, which is induced by the binding site of the hydrophobic portion and the catalytic site respectively (Meereboer 2020). Accelerated by enzymes, surface degradation is much faster, especially in soil, and over time causes an increase in surface and roughness of the biopolymer and consequently higher hydrophilicity (Meereboer 2020, Muthukumar 2015).

4 Analytical investigation

As bioplastics continue to enter the environment, understanding their qualitative and quantitative impact is vital to addressing their potential environmental pollution. Bioplastics can enter the environment as small particles, which can lead to a significant biological and toxicological impact (González-Pleiter 2019). In this regard, the ability to quantify and identify the nature of particles smaller than 10 μm has become a challenge. The following step, in the possible environmental pollution of bioplastics, is the production, due to the degradation process, of both solid microparticles and soluble compounds. These two ways are in the field of analytical sciences very complex challenges in the identification and quantification of bioplastic degradation products. For this reason, we will discuss in this paragraph the last analytical techniques used in the quali-quantitative analysis of bioplastic degradation products.

4.1 Qualitative studies

Qualitative analysis of building blocks in bioplastics is possible by spectroscopic methods such as fluorescence, nuclear magnetic resonance (NMR), Fourier-transform infrared spectroscopy (FTIR), or UV-VIS spectrophotometric



SCHEME 1
Experimental techniques for the study of (bio) plastic materials.

techniques (Kumar 2017; Akdoğan 2018). Qualitative aspects of bioplastic degradation are of critical importance to planning, when possible, the following quantitative studies. Microparticles can be determined analytically either by analyzing them as they are or by analyzing them after dissolution in solvents. FT-IR micro imaging, gas chromatography with mass spectrometry detector, and thermal analysis represent the most used analytical techniques for the analysis of the solid debris of microparticles, while liquid chromatography, always with mass spectrometry detection, is currently the most widely used technique in the analysis of the dissolved microplastics or of their fractions (Sikorska 2020; Ye 2022; Yusuf 2022). Microparticles can be determined in their native status, or after dissolution in solvents. FT-IR micro imaging, gas chromatography coupled with mass spectrometry (GC-MS), and thermal analysis represent the most used analytical techniques for the investigation of solid microparticles. Liquid chromatography, coupled with mass spectrometry (LC-MS) detection, is currently widely used for dissolved microplastic fractions, (Sikorska 2020; Ye 2022; Yusuf 2022).

4.1.1 Fourier transform infrared spectroscopy

FT-IR analysis has the advantage of being a non-destructive and rapid technique, with minimal sample preparation. The PHAs analysis is based on the study of the variation of the intensity of the stretching band of the carbonyl of PHAs as a function of concentration, in the range of 1728–1740 cm^{-1} of wave numbers (Godbole 2016; Isak 2016). However, in the last years, to investigate particles up to 10 µm, the more helpful instrument is the FT-IR micro imaging system, (µFT-IR Imaging). µFT-IR is an instrument with a state-of-the-art infrared detector that simultaneously generates a high number of spatially resolved spectra and analyses large sets of microplastic data showing a "visible" image of the sample. Through appropriate software, it compares the spectra of the microparticles present in environmental matrices with a database of the reference spectra, allowing a very good identification of the microplastic by size, volume, and mass (Karami 2018, Liebezeit 2014).

4.1.2 UV-vis spectrophotometry

This classical and easy technique finds an interesting use in the determination of PHB by exploiting the degradation of the molecule of P (3HB) to crotonic acid by heating in concentrated sulphuric acid and determining its content by studying the absorbance mass of the crotonic acid band at 235 nm (Duvigneau 2021). This technique nowadays, for its easiness, is still used, though do not allow us to determine PHB copolymers.

4.1.3 Fluorescence spectroscopy

The application of this technique in PHAs analysis is based on the fluorescence of Nile-Red, a lipid fluorochrome, that easily penetrates the suspended cells making fluorescent the polymer portion contained in them. The concentration of polymer in the cells can be determined from the analysis of the fluorescence intensity. The intensity of the fluorescence emission of red-stained cells with Nile-Red increases with the biopolymer concentration. This method for the determination of the biopolymer concentration has several advantages: it is fast and reproducible, measurements can be made immediately after sampling, sample preparation time is shorter than traditional methods and sample volumes for analytical determination are very small (Godbole 2016; Rajankar 2018).

However, Nile Red can stain not only biopolymers (PHAs or PLA) but also other lipophilic compounds (Arikawa 2017) and for this reason, fluorescence spectroscopy can be classified as a qualitative rather than quantitative technique.

4.1.4 Qualitative thermal analysis

Among the different techniques available, thermal techniques are widely used in the design, preparation, and characterization of polymeric materials.

Thermal analysis (Differential Scanning Calorimetry and Thermogravimetric Analysis) offers, in addition to high precision in measurement, smart execution, allowing to obtain with a very limited amount of material valuable information regarding the property-structure correlation (Blanco 2021).

4.2 Quantitative studies

4.2.1 Gas chromatography

Gas chromatography has the advantage of providing very detailed, accurate, reproducible, and precise measurements, but conversely uses solvents harmful to the environment and requests long sample pre-treatment and large quantities of the sample (Khok 2020).

The most common method used to determine the PHA content in cells is gas chromatography with a flame ionization detector (GC-FID). This method is quite laborious, but it has high accuracy and provides extensive information on the composition of the monomer of PHAs (Isak 2016).

GC-MS allows the determination of PHB content in cell biomass after an initial stage of methanolysis (Khok 2020), P (3HB) content after acidic or basic digestion, and PHA content from freeze-dried bacteria or natural sample extracts after acidic digestion (Godbole 2016).

The GC-MS drawback is the use of not eco-friendly solvents. To overcome this side effect, it is better to use the pyrolysis technique directly coupled with gas chromatography (Py-GC), which is a valid method in the direct analysis of the content of PHB and its copolymers in prokaryotes (Baidurah 2016; Khang 2021).

4.2.2 Quantitative thermal analyses

Thermogravimetric analysis associated with mass spectrometry (TGA-MS) is a direct method for the quantitative determination of PHB and PLA in soil. This technique is based on the analysis of the masses of the products developed during gaseous pyrolysis in an inert atmosphere. A portion of gas degradation products is transferred to a quadrupole mass spectrometer via a heated capillary. The loss of mass at a specific temperature may be related to the mass signal of the gaseous pyrolysis products. These pyrolysis products' formation can be related to their specific degradation temperatures determined by the TGA. The advantages of the method are the absence of sample pre-treatment and the use of an internal standard but the sample to be measured is often of some micrograms giving problems of homogeneity and significance in sampling (dslu).

4.2.3 High-performance liquid chromatography-HPLC

HPLC is a valid method in the analysis of the soluble fraction of biopolymer degradation products. In the case of PHB analysis the degradation products such as crotonic acid and 2-pentenoic acid, are easily separable and can be quantified. The analytical results are comparable to those obtained with GC-MS, but with shorter analysis times (Duvigneau 2021) and easier sample treatment.

5 Remarks

A wide variety of bioplastics such as PHA, PHB, and PLA have been introduced to address the environmental challenges associated with conventional petroleum-derived plastics. However, also bioplastics have some shortcomings. The information shows that even bio-based plastics cannot be easily recycled. Therefore, bioplastics are also collected in landfills, wherein gradually undergo degradation, leading to CO_2 and methane formation. Nevertheless, it is important to assess the environmental impact of bioplastics compared to the damage caused by conventional plastics. It is clear that, now, the side effects associated with bioplastics are less serious than that associated with conventional plastics. A critical point concerns the lack of analytical methodologies to determine in aquatic ecosystems the concentrations of soluble fractions resulting from the degradation of biopolymers. According to the literature (Scheme 1) the available quantitative analytical techniques, i.e., HPLC, can measure the concentration of some degradation products under controlled laboratory test conditions, far from the environmental conditions of aquatic ecosystems.

So, it becomes increasingly necessary to develop analytical methods and procedures capable of monitoring these substances in real environments. Since bioplastics are a subject of current interest and scientific study, it is also plausible that their disadvantages can be overcome in the future. Kim et al., 2009.

Author contributions

Coordination of manuscript—DP Preparation of the manuscript—VC Qualitative analysis assessments—DB, FS Quantitative analysis assessments—SI, AN.

Conflict of interest

The authors declare that the research was conducted in the absence of any commercial or financial relationships that could be construed as a potential conflict of interest.

Publisher's note

All claims expressed in this article are solely those of the authors and do not necessarily represent those of their affiliated organizations, or those of the publisher, the editors and the reviewers. Any product that may be evaluated in this article, or claim that may be made by its manufacturer, is not guaranteed or endorsed by the publisher.

References

Abe, M. M., Ribeiro Martins, J., Bertolino Sanvezzo, P., Macedo, J. V., Branciforti, M. C., Halley, P., et al. (2021). Advantages and disadvantages of bioplastics production from starch and lignocellulosic components. *Polymers* 13, 2484. doi:10.3390/polym13152484

Akdoğan, M., and Çelik, E. (2018). Purification and characterization of polyhydroxyalkanoate (PHA) from a Bacillus megaterium strain using various dehydration techniques: PHA purification from B. Megaterium using various dehydration techniques. *J. Chem. Technol. Biotechnol.* 93, 2292–2298. doi:10.1002/jctb.5572

Akinmulewo, A. B., and Nwinyi, O. C. (2019). Polyhydroxyalkanoate: A biodegradable polymer (a mini-review). *J. Phys. Conf. Ser.* 1378, 42007. doi:10.1088/1742-6596/1378/4/042007

Albuquerque, P. B. S., and Malafaia, C. B. (2018). Perspectives on the production, structural characteristics and potential applications of bioplastics derived from polyhydroxyalkanoates. *Int. J. Biol. Macromol.* 107, 615–625. doi:10.1016/j.ijbiomac.2017.09.026

Arikan, E. B., and Ozsoy, H. D., 2015. A review: Investigation of bioplastics. *J. Civ. Eng. Archit.* 9, 188–192. doi:10.17265/1934-7359/2015.02.007

Arikawa, H., Sato, S., Fujiki, T., and Matsumoto, K. (2017). Simple and rapid method for isolation and quantitation of polyhydroxyalkanoate by SDS-sonication treatment. *J. Biosci. Bioeng.* 124, 250–254. doi:10.1016/j.jbiosc.2017.03.003

Atiwesh, G., Mikhael, A., Parrish, C. C., Banoub, J., and Le, T.-A. T. (2021). Environmental impact of bioplastic use: A review. *Heliyon* 7, e07918doi:10.1016/j.heliyon.2021.e07918

Baidurah, S., Murugan, P., Joyyi, L., Fukuda, J., Yamada, M., Sudesh, K., et al. (2016). Validation of thermally assisted hydrolysis and methylation-gas chromatography for rapid and direct compositional analysis of poly(3-hydroxybutyrate-co-3-hydroxyhexanoate) in whole bacterial cells. *J. Chromatogr. A* 1471, 186–191. doi:10.1016/j.chroma.2016.10.019

Banerjee, S., and Mazumdar, S. (2012). Electrospray ionization mass spectrometry: A technique to access the information beyond the molecular weight of the analyte. *Int. J. Anal. Chem.* 282574, 1–40. doi:10.1155/2012/282574

Biale, G., La Nasa, J., Mattonai, M., Corti, A., Vinciguerra, V., Castelvetro, V., et al. (2021). A systematic study on the degradation products generated from artificially aged microplastics. *Polymers* 13 (12). doi:10.3390/polym13121997

Blanco, I., and Siracusa, V. (2021). The use of thermal techniques in the characterization of bio-sourced polymers. *Materials* 14, 1686. doi:10.3390/ma14071686

Chen, Y. J. (2014). Bioplastics and their role in achieving global sustainability. *J. Chem. Pharm. Res.* 6, 226–231.

Coppola, G., Gaudio, M. T., Lopresto, C. G., Calabro, V., Curcio, S., and Chakraborty, S. (2021). Bioplastic from renewable biomass: A facile solution for a greener environment. *Earth Syst. Environ.* 5, 231–251. doi:10.1007/s41748-021-00208-7

Di Bartolo, A., Infurna, G., and Dintcheva, N. T. (2021). A review of bioplastics and their adoption in the circular economy. *Polymers* 13, 1229. doi:10.3390/polym13081229

Duvigneau, S., Kettner, A., Carius, L., Griehl, C., Findeisen, R., and Kienle, A. (2021). Fast, inexpensive, and reliable HPLC method to determine monomer fractions in poly(3-hydroxybutyrate-co-3-hydroxyvalerate). *Appl. Microbiol. Biotechnol.* 105, 4743–4749. doi:10.1007/s00253-021-11265-3

Falkenstein, P., Wei, R., Matysik, J., and Song, C. "2021 from Chapter eleven - mechanistic investigation of enzymatic degradation of polyethylene terephthalate by nuclear magnetic resonance,".*Methods Enzym.* Editors G. Weber, U. T. Bornscheuer, and R. Wei (Academic Press), 648, 231–252. doi:10.1016/bs.mie.2020.11.002

Filho, W. L., Saari, U., Fedoruk, M., Iital, A., Moora, H., Klõga, M., et al. (2019). An overview of the problems posed by plastic products and the role of extended producer responsibility in Europe. *J. Clean. Prod.* 214, 550–558. doi:10.1016/j.jclepro.2018.12.256

Filho, W. L., Salvia, A. L., Bonoli, A., Saari, U. A., Voronova, V., Klõga, M., et al. (2021). An assessment of attitudes towards plastics and bioplastics in Europe. *Sci. Total Environ.* 755, 142732. doi:10.1016/j.scitotenv.2020.142732

Fojt, J., Románeková, I., Procházková, P., David, J., Brtnický, M., and Kučerík, J. (2022). A simple method for quantification of polyhydroxybutyrate and polylactic acid micro-bioplastics in soils by evolved gas analysis. *Molecules* 27, 1898. doi:10.3390/molecules27061898

Ghasemlou, M., Daver, F., Murdoch, B. J., Ball, A. S., Ivanova, E. P., and Adhikari, B. (2022). Biodegradation of novel bioplastics made of starch, polyhydroxyurethanes and cellulose nanocrystals in soil environment. *Sci. Total Environ.* 815, 152684. doi:10.1016/j.scitotenv.2021.152684

Godbole, S. (2016). Methods for identification, quantification and characterization of polyhydroxyalkanoates. *Int. J. Bioassays* 54, 4977–4983. doi:10.21746/ijbio.2016.04.005

González-Pleiter, M., Tamayo-Belda, M., Pulido-Reyes, G., Amariei, G., Leganés, F., Rosal, R., et al. (2019). Secondary nanoplastics released from a biodegradable microplastic severely impact freshwater environments. *Environ. Sci. Nano* 6, 1382–1392. doi:10.1039/C8EN01427B

Gu, F., Guo, J., Zhang, W., Summers, P. A., and Hall, P. (2017). From waste plastics to industrial raw materials: A life cycle assessment of mechanical plastic recycling practice based on a real-world case study. *Sci. Total Environ.* 601-602, 1192–1207. doi:10.1016/j.scitotenv.2017.05.278

Han, J., Shin, S. H., Park, K. M., and Kim, K. M. (2015). Characterization of physical, mechanical, and antioxidant properties of soy protein-based bioplastic films containing carboxymethylcellulose and catechin. *Food Sci. Biotechnol.* 24 (3), 939–945. doi:10.1007/s10068-015-0121-0

Indelicato, S., Bongiorno, D., Ceraulo, L., Calabrese, V., Piazzese, D., Napoli, A., et al. (2016). Electrospray ion mobility mass spectrometry of positively and negatively charged (1R, 2S)-dodecyl(2-hydroxy-1-methyl-2-phenylethyl)dimethylammonium bromide aggregates. *Rapid Commun. Mass Spectrom.* 30, 230–238. doi:10.1002/rcm.7422

Isak, I., Patel, M., Riddell, M., West, M., Bowers, T., Wijeyekoon, S., et al. (2016). Quantification of polyhydroxyalkanoates in mixed and pure cultures biomass by fourier transform infrared spectroscopy: Comparison of different approaches. *Lett. Appl. Microbiol.* 63, 139–146. doi:10.1111/lam.12605

Iwata, T. (2015). Biodegradable and bio-based polymers: Future prospects of eco-friendly plastics. *Angew. Chem. Int. Ed.* 54, 3210–3215. doi:10.1002/anie.201410770

Jiménez, L., Mena, M. J., Prendiz, J., Salas, L., and Vega-Baudrit, J. (2019). Polylactic acid (PLA) as a bioplastic and its possible applications in the food industry. *Food Sci. Nutr.* 5, 1–6. doi:10.24966/FSN-1076/100048

Karami, A., Golieskardi, A., Choo, C. K., Larat, V., Karbalaei, S., and Salamatinia, B. (2018). Microplastic and mesoplastic contamination in canned sardines and sprats. *Sci. Total Environ.* 612, 1380–1386. doi:10.1016/j.scitotenv.2017.09.005

Kasavan, S., Yusoff, S., Rahmat Fakri, M. F., and Siron, R. (2021). Plastic pollution in water ecosystems: A bibliometric analysis from 2000 to 2020. *J. Clean. Prod.* 313, 127946doi:10.1016/j.jclepro.2021.127946

Khang, T. U., Kim, M.-J., Yoo, J. I., Sohn, Y. J., Jeon, S. G., Park, S. J., et al. (2021). Rapid analysis of polyhydroxyalkanoate contents and its monomer compositions by pyrolysis-gas chromatography combined with mass spectrometry (Py-GC/MS). *Int. J. Biol. Macromol.* 174, 449–456. doi:10.1016/j.ijbiomac.2021.01.108

Khok, Y. S., Suwa, M., Ito, H., Hazwan Hussin, M., Ishida, Y., Sudesh, K., et al. (2020). Comparison of quantification methods and subsequent characterization of polyhydroxybutyrate film sample utilizing pretreated cane molasses as carbon source. *IOP Conf. Ser. Mat. Sci. Eng.* 716, 12013. doi:10.1088/1757-899X/716/1/012013

Kim, D., Kim, B., Cho, Y., Han, M., and Kim, B.-S. (2009). Kinetics of polycarbonate glycolysis in ethylene glycol. *Ind. Eng. Chem. Res.* 48, 685–691. doi:10.1021/ie8010947

Krawczyk-Walach, M., Gzyra-Jagieła, K., Milczarek, A., and Jóźwik-Pruska, J. (2021). Characterization of potential pollutants from poly(lactic acid) after the degradation process in soil under simulated environmental conditions. *AppliedChem* 1, 156–172. doi:10.3390/appliedchem1020012

Kumar, M., Singhal, A., Verma, P. K., and Thakur, I. S. (2017). Production and characterization of polyhydroxyalkanoate from lignin derivatives by pandoraea sp. ISTKB. *ACS Omega* 2, 9156–9163. doi:10.1021/acsomega.7b01615

Lamberti, F. M., Román-Ramírez, L. A., and Wood, J. (2020). Recycling of bioplastics: Routes and benefits. *J. Polym. Environ.* 28, 2551–2571. doi:10.1007/s10924-020-01795-8

Liebezeit, G., and Liebezeit, E. (2014). Synthetic particles as contaminants in German beers. *Food Addit. Contam. Part A* 31, 1574–1578. doi:10.1080/19440049.2014.945099

Masutani, K., and Kimura, Y. (2014). "Chapter 1. PLA synthesis. From the monomer to the polymer," in *Polymer Chemistry series*. Editors A. Jiménez, M. Peltzer, and R. Ruseckaite (Cambridge, UK: Royal Society of Chemistry), 1–36. doi:10.1039/9781782624806-00001

McAdam, B., Brennan Fournet, M., McDonald, P., and Mojicevic, M. (2020). Production of polyhydroxybutyrate (PHB) and factors impacting its chemical and mechanical characteristics. *Polymers* 12, 2908. doi:10.3390/polym12122908

Meereboer, K. W., Misra, M., and Mohanty, A. K. (2020). Review of recent advances in the biodegradability of polyhydroxyalkanoate (PHA) bioplastics and their composites. *Green Chem.* 22, 5519–5558. doi:10.1039/D0GC01647K

Millican, J. M., and Agarwal, S. (2021). Plastic pollution: A material problem? *Macromolecules* 54, 4455–4469. doi:10.1021/acs.macromol.0c02814

Muniyandi, K., Punamalai, G., Sachithanantham, P., Chardrasekaran, N., and Kamaraj, Y. (2020). Perspectives of bioplastics-A review. *Int. J. Sci. Technol. Res.* 9, 374–381.

Muthukumar, A., and Veerappapillai, S. (2015). Biodegradation of plastics - a brief review -. *Int. J. Pharm. Sci. Rev. Res.* 31 (2), 204–209.

Nandakumar, A., Chuah, J.-A., and Sudesh, K. (2021). Bioplastics: A boon or bane? *Renew. Sustain. Energy Rev.* 147, 111237. doi:10.1016/j.rser.2021.111237

Naser, A. Z., Deiab, I., and Darras, B. M. (2021). Poly(lactic acid) (PLA) and polyhydroxyalkanoates (PHAs), green alternatives to petroleum-based plastics: A review. *RSC Adv.* 11, 17151–17196. doi:10.1039/D1RA02390J

Piemonte, V., Sabatini, S., and Gironi, F. (2013). Chemical recycling of PLA: A great opportunity towards the sustainable development? *J. Polym. Environ.* 21, 640–647. doi:10.1007/s10924-013-0608-9

Rajankar, M. P., Ravindranathan, S., Rajamohanan, P. R., and Raghunathan, A. (2018). Absolute quantitation of poly(R)-3-hydroxybutyric acid using spectrofluorometry in recombinant *Escherichia coli*. *Biol. Methods Protoc.* 3, bpy007doi:10.1093/biomethods/bpy007

RoohiZaheer, M. R., and Kuddus, M. (2018). PHB (poly-β-hydroxybutyrate) and its enzymatic degradation. *Polym. Adv. Technol.* 29, 30–40. doi:10.1002/pat.4126

Rosenboom, J. G., Langer, R., and Traverso, G. (2022). Bioplastics for a circular economy. *Nat. Rev. Mat.* 7, 117–137. doi:10.1038/s41578-021-00407-8

Shah, M., Rajhans, S., Pandya, H. M., and Mankad, A. U. (2021). Bioplastic for future: A review then and now. *World J. Adv. Res. Rev.* 9, 56–67. doi:10.30574/wjarr.2021.9.2.0054

Sikorska, W., Zi, M., Musioł, M., Kowalczuk, M., Janeczek, H., Chaber, P., et al. (2020). Forensic engineering of advanced polymeric materials - Part VII: Degradation of biopolymer welded joints. *Polym. (Basel).* 12, 1167. doi:10.3390/polym12051167

Suzuki, M., Tachibana, Y., and Kasuya, K. (2021). Biodegradability of poly(3-hydroxyalkanoate) and poly(ε-caprolactone) via biological carbon cycles in marine environments. *Polym. J.* 53, 47–66. doi:10.1038/s41428-020-00396-5

Vahabi, H., Michely, L., Moradkhani, G., Akbari, V., Cochez, M., Vagner, C., et al. (2019). Thermal stability and flammability behavior of poly(3-hydroxybutyrate) (PHB) based composites. *Materials* 12, 2239. doi:10.3390/ma12142239

Van Roijen, E. C., and Miller, S. A. (2022). A review of bioplastics at end-of-life: Linking experimental biodegradation studies and life cycle impact assessments. *Resour. Conserv. Recycl.* 181, 106236. doi:10.1016/j.resconrec.2022.106236

Venkatachalam, H., and Palaniswamy, R. (2020). Bioplastic world: A review. *J. Adv. Sci. Res.* 11, 43–53.

World Economic Forum (2016). *World economic Forum annual meeting 2016*. Davos-Klosters, Switzerland): World Economic Forum Davos

Yang, Y. H., Jeon, J. M., Yi, D. H., Kim, J. H., Seo, H. M., Rha, C., et al. (2015). Application of a non-halogenated solvent, methyl ethyl ketone (MEK) for recovery of poly(3-hydroxybutyrate-co-3-hydroxyvalerate) [P(HB-co-HV)] from bacterial cells. *Biotechnol. Bioprocess Eng.* 20, 291–297. doi:10.1007/s12257-014-0546-y

Ye, Y., Yu, K., and Zhao, Y. (2022). The development and application of advanced analytical methods in microplastics contamination detection: A critical review. *Sci. Total Environ.* 818, 151851doi:10.1016/j.scitotenv.2021.151851

Yusuf, A., Sodiq, A., Giwa, A., Eke, J., Pikuda, O., Eniola, J. O., et al. (2022). Updated review on microplastics in water, their occurrence, detection, measurement, environmental pollution, and the need for regulatory standards. *Environ. Pollut.* 292, 118421doi:10.1016/j.envpol.2021.118421

Zhao, C., Liu, M., Du, H., and Gong, Y. (2021). The evolutionary trend and impact of global plastic waste trade network. *Sustainability* 13, 3662. doi:10.3390/su13073662

frontiers | Frontiers in Chemistry

TYPE Review
PUBLISHED 23 September 2022
DOI 10.3389/fchem.2022.972494

Check for updates

OPEN ACCESS

EDITED BY
Anna Zielińska-Jurek,
Gdansk University of Technology, Poland

REVIEWED BY
Giovanni Palmisano,
Khalifa University, United Arab Emirates
Vincenzo Vaiano,
University of Salerno, Italy
Juan Carlos Colmenares,
Institute of Physical Chemistry (PAN), Poland

*CORRESPONDENCE
Ewa Kowalska,
kowalska@cat.hokudai.ac.jp

SPECIALTY SECTION
This article was submitted to Photocatalysis and Photochemistry, a section of the journal Frontiers in Chemistry

RECEIVED 18 June 2022
ACCEPTED 05 September 2022
PUBLISHED 23 September 2022

CITATION
Wang K and Kowalska E (2022), Property-governed performance of platinum-modified titania photocatalysts. *Front. Chem.* 10:972494. doi: 10.3389/fchem.2022.972494

COPYRIGHT
© 2022 Wang and Kowalska. This is an open-access article distributed under the terms of the Creative Commons Attribution License (CC BY). The use, distribution or reproduction in other forums is permitted, provided the original author(s) and the copyright owner(s) are credited and that the original publication in this journal is cited, in accordance with accepted academic practice. No use, distribution or reproduction is permitted which does not comply with these terms.

Property-governed performance of platinum-modified titania photocatalysts

Kunlei Wang and Ewa Kowalska*

Institute for Catalysis (ICAT), Hokkaido University, Sapporo, Japan

Titania is probably the most widely investigated semiconductor photocatalyst because of various advantages, such as high activity, thermal and chemical stability, low price, abundance, and negligible toxicity. However, pristine titania is also characterized by charge carriers' recombination, and thus lower quantum yields of photocatalytic reactions than theoretical 100%. Moreover, its wide bandgap, despite being recommended for excellent redox properties, means also inactivity under visible part of solar radiation. Accordingly, titania has been surface modified, doped and coupled with various elements/compounds. For example, platinum deposited on the surface of titania has shown to improve both UV activity and the performance under vis. Although the studies on titania modification with platinum started almost half a century ago, and huge number of papers have been published up to now, it is unclear which properties are the most crucial and recommended to obtain highly efficient photocatalyst. In the literature, the opposite findings could be found on the property-governed activities that could result from huge differences in the reaction systems, and also examined photocatalysts. Considering the platinum properties, its content, the size of nanoparticles and the oxidation state, must be examined. Obviously, the characteristics of titania also influence the resultant properties of deposited platinum, and thus the overall photocatalytic performance. Although so many reports on Pt/TiO_2 have been published, it is hardly possible to give indispensable advice on the recommended properties. However, it might be concluded that usually fine platinum NPs uniformly deposited on the titania surface result in high photocatalytic activity, and thus in the low optimal content of necessary platinum. Moreover, the aggregation of titania particles might also help in the lowering the necessary platinum amount (even to 0.2 wt%) due to the interparticle electron transfer mechanism between titania particles in one aggregate. In respect of platinum state, it is thought that it is highly substrate-specific case, and thus either positively charged or zero valent platinum is the most recommended. It might be concluded that despite huge number of papers published on platinum-modified titania, there is still a lack of comprehensive study showing the direct correlation between only one property and the resultant photocatalytic activity.

KEYWORDS

platinum, titania, photocatalysis, surface modifacation, photodeposition

Introduction

In 1839, Becquerel reported that a silver chloride (AgCl) electrode in acidic solution exposed to sunlight could be a source of electricity, i.e., the photovoltaic effect – also known as the "Becquerel effect" (Becquerel, 1839). Almost a century later (1921), the first report on "photocatalysis" was published by Renz, which presented the pigment fading, i.e., showing that irradiated oxides could decompose organic dyes and binders of paints (Renz, 1921). Although, these were the first reports on the light-activated reactions, the real interest in this topic has started with the famous paper by Fujishima and Honda on UV-initiated evolution of oxygen and hydrogen (water splitting) on titania and platinum electrodes, respectively (Fujishima and Honda, 1972). Since then, many reports have been published on the activity enhancement, mechanism clarifications (for various reactions), property-governed performance, and possible applications, including several crucial review papers and even books (Fox and Dulay, 1993; Hoffmann et al., 1995; Abe, 2010; Ohtani, 2010; Ibhadon and Fitzpatrick, 2013; Pichat, 2013; Marci et al., 2019; Garcia Lopez et al., 2021; Strunk, 2021).

Considering the basic mechanism of heterogeneous photocatalysis, the "photocatalyst" (usually oxide semiconductor) is excited under irradiation with light of energy equal or larger than its bandgap, i.e., photo-generated electrons are transferred from the valence band (VB) to the conduction band (CB), as shown in Figure 1A. The electrons and positive holes (simultaneously formed in VB) initiate reactions that cannot proceed spontaneously without photocatalyst (and without irradiation). Moreover, same as in the case of catalytic ("dark") reactions, photocatalysts (like catalysts) should not be changed during reactions. Although photocatalytic and catalytic reactions are similar, considering the necessary stability of (photo)catalysts, the main difference lies in the fundamental mechanism, i.e., the "dark reactions" can proceed in the absence of catalysts (being just accelerated after catalyst addition), whereas in the case of photocatalysis, usually there is no reaction in the absence of photocatalyst or light.

Regarding the semiconductor photocatalysts, the width of bandgap determines the photoabsorption properties (Klein, 1968; Wilson, 1981; Hamberg et al., 1985; Horan and Blau, 1987; Madhusudan Reddy et al., 2003). Of course, various semiconductors are characterized by different electronic properties, such as bandgap energy and localization of CB and VB. More positive VB and more negative CB mean the higher ability of oxidation and reduction, respectively. Therefore, the wide bandgap results in the efficient redox properties, e.g., simultaneous reduction and oxidation of water. However, the wide bandgap also means the inactivity under visible part of solar spectrum. For example, the most famous semiconductor photocatalyst – titania (titanium(IV) oxide) with wide bandgap of ca. 3.0–3.2 eV (depending on the polymorphic form) is well known from high photocatalytic activity under UV, but also inactivity under visible light (vis). Accordingly, many studies have been performed to modify the structure of titania (and other wide-bandgap semiconductors) via doping, surface modification and coupling with other materials (Khalil et al., 1998; Wu et al., 1998; Zang et al., 2000; Asahi et al., 2001; Ohno et al., 2003; Mitoraj et al., 2007; Zaleska, 2008; Dai et al., 2009; Etacheri et al., 2015; Janczarek et al., 2015; Wang et al., 2016; Babu et al., 2017; Khan et al., 2017; Salehi-Abar and Kazempour, 2017; Sun et al., 2017).

Moreover, in the case of semiconductor photocatalysts, the quantum yields of photocatalytic reactions (even under UV irradiation) do not reach the theoretical value of 100% because of the charge carriers' recombination (surface or bulk (Herrmann, 1999)). Therefore, numerous studies on the performance improvements have been carried out, focusing on the following aspects: (i) controlled synthesis conditions to improve the properties of photocatalysts (e.g., high crystallinity, a lack of defects, large specific surface area, pure polymorphic forms or fixed ratio of different polymorphs), (ii) morphology architecture, such as the preparation of photocatalysts with exposed facets, different dimensions, advanced morphologies (e.g., inverse opals, nanotubes, nanowires), and (iii) preparation of composite photocatalysts, e.g., by using the metallic or/and nonmetallic elements, and different

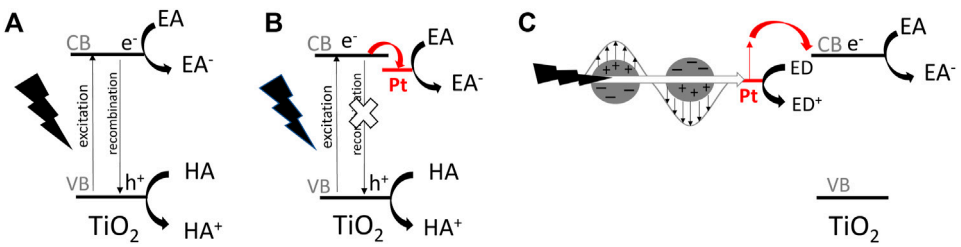


FIGURE 1
The schematic drawings of simplified mechanisms for photocatalytic reactions on titania-based photocatalyst: **(A)** pristine titania under UV excitation, **(B)** Pt-modified titania under UV excitation, **(C)** Pt-modified titania under vis excitation (considering an electron transfer mechanism); EA—electron acceptor, ED-electron donor, HA—hole acceptor.

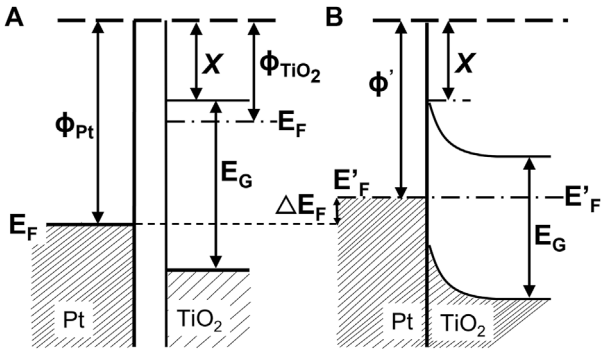


FIGURE 2
Energy band diagram under UV: before **(A)** and after **(B)** contact between Pt and TiO_2: X and E_G are the electron affinity (ca. 4 eV) and energy bandgap (ca. 3 eV), respectively; Φ_{TiO2} is the work function of illuminated TiO_2, estimated to be close to the reduced state (ca. 4.6 eV); Φ_{Pt} is the work function of Pt (ca. 5.36 eV); $\Delta EF = \Phi_{Pt} - \Phi'_{Pt}$ is the increase in the Fermi level of Pt after contact with illuminated TiO_2; drawn based on the report by Disdier et al., 1983.

compounds, to modify the surface or/and the structure of photocatalysts (Bakar and Ribeiro, 2016; Cai et al., 2016; Cheng et al., 2016; Lee et al., 2021; Wang T. M. et al., 2022; Dey et al., 2022; Korosi et al., 2022; Shehab et al., 2022; Shukla and Angappane, 2022). It should be mentioned that for both purposes, i.e., an appearance of vis response and activity enhancement under UV, similar methods have been used for the modifications of wide-bandgap semiconductors, i.e., doping, surface modification, coupling, and nanoarchitecture design (Sun et al., 2019; Huang et al., 2020; Yoshimura et al., 2020; Luo et al., 2021).

Among various strategies, the surface modification of wide-bandgap semiconductors with noble metals (NMs), such as gold, silver, platinum, has probably been the most popular. Kraeutler and Bard were first who found that platinum could scavenge photogenerated electrons (Figure 1B), and thus hinder the charge carriers' recombination (Kraeutler and Bard, 1978), as illustrated by Disdier et al., in 1983, and presented here in Figure 2 (Disdier et al., 1983). Since then, huge number of papers have been published on UV-activity enhancement by NMs (Pichat et al., 1981; Pichat et al., 1982; Nishimoto et al., 1985; Jakob et al., 2003; Subramanian et al., 2003; Kowalska et al., 2008; Azri et al., 2014). For example, Hu et al. proved that platinum hinders charge carriers' recombination by photoluminescence and transient fluorescence spectroscopy, resulting in longer lifetime of photogenerated charge carriers (Hu et al., 2019). Similarly, time-resolved microwave conductivity (TRMC) method was used to show the scavenging of photogenerated electrons by platinum (both originated from inorganic salts and Chini clusters) deposited on the titania surface, which correlates well with the enhanced photocatalytic activity for oxidative decomposition of phenol and rhodamine B (Kowalska et al., 2008), as exemplary presented in Figure 3. Here, improved performance for Pt-modified titania was shown under both UV and vis irradiation. The vis response was explained as originating from the light absorption by Pt-based compounds (sensitization mechanism), i.e., salts, complexes or/and clusters (Macyk et al., 2003; Kisch et al., 2004; Kowalska et al., 2008; Macyk et al., 2010).

In contrast to many reports, Benz et al. have proposed that platinum could work also as a recombination center under anaerobic conditions (Benz et al., 2020). The deposited platinum (0.04–3 wt%) on titania P25 was tested for UV degradation of acid blue nine and rhodamine B in the presence or absence of oxygen in the system. Although, the function of platinum as an electron scavenger has been proven by TRMC method (Figure 4), the decreased activity under anaerobic conditions could suggest that these electrons migrate back to titania. In contrast, under aerobic conditions, superoxide radicals could be efficiently formed on the surface of platinum (electron transfer from titania via platinum to oxygen), as commonly reported. However, it should be mentioned that usually degradation of organic compounds proceeds via oxidative pathways, and thus experiments are performed under aerobic conditions (the participation of reactive oxygen species (ROS); oxygen or air is even continuously bubbled into the reaction system (Gorska et al., 2008; Kowalska et al., 2008)). Additionally, for the reduction pathways, e.g., alcohol dehydrogenation and water splitting, photogenerated electrons are efficiently scavenged by a proton (H^+). Therefore, obviously, the lack of an electron acceptor (oxygen/proton) should result in charge carriers' recombination. Moreover, it should be pointed out that platinum could also work as a shield, causing less efficient photon absorption by titania, and thus resulting in lower efficiency, as discussed latter.

In 2005, another property of NMs has been used for the activation of wide-bandgap semiconductors towards vis response, i.e., plasmon resonance, as exemplary shown in Figure 1C. Tian and Tatsuma proposed the electron transfer from photoexcited gold NPs (due to plasmon resonance) to CB of titania, with simultaneous transfer of compensative electrons from the solution to gold NPs (Tian and Tatsuma, 2005). Since then, many reports showed vis activity of NM modified wide-bandgap semiconductors, resulting from plasmonic activation, known as "plasmonic photocatalysis" (Furube et al., 2007; Kowalska et al., 2009; Mukherjee et al., 2013; Panayotov et al., 2013; Sugawa et al., 2015; Verbruggen, 2015; Verma et al., 2018; Endo-Kimura and Kowalska, 2020; Raja-Mogan et al., 2020; Wei et al., 2020).

Moreover, another function of NMs should also be pointed out, i.e., co-catalytic. In the case of some reactions, pristine photocatalysts might be almost inactive, e.g., alcohol dehydrogenation and water splitting. Titania and other wide-bandgap semiconductors are hardly active due to high

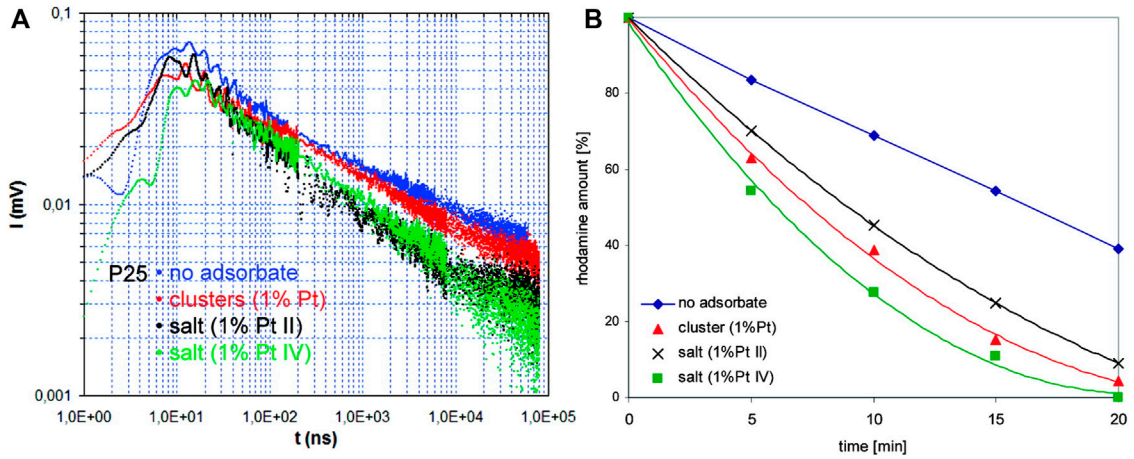


FIGURE 3
Experimental evidence for electrons' scavenging by deposited platinum on the titania surface (platinum originated from platinum salts and Chini clusters): **(A)** TRMC results, and **(B)** photocatalytic activity data for oxidative decomposition of rhodamine B. Adapted from (Kowalska et al., 2008) with permission from ACS.

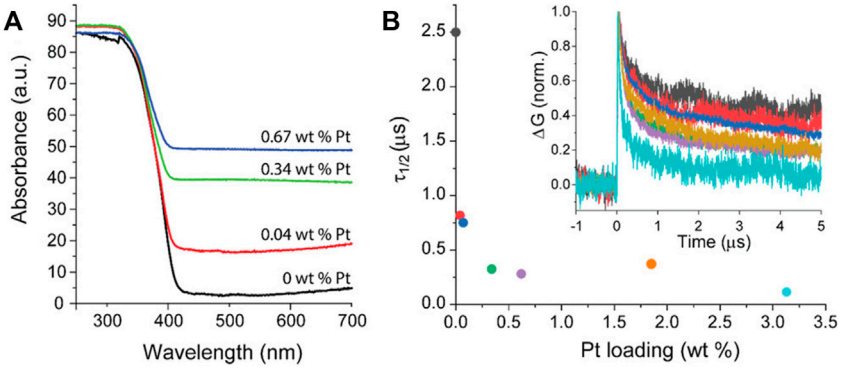


FIGURE 4
(A) DRS spectra for P25 titania loaded with different content of platinum; **(B)** Half time (τ1/2) of the mobile charge carriers measured by TRMC. Inset: transient decay of the mobile charge carrier. Adapted from (Benz et al., 2020), CC-BY-NC-ND license.

overvoltage for both hydrogen and oxygen evolution (Bandara et al., 2005; Abe et al., 2008; Kowalska et al., 2015; Takanabe, 2017; Yoshiiri et al., 2022). Accordingly, it has been found that NM co-catalysts, deposited on the surface of wide-bandgap semiconductors, are highly efficient for hydrogen evolution reactions. For example, Pt-deposition on P25 titania (commercial sample with one of the highest photocatalytic activities) results in activity enhancement by more than one order in magnitude (Wang et al., 2018; Wang K. et al., 2022; Paszkiewicz et al., 2022). Obviously, the properties of these deposits as well as the interface between NMs and semiconductor are decisive for the overall performance. However, the contrary results might be found in the literature. Additionally, the oxidation state of platinum could also play important impact on the photocatalytic activity. Accordingly, this review aims to revised various studies on the most active NM-modified semiconductors, i.e., platinum-modified titania, to clarify the key factors of photocatalytic activity, and to propose what properties are the most recommended for specific reactions.

Considering platinum-modified titania samples, more than 5000 papers could be found in Web of Science (2022/06/16 search for: (i) Pt/TiO_2, (ii) platinum and titania, and (iii) platinum and titanium dioxide). Most of the studies discuss titania samples modified with nanoparticles (NPs) of platinum for various photocatalytic reactions. However, many reports deal

with "dark" activity of platinum (not photocatalytic) where titania is only the support – inert or participating slightly in the overall mechanism, e.g., Pt/TiO_2 has been used as catalyst, electrocatalyst, sonocatalyst, sensor and for resistive switching memory (RSM) devices (Makouangou et al., 1994; Fukuoka et al., 1999; Lee et al., 2009; Song et al., 2011; Takakusagi et al., 2014; Dhanasekaran et al., 2016; Komanoya et al., 2016; Touchy et al., 2016; Ammal and Heyden, 2017; Kon et al., 2017; Nakajima et al., 2021). Additionally, there are some reports suggesting the doping of titania with platinum (Ambrozova et al., 2018; Zener et al., 2018; Ihnatiuk et al., 2020), and photocatalytic activity of titania modified with platinum single atoms (Qin et al., 2022). Moreover, the surface modification of titania with other forms of platinum (not NPs), such as compounds, complexes and clusters, have also been proposed for both UV and vis activity (Macyk and Kisch, 2001; Kisch et al., 2004; Mitoraj et al., 2007; Kowalska et al., 2008; Kisch, 2011; Khnayzer et al., 2012). However, because of huge number of various papers on Pt/TiO_2, and thus impossibility to comprehensively present them in one review paper, only titania photocatalysts modified with platinum NPs are discussed in detail in this review.

Synthesis of platinum-modified titania photocatalysts

The large number of scientific papers on Pt/TiO_2 photocatalysts corresponds obviously to various synthesis procedures of their preparation. Considering the titania aspect, both commercial and self-synthesized samples are used. Here, the most typical methods/samples are titania P25 (from Evonik/Degussa; composed of anatase (78%), rutile (14%) and non-crystalline phase (8%); with specific surface area of ca. 52 $m^2 g^{-1}$, and one of the highest photocatalytic activities in various reaction systems (Ohtani et al., 2010; Wang et al., 2018)) and hydrolysis of titania precursor (titanium alkoxides: isopropoxide and butoxide), respectively (Hufschmidt et al., 2002; Zhao et al., 2002; Coleman et al., 2005; Kowalska et al., 2008; Rosario and Pereira, 2014; Zielinska-Jurek et al., 2015; Haselmann and Eder, 2017; Yurdakal et al., 2017). Of course, other synthesis methods were also proposed, such as, gas-phase reaction (e.g., titanium(IV) chloride with oxygen), hydrothermal reaction (e.g., from titanate nanowires), and anodization of titanium (Nam and Han, 2007; Khan et al., 2008; Amano et al., 2010; Wei et al., 2014; Janczarek et al., 2016; Zielinska-Jurek et al., 2019; Momeni and Jalili, 2022). Then, either pre-synthesized Pt colloid/NPs or its precursor (usually chloroplatinic acid hexahydrate – $H_2PtCl_6 \cdot 6H_2O$) was used for the modification of the titania surface by various methods, including photodeposition (the most popular), impregnation, microemulsion, chemical and thermal reduction, electrostatic adsorption, ion exchange, incipient wetness, atomic layer deposition (ALD), complete decomposition of surface-anchored platinum complexes (Pt (dcbpy)Cl_2; dcbpy = 4,4′-dicarboxy-2,2′-bipyridine), and sputtering (Herrmann et al., 1986; Li et al., 2006; Nam and Han, 2007; Li et al., 2013; Bear et al., 2015; Samad et al., 2015; Shahgaldi and Hamelin, 2015; Zielinska-Jurek et al., 2015; Zielinska-Jurek et al., 2019; Benz et al., 2020). In some cases, titania was pre-treated by heating, sonication or irradiation. Heating was used to: (i) change the properties, e.g., crystallinity, crystal composition, specific surface area, (ii) stabilize the titania surface, and (iii) allow better adsorption of platinum (Li et al., 2006; Bear et al., 2015). Whereas, ultrasonication and UV irradiation were proposed for the generation of oxygen vacancies in the bulk and on the surface, respectively (Haselmann and Eder, 2017). It has also been shown that the kind of platinum salt might influence the resultant properties. For example, chloroplatinate ions in the solution reach the reduction sites via diffusion (photodeposition method), causing Pt enlargement of islets, whereas platinum compounds that strongly adsorbs onto titania (e.g., PtI_2^{-6}) cause that [Pt] in solution phase is minimal (Senevirathna et al., 2006). In contrast, different method of deposition even for the same platinum salt (chloroplatinate acid) might result in either uniform distribution of fine Pt NPs or their aggregation, as shown for impregnation ($[PtCl_6]^{2-}$ adsorbs on the positively charged titania surface quite uniformly due to the high acidity of the solution.) and photodeposition, respectively (Kozlova et al., 2011). Additionally, some reports suggest also the post-treatment operations (annealing, sonication, H_2 reduction) for: (i) stabilization and/or better connection between platinum and titania, (ii) increasing specific surface area, (iii) strong metal-support interaction (SMSI) effect (e.g., electron migration from titania to platinum), (iv) uniform distribution, and (v) the change of the oxidation state of platinum, e.g., from zero-valent to divalent, resulting from the diffusion of platinum from its NPs into the lattice of titania grains and substitution for Ti^{4+} (Colmenares et al., 2006; Li et al., 2006; Khan et al., 2008; Colmenares et al., 2011; Dessal et al., 2019).

Photodeposition of platinum on the titania surface is probably the most common (examples shown in Table 1) due to many advantages, such as:

- short time (for platinum ca. 5–10 min of induction time – complete deposition (Wei et al., 2017a)),
- a good contact between titania and platinum (Since metal cations are reduced by photogenerated electrons directly on the titania surface.),
- complete deposition of all platinum cations (from platinum salt),
- low cost and simple procedure (Only irradiation source is necessary—daylight could also be applied.),
- the ability to monitor *in-situ* the photocatalytic activity during platinum deposition, e.g., by hydrogen evolution (Senevirathna et al., 2006).

TABLE 1 The examples of Pt/TiO_2 photocatalysts' preparation by photodeposition method.

Platinum			Titania				Photodeposition Condition	References
Content (%)	Size (nm)	Distribution	BET (m^2/g)	Size (nm)		Type		
	PPA			PPA	SPA			
0.2	nd	nd	71–131	2–10	nd	A, AR, (pH depending) homemade	UV, 7 h	Huang et al. (2018)
0–0.3	nd	nd	nd	nd	nd	A/R, P25	UV, anaerobic, 1 h	Senevirathna et al. (2006)
0.50	4	nd	49	20	nd	A/R, P25	UV, 12 h	Cubillos-Lobo et al. (2017)
1	4	nd	nd	nd	10	A, homemade RGO-TiO2	UV, 3 h	Shinde et al. (2018)
0.2–3.0	<2	nd	nd	nd	nd	A, homemade	UV, 8 h	Zheng et al. (2009a)
2.1	2–3	nd	17.9	45 for homemade	nd	A/R P25, A Hombikat UV100, A homemade	UV, anaerobic, 6 h	López et al. (2015)
0.08–1.8	nd	nd	54	ND	nd	A/R, P25	solar simulator	Chowdhury et al. (2013)
0.5–2.0	3–12	nd	64	14.8	nd	A, homemade	UV, 3 h	Selvam and Swaminathan, (2011)
0.50	nd	nd	ca.70	ND	nd	A, homemade	UV, 2 h	Vaiano et al. (2018)
0.5 and 2	3–5, 10	agg	ca.50	ND	nd	A, homemade	UV, 15–240 min	Murcia et al. (2014)
0.5 and 1	1.5	uniform	300	8	nd	A, Hombikat UV100	UV	Al-Madanat et al. (2021)
0.1–1.0	0.5–0.7	agg	—	—	—	A/R, modified P25	455 nm, 70 min	Vasilchenko et al. (2020)
	—	—	56	5–10	nd	A, zeolite-TiO2 (P25)	365 nm, 2 h	López-Tenllado et al. (2022)
0.9	1–5	Nd	nd	nd	nd	P25	UV, 0.5–1 h	Bamwenda et al. (1997)

A—anatase, agg.—aggregated, nd-not determined, R-rutile, RGO—reduced graphene oxide.

Photodeposition method is based on the main feature of photocatalysis, that is the formation of charge carriers under irradiation, i.e., the photogenerated electrons reduce platinum cations. Usually, photodeposition is performed in the absence of oxygen (to avoid electron scavenging) and in the presence of a hole scavenger, here, methanol is the most popular (to limit hole-electron recombination). After the reaction completion, Pt/TiO_2 is washed (usually first with methanol to remove all adsorbed organic products from the hole scavenger oxidation, and then with water), dried (Common drying in the presence of air is used as both components are not easily oxidized, in the contrast to silver- or copper-modified samples when freeze drying is recommended (Janczarek et al., 2017)), and ground. Since in the case of platinum, the photodeposition is very fast (completed within few minutes), which might result in platinum aggregation, the modified photodeposition method has also been proposed. For example, photodeposition performed in the initial presence of oxygen or air in the system (aerobic system) might be used, i.e., the samples containing titania, platinum salt and methanol are sealed but the pre-bubbling with inert gas (e.g., argon or nitrogen) is not applied. Accordingly, during irradiation the photogenerated electrons are simultaneously scavenged by oxygen and also used to reduce platinum cations, which causes the formation of smaller and more uniformly distributed platinum NPs (Wei et al., 2017a; Paszkiewicz et al., 2022). However, it might also mean the change in the surface oxidation state of platinum. Indeed, samples prepared in the initial presence of oxygen contain larger content of positively charged platinum than those prepared under anaerobic conditions (Wei et al., 2017a; Paszkiewicz et al., 2022).

The method of synthesis obviously governs the resultant properties of Pt/TiO_2 photocatalysts. For example, smaller and more uniformly distributed Pt NPs have been deposited on the titania by: (i) decomposition of surface-anchored platinum complexes than photodeposition method (Li et al., 2013), (ii) ion exchange (2 nm) than impregnation (12 nm) method (Khan et al., 2008), (iii) photodeposition in the initial presence of oxygen than under anaerobic conditions (Wei et al., 2017a; Paszkiewicz et al., 2022), (iv) thermal reduction (2, 5 and 9 nm) than chemical reduction (3, 6 and 17 nm, respectively, on different titania samples: ST01-fine anatase, P25 and decahedral anatase particles (DAP)) (Zielinska-Jurek et al., 2019).

TABLE 2 The examples of enhanced photocatalytic activity after platinum deposition on titania.

Pt/TiO_2		Tested reaction		Main findings	References
Content (%)	Type	UV	Vis		
0.20	A, A/R	dye decolorization	—	low charge recombination rate	Huang et al. (2018)
0–0.3	A/R	CH_3OH dehydrog	—	increased quantum efficiency from 12.5 to 42.5%	Senevirathna et al. (2006)
0.50	A/R	phenol and methyl orange degr	phenol and methyl orange photodegradation	Pt on sulphated TiO_2 - vis response	Cubillos-Lobo et al. (2017)
1	A	CH_3OH dehydrog., propranolol degr	—	94% under solar	Shinde et al. (2018)
0.2–3.0	A	H_2 generation from HAc	—	optimized Pt amount	Zheng et al. (2009a)
2.1	A	H_2 generation	—	methanol > ethanol > ethyleneglycol > glycerol	López et al. (2015)
0.08–1.8	A/R	H_2 generation from formaldehyde (40–4600 ppm)	H_2 generation from formaldehyde (40–4600 ppm)	Langmuir-type model; platinum (wt%), catalyst dose, light intensity, and initial concentration	Chowdhury et al. (2013)
0.5–2.0	A	synthesis of 2-methylquinolines	—	improved activity	Selvam and Swaminathan, (2011)
0.5	A	H_2 generation from glycerol	—	improved activity	Vaiano et al. (2018)
0.5 and 2	A	phenol degr	—	small Pt NPs - phenolates formation; large Pt NPs - surface interaction	Murcia et al. (2014)
0.5 and 1.0	A	photocatalytic reforming of naphthalene and methanol	—	strong interaction between Pt NPs and TiO_2 surface	Al-Madanat et al. (2021)
0.1–1.9	A/R	CH_3OH dehydrog	—	the low Pt content—high activity	Vasilchenko et al. (2020)
	A	glycerol degr	—	increased activity	Lopez-Tenllado et al. (2022)
1	A	—	HCHO degr	increased activity	Zhu and Wu, (2015)
1%	A/R	hydrogenation of phenylacetylene to styrene		high selectivity and conversion	Lian et al. (2020)

A—anatase, degr—degradation, dehydrog.—dehydrogenation, R-rutile.

Similarly, the procedure of platinum deposition obviously influences the surface oxidation state of platinum. For example, it has been shown that chemical reduction and photodeposition methods result in the preparation of samples with mainly zero-valent and positively charged platinum NPs, respectively (Kozlova et al., 2011). However, other reports show that photodeposition causes the formation of mainly zero-valent platinum (Wei et al., 2018). Therefore, it is though that the slight change in the photodeposition conditions (irradiation source, light intensity and the absence/presence of oxygen) might result in significant change in the properties, and thus in the resultant activities. Other studies indicate that more positively charged platinum is obtained when photodeposition is performed in the initial presence of oxygen in the system than that performed under anaerobic conditions (Wei et al., 2017a; Paszkiewicz et al., 2022). Moreover, post-treatment operations, such as thermal treatment, might cause the change of oxidation state of platinum, e.g., from Pt^0 to Pt^{2+}, due to titania doping with diffused platinum from its NPs (Li et al., 2006).

Property-governed activity of platinum-modified titania photocatalysts

Like pristine titania, platinum-modified titania photocatalysts have been applied for plenty different reactions, including environmental purification (water/air purification, wastewater treatment, self-cleaning surfaces), energy conversion (water splitting, photocurrent generation), and organic synthesis, as shown in Table 2. For example, Avila et al. found in 1998 that Pt/TiO_2 was efficient for the destruction of traces of organic pollutants present in gaseous emissions (Avila et al., 1998). Then, various studies have been performed under UV irradiation. However, considering the high cost of artificial sources of irradiation, the recent study has mainly focused on the activity tests performed under natural solar light (or solar simulator) and the sole vis irradiation. Indeed, many reports have already proven that titania modification with platinum results in vis response (Kowalska et al., 2008; Zielinska-Jurek et al., 2015; Zielinska-Jurek et al., 2019). Moreover, considering high costs of platinum, the

TABLE 3 Exemplary results for the optimization of platinum content.

Tested Content of Pt	Optimal Pt amount (wt%)	Tested Compound	Irradiation	References
0.2–1.0 wt%	1.0	Acetic acid	UV/vis	Zheng et al. (2009a)
0–1.8 wt%	0.25	Formaldehyde	simulated solar and vis	Chowdhury et al. (2013)
0.005–2 wt%	0.2, 1.0, 2.0	methanol	UV/vis	Wang et al. (2018)
2–30 mg L^{-1}	0.057, 0.3 and 2.0	methanol	UV	Senevirathna et al. (2006)
0.5%, 2.0 wt%	0.5	phenol/methyl orange	UV	Murcia et al. (2014)

experiments with low its content (below 1 wt%) have been prioritized. In most cases, the application of platinum has significantly improved the photocatalytic activity of titania. For example, the reaction rate of toluene conversion has increased by ca. four times after platinum deposition on titania (Avila et al., 1998). The most significant activity enhancement is obviously observed for gas evolution reactions and activity under vis since pristine titania is practically inactive (as discussed in Introduction).

The most important question is: What parameters and properties should be considered to design efficient photocatalysts, based on platinum-modified titania? Of course, methods of preparation are crucial since they govern the resultant properties. Considering the properties, it seems that three are the most important: the platinum content, the platinum size (and its distribution) and its surface oxidation state. All these aspects are shortly presented and discussed below.

In the case of platinum content, the contrary reports have been published, suggesting that smaller or larger amount is better (Hufschmidt et al., 2002). However, usually the optimal amount (Table 3) has been suggested, ranging from 0.06 to 2 wt%, e.g., (i) 1.5 wt% for methyl orange degradation under UV/vis (Hu et al., 2012); (ii) 0.025 wt% for degradation of dichloromethane under UV (Ma et al., 2011), (iii) 0.5 wt% for UV methanol dehydrogenation (Ahmed et al., 2014), (iv) 0.2 wt%, 1 wt% or 2 wt% for methanol dehydrogenation, depending on the titania type (Wang et al., 2018), (v) 0.1 wt% for phenol degradation under UV and vis irradiation (Zielinska-Jurek et al., 2019), (vi) 0.057 wt%, 0.3 wt% and 2 wt% for methanol dehydrogenation, depending on the method of Pt deposition (Senevirathna et al., 2006), (viii) 0.1 wt% for hydrogen generation from acetic acid under UV (Zheng et al., 2009), (ix) 0.5 wt% for hydrogen evolution under simulated solar radiation (Hu et al., 2019), (x) 1 wt% for selective hydrogenation of phenylacetylene to styrene under UV (Lian et al., 2020), and (xi) 0.2 wt% for UV synthesis of benzimidazoles (Shiraishi et al., 2010). Interestingly, it has been found that the reaction conditions (pH value), irradiation intensity, the type of titania, kind of tested compounds and their concentration are also decisive, influencing the optimal content of platinum (Hufschmidt et al., 2002; Ma et al., 2011). The type of titania relates to the surface properties, such as specific surface area and crystallinity, and thus obviously different number of platinum NPs should be optimal for titania with different properties.

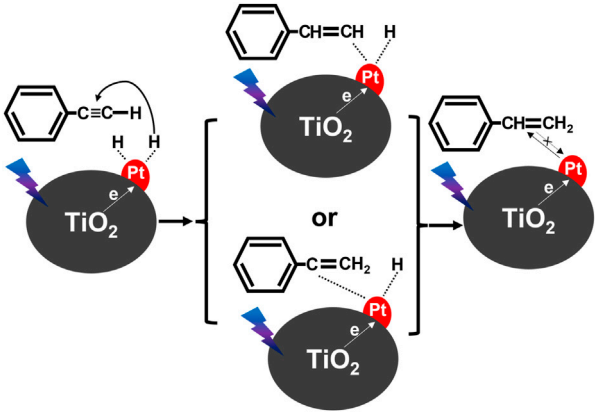


FIGURE 5
Proposed photocatalytic reaction mechanism for semi-hydrogenation of PLE over Pt/TiO_2; drawn based on the report by (Lian et al., 2020).

In the case of organic synthesis, it has been proposed that the amount of deposited platinum is a decisive factor for both high conversion and selectivity. For example, Lian et al. found that 1 wt% of Pt deposited on titania was the most efficient for the photocatalytic conversion of phenylacetylene (PLE) to styrene (STE) under monochromatic light (385 nm) irradiation (Lian et al., 2020), reaching 92.4% (conversion) and 91.3% (selectivity). It has been proposed that photogenerated electrons (from titania) migrate to Pt NPs, whereas methanol as both hydrogenation source and electron donor (holes' scavenger) dissociates (H^+). Then, active hydrogen species, formed on the surface of platinum, hydrogenate PLE (H-Pt), and thus formed STE detaches from the photocatalyst surface, as shown in Figure 5. It has been proposed that the selectivity towards STE is caused by the increased electron density of photocatalyst (electron cumulation on platinum), decreasing the adsorption strength of intermediate STE.

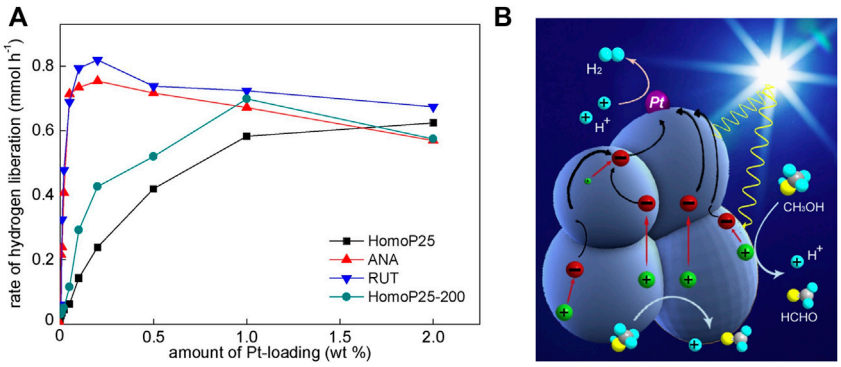


FIGURE 6
(A) The influence of platinum content on the photocatalytic activity during methanol dehydrogenation; **(B)** the schematic image showing the IPET in aggregated single-phase titania particles. Adapted from (Wang et al., 2018) with permission from Elsevier.

It should be pointed out that usually only several different photocatalysts have been tested, and thus with only two to four different contents of platinum. Therefore, it is hardly possible to classify these studies as "optimization". Fortunately, there are also comprehensive reports showing the influence of platinum content in the wide range of concentrations. For example, Zheng et al. investigated nine different contents of platinum (0.2, 0.4, 0.6, 0.8, 1.0, 1.2, 1.4, 2.0 and 3.0 wt%) deposited on self-synthesized titania, with 1.0 wt% being the most active for hydrogen evolution from acetic acid solution (Zheng et al., 2009). Similarly, nine different concentrations of platinum salt have been investigated by Senevirathna et al. to find that 4.5 mg L^{-1} is the most recommended for methanol dehydrogenation under UV (Senevirathna et al., 2006). Table 3 presents exemplary results for the optimization of platinum content on the titania surface.

In respect of this, it is thought that our previous report on platinum-modified titania, in which 36 samples have been tested, might be also very meaningful (Wang et al., 2018). In this study, nine different amounts of platinum (0.05, 0.01, 0.02, 0.05, 0.1, 0.2, 0.5, 1.0 and 2.0 wt%) and four titania samples, originated from the famous P25 titania, i.e., homogenized P25 (HomoP25), homogenized P25 thermally treated at 200 °C (HomoP25-200), anatase isolated from HomoP25 and purified by annealing at 200 °C (ANA) and rutile isolated from HomoP25 and purified by NaOH washing and annealing at 200 °C (RUT), were tested. It has been found that optimal content of platinum (tested during methanol dehydrogenation) depends on the titania feature, reaching 0.2 wt% for ANA and RUT, 1 wt% for HomoP25-200 and 2 wt% for HomoP25, as shown in Figure 6A. It should be pointed out that here, ANA and RUT have been obtained from HomoP25, and thus these samples are characterized by similar properties that those in P25. It has been concluded that much different activities and optimal properties come from the aggregation of titania, caused by thermal treatment (used for samples' purification). It should be remembered that in the case of methanol dehydrogenation one platinum deposit on one titania particle (e.g., aggregate) is sufficient for efficient hydrogen evolution (Ohtani et al., 1997), whereas an increase in platinum NPs' number might cause the "shielding effect", i.e., the competition between titania and platinum for photons (also known as "light-shading effect" (Lian et al., 2020)). Accordingly, it has been concluded that interparticle electron transfer (IPET; photogenerated electrons within one aggregate moving to one platinum deposit) is also possible within the same polymorph (anatase-anatase, rutile-rutile), and it has been named as Homo-IPET, as illustrated in Figure 6B.

Interesting study has been presented by Senevirathna et al. for P25 titania modified with platinum by three methods: photodeposition from hexaiodoplatinic acid, photodeposition from chloroplatinic acid and impregnation (chloroplatinic acid) with thermal treatment (Senevirathna et al., 2006). It has been shown that optimal content of platinum depends on both the method of preparation and the platinum salt, reaching 0.057 wt%, 0.3 wt% and 2 wt%, respectively. It has been proposed that the uniform distribution of fine Pt NPs, allowed by strong adsorption of PtI_2^{-6} on the titania surface, results in the highest photocatalytic activity.

Similar to platinum content, the contrary reports on the best size of platinum deposits have been reported, i.e., showing that smaller, larger or optimal size is the most recommended. It should be pointed out that the opposite results could be caused by different application, i.e., photocatalytic reactions under UV or vis irradiation, where better distribution (fine NPs uniformly deposited on titania) or aggregates of more efficient light harvesting ability, respectively, are recommended (Villani et al., 2006; Ting et al., 2015; Wei et al., 2017a; Wei et al., 2017b; Zielinska-Jurek et al., 2019). For example, Li et al. have shown that smaller and highly

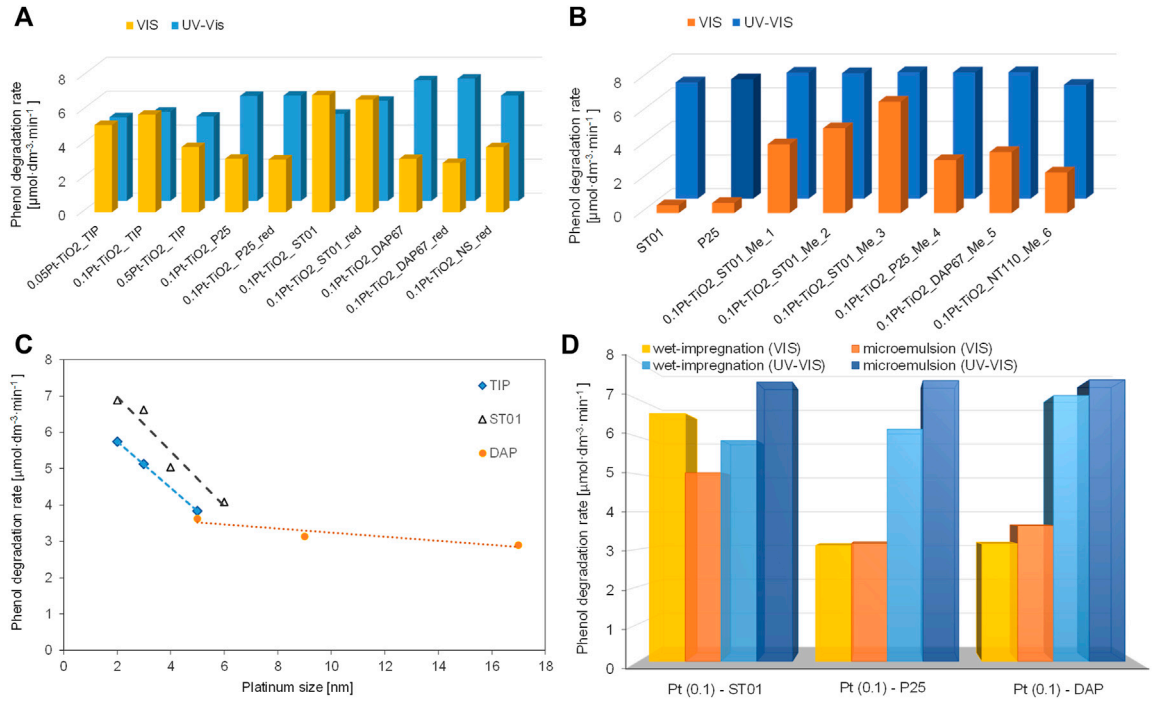


FIGURE 7
(A,B) Photocatalytic activity of Pt-TiO_2 samples obtained by: **(A)** wet-impregnation method, **(B)** microemulsion method; **(C)** Correlation between Pt NPs' size and photocatalytic activity of TIP (self-synthesized titania from titanium isopropoxide), ST01 (commercial samples of fine anatase) and DAP, **(D)** Comparison of UV-vis and visible-light photocatalytic activity for Pt-modified titania samples. Adapted from (Zielinska-Jurek et al., 2019), under Creative Common CC BY license.

dispersed platinum NPs on titania result in higher activity for hydrogen evolution both under UV and vis irradiation (vis activity due to co-adsorbed ruthenium complex) (Li et al., 2013). Zielinska-Jurek et al. investigated simultaneously the influence of various factors on the resultant activity, i.e., the properties of titania (morphology, specific surface area, crystal size, etc.), the preparation method (commercial and self-synthesized titania by different methods for both titania synthesis and platinum deposition: hydrolysis, gas-phase, micoremulsion, impregnation, thermal and chemical reduction), platinum properties (size and shape: spherical or cubic) and the contact between titania and platinum (Zielinska-Jurek et al., 2019). In contrast to other reports, suggesting that under vis irradiation the larger and polydisperse NM particles are important for efficient light harvesting, i.e., broad plasmon peak (Kowalska et al., 2009; Kowalska et al., 2010; Wei et al., 2017a; Wei et al., 2017b), higher activity with a decrase in Pt size was shown, as presented in Figure 7. However, it should be remembered that titania properties (and even its type) have also been changed, and thus the least active sample under vis is characterized by largest Pt NPs deposited on faceted anatase particles with decahedral shape (DAP). In another study, it has been proven that this morphology, despite being highly active under UV (one of the most active titania photocatalysts (Amano et al., 2009; Tachikawa et al., 2011; Janczarek et al., 2016)), is detrimental for vis activity of plasmonic photocatalysts, because of the fast back "hot" electron transfer (Au→TiO_2→Au) (Wei et al., 2019). Therefore, it is thought that for fruitful discussion it is recommended to change only one factor, e.g., platinum size/amount or titania type/properties, and thus direct correlation between only one specific property and activity could be drawn.

Interestingly, it has also been proposed that smaller Pt NPs (ca. 2 nm) on titania nanotubes obtained by ion exchange method than those prepared by impregnation (ca. 12 nm) result in bandgap narrowing, and thus vis response—stoichiometric generation of hydrogen and oxygen (water splitting) (Khan et al., 2008).

Next, the oxidation state of platinum should also be discussed. Of course, the platinum NP means that it is composed of zero-valent platinum, but at the same the charge on its surface could vary. Here, similarly to the influence of platinum content and Pt NPs' size, the contrary reports could be found, suggesting that zero-valent or positively charged platinum is better. For example, Li et al. have shown that the formation of positively charged platinum (e.g., by the thermally initiated diffusion of platinum from its NPs inside the titania lattice) results in higher photocatalytic activity for CO oxidation due to a decrease in the contacted resistance on the interface, being

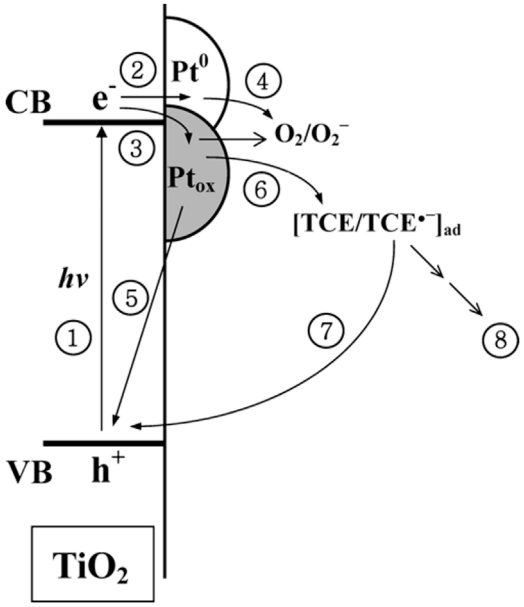


FIGURE 8
The schematic drawing showing the proposed photoinduced electron transfer paths on platinum-modified titania (Pt_{ox}-oxidized form of platinum; Pt^0—zero-valent platinum) in the presence of TCE; The numbers indicate major electronic pathways: (1) band gap excitation; (2) electron trapping in the Pt^0 phase; (3) electron trapping in the Pt_{ox} phase; (4) trapped electron transfer to O_2; (5) Pt_{ox}-mediated recombination; (6) trapped electron transfer to TCE; (7) TCE-mediated recombination; (8) reductively initiated degradation of TCE. Adapted with permission from (Lee and Choi, 2005) with permission from ACS.

beneficial for the transfer of the photo-generated electron (Li et al., 2006). Similarly, positively charged platinum NPs (Pt^{2+} and Pt^{4+}) deposited on P25 titania exhibit higher antimicrobial activity against Gram-negative bacteria in rotating magnetic field (instead of UV irradiation), possibly due to electrostatic attractions (Paszkiewicz et al., 2022). In contrast, Gram-positive bacteria are more sensitive to the photocatalyst with larger content of zero-valent platinum. Furthermore, in the case of gas-phase UV photocatalytic oxidation of dimethyl methylphosphonate (Kozlova et al., 2011) and methanol dehydrogenation (Wei et al., 2017a), samples with the larger content of zero-valent platinum show to be more efficient. However, in the case of oxidative decomposition of acetic acid, the samples with larger content of positively charged platinum show higher photocatalytic activity under UV (Wei et al., 2017a; Paszkiewicz et al., 2022). Similarly, in the case of organic synthesis, the selectivity towards organic products, e.g., during conversion of phenylacetylene to styrene, is preferable when oxidized form of platinum is applied (Lian et al., 2020).

Very interesting study was performed by Lee and Choi on different Pt/TiO_2 photocatalysts for photocatalytic degradation of chlorinated organic compounds (trichloroethylene (TCE), perchloroethylene (PCE), dichloroacetate (DC)) under UV irradiation (Lee and Choi, 2005). They found that among various properties, the oxidation state of platinum was the most decisive, and thus samples with larger content of zero-valent platinum were the most active for all tested compounds. Positively charged platinum (Pt_{Ox}) strongly inhibited the oxidation of TCE and PCE, but it was still more reactive than pristine titania for PCD. It was proposed, based on the photoelectrochemical studies (lower photocurrents for an electrode with positively charged platinum), that Pt_{Ox} species worked as a recombination center. The mediated charge recombination on Pt_{Ox} through the redox cycle of TCE was proposed, as shown in Figure 8. Accordingly, it has been concluded that the effect of platinum in photocatalysis is highly substrate specific, and both the properties of platinum and the interactions between platinum and substrate influence the overall activity.

Conclusion

Many attempts have been performed to find the property-governed activity for Pt/TiO_2 photocatalysts. In those studies, different factors have been considered, such as platinum content, platinum properties (size, aggregation/uniform distribution, oxidation state), titania properties (size, crystallinity, specific surface area, polymorphic form, defect density, morphology, surface characteristics) and the contact between platinum and titania. Unfortunately, usually only few factors have been varied at the same time. The most common studies have been performed for only several different samples, e.g., (i) pristine titania and titania modified with two/three different contents of platinum, (ii) two-four different titania samples modified with the same content of platinum, (iii) pristine titania and titania modified with platinum by two/three different methods. Additionally, though the properties of Pt/TiO_2 samples have been well characterized in many cases by various advanced methods, usually these properties have neither been controlled nor designed. Moreover, the photocatalytic activities have been tested for quite different reactions and in different systems (photoreactors, light intensity, spectrum range). It should be pointed out that even studies showing quantum yields are difficult for comparison when performed in different laboratories since only apparent quantum yields are usually estimated (emitted but not absorbed photons). Accordingly, even after so many years and huge number of published reports in the field, it is still hardly possible to draw the general conclusions on the property-governed activity of platinum-modified titania.

However, it might be proposed that in many cases, fine platinum NPs uniformly distributed on the titania support results in high photocatalytic activity. Moreover, the

preparation of this kind of photocatalyst might cause that optimal content of platinum is really low (below 1 wt%), and thus the photocatalyst even containing platinum could be reasonably cheap. Additionally, the aggregation of titania particles might also be recommended to decrease the necessary amount of platinum (e.g., 0.2 wt%), since IPET between same titania NPs (in one aggregate) allows an efficient electron transfer to platinum deposits. In the case of oxidation state of platinum, it is though that very important is the reagent, and thus its easy adsorption on the photocatalyst surface. Therefore, either positively charged or zero-valent platinum could be beneficial for the specific reaction.

Finally, it might be concluded that platinum is probably the most efficient modifier of titania, resulting in significant enhancement of quantum yields of photocatalytic reactions. Additionally, platinum-modified titania has also shown activity under visible range of solar spectrum, and thus being highly efficient under natural solar radiation. However, the price of platinum and its possible negative influence on the environment (e.g., in the case of the leakage from the photocatalyst surface) are the main shortcomings of its application. Accordingly, a decrease in its content and strong adsorption to titania must be achieved for possible commercial application. Additionally, there is a lack of comprehensive studies, in which only one property could be controlled and analyzed in detail for various photocatalytic reactions. Accordingly, our research is focused on this aspect now, and it is thought that the final conclusions on the property-governed activity of platinum-modified titania could be drawn in the nearest future.

Author contributions

KW: Writing, Visualization. EK: Conceptualization, Supervision, Writing—review and editing.

Funding

The project is co-financed by the Polish National Agency for Academic Exchange within Polish Returns Programme (BPN/PPO/2021/1/00037).

Conflict of interest

The authors declare that the research was conducted in the absence of any commercial or financial relationships that could be construed as a potential conflict of interest.

The handling editor AZ declared a past co-authorship with the authors KW and EK.

Publisher's note

All claims expressed in this article are solely those of the authors and do not necessarily represent those of their affiliated organizations, or those of the publisher, the editors and the reviewers. Any product that may be evaluated in this article, or claim that may be made by its manufacturer, is not guaranteed or endorsed by the publisher.

References

Abe, R. (2010). Recent progress on photocatalytic and photoelectrochemical water splitting under visible light irradiation. *J. Photochem. Photobiol. C Photochem. Rev.* 11, 179–209. doi:10.1016/j.jphotochemrev.2011.02.003

Abe, R., Takami, H., Murakami, N., and Ohtani, B. (2008). Pristine simple oxides as visible light driven photocatalysts: Highly efficient decomposition of organic compounds over platinum-loaded tungsten oxide. *J. Am. Chem. Soc.* 130, 7780–7781. doi:10.1021/ja800835q

Ahmed, L. M., Ivanova, I., Hussein, F. H., and Bahnemann, D. W. (2014). Role of platinum deposited on TiO_2 in photocatalytic methanol oxidation and dehydrogenation reactions. *Int. J. Photoenergy* 2014, 1–9. doi:10.1155/2014/503516

Al-Madanat, O., Curti, M., Gunnemann, C., Alsalka, Y., Dillert, R., and Bahnemann, D. W. (2021). TiO_2 photocatalysis: Impact of the platinum loading method on reductive and oxidative half-reactions. *Catal. Today* 380, 3–15. doi:10.1016/j.cattod.2021.07.013

Amano, F., Prieto-Mahaney, O. O., Terada, Y., Yasumoto, T., Shibayama, T., and Ohtani, B. (2009). Decahedral single-crystalline particles of anatase titanium(IV) oxide with high photocatalytic activity. *Chem. Mat.* 21, 2601–2603. doi:10.1021/cm9004344

Amano, F., Yasumoto, T., Mahaney, O. O. P., Uchida, S., Shibayama, T., Terada, Y., et al. (2010). Highly active titania photocatalyst particles of controlled crystal phase, size, and polyhedral shapes. *Top. Catal.* 53, 455–461. doi:10.1007/s11244-010-9472-1

Ambrozova, N., Reli, M., Sihor, M., Kustrowski, P., Wu, J. C. S., and Koci, K. (2018). Copper and platinum doped titania for photocatalytic reduction of carbon dioxide. *Appl. Surf. Sci.* 430, 475–487. doi:10.1016/j.apsusc.2017.06.307

Ammal, S. C., and Heyden, A. (2017). Water-gas shift activity of atomically dispersed cationic platinum versus metallic platinum clusters on titania supports. *ACS Catal.* 7, 301–309. doi:10.1021/acscatal.6b02764

Asahi, R., Morikawa, T., Ohwaki, T., Aoki, K., and Taga, Y. (2001). Visible-light photocatalysis in nitrogen-doped titanium oxides. *Science* 293, 269–271. doi:10.1126/science.1061051

Avila, P., Bahamonde, A., Blanco, J., Sanchez, B., Cardona, A. I., and Romero, M. (1998). Gas-phase photo-assisted mineralization of volatile organic compounds by monolithic titania catalysts. *Appl. Catal. B Environ.* 17, 75–88. doi:10.1016/s0926-3373(97)00104-5

Azri, Z. H. N. A., Jovic, V., Chen, W. T., Waterhouse, D. S., Metson, J. B., and Waterhouse, G. I. N. (2014). Performance evaluation of Pd/TiO<SUB align="right">2 and Pt/TiO<SUB align="right">2 photocatalysts for hydrogen production from ethanol-water mixtures. *Int. J. Nanotechnol.* 11, 695. doi:10.1504/ijnt.2014.060592

Babu, B., Kadam, A. N., Ravikumar, R., and Byon, C. (2017). Enhanced visible light photocatalytic activity of Cu-doped SnO2 quantum dots by solution combustion synthesis. *J. Alloys Compd.* 703, 330–336. doi:10.1016/j.jallcom.2017.01.311

Bakar, S. A., and Ribeiro, C. (2016). Low temperature synthesis of N-doped TiO_2 with rice-like morphology through peroxo assisted hydrothermal route: Materials characterization and photocatalytic properties. *Appl. Surf. Sci.* 377, 121–133. doi:10.1016/j.apsusc.2016.03.137

Bamwenda, G. R., Tsubota, S., Nakamura, T., and Haruta, M. (1997). The influence of the preparation methods on the catalytic activity of platinum and

gold supported on TiO_2 for CO oxidation. *Catal. Lett.* 44, 83–87. doi:10.1023/a:1018925008633

Bandara, J., Udawatta, C. P. K., and Rajapakse, C. S. K. (2005). Highly stable CuO incorporated TiO_2 catalyst for photocatalytic hydrogen production from H2O. *Photochem. Photobiol. Sci.* 4, 857–861. doi:10.1039/b507816d

Bear, J. C., Gomez, V., Kefallinos, N. S., Mcgettrick, J. D., Barron, A. R., and Dunnill, C. W. (2015). Anatase/rutile bi-phasic titanium dioxide nanoparticles for photocatalytic applications enhanced by nitrogen doping and platinum nano-islands. *J. Colloid Interface Sci.* 460, 29–35. doi:10.1016/j.jcis.2015.08.027

Becquerel, M. (1839). Mémoire sur les effets électriques produits sous l'influence des rayons solaires. *Comptes rendus Hebd. séances l'Académie Sci.* 9, 561–567.

Benz, D., Felter, K. M., Köser, J., Thöming, J., Mul, G., Grozema, F. C., et al. (2020). Assessing the role of Pt clusters on TiO_2 (P25) on the photocatalytic degradation of acid blue 9 and rhodamine B. *J. Phys. Chem. C* 124, 8269–8278. doi:10.1021/acs.jpcc.0c00926

Cai, J. B., Wu, X. Q., Li, S. X., and Zheng, F. Y. (2016). Synthesis of TiO2@WO3/Au nanocomposite hollow spheres with controllable size and high visible-light-driven photocatalytic activity. *ACS Sustain. Chem. Eng.* 4, 1581–1590. doi:10.1021/acssuschemeng.5b01511

Cheng, T., Zhang, G. Q., Xia, Y. G., Ji, Q., Xiao, Y., Wang, X. Y., et al. (2016). Template-free synthesis of titania architectures with controlled morphology evolution. *J. Mat. Sci.* 51, 3941–3956. doi:10.1007/s10853-015-9713-6

Chowdhury, P., Malekshoar, G., Ray, M. B., Zhu, J., and Ray, A. K. (2013). Sacrificial hydrogen generation from formaldehyde with Pt/TiO2 photocatalyst in solar radiation. *Ind. Eng. Chem. Res.* 52, 5023–5029. doi:10.1021/ie3029976

Coleman, H. M., Chiang, K., and Amal, R. (2005). Effects of Ag and Pt on photocatalytic degradation of endocrine disrupting chemicals in water. *Chem. Eng. J.* 113, 65–72. doi:10.1016/j.cej.2005.07.014

Colmenares, J. C., Aramendía, M. A., Marinas, A., Marinas, J. M., and Urbano, F. J. (2006). Synthesis, characterization and photocatalytic activity of different metal-doped titania systems. *Appl. Catal. A General* 306, 120–127. doi:10.1016/j.apcata.2006.03.046

Colmenares, J. C., Magdziarz, A., Aramendia, M. A., Marinas, A., Marinas, J. M., Urbano, F. J., et al. (2011). Influence of the strong metal support interaction effect (SMSI) of Pt/TiO_2 and Pd/TiO_2 systems in the photocatalytic biohydrogen production from glucose solution. *Catal. Commun.* 16, 1–6. doi:10.1016/j.catcom.2011.09.003

Cubillos-Lobo, J. A., Murcia-Mesa, J. J., Guarin-Romero, J. R., Rojas-Sarmiento, H. A., Hidalgo-Lopez, M. D., and Navio-Santos, J. (2017). Study of the visible light activity of Pt and Au-TiO2 photocatalysts in organic pollutants degradation. *Rev. Fac. De. Ingenieria-Universidad De. Antioquia* 2017, 20–30. doi:10.17533/udea.redin.n83a03

Dai, Z.-M., Burgeth, G., Parrino, F., and Kisch, H. (2009). Visible light photocatalysis by a Titania-Rhodium(III) complex. *J. Organomet. Chem.* 694, 1049–1054. doi:10.1016/j.jorganchem.2008.09.048

Dessal, C., Martínez, L., Maheu, C., Len, T., Morfin, F., Rousset, J. L., et al. (2019). Influence of Pt particle size and reaction phase on the photocatalytic performances of ultradispersed Pt/TiO_2 catalysts for hydrogen evolution. *J. Catal.* 375, 155–163. doi:10.1016/j.jcat.2019.05.033

Dey, B., Bulou, S., Ravisy, W., Gautier, N., Richard-Plouet, M., Granier, A., et al. (2022). Low-temperature deposition of self-cleaning anatase TiO2 coatings on polymer glazing via sequential continuous and pulsed PECVD. *Surf. Coat. Technol.* 436, 128256. doi:10.1016/j.surfcoat.2022.128256

Dhanasekaran, P., Selvaganesh, S. V., Giridhar, V. V., and Bhat, S. D. (2016). Iron and nitrogen co-doped titania framework as hybrid catalyst support for improved durability in polymer electrolyte fuel cells. *Int. J. Hydrogen Energy* 41, 18214–18220. doi:10.1016/j.ijhydene.2016.08.112

Disdier, J., Herrmann, J. M., and Pichat, P. (1983). Platinum titanium-dioxide catalysts - a photoconductivity study of electron-transfer from the ultraviolet-illuminated support to the metal and of the influence of hydrogen. *J. Chem. Soc. Faraday Trans. 1.* 79, 651–660. doi:10.1039/f19837900651

Endo-Kimura, M., and Kowalska, E. (2020). Plasmonic photocatalysts for microbiological applications. *Catalysts* 10, 824. doi:10.3390/catal10080824

Etacheri, V., Di Valentin, C., Schneider, J., Bahnemann, D., and Pillai, S. C. (2015). Visible-light activation of TiO_2 photocatalysts: Advances in theory and experiments. *J. Photochem. Photobiol. C Photochem. Rev.* 25, 1–29. doi:10.1016/j.jphotochemrev.2015.08.003

Fox, M. A., and Dulay, M. T. (1993). Heterogeneous photocatalysis. *Chem. Rev.* 93, 341–357. doi:10.1021/cr00017a016

Fujishima, A., and Honda, K. (1972). Electrochemical photolysis of water at a semiconductor electrode. *Nat. Lond. United Kingdom)* 238, 37–38. doi:10.1038/238037a0

Fukuoka, A., Osada, M., Shido, T., Inagaki, S., Fukushima, Y., and Ichikawa, M. (1999). Ship-in-bottle' synthesis of platinum carbonyl clusters in titania- or zirconia-modified mesoporous channels of FSM-16. Structural characterization and catalysis in CO hydrogenation. *Inorganica Chim. Acta* 294, 281–284. doi:10.1016/s0020-1693(99)00245-5

Furube, A., Du, L., Hara, K., Katoh, R., and Tachiya, M. (2007). Ulltrafast plasmon-induced electron transfer from gold nanodots into TiO_2 nanoparticles. *J. Am. Chem. Soc.* 129, 14852–14853. doi:10.1021/ja076134v

Garcia Lopez, E., and Palmisano, L. (2021). *Materials science in photocatalysis*. Amsterdam, Netherlands; Oxford, United Kingdom ; Cambridge, MA: Elsevier.

Gorska, P., Zaleska, A., Kowalska, E., Klimczuk, T., Sobczak, J. W., Skwarek, E., et al. (2008). TiO_2 photoactivity in vis and UV light: The influence of calcination temperature and surface properties. *Appl. Catal. B Environ.* 84, 440–447. doi:10.1016/j.apcatb.2008.04.028

Hamberg, I., Granqvist, C. G., Berggren, K. F., Sernelius, B. E., and Engström, L. (1985). Bandgap widening in heavily doped oxide semiconductors used as transparent heat-reflectors. *Sol. Energy Mater.* 12, 479–490. doi:10.1016/0165-1633(85)90041-3

Haselmann, G. M., and Eder, D. (2017). Early-stage deactivation of platinum-loaded TiO_2 using *in situ* photodeposition during photocatalytic hydrogen evolution. *ACS Catal.* 7, 4668–4675. doi:10.1021/acscatal.7b00845

Herrmann, J.-M., Disdier, J., and Pichat, P. (1986). Photoassisted platinum deposition on TiO_2 powder using various platinum complexes. *J. Phys. Chem.* 90, 6028–6034. doi:10.1021/j100280a114

Herrmann, J. M. (1999). Heterogeneous photocatalysis: Fundamentals and applications to the removal of various types of aqueous pollutants. *Catal. Today* 53, 115–129. doi:10.1016/s0920-5861(99)00107-8

Hoffmann, M. R., Martin, S. T., Choi, W. Y., and Bahnemann, D. W. (1995). Environmental applications of semiconductor photocatalysis. *Chem. Rev.* 95, 69–96. doi:10.1021/cr00033a004

Horan, P., and Blau, W. (1987). Optical nonlinearity near the bandgap in semiconductors. *Contemp. Phys.* 28, 59–68. doi:10.1080/00107518708211040

Hu, S., Qiao, P., Fu, Y., Li, F., Xiao, X., Zhao, C., et al. (2019). *In-situ* platinum plasmon resonance effect prompt titanium dioxide nanocube photocatalytic hydrogen evolution. *Chem. Asian J.* 14, 592–596. doi:10.1002/asia.201801893

Hu, X. J., Zhu, B. L., Dong, J. X., Zhao, W. L., Wang, S. R., Zhang, S. M., et al. (2012). The influence of platinum on the structure and photocatalytic performance of hydrogen titanate nanotubes. *J. Chil. Chem. Soc.* 57, 1008–1011. doi:10.4067/s0717-97072012000100012

Huang, B. S., Su, E. C., Huang, Y. Y., and Tseng, H. H. (2018). Tailored Pt/TiO_2 photocatalyst with controllable phase prepared via a modified sol-gel process for dye degradation. *J. Nanosci. Nanotechnol.* 18, 2235–2240. doi:10.1166/jnn.2018.14237

Huang, H. C., Wang, J., Li, J., Zhao, Y., Dong, X. X., Chen, J., et al. (2020). Surface modification strategy for promoting the performance of non-noble metal single-atom catalysts in low-temperature CO oxidation. *ACS Appl. Mat. Interfaces* 12, 19457–19466. doi:10.1021/acsami.0c00811

Hufschmidt, D., Bahemann, D., Testa, J. J., Emilio, C. A., and Litter, M. I. (2002). Enhancement of the photocatalytic activity of various TiO_2 materials by platinisation. *J. Photochem. Photobiol. A Chem.* 148, 223–231. doi:10.1016/s1010-6030(02)00048-5

Ibhadon, A. O., and Fitzpatrick, P. (2013). Heterogeneous photocatalysis: Recent advances and applications. *Catalysts* 3, 189–218. doi:10.3390/catal3010189

Ihnatiuk, D., Tossi, C., Tittonen, I., and Linnik, O. (2020). Effect of synthesis conditions of nitrogen and platinum Co-doped titania films on the photocatalytic performance under simulated solar light. *Catalysts* 10, 1074. doi:10.3390/catal10091074

Jakob, M., Levanon, H., and Kamat, P. V. (2003). Charge distribution between UV-irradiated TiO_2 and gold nanoparticles: Determination of shift in the Fermi level. *Nano Lett.* 3, 353–358. doi:10.1021/nl0340071

Janczarek, M., Kowalska, E., and Ohtani, B. (2016). Decahedral-shaped anatase titania photocatalyst particles: Synthesis in a newly developed coaxial-flow gas-phase reactor. *Chem. Eng. J.* 289, 502–512. doi:10.1016/j.cej.2016.01.008

Janczarek, M., Wei, Z., Endo, M., Ohtani, B., and Kowalska, E. (2017). Silver- and copper-modified decahedral anatase tiania particles as visible light-responsive plasmonic photocatalyst. *J. Photonics Energy* 7, 1–16. doi:10.1117/1.JPE.7.012008

Janczarek, M., Zielinska-Jurek, A., Markowska, I., and Hupka, J. (2015). Transparent thin films of Cu-TiO_2 with visible light photocatalytic activity. *Photochem. Photobiol. Sci.* 14, 591–596. doi:10.1039/c4pp00271g

Khalil, L. B., Mourad, W. E., and Rophael, M. W. (1998). Photocatalytic reduction of environmental pollutant Cr(VI) over some semiconductors under UV/visible

light illumination. *Appl. Catal. B Environ.* 17, 267–273. doi:10.1016/s0926-3373(98)00020-4

Khan, M. A., Akhtar, M. S., Woo, S. I., and Yang, O. B. (2008). Enhanced photoresponse under visible light in Pt ionized TiO_2 nanotube for the photocatalytic splitting of water. *Catal. Commun.* 10, 1–5. doi:10.1016/j.catcom.2008.01.018

Khan, M., Yi, Z., Gul, S. R., Wang, Y. Z., and Fawad, U. (2017). Visible-light-active silver-vanadium-codoped TiO_2 with improved photocatalytic activity. *J. Mat. Sci.* 52, 5634–5640. doi:10.1007/s10853-017-0798-y

Khnayzer, R. S., Thompson, L. B., Zamkov, M., Ardo, S., Meyer, G. J., Murphy, C. J., et al. (2012). Photocatalytic hydrogen production at titania-supported Pt nanoclusters that are derived from surface-anchored molecular precursors. *J. Phys. Chem. C* 116, 1429–1438. doi:10.1021/jp206943s

Kisch, H., Burgeth, G., and Macyk, W. (2004). Visible light photocatalysis by a titania transition metal complex. *Adv. Inorg. Chem.* 56, 241–259. doi:10.1016/s0898-8838(04)56008-7

Kisch, H. (2011). Visible light photocatalysis by metal halide complexes containing titania as a semiconductor ligand. *Adv. Inorg. Chem. Inorg. Photochem.* 63, 371–393. doi:10.1016/B978-0-12-385904-4.00002-0

Klein, C. A. (1968). Bandgap dependence and related features of radiation ionization energies in semiconductors. *J. Appl. Phys.* 39, 2029-+.2038. doi:10.1063/1.1656484

Komanoya, T., Suzuki, A., Nakajima, K., Kitano, M., Kamata, K., and Hara, M. (2016). A combined catalyst of Pt nanoparticles and TiO_2 with water-tolerant lewis acid sites for one-pot conversion of glycerol to lactic acid. *Chemcatchem* 8, 1094–1099. doi:10.1002/cctc.201501197

Kon, K., Toyao, T., Onodera, W., Siddiki, S. M. a. H., and Shimizu, K. (2017). Hydrodeoxygenation of fatty acids, triglycerides, and ketones to liquid alkanes by a Pt-MoO_x/TiO_2 catalyst. *Chemcatchem* 9, 2822–2827. doi:10.1002/cctc.201700219

Korosi, L., Bognar, B., Czegeny, G., and Lauciello, S. (2022). Phase-selective synthesis of anatase and rutile TiO2 nanocrystals and their impacts on grapevine leaves: Accumulation of mineral nutrients and triggering the plant defense. *Nanomaterials* 12, 483. doi:10.3390/nano12030483

Kowalska, E., Abe, R., and Ohtani, B. (2009). Visible light-induced photocatalytic reaction of gold-modified titanium(IV) oxide particles: Action spectrum analysis. *Chem. Commun.*, 241–243. doi:10.1039/b815679d

Kowalska, E., Mahaney, O. O. P., Abe, R., and Ohtani, B. (2010). Visible-light-induced photocatalysis through surface plasmon excitation of gold on titania surfaces. *Phys. Chem. Chem. Phys.* 12, 2344–2355. doi:10.1039/b917399d

Kowalska, E., Remita, H., Colbeau-Justin, C., Hupka, J., and Belloni, J. (2008). Modification of titanium dioxide with platinum ions and clusters: Application in photocatalysis. *J. Phys. Chem. C* 2, 1124–1131. doi:10.1021/jp077466p

Kowalska, E., Yoshiiri, K., Wei, Z., Zheng, S., Kastl, E., Remita, H., et al. (2015). Hybrid photocatalysts composed of titania modified with plasmonic nanoparticles and ruthenium complexes for decomposition of organic compounds. *Appl. Catal. B Environ.* 178, 133–143. doi:10.1016/j.apcatb.2014.10.003

Kozlova, E. A., Lyubina, T. P., Nasalevich, M. A., Vorontsov, A. V., Miller, A. V., Kaichev, V. V., et al. (2011). Influence of the method of platinum deposition on activity and stability of Pt/TiO_2 photocatalysts in the photocatalytic oxidation of dimethyl methylphosphonate. *Catal. Commun.* 12, 597–601. doi:10.1016/j.catcom.2010.12.007

Kraeutler, B., and Bard, A. J. (1978). Heterogeneous photocatalytic preparation of supported catalysts. Photodeposition of platinum on TiO_2 powder and other substrates. *J. Am. Chem. Soc.* 100, 4317–4318. doi:10.1021/ja00481a059

Lee, C., Kim, I., Shin, H., Kim, S., and Cho, J. (2009). Nonvolatile resistive switching memory properties of thermally annealed titania precursor/polyelectrolyte multilayers. *Langmuir* 25, 11276–11281. doi:10.1021/la902649y

Lee, J., and Choi, W. (2005). Photocatalytic reactivity of surface platinized TiO_2: Substrate specificity and the effect of Pt oxidation state. *J. Phys. Chem. B* 109, 7399–7406. doi:10.1021/jp044425+

Lee, J. H., Kim, T., Kim, E. R., Cho, E. B., and Jung, S. C. (2021). Microwave-assisted synthesis of various Cu2O/Cu/TiO2 and CuxS/TiO2 composite nanoparticles towards visible-light photocatalytic applications. *Mater. Chem. Phys.* 259, 123986. doi:10.1016/j.matchemphys.2020.123986

Li, J., E, Y., Lian, L., and Ma, W. (2013). Visible light induced dye-sensitized photocatalytic hydrogen production over platinized TiO_2 derived from decomposition of platinum complex precursor. *Int. J. Hydrogen Energy* 38, 10746–10753. doi:10.1016/j.ijhydene.2013.02.121

Li, Q., Wang, K., Zhang, S., Zhang, M., Yang, J., and Jin, Z. (2006). Effect of photocatalytic activity of CO oxidation on Pt/TiO_2 by strong interaction between Pt and TiO_2 under oxidizing atmosphere. *J. Mol. Catal. A Chem.* 258, 83–88. doi:10.1016/j.molcata.2006.05.030

Lian, J., Chai, Y., Qi, Y., Guo, X., Guan, N., Li, L., et al. (2020). Unexpectedly selective hydrogenation of phenylacetylene to styrene on titania supported platinum photocatalyst under 385 nm monochromatic light irradiation. *Chin. J. Catal.* 41, 598–603. doi:10.1016/s1872-2067(19)63453-4

López, C. R., Melián, E. P., Ortega Méndez, J. A., Santiago, D. E., Doña Rodríguez, J. M., and González Díaz, O. (2015). Comparative study of alcohols as sacrificial agents in H_2 production by heterogeneous photocatalysis using Pt/TiO2 catalysts. *J. Photochem. Photobiol. A Chem.* 312, 45–54. doi:10.1016/j.jphotochem.2015.07.005

López-Tenllado, F. J., Estévez, R., Hidalgo-Carrillo, J., López-Fernández, S., Urbano, F. J., and Marinas, A. (2022). Hydrogen photo-production from glycerol on platinum, gold and silver-modified TiO_2-USY62 catalysts. *Catal. Today* 390-391, 92–98. doi:10.1016/j.cattod.2021.11.043

Luo, X. F., Lai, W. C., and Liu, X. Y. (2021). Multiple modification of titanium dioxide to enhance its photocatalytic performance. *ChemistrySelect* 6, 39–46. doi:10.1002/slct.202003916

Ma, C. M., Lee, Y. W., Hong, G. B., Su, T. L., Shie, J. L., and Chang, C. T. (2011). Effect of platinum on the photocatalytic degradation of chlorinated organic compound. *J. Environ. Sci.* 23, 687–692. doi:10.1016/s1001-0742(10)60480-9

Macyk, W., Burgeth, G., and Kisch, H. (2003). Photoelectrochemical properties of platinum(IV) chloride surface modified TiO_2. *Photochem. Photobiol. Sci.* 2, 322–328. doi:10.1039/b211583b

Macyk, W., and Kisch, H. (2001). Photosensitization of crystalline and amorphous titanium dioxide by platinum(IV) chloride surface complexes. *Chem. (Basel).* 7, 1862–1867. doi:10.1002/1521-3765(20010504)7:9<1862::aid-chem1862>3.0.co;2-g

Macyk, W., Szacilowski, K., Stochel, G., Buchalska, M., Kuncewicz, J., and Labuz, P. (2010). Titanium(IV) complexes as direct TiO_2 photosensitizers. *Coord. Chem. Rev.* 254, 2687–2701. doi:10.1016/j.ccr.2009.12.037

Madhusudan Reddy, K., Manorama, S. V., and Ramachandra Reddy, A. (2003). Bandgap studies on anatase titanium dioxide nanoparticles. *Mater. Chem. Phys.* 78, 239–245. doi:10.1016/s0254-0584(02)00343-7

Makouangou, R. M., Murzin, D. Y., Dauscher, A. E., and Touroude, R. A. (1994). Kinetics of crotonaldehyde hydrogenation over a titania-supported platinum catalyst. *Ind. Eng. Chem. Res.* 33, 1881–1888. doi:10.1021/ie00032a001

Marci, G., and Palmisano, L. (2019). *Heterogeneous photocatalysis : Relationships with heterogeneous catalysis and perspectives*. Amsterdam, Netherlands: Elsevier.

Mitoraj, D., Janczyk, A., Strus, M., Kisch, H., Stochel, G., Heczko, P. B., et al. (2007). Visible light inactivation of bacteria and fungi by modified titanium dioxide. *Photochem. Photobiol. Sci.* 6, 642–648. doi:10.1039/b617043a

Momeni, M. M., and Jalili, P. (2022). Developing an efficient approach for preparation of high-performance visible-light assisted ethanol electro-oxidation materials based on Pd, Pt and Pd-Pt nanoparticles supported on iron doped titania nanotube films. *Int. J. Hydrogen Energy* 47, 6789–6798. doi:10.1016/j.ijhydene.2021.12.016

Mukherjee, S., Libisch, F., Large, N., Neumann, O., Brown, L. V., Cheng, J., et al. (2013). Hot electrons do the impossible: Plasmon-induced dissociation of H_2 on Au. *Nano Lett.* 13, 240–247. doi:10.1021/nl303940z

Murcia, J. J., Hidalgo, M. C., Navio, J. A., Arana, J., and Dona-Rodriguez, J. M. (2014). Correlation study between photo-degradation and surface adsorption properties of phenol and methyl orange on TiO2 Vs platinum-supported TiO2. *Appl. Catal. B Environ.* 150, 107–115. doi:10.1016/j.apcatb.2013.12.010

Nakajima, H., Tanigaki, T., Toriyama, T., Yamamoto, M., Tanaka, H., and Murakami, Y. (2021). Electrostatic potential measurement at the Pt/TiO2 interface using electron holography. *J. Appl. Phys.* 129, 174304. doi:10.1063/5.0046501

Nam, W., and Han, G. Y. (2007). Preparation and characterization of anodized Pt-TiO_2 nanotube arrays for water splitting. *J. Chem. Eng. Jpn.* 40, 266–269. doi:10.1252/jcej.40.266

Nishimoto, S. I., Ohtani, B., and Kagiya, T. (1985). Photocatalytic dehydrogenation of aliphatic-alcohols by aqueous suspensions of platinized titanium-dioxide. *J. Chem. Soc. Faraday Trans. 1.* 81, 2467–2474. doi:10.1039/f19858102467

Ohno, T., Mitsui, T., and Matsumura, M. (2003). Photocatalytic activity of S-doped TiO_2 photocatalyst under visible light. *Chem. Lett.* 32, 364–365. doi:10.1246/cl.2003.364

Ohtani, B., Iwai, K., Nishimoto, S.-I., and Sato, S. (1997). Role of platinum deposits on titanium(IV) oxide particles: Structural and kinetic analyses of photocatalytic reaction in aqueous alcohol and amino acid solutions. *J. Phys. Chem. B* 101, 3349–3359. doi:10.1021/jp962060q

Ohtani, B. (2010). Photocatalysis A to Z-What we know and what we do not know in a scientific sense. *J. Photochem. Photobiol. C Photochem. Rev.* 11, 157–178. doi:10.1016/j.jphotochemrev.2011.02.001

Ohtani, B., Prieto-Mahaney, O. O., Li, D., and Abe, R. (2010). What is degussa (Evonik) P25? Crystalline composition analysis, reconstruction from isolated pure particles and photocatalytic activity test. *J. Photochem. Photobiol. A Chem.* 216, 179–182. doi:10.1016/j.jphotochem.2010.07.024

Panayotov, D. A., Desario, P. A., Pietron, J. J., Brintlinger, T. H., Szymczak, L. C., Rolison, D. R., et al. (2013). Ultraviolet and visible Photochemistry of methanol at 3D mesoporous networks: TiO_2 and Au-TiO_2. *J. Phys. Chem. C* 117, 15035–15049. doi:10.1021/jp312583w

Paszkiewicz, O., Wang, K., Rakoczy, R., Kordas, M., Leniec, G., Kowalska, E., et al. (2022). Antimicrobial properties of pristine and Pt-modified titania P25 in rotating magnetic field conditions. *Chem. Eng. Process. - Process Intensif.* 178, 109010. doi:10.1016/j.cep.2022.109010

Pichat, P., Herrmann, J. M., Disdier, J., Courbon, H., and Mozzanega, M. N. (1981). Photocatalytic hydrogen production from aliphatic alcohols over a bifunctional platinum on titanium dioxide catalyst. *Nouv. J. Chim.* 5, 627–636.

Pichat, P., Mozzanega, M. N., Disdier, J., and Herrmann, J. M. (1982). Platinum content and temperature effects on the photocatalytic hydrogen production from aliphatic alcohols over platinum/titanium dioxide. *Nouv. J. Chim.* 6, 559–564.

Pichat, P. (2013). *Photocatalysis and water purification*. Weinheim Chichester: Wiley-VCH, John Wiley distributor.

Qin, S., Denisov, N., Will, J., Kolarik, J., Spiecker, E., and Schmuki, P. (2022). A few Pt single atoms are responsible for the overall Co-catalytic activity in Pt/TiO_2 photocatalytic H_2 generation. *Sol. RRL* 6, 2101026. doi:10.1002/solr.202101026

Raja-Mogan, T., Ohtani, B., and Kowalska, E. (2020). Photonic crystals for plasmonic photocatalysis. *Catalysts* 10, 827. doi:10.3390/catal10080827

Renz, C. (1921). Lichtreaktionen der Oxyde des Titans, Cers und der Erdsäuren. *Helv. Chim. Acta* 4, 961–968. doi:10.1002/hlca.192100401101

Rosario, A. V., and Pereira, E. C. (2014). The role of Pt addition on the photocatalytic activity of TiO_2 nanoparticles: The limit between doping and metallization. *Appl. Catal. B Environ.* 144, 840–845. doi:10.1016/j.apcatb.2013.07.029

Salehi-Abar, P., and Kazempour, A. (2017). Effect of N and F doping on the electronic properties of rutile TiO_2 quantum dot solar cells: A first principle study. *Chem. Phys. Lett.* 673, 56–61. doi:10.1016/j.cplett.2017.02.001

Samad, J. E., Hoenig, S., and Regalbuto, J. R. (2015). Synthesis of platinum catalysts over thick slurries of oxide supports by strong electrostatic adsorption. *ChemCatChem* 7, 3460–3463. doi:10.1002/cctc.201500595

Selvam, K., and Swaminathan, M. (2011). Novel redox photocatalyst Pt-TiO2 for the synthesis of 2-methylquinolines from nitroarenes. *Bull. Chem. Soc. Jpn.* 84, 953–959. doi:10.1246/bcsj.20110091

Senevirathna, M. K. I., Pitigala, P. K. D. D. P., and Tennakone, K. (2006). High quantum efficiency Pt/TiO_2 catalyst for sacrificial water reduction. *Sol. Energy Mater. Sol. Cells* 90, 2918–2923. doi:10.1016/j.solmat.2006.05.004

Shahgaldi, S., and Hamelin, J. (2015). The effect of low platinum loading on the efficiency of PEMFC's electrocatalysts supported on TiO_2-Nb, and SnO_2-Nb: An experimental comparison between active and stable conditions. *Energy Convers. Manag.* 103, 681–690. doi:10.1016/j.enconman.2015.06.050

Shehab, M. A., Sharma, N., Valsesia, A., Karacs, G., Kristaly, F., Koos, T., et al. (2022). Preparation and photocatalytic performance of TiO_2 nanowire-based self-supported hybrid membranes. *Molecules* 27, 2951. doi:10.3390/molecules27092951

Shinde, Y., Wadhai, S., Ponkshe, A., Kapoor, S., and Thakur, P. (2018). Decoration of Pt on the metal free RGO-TiO_2 composite photocatalyst for the enhanced photocatalytic hydrogen evolution and photocatalytic degradation of pharmaceutical pollutant β blocker. *Int. J. Hydrogen Energy* 43, 4015–4027. doi:10.1016/j.ijhydene.2017.10.089

Shiraishi, Y., Sugano, Y., Tanaka, S., and Hirai, T. (2010). One-pot synthesis of benzimidazoles by simultaneous photocatalytic and catalytic reactions on Pt@TiO_2 nanoparticles. *Angew. Chem. Int. Ed. Engl.* 49, 1700–1704. doi:10.1002/ange.200906573

Shukla, G., and Angappane, S. (2022). Dimensional constraints favour high temperature anatase phase stability in TiO2 nanorods. *Appl. Surf. Sci.* 577, 151874. doi:10.1016/j.apsusc.2021.151874

Song, Y. Y., Gao, Z. D., Lee, K., and Schmuki, P. (2011). A self-cleaning nonenzymatic glucose detection system based on titania nanotube arrays modified with platinum nanoparticles. *Electrochem. Commun.* 13, 1217–1220. doi:10.1016/j.elecom.2011.08.040

Strunk, J. (2021). *Heterogeneous photocatalysis : Fundamental processes and applications in energy conversion and depollution*. Weinheim, Germany: Wiley VCH.

Subramanian, V., Wolf, E. E., and Kamat, P. V. (2003). Influence of metal/metal ion concentration on the photocatalytic activity of TiO2-Au composite nanoparticles. *Langmuir* 19, 469–474. doi:10.1021/la026478t

Sugawa, K., Tahara, H., Yamashita, A., Otsuki, J., Sagara, T., Harumoto, T., et al. (2015). Refractive index susceptibility of the plasmonic palladium nanoparticle: Potential as the third plasmonic sensing material. *ACS Nano* 9, 1895–1904. doi:10.1021/nn506800a

Sun, S. C., Zhang, J. J., Gao, P., Wang, Y., Li, X. B., Wu, T. T., et al. (2017). Full visible-light absorption of TiO_2 nanotubes induced by anionic S-2(2-) doping and their greatly enhanced photocatalytic hydrogen production abilities. *Appl. Catal. B Environ.* 206, 168–174. doi:10.1016/j.apcatb.2017.01.027

Sun, X. T., Yan, L. T., Xu, R. X., Xu, M. Y., and Zhu, Y. Y. (2019). Surface modification of TiO_2 with polydopamine and its effect on photocatalytic degradation mechanism. *Colloids Surfaces A Physicochem. Eng. Aspects* 570, 199–209. doi:10.1016/j.colsurfa.2019.03.018

Tachikawa, T., Yamashita, S., and Majima, T. (2011). Evidence for crystal-face-dependent TiO_2 photocatalysis from single-molecule imaging and kinetic analysis. *J. Am. Chem. Soc.* 133, 7197–7204. doi:10.1021/ja201415j

Takakusagi, S., Ogawa, T., Uehara, H., Ariga, H., Shimizu, K., and Asakura, K. (2014). Electrodeposition study on a single-crystal titanium dioxide electrode: Platinum on a niobium-doped titanium dioxide(110) electrode. *Chem. Lett.* 43, 1797–1799. doi:10.1246/cl.140706

Takanabe, K. (2017). Photocatalytic water splitting: Quantitative approaches toward photocatalyst by design. *ACS Catal.* 7, 8006–8022. doi:10.1021/acscatal.7b02662

Tian, Y., and Tatsuma, T. (2005). Mechanisms and applications of plasmon-induced charge separation at TiO_2 films loaded with gold nanoparticles. *J. Am. Chem. Soc.* 127, 7632–7637. doi:10.1021/ja042192u

Ting, C. C., Liu, C. H., Tai, C. Y., Hsu, S. C., Chao, C. S., and Pan, F. M. (2015). The size effect of titania-supported Pt nanoparticles on the electrocatalytic activity towards methanol oxidation reaction primarily via the bifunctional mechanism. *J. Power Sources* 280, 166–172. doi:10.1016/j.jpowsour.2015.01.081

Touchy, A. S., Siddiki, S. M. a. H., Onodera, W., Kona, K., and Shimizu, K. (2016). Hydrodeoxygenation of sulfoxides to sulfides by a Pt and MoOx co-loaded TiO_2 catalyst. *Green Chem.* 18, 2554–2560. doi:10.1039/c5gc02806j

Vaiano, V., Lara, M. A., Iervolino, G., Matarangolo, M., Navio, J. A., and Hidalgo, M. C. (2018). Photocatalytic H2 production from glycerol aqueous solutions over fluorinated Pt-TiO_2 with high {001} facet exposure. *J. Photochem. Photobiol. A Chem.* 365, 52–59. doi:10.1016/j.jphotochem.2018.07.032

Vasilchenko, D., Topchiyan, P., Tsygankova, A., Asanova, T., Kolesov, B., Bukhtiyarov, A., et al. (2020). Photoinduced deposition of platinum from $(Bu_4N)_2[Pt(NO_3)_6]$ for a low Pt-loading Pt/TiO2 hydrogen photogeneration catalyst. *ACS Appl. Mat. Interfaces* 12, 48631–48641. doi:10.1021/acsami.0c14361

Verbruggen, S. W. (2015). TiO_2 photocatalysis for the degradation of pollutants in gas phase: From morphological design to plasmonic enhancement. *J. Photochem. Photobiol. C Photochem. Rev.* 24, 64–82. doi:10.1016/j.jphotochemrev.2015.07.001

Verma, P., Yuan, K., Kuwahara, Y., Mori, K., and Yamashita, H. (2018). Enhancement of plasmonic activity by Pt/Ag bimetallic nanocatalyst supported on mesoporous silica in the hydrogen production from hydrogen storage material. *Appl. Catal. B Environ.* 223, 10–15. doi:10.1016/j.apcatb.2017.05.017

Villani, K., Vermandel, W., Smets, K., Liang, D., Van Tendeloo, G., and Martens, J. A. (2006). Platinum particle size and support effects in NO_x mediated carbon oxidation over platinum catalysts. *Environ. Sci. Technol.* 40, 2727–2733. doi:10.1021/es051871h

Wang, K. L., Wei, Z. S., Ohtani, B., and Kowalska, E. (2018). Interparticle electron transfer in methanol dehydrogenation on platinum-loaded titania particles prepared from P25. *Catal. Today* 303, 327–333. doi:10.1016/j.cattod.2017.08.046

Wang, K., Wei, Z., Colbeau-Justin, C., Nitta, A., and Kowalska, E. (2022). P25 and its components - electronic properties and photocatalytic activities. *Surfaces Interfaces* 31, 102057. doi:10.1016/j.surfin.2022.102057

Wang, L. J., Zhang, X., Gao, H. Q., Hu, J. H., Mao, J., Liang, C. H., et al. (2016). 3D CuO network supported TiO2 nanosheets with applications for energy storage and water splitting. *Sci. Adv. Mat.* 8, 1256–1262. doi:10.1166/sam.2016.2714

Wang, T. M., Chen, Y. X., Tong, M. H., Lin, S. W., Zhou, J. W., Jiang, X., et al. (2022). Self-organized TiO2 nanotube Arrays with controllable geometric parameters for highly efficient PEC water splitting. *Chin. J. Struct. Chem.* 41, 2202159–2202167. doi:10.14102/j.cnki.0254-5861.2011-3280

Wei, Z., Endo, M., Wang, K., Charbit, E., Markowska-Szczupak, A., Ohtani, B., et al. (2017a). Noble metal-modified octahedral anatase titania particles with enhanced activity for decomposition of chemical and microbiological pollutants. *Chem. Eng. J.* 318, 121–134. doi:10.1016/j.cej.2016.05.138

Wei, Z., Janczarek, M., Endo, M., Wang, K. L., Balcytis, A., Nitta, A., et al. (2018). Noble metal-modified faceted anatase titania photocatalysts: Octahedron versus decahedron. *Appl. Catal. B Environ.* 237, 574–587. doi:10.1016/j.apcatb.2018.06.027

Wei, Z., Janczarek, M., Wang, K., Zheng, S., and Kowalska, E. (2020). Morphology-governed performance of plasmonic photocatalysts. *Catalysts* 10, 1070. doi:10.3390/catal10091070

Wei, Z., Rosa, L., Wang, K., Endo, M., Juodkazi, S., Ohtani, B., et al. (2017b). Size-controlled gold nanoparticles on octahedral anatase particles as efficient plasmonic photocatalyst. *Appl. Catal. B Environ.* 206, 393–405. doi:10.1016/j.apcatb.2017.01.043

Wei, Z. S., Endo-Kimura, M., Wang, K. L., Colbeau-Justin, C., and Kowalska, E. (2019). Influence of semiconductor morphology on photocatalytic activity of plasmonic photocatalysts: Titanate nanowires and octahedral anatase nanoparticles. *Nanomaterials* 9, 1447. doi:10.3390/nano9101447

Wei, Z. S., Kowalska, E., and Ohtani, B. (2014). Enhanced photocatalytic activity by particle morphology: Preparation, characterization, and photocatalytic activities of octahedral anatase titania particles. *Chem. Lett.* 43, 346–348. doi:10.1246/cl.130985

Wilson, B. A. (1981). Super-bandgap radiation in amorphous-semiconductors. *Bull. Am. Phys. Soc.* 26, 387.

Wu, T. X., Liu, G. M., Zhao, J. C., Hidaka, H., and Serpone, N. (1998). Photoassisted degradation of dye pollutants. V. Self-photosensitized oxidative transformation of Rhodamine B under visible light irradiation in aqueous TiO2 dispersions. *J. Phys. Chem. B* 102, 5845–5851. doi:10.1021/jp980922c

Yoshiiri, K., Karabiyik, B., Wang, K., Wei, Z., Colbeau-Justin, C., and Kowalska, E. (2022). The property-governed activity of silver-modified titania photocatalysts: The influence of titania matrix. *J. Chem. Phys.* 156, 244706. doi:10.1063/5.0097762

Yoshimura, N., Kobayashi, A., Yoshida, M., and Kato, M. (2020). Enhancement of photocatalytic activity for hydrogen production by surface modification of Pt-TiO2 nanoparticles with a double layer of photosensitizers. *Chem. Eur. J.* 26, 16939–16946. doi:10.1002/chem.202003990

Yurdakal, S., Tek, B. S., Degirmenci, C., and Palmisano, G. (2017). Selective photocatalytic oxidation of aromatic alcohols in solar-irradiated aqueous suspensions of Pt, Au, Pd and Ag loaded TiO2 catalysts. *Catal. Today* 281, 53–59. doi:10.1016/j.cattod.2016.05.054

Zaleska, A. (2008). Doped-TiO_2: A review. *Recent Pat. Eng.* 2, 157–164. doi:10.2174/187221208786306289

Zang, L., Macyk, W., Lange, C., Maier, W. F., Antonius, C., Meissner, D., et al. (2000). Visible-light detoxification and charge generation by transition metal chloride modified titania. *Chem. Eur. J.* 6, 379–384. doi:10.1002/(sici)1521-3765(20000117)6:2<379::aid-chem379>3.0.co;2-z

Zener, B., Matoh, L., Carraro, G., Miljevic, B., and Korosec, R. C. (2018). Sulfur-nitrogen- and platinum-doped titania thin films with high catalytic efficiency under visible-light illumination. *Beilstein J. Nanotechnol.* 9, 1629–1640. doi:10.3762/bjnano.9.155

Zhao, W., Chen, C. C., Li, X. Z., Zhao, J. C., Hidaka, H., and Serpone, N. (2002). Photodegradation of sulforhodamine-B dye in platinized titania dispersions under visible light irradiation: Influence of platinum as a functional co-catalyst. *J. Phys. Chem. B* 106, 5022–5028. doi:10.1021/jp020205p

Zheng, X.-J., Wei, L.-F., Zhang, Z.-H., Jiang, Q.-J., Wei, Y.-J., Xie, B., et al. (2009). Research on photocatalytic H_2 production from acetic acid solution by Pt/TiO_2 nanoparticles under UV irradiation. *Int. J. Hydrogen Energy* 34, 9033–9041. doi:10.1016/j.ijhydene.2009.09.019

Zhu, Z., and Wu, R. J. (2015). The degradation of formaldehyde using a Pt@TiO_2 nanoparticles in presence of visible light irradiation at room temperature. *J. Taiwan Inst. Chem. Eng.* 50, 276–281. doi:10.1016/j.jtice.2014.12.022

Zielinska-Jurek, A., Wei, Z. S., Janczarek, M., Wysocka, I., and Kowalska, E. (2019). Size-controlled synthesis of Pt particles on TiO_2 surface: Physicochemical characteristic and photocatalytic activity. *Catalysts* 9, 940. doi:10.3390/catal9110940

Zielinska-Jurek, A., Wei, Z., Wysocka, I., Szweda, P., and Kowalska, E. (2015). The effect of nanoparticles size on photocatalytic and antimicrobial properties of Ag-Pt/TiO_2 photocatalysts. *Appl. Surf. Sci.* 353, 317–325. doi:10.1016/j.apsusc.2015.06.065

frontiers | Frontiers in Chemistry

TYPE Original Research
PUBLISHED 28 October 2022
DOI 10.3389/fchem.2022.996604

Check for updates

OPEN ACCESS

EDITED BY
Jianrong Xu,
Shanghai University of Traditional Chinese Medicine, China

REVIEWED BY
Ping Yu,
Shanghai Jiao Tong University, China
Changlin Liu,
Central China Normal University, China

*CORRESPONDENCE
Hongli Wu,
Hongli.wu@unthsc.edu
Kayla N. Green,
kayla.green@tcu.edu

†These authors have contributed equally to this work and share senior authorship

SPECIALTY SECTION
This article was submitted to Chemical Biology, a section of the journal Frontiers in Chemistry

RECEIVED 18 July 2022
ACCEPTED 05 October 2022
PUBLISHED 28 October 2022

CITATION
Zhang J, Yu Y, Mekhail MA, Wu H and Green KN (2022), A macrocyclic molecule with multiple antioxidative activities protects the lens from oxidative damage.
Front. Chem. 10:996604.
doi: 10.3389/fchem.2022.996604

COPYRIGHT
© 2022 Zhang, Yu, Mekhail, Wu and Green. This is an open-access article distributed under the terms of the Creative Commons Attribution License (CC BY). The use, distribution or reproduction in other forums is permitted, provided the original author(s) and the copyright owner(s) are credited and that the original publication in this journal is cited, in accordance with accepted academic practice. No use, distribution or reproduction is permitted which does not comply with these terms.

A macrocyclic molecule with multiple antioxidative activities protects the lens from oxidative damage

Jinmin Zhang[1], Yu Yu[1], Magy A. Mekhail[2], Hongli Wu[1,3*†] and Kayla N. Green[2*†]

[1]Pharmaceutical Sciences, College of Pharmacy, University of North Texas Health Science Center, Fort Worth, TX, United States, [2]Department of Chemistry and Biochemistry, Texas Christian University, Fort Worth, TX, United States, [3]North Texas Eye Research Institute, University of North Texas Health Science Center, Fort Worth, TX, United States

Growing evidence links oxidative stress to the development of a cataract and other diseases of the eye. Treatments for lens-derived diseases are still elusive outside of the standard surgical interventions, which still carry risks today. Therefore, a potential drug molecule $^{OH}Py_2N_2$ was explored for the ability to target multiple components of oxidative stress in the lens to prevent cataract formation. Several pathways were identified. Here we show that the $^{OH}Py_2N_2$ molecule activates innate catalytic mechanisms in primary lens epithelial cells to prevent damage induced by oxidative stress. This protection was linked to the upregulation of Nuclear factor erythroid-2-related factor 2 and downstream antioxidant enzyme for glutathione-dependent glutaredoxins, based on Western Blot methods. The anti-ferroptotic potential was established by showing that $^{OH}Py_2N_2$ increases levels of glutathione peroxidase, decreases lipid peroxidation, and readily binds iron (II) and (III). The bioenergetics pathway, which has been shown to be negatively impacted in many diseases involving oxidative stress, was also enhanced as evidence by increased levels of Adenosine triphosphate product when the lens epithelial cells were co-incubated with $^{OH}Py_2N_2$. Lastly, $^{OH}Py_2N_2$ was also found to prevent oxidative stress-induced lens opacity in an *ex vivo* organ culture model. Overall, these results show that there are multiple pathways that the $^{OH}Py_2N_2$ has the ability to impact to promote natural mechanisms within cells to protect against chronic oxidative stress in the eye.

KEYWORDS

$^{OH}Py_2N_2$, lens, oxidative stress, Nrf2, glutaredoxin, ferroptosis

Introduction

Cataracts are the most common cause of vision loss in individuals over the age of 60 as well as the leading cause of blindness in the world. According to the latest assessment from the World Health Organization, more than half of the cases of blindness worldwide are attributed to cataracts (Organization, 2019). Moreover, the trend toward an increased

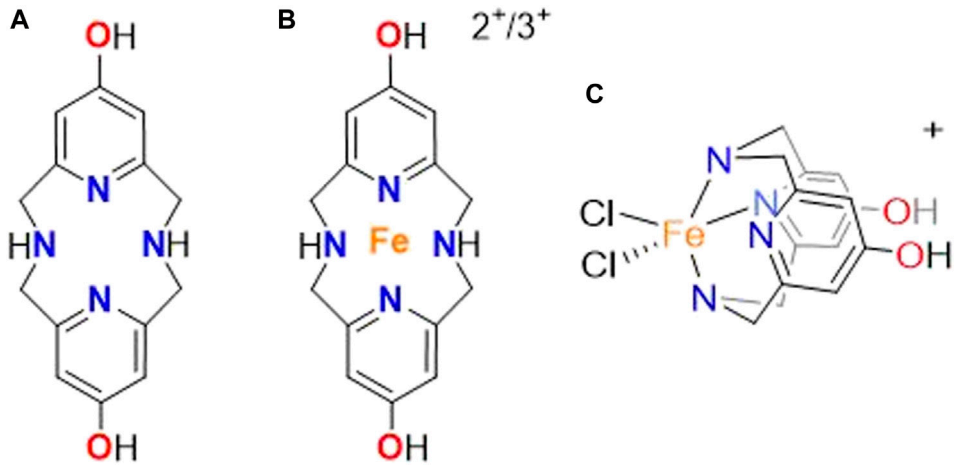


FIGURE 1
Structure of the **(A)** $^{OH}Py_2N_2$ molecule along with the connectivity of the **(B)** iron (II) and (III) complex and **(C)** orientation of the iron in the $^{OH}Py_2N_2$ ligand based on UV-vis studies.

aging population has built global attention to reducing the prevalence of cataract. Currently, the only treatment option to correct a cataract patient's vision is surgery. Though cataract surgery is a well-established procedure, complications may still arise, especially in patients of advanced age. Surgery-related complications such as posterior capsular opacity, intraocular lens dislocation, eye inflammation, photopsia, ocular hypertension, and macular edema may cause irreversible blindness (Chan et al., 2010). Therefore, there is still a great need to identify non-surgical therapeutic options with benefits outweighing the risks of surgery.

Oxidative stress encompasses a range of deficiencies in the balance between pro-oxidant and antioxidant regulatory pathways and the related damage to biological structures (Naik et al., 2014; Czerska et al., 2015). The eye is a prominent target of oxidative stress. It is continuously exposed to various oxidative conditions, such as photo-oxidation, ultraviolet (UV) radiation, smoke, and various forms of pollutants. Thus, oxidative stress has been associated with many ocular disorders, notably age-related macular degeneration (AMD) and cataracts (Spector, 1995; Beatty et al., 2000; Lou, 2003; Yildirim et al., 2011). Chronic exposure to light from the Sun, the largest source of UV radiation in our environment, can significantly increase the risk of a cataract, particularly if the recipient is over 40 years of age (Wolff, 1994). Solar UV that penetrates the atmosphere is mainly composed of UVA (320–400 nm) and UVB (290–320 nm) radiation (Zigman, 1995). This strong UV energy induces overproduction of reactive oxygen species (ROS) that damage lens epithelial cells (LECs), disturb the energy metabolism pathways, promote insoluble protein aggregation, and eventually lead to lens opacity (Lofgren, 2017). Therefore, the need to rebalance ROS to prevent chronic disease like this in the eye continues to be a driving force for the development of new, targeting molecules and studies to understand the mechanisms of their action(s).

Creating interventions for uncontrolled ROS is challenging, but there is strong evidence that antioxidant approaches to prevent or curb disease have positive impacts and show this is a feasible approach (Pisoschi et al., 2021; Woo et al., 2014; Bosco et al., 2011; DeCensi et al., 2010; Goodson et al., 2009; Zhang, 2019; D'Souza et al., 2020; Nechuta et al., 2011; Sotgia et al., 2011; Giem et al., 1993; Fraser, 2009; Singh et al., 2003; Cooper et al., 2009; Zhang et al., 2014a; Farrawell et al., 2018; Rowe et al., 2020; Ikawa et al., 2015; Williams et al., 2016). For example, the Age Related Eye Disease Study sponsored by the National Eye Institute strongly support that high levels of antioxidant vitamins and zinc can reduce the risk of advanced AMD and its associated vision loss (Age-Related Eye Disease Study Research Group, 2001; Chew et al., 2013). Nevertheless, there remains a gap between the current understanding of oxidative stress in disease pathologies and the development of new therapeutic molecules that successfully target this etiology (Lannfelt et al., 2008; Alzheimer's Disease Facts, 2016; Jarvis, 2015; Ratner, 2015; Niedzielska et al., 2016; Doig et al., 2017; Kingwell, 2017; Crielaard et al., 2017; Patel, 2016). During drug design for a disease, therapeutics are typically targeted toward one causative agent ex: cholesterol, an enzyme, or gene. However, such an approach is complicated for diseases involving oxidative stress because the etiology of oxidative stress is multifactorial. Identification of a therapeutic agent that can target multiple antioxidant pathways or induce defense mechanisms innate to the cell could prove powerful in fighting these diseases.

As a result of the current challenges for diseases that involve oxidative stress, we designed the $^{OH}Py_2N_2$ multimodal small molecule (Figure 1) with direct targeting reactivity against ROS (Johnston et al., 2019). Several benchtop assays validated our initial hypothesis that the water soluble molecule could function as a direct antioxidant molecule. Integration of a hydroxyl substituted pyridine group within a tetra-aza macrocyclic ring generates the $^{OH}Py_2N_2$ small molecule that can readily scavenge free radicals as well as bind mis-regulated transition metal ions, halting toxic metal redox processes (Green et al., 2019; Johnston et al., 2019). Interestingly and not part of our initial design, which focused on direct reactivity with ROS, $^{OH}Py_2N_2$ showed the potential to activate cellular antioxidant defense capacity *via* activation of the Nrf2 (Nuclear factor erythroid 2-related factor 2) signaling pathway in neuronal cell culture along with low toxicity, high metabolic stability, and proving to be highly water soluble (Johnston et al., 2019). Nrf2 is a transcription factor that plays key roles in antioxidant and detoxification responses, particularly in the eye. Nrf2 activates more than 250 antioxidant enzymes and pro-survival genes (Ma, 2013). It is commonly referred to as the gatekeeper to coordinated induction of cytoprotective and antioxidant genes or master antioxidant transcriptional regulator (Kaspar et al., 2009). Increased Nrf2 activity correlates with cellular survival and protection from oxidative injury to RPE cells and pathogenic processes (Johnson et al., 2009; Zhang et al., 2014b; Cuadrado et al., 2018; Tang et al., 2018; Bahn et al., 2019; Han et al., 2019; Kitaoka et al., 2019; Sotolongo et al., 2020). Likewise, lower Nrf2 expression is associated with an increased risk or early onset of diseases of the eye (Zhao et al., 2011; von Otter et al., 2010). Therefore, activation of Nrf2 pathways has garnered significant interest as a potential target for therapeutic design. The ability for $^{OH}Py_2N_2$ to activate this pathway piqued our interest to further explore the catalytic (enzyme based) and cellular pathways that this molecule might unlock to provide protection against oxidative stress.

The recently established understanding of the direct antioxidant activity of $^{OH}Py_2N_2$ through radical and transition metal scavenging, along with preliminary results suggesting catalytic protection *via* the Nrf2 pathway prompted the present studies focused on the therapeutic potential and activation of defensive antioxidant mechanisms induced by $^{OH}Py_2N_2$ to protect against oxidative stress in the eye (Johnston et al., 2019). To explore this potential, human lens epithelial cells were exposed to conditions that model oxidative stress and showed excellent cell viability when treated with $^{OH}Py_2N_2$. The levels of Nrf2 and downstream antioxidant enzyme GSH-dependent glutaredoxins (Grx1 and Grx2), important components that protect protein thiols from oxidation, increased ATP expression, and antiferroptotic potential were then measured to elucidate the catalytic protective mechanisms initiated by $^{OH}Py_2N_2$ treatment. Lastly, $^{OH}Py_2N_2$ was also found to prevent oxidative stress-induced lens opacity in an *ex vivo* organ culture model.

Materials and methods

General methods and materials

Ligand $^{OH}Py_2N_2$ was produced as the trihydrochloride salt using previously published methods (Johnston et al., 2019). Dulbecco's modified Eagle's medium (DMEM), fetal bovine serum (FBS), gentamicin, penicillin, and 0.05% trypsin were all purchased from Thermo Fisher Scientific (Waltham, MA, United States). Hydrogen peroxide and all chemicals were obtained from Sigma Chemical Co. (St. Louis, MO, United States) unless otherwise stated. Antibodies against Grx1 (ab45953) and Grx2 (ab45953) were purchased from Abcam (Waltham, MA, United States). Nrf2 (#12721) and GPX4 (#52455) antibodies were purchased from Cell Signaling (Denver, CO, United States). CellROX Deep Red was purchased from Thermo Fisher Scientific (Waltham, MA, United States). Colorimetric cell viability kit I (WST-8) was purchased from PromoKine (Heidelberg, Baden-Württemberg, Germany).

Potentiometric methods

The concentration of the $^{OH}Py_2N_2$ ligand, as well as an estimation of the stability constant of the iron (II) complex, were determined *via* pH-potentiometric titrations. Challenges with solubility prevented a high level of accuracy in the models. A Metrohm 888 Titrando equipped with a Metrohm 6.0234.100 combined electrode was used to measure the pH in the titration experiments. For the calibration of the electrode, KH-phthalate (pH 4.008) and borax (pH 9.177) buffers were used (Manov et al., 1945; Manov et al., 1946). The calculation of $[H^+]$ from the measured pH values was performed with the use of the method proposed by Irving *et al.* by titrating a 0.02 M HCl solution with a standardized NaOH solution (0.2 M) (Irving et al., 1967). The differences between the measured and calculated pH values were used to obtain the $[H^+]$ concentrations from the pH-data collected in the titrations. The ion product of water was determined from the same experiment in the pH range 11.40–12.00. The ionic strength in the titrated and thermostat controlled (at 25°C) samples of 6.00 ml was kept constant and set to 0.15 M NaCl. The samples were stirred by a magnetic stir bar and kept under inert gas atmosphere (N_2) to avoid the effect of CO_2. The protonation constants of the ligands were obtained from previously reported data (Johnston et al., 2019). Validation of the formation of the metal complex was determined using the direct pH-potentiometric method by titrating samples with 1:1 metal-to-ligand ratios (the number of data pairs were between 100 and

250), allowing 1 min for sample equilibration to occur. Models of the formation were obtained from the titration data with the PSEQUAD program (Bush, 2011). The protonation and metal complex stability pH titration were plotted against the first derivative of the slope to emphasis the formation of the iron (II) complex of the $^{OH}Py_2N_2$.

Primary mouse lens epithelial cell (LEC) culture

Primary LEC cultures were isolated from C57BL/6J mice. Mouse lens capsules were cut into small pieces and treated with 0.05% trypsin at 37°C for 10–20 min. The cells loosened from the capsule were placed into a 24-well plate containing 1 ml DMEM with 20% FBS and 50 μg/ml gentamicin per well. The cultures were incubated for 1 week in a humid atmosphere with 5% CO_2 at 37°C. Medium was changed every 2 days. After the primary cultures achieved confluence, the cells were subcultured by using 0.05% trypsin.

Lens organ culture

All experiments using mice were in accordance with the ARVO Statement for the Use of Animals in Ophthalmic and Vision Research and an approved institutional animal care and use committee protocol at the University of North Texas Health Science Center (Protocol Number: IACUC-2019-0003 and IACUC-2022-0008). The mouse lenses from C57BL/6J mice were carefully dissected out of the eye using a posterior approach to avoid the surgical tools damaging the lens. The lenses were cultured in modified TC-199 media by following previously published method (Cui and Lou, 1993). Briefly, the lenses were placed in a 24-well plate of TC-199 media with an osmolarity ranging from 300–320 mOsm. The medium was pre-incubated in an organ culture incubator at 37°C with 5% CO_2 for 2 h prior to the addition of the lenses. The lenses were then incubated in the medium for 24 h. Those lenses became opaque, an indication of potential damage due to dissection, were excluded from the following experiments. Cultured lenses were incubated with 10–100 μL $^{OH}Py_2N_2$ for 24 h and then exposed to 200 μm H_2O_2 for another 6 h. The lens morphological changes were recorded under a dissecting microscope (Nikon) using darkfield illuminations. Lenses incubated with media alone served as the control.

Cell viability assay

Cell viability was measured by a colorimetric cell viability kit (Promokine, Heidelberg, Germany) with the tetrazolium salt WST-8 (2-(2-methoxy-4-nitrophenyl)-3-(4-nitrophenyl)-5-(2,4-disulfophenyl)-2H-tetrazolium, monosodium salt), which can be bioreduced to a water-soluble orange formazan dye by dehydrogenases present in the viable cells. The amount of formazan produced is directly proportional to the number of living cells. Cells were seeded at a density of 5000 cells/well (100 μL total volume/well) in a 96-well assay. Cells were incubated with or without $^{OH}Py_2N_2$ (10 and 100 μm) for 24 h and then treated with 200 μm of H_2O_2 for 6 h. After treatment, 10 μL of WST-8 solution was added to each well of the culture plate and incubated for 2 h in the incubator. The absorption was evaluated at 450 nm using a microplate reader (BioTek, Winooski, VT). The cell morphology was observed under phase-contrast microscopy.

Cellular ROS assay

Intracellular ROS levels were determined using the fluorescent probe CellROX Orange Reagent. After pretreatment with $^{OH}Py_2N_2$ for 24 h, LECs were exposed to 200 μm H_2O_2 for another 30 min. After treatment, the cells were loaded with 5 mm CellROX Orange Reagent for 30 min at 37°C, washed with DPBS and immediately imaged on a fluorescence microscope (Olympus, Center Valley, PA). The cellular fluorescence was quantified using the ImageJ software, after background subtraction for each image.

Western blot analysis

Protein concentration was determined with a BCA assay kit (Thermo Scientific, Rockford, IL). Equal amounts of protein were boiled in Laemmli buffer (Bio-Rad, Bio-Rad, Richmond, CA, United States) and loaded onto 12% SDS-PAGE gel and transferred to a 0.2 μm polyvinylidene difluoride membrane (GE Healthcare, Boulder, CO). The membranes were incubated with appropriate primary antibodies for overnight at 4°C and were then incubated with the appropriate secondary antibodies for 1 h. Detection was performed using the ECL Western blotting detection system (Thermo Scientific, Rockford, IL). The immunoblot was analyzed with a Bio-Rad imaging system (Versadoc 5000 MP Imaging System, Bio-Rad, Richmond, CA, United States).

Glutaredoxin activity

The enzyme activities of Grx1 and Grx2 were examined using 2-Hydroxyethyl disulfide (HEDS) as the substrate according to the method described in Raghavachari and Lou (Gladyshev et al., 2001). In brief, the cell lysate was mixed with potassium phosphate buffer (200 mm, pH7.5) containing 0.5 mm glutathione (GSH), 0.4 U/mL glutathione reductase (GR),

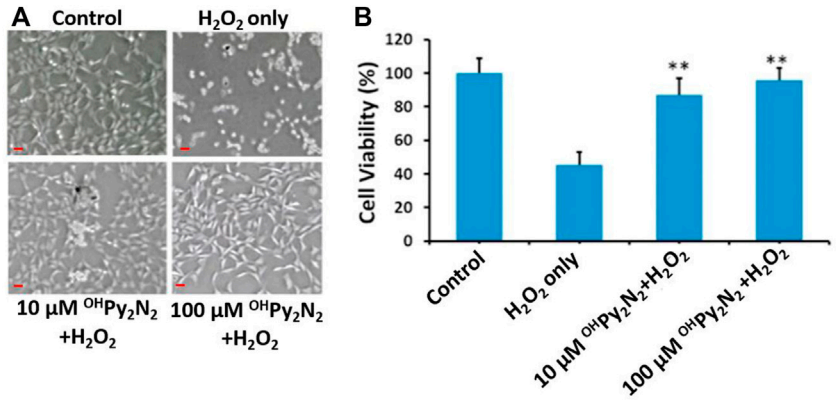


FIGURE 2
Cytoprotective effects of $^{OH}Py_2N_2$ in primary LEC against treatment with H_2O_2. Cells were incubated with or without $^{OH}Py_2N_2$ (10 and 100 μM) for 24 h and then treated with 200 μM of H_2O_2 for 6 h. After treatment, 10 μL of WST-8 solution was added to each well of the culture plate and incubated for 2 h in the incubator. **(A)** Images of cells (Scale bar = 50 μm), **(B)** Cell viability. n = 6, $^{**}p < 0.01$.

0.2 mm β-nicotinamide adenine dinucleotide phosphate, reduced tetra (cyclohexylammonium) salt (NADPH), and 2 mm hydroxyethyl disulfide (HED). The reaction was carried out at 30°C, and the decrease in absorbance at 340 nm was monitored for 5 min and used to determine the activity.

ATP Quantification

ATP level was measured with an ATP bioluminescence assay kit CLS II (Roche Applied Science, Penzberg, Germany) according to the manufacturer's recommendation (Wu et al., 2014). Briefly, lens homogenates were mixed with nine volumes of boiling solution (PBS containing 100 mm Tris and 4 mm EDTA) and incubated for 2 min at 100°C. The sample mix was then centrifuged at 1000 × g for 1 min, and 50 μL of the supernatant was mixed with 50 μL of luciferase reagent by automated injection. The luminescence intensity was detected by a Fluostar Optima microplate reader (BMG Labtech, Offenburg, Germany), and integrated for 1–10 s.

Malondialdehyde (MDA) measurement

Cells were seeded at a density of 10,000 cells/well in a 96-well assay. Cells were incubated with or without $^{OH}Py_2N_2$ (1, 10 and 100 μm) for 24 h and then treated with 200 μm of H_2O_2 for 6 h. MDA was measured by using the MDA assay kit (Abcam, Cambridge, MA, United States, ab118970) based on the thiobarbituric acid (TBA) reaction. The intensity of the resulting MDA-TBA adduct was read at RFU at Ex/Em = 532/553 nm and the data were expressed as nmol/mg protein.

Statistics

Each experiment was performed at least three times and statistical analyses were performed using Student's t-test when comparing between two groups and one-way ANOVA followed by Bonferroni's test as a post hoc test when comparing among three or more groups with the Prism software (GraphPad, La Jolla, CA). The number of experimental samples used in each group is presented in the figure legends. All data are expressed as means ± SD and differences were considered significant at $p < 0.05$.

Results and discussion

Previous work has shown that pyridinophane type molecules are low molecular weight entities that display potent antioxidant ability, low toxicity, and high metabolic stability in neuronal cell culture models, suggesting they could serve as potential agents to treat Alzheimer's and other neurodegenerative diseases (Lincoln et al., 2013; Green et al., 2019; Johnston et al., 2019). Among these molecules, the $^{OH}Py_2N_2$ pyridinophane (Figure 1) showed higher pharmacological efficacy and increased biological compatibility compared to the parent systems (Johnston et al., 2019). As a result of this success, disorders of the eye were next explored to understand the extent to which the protective nature of $^{OH}Py_2N_2$ could be utilized and as models to understand the mechanisms of this protective reactivity.

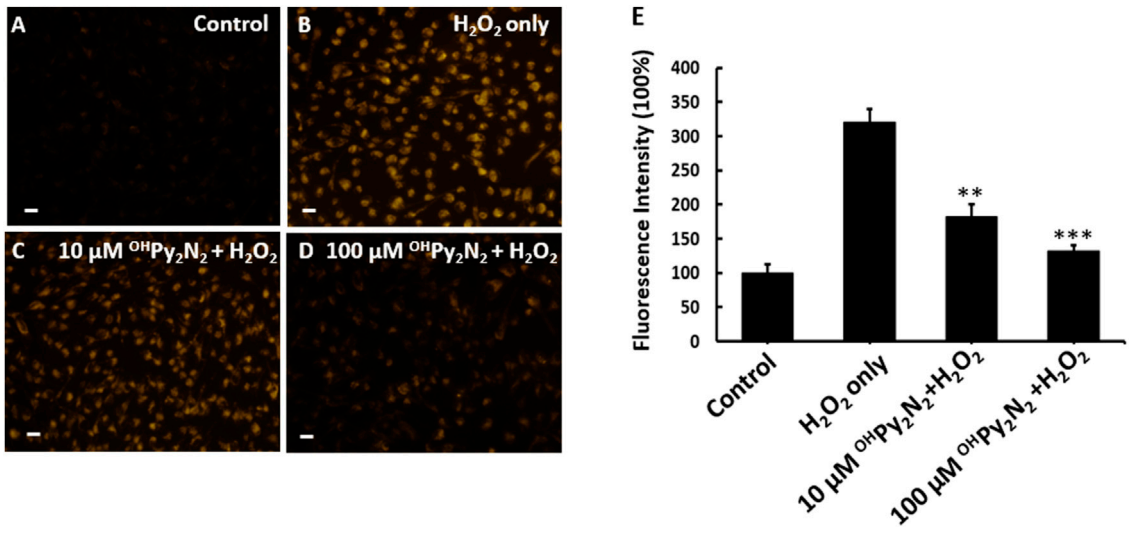


FIGURE 3
$^{OH}Py_2N_2$ reduces ROS production in H_2O_2-treated LECs. **(A)** LECs as a control with no treatment, **(B)** 200 μM H_2O_2 treatment for 30 min, and **(C,D)** pretreatment with 10 or 100 μM $^{OH}Py_2N_2$ for 24 h followed by 200 μM H_2O_2 treatment for 30 min. **(E)** Fluorescence was detected using the probe CellROX orange reagent for all groups; fluorescence intensity quantified and represented as the mean mean ± SEM of three independent experiments, $^{**}p < 0.01$, $^{***}p < 0.01$ compared with the H_2O_2-only group ($n = 3$). Scale bar = 50 μm.

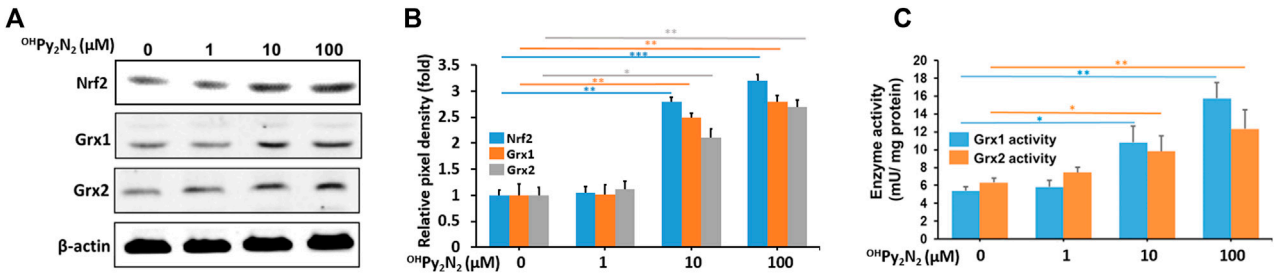


FIGURE 4
$^{OH}Py_2N_2$ upregulates Nrf2, Grx1, and Grx2 in LECs.**(A)** Western blot analysis showing the increased expression of antioxidant transcription factor Nrf2 along with enzymes Grx1, and Grx2. **(B)** The relative pixel density of Nrf2, Grx1, and Grx2 over loading control. **(C)** Grx1 and Grx2 enzymatic activity increased as a result of exposure to $^{OH}Py_2N_2$. ($^{*}p < 0.05$; $^{**}p < 0.01$; $^{***}p < 0.001$) ($n = 3$).

$^{OH}Py_2N_2$ prevents LECs from H_2O_2-induced damage

To test the cytoprotective effects in the lens, primary LECs were treated with $^{OH}Py_2N_2$ for 24 h followed by a 200 μm H_2O_2 challenge for 6 h H_2O_2 treatment alone caused approximately 60% cell viability loss in mLECs (Figure 2). In contrast, treatments of $^{OH}Py_2N_2$ at concentrations of both 10 μm and 100 μm $^{OH}Py_2N_2$ protected cells from oxidative stress-induced cell damage, with the later showing the largest (90%) improvement. The cell morphology was then observed under phase-contrast microscopy. Following exposure to 200 μm H_2O_2 for 6 h, LECs showed a marked decrease in number concomitant to shrinkage in size and loss of adhesion. Pretreatment with different doses of $^{OH}Py_2N_2$ (10 and 100 μm) attenuated H_2O_2-induced cell morphological changes. These results suggest that the $^{OH}Py_2N_2$ molecule can prevent cell death induced by oxidative stress in multiple models, making its translation to multiple disease states arising from oxidative stress promising.

$^{OH}Py_2N_2$ prevents ROS production

Intracellular ROS levels were measured to determine if the protection demonstrated by $^{OH}Py_2N_2$ against H_2O_2 (Figure 2) induced cell death as a result of lowering the oxidative stress in the LECs. For this study, cells were preloaded with CellROX Orange followed by stimulation with H_2O_2 to monitor the resulting ROS sensitive fluorescent product (Figure 3). Separately, LECs were pretreated with $^{OH}Py_2N_2$ for 24 h and subsequently treated with H_2O_2 at 200 μm for another 30 min. As compared with non-treated control cells (Figure 3A), H_2O_2 treatment significantly increased the fluorescence intensity of ROS (Figure 3B). $^{OH}Py_2N_2$ treatment dose-dependently decreased the production of ROS (Figures 3C,D). Quantitative fluorescence intensities of CellROX Orange in the various groups are shown in Figure 3E to support the visual results and validate that the $^{OH}Py_2N_2$ molecule protects against ROS induced cell death by H_2O_2 by decreasing the oxidative stress in the LECs.

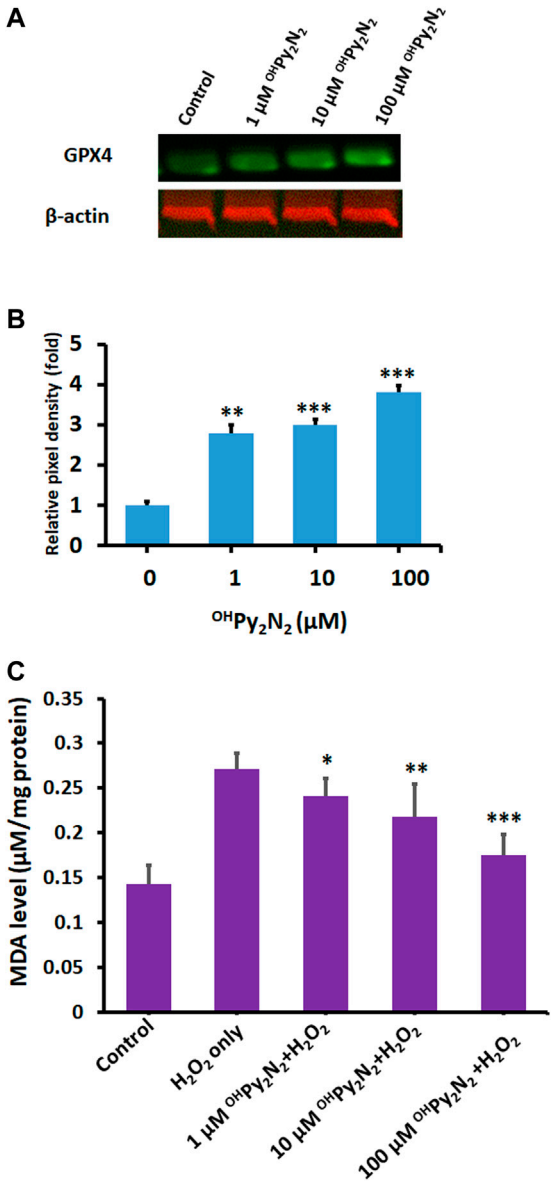


FIGURE 5
Anti-ferroptotic effects of $^{OH}Py_2N_2$ in LECs. **(A)** $^{OH}Py_2N_2$ upregulates GPX4 expression. LECs were treated with (1–100 μM) $^{OH}Py_2N_2$ for 24 h. Control cells were treated identically but without additional of $^{OH}Py_2N_2$. **(B)** The relative pixel density of GPX4 over loading control. Data presented are a typical representation of triplicate experiments. (**$p < 0.01$; ***$p < 0.001$). **(C)** $^{OH}Py_2N_2$ inhibits H_2O_2-induced MDA formation. Cells were incubated with or without $^{OH}Py_2N_2$ (1, 10 and 100 μM) for 24 h and then treated with 200 μm of H_2O_2 for 6 h. MDA level in each group was measured. (*$p < 0.05$; **$p < 0.01$; ***$p < 0.001$) ($n = 3$).

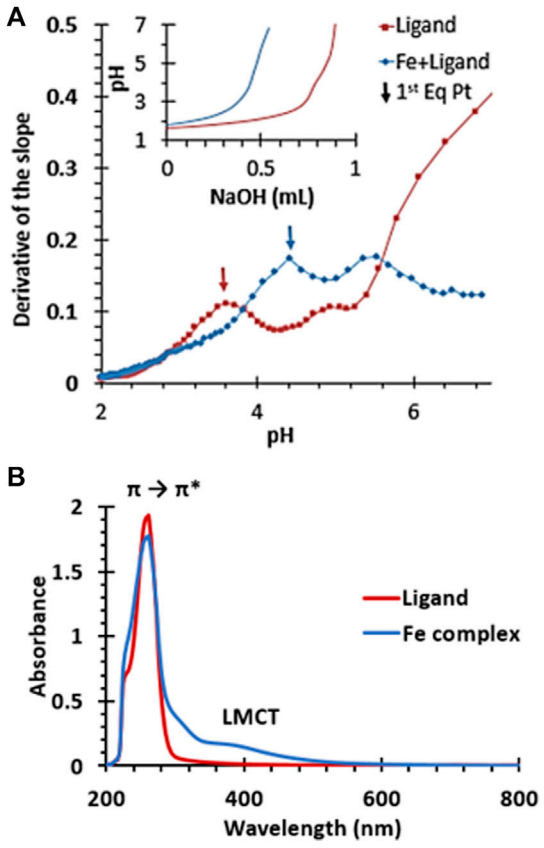


FIGURE 6
(A) First derivative of the potentiometric titration of $^{OH}Py_2N_2$ and the iron (II) complex. Inset shows original titration data. **(B)** UV-vis spectra of an aqueous solution of $^{OH}Py_2N_2$ (red) and **(B)** the iron (III) complex of $^{OH}Py_2N_2$.

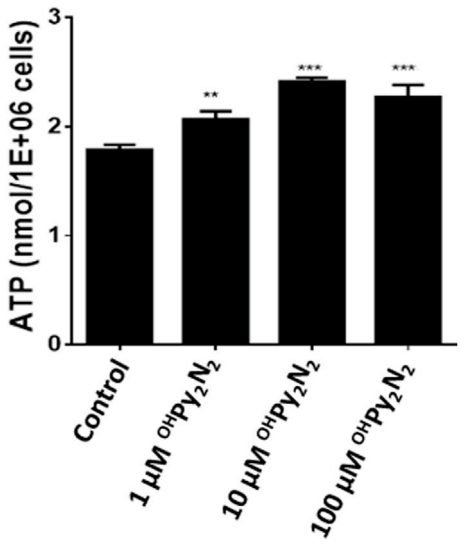


FIGURE 7
ATP production is increased with the addition of $^{OH}Py_2N_2$. LECs were treated with (1–100 μm) $^{OH}Py_2N_2$ for 24 h. Control cells were treated identically but without additional of $^{OH}Py_2N_2$. Whole cell homogenates were used for ATP measurement with an ATP assay kit (n = 6, $^{**}p < 0.01$, $^{***}p < 0.001$).

$^{OH}Py_2N_2$ activates Nrf2 and increases glutaredoxin (Grx) expression

Nrf2 is the central regulator of a comprehensive and protective biological antioxidant response. Activation of Nrf2 leads to the transcriptional activation of a broad range of antioxidant enzymes including NADPH dehydrogenase, heme oxygenase-1, superoxide dismutase, catalase, glutathione peroxidase (GPX), thioredoxin, and more. Our previous study has shown that $^{OH}Py_2N_2$ could dose-dependently upregulate Nrf2 in neuronal cell culture (Johnston et al., 2019). Therefore, LECs were treated with $^{OH}Py_2N_2$ at 1, 10, and 100 μm for 24 h to further investigate the effect on the Nrf2 pathway in this particular model. Western blot analysis showed a dose-dependent increase of Nrf2 protein expression (Figure 4A). This result indicates that the mode of antioxidant action (Nrf2 expression) is translated between neuronal and lens cell culture showing the portability of this molecule toward treating conditions rising from oxidative stress. As a result of this success, we next explored what mechanisms could be activated as a result of Nrf2 expression upon treatment with $^{OH}Py_2N_2$ resulting in the protective effects observed to date.

To maintain intracellular redox homeostasis, mammalian tissues including the lens have well-designed repair systems to protect protein thiols from oxidation (Holmgren, 1989; Lillig et al., 2008). The first is the GSH-dependent glutaredoxin (Grx) system, which are a group oxidoreductases that catalyze the reduction of glutathione-protein mixed disulfides. The Grx system has two major isozymes: glutaredoxin 1 (Grx1, also known as thioltransferease or TTase) and the recently discovered glutaredoxin 2 (Grx2) (Holmgren, 1976; Gladyshev et al., 2001; Lundberg et al., 2001). Previous studies suggest that enhancing Grx system may be a potential therapeutic strategy for delaying or slowing down the age-related cataracts (Xing and Lou, 2010; Kronschläger et al., 2012; Wu et al., 2014; Fan et al., 2022). In our study, we found $^{OH}Py_2N_2$ could boost activity of the Grx system. The enzymatic activity of Grx1 and Grx2 were observed to increase in cell lysates treated with $^{OH}Py_2N_2$ (1–100 μm) in a dose-dependently manner (Figure 4B) along with the protein levels of Grx1 and Grx2 (Figure 4A). From this series of studies, it can be concluded that the addition of $^{OH}Py_2N_2$ to LECs activates the translocation of Nrf2 and the expression of antioxidant enzymes, including Grx1 and Grx2 as a mechanism that results in the catalytic protection of LECs against ROS assaults. To our knowledge this is the first example of a such a low molecular weight, macrocyclic small molecule of this type,

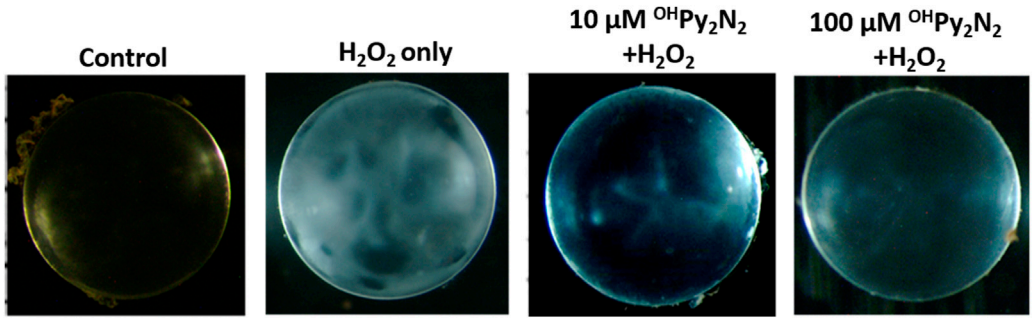


FIGURE 8
$^{OH}Py_2N_2$ prevented H_2O_2-induced opacity in culture mouse lenses. Cultured lenses were incubated with 10–100 μm $^{OH}Py_2N_2$ for 24 h and then exposed to 200 μm H_2O_2 for another 6 h (n = 3).

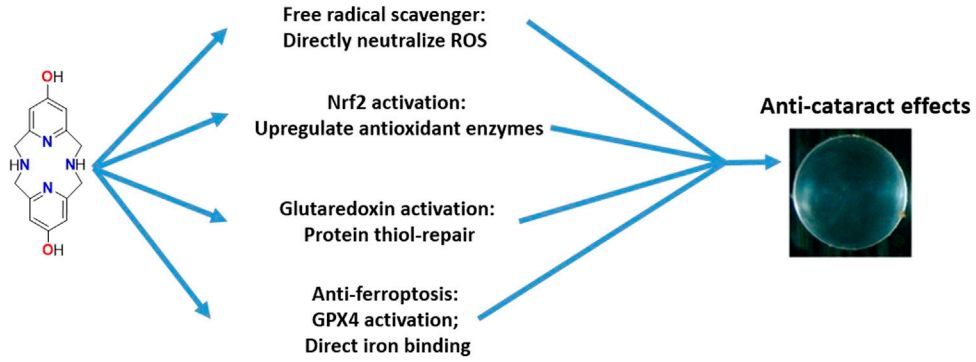


FIGURE 9
Multiple pathways are activated upon exposure to $^{OH}Py_2N_2$ that can result in protection against oxidative stress and cataract formation.

particularly a pyridinophane, that can activate cellular mechanisms of protection against oxidative stress.

$^{OH}Py_2N_2$ demonstrates anti-ferroptotic effects and iron binding

Ferroptosis is a newly identified form of non-apoptotic regulated cell death that is initiated by excessive iron-dependent lipid peroxidation (Jiang et al., 2021). Glutathione peroxidase (GPX4) is the key regulator of this form of cell death (Lei et al., 2022). Compounds that up-regulate GPX4 have been proposed as ferroptosis inhibitors (Chen et al., 2020; Li et al., 2020; Lei et al., 2022). In fact, inhibiting ferroptosis has the potential to be a useful therapeutic method for age-related diseases, including cataract (Wei et al., 2021). In our study, we found $^{OH}Py_2N_2$ dose-dependently upregulate GPX4 in LECs (Figures 5A,B), indicating $^{OH}Py_2N_2$, thus enhancing a natural defense mechanism against ferroptosis.

Ferroptosis is associated with two major biochemical hallmarks, lipid peroxidation and iron accumulation (Tang et al., 2021). Malondialdehyde (MDA), the final product of polyunsaturated fatty acid peroxidation, is one of the most important biomarkers of lipid peroxidation. Previous studies have shown that MDA accumulation plays a pivotal role in senile cataractogenesis (Bhuyan et al., 1986). As shown in Figure 5C, as compared with the control group, the MDA level was significantly increased after H_2O_2 treatment (control: 0.14 ± 0.021 vs. H_2O_2 alone: 0.27 ± 0.0172 nmol/mg protein, $p <$ 0.001). Conversely, $^{OH}Py_2N_2$ prevented H_2O_2-induced MDA accumulation in a dose-dependent manner (1 μM $^{OH}Py_2N_2$: 0.24 ± 0.022 nmol/mg protein $p < 0.05$ vs. 10 μm $^{OH}Py_2N_2$: 0.21 ± 0.035 nmol/mg protein $p < 0.01$ vs. 100 μM $^{OH}Py_2N_2$: 0.17 ± 0.023 nmol/mg protein $p < 0.001$). Our data indicate that $^{OH}Py_2N_2$ effectively prevented oxidative stress-induced lipid peroxidation.

Additionally, iron-chelating capacity is also strongly linked with anti-ferroptotic effects (Chen et al., 2020; Lei et al., 2022).

The metal binding halts the Fenton reaction that leads to ferroptotic lipid peroxidation. Molecule $^{OH}Py_2N_2$ has previously been shown to bind copper (II) effectively and molecules within this pyridinophane family are well-known to interact strongly with a range of transition metal-ions including iron (II) and (III) (Brewer et al., 2018; Johnston et al., 2019; Mekhail et al., 2020; Brewer et al., 2021). Potentiometric titrations of $^{OH}Py_2N_2$ and iron (II) in aqueous solution (Figure 6) validate complexation based on the shift in the titration curve compared to the chelate molecule alone. This curve is very similar to our previous studies of similar iron (II) titrations showing complex formation around a pH of four and is consistent with a log β in the range of 12–13, which is in range or higher than metal-binding agents explored to date (Chen et al., 2020; Mekhail et al., 2020). Furthermore, addition of iron (III) to an aqueous solution of $^{OH}Py_2N_2$ resulted in a color change from pale yellow to dark yellow. UV-vis analysis of the resulting solution showed ligand to metal charge transfer bands at 313 and 390 nm (Figure 6) and a ligand based π to π* transition at 290 nm. This spectroscopy is consistent with an Fe(III) ($^{OH}Py_2N_2$)Cl_2 complex of the geometry shown in Figure 1 (Mekhail et al., 2020; Brewer et al., 2021). Together, these results serve as evidence that the $^{OH}Py_2N_2$ scaffold is a good agent for binding iron (II) and (III) and could be a contributing mechanism for antiferroptotic activity to explore in depth in the future.

$^{OH}Py_2N_2$ treatment promotes ATP production

Adenosine triphosphate (ATP) is often referred to as the "energy currency" because it is used to fill any energy needs of the cell. Reduced energy levels threaten cellular homeostasis and may trigger cataract formation (Greiner and Glonek, 2020). As a result of these foundations, the ability for $^{OH}Py_2N_2$ to elevate ATP production as a means of preventing oxidative stress induced cataract formation was explored using an established luciferase based bioluminescence assay method (Wu et al., 2014). The $^{OH}Py_2N_2$ molecule promoted a dose-dependently ATP production, suggesting that $^{OH}Py_2N_2$ may enhance mitochondrial function and improve bioenergetic function to help LECs to fight against oxidative stress (Figure 7).

$^{OH}Py_2N_2$ protects the lens from H_2O_2-induced opacity

Encouraged by the above positive results, we further tested if $^{OH}Py_2N_2$ treatments could prevent H_2O_2-induced lens opacity. Cultured lenses extracted from C57BL/6J mice were incubated with $^{OH}Py_2N_2$ (10–100 μm) for 24 h and then exposed to 200 μm H_2O_2 for another 6 h. As shown in Figure 8, pretreatment with 10 and 100 μm $^{OH}Py_2N_2$, followed by H_2O_2 induction, resulted in reduced opacities compared to cataract induction alone.

Conclusion

The studies show that the ability for $^{OH}Py_2N_2$ to induce protection against peroxide induced cell death over to LECs (Figure 9). Although $^{OH}Py_2N_2$ was designed to serve as a direct antioxidant that functions through radical scavenging and metal-binding, the studies described herein show that the molecule activates multiple biological pathways innate to cells that promote the cells to protect against oxidative stress. The ability for $^{OH}Py_2N_2$ to turn-on Nrf2 expression as well as Grx1 and Grx2 catalytic pathways impacted by the small molecule. The molecule also upregulates GPX4 and binds iron (II) and (III) ions, which suggests that it should be explored further for the details regarding its anti-ferroptotic abilities in more detail. The bioenergetic pathway is also upregulated by treatment with $^{OH}Py_2N_2$ as evidenced by increased levels of ATP. Lastly, cultured lenses were protected from H_2O_2-induced lens opacity by this multimodal small molecule, showing the ultimate potential of this water-soluble small molecule. Altogether, this work opens up several new fields of exploration that marry the organic and inorganic design of small molecules with studies that function to elucidate an understanding of their potential to impact diseases in the eye. Moreover, understanding what structural components of the $^{OH}Py_2N_2$ molecule are responsible for activating these pathways is of urgent interest. This work also leads to the need to understand at what point(s) in the immune response pathway for protecting against oxidative stress the $^{OH}Py_2N_2$ interacts, leading to the responses described herein.

Data availability statement

The original contributions presented in the study are included in the article, further inquiries can be directed to the corresponding authors.

Author contributions

The manuscript was written through contributions of all authors. All authors have given approval to the final version of the manuscript.

Funding

The authors acknowledge National Institutes of Health 2R15GM123463-02 (to KG and HW) and Welch Foundation P-2063-20210327 (to KG). BrightFocus Foundation [rant no: M2015180 (HW)]; California Table Grape Commission

Research Grant (HW); and the United States Department of Defense [VRP Research Award no: W81XWH2010896 (HW)].

Conflict of interest

The authors declare that the research was conducted in the absence of any commercial or financial relationships that could be construed as a potential conflict of interest.

Publisher's note

All claims expressed in this article are solely those of the authors and do not necessarily represent those of their affiliated organizations, or those of the publisher, the editors and the reviewers. Any product that may be evaluated in this article, or claim that may be made by its manufacturer, is not guaranteed or endorsed by the publisher.

References

Age-Related Eye Disease Study Research Group (2001). A randomized, placebo-controlled, clinical trial of high-dose supplementation with vitamins C and E, beta carotene, and zinc for age-related macular degeneration and vision loss: AREDS report no. 8. *Arch. Ophthalmol.* 119 (10), 1417–1436. doi:10.1001/archopht.119.10.1417

Alzheimer's Disease Facts (2016). Figures, Alzheimer's & dementia. *Alzheimer's Assoc.* 12 (4).

Bahn, G., Park, J.-S., Yun, U. J., Lee, Y. J., Choi, Y., Park, J. S., et al. (2019). NRF2/ARE pathway negatively regulates BACE1 expression and ameliorates cognitive deficits in mouse Alzheimer's models. *Proc. Natl. Acad. Sci. U. S. A.* 116 (25), 12516–12523. doi:10.1073/pnas.1819541116

Beatty, S., Koh, H.-H., Phil, M., Henson, D., and Boulton, M. (2000). The role of oxidative stress in the pathogenesis of age-related macular degeneration. *Surv. Ophthalmol.* 45 (2), 115–134. doi:10.1016/s0039-6257(00)00140-5

Bhuyan, K. C., Bhuyan, D. K., and Podos, S. M. (1986). Lipid peroxidation in cataract of the human. *Life Sci.* 38 (16), 1463–1471. doi:10.1016/0024-3205(86)90559-x

Bosco, J. L. F., Antonsen, S., Sorensen, H. T., Pedersen, L., and Lash, T. L. (2011). Metformin and incident breast cancer among diabetic women: A population-based case-control study in Denmark. *Cancer Epidemiol. Biomarkers Prev.* 20 (1), 101–111. doi:10.1158/1055-9965.epi-10-0817

Brewer, S. M., Schwartz, T. M., Mekhail, M. A., Turan, L. S., Prior, T. J., Hubin, T. J., et al. (2021). Mechanistic insights into iron-catalyzed C–H bond activation and C–C coupling. *Organometallics* 40 (15), 2467–2477. doi:10.1021/acs.organomet.1c00211

Brewer, S. M., Wilson, K. R., Jones, D. G., Reinheimer, E. W., Archibald, S. J., Prior, T. J., et al. (2018). Increase of direct C–C coupling reaction yield by identifying structural and electronic properties of high-spin iron tetra-azamacrocyclic complexes. *Inorg. Chem.* 57 (15), 8890–8902. doi:10.1021/acs.inorgchem.8b00777

Bush, A. I. (2011). A copper binding site within the pathological conformer epitope of mutant SOD1. *Front. Neurosci.* 2, 97. doi:10.3389/fnins.2011.00097

Chan, E., Mahroo, O. A., and Spalton, D. J. (2010). Complications of cataract surgery. *Clin. Exp. Optom.* 93 (6), 379–389. doi:10.1111/j.1444-0938.2010.00516.x

Chen, X., Yu, C., Kang, R., and Tang, D. (2020). Iron metabolism in ferroptosis. *Front. Cell Dev. Biol.* 8, 590226. doi:10.3389/fcell.2020.590226

Chew, E. Y., Clemons, T. E., Agrón, E., Sperduto, R. D., SanGiovanni, J. P., Kurinij, N., et al. (2013). Long-term effects of vitamins C and E, β-carotene, and zinc on age-related macular degeneration: AREDS report no. 35. *Ophthalmology* 120 (8), 1604–1611.e4. e4. doi:10.1016/j.ophtha.2013.01.021

Cooper, G., Young, A., Gamble, G., Occleshaw, C., Dissanayake, A., Cowan, B., et al. (2009). A copper (II)-selective chelator ameliorates left-ventricular hypertrophy in type 2 diabetic patients: A randomised placebo-controlled study. *Diabetologia* 52 (4), 715–722. doi:10.1007/s00125-009-1265-3

Crielaard, B. J., Lammers, T., and Rivella, S. (2017). Targeting iron metabolism in drug discovery and delivery. *Nat. Rev. Drug Discov.* 16 (6), 400–423. doi:10.1038/nrd.2016.248

Cuadrado, A., Kügler, S., and Lastres-Becker, I. (2018). Pharmacological targeting of GSK-3 and NRF2 provides neuroprotection in a preclinical model of tauopathy. *Redox Biol.* 14, 522–534. doi:10.1016/j.redox.2017.10.010

Cui, X.-L., and Lou, M. F. (1993). The effect and recovery of long-term H2O2 exposure on lens morphology and biochemistry. *Exp. eye Res.* 57 (2), 157–167. doi:10.1006/exer.1993.1111

Czerska, M., Mikolajewska, K., Zielinski, M., Gromadzinska, J., and Wasowicz, W. (2015). Today's oxidative stress markers. *Med. Pr.* 66 (3), 393–405. doi:10.13075/mp.5893.00137

D'Souza, L. C., Mishra, S., Chakraborty, A., Shekher, A., Sharma, A., and Gupta, S. C. (2020). Oxidative stress and cancer development: Are noncoding RNAs the missing links? *Antioxidants Redox Signal.*

DeCensi, A., Puntoni, M., Goodwin, P., Cazzaniga, M., Gennari, A., Bonanni, B., et al. (2010). Metformin and cancer risk in diabetic patients: A systematic review and meta-analysis. *Cancer Prev. Res. (Phila).* 3 (11), 1451–1461. doi:10.1158/1940-6207.capr-10-0157

Doig, A. J., Del Castillo-Frias, M. P., Berthoumieu, O., Tarus, B., Nasica-Labouze, J., Sterpone, F., et al. (2017). Why is research on amyloid-beta failing to give new drugs for alzheimer's disease? *ACS Chem. Neurosci.* 8 (7), 1435–1437. doi:10.1021/acschemneuro.7b00188

Fan, Q., Li, D., Zhao, Z., Jiang, Y., and Lu, Y. (2022). Protective effect of Glutaredoxin 1 against oxidative stress in lens epithelial cells of age-related nuclear cataracts. *Mol. Vis.* 28, 70–82.

Farrawell, N. E., Yerbury, M. R., Plotkin, S. S., McAlary, L., and Yerbury, J. J. (2018). CuATSM protects against the *in vitro* cytotoxicity of wild-type-like copper–zinc superoxide dismutase mutants but not mutants that disrupt metal binding. *ACS Chem. Neurosci.* 10 (3), 1555–1564. doi:10.1021/acschemneuro.8b00527

Fraser, G. E. (2009). Vegetarian diets: What do we know of their effects on common chronic diseases? *Am. J. Clin. Nutr.* 89 (5), S1607–S1612. doi:10.3945/ajcn.2009.26736k

Giem, P., Beeson, W. L., and Fraser, G. E. (1993). The incidence of dementia and intake of animal products - preliminary findings from the adventist health study. *Neuroepidemiology* 12 (1), 28–36. doi:10.1159/000110296

Gladyshev, V. N., Liu, A., Novoselov, S. V., Krysan, K., Sun, Q. A., Kryukov, V. M., et al. (2001). Identification and characterization of a new mammalian glutaredoxin (thioltransferase), Grx2. *J. Biol. Chem.* 276 (32), 30374–30380. doi:10.1074/jbc.m100020200

Goodson, A. G., Cotter, M. A., Cassidy, P., Wade, M., Florell, S. R., Liu, T., et al. (2009). Use of oral N-acetylcysteine for protection of melanocytic nevi against UV-induced oxidative stress: Towards a novel paradigm for melanoma chemoprevention. *Clin. Cancer Res.* 15 (23), 7434–7440. doi:10.1158/1078-0432.ccr-09-1890

Green, K. N., Pota, K., Tircsó, G., Gogolák, R. A., Kinsinger, O., Davda, C., et al. (2019). Dialing in on pharmacological features for a therapeutic antioxidant small molecule. *Dalton Trans.* 48, 12430–12439. doi:10.1039/c9dt01800j

Greiner, J. V., and Glonek, T. (2020). Hydrotropic function of ATP in the crystalline lens. *Exp. Eye Res.* 190, 107862. doi:10.1016/j.exer.2019.107862

Han, Y., Nan, S., Fan, J., Chen, Q., and Zhang, Y. (2019). Inonotus obliquus polysaccharides protect against Alzheimer's disease by regulating Nrf2 signaling

and exerting antioxidative and antiapoptotic effects. *Int. J. Biol. Macromol.* 131, 769–778. doi:10.1016/j.ijbiomac.2019.03.033

Holmgren, A. (1976). Hydrogen donor system for *Escherichia coli* ribonucleoside-diphosphate reductase dependent upon glutathione. *Proc. Natl. Acad. Sci. U. S. A.* 73 (7), 2275–2279. doi:10.1073/pnas.73.7.2275

Holmgren, A. (1989). Thioredoxin and glutaredoxin systems. *J. Biol. Chem.* 264 (24), 13963–13966. doi:10.1016/s0021-9258(18)71625-6

Ikawa, M., Okazawa, H., Tsujikawa, T., Matsunaga, A., Yamamura, O., Mori, T., et al. (2015). Increased oxidative stress is related to disease severity in the ALS motor cortex: A PET study. *Neurology* 84 (20), 2033–2039. doi:10.1212/wnl.0000000000001588

Irving, H. M., Miles, M. G., and Pettit, L. D. (1967). A study of some problems in determining the stoicheiometric proton dissociation constants of complexes by potentiometric titrations using a glass electrode. *Anal. Chim. Acta* 38 (4), 475–488. doi:10.1016/s0003-2670(01)80616-4

Jarvis, L. M. (2015). Alzheimer's next chapter. *Chem. Eng. News Arch.* 93, 11–15. doi:10.1021/cen-09322-cover

Jiang, X., Stockwell, B. R., and Conrad, M. (2021). Ferroptosis: Mechanisms, biology and role in disease. *Nat. Rev. Mol. Cell Biol.* 22 (4), 266–282. doi:10.1038/s41580-020-00324-8

Johnson, J., Maher, P., and Hanneken, A. (2009). The flavonoid, eriodictyol, induces long-term protection in ARPE-19 cells through its effects on Nrf2 activation and phase 2 gene expression. *Invest. Ophthalmol. Vis. Sci.* 50 (5), 2398–2406. doi:10.1167/iovs.08-2088

Johnston, H. M., Pota, K., Barnett, M. M., Kinsinger, O., Braden, P., Schwartz, T. M., et al. (2019). Enhancement of the antioxidant activity and neurotherapeutic features through pyridol addition to tetraazamacrocyclic molecules. *Inorg. Chem.* 58 (24), 16771–16784. doi:10.1021/acs.inorgchem.9b02932

Kaspar, J. W., Niture, S. K., and Jaiswal, A. K. (2009). Nrf2:INrf2 (Keap1) signaling in oxidative stress. *Free Radic. Biol. Med.* 47 (9), 1304–1309. doi:10.1016/j.freeradbiomed.2009.07.035

Kingwell, K. (2017). Zeroing in on neurodegenerative alpha-synuclein. *Nat. Rev. Drug Discov.* 16 (6), 371–373. doi:10.1038/nrd.2017.95

Kitaoka, Y., Tamura, Y., Takahashi, K., Takeda, K., Takemasa, T., and Hatta, H. (2019). Effects of Nrf2 deficiency on mitochondrial oxidative stress in aged skeletal muscle. *Physiol. Rep.* 7 (3), e13998. doi:10.14814/phy2.13998

Kronschläger, M., Galichanin, K., Ekström, J., Lou, M. F., and Söderberg, P. G. (2012). Protective effect of the thioltransferase gene on *in vivo* UVR-300 nm–induced cataract. *Invest. Ophthalmol. Vis. Sci.* 53 (1), 248–252. doi:10.1167/iovs.11-8504

Lannfelt, L., Blennow, K., Zetterberg, H., Batsman, S., Ames, D., Harrison, J., et al. (2008). Safety, efficacy, and biomarker findings of PBT2 in targeting aβ as a modifying therapy for alzheimer's disease: A phase IIa, double-blind, randomised, placebo-controlled trial. *Lancet Neurol.* 7 (9), 779–786. doi:10.1016/s1474-4422(08)70167-4

Lei, G., Zhuang, L., and Gan, B. (2022). Targeting ferroptosis as a vulnerability in cancer. *Nat. Rev. Cancer* 22 (7), 381–396. doi:10.1038/s41568-022-00459-0

Li, J., Cao, F., Yinliang, H., Huangjian, Z., Lintao, Z., Mao, N., et al. (2020). Ferroptosis: Past, present and future. *Cell Death Dis.* 11 (2), 88. doi:10.1038/s41419-020-2298-2

Lillig, C. H., Berndt, C., and Holmgren, A. (2008). Glutaredoxin systems. *Biochimica Biophysica Acta - General Subj.* 1780 (11), 1304–1317. doi:10.1016/j.bbagen.2008.06.003

Lincoln, K. M., Gonzalez, P., Richardson, T. E., Rutter, L., Julovich, D. A., Simpkins, J. W., et al. (2013). A potent antioxidant small molecule aimed at targeting metal-based oxidative stress in neurodegenerative disorders. *Chem. Commun.* 49, 2712–2714. doi:10.1039/c2cc36808k

Lofgren, S. (2017). Solar ultraviolet radiation cataract. *Exp. Eye Res.* 156, 112–116. doi:10.1016/j.exer.2016.05.026

Lou, M. F. (2003). Redox regulation in the lens. *Prog. Retin. eye Res.* 22 (5), 657–682. doi:10.1016/s1350-9462(03)00050-8

Lundberg, M., Johansson, C., Chandra, J., Enoksson, M., Jacobsson, G., Ljung, J., et al. (2001). Cloning and expression of a novel human glutaredoxin (Grx2) with mitochondrial and nuclear isoforms. *J. Biol. Chem.* 276 (28), 26269–26275. doi:10.1074/jbc.m011605200

Ma, Q. (2013). Role of nrf2 in oxidative stress and toxicity. *Annu. Rev. Pharmacol. Toxicol.* 53, 401–426. doi:10.1146/annurev-pharmtox-011112-140320

Manov, G. G., Delollis, N. J., and Acree, S. F. (1945). Comparative liquid-junction potentials of some ph buffer standards and the calibration of ph meters. *J. Res. Natl. Bur. Stand. (1977).* 34 (2), 115–127. doi:10.6028/jres.034.002

Manov, G. G., Delollis, N. J., Lindvall, P. W., and Acree, S. F. (1946). Effect of sodium chloride on the apparent ionization constant of boric acid and the ph values of borate solutions. *J. Res. Natl. Bur. Stand. (1977).* 36 (6), 543–558. doi:10.6028/jres.036.033

Mekhail, M. A., Pota, K., Schwartz, T. M., and Green, K. N. (2020). Functionalized pyridine in pyclen-based iron (iii) complexes: Evaluation of fundamental properties. *RSC Adv.* 10 (52), 31165–31170. doi:10.1039/d0ra05756h

Naik, P., Fofaria, N., Prasad, S., Sajja, R. K., Weksler, B., Couraud, P. O., et al. (2014). Oxidative and pro-inflammatory impact of regular and denicotinized cigarettes on blood brain barrier endothelial cells: Is smoking reduced or nicotine-free products really safe? *BMC Neurosci.* 15, 51. doi:10.1186/1471-2202-15-51

Nechuta, S., Lu, W., Chen, Z., Zheng, Y., Gu, K., Cai, H., et al. (2011). Vitamin supplement use during breast cancer treatment and survival: A prospective cohort study. *Cancer Epidemiol. Biomarkers Prev.* 20 (2), 262–271. doi:10.1158/1055-9965.epi-10-1072

Niedzielska, E., Smaga, I., Gawlik, M., Moniczewski, A., Stankowicz, P., Pera, J., et al. (2016). Oxidative stress in neurodegenerative diseases. *Mol. Neurobiol.* 53 (6), 4094–4125. doi:10.1007/s12035-015-9337-5

Organization, W. H. (2019). *World report on vision*.

Patel, M. (2016). Targeting oxidative stress in central nervous system disorders. *Trends Pharmacol. Sci.* 37 (9), 768–778. doi:10.1016/j.tips.2016.06.007

Pisoschi, A. M., Pop, A., Iordache, F., Stanca, L., Predoi, G., and Serban, A. I. (2021). Oxidative stress mitigation by antioxidants - an overview on their chemistry and influences on health status. *Eur. J. Med. Chem.* 209, 112891. doi:10.1016/j.ejmech.2020.112891

Ratner, M. (2015). Biogen's early Alzheimer's data raise hopes, some eyebrows. *Nat. Biotechnol.* 33 (5), 438. doi:10.1038/nbt0515-438

Rowe, D., Mathers, S., Noel, K., and Rosenfeld, C. (2020). CuATSM phase 2a study confirms disease-modifying effects in patients with sporadic ALS observed in the phase 1 study (1338). *Neurology* 95 (15 Supplement), 1338.

Singh, P. N., Sabate, J., and Fraser, G. E. (2003). Does low meat consumption increase life expectancy in humans? *Am. J. Clin. Nutr.* 78 (3), 526s–532s. doi:10.1093/ajcn/78.3.526s

Sotgia, F., Martinez-Outschoorn, U. E., and Lisanti, M. P. (2011). Mitochondrial oxidative stress drives tumor progression and metastasis: Should we use antioxidants as a key component of cancer treatment and prevention? *BMC Med.* 9 (11), 62. doi:10.1186/1741-7015-9-62

Sotolongo, K., Ghiso, J., and Rostagno, A. (2020). Nrf2 activation through the PI3K/GSK-3 axis protects neuronal cells from Aβ-mediated oxidative and metabolic damage. *Alz. Res. Ther.* 12 (1), 13–22. doi:10.1186/s13195-019-0578-9

Spector, A. (1995). Oxidative stress-induced cataract: Mechanism of action. *FASEB J.* 9 (12), 1173–1182. doi:10.1096/fasebj.9.12.7672510

Tang, D., Chen, X., Kang, R., and Kroemer, G. (2021). Ferroptosis: Molecular mechanisms and health implications. *Cell Res.* 31 (2), 107–125. doi:10.1038/s41422-020-00441-1

Tang, M., Ji, C., Pallo, S., Rahman, I., and Johnson, G. V. W. (2018). Nrf2 mediates the expression of BAG3 and autophagy cargo adaptor proteins and tau clearance in an age-dependent manner. *Neurobiol. Aging* 63, 128–139. doi:10.1016/j.neurobiolaging.2017.12.001

von Otter, M., Landgren, S., Nilsson, S., Zetterberg, M., Celojevic, D., Bergström, P., et al. (2010). Nrf2-encoding NFE2L2 haplotypes influence disease progression but not risk in Alzheimer's disease and age-related cataract. *Mech. Ageing Dev.* 131 (2), 105–110. doi:10.1016/j.mad.2009.12.007

Wei, Z., Hao, C., Huangfu, J., Srinivasagan, R., Zhang, X., and Fan, X. (2021). Aging lens epithelium is susceptible to ferroptosis. *Free Radic. Biol. Med.* 167, 94–108. doi:10.1016/j.freeradbiomed.2021.02.010

Williams, J. R., Trias, E., Beilby, P. R., Lopez, N. I., Labut, E. M., Bradford, C. S., et al. (2016). Copper delivery to the CNS by CuATSM effectively treats motor neuron disease in SODG93A mice co-expressing the copper-chaperone-for-SOD. *Neurobiol. Dis.* 89, 1–9. doi:10.1016/j.nbd.2016.01.020

Wolff, S. P. (1994). Cataract and UV radiation. *Doc. Ophthalmol.* 88 (3-4), 201–204. doi:10.1007/bf01203674

Woo, S. Y., Kim, J. H., Moon, M. K., Han, S. H., Yeon, S. K., Choi, J. W., et al. (2014). Discovery of vinyl sulfones as a novel class of neuroprotective agents toward Parkinson's disease therapy. *J. Med. Chem.* 57 (4), 1473–1487. doi:10.1021/jm401788m

Wu, H., Yu, Y., David, L., Ho, Y. S., and Lou, M. F. (2014). Glutaredoxin 2 (Grx2) gene deletion induces early onset of age-dependent cataracts in mice. *J. Biol. Chem.* 289 (52), 36125–36139. doi:10.1074/jbc.m114.620047

Xing, K.-Y., and Lou, M. F. (2010). Effect of age on the thioltransferase (glutaredoxin) and thioredoxin systems in the human lens. *Invest. Ophthalmol. Vis. Sci.* 51 (12), 6598–6604. doi:10.1167/iovs.10-5672

Yildirim, Z., Ucgun, N. I., and Yildirim, F. (2011). The role of oxidative stress and antioxidants in the pathogenesis of age-related macular degeneration. *Clinics* 66 (5), 743–746. doi:10.1590/s1807-59322011000500006

Zhang, H., Liu, Y.-y., Jiang, Q., Li, K.-r., Zhao, Y.-x., Cao, C., et al. (2014). Salvianolic acid A protects RPE cells against oxidative stress through activation of Nrf2/HO-1 signaling. *Free Radic. Biol. Med.* 69, 219–228. doi:10.1016/j.freeradbiomed.2014.01.025

Zhang, S., Liu, H., Amarsingh, G. V., Cheung, C. C., Hogl, S., Narayanan, U., et al. (2014). Diabetic cardiomyopathy is associated with defective myocellular copper regulation and both defects are rectified by divalent copper chelation. *Cardiovasc. Diabetol.* 13 (1), 100. doi:10.1186/1475-2840-13-100

Zhang, W. C. (2019). microRNAs tune oxidative stress in cancer therapeutic tolerance and resistance. *Int. J. Mol. Sci.* 20 (23), 6094. doi:10.3390/ijms20236094

Zhao, Z., Chen, Y., Wang, J., Sternberg, P., Freeman, M. L., Grossniklaus, H. E., et al. (2011). Age-related retinopathy in NRF2-deficient mice. *PloS one* 6 (4), e19456. doi:10.1371/journal.pone.0019456

Zigman, S. (1995). Environmental near-UV radiation and cataracts. *Optom. Vis. Sci.* 72 (12), 899–901. doi:10.1097/00006324-199512000-00008

frontiers | Frontiers in Chemistry

TYPE Mini Review
PUBLISHED 31 October 2022
DOI 10.3389/fchem.2022.1042658

Check for updates

OPEN ACCESS

EDITED BY
Jyotirmayee Mohanty,
Bhabha Atomic Research Centre (BARC), India

REVIEWED BY
Padmaja Prasad Mishra,
Saha Institute of Nuclear Physics (SINP), India
Pratik Sen,
Indian Institute of Technology Kanpur, India

*CORRESPONDENCE
Mercedes Novo,
m.novo@usc.es

SPECIALTY SECTION
This article was submitted to Supramolecular Chemistry, a section of the journal Frontiers in Chemistry

RECEIVED 12 September 2022
ACCEPTED 12 October 2022
PUBLISHED 31 October 2022

CITATION
Novo M and Al-Soufi W (2022), Supramolecular association studied by Fluorescence correlation spectroscopy. *Front. Chem.* 10:1042658. doi: 10.3389/fchem.2022.1042658

COPYRIGHT
© 2022 Novo and Al-Soufi. This is an open-access article distributed under the terms of the Creative Commons Attribution License (CC BY). The use, distribution or reproduction in other forums is permitted, provided the original author(s) and the copyright owner(s) are credited and that the original publication in this journal is cited, in accordance with accepted academic practice. No use, distribution or reproduction is permitted which does not comply with these terms.

Supramolecular association studied by Fluorescence correlation spectroscopy

Mercedes Novo* and Wajih Al-Soufi

Single-molecule Research Unit, Biophysical Chemistry, Photophysics and Spectroscopy Group, Faculty of Sciences, University of Santiago de Compostela, Lugo, Spain

A comprehensive description of a supramolecular system involves a full understanding of its thermodynamic and dynamic properties, as well as detailed knowledge of its structure. Fluorescence Correlation Spectroscopy (FCS) constitutes a powerful technique to acquire this information. Fluorescence correlation curves show a characteristic diffusion term that is related to the binding equilibrium constant or other thermodynamic properties of the supramolecular system. The association and dissociation rate constants of the binding process can be determined in FCS when the relaxation time of the binding is faster than the observation time—a regime called fast-exchange dynamics - in opposition to the slow-exchange regime. In all cases, structural information can be inferred from the diffusional properties of the supramolecular complexes. A short overview of the use of FCS for the study of supramolecular systems is given with examples which belong to the fast and slow regime.

KEYWORDS

Fluorescence Correlation Spectroscopy, supramolecular association, slow exchange, fast exchange, binding constant, association dynamics

1 Introduction

Supramolecular systems are assemblies of molecules maintained by non-covalent, weak interactions. They resemble biological systems regarding important aspects such as molecular recognition, self-assembly or host-guest binding. A key feature of these systems is their reversibility, which is a consequence of the weak intermolecular interactions between molecules and determines their function.

Structure, thermodynamics, and dynamics are needed to obtain a full picture of a supramolecular system (Bohne, 2011). Structure is defined by the stoichiometry of the building blocks and their spatial arrangement, whereas thermodynamics gives the stability and the specificity of the association. Dynamics is important to characterize the reactivity of these systems and understand their reversibility.

In contrast to molecules, supramolecular systems are highly dynamic with a high-order organization, which is often polydisperse and which determines their function (Bohne, 2014). Therefore, traditional chemical characterization methods in ensemble average are frequently insufficient and single-molecule approaches are needed to fully understand their behavior (Selvin and Ha, 2008). Single-molecule techniques have

demonstrated to reveal individual behaviors typical of complex local environments and to give dynamic information of these systems while staying at the equilibrium, both in solution and in cell culture (Zander et al., 2002; Yanagida and Ishii, 2009). Among them, Fluorescence Correlation Spectroscopy (FCS) is a powerful technique that allows for the investigation of structure, thermodynamics and dynamics of supramolecular systems (Al-Soufi et al., 2005).

2 Supramolecular association studied by Fluorescence Correlation Spectroscopy

2.1 Fluorescence Correlation Spectroscopy

FCS is a free diffusion single-molecule technique monitoring the intensity fluctuations of a small number of fluorescent molecules (N = 1–10) as they diffuse through an open sample volume. The fluorescence probe has typically nanomolar concentration and the very small observation volume of femtoliters is defined by the focus of a collimated laser beam in a confocal microscope with a high aperture objective. A fluorescent molecule which diffuses into this sample volume is excited by the laser light and generates a burst of fluorescence photons which are collected and monitored as a function of time. Then the autocorrelation function of the intensity trace is calculated in order to extract the physicochemical information of the system under study (Elson, 2011; Wohland et al., 2020).

The observed fluctuations of the fluorescence intensity can be due to diffusion, chemical reactions, photophysical processes, structural changes or any other processes which modulate the fluorescence signal of the probe around the equilibrium value. Each of these processes appears in the autocorrelation function as a "term" at a typical correlation time. In all cases, the random diffusion of the probe through the solution leads to a term at the diffusion correlation time τ_D, which is related to its translational diffusion coefficient D and hence to the size and shape of the diffusing particle. Therefore, the diffusion time yields direct information about the supramolecular systems, both regarding structure and thermodynamics of the species involved (Novo et al., 2011).

Typical processes in supramolecular systems such as host-guest interactions or self-assembly may also generate an additional correlation term, characterized by the reaction correlation time τ_R, which is the relaxation time of the process. This reaction time yields dynamic information of the system at equilibrium with no need of an external synchronization.

In the following sections we will analyze these two terms in more detail, taking into account the type of dynamics of the supramolecular system.

2.2 Slow *versus* fast-exchange dynamics

The stability of supramolecular systems is characterized by the binding equilibrium constant K (note that often the reciprocal value, i.e. the dissociation constant K_D, is used). A large value of K (or small K_D) indicates high affinity between the building blocks. Thermodynamic studies also give information about the association stoichiometry and the number of binding sites, as well as the specificity of a certain ligand to different receptors.

However, no dynamic information can be inferred from the binding equilibrium constant (Bohne, 2014). For a certain value of K, a wide range of association and dissociation rate constants are possible (Novo et al., 2011). For example, for an intermediate 1:1 binding constant of 10^3 M^{-1}, the association rate constant k_+ may vary within many orders of magnitude, with only a higher limit imposed by the diffusion controlled rate of about 10^{10} M^{-1} s^{-1}. Given the relationship $K = k_+/k_-$, it follows that the corresponding dissociation rate constant, k_-, ranges from 10^7 s^{-1} to values as low as 1 s^{-1} or even lower. Knowledge about these rate constants is crucial for the understanding of a supramolecular system, being k_+ mainly related to the geometric and steric requirements for the binding and k_- to the strength of the interactions between the building blocks (Al-Soufi et al., 2005; Novo et al., 2007; Al-Soufi et al., 2008; Bordello et al., 2010; Bordello et al., 2012; Bordello et al., 2015).

The broad dynamic range of supramolecular association yields relaxation times as short as a few nanoseconds or as long as seconds. Diffusion correlation times are usually in the range from tenth to several thousands of microseconds, whereas the reaction correlation time can vary from a few microseconds to hundreds of microseconds. For a given experimental observation time in a FCS experiment two limiting time regimes have to be distinguished: "slow-exchange", with long relaxation times with respect to the observation time, and "fast-exchange" where the binding dynamics is much faster than the observation time, with the reaction time at least one order of magnitude shorter than the diffusion time. Only in the second case dynamic information can be inferred from FCS, providing that the observed physical property changes during the binding process.

Figure 1 illustrates these two limiting regimes for host-guest supramolecular systems, slow-exchange dynamics on the left and fast-exchange on the right. The panel on the left, illustrates that the labelled guest passes through the observation volume either free or bound to the host, being the diffusion faster for the free guest. The rates of association and dissociation are too slow for these processes to occur during the time that the guest is observed. Therefore, two species are detected, the free guest and the host-guest complex, with different diffusional properties and contributions proportional to their equilibrium concentrations.

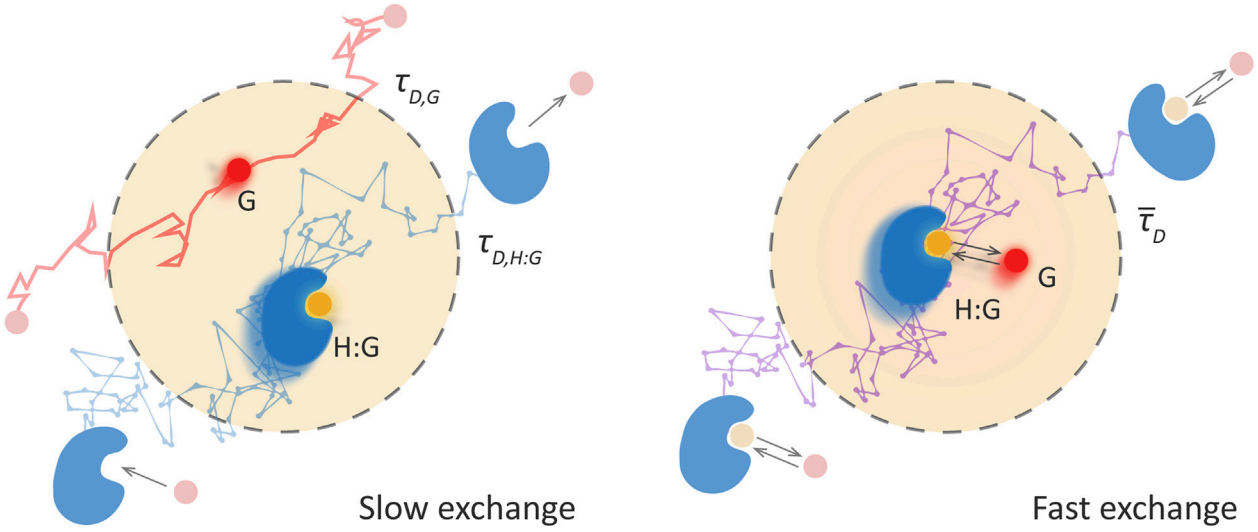


FIGURE 1
The two limiting regimes for the study of the association dynamics of host-guest supramolecular systems by FCS. The dashed grey line indicates the observation volume. Left panel: "Slow exchange"—the association dynamics are much slower than the diffusion time across the observation volume. The probability of an association or dissociation event during the observation is very low and the free guest, G, and the host-guest, H:G, are detected as separate species, each with its own diffusion time, $\tau_{D,G}$ and $\tau_{D,H:G}$, respectively. Right panel: "Fast exchange"—the association dynamics are fast enough to occur many times during the transit and, therefore, only one mean diffusion time, $\bar{\tau}_D$, is observed. Its value depends on the fraction of time the fluorescent species is free or bound during the transit, which, on the other hand, depends on the equilibrium constant and the concentration of the host.

On the contrary, in the fast exchange regime (Figure 1, panel on the right), the labelled guest binds to hosts and separates several times during its diffusion through the observation volume. This leads to the detection of a single diffusing species, with a mean diffusion time which is a weighted average between that of free and bound guest. If, additionally, the fluorescence intensity of the labelled guest changes upon binding, also faster fluorescence fluctuations are observed that are directly related to the exchange dynamics.

In the following sections we will show the FCS curves typical of these limiting regimes and discuss the information that can be obtained from them. Then, different examples of supramolecular systems with these two dynamic regimes will be shown.

2.3 Slow-exchange dynamics

Slow-exchange dynamics is typical of highly stable supramolecular systems, with large values of the binding equilibrium constant and long relaxation times. In FCS experiments, this kind of systems show two diffusion correlation times, a shorter one related to the free labelled molecule and a longer one due to the bound labelled molecule, with a higher mass and slower diffusion. The contributions of these two correlation terms to the correlation curve depend on the concentrations of the two species and on their brightness (often the fluorescence properties of the dye change upon binding). No reaction term is observed in this case, since the relaxation time is longer than the diffusion time and no exchange takes place during the observation time.

Figure 2, left panel, shows typical FCS curves of supramolecular binding with slow-exchange dynamics. Two diffusion times are observed, a shorter correlation time τ_{D1} for the free labelled molecule and a second, longer time τ_{D2} for the supramolecular complex. The amplitude of the correlation curve is inversely proportional to the total number of diffusing species N. The contributions of each species to the correlation curve, giving by parameters r and $1\text{-}r$ for τ_{D1} and τ_{D2}, respectively, and depend on the concentrations and on the brightnesses of the corresponding species. The analysis of all these parameters yields thermodynamic information of the supramolecular system, such as the binding equilibrium constant and the stoichiometry of the supramolecular complex. However, small size differences between the building blocks of the supramolecular system may hinder the discrimination of high stoichiometry complexes, due to the limitation of FCS to differentiate two diffusion times which are close to each other.

Usually self-assembly systems present such slow-exchange dynamics, with intermolecular cooperative forces that lead to stable aggregates above a critical concentration of monomers. An example of this kind of systems is the early aggregation of the peptide Amyloid-β(1–42) (Aβ42), which is thought to initiate the

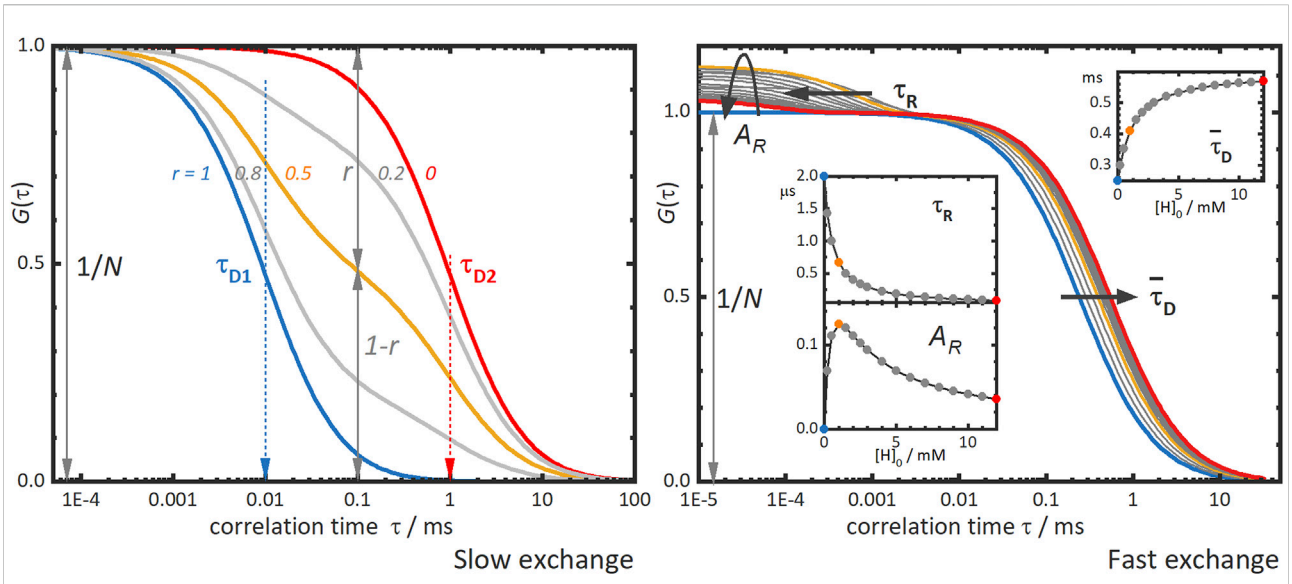


FIGURE 2
Simulated fluorescence correlation curves obtained in the slow and fast exchange regimes. Left panel: "Slow exchange"—the correlation curve shows two diffusion terms, one for each diffusing species, a fast one with τ_{D1}, and another slower one with τ_{D2}. In host-guest systems as that depicted in Figure 1, these species correspond to the guest with or $\tau_{D,G}$, and the complex with $\tau_{D,H:G}$, respectively. The different correlation curves in the panel correspond to different contributions of the two species to the curve as given by the parameter r. The blue curve with $r = 1$ and the red one with $r = 0$ would be obtained for solutions of only fast or slow species, respectively. The grey and orange intermediate curves correspond to mixtures of fast and slow species with r-values as indicated in the figure. Right panel: "Fast exchange"—the correlation curve shifts towards longer correlation times as the concentration of host is increased. The blue curve corresponds to that of free guest alone and the grey, orange, and red curves to increasing concentrations of host. The inserts show the dependence on the total host concentration, $[H]_0$, of the mean diffusion time, $\bar{\tau}_D$, the relaxation time, τ_R, and the amplitude, A_R, of the reaction term. In both regimes, the amplitude of the diffusion term is given by the inverse of the total number of diffusing species, N.

neurodegeneration process in Alzheimer's disease (Hardy et al., 2014). FCS titrations using a labelled peptide (Aβ42*) as probe were used to determine the concentrations and the diffusional properties of the species involved in the aggregation process (Novo et al., 2018). The results demonstrate that monomeric Aβ42 undergoes aggregation when its concentration exceeds a critical aggregation concentration (*cac*) of about 90 nM. Moreover, the aggregates formed are micelle-like oligomers, whose size and shape is independent of the incubation time or the peptide concentration.

2.4 Fast-exchange dynamics

As illustrated in Figure 1, right panel, in systems with fast binding dynamics, the association and dissociation processes take place during the time that the species diffuse through the observation volume. If, additionally, the fluorescent probe changes its brightness upon binding, both thermodynamic and kinetic information can be obtained in one and the same experiment.

The first effect of fast-exchange dynamics on the FCS curves is the observation of a single diffusion correlation term with a mean diffusion time, $\bar{\tau}_D$, which is a weighted average of the diffusion times of the species forming the supramolecular system (Al-Soufi et al., 2005; Novo et al., 2011). The value of this mean diffusion time is related to the binding equilibrium constant and increases with the concentration of the supramolecular complex. As for the slow-exchange dynamics, the amplitude of the diffusion term is the inverse of the total number of diffusing particles, N. Figure 2, right panel, shows simulated FCS curves for a host-guest system with fast-exchange dynamics. The diffusion term moves towards longer times as the concentration of the unlabelled host is increased. From the variation of the mean diffusion time with the host concentration the binding equilibrium constant K can be obtained, as well as the diffusion coefficients of the free guest and the host-guest complex.

We showed how FCS can be used to determine high binding equilibrium constants in non-fluorescent host-guest systems (Granadero et al., 2010). A suitable labelling of the guest, usually the smaller molecule, allows for the determination of the binding constant from the change of the mean diffusion time with the host concentration. The very low concentration of the fluorophore which is needed in FCS makes it possible to have an excess of host even for systems with very high binding affinities.

Stoichiometry of the host-guest complexes can also be inferred from the profile of the variation of the mean

diffusion time with the host concentration and the diffusional properties of the complex as compared to those of the free molecules. The sensibility of the FCS curves to different stoichiometries is especially high when a labelled guest is used and the size difference between guest and host is large.

The second effect in the FCS curves is the emergence of an additional term at shorter correlation times than the diffusion term (Figure 2, right panel). This "reaction" term is characterized by a reaction correlation time, τ_R, which is given by the relaxation time of the binding process, defined by the association and dissociation rate constants, k_+ and k_-, respectively, For a host-guest system, with a fluorescent-labelled guest, the reaction time is given by $\tau_R = (k_+[\mathrm{H}] + k_-)^{-1}$, with [H] being the total concentration of the unlabeled host. The amplitude of the reaction term, A_R, depends strongly on the brightness ratio between the free and the bound labelled molecule and shows a complex dependency with the binding equilibrium constant K (inset in the right panel of Figure 2). Both the reaction time and its amplitude vary with the concentration of host as shown in Figure 2, right panel, allowing for the determination of the different physicochemical parameters involved from FCS titrations.

Moreover, from the translational diffusion coefficients of the species determined form the FCS data, the limiting diffusion-controlled collisional rate constant of the association process can be estimated, making it possible to compare the observed association rate constant with this upper limit (Al-Soufi et al., 2005). This provides very useful information for the proposition of the corresponding kinetic mechanism of the binding process.

Our research group has pioneered the application of FCS to the study of fast supramolecular dynamics in host-guest systems (Al-Soufi et al., 2005). Fluorescent probes or fluorescent-labelled molecules suitable for FCS were used as guests to study different types of hosts, going from rigid cages such as cyclodextrins, which form inclusion complexes, to flexible micelles of surfactants and to biopolymers with binding capability.

Our FCS studies on the binding dynamics of pyronines with cyclodextrins explained the great differences in the stability of the formed inclusion complexes (Al-Soufi et al., 2005; Al-Soufi et al., 2008). The stability is dictated by the dissociation rate constants and not by the rate of the association process, as it may be expected. The association rate constants have the same order of magnitude for all systems under study, being among the highest reported for this kind of systems, but are significantly lower than the diffusion-controlled collision rate constant. From this information a two-step model is proposed. Firstly, an encounter complex is formed followed by an unimolecular inclusion reaction as the rate-limiting step. The rate of this second step seems to be controlled by geometrical and orientational requirements.

Comparing these binding dynamics of the relatively rigid cyclodextrins with those of the much more flexible micelles, one finds great differences in the association process. The association rate constants of dyes to micelles are much higher, and of the same order of magnitude as the estimated diffusion-controlled collision rate constants (Al-Soufi et al., 2008; Novo et al. 2011). The rate-limiting step is not the inclusion into the micelles, but the diffusion of dye and micelle to form the encounter complex. Based on this different behavior, we called micelles "soft cages", with no geometrical or orientational requirements for the formation of the supramolecular complex, whereas cyclodextrins behave as "hard cages", imposing geometric restrictions during the inclusion step.

We also used FCS to study the binding dynamics of small molecules to the minor groove of double stranded DNA (Bordello et al., 2012; Bordello et al., 2015). Again, the stabilities of the complexes formed were determined by the dissociation rate constants, quite high for the minor-groove binders under study due to the influence of the negatively charged fluorescent label. The association rate constants were at least two orders of magnitude smaller than the diffusion-controlled limit and were mainly responsible for the high specificity of the binders to AT sequences. The effect of salt concentration and the potential gliding mechanisms were analyzed with the help of a two-step mechanism with two types of encounter complexes (Bordello et al., 2012).

2.5 Structural studies of supramolecular systems by FCS

Beside thermodynamic and kinetic parameters, FCS studies yield also useful structural and geometric information. The diffusion correlation time τ_D is inversely proportional to the translational diffusion coefficient D and therefore related to the size and the shape of the diffusing species (Novo et al., 2011). Using the relationship between the diffusion coefficient and the mass, the size of the supramolecular complex can be obtained. This is especially useful for self-assembly systems, where the aggregation number of the aggregates can be estimated (Novo et al., 2018). From the dependency of the diffusion coefficient with the mass, information about the shape and conformation of the supramolecular complex or aggregate can be inferred (Al-Soufi et al., 2008; Bordello et al., 2009; Novo et al., 2018). Moreover, using the Stokes-Einstein relation the hydrodynamic radii of the supramolecular complexes can be estimated from the diffusion coefficients.

Our FCS study on the early aggregation of the Aβ42 allowed us to determine the conformational parameter ν, exponent of the diffusion coefficient *versus* molar mass dependency ($D \sim M^{-\nu}$), both for the monomeric species and for the aggregates (Novo et al., 2018). The value of $\nu = 0.44$ for Aβ42 monomers indicates a random coil conformation with some structured regions of the peptide. For the oligomers a value of $\nu = 0.75$ suggests an elongated conformation in agreement with the reported cylindrical geometry of the aggregates of a similar peptide

(Yong et al., 2002). Furthermore, the size statistical distribution and the mean aggregation number of about 50 Aβ42 monomers per aggregate were obtained from the analysis of the experimental diffusion correlation times of the aggregates. From these parameters, also the hydrodynamic radii of the monomers and the oligomers could be estimated using Stokes-Einstein equation.

Similar studies of host-guest systems formed by a small fluorescent molecule and cyclodextrins yielded a power law for the diffusion coefficients of the complexes of $D \sim M^{-0.4}$, a mass dependency in between the conformational parameter $\nu = 0.33$ expected for compact spherical particles and the value $\nu = 0.5$ which characterizes random coil conformation (Al-Soufi et al., 2005; Al-Soufi et al., 2008). This dependency was also found for micelles as hosts (Al-Soufi et al., 2008), allowing for the mean aggregation number determination.

3 Discussion

FCS is a very powerful technique for the study of supramolecular systems. Thermodynamic, dynamic, and structural information about these systems can be obtained from the same measurement or titration series. FCS is especially useful for the determination of association and dissociation rate constants in host-guest systems, where few other techniques are available. Nevertheless, to extract dynamic information from FCS measurements the system must fulfill two conditions: i) to be in the fast-exchange regime and ii) to show a significant change in the fluorescence intensity upon binding.

To comply with the first requirement the reaction time, τ_R, must be much shorter than the diffusion time $\bar{\tau}_D$, differing in at least one order of magnitude. Both, the reaction time, and the mean diffusion time, can be slightly tuned varying the host concentration (see Figure 2, right panel). More effectively, a significantly larger shift of the diffusion term can be achieved by changing the size of the observation volume, using different focus diameters. An increase of about one order of magnitude of the mean diffusion time can be obtained in this way. When, in spite of this, the reaction term and the diffusion term overlap, other single-molecule techniques with immobilized molecules may be used, such as smTIRF (Selvin and Ha, 2008). The second condition can be satisfied selecting a suitable fluorescent dye and the proper labelling site.

Author contributions

Equal contribution and last authorship: These authors contributed equally to this work and share last authorship.

Funding

We acknowledge funding by the Spanish Government (Ministerio de Ciencia e Innovación, grant PID 2020-120378RB-I00) and the Galician Government (Xunta de Galicia, grant ED431B 2019/18).

Conflict of interest

The authors declare that the research was conducted in the absence of any commercial or financial relationships that could be construed as a potential conflict of interest.

Publisher's note

All claims expressed in this article are solely those of the authors and do not necessarily represent those of their affiliated organizations, or those of the publisher, the editors and the reviewers. Any product that may be evaluated in this article, or claim that may be made by its manufacturer, is not guaranteed or endorsed by the publisher.

References

Al-Soufi, W., Reija, B., Felekyan, S., Seidel, C. A., and Novo, M. (2008). Dynamics of supramolecular association monitored by fluorescence correlation spectroscopy. *ChemPhysChem* 9, 1819–1827. doi:10.1002/cphc.200800330

Al-Soufi, W., Reija, B., Novo, M., Felekyan, S., Kühnemuth, R., and Seidel, C. A. M. (2005). Fluorescence correlation spectroscopy, a tool to investigate supramolecular dynamics: Inclusion complexes of pyronines with cyclodextrin. *J. Am. Chem. Soc.* 127, 8775–8784. doi:10.1021/ja0508976

Bohne, C. (2011). *Dynamics of guest binding to supramolecular assemblies*. New Jersey, United States: Wiley Online Library, 1–51. doi:10.1002/9781118095300.ch1

Bohne, C. (2014). Supramolecular dynamics. *Chem. Soc. Rev.* 43, 4037–4050. doi:10.1039/c3cs60352k

Bordello, J., Granadero, D., Novo, M., and Al-Soufi, W. The influence of hydrophobic fluorescent probes on surfactant premicellization studied by fluorescence correlation spectroscopy, (2009)

Bordello, J., Novo, M., and Al-Soufi, W. (2010). Exchange-dynamics of a neutral hydrophobic dye in micellar solutions studied by fluorescence correlation spectroscopy. *J. Colloid Interface Sci.* 345, 369–376. doi:10.1016/j.jcis.2010.01.064

Bordello, J., Sánchez, M. I., Vázquez, M. E., Mascareñas, J. L., Al-Soufi, W., and Novo, M. (2015). Fluorescence-labeled bis-benzamidines as fluorogenic DNA minor-groove binders: Photophysics and binding dynamics. *Chem. Eur. J.* 21, 1609–1619. doi:10.1002/chem.201404926

Bordello, J., Sánchez, M. I., Vázquez, M. E., Mascareñas, J. L., Al-Soufi, W., and Novo, M. (2012). Single-molecule approach to DNA minor-groove association dynamics. *Angew. Chem. Int. Ed.* 51, 7541–7544. doi:10.1002/anie.201201099

Elson, E. (2011). Fluorescence correlation spectroscopy: Past, present, future. *Biophys. J.* 101, 2855–2870. doi:10.1016/j.bpj.2011.11.012

Granadero, D., Bordello, J., Pérez-Alvite, M. J., Novo, M., and Al-Soufi, W. (2010). Host-guest complexation studied by fluorescence correlation spectroscopy:

Adamantane–cyclodextrin inclusion. *Int. J. Mol. Sci.* 11, 173–188. doi:10.3390/ijms11010173

Hardy, J., Bogdanovic, N., Winblad, B., Portelius, E., Andreasen, N., Cedazo-Minguez, A., et al. (2014). Pathways to Alzheimer's disease. *J. Intern. Med.* 275, 296–303. doi:10.1111/joim.12192

Novo, M., Felekyan, S., Seidel, C. A. M., and Al-Soufi, W. (2007). Dye-exchange dynamics in micellar solutions studied by fluorescence correlation spectroscopy. *J. Phys. Chem. B* 111, 3614–3624. doi:10.1021/jp0657639

Novo, M., Granadero, D., Bordello, J., and Al-Soufi, W. (2011). Host-guest association studied by fluorescence correlation spectroscopy. *J. Inclusion. Phenom. Macrocyclic. Chem.*, 1–10.

Novo, M., Freire, S., and Al-Soufi, W. (2018). Critical aggregation concentration for the formation of early Amyloid-β (1-42) oligomers. *Sci. Rep.* 8, 1783. doi:10.1038/s41598-018-19961-3

Selvin, P. R., and Ha, T. (2008). *Single-molecule techniques: A laboratory manual*. Cold spring harbor. New York: Cold Spring Harbor Laboratory Press, c2008.

Wohland, T., Maiti, S., and Macháň, R. (2020). *An introduction to fluorescence correlation spectroscopy*. Bristol, UK: Institute of Physics Publishing.

Yanagida, T., and Ishii, Y. (2009). *Single molecule dynamics in life science*. New Jersey, United States: Wiley Online Library.

Yong, W., Lomakin, A., Kirkitadze, M. D., Teplow, D. B., Chen, S. H., and Benedek, G. B. (2002). Structure determination of micelle-like intermediates in amyloid beta -protein fibril assembly by using small angle neutron scattering. *Proc. Natl. Acad. Sci. U. S. A.* 99, 150–154. doi:10.1073/pnas.012584899

Zander, C., Enderlein, J., and Keller, R. A. (2002). *Single-molecule detection in solution - methods and applications*. Berlin/New York: VCH-Wiley.

frontiers | Frontiers in Chemistry

TYPE Original Research
PUBLISHED 31 October 2022
DOI 10.3389/fchem.2022.1017394

Check for updates

OPEN ACCESS

EDITED BY
Rachelle J. Bienstock,
RJB Computational Modeling LLC,
United States

REVIEWED BY
Pranab Kishor Mohapatra,
C. V. Raman Global University, India
Shizhong Dai,
Stanford University, United States

*CORRESPONDENCE
Mary Jo Ondrechen,
mjo@neu.edu

SPECIALTY SECTION
This article was submitted to Theoretical and Computational Chemistry, a section of the journal Frontiers in Chemistry

RECEIVED 12 August 2022
ACCEPTED 10 October 2022
PUBLISHED 31 October 2022

CITATION
Iyengar SM, Barnsley KK, Vu HY, Bongalonta IJA, Herrod AS, Scott JA and Ondrechen MJ (2022), Identification and characterization of alternative sites and molecular probes for SARS-CoV-2 target proteins.
Front. Chem. 10:1017394.
doi: 10.3389/fchem.2022.1017394

COPYRIGHT
© 2022 Iyengar, Barnsley, Vu, Bongalonta, Herrod, Scott and Ondrechen. This is an open-access article distributed under the terms of the Creative Commons Attribution License (CC BY). The use, distribution or reproduction in other forums is permitted, provided the original author(s) and the copyright owner(s) are credited and that the original publication in this journal is cited, in accordance with accepted academic practice. No use, distribution or reproduction is permitted which does not comply with these terms.

Identification and characterization of alternative sites and molecular probes for SARS-CoV-2 target proteins

Suhasini M. Iyengar, Kelly K. Barnsley, Hoang Yen Vu, Ian Jef A. Bongalonta, Alyssa S. Herrod, Jasmine A. Scott and Mary Jo Ondrechen*

Department of Chemistry and Chemical Biology, Northeastern University, Boston, MA, United States

Three protein targets from SARS-CoV-2, the viral pathogen that causes COVID-19, are studied: the main protease, the 2′-O-RNA methyltransferase, and the nucleocapsid (N) protein. For the main protease, the nucleophilicity of the catalytic cysteine C145 is enabled by coupling to three histidine residues, H163 and H164 and catalytic dyad partner H41. These electrostatic couplings enable significant population of the deprotonated state of C145. For the RNA methyltransferase, the catalytic lysine K6968 that serves as a Brønsted base has significant population of its deprotonated state *via* strong coupling with K6844 and Y6845. For the main protease, Partial Order Optimum Likelihood (POOL) predicts two clusters of biochemically active residues; one includes the catalytic H41 and C145 and neighboring residues. The other surrounds a second pocket adjacent to the catalytic site and includes S1 residues F140, L141, H163, E166, and H172 and also S2 residue D187. This secondary recognition site could serve as an alternative target for the design of molecular probes. From *in silico* screening of library compounds, ligands with predicted affinity for the secondary site are reported. For the NSP16-NSP10 complex that comprises the RNA methyltransferase, three different sites are predicted. One is the catalytic core at the conserved K-D-K-E motif that includes catalytic residues D6928, K6968, and E7001 plus K6844. The second site surrounds the catalytic core and consists of Y6845, C6849, I6866, H6867, F6868, V6894, D6895, D6897, I6926, S6927, Y6930, and K6935. The third is located at the heterodimer interface. Ligands predicted to have high affinity for the first or second sites are reported. Three sites are also predicted for the nucleocapsid protein. This work uncovers key interactions that contribute to the function of the three viral proteins and also suggests alternative sites for ligand design.

KEYWORDS

SARS-CoV-2, main protease, RNA methyltransferase, Nucleocapsid, POOL, coupled amino acids, secondary sites

Introduction

Severe acute respiratory syndrome coronavirus 2 (SARS-CoV-2), the pathogen that causes the COVID-19 global pandemic (Wu F. et al, 2020; Zhou et al., 2020), has currently led to more than 620 million confirmed cases and more than six million deaths in over 200 countries according to the World Health Organization (https://covid19.who.int/). Oral antiviral drugs that act directly on the target of interest are a foundation for the treatment of viral diseases and two oral antiviral medications, Paxlovid and Lagevrio, have received emergency use authorization from the United States Food and Drug Administration (FDA) for the treatment of COVID-19. Given the heavy toll that COVID-19 has taken on human lives and health, as well as the serious social and economic impacts, we must learn as much as possible to characterize the viral components and how they function. Because a wider array of treatments is desired, further characterization of individual viral protein targets is required to develop future chemical probes and high-affinity ligands for COVID-19 and other potential related coronavirus infections.

The SARS-CoV-2 virus is a beta-coronavirus closely related to SARS-CoV and MERS-CoV. SARS-CoV-2 is a positive-strand RNA virus with a single-stranded RNA genome that consists of ~29800 bases which encodes up to 14 open reading frames (ORFs) (Wu A. et al, 2020). The viral genome encodes four structural proteins, Spike (S), envelope (E), membrane (M) and nucleocapsid (N), and 16 non-structural (NSP1-NSP16), proteins that are essential for the life cycle of the virus (Snijder et al., 2016; Wu A. et al, 2020). It is critical to understand how the viral proteins function and how their function may be modulated. The current drug discovery efforts primarily target the main protease, also called the 3CL-protease (MPro, NSP5, 3CL-Pro), the RNA-dependent RNA polymerase, and the Spike protein (Ramajayam et al., 2011; Wrapp et al., 2020). In this study, the targets of interest are the main protease (MPro), the RNA methyltransferase (MTase, NSP16) and the nucleocapsid protein (N protein). A greater understanding of the function of viral proteins can add to the knowledge of the viral life cycle at the atomic and molecular level. The results of this study can help to understand the function of these viral proteins and to guide strategies for the accelerated development of interventions to mitigate COVID-19.

MPro is one of two internally encoded proteases that hydrolyze the polyproteins at specific locations. Because MPro is essential for viral replication it is a validated drug target for SARS-CoV-2 (Gao et al., 2021; Cao et al., 2022; Huff et al., 2022). The MPro is made up of three domains: domains I (residues 10–99) and II (residues 100–182) have an antiparallel β-barrel structure. Domain III (residues 198–303) has a cluster of helices (Jin et al., 2020; Zhang et al., 2020). During the first step of the hydrolysis reaction, C145 acts as a nucleophile, assisted by H41 that acts as a base catalyst. There are also several binding sites in the catalytic machinery, with the S1 site defining the enzyme's affinity for glutamine at the P1 position of the peptide substrate. Domain III is involved in MPro dimerization, with the homodimer being proposed to be the active form of the enzyme (Hilgenfeld, 2014). Serial truncation experiments have also demonstrated that the last C-terminal helix in domain III is critical for dimerization (Hsu et al., 2005).

Capping of the viral RNA is critical for the survival and further replication of the virus in cells. For SARS-CoV-2, the 2′-O-methyltransferase (NSP16), with its partner protein NSP10, catalyzes a key step in the capping process. Thus it has been identified as a therapeutic target (Ahmed-Belkacem et al., 2022; Rowaiye et al., 2022; Sulimov et al., 2022). SARS-CoV-2 NSP16 has twelve strands, seven helices, and five 3_{10} helices, whereas NSP10 has a central antiparallel pair of strands and a helical domain with two zinc fingers. The NSP10 zinc coordinating residues are highly conserved across beta-coronaviruses, underlining the necessity for zinc coordination. The X-ray crystal structures highlight the *S*-adenosyl-L-methionine (SAM) and RNA cap substrate-binding pockets, together with the NSP10/NSP16 interface, as potential therapeutic targets. The NSP16 protein catalyzes the transfer of the methyl group from SAM to Cap-0, resulting in the reaction products S-adenosyl homocysteine (SAH) and Cap-1. The catalytic site of NSP16 is a highly conserved motif among class I MTases (K-D-K-E) and contains the residues K6839, D6928, K6968, and E7001 (Bollati et al., 2009; Chen et al., 2011; Decroly et al., 2011). Nsp10-derived peptide inhibitors have been identified as attractive therapeutic targets because they inhibit 2′-O-methyltransferase activity and impair viral replication (Ke et al., 2012; Wang et al., 2015; Ahmed-Belkacem et al., 2022; Sulimov et al., 2022). This 2′-O methyltransferase (MTase) has been shown to be required for coronavirus replication in cell cultures (Decroly et al., 2008; Daffis et al., 2010). NSP10 is an important cofactor for NSP16 and significantly increases NSP16 activity (Sawicki et al., 2005; Minskaia et al., 2006; Decroly et al., 2008; Daffis et al., 2010; Ma et al., 2015; Wang et al., 2015).

The nucleocapsid protein (N protein) is a key component of the viral envelope. The SARS-CoV-2 N protein is a multifunctional RNA-binding protein that is required by the virus for RNA transcription and replication. It plays important roles in the formation of helical ribonucleoproteins during the packaging of the viral RNA genome, controlling viral RNA synthesis in replication/transcription, and modulating infected cell metabolism (Stohlman et al., 1988; Nelson et al., 2000; Cong et al., 2020). Because of its essential roles in the viral lifecycle, the N protein is regarded as a therapeutic target (Wang et al., 2022). A conserved architecture with a β-sheet core of five antiparallel β-sheets, an extended β3-4 hairpin, and an acidic loop with a 3_{10}

TABLE 1 Selected SARS-COV-2 protein structures retrieved from the PDB.

PDB Code	Structure	Resolution (Å)	Reference
6LU7	MPro in complex with an inhibitor N3	2.16	Jin et al. (2020)
6W4H	NSP16-NSP10 Complex	1.80	Rosas-Lemus et al. (2020)
7DE1	Nucleocapsid protein C-terminal RNA binding domain	2.00	Yang et al. (2020)

helix is revealed in the structures of the SARS-CoV-2 N protein RNA binding domain. The primary functions of N protein are to bind to the viral RNA genome and pack it into a long helical nucleocapsid structure or ribonucleoprotein (RNP) complex (Masters & Sturman, 1990; McBride et al., 2014). The conservation of the N protein sequence across coronaviruses and its high immunogenicity make the N Protein an attractive therapeutic target for testing *in silico* (Luo et al., 2006; Yu et al., 2006; Peng et al., 2008; Tatar et al., 2021).

We report herein on the computationally predicted binding sites, on interactions between these sites, and on library compounds that possibly bind to these sites, for three SARS-CoV-2 protein targets: the main protease (MPro, NSP5, 3CL-Pro), the 2′-O-methyltransferase (MTase, NSP16), and the nucleocapsid protein (N protein).

Materials and methods

Protein structure retrieval and preparation

Protein preparation steps for structures retrieved from the PDB

Recently deposited structures of the SARS-CoV-2 MPro, MTase and N protein were obtained from the protein data bank (PDB) (Table 1). A Protein Reliability Report using Maestro was created with a structure analysis panel to compare the reliability of the structures (Supplementary Figure S1). Before running POOL (Tong et al., 2009; Somarowthu et al., 2011; Somarowthu & Ondrechen, 2012) on these structures, they were prepared and analyzed in YASARA (Krieger & Vriend, 2014). Each structure was loaded into a new YASARA workspace from the PDB, then cleaned to add any missing atoms. Water molecules, cofactors, and ligands were deleted. A simulation cell extending 5.0 Å around all atoms was created, solvated with a 0.999% solution of NaCl at pH = 7.0, and then pK_a prediction and energy minimization were performed using the YAMBER3 force field. The resulting cleaned structures were used as the input structures for POOL. The Protein Preparation Wizard (Sastry et al., 2013) in Maestro was used to further prepare them before docking with Glide (Halgren et al., 2004). The final step is restricted minimization, which provides controls for optimizing the corrected structure, easing any strain, and fine-tuning the placement of functional groups.

Protein preparation steps for homology models

The N Protein N-terminal RNA binding domain model structure was built with the homology model module in YASARA (Krieger et al., 2009) using a series of templates from the PDB. These structures were obtained from a BLAST search of the N Protein sequence (UniProtKB accession #P59595) (https://covid-19.uniprot.org/uniprotkb/P59595#Names%20&%20Taxonomy) on the PDB sequence database. The model was built from selected template structures with sequence homology to N Protein: SARS-CoV-2 nucleocapsid protein N-terminal binding domain (PDB ID: 6M3M) (Kang et al., 2020); RNA binding domain of nucleocapsid phosphoprotein from SARS-CoV-2 (PDB ID: 6VYO) (https://www.rcsb.org/structure/6VYO); C-terminal dimerization domain of Nucleocapsid Phosphoprotein from SARS-CoV-2 (PDBID: 6WJI) (https://www.rcsb.org/structure/6WJI); and the N-Terminal binding domain of the SARS-CoV-2 nucleocapsid phosphoprotein (PDBID: 6YI3) (Dinesh et al., 2020). Using these four structures as templates, a hybrid model for the N-terminal RNA binding domain of N protein was built in YASARA. Figure 1A shows the hybrid model generated for SARS-CoV-2 N Protein. In addition, a full-length model consisting of the entire N Protein structure was also built using the I-TASSER Server (Yang et al., 2015). Figure 1B shows the full-length model generated for SARS-CoV-2 N Protein. Both these N Protein models were further validated using structure evaluation servers, including ERRAT (Colovos & Yeates, 1993), VERIFY-3D (Eisenberg et al., 1997), the servers in the Structural Analysis and Verification Server (SAVES) (Lüthy et al., 1992), and QMean (Benkert et al., 2011) (Supplementary Figure S2). Then, the model structures were prepared as described above before running POOL (Tong et al., 2009; Somarowthu et al., 2011; Somarowthu & Ondrechen, 2012) and docking.

Ligand database retrieval and preparation

The ligands were obtained from the following databases: a) ZINC FDA library (https://zinc15.docking.org/substances/subsets/fda/) b) CAS Antiviral set (https://www.cas.org/covid-19-antiviral-compounds-dataset) c) Enamine FDA library (https://enamine.net/hit-finding/compound-collections/bioreference-compounds/fda-approved-drugs-collection) and d) Antiviral library consisting of compounds from: Selleck Chemicals Antiviral Library, Enamine Antiviral Library, and Asinex Antiviral Library. The ligands were

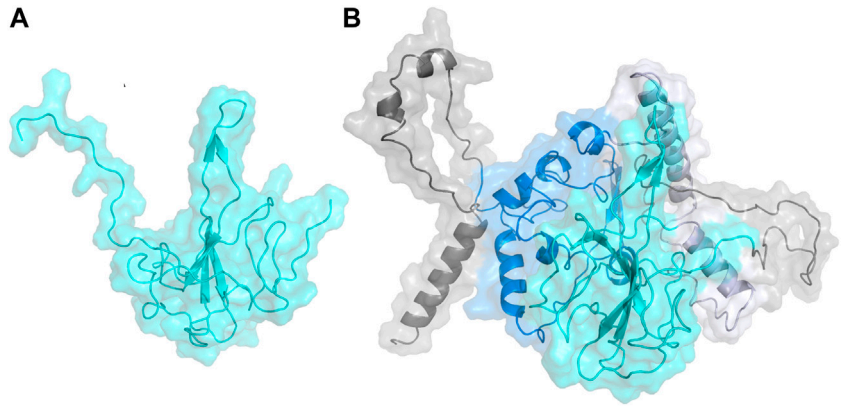


FIGURE 1
(A) Homology model built on YASARA for N-terminal domain of the Nucleocapsid protein shown in cyan. **(B)** Homology model built on I-TASSER for the full length Nucleocapsid protein with domains colored as: N-terminal domain—cyan; C-terminal domain—blue; linker region—lavender; other regions—gray.

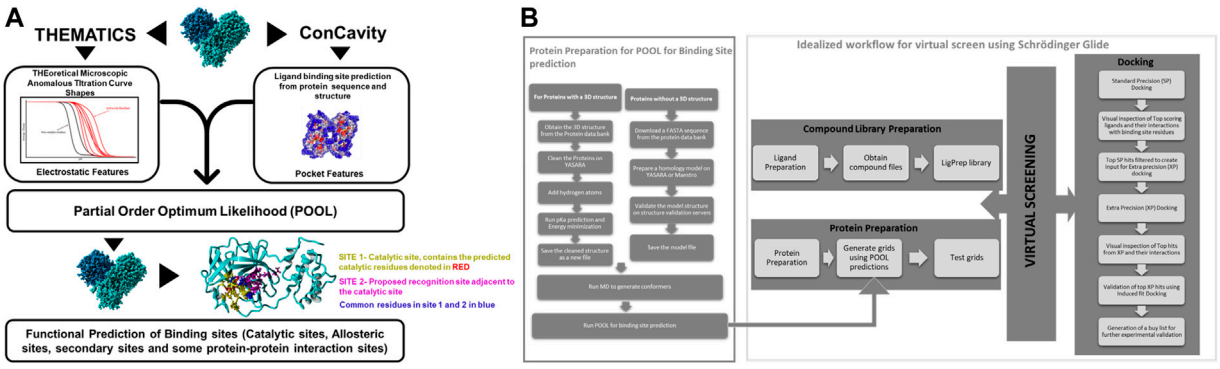


FIGURE 2
(A) A schematic representation of Partial Order Optimum Likelihood (POOL), our machine learning method to predict biochemically active sites. **(B)** Virtual screening workflow adopted in this project in conjunction with POOL.

prepared using the LigPrep (Schrödinger Release 2020–2: LigPrep, Schrödinger, LLC, New York, NY, 2021) tool.

Binding Site detection

For the binding site prediction, Partial Order Optimum Likelihood (POOL) (Tong et al., 2009; Somarowthu et al., 2011; Somarowthu and Ondrechen, 2012) was used (Figure 2A). POOL is a machine learning method that predicts biochemically active sites, including catalytic sites, allosteric sites, and exosites, some of which may not be detected by other predictive methods, from the 3D structure. POOL generates a rank-ordered list of all the amino acids in the protein structure in the order of likelihood of biochemical activity and the top 10% of the rank-ordered list are further visualized to predict the binding site pockets. The input features for POOL consist of electrostatic properties of the local environment (Ko et al., 2005; Wei et al., 2007; Tong et al., 2009; Somarowthu et al., 2011) and surface topological metrics from the structure-only version of ConCavity (Capra et al., 2009).

Virtual screening and analysis

Molecular Docking was performed using Schrödinger Glide (Friesner et al., 2004). For docking in Schrödinger Glide, the protein was minimized and optimized using the Protein

Preparation Wizard and the grid for docking was prepared using Receptor Grid Generation using clusters of residues from the top 10% of the POOL predicted residues as the centroid for ligand placement in Schrödinger 2020–3. Molecular Docking was performed on the Discovery Cluster at the Massachusetts Green High-Performance Computing Center using Glide. Glide Standard Precision (SP) (Halgren et al., 2004) was used as an initial screen and top predicted ligands with docking score of <=-7 kcal/mol were then docked with Glide Extra Precision (XP) (Friesner et al., 2006). The top hits from Glide XP were further used as input for the Induced Fit Docking (Sherman et al., 2006a; Sherman et al., 2006b; Farid et al., 2006) method in some cases on Schrödinger to account for the conformational flexibility of the protein and the ligand at the docking site. The top hits from each XP simulation were used to perform postprocessing using Schrodinger's Virtual Screening Workflow and Prime molecular mechanics/generalized Born surface area (MM- GBSA) calculations using the default settings. The protein-ligand complexes were then ranked on the basis of their binding free energy calculations. The workflow of our strategic modeling and *in-silico* screening is shown in detail in Figure 2B.

Residue interaction analysis

Pairwise Coulomb potential energies of interaction between amino acid side chains, and the free energies of desolvation of the amino acid side chains, were calculated by a linear Poisson-Boltzmann method (Antosiewicz et al., 1994; Baker et al., 2001; Shen et al., 2003; Dolinsky et al., 2004). The intrinsic pK_as were calculated from the desolvation energy as (Ullmann, 2003; Coulther et al., 2021; Iyengar et al., 2022):

$$\mathrm{p}K_a\,(\text{intrinsic}) = \mathrm{p}K_a\,(\text{model}) - \gamma \cdot \Delta\Delta G / [\ln(10)\mathrm{RT}] \qquad (1)$$

where the intrinsic pK_a is the pK_a of an amino acid side chain in the hypothetical protein structure where all other ionizable groups are in their electrically neutral state. The model pK_a is the pK_a of the side chain of the free amino acid in solution. For cation-forming side chains, $\gamma = +1$; $\gamma = -1$ for anion-forming side chains. $\Delta\Delta G$ is the Gibbs free energy of desolvation of the side chain in the hypothetical neutral protein structure, relative to the free amino acid in aqueous solution.

Results and discussion

Main protease (MPro, 3CL-Pro or NSP5)

POOL predicts a secondary recognition site for the main protease

The SARS-CoV-2 MPro structure consists of three domains: domain I has residues 10–99; domain II residues 100–182, and domain III residues 198–303. The active site is located on a cleft between domains I and II and includes a H41- C145 catalytic dyad. The major subsites in the MPro active site, where the substrate binds, have been identified (Jin et al., 2020). F140, L141, N142, H163, E166, and H172 make up the S1 subsite. A small portion of S1 subsite is further separated by N142 making up the S1' subsite, which consists of Y25, Y26, and L27, whereas H41, M49, Y54, M165, and D187 make up the hydrophobic S2 subsite. M165, L167, F185, Q189, and Q192 amino acids make up the S4 binding subsite.

The POOL-predicted residues for the Main Protease monomer (PDB ID: 6LU7, Figure 3) form two clusters near the site of proteolysis. One surrounds a pocket containing the catalytic site and consists of: L27, C38, P39, H41, V42, N142, G143, C145, M165, F181, R188, and Q189, including the two catalytic residues H41 and C145. This cluster also includes N142, L27, and M165, previously labeled as S1, S2, and S4, respectively. POOL predicts a second cluster that surrounds a pocket adjacent to the catalytic site and consists of: R40, Y54, C85, R105, Q110, C128, F140, L141, S144, C160, Y161, H163, H164, E166, H172, A173, Y182, and D187. This secondary recognition site includes S1 residues from Domain II, F140, L141, H163, E166, and H172. It also includes D187, previously identified as a member of S2.

Recognition peptide sequence docked on the main protease interacts with the POOL predicted residues

The main protease recognition sequence is LQ↓SAG. To understand the how the polypeptide sequence interacts with the residues around the active site of the main protease, a peptide fragment, capped on the N- and C- terminal sides with two glycine residues, GG-LQSAG-GG was docked into the protease dimer structure using the Schrodinger Peptide Docking algorithm. The peptide was docked at the catalytic site to identify its interactions with the amino acids surrounding the active site pocket. The docking scores of the complex with the MPro receptor are represented in Table 2. The peptide GG-LQSAG-GG binds to the catalytic pocket with the recognition sequence approaching the two catalytic residues H41-C145, as seen in Figure 4. It has a good docking score and interactions with some of the residues within the S1, S1', S2, and S4 subsites including the active site residues H41 and C145. The peptide GG-LQSAG-GG (Figures 4A,B) gives a docking score of -9.15 kcal/mol and MM-GBSA Binding energy of -31.04 kcal/mol. The GG-LQSAG-GG peptide lies in a pocket (A chain) formed by F140, L141, N142, H163 and E166 which belong to the S1 subsite, T25, T26, and L27 which belong to the S1' subsite, H41, M49 and D187 from the hydrophobic S2 subsite and M165, and Q189 belonging to the hydrophobic S4 subsite. Some other residues forming a pocket around the peptide are C44, T45, S46, H164, G143, S144, C145, and R188 from the A Chain and Ser1 from the B Chain. Four hydrogen bonds are found between the peptide and T26, S46, N142, and E166, from the A Chain (Figures 4A,B).

10.3389/fchem.2022.1017394

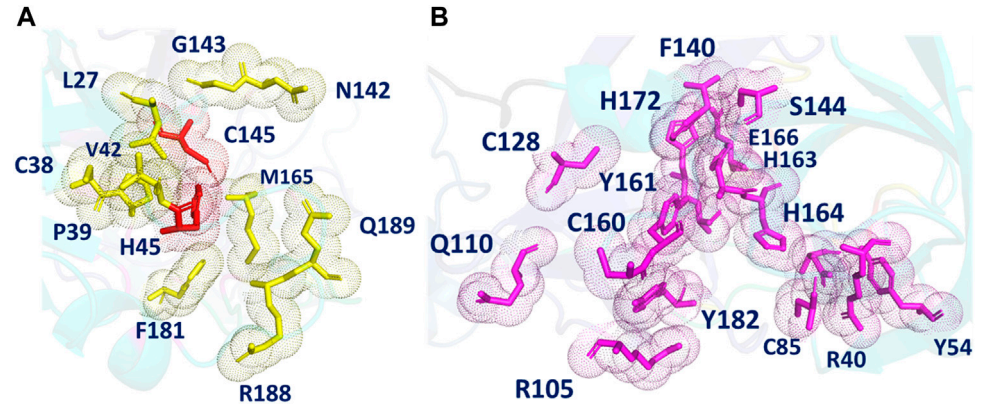


FIGURE 3
(A) The different POOL-predicted pockets for the SARS-CoV-2 Main Protease (PDB ID: 6LU7). The POOL predicted residues in pocket one shown in yellow include the catalytic dyad H41-C145, shown in red. **(B)** The POOL-predicted secondary recognition pocket, shown in magenta, are the residues surrounding the catalytic dyad.

TABLE 2 Peptide Docking scores with the SARS-CoV-2 Main Protease.

Peptide name	Sequence	Docking score (kcal/mol)	MM-GBSA score (kcal/mol)
GG-LSQAG-GG	GGLQSAGGG	-9.15	-31.0

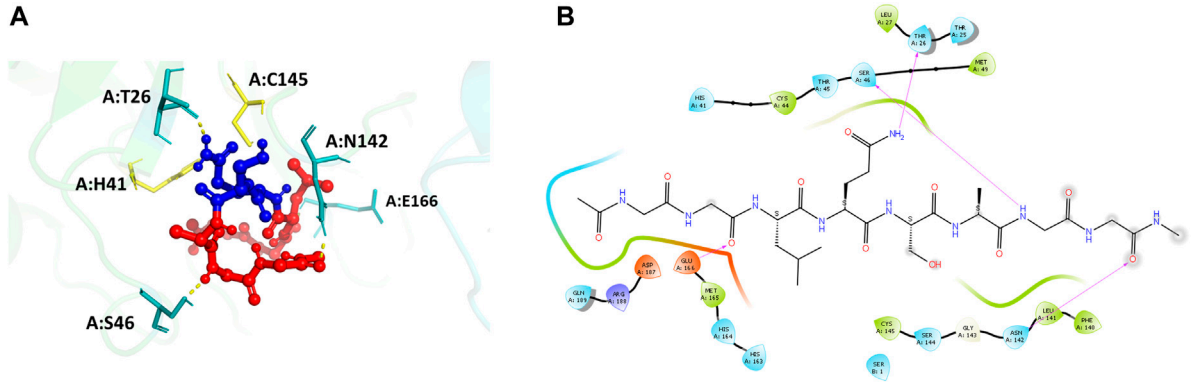


FIGURE 4
(A) Docking pose of the recognition peptide LQ↓SAG with two glycine caps (GG-LQSAG-GG) docked at the active site (in yellow) of the SARS-CoV-2 MPro with chain A in green and chain B in cyan. The peptide GG-LQSAG-GG is shown as red balls and sticks with the cleavage sequence Q↓S shown in blue. The H-bond interactions are shown in yellow and the interacting residues in teal. **(B)** The ligand interaction diagram showing the docked pose of GG-LQSAG-GG and the residues forming a pocket around it.

Key interactions with the catalytic residues for MPro

Key interactions that facilitate the catalytic activity of H41 and C145 were analyzed. C145, in order to serve as a nucleophile, must have significant population of the deprotonated state of its side chain. This is achieved through coupling to three nearby histidine residues, the dyad partner H41, the S1 residue H163, and H164, as shown in Table 3. The strong electrostatic coupling between C145 and these three histidines, with the intrinsic pK_a of the anion-forming residue higher than that of each of the cation-forming residues, leads to an expanded buffer range and significant populations of both

TABLE 3 Computed pairwise energies of electrostatic interaction (kcal/mol) between the two catalytic residues C145 and H41 and their strongest coupling partners in the SARS-CoV-2 main protease. Intrinsic pK_as for each residue are also listed.

Top couplers to C145: pK_a (intrinsic) = 8.9			Top couplers to H41: pK_a (intrinsic) = 5.6		
Residue	**|E|(kcal/mol)**	**pK_a (intrinsic)**	**Residue**	**|E|(kcal/mol)**	**pK_a (intrinsic)**
H41	1.3	5.6	Y54	1.7	11.7
H163	1.0	5.0	H164	1.7	5.1
H164	0.94	5.1	C145	1.3	8.9
Y54	0.58	11.7	D187	1.2	5.2
Y161	0.56	11.9	C44	1.0	9.7

protonation states that is necessary for catalysis (Koumanov et al., 2002; Ringe et al., 2004; Coulther et al., 2021; Iyengar et al., 2022). Indeed, significant population of the deprotonated state of C145 has been implied in a recent report suggesting covalent binding of selected ligands by C145 (Mohapatra et al., 2021). Similarly, the catalytic H41 must have significant population of both protonation states to exchange a proton with the thioester intermediate. This is achieved through the coupling to C145, and also to H164, wherein the two like-charged histidine side chains are strongly coupled to each other and have matched (<1 pH unit difference) intrinsic pK_as (Table 3) (Koumanov et al., 2002; Coulther et al., 2021; Iyengar et al., 2022).

Potential SARS-CoV-2 main protease inhibitors that bind to the secondary recognition MPro POOL predicted site

Docking reveals potential ligand candidates that bind to the MPro secondary recognition site predicted by POOL; the top five are: 989–51–5 (Epigallocatechin gallate); ZINC000085540219 (Ioxilan); Z1563146136 (Acarbose); ZINC000003914596 (Saquinavir) and ZINC000003830947 (Iopamidol) (Supplementary Table S1). Supplementary Table S1 shows the Glide docking method, docking scores and details of the ligand-protein interactions. The list includes antidiabetic agents and protease inhibitors. The docking score ranges for Induced fit docking on Glide were between -14 and -11 kcal/mol. The interactions between the ligand-protein complex are shown in Supplementary Figure S3 and listed in Supplementary Table S4. All the compounds bind at the POOL predicted secondary site and some of the important H-bond interactions are observed with the residues N142, H164, E166, and Q189; these are similar to the interactions observed with the recognition peptide sequences. Some of the important π- π interactions are observed with H41 and H164.

Epigallocatechin gallate (Figures 5A,B), the top hit, binds to the MPro secondary recognition site with an IFD-XP Score of -14.12 kcal/mol. It forms 11 H-bond interactions with the residues T26, H41, Y54, N142, H163, H164, E166, and Q189 and a π- π interaction is observed with H41. The residues forming a pocket around the binding pose of Epigallocatechin gallate are T25, T26, L27, H41, C44, M49, P52, Y54, F140, L141, N142, G143, S144, C145, H163, H164, M165, E166, D187, R188 and Q189.

Methyltransferase (MTase, NSP16/NSP10 complex)

POOL predicts multiple sites for the methyltransferase

The NSP16 crystal structure (PDB ID: 6W4H) is made up of the polyprotein pp1ab residues 6,799 to 7,096. The catalytic core of the NSP16 forms a Rossmann-like beta-sheet fold with seven β-strands and one antiparallel β-strand (β7) which is sandwiched between 11 α-helices and 20 loops. There are three β-strands (β′1, β′2, and β′3) in the NSP10 protein, which have pp1a residues 4,272–4,392, that form a central antiparallel β-sheet at its core. On one side of the β -sheet is a large loop that directly interacts with NSP16 and stabilizes the heterodimer complex. On the other side of this β-sheet, six helices and loops form two zinc finger motifs. It has been reported that coronaviruses use zinc fingers to non-specifically bind RNA (Matthes et al., 2006; Chen et al., 2011). There are two Zn^{2+}-binding sites; the first one is coordinated by C4327, C4330, H4336, and C4343 and the second one is coordinated by C4370, C4373, C4381, and C4383. The NSP16 protein catalyzes the transfer of the methyl group from SAM to Cap-0, resulting in the reaction products S-adenosyl homocysteine (SAH) and Cap-1 (Nencka et al., 2022). The adenosine moiety is stabilized by residues F6947, D6912, L6898, C6913, and M6929. The sugar moiety is stabilized by G6871 and D6897 residues, as well as two molecules of water which interact with N6899. The methionine moiety interacts with the residues D6928, Y6845, N6841, and G6871.

The POOL-predicted residues for the methyltransferase form three clusters, as shown in Figure 6. The first one is

10.3389/fchem.2022.1017394

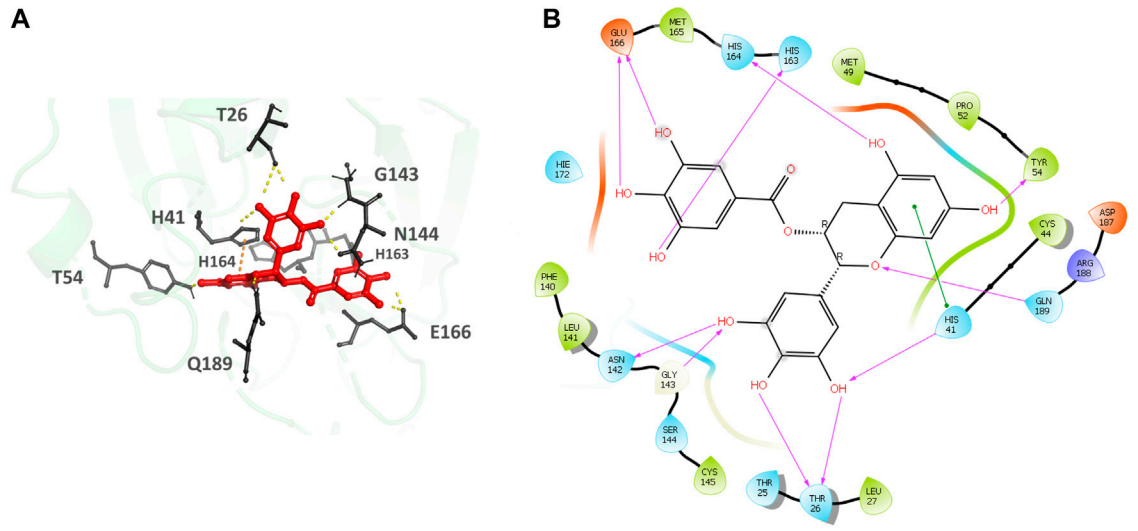


FIGURE 5
(A) Epigallocatechin gallate bound to the monomer of the SARS-CoV-2 MPro at the POOL predicted secondary site. The protein backbone is shown in green cartoon representation, ligand in red with the residues in gray. The hydrogen bonds are shown as yellow dashes and π- π stacking interactions as orange dashes. **(B)** Ligand interaction diagram of Epigallocatechin gallate at the secondary site. The hydrogen bonds are shown as pink arrows and π- π stacking interactions are shown as green lines.

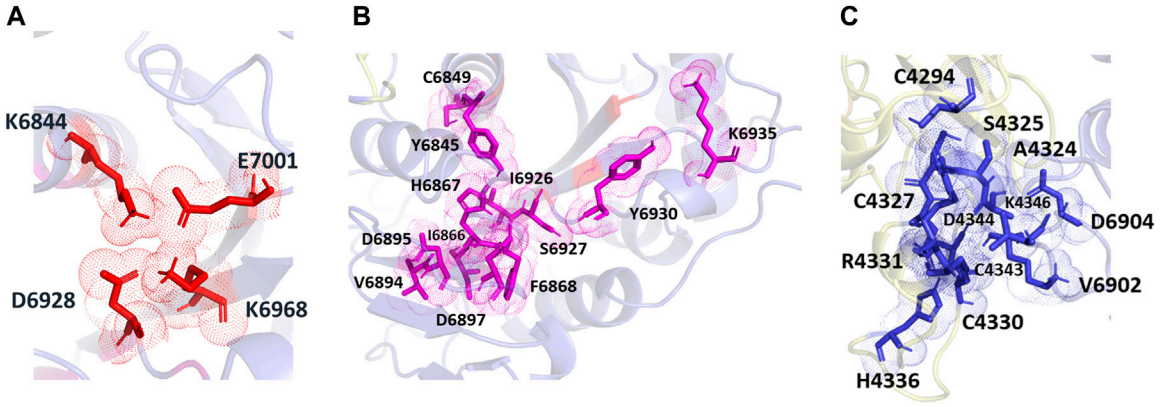


FIGURE 6
The different POOL predicted sites for the SARS-CoV-2 RNA methyltransferase (NSP16/NSP10 complex) **(A)** The POOL-predicted residues in site 1, which contains the D-K-E part of the K-D-K-E conserved catalytic motif (D6928, K6968, and E7001) with an additional K6844, are shown in red **(B)** POOL-predicted site 2, containing residues surrounding the catalytic motif, is shown in magenta. **(C)** Site 3, and the POOL-predicted residues at the dimer interface, in blue.

located at the conserved catalytic K-D-K-E motif found in methyltransferases, and includes the catalytic D6928, K6968, and E7001, with an additional K6844 residue (colored in red). The second cluster surrounds the catalytic pocket and includes Y6845, C6849, I6866, H6867, F6868, V6894, D6895, D6897, I6926, S6927, Y6930, and K6935 (shown in magenta). The third POOL-predicted site for the NSP16-NSP10 complex lies at the heterodimer interface and consists of C4294, A4324, S4325, C4327, C4330, R4331, D4335, H4336, C4343, D4344, K4346, and C4383 of the NSP10 chain and V6902, D6904 of the NSP16 chain (shown in blue).

Key interactions with the catalytic residues for the methyltransferase

For each of the catalytic residues in the K-D-K-E motif, the top five couplers with the highest pairwise potential energies of

TABLE 4 Computed pairwise energies of electrostatic interaction (kcal/mol) between three of the members of the catalytic tetrad D-K-E, D6928, K6968, and K7001, plus the coupled K6844, and their five strongest coupling partners for each, in the SARS-CoV-2 RNA methyltransferase. Intrinsic pK_as for each residue are also listed.

Top couplers to D6928: pK_a (intrinsic) = 4.6			**Top couplers to E7001: pK_a (intrinsic) = 5.0**		
Residue	**|E|(kcal/mol)**	**pK_a (intrinsic)**	**Residue**	**|E|(kcal/mol)**	**pK_a (intrinsic)**
K6968	2.6	9.8	K6844	2.4	9.4
Y6845	2.4	10.7	K6968	2.0	9.8
K6844	1.5	9.4	D6928	1.2	4.6
E7001	1.2	5.0	Y7026	0.90	12.5
H6867	1.0	3.1	Y6845	0.78	10.7
Top couplers to K6844: pK_a(intrinsic) = 9.4			**Top couplers to K6968: pK_a(intrinsic) = 9.8**		
Residue	**|E|(kcal/mol)**	**pK_a(intrinsic)**	**Residue**	**|E|(kcal/mol)**	**pK_a(intrinsic)**
E7001	2.4	5.0	D6928	2.6	4.6
K6968	1.8	9.8	E7001	2.0	5.0
D6928	1.5	4.6	K6844	1.8	9.4
Y6845	0.91	10.7	Y6845	0.91	10.7
Y6930	0.53	10.2	Y6930	0.77	10.2

interaction are shown in Table 4. Lysine-6968 serves as the base that enables the 2' oxygen atom of the RNA to attack the methyl group of SAM (Nencka et al., 2022). The deprotonated state of K6968 is significantly populated, first by the strong electrostatic coupling to K6844, wherein the two lysine residues have closely matched intrinsic pK_as (Table 4), and second by strong coupling to Y6845 (and to a lesser extent to Y6930), wherein the anion-forming tyrosine has an intrinsic pK_a higher than that of the lysine (Koumanov et al., 2002; Coulther et al., 2021; Iyengar et al., 2022). Strong coupling to the two anion-forming residues, D6928 and E7001, strengthens the basicity of K6968.

Potential SARS-CoV-2 Methyltransferase (NSP16/NSP10 Complex) inhibitors that bind to the MTase POOL-predicted site containing the conserved catalytic motif

To verify the docking method, the known ligand sinefungin was docked into the catalytic site, resulting in a pose similar to that of the reported complex structure (PDB ID 6WKQ) (Rosas-Lemus et al., 2020) with a docking score of -8.2 kcal/mole. Docking studies and analysis yield potential ligand candidates that bind to the MTase conserved catalytic motif. Examples are mostly from the Chemical Abstracts Service (CAS) Antiviral Database and include: CAS ID# 435297–57–7 (1H-1,2,4-Triazole-3-carboxamide, 1-β-D-ribofuranosyl-, 5′-[6-hydrogen (2R)-2-aminohexanedioate); 435297-58-8 (1H-1,2,4-Triazole-3-carboxamide, 1-β-D-ribofuranosyl-, 5′-[6-hydrogen (2S)-2-aminohexanedioate); 1312805-81-4 (Adenosine, 1′-[3-(aminocarbonyl)-1H-1,2,4-triazol-1-yl]-1′-de (6-amino-9H-purin-9-yl)adenylyl-(2′→5′)-1′-[3-(aminocarbonyl)-1H-1,2,4-triazol-1-yl]-1′-de (6-amino-9H-purin-9-yl)adenylyl-(2′→5′)-1′-[3-(aminocarbonyl)-1H-1,2,4-triazol-1-yl]-1′-de (6-amino-9H-purin-9-yl)-(Acl))); 1002334-92-0 (1H-1,2,4-Triazole-3-carboxamide, 1-[5-O-[5-(β-D-galactopyranosyloxy)-1-oxopentyl]-β-D-ribofuranosyl]-(Acl)); and 435297-32-8 (L-Arginine, 5′-ester with 1-β-D-ribofuranosyl-1H-1,2,4-triazole-3-carboxamide- (9Cl)) (Supplementary Table S2). Supplementary Table S2 shows the Glide docking method, docking scores, and MM-GBSA scores, along with the specific ligand-protein interactions. The docking score ranges for Extra Precision (XP) Gscore from Glide were between -14 and -13 kcal/mol. The interactions in the ligand-protein complex are shown in Supplementary Figure S4 and listed in Supplementary Table S2. All the compounds bind at the POOL-predicted site containing the conserved catalytic motif and important H-bond interactions are observed with the residues K6844, G6911, C6913, D6928, and K6968.

435297-57-7 (1H-1,2,4-Triazole-3-carboxamide, 1-β-D-ribofuranosyl-, 5′-[6-hydrogen (2R)-2-aminohexanedioate) (Figures 7A,B), the top hit, binds to the MTase conserved catalytic pocket with an XP Gscore of-14.88 kcal/mol. It forms seven H-bonds and interactions with the residues S6896, D6897, G6869, G6911, C6913, Y6930 and K6968. The residues forming a pocket around the binding pose of 435297-57-7 are N6841, K6844, A6870, G6869, F6868, S6872, G6871, G6911, D6912, C6913, V6916, D6928, M6929, Y6930, D6931, F6947, K6968.

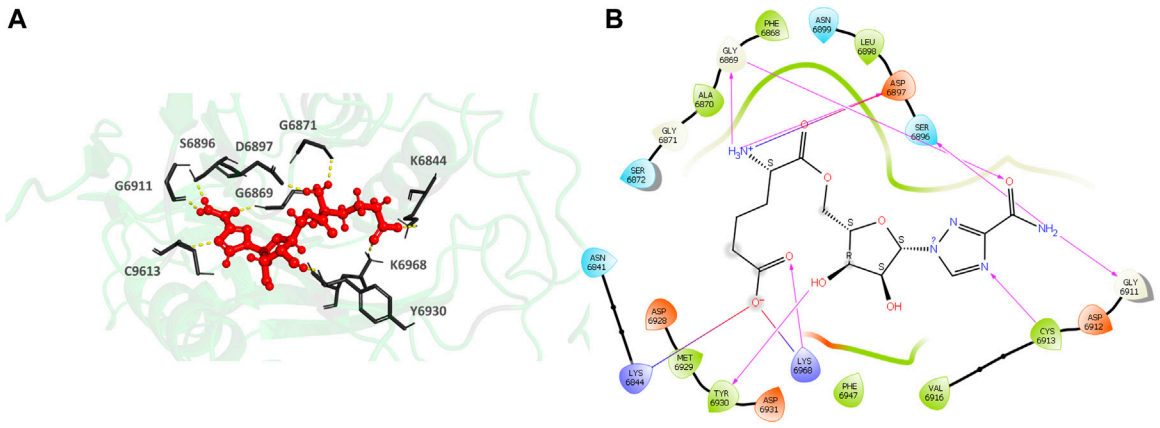


FIGURE 7
(A) CAS#435297–57–7 bound to the SARS-CoV-2 NSP16/NSP10 complex (MTase) at the POOL-predicted site including the conserved catalytic motif. The protein backbone is shown in cartoon representation in green, ligand in red with the residue side chains in gray. The hydrogen bonds are shown as yellow dashes. **(B)** Ligand interaction diagram of CAS#435297–57–7 at the POOL-predicted site containing the conserved catalytic motif. The hydrogen bonds are shown as pink arrows and salt bridges in a bluish-red line.

Potential SARS-CoV-2 Methyltransferase (NSP16/NSP10 Complex) inhibitors that bind to the MTase second POOL-predicted pocket surrounding the conserved catalytic motif

Docking studies and analysis yield potential ligand candidates that bind to the second POOL-predicted NSP16 pocket surrounding the catalytic motif. Examples include: CAS ID# 926902-14-9 (Adenosine, 5′→P-ester with thiotetraphosphoric acid ([(HO) (HS)P(O)OP(O) (SH)]2O), P‴→5′-ester with uridine); 162754-90-7 (β-D-arabino-Adenosine, 5′-O-phosphonoadenylyl-(2′→5′)-adenylyl-(2′→5′)- (9Cl)); 188560-02-3 (Inosine 5′-(pentahydrogen tetraphosphate), P′→5′-ester with inosine); 217807-08-4 (Adenosine, 5′-O-[hydroxy [[hydroxy (phosphonooxy) phosphinyl]oxy] phosphinyl]adenylyl-(2′→5′)-adenylyl-(2′→5′)-1′-[3-(aminocarbonyl)-1H-1,2,4-triazol-1-yl]-1′-de (6-amino-9H-purin-9-yl)- (9Cl)); and 217807-10-8 (Adenosine, 5′-O-[hydroxy (phosphonooxy)phosphinyl]adenylyl-(2′→5′)-1′-[3-(aminocarbonyl)-1H-1,2,4-triazol-1-yl]-1′-de (6-amino-9H-purin-9-yl)adenylyl-(2′→5′)- (9Cl)), (Supplementary Table S3). Supplementary Table S3 shows the Glide docking method, docking scores, MM-GBSA scores and the specific interactions with amino acids. The list consists mainly of antiviral ligands from the Chemical Abstract Service (CAS) Antiviral Database. The docking score ranges for Extra Precision (XP) docking on Glide were between -14 and -13 kcal/mol. The interactions between the ligand-protein complex are shown in Supplementary Figure S5 and listed in Supplementary Table S3. All the compounds bind at the POOL predicted NSP16 pocket surrounding the catalytic motif and some of the important H-Bond interactions are observed with the residues K6844, D6897, D6912, C6913, D6928, Y6930, and K6935. Some of the important π- π interactions are observed with Y6828 and F6947 of the NSP16 chain.

926902-14-9 (Adenosine, 5′→P-ester with thiotetraphosphoric acid ([(HO) (HS)P(O)OP(O) (SH)]2O), P‴→5′-ester with uridine) (Figures 8A,B), the top hit, binds to the MTase POOL predicted NSP16 pocket surrounding the catalytic motif with an XP Gscore of -14.41 kcal/mol. It forms nine H-bonds and interactions with the residues G6829, L6898, D6897, N6899, D6912, C6913, Y6930, F6947, K6968, and N6996. It also forms two π- π interactions with Y6828 and F6947. The residues forming a pocket around the binding pose of **926902-14-9** are Y6828, G6829, D6830, M6840, N6841, K6844, G6869, G6871, S6872 D6897, L6898, N6899, D6912, C6913, A6914, D6928, M6929, Y6930, D6931, P6932, K6935, F6947, N6996, S6998, S6999, S7000, and E7001.

Nucleocapsid protein (N-Cap)

POOL predicts multiple sites for the nucleocapsid protein

The SARS-CoV-2 N protein is divided into five domains: a predicted intrinsically disordered N-terminal domain (N-NTD); an RNA-binding domain; a predicted disordered central linker (LKR) within a Ser/Arg rich (S/R) domain; a dimerization domain; and a predicted disordered C-terminal domain (N-CTD). SARS-CoV has been shown to bind viral RNA *via* the N-NTD, N-CTD, and C-tail domains (Huang et al., 2004; Chen et al., 2007; Takeda et al., 2008). It has been reported that the LKR's SR-rich region regulates N protein oligomerization upon phosphorylation (Peng et al., 2008) and the N-protein self-association is required for viral RNP assembly (Luo et al., 2006). The N-CTD has been shown to play a direct role in N

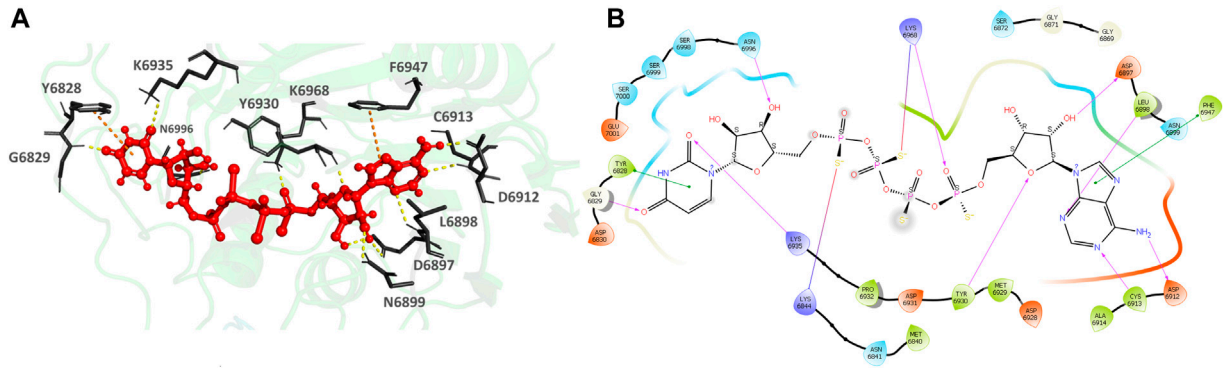


FIGURE 8
(A) CAS# 926902–14–9 bound to SARS-CoV-2 NSP16/NSP10 complex (MTase) at the POOL-predicted residues surrounding the conserved catalytic motif, Site 2. The protein backbone is shown in cartoon representation in green, ligand in red with the residue side chains in gray. The hydrogen bonds are shown as yellow dashes. **(B)** Ligand interaction diagram of CAS# 926902–14–9 and the POOL-predicted residues surrounding the conserved catalytic motif, Site 2. The hydrogen bonds are shown as pink arrows and salt bridges in a bluish-red line.

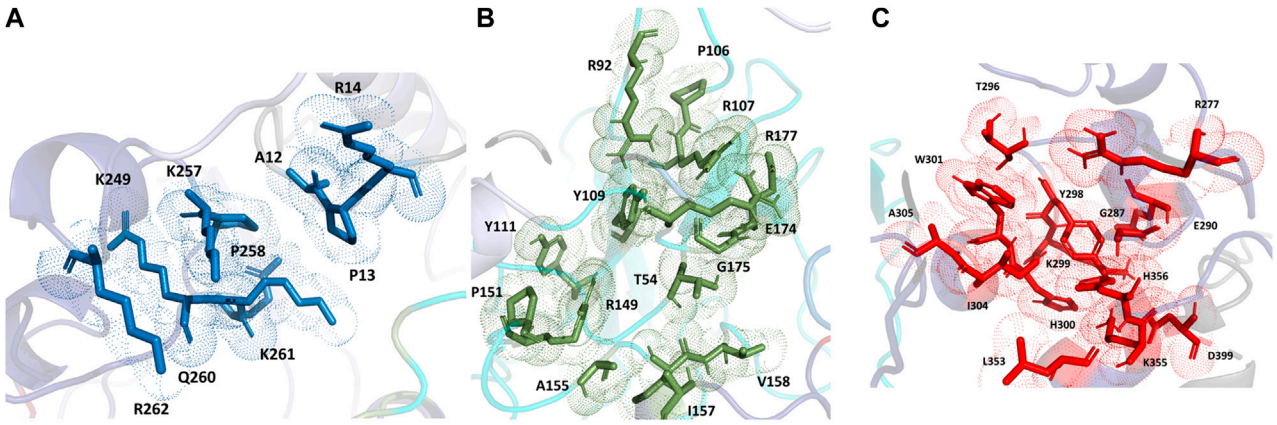


FIGURE 9
The different POOL-predicted sites for the SARS-CoV-2 Nucleocapsid protein. POOL-predicted sites for the full-length SARS-CoV-2 Nucleocapsid protein built on I-TASSER. **(A)** Site 1 shown in blue, **(B)** Site 2 in green and **(C)** Site 3 in red.

protein dimerization and oligomerization (Luo et al., 2006; Yu et al., 2006; Chen et al., 2007; Takeda et al., 2008). Some important residues that interact with antiviral compounds from the RNA Binding domain are F66, R68, G69, Y123, I131, W132, V133, and A134 (Tatar et al., 2021).

For the full-length nucleocapsid protein model POOL predicted three distinct clusters of residues in surface pockets. Site 1 (Figure 9A) consists of residues A12, P13, R14, K249, K257, Q260, K261, and R262, Site 2 (Figure 9B) consists of T54, R92, R107, Y109, Y111, R149, P151, A155, I157, V158, E174, G175, R177, G178, G179 and A311, while Site 3 (Figure 9C) consists of R259, R277, G287, E290, T296, Y298, K299, H300, W301, I304, A305, L353, K355, H356, and D399. For the N-terminus model of Nucleocapsid protein, POOL predicts the following residues (Figure 10): T49, A50, S51, V72, P73, Y86, Y87, R88, R92, R107, Y109, F110, Y111, Y112, and R149. For the C-terminus Nucleocapsid protein structure (PDB ID: 7DE1), the POOL predicted residues are (Figure 10): R259, R262, R277, D288, Y298, K299, H300, W301, I304, A305, K355, and H356.

For the SARS-CoV-2 N-terminal domain of the nucleocapsid protein, it has been reported that residues R92, R107, Y109 and R149 interact with the RNA (Dinesh et al., 2020); these residues are included in the POOL predictions for both the full-length N protein (Site 2) and the N-terminus model structure. We note that the POOL

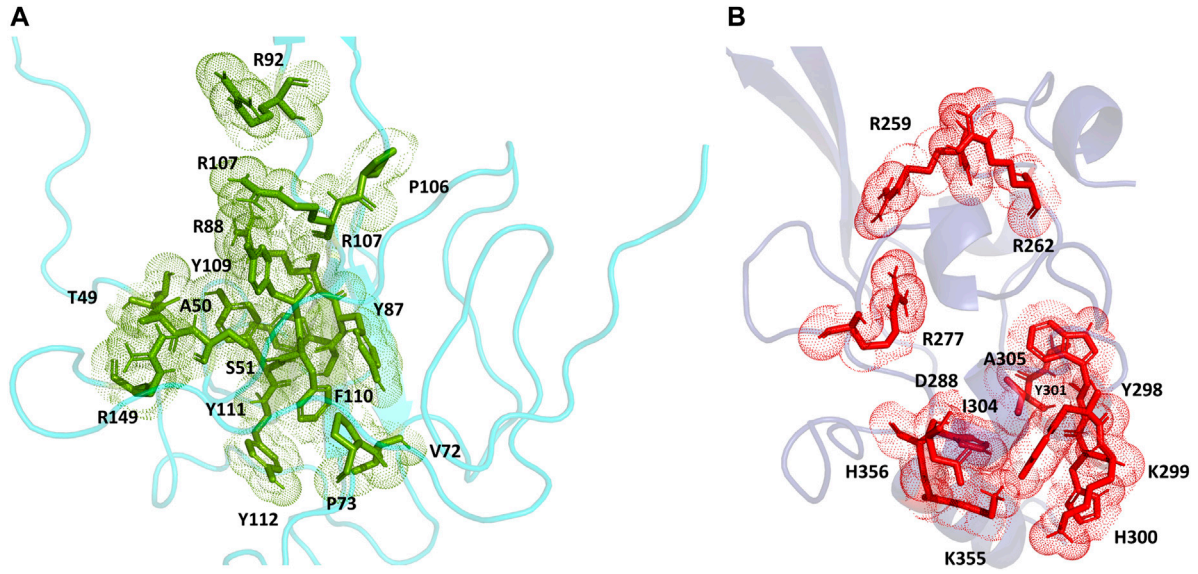


FIGURE 10
(A) The POOL-predicted residues for the SARS-CoV-2 Nucleocapsid protein N-terminal model built in YASARA **(B)** The POOL-predicted residues for the SARS-CoV-2 Nucleocapsid protein C-terminal structure from the PDB (PDB ID: 7DE1).

predictions for Site three for the full-length nucleocapsid model and for the C-terminal Nucleocapsid structure (PDB: 7DE1) are in good agreement.

Potential SARS-CoV-2 full length nucleocapsid protein inhibitors that bind to the NCap POOL-predicted site 1

Based on our docking studies and analysis, the potential ligand candidates that bind to full length Nucleocapsid protein POOL-predicted site one are ligands from the Enamine Covid library, Life Chemicals SARS-CoV-2 library and ZINC Database with ID# ZINC000085537017 (Cangrelor); Z1455181379 ((3-(1-(2,4-difluorophenyl)-2,5-dioxoimidazolidin-4-yl)propanoyl) proline); Z57170530 (4-hydroxy-3-((5-hydroxy-7-oxo-7,8-dihydro-1l3-chromen-6-yl))-2H-chromen-2-one); F0916-5053 (N (3chlorobenzyl)-4 [4-oxo-2 [(2-oxo-2{[3 (trifluoromethyl)phenyl]amino}ethyl)thio]quinazolin-3(4H) yl]butanamide); and Z1444935835 (3-{[2-(6-fluoro-1H-indol-3-yl)acetamido]methyl}benzoic acid), (Supplementary Table S4). Supplementary Table S4 shows the Glide docking method, docking scores, MM-GBSA scores along with the details about ligand-protein interactions. The list consists of mainly ligands from the Enamine Covid library, Life Chemicals SARS-CoV-2 library and ZINC Database. The docking score ranges for Extra Precision (XP) docking on Glide were -15 to -9 kcal/mol. The interactions between the ligand-protein complex are shown in the Supplementary Figure S6 and listed in Supplementary Table S4. All the compounds bind to the Ncap POOL-predicted sites and important H-bond interactions are observed with the residues R177, Q260, K261 and W301. Important π- π interactions are observed with W301.

ZINC000085537017 (Cangrelor), the top hit, is an ATP mimic and ubiquitous binder to multiple sites and targets. The second-best scoring hit, Z1455181379 (3-(1-(2,4-difluorophenyl)-2,5-dioxoimidazolidin-4-yl)propanoyl)proline) (Supplementary Figure S9), binds to full length Nucleocapsid protein at the POOL-predicted site 1 with an XP GScore of -11.05. It forms three hydrogen bonds with R177, T263, and A264. The residues forming a pocket around the binding pose of Z1455181379 are G175, R177, Q260, K261, R262, T263, A264, V270, F274, R277, F286, G287, L291, G295, T296, and W301.

Potential SARS-CoV-2 full length nucleocapsid protein inhibitors that bind to the NCap POOL-predicted site 2

Based on our docking studies and analysis, the potential ligand candidates that bind to full length Nucleocapsid protein POOL predicted site two are ligands from the ZINC Database with ID# ZINC000028467879 (Ceftriaxone), ZINC000004468778 (Cefixime), ZINC000003989268 (Ceftaroline Fosamil), ZINC000001540998 (Pemetrexed), and ZINC000004468778_2 (Cefixime), (Supplementary Table S5). Supplementary Table S5 shows the Glide docking method, docking scores, and MM-GBSA scores, along with the details about ligand-protein interactions. The docking score ranges for Extra Precision (XP) docking on Glide were between −15 and

−9 kcal/mol. The interactions between the ligand-protein complex are shown in Supplementary Figure S7 and listed in Supplementary Table S5. All the compounds bind to the Ncap POOL predicted site two and important H-bond interactions are observed with the residues G175, R177, Q260, K261 and W301. Important π- π and π-cation interactions were observed with W301, R177, and K261.

ZINC000028467879 (Ceftriaxone), (Supplementary Figure S9) the top hit, binds to full length Nucleocapsid protein at the POOL predicted site 2 with an XP GScore of −11.53 kcal/mol. It forms five H-bond interactions with the residues S176, R177, Q260, T263 and A264. The residues forming a pocket around the binding pose of ZINC000028467879 are T54, A155, A156, V158, G175, S176, R177, Q260, K261, R262, T263, A264, V270, F274, R277, L291, G295, T296, TW301, A305, A308, P309, S310, and A311.

Potential SARS-CoV-2 full length nucleocapsid protein inhibitors that bind to the NCap POOL predicted site 3

Based on our docking studies and analysis, the potential ligand candidates that bind to full length Nucleocapsid protein POOL-predicted site three are ligands from the DrugBank and ZINC Database with ID# DB02738 (Adenosine-5′-Pentaphosphate), ZINC000085537017 (Cangrelor), DB03732 (Etheno-Nadp), DB04158 (6-(adenosine tetraphosphate-methyl)-7,8-dihydropterin), and DB02355 (Adenosine-5′-Rp-Alpha-Thio-Triphosphate), (Supplementary Table S6). Supplementary Table S6 shows the Glide docking method, docking scores, MM-GBSA scores, along with the details about ligand-protein interactions. The docking score ranges for Extra Precision (XP) docking on Glide were between -19 and -14 kcal/mol. The interactions between the ligand-protein complex are shown in Supplementary Figure S8 and listed in Supplementary Table S6. All the compounds bind to the Ncap POOL predicted site three and important H-bond interactions are observed with the residues G175, R177, Q260, K261 and W301. Important π- π and π-cation interactions were observed with W301, and R177. These compounds, as might be anticipated, are nucleotide-like.

Conclusion

Some new insights into the functioning of three viral proteins have emerged. The nucleophilic C145 of the main protease is assisted by strong electrostatic coupling to H41, H163, and H164, so that it can be deprotonated and available to affect nucleophilic attack at neutral pH. H41, which exchanges a proton with the thioester intermediate, is assisted by strong coupling to C145 and H164. K6968, the catalytic base of the RNA methyltransferase, has a significant population of its deprotonated state at neutral pH, and therefore is able to act as a Brønsted base, through strong coupling to K6844 and Y6845. Its strength of basicity is enhanced by strong coupling to two acidic residues, D6928 and E7001. These two catalytic acidic residues of the RNA methyltransferase are strongly coupled to each other; the buffer range of D6928 is also expanded through strong coupling to H6867.

Multiple sites of likely biochemical significance are predicted for each of the three proteins, with multiple examples of ligands that may bind and interact with these sites. These sites represent alternative targets for the design of ligands to serve as chemical probes or inhibitors for these viral proteins.

Data availability statement

The original contributions presented in the study are included in the article/Supplementary Material, further inquiries can be directed to the corresponding author.

Author contributions

SI designed the study, assisted in acquiring the funding, performed calculations, analyzed the data, wrote the first draft and edited the final draft. KB designed the study, assisted in acquiring the funding, performed calculations, analyzed results, and contributed to the editing and finalization of the manuscript. HV, IB, AH, and JS performed calculations, analyzed results, and contributed to the finalization of the manuscript. MO designed the study, acquired the funding, performed calculations, analyzed results, and wrote the first draft and edited the final draft.

Funding

Support from the National Science Foundation under grants # CHE-2030180 and CHE-1905214 to MO is gratefully acknowledged. Grant CHE-2030180 was funded under the RAPID mechanism in response to the COVID-19 emergency. IB, AH, and JS were supported by the NSF Research Experiences for Undergraduates (REU) program under grant # DBI-2031778.

Conflict of interest

The authors declare that the research was conducted in the absence of any commercial or financial relationships that could be construed as a potential conflict of interest.

Publisher's note

All claims expressed in this article are solely those of the authors and do not necessarily represent those of their

affiliated organizations, or those of the publisher, the editors and the reviewers. Any product that may be evaluated in this article, or claim that may be made by its manufacturer, is not guaranteed or endorsed by the publisher.

Supplementary material

The Supplementary Material for this article can be found online at: https://www.frontiersin.org/articles/10.3389/fchem.2022.1017394/full#supplementary-material

References

Ahmed-Belkacem, R., Hausdorff, M., Delpal, A., Sutto-Ortiz, P., Colmant, A. M. G., Touret, F., et al. (2022). Potent inhibition of SARS-CoV-2 nsp14 N7-methyltransferase by sulfonamide-based bisubstrate analogues. *J. Med. Chem.* 65 (8), 6231–6249. doi:10.1021/acs.jmedchem.2c00120

Antosiewicz, J., McCammon, J. A., and Gilson, M. K. (1994). Prediction of pH-dependent properties of proteins. *J. Mol. Biol.* 238, 415–436. doi:10.1006/jmbi.1994.1301

Baker, N. A., Sept, D., Joseph, S., Holst, M. J., and McCammon, J. A. (2001). Electrostatics of nanosystems: Application to microtubules and the ribosome. *Proc. Natl. Acad. Sci. U. S. A.* 98, 10037–10041. doi:10.1073/pnas.181342398

Benkert, P., Biasini, M., and Schwede, T. (2011). Toward the estimation of the absolute quality of individual protein structure models. *Bioinformatics* 27 (3), 343–350. doi:10.1093/bioinformatics/btq662

Bollati, M., Milani, M., Mastrangelo, E., Ricagno, S., Tedeschi, G., Nonnis, S., et al. (2009). Recognition of RNA cap in the wesselsbron virus NS5 methyltransferase domain: Implications for RNA-capping mechanisms in flavivirus. *J. Mol. Biol.* 385 (1), 140–152. doi:10.1016/j.jmb.2008.10.028

Cao, W., Cho, C. C. D., Geng, Z. Z., Shaabani, N., Ma, X. R., Vatansever, E. C., et al. (2022). Evaluation of SARS-CoV-2 main protease inhibitors using a novel cell-based assay. *ACS Cent. Sci.* 8 (2), 192–204. doi:10.1021/acscentsci.1c00910

Capra, J. A., Laskowski, R. A., Thornton, J. M., Singh, M., and Funkhouser, T. A. (2009). Predicting protein ligand binding sites by combining evolutionary sequence conservation and 3D structure. *PLoS Comput. Biol.* 5 (12), e1000585. doi:10.1371/journal.pcbi.1000585

Chen, C. Y., Chang, C. K., Chang, Y. W., Sue, S. C., Bai, H. I., Riang, L., et al. (2007). Structure of the SARS coronavirus nucleocapsid protein RNA-binding dimerization domain suggests a mechanism for helical packaging of viral RNA. *J. Mol. Biol.* 368 (4), 1075–1086. doi:10.1016/j.jmb.2007.02.069

Chen, Y., Su, C., Ke, M., Jin, X., Xu, L., Zhang, Z., et al. (2011). Biochemical and structural insights into the mechanisms of SARS coronavirus RNA ribose 2'-O-methylation by nsp16/nsp10 protein complex. *PLoS Pathog.* 7 (10), e1002294. doi:10.1371/journal.ppat.1002294

Colovos, C., and Yeates, T. O. (1993). Verification of protein structures: Patterns of nonbonded atomic interactions. *Protein Sci.* 2 (9), 1511–1519. doi:10.1002/pro.5560020916

Cong, Y., Ulasli, M., Schepers, H., Mauthe, M., V'Kovski, P., Kriegenburg, F., et al. (2020). Nucleocapsid protein recruitment to replication-transcription complexes plays a crucial role in coronaviral life cycle. *J. Virol.* 94 (4), 019255–e2019. doi:10.1128/jvi.01925-19

Coulther, T. A., Ko, J., and Ondrechen, M. J. (2021). Amino acid interactions that facilitate enzyme catalysis. *J. Chem. Phys.* 154, 195101. doi:10.1063/5.0041156

Daffis, S., Szretter, K. J., Schriewer, J., Li, J., Youn, S., Errett, J., et al. (2010). 2'-O methylation of the viral mRNA cap evades host restriction by IFIT family members. *Nature* 468 (7322), 452–456. doi:10.1038/nature09489

Decroly, E., Debarnot, C., Ferron, F., Bouvet, M., Coutard, B., Imbert, I., et al. (2011). Crystal structure and functional analysis of the SARS-coronavirus RNA cap 2'-O-methyltransferase nsp10/nsp16 complex. *PLoS Pathog.* 7 (5), e1002059. doi:10.1371/journal.ppat.1002059

Decroly, E., Imbert, I., Coutard, B., Bouvet, M., Selisko, B., Alvarez, K., et al. (2008). Coronavirus nonstructural protein 16 is a cap-0 binding enzyme possessing (nucleoside-2'O)-methyltransferase activity. *J. Virol.* 82 (16), 8071–8084. doi:10.1128/jvi.00407-08

Dinesh, D. C., Chalupska, D., Silhan, J., Koutna, E., Nencka, R., Veverka, V., et al. (2020). Structural basis of RNA recognition by the SARS-CoV-2 nucleocapsid phosphoprotein. *PLoS Pathog.* 16 (12), e1009100. doi:10.1371/journal.ppat.1009100

Dolinsky, T. J., Nielsen, J. E., McCammon, J. A., and Baker, N. A. (2004). PDB2PQR: An automated pipeline for the setup of Poisson-Boltzmann electrostatics calculations. *Nucleic Acids Res.* 32, W665–W667. doi:10.1093/nar/gkh381

Eisenberg, D., Lüthy, R., and Bowie, J. U. (1997). *VERIFY3D: Assessment of protein models with three-dimensional profiles,* Methods in Enzymology. Amsterdam, Netherlands: Academic Press, 396–404.

Farid, R., Day, T., Friesner, R. A., and Pearlstein, R. A. (2006). New insights about HERG blockade obtained from protein modeling, potential energy mapping, and docking studies. *Bioorg. Med. Chem.* 14 (9), 3160–3173. doi:10.1016/j.bmc.2005.12.032

Friesner, R. A., Banks, J. L., Murphy, R. B., Halgren, T. A., Klicic, J. J., Mainz, D. T., et al. (2004). Glide: A new approach for rapid, accurate docking and scoring. 1. Method and assessment of docking accuracy. *J. Med. Chem.* 47 (7), 1739–1749. doi:10.1021/jm0306430

Friesner, R. A., Murphy, R. B., Repasky, M. P., Frye, L. L., Greenwood, J. R., Halgren, T. A., et al. (2006). Extra precision Glide: Docking and scoring incorporating a model of hydrophobic enclosure for Protein–Ligand complexes. *J. Med. Chem.* 49 (21), 6177–6196. doi:10.1021/jm051256o

Gao, K., Wang, R., Chen, J., Tepe, J. J., Huang, F., and Wei, G.-W. (2021). Perspectives on SARS-CoV-2 main protease inhibitors. *J. Med. Chem.* 64 (23), 16922–16955. doi:10.1021/acs.jmedchem.1c00409

Halgren, T. A., Murphy, R. B., Friesner, R. A., Beard, H. S., Frye, L. L., Pollard, W. T., et al. (2004). Glide: A new approach for rapid, accurate docking and scoring. 2. Enrichment factors in database screening. *J. Med. Chem.* 47 (7), 1750–1759. doi:10.1021/jm030644s

Hilgenfeld, R. (2014). From SARS to MERS: Crystallographic studies on coronaviral proteases enable antiviral drug design. *Febs J.* 281 (18), 4085–4096. doi:10.1111/febs.12936

Hsu, W.-C., Chang, H.-C., Chou, C.-Y., Tsai, P.-J., Lin, P.-I., and Chang, G. G. (2005). Critical assessment of important regions in the subunit association and catalytic action of the severe acute respiratory syndrome coronavirus main protease. *J. Biol. Chem.* 280 (24), 22741–22748. doi:10.1074/jbc.m502556200

Huang, Q., Yu, L., Petros, A. M., Gunasekera, A., Liu, Z., Xu, N., et al. (2004). Structure of the N-terminal RNA-binding domain of the SARS CoV nucleocapsid protein. *Biochemistry* 43 (20), 6059–6063. doi:10.1021/bi036155b

Huff, S., Kummetha, I. R., Tiwari, S. K., Huante, M. B., Clark, A. E., Wang, S., et al. (2022). Discovery and mechanism of SARS-CoV-2 main protease inhibitors. *J. Med. Chem.* 65 (4), 2866–2879. doi:10.1021/acs.jmedchem.1c00566

Iyengar, S. M., Barnsley, K. K., Xu, R., Prystupa, A., and Ondrechen, M. J. (2022). Electrostatic fingerprints of catalytically active amino acids in enzymes. *Protein Sci.* 31 (5), e4291. doi:10.1002/pro.4291

Jin, Z., Du, X., Xu, Y., Deng, Y., BingLi, X., Zhang, L., et al. (2020). Structure of Mpro from COVID-19 virus and discovery of its inhibitors. bioRxiv.

Kang, S., Yang, M., Hong, Z., Zhang, L., Huang, Z., Chen, X., et al. (2020). Crystal structure of SARS-CoV-2 nucleocapsid protein RNA binding domain reveals potential unique drug targeting sites. *Acta Pharm. Sin. B* 10 (7), 1228–1238. doi:10.1016/j.apsb.2020.04.009

Ke, M., Chen, Y., Wu, A., Sun, Y., Su, C., Wu, H., et al. (2012). Short peptides derived from the interaction domain of SARS coronavirus nonstructural protein nsp10 can suppress the 2'-O-methyltransferase activity of nsp10/nsp16 complex. *Virus Res.* 167 (2), 322–328. doi:10.1016/j.virusres.2012.05.017

Ko, J., Murga, L. F., André, P., Yang, H., Ondrechen, M. J., Williams, R. J., et al. (2005). Statistical criteria for the identification of protein active sites using theoretical microscopic titration curves. *Proteins.* 59 (2), 183–195. doi:10.1002/prot.20418

Koumanov, A., Rüterjans, H., and Karshikoff, A. (2002). Continuum electrostatic analysis of irregular ionization and proton allocation in proteins. *Proteins.* 46 (1), 85–96. doi:10.1002/prot.10034

Krieger, E., Joo, K., Lee, J., Lee, J., Raman, S., Thompson, J., et al. (2009). Improving physical realism, stereochemistry, and side-chain accuracy in homology modeling: Four approaches that performed well in CASP8. *Proteins.* 77 (9), 114–122. doi:10.1002/prot.22570

Krieger, E., and Vriend, G. (2014). YASARA View - molecular graphics for all devices - from smartphones to workstations. *Bioinformatics* 30, 2981–2982. doi:10.1093/bioinformatics/btu426

Luo, H., Chen, J., Chen, K., Shen, X., and Jiang, H. (2006). Carboxyl terminus of severe acute respiratory syndrome coronavirus nucleocapsid protein: Self-association analysis and nucleic acid binding characterization. *Biochemistry* 45 (39), 11827–11835. doi:10.1021/bi0609319

Lüthy, R., Bowie, J. U., and Eisenberg, D. (1992). Assessment of protein models with three-dimensional profiles. *Nature* 356 (6364), 83–85. doi:10.1038/356083a0

Ma, Y., Wu, L., Shaw, N., Gao, Y., Wang, J., Sun, Y., et al. (2015). Structural basis and functional analysis of the SARS coronavirus nsp14-nsp10 complex. *Proc. Natl. Acad. Sci. U. S. A.* 112 (30), 9436–9441. doi:10.1073/pnas.1508686112

Masters, P. S., and Sturman, L. S. (1990). Background paper Functions of the coronavirus nucleocapsid protein. *Adv. Exp. Med. Biol.* 276, 235–238. doi:10.1007/978-1-4684-5823-7_32

Matthes, N., Mesters, J. R., Coutard, B., Canard, B., Snijder, E. J., Moll, R., et al. (2006). The non-structural protein Nsp10 of mouse hepatitis virus binds zinc ions and nucleic acids. *FEBS Lett.* 580 (17), 4143–4149. doi:10.1016/j.febslet.2006.06.061

McBride, R., van Zyl, M., and Fielding, B. C. (2014). The coronavirus nucleocapsid is a multifunctional protein. *Viruses* 6 (8), 2991–3018. doi:10.3390/v6082991

Minskaia, E., Hertzig, T., Gorbalenya, A. E., Campanacci, V., Cambillau, C., Canard, B., et al. (2006). Discovery of an RNA virus 3'->5' exoribonuclease that is critically involved in coronavirus RNA synthesis. *Proc. Natl. Acad. Sci. U. S. A.* 103 (13), 5108–5113. doi:10.1073/pnas.0508200103

Mohapatra, P. K., Chopdar, K. S., Dash, G. C., Mohanty, A. K., and Raval, M. K. (2021). *In silico* screening and covalent binding of phytochemicals of Ocimum sanctum against SARS-CoV-2 (COVID 19) main protease. *J. Biomol. Struct. Dyn.* 1, 1–10. doi:10.1080/07391102.2021.2007170

Nelson, G. W., Stohlman, S. A., and Tahara, S. M. (2000). High affinity interaction between nucleocapsid protein and leader/intergenic sequence of mouse hepatitis virus RNA. *Microbiology* 81 (1), 181–188. doi:10.1099/0022-1317-81-1-181

Nencka, R., Silhan, J., Klima, M., Otava, T., Kocek, H., Krafcikova, P., et al. (2022). Coronaviral RNA-methyltransferases: Function, structure and inhibition. *Nucleic Acids Res.* 50 (2), 635–650. doi:10.1093/nar/gkab1279

Peng, T. Y., Lee, K. R., and Tarn, W. Y. (2008). Phosphorylation of the arginine/serine dipeptide-rich motif of the severe acute respiratory syndrome coronavirus nucleocapsid protein modulates its multimerization, translation inhibitory activity and cellular localization. *Febs J.* 275 (16), 4152–4163. doi:10.1111/j.1742-4658.2008.06564.x

Ramajayam, R., Tan, K. P., and Liang, P. H. (2011). Recent development of 3C and 3CL protease inhibitors for anti-coronavirus and anti-picornavirus drug discovery. *Biochem. Soc. Trans.* 39 (5), 1371–1375. doi:10.1042/bst0391371

Ringe, D., Wei, Y., Boino, K. R., and Ondrechen, M. J. (2004). Protein structure to function: Insights from computation. *Cell. Mol. Life Sci.* 61, 387–392. doi:10.1007/s00018-003-3291-5

Rosas-Lemus, M., Minasov, G., Shuvalova, L., Inniss, N. L., Kiryukhina, O., Brunzelle, J., et al. (2020). High-resolution structures of the SARS-CoV-2 2'-O-methyltransferase reveal strategies for structure-based inhibitor design. *Sci. Signal.* 13 (651), eabe1202. doi:10.1126/scisignal.abe1202

Rowaiye, A. B., Oli, A. N., Onuh, O. A., Emeter, N. W., Bur, D., Obideyi, O. A., et al. (2022). Rhamnetin IS a better inhibitor of sars-cov-2 2'-O-methyltransferase than dolutegravir: A computational prediction. *Afr. J. Infect. Dis.* 16 (2), 80–96. doi:10.21010/ajid.v16i2.9

Sastry, G. M., Adzhigirey, M., Day, T., Annabhimoju, R., and Sherman, W. (2013). Protein and ligand preparation: Parameters, protocols, and influence on virtual screening enrichments. *J. Comput. Aided. Mol. Des.* 27 (3), 221–234. doi:10.1007/s10822-013-9644-8

Sawicki, S. G., Sawicki, D. L., Younker, D., Meyer, Y., Thiel, V., Stokes, H., et al. (2005). Functional and genetic analysis of coronavirus replicase-transcriptase proteins. *PLoS Pathog.* 1 (4), e39. doi:10.1371/journal.ppat.0010039

Shen, T., Wong, C. F., and McCammon, J. A. (2003). Brownian dynamics simulation of helix-capping motifs. *Biopolymers* 70 (2), 252–259. doi:10.1002/bip.10466

Sherman, W., Beard, H. S., and Farid, R. (2006a). Use of an induced fit receptor structure in virtual screening. *Chem. Biol. Drug Des.* 67 (1), 83–84. doi:10.1111/j.1747-0285.2005.00327.x

Sherman, W., Day, T., Jacobson, M. P., Friesner, R. A., and Farid, R. (2006b). Novel procedure for modeling ligand/receptor induced fit effects. *J. Med. Chem.* 49 (2), 534–553. doi:10.1021/jm050540c

Snijder, E. J., Decroly, E., and Ziebuhr, J. (2016). The nonstructural proteins directing coronavirus RNA synthesis and processing. *Adv. Virus Res.* 96, 59–126. doi:10.1016/bs.aivir.2016.08.008

Somarowthu, S., and Ondrechen, M. J. (2012). POOL server: Machine learning application for functional site prediction in proteins. *Bioinformatics* 28 (15), 2078–2079. doi:10.1093/bioinformatics/bts321

Somarowthu, S., Yang, H., Hildebrand, D. G. C., and Ondrechen, M. J. (2011). High-performance prediction of functional residues in proteins with machine learning and computed input features. *Biopolymers* 95 (6), 390–400. doi:10.1002/bip.21589

Stohlman, S. A., Baric, R. S., Nelson, G. N., Soe, L. H., Welter, L. M., and Deans, R. J. (1988). Specific interaction between coronavirus leader RNA and nucleocapsid protein. *J. Virol.* 62 (11), 4288–4295. doi:10.1128/jvi.62.11.4288-4295.1988

Sulimov, A., Kutov, D., Ilin, I., Xiao, Y., Jiang, S., and Sulimov, V. (2022). Novel inhibitors of 2'-O-methyltransferase of the SARS-CoV-2 coronavirus. *Molecules* 27 (9), 2721. doi:10.3390/molecules27092721

Takeda, M., Chang, C. K., Ikeya, T., Güntert, P., Chang, Y. H., Hsu, Y. L., et al. (2008). Solution structure of the c-terminal dimerization domain of SARS coronavirus nucleocapsid protein solved by the SAIL-NMR method. *J. Mol. Biol.* 380 (4), 608–622. doi:10.1016/j.jmb.2007.11.093

Tatar, G., Ozyurt, E., and Turhan, K. (2021). Computational drug repurposing study of the RNA binding domain of SARS-CoV-2 nucleocapsid protein with antiviral agents. *Biotechnol. Prog.* 37 (2), e3110. doi:10.1002/btpr.3110

Tong, W., Wei, Y., Murga, L. F., Ondrechen, M. J., and Williams, R. J. (2009). Partial Order Optimum Likelihood (POOL): Maximum likelihood prediction of protein active site residues using 3D structure and sequence properties. *PLoS Comput. Biol.* 5 (1), e1000266. doi:10.1371/journal.pcbi.1000266

Ullmann, G. M. (2003). Relations between protonation constants and titration curves in polyprotic acids: A critical view. *J. Phys. Chem. B* 107 (5), 1263–1271. doi:10.1021/jp026454v

Wang, Y., Sun, Y., Wu, A., Xu, S., Pan, R., Zeng, C., et al. (2015). Coronavirus nsp10/nsp16 methyltransferase can Be targeted by nsp10-derived peptide *in vitro* and *in vivo* to reduce replication and pathogenesis. *J. Virol.* 89 (16), 8416–8427. doi:10.1128/jvi.00948-15

Wang, Y. T., Long, X. Y., Ding, X., Fan, S. R., Cai, J. Y., Yang, B. J., et al. (2022). Novel nucleocapsid protein-targeting phenanthridine inhibitors of SARS-CoV-2. *Eur. J. Med. Chem.* 227, 113966. doi:10.1016/j.ejmech.2021.113966

Wei, Y., Ko, J., Murga, L., and Ondrechen, M. J. (2007). Selective prediction of interaction sites in protein structures with THEMATICS. *BMC Bioinforma.* 8 (1), 119. doi:10.1186/1471-2105-8-119

Wrapp, D., Wang, N., Corbett, K. S., Goldsmith, J. A., Hsieh, C. L., Abiona, O., et al. (2020). Cryo-EM structure of the 2019-nCoV spike in the prefusion conformation. *Science* 367 (6483), 1260–1263. doi:10.1126/science.abb2507

Wu, A., Peng, Y., Huang, B., Ding, X., Wang, X., Niu, P., et al. (2020a). Genome composition and divergence of the novel coronavirus (2019-nCoV) originating in China. *Cell. Host Microbe* 27 (3), 325–328. doi:10.1016/j.chom.2020.02.001

Wu, F., Zhao, S., Yu, B., Chen, Y.-M., Wang, W., Song, Z.-G., et al. (2020b). A new coronavirus associated with human respiratory disease in China. *Nature* 579 (7798), 265–269. doi:10.1038/s41586-020-2008-3

Yang, J., Yan, R., Roy, A., Xu, D., Poisson, J., and Zhang, Y. (2015). The I-tasser suite: Protein structure and function prediction. *Nat. Methods* 12 (1), 7–8. doi:10.1038/nmeth.3213

Yang, M., He, S., Chen, X., Huang, Z., Zhou, Z., Zhou, Z., et al. (2020). Exploiting double exchange diels-alder cycloadditions for immobilization of peptide nucleic acids on gold nanoparticles *Front. Chem.* 8, 4. doi:10.3389/fchem.2020.00004

Yu, I. M., Oldham, M. L., Zhang, J., and Chen, J. (2006). Crystal structure of the severe acute respiratory syndrome (SARS) coronavirus nucleocapsid protein dimerization domain reveals evolutionary linkage between corona- and arteriviridae. *J. Biol. Chem.* 281 (25), 17134–17139. doi:10.1074/jbc.m602107200

Zhang, L., Lin, D., Sun, X., Curth, U., Drosten, C., Sauerhering, L., et al. (2020). Crystal structure of SARS-CoV-2 main protease provides a basis for design of improved α-ketoamide inhibitors. *Science* 368, 409–412. doi:10.1126/science.abb3405

Zhou, P., Yang, X.-L., Wang, X.-G., Hu, B., Zhang, L., Zhang, W., et al. (2020). A pneumonia outbreak associated with a new coronavirus of probable bat origin. *Nature* 579 (7798), 270–273. doi:10.1038/s41586-020-2012-7

frontiers | Frontiers in Chemistry

TYPE Original Research
PUBLISHED 13 December 2022
DOI 10.3389/fchem.2022.1038796

Check for updates

OPEN ACCESS

EDITED BY
Sarah Pike,
University of Birmingham, United Kingdom

REVIEWED BY
Lanlan Yu,
Chinese Academy of Medical Sciences and Peking Union Medical College, China
Carlo Diaferia,
University of Naples Federico II, Italy

*CORRESPONDENCE
Umberto Piarulli,
Umberto.piarulli@uninsubria.it
Silvia Gazzola,
s.gazzola@uninsubria.it

†PRESENT ADDRESSES
Giulia Alboreggia, Division of Biomedical Sciences, School of Medicine, University of California Riverside, Riverside, CA, United States; Francesco Oliva, Department of Physics, University of Cagliari, Cagliari, Italy

SPECIALTY SECTION
This article was submitted to Supramolecular Chemistry, a section of the journal Frontiers in Chemistry

RECEIVED 07 September 2022
ACCEPTED 29 November 2022
PUBLISHED 13 December 2022

CITATION
Fasola E, Alboreggia G, Pieraccini S, Oliva F, Agharbaoui FE, Bollati M, Bertoni G, Recchia S, Marelli M, Piarulli U, Pellegrino S and Gazzola S (2022), Conformational switch and multiple supramolecular structures of a newly identified self-assembling protein-mimetic peptide from *Pseudomonas aeruginosa* YeaZ protein. *Front. Chem.* 10:1038796. doi: 10.3389/fchem.2022.1038796

COPYRIGHT
© 2022 Fasola, Alboreggia, Pieraccini, Oliva, Agharbaoui, Bollati, Bertoni, Recchia, Marelli, Piarulli, Pellegrino and Gazzola. This is an open-access article distributed under the terms of the Creative Commons Attribution License (CC BY). The use, distribution or reproduction in other forums is permitted, provided the original author(s) and the copyright owner(s) are credited and that the original publication in this journal is cited, in accordance with accepted academic practice. No use, distribution or reproduction is permitted which does not comply with these terms.

Conformational switch and multiple supramolecular structures of a newly identified self-assembling protein-mimetic peptide from *Pseudomonas aeruginosa* YeaZ protein

Elettra Fasola[1], Giulia Alboreggia[1†], Stefano Pieraccini[2], Francesco Oliva[2†], Fatima Ezzahra Agharbaoui[2], Michela Bollati[3], Giovanni Bertoni[4], Sandro Recchia[1], Marcello Marelli[5], Umberto Piarulli[1*], Sara Pellegrino[6] and Silvia Gazzola[1*]

[1]Science and High Technology Department, University of Insubria, Como, Italy, [2]Chemistry Department, University of Milan, Milan, Italy, [3]CNR and Department of Biosciences, Institute of Biophysics, University of Milan, Milan, Italy, [4]Department of Bioscience, University of Milan, Milan, Italy, [5]CNR-SCITEC—Istituto di Scienze e Tecnologie Chimiche "Giulio Natta", Milan, Italy, [6]Pharmaceutical Science Department, University of Milan, Milan, Italy

Protein-mimetic peptides (PMPs) are shorter sequences of self-assembling proteins, that represent remarkable building blocks for the generation of bioinspired functional supramolecular structures with multiple applications. The identification of novel aminoacidic sequences that permit the access to valuable biocompatible materials is an attractive area of research. In this work, *in silico* analysis of the *Pseudomonas aeruginosa* YeaZ protein (*Pa*YeaZ) led to the identification of a tetradecapeptide that represents the shortest sequence responsible for the YeaZ-YeaZ dimer formation. Based on its sequence, an innovative 20-meric peptide, called PMP-2, was designed, synthesized, and characterized in terms of secondary structure and self-assembly properties. PMP-2 conserves a helical character and self-assembles into helical nanofibers in non-polar solvents (DMSO and trifluoroethanol), as well as in dilute (0.5 mM) aqueous solutions. In contrast, at higher concentrations (>2 mM) in water, a conformational transition from α-helix to β-sheet occurs, which is accompanied by the Protein-mimetic peptide aggregation into 2D-sheets and formation supramolecular gel in aqueous environment. Our findings reveal a newly identified Protein-mimetic peptide that could turn as a promising candidate for future material applications.

KEYWORDS

protein-mimetic peptide, self-assembly, peptide material, motif design, supramolecular gel, YeaZ protein

1 Introduction

The supramolecular self-assembly of proteins plays a fundamental role in generating highly complex hierarchical macrostructures with specific biological functions in living organisms (Bai et al., 2016). Protein folding (Kim et al., 2022), the reversible assembly of tubulin (Fletcher and Mullins, 2010) and collagen fibers (Pins et al., 1997), and the interaction of proteins to form complexes with a wide range of bio-functionalities (Bai et al., 2016) are just a few of the numerous examples that nature offers. The discovery that protein-mimetic peptides (PMPs), i.e., shorter sequences of self-assembling proteins, can lead to sophisticated supramolecular structures like nanofibers, micelles, ribbons, or spheres, paved the way to the generation of peptide-based functional bioinspired nanomaterials (Zhang et al., 1993; Goerbitz, 2006; Levin et al., 2020; Locarno et al., 2020; La Manna et al., 2021). These peptide materials are characterized by high biocompatibility and biodegradability, as well as facile synthesis, thus finding several applications in the development of biomaterials for tissue engineering (Gomes et al., 2011; Xu et al., 2015; Berns et al., 2016; Shen et al., 2022), drug delivery (Abbas et al., 2010; Zou et al., 2020), and bioinspired technology (Fu et al., 2009; Assal et al., 2013; Matsuura et al., 2020). In this context, the elucidation of novel protein sequences that permit the access to valuable biocompatible materials is an attractive area of research (Castelletto and Hamly, 2022). Among the identified PMPs (Zhang et al., 2018), sequences deriving from α-helical domains have been less explored due to the intrinsic thermodynamical instability of the helix when it is extracted from the native protein.

On the other hand, α–helices are the most common motif in globular proteins (Mondal and Gazit, 2016), and they are often involved in biological relevant protein-protein interactions (PPIs) (Araghi and Keating., 2016; Zanella et al., 2019). The assembly of two or more α-helices forms coiled-coils, that are a structural element identified in several proteins, and are considered the most stable and regular protein folding known so far (Lupas, 1996; Wolf et al., 1997; Apostolovic et al., 2010; Lupas and Bassler, 2017). For these reasons, self-assembling α–helices provide a promising starting point for the design of novel functional materials with nature-like mechanical features (Lupas and Bassler, 2017).

In this work we present the design of a novel promising PMP, called PMP-2, starting from the recently solved X-ray crystal structure of *Pseudomonas aeruginosa* YeaZ (*Pa*YeaZ, PDB: 4Y0W; Vecchietti et al., 2016). In bacteria, the homodimeric protein YeaZ participates to the formation of protein networks thar are involved in the biosynthesis of an essential tRNA modification, and for this reason YeaZ is receiving growing interest as potential novel target for antibacterial development (Swinehart et al., 2020). Interestingly, the YeaZ homodimers mainly bind through the interaction of the two α2 α-helices to form a coiled-coil-like structure. Based on this evidence, the assembling mode of YeaZ protein was here investigated for the first time through computational studies, and we identified the sequence primarily responsible for the dimer formation within a shorter fragment of the α2 helix. The remarkable self-assembling properties of this new PMP, conveniently functionalized, were studied by a combination of Circular Dichroism Analysis, Electron Microscopy techniques, Dynamic Light Scattering and Infrared Spectroscopy. The results indicated that PMP-2 self-assembles into supramolecular nanofilaments with defined diameter. By modulating the experimental conditions, these nanofibers can transform to 2D-sheets and form gels in aqueous environment, and this transformation is accompanied by a conformational switch of PMP-2 from α-helix to β-sheet secondary structure. Our finding led to the discovery a new PMP deriving from a α-helix domain of a bacterial protein that shows the potential to be used as a building block for generating functional materials (Meng et al., 2014; Mondal and Gazit, 2016; Ruffoni et al., 2016; Li et al., 2017; Zhang et al., 2018). Additionally, the elucidation of the assembly mode of *Pa*YeaZ homodimer that could have potential relevance in drug discovery in the future.

2 Materials and methods

2.1 Computational studies

The model of YeaZ homodimer was obtained using the published crystal structure (PDB ID code 4Y0W, Vecchietti et al., 2016). We extracted two monomers from the crystal structure. The system was simulated in explicit water solvent with periodic boundary conditions. The protein was described using the amber99SB-ILDN force field (Lindorff-Larsen et al., 2010), while TIP3P model (Jorgensen et al., 1983) was adopted for water. The system was submitted to geometry optimization using the steepest descent method (50,000 steps). Then, we carried out a 200 ps equilibration in the NVT ensemble followed by a second equilibration of further 200 ps in the NPT ensemble. During the equilibration, cα were restrained to crystallographic positions. Equilibration phase was followed by a 100 ns long unrestrained production run in the NPT ensemble. Temperature and pressure were kept constant to their reference values (1 bar, 300 K respectively) through the velocity rescale algorithm (Bussi et al., 2007) and the Berendsen barostat (Berendsen et al., 1984). A 14 Å cutoff was applied for non-bonded interactions and the Particles Mesh Ewald algorithm (Darden et al., 1993) was employed to calculate long range electrostatic interactions. During the MD simulations all bond lengths were constrained to their equilibrium values with the LINCS algorithm (Hess et al., 1997), allowing time step of 2 fs. Simulations and subsequent analysis were performed with the GROMACS 5.0.7 program suite (Van der Spoel et al., 2005).

500 snapshots were extracted from the last 20 ns of the dynamics of the YeaZ complex (one snapshot every 40 ps). The contribution of each of the amino acids at the protein-protein interface to the binding energy has been estimated through computational alanine scanning (CAS). This technique calculates the difference in binding free energy between the protomers forming the complex upon mutation of each of the interfacial residues into alanine (ΔΔG). This evaluation has been performed using the molecular mechanics/Poisson–Boltzmann surface area (MM/PBSA) approach (Massova and Kollman, 2000). A positive ΔΔG value means that the associated residue mutation into alanine reduces the binding energy, while a negative ΔΔG value means that the protein-protein binding energy is increased upon mutation. Residues exhibiting the largest ΔΔG values are thus those contributing most to the complex formation. CAS was performed only for residues located at the interface, that were identified as the ensemble of residues with a different solvent accessible surface area (SASA) in the complex and in the apo-protein. SASA of each residue was calculated using Naccess (S. Hubbard and J. Thornton, 1992–6), ΔG of binding was calculated with the MM/PBSA approach as implemented in the GMXPBSA 2.0 suite (Paissoni et al., 2014). This protocol implicitly assumes that point mutations in the protein do not significantly affect its conformation. The validity of this assumption in computational alanine scanning has been widely confirmed in the literature, when applied to PPIs. A dielectric constant of two was chosen for the protein interior. The initial secondary structures of the synthesized peptides have been obtained with the Pepfold3 server (Lamiable et al., 2016). Each system has been simulated using periodic boundary conditions and explicit solvent model (either water or TFE). The peptides were described using the amber99SB-ILDB (Lindorff-Larsen et al., 2010) force field, while the TIP3P (Jorgensen et al., 1983) model was adopted for water and the Generalized Amber Force Field (GAFF) (Wang et al., 2004) for TFE. Each system was simulated with the protocol described above, except for the production run that was 500 ns long. Three replicas of each simulation have been performed. Cluster analysis has been performed using the Gromos algorithm (Daura et al., 1999) and secondary structure has been calculated with the DSSP software (Kabsch and Sander, 1983).

2.2 Peptide synthesis

All the commercially available reagents and resins were used as purchased from Sigma-Aldrich®, TCI, Fluorochem©, and HPLC grade solvents were employed. Synthesis of peptides was performed by manual solid phase synthesis by the Fmoc-strategy on Fmoc-Gly preloaded Wang resin (commercially reported loading 0.4–0.9 mmol/g). HPLC purifications were performed with SHIMADZU LC-20AP equipped with diode array UV detector and Phenomenex Fusion-RP 80Å column. High resolution mass spectra were obtained with Thermo Fisher Scientific Orbitrap Exploris™ 120 equipped with UHPLC and C18 column. The purities of the synthesized peptides were analyzed by analytical HPLC SHIMADZU LC-20AP equipped with diode array UV detector and C18 column.

2.3 Circular Dichroism Analysis

Circular Dichroism experiments were performed on a CD-spectropolarimeter Jasco 820 with a 0.1 cm quartz cuvette. Spectra were acquired from 195 to 250 nm with a 0.1 nm step and 1 s collection time per step, taking three averages. The spectrum of the solvent was subtracted to eliminate interference from cell, solvent, and optical equipment. The CD spectra were plotted as mean residue ellipticity θ (degree·cm^2·d^{-1}·mol^{-1}) versus wavelength λ (nm). Noise-reduction was obtained using a Fourier-transform filter program from Jasco. Secondary structure analysis was performed using the CONTIN algorithm (Whitmore and Wallace, 2008) and the reference set 7 (Sreerama and Woody, 2000). CD spectra were registered at 0.07–0.18 mM concentrations, using pure TFE or TFE and buffer solutions to test different pH ranges.

2.4 Fourier transform-attenuated total reflection (FT-ATR) analysis

For ATR spectra, Nicolet iS10 Thermo Fisher Scientific spectrometer was employed. Spectra are plotted as Absorbance versus wave numbers (cm^{-1}), with resolution 4 cm^{-1} and 32 scans. Solvent subtraction and spectra deconvolution were performed with OMNIC™ Spectra Software.

2.5 Trasmission Electron Microscopy analysis

TEM samples were prepared by the same technique from a 2 mM DMSO solution to afford 0.1 mM final concentration in Milli-Q water at different pHs. After deposition onto the carbon/Formvar TEM grid, water was eliminated by lyophilization. Operating conditions: low vacuum mode 1 Torr; accelerating voltage 10 kV; working distance 7.5 mm, GSE detector; magnifications: ×800, ×1,600, ×3,200, ×6,400, and ×12,800. Transmission Electron Microscopy (TEM) and Scanning TEM (STEM) images were collected by a ZEISS LIBRA200FE with in-column Ω-filter and accelerating voltage 200 kV. Samples were treated with UranyLess solution (EMS) for negative staining.

2.6 Dynamic Light Scattering analysis

Malvern Zetasizer Nano instrument (Malvern Panalytical, Ltd.) was employed for Dynamic Light Scattering (DLS) analysis, performed at 25°C. The instrument is equipped with a 633 nm solid-state He–Ne laser at a scattering angle of 173°. All the samples used to analyze the stability of the PMP-2 aggregates as a function of different DMSO/water ratio were prepared by solvent displacement technique starting from concentrated solutions in 100% DMSO (0.125, 0.2, 0.5, 2, 4, and 10 mM) to obtain 0.1 mM final concentrations in Milli-Q water, with 80%, 50%, 20%, 10%, 5%, 2.5% and 1% v/v of DMSO, respectively. All the samples used to analyze the stability of the PMP-2 aggregates as a function of concentration were prepared starting from 0.1 mM in Milli-Q water with 5% *v/v* of DMSO and diluting with Milli-Q water to obtain the final concentration of 0.05, 0.01, 0.005, and 0.001 mM. The corresponding refractive index and viscosity data of DMSO/water mixtures are reported in the literature (LeBel and Goring, 1962) and the samples were aged 24 h at room temperature before the measurements.

2.7 Scanning Electron Microscopy analysis

Scanning Electron Microscopy (SEM) images were acquired with Philips ESEM FEG Mod. XL 30 without sample coating and in the low vacuum mode (under 1 Torr) of water vapor pressure, to avoid possible morphological modifications. SEM aqueous samples were prepared by solvent displacement technique: DMSO concentrated stock solutions of the synthesized peptides were added dropwise to a proper volume of Milli-Q water at different pHs, to afford a final concentration of 0.5 mM. The samples were lyophilized before the analysis, while the hydrogels were transferred as such.

2.8 Thioflavin T fluorescence analysis

Aggregation kinetics were followed using Thioflavin-T (ThT) as fluorescent dye, specific for β sheet-rich structures (LeVine 3rd, 1993). PMP-2, was dissolved in Milli-Q water to reach the final concentration of 0.1 or 2 mM, and heated at 60°C. After 24 h, 100 µl samples were incubated at 25°C in the presence of 20 µM ThT. Fluorescence signal was measured every 20 min for 30 h in a quartz cuvette using a Cary Eclipse Fluorescence Spectrometer. The dye was excited at 450 nm, and the emission was measured at 480 nm.

2.9 Hydrogel preparation

To prepare the hydrogels at different concentration, the lyophilized PMP-2 was dissolved in the suitable amount of Milli-Q water (final concentration of the prepared solutions: 0.1, 1, 2, 5, 10, and 20 mM) heating at 60°C for 3 min and sonicating for 1 min. The clear solutions were left cooling at rt. After 24 h of aging the hydrogel formation was verified at concentrations above 2 mM by the stable-to-inversion method. The 20 mM hydrogel was kept at room temperature for 10 months, and it showed complete stability.

3 Results and discussion

3.1 Design, synthesis and structural characterization of the novel YeaZ-derived PMP

3.1.1 *In silico* identification of the *Pa*YeaZ peptide sequence of the α2 domain responsible for the YeaZ-YeaZ homodimer formation

To predict the sequence responsible for the YeaZ-YeaZ homodimer formation, we performed a computational alanine scanning (CAS), a technique that identifies the smallest subset of amino acids, also known as "hot spots" (Sousa et al., 2007; Keskin et al., 2008; Pieraccini et al., 2009), at the intradimer interface that are responsible for the binding energy of the protein-protein complex formation. The results (Supplementary Material; Section 2.1) revealed four residues having a ΔΔG>2 kcal/mol, namely Ile74, Val78, Leu82, and Phe84, thus crucial for the PPIs. All residues are located on the α2-helix of *Pa*YeaZ, within the coiled-coil-like structure at the protein-protein interface (Supplementary Material; Supplementary Table S1). Based on this prediction, we first selected the sequence RIAIGVVQGLAFAL (Arg73-Leu86) (PMP-1, Figure 1), which was subjected to further modification consisting in the replacement of Arg73 with Ala, as suggested by the better negative ΔΔG value from CAS analysis (Supplementary Material; Supplementary Table S4), and in the addition of a charged tag at the C-terminus. Indeed, the α-helices that naturally assemble in proteins are often amphipathic. Their folding in coiled-coil structure leads to an increased stabilization of the helical structure thanks to additional van der Waals forces, as well as to the shielding of the hydrophobic segments from the aqueous environment (Missirlis et al., 2010; Han et al., 2013). We linked the cationic sequence KKK at the C-terminus of PMP-1 through an additional GG-spacer, generating the amphiphilic structure PMP-2 (Figure 1). The conservation of the helical conformation was ensured by inserting the Lys-tag at the C-terminus, which allows the correct alignment of the charged residues at neutral pH with the helix dipole (Hol, W.G., 1985). In addition, the GG-spacer helps to minimize the effect of the tag to the peptide secondary structure, as reported by Morales and co-workers (Morales and Jimenez, 2019).

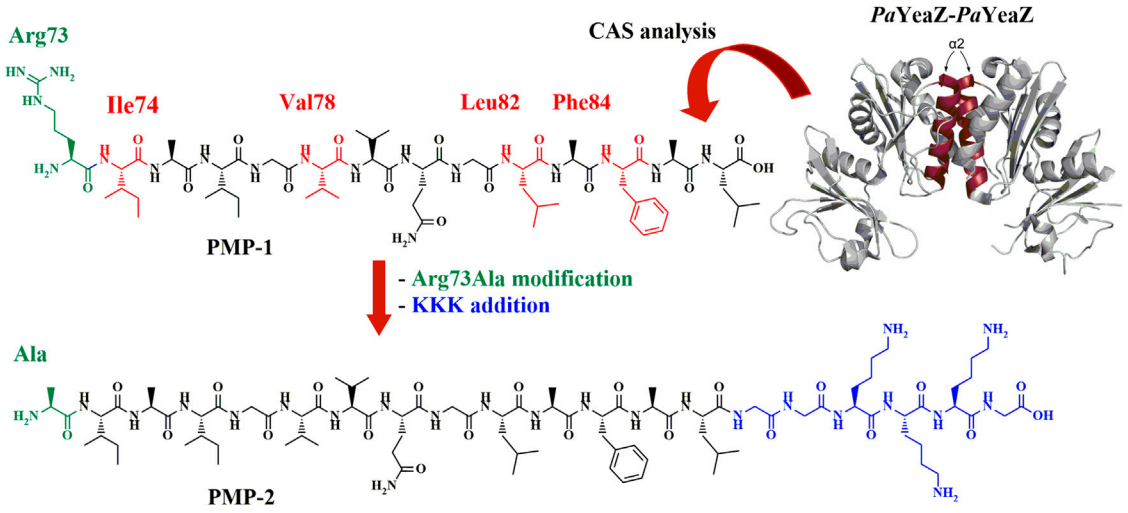


FIGURE 1
*Pa*YeaZ dimer crystal structure (PDB: 4Y0W, the two α2 helix of each subunit are colored in ruby red), the computationally identified PMP-1 sequence (Arg73-Leu86) and the final amphiphilic PMP-2, object of this study. Hot spots are shown in red in PMP-1, further Arg73Ala modification is highlighted in green and GGKKKG C-terminal sequence is shown in blue.

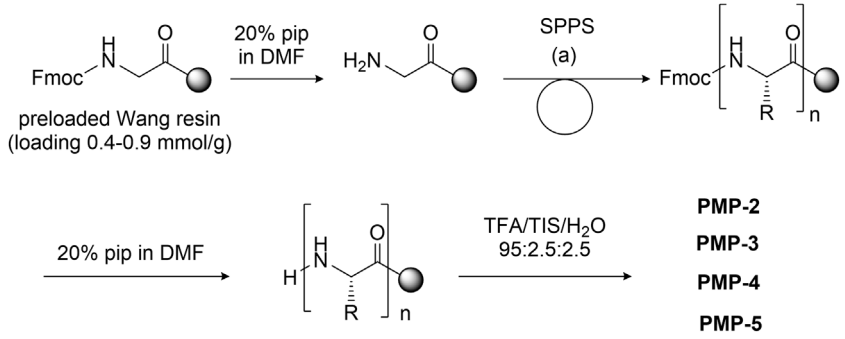
Due to the further modification of the sequence, we decided to simulate the secondary structure of the designed PMP-2 by Molecular Dynamics (MD) calculation. MD were carried out both in trifluoroethanol (TFE) and in water to mimic a hydrophobic and hydrophilic environment, respectively. The results suggested that in TFE the α-helical structure is the predominant conformation (28%), and the Lys-tag seems to not hamper the formation of the helix, whereas in water only 3% of helical structure is present, and the major contribution is given by a β-strand structure (15%). Considering that the original sequence is naturally present in the higher hydrophobic core of the protein, it is not surprising that the helix is conserved better in TFE rather than in water. On the other hand, the possible self-assembly process of the PMP showing α-helical predominant conformation, could stabilize the helix also in water thanks to the added polar head, and finally generating supramolecular structures like nanofibers (Lupas and Bassler, 2017). To verify our hypothesis, we synthesized PMP-2 and we studied its secondary structure as well as the predicted self-assembling behavior. Finally, shorter derivatives of PMP-2 were also prepared and investigated to understand the influence of the PMP-1 sequence on the secondary structure and self-assembly properties.

3.1.2 Synthesis of PMP-2 and of the shorter derivatives PMP-3-5

PMP-2 and its shorter derivatives PMP-3-5 were synthesized by manual solid phase peptide synthesis (SPPS) on Fmoc-Gly preloaded Wang resin (commercially reported loading 0.4–0.9 mmol/g) using the Fmoc strategy. COMU® (3 eq) and *N,N*-diisopropylethylamine (8.5 eq) or *N,N′*-di*iso*propylcarbodiimide (3 eq)/OxymaPure® (3 eq) were used as coupling reagents, depending on the amino acid residue (see Supplementary Information, Section 3.1 for the details). After cleavage from the resin with TFA/H_2O/TIS 95: 2.5:2.5, the peptides was purified by RP-HPLC and fully characterized by HRMS. The general synthetic scheme, yields and purities of the synthesized peptides are reported in Figure 2.

3.1.3 Secondary structure determination by circular dichroism analysis

CD experiments were initially performed in TFE at 0.1 mM (Figure 3), to directly compare the MD simulations with the experimental analysis. In TFE, the strong positive band at around 195 nm (amide π-π* transition), the negative band close to 205 nm (amide π-π* transition), and the negative band at 222 nm (amide n-π* transition) observed in the recorded spectra suggested a predominant helical conformation at this concentration, thus confirming the theoretical calculation. CD spectra were also measured at pH = 4 (acetate buffer/TFE 1:1) and pH = 11 (NaOH aqueous solution/TFE 1:1) to modulate the protonation of Lys side chains (Supplementary Material, Supplementary Figure S13) (calculated isoelectric point of PMP-2: 10.4). In both cases the α-helix was conserved, suggesting that the protonation of the C-terminal KKK sequence does not influence the secondary structure of PMP-2. To better understand the influence of the aqueous environment on the stability of the helix, the water content of



Name	Sequence	Yield	HPLC purity
PMP-2	AIAIGVVQGLAFALGGKKKG	60%	96%
PMP-3	VVQGLAFALGGKKKG	42%	97%
PMP-4	LAFALGGKKKG	25%	95%
PMP-5	AIAIGVVQGGKKKG	36%	98%

FIGURE 2
General synthetic scheme [coupling condition (a): conditions: Fmoc-aa-OH 3-5 eq, DIPEA 9-15 eq, COMU 3-5 eq.] and sequence of peptides PMP-3-5 with the isolated yield and HPLC purity.

the solution was increased, and PMP-2 was dissolved in TFE/acetate buffer 1:2 and 1:4 (a major content of water led to precipitation of the peptide). Interestingly, the helical contribution was maintained, indicating a good tendency of the peptide to preserve its α-helix structure even in a more polar solvent (Figure 3).

In order to unravel the molecular determinants of the helical conformation, shorter derivatives of PMP-2 were designed and synthesized (PMP-3-5, Figure 2). PMP-3 and PMP-4 derive from the deletion of subsequent sequences from the N-terminus of PMP-2 (the pentapeptide AIAIG and the non-apeptide AIAIGVVQG respectively), whereas PMP-5 derives from the deletion of the hexapeptide GLAFAL bearing the Phe residue, which represents one of the most important hot-spots for interaction in the *Pa*YeaZ homodimer. A lack of helical structure in all the three derivatives was observed in the MD simulation, and this was confirmed later by CD-spectra (Figure 3). These findings clearly indicated the importance of the whole bacterial α2 sequence of PMP-1 for the maintenance of the α-helix.

3.2 Supramolecular aggregation studies of the new PMPs

3.2.1 Trasmission electron microscopy analysis of PMP-2

The remarkable attitude of PMP-2 to self-assemble was analyzed by Transmission Electron Microscopy (TEM). To trigger the self-assembling process of PMP-2 through the polarization of the solvent, the samples were prepared following the solvent displacement technique, which has been used by us (Impresari et al., 2022; Bonetti et al., 2015) and others (Heimburg et al., 1999; Reches and Gazit. 2003; Bucci et al. 2020) with Phe-containing peptides. Lyophilized PMP-2 was dissolved in DMSO to reach a 2 mM concentration, and the resulting solution was added dropwise into Milli-Q water to reach the final concentration of 0.1 mM in 95:5 water/DMSO ratio. Although the CD studies were carried out in TFE, we switched to DMSO due to its higher capability to dissolve PMP-2 compared to TFE, limiting the amount of the hydrophobic solvent in the final aqueous solution. Additionally, the direct comparison of FT-ATR spectra of PMP-2 dissolved in DMSO as well as in TFE (at 10 mM concentration) indicated the adoption of the helical conformation in both cases, thus confirming the possibility of using such solvent for our planned investigations without altering the experimental conditions (Supplementary Material, Supplementary Figures S22, S23).

The resulting 0.1 mM solution was dropped onto a C/Formvar TEM grid, lyophilized, and analyzed. Representative TEM micrographs are reported in Figure 4 (Supplementary Material, Supplementary Figure S18), and they showed the formation of an entangled fibrillar network clearly visible at the 200 nm scale, similar to those fibrillar structures reported in the literature for other α-helical dominant peptide sequences (Potekhin et al., 2001; Cieslik-Boczula 2017). The subunits of these fibers have a diameter of 6 nm, and they are

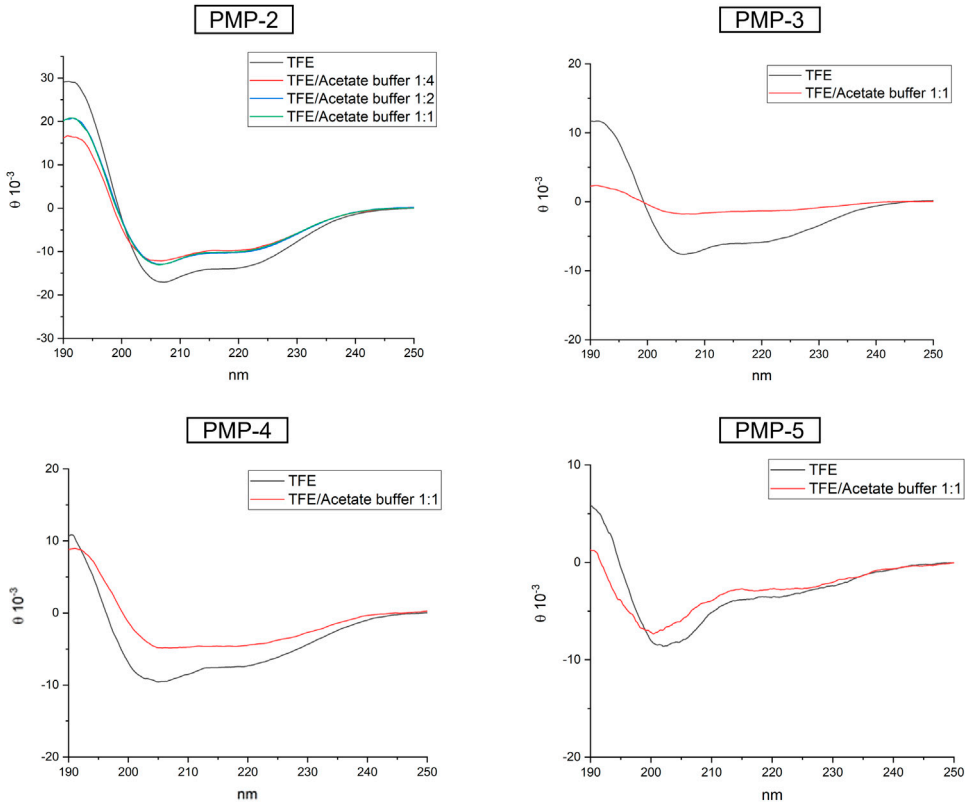


FIGURE 3
CD spectra of PMP-2-5 measured at 0.1 mM solution in pure TFE (black), or in different ratio of TFE/acetate buffer.

intertwined into bundled filaments (in a range from 3 to 8). Considering the stability of the α-helical conformation of PMP-2 observed through CD analysis by increasing the water content, (Figure 3; Supplementary Material; Supplementary Figure S13), the initial fibrillar formation may effectively arise from the peptide that adopts a helical structure in a hydrophobic environment (DMSO), which is retained in water thanks to the self-aggregation and consequent helical stabilization of PMP-2 (Missirlis et al., 2010; Han et al., 2013). A possible contribution of the positively charged head group to promote the PMP-2 self-assembly into this type of nanostructures is suggested by pH-dependent aggregation studies. Whereas at pH = 4 a similar behavior to the neutral aqueous solution was observed with the formation of the same filaments (Figures 4B,C), at pH 11 the observed few filaments co-existed with an undefined reticular structure, which is not stable under the experimental conditions. (Supplementary Material; Supplementary Figure S18D). Although this result is still under investigation, the possible control of the self-assembly by changing the pH might be an advantage in terms of future application as functional material.

3.2.2 Scanning Electron Microscopy analysis of PMP-2

To further investigate the capacity of these fibers to bundle into bigger filaments, Scanning Electron Microscopy (SEM) analyses were carried out at an increased concentration of 0.5 mM in water obtained by the solvent displacement technique. SEM images were collected in the low vacuum mode, under 1 Torr of water vapor pressure, to avoid possible morphological modifications induced by a preliminary gold coating. As shown in Figures 4D,E, PMP-2 forms helical fibers of several micrometers size, resulting from the aggregation of multiple bundled filaments. These micrometer long fibers are well visible at the edge of the sample holder, while in the middle we found the co-existence of parallel fibers and a 2D sheet-like structure as the one shown in Figure 4F. This effect might be a consequence of a concentration gradient in the sample drop during the lyophilization (increasing from the edge to the center), thereby a conformational switch, and consequently a morphological transformation, can occur as function of a different concentration. To support this hypothesis, we performed FT-ATR and ThT fluorescence analysis, which are reported in paragraph 2.3.

10.3389/fchem.2022.1038796

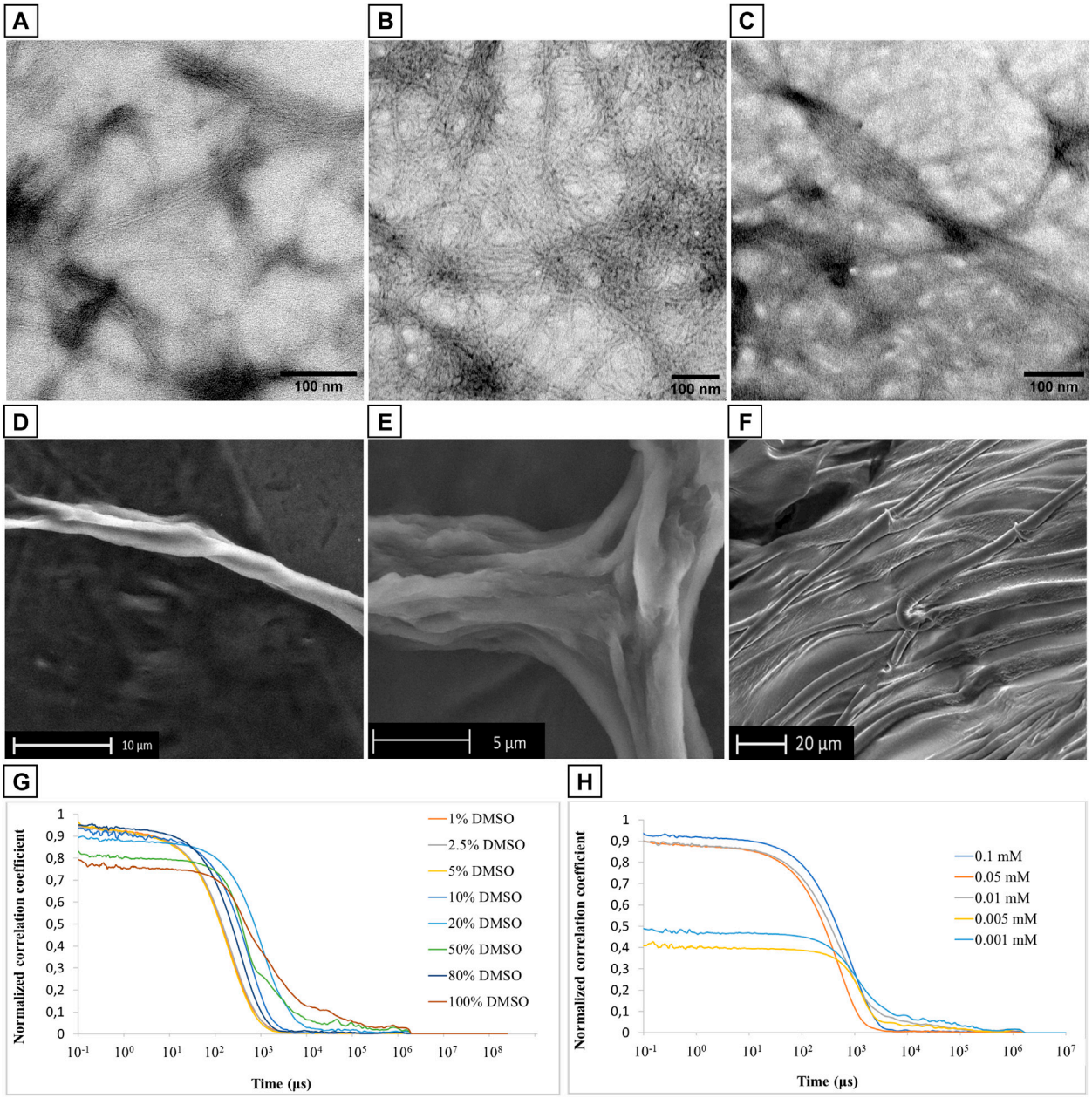


FIGURE 4
(A–C): TEM micrographs of filamentous assembly of PMP-2 from 0.1 mM solution at pH 7.6 **(A)**, and pH 4 **(B,C)**. **(D–F)**: SEM images of PMP-2 from 0.5 mM solution at measured pH = 7.6. **(G,H)**: DLS measurements of PMP-2: **(G)** Normalized autocorrelation functions at different DMSO/water mixture, and **(H)** normalized autocorrelation functions at different concentration **(H)**.

3.2.3 Dynamic Light Scattering analysis

Dynamic Light Scattering analysis was used to analyze the stability of the PMP-2 aggregates as a function of different DMSO/water ratio at 0.1 mM. A very poor scattering power was observed when PMP-2 was dissolved in 100, 80, and 50% *v/v* DMSO/water, whereas a more stable correlogram was obtained with 20% and 10% of DMSO, indicating the formation of some stable aggregates. A perfect overlap of the correlograms was achieved when the water content was increased, and PMP-2 was dissolved in 5, 2.5, and 1% *v/v* DMSO/water solutions (Figure 4G). The obtained curves, reproducible over several acquisitions, confirmed the presence of stable aggregates at the conditions used for TEM and SEM analysis (5% and 2.5% DMSO *v/v* respectively). The aggregation tendency of PMP-2 was also

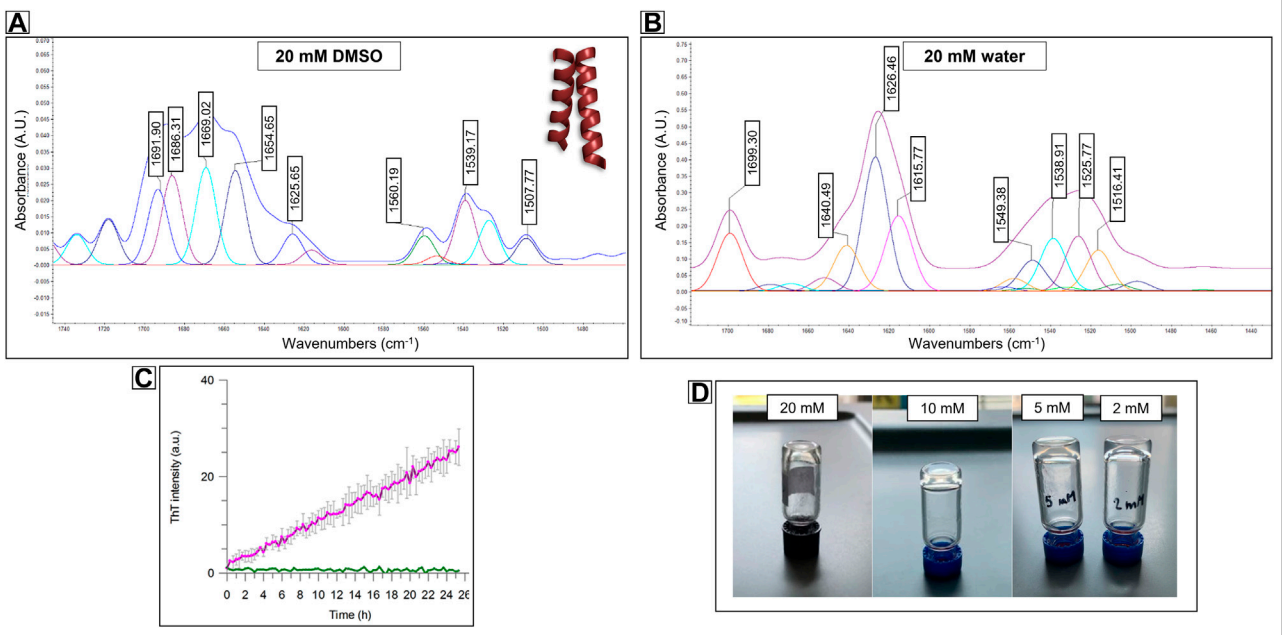


FIGURE 5
FT-ATR spectra of Compound PMP-2 at 20 mM concentration in **(A)** DMSO and **(B)** in water. In DMSO the pentameric signal of a coiled-coil like structure can be recognize, while in water the β-sheet conformation is predominant. **(C)** Stable-to-inversion gel test on PMP-2 in Milli-Q water at 20 mM, 10 mM and 5 mM and 2 mM, respectively. **(D)** ThT fluorescence assays showing 2 mM PMP-2 (purple trace) aggregation over 24 h. The concentration of the control PMP-2 is 0.1 mM (green trace).

investigated as function of concentration. The 0.1 mM solution of PMP-2 dissolved in 2.5% v/v DMSO/water was diluted to 0.05 and 0.001 mM with Milli-Q water, and a good fitting was obtained in both cases (Figure 4H). By contrast, no reliable correlograms were obtained at 0.005 and 0.0001 mM, probably due to the poor scattering power of the solutions and to the limit of detection of the instrument.

3.2.4 Electron microscopy analysis of PMP-3-5

TEM and SEM studies were carried out for the shorter derivatives PMP-3-5 by preparing the respective final 0.1 mM solutions and 0.5 mM solutions by solvent displacement. The obtained micrographs showed a different behavior of the three peptides compared to PMP-2, and no similar nanofibers were observed (Supplementary Material, Supplementary Section 4.1). These results highlighted the importance of the α-helix conformation assumed by the entire bacterial amino acid sequence present in PMP-2 to generate nanofibers.

3.3 Conformational switch

3.3.1 FT-ATR studies

The experimental evidence observed during the SEM analysis of PMP-2, in particular the co-existence of parallel fibers and a 2D sheet-like structure showed in Figure 4F, suggested that PMP-2 can adopt different conformations by varying the concentration. In addition, the increasing contribution of β-sheet conformation observed in the CD spectra upon changing the hydrophilicity of the solution (from 10% in pure TFE to 17% in the 1:2 and 1:4 TFE/water solutions), supported the hypothesis that also the hydrophilicity could have a crucial role in the final secondary structure of PMP-2. A change in the solution parameters can thus trigger a conformational switch, and this can lead to different aggregates. This tunable behavior of specific sequences is recently gaining growing attention because of the possibility to generate multiple morphologies from a single compound (Kaur at al., 2020; Ghosh et al., 2022). The conformation of PMP-2 in the highly concentrated 20 mM DMSO solution was thus investigated by AFT-ATR analysis, where a dimeric coiled-coil profile deriving from helical peptide self-assembly could be recognized (Figure 5A) by the pentameric signals revealed by the deconvolution process (Kammerer et al., 2004; Hendricks et al., 2017). This behavior is indicative of the attitude of the bacterial sequence to self-assemble as coiled coil when located in the hydrophobic environment of the native *Pa*YeaZ protein. As showed by the spectra obtained from the 10 mM DMSO solution, this coiled coil-like structure is destabilized by

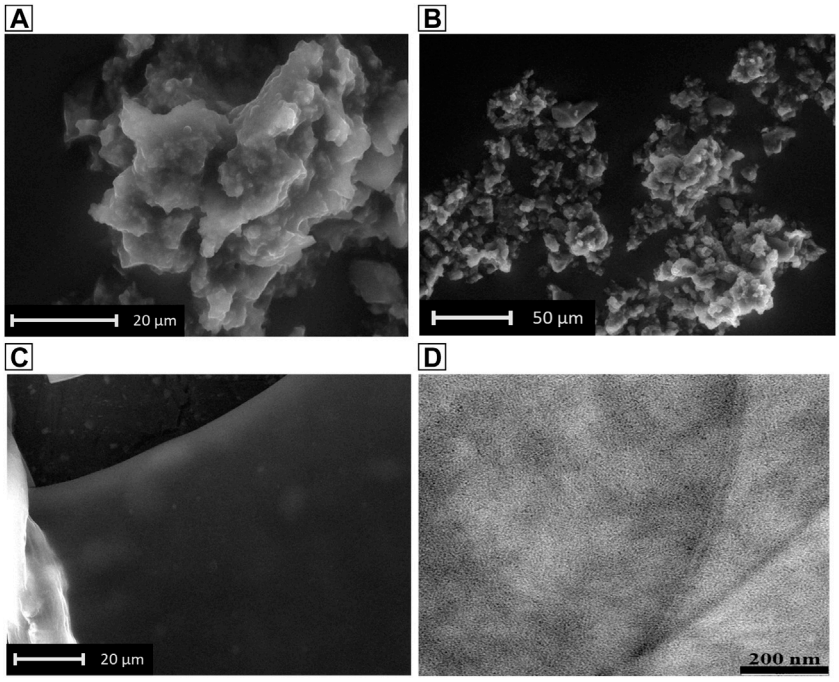


FIGURE 6
SEM images of the hydrogel in dry form **(A)**, and in wet form **(B,C)**. **(D)**: TEM image of the 2 mM hydrogel in dry form.

dilution, although still present, suggesting that molecular interactions are needed to stabilize the helical conformation.

For a direct comparison, we tried to achieve a similar concentration of PMP-2 in water although its low solubility at room temperature. Interestingly, after sonicating and heating at 60°C, the 20 mM solution of PMP-2 in Milli-Q water, a transparent hydrogel-like morphology was obtained after aging overnight. The Minimum Gelation Concentration (MGC) was found at 2 mM (3.8 mg/ml) by the stable-to-inversion test method, and the final pH of the hydrogel was 8.4 (Figure 5D). In contrast to the DMSO solution, the FT-ATR spectrum of the 20 mM hydrogel clearly shows a β-sheet conformation, with a peak at 1,626 cm^{-1}, and a peak at 1,690 cm^{-1} that can be attributed to a β-strand aggregation (Figure 5B). Same FT-ATR spectra profiles were obtained with the more diluted hydrogels at concentration 10, 5, 2 mM, suggesting the occurring of a conformational switch from α-helix to β-sheet, as we previously hypothesized. (Supplementary Material, Supplementary Figure S25).

3.3.2 ThT fluorescence analysis

To assess the secondary structure content of the hydrogels, we tested the propensity of PMP-2 dissolved in Milli-Q and heated at 60°C to form β-rich aggregates *in vitro* by Thioflavin T (ThT) assay. This benzothiazole salt is a commonly used fluorogenic compound specific for β-amyloid-like structures. Upon the binding to β-sheet-rich structures, the dye displays enhanced fluorescence at 480 nm. Figure 5C shows the increased ThT signal of PMP-2 at the lowest hydrogel concentration of 2 mM over 2 days' incubation at 25°C, suggesting the formation of β-like structure, while at 0.1 mM concentration, at which PMP-2 does not form the gel, no signal increase was observed.

3.3.3 Electron microscopy analysis

The effect of the conformational switch was observed through Electron Microscopy Techniques. In particular, the 20 mM hydrogel was analyzed by SEM as wet form and dried form. In the first case, SEM analysis showed a fractal-like morphology that alternatively grows and gets smaller through the successive wet and dry cycles directly into the instrument, (Figures 6A,B). This experiment was done by changing the relative humidity directly inside the environmental SEM chamber, through slight changes in the cooled sample holder, and suggests the ability of the hydrogel to regenerate by simply absorbing aqueous vapors. By contrast, the thick film observed analyzing the xerogel (Figure 6C), support the correlation between the β-sheet secondary structure and 2D-sheet formation previously observed in Figure 4E. The fine structure of the film was subsequently observed by TEM (from the 2 mM concentration) that showed again the formation of a thick 2D-sheet, in which the typical hydrogel fiber network can be distinguished (Figure 6D).

4 Conclusion

In this work, we reported the discovery of a novel PMP sequence deriving from the α-helix domain α2 of *Pa*YeaZ that undergoes a conformational switch from α-helix to β-sheet, and it is able to generate multiple morphologies. This essential protein in bacteria forms protein networks to exploit its biological function, and the X-ray structure of the homodimer was recently solved (Vecchietti et al., 2016). By molecular dynamic simulations and CAS analysis, we identified the shortest amino-acidic sequence (PMP-1) responsible for the dimer formation. A further chemical modification was introduced to stabilize the helical conformation and increase the water solubility of the otherwise very hydrophobic PMP sequence. The remarkable attitude of the helical PMP-1 to self-assemble was investigated after chemical modifications that led to the final peptide structure PMP-2. Overall, conformational analysis by CD and FT-ATR experiments indicate that PMP-2 conserves its helical character in hydrophobic environment like TFE and DMSO. At the highest reachable concentration in DMSO (20 mM), a dimeric coiled-coil profile can be recognized by FT-ATR spectra. Interestingly, the pose of the interacting helices of the *Pa*YeaZ homodimer in the X-ray crystal structure can be attributed to a dimeric coiled-coil as well, thus giving a further indication that the helical conformation of *Pa*YeaZ in solution (at least in hydrophobic solvents or in diluted water solutions, <0.5 mM) is maintained in the solid state (Vecchietti et al., 2016). Additionally, an increased water content up to 80% does not abolish the α-helix as shown by CD analysis, proving a stabilization of this secondary motif also in water, although to a lower extent. The nanoaggregates of PMP-2 formed in 95:5 water/DMSO solution at 0.1 mM concentration were studied by DLS and TEM, the latter showing the formation of filaments that are formed by the intertwining of 3–8 nanofibers having diameter of 6 nm. By increasing the concentration and the water content (97.5:2.5 water/DMSO at 0.5 mM), a conformational transition occurs, and PMP-2 adopts a β-sheet structure, as shown by the FT-ATR spectra. Probably, higher concentrations in a polar solvent emphasize the amphiphilic character of PMP-2, thus facilitating β-sheet rich structures as reported in the literature (Kammerer et al., 2004; Hendricks et al., 2017). Above 2 mM, the formation of a hydrogel-like morphology is recognized by dissolving **PMP-2** in 100% Milli-Q water and heating the sample to 60 °C. The secondary β-sheet structure adopted by the **PMP-2** also in this morphology was proven by FT-ATR and ThT analysis, confirming the occurrence of a conformational transition.

The unraveling of the molecular features (sequences, secondary structures, and intermolecular forces) that determine the proteins folding and assembly, is the driving force for the design of supramolecular architectures with potential useful applications (Baldwin, 1989). The additional ability of certain protein sequences to switch to different secondary structural elements (α-helix, β-sheet), as well as to form different aggregate types by a fine tuning of the external conditions, is known, and represents a topic of high interest due to the possibility to generate multi-stimuli responsive materials from a single building block. In addition, naturally occurring conformational switches are often involved in important biological processes (Wang et al., 2019). Thus, our findings may have potential utility for generating novel responsive biocompatible materials, as well as have relevance to fostering the understanding of the bacterial protein network formation, which could turn into a new biological target. Further investigations currently ongoing in our laboratories aim at determining the antimicrobial activity and cytotoxicity of PMP-2, and the mechanical and functional properties of this hydrogel like material.

Data availability statement

The original contributions presented in the study are included in the article/Supplementary Material, further inquiries can be directed to the corresponding authors.

Author contributions

The manuscript was written by SG with the contributions of all the authors. EF worked on the synthesis of peptides, hydrogel formation, preparation of samples for conformational studies, and she performed DLS analysis. GA work on the synthesis of PMP-2. STP, FO, and FA did the computational studies. MB performed the ThT fluorescence assays. GB started the analysis of *Pa*YeaZ self-assembly on the X-Ray structure. SR performed the SEM analysis together with EF, and MM performed the TEM analysis. UP funded the project and contribute to the supervision of the project. SAP did the CD analysis and contributed to the design methodology and the data evaluation. SG conceptualized and supervised the project and contribute to the experimental analysis. All authors critically revised the article.

Acknowledgments

We acknowledge Dr. Cristina Corti for her help with FT-ATR instrument, and Professor Angelo Maspero for the technical support. We gratefully acknowledge Ministero dell'Università e della Ricerca (PRIN 2020 project 2020833Y75), and the European Commission (Marie Skłodowska-Curie ITN MAGICBULLET:RELOADED 861316). We also thank Regione Lombardia, regional law n° 9/2020, resolution n° 3,776/2020, for financial support.

Conflict of interest

The authors declare that the research was conducted in the absence of any commercial or financial relationships that could be construed as a potential conflict of interest.

Publisher's note

All claims expressed in this article are solely those of the authors and do not necessarily represent those of their affiliated organizations, or those of the publisher, the editors and the reviewers. Any product that may be evaluated in this article, or claim that may be made by its manufacturer, is not guaranteed or endorsed by the publisher.

Supplementary material

The Supplementary Material for this article can be found online at: https://www.frontiersin.org/articles/10.3389/fchem.2022.1038796/full#supplementary-material

References

Abbas, O., Richards, J. E., and Mahalingam, M. (2010). Fibroblast-activation protein: A single marker that confidently differentiates morpheaform/infiltrative basal cell carcinoma from desmoplastic trichoepithelioma. *Mod. Pathol.* 23, 1535–1543. doi:10.1038/modpathol.2010.142

Apostolovic, B., Danial, M., and Klok, H. A. (2010). Coiled coils: Attractive protein folding motifs for the fabrication of self-assembled, responsive and bioactive materials. *Chem. Soc. Rev.* 39, 3541–3575. doi:10.1039/B914339B

Araghi, R. R., and Keating, A. E. (2016). Designing helical peptide inhibitors of protein–protein interactions. *Curr. Opin. Struct. Biol.* 39, 27–38. doi:10.1016/j.sbi.2016.04.001

Assal, Y., Mie, M., and Kobatake, E. (2013). The promotion of angiogenesis by growth factors integrated with ECM proteins through coiled-coil structures. *Biomaterials* 34, 3315–3323. doi:10.1016/j.biomaterials.2013.01.067

Bai, Y., Luo, Q., and Liu, J. (2016). Protein self-assembly via supramolecular strategies. *Chem. Soc. Rev.* 45, 2756–2767. doi:10.1039/C6CS00004E

Baldwin, R. L. (1989). How does protein folding get started? *Trends biochem. Sci.* 14, 291–294. doi:10.1016/0968-0004(89)90067-4

Berendsen, H. J., Postma, J. V., Van Gunsteren, W. F., DiNola, A. R. H. J., and Haak, J. R. (1984). Molecular dynamics with coupling to an external bath. *J. Chem. Phys.* 81 (8), 3684–3690. doi:10.1063/1.448118

Berns, E. J., Álvarez, Z., Goldberger, J. E., Boekhoven, J., Kessler, J. A., Kuhn, H. G., et al. (2016). A tenascin-C mimetic peptide amphiphile nanofiber gel promotes neurite outgrowth and cell migration of neurosphere-derived cells. *Acta Biomater.* 37, 50–58. doi:10.1016/j.actbio.2016.04.010

Bonetti, A., Pellegrino, S., Das, P., Yuran, S., Bucci, R., Ferri, N., et al. (2015). Dipeptide nanotubes containing unnatural fluorine-substituted β2, 3-diarylamino acid and L-alanine as candidates for biomedical applications. *Org. Lett.* 17 (18), 4468–4471. doi:10.1021/acs.orglett.5b02132

Bucci, R., Bossi, A., Erba, E., Vaghi, F., Saha, A., Yuran, S., et al. (2020). Nucleobase morpholino β amino acids as molecular chimeras for the preparation of photoluminescent materials from ribonucleosides. *Sci. Rep.* 10 (1), 19331. doi:10.1038/s41598-020-76297-7

Bussi, G., Donadio, D., and Parrinello, M. (2007). Canonical sampling through velocity rescaling. *J. Chem. Phys.* 126, 014101. doi:10.1063/1.2408420

Castelletto, V., and Hamley, I. W. (2022). Amyloid and hydrogel formation of a peptide sequence from a coronavirus spike protein. *ACS Nano* 16 (2), 1857–1867. doi:10.1021/acsnano.1c10658

Cieślik-Boczula, K. (2017). Alpha-helix to beta sheet transition in long-chain poly-L-lysine: Formation of alpha-helical fibrils by poly-L-lysine. *Biochimie* 137, 106–114. doi:10.1016/j.biochi.2017.03.006

Darden, T., York, D., and Pedersen, L. (1993). Particle mesh Ewald: An N log (N) method for Ewald sums in large systems. *J. Chem. Phys.* 98 (12), 10089–10092. doi:10.1063/1.464397

Daura, X., Gademann, K., Jaun, B., Seebach, D., Van Gunsteren, W. F., and Mark, A. E. (1999). Peptide folding: When simulation meets experiment. *Angew. Chem. Int. Ed.* 38, 236–240. doi:10.1002/(sici)1521-3773(19990115)38:1/2<236:aid-anie236>3.0.co;2-m

Fletcher, D. A., and Mullins, R. D. (2010). Cell mechanics and the cytoskeleton. *Nature* 463, 485–492. doi:10.1038/nature08908

Fu, C., Shao, Z., and Fritz, V. (2009). Animal silks: Their structures, properties and artificial production. *Chem. Commun.* 43, 6515–6529. doi:10.1039/B911049F

Ghosh, G., Barman, R., Mukherjee, A., Ghosh, U., Ghosh, S., and Fernandez, G. (2022). Control over multiple Nano- and secondary structures in peptide self-assembly. *Angew. Chem. Int. Ed. Engl.* 61, e202113403. doi:10.1002/anie.202113403

Goerbitz, C. H. (2006). The structure of nanotubes formed by diphenylalanine, the core recognition motif of Alzheimer's β-amyloid polypeptide. *Chem. Commun.* 2006, 2332–2334. doi:10.1039/b603080g

Gomes, S., Numata, K., Leonor, I. B., Mano, J. F., Reis, R. L., and Kaplan, D. L. (2011). AFM study of morphology and mechanical properties of a chimeric spider silk and bone sialoprotein protein for bone regeneration. *Biomacromolecules* 12, 1675–1685. doi:10.1021/bm2000605

Han, S. H., Lee, M. K., and Lim, Y. B. (2013). Bioinspired self-assembled peptide nanofibers with thermostable multivalent α-helices. *Biomacromolecules* 14, 1594–1599. doi:10.1021/bm400233x

Heimburg, T., Schünemann, J., Weber, K., and Geisler, N. (1999). FTIR-spectroscopy of multistranded coiled coil proteins. *Biochemistry* 38, 12727–12734. doi:10.1021/bi983079h

Hendricks, M. P., Sato, K., Palmer, L. C., and Stupp, S. I. (2017). Supramolecular assembly of peptide amphiphiles. *Acc. Chem. Res.* 50, 2440–2448. doi:10.1021/acs.accounts.7b00297

Hess, B., Bekker, H., Berendsen, H. J., and Fraaije, J. G. (1997). Lincs: A linear constraint solver for molecular simulations. *J. Comput. Chem.* 18 (12), 1463–1472. doi:10.1002/(sici)1096-987x(199709)18:12<1463:aid-jcc4>3.0.co;2-h

Hol, W. G. (1985). The role of the alpha-helix dipole in protein function and structure. *Prog. Biophys. Mol. Biol.* 45, 149–195. doi:10.1016/0079-6107(85)90001-x

Jorgensen, W. L., Chandrasekhar, J., Madura, J. D., Impey, R. W., and Klein, M. L. (1983). Comparison of simple potential functions for simulating liquid water. *J. Chem. Phys.* 79 (2), 926–935. doi:10.1063/1.445869

Kabsch, W., and Sander, C. (1983). Dictionary of protein secondary structure: Pattern recognition of hydrogen-bonded and geometrical features. *Biopolymers* 22 (12), 2577–2637. doi:10.1002/bip.360221211

Kammerer, R. A., Kostrewa, D., Zurdo, J., Detken, A., Garcìa Echeverrìa, C., Green, J. D., et al. (2004). Exploring amyloid formation by a *de novo* design. *Proc. Natl. Acad. Sci. U. S. A.* 101, 4435–4440. doi:10.1073/pnas.0306786101

Kaur, H., Jain, R., and Roy, S. (2020). Pathway-dependent preferential selection and amplification of variable self-assembled peptide nanostructures and their biological activities. *ACS Appl. Mat. Interfaces* 12, 52445–52456. doi:10.1021/acsami.0c16725

Keskin, O., Gursoy, A., Ma, B., and Nussinov, R. (2008). Principles of Protein–Protein interactions: What are the preferred ways for proteins to interact? *Chem. Rev.* 108, 1225–1244. doi:10.1021/cr040409x

Kim, N. H., Choi, H., Shahzad, Z. M., Ki, H., Lee, J., Chae, H., et al. (2022). Supramolecular assembly of protein building blocks: From folding to function. *Nano Converg.* 9, 4. doi:10.1186/s40580-021-00294-3

La Manna, S., Di Natale, C., Onesto, V., and Marasco, D. (2021). Self-assembling peptides: From design to biomedical applications. *Int. J. Mol. Sci.* 22, 12662. doi:10.3390/ijms222312662

Lamiable, A., Thévenet, P., Rey, J., Vavrusa, M., Derreumaux, P., and Tufféry, P. (2016). PEP-FOLD3: Faster *de novo* structure prediction for linear peptides in solution and in complex. *Nucleic Acids Res.* 8, W449–W454. doi:10.1093/nar/gkw329

LeBel, R. G., and Goring, D. A. I. (1962). Density, viscosity, refractive index, and hygroscopicity of mixtures of water and dimethyl sulfoxide. *J. Chem. Eng. Data* 7 (1), 100–101. doi:10.1021/je60012a032

Levin, A., Hakala, T. A., Schnaider, L., Bernardes, G. J. L., Gazit, E., and Knowles, T. P. J. (2020). Biomimetic peptide self-assembly for functional materials. *Nat. Rev. Chem.* 4, 615–634. doi:10.1038/s41570-020-0215-y

Li, Y., Wang, Y., Ou, S. H., Lock, L. L., Xu, X., Ghose, S., et al. (2017). Conformation preservation of α-helical peptides within supramolecular filamentous assemblies. *Biomacromolecules* 18, 3611–3620. doi:10.1021/acs.biomac.7b00992

Lindorff-Larsen, K., Piana, S., Palmo, K., Maragakis, P., Klepeis, J. L., Dror, R. O., et al. (2010). Improved side-chain torsion potentials for the Amber ff99SB protein force field. *Proteins.* 78 (8), 1950–1958. doi:10.1002/prot.22711

Locarno, S., Argentiere, S., Ruffoni, A., Maggioni, D., Soave, R., Bucci, R., et al. (2020). Self-assembled hydrophobic ala-aib peptide encapsulating curcumin: A convenient system for water insoluble drugs. *RSC Adv.* 10, 9964–9975. doi:10.1039/C9RA10981A

Lupas, A. (1996). Coiled coils: New structures and new functions. *Trends biochem. Sci.* 21, 37510052–37513829. doi:10.1016/s0968-0004(96)10052-9

Lupas, A. N., and Bassler, J. (2017). Coiled coils – a model system for the 21st century. *Trends biochem. Sci.* 42, 130–140. doi:10.1016/j.tibs.2016.10.007

Massova, I., and Kollman, P. A. (2000). Combined molecular mechanical and continuum solvent approach (MM-PBSA/GBSA) to predict ligand binding. *Perspect. Drug Discov. Des.* 18, 113–135. doi:10.1023/A:1008763014207

Matsuura, K., Ota, J., Fujita, S., Shiomi, Y., and Inaba, H. (2020). Construction of ribonuclease-decorated artificial virus-like capsid by peptide self-assembly. *J. Org. Chem.* 85, 1668–1673. doi:10.1021/acs.joc.9b02295

Meng, Q., Kou, Y., Ma, X., Guo, L., and Liu, K. (2014). Nanostructures from the self-assembly of α-helical peptide amphiphiles. *J. Pept. Sci.* 20, 223–228. doi:10.1002/psc.2606

Missirlis, D., Farine, M., Kastantin, M., Ananthanarayanan, B., Neumann, T., and Tirrel, M. (2010). Linker Chemistry determines secondary structure of $p53_{14–29}$ in peptide amphiphile micelles. *Bioconjug. Chem.* 21, 465–475. doi:10.1021/bc900383m

Mondal, S., and Gazit, E. (2016). The self-assembly of helical peptide building blocks. *ChemNanoMat* 2, 323–332. doi:10.1002/cnma.201600048

Morales, P., and Jiménez, M. A. (2019). Design and structural characterisation of monomeric water-soluble α-helix and β-hairpin peptides: State-of-the-art. *Arch. Biochem. Biophys.* 661, 149–167. doi:10.1016/j.abb.2018.11.014

Paissoni, C., Spiliotopoulos, D., Musco, G., and Spitaleri, A. (2014). Gmxpbsa 2.0: A GROMACS tool to perform MM/PBSA and computational alanine scanning. *Comput. Phys. Commun.* 185 (11), 2920–2929. doi:10.1016/j.cpc.2014.06.019

Pieraccini, S., Saladino, G., Cappelletti, G., Cartelli, D., Francescato, P., Speranza, G., et al. (2009). *In silico* design of tubulin-targeted antimitotic peptides. *Nat. Chem.* 1, 642–648. doi:10.1038/nchem.401

Pins, G. D., Christiansen, D. L., Patel, R., and Silver, F. H. (1997). Self-assembly of collagen fibers. Influence of fibrillar alignment and decorin on mechanical properties. *Biophys. J.* 73 (4), 2164–2172. doi:10.1016/S0006-3495(97)78247-X

Potekhin, S. A., Melnik, T. N., Popov, V., Lanina, N. F., Vazina, A. A., Rigler, P., et al. (2001). De novo design of fibrils made of short α-helical coiled coil peptides. *Chem. Biol.* 8, 1025–1032. doi:10.1016/s1074-5521(01)00073-4

Reches, M., and Gazit, E. (2003). Casting metal nanowires within discrete self-assembled peptide nanotubes. *Science* 300 (5619), 625–627. doi:10.1126/science.1082387

Ruffoni, A., Cavanna, M. V., Argentiere, S., Locarno, S., Pellegrino, S., Gelmi, M. L., et al. (2016). Aqueous self-assembly of short hydrophobic peptides containing norbornene amino acid into supramolecular structures with spherical shape. *RSC Adv.* 6, 90754–90759. doi:10.1039/c6ra17116h

Shen, Y., Wang, X., Wang, Y., Guo, X., Keda, Y., Dong, K., et al. (2022). Bilayer silk fibroin/sodium alginate scaffold promotes vascularization and advances inflammation stage in full-thickness wound. *Biofabrication* 14, 035016. doi:10.1088/1758-5090/ac73b7

Sousa, S. F., Fernandes, P. A., and Ramos, M. J. (2007). Theoretical studies on farnesyltransferase: The distances paradox explained. *Proteins.* 66, 205–218. doi:10.1002/prot.21219

Sreerama, N., and Woody, R. W. (2000). Estimation of protein secondary structure from circular dichroism spectra: Comparison of CONTIN, SELCON, and CDSSTR methods with an expanded reference set. *Anal. Biochem.* 287 (2), 252–260. doi:10.1006/abio.2000.4880

Swinehart, W., Deutsch, C., Sarachan, K. L., Luthra, A., Bacusmo, J. M., de Crécy-Lagard, V., et al. (2020). Specificity in the biosynthesis of the universal tRNA nucleoside N6-threonylcarbamoyl adenosine (t6A)-TsaD is the gatekeeper. *RNA* 26, 1094–1103. doi:10.1261/rna.075747.120

Van Der Spoel, D., Lindahl, E., Hess, B., Groenhof, G., Mark, A. E., and Berendsen, H. J. (2005). Gromacs: Fast, flexible, and free. *J. Comput. Chem.* 26 (16), 1701–1718. doi:10.1002/jcc.20291

Vecchietti, D., Ferrara, S., Rusmini, R., Macchi, R., Milani, M., and Bertoni, G. (2016). Crystal structure of YeaZ from *Pseudomonas aeruginosa*. *Biochem. Biophys. Res. Commun.* 470, 460–465. doi:10.1016/j.bbrc.2016.01.008

Wang, H., Feng, Z., and Xu, B. (2019). Assemblies of peptides in a complex environment and their applications. *Angew. Chem. Int. Ed.* 58, 10423–10432. doi:10.1002/anie.201814552

Wang, J., Wolf, R. M., Caldwell, J. W., Kollman, P. A., and Case, D. A. (2004). Development and testing of a general amber force field. *J. Comput. Chem.* 25, 1157–1174. doi:10.1002/jcc.20035

Whitmore, L., and Wallace, B. A. (2008). Protein secondary structure analyses from circular dichroism spectroscopy: Methods and reference databases. *Biopolymers* 89 (5), 392–400. doi:10.1002/bip.20853

Wolf, E., Kim, P. S., and Berger, B. (1997). MultiCoil: A program for predicting two-and three-stranded coiled coils. *Protein Sci.* 6, 1179–1189. doi:10.1002/pro.5560060606

Xu, Z., Yang, Y., Zhao, W., Wang, Z., Landis, W. J., Cui, Q., et al. (2015). Molecular mechanisms for intrafibrillar collagen mineralization in skeletal tissues. *Biomaterials* 39, 59–66. doi:10.1016/j.biomaterials.2014.10.048

Zanella, S., Bocchinfuso, G., De Zotti, M., Arosio, D., Marino, F., Raniolo, S., et al. (2019). Rational Design of Antiangiogenic helical oligopeptides targeting the vascular endothelial growth factor receptors. *Front. Chem.* 7, 170. doi:10.3389/fchem.2019.00170

Zhang, S., Holmes, T., Lockshin, C., and Rich, A. (1993). Spontaneous assembly of a self-complementary oligopeptide to form a stable macroscopic membrane. *Proc. Natl. Acad. Sci. U. S. A.* 90, 3334–3338. doi:10.1073/pnas.90.8.3334

Zhang, W., Yu, X., Li, Y., Su, Z., Jandt, K., and Wei, G. (2018). Protein-mimetic peptide nanofibers: Motif design, self-assembly synthesis, and sequence-specific biomedical applications. *Prog. Polym. Sci.* 80, 94–124. doi:10.1016/j.progpolymsci.2017.12.001

Zou, Q., Chang, R., Xing, R., Yuan, C., and Yan, X. (2020). Injectable self-assembled bola-dipeptide hydrogels for sustained photodynamic prodrug delivery and enhanced tumor therapy. *J. Control. Release* 319, 344–351. doi:10.1016/j.jconrel.2020.01.002

frontiers | Frontiers in Chemistry

TYPE Original Research
PUBLISHED 13 January 2023
DOI 10.3389/fchem.2022.1009468

Check for updates

OPEN ACCESS

EDITED BY
Rajni Verma,
The University of Melbourne, Australia

REVIEWED BY
Soumen Saha,
Duke University, United States
Manzar Abbas,
Khalifa University, United Arab Emirates

*CORRESPONDENCE
Céline Valéry,
celine.valery@rmit.edu.au

SPECIALTY SECTION
This article was submitted to Nanoscience, a section of the journal Frontiers in Chemistry

RECEIVED 01 August 2022
ACCEPTED 12 December 2022
PUBLISHED 13 January 2023

CITATION
Cardoso P, Appiah Danso S, Hung A, Dekiwadia C, Pradhan N, Strachan J, McDonald B, Firipis K, White JF, Aburto-Medina A, Conn CE and Valéry C (2023), Rational design of potent ultrashort antimicrobial peptides with programmable assembly into nanostructured hydrogels. *Front. Chem.* 10:1009468. doi: 10.3389/fchem.2022.1009468

COPYRIGHT
© 2023 Cardoso, Appiah Danso, Hung, Dekiwadia, Pradhan, Strachan, McDonald, Firipis, White, Aburto-Medina, Conn and Valéry. This is an open-access article distributed under the terms of the Creative Commons Attribution License (CC BY). The use, distribution or reproduction in other forums is permitted, provided the original author(s) and the copyright owner(s) are credited and that the original publication in this journal is cited, in accordance with accepted academic practice. No use, distribution or reproduction is permitted which does not comply with these terms.

Rational design of potent ultrashort antimicrobial peptides with programmable assembly into nanostructured hydrogels

Priscila Cardoso[1,2], Samuel Appiah Danso[1,3], Andrew Hung[2], Chaitali Dekiwadia[4], Nimish Pradhan[1], Jamie Strachan[1,2], Brody McDonald[1], Kate Firipis[5,6], Jacinta F. White[3], Arturo Aburto-Medina[2], Charlotte E. Conn[2] and Céline Valéry[1]*

[1]School of Health and Biomedical Sciences, Translational Immunology and Nanotechnology Theme, NanoBioPharm Research Group, RMIT University, Bundoora, VIC, Australia, [2]School of Science, STEM College, RMIT University, Melbourne, VIC, Australia, [3]Materials Characterisation and Modelling, Manufacturing, CSIRO, Clayton, VIC, Australia, [4]RMIT Microscopy and Microanalysis Facility (RMMF), RMIT University, Melbourne, VIC, Australia, [5]BioFab3D, Aikenhead Centre for Medical Discovery, St Vincent's Hospital Melbourne, Fitzroy, VIC, Australia, [6]Biomedical and Electrical Engineering, School of Engineering, RMIT University, Melbourne, VIC, Australia

Microbial resistance to common antibiotics is threatening to cause the next pandemic crisis. In this context, antimicrobial peptides (AMPs) are receiving increased attention as an alternative approach to the traditional small molecule antibiotics. Here, we report the bi-functional rational design of Fmoc-peptides as both antimicrobial and hydrogelator substances. The tetrapeptide Fmoc-WWRR-NH_2—termed Priscilicidin—was rationally designed for antimicrobial activity and molecular self-assembly into nanostructured hydrogels. Molecular dynamics simulations predicted Priscilicidin to assemble in water into small oligomers and nanofibrils, through a balance of aromatic stacking, amphiphilicity and electrostatic repulsion. Antimicrobial activity prediction databases supported a strong antimicrobial motif *via* sequence analogy. Experimentally, this ultrashort sequence showed a remarkable hydrogel forming capacity, combined to a potent antibacterial and antifungal activity, including against multidrug resistant strains. Using a set of biophysical and microbiology techniques, the peptide was shown to self-assemble into viscoelastic hydrogels, as a result of assembly into nanostructured hexagonal mesophases. To further test the molecular design approach, the Priscilicidin sequence was modified to include a proline turn—Fmoc-WPWRR-NH_2, termed P-Priscilicidin–expected to disrupt the supramolecular assembly into nanofibrils, while predicted to retain antimicrobial activity. Experiments showed P-Priscilicidin self-assembly to be effectively hindered by the presence of a proline turn, resulting in liquid samples of low viscosity. However, assembly into small oligomers and nanofibril precursors were evidenced. Our results augur well for fast, adaptable, and cost-efficient antimicrobial peptide design with programmable physicochemical properties.

KEYWORDS

antimicrobial peptide (AMP), peptide hydrogels, molecular engineering, molecular self assembly, fmoc-peptides

Introduction

Microbial resistance to common antibiotics is threatening to cause the next pandemic crisis (WHO, 2020). In this context, antimicrobial peptides (AMPs) are receiving increased attention as an alternative approach to the traditional small molecule antibiotics (WHO, 2020).

Indeed, peptides are relatively easy to synthetise while exhibiting broad-spectrum antimicrobial activity, decreased microbial resistance and intrinsic biocompatibility. The emergence of molecular engineering principles to design antimicrobial peptide sequences has made rational sequence design a promising approach for rapid and adaptive design of novel antimicrobial therapeutics. Recent works demonstrated that sequences as short as 2–5 natural residues can display antimicrobial activity (Glossop et al., 2019; Cardoso et al., 2021). In parallel, a few natural and synthetic AMPs were reported to self-assemble in solution into nanostructures, a process that can be harnessed for drug delivery and material design (Cardoso et al., 2021).

Here we report the bi-functional rational design of Fmoc-tetrapeptides for potent antimicrobial activity and control of peptide hydrogelation through molecular self-assembly. Peptide molecular self-assembly is mediated through intermolecular non-covalent interactions such as hydrogen bonding, hydrophobic, ionic, and π–π stacking interactions (Cardoso et al., 2021). Pioneering works in this domain established that two nanostructure-forming short synthetic sequences - the diphenylalanine peptide and cyclic D,L-alpha alanine peptide—interact with bacterial membranes and display antibacterial activity (Fernandez-Lopez et al., 2001; Schnaider et al., 2017). The antimicrobial action of AMPs is known to mainly arise from a combination of electrostatic and hydrophobic interactions with microbial membrane components. Sequence motifs that favor antimicrobial activity have been reported, especially: i) presence of cationic amino acids ii) primary structure characterized by a net positive charge of 2–9, iii) presence of aromatic amino acids, iv) amphipathic character of primary sequence (Tian et al., 2015; Li et al., 2017; Cardoso et al., 2021).

Although there is still debate on a direct relationship between self-assembly and antimicrobial activity, networks of peptide self-assembled nanostructures present the advantage of potentially resulting into hydrogels through reticulation of the aqueous media. Such supramolecular hydrogels can be exploited to create biomaterials with various applications, including as drug delivery vehicles, tissue engineering scaffolds, or as precursors for creating nanostructured surfaces (Das and Gavel, 2020; Cardoso et al., 2021; Shi et al., 2021). Specifically, the use of a fluorenylmethyloxycarbonyl (Fmoc) group located at the N-terminal of the sequence was previously reported to drive peptide supramolecular assembly into biocompatible hydrogels (Fleming et al., 2013; Tao et al., 2016; Firipis et al., 2021).

By applying a bottom-up approach supported by molecular dynamics and online antimicrobial prediction tools detailed below, we designed two Fmoc-peptide sequences of four to five amino-acids. Both sequences entail motifs for antimicrobial and self-assembling, as detailed in the results section. Our rational design predicted both peptides to exhibit antimicrobial activity; however, with one sole hydrogelator sequence. Using a large set of biophysical and microbiological techniques, we investigated for both designed sequences: i) the self-assembly into different molecular species; ii) the kinetics and mechanisms of hydrogelation and iii) antimicrobial activity on different strains.

Materials and methods

Chemicals and reagents

Indolicidin (sequence: ILPWKWPWWPWRR-NH_2, molecular weight: 1,906.3 g/mol) and FMOC-WWRR-NH_2 (molecular weight: 924.1) were obtained from ChemPep (USA) as lyophilized powder and acetate salts with a purity >95%. Ethanol and Congo red were purchased from Sigma-Aldrich (Australia). Sodium chloride was purchased from Alfa Aesar (United Kingdom). The negative staining agent phosphotungstic acid was purchased from Proscitech (Australia). A Milipore filter system was utilized to obtain Milli-Q water. BD Difco Mueller Hinton Broth (MHB) and Sabouraud broth (SB) were purchased from Cell biosciences (Australia). Strains: *E. coli* NCTC 10418, *P. aeruginosa* ATCC 9721, *E. faecalis* ATCC 19433, *S. aureus* ATCC 25923, *S. aureus* ATCC BAA-1756 (methicillin resistant), *Streptococcus pneumoniae* ATCC 49619, *Candida albicans* ATCC 10231 and *Candida auris* DSM 21092 (Fluconazole resistant) were provided by the RMIT microbial culture collection. Bacterial strains were stored in 50% glycerol at −20 and −80°C.

Peptide samples

The peptides were prepared by mixing the lyophilized peptide directly with type 1 water, vortexed for a few seconds to obtain an isotropic solution and stored at 4°C–5°C in between experiments.

Molecular dynamics

The Fmoc-WWRR-NH_2 and Fmoc-WPWRR-NH_2 peptide structures were prepared using Swiss-PdbViewer (Deepview) (Guex and Peitsch, 1997) and Discovery Studio Visualizer

(BIOVIA, Dassault Systèmes, Discovery Studio Visualizer, 2021 San Diego, CA). Molecular dynamics simulation cells for modelling peptide self-assembly were constructed by arranging smaller cubic 'subcells' containing a single peptide into larger cubic simulation cells composed of 3 × 3 × 3 subcells, in a crystalline structure, resulting in final cell sizes of 9 × 9 × 9 nm^3 (WWRR) or 9.6 × 9.6 × 9.6 nm^3 (WPWRR). Each of the simulation cells therefore contains 27 of the respective peptides initially in random orientations. Each box was filled with 23,054 (WWRR) or 28,273 (WPWRR) TIP4P water molecules. Cl^- counterions were added to neutralise the net positive charge of each system. GROMACS version 2019.3 (Van Der Spoel et al., 2005; Pronk et al., 2013) was used for all simulations, using the OPLS-AA forcefield (Jorgensen et al., 1996; Kaminski et al., 2001) for the peptides and the TIP4P model for water molecules (Jorgensen et al., 1983). Fmoc parameters were adapted from Mu et al. (2012). For all simulations, the integration time step was set to 2 fs. Electrostatic interactions were evaluated using the fast smooth particle-mesh Ewald (PME) method with a Coulombic potential cut-off of 1.2 nm (Essmann et al., 1995). For the peptides, covalent bonds involving hydrogen atoms were constrained using the LINCS algorithm (Hess et al., 1997). The systems were firstly energy minimized using the steepest descent algorithm for a maximum of 10,000 steps. Subsequent simulations were performed at 310 K temperature. Each system was equilibrated by running preparatory simulations in which all non-solvent heavy atoms were positionally restrained, firstly under a constant particle number, velocity, and temperature (NVT) ensemble for 100 ps, followed by a constant particle number, pressure, and temperature (NPT) simulation for another 100 ps. In the equilibration simulations, the temperature and pressure were coupled using the Berendsen thermostat and barostat (Berendsen et al., 1984). After the equilibration steps, all restraints were removed, and 800 ns production MD simulations were performed for both WWRR and WPWRR peptide self-assembly systems. For the production simulations, the velocity rescale thermostat of Bussi et al. (2007), with a coupling time constant of 0.1 ps, was used to maintain the temperature at 310 K, while the pressure was maintained at 1 bar using isotropic coupling with the Parrinello-Rahman barostat algorithm (Parrinello and Rahman, 1981). Molecular structures were visualized using Visual Molecular Dynamics version 1.9.3 (VMD) (Humphrey et al., 1996).

Activity predictions using antimicrobial sequence databases

The probability of antimicrobial activity for the designer tetrapeptide was evaluated using the prediction models Support Vector Machines (SVMs), Random Forests (RF), Discriminant analysis (DA) and Artificial Neural Network classifier (ANN) from the Collection of Anti-Microbial Peptides (CAMP) online (Waghu et al., 2016). The higher the score (max = 1), the greater is the likelihood of the sequence being antimicrobial. Peptides within the score between 0.5 and 1 are considered antimicrobial by those prediction tools. Given that only natural amino acids are considered by the algorithms without any possibility of modification, the Fmoc group was replaced by the aromatic phenylalanine (F) and the C-termini were as free carboxylic acids instead of amidated.

Minimal inhibitory concentration assays (MIC)

Minimal inhibitory concentration (MIC) assays were performed following a standard broth dilution procedure (Wiegand et al., 2008) in which bacteria were grown in MHB and fungal in SB overnight. The overnight bacterial suspension was adjusted to 10^6 CFU/ml in broth according to MacFarlane standard. Bacterial solutions were mixed in 96-well plates with the peptide solution to reach final concentrations of peptides ranging from 1,082 to 2 μM, including inhibition control (Indolicidin), growth control, and sterility control. Within each MIC experiment, each peptide was tested in triplicate across this concentration range and repeated on 3 independent days. Media and glassware were sterilized at 120°C for 1 h with an autoclave prior to all bioassays.

Fluorescence assisted cell sorting (FACS)

FACS assay was performed following the LIVE/DEAD™ BacLight™ Bacterial Viability Kit (L7012) instructions and stablished procedures (Berney et al., 2007; Robertson et al., 2019), in which bacteria were grown in Mueller Hinton Broth and fungal in Sabouraud Broth overnight to a late–log phase. Then, 900 μl of the cell suspension was added to 100 μl of five different concentrations of peptides solution and incubated overnight at 36°C–37°C. On the next day, the suspension was centrifuged at 10,000 × g for 10 min and the supernatant fraction was removed from the samples. The pellets were resuspended with 1 ml of PBS buffer and incubated at room temperature for 1 h, mixing every 15 min. The sample was centrifuged at 10,000 × g for 10 min, the supernatant removed followed by the resuspension of the pellet in 1 ml of PBS. The washing steps were repeated twice. To perform the staining of the cells, equal volumes of SYTO® 9 and propidium iodide were combined in a microfuge tube and 3 μl of the dye mixture was added to each microbial suspension. The sample was incubated at room temperature in the dark for 15 min. The evaluation of cell viability was performed through the calculation of the red to green fluorescence ratio to determine the proportion of live cells in a sample.

Scanning electron microscopy (SEM) of microbial cells

Pure peptide samples were prepared according to the procedure described in paragraph 2.2. Bacterial samples were prepared by diluting an overnight growth culture of bacteria to OD600 of 0.3–4 and incubating the resultant bacterial solution with the appropriate concentration of peptide for 1 h at 36°C, after which the bacteria were washed four times with PBS by centrifugation, and the resultant bacterial pellets were fixed in a solution of 2.5% glutaraldehyde in PBS for 30 min at 25°C. Control samples were prepared in the same manner but were not incubated with the peptide. The glutaraldehyde solution was washed thrice from the bacteria. The samples were then dehydrated in an incremental manner with 30%–100% EtOH, with a holding time of 15 min for each step, followed by final dehydration in 100% dry EtOH (Hartmann et al., 2010; Glossop et al., 2019). The samples were placed on silicon wafers and coated with iridium to increase its surface conductivity. SEM was performed on a FEI Quanta 200 SEM (2002) operating at 30 kV accelerating voltage.

Attenuated total reflectance fourier transform infrared spectroscopy (ATR-FTIR)

Data was recorded at 25°C using a Tensor-II spectrometer (Bruker, Germany) equipped with a Bio-ATR attachment (Bruker, Germany) by directly depositing the samples on the ATR crystal as previous reported by our group (Dharmadana et al., 2019). Spectra were collected over 32 scans within 4,000–400 cm^{-1} wavenumber range at a resolution of 4 cm^{-1}. Associated water signal was subtracted from the resulting spectra, and secondary derivatives were calculated using OPUS software (Bruker, Germany).

Polarized light optical microscopy (PLOM)

Polarizing light optical microscopy (PLOM) was performed with a Zeiss Axioskop microscope (Germany) with crossed polarizers at a magnification of × 10 and × 20 on samples conditioned in thin layers between glass coverslip and slide as previously. Images were recorded using a Nikon digital camera and the Zen freeware (bruker, Germany)

Negative staining for transmission electron microscopy imaging (TEM)

Carbon-coated grids (EMSCF200H-CU-TH, ProSciTech) were glow discharged to render them hydrophilic. A 1–5 µl aliquot of sample was applied to an upturned grid held in anti-capillary forceps, over moist filter paper, and left for 5 min over moistened filter paper to adsorb. Excess liquid was then removed with filter paper, the grid was then inverted onto a drop of 2% PTA stain, pH 6.9 on Parafilm, for 1 min. The grid was removed, the stain wicked away with filter paper and allowed to dry before viewing in the microscope. The samples were examined using Tecnai 12 Transmission Electron Microscope (FEI, Eindhoven, Netherlands) at an operating voltage of 120 kV. Images were recorded using a FEI Eagle 4 k × 4 k CCD camera and AnalySIS v3.2 camera control software (Olympus).

Cryogenic transmission electron microscopy (cryo-TEM)

A laboratory-built humidity-controlled vitrification system was used to prepare the samples for Cryo-TEM. Humidity was kept at 80% for all experiments, and ambient temperature was 22°C. 300-mesh copper grids coated with perforated carbon film (Lacey carbon film: ProSciTech GSCU300FL-50, Kirwan, Qld, Australia) were glow discharged using a Pelco EasiGlow Glow Discharge unit to render the carbon film hydrophilic. 3 µl aliquots of the sample were pipetted onto each grid prior to plunging. After 5 s adsorption time the grid was blotted manually using Whatman 541 filter paper, for 4 s. The grid was then plunged into liquid ethane cooled by liquid nitrogen. Frozen grids were stored in liquid nitrogen until required. The samples were examined using a Gatan 626 cryoholder (Gatan, Pleasanton, CA, USA) and Tecnai 12 Transmission Electron Microscope (FEI, Eindhoven, Netherlands) at an operating voltage of 120 kV. At all times low dose procedures were followed, using an electron dose of less than 5 electrons/$Å^2$ for all imaging. Images were recorded using a FEI Eagle 4 k × 4 k CCD camera at a range of magnifications using AnalySIS v3.2 camera control software (Olympus).

Cryogenic scanning electron microscopy (cryo-SEM)

Carbon-coated Lacy Formvar 300-mesh copper grids (GSCU300FL-50, ProSciTech, Australia) were glow discharged to render them hydrophilic. A 1 µl drop of peptide sample (5% w/w) at day 19 was applied on an upturned grid held in place by a tweezer. This was then turned upside down and gently smeared the sample on a Parafilm 'M'. The samples were vitrified by plunging them into liquid ethane, which was pre-cooled in liquid nitrogen. The vitrified samples were stored within a precooled grid

holder. The grids were transferred onto the brass grid holder under liquid nitrogen. The grid holder with samples was transferred in liquid nitrogen slush under vacuum into the cryogenic preparation chamber (Gatan ALTO 2500, UK) using the transfer arm. In the preparation chamber, the samples were sublimed at −80°C for 60 min and subsequently coated using platinum at ≤ −140°C for 120 s using a current of 10 mA. The cryogenically processed samples were transferred under vacuum onto the liquid nitrogen cooled stage within the Field Emission Scanning Electron Microscope (FE-SEM) chamber for imaging. The samples were imaged using a Zeiss Sigma 300 VP SEM (Germany) operated in the secondary electron (SE) mode. An accelerating voltage of 2 kV with a probe current of 80 pA was used for imaging. The location for imaging was taken in the region of 200 nm from the edge of the grid beyond the grid holder.

Synchrotron small-angle and wide-angle X-ray scattering (SAXS/WAXS)

Samples were prepared within wax-sealed quartz glass capillaries of 0.01 mm wall thickness and 1.5 mm outer diameter (Hilgenberg GmbH, Germany). SAXS and WAXS experiments were performed on the SAXS/WAXS beamline operated at 11 KeV at the Australian Synchrotron (Melbourne, Australia). The capillaries were introduced into a capillary holder accommodating 20 capillaries and the temperature was controlled at 25°C and at 37°C. The SAXS/WAXS patterns were recorded for a sample-detector distance of 1.6 m with an exposure time of 1 s, providing a q range of 0.01–1.5 $Å^{-1}$. Scattering patterns were recorded using 1 M Pilatus detector for SAXS and a 200 k Pilatus detector for WAXS. Each pattern resulted from radial integration and subtraction of solvent scattering using the in-house Scatterbrain (Synchrotron). The SaSView (SaSView application) application and Primus suite (Konarev et al., 2003) were used to perform the Guinier and form factor analysis. The hexagonal parameter (a) was calculated from the position q) of the first diffraction peak using Eq. 1 (Alexandridis et al., 1998).

$$Q = 4\pi/(a\sqrt{3}) \quad (1)$$

Rheology

Rheology was undertaken on a calibrated rheometer (Anton Paar MCR 301, Anton Paar Pty. Ltd. Austria) fitted with a 15 mm cone plate fixture with a cone angle of 1° (CP15-1, Anton Paar Pty. Ltd. Austria). Shear strain tests were collected between 0.05% and 100% with a constant angular frequency of 3 $rad{\cdot}s^{-1}$. All measurements were carried out in triplicate with the mean and standard deviation shown, calculated and plotted in GraphPad Prism.

Results

Rational design of bi-functional peptide sequences

To design a simple chemical sequence that minimises the cost of synthesis, we chose a combination of natural aromatic and cationic residues to target the microbial lipid membrane, through respectively: i) hydrophobic insertion within the lipid bilayer, ii) electrostatic interactions with membrane phospholipid head groups and other microbial anionic compounds, such as lipopolysaccharides or teichoic acid respectively found in Gram-negative and Gram-positive bacteria cell wall. The high occurrence of two repeats of tryptophan (W, aromatic) and arginine (R, cationic) residues in natural AMPs led us to consider double repeats of each of these amino-acids (Cardoso et al., 2021). A typical example is the potent natural antimicrobial peptide indolicidin, isolated from bovine neutrophils and of sequence ILPWKWPWWPWRR-NH_2, which contains seven residues as tryptophan or arginine over a total of thirteen amino-acids (Selsted et al., 1992; Subbalakshmi and Sitaram, 1998; Batista Araujo et al., 2022). The antimicrobial activity of the tryptophan-arginine motif in natural AMPs is generally rationalised by the arginine guanidinium group that can either interact with negatively charged microbial membranes *via* electrostatic interactions or participate in cation–π interactions with the indole group of tryptophan. This duality is believed to favour AMP penetration into the microbial lipid bilayer (Chan et al., 2006; Saravanan et al., 2014). In our designer sequences, we hence included W and R repeats (Figure 1).

Capping the charged peptide termini by neutral and aromatic groups was included in our sequences to optimize the polarity and amphiphilic properties of the peptide, as critical physicochemical features for self-assembly and antimicrobial propensity. In fact, these modifications enhance the segregation of aromatic groups (Fmoc, W) from charged-aliphatic groups (R, amide) in the peptide primary sequence. Common chemical modifications of peptide termini were chosen, respectively amidation found in natural sequences, e.g., indolicidin, and the synthetic fluorenylmethoxycarbonyl (Fmoc) group used as a common conjugation step in peptide solid phase synthesis. Amidation was further reported to limit enzymatic proteolysis and enhance stability (Sforça et al., 2004; Mura et al., 2016). The insertion of the highly aromatic Fmoc at the N-terminal was expected to also favour peptide self-assembly through π-stacking, as previously

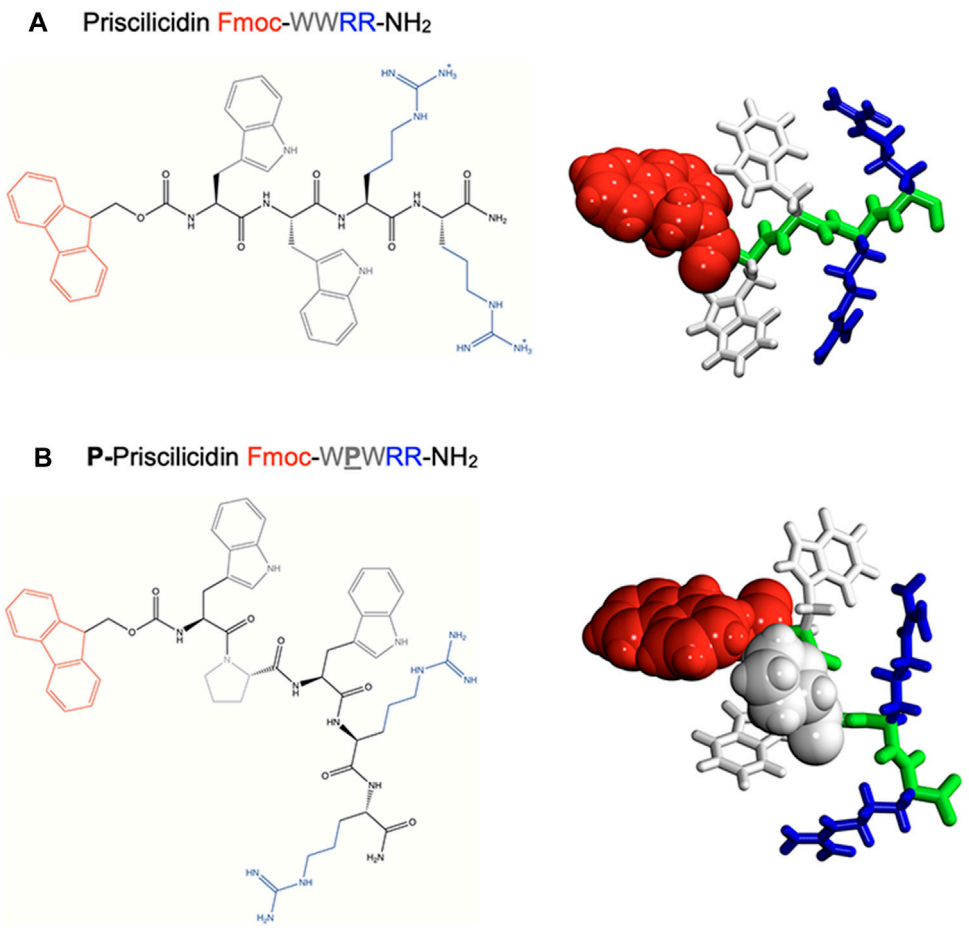


FIGURE 1
Molecular structure of the rationally designed peptides **(A)** Priscilicidin and **(B)** P-Priscilicidin. Left panel: developed amino-acid sequences. Right panels: *ab-initio* monomers for molecular dynamics simulations.

reported for single to tetrapeptide Fmoc-containing sequences (Smith et al., 2008; Orbach et al., 2009), including antimicrobial sequences based on the Fmoc-FF motif or bearing unnatural amino-acids (McCloskey et al., 2017; Schnaider et al., 2017; Misra et al., 2021; Prakash et al., 2022).

In accordance with reported AMP motifs, the resulting designer tetrapeptide Fmoc-WWRR-NH_2 (Figure 1A) exhibits a net charge of +2 for a wide range of pH, a rich content in aromatic and cationic residues as well as a highly polar and amphiphilic sequence. To test the influence of backbone conformation in our approach, we designed a second peptide, P-Priscilicidin (Figure 1B) that includes a proline turn to disrupt backbone linearity and potentially peptide self-assembly. The amino-acid sequence of P-Priscilicidin corresponds to the C-terminal sequence of indolicidin, a natural potent antimicrobial peptide biosynthesised by bovine neutrophils (Selsted et al., 1992; Subbalakshmi and Sitaram, 1998; Batista Araujo et al., 2022).

Predicted *versus* experimental antimicrobial activity

The designer Fmoc-peptides were submitted to online antimicrobial prediction algorithms embedded within the CAMP database of antimicrobial peptides. A phenylalanine was used *in lieu* of Fmoc as these tools only consider natural amino-acids (Waghu et al., 2016). All prediction algorithms returned a good probability of antimicrobial activity for both peptides when compared to the indolicidin control; except for the RF algorithm that returned a less probable activity (Table 1). Given the approximation in sequences and the high dependence on the algorithm data source, this difference cannot be easily explained.

The antimicrobial activities of the Priscilicidin, P-Priscilicidin were experimentally tested on bacterial and fungal strains using Minimum Inhibitory Concentration

TABLE 1 Antimicrobial activity predictions from different algorithms in the CAMP database.

Peptide sequence in database	SVM	RF	ANN	DA
Indolicidin-like ILPWKWPWWPWRR (free N, C-termini)	0.999	0.991	AMP	0.997
Priscilicidin (Pris) -like (F)-WWRR (free N, C-termini)	1.000	0.568	AMP	0.997
P-Priscilicidin (P-Pris) -like (F)-WPWRR (free N, C-termini)	1.000	0.572	AMP	0.972

Green data indicate prediction for antimicrobial activity. Red data indicate prediction for non-antimicrobial activity.

TABLE 2 Experimental antimicrobial activities of indolicidin (control), Priscilicidin (Fmoc-WWRR-NH2) and P-Priscilicidin (Fmoc-WPWRR-NH2) from minimum inhibitory concentration assays (MIC) and verified by fluorescence-assisted cell sorting assays (FACS) for the most critical strains (results given for >90% dead cells).

		Gram-negative bacteria		Gram-positive bacteria				Fungi	
Peptide sequence	Assay	E. *coli*	*P. aeruginosa*	*E. faecalis*	*E. faecium*	*S. aureus/ Methicillin resistant*	*S. pneumoniae*	*C. albicans*	*C. auris* Fluconazole resistant
Indolicidin (control) ILPWKWPWWPWRR-NH_2	MIC FACS	16 μM 10 μM	33 μM	33 μM	33 μM	16/ 33 μM >42 μM I	16 μM	4 μM	16 μM 21 μM
Indolicidin C-terminus WPWRR-NH_2	MIC	313 μM	313 μM	*N/A*	*N/A*	*N/A*	*N/A*	*78 μM*	*313 μM*
Di-Tryptophan (control) WW	MIC	*N/A*	*N/A*	*N/A*	*N/A*	*N/A*	*N/A*	*N/A*	*N/A*
Priscilicidin (Pris) Fmoc-WWRR-NH_2	MIC FACS	68 μM 54 μM	68 μM	68 μM	**34 μM**	**17/34 μM** **27 I (R)**	**17 μM**	**8 μM**	**17 μM 24 μM**
P-Priscilicidin (P-Pris) Fmoc-WPWRR-NH_2	MIC FACS	122 μM 196 μM	61 μM	61 μM	61 μM	**31**/61 μM 196 μM R)	**31 μM**	**15 μM**	**31 μM** 54 μM

Bold values indicate potent antimicrobial activity when compared to the indolicidin control. Italic data indicate low antimicrobial activity when compared to indolicidin control. N/A stands for non-applicable and corresponds to values >1,000 μM.

(MIC) assays and verified by Fluorescence Assisted Cell Sorting (FACS) assays for the most critical strains, including the resistant ones (Table 2; Supplementary Table S1). Indolicidin was used as a control. The FACS results are here given as the minimum concentration showing over 90% dead microbes, while the full results are provided in Supplementary Table S1; Supplementary Figures S2–S16.

Priscilicidin exhibited antimicrobial activity in the low micromolar range (under 50 μM) against Gram-positive bacteria (*E. faecium*, *S. aureus*, methicillin-resistant-*S. aureus*, *S. pneumoniae*) and fungal strains (*C. albicans* and fluconazole-resistant *C. auris*), with similar inhibitory concentrations to the indolicidin control. However, the Priscilicidin peptide was found less active against representative Gram-negative bacteria (*E. coli*, *P. aeruginosa*) with MICs and FACS results in the high micromolar range. Similar values were obtained for P-Priscilicidin but for *E. faecium* and resistant strains.

For one representative strain of each microbial type, activity assays were complemented with direct observations of the peptide impact on microbial cells using scanning electron microscopy. A range of peptide concentrations was tested, including the inhibitory concentration found by MIC and FACS assays for each strain (Figure 2; Supplementary Table S1; Supplementary Figures S17–S25). For peptide concentrations above the inhibitory concentrations obtained by MIC and FACS assays, electron micrographs revealed the cells of E. *coli* (Gram-negative bacteria), S. *aureus* (Gram-positive bacteria) and fluconazole-resistant C. *auris* (fungi) to exhibit i) higher propensity to agglomerate and ii) damaged or perforated cell membranes, as evidenced by the numerous observed defects at the cell surfaces compared to control samples. These observations hence reveal the peptides to impact the structure of the microbial cell membranes.

Altogether, activity assays (MIC, FACS) and electron microscopy of treated microbes reveal that the rationally designed peptides Priscilicidin and P-Priscilicidin display a similar antimicrobial activity to the potent indolicidin peptide for representative Gram-positive bacteria and fungi, besides

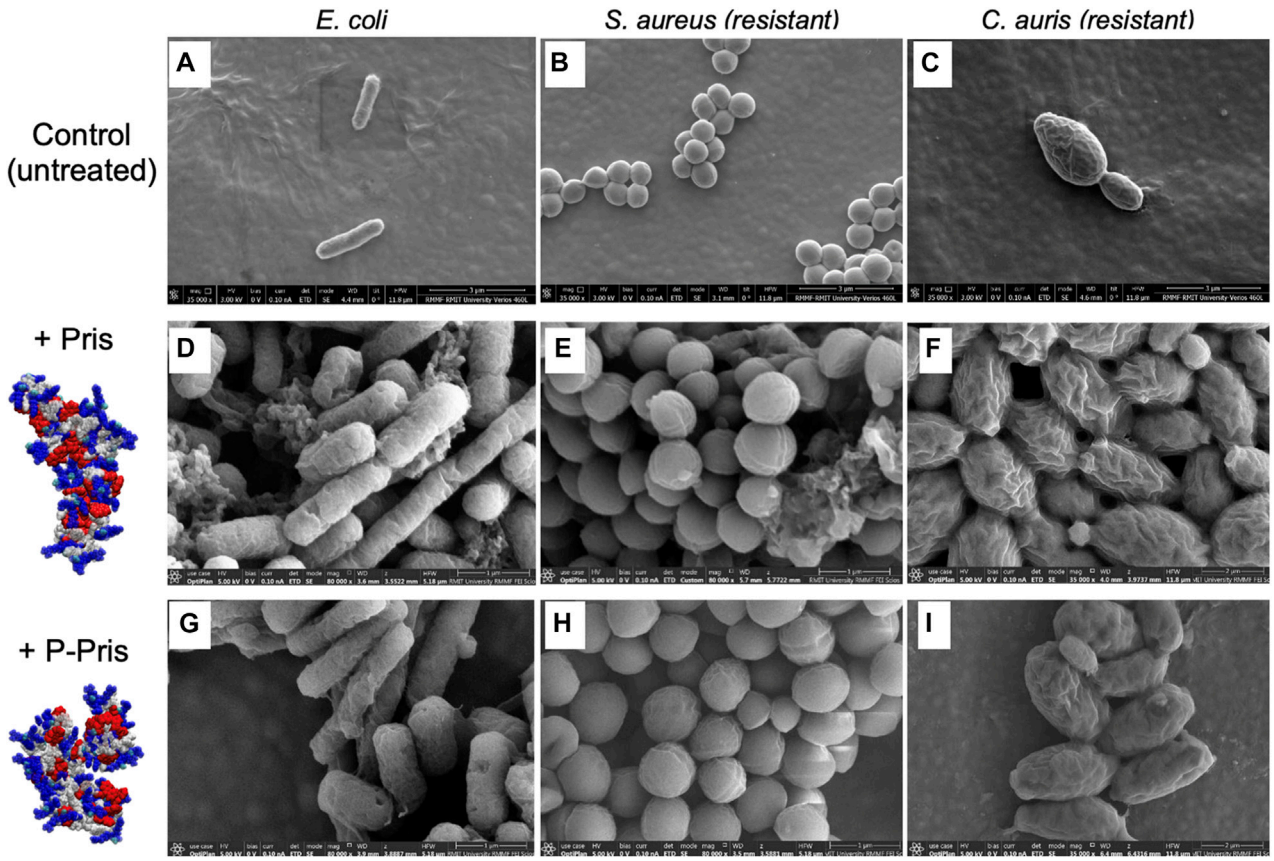


FIGURE 2
Representative scanning electron micrographs (SEM) of untreated (control, **A–C**) and treated bacterial/fungal cells with Priscilicidin **(D–F)** and P-Priscilicidin **(G–I)**. Priscilicidin was added at 2.4 times MIC **(D–F)** and the peptide P-Priscilicidin at 1.2 times MIC **(G–I)** (other concentrations are shown in Supplementary Figures S17–S25).

significantly shorter sequences. Interestingly, the addition of the Fmoc-moiety at the C-terminus significantly enhanced antimicrobial activity, as shown by the lower activity of the indolicidin C-terminus sequence when compared to P-Priscilicidin (Table 2). The linearity of the Priscilicidin backbone further provides increased activity (Table 2; Figure 2). To summarise, the antimicrobial activity of the short sequences can be ranked as: WPWRR-NH_2 (indolicidin C-terminus) < Fmoc-WPWRR-NH_2 (P-Pris) < Fmoc-WWRR-NH_2 (Pris).

Molecular dynamics support sequence-controlled peptide self-assembly

Molecular dynamics simulations were performed on the designer peptides to verify the self-assembly principles hypothesized in our rational sequence design (Figures 3, 4).

Molecular dynamics simulations up to 397 ns predicted the self-assembly of Priscilicidin into extended chains, stabilised by continuous intermolecular pi-stacking of the aromatic and hydrophobic Fmoc groups in the central core of the structure (Figures 3A, 4A). The Pris extended oligomers displayed a Tryptophan and Arginine coat protecting the Fmoc hydrophobic core structure. Further simulation to 800 ns further stabilised the elongated Fmoc stacks and displayed limited lateral growth of the oligomers, supporting elongation into nanofibrils.

For P-Priscilicidin, molecular dynamics predicted the proline turn to disrupt the formation of continuous Fmoc stacks, leading to partial clumping of oligomers with discontinuous intermolecular Fmoc pi-stacking (Figures 3B, 4B). The resulting oligomeric structure displayed Fmoc groups that are partially exposed to the solvent and not exclusively located within a hydrophobic core as for Priscilicidin. These simulations support the formation of

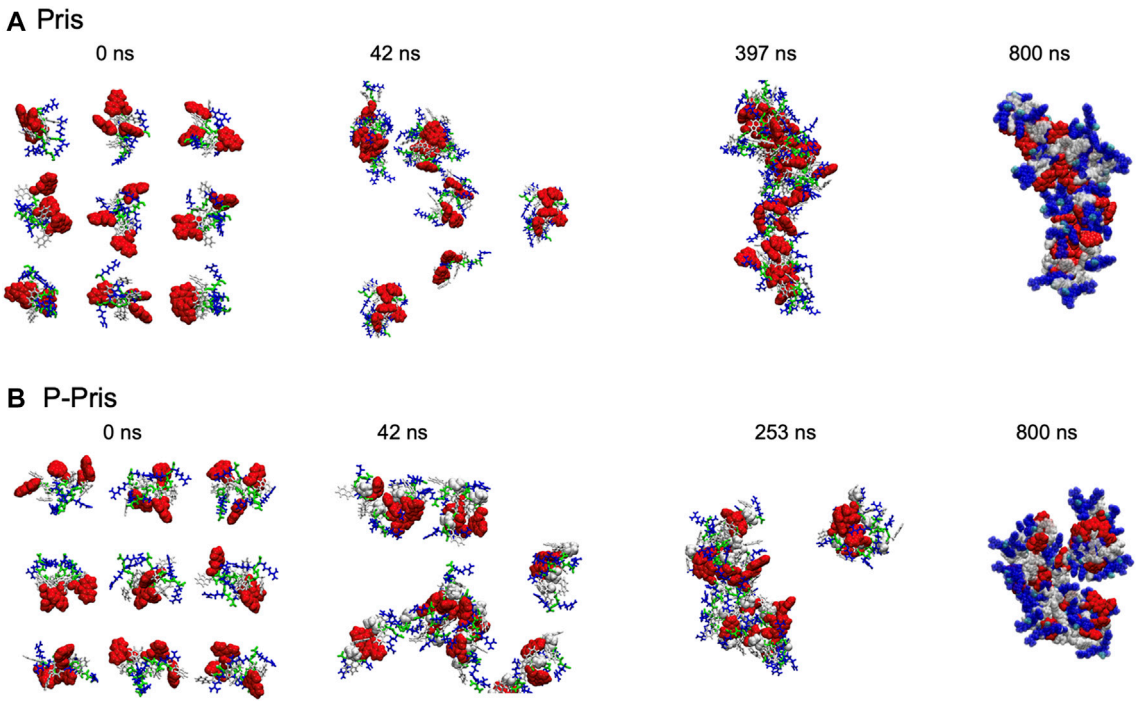


FIGURE 3
Priscilicidin **(A)** and P-Priscilicidin **(B)** molecular dynamics simulations.

P-Pris globular oligomeric species with unfavored elongation into nanofibrils or nanostructures.

Molecular spectroscopy insights into arginine side-chain solvent exposure

The peptide conformation in solution was experimentally characterized by attenuated total reflectance Fourier-transform infrared spectroscopy (ATR-FTIR), as a function of peptide acetate concentration in water and time after sample mixing at room temperature (Table 3; Supplementary Figure S26). For ATR-FTIR, analysis was focused on the amide I and Arginine range of vibrations (Venyaminov and Kalnin, 1990; Surewicz et al., 1993). The main difference between IR spectra was observed on the arginine side-chain vibrations, being recorded as either i) two vibrations with a smaller split between wavenumber values (around 1,680 + 1,630 cm^{-1}), similarly to reported vibrations for single amino-acid arginine side-chain in solution (around 1,670 + 1,630 cm^{-1}); which were assigned to solvent-exposed arginine side-chain in peptide monomer or globular oligomer, as indicated by molecular dynamics; or ii) two vibrations with a larger split between wavenumber values, similarly to arginine side-chain buried within protein hydrophobic pockets; which were interpreted as arginine side-chain buried within the core of peptide Fmoc-stacked assemblies, as indicated by molecular dynamics (Table 3; Supplementary Figure S26) (Venyaminov and Kalnin, 1990; Surewicz et al., 1993).

For Priscilicidin, the IR data support the formation of peptide self-assemblies with Arginine side-chains embedded within a hydrophobic core–i.e., Fmoc-stacks according to molecular dynamics–(MD)—with concentration and time increase. This is consistent with a cooperative intrinsic self-assembly process based on Fmoc-stacking as indicated by molecular dynamics. However, IR data indicate that P-Priscilicidin data does not undergo such a process but remains in a state with solvent-exposed Arginine sidechains, consistently with molecular dynamics.

Experimental evidence of molecular self-assembly into oligomers, nanoribbons and nanofibrils

Transmission electron microscopy imaging of the peptide samples in water was performed for [1–10] % wt peptide acetate from a few hours to 1 month of incubation at 4°C–5°C, using the negative staining technique (TEM) and cryogenic sample

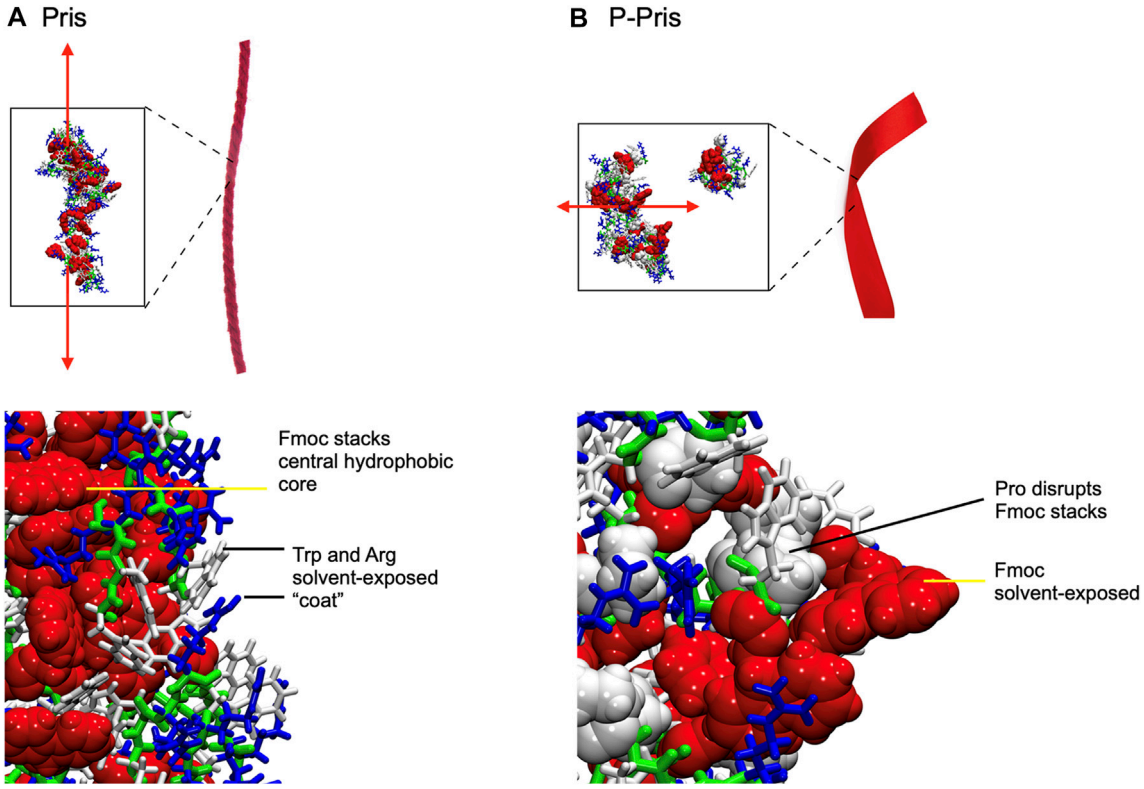


FIGURE 4
Final Molecular Dynamics simulation snapshots of Priscilicidin **(A)** and P-Priscilicidin **(B)**, with conceptual cartoon representations of extended fibrils (red ribbons) drawn for illustration only. Fmoc groups form partially ordered ring stacks in Priscilicidin, sequestered from solvent by Trp and Arg **(A)**, which in contrast are disordered and solvent-exposed in P-Priscilicidin **(B)**.

preparation (cryoTEM, cryoSEM) (Figures 5, 6, Supplementary Figure S27).

For short incubation times of a few hours, three different Priscilicidin oligomeric structures were imaged by transmission electron microscopy as a function of peptide concentration (Figure 5; Supplementary Figure S26): i) extended oligomers, as predicted by molecular dynamics (background in Figures 5A, B), ii) nanoribbons and iii) nanofibrils, consistently with bidirectional assembly of the extended oligomers (negative staining in Figures 5C, D, cryo-TEM in Supplementary Figure S27). The critical concentration of self-assembly is below 1% wt, while for the highest concentrations (5%, 10% wt), the nanofibrils were observed to associate into nanofibers and large bundles by tight close contacts (Figures 5C, D, 6A,6B). These observations support the nanosheets to be transient species towards the formation of nanofibrils and nanofibers. We hence propose Priscilicidin self-assembly to proceed from extended oligomers to nanosheets, which fold into nanofibrils within a few hours. These nanofibrils then align into large clusters that can tighten into nanofibers.

Synchrotron small angle X-ray scattering was recorded at room temperature (25°C) and at 37°C for [1–10] % wt Priscilicidin and P-Priscilicidin (as acetate salts) in water, for incubation times of a few days to 1 month, as kept at 5°C in between experiments (Figures 5E,F; Supplementary Figures S28–S29; Table 4).

Consistently with the molecular dynamics, molecular spectroscopy and TEM, SAXS showed Priscilicidin to undergo self-assembly into extended oligomers, nanoribbons, nanofibrils and hexagonally-aligned nanofibrils into nanofibers, with concentration and time increase.

For P-Priscilicidin (Figure 7A; Supplementary Figure S30–S31), the only nanostructures that could be imaged were nanoribbons for the highest concentration tested (10% wt in water) after 1 month incubation, in coexistence with globular oligomers. Consistently, SAXS patterns did not show any form or structure factor, but a correlation peak and a SAXS slope supporting the formation of oligomers and nanoribbons for 10% wt peptide acetate in water after 1 month (Figure 7B).

Sequence-controlled hydrogelation into nanostructured mesophases

Priscilicidin hydrogel characterisation was performed using electron microscopy, polarised light optical

TABLE 3 ATR-FTIR shifting vibrations in the amide I region (1,700–1,600 cm^{-1}), assigned as solvent-exposed arginine side-chain within peptide monomer/small oligomer (blue) or arginine side-chain buried within peptide self-assembly Fmoc-stacked core (orange).

			Single amino-acid arg vibrations (cm^{-1})	Protein arg vibrations (cm^{-1})	
		References	1,672–1,673 + 1,633–1,636	1,688–1,695 + 1,576–1,577	
Peptide sequences	Conc (% wt)	Time after mixing	Solvent-exposed Arg	Buried Arg within hydrophobic pocket	Interpretation for peptide assembly according to MD
Priscilicidin (Pris) Fmoc-WWRR-NH_2	1	0	1,680 + 1,634		monomer/globular oligomer
		3 days	1,680 + 1,630		
		5 days	1,684 + 1,632		
		30 days	1,680 + 1,635		
	5	0	1,680 + 1,629		monomer/globular oligomer
		3 days		1,694 + 1,634	Fmoc-stacked assembly
		5 days		1,695 + 1,634	
		30 days		1,695 + 1,634	
	10	0	1,679 + 1,629		monomer/globular oligomer
		3 days		1,694 + 1,634	Fmoc-stacked assembly
		5 days		1,695 + 1,634	
		30 days		1,695 + 1,634	
P-Priscilicidin (P-Pris) Fmoc-WPWRR-NH_2	1	0	1,670 + 1,629		monomer/globular oligomer
		30 days	1,680 + 1,634		
	5	0	1,679 + 1,629		
		30 days	1,679 + 1,630		
	10	0	1,678 + 1,629		
		30 days	1,679 + 1,630		

microscopy, and oscillatory rheology (Figure 6; Supplementary Figure S32). For incubation times of a few days, Priscilicidin was observed to spontaneously form homogeneous hydrogel, from around 5% w/w of peptide acetate in pure water. The peptide could be easily solubilised in pure water at concentrations of at least 10% w/w (higher concentrations not explored). The sample then developed over time viscoelastic and self-healing gel behaviour when manipulated (Figure 6C). After 1 month of incubation, transmission electron microscopy (TEM, Figure 6A) on dried 10% Priscilicidin samples confirmed the formation of a few microns long, semi-flexible nanofibers resulting from nanofibrils in close contact. The formation of nanofibril bundles is consistent with the hexagonal networks revealed by SAXS, while the nanostructure semi-flexibility supports liquid crystalline properties. The mesophasic state of Priscilicidin hydrogels was further supported by the observation of birefringence and nematic optical textures under polarised light microscopy (Figure 6C). Cryogenic scanning electron microscopy (cryoSEM, Figure 6B) revealed reticulation of the whole hydrogel volume by nanofibrillar structures, hence confirming the hydrogel homogeneity.

The rheological behaviour of Priscilicidin (Figures 6D, 7C) and P-Priscilicidin (Figure 7C) was characterised through measuring the storage (G′) and loss (G″) moduli as a function of peptide concentration and time. The peptides generally had a non-linear behaviour with time, assigned to unfinished self-assembly process from monomers to oligomers to nanoribbons (both peptides), to nanofibrils or mature nanofibers (Priscilicidin) as evidenced above by electron microscopy and SAXS. The Priscilicidin samples rapidly assemble and continue to form a soft gel network from day 0 to day 5. When comparing the rheological data from day 5 to day 30, there is no looking at the significant increase in gel formation after day 5 except for the 1% wt

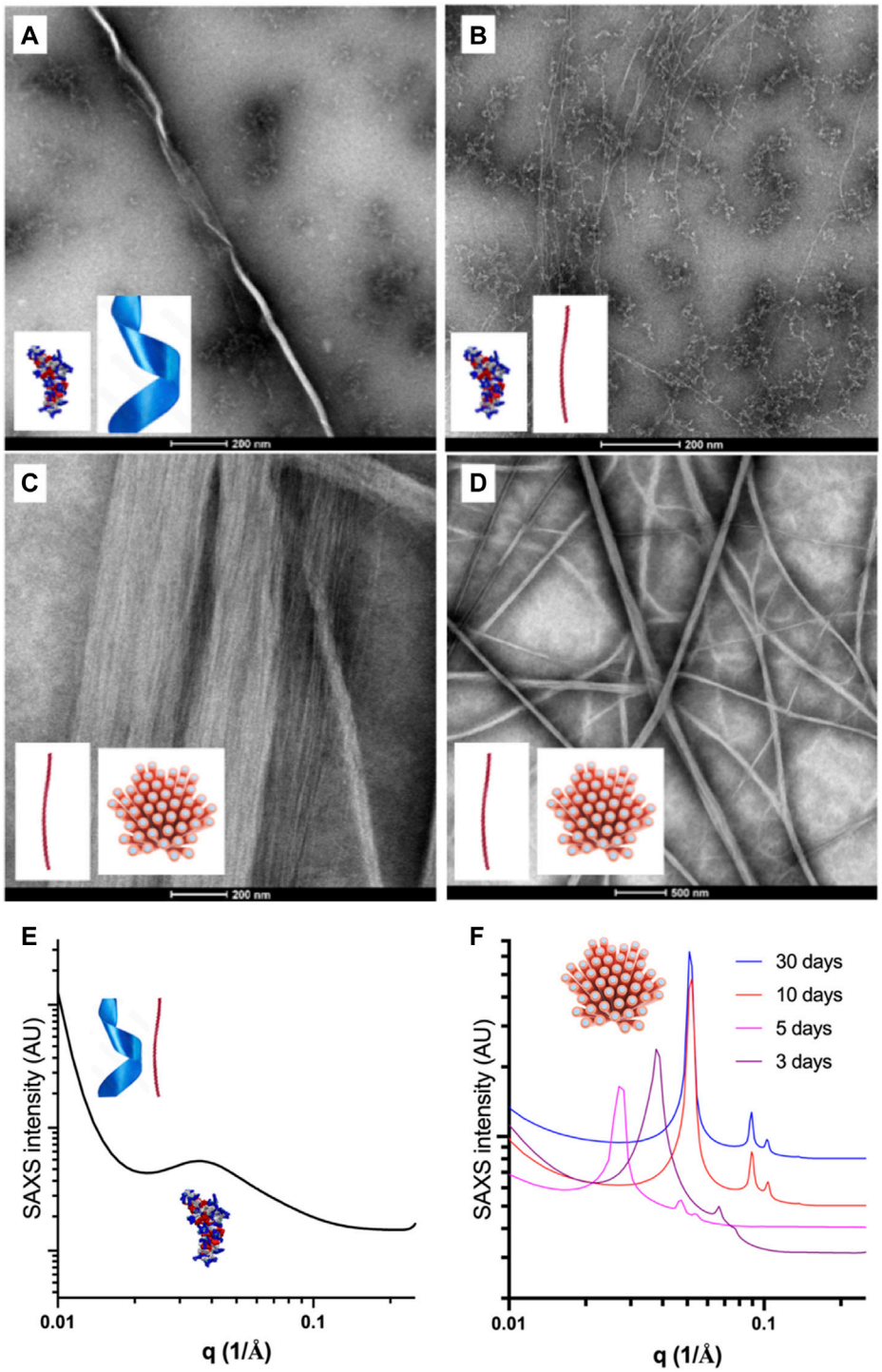


FIGURE 5
Representative transmission electron micrographs and SAXS patterns of the self-assembled species formed in water by Priscilicidin (Fmoc-WWRR-NH_2) over the concentration-time space. **(A)** Nanoribbon and oligomers for 1% wt Pris ac, 1 week. Scale bar 200 nm; **(B)** Nanofibrils and extended oligomers for 5% wt Pris ac < 12 h. Scale bar 200 nm; **(C)** Single and aligned nanofibrils (into nanofibers) for 5% Pris ac, 1 week. Scale bar 200 nm; **(D)** Single and aligned nanofibrils (into nanofibers) for 5% Pris ac, 7 days. Scale bar 500 nm. **(E)** SAXS patterns recorded at 25°C for 1% Pris ac, 30 days interpreted as a coexistence of oligomers, nanoribbons and nanofibrils (Table 4); **(F)** SAXS patterns recorded at 25°C for 10% Pris ac as a function of time interpreted as maturing hexagonal networks of nanofibrils (Table 4).

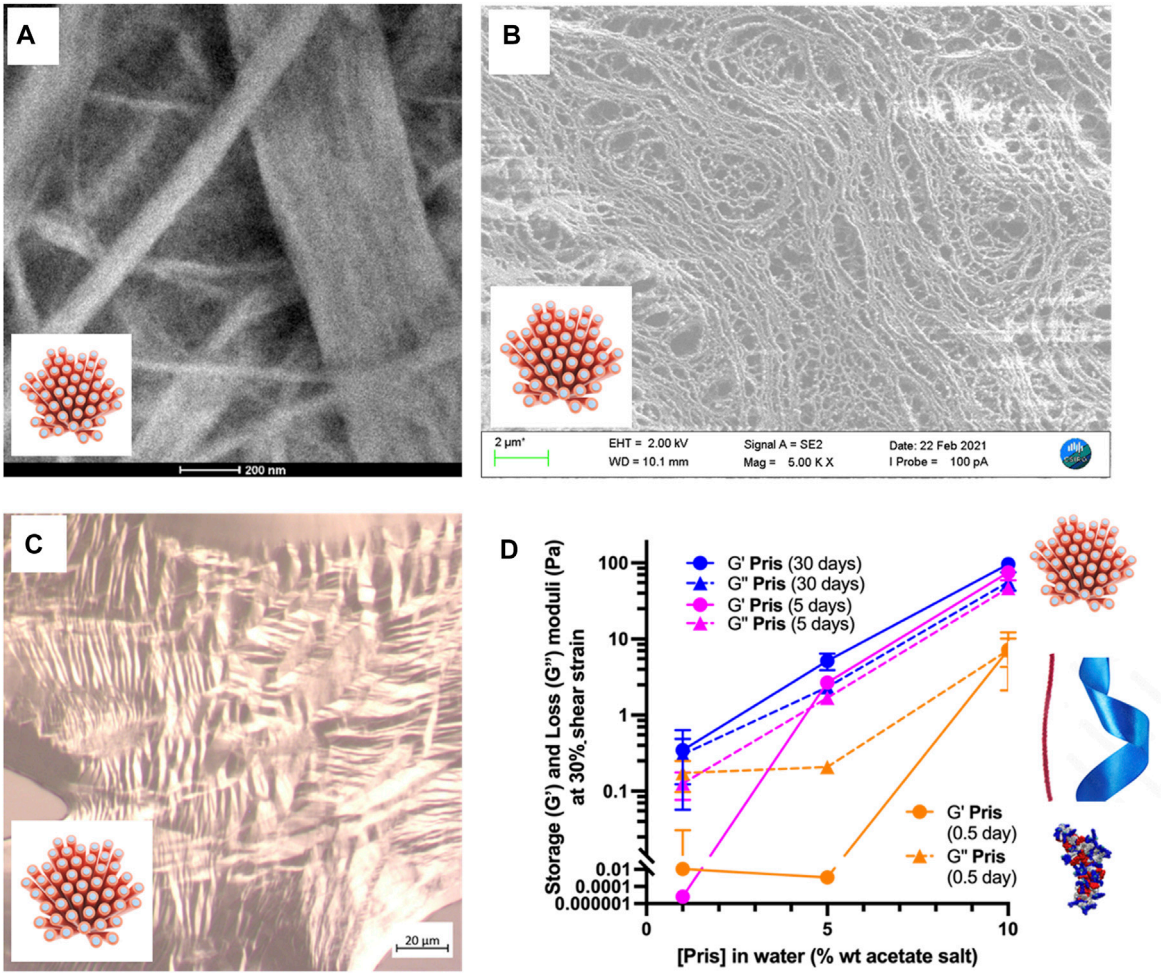


FIGURE 6
Priscilicidin nanostructured samples: mesophasic and viscoelastic properties. **(A)** 10% at t = 5 days. Scale bar 200 nm; **(B)** 5% at t = 5 days. Scale bar 2 µm; **(C)** 10% w/w hydrogel (3 days old), dried on slide showing nematic optical textures. Scale bar 20 µm; **(D)** G′ and G″ values at 30% strain over Priscilicidin concentration and time space.

TABLE 4 Small angle X-ray scattering fits and assignments for Priscilicidin as a function of peptide acetate concentration in water, temperature, and incubation time.

[Pris ac]% wt in water	Incubation time at 5°C	Structure factor	SAXS slope q^{-x} x)	Lattice parameter (a_{hex}) nm	Interpretation on peptide assemblies (Dharmadana et al., 2020)
1	3 days	None	1.57 (25°C)| 1.77 (37°C)	N/A	Coexistence of q^{-1}: rod-like oligomers/nanofibrils and q^{-2}: flat 2D-structures/nanoribbons
	10 days		1.44 (25°C)| 1.51 (37°C)		
	30 days		1.56 (25°C)| 1.69 (37°C)		
5	3 days	Hexagonal network	N/A	15 (25°C)|14 (37°C)	Maturing hexagonal networks of laterally aligned nanofibrils (nanofibers)
	10 days			15 (25°C)|14 (37°C)	
	30 days			15 (25°C)|15 (37°C)	
10	3 days	Hexagonal network	N/A	13 (25°C)|13 (37°C)	Maturing hexagonal networks of laterally aligned nanofibrils (nanofibers)
	10 days			14 (25°C)|13 (37°C)	
	30 days			14 (25°C)|13 (37°C)	

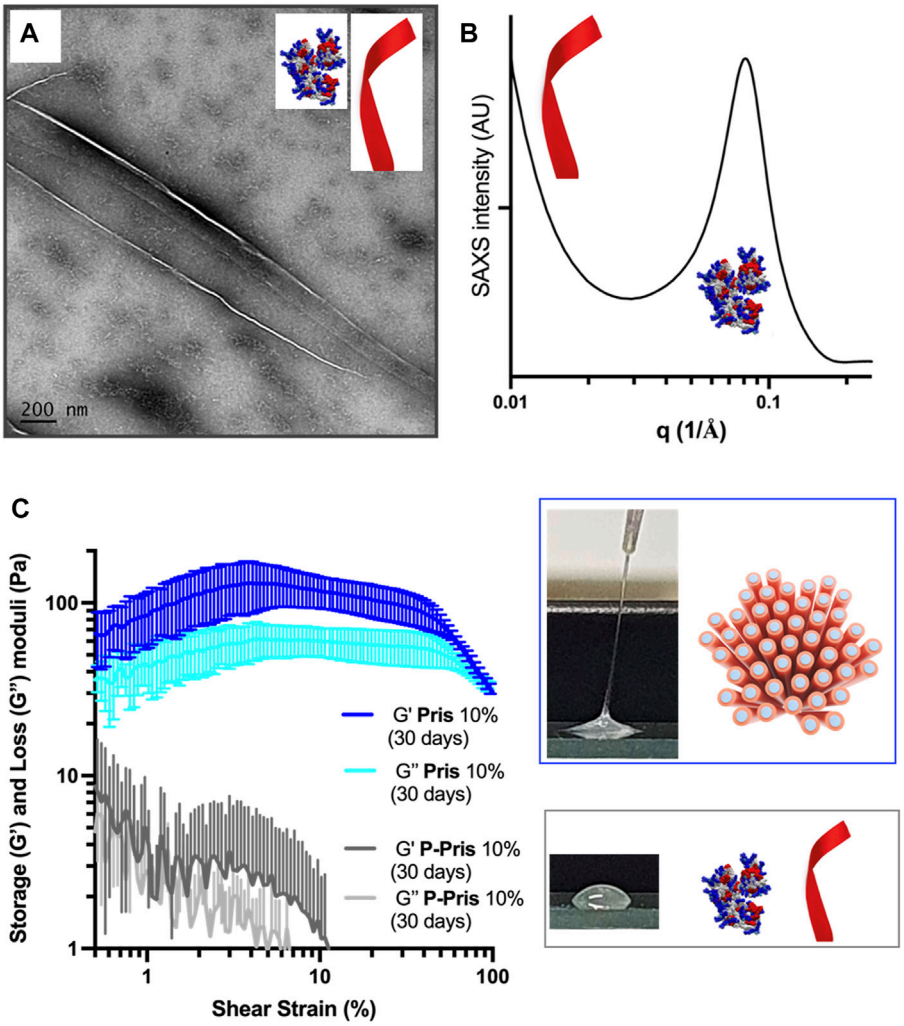


FIGURE 7
Peptide species **(A,B)** and rheological behaviour **(C)** of 10% wt P-Priscilicidin pure water solutions aged for 30 days at 5°C compared to **(C)** the rheological behaviour and macroscopic appearance of 10% wt Priscilicidin hydrogels aged under the same conditions. Image **(A)**: scale bar 200 nm.

Priscilicidin sample (Figure 6D; Supplementary Figure S29). On the contrary, P-Priscilicidin forms very weak and unstable gels under shear strain (Figure 7C; Supplementary Figure S29).

In summary, Priscilicidin forms viscoelastic nanostructured mesophases, while P-Priscilicidin forms colloidal solutions of low viscosity.

Discussion and conclusion

Molecular dynamics simulations predicted Priscilicidin to assemble in water into small oligomers and nanofibrils, through a balance of aromatic stacking, amphiphilicity and electrostatic repulsion. The resulting extended oligomer consists of solvent protected Fmoc at the core, protected by an exposed hydrophilic layer of Arg and Trp. It is noteworthy that a similar supramolecular assembly of ordered, elongated Fmoc stacking was previously observed in simulations of a prototypical dipeptide, Fmoc-AA (Mu et al., 2012; Guo et al., 2015). 'Worm-like' extended nanostructures have also been observed to form in water for Fmoc-FF and Fmoc-FFD (Li et al., 2018). The appearance of a broadly similar superstructure in Priscilicidin (Fmoc-WWRR-NH_2), with an amino acid sequence distinct from these previously studied peptides, highlights the vital contribution of the Fmoc-Fmoc interaction in peptide self-assembly. On the other hand, we have demonstrated that introduction of a single proline, in the form of P-Priscilicidin, is sufficient to alter the structures of Pris monomers, ultimately translating into formation of a far less ordered, roughly globular oligomeric complex. This

result highlights the importance of structurally disruptive residues on reducing the fibrillogenic potential of peptides which otherwise strongly favour elongation.

Fmoc-FF–a reference ultrashort self-assembling Fmoc-peptide–is a poorly water-soluble substance. Complete solubilisation for homogeneous lyotropic self-assembly of Fmoc-FF in water can only be achieved by i) dissolution in dimethyl sulfoxide (DMSO) followed by a dilution step in water and change of pH, or ii) by heating the peptide initial aqueous solution up to 90°C for peptide solubilisation before a cooling step (Smith et al., 2008; Tang et al., 2009). Depending on conditions, Fmoc-FF displays polymorphism between a hydrogel state and precipitates (Tang et al., 2009). Comparatively, the Fmoc peptides reported here display a largely improved water solubility and sample physicochemical stability. From a pharmaceutical sciences point of view, these new peptides offer the advantage of a simple hydrogel preparation protocol, under standard soft mixing conditions, with no observed polymorphism nor precipitation, for at least 1 month after preparation.

We here provide a proof of concept for bi-functional molecular design on Fmoc-peptides containing 4 and 5 amino-acids. Using minimalistic molecular engineering principles, we designed peptides that form antimicrobial hydrogels of different viscoelastic properties. Given the broad applications of peptide nanostructured hydrogels as, for instance, pharmaceutical or cosmetic biomaterials, our results augur well for fast, adaptive, and cost-efficient antimicrobial peptide design with programmable physicochemical properties.

Data availability statement

The original contributions presented in the study are included in the article/Supplementary material, further inquiries can be directed to the corresponding author.

Author contributions

PC and CV conceptualised the project and designed the peptides. All authors performed experiments, analysed data, interpreted data and contributed to collegial discussions. PC, AH, and CV wrote the paper. AAB, DK, and JW edited the article.

Funding

This project was funded by a RMIT Biomedical and Health Innovation Capability Fund to PC, CC, and CV. Synchrotron SAXS beam time was funded by ANSTO (Australian government) under award of merit grants to PC, CC, JS, and CV. PC is the recipient of a PhD LATAM scholarship from the Australian Technology Network (ATN). SAD is the recipient of a MSc CSIRO-RMIT scholarship. BM is the recipient of a PhD Research Training Program (RTP) scholarship from the Australian government This work benefited from the use of the SasView application, originally developed under NSF award DMR-0520547. SasView contains code developed with funding from the European Union's Horizon 2020 research and innovation programme under the SINE2020 project, grant agreement No 654000. Computational simulations were made possible by use of facilities provided by the National Computational Infrastructure (NCI), which is funded by the Australian Government; the Pawsey Supercomputing Research Centre, which is funded by the Australian Government and the Government of Western Australia; and the LIEF HPC-GPGPU Facility hosted at the University of Melbourne, which was established with the assistance of LIEF Grant LE170100200.

Acknowledgments

The authors are grateful to the Australian Synchrotron SAXS/WAXS beam line scientists Tim Ryan and Nigel Kirby for their experimental help and fruitful discussions on nanostructure diffraction and scattering. The authors acknowledge the facilities, and the scientific and technical assistance of the RMIT University's Microscopy and Microanalysis Facility, a linked laboratory of Microscopy Australia. The authors acknowledge the use of the Cryo FE-SEM within the Materials Characterisation and Modelling Program CSIRO.

Conflict of interest

The authors declare that the research was conducted in the absence of any commercial or financial relationships that could be construed as a potential conflict of interest.

Publisher's note

All claims expressed in this article are solely those of the authors and do not necessarily represent those of their affiliated organizations, or those of the publisher, the editors and the reviewers. Any product that may be evaluated in this article, or claim that may be made by its manufacturer, is not guaranteed or endorsed by the publisher.

Supplementary material

The Supplementary Material for this article can be found online at: https://www.frontiersin.org/articles/10.3389/fchem.2022.1009468/full#supplementary-material

References

Alexandridis, P., Olsson, U., and Lindman, B. (1998). A record nine different phases (four cubic, two hexagonal, and one lamellar lyotropic liquid crystalline and two micellar solutions) in a ternary isothermal system of an amphiphilic block copolymer and selective solvents (water and oil). *Langmuir* 14 (10), 2627–2638. doi:10.1021/la971117c

Batista Araujo, J., Sastre de Souza, G., and Lorenzon, E. N. (2022). Indolicidin revisited: Biological activity, potential applications and perspectives of an antimicrobial peptide not yet fully explored. *World J. Microbiol. Biotechnol.* 38 (3), 39. doi:10.1007/s11274-022-03227-2

Berendsen, H. J. C., Postma, J. P. M., van Gunsteren, W. F., DiNola, A., and Haak, J. R. (1984). Molecular dynamics with coupling to an external bath. *J. Chem. Phys.* 81 (8), 3684–3690. doi:10.1063/1.448118

Berney, M., Hammes, F., Bosshard, F., Weilenmann, H. U., and Egli, T. (2007). Assessment and interpretation of bacterial viability by using the LIVE/DEAD BacLight Kit in combination with flow cytometry. *Appl. Environ. Microbiol.* 73 (10), 3283–3290. doi:10.1128/aem.02750-06

Bussi, G., Donadio, D., and Parrinello, M. (2007). Canonical sampling through velocity rescaling. *J. Chem. Phys.* 126 (1), 014101. doi:10.1063/1.2408420

Cardoso, P., Glossop, H., Meikle, T. G., Aburto-Medina, A., Conn, C. E., Sarojini, V., et al. (2021). Molecular engineering of antimicrobial peptides: Microbial targets, peptide motifs and translation opportunities. *Biophys. Rev.* 13 (1), 35–69. doi:10.1007/s12551-021-00784-y

Chan, D. I., Prenner, E. J., and Vogel, H. J. (2006). Tryptophan- and arginine-rich antimicrobial peptides: Structures and mechanisms of action. *Biochim. Biophys. Acta* 1758 (9), 1184–1202. doi:10.1016/j.bbamem.2006.04.006

Das, A. K., and Gavel, P. K. (2020). Low molecular weight self-assembling peptide-based materials for cell culture, antimicrobial, anti-inflammatory, wound healing, anticancer, drug delivery, bioimaging and 3D bioprinting applications. *Soft Matter* 16 (44), 10065–10095. doi:10.1039/d0sm01136c

Dharmadana, D., Adamcik, J., Ryan, T. M., Appiah Danso, S., Chong, C. J. H., Conn, C. E., et al. (2020). Human neuropeptide substance P self-assembles into semi-flexible nanotubes that can be manipulated for nanotechnology. *Nanoscale* 12 (44), 22680–22687. doi:10.1039/d0nr05622g

Dharmadana, D., Reynolds, N. P., Conn, C. E., and Valéry, C. (2019). pH-dependent self-assembly of human neuropeptide hormone GnRH into functional amyloid nanofibrils and hexagonal phases. *ACS Appl. Bio Mater.* 2 (8), 3601–3606. doi:10.1021/acsabm.9b00468

Essmann, U., Perera, L., Berkowitz, M. L., Darden, T., Lee, H., and Pedersen, L. G. (1995). A smooth particle mesh Ewald method. *J. Chem. Phys.* 103 (19), 8577–8593. doi:10.1063/1.470117

Fernandez-Lopez, S., Kim, H-S., Choi, E. C., Delgado, M., Granja, J. R., Khasanov, A., et al. (2001). Antibacterial agents based on the cyclic d, l-α-peptide architecture. *Nature* 412 (6845), 452–455. doi:10.1038/35086601

Firipis, K., Nisbet, D. R., Franks, S. J., Kapsa, R. M., Pirogova, E., Williams, R. J., et al. (2021). Enhancing peptide biomaterials for biofabrication. *Polymers* 13 (16), 2590. doi:10.3390/polym13162590

Fleming, S., Debnath, S., Frederix, P. W., Tuttle, T., and Ulijn, R. V. (2013). Aromatic peptide amphiphiles: Significance of the Fmoc moiety. *Chem. Commun.* 49 (90), 10587–10589. doi:10.1039/c3cc45822a

Glossop, H. D., De Zoysa, G. H., Hemar, Y., Cardoso, P., Wang, K., Lu, J., et al. (2019). Battacin-Inspired ultrashort peptides: Nanostructure analysis and antimicrobial activity. *Biomacromolecules* 20 (7), 2515–2529. doi:10.1021/acs.biomac.9b00291

Guex, N., and Peitsch, M. C. (1997). SWISS-MODEL and the Swiss-PdbViewer: An environment for comparative protein modeling. *Electrophoresis* 18 (15), 2714–2723. doi:10.1002/elps.1150181505

Guo, K. Z., HengSun, J., and Yuan, S. (2015). Chengbu. Molecular dynamics simulation on self-assembly of fmoc-FF dipeptide. *Chem. J. Chin. Univ. -Chinese Edition-* 36 (11), 2171.

Hartmann, M., Berditsch, M., Hawecker, J., Ardakani, M. F., Gerthsen, D., and Ulrich, A. S. (2010). Damage of the bacterial cell envelope by antimicrobial peptides gramicidin S and PGLa as revealed by transmission and scanning electron microscopy. *Antimicrob. Agents Chemother.* 54 (8), 3132–3142. doi:10.1128/aac.00124-10

Hess, B., Bekker, H., Berendsen, H. J. C., and Fraaije, J. G. E. M. (1997). Lincs: A linear constraint solver for molecular simulations. *J. Comput. Chem.* 18 (12), 1463–1472. doi:10.1002/(sici)1096-987x(199709)18:12<1463:aid-jcc4>3.0.co;2-h

Humphrey, W., Dalke, A., and Schulten, K. (1996). Vmd: Visual molecular dynamics. *J. Mol. Graph* 14 (133-8), 33–38. doi:10.1016/0263-7855(96)00018-5

Jorgensen, W. L., Chandrasekhar, J., Madura, J. D., Impey, R. W., and Klein, M. L. (1983). Comparison of simple potential functions for simulating liquid water. *J. Chem. Phys.* 79 (2), 926–935. doi:10.1063/1.445869

Jorgensen, W. L., Maxwell, D. S., and Tirado-Rives, J. (1996). Development and testing of the OPLS all-atom force Field on conformational energetics and properties of organic liquids. *J. Am. Chem. Soc.* 118 (45), 11225–11236. doi:10.1021/ja9621760

Kaminski, G. A., Friesner, R. A., Tirado-Rives, J., and Jorgensen, W. L. (2001). Evaluation and reparametrization of the OPLS-AA force Field for proteins via comparison with accurate quantum chemical calculations on peptides. *J. Phys. Chem. B* 105 (28), 6474–6487. doi:10.1021/jp003919d

Konarev, P. V., Volkov, V. V., Sokolova, A. V., Koch, M. H. J., and Svergun, D. I. (2003). Primus: A windows PC-based system for small-angle scattering data analysis. *J. Appl. Crystallogr.* 36 (5), 1277–1282. doi:10.1107/s0021889803012779

Li, J., Koh, J-J., Liu, S., Lakshminarayanan, R., Verma, C. S., and Beuerman, R. W. (2017). Membrane active antimicrobial peptides: Translating mechanistic insights to design. *Front. Neurosci.* 11 (73), 73. doi:10.3389/fnins.2017.00073

Li, Q., Zhang, J., Wang, Y., Qi, W., Su, R., and He, Z. (2018). Peptide-templated synthesis of TiO2 nanofibers with tunable photocatalytic activity. *Chem. – A Eur. J.* 24 (68), 18123–18129. doi:10.1002/chem.201804514

McCloskey, A. P., Draper, E. R., Gilmore, B. F., and Laverty, G. (2017). Ultrashort self-assembling Fmoc-peptide gelators for anti-infective biomaterial applications. *J. Peptide Sci.* 23 (2), 131–140. doi:10.1002/psc.2951

Misra, S., Mukherjee, S., Ghosh, A., Singh, P., Mondal, S., Ray, D., et al. (2021). Single amino-acid based self-assembled biomaterials with potent antimicrobial activity. *Chemistry–A Eur. J.* 27 (67), 16744–16753. doi:10.1002/chem.202103071

Mu, X., Eckes, K. M., Nguyen, M. M., Suggs, L. J., and Ren, P. (2012). Experimental and computational studies reveal an alternative supramolecular structure for fmoc-dipeptide self-assembly. *Biomacromolecules* 13 (11), 3562–3571. doi:10.1021/bm301007r

Mura, M., Wang, J., Zhou, Y., Pinna, M., Zvelindovsky, A. V., Dennison, S. R., et al. (2016). The effect of amidation on the behaviour of antimicrobial peptides. *Eur. Biophys. J.* 45 (3), 195–207. doi:10.1007/s00249-015-1094-x

Orbach, R., Adler-Abramovich, L., Zigerson, S., Mironi-Harpaz, I., Seliktar, D., and Gazit, E. (2009). Self-assembled fmoc-peptides as a platform for the formation of nanostructures and hydrogels. *Biomacromolecules* 10 (9), 2646–2651. doi:10.1021/bm900584m

Parrinello, M., and Rahman, A. (1981). Polymorphic transitions in single crystals: A new molecular dynamics method. *J. Appl. Phys.* 52 (12), 7182–7190. doi:10.1063/1.328693

Prakash, V., Christian, Y., Redkar, A. S., Roy, A., Anandalakshmi, R., and Ramakrishnan, V. (2022). Antibacterial hydrogels of aromatic tripeptides. *Soft Matter* 18 (34), 6360–6371. doi:10.1039/d2sm00606e

Pronk, S., Páll, S., Schulz, R., Larsson, P., Bjelkmar, P., Apostolov, R., et al. (2013). Gromacs 4.5: A high-throughput and highly parallel open source molecular simulation toolkit. *Bioinformatics* 29 (7), 845–854. doi:10.1093/bioinformatics/btt055

Robertson, J., McGoverin, C., Vanholsbeeck, F., and Swift, S. (2019). Optimisation of the protocol for the LIVE/DEAD(®) BacLight(TM) bacterial viability Kit for rapid determination of bacterial load. *Front. Microbiol.* 10, 801. doi:10.3389/fmicb.2019.00801

Saravanan, R., Li, X., Lim, K., Mohanram, H., Peng, L., Mishra, B., et al. (2014). Design of short membrane selective antimicrobial peptides containing tryptophan and arginine residues for improved activity, salt-resistance, and biocompatibility. *Biotechnol. Bioeng.* 111 (1), 37–49. doi:10.1002/bit.25003

SaSView. (2022). SaSView application. Available at: https://www.sasview.org/.

Schnaider, L., Brahmachari, S., Schmidt, N. W., Mensa, B., Shaham-Niv, S., Bychenko, D., et al. (2017). Self-assembling dipeptide antibacterial nanostructures with membrane disrupting activity. *Nat. Comm.* 8 (1), 1365. doi:10.1038/s41467-017-01447-x

Selsted, M. E., Novotny, M. J., Morris, W. L., Tang, Y. Q., Smith, W., and Cullor, J. S. (1992). Indolicidin, a novel bactericidal tridecapeptide amide from neutrophils. *J. Biol. Chem.* 267 (7), 4292–4295. doi:10.1016/s0021-9258(18)42830-x

Sforça, M. L., Oyama, S., Jr., Canduri, F., Lorenzi, C. C., Pertinhez, T. A., Konno, K., et al. (2004). How C-terminal carboxyamidation alters the biological activity of peptides from the venom of the eumenine solitary wasp. *Biochemistry* 43 (19), 5608–5617. doi:10.1021/bi0360915

Shi, Y., Wareham, D. W., Phee, L. M., and Azevedo, H. S. (2021). "Self-assembled peptide nanostructures for antibacterial applications," in *Peptide-based biomaterials. Soft matter series*. Editor M. O. Guler (Cambridge, UK: The Royal Society of Chemistry), 395.

Smith, A. M., Williams, R. J., Tang, C., Coppo, P., Collins, R. F., Turner, M. L., et al. (2008). Fmoc-diphenylalanine self assembles to a hydrogel via a novel architecture based on π–π interlocked β-sheets. *Adv. Mater.* 20 (1), 37–41. doi:10.1002/adma.200701221

Subbalakshmi, C., and Sitaram, N. (1998). Mechanism of antimicrobial action of indolicidin. *FEMS Microbiol. Lett.* 160 (1), 91–96. doi:10.1111/j.1574-6968.1998.tb12896.x

Surewicz, W. K., Mantsch, H. H., and Chapman, D. (1993). Determination of protein secondary structure by fourier transform infrared spectroscopy: A critical assessment. *Biochemistry* 32 (2), 389–394. doi:10.1021/bi00053a001

Tang, C., Smith, A. M., Collins, R. F., Ulijn, R. V., and Saiani, A. (2009). Fmoc-diphenylalanine self-assembly mechanism induces apparent pKa shifts. *Langmuir* 25 (16), 9447–9453. doi:10.1021/la900653q

Tao, K., Levin, A., Adler-Abramovich, L., and Gazit, E. (2016). Fmoc-modified amino acids and short peptides: Simple bio-inspired building blocks for the fabrication of functional materials. *Chem. Soc. Rev.* 45 (14), 3935–3953. doi:10.1039/c5cs00889a

Tian, X., Sun, F., Zhou, X. R., Luo, S. Z., and Chen, L. (2015). Role of peptide self-assembly in antimicrobial peptides. *J. Pept. Sci.* 21 (7), 530–539. doi:10.1002/psc.2788

Van Der Spoel, D., Lindahl, E., Hess, B., Groenhof, G., Mark, A. E., and Berendsen, H. J. (2005). Gromacs: Fast, flexible, and free. *J. Comput. Chem.* 26 (16), 1701–1718. doi:10.1002/jcc.20291

Venyaminov, S. Y., and Kalnin, N. N. (1990). Quantitative IR spectrophotometry of peptide compounds in water (H_2O) solutions. I. Spectral parameters of amino acid residue absorption bands. *Biopolymers* 30 (13-14), 1243–1257. doi:10.1002/bip.360301309

Waghu, F. H., Barai, R. S., Gurung, P., and Idicula-Thomas, S. (2016). $CAMP_{R3}$: A database on sequences, structures and signatures of antimicrobial peptides: Table 1. *Nucleic Acids Res.* 44 (D1), D1094–D1097. doi:10.1093/nar/gkv1051

WHO (2020). Antimicrobial resistance Geneva2020. Available at: https://www.who.int/news-room/fact-sheets/detail/antimicrobial-resistance.

Wiegand, I., Hilpert, K., and Hancock, R. E. (2008). Agar and broth dilution methods to determine the minimal inhibitory concentration (MIC) of antimicrobial substances. *Nat. Protoc.* 3 (2), 163–175. doi:10.1038/nprot.2007.521

frontiers | Frontiers in Chemistry

TYPE Original Research
PUBLISHED 10 February 2023
DOI 10.3389/fchem.2023.1089714

Check for updates

OPEN ACCESS

EDITED BY
Rachelle J. Bienstock,
RJB Computational Modeling LLC,
United States

REVIEWED BY
Emanuele Carosati,
University of Trieste, Italy
Marcus Fischer,
St. Jude Children's Research Hospital,
United States

*CORRESPONDENCE
Esther Kellenberger,
ekellen@unistra.fr

SPECIALTY SECTION
This article was submitted to Theoretical and Computational Chemistry, a section of the journal Frontiers in Chemistry

RECEIVED 04 November 2022
ACCEPTED 27 January 2023
PUBLISHED 10 February 2023

CITATION
Revillo Imbernon J, Chiesa L and Kellenberger E (2023), Mining the Protein Data Bank to inspire fragment library design.
Front. Chem. 11:1089714.
doi: 10.3389/fchem.2023.1089714

COPYRIGHT
© 2023 Revillo Imbernon, Chiesa and Kellenberger. This is an open-access article distributed under the terms of the Creative Commons Attribution License (CC BY). The use, distribution or reproduction in other forums is permitted, provided the original author(s) and the copyright owner(s) are credited and that the original publication in this journal is cited, in accordance with accepted academic practice. No use, distribution or reproduction is permitted which does not comply with these terms.

Mining the Protein Data Bank to inspire fragment library design

Julia Revillo Imbernon, Luca Chiesa and Esther Kellenberger*

Laboratoire d'Innovation Thérapeutique, Faculté de Pharmacie, UMR7200 CNRS Université de Strasbourg, Illkirch-Graffenstaden, France

The fragment approach has emerged as a method of choice for drug design, as it allows difficult therapeutic targets to be addressed. Success lies in the choice of the screened chemical library and the biophysical screening method, and also in the quality of the selected fragment and structural information used to develop a drug-like ligand. It has recently been proposed that promiscuous compounds, i.e., those that bind to several proteins, present an advantage for the fragment approach because they are likely to give frequent hits in screening. In this study, we searched the Protein Data Bank for fragments with multiple binding modes and targeting different sites. We identified 203 fragments represented by 90 scaffolds, some of which are not or hardly present in commercial fragment libraries. By contrast to other available fragment libraries, the studied set is enriched in fragments with a marked three-dimensional character (download at 10.5281/zenodo.7554649).

KEYWORDS

scaffold, binding mode, site comparison, interaction graph, similarity, FBDD, PDB

1 Introduction

Over the past 25 years, the fragment-based approach has demonstrated its value to drug discovery by producing fifty-eight successful fragment-to-lead developments, including six approved drugs (Erlanson, 2021; de Esch et al., 2022). A fragment-based drug discovery (FBDD) project begins with the discovery of a molecule characterized by low molecular weight, low chemical structure complexity, and low binding affinity for the assayed protein target (Keserü et al., 2016; Li, 2020). It generally relies on biophysical methods, which are sensitive, and three-dimensional binding mode information, which facilitates the elaboration of the fragment hit into a drug-like lead. Compared to high-throughput screening campaigns, fragment screening has the advantage of a reduced scale for screening while efficiently exploring chemical space, the possible combinations between fragments giving access to multiple complex compounds (Shi and von Itzstein, 2019).

The fragment quality is critical to the success of drug design. Fragment must be stable in buffers and biological media, have high solubility in water, and have a well-defined synthetic pathway to allow for follow-up discovery to develop a drug candidate. Accordingly, fragment libraries present a preferred range of physico-chemical descriptors, e.g., following the rule of three (molecular weight ≤300; number of hydrogen bond donors ≤3; number of hydrogen bond acceptors ≤3; logP ≤3; number of rotatable bonds ≤3), and have generally been filtered to exclude unwanted compounds, e.g., reactive or poorly soluble compounds (Congreve et al., 2003). Recommended cut-off values for molecular weight have fluctuated in response to questions about ideal size and complexity.

In 2021, approximately half a million fragments were marketed in 81 libraries by 14 chemical suppliers (Revillo Imbernon et al., 2022). Collections vary both in size and content. Large catalogs, which contain up to 172,000 fragments, allow the assembly of custom libraries based on specific criteria. Numerous medium to small size libraries (80–8,968 fragments) are adapted to particular purposes, e.g., collections of fluorinated

fragments are suitable for screening by NMR (Troelsen and Clausen, 2020; Shinya et al., 2022). Several commercial libraries focus on diversity, aiming for good fragment space coverage and the ability to deliver hits to most targets. Academic initiatives have also proposed libraries of fragments built by maximizing structural or shape diversity, such as libraries developed based on diversity-oriented synthetic (DOS) strategy (Kidd et al., 2018). The diverse fragment libraries can serve different purposes, ranging from being a tool to study ligand-protein interactions or to facilitate bioisosteric replacement (Heidrich et al., 2019; Ferri et al., 2020) to the screening collection applicable to a wide variety of target proteins, such as the Diamond iNext Poised library of the Structural Genomics Consortium (DSiP) and the F2X chemical library, which both have been designed taking into account the diversity of chemical structures (Cox et al., 2016; Wollenhaupt et al., 2020). The diversity of chemical structures, however, does not presage the ability to provide hits for different proteins, as structurally dissimilar fragments may exhibit the same biological activity. XChem's analysis of DSiP screening campaigns thus demonstrated that structurally dissimilar fragments can form the same interactions, consistent with the pharmacophore concept (Carbery et al., 2022). The investigation of 309 protein-fragment structures obtained for 10 unrelated targets and 225 fragments led the authors to propose a strategy for selecting functionally diverse fragments based on the interactions formed with multiple proteins, as encoded in interaction fingerprints. Applied to DSiP hits, it yielded an ensemble of hundred functionally diverse fragments. The pharmacophore concept is also the basis for the development of the SpotXplorer library, which is composed of 96 fragments selected from commercial collections in order to maximize pharmacophore diversity while covering as much as possible of the 425 2-point and 3-point binding pharmacophores present in the Protein Data Bank (PDB) hotspots (Bajusz et al., 2021). SpotXplorer library has delivered hits for both well-studied proteins (G-protein coupled receptors and kinases) and novel targets (e.g., histone methyl transferase).

In this study, we further mine the PDB for relevant fragments, looking for small molecules able to adapt their binding mode to the protein context. We thus systematically compared the binding modes as well as the binding sites of a fragment if present in more than one PDB entry. We identified 203 fragments exhibiting two or more binding modes and binding to two or more different protein sites. This set of versatile PDB fragments overlaps with commercial libraries, contains approved drugs and approved drugs substructures, and reveals scaffolds that are still little exploited.

2 Material and methods

2.1 Collection of versatile PDB fragments

Fragment is here defined as a small molecular compound (molecular weight below 300 Da, non-hydrogen atoms count ranging from 2 to 18) that is not a monosaccharide, an organometallic compound, a prosthetic group, a crystallization additive (solvent, detergent, buffer, polyalcohol, etc.) (Desaphy et al., 2015; Drwal et al., 2018), a simple polyatomic ion (phosphate, sulfate or carboxylic acid), a small polyhalogenated compound, or a linear aliphatic compound.

Three-dimensional structures of protein in complex with a fragment were selected in the PDB if the deposition date is after 1 January 2000 and the resolution is below 3 Å. Their mmCIF files were downloaded from the RCSB website (Berman et al., 2000; RCSB, 2022). The preparation and standardization of the data followed the previously published protocol for the creation and maintenance of the sc-PDB, which provides, in an all-atom and annotated description, the druggable sites of the PDB and their ligands (Kellenberger et al., 2006; Desaphy et al., 2015). Briefly, the entries were filtered on the basis of molecular completeness and hydrogen atoms were added using protoss (v4.0, ZBH, University of Hamburg, Germany) (Bietz et al., 2014). For each PDB entry, the fragments, and their protein target (here including only amino acid residues) were saved in separate MOL2 files.

The frequency of each fragment in the data sample was evaluated by considering the occurrence of its HET code. Only fragments present in more than one PDB file were further considered.

The binding mode of a fragment to a protein site was described as an interaction graph. Hydrogen bond, ionic bond, aromatic stacking, and hydrophobic contacts were detected based on geometric rules using IChem (v5.2.8, University of Strasbourg, France) (Desaphy et al., 2013; Da Silva et al., 2018). For each interaction, a pseudo-atom is placed on the ligand interacting atom and labeled according to the nature of the interaction. In the case of hydrogen bond, a second pseudo-atom is defined halfway to the protein interacting atom to account for the directionality of the bond. The pseudo-atoms constitute the nodes of the interaction graph. Edges are defined between all pairs of nodes and labeled with the corresponding Euclidian distance. All graphs generated for the same fragment were compared to each other using a Subgraph Matching Kernel (max nodes = 3). Edge similarity was obtained *via* a normalized distance function (max distance = 1) (Siglidis et al., 2020). The kernel yields a similarity score value ranging between 0 and 1. The number of binding modes of a fragment was inferred from density-based clustering using Sklearn (eps = 0.23, N = 2) (Pedregosa et al., 2011). A correction of this number was applied based on shape similarity using ROCS (v3.4.1, OpenEye, Cadence Design Systems, Inc.). Two clusters were merged if the graphs of one cluster are subgraphs of the other cluster (TverskyCombo score ≥2). Only fragments showing two or more binding modes were further considered.

The binding cavity of a fragment was described as a cloud of points colored with pharmacophoric properties using Volsite tool in IChem and considering a maximal distance of 4 Å between the points and the non-hydrogen atoms of the fragment (Desaphy et al., 2012; Da Silva et al., 2018). All clouds of points generated for the same fragment were compared to each other using ProCare (Eguida and Rognan, 2020). Procare benchmarking, conducted by its authors, indicated that the comparison of dissimilar cavities yields a score below 0.47. Comparisons were made twice (cavity 1 vs. cavity 2 and cavity 2 vs. cavity 1), and the best score was retained. The number of cavities of a fragment was inferred from density-based clustering using Sklearn (eps = 0.47, N = 2) (Pedregosa et al., 2011). Only fragments showing two or more binding cavities were further considered.

Pan-assay interference compounds (PAINS) (Baell and Holloway, 2010) were identified based on 652 rules using Filter (v.2.5.1.4; Openeye Scientific Software, Santa Fe) and removed from the dataset.

2.2 Analysis of versatile PDB fragments

Molecular descriptors were computed for the PDB fragments using Pipeline Pilot (v.22.1.0.2935, BIOVIA, Dassault Systèmes, Pipeline Pilot): molecular weight, AlogP, molecular polar surface area, number of hydrogen bond acceptors and donors, aqueous solubility, number of positively and negatively charged atoms, number of rotatable bonds, number of rings, number of stereocenters, number of heavy atoms and solvent accessible surface area. The Plane of Best Fit (PBF) was calculated using Openeye libraries (v2019.10.2, OpenEye, Cadence Design Systems, Inc.) from a low energy conformer generated by corina (v3.40, Molecular Networks GmbH, Nürnberg, Germany).

The modeling confidence of the binding sites and fragments was assessed by the Real Space Correlation Coefficient (RSCC). The validation XML files of each PDB entry was downloaded from the PDB website (RCSB, 2022), and the mean RSCC of the residues in the fragment binding site was calculated. The coefficient of the fragment was directly extracted from the validation XML file. Model's quality was assigned based on Twilight classification: RSCC >0.9 for a model that fits the density, 0.9 ≥ RSCC ≥0.8 for a model that partially fits the electronic density and RSCC <0.8 for a model with significant parts are missing from the density (Weichenberger et al., 2013; Deller and Rupp, 2015).

The sequence conservation between the proteins binding the same fragment was evaluated by local alignment using the EMBOSS water package (v.6.6.0.0, EMBL-EBI, Cambridgeshire, United Kingdom). EBLOSUM62 was used as score matrix. Penalties for gap opening and gap extension were set to 10 and 0.5, respectively. For each PDB complex of a fragment, the protein chain containing more than half of the amino-acids forming the fragment binding site was saved in FASTA format. Proteins were clustered based on sequence identity through density-based clustering using Sklearn (eps = 0.10 or eps = 0.75, N = 2) (Pedregosa et al., 2011). Only alignments which contains at least hundred amino-acids were considered.

The structural conservation between the proteins binding the same fragment was evaluated by local 3D-alignment using CE with default settings (v1.02.2, San Diego Supercomputer Center, United States). The root mean square deviation (RMSD) between backbone atom coordinates was computed between identical and homologous proteins only. The RMSD analysis focused on the maximal values obtained from the all-against-all comparison of proteins binding the same fragment.

The conservation of the conformation of the same ligand in all its bound forms was evaluated by rigid body fit using PyMOL (v2.3.5, Schrodinger, LLC).

Structural similarity to XChem's functionally diverse fragments and SpotXplorer library was evaluated using ECFP4 molecular fingerprints and Tanimoto's coefficient (Tc) using Pipeline Pilot. The maximal similarity was reported for each versatile PDB fragment for the two compared sets.

Chemical scaffolds in the versatile PDB fragments were identified following the Bemis and Murcko approach (Bemis and Murcko, 1996) implemented in ADMET predictor (ADMET Predictor, Simulations Plus, Inc., Lancaster, California, United States). Fragments were standardized, neutralized, then classified using the option "Frameworks".

How the versatile PDB fragments populate the chemical space defined by the commercial fragments libraries was investigated by projecting the versatile PDB fragments in the published GTM map (Revillo Imbernon et al., 2022). Fragments were standardized using Standardizer (v16.10.17.0; ChemAxon Ltd.) and transformed into IIAB (2–4)_cycle ISIDA descriptors using ISIDA/Fragmentor (v.2019, Faculté de Chimie, Université de Strasbourg, France). The map was explored using GTM tools (Kireeva et al., 2012).

The versatile PDB fragments were searched in the drug-like collection of on-the-shelf commercially available compounds (Perebyinis and Rognan, 2022) and in Drugbank (Wishart et al., 2018). Compound standardization and substructure search were performed using RDKit (RDKit: Open-source cheminformatics, https://www.rdkit.org, https://doi.org/10.5281/zenodo.7415128). The molecules were neutralized, and their canonical tautomeric state was determined. The substructure search was performed using the fragment as the substructure query, and the commercial library or DrugBank compounds as the target. The chirality of both the query and the target were considered during the search. The contribution of each fragment to its corresponding superstructure was determined as the fraction of bonds in the query, over the number of bonds in the target. The result of the search was considered an exact match if the ratio between the number of bonds in the query and the target was equal to 1, otherwise it was considered as a substructure.

Datasets are available on Zenodo (doi: 10.5281/zenodo.7554649). The repository contains the MOL2 files of the crystallographic structures of the PDB versatile fragments, their binding proteins, their binding cavity, and interaction pseudoatoms. The repository also contains five CSV files: One including the versatile PDB fragments, their SMILES string, their number of binding modes and their number of binding cavities; another one containing the HET code and SMILES of the 521 fragments maintained after the PDB and ligand type filtering; the third CSV file groups the starting PDB information downloaded from the website (RCSB, 2022); another one containing the RSCC scores of fragments and binding sites; the last one summarizes the results of the search for the versatile PDB fragments in Drugbank and commercial drug-like libraries.

3 Results

The versatile fragments were selected from the PDB following a protocol comprising five filtering steps: 1) Unwanted molecules that do not meet the definition of a fragment, 2) molecules present in a single entry, 3) molecules that show only a single binding mode, 4) molecules that are described only in binding sites that are similar, and 5) PAINS compounds which are likely to interfere with bioassays (Figure 1). At the end of step 2, a total of 521 fragments were retained. For each of them, binding modes were grouped following a density-based clustering using pairwise comparisons by subgraph matching. The distance threshold for clustering was defined on the inflection point in a polynomial projection of the distribution of the comparison data of all the 521 fragments. The visual examination of the clusters revealed cases of separation of binding modes when one is included in the other. Therefore, we applied a correction aiming to group them together. A total of 427 fragments showed two or more binding modes. The ability of these fragments to adapt to different protein environments was then assessed using a new protein comparison method which focuses on local 3D alignment. Protein cavities were delineated based on the shape and size of the bound fragment. The

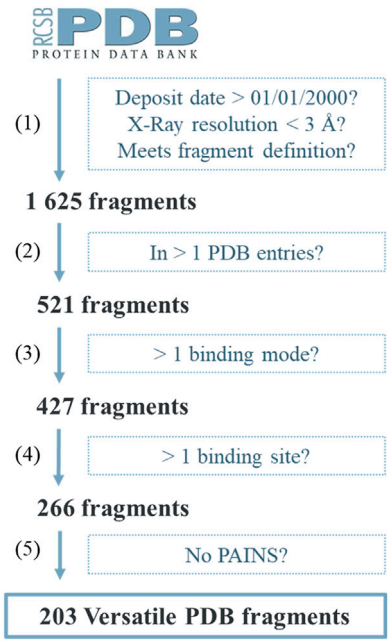


FIGURE 1
Overall workflow.

distribution of similarity scores is bimodal, with a first maximum at 0.86 corresponding to the median value obtained for the comparison of two copies of the same site in the same protein, and a second maximum at 0.34 corresponding to the median value for the random comparison of two unrelated sites. Density-based clustering using the recommended threshold for detecting similar sites (0.47) tended to cluster overlapping sub-sites of a pocket while well separating cavities with no visible commonalities. A total of 266 fragments were found in complex with two or more dissimilar binding sites. Of this set, 63 fragments were discarded because they contained quaternary pyridines, phosphorus, catechol among other structural motifs prevalent in problematic screening compounds.

The structure quality was assessed based on the correlated quality indicator RSCC, available for 4,997 of the 5,220 structures of the 203 versatile fragments. The protein binding site structures are mostly very well resolved (97% of the binding site structures fit to the density). Overall, the fragment structures are also well defined (72% and 18% of the fragment structures fit and partly fit the electron density, respectively). The 10% of structures where part of the fragment is not in the density concern 115 fragments. All data was used in the analysis that follows. If the lower quality structures had been discarded, one fragment would have been excluded for lack of binding mode diversity (HET code: NBO) and eleven fragments would have been excluded for lack of binding site diversity (HET code: IBP, M2S, PEA, 2EC, LTN, 4BX, 2UP, 1FL, MOK, FMK, and AJD).

The 203 versatile fragments identified in the PDB mostly comply with the rule of three, with 130 presenting no rules' violation, 46 one rules' violation, 26 two rules' violations, and only one three rules' violations. Rules violations are mostly linked to the number of hydrogen bond donor (24) and acceptor groups (49), the number of rotatable bonds (27), and only in one instance the logP. Figure 2 shows the absence of molecular obesity in the set (panel A), and provides an overview of the molecular complexity (panel B) and three-dimensionality (panel C) of the selected fragments. For more details, the molecular weight of 91 fragments falls in the 175–250 range. All fragments contain 6 to 18 non-hydrogen atoms (Figure 2A). Fragments are weakly lipophilic (107 fragments with $0 \leq \log P < 3$) or hydrophilic (95 fragments with $\log P < 0$). A total of 175 fragments contains one or two rings (Figure 2B). Consistent with ring aromaticity, there are 66 flat fragments, as indicated by the zero PBF value (Figure 2C), yet they only represent one-third of the entire set. The number of rotatable bonds does not exceed three for almost 87% of the fragments.

The 203 versatile fragments are present in 2,303 crystallographic PDB structures, representing 5,220 structures of fragment-protein complexes. About 82% of versatile PDB fragments bind to two or three different cavities, and accordingly using a small number of binding modes (Figure 2D). Exceptions are nucleosides such as thymidine, which shows 26 binding modes in two cavities, and flexible linear fragments such as the amino acid arginine, which shows six binding modes in two cavities. A total of twelve fragments are present in five or more cavities: six amino acids (lysine, canavanin, methionine, phenylalanine, leucine and pidolic acid), one nucleobase (guanine), two molecules naturally present in the organism and three exogenous molecules. The highly versatile natural molecules are both small ring system substituted with oxygenated group: the gamma-butyrolactone, which is a precursor of gamma-hydroxybutyrate (HET code: GBL) and the vitamin C or ascorbic acid (HET code: ASC). The three exogenous molecules target five to seven cavities: Afegostat, an iminosugar which failed a phase II clinical trial for Gaucher's Disease (PDB code: IFM), 4-bromo-1H-pyrazole (HET code: BYZ), and thiophene-2-carboxylic acid (HET code: C21).

Sequence comparison between the proteins binding the same fragment revealed that 140 fragments bind to non-related proteins (identity <25%), specifically with two to three proteins for 93 fragments and more than 40 proteins for four fragments (resorcinol RCO: 82, styrene oxide RSO: 58, uridine URI: 41, and phenylalanine PHE: 64). Only eight of the fragments are in complex with the same protein or close homologs (identity ≥90%), whose overall structure is well conserved (maximum pairwise RMSD ≤1.42 Å). The remaining 55 fragments bind to more distant homologs (25% ≤ identity ≤90%), whose overall structure is either well conserved (maximal pairwise RMSD ~1 Å for 14 fragments) or else very different (maximal pairwise RMSD ~6 Å for 41 fragments). Thus, a total of 22 of the fragments explore several local sites in proteins that are similar in sequence and overall structure.

The conformations of the fragments were compared to assess whether structural plasticity can account for the versatility of binding. About 43% of the 203 versatile fragments show a conformation which is conserved in all their binding sites (maximum pairwise RMSD ≤0.5 Å) and only 11 fragments use very different conformations to adapt to their different protein environments (maximum pairwise RMSD >2 Å). On average, fragment conformation is more variable for fragments that bind to homologs than for fragments that bind to proteins that are unrelated in sequence: the mean value of the maximum pairwise RMSD is equal to 0.78 Å ± 0.69 for the 140 fragments binding to non-related proteins, to 0.88 Å ± 0.72 for 55 fragment binding to distant homologs, and 0.97 Å ± 0.58 for the eight fragments binding to the same protein or close homologs.

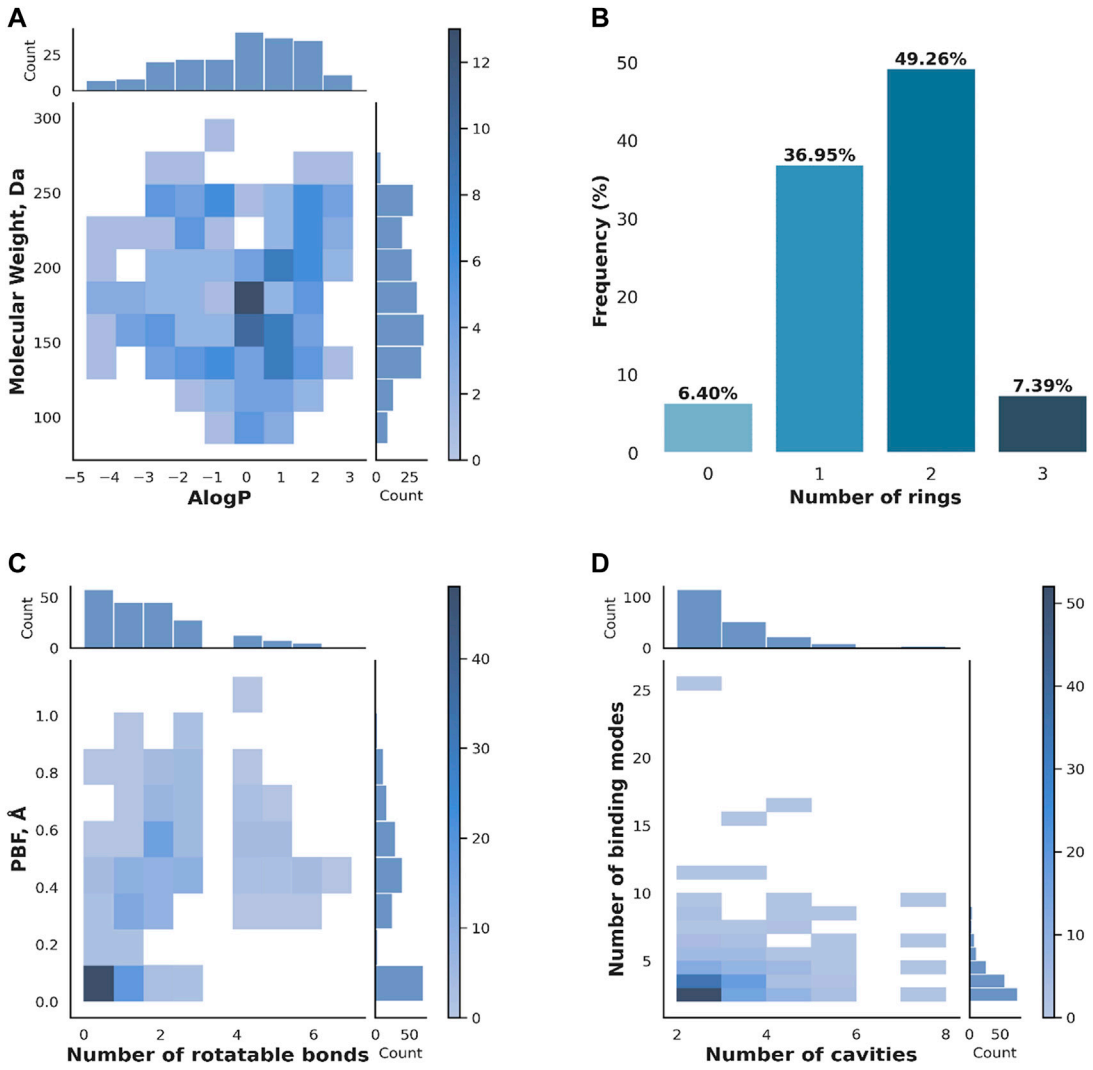


FIGURE 2
Properties of the versatile PDB fragments. **(A)** Molecular weight vs. AlogP **(B)** Number of rings **(C)** PBF vs. Number of rotatable bonds **(D)** Number of binding modes vs. Number of binding cavities. The distributions of individual properties are given on the top and side of the heat maps in **(A)**, **(C)** and **(D)**. The color scale on the side of the heat maps in **(A)**, **(C)** and **(D)** refers to the number of fragments.

Two examples of versatile fragments are discussed below and illustrate how a fragment adapts its binding mode to unrelated proteins (Figure 3A), and to different sites in the same protein (Figure 3B). The first example involves a pyrrolo-pyrimidine fragment (HET code: PQ0). This fragment shows three binding modes in two protein cavities found in two types of proteins, tRNA-guanine transglycolase (PDB codes: 1IT8, 1P0B, 2PWV, and 2QII) and nitryl reductase QueF (PDB code: 4FGC). The three binding modes are dominated by hydrogen bonds. Changes involve the pyrrole moiety, which does not interact with the protein or interact with a tyrosine side chain depending on local structural variation of tRNA-guanine transglycolases binding site. More importantly, different protonation states of the fragment allow for different hydrogen bonding patterns in the two proteins. Last, although it is not the focus of the present study, this fragment also binds to RNA (PDB code: 3GCA) (Berman et al., 2000).

The second example consists of a furanone (HET code: H3M), which is in complex twice with the strigolactone esterase D14 (PBD code: 6BRT and 3WIO), yet shows a 4 Å shift in the main cavity, thereby defining two non-overlapping subpockets (Figure 3B). The two corresponding binding modes are dominated by π interactions which are frequently observed in RNA-protein complexes (Wilson et al., 2021), but they differ in the hydrogen bonds formed with the protein, which either involve a tryptophan indole ring, or a cysteine sulfhydryl and a protein-bound water molecule. Of note, the binding mode comparison method used here ignored weak hydrogen bonds and water mediated interactions yet was nevertheless able to differentiate the two binding modes. Interestingly, the three-dimensional structures of furanone ring are not identical in the two complexes, suggesting that despite the absence of rotatable bonds this scaffold is able to adapt its shape to the local environment.

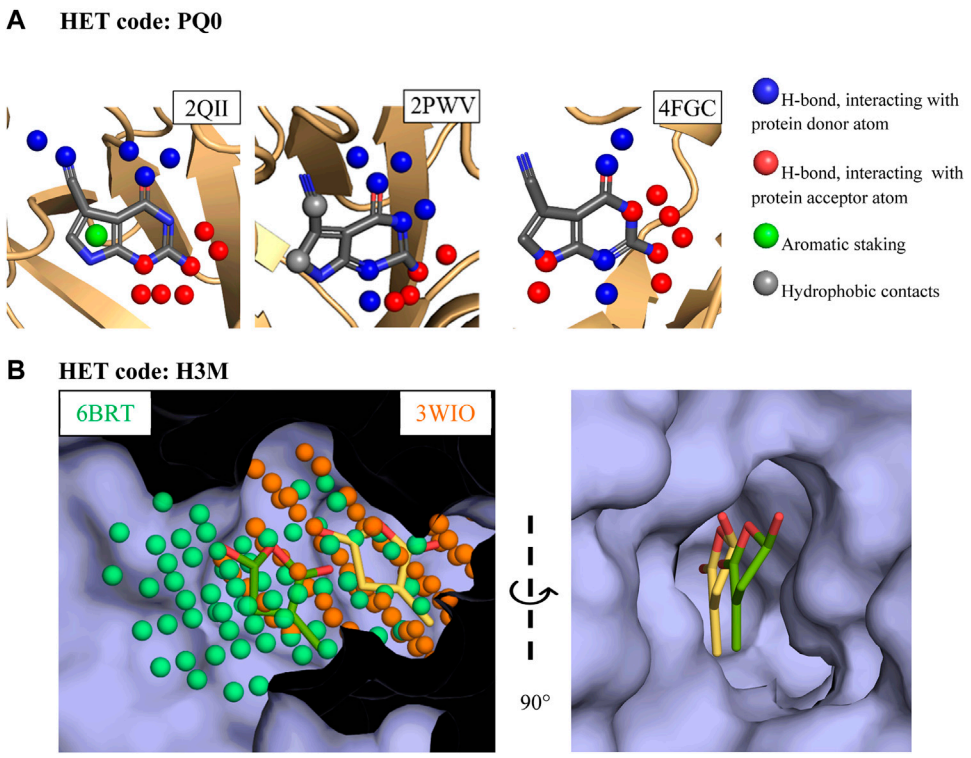


FIGURE 3
Examples of three-dimensional structures of PDB versatile fragments **(A)** Interactions formed by pyrrolo-pyrimidine in tRNA-guanine transglycolase and nitryl reductase QueF. **(B)** Substituted furanone binding to two adjacent subpockets in strigolactone esterase D14. The cavity points representing the two subpockets and used for the comparison of the two sites are shown in the left image.

The versatile PDB fragments were compared to two academic collections, the XChem's functionally diverse fragments and SpotXplorer library. The distribution of maximal similarity between versatile PDB fragments and XChem's functionally diverse fragments had a median maximal value equal to 0.21 (Supplementary Figure S1). Thirteen versatile PBD fragments share common chemical structures with XChem's functionally diverse fragments (Tc > 0.45). One single fragment is common to both sets. This fragment is a sulfapyridine (HET code: SFY), which shows two binding modes in three cavities. It contains multiple pharmacophoric features (two hydrophobic rings, three hydrogen bond donors, two hydrogen bond acceptors), allowing adaptation to different protein environments. The chemical structures of versatile PDB fragments and SpotXplorer library do not overlap, with a median maximal similarity value equal to 0.23. A total of six versatile PBD fragments share common chemical structures with SpotXplorer library (Tc > 0.45).

The versatile PDB fragments were compared to the commercially available fragments using two approaches: shared Bemis and Murcko scaffolds and generative topographic map (GTM), which represents the chemical space in a 2D map, here based on topological descriptors (Kireeva et al., 2012). The 203 fragments are covered by 90 scaffolds. The commercial chemical space of fragments was described with about 60,000 scaffolds (https://gtmfrag.drugdesign.unistra.fr/) ranging from very simple (benzene) to very complex (adamantane) (Revillo Imbernon et al., 2022). We identified four absent scaffolds and 20 rare scaffolds, which were observed in twenty or less commercially available fragments (Figure 4). These 24 scaffolds represent a total of 32 fragments (Supplementary Figure S2). They show on average more oxygen atoms than commercial fragments (1–6 O in 79% of PDB scaffolds; 1–3 O in 31% of commercial scaffolds), and conversely fewer nitrogen atoms (1–5 N in 79% of PDB scaffolds; 1–6 N in 93% of commercial scaffolds). The coverage of the fragment space by the versatile PDB fragments was further analyzed through a GTM model recently developed to compare commercial libraries, based on the likelihood of the compounds projected onto the common frame (Figure 5). The versatile PDB fragments populate three regions which show a low density among the general commercial fragments set (Figure 5B): **A4**, **C2**, and **C4**. The region **A4** groups together three-dimensional molecules, mostly non-aromatic heterocycles which contain oxygen atoms. The region **C2** includes aromatic rings fused and substituted with alcohol, ketone or carboxylic acid groups. The region **C4** shows many purine derivatives with amino substituents on the pyrimidine ring. Noteworthy, the patterns observed in regions **A4** and **C2** have a low likelihood among the general commercial fragments set (Figure 5B) but are characteristic of nature-product like fragments of commercial libraries (Figure 5C).

The 203 versatile PDB fragments were further characterized by querying a repository of approved drugs, Drugbank (Wishart et al., 2018), and screening collections of commercial catalogs. A total of 45 fragments are registered as approved small molecule drugs in DrugBank. Among these, seven are also nutraceuticals and sixteen in clinical trials. Around half of the fragments (98) were identified as substructures of 1,436 approved drugs. The fragments generally represent a small portion of the corresponding superstructures,

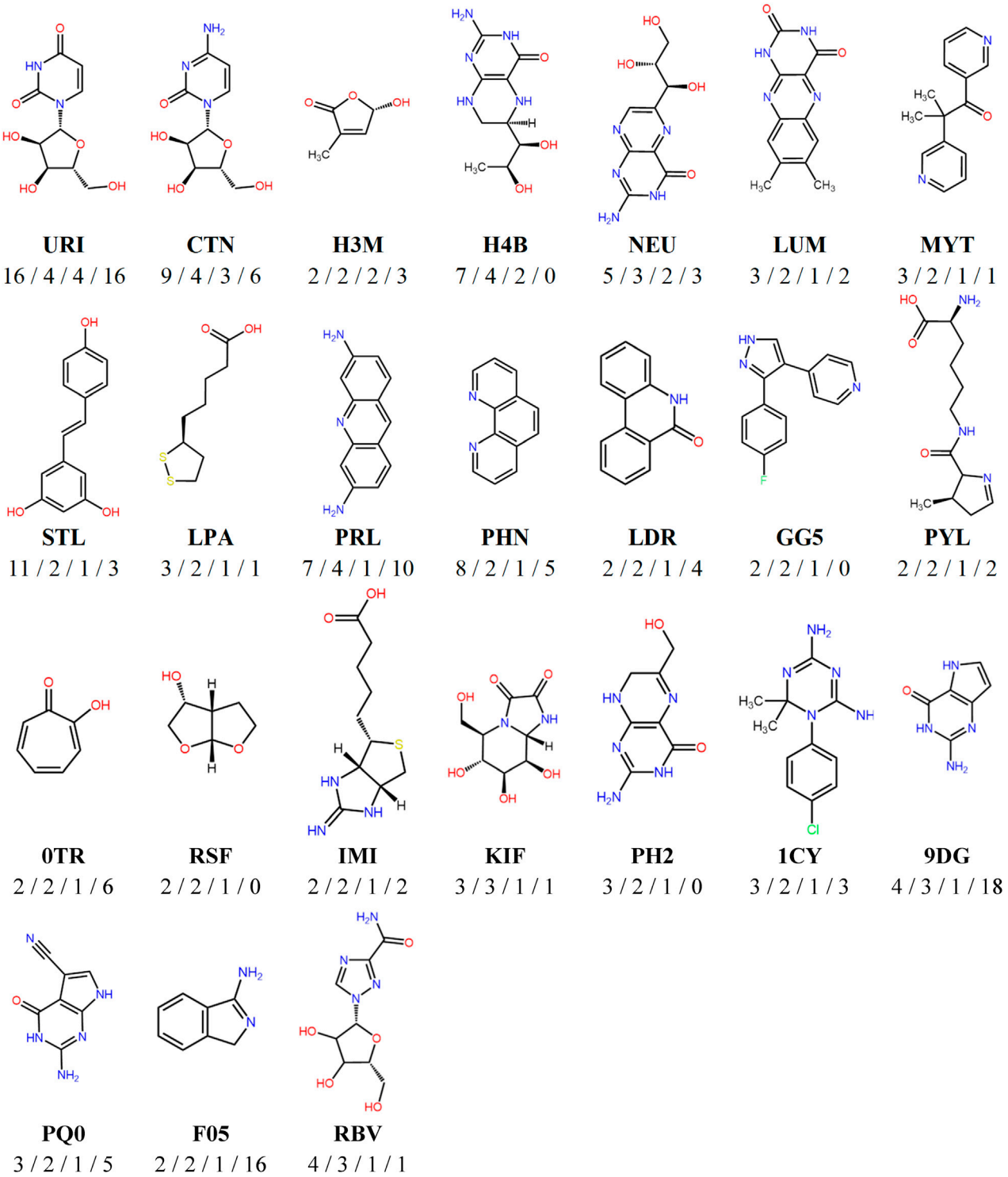


FIGURE 4
Representative chemical structures of the versatile PDB fragments which are absent or poorly represented in commercial fragments libraries. Below each fragment structure are indicated the HET code, then the number of binding modes/the number of different cavities/the number of versatile PDB fragments containing the same scaffold/the number of commercial fragments containing the same scaffold.

with the bonds in the fragment representing less than 50% of the bonds in the superstructure for 88% of the fragment-superstructure pairs. While 22 fragments are substructures of only a single drug, 48 are found in at least five drugs. Larger fragments (MW > 175) account for 28 of the 45 identified drugs, while 37 represent a substructure of 134 drugs. The exploration of commercial catalogs identified 95 purchasable fragments, and 163 fragments substructures of a huge number of commercially available screening compounds (4,769,862). The fragments represent however less than 50% of the superstructures' bonds in 97% of the fragment-compound pairs.

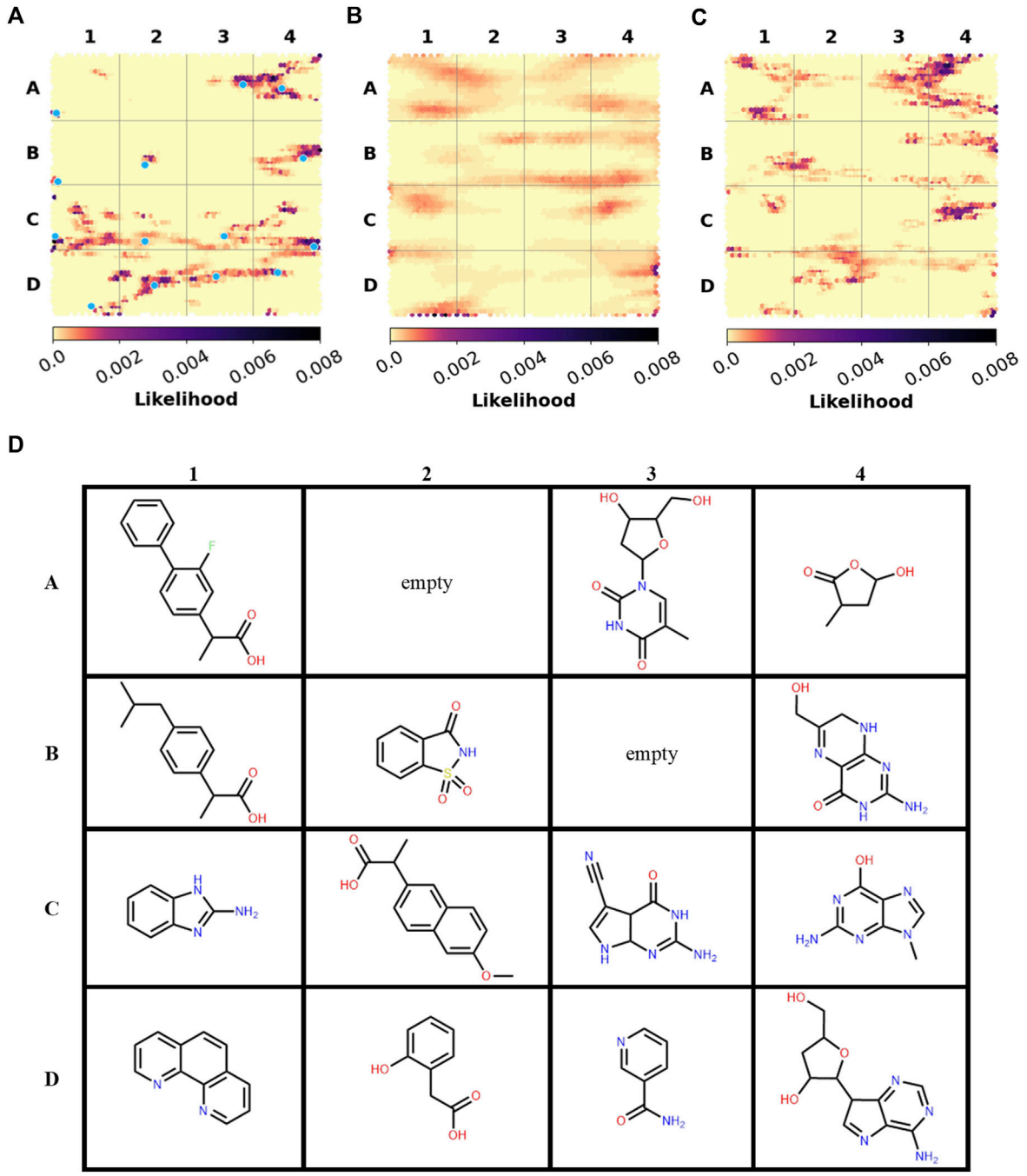


FIGURE 5
Spatial distribution of the fragments in GTM Landscapes **(A)** Versatile PDB fragments **(B)** All commercially-available fragments **(C)** Ensemble of nature-product like commercial libraries. **(D)** Examples of versatile PDB fragments. Their projection points are marked with blue dots on the map **(A)**. Figures 5B, C are adapted from (Revillo Imbernon et al., 2022).

4 Discussion

The PDB is an essential resource for structure-based drug discovery. Most drugs that have been approved by the FDA over the past decade were developed when structural information was freely available for the protein target (Westbrook and Burley, 2019). Additionally, with 38,790 entries in the Chemical Component Dictionary in 2022, the PDB provides important material for characterizing recognition between small molecular entities and proteins. The number of fragment-sized chemical entities (MW ≤ 300 Da) amounts to 13,965. Our analysis of the PDB identified only 203 versatile fragments, able to adopt at least two binding modes and to bind to at least two distinct sites. Most of these fragments target multiple proteins that differ in sequence, but we also highlighted eight fragments that bind differently to the same protein or close homologs.

Do the properties of the 203 versatile PDB fragments meet FBDD expectations? Lipophilicity and molecular weight are two widely used criteria, as they are related to solubility, metabolism

and selectivity, and a *sweet spot* has been suggested around a molecular weight 400 Da and a logP around 3 (Hann, 2011; Hann and Keserü, 2012). These values are shifted down in commercial fragment libraries with molecular weight in the range 200–300 Da and logP in the range 0–2 (Revillo Imbernon et al., 2022). A minimal molecular weight around 175 Da was suggested by the study of the conservation of the binding mode of the fragments in their drug-like superstructures (Jacquemard and Kellenberger, 2019). The same threshold was proposed following the analysis of XChem's screening campaigns which revealed that fragments that have never been shown to bind to a target tend to have a low molecular weight compared to fragments that bind to one or more targets (Carbery et al., 2022). According to the size criterion, about half of the versatile PDB fragments may provide a valid base for fragment growing (105 fragments with MW > 175 Da). A total of 38 fragments show a logP in the 0–2 range, yet there are also 50 hydrophilic fragments (logP <0). The combinations of lipophilicity and molecular weight which are little explored by recently developed synthetic oral drugs should not be overlooked since they may correspond to molecules of therapeutic interest such as natural products (e.g., antibiotics) (Young et al., 2022). Thus, we did not exclude hydrophilic fragments from the analysis. In addition, these fragments have the advantage of good aqueous solubility.

Are the 203 versatile PDB fragments original? To answer this question, we compared this set to XChem's functionally diverse fragments and SpotXplorer library, to the chemical space covered by commercial fragment libraries, and to screening collections of drug-like molecules. The XChem's functionally diverse fragments and SpotXplorer library are two collections comprising a wide diversity of pharmacophores evidenced by the binding modes observed in the structural data (Bajusz et al., 2021; Carbery et al., 2022). The comparison of chemical structures revealed that these two collections and the 203 versatile PDB fragments hardly overlap. The XChem's functionally diverse fragments and SpotXplorer library being assembled from commercial catalogs, we therefore sought to assess whether the scaffolds of the 203 versatile PDB fragments were indeed present in the fragment's libraries provided by chemical suppliers. According to our 2021 inventory (Revillo Imbernon et al., 2022), 198 versatile PDB fragments or structural analogs are commercially available, but 27 of them are rare in commercial fragment libraries. The five fragments whose scaffold is missing from commercial fragment libraries also cannot be purchased from commercial drug-like collections. These fragments are all the more original as only two of them are substructures of an available compound (HET code GG5 and RSF, representing 71% and 47% of the superstructure bonds in their respective best fragment/compound pair). In summary, if a large part of the versatile PDB fragments can be purchased from chemical suppliers, 24 of their scaffolds are little or not represented in commercial fragment libraries (Figure 4).

Many of the versatile PDB fragments that are not or rarely present in commercial fragment libraries are enriched in oxygen atom. Oxygen containing functional groups, such as ether, are more common in natural products than in synthetic molecules (Ertl and Schuhmann, 2019). Among oxygen-containing versatile PDB fragments are eight nucleosides and close analogs. The phosphorylated nucleoside, i.e., nucleotides, are common cofactors, therefore recognized by numerous protein sites. They have already widely inspired medicinal chemists, allowing for example the development of many anti-viral drugs (Seley-Radtke and Yates, 2018; Yates and Seley-Radtke, 2019).

Have all the 203 versatile PDB fragments already been exploited in drug discovery? To answer this question, we explored Drugbank thus identifying 45 approved drugs. According to Drugbank annotations, 29 of these drugs have more than one known target. For example, acetazolamide used to treat edema, certain types of epilepsy and glaucoma, has been reported to target nine types of carbonic anhydrase and aquaporin-1. The PDB structures provide eight binding modes of acetazolamide in multiple enzyme types: carbonic anhydrase, chitinase, deacetylase and synthase (HET code: AZM). The 16 other drugs have a single known target or no targets. For example, sulfapyridine is a sulfonamide antibiotic targeting dihydropteroate synthase type-1. The PDB structures provide four binding modes of sulfapyridine in multiple protein types: reductase, kinase, proteinase, erythrocine membrane protein and synthase (HET code SFY). As an example of drug with no known target, piracetam was crystallized in glutamate receptor 2 and glutamate receptor 3 (HET code PZI). Interestingly, 123 of the versatile PDB fragments are substructures of approved drugs, including drugs with a single known target. The data revealed examples of promiscuous fragment embedded into a selective drug, such as indole-3-carboxylic acid (HET code ICO) which was crystallized in complex with four types of protein (androgen receptor, integrase, malate synthase G, and a transcriptional regulator), and which also represents about half of tropisetron, a 5HT-3 receptor antagonist used as an antiemetic in the treatment of chemotherapy-induced nausea and vomiting (Ki = 2.70 nM, BindingDB entry BDBM50108392 (Chen et al., 2001)). In summary, we have identified 80 versatile PDB fragments that have not been yet exploited in drugs. Moreover, structural data on the 203 versatile PDB fragments reveal new off-targets for existing drugs and show that a versatile fragment can evolve into a drug with high affinity for its target. This data, freely available on zenodo, provides fragment-focused insights complementing previous studies of multi-target PDB ligands (Sturm et al., 2012; Barelier et al., 2015; Pottel et al., 2018; Feldmann and Bajorath, 2020; Pinzi and Rastelli, 2020) that can be used to better understand polypharmacology (Chaudhari et al., 2017; Proschak et al., 2019).

5 Conclusion

The clustering of the binding modes and binding sites of PDB fragments issued a set of 203 low molecular weight compounds able to adapt to different protein environments and to exploit several combinations of interacting atoms. The versatile PDB fragments constitute an ensemble which contains many structures that can be purchased directly yet also a few scaffolds that are poorly represented in fragment screening collections. The presence of oxygenated compounds in rare and original scaffolds calls for renewed interest in natural products. Since the PDB provides structural insights into well-studied biological functional systems, a significant amount of versatile PDB fragments (45/203) are approved drugs. Moreover, many promiscuous fragments are a substructure of selective drug, suggesting their utility for FBDD.

Data availability statement

The datasets presented in this study can be found in online repositories. The names of the repository/repositories and accession number(s) can be found in the article/Supplementary Material.

Author contributions

Conceptualization: EK; Methodology: JRI and EK; Implementation of the protocol: JRI and LC; Data preparation: JRI; Formal analysis: JRI and EK; Writing—original draft preparation: JRI and EK; Writing—review and editing: JRI, LC, and EK; project management: EK.

Acknowledgments

The authors thank Guillaume Bret for technical assistance and helpful discussion. The authors thank the Institut du Médicament (IMS) for financial support.

Conflict of interest

The authors declare that the research was conducted in the absence of any commercial or financial relationships that could be construed as a potential conflict of interest.

Publisher's note

All claims expressed in this article are solely those of the authors and do not necessarily represent those of their affiliated organizations, or those of the publisher, the editors and the reviewers. Any product that may be evaluated in this article, or claim that may be made by its manufacturer, is not guaranteed or endorsed by the publisher.

Supplementary material

The Supplementary Material for this article can be found online at: https://www.frontiersin.org/articles/10.3389/fchem.2023.1089714/full#supplementary-material

References

Baell, J. B., and Holloway, G. A. (2010). New substructure filters for removal of Pan assay interference compounds (PAINS) from screening libraries and for their exclusion in bioassays. *J. Med. Chem.* 53, 2719–2740. doi:10.1021/jm901137j

Bajusz, D., Wade, W. S., Satała, G., Bojarski, A. J., Ilaš, J., Ebner, J., et al. (2021). Exploring protein hotspots by optimized fragment pharmacophores. *Nat. Commun.* 12, 3201. doi:10.1038/s41467-021-23443-y

Barelier, S., Sterling, T., O'Meara, M. J., and Shoichet, B. K. (2015). The recognition of identical ligands by unrelated proteins. *ACS Chem. Biol.* 10, 2772–2784. doi:10.1021/acschembio.5b00683

Bemis, G. W., and Murcko, M. A. (1996). The properties of known drugs. 1. Molecular frameworks. *J. Med. Chem.* 39, 2887–2893. doi:10.1021/jm9602928

Berman, H. M., Westbrook, J., Feng, Z., Gilliland, G., Bhat, T. N., Weissig, H., et al. (2000). The protein Data Bank. *Nucleic Acids Res.* 28, 235–242. doi:10.1093/nar/28.1.235

Bietz, S., Urbaczek, S., Schulz, B., and Rarey, M. (2014). Protoss: A holistic approach to predict tautomers and protonation states in protein-ligand complexes. *J. Cheminformatics* 6, 12. doi:10.1186/1758-2946-6-12

Carbery, A., Skyner, R., von Delft, F., and Deane, C. M. (2022). Fragment libraries designed to Be functionally diverse recover protein binding information more efficiently than standard structurally diverse libraries. *J. Med. Chem.* 65, 11404–11413. doi:10.1021/acs.jmedchem.2c01004

Chaudhari, R., Tan, Z., Huang, B., and Zhang, S. (2017). Computational polypharmacology: A new paradigm for drug discovery. *Expert Opin. Drug Discov.* 12, 279–291. doi:10.1080/17460441.2017.1280024

Chen, X., Liu, M., and Gilson, M. (2001). BindingDB: A web-accessible molecular recognition database. *Comb. Chem. High. Throughput Screen.* 4, 719–725. doi:10.2174/1386207013330670

Congreve, M., Carr, R. A. E., Murray, C. W., and Jhoti, H. (2003). A 'Rule of Three' for fragment-based lead discovery? *Drug Discov. Today* 8, 876–877. doi:10.1016/s1359-6446(03)02831-9

Cox, O. B., Krojer, T., Collins, P., Monteiro, O., Talon, R., Bradley, A., et al. (2016). A poised fragment library enables rapid synthetic expansion yielding the first reported inhibitors of PHIP(2), an atypical bromodomain. *Chem. Sci.* 7, 2322–2330. doi:10.1039/C5SC03115J

Da Silva, F., Desaphy, J., and Rognan, D. (2018). IChem: A versatile toolkit for detecting, comparing, and predicting protein–ligand interactions. *ChemMedChem* 13, 507–510. doi:10.1002/cmdc.201700505

de Esch, I. J. P., Erlanson, D. A., Jahnke, W., Johnson, C. N., and Walsh, L. (2022). Fragment-to-Lead medicinal chemistry publications in 2020. *J. Med. Chem.* 65, 84–99. doi:10.1021/acs.jmedchem.1c01803

Deller, M. C., and Rupp, B. (2015). Models of protein–ligand crystal structures: Trust, but verify. *J. Comput. Aided Mol. Des.* 29, 817–836. doi:10.1007/s10822-015-9833-8

Desaphy, J., Azdimousa, K., Kellenberger, E., and Rognan, D. (2012). Comparison and druggability prediction of protein–ligand binding sites from pharmacophore-annotated cavity shapes. *J. Chem. Inf. Model.* 52, 2287–2299. doi:10.1021/ci300184x

Desaphy, J., Bret, G., Rognan, D., and Kellenberger, E. (2015). sc-PDB: a 3D-database of ligandable binding sites-10 years on. *Nucleic Acids Res.* 43, D399–D404. doi:10.1093/nar/gku928

Desaphy, J., Raimbaud, E., Ducrot, P., and Rognan, D. (2013). Encoding protein–ligand interaction patterns in fingerprints and graphs. *J. Chem. Inf. Model.* 53, 623–637. doi:10.1021/ci300566n

Drwal, M. N., Bret, G., Perez, C., Jacquemard, C., Desaphy, J., and Kellenberger, E. (2018). Structural insights on fragment binding mode conservation. *J. Med. Chem.* 61, 5963–5973. doi:10.1021/acs.jmedchem.8b00256

Eguida, M., and Rognan, D. (2020). A computer vision approach to align and compare protein cavities: Application to fragment-based drug design. *J. Med. Chem.* 63, 7127–7142. doi:10.1021/acs.jmedchem.0c00422

Erlanson, D. (2021). Practical fragments: Fragments in the clinic: 2021 edition. Pract. Fragm. Available at: https://practicalfragments.blogspot.com/2021/11/fragments-in-clinic-2021-edition.html (Accessed October 10, 2022).

Ertl, P., and Schuhmann, T. (2019). A systematic cheminformatics analysis of functional groups occurring in natural products. *J. Nat. Prod.* 82, 1258–1263. doi:10.1021/acs.jnatprod.8b01022

Feldmann, C., and Bajorath, J. (2020). Biological activity profiles of multitarget ligands from X-ray structures. *Molecules* 25, 794. doi:10.3390/molecules25040794

Ferri, M., Alunno, M., Greco, F. A., Mammoli, A., Saluti, G., Carotti, A., et al. (2020). Fragment based drug design and diversity-oriented synthesis of carboxylic acid isosteres. *Bioorg. Med. Chem.* 28, 115731. doi:10.1016/j.bmc.2020.115731

Hann, M. M., and Keserü, G. M. (2012). Finding the sweet spot: The role of nature and nurture in medicinal chemistry. *Nat. Rev. Drug Discov.* 11, 355–365. doi:10.1038/nrd3701

Hann, M. M. (2011). Molecular obesity, potency and other addictions in drug discovery. *MedChemComm* 2, 349–355. doi:10.1039/C1MD00017A

Heidrich, J., Sperl, L. E., and Boeckler, F. M. (2019). Embracing the diversity of halogen bonding motifs in fragment-based drug discovery—construction of a diversity-optimized halogen-enriched fragment library. *Front. Chem.* 7, 9. doi:10.3389/fchem.2019.00009

Jacquemard, C., and Kellenberger, E. (2019). A bright future for fragment-based drug discovery: What does it hold? *Expert Opin. Drug Discov.* 14, 413–416. doi:10.1080/17460441.2019.1583643

Kellenberger, E., Muller, P., Schalon, C., Bret, G., Foata, N., and Rognan, D. (2006). Sc-PDB: An annotated database of druggable binding sites from the protein Data Bank. *J. Chem. Inf. Model.* 46, 717–727. doi:10.1021/ci050372x

Keserü, G. M., Erlanson, D. A., Ferenczy, G. G., Hann, M. M., Murray, C. W., and Pickett, S. D. (2016). Design principles for fragment libraries: Maximizing the value of learnings from pharma fragment-based drug discovery (FBDD) programs for use in academia. *J. Med. Chem.* 59, 8189–8206. doi:10.1021/acs.jmedchem.6b00197

Kidd, S. L., Osberger, T. J., Mateu, N., Sore, H. F., and Spring, D. R. (2018). Recent applications of diversity-oriented synthesis toward novel, 3-dimensional fragment collections. *Front. Chem.* 6, 460. doi:10.3389/fchem.2018.00460

Kireeva, N., Baskin, I. I., Gaspar, H. A., Horvath, D., Marcou, G., and Varnek, A. (2012). Generative topographic mapping (GTM): Universal tool for data visualization, structure-activity modeling and dataset comparison. *Mol. Inf.* 31, 301–312. doi:10.1002/minf.201100163

Li, Q. (2020). Application of fragment-based drug discovery to versatile targets. *Front. Mol. Biosci.* 7, 180. doi:10.3389/fmolb.2020.00180

Pedregosa, F., Varoquaux, G., Gramfort, A., Michel, V., Thirion, B., Grisel, O., et al. (2011). Scikit-learn: Machine learning in Python. *J. Mach. Learn. Res.* 12, 2825–2830.

Perebyinis, M., and Rognan, D. (2022). Overlap of on-demand ultra-large combinatorial spaces with on-the-shelf drug-like libraries. *Mol. Inf.* 41, 2200163. doi:10.1002/minf.202200163

Pinzi, L., and Rastelli, G. (2020). Identification of target associations for polypharmacology from analysis of crystallographic ligands of the protein Data Bank. *J. Chem. Inf. Model.* 60, 372–390. doi:10.1021/acs.jcim.9b00821

Pottel, J., Levit, A., Korczynska, M., Fischer, M., and Shoichet, B. K. (2018). The recognition of unrelated ligands by identical proteins. *ACS Chem. Biol.* 13, 2522–2533. doi:10.1021/acschembio.8b00443

Proschak, E., Stark, H., and Merk, D. (2019). Polypharmacology by design: A medicinal chemist's perspective on multitargeting compounds. *J. Med. Chem.* 62, 420–444. doi:10.1021/acs.jmedchem.8b00760

RCSB (2022). Pdb: Homepage (n.d.). Available at: https://www.rcsb.org/ (Accessed April 1, 2022).

Revillo Imbernon, J., Jacquemard, C., Bret, G., Marcou, G., and Kellenberger, E. (2022). Comprehensive analysis of commercial fragment libraries. *RSC Med. Chem.* 13, 300–310. doi:10.1039/D1MD00363A

Seley-Radtke, K. L., and Yates, M. K. (2018). The evolution of nucleoside analogue antivirals: A review for chemists and non-chemists. Part 1: Early structural modifications to the nucleoside scaffold. *Antivir. Res.* 154, 66–86. doi:10.1016/j.antiviral.2018.04.004

Shi, Y., and von Itzstein, M. (2019). How size matters: Diversity for fragment library design. *Molecules* 24, 2838. doi:10.3390/molecules24152838

Shinya, S., Katahira, R., Furuita, K., Sugiki, T., Lee, Y.-H., Hattori, Y., et al. (2022). ^{19}F chemical library and ^{19}F-NMR for a weakly bound complex structure. *RSC Med. Chem.* 13, 1100–1111. doi:10.1039/D2MD00170E

Siglidis, G., Nikolentzos, G., Limnios, S., Giatsidis, C., Skianis, K., and Vazirgiannis, M. (2020). GraKeL: A graph kernel library in Python. *J. Mach. Learn. Res.* 21, 1–5.

Sturm, N., Desaphy, J., Quinn, R. J., Rognan, D., and Kellenberger, E. (2012). Structural insights into the molecular basis of the ligand promiscuity. *J. Chem. Inf. Model.* 52, 2410–2421. doi:10.1021/ci300196g

Troelsen, N. S., and Clausen, M. H. (2020). Library design strategies to accelerate fragment-based drug discovery. *Chem. Eur. J.* 26, 11391–11403. doi:10.1002/chem.202000584

Weichenberger, C. X., Pozharski, E., and Rupp, B. (2013). Visualizing ligand molecules in twilight electron density. *Acta Crystallogr. Sect. F. Struct. Biol. Cryst. Commun.* 69, 195–200. doi:10.1107/S1744309112044387

Westbrook, J., and Burley, S. K. (2019). How structural biologists and the protein Data Bank contributed to recent FDA new drug approvals. *Struct. Lond. Engl.* 27, 211–217. doi:10.1016/j.str.2018.11.007

Wilson, K. A., Kung, R. W., D'souza, S., and Wetmore, S. D. (2021). Anatomy of noncovalent interactions between the nucleobases or ribose and π-containing amino acids in RNA–protein complexes. *Nucleic Acids Res.* 49, 2213–2225. doi:10.1093/nar/gkab008

Wishart, D. S., Feunang, Y. D., Guo, A. C., Lo, E. J., Marcu, A., Grant, J. R., et al. (2018). DrugBank 5.0: A major update to the DrugBank database for 2018. *Nucleic Acids Res.* 46, D1074–D1082. doi:10.1093/nar/gkx1037

Wollenhaupt, J., Metz, A., Barthel, T., Lima, G. M. A., Heine, A., Mueller, U., et al. (2020). F2X-Universal and F2X-entry: Structurally diverse compound libraries for crystallographic fragment screening. *Structure* 28, 694–706. e5. doi:10.1016/j.str.2020.04.019

Yates, M. K., and Seley-Radtke, K. L. (2019). The evolution of antiviral nucleoside analogues: A review for chemists and non-chemists. Part II: Complex modifications to the nucleoside scaffold. *Antivir. Res.* 162, 5–21. doi:10.1016/j.antiviral.2018.11.016

Young, R. J., Flitsch, S. L., Grigalunas, M., Leeson, P. D., Quinn, R. J., Turner, N. J., et al. (2022). The time and place for nature in drug discovery. *JACS Au* 2, 2400–2416. doi:10.1021/jacsau.2c00415

frontiers | Frontiers in Chemistry

TYPE Original Research
PUBLISHED 10 February 2023
DOI 10.3389/fchem.2023.969865

Check for updates

OPEN ACCESS

EDITED BY
Giusy Lofrano,
University of Salerno, Italy

REVIEWED BY
Abhishek Mandal,
Indian Agricultural Research Institute (ICAR), India
Michele Iafisco,
National Research Council (CNR), Italy

*CORRESPONDENCE
Giuseppina Cerrato,
giuseppina.cerrato@unito.it

SPECIALTY SECTION
This article was submitted to Green and Sustainable Chemistry, a section of the journal Frontiers in Chemistry

RECEIVED 15 June 2022
ACCEPTED 23 January 2023
PUBLISHED 10 February 2023

CITATION
Giordana A, Malandrino M, Zambon A, Lusvardi G, Operti L and Cerrato G (2023), Biostimulants derived from organic urban wastes and biomasses:
An innovative approach.
Front. Chem. 11:969865.
doi: 10.3389/fchem.2023.969865

COPYRIGHT
© 2023 Giordana, Malandrino, Zambon, Lusvardi, Operti and Cerrato. This is an open-access article distributed under the terms of the Creative Commons Attribution License (CC BY). The use, distribution or reproduction in other forums is permitted, provided the original author(s) and the copyright owner(s) are credited and that the original publication in this journal is cited, in accordance with accepted academic practice. No use, distribution or reproduction is permitted which does not comply with these terms.

Biostimulants derived from organic urban wastes and biomasses: An innovative approach

Alessia Giordana[1], Mery Malandrino[1], Alfonso Zambon[2], Gigliola Lusvardi[2], Lorenza Operti[1] and Giuseppina Cerrato[1]*

[1]Dipartimento di Chimica, Università degli Studi di Torino, Turin, Italy, [2]Dipartimento di Scienze Chimiche e Geologiche, Università degli Studi di Modena e Reggio Emilia, Modena, Italy

We used humic and fulvic acids extracted from digestate to formulate nanohybrids with potential applications in agronomy. In order to obtain a synergic co-release of plant-beneficial agents, we functionalized with humic substances two inorganic matrixes: hydroxyapatite ($Ca_{10}(PO_4)_6(OH)_2$, HP) and silica (SiO_2) nanoparticles (NPs). The former is a potential controlled-release fertilizer of P, and the latter has a beneficial effect on soil and plants. SiO_2 NPs are obtained from rice husks by a reproducible and fast procedure, but their ability to absorb humic substances is very limited. HP NPs coated with fulvic acid are instead a very promising candidate, based on desorption and dilution studies. The different dissolutions observed for HP NPs coated with fulvic and humic acids could be related to the different interaction mechanisms, as suggested by the FT-IR study.

KEYWORDS

biostimulant, hydroxyapatite, silica, rice husk, humic acid, fulvic acid, nanofertilizer

1 Introduction

One of the major challenges for the future is the increasing worldwide demand for food and fuel that comes with a growing global population (National Academies of Sciences et al., 2019). Further intensification of current agricultural practices is unsustainable because they have led to unacceptable levels of environmental degradation (European Environment Agency., 2020). The poor efficiency and overuse of NPK fertilizers lead to losses in energy and water and present critical environmental implications such as eutrophication of surface waters and soil degradation caused by leaching of organic matter and salinization (National Academies of Sciences et al., 2019). Innovative agricultural interventions need to be implemented to safeguard ecosystems, biodiversity, and climate; nanotechnology has been suggested as a promising approach to this end because nanoscale materials can provide time-controlled, target-specific, self-regulated, and multi-functional capabilities (Lowry et al., 2019). Nanomaterials can, for example, deliver fertilizers, pesticides, and herbicides in an 'on-demand' manner, thus avoiding repeated applications and reducing adverse effects on plants and the environment (Wang et al., 2016). In particular, nanofertilizers may improve nutrient delivery efficiency and enhance productivity by ensuring gradual release of these nutrients (Verma et al., 2022). Among the strategies proposed, the use of biostimulants offers a potential route to reduce the dependency on fertilizers and pesticides.

Biostimulants are classified as any substance or microorganism, which even if not delivering nutrients, when applied to plants enhance nutritional efficiency, abiotic stress tolerance, and/or crop quality traits (du Jardin, 2015). Among the various biostimulants, an important class of compounds is represented by humic substances. Their role in soil fertility is well known, and the stimulation of plant growth by humic substances is well documented in the literature (Calvo

et al., 2014; Canellas et al., 2015). Nowadays, commercial products are obtained from non-renewable sources such as leonardite, peat, and coal. The aim of this work is thus to valorize the residual product of a transformation chain of the organic fraction of the solid urban waste, a basic extract of a solid digestate rich in humic and fulvic acids (indicated as HAs and FAs, respectively), which may represent a renewable source of humic substances. It is impossible to define a molecular formula for these heterogeneous and complex molecular systems, whose chemical composition varies depending on the source and generation condition. Humic substances are classified according to their solubility as a function of pH change. FAs represent the fraction always soluble, while HAs represent the fraction insoluble at a pH < 2. Moreover, all these humic substances contain many oxygen-based functional groups (such as phenol and carboxylic acid) that allow their adsorption on an inorganic substrate (Vekariya et al., 2016). By selecting proper solids, it is possible to obtain multi-functional and non-toxic nanocomposites that could find applications in agronomy being capable of conducting multiple beneficial actions including crop nutrition, plant stimulation, and soil amendments.

As inorganic substrates, we choose hydroxyapatite ($Ca_{10}(PO_4)_6(OH)_2$, HP) and silica (SiO_2) nanoparticles (NPs): the former is a potential solid fertilizer of P and the latter has beneficial effects on soil and plants. Even though Si is not considered an essential element, the beneficial effects of Si on plants and soil have been demonstrated by several studies using pot, hydroponic, and field experiments (Guntzer et al., 2012).

HP is a biocompatible and biodegradable material rich in P. Given its high solubility under acidic conditions and thus in gastric juices, HP does not raise concerns over bioaccumulation through the food chain and negative effects on human health. HP solubility decreases with the increasing pH value, allowing a slow release of nutrients at soil pH. HP NPs have been proposed as a controlled-release fertilizer of P, but their use is still limited due to low solubility in neutral and alkaline soils and their tendency to agglomerate. A strategy proposed to improve dissolution and bioavailability of HP NPs is to modify their surface with plant- or soil-friendly materials. Surface engineering with urea afforded nanohybrid fertilizers with high contents of N (Kottegoda et al., 2017; Sharma et al., 2022) with synergic effects on nutrient use efficiency, decreasing urea solubility and increasing HP dissolution. Surface modification with citric acid has been proven to modulate P-realizing kinetics, providing the optimal concentration of P for crops during their growth (Samavini et al., 2018). Humic acids have been used to modify the surface acidity of HP, in virtue of their ability to stimulate plant growth, to obtain a multi-functional material with multiple beneficial actions (Yoon et al., 2020). In this study, the authors functionalized HP NPs with commercial and synthetized humic substances and tested the resulting materials on *Zea mays*, noting significant improvements in terms of early plant growth, corn productivity, and resistance to abiotic stresses. These effects were ascribed to the co-release of P (as phosphate ions) and humic substances and to their synergic effect as plant-beneficial agents.

As possible oxidic substrates, we employed SiO_2 NPs obtained from rice husks, a common agricultural waste in Piedmont. Si is recognized as fundamental in agriculture, especially when stress conditions are afflicting plants, even though it is not recognized as "essential" for plant growth (Luyckx et al., 2017). Moreover, many widespread crops are Si accumulators (such as rice, wheat, sugarcane, and soybean), and their absorption depends on its availability (Guntzer et al., 2012). Furthermore, various studies have demonstrated the beneficial effect of Si on soil (Aksakal et al., 2013) and suggested that Si can make P in soil more available (Guntzer et al., 2012). Moreover, Si protects plants against various pathogens, as its presence enhances the cell wall resistance to fungal attacks. Rice husks are costless and widely available agricultural wastes, and they contain 15–20 wt% of silica in hydrated amorphous forms, depending on the variety, climate, and geographic location of production (Sun and Gong, 2001; Chandrasekhar et al., 2004). Rice husks represent a safer, less expensive, and more environmentally friendly silica precursor with respect to commonly employed alkoxysilane compounds. On the other hand, Si in the form of SiO_2 might be obtained from rice husks by several different procedures, such as thermal/hydrothermal treatments, chemical attacks, or biological digestion (Shen, 2017; Hossain et al., 2018), leading to a possible re-use of a typical agricultural waste in a "circular economy" approach (rather than dumping or burning it in open spaces), including its use as raw materials in the chemical industry or as an alternative fuel to produce energy (Bakar et al., 2016). Nitric acid digestion permits the extraction of amorphous SiO_2 from rice husks with high purity and interesting properties as the adsorbent of organic dyes (Tolba et al., 2015).

Self-assembly of HAs and FAs on the surface of HP and SiO_2 NPs was performed by water dipping. NPs coated with HAs and FAs were characterized, and acid desorption and HP dissolution were also evaluated, comparing the effect of FAs and HAs. An FT-IR study was performed to investigate the nature of the interaction between humic substances and the inorganic substrate.

This experimental approach is novel as, to the best of our knowledge, no other studies report the following: (i) the approach to self-assembling humic substances derived from a recycling plant onto inorganic substrates; (ii) the use of silica support derived from waste materials, and (iii) the study of the release of elements/substances (even in a simple medium, like water) from the self-assembled composite(s).

2 Materials and methods

2.1 Materials

Calcium hydroxide ($Ca(OH)_2$, 95%) was purchased from Thermo Scientific. Hydrochloric acid (HCl, p.a. ≥37%), ammonia solution (NH_3, p.a. 28%–30%), and nitric acid (HNO_3, p.a. 65%) were purchased from Merck. Phosphoric acid (H_3PO_4; 85%) was purchased from CARLO ERBA. $NaHCO_3$ was purchased from Fluka. All commercial reagents were used as received without any further purification. The basic extract of the solid digestate containing 7 wt% of HAs and FAs was obtained by a pilot implant treating urban organic wastes (ACEA Pinerolese SpA, Pinerolo (TO), Italy). Rice husks were provided by a local farm (Azienda Agricola Risicola Allocco, Bra (CN), Italy).

2.2 Preparation of inorganic substrates

HP NPs were synthesized according to a previously reported precipitation method (Aina et al., 2012). Briefly, 0.1 mol of

$Ca(OH)_2$ was stirred in 200 mL of water for 20 min until a homogeneous suspension was obtained. Then, 0.06 mol of H_3PO_4 (diluted with 200 mL of water) was slowly added dropwise, with continuous stirring. During the reaction, the pH is controlled and maintained above 10.5 by addition of ammonia solution, as necessary. The suspension was stirred for further 2 h and then allowed to stand overnight, and the final product was filtered and dried under ambient conditions. The overall yield is 9.05 g (99.0%).

Rice husk was washed with water to remove the residual of rice and earth. Then, it was dried in an oven at 60°C. Acid digestion was conducted under hydrothermal conditions: rice husk, HNO_3, and pure water taken in a weight ratio of 1:5:5 were allowed to react at 160°C for 2 h. The solid product was separated by filtration under suction, washed with distilled water, and dried under ambient conditions. Using 2.0 g of rice husks, 10 mL of water, and 7.0 mL of HNO_3, 248 mg of SiO_2 was obtained (yield: 12.4 wt%).

2.3 Formulation of solid biostimulants

The basic extract was centrifuged (3,000 rpm; 15 min) to eliminate solid residues. Then, HAs and FAs were separated according to different solubility fractions depending on the pH value. In detail, HCl solution (1.0 M) was added to the black dense solution until pH~1 was achieved, thus allowing the precipitation of a fraction of HAs. The obtained black powder was separated by centrifugation (5,000 rpm; 10 min) and dried in an oven at 55°C. The supernatant solution containing FAs was dried in an oven at 55°C to obtain a solid product.

Solid HAs and FAs were dissolved in either $NaHCO_3$ solution (0.05 M) or water. To favor a complete dissolution, solutions were sonicated for 5 min and then centrifugated to separate undissolved residues (2,500 rpm, 5 min). Either HP (1.0 g) or SiO_2 (0.5 g) NPs were added to 40 or 20 mL of humic substance solutions and shook for 2 h. The coated NPs were isolated *via* centrifugation (5,000 rpm; 5 min) and dried at 60°C. The amount of adsorbed acids was calculated by the difference in concentration between starting and separated solutions, by the spectrometric detention of absorbance at 254 nm. Calibrations were performed with solutions with known concentrations, according to the Beer–Lambert law. UV-vis spectra were recorded using the Perkin Elmer Lambda 900 spectrophotometer, utilizing quartz cells with an optical path of 1 cm.

2.4 Acid and ion release studies

To evaluate the release of humic substances and dissolution of the matrix, biostimulants based on HP (0.26 g) were suspended in 12 mL of pure water. Every 24 h, the solid was separated by centrifugation (5,000 rpm; 5 min), and the same volume of fresh water was re-added. HAs and FAs desorption was quantified by the spectrometric detention on the separated solution, as described previously. The released P and Ca ions were quantified by inductively coupled plasma atomic emission spectroscopy (ICP-AES) (PerkinElmer, model Optima 7000 DV). The wavelengths were 213.617 and 317.933 nm for P and Ca, respectively. Calibrations were performed with standard solutions. The concentration of Ca and P on the used coated HP was determined in the same way by diluting in water the solution obtained after digestion of 0.24 mg of each sample in aqua regia.

2.5 Instrumental characterization

Identification and characterization of crystalline phases of pure and coated inorganic substrates were carried out by several solid-state techniques.

PXRD, using a X'Pert powder diffractometer operating in the Bragg–Brentano geometry, equipped with a graphite crystal monochromator, and using Cu(Kα1) radiation (λ = 1.5406 Å), was collected in the range of 5°–70° with a step size of 0.02°.

FT-ATR (Attenuated Total Reflection) spectra were obtained in solid samples using the Bruker VERTEX 70 spectrophotometer equipped with Harrick MVP2 ATR cells and a DTGS detector (64 scan, 4 cm^{-1} resolution).

Thermogravimetric analyses were carried out on TA Instruments (TGA 2950 hr) in the air flow, with the ramp rate 10°C/min, from rt to 750°C.

The general morphology/topography of various samples was assessed by means of a scanning electron microscope operating with a field emission source (model: TESCAN S9000G; source: Schottky type FEG; resolution: 0.7 nm at 15 keV (in In-Beam SE mode), fitted with an EDS detector (Oxford EDS Ultim Max operating with Aztec software). Before the investigations, all samples were coated with Au in order to enhance the conductivity.

Analyses relative to the ultimate morphology of the samples were performed on a HR-TEM JEOL 3010-UHR (Tokyo, Japan) high-resolution transmission electron microscope (acceleration potential: 300 kV, LaB_6 filament) fitted with an Oxford INCA X-ray energy-dispersive spectrometer (X-EDS) with a PentaFET Si(Li) detector. The samples were dry dispersed before the investigation on Cu grids covered with lacey carbon without any further treatment.

Specific surface areas were evaluated from N_2 adsorption/desorption isotherms under subcritical conditions (196°C), obtained by means of an ASAP 2020 instrument. The surface area was calculated using the B.E.T. model.

FT-IR spectra were recorded using a Bruker Equinox 55 spectrometer, equipped with an MCT detector at 4 cm^{-1} resolution. The solid samples, in the form of self-supported pellets (≈10 mg/cm^2), were inserted into a conventional quartz vacuum cell equipped with KBr windows connected to a glass vacuum line (residual pressure <10^{-5} Torr) that allows the performance of *in situ* adsorption/desorption runs. The samples were activated at 120°C. Adsorption/desorption tests of water were carried out at 25°C.

3 Results

3.1 Characterization of inorganic substrates

The synthetized HP NPs exhibit physico-chemical characteristics similar to those reported in the literature (Aina et al., 2012). The PXRD pattern indicates the formation of a crystalline product, and both peak positions and relative intensities are the characteristics of the HP pure crystalline phase (ICDD card PDF n. 01-074-0565), as reported in Supplementary Material S1 (Supplementary Figure S1). All peaks are broad, suggesting the formation of NPs. In the FT-ATR spectrum (see Supplementary Figure S2), it is possible to recognize intense bands originating from PO_4^{3-} groups (Koutsopoulos, 2002). The most intense and broad band with the maximum at 1,024 cm^{-1} is assigned to the asymmetric stretching mode (ν_3) of the P–O bond, whereas the sharp

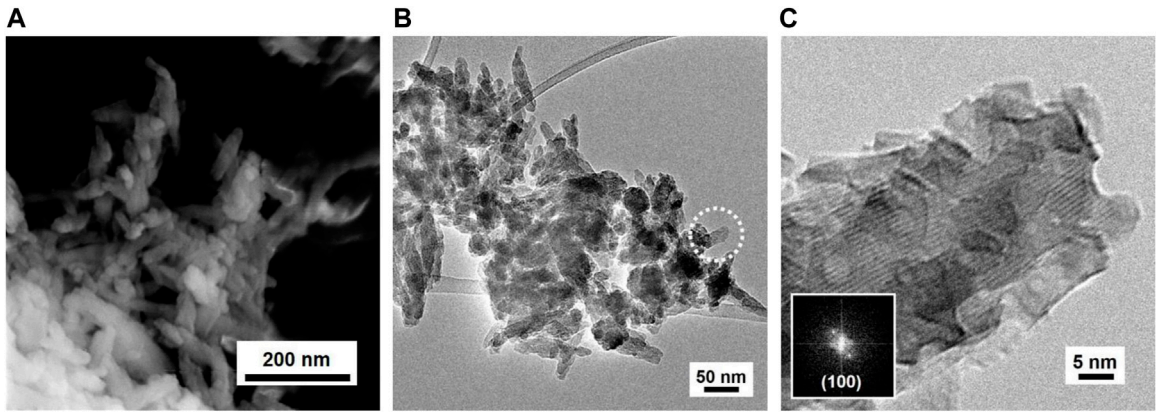


FIGURE 1
SEM **(A)** and TEM **(B, C)** images of the obtained HP NPs.

signals at 627, 601, and 560 cm^{-1} are ascribable to the bending modes (ν_4) of the O–P–O group and the weak component at 963 cm^{-1} is assigned to the symmetric mode (ν_1) of P–O. The spectral component typical of free hydroxyl groups is covered by the presence of a broad band centered at 3,400 cm^{-1}, due to the stretching mode of water molecules/OH groups interacting via H-bonding, either in bulk or adsorbed at the surface: their relevant bending mode is observable at 1,640 cm^{-1} (Sakhno et al., 2015). Three other spectral components are also well evident: a shoulder, located at 875 cm^{-1}, corresponding to the out-of-plane bending mode (ν_2) and multiple bands at 1,420, 1,455, and 1,487 cm^{-1}, attributable to the asymmetric stretching mode (ν_3), all of them being characteristic of surface carbonate species (Ren et al., 2014). The FESEM image (Figure 1A) indicates the formation of aggregates of prismatic NPs with average dimensions below 200 nm, mostly having a needle-like shape. NPs seem to be homogeneous in shape and dimension, as also confirmed by TEM images (Figures 1B, C and Supplementary Figure S3). As shown in Figure 1C, HP consists of prismatic elongated NPs grown along a crystallographic direction, mainly referred to that of the (101) planes. The SSA is calculated as 122 m^2/g.

The white powder obtained from the acid digestion of rice husks consists of pure SiO_2 NPs. The hydrothermal acid digestion was repeated different times, always affording analogous products and similar yields. TGA was used to verify the purity of the product. In the thermal degradation of rice husks (in Supplementary Figure S4), a weight loss of 5.2% was observed below 100°C that can be related to the loss of residual water. The majority of the weight loss (78.6%) takes place between 220°C and 500°C and can be related to the decomposition of organic molecules, such as lignin and cellulose. The residual weight at 750°C is 12.8%, very similar to that of the acid digestion synthetic yield. The residual white product collected after thermal degradation of rice husks was also analyzed by FT-ATR and resulted to be composed of SiO_2, as the main components can easily be ascribed to those of pure SiO_2 (Bellamy, 1968; Legrand, 1999). Conversely, the main weight loss of the white powder obtained after acid digestion is very low (4%) and is related to water removal at around 100°C, while a very low loss (0.4%) is observed at 310°C and can be related to the decomposition of the organic residue. Vibrational data obtained for this sample (reported in Figure 2) confirm the formation of SiO_2, presenting

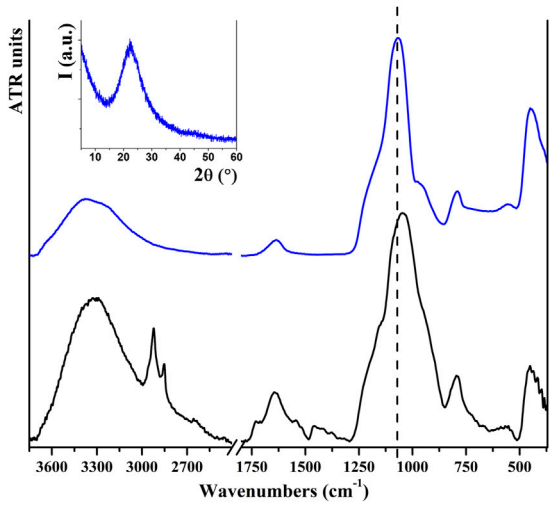


FIGURE 2
FT-ATR spectra of rice husks (black) and the product obtained after acid digestion (blue). Inset shows the PXRD pattern of the obtained SiO_2 NPs.

strong signals at 1,065, 793, and 450 cm^{-1} that represent characteristic modes related to the presence of Si–O–Si bonds. It is also possible to observe two other bands, located at 3400 e 1630 cm^{-1}, respectively, related to water stretching and scissor modes, but no signals of organic residue are detectable, confirming the TGA results. The characteristic signals of rice husks, as stretching modes of the C–H bond (around 2,900 cm^{-1}) and C–C/C–O bond (around 1,000 cm^{-1}), are not present in the spectrum of the product. The intense signal at 1,050 cm^{-1} observed for the rice husk could be due to the superimposition of C–O and Si–O–Si modes, and in the final product we observe a shift at 15 cm^{-1}. PXRD analysis indicates that the obtained material is amorphous, as evident from the inset to Figure 2. FESEM images indicate the presence of aggregates of small NPs that maintain an aggregation similar to that observed in the starting material (Supplementary Figure S5). The SSA is calculated as 202 m^2/g.

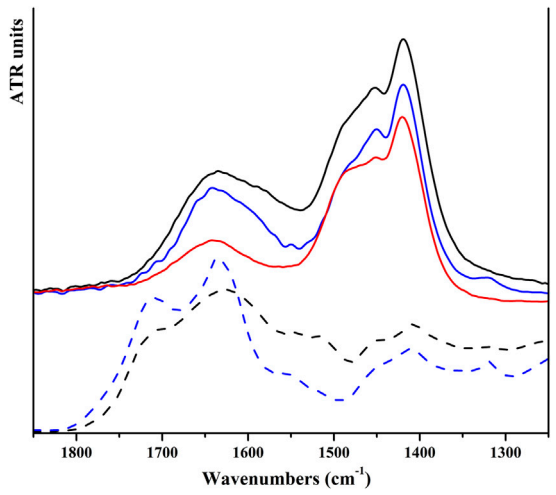


FIGURE 3
FT-ATR spectra of HP NPs (solid red line), solid HAs (black dash line), solid FAs (blue dash line), and HP NPs coated with HAs (solid black line) and FAs (solid blue line) in the spectral range of 1,250–1,850 cm^{-1}.

3.2 Adsorption of humic substances on inorganic matrixes

The solid fractions obtained by the separation of the basic extract were characterized by FT-ATR spectroscopy (see Supplementary Figure S6). HAs and FAs present similar functional groups (phenolic and alcoholic hydroxyl groups, aromatic and aliphatic carboxyl species and carbonyl groups, aliphatic chains and amides) and give then very similar FT-IR spectra but with some differences in the relative content of these groups (supported semi-quantitatively by the intensities of the relevant spectral components), and a careful analysis can reveal specific characteristics of the two fractions. Spectra are dominated by a broad band in the range of 3,700–2,500 cm^{-1}, ascribable to the stretching mode of hydroxyl groups of carboxyl species and phenolic and alcoholic functional groups interacting via H-bonding. For FAs, this component is very intense and exhibits a shoulder at 3,240 cm^{-1} that could be attributable to N–H aminic stretching vibrations. Vibrational features of HAs are represented by a couple of bands located at 2,925 and 2,855 cm^{-1}, ascribable to the stretching mode of aliphatic C–H in methyl (–CH_3) and methylenic (–CH_2–) units, respectively, which are superimposed to the OH stretching band and more evident with respect to FAs, consistent with the literature (Giovanela et al., 2004). The higher concentration of carboxylic groups in FAs can be related to the higher intensity of the bands lying above 1,600 cm^{-1} (Giovanela et al., 2004; Tatzber et al., 2007). Finally, the broad signal at 1,210 cm^{-1} is ascribable to the C–O stretching mode of alcoholic and phenolic groups, and it is more intense for HAs. An additional band is evident at 1,320 cm^{-1}, which is most likely due to bending modes of aromatic amine and, in fact, it is more intense for FAs.

NPs of both products were dipped in HAs and FAs solutions, having a concentration near saturation. To dissolve HAs, it was necessary to use a $NaHCO_3$ solution (0.05 M); the pH of the final solution is 8.5. Of note, commercial HA salts also dissolve giving a basic solution. Instead, FAs were dissolved in water, and the final solutions have a pH of 4.5. For HP NPs, the reciprocal affinity of the two materials resulted in a fast functionalization, as evident by (i) a drastic color change of the solid from white to brown and (ii) the discoloration of the supernatant solution. Conversely, on SiO_2 NPs, no evident chromogenic features of humic substances are observed. UV-vis analysis of supernatant solutions was used to determine the amount of acids adsorbed on all solids. For both inorganic substrates, a higher amount of FAs is absorbed with respect to HAs, as shown in Table 1. We can observe that HP is able to absorb more humic substances from solutions with respect to silica and that humic substances are absorbed on each substrate in similar amounts, independent of the kind of acid (average value: 32.5 for HP and 12.9 for SiO_2). The amount of adsorbed acids is very low for silica-based materials, and no evidence of functionalization is observable in the vibrational spectra and by means of other characterization techniques. Meanwhile, for HP-based materials, FT-ATR spectra present typical features of HP and humic substances; this is better visible in Figure 3, in which a magnified view in the 1,250–1,850 cm^{-1} range has been reported. Within this region, the spectrum of HP is featured by the spectral component ascribable to water and carbonate species, whereas the spectra of HAs and FAs are characterized by broad bands above 1,600 cm^{-1}, ascribable to COO^- and aromatic groups (as discussed previously). The bands of HAs and FAs were superimposed to those of the inorganic substrate, but in the spectra of coated materials, a broad shoulder at around 1,590 cm^{-1} is observable. PXRD patterns indicate that the coated HP NPs retain a higher degree of crystallinity, without any peculiar phase modification (Supplementary Figure S7). FESEM images suggest that both morphology and dimensions are maintained after the functionalization step (see Figure 4). EDS maps of carbon provide evidence that a higher density of organic molecules is observed for FAs derivatives that seems to form a coated film on top of the HP crystallites.

3.3 Co-release of ions and humic substances in water

To understand if there are differences in HP dissolution depending on the nature of adsorbed organic acids (HAs or FAs), a specific test was performed (as reported in Section 2.4), aimed at quantifying the concentration of relased acids and revealiong the amount of phosphate and calcium ions released in water by coated HP (in steps of 24 h), as shown in Figure 5 and Supplementary Material S1 (Supplementary Table S1; Supplementary Table S2). Results indicate that for both HAs and FAs, a maximum concentration is reached after the first 24 h (9.1 and 4.3 mg/mL, respectively), but in the successive steps, the release is almost constant (see the solid line in Figure 5A). The difference in concentration can be related to the different amount of adsorbed acids on HP, but comparing the percentage of released acids (see the dash line in Figure 5A) a very similar trend between HAs and FAs is observed. The same is not true for HP dissolution, as shown in Figure 5B. In fact, for HP coated with FAs, the concentration of both P and Ca species in water is virtually constant during the week (average values are 0.12 and 0.26 mmol/L, respectively). On the contrary, for the material coated with HAs, the concentration of P is very high after the first 24 h (0.53 mmol/L) and then it drastically decreases (0.25 mmol/L after 48 h down to 0.12 mmol/L after 72 h), whereas the concentration of Ca slowly increases during the week (starting from 0.071 mmol/L after 24 h and reaching 0.16 mmol/L after 96 h). The same trend is visible when observing the percentage in weight of released Ca and P (in the inset in Figure 5B), suggesting that dissolution

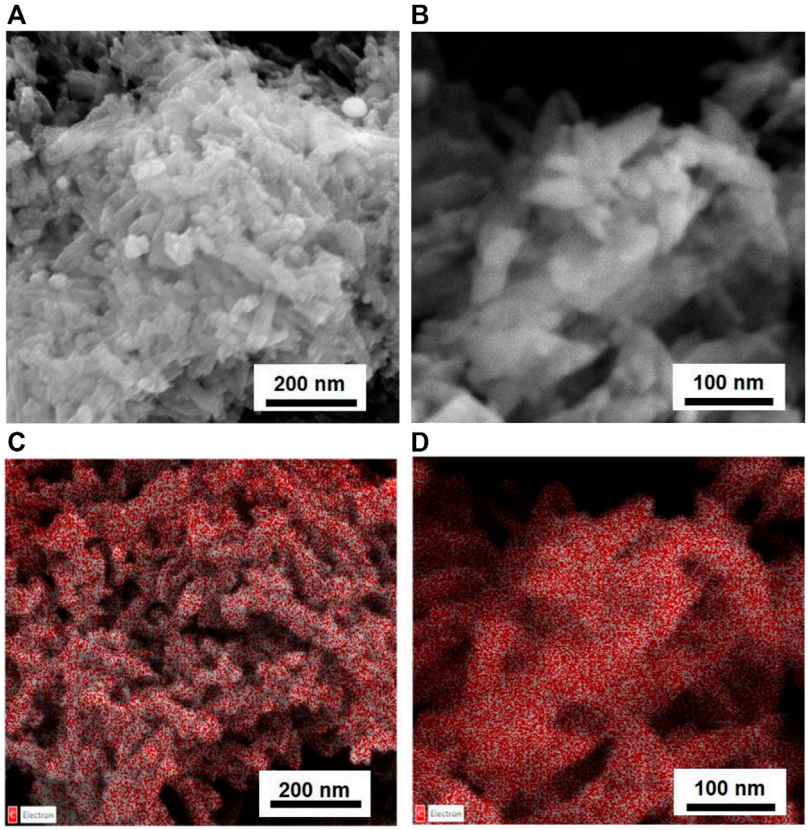


FIGURE 4
SEM images of HP NPs coated with HAs **(A)** and FAs **(B)** and EDS carbon maps **(C)** for HAs and **(D)** FAs.

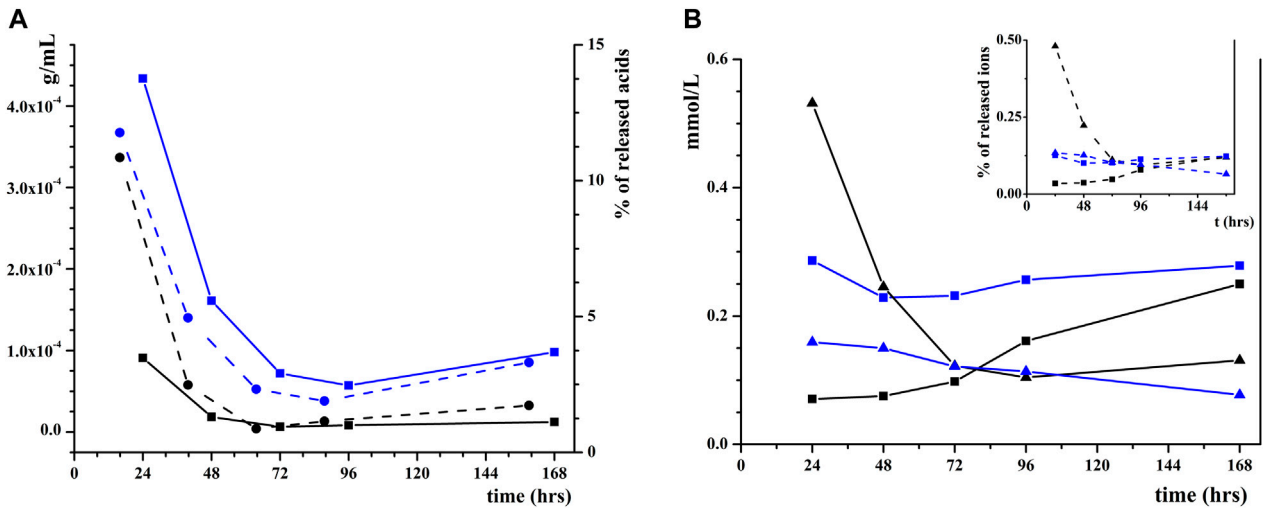


FIGURE 5
(A) Concentrations of HAs (black squares) and FAs (blue squares) released in pure water and wt% of the released HAs (black circles) and FAs (blue circles); **(B)** Concentrations and wt% (in the inset) of solubilized P (triangles) and Ca (squares) from HP NPs coated with HAs (black) or FAs (blue).

is influenced by the kind of acid adsorbed on the surface. Comparing the total amount of ions present in the solution, a higher amount of HP is dissolved when the surface is coated with FA (0.85 mg, 0.23 of P and 0.62 of Ca) than HA (0.73 mg, 0.42 of P and 0.31 of Ca).

3.4 FT-IR study of the interaction mechanism

A FT-IR study was performed to investigate the nature of the interaction between HP and humic substances. For the system coated

TABLE 1 Amount of HAs and FAs adsorbed on inorganic matrixes.

	wt% of acids on the substrate	mg of absorbed acids	Concentration of the initial solution (mg/mL)	wt% of acids adsorbed from the initial solution
HP + HAs	5.37	26.8 ± 1.5	4.59 ± 0.08	29.2
SiO_2 + HAs	3.28	16.4 ± 0.2	5.86 ± 0.08	14.0
HP + FAs	13.4	67.2 ± 2.2	9.38 ± 0.11	35.8
SiO_2 + FAs	5.23	26.1 ± 23.4	11.2 ± 01.2	11.7

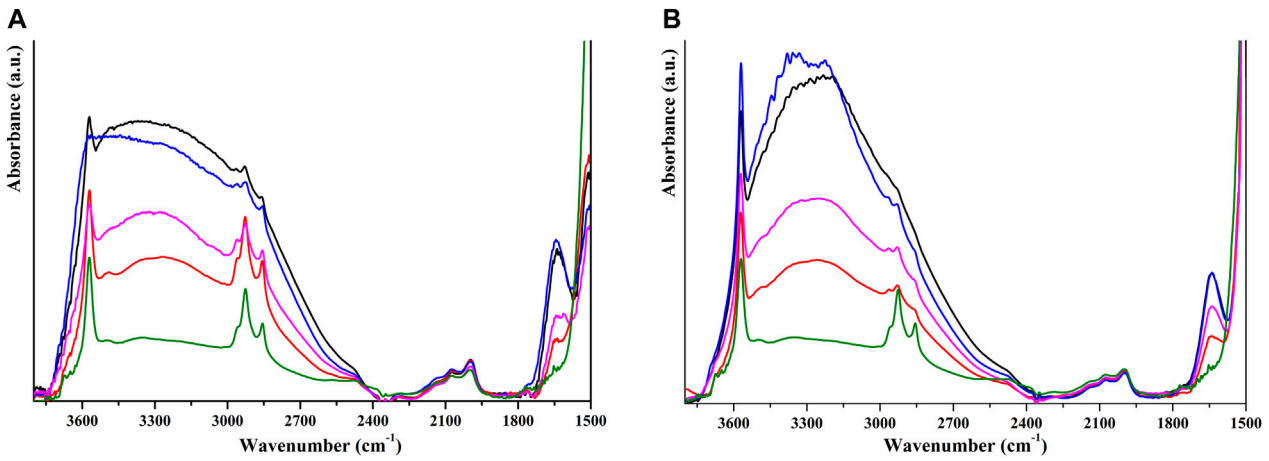


FIGURE 6
FT-IR spectra of self-supported pellets of HP NPs coated with FAs **(A)** and HAs **(B)** after outgassing (black lines), thermal activation at 120°C (red lines), addition of water vapor (blue lines) and outgassing (pink lines). Spectra of starting HP NPs after thermal activation at 120°C are reported as green line.

with FAs, in the spectrum of the sample after outgassing (black line in Figure 6A), it is possible to recognize the signals of HP, particularly the overtones of the phosphate group (between 1,950 and 2,200 cm^{-1}) and the stretching mode of surface-isolated hydroxyl species at 3,570 cm^{-1}. It is also possible to recognize the stretching modes of aliphatic moieties of FAs around 2,925 cm^{-1} and the stretching mode of carboxylic groups around 1,650 cm^{-1}. These signals are superimposed to the typical HP band. We can observe that the signals of C–H stretching are more intense in the coated materials, suggesting that this is in part related to the presence of FAs. The band of physisorbed water can be removed by thermal treatment at 120°C, and comparing coated and pristine HP (red and green lines in Figure 6A, respectively), we can attribute these signals to FAs. We can hypothesize that FAs and HP mainly interact through H-bonding of carboxylate and hydroxyl groups with phosphate and hydroxyl surface groups, as supported by the presence of a signal at 3,490 cm^{-1} that can be assigned to columnar OH groups interacting *via* H-bonding with the carboxylate group (Bertinetti et al., 2007) and by the broad band centered at 3,300 cm^{-1}, related to OH groups interacting *via* H-bonding. After water re-addition, the disappearance of stretching modes of the isolated OH surface group is observed (blue line in Figure 6A), suggesting that part of these surface groups is not involved in the interaction with FAs and is still free to interact with water molecules. This interaction with water is weak as a simple outgassing at room temperature brings about its removal. When the same experiment is carried out on HP coated with HAs, it can be noted that the signal of isolated OH groups is more evident in every step and that the interaction with water is also hindered at high water pressure, as shown in Figure 6B. The bands around 2,900 cm^{-1} are less evident, and this can be related to the low percentage of HAs on the HP surface. The signal at 3,490 cm^{-1} is less evident with respect to HP coated with FAs, suggesting that in this system the interaction *via* H-bonding is less important and part of HAs may interact by Lewis acid–basic interaction with Ca ions, as reflected in different behaviors observed during the dissolution of coated HP.

We also performed the same experiment on coated SiO_2, but no signals ascribable to humic substances can be observed, probably because of their low amount. Thermal activation at 120°C is not sufficient to remove physisorbed water, but a higher temperature treatment would cause HAs and FAs degradation, so no indication about the substrate–acid interaction has been obtained for these systems.

4 Discussion

Crystalline HP NPs were obtained by aqueous precipitation and coating with HAs and FAs, obtained from the valorization of urban

organic waste. HP coated with our HAs presents characteristics similar to those reported for HP coated with commercial HAs (Yoon et al., 2020). A higher amount of FAs is adsorbed on the HP surface with respect to HAs (13 vs. 5.4 wt%, respectively). FAs and HAs present similar functional groups, but in model structures FAs have less condensed aromatic rings, a higher fraction of aliphatic chains, and a higher density of carboxylic acid groups (Aiken, 1985). Analysis of spectroscopical data on FAs and HAs obtained from organic waste also indicate the same trend in our samples, suggesting a similarity with soil humic substances (Giovanela et al., 2004; Tatzber et al., 2007). It is known that humic substances have a tendency to agglomerate depending on pH conditions (de Melo et al., 2016), and it is important to note the different pH values of HAs and FAs solutions in the adsorption step. To re-dissolve solid HAs, it is necessary to basify the solution till pH reaches around 8.5. In the basic environment, phenolic and carboxylic groups are deprotonated, and the repulsion of these negatively charged groups causes molecules to assume a stretched configuration. We can presume that this structure is maintained after adsorption, preventing free hydroxyl groups to interact with water during the FT-IR experiment, possibly due to steric reasons. The solution of FAs instead has a pH of around 4.5, and in the acid condition, most phenolic and carboxylic groups are protonated, the repulsion is minimized, and the molecules adopt a coiled and compact structure. These can also explain the different amount of adsorbed species because folded molecules can be absorbed in higher quantity with respect to those having a stretched configuration.

HAs and FAs present a similar behavior in desorption from HP, while the nature of the acid influences the dissolution mechanism of coated HP. HP dissolution is more effective for FAs systems, where it is constant with time and more concentrated in Ca. For HA systems, the release is less constant, and after the first step (24 h) the concentration of P released in the solution drastically decreases, while the concentration of Ca increases with time. In a recent study on the dissolution of HP obtained from fish bones, similar values of P dissolution were obtained suspending the material in a citric acid solution (Sittitut et al., 2022), suggesting that surface coverage with HAs and FAs generates a local acid environment in the presence of water that favors HP dissolution. Our results suggest that HP NPs coated with FAs is a potential material for a synergic release of crop nutrients and stimulants, presenting a more controlled and efficient dissolution with respect to HP coated with HAs.

HP coated with FAs and HAs has shown a different behavior in the adsorption step and a different effect on HP dissolution. These could be correlated to a different interaction mechanism between the substrate and organic acids. The literature suggests that oxygen-based functional groups on the surface of HP nanoparticles can bind with two competing mechanisms, i.e., H-bonding interaction or chelation of Ca^{2+} ions (de Melo et al., 2016; Yoon et al., 2020). FT-IR studies (see Figure 6) suggest that the competition between interaction mechanisms is more pronounced on HP coated with HAs, in which a large fraction of OH groups remains free from interactions; conversely, the H-bonding interaction seems to be predominant when the material is coated with FAs. As this is a stronger interaction, we could suppose that desorption of FAs and HAs interacting *via* H-bonding promotes HP dissolution more than the desorption of HAs, which interact with Ca^{2+}, as also suggested by the desorption study.

Finally, we have shown that it is possible to obtain pure SiO_2 NPs from rice husks in a more sustainable way with respect to other previously reported procedures (Sun and Gong, 2001; Hossain et al., 2018) using water as a solvent and without any combustion treatment. This hydrothermal digestion procedure is fast, reproducible, and allows to obtain amorphous NPs with a high surface area (202 m^2/g). Despite the material characteristics being promising as humic substance adsorbers, having a high SSA and a certain amount of surface hydroxyl groups indicate that a very low amount of humic species can be really adsorbed. Due to the interesting properties of SiO_2 obtained from rice husks, further studies will be performed in order to investigate the possible functionalization of the surface to obtain a catalyst from a worldwide common agricultural waste.

Some preliminary conclusions drawn regarding this study are as follows: first, we demonstrated that it is possible to obtain a composite material (by self-assembly) to be employed in a gradual delivery process starting from waste materials: in our opinion, this is a result that might boost the interest towards such applications, particularly for circular economy applications and processes. Second, the physico-chemical characterization (mainly carried out by means of vibrational spectroscopy but not restricted to this) demonstrated that the different dissolution behaviors exhibited by the composite materials might be due to the different interaction mechanisms that regulate the adsorption/desorption of humic substances to/from the inorganic supports. Finally, the opportunity of obtaining silica NPs from another waste product (from agriculture) is in our opinion a very promising approach that deserves further investigations to shed some more light onto the general valorization process of wastes.

Data availability statement

The original contributions presented in the study are included in the article/Supplementary Material; further inquiries can be directed to the corresponding author.

Author contributions

Methodology: AG, GC, and LO; formal analysis: AG and MM; investigation: AG, GC, and MM; conceptualization: AG and GC; writing—original draft: AG and GC; supervision: GL and LO; writing—review and editing: AZ and GL; project administration: GC; funding acquisition: AG and GC.

Funding

Partial funding was obtained by the SATURNO project (Scarti organici e Anidride carbonica Trasformati in carbURanti, fertilizzanti e prodotti chimici; applicazione concreta dell'ecoNOmia circolare): this is a Piedmont regional project for the activities devoted to circular economy, active in the framework of POR F.E.S.R. 2014/2020 funding from the European Commission (Actions I.1b.2.2 and 1.8.II.2.3.1) at https://saturnobioeconomia.it/.

Acknowledgments

The authors would like to acknowledge Marisa Filippi's contribution to all the measurements carried out during her Master's thesis stage.

Conflict of interest

The authors declare that the research was conducted in the absence of any commercial or financial relationships that could be construed as a potential conflict of interest.

Publisher's note

All claims expressed in this article are solely those of the authors and do not necessarily represent those of their affiliated organizations, or those of the publisher, the editors, and the reviewers. Any product that may be evaluated in this article, or claim that may be made by its manufacturer, is not guaranteed or endorsed by the publisher.

Supplementary material

The Supplementary Material for this article can be found online at: https://www.frontiersin.org/articles/10.3389/fchem.2023.969865/full#supplementary-material

References

Aiken G. R. (Editor) (1985). *Humic substances in soil, sediment, and water: Geochemistry, isolation, and characterization* (New York: Wiley).

Aina, V., Lusvardi, G., Annaz, B., Gibson, I. R., Imrie, F. E., Malavasi, G., et al. (2012). Magnesium- and strontium-co-substituted hydroxyapatite: The effects of doped-ions on the structure and chemico-physical properties. *J. Mat. Sci. Mat. Med.* 23, 2867–2879. doi:10.1007/s10856-012-4767-3

Aksakal, E. L., Angin, I., and Oztas, T. (2013). Effects of diatomite on soil consistency limits and soil compactibility. *CATENA* 101, 157–163. doi:10.1016/j.catena.2012.09.001

Bakar, R. A., Yahya, R., and Gan, S. N. (2016). Production of high purity amorphous silica from rice husk. *Procedia Chem.* 19, 189–195. doi:10.1016/j.proche.2016.03.092

Bellamy, L. J. (1968). *Advances in infrared group frequencies*. London: Methuen.

Bertinetti, L., Tampieri, A., Landi, E., Ducati, C., Midgley, P. A., Coluccia, S., et al. (2007). Surface structure, hydration, and cationic sites of nanohydroxyapatite: UHR-TEM, IR, and microgravimetric studies. *J. Phys. Chem. C* 111, 4027–4035. doi:10.1021/jp066040s

Calvo, P., Nelson, L., and Kloepper, J. W. (2014). Agricultural uses of plant biostimulants. *Plant Soil* 383, 3–41. doi:10.1007/s11104-014-2131-8

Canellas, L. P., Olivares, F. L., Aguiar, N. O., Jones, D. L., Nebbioso, A., Mazzei, P., et al. (2015). Humic and fulvic acids as biostimulants in horticulture. *Sci. Hortic.* 196, 15–27. doi:10.1016/j.scienta.2015.09.013

Chandrasekhar, S., Satyanarayana, K. G., Pramada, P. N., Raghavan, P., and Gupta, T. N. (2004). Review. Processing, properties and applications of reactive silica from rice husk — an overview. *ChemInform* 35. doi:10.1002/chin.200406243

de Melo, B. A. G., Motta, F. L., and Santana, M. H. A. (2016). Humic acids: Structural properties and multiple functionalities for novel technological developments. *Mat. Sci. Eng. C* 62, 967–974. doi:10.1016/j.msec.2015.12.001

du Jardin, P. (2015). Plant biostimulants: Definition, concept, main categories and regulation. *Sci. Hortic.* 196, 3–14. doi:10.1016/j.scienta.2015.09.021

European Environment Agency (2020). *Healthy environment, healthy lives: How the environment influences health and well being in europe*. LU: Publications Office.

Giovanela, M., Parlanti, E., Soriano-Sierra, E. J., Soldi, M. S., and Sierra, M. M. D. (2004). Elemental compositions, FT-IR spectra and thermal behavior of sedimentary fulvic and humic acids from aquatic and terrestrial environments. *Geochem. J.* 38, 255–264. doi:10.2343/geochemj.38.255

Guntzer, F., Keller, C., and Meunier, J.-D. (2012). Benefits of plant silicon for crops: A review. *Agron. Sustain. Dev.* 32, 201–213. doi:10.1007/s13593-011-0039-8

Hossain, S. S., Mathur, L., and Roy, P. K. (2018). Rice husk/rice husk ash as an alternative source of silica in ceramics: A review. *J. Asian Ceram. Soc.* 6, 299–313. doi:10.1080/21870764.2018.1539210

Kottegoda, N., Sandaruwan, C., Priyadarshana, G., Siriwardhana, A., Rathnayake, U. A., Berugoda Arachchige, D. M., et al. (2017). Urea-hydroxyapatite nanohybrids for slow release of nitrogen. *ACS Nano* 11, 1214–1221. doi:10.1021/acsnano.6b07781

Koutsopoulos, S. (2002). Synthesis and characterization of hydroxyapatite crystals: A review study on the analytical methods. *J. Biomed. Mat. Res.* 62, 600–612. doi:10.1002/jbm.10280

A. P. Legrand (Editor) (1999). *The surface properties of silicas, Reprinted* (Chichester: Wiley).

Lowry, G. V., Avellan, A., and Gilbertson, L. M. (2019). Opportunities and challenges for nanotechnology in the agri-tech revolution. *Nat. Nanotechnol.* 14, 517–522. doi:10.1038/s41565-019-0461-7

Luyckx, M., Hausman, J.-F., Lutts, S., and Guerriero, G. (2017). Silicon and plants: Current knowledge and technological perspectives. *Front. Plant Sci.* 8, 411. doi:10.3389/fpls.2017.00411

National Academies of Sciences, Engineering, and Medicine (2019). *Science breakthroughs to advance food and agricultural research by 2030*. Medicine, Committee on Science Breakthroughs 2030: A Strategy for Food and Agricultural Research, National Academies of Sciences, E., and Medicine (U.S.)., Board on Agriculture and Natural Resources, National Academies of Sciences, E., and Medicine (U.S.)., Board on Life Sciences, National Academies of Sciences, E., and Medicine (U.S.)., Water Science and Technology Board, National Academies of Sciences, E., and Medicine (U.S.)., Board on Environmental Change and Society.

Ren, F., Ding, Y., and Leng, Y. (2014). Infrared spectroscopic characterization of carbonated apatite: A combined experimental and computational study: Ir spectroscopic characterization of CAp. *J. Biomed. Mat. Res. A* 102, 496–505. doi:10.1002/jbm.a.34720

Sakhno, Y., Ivanchenko, P., Iafisco, M., Tampieri, A., and Martra, G. (2015). A step toward control of the surface structure of biomimetic hydroxyapatite nanoparticles: Effect of carboxylates on the {010} P-rich/Ca-rich facets ratio. *J. Phys. Chem. C* 119, 5928–5937. doi:10.1021/jp510492m

Samavini, R., Sandaruwan, C., Silva, M. D., Priyadarshana, G., Kottegoda, N., and Karunaratne, V. (2018). Effect of citric acid surface modification on solubility of hydroxyapatite nanoparticles. *J. Agric. Food Chem.* 8, 3330–3337. doi:10.1021/acs.jafc.7b05544

Sharma, B., Shrivastava, M., Afonso, L. O. B., Soni, U., and Cahill, D. M. (2022). Zinc- and magnesium-doped hydroxyapatite nanoparticles modified with urea as smart nitrogen fertilizers. *ACS Appl. Nano Mat.* 5, 7288–7299. doi:10.1021/acsanm.2c01192

Shen, Y. (2017). Rice husk silica derived nanomaterials for sustainable applications. *Renew. Sustain. Energy Rev.* 80, 453–466. doi:10.1016/j.rser.2017.05.115

Sittitut, U., Jettanasen, J., Supothina, S., and Rattanakam, R. (2022). Dissolution performance of carbon/hydroxyapatite nanocomposite prepared from fish scales. *Inorganics* 10, 242. doi:10.3390/inorganics10120242

Sun, L., and Gong, K. (2001). Silicon-based materials from rice husks and their applications. *Ind. Eng. Chem. Res.* 40, 5861–5877. doi:10.1021/ie010284b

Tatzber, M., Stemmer, M., Spiegel, H., Katzlberger, C., Haberhauer, G., Mentler, A., et al. (2007). FTIR-spectroscopic characterization of humic acids and humin fractions obtained by advanced NaOH, $Na_4P_2O_7$, and Na_2CO_3 extraction procedures. *J. Plant Nutr. Soil Sci.* 170, 522–529. doi:10.1002/jpln.200622082

Tolba, G. M. K., Barakat, N. A. M., Bastaweesy, A. M., Ashour, E. A., Abdelmoez, W., El-Newehy, M. H., et al. (2015). Effective and highly recyclable nanosilica produced from the rice husk for effective removal of organic dyes. *J. Ind. Eng. Chem.* 29, 134–145. doi:10.1016/j.jiec.2015.03.025

Vekariya, R. L., Sonigara, K. K., Fadadu, K. B., Vaghasiya, J. V., and Soni, S. S. (2016). Humic acid as a sensitizer in highly stable dye solar cells: Energy from an abundant natural polymer soil component. *ACS Omega* 1, 14–18. doi:10.1021/acsomega.6b00010

Verma, K. K., Song, X.-P., Joshi, A., Tian, D.-D., Rajput, V. D., Singh, M., et al. (2022). Recent trends in nano-fertilizers for sustainable agriculture under climate change for global food security. *Nanomaterials* 12, 173. doi:10.3390/nano12010173

Wang, P., Lombi, E., Zhao, F.-J., and Kopittke, P. M. (2016). Nanotechnology: A new opportunity in plant Sciences. *Trends Plant Sci.* 21, 699–712. doi:10.1016/j.tplants.2016.04.005

Yoon, H. Y., Lee, J. G., Esposti, L. D., Iafisco, M., Kim, P. J., Shin, S. G., et al. (2020). Synergistic release of crop nutrients and stimulants from hydroxyapatite nanoparticles functionalized with humic substances: Toward a multifunctional nanofertilizer. *ACS Omega* 5, 6598–6610. doi:10.1021/acsomega.9b04354

frontiers | Frontiers in Chemistry

TYPE Original Research
PUBLISHED 21 March 2023
DOI 10.3389/fchem.2023.1106349

Check for updates

OPEN ACCESS

EDITED BY
Lara Massai,
University of Florence, Italy

REVIEWED BY
Sanja Grguric-Sipka,
University of Belgrade, Serbia
Thomas Scattolin,
University of Padua, Italy

*CORRESPONDENCE
Éva A. Enyedy,
enyedy@chem.u-szeged.hu
Ceyda Acilan,
cayhan@ku.edu.tr
Isabel Correia,
icorreia@tecnico.ulisboa.pt

†These authors have contributed equally to this work

SPECIALTY SECTION
This article was submitted to Inorganic Chemistry, a section of the journal Frontiers in Chemistry

RECEIVED 23 November 2022
ACCEPTED 28 February 2023
PUBLISHED 21 March 2023

CITATION
Ribeiro N, Bulut I, Sergi B, Pósa V, Spengler G, Sciortino G, André V, Ferreira LP, Biver T, Ugone V, Garribba E, Costa-Pessoa J, Enyedy ÉA, Acilan C and Correia I (2023), Promising anticancer agents based on 8-hydroxyquinoline hydrazone copper(II) complexes. *Front. Chem.* 11:1106349. doi: 10.3389/fchem.2023.1106349

COPYRIGHT
© 2023 Ribeiro, Bulut, Sergi, Pósa, Spengler, Sciortino, André, Ferreira, Biver, Ugone, Garribba, Costa-Pessoa, Enyedy, Acilan and Correia. This is an open-access article distributed under the terms of the Creative Commons Attribution License (CC BY). The use, distribution or reproduction in other forums is permitted, provided the original author(s) and the copyright owner(s) are credited and that the original publication in this journal is cited, in accordance with accepted academic practice. No use, distribution or reproduction is permitted which does not comply with these terms.

Promising anticancer agents based on 8-hydroxyquinoline hydrazone copper(II) complexes

Nádia Ribeiro[1], Ipek Bulut[2†], Baris Sergi[2†], Vivien Pósa[3], Gabriella Spengler[3,4], Giuseppe Sciortino[5], Vânia André[1], Liliana P. Ferreira[6,7], Tarita Biver[8], Valeria Ugone[9], Eugenio Garribba[10], João Costa-Pessoa[1], Éva A. Enyedy[3]*, Ceyda Acilan[11,12]* and Isabel Correia[1]*

[1]Centro de Química Estrutural, Institute of Molecular Sciences, and Departamento de Engenharia Química, Instituto Superior Técnico, Universidade de Lisboa, Lisbon, Portugal, [2]Graduate School of Health Sciences, Koc University, Istanbul, Türkiye, [3]MTA-SZTE Lendület Functional Metal Complexes Research Group, Department of Inorganic and Analytical Chemistry, University of Szeged, Szeged, Hungary, [4]Department of Medical Microbiology, Albert Szent-Györgyi Health Center and Faculty of Medicine, University of Szeged, Szeged, Hungary, [5]Institute of Chemical Research of Catalonia (ICIQ), The Barcelona Institute of Science and Technology, Tarragona, Spain, [6]Department of Physics, University of Coimbra, Coimbra, Portugal, [7]Biosystems and Integrative Sciences Institute (BioISI), Faculdade de Ciências, Universidade de Lisboa, Lisbon, Portugal, [8]Department of Chemistry and Industrial Chemistry, University of Pisa, Pisa, Italy, [9]Istituto di Chimica Biomolecolare, Consiglio Nazionale delle Ricerche, Sassari, Italy, [10]Dipartimento di Medicina, Chirurgia e Farmacia, Università di Sassari, Sassari, Italy, [11]School of Medicine, Koc University, Istanbul, Türkiye, [12]Research Center for Translational Medicine (KUTTAM), Koc University, Istanbul, Türkiye

We report the synthesis and characterization of a group of benzoylhydrazones (L^n) derived from 2-carbaldehyde-8-hydroxyquinoline and benzylhydrazides containing distinct *para* substituents (R = H, Cl, F, CH_3, OCH_3, OH and NH_2, for $L^{1\text{-}7}$, respectively; in L^8 isonicotinohydrazide was used instead of benzylhydrazide). Cu(II) complexes were prepared by reaction of each benzoylhydrazone with Cu(II) acetate. All compounds were characterized by elemental analysis and mass spectrometry as well as by FTIR, UV-visible absorption, NMR or electron paramagnetic resonance spectroscopies. Complexes isolated in the solid state (**1–8**) are either formulated as [Cu(HL) acetate] (with L^1 and L^4) or as $[Cu(L^n)]_3$ (*n* = 2, 3, 5, 6, 7 and 8). Single crystal X-ray diffraction studies were done for L^5 and $[Cu(L^5)]_3$, confirming the trinuclear formulation of several complexes. Proton dissociation constants, lipophilicity and solubility were determined for all free ligands by UV-Vis spectrophotometry in 30% (v/v) DMSO/H_2O. Formation constants were determined for [Cu(LH)], [Cu(L)] and [Cu(LH_{-1})] for L = L^1, L^5 and L^6, and also [Cu(LH_{-2})] for L = L^6, and binding modes are proposed, [Cu(L)] predominating at physiological pH. The redox properties of complexes formed with L^1, L^5 and L^6 are investigated by cyclic voltammetry; the formal redox potentials fall in the range of +377 to +395 mV vs. NHE. The binding of the Cu(II)-complexes to bovine serum albumin was evaluated by fluorescence spectroscopy, showing moderate-to-strong interaction and suggesting formation of a ground state complex. The interaction of L^1, L^3, L^5 and L^7, and of the corresponding complexes with *calf thymus* DNA was evaluated by thermal denaturation. The antiproliferative activity of all compounds was evaluated in malignant melanoma (A-375) and lung (A-549) cancer cells. The complexes show higher activity than the corresponding free ligand, and most complexes are more active than cisplatin. Compounds **1, 3, 5**, and **8** were selected for additional studies: while these complexes induce reactive oxygen species and double-strand

breaks in both cancer cells, their ability to induce cell-death by apoptosis varies. Within the set of compounds tested, **8** emerges as the most promising one, presenting low IC_{50} values, and high induction of oxidative stress and DNA damage, which eventually lead to high rates of apoptosis.

KEYWORDS

Schiff bases, anticancer, speciation, antibacterial, 8-hydoxyquinoline, copper complexes

1 Introduction

Cancer is a leading cause of death in developed countries, with a significant expense to human lives. Despite the success of platinum metallodrugs, drawbacks such as intrinsic and acquired chemoresistance, as well as unspecific action leading to toxic side effects, drive researchers towards the search for alternative and safer chemotherapeutics, which may also take advantage of their different mechanisms of action. One alternative is the use of metallodrugs in which distinct metal ions may be explored to overcome these drawbacks and take advantage of different reactivity, electronic features and redox chemistry.

Copper is a signalling metal ion involved in cell growth and proliferation. The field of cuproplasia (regulated copper-dependent cell proliferation) has just begun to be explored, but has already given proof of its importance in fighting cancer (Ge et al., 2022). It is known that during tumour growth and metastasis cancer cells have an increased need for copper since this metal ion is involved in cellular processes such as signalling, oxidative phosphorylation, cell growth, proliferation, angiogenesis and autophagy (Lelièvre et al., 2020). This may be used as a strategy to target cancer cells, and develop anticancer treatments to interrupt, deplete, or increase copper concentration in tumours.

Despite being an essential nutrient to humans, copper homeostasis must be strictly maintained. Under biological conditions, copper is mostly bound to peptides and proteins, preventing uncontrolled redox activity. Its deficiency is detrimental, but its excess results in increased cellular oxidative stress. Organic molecules which act as chelating moieties can bind and sequester metal ions, or can act as ionophores that cross the cell membrane when still bound to the metal ion and release it inside the cell (Denoyer et al., 2015). In the intracellular environment, the Cu(II) complexes can be reduced by cellular reductants such as glutathione (GSH); the formed Cu(I) complex can be re-oxidized producing reactive oxygen species (ROS), or as Cu(I) has high affinity for GSH, the release of the original ligand is also possible.

8-Hydroxyquinoline (8HQ) and its derivatives are versatile compounds and have been explored in the design of various classes of anticancer compounds, acting through different mechanisms of action (Song et al., 2015). Numerous studies provided proof of the direct relationship between the ability of these molecules to act as metal chelators and their antiproliferative activity (Prachayasittikul et al., 2013). Binding of biologically active molecules to metal ions may alter their pharmacokinetic characteristics and improve their therapeutic potential, thus the prospective synergistic effect of having the 8HQ scaffold, with known therapeutic activity (Zhai et al., 2010; Jiang et al., 2011; Oliveri et al., 2012; Prachayasittikul et al., 2013; Song et al., 2015; Oliveri and Vecchio, 2016; Gupta et al., 2021), chelated to a metal ion, with its potential for involvement in redox processes and its diversity in structure and electronic features, has been considered an attractive approach to develop therapeutic drugs (Correia et al., 2014; Ndagi et al., 2017; Pape et al., 2018; Matos et al., 2019; Ribeiro et al., 2022). For example, zinc and copper complexes of 5,7-dihalo-substituted-8-hydroxyquinolines were reported as highly cytotoxic agents against hepatoma, ovarian and non-small-cell lung human tumour cells, with IC_{50} values from 1.4 nM to 32.13 μM (Liu et al., 2013).

8-Hydroxy-2-quinolinecarbaldehyde showed promising antiproliferative results both *in vitro* and *in vivo* (Chan et al., 2013; Lam et al., 2016). Moreover, it can be used as starting material for the synthesis of new 8HQ-based ligands, which allow expanding the coordination ability of the parent 8HQ (Albrecht et al., 2005). Also, its coordination to metal ions further fosters the design and development of new anticancer agents since metal ions chelation by 8HQs has been highlighted as a key factor in their ability to induce cell death (Zhang et al., 2008; Hickey et al., 2011; Xie and Peng, 2017; Zhu et al., 2019). Barilli *et al.* reported on a family of 2-substituted-8HQs, that showed promising antiproliferative results on HeLa cervical cancer cells in the presence of iron and copper (Barilli et al., 2014). Chen and co-workers showed that Cu(II) and Ni(II) complexes with 2-((2-(pyridin-2-yl)hydrazono)methyl)quinoline-8-ol present high cytotoxic activity against seven different cancer cells. The Cu(II) compound induced caspase-dependent apoptosis and caused cancer cell cycle arrest in the S phase (Chang et al., 2016). Rigolino and co-workers (Rogolino et al., 2017) reported on a series of 8-hydroxyquinoline thiosemicarbazones and their Cu(II) and Zn(II) complexes which displayed cytostatic activity in different cancer cells, the most active Cu(II) complex showing an IC_{50} value lower than 1 μM. Ali *et al.* studied mixed ligand Cu(II) complexes with 8HQ derivatives and their antiproliferative effect in breast cancer cells (Ali et al., 2021).

Recently, we reported on a series of six 8HQ-benzohydrazones and their coordination to V(IV)O ions (Ribeiro et al., 2022). Cytotoxicity on a melanoma cell line occurred in the low micromolar range and increased generation of ROS-induced DNA damage was observed. Annexin V and Caspase 3/7 flow cytometry assays indicated cell death by apoptosis. The fluoro-substituted metal complex was identified as the one showing the highest apoptosis and induction of DNA double-strand breaks. In this report, we synthesized two new ligands and Cu(II) complexes with the full series. The Cu(II) complexes show high potential as anticancer agents. The assays performed *in vitro* regarding their chemical and biological behaviour indicate that their redox properties are, at least partly, responsible for their cytotoxic action. They can interact with GSH and ascorbic acid (AA), increasing the ROS concentration in the cells, and triggering cell defences that lead to cell death.

2 Experimental

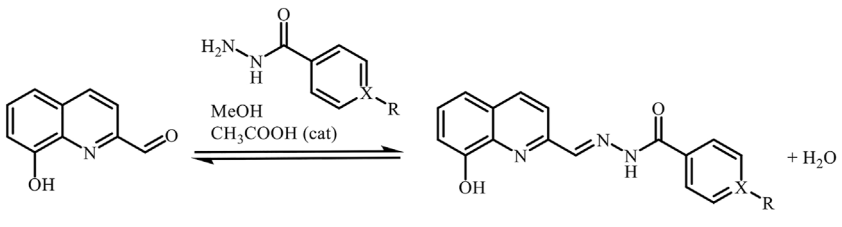
Details on the experimental part are included in Supplementary Material, section S1, and only the synthetic procedure/characterization aspects are included here.

2.1 Chemicals and apparatuses

Benzoic hydrazide (98%), 4-chlorobenzhydrazide (98%), 4-fluorobenzoic hydrazide (96%), 4-methoxybenzhydrazide (97%), *p*-toluic hydrazide (99%), and 4-aminobenzoic hydrazide (95%) were all from Aldrich, while 4-hydroxybenzhydrazide (puriss) was from Merck and isoniazid (≥99%) was from Fluka. $[Cu(AcO)_2]\cdot H_2O$ from Panreac was used as received. Dioxane (Fluka), dimethyl sulfoxide (DMSO, Riedel-de-Haën), methanol (MeOH, Riedel-de-Haën) and ethanol (EtOH, Fluka) were all analytical grade and used without further purification. 4-(2-Hydroxyethyl)-1-piperazineethanesulfonic acid (HEPES), tetrabutylammonium nitrate (TBAN), glutathione and ascorbic acid were purchased from Sigma-Aldrich in puriss quality. KCl, HCl, KOH, DMSO, EDTA and potassium hydrogenphtalate were obtained from Molar Chemicals (Hungary) and used without further purification. Milli-Q ultra-pure water was used for the preparation of all solutions. For the reactions with AA and GSH, the pH of the solutions was adjusted to 7.4 with HEPES (50 mM). $CuCl_2$ stock solution was prepared by the dissolution of $CuCl_2$ in water and the concentration was determined by complexometry. When necessary, the pH was set to the appropriate value by the addition of HCl or KOH solutions. Elemental analysis for C, H and N, were carried out on a FISONS EA 1108 CHNS-O apparatus at *Laboratório de Análises of Instituto Superior Técnico*, while ESI-MS spectra of methanolic solutions of the compounds in both positive and negative modes were measured in a 500-M Varian Ion Trap Mass Spectrometer. Proton, carbon and correlation NMR spectra were obtained on a Bruker Avance II + 300 (UltraShieldTM Magnet) spectrometer operating at 300 MHz for proton and at 75.4 MHz for carbon, at room temperature; the chemical shifts are reported in ppm using tetramethylsilane as the internal reference. A JASCO FT/IR 4100 spectrophotometer was used for recording the infra-red spectra and electronic absorption spectra (UV-Vis) were recorded ether with a Perkin Elmer Lambda 35 (in the characterization studies) or an Agilent Cary 8,454 diode array spectrophotometer (in the spectrophotometric speciation studies). UV-vis spectrophotometers were thermostated to within ±0.1°C by Haake water baths. EPR spectra were recorded at 120 K with an X-band (9.4 GHz) Bruker EMX spectrometer equipped with an HP 53150 A microwave frequency counter with the following instrumental settings: microwave frequency, 9.40–9.41 GHz; microwave power, 20 mW; time constant, 163.8 m; modulation frequency, 100 kHz; modulation amplitude, 4 G; sweep time, 335.5 s; resolution 4,096 points. Magnetization measurements as a function of temperature were performed using a SQUID magnetometer (Quantum Design MPMS). The molar magnetic susceptibility values were subtracted for diamagnetism of the constituent atoms, estimated from Pascal constants, to isolate the copper spin contribution; the corrected molar susceptibility is designated by χ_m. Software PHI (Chilton et al., 2013) was used to fit an isotropic spin Hamiltonian (exchange coupling and Zeeman effect components) to the χ_m, χ_m^{-1}, and $\chi_m T$ vs. temperature curves.

2.2 Synthesis of the ligand precursors

The synthesis of the ligand precursors was done by adapting a published procedure (Liu and Yang, 2009a) – Scheme 1. The synthesis and characterization of L^1-L^6 were described in a



	X	R
L^1	C	H
L^2	C	Cl
L^3	C	F
L^4	C	CH_3
L^5	C	OCH_3
L^6	C	OH
L^7	C	NH_2
L^8	N	-----

SCHEME 1
General scheme for the ligand precursors' syntheses. Abbreviations L^1 – L^8 represent globally all possible protonation forms of the compounds. Only when specifying a particular protonation form, the protons will be included in the abbreviation (LH_n or H_nL).

previous publication (Ribeiro et al., 2022). Briefly, the carbaldehyde was dissolved in *ca.* 10 mL of MeOH and stirred with a few drops of glacial acetic acid. The corresponding benzohydrazide was added as a solid to the previous solution and left to reflux for 6 h. When a solid started to separate from the reaction mixture, it was allowed to cool to room temperature and then in the freezer for further precipitation. The solid product was finally collected by filtration, washed with ice-cold MeOH and dried under vacuum in a desiccator over silica-gel.

Crystals of L^5 suitable for single crystal X-ray diffraction (SCXRD) were obtained from an acetone solution of the compound kept at room temperature for a few weeks.

L^7: Bright yellow solid. Yield: 62.3%. Elem. analysis for $C_{17}H_{14}N_4O_2{\cdot}0.25H_2O$ [found (calcd.)]: C, 65.5% (65.69%); H, 4.5% (4.70%); N, 18.0% (18.03%). ESI-MS *m/z* (−) 305.40 (calcd. for $[C_{17}H_{14}N_4O_2{-}H]^-$ 305.31) (+) 306.99 (calcd. for $[C_{17}H_{14}N_4O_2{+}H]^+$ 307.31). FTIR (KBr pellet, cm^{-1}) 3,441–3,318 (OH and primary amine), 3,212 (br), 3,109–3,046 (aromatic CH), 1,645 (carbonyl), 1,625 ($CN_{quinoline}$), 1,548 (imine). UV-Vis [DMSO, λ, nm (ε, $M^{-1}cm^{-1}$)] 265 (2.2×10^4), 284 (2.8×10^4), 295 (2.9×10^4), 350 (2.4×10^4).

L^8: Bright yellow solid. Yield: 71.1%. Elem. analysis for $C_{16}H_{12}N_4O_2{\cdot}0.25H_2O$ [found (calcd.)]: C, 64.8% (64.75%); H, 4.2% (4.24%); N, 18.8% (18.88%). ESI-MS *m/z* (−) 291.21 (calcd. for $[C_{16}H_{12}N_4O_2{-}H]^-$ 291.28) (+) 293.13 (calcd. for $[C_{16}H_{12}N_4O_2{+}H]^+$ 293.30). FTIR (KBr pellet, cm^{-1}) 3,445, 3,326, 3,046 (aromatic CH), 2,860 (azomethine CH), 1,679 (carbonyl), 1,549 (imine). UV-Vis [DMSO, λ, nm (ε, $M^{-1}cm^{-1}$)] 260 (2.0×10^4), 295 (2.35×10^4), 344 (1.3×10^4), 356 (1.37×10^4), 400 (1.5×10^3).

2.3 Synthesis of the copper(II) complexes

In a round-bottom flask, 0.25 mmol of the corresponding ligand precursor were suspended in *ca.* 10 ml of MeOH. A few drops of 0.1 M KOH solution in MeOH were added till pH ≈ 9. In a vial, 0.25 mmol of $[Cu(AcO)_2]{\cdot}H_2O$ were dissolved in MeOH and added to the ligand precursors' solution. The mixture was stirred for *ca.* 4 h at room temperature. In general, the ligand's suspensions presented a yellow-milky aspect and, upon the addition of the blue copper solution, the reaction mixture gained a darker colour with the formation of a reddish-brown solid. The solids were collected by filtration, washed with ice-cold MeOH and dried under vacuum in a desiccator over silica-gel.

[Cu(HL^1)(AcO)] (**1**): Red solid. Yield: 85.7%. Elem. analysis for $C_{19}H_{15}N_3O_4Cu{\cdot}H_2O$ [found (calcd.)]: C, 52.8% (52.96%); H, 3.5% (3.98%); N, 9.7% (9.75%). ESI-MS *m/z* (−) 410.96 (calcd. for $[C_{19}H_{15}N_3O_4Cu{-}H]^-$ 411.03). FTIR (KBr pellet, cm^{-1}) 3,415 (br), 3,054, 1,664 (br), 1,586, 1,512, 1,491, 1,454. UV-Vis [DMSO, λ, nm (ε, $M^{-1}cm^{-1}$)] 277 (2.18×10^4), 331 (2.3×10^4), 390 (1.2×10^4), 478 (2.4×10^3).

[Cu(L^2)]$_3$ (**2**): Red solid. Yield: 95.3%. Elem. analysis for $3{\times}\{C_{17}H_{10}N_3O_2ClCu{\cdot}0.5H_2O{\cdot}0.25MeOH\}$ [found (calcd.)]: C, 51.0% (51.25%); H, 2.7% (2.99%); N, 10.1% (10.39%). ESI-MS *m/z* (−) 385.23 (calcd. for $[C_{17}H_{10}N_3O_2ClCu{-}H]^-$ 384.97). FTIR (KBr pellet, cm^{-1}) 3,428 (br), 3,021, 1,662 (br), 1,593, 1,506, 1,487, 1,446. UV-Vis [DMSO, λ, nm (ε, $M^{-1}cm^{-1}$)] 282 (sh, 9.0×10^3), 332 (8.0×10^3), 405 (6.0×10^3), 428 (5.5×10^3), 556 (3.8×10^3).

[Cu(L^3)]$_3$ (**3**): Dark red solid. Yield: 66.2%. Elem. analysis for $3{\times}\{C_{17}H_{10}N_3O_2FCu{\cdot}1.25H_2O\}$ [found (calcd.)]: C, 52.1% (51.91%); H, 2.8% (3.20%); N, 10.5% (10.68%). ESI-MS *m/z* (−) 369.39 (calcd. for $[C_{17}H_{10}N_3O_2FCu{-}H]^-$ 369.00); *m/z* (+) 371.08 (calcd. for $[C_{17}H_{10}N_3O_2FCu + H]^+$ 371.02). FTIR (KBr pellet, cm^{-1}) 3,423 (br), 3,020, 1,662 (br), 1,601, 1,509, 1,493, 1,446. UV-Vis [DMSO, λ, nm (ε, $M^{-1}cm^{-1}$)] 280 (sh, 1.3×10^4), 327 (1.25×10^4), 394 (7.0×10^3), 425 (4.5×10^3), 535 (1.8×10^3).

[Cu(HL^4)(AcO)] (**4**): Reddish-brown solid. Yield: 74.9%. Elem. analysis for $C_{20}H_{17}N_3O_4Cu{\cdot}0.5H_2O$ [found (calcd.)]: C, 54.9% (55.11%); H, 4.0% (4.16%); N, 9.6% (9.64%). ESI-MS *m/z* (+) 367.10 (calcd. for $[C_{20}H_{17}N_3O_4Cu{-}AcO]^+$ 367.04). FTIR (KBr pellet, cm^{-1}) 3,420 (br), 3,052, 1,662 (br), 1,608, 1,518, 1,496, 1,452. UV-Vis [DMSO, λ, nm (ε, $M^{-1}cm^{-1}$)] 278 (2.35×10^4), 327 (2.0×10^4), 402 (1.25×10^4), 426 (sh, 7.0×10^3), 540 (br, 1.0×10^3).

[Cu(L^5)]$_3$ (**5**): Reddish-brown solid. Yield: 39.9%. Elem. analysis for $3{\times}\{C_{18}H_{13}N_3O_3Cu{\cdot}1.75H_2O\}$ [found (calcd.)]: C, 52.1% (52.17%); H, 3.6% (4.01%); N, 9.7% (10.14%). ESI-MS *m/z* (+) 383.08 (calcd. for $[C_{18}H_{15}N_3O_4Cu + H]^+$ 383.03). FTIR (KBr pellet, cm^{-1}) 3,386 (br), 3,046, 1,657 (br), 1,603, 1,506, 1,485, 1,449. UV-Vis [DMSO, λ, nm (ε, $M^{-1}cm^{-1}$)] 281 (1.45×10^4), 335 (1.5×10^4), 399 (9.0×10^3), 429 (sh, 6.0×10^3), 560 (br, 9.0×10^2). Crystals suitable for SCXRD were obtained after a few weeks from the mother liquor (methanol).

[Cu(L^6)]$_3$ (**6**)**:** Brown solid. Yield: 62.0%. Elem. analysis for $3{\times}\{C_{17}H_{11}N_3O_3Cu{\cdot}1.5H_2O\}$ [found (calcd.)]: C, 51.7% (51.58%); H, 3.2% (3.56%); N, 10.5% (10.61%). ESI-MS *m/z* (+) 367.23 (calcd. for $[C_{17}H_{13}N_3O_4Cu{-}H]^-$ 367.00). FTIR (KBr pellet, cm^{-1}) 3,414 (br), 3,060, 1,648 (br), 1,605, 1,524, 1,496, 1,454. UV-Vis [DMSO, λ, nm (ε, $M^{-1}cm^{-1}$)] 281 (2.25×10^4), 332 (1.9×10^4), 407 (1.2×10^4), 478 (br, 3.0×10^3), 549 (br, 1.1×10^3).

[Cu(L^7)]$_3$ (**7**)**:** Brown solid. Yield: 59.0%. Elem. analysis for $3{\times}\{C_{17}H_{12}N_4O_2Cu{\cdot}2.5MeOH\}$ [found (calcd.)]: C, 50.0% (50.06%); H, 3.9% (4.32%); N, 13.2% (13.34%). ESI-MS *m/z* (+) 399.51 (calcd. for $[C_{17}H_{12}N_4O_2Cu + MeOH + H]^+$ 400.06). FTIR (KBr pellet, cm^{-1}) 3,440 (br), 3,342, 3,216, 3,036, 1,625, 1,602, 1,523, 1,493, 1,454. UV-Vis [DMSO, λ, nm (ε, $M^{-1}cm^{-1}$)] 291 (2.9×10^4), 345 (sh, 1.55×10^4), 417 (1.3×10^4), 535 (br, 1.4×10^3).

[Cu(L^8)]$_3$ (**8**)**:** Reddish-brown solid. Yield: 52.7%. Elem. analysis for $3{\times}\{C_{16}H_{10}N_4O_2Cu{\cdot}1.75H_2O{\cdot}0.25MeOH\}$ [found (calcd.)]: C, 49.5% (49.62%); H, 3.3% (3.72%); N, 14.0% (14.24%). ESI-MS *m/z* (+) 354.08 (calcd. for $[C_{16}H_{10}N_4O_2Cu + H]^+$ 354.02). FTIR (KBr pellet, cm^{-1}) 3,435 (br), 3,047, 1,628, 1,595, 1,521, 1,499, 1,460. UV-Vis [DMSO, λ, nm (ε, $M^{-1}cm^{-1}$)] 276 (1.1×10^4), 340 (9.0×10^3), 387 (6.0×10^3), 495 (br, 1.6×10^3).

3 Results and discussion

3.1 Synthesis and characterization

The organic compounds here described are benzohydrazide-hydrazone derivatives of 8-hydroxy-2-quinolinecarbaldehyde

(8HQ-2CHO). The synthesis, solid state and solution characterization (including pK_a values) of L^1 - L^6, have already been included in a previous publication in which their binding to V(IV)O was also disclosed (Ribeiro et al., 2022). Compounds labelled L^7 and L^8 are related to the previously described compounds, corresponding to the new condensation products of 8HQ-2CHO with 4-aminobenzoic hydrazide and isoniazid, respectively. Their characterization will now be briefly described. The NMR spectra of both compounds were measured in DMSO_d_6 and the chemical shifts are in good agreement with the other compounds of this family: the imine proton appears at 7.76 and 7.96 ppm for L^7 and L^8, respectively (Supplementary Table S2 in Supplementary Material, SM) and the corresponding carbons at 136.5 and 140.2 ppm. In both compounds, the proton from the hydroxyl group is present at 10.86 ppm, while the NH is at 15.50 ppm for L^7 and 16.08 ppm for L^8. The protons from the amino benzyl substituent in L^7 resonate at 5.93 ppm.

Copper complexes are all new and were synthesized in moderate to good yields from the Cu(II) acetate salt. Elemental analysis and mass spectrometry reveal a 1:1 ligand-to-metal stoichiometric ratio for all. Interestingly, while with L^1 (no substituent) and L^4 (methyl substituted) an acetate anion from the original salt seems to be maintained in the solid-state complex, in all other complexes double deprotonation of the ligand is assumed. Regarding the substituent effects, unsubstituted or substituents with inductive charge effect, like CH_3, do not seem to be enough to doubly deprotonate the ligand. The other substituents, having a resonance effect on the aromatic ring, allow for the double deprotonation of the ligand and the coordination to the Cu(II) centre in a di-anionic form. All complexes were spectroscopically characterized, however, and due to the large number of compounds synthesized, with some techniques only selected compounds will be evaluated.

The infra-red absorption spectra (FTIR, Supplementary Figure S1) of the two new ligand precursors are consistent with those already reported for the related compounds (Ribeiro et al., 2022), presenting narrow, strong bands in the region around 3,400 cm^{-1}, assigned to OH and NH stretching vibrations. A set of bands between 1,680 and 1,500 cm^{-1}, due to vibrations of double bonds in the carbonyl and imine moieties, as well as in the aromatic rings, is observed. Coordination to copper leads to the disappearance of the sharp OH and NH bands, with a broad band appearing in the same region, probably associated with hydrogen-bonded OH and NH groups and solvent molecules retained in the solid matrixes (Supplementary Figure S2 and Supplementary Table S3). Significant changes are also registered in the region 1,680 – 1,500 cm^{-1} upon metal binding, showing the involvement of both carbonyl and nitrogen atoms of amide, imine and quinoline moieties in the metal coordination.

All compounds were characterized by UV-Vis absorption spectroscopy in DMSO (Supplementary Table S3, Supplementary Figure S3, S4). The organic compounds, L^1-L^8, show electronic transitions typical for this type of compounds, namely, $\pi \rightarrow \pi^*$ and $n \rightarrow \pi^*$ transitions (Liu and Yang, 2009b; Ribeiro et al., 2022). Cu(II) complexes spectra show the presence of the same bands, although shifted, and new ones at higher wavelengths with lower molar extinction coefficients, consistent with charge transfer bands between the ligand and the metal centre.

3.2 Structural characterization by SCXRD

Single crystals of L^5 and its Cu-complex **5** were obtained from acetone and methanol, respectively. L^5 crystallized in the triclinic system, space group P−1, and the asymmetric unit consists of two molecules of L^5 and three water molecules engaged in hydrogen bonds with the protonated phenol-O and carbonyl-O atoms (Supplementary Table S4). The compound adopts an *E* configuration relative to the hydrazonic C12=N13 linkage (Figure 1A). The C8-C12-N13-N14 dihedral angle is 179.5(7)° in L^5, while in the complex, after reorientation of the nitrogen in relation to the quinoline ring, twisting and bending of the molecule, it becomes 2.9(19)°. Complex **5** crystallizes as a trimer in the trigonal system, space group P−3. Each ligand acts as a dibasic pentadentate ligand being shared by two different pentacoordinated Cu(II) metal centres (Figure 1B). Each copper centre is surrounded by the following donors from two ligand molecules: [(O^-, N, N^2_{im}); (N^1_{im}, CO^-)]. Both carbonyl oxygen atoms are deprotonated since enolization and deprotonation of the amide group occur upon coordination, decreasing the C15-N14 bond by 0.02 Å and increasing the C15-O17 bond by 0.026 Å (Table 1) (Das et al., 2014). At the same time, the N14-C15-O17 angle increases by 5.3°, while the C16-C15-O17 and C15-N14-N13 angles decrease by 5.5° and 8.1°, respectively, due to the enolization and coordination of this part of the molecule. The three Cu(II) atoms form an equilateral triangle with a distance of 4.780(3) Å between metal centres (Figure 1C).

3.3 SQUID magnetometry

To gain further insight into the structure of the compounds in the solid-state, magnetization measurements of crystals of complex **5** were performed as a function of temperature (from 10 to 300 K, under an applied magnetic field of 0.1 T). Supplementary Figure S5 displays the thermal variation of the molar magnetic susceptibility, χ_m (= M/H, where M is the molar magnetization and H is the applied magnetic field), after diamagnetic contribution subtraction, as well as the product $\chi_m T$ vs. temperature. The $\chi_m T$ product is practically constant over all the temperature range, varying between 0.86 and 0.97 $cm^3\ K\ mol^{-1}$. Assuming the spin-only model with S = ½ (g = 2) for each of three non-interacting Cu(II) ions, the value expected for $\chi_m T$ is 1.25 $cm^3\ K\ mol^{-1}$ for all spins aligned with the external applied magnetic field (↑↑↑) and 0.38 $cm^3\ K\ mol^{-1}$ for a configuration of Cu(II) spins with total spin S = ½ (↑↓↑). The experimental result is far from these two values, indicating the need to consider interactions between the copper spins. Different approaches were considered to fit simultaneously χ_m, χ_m^{-1}, $\chi_m T$ vs. T curves, and program PHI (Chilton et al., 2013) with the isotropic Spin Hamiltonian:

$$\hat{H} = -2\left[J_{12}\left(\hat{S}_1 \cdot \hat{S}_2\right) + J_{13}\left(\hat{S}_1 \cdot \hat{S}_3\right) + J_{23}\left(\hat{S}_2 \cdot \hat{S}_3\right)\right] + \mu_B\left(g_1\hat{S}_1 + g_2\hat{S}_2 + g_3\hat{S}_3\right) \quad (1)$$

The results indicate a rather weak interaction between the three S = ½ Cu(II) ions, either pointing to a weak isotropic parallel coupling ($0<J<1$) cm^{-1} (Supplementary Figure S5), or to a weak antiparallel one, which indicates the existence of magnetic

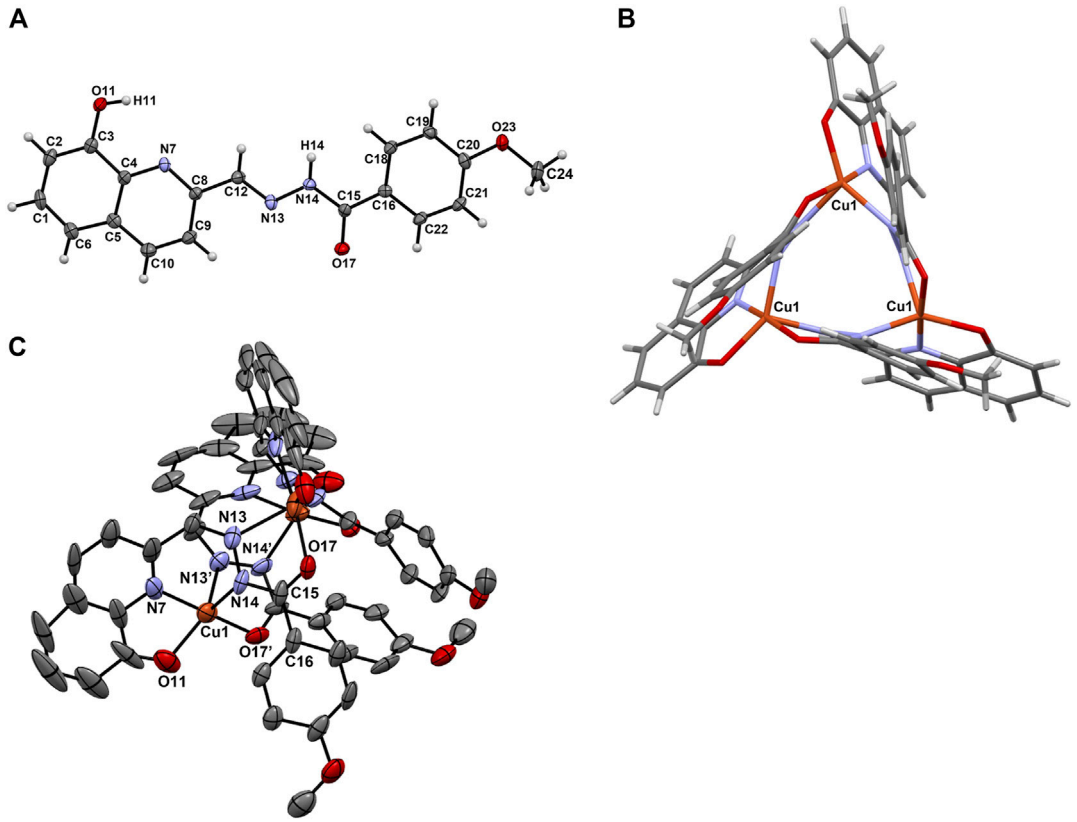


FIGURE 1
(A) ORTEP diagram of L^5 with thermal ellipsoids at 40% probability level along with the atom numbering scheme; **(B)** View of the binding in the equilateral triangle formed between the Cu(II) centres in $[Cu(L^5)]_3$ (**5**) and **(C)** ORTEP diagram of $[Cu(L^5)]_3$ with thermal ellipsoids at 40% probability level. Hydrogen atoms are omitted for clarity.

frustration among the three Cu ions ($-1 < J < 0$) cm^{-1}. The small value obtained for J can be explained by the indirect bonding between the Cu(II) ions.

Both spin configurations are consistent with three $S = ½$ Cu(II) ions at the same distance from each other, in equivalent local symmetry sites, in perfect agreement with the Cu equilateral triangle configuration obtained from crystallographic data.

3.4 EPR characterization

For selected complexes (**1**, **5**, **6** and **7**) electron paramagnetic resonance (EPR) spectra were recorded at 120 K on amorphous (polycrystalline) powder samples, and these are reported in Figure 2A. They exhibit a single isotropic feature with g values of 2.114, 2.118, 2.115 and 2.110, respectively. The spectrum recorded on the crystals of $[Cu(L^5)]_3$ (**5**) (with g = 2.112) is very similar to that collected on the polycrystalline powder of the same compound and this demonstrates that the two structures are comparable. The detected isotropic absorptions are usually the result of the dipolar interaction and intercentre exchange between neighbouring units that broaden the hyperfine lines (Rizzi et al., 2016) and support the trinuclear nature observed by SCXRD analysis. Notably, the same features have also been revealed for other trimeric Cu(II) complexes (Thakurta et al., 2008; Saha et al., 2014).

When the complexes are dissolved in DMSO, the spectral pattern does not change significantly and the signal is dominated by an almost and little resolved isotropic band (Figure 2B and Supplementary Figure S6). This suggests that the complexes partly keep their structure in the organic solution. However, in the parallel region, the hyperfine coupling between an unpaired electron and the Cu(II) nucleus is observed. The resonances of this mononuclear complex are indicated with **IIa** and coincide with those of the species that the spectrophotometric titrations interpreted as [Cu(L)] (see *infra*). Considering that in the X-ray structure of complex **5**, the L^5 ligand adopts a trinuclear coordination with the donor set (O^-, N, N^2_{im}), the resonances **IIa** could be assigned to a complex with equatorial coordination of [(O^-, N, N^2_{im}); DMSO]. In other words, in DMSO and H_2O the equilibrium (Eq. 2) is established:

$$[Cu(L)]_3 + 3\,DMSO/H_2O \rightleftarrows 3\,[Cu(L)(DMSO/H_2O)] \quad (2)$$

In DMSO the two species $[Cu(L)]_3$ and [Cu(L)(DMSO)] coexist (see Figure 2B), while in water the formation of $[Cu(L)(H_2O)]$ is favoured (see *infra*, section 3.7). The resonances at 309.4 mT, denoted by the dashed line in Figure 2B, can be considered distinctive of the presence in solution of the trinuclear complex $[Cu(L)]_3$. The comparison between the behaviour of the crystalline

TABLE 1 Selected bond lengths (Å) and angles (°) for L^5 and $[Cu(L^5)]_3$ (**5**). Atoms labelled with a prime (′) belong to a second ligand molecule coordinated to the same Cu(II) centre.

	L^5	$[Cu(L^5)]_3$ (**5**)
Bond lengths (Å)		
C3-O11	1.347(10)	1.263(18)
C4-N7	1.359(9)	
C8-N7	1.323(12)	
C12-N13	1.286(13)	1.284(11)
N13-N14	1.381(10)	1.390(10)
C15-N14	1.359(13)	1.339(12)
C15-O17	1.236(10)	1.262(12)
Cu1-O11		1.959(8)
Cu1-N7		1.940(9)
Cu1-N14		2.010(10)
Cu1-N13′		2.204(8)
Cu1-O17′		1.956(6)
Bond angles (°)		
O11-C3-C4	120.5(8)	116.6(8)
C4-N7-C8	118.4(7)	121.9(9)
C12-N13-N14	116.0(7)	119.4(7)
C15-N14-N13	118.3(7)	110.2(8)
O17-C15-N14	120.1(7)	125.4(8)
O17-C15-C16	122.3(8)	116.8(8)
C16-C15-N14	117.6(7)	117.8(9)
O11-Cu1-N7		82.5(4)
N7-Cu1-N14		86.9(4)
N14-Cu1-N13′		95.0(4)
N13′-Cu1-O17′		76.0(3)
O17′-Cu1-O11		95.5(4)
O17′-Cu1-N7		173.1(4)
O17′-Cu1-N14		98.3(4)
O11-Cu1-N14		146.0(4)
O11-Cu1-N13′		118.5(4)

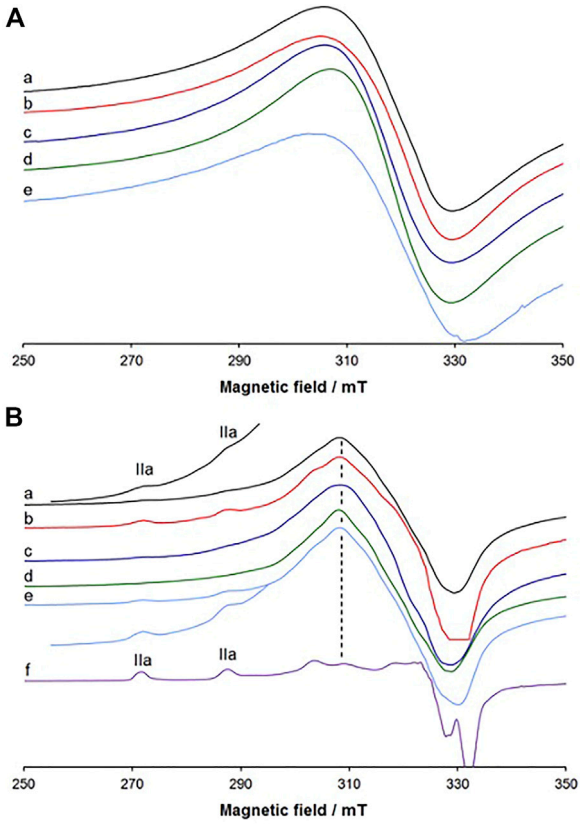


FIGURE 2
(A) X-band EPR spectra recorded at 120 K on: **(A)** polycrystalline samples of **1** (a), crystalline **5** (b), polycrystalline **5** (c), **6** (d) and **7** (e); **(B)** polycrystalline samples of **1** (a), **4** (b), polycrystalline **5** (c), crystalline **5** (d), and **6** (e) dissolved in DMSO. The region between 255.0 and 295.0 mT of the traces (a) and (e) is amplified by four and three times, respectively. In (f) the spectrum recorded in the system Cu(II)/H_2L^4 1:1 at pH 6.50 in the mixture of 80% (v/v) DMSO/H_2O is also shown. **IIa** indicates the first two parallel resonances of the complex [Cu(L)] with [(O^-, N, N^2_{im}); DMSO] binding set, and the dashed line indicates the distinctive resonance of the trinuclear species $[Cu(L)]_3$.

and polycrystalline samples is highlighted in Supplementary Figure S7, which demonstrates that the two forms behave similarly according to reaction in Eq. 2.

It is worth noting that, in contrast with other reported polynuclear Cu(II) complexes, which in organic solvents give the mononuclear units (Alves et al., 2004; Ali et al., 2005; Koval et al., 2006; Pradeep and Das, 2009; Ray et al., 2010; Thakurta et al., 2010; Shit et al., 2013), in our $[Cu(L)]_3$ complexes, the bridges are strong enough to survive to some extent in DMSO solution and are not broken; this is probably due to the nature of the bridge, disclosed by the SCXRD study, which shows a tridentate behaviour of the ligand L on one side, with the set (O^-, N, N^2_{im}), and bidentate on the other side with the donor set (N^1_{im}, CO^-). In aqueous solution we expect the predominance of the $[Cu(L)(H_2O)]$ species, as shown in the next section.

3.5 Proton dissociation processes and solubility of the ligand precursors

Investigation of the proton dissociation processes of a bioactive compound is necessary for the interpretation of the results of the biological assays since based on the pK_a values one can determine the actual chemical form and charge at a given pH. The pK_a values for the related 8-hydroxyquinoline-hydrazone conjugates ($L^{1\text{-}6}$) were already determined in our previous work (Ribeiro et al., 2022) by UV-Vis spectrophotometric titrations in 30% (v/v) DMSO/H_2O (Supplementary Table S5). For the reference compound L^1 three pK_a values could be calculated based on the spectral changes, and pK_{a1},

TABLE 2 pK_a values of the studied ligand precursors determined by UV-Vis spectrophotometric titrations in 30% (v/v) DMSO/H_2O in addition to their thermodynamic solubility ($S_{7.4}$). [t = 25.0°C; I = 0.1 M (KCl)].

	L^7	L^8	L^{1a}
R =	**NH_2**	**H, X = N**	**H**
pK_{a1}	2.37 ± 0.01	2.61 ± 0.01	2.24
pK_{a2}	9.41 ± 0.01	8.95 ± 0.01	9.51
pK_{a3}	12.25 ± 0.01	11.14 ± 0.01	11.45
$S_{7.4}$ (μM)	1.4 ± 0.1	2.1 ± 0.2	3.7

[a]Data taken from Ref. (Ribeiro et al., 2022).

pK_{a2} and pK_{a3} were assigned to the deprotonation of the quinolinium NH^+, the hydroxyl and the benzohydrazide NH moieties, respectively. The various substituents (Cl, F, CH_3, OCH_3) have negligible influence on these pK_a values. For L^6 with the additional OH group also three pK_a values were obtained, although pK_{a2} and pK_{a3} were attributed to the two hydroxyl moieties, and the pK_a of the benzohydrazide NH was fairly high (>12) (Ribeiro et al., 2022).

Both L^7 and L^8 have one more dissociable proton than L^1, namely, L^7 has the ammonium group and L^8 the pyridinium nitrogen, which may dissociate in the acidic pH range (ChemAxon, 2012). Three pK_a values could be calculated for L^7 and L^8 under the same experimental conditions and are collected in Table 2. Supplementary Figure S8 shows the spectra of L^8 and the computed molar absorbance spectra of the ligand in the different protonation states. As the deprotonation of the ammonium (L^7) and the pyridinium nitrogen (L^8) are assumed to take place in the same pH range as the quinolinium NH^+, it is not possible to assign the pK_{a1} to a particular moiety, while pK_{a2} and pK_{a3} undoubtedly belong to the hydroxyl and the benzohydrazide NH groups, respectively. Despite the relatively small differences found, L^7 and L^8 are also present in solution in their neutral H_2L form at physiological pH, similarly to ligands L^1-L^5 (Ribeiro et al., 2022), as the concentration distribution curves show in Supplementary Figure S9.

The thermodynamic solubility (*S*) of both ligand precursors was also determined at pH 7.4 in water at 0.1 M KCl ionic strength (Table 2) revealing low values, as observed for the rest of the ligand series and a minor impact of the derivatization.

3.6 Solution stability of Cu(II) complexes formed with selected ligand precursors

The complex formation processes of L^1, L^5 and L^6 with Cu(II) ions were studied by UV-Vis spectrophotometry in 30% (v/v) DMSO/H_2O using relatively low concentrations (c_L = 50–60 μM), due to the limited water solubility of the ligand precursors as well as of the Cu(II) complexes (see thermodynamic solubility data in aqueous media in Table 2 and Table 3). L^1 was selected as the simplest compound of the studied ligand series, whereas L^5 and L^6 were selected to compare with the oxidovanadium(IV) system (Ribeiro et al., 2022). The solution stability and stoichiometry of the Cu(II) complexes were determined by the evaluation of the UV-Vis spectra recorded at various pH values (representative spectra are shown for the Cu(II) − L^1 and Cu(II) − L^6 systems in Figures 3A,B and for Cu(II) − L^5 in Supplementary Figure S10A). The computed overall stability constants and pK_a values of the complexes are collected in Table 3. The formation of only mono-ligand complexes was found with $[Cu(LH)]^+$, [Cu(L)], and $[Cu(LH_{-1})]^-$ (and $[Cu(LH_{-2})]^{2-}$ in the case of L^6) compositions, and their computed molar absorbance spectra are shown in Figures 3C, D, Supplementary Figure S10B. The differences found in the intra-ligand and charge-transfer bands of these species suggest several different coordination modes; however, based on these spectra, it is difficult to judge the actual binding types, thus, EPR spectroscopic measurements were also done (*vide infra*).

In the $[Cu(LH)]^+$ species most probably the ligand coordinates *via* the (O^-, N) donor set of the 8HQ scaffold, while the benzohydrazide NH moiety is still protonated. Considering the much lower pK_a value of $[Cu(LH)]^+$ (Table 3) than that of the benzohydrazide NH of the ligand precursors (pK_{a3} in the case of L^1, L^5, and pK_{a4} in the case of L^6), upon the deprotonation of $[Cu(LH)]^+$ the binding of the benzohydrazide N^2_{im} donor atom is highly probable in the species [Cu(L)], adding to (O^-, N) donor set, also in agreement with the SCXRD structure that showed one of the ligands assuming this binding mode. It is worth noting that an equilibrium between [Cu(L)] and the trinuclear complex $[Cu(L)]_3$ (found by X-ray diffraction analysis, SQUID magnetometry and EPR spectroscopy) is possible; however, under the conditions used

TABLE 3 Overall (logβ) stability and proton dissociation (pK_a) constants of the Cu(II) complexes formed with L^1, L^5 and L^6 determined by UV-Vis spectrophotometric titrations in 30% (v/v) DMSO/H_2O in addition to their thermodynamic solubility ($S_{7.4}$) and distribution coefficients (log$D_{7.4}$) at pH 7.40 (these determined experimentally *via n*-octanol/water partitioning). [t = 25.0°C; I = 0.10 M (KCl)]. pCu (= −log[Cu(II)]) values were computed with the use of the stability constants at pH 7.4, at 1 μM Cu(II) and i) 1 μM or ii) 10 μM ligand concentrations. Formal potential values ($E_{1/2}$) vs NHE and peak separations (ΔE) measured for the Cu(II) complexes by cyclic voltammetry [see the conditions in the legend of Supplementary Figure S14].

	L^1	L^5	L^6
R =	H	OCH_3	OH
logβ $[Cu(LH)]^+$	23.41 ± 0.02	22.75 ± 0.05	16.91 ± 0.03
logβ [Cu(L)]	17.79 ± 0.02	18.26 ± 0.04	11.67 ± 0.03
logβ $[Cu(LH_{-1})]^-$	7.39 ± 0.03	7.18 ± 0.04	2.50 ± 0.03
logβ $[Cu(LH_{-2})]^{2-}$	–	–	−7.40 ± 0.04
pK_a $[Cu(LH)]^+$	5.62	4.49	5.24
pK_a [Cu(L)]	10.40	11.08	9.17
pCu [a]	8.96	9.03	7.26
pCu [b]	12.59	12.69	9.44
$S_{7.4}$ (μM) [c]	5.8 ± 0.3	<1	1.3 ± 0.1
log$D_{7.4}$	+1.9 ± 0.1	+2.4 ± 0.1	+2.0 ± 0.1
$E_{1/2}$ (mV)	+395	+377	+380
ΔE (mV)	166	144	150

[a]$c_{Cu(II)}$ = 1 μM; c_L = 1 μM.
[b]$c_{Cu(II)}$ = 1 μM; c_L = 10 μM.
[c]$S_{7.4}$ determined for complex **2**: <1 μM; **3**: <1 μM; **4**: 4.0 ± 0.2; **7**: 4.2 ± 0.1; **8**: 3.3 ± 0.3.

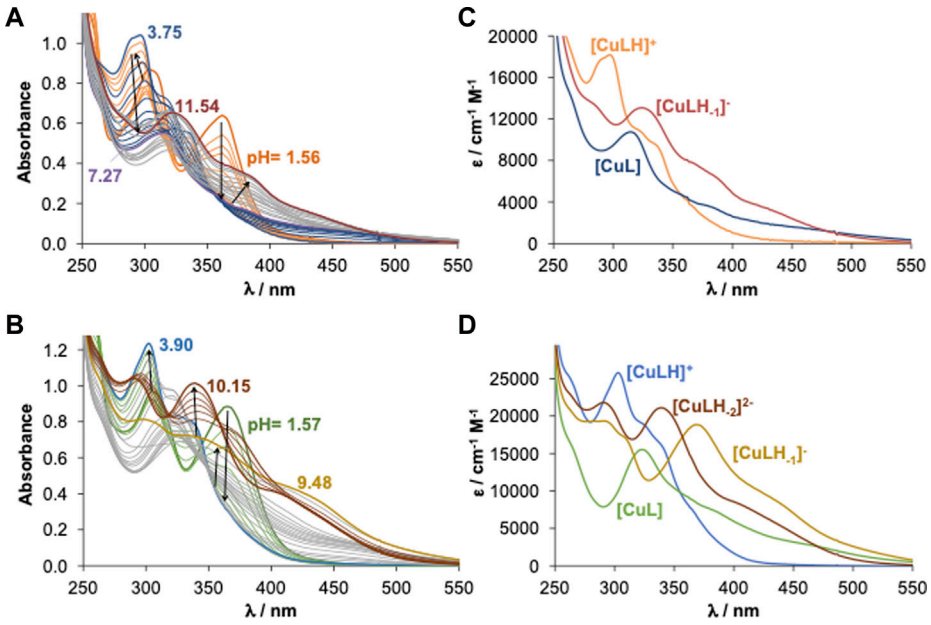


FIGURE 3
UV-Vis spectra of the **(A)** Cu(II) – L^1 (1:1) and **(B)** Cu(II) – L^6 (1:1) systems recorded at various pH values. Calculated spectra (extinction coefficients) of individual species of the **(C)** L^1 and **(D)** L^6 complexes. [$c_{Cu(II)} = c_L$ = 50 μM; pH = 1.5–11.0; t = 25.0°C; I = 0.10 M (KCl); ℓ = 1.0 cm; 30% (v/v) DMSO/H_2O].

for the UV-Vis titrations (very low concentration, presence of the weakly coordinating DMSO), the percent amount of polynuclear species is assumed to be rather low. $[Cu(LH_{-1})]^-$ is most likely a mixed hydroxido complex (=$[Cu(L)(OH)]^-$ with [(O^-, N, N^2_{im}); OH^-] binding mode) in the case of L^1 and L^5, while it is formed by the deprotonation of the additional OH group of L^6 based on the much lower pK_a of [Cu(L)]. Additionally, the development of a new band at 368 nm upon the formation of $[Cu(LH_{-1})]^-$ from [Cu(L)] also supports this suggestion (Figure 3D), which is not present in the case of L^1 and L^5. Formation of $[Cu(LH_{-2})]^{2-}$ was only found with L^6 and this species is suggested to be a mixed hydroxido species.

Concentration distribution curves (Figure 4) show that [Cu(L)] species predominate at physiological pH. To compare the Cu(II) binding ability of the studied ligands, the pCu (= –log [Cu(II)]) was computed at 1 μM metal ion concentration, and 1 and 10 μM ligand concentrations at pH 7.4, based on the obtained stability constants (Table 3). The higher pCu indicates stronger metal ion binding under the given conditions. These values reflect the similar Cu(II)-binding strength of L^1 and L^5, whereas L^6 forms somewhat lower stability complexes in comparison to the other two ligands, which suggests that the benzohydrazide N^2_{im} donor is not involved in the coordination in complex **6**. These Cu(II) complexes are the most stable species at physiological pH, with a level of dissociation at 1 μM concentration corresponding to only ca. 5% for complex **6**.

As the complex formation of ligands L^4 and L^6 was also studied with oxidovanadium(IV) the speciation data obtained here for the Cu(II) complexes were compared and detailed in the SI (Supplementary Figure S11B and its legend). It was pointed out that the binding of these ligands to Cu(II) at pH > 7 is much stronger than to oxidovanadium(IV).

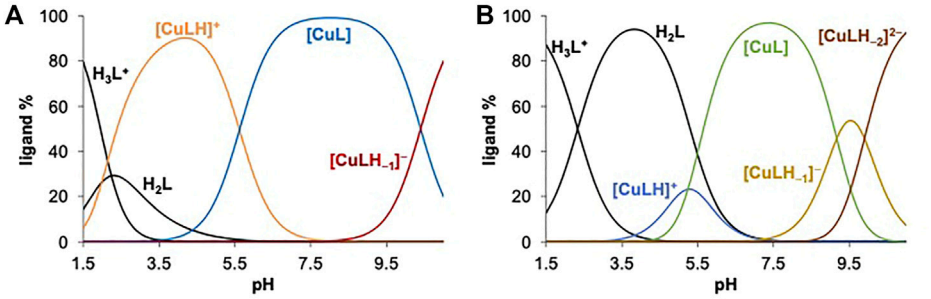


FIGURE 4
Concentration distribution curves calculated for the **(A)** Cu(II) – L^1 (1:1) and **(B)** Cu(II) – L^6 (1:1) systems. [$c_{Cu(II)} = c_L$ = 50 μM; t = 25.0°C; I = 0.10 M (KCl); 30% (v/v) DMSO/H_2O].

3.7 EPR spectra in solution

The Cu(II) binding modes in solution were studied by EPR spectroscopy at 120 K in a mixture of 80% (v/v) DMSO/H_2O in the systems containing L^4 or L^6 with molar ratio 1:1.

The spectra measured with L^6 are depicted in Figure 5, while the spin Hamiltonian parameters are listed in Table 4. The complexation starts with the formation of $[Cu(LH)]^+$ with the coordination of 8-hydroxyquinoline moiety and [(O^-, N); H_2O; H_2O] equatorial donor set. Its first three parallel resonances are indicated with **I** in Figure 5.

Upon increasing the pH, another complex is observed (**IIa** in Figure 5) with g_z = 2.273 and $|A_z|$ = 169.5 × 10^{-4} cm^{-1}. For this species, whose composition is [Cu(L)] according to the spectrophotometric data, several coordination modes could be possible: [(O^-, N, N^2_{im}); H_2O] [(O^-, N, N^1_{im}); H_2O] or [(O^-, N, N^1_{im}, CO^-)]. The values of ΔG_{aq}^{calcd} are −9.0 kcal mol^{-1}, −2.3 kcal mol^{-1}, and −3.4 kcal mol^{-1} (Supplementary Figure S12), respectively, suggesting that the donor set [(O^-, N, N^2_{im}); H_2O] is the most stable since it shows the lowest value of ΔG_{aq}^{calcd}. This is in agreement with the SCXRD structure that suggests that each Cu(II) ion is bound to the same donors from one molecule, and with the EPR spectra collected after dissolving the solid compounds in DMSO solution (see Figure 2). Moreover, the tridentate binding (O^-, N, N^2_{im}) is the only one that makes possible the bidentate coordination (N^1_{im}, CO^-) to an adjacent [Cu(L)] unit. It must be noted that [Cu(L)] predominates in solution from pH 6 to pH 8, in line with the distribution curves in Figure 4; furthermore, in the pH range of existence of [Cu(L)] the distinctive resonance of $[Cu(L)]_3$ appears (Figure 5), indicating that equilibrium in Eq. 2 happens in DMSO/H_2O mixtures as well (but is shifted towards the right), and that the species [Cu(L)] (with a water molecule that occupies the fourth metal equatorial site) and $[Cu(L)]_3$ coexist in solution. As equilibrium in Eq. 2 is not pH dependent and due to the low solubility of the complexes, individual characterization of [Cu(L)] and $[Cu(L)]_3$ by spectrophotometry is difficult (see Section 3.6).

The formation of the complex [Cu(L)] with coordination [(O^-, N, N^2_{im}); H_2O] allows also accounting for the appearance of another species at pH higher than 8.0 (**III** in Figure 5), to which the UV-Vis spectrophotometric titrations assign the stoichiometry $[Cu(LH_{-1})]^-$. It has g_z = 2.223 and $|A_z|$ = 182.0 × 10^{-4} cm^{-1}. It is plausible that this latter species is originated from [Cu(L)] upon the deprotonation of an equatorial water molecule to give the binding mode [(O^-, N, N^2_{im}); OH^-]; the coordination of an OH^- in the equatorial plane of Cu(II) ion, which replaces a water ligand, agrees well with the decrease of g_z and the increase of A_z.

Finally, the deprotonation with a pK_a of 9.90, suggested by spectrophotometry, can be ascribed to the non-coordinating phenolic–OH on the phenyl ring; since this deprotonation does not change the coordination mode, the spin Hamiltonian EPR parameters remain the same up to the formation of the hydroxo complex $[Cu(OH)_4]^{2-}$, denoted with **OH** in Figure 5, that appears in solution at pH > 13.

The behaviour of the system with L^4 is shown in Supplementary Figure S13. The first observed resonances, after the solvated Cu^{2+} ion, are those indicated by **I**. The EPR parameters are comparable to those of the similar species detected with L^6 and the same equatorial coordination mode, [(O^-, N); H_2O; H_2O], is assigned (Table 4).

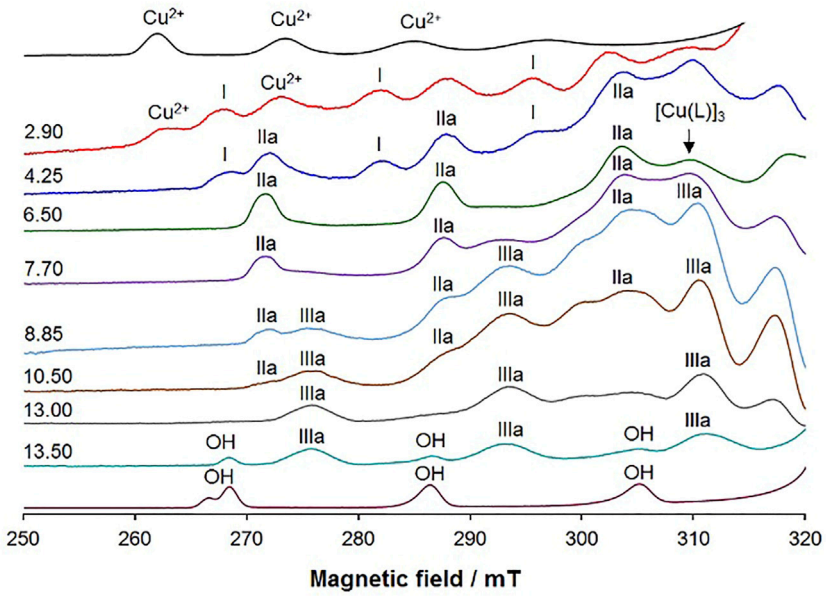


FIGURE 5
Low field region of the X-band anisotropic EPR spectra recorded as a function of pH at 120 K in a mixture DMSO/H_2O 80/20 (v/v) containing ^{63}Cu(II) and L^6 (molar ratio 1:1 and Cu(II) concentration 1.0 mM). The first and last spectra were recorded on solutions containing the solvated and hydroxide complexes. With **I** are indicated the first three equatorial resonances of $[Cu(LH)]^+$, with **IIa** of [Cu(L)] with the donor set [(O^-, N, N^2_{im}); H_2O], and with **IIIa** of $[Cu(LH_{-1})]^-$ with the donor set [(O^-, N, N^2_{im}); OH^-]. With **Cu^{2+}** and **OH** are denoted the resonances of solvated Cu^{2+} ion and hydroxo $[Cu(OH)_4]^{2-}$ complexes, taken as references. Moreover, the position of the resonance distinctive of the trinuclear complex $[Cu(L)]_3$ is also indicated by the arrow.

TABLE 4 Experimental spin Hamiltonian parameters for Cu(II) complexes formed by L^6 and L^4.

Ligand	Species	g_z	$\|A_z\|$ (^{63}Cu)[a]	Equatorial donor set
L^6 (R = OH)	$[Cu(LH)]^+$ (**I**)	2.325	152.3	[(O^-, N); H_2O; H_2O]
	[Cu(L)] (**IIa**)	2.273	169.5	[(O^-, N, N^2_{im}); H_2O]
	$[Cu(LH_{-1})]^-$ (**IIIa**)	2.223	182.0	[(O^-, N, N^2_{im}); OH^-]
L^4 (R = CH_3)	$[Cu(LH)]^+$ (**I**)	2.326	150.7	[(O^-, N); H_2O; H_2O]
	[Cu(L)] (**IIa**)	2.273	170.0	[(O^-, N, N^2_{im}); H_2O]
	[Cu(L)] (**IIb**)	2.217	183.6	[(O^-, N, N^1_{im}); H_2O] or [(O^-, N, N^1_{im}, CO^-)]
	$[Cu(LH_{-1})]^-$ (**IIIa**)	2.224	183.8	[(O^-, N, N^2_{im}); OH^-]
	$[Cu(LH_{-1})]^-$ (**IIIb**)	2.296	~174	[(O^-, N, N^1_{im}); OH^-]

[a]Hyperfine coupling constant reported in 10^{-4} cm^{-1} units.

This corresponds to $[Cu(LH)]^+$, determined also by spectrophotometric titrations.

Upon increasing the pH to ~4, two new species appear in solution, indicated by **IIa** and **IIb** in Supplementary Figure S13, which are the major species in solution, from pH 5.5 to 8.5. According to the concentration distribution curves in Figure 4, they should correspond to [Cu(L)]. The fact that the intensity ratio of the two sets of resonances remains unaltered in a wide pH range suggests that they could be isomers with the ligand in the same protonation degree and a different coordination mode around Cu(II) ion. Species **IIa** is characterized by spin Hamiltonian parameters very close to the similar species detected in the system with L^6 and after the dissolution of the solid complexes: g_z is 2.273 and $|A_z| = 170.0 \times 10^{-4}$ cm^{-1}; thus, an identical donor set [(O^-, N, N^2_{im}); H_2O], is assigned. The species **IIb** has $g_z = 2.217$ and $|A_z| = 183.6 \times 10^{-4}$ cm^{-1}. For this species, the superhyperfine coupling with ^{14}N is detected; the number of lines (five) with a ratio 1:2:3:2:1 and a mean coupling constant A_z (^{14}N) of 14.8×10^{-4} cm^{-1} indicate the binding of two nitrogen atoms to copper (Xu and Chen, 1996; Klement et al., 1999; Thakurta et al., 2008). For **IIb** two donor sets are possible: the ligand in a tetradentate mode with [(O^-, N, N^1_{im}, CO^-)] or in a tridentate mode with the binding set [(O^-, N, N^1_{im}); H_2O] without the coordination of the negative CO^- donor group. Moreover, it must be observed that, in the pH range 5.5–8.5, the presence of a minor amount of $[Cu(L)]_3$ in equilibrium with [Cu(L)] cannot be excluded (Supplementary Figure S13).

Above pH 10, two new sets of resonances are revealed, indicated by **IIIa** and **IIIb** (Supplementary Figure S13). **IIIa** has $g_z = 2.224$ and $|A_z| = 183.8 \times 10^{-4}$ cm^{-1} and is assigned to $[Cu(LH_{-1})]^-$, found by spectrophotometric titrations. Its coordination set is proposed as [(O^-, N, N^2_{im}); OH^-], similarly to what was detected with L^6. **IIIb** coexists with **IIIa**, and its detection could be explained by the transformation of [Cu(L)] with [(O^-, N, N^1_{im}); H_2O] donor set to $[Cu(LH_{-1})]^-$ with [(O^-, N, N^1_{im}); OH^-]. At pH > 12, the resonances of $[Cu(OH)_4]^{2-}$ (**OH**) are observed.

Overall, both spectroscopic techniques agree concerning the pH speciation of the system. EPR also evidences the coexistence of mononuclear and trinuclear species, which spectrophotometric techniques are unable to disclose due to the similar stoichiometry of both. At physiological pH the complexes are in the neutral form [Cu(L)] and the coordination probably involves the tridentate ligand with the donor atoms (O^-, N, N^2_{im}).

3.8 Redox properties of selected Cu(II) complexes

Copper is a redox-active metal that can react with intracellular reducing agents and induce the formation of ROS. These processes may change the redox state of the cell and impact several important metabolic and signalling processes, which in the end may lead to cell death. The redox properties of selected compounds (**1**, **5** and **6**) were investigated by cyclic voltammetry in 9:1 (v/v) DMSO:HEPES (0.01 M, pH 7.4) with 0.1 M TBAN background electrolyte. These conditions were chosen to provide sufficient solubility of the complexes (1 mM), even though the pH scaling differs from that used for the UV-Vis titrations. Normalized cyclic voltammograms are shown in Supplementary Figure S14, and the electrochemical data are collected in Table 3. Both cathodic and anodic peaks could be detected; the peak separation was fairly large indicating irreversible electrochemical processes. The formal redox potentials obtained for the complexes fall in the range 377–395 mV vs. NHE which is higher than the reported redox potentials of the GSSG/GSH (−260 mV) (Schafer and Buettner, 2001) and dehydro-L-ascorbic acid/AA (+50 mV) (Hartinger et al., 2006) redox pairs.

The direct redox reaction between the copper complexes and GSH and AA was monitored spectrophotometrically under anaerobic conditions at pH 7.4 in the presence of 5% (v/v) DMSO using a tandem cuvette. After the addition of both reducing agents (100 equiv. since a high excess is feasible under physiologically relevant conditions) to the Cu(II) complexes significant spectral changes were observed, and the redox reactions reached the equilibrium within 20 or 60 min for GSH and AA, respectively (Figure 6). These indicate the liberation of the free ligand during the redox reaction since most probably the generated Cu(I) complex dissociates and a stable Cu(I) complex is formed with GSH (or AA), which is present in a high excess when

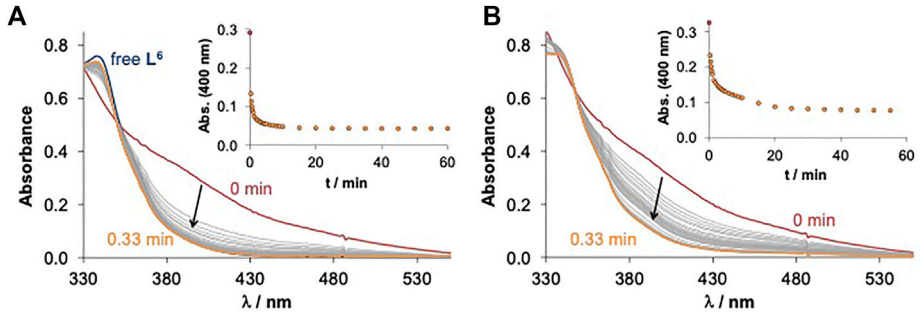


FIGURE 6
Time-dependent changes of the UV-Vis spectra of the Cu(II) complex **6** (40 μM) in the presence of 100 equiv. **(A)** GSH (4 mM) and **(B)** AA (4 mM) at pH 7.4 in 5% (v/v) DMSO/H_2O under anaerobic conditions. Inserted figures show the changes in absorbance values plotted against time at 400 nm [t = 25.0°C; I = 0.10 M (KCl)].

compared to the 8HQ-based ligand. The recorded absorbance–time curves were further analysed and changes were compared (Supplementary Figure S15). Our description of these kinetic runs is only semi-quantitative; however, it can give information about differences in reaction rates. Observed rate constants (k_{obs}) were calculated as the slope of the ln (A/A_0) vs. time plots (see an example in Supplementary Figure S16 for the reaction of complex **5** with GSH) and the calculated values are collected in Supplementary Figure S15. It can be concluded that the redox reaction is faster with GSH in all cases and the reaction rates for the complexes gave the following trend: **1** ~ **6** > **5**.

3.9 Stability in aqueous media

UV-Vis absorption spectra of the compounds were measured in an aqueous buffer (HEPES, 0.01 M, 0.1 M KCl, pH 7.4) by dilution of DMSO stock solutions (Supplementary Figures S17, S18). The complexes showed no decomposition or hydrolysis but simply a decrease in the intensity of the absorption bands, due to precipitation.

3.10 Binding to macromolecules

The analysis of the interaction of newly synthesized compounds with bovine serum albumin (BSA) is the first model in the evaluation of their transport in blood, upon administration. It was monitored by studying the quenching of albumin's fluorescence emission with increasing concentrations of the complexes (Carter and Ho, 1994). The Stern–Volmer analysis (see Supplementary Figure S19 and Supplementary Table S6) confirmed the formation of a ground state metal complex–protein adduct. Overall, data showed moderate to strong interaction between BSA and the synthesized complexes.

The ability to interact with DNA was studied for selected compounds with different techniques, which are detailed in SM (see Supplementary Figures S20–S23 and Supplementary Table S7): DNA thermal denaturation and DNA-ethidium bromide fluorescence competition assays. Overall, the results point to weak interactions of all compounds with DNA and, most likely, occurring at the external surface of the biomolecule.

To further investigate the nature of the interaction between the complexes and DNA, cell-free DNA binding assays followed by gel electrophoresis were performed. The ligand precursors had little to no effect on DNA migration except L^7 (Supplementary Figure S24A). On the other hand, incubation of plasmid DNA with complexes **1**-**8** confirmed binding to DNA and changed the supercoiling status by increasing the nicked circular form. The most dramatic response was obtained with **1**, with the highest nicking efficiency. To understand whether the induction of DNA nicks requires ROS, the samples were pre-incubated with a singlet oxygen scavenger, NaN_3. The change in DNA migration was reversed, suggesting that singlet oxygen is involved in the induced DNA nicking by the complexes. Overall, complexes **1**-**8** appear to be promising species with little activity of their corresponding ligands.

3.11 Anticancer activity of the compounds

Copper compounds were tested, along with the free ligands and cisplatin as the positive control, for their cytotoxicity on both melanoma (A-375) and lung adenocarcinoma (A-549) cell lines in the concentration range 0.78–50 μM. Following 72 h of incubation, cell viability was measured *via* sulforhodamine B (SRB) assay (Supplementary Figure S25). Compared to their free ligand counterparts, all complexes proved to be more effective/cytotoxic in both A-375 and A-549 cells, with all complexes, except **6**, exhibiting IC_{50} values <10 μM in both cell lines (Table 5, Supplementary Figure S25). Moreover, all selected Cu(II)-complexes showed higher cytotoxicity than the positive control cisplatin in both cells (except **6**). Therefore, the treatment of cells with copper compounds resulted in cell survival loss, albeit with varying efficacy.

We have previously shown that all the oxidovanadium(IV) complexes of the same ligands (L^1-L^6) were also cytotoxic at μM doses (Ribeiro et al., 2022). Since the V(IV)O complex of L^4 was not very effective for the induction of apoptosis in our previous analysis, we did not proceed further with **4**. Additionally, complex **7** does not have a V-counterpart, and its ligand is quite cytotoxic, so we excluded it

TABLE 5 IC_{50} values of selected copper complexes 1–8, free ligands (L) and cisplatin (μM ± SD) on A-375 and A-549 cell lines.

IC_{50} (μM ± SD)							
A-375				A-549			
1	2.7 ± 0.03	L^1	12.3 ± 0.5	**1**	4.2 ± 0.2	L^1	>50
2	6.5 ± 0.8	L^2	>50	**2**	9.3 ± 0.4	L^2	>50
3	5.1 ± 0.3	L^3	23.9 ± 1.5	**3**	8.9 ± 0.2	L^3	>50
4	2.0 ± 1.3	L^4	>50	**4**	3.9 ± 0.6	L^4	>50
5	3.4 ± 0.1	L^5	30.9 ± 0.3	**5**	5.1 ± 0.01	L^5	>50
6	13.6 ± 0.9	L^6	21.2 ± 0.2	**6**	16.0 ± 0.3	L^6	46.9 ± 0.8
7	5.1 ± 0.4	L^7	12.4 ± 0.2	**7**	9.3 ± 0.2	L^7	23.6 ± 0.2
8	2.8 ± 0.4	L^8	9.1 ± 1.9	**8**	5.1 ± 0.2	L^8	45.1 ± 2.7
cisplatin	11.2 ± 0.3			cisplatin	16.5 ± 3.4		

from further studies and kept complex **8,** which has lower IC_{50} values and a ligand which presents much lower activity in A-549 cells. Complex **1** was the one that showed the highest ability to target DNA (highest ΔT_m and nicking efficiency) and **3** was selected to compare the metal effect since the vanadium complex of ligand L^3 was the most effective in the melanoma cell line (Ribeiro et al., 2022). Additional reasons to choose **5** and **8** are the presence of groups with H-acceptor ability that seem to present better cytotoxic profiles than H-donor groups. Therefore compounds **1, 3, 5** and **8** were selected for additional studies.

3.12 Formation of reactive oxygen species and DNA double-strand breaks

Since reactive oxygen species appeared to be involved in the nicking activity of the complexes (Supplementary Figure S24), we investigated whether there was an increase in ROS formation in cells upon drug treatment. Dihydroethidium (DHE) is a reduced form of ethidium, after oxidation with superoxide (ROS), it is converted into 2-hydroxy ethidium, which is a chemical that emits red fluorescence and intercalates DNA. Not surprisingly, there was an induction of ROS upon treatment with all complexes under study at levels more than or at least comparable to cisplatin in A-375 cells (Figure 7A). Similar results were obtained using A-549 cells, but with much milder induction of ROS except for **8**, which remained high (Supplementary Figure S26). Complex **5** was the one which produced the milder ROS induction in these cells.

Additionally, to assess whether the ROS induction contributed to the cytotoxicity triggered by these complexes, we used a ROS scavenger, N-acetyl-cysteine (NAC), in combination with **1**, **3**, **5** or **8**. Our data showed that among the tested compounds, the cytotoxicity of **1**, **3**, and **8**, but not **5** was significantly reduced upon addition of NAC to the cell culture (Supplementary Figure S27), in both cell lines. Interestingly, NAC is known to scavenge some types of ROS (it directly interacts with $^{\bullet}OH$ and HOCl), but not others (i.e., H_2O_2, and $O_2^{\bullet-}$). Therefore, this data suggested that while **1**, **3** and **8** potentially act through generation of $^{\bullet}OH$ and HOCl, **5** seems to act through other intermediates. Indeed, it is also possible that the cytotoxicity induced by **5** is not by ROS, despite the induction observed in Figure 7A.

Indeed, we examined whether DNA nicks induced by the complexes on pure plasmid DNA would reflect in cell culture as increased DNA break formation. To test this, A-375 cells were

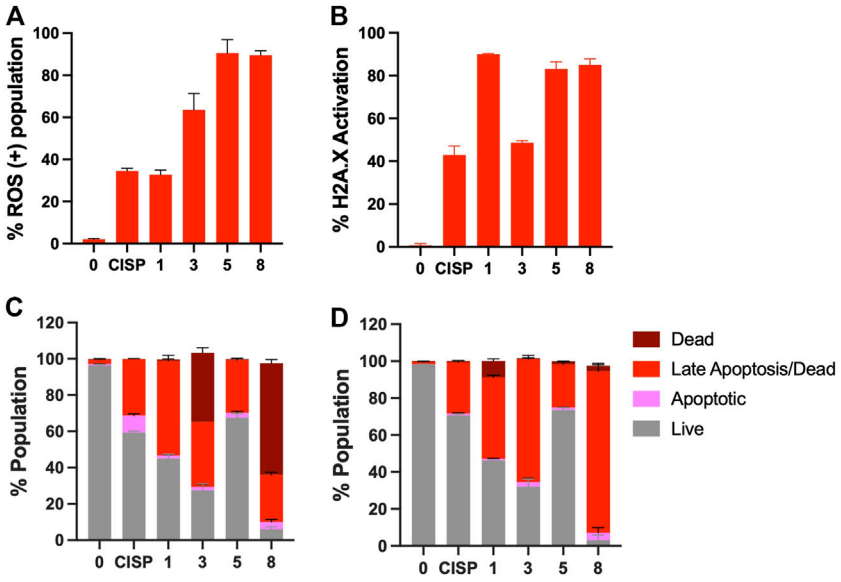


FIGURE 7
Induction of oxidative stress and DNA double strand breaks upon treatment with Cu(II) complexes. **(A)** A-375 cells were treated with cisplatin (CISP) or **1**, **3**, **5**, **8** and assessed for ROS activation *via* dihydroethidium staining. **(B)** A-375 cells were stained with antiphospho-Histone H2A.X (Ser139), Alexa Fluor® 555 and anti-Histone H2A.X, PECy5 conjugated antibodies, following cisplatin or **1**, **3**, **5**, **8** treatment. The cells were scored using Muse Cell Analyzer. Induction of apoptosis upon treatment with the Cu-complexes. Flow cytometric analyses of **(C)** Annexin V/7-AAD positivity and **(D)** Caspase 3/7 activity on A-375 cells. Cells were exposed to **1, 3, 5** and **8** or cisplatin at half inhibitory concentrations for 48 h and counted with Muse Cell Analyzer.

stained using γH2AX, which is a common marker for DSBs (Figure 7B). Mostly in accordance with ROS levels, cells were positive for γH2AX foci and **1**, **5** and **8** exhibited the highest levels of DSB induction. Interestingly, while **3** was able to induce a significant amount of ROS (60% positivity), the amount of DNA breaks did not correlate with the ROS levels, suggesting that the oxidative species generated by **3** may be more efficiently cleared in cells compared to those generated by other complexes. For complex **1** the opposite effect was observed and despite its lower ability to induce ROS formation, the DSB were the highest among the group.

3.13 Induction of apoptosis in response to Cu(II) complexes

To determine the mode of cell death, A-375 cells were incubated with the Cu complexes and cisplatin for 48 h and, induction of apoptosis was evaluated using both Annexin-V staining and activation of caspase 3/7 in response to drug treatment. While Annexin-V staining relies on the loss of plasma membrane asymmetry, caspases 3 and 7 are critical proteases, which are responsible for the cleavage of many cellular proteins. Based on the selected assays that rely on different mechanisms, cells exhibited a dramatic increase in both the early and late apoptosis population, and once again **8** appeared as the most effective drug among the complexes tested herein (Figure 7). Complex **3** also performed well. All complexes appeared to be superior to cisplatin in terms of induction of Annexin-V and caspase 3/7 staining except for **5**, which triggered apoptosis only mildly (Figures 7C, D) despite the significant increase in oxidative stress and DNA breaks (~80%, Figures 7A,B). Similar results were obtained in A-549 cells (Supplementary Figure S28).

3.14 Antibacterial activity of the ligand precursors and their Cu(II) complexes

The Cu(II) complexes selected for cell studies (**1**, **3**, **5**, **8**) as well as **6** and **7** and their ligand precursors were further investigated to reveal their antibacterial activity on the Gram-negative *Escherichia coli* and *Klebsiella pneumoniae* strains and the Gram-positive *S. aureus* using the sensitive (ATCC 25928) and the methicillin-resistant (MRSA 272123) subspecies (Supplementary Table S8). Neither the ligand precursors nor the Cu(II) salt had activity on the tested bacteria (MIC >100 μM). While complexes **6** and **8** had no measurable effect, **1** and **3** and **5** exerted effects with 50 and 100 μM MIC values against the sensitive and the methicillin-resistant subspecies, respectively. Complex **7** was found to be the most active with 12.5 μM (ATCC 25928) and 50 μM (MRSA) MIC values. It should be noted that *Staphylococcus aureus* causes a wide variety of clinical diseases, and the resistant MRSA subspecies is responsible for several community and hospital-acquired infections (Bal et al., 2017).

4 Conclusion

Several new benzoylhydrazones (L^n, n = 1–8) were synthesized as well as eight new Cu(II) complexes by reaction of the ligand precursors (L^n) with Cu(II) acetate. All compounds were characterized and the crystal and molecular structure of both L^5 and its Cu-complex were obtained by SCXRD. The trinuclear structure was established for $[Cu(L^5)]_3$, and a similar formulation is proposed for $[Cu(L^n)]_3$ (n = 2, 3, 6, 7 and 8) in the solid phase. For **1** and **4** the presence of acetate in the solid-state structural formula of the complexes, precluded the formation of the oligomer.

All compounds present low solubility in water, but they are moderately soluble in DMSO, thus most studies in solution were carried out in media also containing DMSO. Solubility, lipophilicity and proton dissociation constants were determined for all ligand precursors, and for the copper(II) complexes formed by L^1, L^5 and L^6 in 30% (v/v) DMSO/H_2O. L^1-L^8 are present in solution in their neutral H_2L form, and species $[Cu(LH)]^+$, $[Cu(L)]$ and $[Cu(LH_{-1})]^-$ form in the Cu(II) – ligand systems (L = L^1, L^5 and L^6), and also $[Cu(LH_{-2})]^{2-}$ in the case of L^6. Their formation constants were determined, and their binding modes were established by analysis of the spectrophotometric and EPR data, as well as by DFT methodologies. $[Cu(L)]$ predominates at physiological pH and the relative amount of trinuclear species is not expected to be relevant in the low μM range of concentrations.

The direct redox reactions between these copper complexes and the physiological reducing agents GSH and AA were also evaluated; it was found that the reactions producing Cu(I) species proceed faster with GSH than with AA. Our data also suggests the release of the free ligand during the redox reaction, and that probably the generated Cu(I) complex also dissociates; Cu(I) complexes probably form with GSH (or AA), which are present in a high excess when compared to the 8HQ-containing ligand.

Based on the stability constants, for the systems with L^1, L^5 and L^6 pCu values (these reflect the binding strength of the ligands) were computed at 1 μM total metal ion, and two different ligand concentrations at pH 7.4. The pCu values are in the range 7.3–9.0 (for c_L = 1 μM) and 9.4 – 12.7 (for c_L = 10 μM). These Cu(II) complexes may be considered as high stability species and the concentration distribution curves show that $[Cu(L)]$ species predominate at physiological pH.

All complexes appeared to be potent on cancer cells, albeit with varying efficiencies in cell lines of different origins. Globally this group of complexes is more active against the melanoma cells (A-375), than in lung (A-549) cancer cells, but in both cases the IC_{50} values are in the low μM range. Moreover, our data show that whilst the Cu complexes under study can induce ROS and DSBs in both melanoma and lung adenocarcinoma cells, their ability to induce an apoptotic form of cell death varies, potentially as a result of different clearance mechanisms or efficiencies within the cells. In terms of induction of apoptosis, **3** was the second most effective complex tested in our analyses, despite its lower efficiency in triggering DSBs. This was consistent with our previous report since the oxidovanadium(IV) complex of L^3 was the most effective among L^1-L^6 complexes. Considering the IC_{50} values, the ability to induce ROS formation, double-strand breaks and cell-death by apoptosis, within the set of compounds tested, **8** seems to be the most promising complex.

Having developed ligands with different substituents we tried to establish a SAR analysis and correlate chemical properties (such as solubility and logD values) with the compounds' biological activity (IC_{50} values and macromolecules' binding parameters), but in general no correlations were found. For the complexes there

seems to be some correlation between higher aqueous solubility and higher biological activity, but we do not have sufficient data to clearly state this. The forces driving the interactions and biological effects cannot be easily explained by the electronic effects of the different substituents in the ligands. The only effect clearly seen is that the presence of nitrogen atoms impacts positively the biological activity more than the presence of oxygen atoms and, concerning the presence of halogens, that the F-containing compounds are more active than those with Cl. Moreover, groups with H-donor ability seem to perform better, especially in the lung A-549 cancer cells.

Interestingly, complex **7** is the one that shows the lowest MIC values in Gram-positive bacteria *S. Aureus* subspecies ATCC 25928 (12.5 μM) and MRSA (50 μM), with complexes **1** (50 μM) and **3** and **5** (100 μM) also showing an effect in the same bacteria.

Data availability statement

The SCXRD structures presented in this study can be found in online repositories. The names of the repository/repositories and accession number(s) can be found below: https://www.ccdc.cam.ac.uk/structures/- CCDC numbers 2182647-2182648.

Author contributions

NR—Investigation: synthesis and characterization of the compounds in solid state and solution; writing of original draft of the manuscript IB and BS—Investigation: Cell studies VP—Investigation: spectrophotometric titrations and solution studies. GaS—Investigation: bacterial studies GiS—Investigation: theoretical calculations VA—Investigation: SCXRD studies LF—Investigation: magnetic studies TB—Methodology and supervision: studies with biomacromolecules (BSA and DNA) VU—Investigation: EPR studies EG—Methodology and supervision: EPR studies JC—Supervision and validation ÉE—Conceptualization, methodology and supervision: spectrophotometric titrations and solution studies CA—Conceptualization, methodology and supervision: cell studies IC—Funding acquisition, project management, conceptualization, methodology and supervision of synthesis and characterization work, writing of first draft of manuscript. All authors have read and agreed to the submited version of the manuscript.

Acknowledgments

This work was supported by Centro de Química Estrutural, which is financed by national funds from Fundação para a Ciência e Tecnologia (FCT), projects UIDB/00100/2020, UIDP/00100/2020 and LA/P/0056/2020, and Programa Operacional Regional de Lisboa 2020. We also thank project PTDC/QUI-QIN/0586/2020; NR acklowledges FCT for SFRH/BD/135797/2018 and VA for CEECIND/00283/2018 grants. This work was supported by the Portuguese-Hungarian Scientific and Technological Cooperation FCT/NKFIH 2019/2020, and TKP-2021-EGA-32 (NKFIH, Hungary). This contribution is based upon work from COST Action CA18202, NECTAR—Network for Equilibria and Chemical Thermodynamics Advanced Research, supported by COST (European Cooperation in Science and Technology). The Portuguese NMR and Mass spectrometry IST-UL are acknowledged for the access to the equipment. This work was also supported by Koç University School of Medicine (KUSOM) and the authors gratefully acknowledge use of the services and facilities of the Koç University Research Center for Translational Medicine (KUTTAM), funded by the Presidency of Turkey, Presidency of Strategy and Budget. The content is solely the responsibility of the authors and does not necessarily represent the official views of the Presidency of Strategy and Budget. GS, VU, EG thank Fondazione di Sardegna (grant FdSGarribba 2017); GS also thank MICINN' Juan de la Cierva program, FJC 2019–039135-I for the financial support. L.P. LF acknowledges financial support from Fundação para a Ciência e a Tecnologia (FCT, Portugal) through grants UIDB/04046/2020 and UIDP/04046/2020 to BioISI and research infrastructure NECL—proj. 22096.

Conflict of interest

The authors declare that the research was conducted in the absence of any commercial or financial relationships that could be construed as a potential conflict of interest.

Publisher's note

All claims expressed in this article are solely those of the authors and do not necessarily represent those of their affiliated organizations, or those of the publisher, the editors and the reviewers. Any product that may be evaluated in this article, or claim that may be made by its manufacturer, is not guaranteed or endorsed by the publisher.

Supplementary material

The Supplementary Material for this article can be found online at: https://www.frontiersin.org/articles/10.3389/fchem.2023.1106349/full#supplementary-material

References

Albrecht, M., Osetska, O., and Fröhlich, R. (2005). 2-[(8-Hydroxyquinolinyl) Methylene]Hydrazinecarboxamide: Expanding the coordination sphere of 8-hydroxyquinoline for coordination of rare-earth metal(III) ions. *Dalton Trans.* (23), 3757–3762. doi:10.1039/B507621H

Ali, A., Banerjee, S., Kamaal, S., Usman, M., Das, N., Afzal, M., et al. (2021). Ligand substituent effect on the cytotoxicity activity of two new copper(II) complexes bearing 8-hydroxyquinoline derivatives: Validated by MTT assay and apoptosis in MCF-7 cancer cell line (human breast cancer). *RCS Adv.* 11 (24), 14362–14373. doi:10.1039/d1ra00172h

Ali, M. A., Mirza, A. H., Fereday, R. J., Butcher, R. J., Fuller, J. M., Drew, S. C., et al. (2005). Synthetic, EPR spectroscopic, magnetic and X-ray crystallographic structural studies on copper(II) complexes of the tridentate N_2S donor ligand formed from 6-methyl-2-formylpyridine and S-methyldithiocarbazate (hmpsme). *Inorg. Chim. Acta* 358 (13), 3937–3948. doi:10.1016/j.ica.2005.06.063

Alves, W. A., Santos, R. HdA., Paduan-Filho, A., Becerra, C. C., Borin, A. C., and Ferreira, A. M. D. C. (2004). Molecular structure and intra- and intermolecular magnetic interactions in chloro-bridged copper(II) dimers. *Inorg. Chim. Acta* 357 (8), 2269–2278. doi:10.1016/j.ica.2004.01.004

Bal, A. M., David, M. Z., Garau, J., Gottlieb, T., Mazzei, T., Scaglione, F., et al. (2017). Future trends in the treatment of methicillin-resistant Staphylococcus aureus (MRSA) infection: An in-depth review of newer antibiotics active against an enduring pathogen. *J. Glob. Antimicrob. Resist.* 10, 295–303. Epub 2017/07/25. doi:10.1016/j.jgar.2017.05.019

Barilli, A., Atzeri, C., Bassanetti, I., Ingoglia, F., Dall'Asta, V., Bussolati, O., et al. (2014). Oxidative stress induced by copper and iron complexes with 8-hydroxyquinoline derivatives causes paraptotic death of hela cancer cells. *Mol. Pharm.* 11 (4), 1151–1163. doi:10.1021/mp400592n

Carter, D. C., and Ho, J. X. (1994). Structure of serum albumin. *Adv. Protein Chem.* 45, 153–203. Epub 1994/01/01. doi:10.1016/s0065-3233(08)60640-3

Chan, S. H., Chui, C. H., Chan, S. W., Kok, S. H. L., Chan, D., Tsoi, M. Y. T., et al. (2013). Synthesis of 8-hydroxyquinoline derivatives as novel antitumor agents. *ACS Med. Chem. Lett.* 4 (2), 170–174. doi:10.1021/ml300238z

Chang, H. Q., Jia, L., Xu, J., Zhu, T. F., Xu, Z. Q., Chen, R. H., et al. (2016). Syntheses, crystal structures, anticancer activities of three reduce Schiff base ligand based transition metal complexes. *J. Mol. Struct.* 1106, 366–372. doi:10.1016/j.molstruc.2015.11.001

ChemAxon (2012). *Marvinsketch*. Budapest, Hungary: ChemAxon.

Chilton, N. F., Anderson, R. P., Turner, L. D., Soncini, A., and Murray, K. S. (2013). PHI: A powerful new program for the analysis of anisotropic monomeric and exchange-coupled polynuclear D- and F-block complexes. *J. Comput. Chem.* 34 (13), 1164–1175. doi:10.1002/jcc.23234

Correia, I., Adao, P., Roy, S., Wahba, M., Matos, C., Maurya, M. R., et al. (2014). Hydroxyquinoline derived vanadium(IV and V) and copper(II) complexes as potential anti-tuberculosis and anti-tumor agents. *J. Inorg. Biochem.* 141, 83–93. doi:10.1016/j.jinorgbio.2014.07.019

Das, S., Dey, A., Biswas, S., Colacio, E., and Chandrasekhar, V. (2014). Hydroxide-free cubane-shaped tetranuclear [Ln_4] complexes. *Inorg. Chem.* 53 (7), 3417–3426. doi:10.1021/ic402827b

Denoyer, D., Masaldan, S., La Fontaine, S., and Cater, M. A. (2015). Targeting copper in cancer therapy: 'Copper that cancer. *Metallomics* 7 (11), 1459–1476. doi:10.1039/C5MT00149H

Ge, E. J., Bush, A. I., Casini, A., Cobine, P. A., Cross, J. R., DeNicola, G. M., et al. (2022). Connecting copper and cancer: From transition metal signalling to metalloplasia. *Nat. Rev. Cancer* 22 (2), 102–113. doi:10.1038/s41568-021-00417-2

Gupta, R., Luxami, V., and Paul, K. (2021). Insights of 8-hydroxyquinolines: A novel target in medicinal chemistry. *Bioorg. Chem.* 108, 104633. doi:10.1016/j.bioorg.2021.104633

Hartinger, C. G., Zorbas-Seifried, S., Jakupec, M. A., Kynast, B., Zorbas, H., and Keppler, B. K. (2006). From bench to bedside-preclinical and early clinical development of the anticancer agent indazolium trans-[tetrachlorobis(1*H*-indazole)ruthenate(III) (KP1019 or FFC14A). *J. Inorg. Biochem.* 100 (5-6), 891–904. Epub 2006/04/11. doi:10.1016/j.jinorgbio.2006.02.013

Hickey, J. L., Crouch, P. J., Mey, S., Caragounis, A., White, J. M., White, A. R., et al. (2011). Copper(II) complexes of hybrid hydroxyquinoline-thiosemicarbazone ligands: Gsk3 beta inhibition due to intracellular delivery of copper. *Dalton Trans.* 40 (6), 1338–1347. doi:10.1039/c0dt01176b

Jiang, H. C., Taggart, J. E., Zhang, X. X., Benbrook, D. M., Lind, S. E., and Ding, W. Q. (2011). Nitroxoline (8-hydroxy-5-nitroquinoline) is more a potent anti-cancer agent than clioquinol (5-chloro-7-iodo-8-quinoline). *Cancer Lett.* 312 (1), 11–17. doi:10.1016/j.canlet.2011.06.032

Klement, R., Stock, F., Elias, H., Paulus, H., Pelikán, P., Valko, M., et al. (1999). Copper(II) complexes with derivatives of salen and tetrahydrosalen: A spectroscopic, electrochemical and structural study. *Polyhedron* 18 (27), 3617–3628. doi:10.1016/S0277-5387(99)00291-0

Koval, I. A., Sgobba, M., Huisman, M., Lüken, M., Saint-Aman, E., Gamez, P., et al. (2006). A remarkable anion effect on the crystal packing of two analogous copper complexes from a thiophene-containing phenol-based ligand. *Inorg. Chim. Acta* 359 (12), 4071–4078. doi:10.1016/j.ica.2006.04.012

Lam, K. H., Lee, K. K., Kok, S. H., Wong, R. S., Lau, F. Y., Cheng, G. Y., et al. (2016). Antiangiogenic activity of 2-formyl-8-hydroxy-quinolinium chloride. *Biom. Pharmacother.* 80, 145–150. Epub 2016/05/03. doi:10.1016/j.biopha.2016.03.014

Lelièvre, P., Sancey, L., Coll, J-L., Deniaud, A., and Busser, B. (2020). The multifaceted roles of copper in cancer: A trace metal element with dysregulated metabolism, but also a target or a bullet for therapy. *Cancers* 12 (12), 3594. doi:10.3390/cancers12123594

Liu, Y-c., and Yang, Z-y. (2009). Synthesis, crystal structure, antioxidation and DNA binding properties of binuclear Ho(III) complexes of Schiff-base ligands derived from 8-hydroxyquinoline-2-carboxyaldehyde and four aroylhydrazines. *J. Organomet. Chem.* 694 (19), 3091–3101. doi:10.1016/j.jorganchem.2009.05.031

Liu, Y. C., Wei, J. H., Chen, Z. F., Liu, M., Gu, Y. Q., Huang, K. B., et al. (2013). The antitumor activity of zinc(II) and copper(II) complexes with 5,7-dihalo-substituted-8-quinolinoline. *Eur. J. Med. Chem.* 69, 554–563. doi:10.1016/j.ejmech.2013.08.033

Liu, Y. C., and Yang, Z. Y. (2009). Crystal structures, antioxidation and DNA binding properties of Dy(III) complexes with Schiff-base ligands derived from 8-hydroxyquinoline-2-carboxaldehyde and four aroylhydrazines. *Eur. J. Med. Chem.* 44 (12), 5080–5089. doi:10.1016/j.ejmech.2009.09.015

Matos, C. P., Yildizhan, Y., Adiguzel, Z., Pavan, F. R., Campos, D. L., Pessoa, J. C., et al. (2019). New ternary iron(III) aminobisphenolate hydroxyquinoline complexes as potential therapeutic agents. *Dalton Trans.* 48 (24), 8702–8716. doi:10.1039/c9dt01193e

Ndagi, U., Mhlongo, N., and Soliman, M. E. (2017). Metal complexes in cancer therapy – an update from drug design perspective. *Drug Des. Dev. Ther.* 11, 599–616. doi:10.2147/Dddt.S119488

Oliveri, V., Giuffrida, M. L., Vecchio, G., Aiello, C., and Viale, M. (2012). Gluconjugates of 8-hydroxyquinolines as potential anti-cancer prodrugs. *Dalton Trans.* 41 (15), 4530–4535. doi:10.1039/c2dt12371a

Oliveri, V., and Vecchio, G. (2016). 8-Hydroxyquinolines in medicinal chemistry: A structural perspective. *Eur. J. Med. Chem.* 120, 252–274. doi:10.1016/j.ejmech.2016.05.007

Pape, V. F. S., May, N. V., Gal, G. T., Szatmari, I., Szeri, F., Fulop, F., et al. (2018). Impact of copper and iron binding properties on the anticancer activity of 8-hydroxyquinoline derived mannich bases. *Dalton Trans.* 47 (47), 17032–17045. doi:10.1039/c8dt03088j

Prachayasittikul, V., Prachayasittikul, S., Ruchirawat, S., and Prachayasittikul, V. (2013). 8-Hydroxyquinolines: A review of their metal chelating properties and medicinal applications. *Drug Des. Dev. Ther.* 7, 1157–1178. Epub 2013/10/12. doi:10.2147/dddt.s49763

Pradeep, C. P., and Das, S. K. (2009). Chiral supramolecular metal-organic architectures from dinuclear copper complexes. *Polyhedron* 28 (3), 630–636. doi:10.1016/j.poly.2008.12.012

Ray, A., Mitra, S., Khalaji, A. D., Atmani, C., Cosquer, N., Triki, S., et al. (2010). Magneto-structural correlations and DFT calculations in two rare tetranuclear copper(II)-clusters with doubly phenoxo and end-on azido bridges: Syntheses, structural variations and EPR studies. *Inorg. Chim. Acta* 363 (13), 3580–3588. doi:10.1016/j.ica.2010.07.014

Ribeiro, N., Bulut, I., Pósa, V., Sergi, B., Sciortino, G., Costa Pessoa, J., et al. (2022). Solution chemical properties and anticancer potential of 8-hydroxyquinoline hydrazones and their oxidovanadium(IV) complexes. *J. Inorg. Biochem.* 235, 111932. doi:10.1016/j.jinorgbio.2022.111932

Rizzi, A. C., Neuman, N. I., González, P. J., and Brondino, C. D. (2016). EPR as a tool for study of isolated and coupled paramagnetic centers in coordination compounds and macromolecules of biological interest. *Eur. J. Inorg. Chem.* 2016 (2), 192–207. doi:10.1002/ejic.201501111

Rogolino, D., Cavazzoni, A., Gatti, A., Tegoni, M., Pelosi, G., Verdolino, V., et al. (2017). Anti-proliferative effects of copper(II) complexes with hydroxyquinoline-thiosemicarbazone ligands. *Eur. J. Med. Chem.* 128, 140–153. doi:10.1016/j.ejmech.2017.01.031

Saha, S., Sasmal, A., Roy Choudhury, C., Gómez-Garcia, C. J., Garribba, E., and Mitra, S. (2014). A new linear double phenoxide-bridged trinuclear Cu(II) Schiff base complex: Synthesis, crystallographic elucidation, magneto-structural correlation and DFT study. *Polyhedron* 69, 262–269. doi:10.1016/j.poly.2013.12.006

Schafer, F. Q., and Buettner, G. R. (2001). Redox environment of the cell as viewed through the redox state of the glutathione disulfide/glutathione couple. *Free Radic. Biol. Med.* 30 (11), 1191–1212. Epub 2001/05/23. doi:10.1016/s0891-5849(01)00480-4

Shit, S., Nandy, M., Rosair, G., Salah El Fallah, M., Ribas, J., Garribba, E., et al. (2013). A hexanuclear copper(II) Schiff base complex incorporating rare "bicapped cubane" core: Structural aspects, magnetic properties and EPR study. *Polyhedron* 52, 963–969. doi:10.1016/j.poly.2012.07.016

Song, Y., Xu, H., Chen, W., Zhan, P., and Liu, X. (2015). 8-Hydroxyquinoline: A privileged structure with a broad-ranging pharmacological potential. *MedChemComm* 6 (1), 61–74. doi:10.1039/C4MD00284A

Thakurta, S., Chakraborty, J., Rosair, G., Tercero, J., El Fallah, M. S., Garribba, E., et al. (2008). Synthesis of two new linear trinuclear Cu^{II} complexes: Mechanism of magnetic coupling through hybrid B3LYP functional and CShM studies. *Inorg. Chem.* 47 (14), 6227–6235. doi:10.1021/ic8001459

Thakurta, S., Rizzoli, C., Butcher, R. J., Gómez-García, C. J., Garribba, E., and Mitra, S. (2010). Sterically-controlled nuclearity in new copper(II) complexes with di-compartmental ligands: Formation of antiferromagnetically coupled angular trimer and mononuclear inclusion complex. *Inorg. Chim. Acta* 363 (7), 1395–1403. doi:10.1016/j.ica.2009.12.053

Xie, F., and Peng, F. Y. (2017). Anti-prostate cancer activity of 8-hydroxyquinoline-2-carboxaldehyde-thiosemicarbazide copper complexes by fluorescent microscopic imaging. *J. Fluoresc.* 27 (6), 1937–1941. doi:10.1007/s10895-017-2133-z

Xu, Y., and Chen, D. (1996). Studies of EPR and ENDOR spectra of ^{14}N and ^{15}N label bis(2-hydroxyacetophenyl ketoxime)-^{63}Cu(II) and -^{65}Cu(II) complexes in disordered system. *Appl. Magn. Reson.* 10 (1), 103–116. doi:10.1007/BF03163102

Zhai, S. M., Yang, L., Cui, Q. C., Sun, Y., Dou, Q. P., and Yan, B. (2010). Tumor cellular proteasome inhibition and growth suppression by 8-hydroxyquinoline and clioquinol requires their capabilities to bind copper and transport copper into cells. *J. Biol. Inorg. Chem.* 15 (2), 259–269. doi:10.1007/s00775-009-0594-5

Zhang, H., Thomas, R., Oupicky, D., and Peng, F. (2008). Synthesis and characterization of new copper thiosemicarbazone complexes with an ONNS quadridentate system: Cell growth inhibition, S-phase cell cycle arrest and proapoptotic activities on cisplatin-resistant neuroblastoma cells. *J. Biol. Inorg. Chem.* 13 (1), 47–55. doi:10.1007/s00775-007-0299-6

Zhu, Z-H., Hu, Q., Pan, H-L., Zhang, Y., Xu, H., Kurmoo, M., et al. (2019). Tracking the multiple-step formation of an iron(III) complex and its application in photodynamic therapy for breast cancer. *Sci. China Chem.* 62 (6), 719–726. doi:10.1007/s11426-019-9464-1

frontiers | Frontiers in Chemistry

TYPE Original Research
PUBLISHED 06 April 2023
DOI 10.3389/fchem.2023.1154219

Check for updates

OPEN ACCESS

EDITED BY
Rajni Verma,
The University of Melbourne, Australia

REVIEWED BY
Sandeep Sharma,
Guru Nanak Dev University, India
Saurabh Pathak,
Seoul National University, Republic of Korea
Komal Jain,
National Physical Laboratory (CSIR), India

*CORRESPONDENCE
Daniela Ghica,
ghica@infim.ro

SPECIALTY SECTION
This article was submitted to Nanoscience, a section of the journal Frontiers in Chemistry

RECEIVED 30 January 2023
ACCEPTED 28 March 2023
PUBLISHED 06 April 2023

CITATION
Vlaicu ID, Stefan M, Radu C, Culita DC, Radu D and Ghica D (2023), Atomic scale insight into the decomposition of nanocrystalline zinc hydroxynitrate toward ZnO using Mn^{2+} paramagnetic probes.
Front. Chem. 11:1154219.
doi: 10.3389/fchem.2023.1154219

COPYRIGHT
© 2023 Vlaicu, Stefan, Radu, Culita, Radu and Ghica. This is an open-access article distributed under the terms of the Creative Commons Attribution License (CC BY). The use, distribution or reproduction in other forums is permitted, provided the original author(s) and the copyright owner(s) are credited and that the original publication in this journal is cited, in accordance with accepted academic practice. No use, distribution or reproduction is permitted which does not comply with these terms.

Atomic scale insight into the decomposition of nanocrystalline zinc hydroxynitrate toward ZnO using Mn^{2+} paramagnetic probes

Ioana D. Vlaicu[1], Mariana Stefan[1], Cristian Radu[1,2], Daniela C. Culita[3], Dana Radu[1] and Daniela Ghica[1]*

[1]National Institute of Materials Physics, Magurele, Romania, [2]Faculty of Physics, University of Bucharest, Magurele, Romania, [3]Ilie Murgulescu Institute of Physical Chemistry, Romanian Academy, Bucharest, Romania

Layered zinc hydroxynitrate (ZHN), with the chemical formula $Zn_5(OH)_8(NO_3)_2{\cdot}2H_2O$, exhibits a range of special properties such as anion-exchange and intercalation capacity, as well as biocompatibility, making it attractive for a large variety of applications in fields from nanotechnology to healthcare and agriculture. In this study nanocrystalline ZHN doped with 1,000 ppm Mn^{2+} was prepared by two synthesis methods (coprecipitation and solid state reaction) using similar environment-friendly precursors. The complex morpho-structural [X-ray diffraction, scanning and transmission electron microscopy, textural analysis] and spectroscopic [Fourier transform infrared and electron paramagnetic resonance (EPR)] characterization of the two ZHN nanopowders showed similar crystalline structures with Mn^{2+} ions localized in the nanocrystals volume, but with differences in their morphological and textural characteristics, as well as in the doping efficiency. ZHN obtained by coprecipitation consists of larger nanoplatelets with more than two times larger specific surface area and pore volume, as well as a dopant concentration than in the ZHN sample obtained by solid state reaction. The thermal stability and the on-set of the structural phase transformation have been investigated at atomic scale with high accuracy by EPR, using Mn^{2+} as paramagnetic probes. The on-set of the ZHN structural phase transformation toward ZnO was observed by EPR to take place at 110°C and 130°C for the samples prepared by coprecipitation and solid state reaction, respectively, evidencing a manganese induced local decrease of the transformation temperature. Our results contribute to the selection of the most appropriate ZHN synthesis method for specific applications and in the development of new green, cost-effective synthesis routes for Mn^{2+} doped nano-ZnO.

KEYWORDS

zinc hydroxynitrate, nanocrystals, electron paramagnetic resonance, Mn^{2+} paramagnetic probe, morpho-structural analysis, structural phase transformation

1 Introduction

After the discovery of polymeric nanocomposite materials containing mineral clays, a considerable increase in the scientific interest for layered compounds was recorded, especially for the layered double hydroxide salts (LDHS) (Braterman et al., 2004; Oh et al., 2009). Meanwhile, the structurally similar layered hydroxide salts (LHS) exhibit the same interesting properties such as anion-exchange and intercalation capacity, which

enable their use as catalysts and matrices of functional nanocomposites with polymers. (Newman and Jones, 1999; Wypych et al., 2005; Biswick et al., 2006; Marangoni et al., 2009; Cursino et al., 2010; Machado et al., 2010; Reinoso et al., 2014; de Oliveira and Wypych, 2016; Ghotbi et al., 2018). Other applications in nanomedicine, agriculture and cosmetics are related to the biocompatibility of these layered materials, e.g., slow releasing drug delivery agents, biomolecule reservoirs, fertilizers, herbicides, sunscreens (Oh et al., 2009; Cursino et al., 2010; Li et al., 2012; Ruiz et al., 2020).

A typical representative of LHS is zinc hydroxynitrate, with molecular formula $Zn_5(OH)_8(NO_3)_2{\cdot}2H_2O$ (ZHN). One of the problems limiting the large scale use of this compound for most of these applications is its thermal stability. The thermal stability of ZHN was investigated in the past five decades by several groups and several different mechanisms for the thermal decomposition to zinc oxide (ZnO) were proposed. However, most of the studies report the same two overlapping steps for the decomposition, below 200°C or between 200°C and 320°C, depending on the synthesis or post-synthesis conditions, steps that involve the formation of intermediates like anhydrous $Zn_5(OH)_8(NO_3)_2$ and $Zn_3(OH)_4(NO_3)_2$ (Stählin and Oswald, 1971; Biswick et al., 2007; Ahmadi et al., 2013).

It is expected that the morpho-structural properties affect material's efficiency for specific applications. Therefore, it is important to establish performant and reproducible synthesis algorithms, resulting in materials with defined morpho-structural characteristics, in view of a larger scale use of ZHN. To our knowledge, there are few reports containing information on the morphology of the investigated ZHN (Hussein et al., 2009; Li et al., 2012; Reinoso et al., 2014; de Oliveira and Wypych, 2016; Ruiz et al., 2020), while the ZHN crystallinity degree and crystallite size are mentioned only by Hussein et al. (2009). No discussion is available in literature on the influence of the ZHN morpho-structural aspects on the material thermal stability and its structural phase transformation path.

Electron paramagnetic resonance (EPR) spectroscopy of lightly doped (nano)-crystals has been successfully used to investigate structural phase transformations at atomic scale using paramagnetic probing ions, resulting in a richer information at atomic level and higher accuracy than in the case of thermal analysis methods (Nistor et al., 2014). Mn^{2+} proved to be a good paramagnetic probe in zinc based compounds, due to the similar charge state and close ionic radii with the host Zn^{2+} ions (Nistor et al., 2013; Stefan et al., 2013; Ghica et al., 2014). In low concentrations (below 1% nominal concentration), the Mn^{2+} doping ions do not affect the host lattice and allow the determination with high sensitivity and accuracy of the on-set of the phase transformations (Ghica et al., 2011; Nistor et al., 2013; Ghica et al., 2019). Moreover, due to the EPR sensitivity which is much higher than that of the X-ray diffraction (XRD) technique, low concentrations of doped minority phases could be identified as well (Ghica et al., 2011; Nistor et al., 2013; Ghica et al., 2016).

In answer to all aspects and problems discussed above, we have synthesized nanostructured ZHN by two cost-effective methods, using the same environment-friendly precursors and investigated the morpho-structural properties and thermal stability of the resulting Mn-doped ZHN nanostructured powders, within an original approach. The localization of the low concentration Mn^{2+} ions and the doping efficiency in the two ZHN nano-systems, of particular interest for applications, were evaluated by EPR. The structural phase transformation was monitored at atomic scale by EPR with the Mn^{2+} probing ions, showing with high accuracy the on-set of the structural transformation toward ZnO and the differences in the two nano-systems.

The importance of this work is better evidenced in a larger context, as it opens the way to applications in a wide range of fields: i) green, cost-effective ZHN synthesis by different methods, for applications from nanotechnology to healthcare and agriculture; ii) developing new cost-effective synthesis routes for Mn^{2+} doped nano-ZnO. ZnO is one of the most intensively studied semiconductor with already a wide range of applications from nano- and/or optoelectronics to multiple bio-medical applications (Fortunato et al., 2009; Hoye et al., 2013; Verma et al., 2021). Furthermore, by doping it is possible to tailor or develop new material properties, extending the range of applications (Sharma et al., 2003; Dietl, 2010; Zhang et al., 2018; Pradhan, 2019; Popescu et al., 2020; Pradeep and Viswanatha, 2020).

2 Materials and methods

2.1 Materials synthesis

$Zn_5(OH)_8(NO_3)_2{\cdot}2H_2O$ has been synthesized by two methods, using the same precursors without any further purification: zinc nitrate hexahydrate [$Zn(NO_3)_2{\cdot}6H_2O$, from Sigma Aldrich], manganese nitrate tetrahydrate [$Mn(NO_3)_2{\cdot}4H_2O$, from Alfa Aesar] and sodium hydroxide [NaOH, from Sigma Aldrich]. The preparation procedures for the two materials, labeled ZHN_{COPP} and ZHN_{SSR} after the coprecipitation and solid state reaction methods used, are detailed below:

ZHN_{COPP}: Coprecipitation method—an aqueous solution containing zinc nitrate and manganese nitrate, in the corresponding amounts for 1,000 ppm Mn^{2+} nominal concentration, was slightly acidified with 250 mL HNO_3 (1 M) and magnetically stirred for several minutes. Afterwards, this mixture was precipitated with a strong basic solution of NaOH 2.4 M (excess was used) added slowly with a peristaltic pump, at nearly 35°C, under continuous magnetic stirring. The suspension thus obtained was allowed to age for 1 hour at the same temperature, under continuous magnetic stirring. The precipitate was collected by centrifugation and washed several times with bi-distilled water and absolute ethanol, and air dried at 60°C.

ZHN_{SSR}: Solid state reaction method—zinc nitrate hexahydrate, manganese nitrate tetrahydrate (the amount corresponding to a 1,000 ppm Mn^{2+} nominal concentration) and sodium hydroxide were thoroughly mixed and ground in an agate mortar, in a molar ratio 1:0.62, without any water or other solvents added, until a homogenous white paste was formed. The paste was collected in a beaker and was carefully washed with bi-distilled water several times. The white precipitate separated by centrifugation was air dried at 60°C.

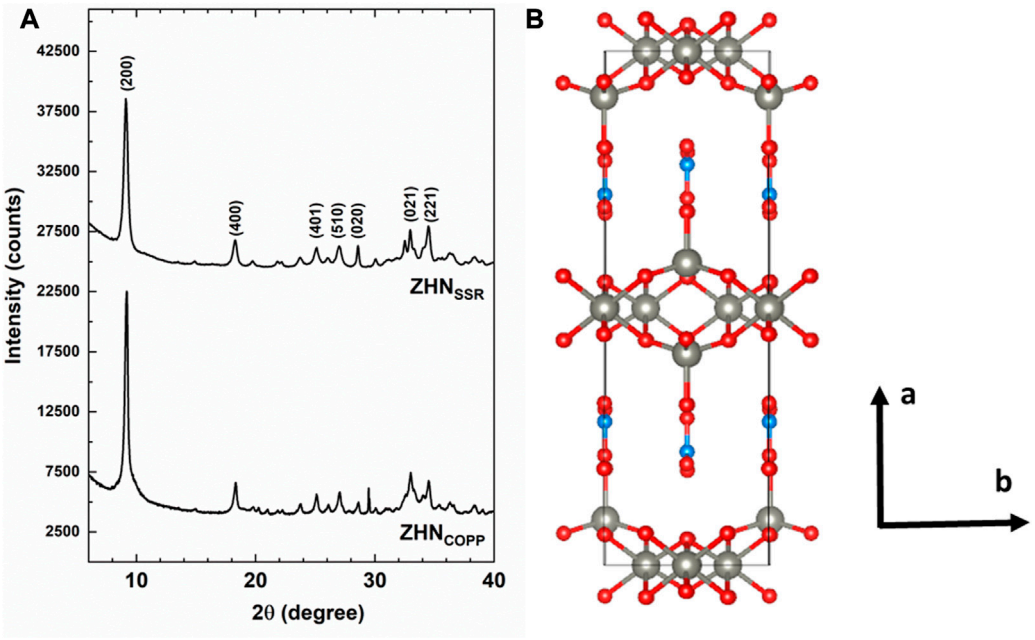


FIGURE 1
(A) XRD patterns of the as-prepared ZHN samples. Only the most intense peaks of the $Zn_5(OH)_8(NO_3)_2(H_2O)_2$ structure have been marked. **(B)** Structural model along the *c-axis* with the following color codes for atoms: grey–Zn, red–oxygen, light blue–nitrogen.

2.2 Materials characterization

XRD patterns were recorded with a Bruker D8 Advance X-ray diffractometer with Cu anode and Ni filter (λ = 0.154184 nm), in Bragg-Brentano geometry. The structural parameters of the identified crystalline phases were determined by Rietveld refinement of the experimental XRD data with the Bruker Topas v. 3 software.

Morpho-structural investigations down to the nano-scale were performed by scanning electron microscopy (SEM) and transmission electron microscopy (TEM) using Tescan Lyra III FEG and JEM 2100 electron microscopes, respectively.

Nitrogen adsorption-desorption isotherms at −196°C were recorded on a Micromeritics ASAP 2020 apparatus. Both samples were degassed at 70°C for 15 h, under vacuum, prior to N_2 adsorption. The analysis of the isotherms allowed us to determine the specific surface area (S_{BET}), according to the Brunauer–Emmett–Teller (BET) equation, the total pore volume (V_{total}) from the amount adsorbed at the relative pressure of 0.995, and the mean pore diameter using Barrett–Joyner–Halenda (BJH) method.

Fourier transform infrared (FTIR) spectra were recorded with a Spectrum BX II (Perkin Elmer) spectrometer in absorbance mode, in the 4,000 cm^{-1}–400 cm^{-1} spectral range, with 32 scans and a resolution of 4 cm^{-1}. The samples were embedded in KBr pellets with a mass-ratio sample: KBr of 1:100.

EPR investigations were performed on weighted amounts of powders inserted in calibrated pure fused silica sample tubes of 2 mm inner diameter. X (9.8 GHz) and Q (34 GHz) -band EPR measurements were performed at room temperature (RT) with the Bruker ELEXSYS E580 and E500 spectrometers, respectively. The magnetic field calibration at the sample was made with a BDPA (alpha, gamma–bisdiphenylene-beta-phenyl allyl) reference sample from Bruker, exhibiting a single EPR line with g = 2.00276. The spin Hamiltonian (SH) parameters of the observed paramagnetic centers were determined with the EASYSPIN v.5.2.28 software (Stoll and Schweiger, 2006). Isochronal annealing experiments from 100°C up to 150°C were performed in air in steps of 10°C for 10 min at each temperature in order to study the thermal evolution of the samples inside the EPR tubes. The samples were sequentially annealed at successive temperatures in a temperature stabilized (±1°C) furnace and cooled down to RT for further measurements. Small amounts of samples extracted from the EPR tube after specific annealing treatments were deposited on a zero-diffraction Si wafer (MTI Corporation, USA) for XRD measurements.

3 Results and discussion

3.1 XRD investigation

Both ZHN_{COPP} and ZHN_{SSR} samples (Figure 1A) exhibit X-ray diffractograms indexed as pure zinc hydroxynitrate hydrate–$Zn_5(OH)_8(NO_3)_2{\cdot}2H_2O$, monoclinic structure, space group C2/m, ICDD 04-011-5271. The Rietveld refinement of the experimental data resulted in similar structural parameters: a = 1.9480 nm, b = 0.6238 nm, c = 0.5517 nm, α = 90°, β = 93.28°, γ = 90°, and average crystallite size d = 25 nm ± 3 nm. A pronounced (200) texture is observed in the case of the ZHN_{COPP} sample, with a corresponding coherence distance on the [200] direction of 40 nm ± 3 nm. As the XRD texture could be associated with the shape anisotropy of the nanocrystals, this aspect has been investigated by electron microscopy in Section 3.2.

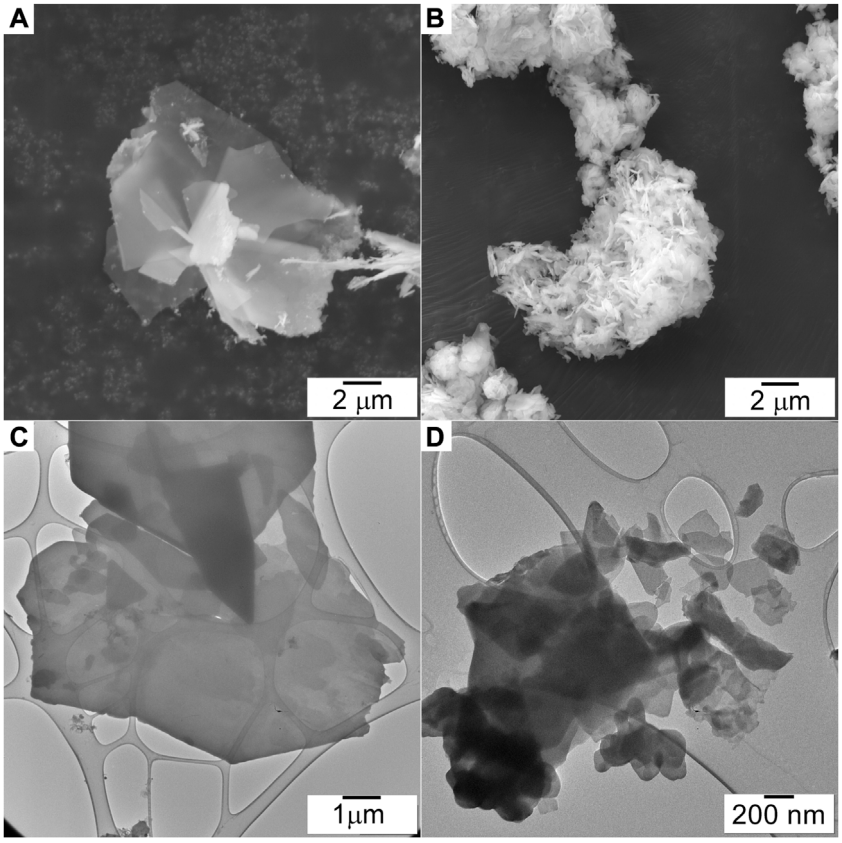


FIGURE 2
SEM images of the ZHN_{COPP} **(A)** and ZHN_{SSR} **(B)** samples. TEM images of the ZHN_{COPP} **(C)** and ZHN_{SSR} **(D)** samples.

Figure 1B presents a view along the *c*-axis of the structural model of the ZHN compound with the structural parameters from above. According to previous structural investigations (Stählin and Oswald, 1970; Stählin and Oswald, 1971; Chouillet et al., 2004; Biswick et al., 2007), the layered structure of $Zn_5(OH)_8(NO_3)_2{\cdot}2H_2O$ consists of Zn $(OH)_2$ layers with CdI_2 type structure. In each such layer one-quarter of the zinc atoms are missing from the octahedral sites, while each occupied octahedron shares its edges with four occupied and two unoccupied octahedral sites. Tetrahedrally coordinated Zn^{2+} cations are located above and below the empty octahedra, coordinated in three corners of the tetrahedron by hydroxide ions from the brucite-like layers and in the fourth corner by a water molecule. The nitrate anions are not directly coordinated to the zinc ions, being located between the sheets and lying in a plane normal to them, preserving the D_{3h} symmetry. The hydrogen bonds holding together the sheets bind the oxygen atoms of the nitrate groups with the water molecule and with two hydroxide ions of the sheet.

It should be mentioned that the presence of the Mn^{2+} ions with 0.1% nominal concentration in the host ZHN lattice would not be observable by XRD investigations. The Mn^{2+} ions have similar charge state and close ionic radii with the host Zn^{2+} ions (Shannon, 1976). The substitution of the tetrahedrally coordinated Zn^{2+} ions (crystal radius R = 0.074 nm) by the slightly larger Mn^{2+} ions (R = 0.080 nm) would produce a small expansion of the host lattice associated with lattice disorder. This would be evidenced by an increase of the lattice parameters and a decrease of the crystallite size, observed in XRD patterns as shifts in the peak positions and line broadening, respectively. However, at low dopant concentration this effect is reduced, and below 1% nominal concentration the Mn^{2+} doping ions would not affect the host lattice in a detectable way (Ghica et al., 2011; Nistor et al., 2013; Ghica et al., 2019), as confirmed by our XRD results. Instead, the localization of the Mn^{2+} ions and the annealing induced changes in their neighborhood/environment were investigated by the more sensitive EPR spectroscopy as presented in Section 3.5.

3.2 Electron microscopy investigations

SEM. SEM images of the ZHN_{COPP} and ZHN_{SSR} samples are shown in Figures 2A, B. Both samples consist of agglomerated platelets shaped as irregular polygons, randomly oriented, but with much larger dimensions (up to about 10 μm) for the ZHN_{COPP} sample. Because of this dimensional difference, the two samples observation had to be performed with different microscope magnitudes, as seen in Figure 2. Both samples display the characteristic plate-like morphology of the layered materials, with nanometric-scale thick platelets, thinner than previously reported (Li et al., 2012; de Oliveira and Wypych, 2016; Ruiz et al., 2020). A

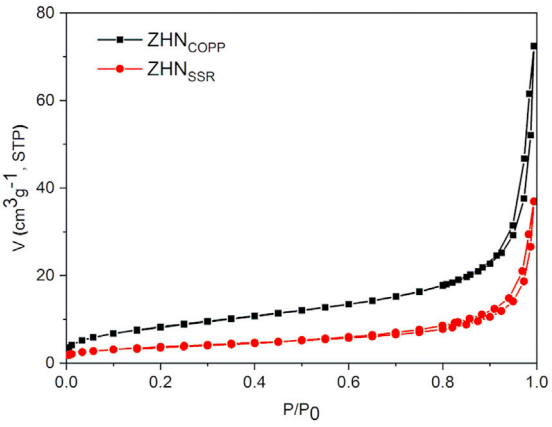


FIGURE 3
N_2 adsorption–desorption isotherms of the samples.

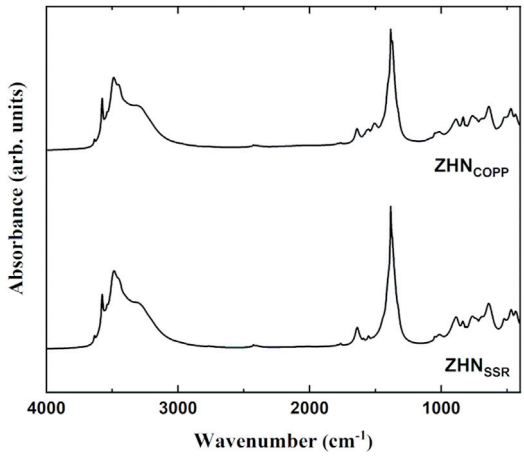


FIGURE 4
Infrared spectra of the ZHN_{COPP} and ZHN_{SSR} samples.

comparison of Figures 2A, B evidences a more pronounced shape anisotropy in the case of the ZHN_{COPP} nanocrystals, which can indeed explain the observed texture in the XRD pattern of this sample.

TEM. Low magnification TEM images of the ZHN_{COPP} and ZHN_{SSR} samples are shown in Figures 2C, D. The ZHN_{COPP} sample consists of platelets of large dimensions (few μm to above 10 μm) and much smaller thickness, proven by the fact that the carbon membrane on which particles are supported is still visible. The ZHN_{SSR} sample also consists of platelets but of smaller size, in the range of a few hundred nanometers. Both samples were very sensitive to the electron beam, a fact that hindered the analysis at higher magnification, although damage prevention measures were taken (the accelerating voltage was set to 80 kV and the images were taken using low beam intensity and longer exposure times).

3.3 Textural analysis

The N_2 adsorption–desorption isotherms of the samples are shown in Figure 3. Both isotherms can be classified as type IV according to IUPAC classification, with small hysteresis loops of H3 type (Sing et al., 1985). Both specific surface area and total pore volume are more than two times larger for the ZHN_{COPP} sample than for the ZHN_{SSR} sample, as seen in Table 1. These values are in agreement with those reported in the literature for materials obtained by similar methods (Reinoso et al., 2014). However, the mean diameter of the pores is smaller for ZHN_{COPP} than for ZHN_{SSR}. The notable differences in the specific surface area and total pore volume are correlated with the different size/morphology observed by electron microscopy for the two ZHN nanostructures. The appearance of the hysteresis loop at relative pressure values higher than 0.9 indicates the existence of relatively large pores, most likely coming from the interparticle voids.

To our knowledge, the results presented in Sections 3.1–3.3 represent the first comparative study of the morpho-structural properties of the ZHN compounds obtained by two different methods. By using two different synthesis methods, but keeping as many synthesis parameters similar as possible, i.e., the same precursors, Mn doping level, precipitate washing process and drying temperature and time, we have obtained ZHN nanostructures with notably different morphological properties. Up to now there are only a few reports on the morphology of the ZHN compounds (Hussein et al., 2009; Li et al., 2012; Reinoso et al., 2014; de Oliveira and Wypych, 2016; Ruiz et al., 2020), and no correlation was made with the synthesis method. It is generally known that the size and morphology at nanoscale are influenced by several factors, including the synthesis method itself, changes in the synthesis or post-synthesis parameters, doping, etc., and changes in just one parameter could result in a spectacular shape change (Yang et al., 2013; Ghica et al., 2016; Guria and Pradhan, 2016). In our case, it is possible that the mechanical stress due to the grinding and also the lack of any solvent (other than the water adsorbed from the atmosphere) affected the growth of the ZHN_{SSR} platelets, impeding the development of highly anisotropic shapes, while for ZHN_{COPP} the preparation conditions were more suitable for the growth of well crystallized platelets, in the solvent presence. Despite intensive research in this field, growth mechanisms are still a difficult issue even for simple oxide, sulfide, selenide structures (ZnO, ZnS, ZnSe, CdSe, etc.) and further experimental and theoretical research is required (Yang et al., 2013; Guria and Pradhan, 2016).

TABLE 1 Textural characteristics of the two ZHN samples.

Sample	S_{BET} (m^2g^{-1})	Total pore volume (cm^3g^{-1})	Average pore size (nm)
ZHN_{COPP}	30.3	0.112	14.9
ZHN_{SSR}	13.1	0.057	18.8

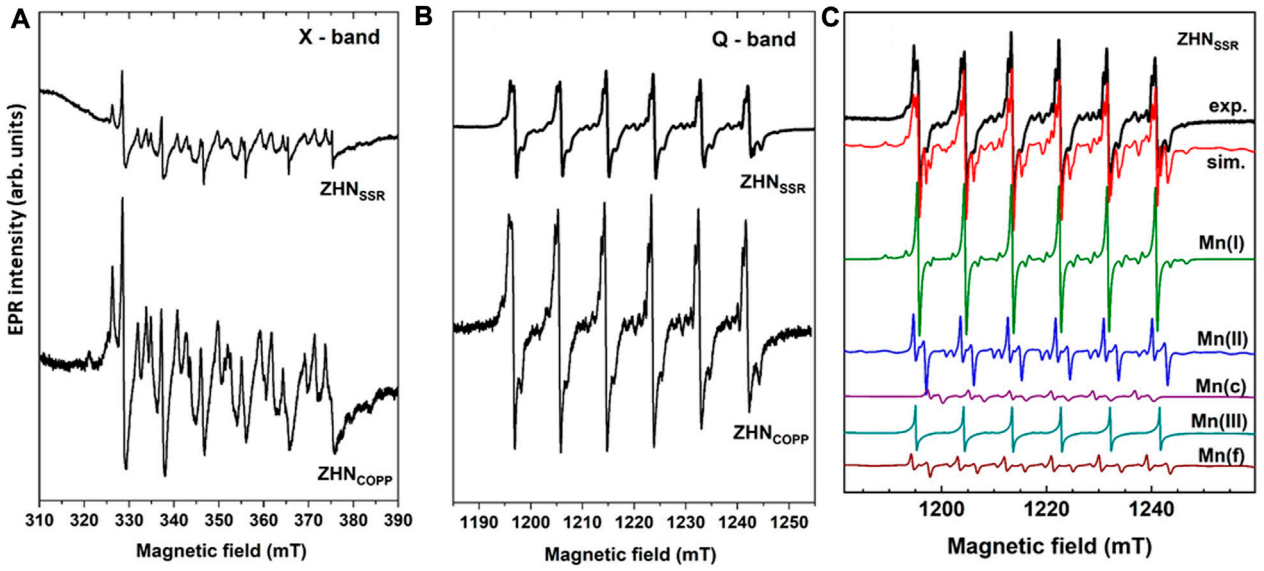


FIGURE 5
EPR spectra of the as-prepared samples measured at RT in X-band (9.86 GHz) **(A)**, and Q-band (34.12 GHz) **(B)**. **(C)** Experimental (exp.) and simulated (sim.) EPR spectrum in Q-band of the ZHN_{SSR} sample. The component spectra of the indicated centers, calculated with the SH parameters from Table 2, are presented below.

3.4 FTIR results

As it can be observed in Figure 4, the two ZHN samples exhibit the same absorption bands previously reported for the $Zn_5(OH)_8(NO_3)_2{\cdot}2H_2O$ compound (Stählin and Oswald, 1971; Chouillet et al., 2004). The sharp peak around 3,570 cm^{-1} and the intense peak at 3,400 cm^{-1} are assigned to various stretching vibrations of the O-H bonds in $Zn_5(OH)_8(NO_3)_2{\cdot}2H_2O$ (Chouillet et al., 2004). The broad band around 3,300 cm^{-1} and the peak around 1,640 cm^{-1} indicate the presence of water molecules in the interlayer space or adsorbed on the surface. For both spectra shown in Figure 4, the most intense peak at about 1,380 cm^{-1} corresponds to the ν_3 vibration (NO_2 stretching mode of a free nitrate ion), while the weak peaks around 1,050 cm^{-1} correspond to the ν_1 vibration (NO stretch of a free nitrate group), 840 cm^{-1} to the ν_2 vibration (out of plane vibration) and 720 cm^{-1} to the ν_4 vibration (NO_2 bend), characteristic to various vibration modes of the nitrate group (Stählin and Oswald, 1971; Chouillet et al., 2004). It should be emphasized that, as observed by Chouillet et al. (2004), the 1,380 cm^{-1} absorption band is not split, in agreement with $Zn_5(OH)_8(NO_3)_2{\cdot}2H_2O$ structure in which the nitrate ion is not coordinated (Louër et al., 1973). Moreover, the weak absorption band at 1,050 cm^{-1} is infrared forbidden and should not appear in a D_{3h} symmetry, but it can be present when the symmetry is slightly distorted (Gatehouse et al., 1957). Below 1,000 cm^{-1} translation and bending vibration modes for Zn-OH, nitrate group and Zn-O bonds, with low intensity, can be observed in the spectra of both compounds (Jnido et al., 2021).

3.5 EPR investigation

The EPR spectra of the as-prepared samples in the X (9.86 GHz) and Q (34.12 GHz) frequency bands, normalized for differences in mass and spectrometer parameters, are presented in Figures 5A, B, respectively. For each sample the EPR spectrum consists of several overlapping individual spectra with a characteristic six-lines hyperfine structure (better observed in Q-band, Figure 5B), attributed to Mn^{2+} ions ($S = 5/2$, $I = 5/2$) localized in different host lattices. The EPR spectra of the two samples are quite similar, with close line widths values and the spectrum of the ZHN_{COPP} sample about three times more intense than the spectrum of the ZHN_{SSR} sample. It can thus be inferred that the Mn^{2+} ions concentration is three times higher in the ZHN_{COPP} sample than in the ZHN_{SSR} sample, pointing to an enhanced doping efficiency when the coprecipitation synthesis route is used. We associate this result to the enhanced shape anisotropy of the ZHN_{COPP} nanocrystals, in agreement with theoretical studies which show that the doping efficiency varies with the morphology and size of the nanocrystals (Erwin et al., 2005; Singh et al., 2010).

The EPR spectra of the Mn^{2+} paramagnetic centers were analyzed using the following spin Hamiltonian (SH), where the first term is the electron Zeeman interaction of the $S = 5/2$ electron spin with the external magnetic field B and the second term is the hyperfine interaction of the electron spin with the $I = 5/2$ nuclear spin of the ^{55}Mn (100% abundance) isotope, responsible for the characteristic six-lines hyperfine structure. The next two terms are zero-field-splitting (*ZFS*) terms describing the interaction of the electron spin with the local crystal field, while the last term is the nuclear Zeeman interaction (Abragam and Bleaney, 1970; Stefan et al., 2014):

TABLE 2 Relative concentration, EPR parameters (*g, A, D* and *a*), broadening parameter σ (*D*) and individual peak-to-peak linewidth (ΔB) of the Mn^{2+} centers in the ZHN samples.

Sample	Center/relative concentration	*g*	*A* [10^{-4} cm^{-1}]	*D* [10^{-4} cm^{-1}]	*a* [10^{-4} cm^{-1}]	σ (*D*) [%*D*]	Δ*B* [mT]
ZHN_{SSR}	Mn(I)/22%	2.0011 ± 0.0002	−84.7 ± 0.2	−18 ± 2	9 ± 2	-	0.6
	Mn(II)/53%	2.0009 ± 0.0002	−85.5 ± 0.5	225 ± 5	0	4 ± 1	0.3
	Mn(c)/5%	2.0012 ± 0.0001	−74.0 ± 0.5	−240 ± 5	-	11 ± 1	0.3
	Mn(III)/3%	2.0011 ± 0.0001	−87.5 ± 0.2	-	-	-	0.15
	Mn(f)/17%	2.0013 ± 0.0001	−84.0 ± 0.5	−270 ± 5	-	5 ± 1	0.3
ZHN_{COPP}	Mn(I)/39%	2.0011 ± 0.0002	−84.7 ± 0.2	−18 ± 2	9 ± 2	-	0.65
	Mn(II)/61%	2.0009 ± 0.0002	−85.5 ± 0.5	225 ± 5	0	6 ± 1	0.5

$$H = \mu_B \mathbf{S}\cdot\mathbf{g}\cdot\mathbf{B} + \mathbf{S}\cdot\mathbf{A}\cdot\mathbf{I} + \frac{a}{6}\left[\left(S_x^4 + S_y^4 + S_z^4\right) - \frac{1}{5}S(S+1)\left(3S^2+3S-1\right)\right] + D\left[S_z^2 - \frac{1}{3}S(S+1)\right] - \mu_N g_N \mathbf{B}\cdot\mathbf{I}$$

For nanostructured materials, the contribution of random strains and lattice disorder is very important, producing a variation in the local crystal field at the paramagnetic ion sites, both in magnitude and orientation, reflected in the broadening of the individual EPR line width. This line broadening is reproduced in the lineshape simulation of the experimental spectra by including a statistical distribution of the axial *ZFS*-parameter value *D*, described by the corresponding standard deviation σ(*D*) (Stefan et al., 2013). The EPR parameters (*g, A, D, a*) of the Mn^{2+} centers, σ(*D*) and individual linewidth (Δ*B*), as determined by simulation and fitting of the Q-band spectrum of the ZHN_{SSR} sample are presented in Table 2. The Mn(I) and Mn(II) centers correspond to Mn^{2+} ions in ZHN, while the Mn(III) centers are Mn^{2+} ions localized in a $Zn_3(OH)_4(NO_3)_2$ phase (Ghica et al., 2019). Mn(c) corresponds to Mn^{2+} ions in crystalline ZnO (Stefan et al., 2013), while Mn(f) is associated to traces of doped precursor. The simulated Q-band spectrum of the ZHN_{SSR} sample with all the above mentioned contributions (Table 2) is presented in Figure 5C. The relative concentrations of the Mn^{2+} centers in the respective hosts, given in Table 2 with an accuracy of ±2%, are proportional to the integrated intensities of the associated spectra. Thus, in the ZHN_{SSR} sample, the concentration of the Mn^{2+} ions in traces of ZnO and precursors is much lower than the concentration of the Mn^{2+} ions in ZHN. On the other hand, the EPR spectrum of the ZHN_{COPP} sample shows that the Mn^{2+} ions are localized substitutionally only in the two Zn^{2+} sites from ZHN.

The observation of the Mn^{2+} ions in a crystalline phase of ZnO in the ZHN_{SSR} EPR spectrum, with a relative concentration of 5%, lead us to check for the possible presence of ZnO peaks in the XRD patterns of both samples. This minority phase would not be distinguishable in diffractograms, as the corresponding XRD peaks with very low intensities are hidden under the main peaks of the ZHN phase. The Rietveld refinement performed by including ZnO alongside $Zn_5(OH)_8(NO_3)_2{\cdot}2H_2O$ resulted in a better fit of the diffractograms and allowed the identification of traces (1%–2%) of ZnO hexagonal phase (space group P63mc, ICDD 01-070-8070) with average crystallite size of ~15 nm in both samples.

The spectral parameters of the two Mn-related centers [Mn(I) and Mn(II)] in ZHN are similar in both samples and correspond to the ones reported by Ghica et al. (2019), indicating the presence of the Mn doping ions in the sample volume for both synthesis methods. Along with the structural investigations, this result shows similar structural quality at atomic scale of both ZHN nano-systems obtained by the two synthesis methods, even though ZHN_{SSR} contains traces of precursor phases.

The thermal decomposition of both ZHN samples has been investigated by EPR using the Mn doping ions as paramagnetic probes. Their EPR spectra after isochronal annealing experiments up to 150°C are represented in Figures 6A, B, where only the first three hyperfine transitions at low-field are displayed for simplicity. At temperatures above 100°C the Mn(I) and Mn(II) EPR spectra become weaker, and new centers are formed. The thermal evolution of the Mn^{2+} centers reflects the evolution of their host material, namely, the decomposition of ZHN and the formation of new phases. A notable increase in the intensity of the EPR spectrum of Mn(c) (Mn^{2+} ions in ZnO nanocrystals) appears at 110°C for the ZHN_{COPP} sample, and at 130°C for the ZHN_{SSR} sample. We should mention that a similar EPR investigation of the thermal decomposition of crystalline $Zn(OH)_2$ showed the on-set of the formation of nanocrystallline ZnO at 120°C (Nistor et al., 2013b). We note that in the ZHN_{COPP} sample, the Mn(III) centers are formed only above 100°C. For both samples the Mn(III) centers decrease in intensity with the annealing temperature increase, being hardly visible at 150°C (Figures 6A, B). For an easier observation of the evolution of the Mn^{2+} spectra from Figure 6A, B we have marked the first hyperfine transition at low-field of the Mn^{2+} centers with a green rectangle for all zinc hydroxynitrate compounds [Mn(I) and Mn(II) in $Zn_5(OH)_8(NO_3)_2{\cdot}2H_2O$ and Mn(III) in $Zn_3(OH)_4(NO_3)_2$], and with a dark red rectangle for ZnO.

After isochronal annealing up to 150°C, the EPR spectra of both samples show mostly the Mn(c) paramagnetic center, meaning that almost all Mn^{2+} ions are localized in the volume of the ZnO phase. However, the corresponding XRD patterns of both samples consist of a mixture of two different crystalline phases: $Zn_3(OH)_4(NO_3)_2$ and ZnO (Figure 6C), with an enhanced transformation towards ZnO in the case of the ZHN_{SSR} sample. It can thus be concluded that the transformation of ZHN into ZnO is initiated at lower temperatures in the sample regions containing manganese than in the pure ones, independent of the synthesis routes, as further

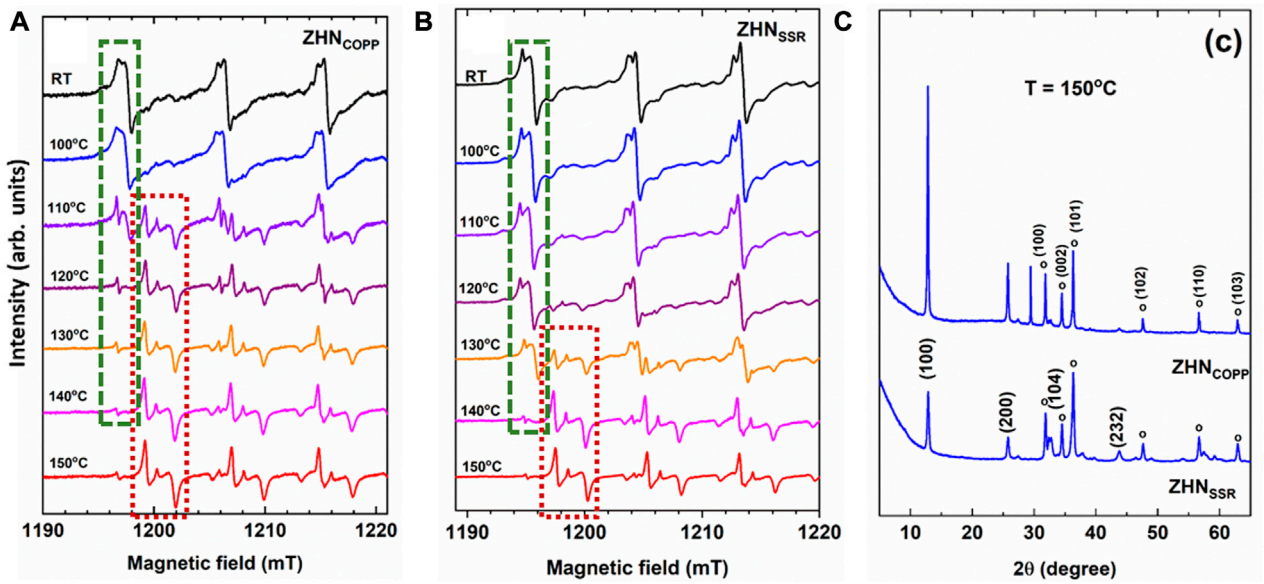


FIGURE 6
Detailed view of the EPR spectra of the Mn^{2+} ions in the ZHN_{COPP} **(A)**, and ZHN_{SSR} **(B)** samples, as-prepared (RT) and isochronally annealed (10 min at each indicated temperature). Only the first three hyperfine transitions at low-field are displayed for simplicity. Transformation of the Mn^{2+} centers in the zinc hydroxynitrate phases into Mn^{2+} centers in ZnO is evidenced with green and dark red dotted lines, respectively, only for the first hyperfine transition, where these centers do not overlap. **(C)** XRD patterns of both samples after isochronal annealing up to 150°C. The ZnO phase is marked with open circles and indexed in the upper pattern, while the $Zn_3(OH)_4(NO_3)_2$ phase is indexed in the lower pattern.

explained. The doping process can be used to change or modulate the morpho-structural properties of nanostructured materials, as the doping ions could influence the nanocrystals growth, affecting both the size and morphology, and even induce structural phase transformations or decomposition toward different compounds (Erwin et al., 2005; Ghica et al., 2016; Guria and Pradhan, 2016; Pradhan, 2019). In a previous report, Ghica et al. (2016) have shown that in the case of the Zn $(OH)_2$ compound, the minute addition of Mn^{2+} ions (1 ppm) re-directed the coprecipitation synthesis toward Mn-doped ZnO instead of Mn-doped Zn $(OH)_2$. It was suggested that this effect could be driven by a coordinative hindrance suffered by Mn^{2+}, which in most compounds assumes an octahedral coordination, when substituting for Zn^{2+} in a site tetrahedrally coordinated by four $(OH)^-$ ligands. As mentioned in Section 3.1, there are two cationic sites in the ZHN compound: One with Zn^{2+} ions octahedrally coordinated by six $(OH)^-$ groups and one with Zn^{2+} ions tetrahedrally coordinated by three $(OH)^-$ groups and one water molecule. It is possible that the Mn^{2+} ions substituting for Zn^{2+} ions in tetrahedral sites could favor the transformation into ZnO by a similar mechanism. The tetrahedrally coordinated sites could thus become nucleation sites for ZnO at a lower temperature than in the undoped material. In our previous study of ZnO nanostructures obtained by coprecipitation followed by annealing (Ghica et al., 2019), we have observed that the transformation of ZHN into ZnO was initiated at lower temperatures in the sample regions containing manganese than in the pure ones. As shown in the present work, the ZHN to ZnO transformation at a lower temperature at the Mn^{2+} sites takes place for both ZHN compounds with different morphologies obtained by two different synthesis methods. This effect is thus the result of the doping process itself, and not dependent on the synthesis method.

On the other hand, the difference in the onset temperature for the phase transformation in the two nanostructured ZHN samples (110°C for ZHN_{COPP} and 130°C for ZHN_{SSR}) is related to their different size and morphology resulted from the specific synthesis method used. This correlation has been detailed in the last paragraph of Section 3.3, following the morpho-structural analysis. Although both ZHN samples have the same nominal doping level, the EPR study has shown that the concentration of the substitutional Mn^{2+} ions is higher in the ZHN_{COPP} sample, therefore providing more nucleation sites for ZnO in the ZHN_{COPP} sample than in the ZHN_{SSR} sample. This result can also explain the lower onset temperature for the transformation into ZnO in the ZHN_{COPP} sample than in the ZHN_{SSR} sample.

Our result points to a more convenient lower temperature synthesis of ZnO nanocrystals by thermal decomposition of ZHN obtained either by coprecipitation or solid state reaction, when ZHN is doped with Mn^{2+} ions. This subject deserves further investigation, towards the identification of new cost-effective synthesis routes of Mn^{2+} doped nano-ZnO. Doping in general and Mn^{2+} doping specifically in the case of nanostructured ZnO can modulate/enhance material properties for different applications (Sharma et al., 2003; Kittilstved and Gamelin, 2006; Dietl, 2010; Hoye et al., 2013; Jiang et al., 2018; Martínez-Carmona et al., 2018; Zhang et al., 2018; Pradhan, 2019; Popescu et al., 2020; Pradeep and Viswanatha, 2020) as a function of the dopant concentration and localization. However, the synthesis of nanostructured doped ZnO is not trivial, as shown by the still not-resolved issues regarding the control and uniformity of the dopant distribution and solubility, agglomeration and formation of minority phases, all depending on

the synthesis method and procedures. Thermal decomposition at low temperatures of Mn^{2+} doped ZHN promises to be a good method to obtain uniformly doped ZnO nanocrystals.

To summarize, a comparison of the two synthesis routes for ZHN seems to incline the balance in favor of the coprecipitation route. The two samples have similar structure and crystallite size, the dopant Mn^{2+} ions are easily incorporated in the host lattices, but the coprecipitation sample has a higher doping efficiency. However, the solid state reaction method has the non-negligible advantage of a cleaner and simpler process, with less reactants involved, and a higher thermal stability of the as-prepared ZHN sample.

4 Conclusion

Nanocrystalline $Zn_5(OH)_8(NO_3)_2{\cdot}2H_2O$ (ZHN), doped with a small amount of Mn^{2+} ions, was prepared by two different synthesis routes, coprecipitation and solid state reaction using the same environment-friendly reactants. The resulting nanocrystalline samples have distinct morpho-structural and textural properties, clearly influenced by the synthesis method. While in both cases the structure and crystallite size are similar, the sample obtained by coprecipitation exhibits much larger platelets with specific surface area and total pore volume more than two times larger than in the case of the sample obtained by solid state reaction. From the analysis of the EPR spectra we determined that the Mn^{2+} dopant ions are localized substitutionally in the Zn^{2+} sites of the host lattice in both samples. The concentration of the Mn^{2+} ions is three times higher in the coprecipitation sample, showing that this synthesis route ensures an enhanced doping efficiency. The on-set of the ZHN structural phase transformation toward ZnO was observed by EPR at 110°C and 130°C for the samples synthesized by coprecipitation and solid state reaction, respectively. A comparison of the EPR results with the structural and compositional XRD results showed that the Mn^{2+} dopant ions promote the local transformation of ZHN into ZnO at lower temperatures. This is the first detailed investigation of the decrease in the ZHN to ZnO transformation temperature initiated by the Mn^{2+} doping.

Our results provide a basis for the selection of the appropriate synthesis method for nanocrystalline ZHN suitable for the envisaged application in nanotechnology, healthcare or agriculture and for the development of new green, cost-effective synthesis routes of Mn^{2+} doped nano-ZnO.

Data availability statement

The original contributions presented in the study are included in the article/supplementary material, further inquiries can be directed to the corresponding author.

Author contributions

DG and IV conceptualized the project and were in charge of overall planning. All authors performed experiments, analyzed and interpreted data and contributed to discussions. DG, IV, and MS drafted the manuscript with support from all authors. All authors have read and agreed to the published version of the manuscript.

Funding

This work is funded by the Core Program of the National Institute of Materials Physics, granted by the Romanian Ministry of Research, Innovation and Digitalization through the Project PC1-PN23080101. The fee for open access publication was supported from the project 35PFE/2021, funded by the Romanian Ministry of Research, Innovation and Digitization.

Conflict of interest

The authors declare that the research was conducted in the absence of any commercial or financial relationships that could be construed as a potential conflict of interest.

Publisher's note

All claims expressed in this article are solely those of the authors and do not necessarily represent those of their affiliated organizations, or those of the publisher, the editors and the reviewers. Any product that may be evaluated in this article, or claim that may be made by its manufacturer, is not guaranteed or endorsed by the publisher.

References

Abragam, A., and Bleaney, B. (1970). *Electron paramagnetic resonance of transition ions*. Oxford: Clarendon Press.

Ahmadi, S. J., Hosseinpour, M., Javadi, F., and Tayebee, R. (2013). Optimization study on formation and decomposition of zinc hydroxynitrates to pure zinc oxide nanoparticles in supercritical water. *Ind. Eng. Chem. Res.* 52, 1448–1454. doi:10.1021/ie3026218

Biswick, T., Jones, W., Pacuła, A., Serwicka, E., and Podobinski, J. (2007). The role of anhydrous zinc nitrate in the thermal decomposition of the zinc hydroxy nitrates Zn5(OH)8(NO3)2·2H2O and ZnOHNO3·H2O. *J. Sol. State Chem.* 180, 1171–1179. doi:10.1016/j.jssc.2007.01.012

Biswick, T., Jones, W., Pacuła, A., and Serwicka, E. (2006). Synthesis, characterisation and anion exchange properties of copper, magnesium, zinc and nickel hydroxy nitrates. *J. Sol. State Chem.* 179, 49–55. doi:10.1016/j.jssc.2005.09.040

Braterman, P. S., Xu, Z. P., and Yarberry, F. (2004). "Layered double hydroxide (LDHs)," in *Handbook of layered materials*. Editors S. M. Auerbach, K. A. Carrado, and P. K. Dutta (New York: Marcel Dekker), 373–474. doi:10.1201/9780203021354.ch8

Chouillet, C., Krafft, J. M., Louis, C., and Lauron-Pernot, H. (2004). Characterization of zinc hydroxynitrates by diffuse reflectance infrared spectroscopy – structural modifications during thermal treatment. *Spectrochim. Acta, Part A* 60, 505–511. doi:10.1016/S1386-1425(03)00255-5

Cursino, A. C. T., da Costa Gardolinski, J. E. F., and Wypych, F. (2010). Intercalation of anionic organic ultraviolet ray absorbers into layered zinc hydroxide nitrate. *J. Colloid Interface Sci.* 347, 49–55. doi:10.1016/j.jcis.2010.03.007

de Oliveira, H. B., and Wypych, F. (2016). Evaluation of layered zinc hydroxide nitrate and zinc/nickel double hydroxide salts in the removal of chromate ions from solutions. *J. Solid State Chem.* 243, 136–145. doi:10.1016/j.jssc.2016.08.019

Dietl, T. (2010). A ten-year perspective on dilute magnetic semiconductors and oxides. *Nat. Mater* 9, 965–974. doi:10.1038/nmat2898

Erwin, S. C., Zu, L., Haftel, M. I., Efros, A. L., Kennedy, T. A., and Norris, D. J. (2005). Doping semiconductor nanocrystals. *Nature* 436, 91–94. doi:10.1038/nature03832

Fortunato, E., Gonçalves, A., Pimentel, A., Barquinha, P., Gonçalves, G., Pereira, L., et al. (2009). Zinc oxide, a multifunctional material: From material to device

applications. *Appl. Phys. A Mat. Sci. Process.* 96, 197–205. doi:10.1007/s00339-009-5086-5

Gatehouse, B. M., Livingstone, S. E., and Nyholm, R. S. (1957). 847. Infrared spectra of some nitrato-co-ordination complexes. *J. Chem. Soc.*, 4222–4225. doi:10.1039/JR9570004222

Ghica, D., Nistor, S. V., Nistor, L. C., Stefan, M., and Mateescu, C. D. (2011). Structural phase transformations in annealed cubic ZnS nanocrystals. *J. Nanopart. Res.* 13 (9), 4325–4335. doi:10.1007/s11051-011-0379-y

Ghica, D., Stefan, M., Ghica, C., and Stan, G. E. (2014). Evaluation of the segregation of paramagnetic impurities at grain boundaries in nanostructured ZnO films. *ACS Appl. Mat. Interfaces* 6, 14231–14238. doi:10.1021/am5035329

Ghica, D., Vlaicu, I. D., Stefan, M., Maraloiu, V. A., Joita, A. C., and Ghica, C. (2019). Tailoring the dopant distribution in ZnO:Mn nanocrystals. *Sci. Rep.* 9, 6894. doi:10.1038/s41598-019-43388-z

Ghica, D., Vlaicu, I. D., Stefan, M., Nistor, L. C., and Nistor, S. V. (2016). On the agent role of Mn2+ in redirecting the synthesis of Zn(OH)2 towards nano-ZnO with variable morphology. *RSC Adv.* 6 (108), 106732–106741. doi:10.1039/c6ra23065b

Ghotbi, M. Y., Javanmard, A., and Soleimani, H. (2018). Three dimensional metal/N-doped nanoplate carbon catalysts for oxygen reduction, the reason for using a layered nanoreactor. *Sci. Rep.* 8, 3404. doi:10.1038/s41598-018-21782-3

Guria, A. K., and Pradhan, N. (2016). Doped or not doped: Ionic impurities for influencing the phase and growth of semiconductor nanocrystals. *Chem. Mat.* 28, 5224–5237. doi:10.1021/acs.chemmater.6b02009

Hoye, R. L. Z., Musselman, K. P., and MacManus-Driscoll, J. L. (2013). Research update: Doping ZnO and TiO2 for solar cells. *Apl. Mater* 1, 060701. doi:10.1063/1.4833475

Hussein, M. Z. b., Ghotbi, M. Y., Yahaya, A. H., and Abd Rahman, M. Z. (2009). The effect of polymers onto the size of zinc layered hydroxide salt and its calcined product. *Solid State Sci.* 11, 368–375. doi:10.1016/j.solidstatesciences.2008.06.006

Jiang, J., Pi, J., and Cai, J. (2018). The advancing of zinc oxide nanoparticles for biomedical applications. *Bioinorg. Chem. Appl.* 2018, 1–18. doi:10.1155/2018/1062562

Jnido, G., Ohms, G., and Viöl, W. (2021). Deposition of zinc oxide coatings on wood surfaces using the solution precursor plasma spraying process. *Coatings* 11 (2), 183. doi:10.3390/coatings11020183

Kittilstved, K. R., and Gamelin, D. R. (2006). Manipulating polar ferromagnetism in transition-metal-doped ZnO: Why manganese is different from cobalt (invited). *J. Appl. Phys.* 99, 08M112. doi:10.1063/1.2167638

Li, P., Xu, Z. P., Hampton, M. A., Vu, D. T., Huang, L., Rudolph, V., et al. (2012). Control preparation of zinc hydroxide nitrate nanocrystals and examination of the chemical and structural stability. *J. Phys. Chem. C* 116, 10325–10332. doi:10.1021/jp300045u

Louër, M., Louër, D., and Grandjean, D. (1973). Etude structurale des hydroxynitrates de nickel et de zinc. I. Classification structurale. *Acta Cryst. B* 29, 1696–1703. doi:10.1107/S0567740873005285

Machado, G. S., Arízaga, G. G. C., Wypych, F., and Nakagaki, S. (2010). Immobilization of anionic metalloporphyrins on zinc hydroxide nitrate and study of an unusual catalytic activity. *J. Catal.* 274, 130–141. doi:10.1016/j.jcat.2010.06.012

Marangoni, R., Ramos, L. P., and Wypych, P (2009). New multifunctional materials obtained by the intercalation of anionic dyes into layered zinc hydroxide nitrate followed by dispersion into poly(vinyl alcohol) (PVA). *J. Colloid Interface Sci.* 330, 303–309. doi:10.1016/j.jcis.2008.10.081

Martínez-Carmona, M., Gun'ko, Y., and Vallet-Regí, M. (2018). ZnO nanostructures for drug delivery and theranostic applications. *Nanomaterials* 8 (4), 268. doi:10.3390/nano8040268

Newman, S. P., and Jones, W. (1999). Comparative study of some layered hydroxide salts containing exchangeable interlayer anions. *J. Solid State Chem.* 148, 26–40. doi:10.1006/jssc.1999.8330

Nistor, S. V., Ghica, D., Stefan, M., and Nistor, L. C. (2013). Sequential thermal decomposition of the shell of cubic ZnS/Zn(OH)2 core-shell quantum dots observed with Mn2+ probing ions. *J. Phys. Chem. C* 117 (42), 22017–22028. doi:10.1021/jp4063093

Nistor, S. V., Ghica, D., Stefan, M., Vlaicu, I. D., Barascu, J. N., and Bartha, C. (2013b). Magnetic defects in crystalline Zn(OH)2 and nanocrystalline ZnO resulting from its thermal decomposition. *J. Alloys Compd.* 548, 222–227. doi:10.1016/j.jallcom.2012.09.016

Nistor, S. V., Stefan, M., and Ghica, D. (2014). Pulse annealing electron paramagnetic resonance with probing transition ions: Application to thermal formation and growth of nanoZnO. *J. Therm. Anal. Calorim.* 118, 1021–1031. doi:10.1007/s10973-014-3743-1

Oh, J. M., Biswick, T. T., and Choy, J. H. (2009). Layered nanomaterials for green materials. *J. Mat. Chem.* 19, 2553–2563. doi:10.1039/b819094a

Popescu, T., Matei, C. O., Vlaicu, I. D., Tivig, I., Kuncser, A. C., Stefan, M., et al. (2020). Influence of surfactant-tailored Mn-doped ZnO nanoparticles on ROS production and DNA damage induced in murine fibroblast cells. *Sci. Rep.* 10, 18062. doi:10.1038/s41598-020-74816-0

Pradeep, K. R., and Viswanatha, R. (2020). Mechanism of Mn emission: Energy transfer vs charge transfer dynamics in Mn-doped quantum dots. *Apl. Mater* 8, 020901. doi:10.1063/1.5140888

Pradhan, N. (2019). Mn-doped semiconductor nanocrystals: 25 Years and beyond. *J. Phys. Chem. Lett.* 10, 2574–2577. doi:10.1021/acs.jpclett.9b01107

Reinoso, D. M., Damiani, D. E., and Tonetto, G. M. (2014). Synthesis of biodiesel from soybean oil using zinc layered hydroxide salts as heterogeneous catalysts. *Catal. Sci. Technol.* 4, 1803–1812. doi:10.1039/c4cy00145a

Ruiz, C. V., Becerra, M. E., and Giraldo, O. (2020). Structural, thermal, and release properties of hybrid materials based on layered zinc hydroxide and caffeic acid. *Nanomaterials* 10, 163. doi:10.3390/nano10010163

Shannon, R. D. (1976). Revised effective ionic radii and systematic studies of interatomic distances in halides and chalcogenides. *Acta Cryst. A* 32, 751–767. doi:10.1107/s0567739476001551

Sharma, P., Gupta, A., Rao, K. V., Owens, F. J., Sharma, R., Ahuja, R., et al. (2003). Ferromagnetism above room temperature in bulk and transparent thin films of Mn-doped ZnO. *Nat. Mater* 2, 673–677. doi:10.1038/nmat984

Sing, K. S. W., Everett, D. H., Haul, R. A. W., Moscou, L., Pierotti, R. A., Rouquerol, J., et al. (1985). Reporting physisorption data for gas/solid systems with special reference to the determination of surface area and porosity (Recommendations 1984). *Pure Appl. Chem.* 57, 603–619. doi:10.1351/pac198557040603

Singh, T., Mountziaris, T. J., and Maroudas, D. (2010). On the transition-metal doping efficiency of zinc oxide nanocrystals. *Appl. Phys. Lett.* 97, 073120. doi:10.1063/1.3478216

Stählin, W., and Oswald, H. R. (1971). The infrared spectrum and thermal analysis of zinc hydroxide nitrate. *J. Sol. State Chem.* 2, 252–255. doi:10.1016/0022-4596(71)90037-5

Stählin, W., and Oswald, H. (1970). The crystal structure of zinc hydroxide nitrate, Zn5(OH)8(NO3)2·2H2O. *Acta Cryst. B* 26, 860–863. doi:10.1107/s0567740870003230

Stefan, M., Nistor, S. V., and Ghica, D. (2013). Correlation of lattice disorder with crystallite size and the growth kinetics of Mn2+ doped ZnO nanocrystals probed by electron paramagnetic resonance. *Cryst. Growth Des.* 13, 1350–1359. doi:10.1021/cg400037c

Stefan, M., Nistor, S. V., and Ghica, D. (2014). "ZnS and ZnO semiconductor nanoparticles doped with Mn^{2+} ions. Size effects investigated by EPR spectroscopy," in *Size effects in nanostructures. Basics and application*. Editors V. Kuncser and L. Miu (Germany: Springer-Verlag Berlin Heidelberg), 3–27.

Stoll, S., and Schweiger, A. (2006). EasySpin, a comprehensive software package for spectral simulation and analysis in EPR. *J. Magn. Reson.* 178, 42–55. doi:10.1016/j.jmr.2005.08.013

Verma, R., Pathak, S., Srivastava, A. K., Prawer, S., and Tomljenovic-Hanic, S. (2021). ZnO nanomaterials: Green synthesis, toxicity evaluation and new insights in biomedical applications. *J. Alloys Compd.* 876, 160175. doi:10.1016/j.jallcom.2021.160175

Wypych, F., Arízaga, G. G. C., and da Costa Gardolinski, J. E. F. (2005). Intercalation and functionalization of zinc hydroxide nitrate with mono- and dicarboxylic acids. *J. Colloid Interface Sci.* 283, 130–138. doi:10.1016/j.jcis.2004.08.125

Yang, Y., Li, Y., Zhu, L., He, H., Hu, L., Huang, J., et al. (2013). Shape control of colloidal Mn doped ZnO nanocrystals and their visible light photocatalytic properties. *Nanoscale* 5, 10461–10471. doi:10.1039/c3nr03160h

Zhang, Y., Han, F., Dai, Q., and Tang, J. (2018). Magnetic properties and photovoltaic applications of ZnO:Mn nanocrystals. *J. Colloid Interface Sci.* 517, 194–203. doi:10.1016/j.jcis.2018.02.002

frontiers | Frontiers in Chemistry

TYPE Original Research
PUBLISHED 19 April 2023
DOI 10.3389/fchem.2023.1152500

Check for updates

OPEN ACCESS

EDITED BY
Weiwei Han,
Jilin University, China

REVIEWED BY
Sanja Josip Armakovic,
University of Novi Sad, Serbia
Tanmoy Chakraborty,
Sharda University, India
Debdutta Chakraborty,
Birla Institute of Technology, Mesra, India

*CORRESPONDENCE
Angela K. Wilson,
akwilson@msu.edu

RECEIVED 27 January 2023
ACCEPTED 03 April 2023
PUBLISHED 19 April 2023

CITATION
North SC, Jorgensen KR, Pricetolstoy J and Wilson AK (2023), Population analysis and the effects of Gaussian basis set quality and quantum mechanical approach: main group through heavy element species.
Front. Chem. 11:1152500.
doi: 10.3389/fchem.2023.1152500

COPYRIGHT
© 2023 North, Jorgensen, Pricetolstoy and Wilson. This is an open-access article distributed under the terms of the Creative Commons Attribution License (CC BY). The use, distribution or reproduction in other forums is permitted, provided the original author(s) and the copyright owner(s) are credited and that the original publication in this journal is cited, in accordance with accepted academic practice. No use, distribution or reproduction is permitted which does not comply with these terms.

Population analysis and the effects of Gaussian basis set quality and quantum mechanical approach: main group through heavy element species

Sasha C. North[1], Kameron R. Jorgensen[2], Jason Pricetolstoy[1] and Angela K. Wilson[1]*

[1]Department of Chemistry, Michigan State University, East Lansing, MI, United States, [2]Department of Biology and Chemistry, Texas A&M International University, Laredo, TX, United States

Atomic charge and its distribution across molecules provide important insight into chemical behavior. Though there are many studies on various routes for the determination of atomic charge, there are few studies that examine the broader impact of basis set and quantum method used over many types of population analysis methods across the periodic table. Largely, such a study of population analysis has focused on main-group species. In this work, atomic charges were calculated using several population analysis methods including orbital-based methods (Mulliken, Löwdin, and Natural Population Analysis), volume-based methods (Atoms-in-Molecules (AIM) and Hirshfeld), and potential derived charges (CHELP, CHELPG, and Merz-Kollman). The impact of basis set and quantum mechanical method choices upon population analysis has been considered. The basis sets utilized include Pople (6-21G**, 6-31G**, 6-311G**) and Dunning (cc-pV*n*Z, aug-cc-pV*n*Z; *n* = D, T, Q, 5) basis sets for main group molecules. For the transition metal and heavy element species examined, relativistic forms of the correlation consistent basis sets were used. This is the first time the cc-pV*n*Z-DK3 and cc-pwCV*n*Z-DK3 basis sets have been examined with respect to their behavior across all levels of basis sets for atomic charges for an actinide. The quantum methods chosen include two density functional (PBE0 and B3LYP), Hartree-Fock, and second-order Møller-Plesset perturbation theory (MP2) approaches.

KEYWORDS

electrostatic potential (ESP) derived charges, volume-based methods, atomic charge, population analysis, orbital-based methods

1 Introduction

Atomic charge is important in the rationalization and elucidation of chemical and structural characteristics of molecules. How this charge is distributed across an atom influences the bonding between (intermolecular) and within (intramolecular) molecules. Insight about the electronic density, and thus, the distribution of the charge across an atom, can be quantified using population analysis approaches.

Population analysis has proven useful for decades to help provide insight about a broad range of chemistry. To provide a number of examples, in recent work, population analysis

has been used to elucidate resins that are more effective for cadmium removal (Zhang et al., 2022) to help understand the dynamics of methanol's main reaction channels (Catone et al., 2021) and to provide insight about the interaction of chloroquine with C_{60} (Novir and Aram, 2020). For a study on endocannabinoid receptors, a therapeutic target for physiological pain treatment and mood regulation, population analysis was used to help indicate the most probable sites to undergo a nucleophilic attack (Rangel-Galván et al., 2022). Electrostatic partial charges, obtained from population analysis, have been used in the parameterization and the development of force fields, essential to molecular dynamics (MD) simulations (Bai et al., 2022; da Silva et al., 2022; Kognole et al., 2022; Uene et al., 2022).

Widely used population analysis schemes include: A) those based on wavefunction partitioning and orbital based schemes [Mulliken (MPA) (Mulliken, 1955), Löwdin (LPA) (Löwdin, 1970), and Natural Population Analysis (NPA) (Reed et al., 1985)]; B) volume-based charge assignment methods [Atoms-in-Molecules (AIM) (Bader, 1990) and Hirshfeld population analysis (Hirshfeld, 1977)]; and, C) electrostatic potential (ESP) approaches [CHELP (Chirlian et al., 1987), CHELPG (Breneman and Wiberg, 1990), and Merz-Kollman (MK) population analysis (Singh and Kollman, 1984; Besler et al., 1990)]. There is a very rich history of population analysis schemes, far too rich to address here. However, a brief overview of these methods and illustrations of modifications that have been made for some of the methods are provided here.

1.1 Wavefunction partitioning and orbital based schemes

For the population methods that are based on wavefunction partitioning and are orbital based (Type A), Mulliken population analysis (Mulliken, 1955) uses orbital partitioning schemes accounting for atomic orbital overlap and overlap population. The Mulliken charge assigned to atom k is calculated using the difference between the atomic number of atom k (Z_k) and the sum over basis functions centered on atom k plus the overlap contribution from basis set functions centered at other atoms (Eq. 1).

$$Q_k = Z_k - \left(\sum_{i\epsilon k} P_{i,i} + \sum_{i\epsilon k} \sum_{j\neq i} S_{ij} P_{ij}\right) \quad (1)$$

Errors arise due to the Mulliken method evenly dividing the overlap population between two atoms without considering atom type or electronegativity (Though there have been suggested modifications to the original Mulliken method such as work by Noell for application to transition metal complexes) (Noell, 1982). In a number of studies, Mulliken charges have been shown to have basis set dependence which can yield inconsistent and poor charge values, depending upon basis set chosen (Mulliken, 1971; Cramer, 2002; Jensen, 2007). For example, in the water molecule, the partial charge on the oxygen atom varied by 0.5263 *e* when using a small basis set (aug-cc-pVDZ) *versus* using a large basis set (aug-cc-pV5Z) (Martin and Zipse, 2005). However, when using Atoms-in-Molecules (AIM), a topological method (described below), the difference in charge assignment between the small and large basis sets was only 0.0078 *e* for oxygen (Martin and Zipse, 2005). Despite the possible basis set dependencies, Mulliken charges continue to be used due to the simplicity of this charge assignment scheme.

Other wavefunction based methods have sought to improve upon Mulliken based charges including Löwdin population analysis (LPA) (Löwdin, 1970), and Natural Population Analysis (NPA) (Reed et al., 1985). LPA uses the Löwdin symmetrically orthogonalized atomic orbitals to assign the electron density maintaining the essential features of Mulliken analysis to reduce basis set dependencies (Mayer, 2004). NPA addresses the basis set dependence of Mulliken by utilizing the Natural Bond Order approach (Foster and Weinhold, 1980; Reed and Weinhold, 1983; Reed and Weinhold, 1985), a bond analysis technique. NPA is based on the construction of a set of "natural atomic orbitals" (NAOs) for a given molecule using an arbitrary atomic orbital basis set. The "natural population analysis" simply represents the occupancies (diagonal one-particle density matrix elements) of these NAOs in the system of interest and enables greater numerical stability and provides a better description of the electronic distribution in compounds with high ionic character than the Mulliken approach.

1.2 Volume based charge assignment methods

(Type B) include Atoms-in-Molecules (AIM) and Hirshfeld population analysis. These methods assign charge based on the volumes occupied by each atom. These calculations are more demanding than Mulliken analysis. For example, the AIM (Bader, 1990) approach divides molecular charge density into atomic contributions based on topology. This requires knowledge of the gradient vector field of the charge densities, and the division of the three-dimensional space of the molecule into atomic volumes containing exactly one nucleus, which acts as a local attractor of the electron density. Hirshfeld population analysis (Hirshfeld, 1977; Ritchie, 1985; Ritchie and Bachrach, 1987) gives the total density of a molecule as a sum of well-defined contributions from its constituent atoms, and thus simply divides the molecular density at each atomic "point" in the molecule in proportion to their respective contributions to the molecular density. Hirshfeld charges have been shown to decrease basis set dependence, however, Hirshfeld charges have been shown to be smaller in absolute value than expected for atomic charges. Among the first to note this difference were Davidson and Chakravorty (1992) and Bultinck et al. (2007) For example, in work by Bultinck, the Hirshfeld charges on the atoms in the $(LiNH_3)^+$ ion were found to be 0.751 for Li, −0.203 for N, and 0.151 for H when ROHF/6-311G** was used, which are smaller than anticipated.

1.3 Electrostatic potential (ESP) approaches

(Type C) rely on the partitioning of electrostatic potentials. These types of methods result in less basis set dependence compared to orbital based methods and are less computationally expensive as compared to topology based methods (Chirlian et al., 1987). The partitioning is accomplished through fitting points across the molecular coordinate system to reproduce the electrostatic potential. Common ESP methods including CHELP (Chirlian

et al., 1987), CHELPG (Breneman and Wiberg, 1990), and Merz-Kollman (MK) (Singh and Kollman, 1984; Besler et al., 1990) differing in their grid points choice and fitting procedure method for the potential. CHELP assigns points on spherical shells around each atom (14 points per shell) at 2.5, 3.5, 4.5, 5.5, and 6.5 Å from each atom excluding points in the van der Waals radii (the radius of an imaginary hard sphere representing the distance of closest approach for another atom) for any atom. CHELPG assigns points on an evenly spaced cubic grid including a much denser packing of points (1 point per 0.3 Å) than CHELP and MK methods, sampling points between 0 and 2.8 Å around each atom, including the van der Waals radii. MK uses nested Connolly surface algorithms, assigning one to five points every 1 Å, including points by scaling atomic radii to multiples of (1.4, 1.6, 1.8 and 2.0) the van der Waals radii, and discarding all points inside the van der Waals volume. Weaknesses of charges determined using ESP methods include that they are not easily transferable between common (molecular) functional groups in related molecules, they have often been conformationally dependent, and large charges can result. The restricted electrostatic potential (RESP) model (Bayly et al., 1993) has been developed for molecule charge assignment to address some of these challenges. Numerous studies have been made using ESP charge assignment models to calculate charge of a single molecule, or of several molecules at a specified Hamiltonian and basis set (Sigfridsson and Ryde, 1998).

1.4 Advances in population analysis methods: Examples

In considering population analysis schemes, many studies have been done to extend or more thoroughly understand the methods. For example, in a critical analysis of Hirshfield population analysis by Bultinck et al. (2007), Bultinck identified a number of weaknesses with the analysis approach, pointing out the unphysical nature of some of the predictions, and the methodology selected for computational convenience. As a result, an extension to the Hirshfeld method was suggested by Bultinck, utilizing a weighted sums of charge atomic densities in an iterative procedure until self-consistent charges are determined. In 2006, Bruhn et al. (2006) used atomic orbital-based population analyses, examining the way these methods are affected by rigid rotation of the molecule. They demonstrated that the Mulliken and pre-orthogonalized Löwdin population analyses are invariant to a general rotation transformation, while the standard non-pre-orthogonalized implementation of the Löwdin formalism may not be invariant to such rotations. In a different study, Hirshfeld and Mulliken population analysis methods were examined to determine if the charge assignment within the methods was consistent with chemical intuition (i.e., consistent with commonly used chemical concepts such as electronegativity). The study suggested improvements for the Hirshfeld method charge partitioning technique such as increasing the magnitude of the atomic charges (Saha et al., 2009). In 2020, a study was done by Cho et al. (2020) that examined the use of a broad range of population analysis methods on the GMTKN55 set of nearly 2,500 main-group molecules using the PBE0 density functional.

In addition to the numerous studies of population methods, there have been many reviews of population analysis schemes. These include works by Wiberg and Rablen, who compared charges obtained using Mulliken population analysis, Natural Population Analysis (NPA), Bader's Atoms-in-Molecules (AIM), CHELPG, and using atomic polar tensors (GAPT), and applied to hydrocarbons (Wiberg and Rablen, 1993). The same authors revisited population analysis schemes 25 years later, when they compared charges obtained using Mulliken, minimal basis set (MBS), NPA, Mertz-Kollman (MK), CHELPG, Hirshfeld, and charge model 5 (CM5) methods, applied to hydrogen charges and hydrogen bonding (Wiberg and Rablen, 2018). Comparison to experimental results from high-resolution spectroscopic studies of deuterated methanes and known energies for H···O hydrogen bonds demonstrated that the Hirshfeld charges were the most reliable as compared to experiment. Bachrach (1994) gave a lengthy review in 1994 on commonly used population methods in "Population Analysis and Electron Densities from Quantum Mechanics." Heidar-Zadeh et al. (2018) reviewed population analysis schemes using information theory, and recently Davidson and Clark (Davidson and Clark, 2022) discussed the historical context that has influenced common conceptions about chemical bonding and reactivity (such as charge), as well as relevant technical considerations of population analyses (primarily from the Schrödinger perspective). For example, the isolated atom does not appear in the Schrödinger equation of a molecule, and thus atomic properties (such as atomic populations) must be obtained from post-processing partitioning of the wavefunction. Therefore, Davidson and Clark discuss algebraic considerations of this partitioning, such as orbital and spatial decomposition schemes of the density matrix.

While there are many studies utilizing population analysis techniques, useful illustrations are needed to demonstrate the role of basis set and quantum mechanical method choice on the assignment of atomic charge across many population analysis schemes. For example, though Cho et al. (2020) examined a wide variety of population analysis schemes and a large, diverse set of molecules, only DFT with the PBE0 functional was considered. Similarly, Wiberg and Rablen considered many classes of population schemes in their works (Wiberg and Rablen, 1993; Wiberg and Rablen, 2018) but focused on the performance of these schemes for hydrogen charges and hydrogen bonding. Another study considered both the basis set and quantum method dependance of the AIM method, using HF and DFT with the B3LYP functional, and used both Dunning and Pople basis sets, but did not consider additional population methods (Jabłoński and Palusiak, 2010). Though these are only a few examples of the many prior studies, they do illustrate the typical focused nature of much of the prior studies.

In the present study, the assignment of charge using several different basis sets, quantum mechanical methods, and molecule type, as well as the effect of molecular polarity on charges, will be examined in this work. Although much development has been done on some of these population analysis methods, such as the iterative Hirshfeld (Bultinck et al., 2007) and pre-orthogonalized Löwdin (Bruhn et al., 2006), this work considers population analysis schemes in their original descriptions, examining their performance with a variety of basis sets and quantum mechanical methods, as these are the methods that are most commonly used by the chemistry community. The current work includes main group,

transition metal, and heavy element species, considering the impact of basis set choices, cc-pV*n*Z-DK3 and cc-pwCV*n*Z-DK3 (Peterson, 2015; Feng and Peterson, 2017), for heavier element species.

2 Computational methods

Atomic charges for HF, LiF, MgO, NaCl, SO_2, CO_2, H_2O, $BeCl_2$, $MgCl_2$, NH_3, BF_3, CH_4, VO, and LrF have been determined. This set of molecules represents a variety of bonding, oxidation states, and structures. Bond electronegativity differences range from 0.45 (C—H) to 3.00 (Li—F) for the main group molecules. Four different *ab initio* and density functional approaches have been used including the B3LYP and PBE0 (Adamo and Barone, 1999) functionals, Hartree-Fock (HF), and second-order Møller–Plesset perturbation theory (MP2).

For main group molecules, the Dunning correlation consistent (cc-pV*n*Z, aug-cc-pV*n*Z, *n* = D,T,Q,5) (Dunning, 1989; Kendall et al., 1992; Prascher et al., 2011) and Pople (6-21G**, 6-31G**, 6-311G**) (Hehre et al., 1972; Hariharan and Pople, 1973; Dill and Pople, 1975; Binkley and Pople, 1977; McLean and Chandler, 1980; Raghavachari et al., 1980; Francl et al., 1982; Gordon et al., 1982) basis sets were used. The *tight-d* basis sets, cc-pV (*n*+*d*)Z, and aug-cc-pV (*n*+*d*)Z (*n* = D,T,Q,5) (Dunning et al., 2001), were used for second-row atoms. Experimental geometries from the NIST Computational Chemistry Comparison and Benchmark Database were used for all calculations (Johnson, 2015). The correlation consistent (cc-pV*n*Z, aug-cc-pV*n*Z, *n* = D,T,Q,5) basis sets (Balabanov and Peterson, 2005; Balabanov and Peterson, 2006), were used for vanadium oxide. For the lawrencium fluoride calculations, cc-pVnZ-DK3 and cc-pwCV*n*Z-DK3 basis sets were used for lawrencium, and the cc-pVnZ-DK basis sets were used for fluorine (*n* = D,T,Q for each atom) (Peterson, 2015; Feng and Peterson, 2017). For LrF, wavefunction based and volume-based population analysis were the focus of the calculations.

Mulliken, Löwdin, NPA, Hirshfeld, AIM, CHELP, CHELPG, and MK population analysis have been done, using Gaussian 16 (Frisch et al., 2016). CHELP initial radii values that were not predefined in Gaussian were set as the covalent radii for beryllium and boron (1.06 and 0.83 Å, respectively) and ionic radii for lithium, sodium, magnesium, and vanadium (0.90, 1.16, 0.86, and 0.93 Å, respectively) (Teatum et al., 1960; Allen et al., 1987). The atom charges for the center atoms in the polyatomic molecules investigated are given (e.g., C in CH_4, O in H_2O) in the present work. For diatomics, cation charges were considered for MgO, NaCl, VO and LrF, and the anion charges were considered for HF and LiF. Orbital-based (Mulliken, Löwdin, NPA) and volume-based (Hirshfeld and AIM) methods were utilized for LrF.

3 Results and discussion

3.1 Main group molecules

3.1.1 Polar bonds

The atomic charge (q_c) determined for each type of molecule investigated, along with method, basis set, and analysis used are provided in Figures 1–3. Figure 1 shows the charges for LiF; Figure 2 provides charges for $BeCl_2$,; Figure 3 gives the charges for BF_3. Charges for the other main group molecules are included in the tables in the Supporting Material (SI).

To consider the assigned charges for molecules with quite different bond polarities, Tables 1 and 2 shows the fluorine charges for the HF and much more polar LiF, molecules. The difference in electronegativity between hydrogen and fluorine is 1.88, and between lithium and fluorine is 3.00. The maximum charge difference between the fluorine in HF and in LiF is 0.82 *e*, as given by Löwdin population analysis using PBE0/aug-cc-pVQZ. On average across all methods there is a fluorine charge difference in HF compared to LiF of 0.34 *e*. The most consistent (least basis set dependent) of the methods is the Hirshfeld method which, on average, results in a fluorine charge difference of 0.37 *e* between HF and LiF. The orbital-based methods are basis set dependent and slightly more so for the polar molecules. The difference between the charges obtained using the various cc-pVnZ basis sets for LiF with PBE0 is 0.97 *e*, while for the HF molecule, the maximum difference between charges obtained using PBE0 and the cc-pV*n*Z sets is 0.91 *e*. Similarly, the maximum difference between charges obtained using HF/cc-pVnZ is 1.03 *e* for LiF, while it is 0.92 *e* for HF. Hirshfeld and electrostatic potential based methods show much less dependence on basis set as compared to orbital based methods.

3.1.2 Wavefunction population analysis

For population analysis methods, ideally, charge assignment should be independent of basis set and level of theory. In reality, the charge can vary significantly with respect to basis set choice for certain population analysis methods as already noted for HF and LiF. The wavefunction based population analysis methods, Löwdin and Mulliken, have the largest basis set sensitivity as indicated by the large span of assigned charges as shown in Figures 1–3. This basis set sensitivity of Mulliken and Löwdin analysis methods is consistent across the molecules investigated, with the largest basis set effect occurring for the boron charge assigned in BF_3 using the Löwdin population analysis method, which varies from −2.86 *e* when using HF/aug-cc-pV5Z to 0.33 *e* using HF/6-211G**. In fact, Löwdin charges have the largest basis set dependence for the main group molecules investigated, with a difference in charge as large as 3.19 *e* as for BF_3. Similar trends in basis set dependence are shown for *ab initio* and DFT methods using Mulliken and NPA schemes (Figure 4). Charges obtained using HF are shown to be consistently larger than the charges assigned using B3LYP, PBE0, and MP2 methods.

Interestingly, despite the electronegativity of fluorine, the Löwdin approach resulted in the assignment of a negative charge to boron when the correlation consistent basis sets were utilized, and for the largest of the Pople style basis sets, 6-311G**. And, in fact, Löwdin charges tend to be unphysical for most of the systems investigated, resulting in negative charges on the cation or on the less electronegative atoms in the compound, particularly when using the correlation consistent basis sets. The charges become larger if diffuse basis functions are used, particularly when there is overlapping electron density originating from neighboring atoms. Figures 4A, D show that the Löwdin method is more dependent on basis set than on the level of theory used in the assignment of atomic charges. However, for basis sets of similar size, the Löwdin atomic charges are similar. For example, using double-ζ correlation consistent basis sets

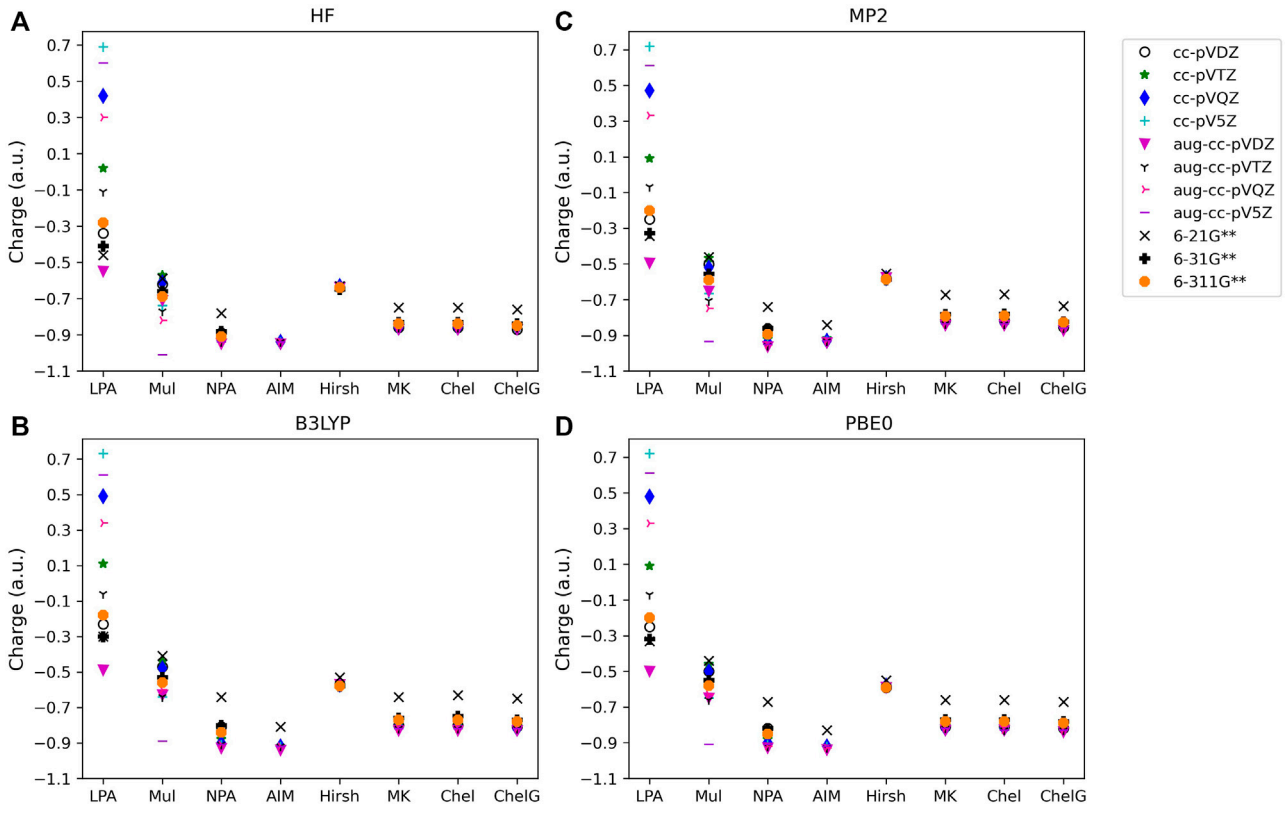


FIGURE 1
Atomic charge determined for noted basis set, analysis method, and quantum mechanical method: **(A)** HF, **(B)** B3LYP, **(C)** MP2, and **(D)** PBE0 for one of the diatomic compounds investigated, LiF. Charges for the remaining three diatomic molecules studied are included in the SI.

are consistent with the charges obtained using the Pople basis sets. Generally, charges predicted with the larger augmented correlation consistent basis sets show larger deviations from the charges predicted with the Pople style basis sets. These general impacts of basis set choices upon the Löwdin charges, as demonstrated in Figures 4A, D, occur for all molecules investigated. The difference between Löwdin atomic charge obtained using the augmented and non-augmented correlation consistent basis sets is often large as well. For example, the difference between the Löwdin atomic charge obtained using the augmented and non-augmented cc-pV5Z basis sets is as large as 0.89 *e*, as shown for CH_4 (Supplementary Figure S1). Six compounds (CH_4, NH_3, H_2O, $BeCl_2$, $MgCl_2$, and HF), have over a 0.44 *e* atomic charge difference between the cc-pV5Z and aug-cc-pV5Z calculations when using the Löwdin population analysis method.

The Mulliken approach resulted in the second widest span of atomic charge predictions for the compounds. As shown in Figure 4B, the Mulliken atomic charge for boron in BF_3 has a maximum difference of ~1.80 *e* for B3LYP/cc-pVDZ and HF/aug-cc-pVQZ, and displays a large basis set dependence. However, unlike the Löwdin approach, the Mulliken approach resulted in a positive charge on the boron, which is to be expected for bonding with the electronegative fluorine atoms. The largest span of charges determined by Mulliken population analysis is for CH_4, with the largest difference of 2.50 *e* occurring for carbon between the MP2/aug-cc-pVTZ ($q_C = -1.25$ *e*) and B3LYP/aug-cc-pVDZ ($q_C = 1.26$ *e*) predictions. Similar as for the Löwdin charges, the Mulliken charges are less basis set dependent when using the smaller Pople style basis sets as compared to the correlation consistent basis sets. This is likely due to the smaller changes between sizes of the Pople basis sets as compared to those of the correlation consistent basis sets with respect to increasing basis set size. It is also important to note that while the correlation consistent basis sets are systematically constructed to converge with increasing basis set quality for energies, this convergence behavior is not necessarily expected for charges. The Mulliken charges do not converge, yet still vary with changes in basis set quality. This non-convergence of Mulliken charges when using correlation consistent basis sets was noted previously, as demonstrated by Martin and Zipse for the Mulliken charge of oxygen on H_2O (Martin and Zipse, 2005).

Of the orbital-based population analysis methods, natural population analysis is the most consistent in the assignment of atomic charge regardless of the basis set or method used with the exception of the HF method. To illustrate, Figure 4C shows the atomic charges for the boron in BF_3 as determined using NPA. NPA results in appropriate signs for the atomic charges for all of the molecules. The NPA population analysis method results in charge differences of up to 0.39 *e* for boron in BF_3 when HF/aug-cc-pVDZ ($q_c = 1.70$) and B3LYP/6-21G**($q_c = 1.31$) were used. The largest atomic charge span between NPA charges was 0.71 *e* for magnesium in MgO, comparing MP2/aug-cc-pVQZ ($q_c = 1.48$) and B3LYP/6-21G** ($q_c = 0.77$). For MgO, MP2 gives a charge on Mg that is closer

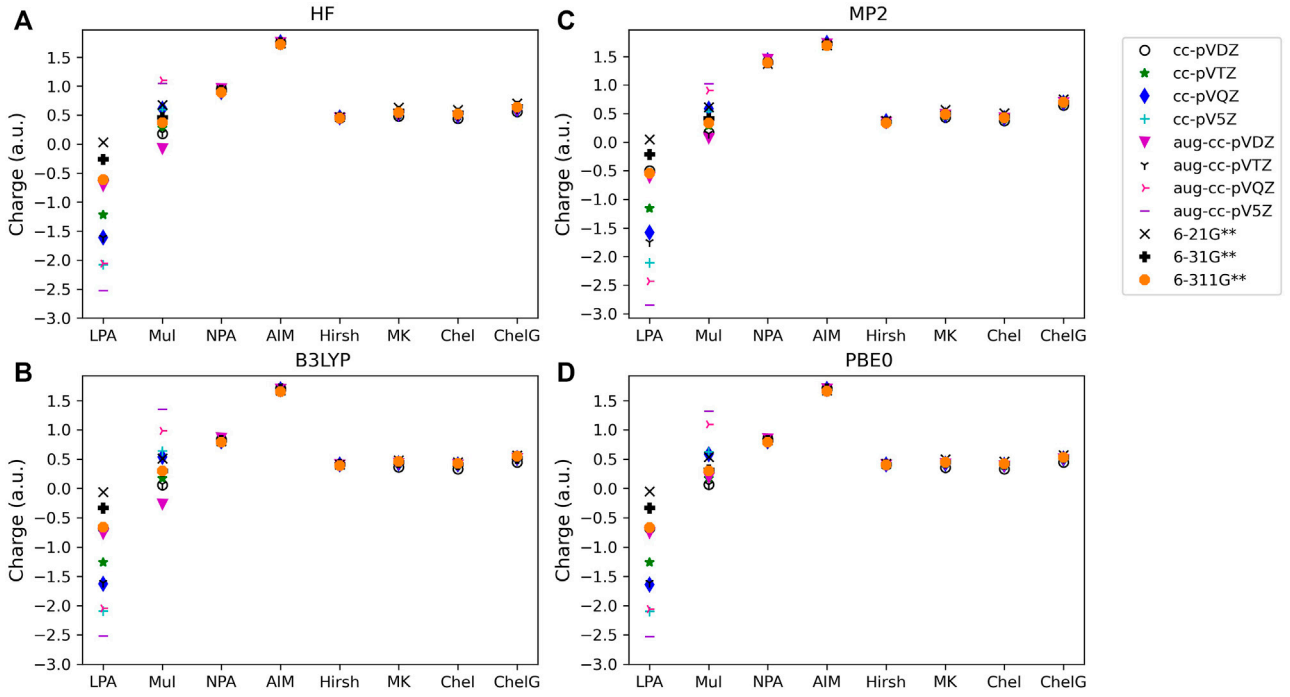


FIGURE 2
Atomic charge determined for noted basis set, analysis method and quantum mechanical method: **(A)** HF, **(B)** B3LYP, **(C)** MP2, and **(D)** PBE0 for one of the triatomic compounds investigated, BeCl2. Charges for the remaining four triatomic compounds studied are included in the SI.

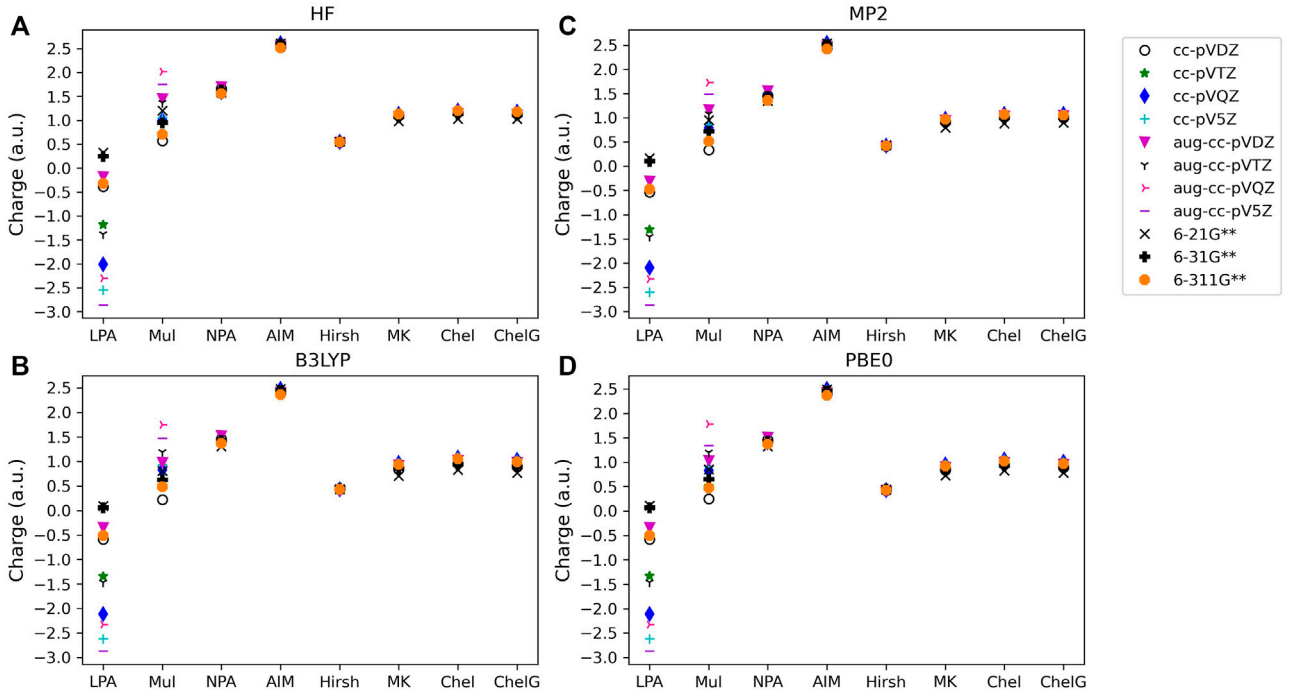


FIGURE 3
Atomic charge determined for noted basis set, analysis method and quantum mechanical method: **(A)** HF, **(B)** B3LYP, **(C)** MP2, and **(D)** PBE0 for one of the triatomic compounds investigated, BF_3. Charges for the two remaining polyatomic compounds are included in the SI.

TABLE 1 Comparison of charges obtained for the most polar (LiF) and least polar (HF) diatomic molecules, using different quantum methods, population analysis schemes, and basis sets.

		Fluorine charge in LiF (ΔEN = 3.00)								Fluorine charge in HF (ΔEN = 1.88)							
		Q_{LPA}	Q_{MPA}	Q_{NPA}	Q_{AIM}	Q_{HPA}	Q_{MK}	Q_{CHELP}	Q_{CHELPG}	Q_{LPA}	Q_{MPA}	Q_{NPA}	Q_{AIM}	Q_{HPA}	Q_{MK}	Q_{CHELP}	Q_{CHELPG}
B3LYP	cc-pVDZ	−0.23	−0.47	−0.81	*	−0.57	−0.80	−0.80	−0.81	−0.06	−0.21	−0.52	−0.72	−0.23	−0.41	−0.40	−0.41
	cc-pVTZ	0.11	−0.44	−0.88	−0.92	−0.57	−0.81	−0.81	−0.81	0.25	−0.32	−0.54	−0.72	−0.22	−0.42	−0.40	−0.42
	cc-pVQZ	0.49	−0.48	−0.90	−0.92	−0.57	−0.81	−0.81	−0.82	0.62	−0.34	−0.55	−0.72	−0.21	−0.42	−0.40	−0.42
	cc-pV5Z	0.73	−0.64	−0.91	−0.92	−0.57	−0.82	−0.82	−0.82	0.85	−0.37	−0.54	−0.73	−0.21	−0.42	−0.40	−0.42
	aug-cc-pVDZ	−0.49	−0.63	−0.93	−0.94	−0.57	−0.83	−0.83	−0.83	0.09	−0.25	−0.56	−0.71	−0.21	−0.41	−0.39	−0.41
	aug-cc-pVTZ	−0.06	−0.64	−0.91	−0.92	−0.57	−0.82	−0.82	−0.82	0.66	−0.33	−0.55	−0.73	−0.21	−0.41	−0.40	−0.41
	aug-cc-pVQZ	0.34	−0.60	−0.91	−0.92	−0.57	−0.82	−0.82	−0.82	1.13	−0.43	−0.55	−0.73	−0.21	−0.41	−0.40	−0.41
	aug-cc-pV5Z	0.61	−0.89	−0.91	−0.92	−0.57	−0.82	−0.82	−0.82	1.35	−0.52	−0.54	−0.73	−0.21	−0.41	−0.40	−0.41
	6-21G**	−0.30	−0.41	−0.64	−0.81	−0.53	−0.64	−0.63	−0.65	−0.18	−0.32	−0.48	−0.65	−0.23	−0.37	−0.36	−0.37
	6-31G**	−0.30	−0.53	−0.80	*	−0.58	−0.76	−0.75	−0.77	−0.25	−0.36	−0.54	−0.70	−0.23	−0.42	−0.40	−0.42
	6-311G**	−0.18	−0.56	−0.84	*	−0.58	−0.77	−0.77	−0.78	−0.04	−0.30	−0.53	−0.69	−0.23	−0.44	−0.42	−0.44
PBE0	cc-pVDZ	−0.25	−0.50	−0.82	*	−0.59	−0.81	−0.81	−0.82	−0.06	−0.21	−0.53	−0.73	−0.23	−0.42	−0.40	−0.42
	cc-pVTZ	0.09	−0.46	−0.88	−0.92	−0.58	−0.81	−0.81	−0.82	0.25	−0.32	−0.54	−0.73	−0.22	−0.42	−0.41	−0.42
	cc-pVQZ	0.48	−0.50	−0.90	−0.92	−0.58	−0.82	−0.82	−0.82	0.62	−0.34	−0.55	−0.74	−0.22	−0.42	−0.40	−0.42
	cc-pV5Z	0.72	−0.65	−0.91	−0.92	−0.58	−0.82	−0.82	−0.83	0.85	−0.37	−0.54	−0.74	−0.21	−0.42	−0.40	−0.42
	aug-cc-pVDZ	−0.50	−0.65	−0.93	−0.94	−0.59	−0.83	−0.83	−0.84	0.08	−0.28	−0.56	−0.72	−0.21	−0.41	−0.40	−0.41
	aug-cc-pVTZ	−0.07	−0.66	−0.92	−0.93	−0.58	−0.82	−0.83	−0.83	0.66	−0.35	−0.55	−0.74	−0.21	−0.42	−0.40	−0.41
	aug-cc-pVQZ	0.33	−0.63	−0.92	−0.93	−0.58	−0.82	−0.83	−0.83	1.13	−0.43	−0.55	−0.74	−0.21	−0.42	−0.40	−0.41
	aug-cc-pV5Z	0.61	−0.91	−0.91	−0.92	−0.58	−0.82	−0.83	−0.83	1.35	−0.54	−0.54	−0.74	−0.21	−0.41	−0.40	−0.41
	6-21G**	−0.33	−0.44	−0.67	−0.83	−0.55	−0.66	−0.66	−0.67	−0.19	−0.34	−0.49	−0.67	−0.23	−0.38	−0.37	−0.38
	6-31G**	−0.32	−0.55	−0.82	*	−0.59	−0.77	−0.77	−0.78	−0.26	−0.36	−0.55	−0.71	−0.24	−0.42	−0.41	−0.42
	6-311G**	−0.20	−0.58	−0.85	*	−0.59	−0.78	−0.78	−0.79	−0.04	−0.30	−0.53	−0.70	−0.23	−0.44	−0.42	−0.44
HF	cc-pVDZ	−0.34	−0.62	−0.89	*	−0.64	−0.86	−0.86	−0.87	−0.07	−0.24	−0.55	−0.77	−0.25	−0.45	−0.43	−0.45
	cc-pVTZ	0.02	−0.57	−0.92	*	−0.64	−0.86	−0.86	−0.86	0.23	−0.35	−0.55	−0.78	−0.24	−0.45	−0.43	−0.45
	cc-pVQZ	0.42	−0.61	−0.93	−0.94	−0.63	−0.86	−0.86	−0.86	0.61	−0.37	−0.55	−0.79	−0.24	−0.44	−0.43	−0.44
	cc-pV5Z	0.69	−0.74	−0.94	−0.94	−0.63	−0.86	−0.86	−0.86	0.85	−0.39	−0.55	−0.79	−0.24	−0.44	−0.43	−0.44

(Continued on following page)

10.3389/fchem.2023.1152500

TABLE 1 (*Continued*) Comparison of charges obtained for the most polar (LiF) and least polar (HF) diatomic molecules, using different quantum methods, population analysis schemes, and basis sets.

		Fluorine charge in LiF (ΔEN = 3.00)								Fluorine charge in HF (ΔEN = 1.88)							
		Q_{LPA}	Q_{MPA}	Q_{NPA}	Q_{AIM}	Q_{HPA}	Q_{MK}	Q_{CHELP}	Q_{CHELPG}	Q_{LPA}	Q_{MPA}	Q_{NPA}	Q_{AIM}	Q_{HPA}	Q_{MK}	Q_{CHELP}	Q_{CHELPG}
	aug-cc-pVDZ	−0.55	−0.71	−0.95	−0.95	−0.64	−0.87	−0.87	−0.87	0.05	−0.32	−0.57	−0.76	−0.23	−0.44	−0.43	−0.44
	aug-cc-pVTZ	−0.11	−0.77	−0.94	−0.94	−0.63	−0.86	−0.86	−0.86	0.64	−0.37	−0.56	−0.78	−0.23	−0.44	−0.43	−0.44
	aug-cc-pVQZ	0.30	−0.82	−0.94	−0.94	−0.63	−0.86	−0.86	−0.86	1.12	−0.43	−0.55	−0.79	−0.23	−0.44	−0.43	−0.44
	aug-cc-pV5Z	0.60	−1.01	−0.94	−0.94	−0.63	−0.86	−0.86	−0.86	1.35	−0.52	−0.55	−0.79	−0.23	−0.44	−0.43	−0.44
	6-21G**	−0.46	−0.59	−0.78	*	−0.63	−0.75	−0.75	−0.76	−0.21	−0.38	−0.51	−0.89	−0.25	−0.41	−0.40	−0.41
	6-31G**	−0.41	−0.66	−0.88	*	−0.65	−0.83	−0.83	−0.84	−0.27	−0.40	−0.57	−0.75	−0.25	−0.45	−0.44	−0.45
	6-311G**	−0.28	−0.69	−0.91	*	−0.64	−0.84	−0.84	−0.85	−0.06	−0.32	−0.54	−0.74	−0.25	−0.46	−0.45	−0.46

*AIM, requires more flexibility in the basis set than permitted by the smallest of the basis sets considered for LiF.

10.3389/fchem.2023.1152500

TABLE 2 Comparison of charges obtained for the most polar (LiF) and least polar (HF) diatomic molecules, using MP2 with different population analysis schemes and basis sets.

		Fluorine charge in LiF (ΔEN = 3.00)								Fluorine charge in HF (ΔEN = 1.88)							
		Q_{LPA}	Q_{MPA}	Q_{NPA}	Q_{AIM}	Q_{HPA}	Q_{MK}	Q_{CHELP}	Q_{CHELPG}	Q_{LPA}	Q_{MPA}	Q_{NPA}	Q_{AIM}	Q_{HPA}	Q_{MK}	Q_{CHELP}	Q_{CHELPG}
MP2	cc-pVDZ	−0.25	−0.50	−0.86	*	−0.58	−0.82	−0.82	−0.87	−0.06	−0.22	−0.52	−0.73	−0.23	−0.42	−0.41	−0.42
	cc-pVTZ	0.09	−0.47	−0.92	−0.92	−0.58	−0.82	−0.82	−0.86	0.25	−0.32	−0.53	−0.74	−0.22	−0.42	−0.40	−0.42
	cc-pVQZ	0.47	−0.52	−0.94	−0.93	−0.58	−0.83	−0.83	−0.86	0.62	−0.34	−0.54	−0.76	−0.22	−0.42	−0.40	−0.42
	cc-pV5Z	0.72	−0.67	−0.95	−0.93	−0.58	−0.83	−0.83	−0.86	0.85	−0.34	−0.53	−0.76	−0.21	−0.42	−0.40	−0.42
	aug-cc-pVDZ	−0.50	−0.65	−0.97	−0.94	−0.58	−0.84	−0.84	−0.85	0.08	−0.27	−0.56	−0.72	−0.21	−0.42	−0.40	−0.41
	aug-cc-pVTZ	−0.07	−0.71	−0.96	−0.93	−0.58	−0.84	−0.84	−0.85	0.66	−0.34	−0.55	−0.75	−0.21	−0.42	−0.40	−0.41
	aug-cc-pVQZ	0.33	−0.75	−0.95	−0.93	−0.58	−0.84	−0.84	−0.86	1.13	−0.39	−0.55	−0.76	−0.21	−0.42	−0.40	−0.41
	aug-cc-pV5Z	0.61	−0.93	−0.95	−0.93	−0.58	−0.84	−0.84	−0.86	1.35	−0.50	−0.53	−0.76	−0.21	−0.42	−0.40	−0.41
	6-21G**	−0.34	−0.46	−0.74	−0.84	−0.55	−0.67	−0.67	−0.74	−0.19	−0.36	−0.49	−0.69	−0.23	−0.39	−0.38	−0.39
	6-31G**	−0.33	−0.56	−0.86	*	−0.59	−0.78	−0.78	−0.82	−0.26	−0.37	−0.54	−0.72	−0.23	−0.43	−0.42	−0.43
	6-311G**	−0.20	−0.59	−0.89	*	−0.59	−0.79	−0.79	−0.83	−0.04	−0.30	−0.52	−0.70	−0.23	−0.44	−0.42	−0.44

*AIM, requires more flexibility in the basis set than permitted by the smallest of the basis sets considered for LiF.

10.3389/fchem.2023.1152500

10.3389/fchem.2023.1152500

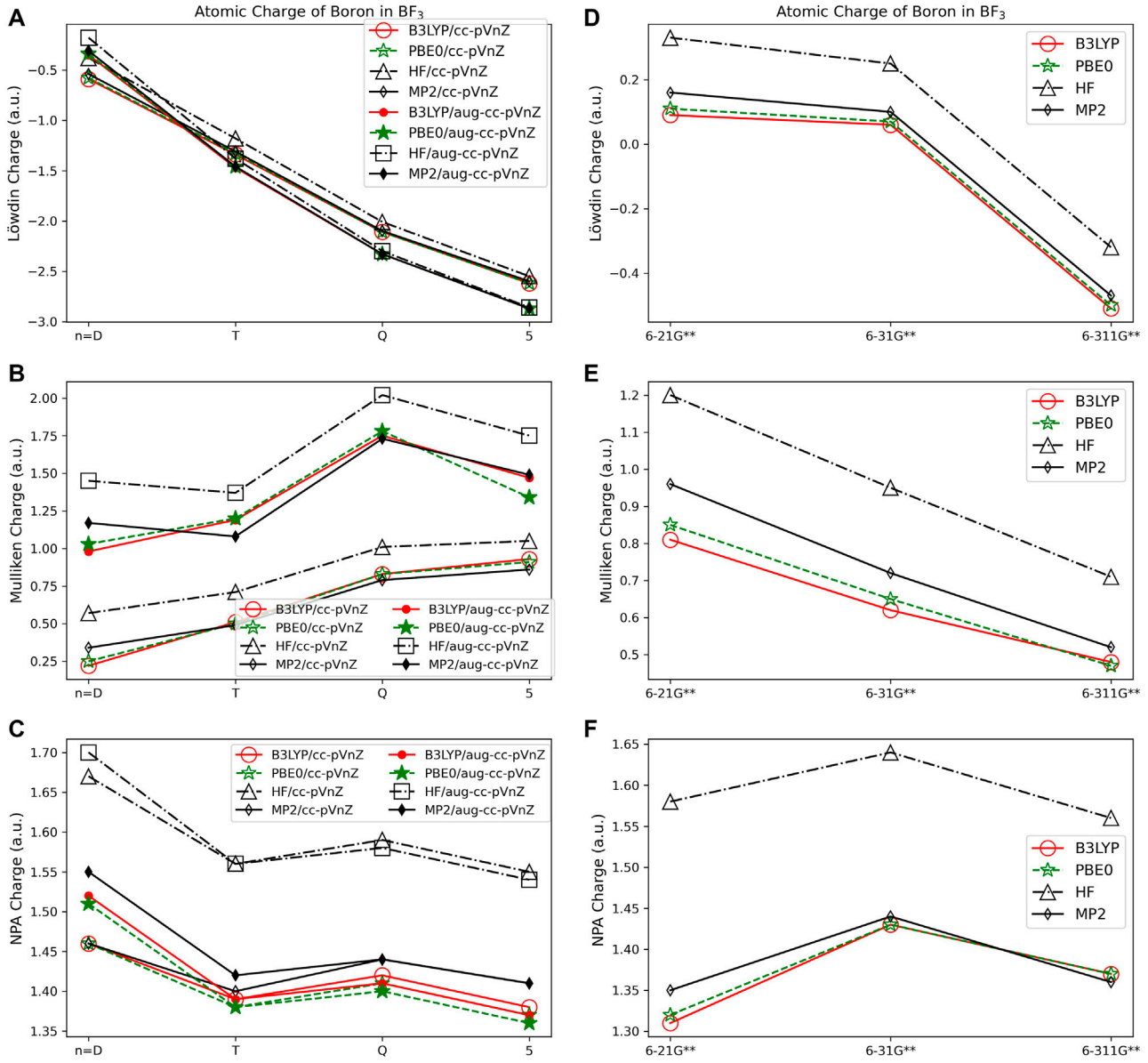


FIGURE 4
Atomic charge of boron in BF_3 determined using a number of different theoretical methods, Dunning style basis sets, and wavefunction-based population analysis methods: **(A)** Löwdin, **(B)** Mulliken, and **(C)** NPA. (*Note that scales vary from one analysis method to another.) Pople style basis sets are presented in **(D)** Löwdin, **(E)** Mulliken, and **(F)** NPA.

to the expected Mg charge of 2+. In Figure 4C the variation in atomic charge is more method dependent than basis set dependent with distinct differences in charges obtained utilizing MP2, PBE0, and B3LYP as compared to those using HF. The NPA atomic charge is higher for cations and lower for anions when utilizing HF as compared to using MP2 or a DFT approach for all of the compounds.

3.1.3 Volume based population analysis

The charges assigned with volume-based methods are less dependent on basis set and quantum method used as compared to the charges obtained using the Löwdin and Mulliken orbital based methods. The AIM approach results in a higher atomic charge for all cations, and lower atomic charge for all anions in comparison to the other population analysis methods (see, for example, LiF in Figure 1). For the atomic charge of boron determined using AIM for BF_3 (Figure 5A) there is a ~0.14 *e* difference between what is predicted with the HF and DFT methods when using the same basis set type; the charges obtained with MP2 fall in between the charges obtained using HF and the DFT methods. The largest AIM charge differences occur for carbon in CO_2, with a 0.60 *e* difference between the

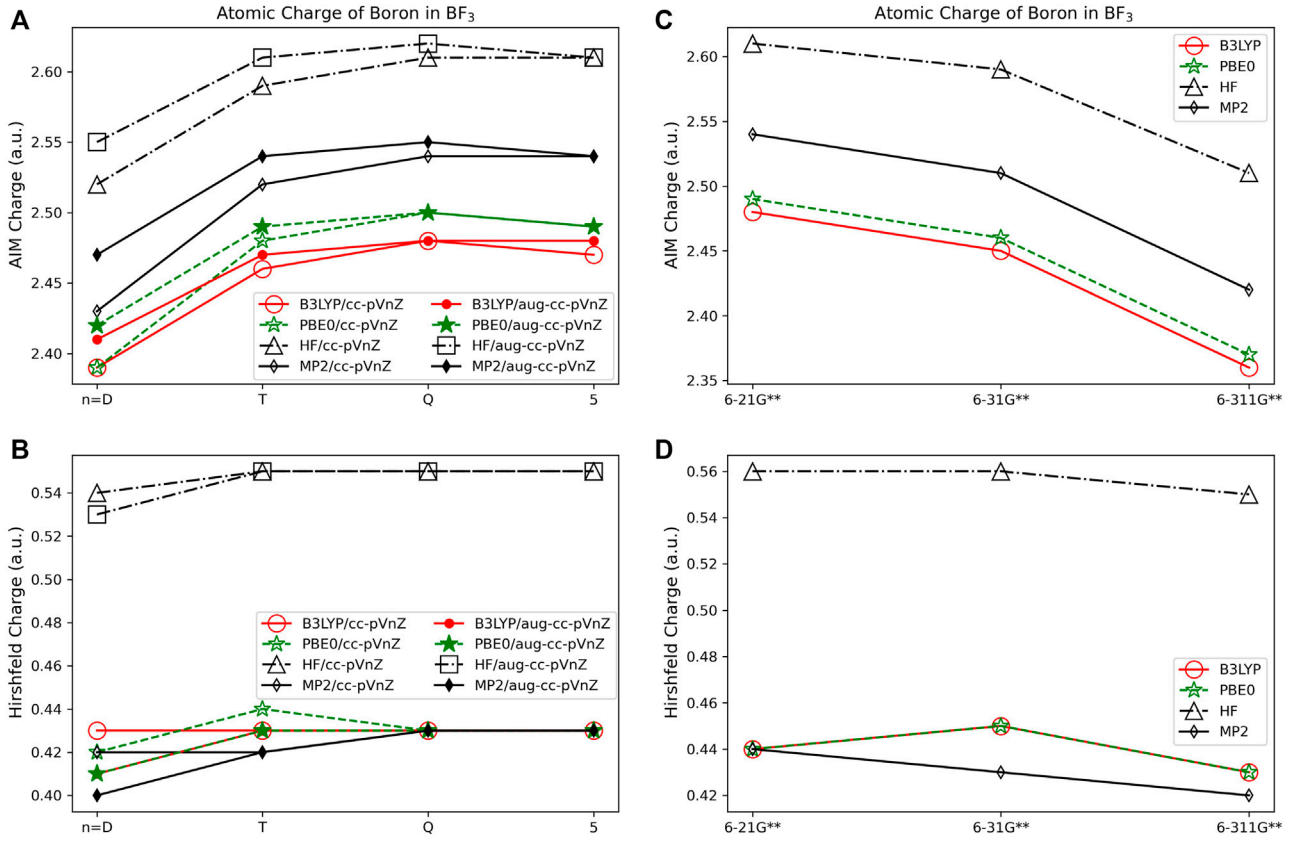


FIGURE 5
Atomic charge of boron in BF_3 determined using a number of theoretical methods, Dunning style basis sets, and population analysis methods: **(A)** AIM, and **(B)** Hirshfeld. Pople style basis sets are presented using **(C)** AIM, and **(D)** Hirshfeld.

predictions from B3LYP/6-311G** (q_C = 2.13 *e*) and HF/aug-cc-pVQZ (q_C = 2.73 *e*). When using AIM, charge assignment is less basis set dependent when using the correlation consistent basis sets *versus* the Pople style basis sets.

In contrast to the Löwdin and Mulliken population analysis methods, Hirshfeld is the most consistent overall with charge assignment having little dependence on the basis set and theoretical method. The Hirshfeld method results in differences in the calculated charges of less than or equal to 0.05 *e* regardless of the chosen basis set or theoretical method utilized for five of the molecules investigated, while three main group compounds investigated have differences in atomic charge greater than 0.12 *e*. Investigating the small differences in assigned atomic charge, Hirshfeld charges are shown to depend slightly more on the choice of theoretical method than on the quality of basis set. In Figure 5B, for example, the boron charge in BF_3 using the Hirshfeld method differs by no more than ~0.15 *e* between methods. HF theory assigns larger charges (in absolute value) to boron in BF_3 than MP2, B3LYP, and PBE0, independent of basis set. This same trend occurs for all of the molecules. In Figure 5 it is shown that basis set variations are nearly eliminated for all but the smallest basis sets, though there is a slightly larger difference between the charges obtained using the Pople basis sets with MP2, as compared to charges obtained using these sets with HF or DFT.

3.1.4 Electrostatic potential based population analysis

Figures 6A–F show the boron charge in BF_3 for Merz-Kollman, CHELP, and CHELPG population analysis schemes. It is important to note that previous work has shown that the Merz-Kollman and CHELP have a dependence on molecular orientation, on average 0.04–0.05 *e*, and CHELPG has a minimal 0.001 *e* dependence upon the rotation of the molecule (Sigfridsson and Ryde, 1998). The charges of the molecule vary by the same magnitude, regardless of the quantum mechanical method, basis set, and molecule examined with these analysis schemes, with the largest charge span of 0.47 *e* for BF_3, and an average atomic charge span of 0.39 *e* considering all quantum methods and basis sets. The three electrostatic potential methods result in similar charge assignments. While electrostatic population analysis methods are less dependent on quantum method and basis set used than Löwdin and Mulliken methods, they are slightly more dependent on quantum method and basis set used than the NPA, Hirshfeld, and AIM population analysis methods. Using HF the magnitude of the charge is increased as compared to the charge from B3LYP and PBE0, with the charges obtained using MP2 often falling between HF and DFT, as for the AIM charges. Charges assigned when using the correlation consistent basis sets show even less variation

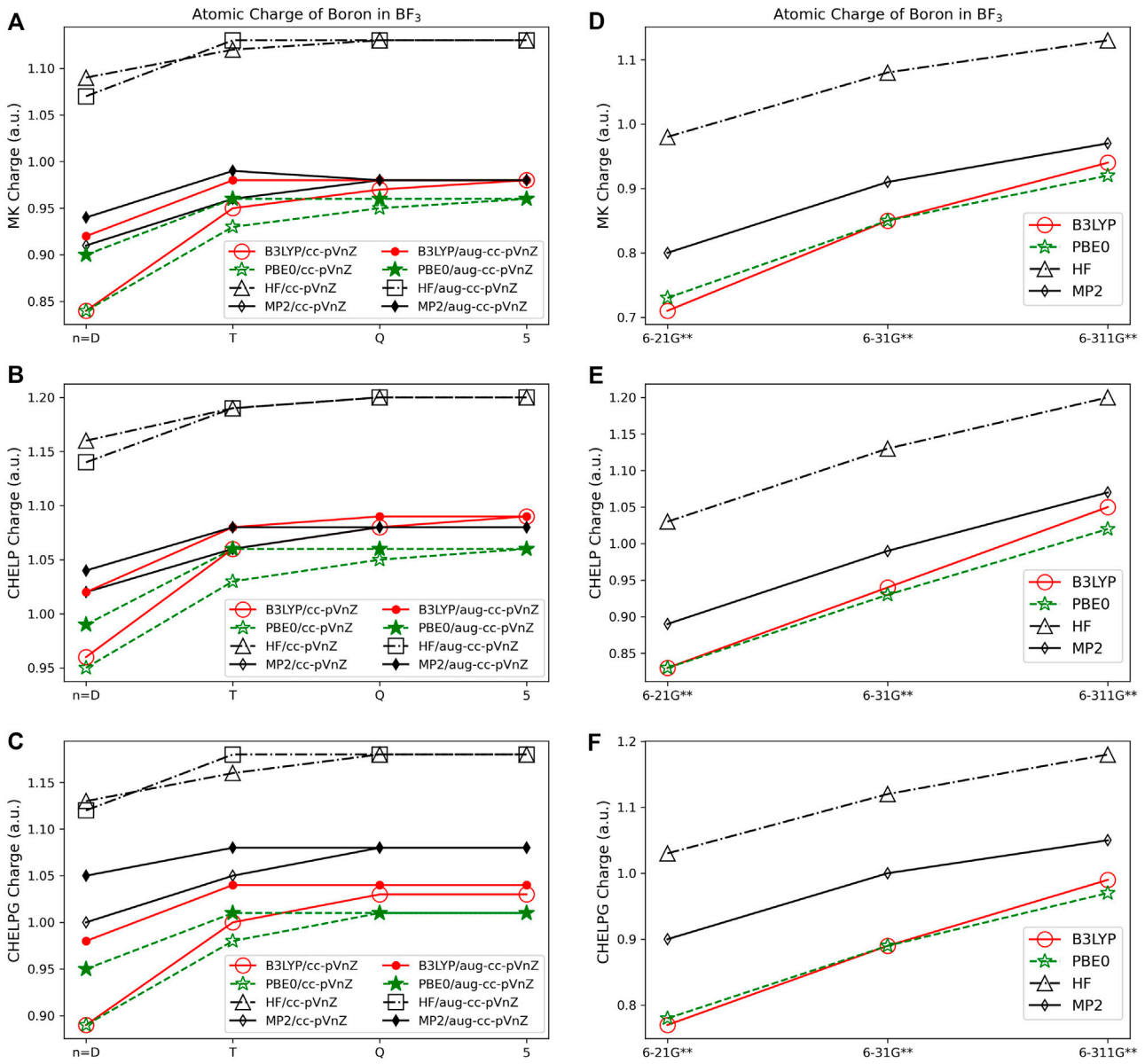


FIGURE 6
Atomic charge of boron in BF_3 determined using a number of theoretical methods, basis sets, and population analysis methods: **(A)** Merz-Kollman, **(B)** CHELP, and **(C)** CHELPG. Pople style charges are presented in **(D)** Merz-Kollman, **(E)** CHELP, and **(F)** CHELPG.

than the Pople sets when the basis set size is increased (see Figure 6). It is also shown that the CHELP atomic charge for carbon in CH_4 is predicted to be positive for most basis set and quantum method combinations (see Supplementary Figure S1). All other ESP methods predict negative values for carbon along with the most numerically stable population analysis method, Hirshfeld. Based on these considerations and the afore mentioned performance of CHELP as compared to CHELPG (Sigfridsson and Ryde, 1998), CHELP is not recommended for atomic charge.

3.2 Vanadium oxide (VO)

To consider a transition metal, vanadium oxide (VO) was investigated. All charges obtained for VO are given in the SI (Supplementary Tables S13, S14). The Mulliken populations obtained in this work (Figure 7B) are consistent with prior work by Miliordos and Mavridis. In their prior extensive study of the electronic structure of the VO molecule, where both its neutral and cationic/anionic forms were examined (Miliordos and Mavridis, 2007) using multireference and coupled cluster methods, Mulliken

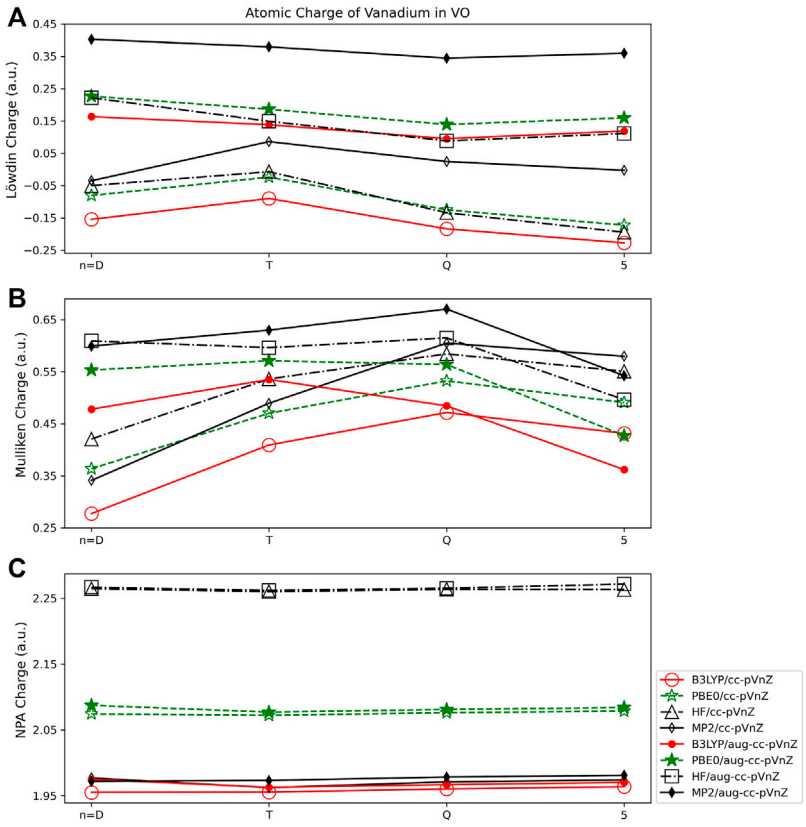


FIGURE 7
Atomic charge of vanadium in VO determined using a number of different theoretical methods, Dunning style basis sets, and wavefunction-based population analysis methods: **(A)** Löwdin, **(B)** Mulliken, and **(C)** NPA (*Note that scales vary from one analysis method to another.).

population analysis indicated an electron transfer of ~0.5 *e* from the V atom to the O atom in neutral VO.

3.2.1 Wavefunction population analysis

For vanadium oxide, the Löwdin population analysis showed less dependence on the size of the basis set than was observed for main group molecules. For example, the largest difference between basis sets for a single quantum method using the Löwdin population scheme is for PBE0, where an absolute charge difference of 0.149 *e* is observed between the cc-pVTZ and cc-pV5Z basis sets (Figure 7A). This is in contrast to an example from the main group species, where for MgO, the difference in Löwdin charge obtained using the cc-pVDZ and cc-pV5Z basis sets is markedly larger, at ~0.5 *e*. However, it should be noted that for several of the calculations, the Löwdin population analysis predicted a negative charge on the vanadium atom when non-augmented basis sets were used. This indicates that the diffuse flexibility in the basis set is important for obtaining charges that are physically meaningful (positive charges on metal atoms), at least for VO. In addition, the Löwdin method displayed a considerable dependence on the quantum method used, with the largest charge difference of 0.25 *e* occurring between the HF (0.11 *e*) and MP2 (0.36 *e*) determinations with the aug-cc-pVQZ basis set.

The basis set size dependence of the Mulliken population analysis (Figure 7B) for VO is similar to that of HF and LiF. For example, the difference in Mulliken charge obtained for the HF molecule using the B3LYP functional was 0.16 *e* (using the cc-pVDZ and cc-pV5Z basis sets), and for LiF using B3LYP the difference in charge obtained using the same basis sets was 0.17 *e*. For the same method and basis sets the charge difference in VO is 0.15 *e*. For the augmented correlation consistent basis sets however, the Mulliken charges vary less with basis set size as compared to the charges arising from use of the non-augmented sets for VO, where the opposite was observed for the HF and LiF molecules. The Mulliken charges obtained using B3LYP and the aug-cc-pVDZ and aug-cc-pV5Z sets for VO differ by just 0.12 *e*, for example, while for the HF molecule using the same basis sets and quantum method the difference is 0.27 *e*. Mulliken population analysis shows slightly less dependence on the quantum method as compared to the Löwdin method when applied to VO, with a maximum difference of 0.19 *e* between the charges obtained using aug-cc-pVQZ in combination with the B3LYP (0.48 *e*) and MP2 (0.67 *e*) methods.

As demonstrated for the main group molecules, of the wavefunction based population schemes, NPA shows much less dependence on basis set than either the Löwdin or Mulliken schemes (Figure 7C). Additionally, unlike for the Löwdin or Mulliken schemes, there is very little (0.02 *e* or smaller) difference between the augmented and non-augmented basis sets of the same *n* (for example, the cc-pVDZ and

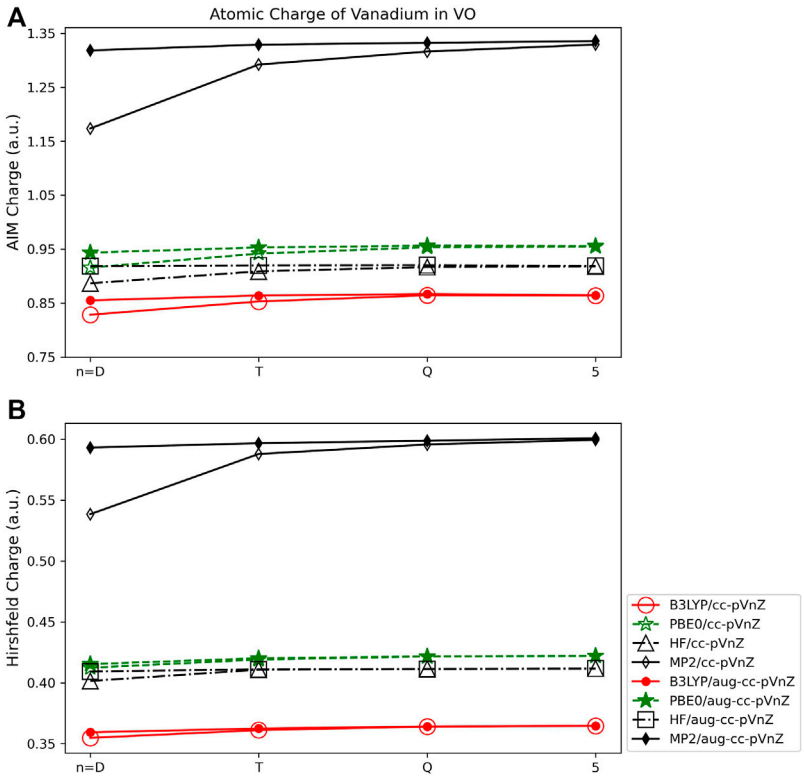


FIGURE 8
Atomic charge of vanadium in VO determined using a number of theoretical methods, Dunning style basis sets, and population analysis methods: **(A)** AIM, and **(B)** Hirshfeld (*Note that scales vary from one analysis method to another.).

aug-cc-pVDZ basis sets) obtained using the same quantum method. The B3LYP and MP2 results are shown to be quite consistent, varying by 0.02 *e* or less, while the NPA charges obtained using PBE0 are ~0.12 *e* larger. Finally, the HF results are furthest from the two DFT and the MP2 results, as was observed for main group molecules, resulting in charges of ~2.26 *e*, regardless of basis set used.

3.2.2 Volume based population analysis

As was observed for the main group molecules, the AIM and Hirshfeld charges show much less basis set and quantum method dependance than the Mulliken and Löwdin wavefunction based methods. The overall basis set level or addition of augmented functions affects the charge very little, usually by ~0.01 *e* or less for any particular quantum method. Though the volume-based methods are in general less dependent on quantum method, from Figure 8 it is clear that the MP2 method results in charges that are less consistent with the HF, B3LYP, and PBE0 results. This is in contrast to the observations in population method trends for the main group species, where HF charges tended to be the least consistent as compared to the charges arising from the other three quantum methods (see, for example, Figure 5). Similar as for main group species, however, is that the Hirshfeld charges are the most independent of basis set or quantum method used, varying by ~0.25 *e* at most (Figure 8B).

3.2.3 Electrostatic potential based population analysis

The Merz-Kollman (MK) and CHELPG population analysis methods when applied to the VO molecule (Figure 9) show similar dependence on quantum method as the Mulliken and AIM approaches. The MK and CHELPG methods are less dependent on quantum method than the Löwdin method, and more so than either the Hirshfeld or NPA approaches. The largest span between charges obtained using MK and CHELPG are both ~0.45 *e* when all basis sets and methods are considered. The CHELP method on the other hand shows much more dependence on quantum method, with a maximum charge difference of ~0.70 (Figure 9B). All three ESP approaches show very little basis set dependence, however, both when the relative size of the basis set and augmented and non-augmented sets are compared. The largest basis set difference is between the cc-pVDZ and aug-cc-pVDZ basis sets when using the MP2 quantum approach (for all three ESP methods). For example, the cc-pVDZ/MK charge is 1.19 *e*, and the aug-cc-pVDZ/MK charge is 1.29 *e*. This difference is shown in Figures 9A–C. For all basis sets other than the double-ζ set, however, the effect of different basis sets for a given quantum method is very small, on the order of 0.01–0.02 *e* for all three ESP methods.

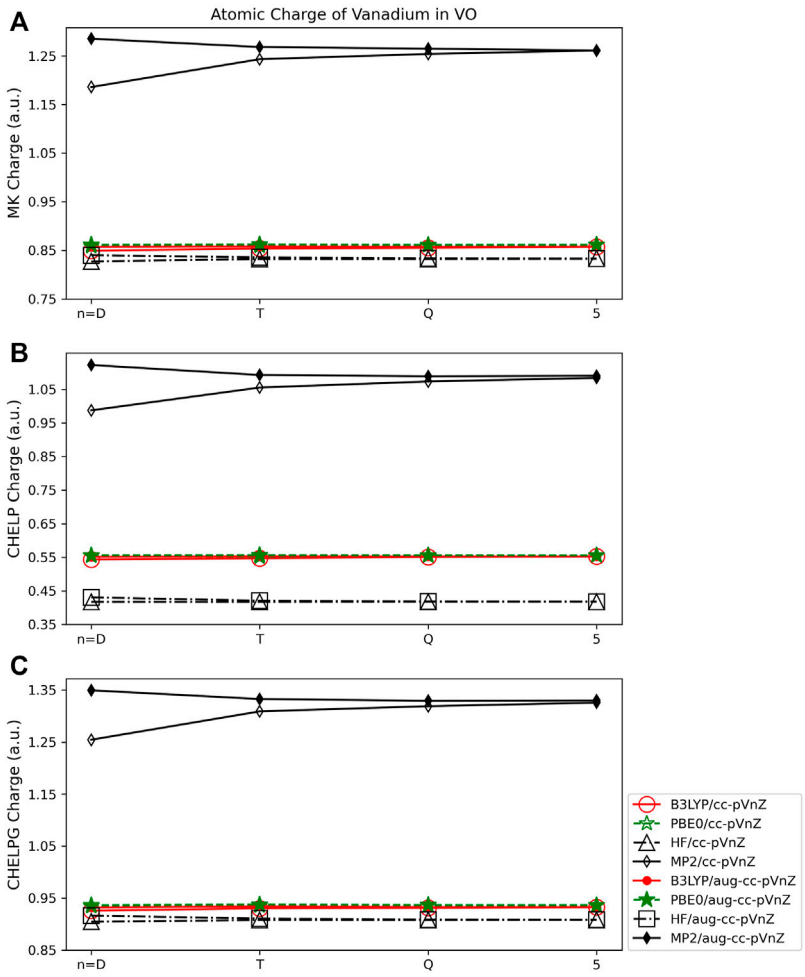


FIGURE 9
Atomic charge of vanadium in VO determined using a number of theoretical methods, basis sets, and population analysis methods: **(A)** Merz-Kollman, **(B)** CHELP, and **(C)** CHELPG (*Note that scales vary from one analysis method to another.).

3.3 Lawrencium fluoride (LrF)

The lawrencium fluoride molecule was chosen to provide insight about the behavior of population analysis on an actinide-containing molecule. All charges obtained for the LrF molecule are given in Supplementary Tables S15, S16 in the SI. There are limited studies of LrF, however, Laerdahl et al. (1998) did calculate the Mulliken population on the Lr atom in LrF using the Dirac-Hartree-Fock (DHF) method and an author-generated gaussian basis set, giving a total charge on the metal of 0.86 *e*. This charge is approximately 0.30 *e* larger than that found in this work using HF/cc-pVQZ-DK3 (Figure 10A). The ground state electronic structure for this molecule is a closed-shell singlet ($^1\Sigma^+$) that is well separated (~22,225 cm^{-1}) from the first excited state, according to recent work done using the multireference configuration interaction method with a Davidson correction (MRCI + Q) (North et al., 2023). For heavy element species, it is important to include relativistic effects in both the basis set and Hamiltonian. The cc-pV*n*Z-DK3 and cc-pwCV*n*Z-DK3 basis sets with *n* = D,T,Q (Peterson, 2015; Feng and Peterson, 2017) were contracted for the third-order Douglas-Kroll-Hess (DKH3) relativistic Hamiltonian (Reiher and Wolf, 2004). This is one of the first, if not the first time that these basis sets have been examined with respect to population analysis methods.

3.3.1 Wavefunction population analysis

The charges on the Lr atom obtained using the Löwdin method are shown to be more dependent on the size of the basis set used than for VO. The charges obtained using HF show the largest basis set dependence for this population scheme. Here, the charge obtained using HF/cc-pVDZ-DK3 is 0.34 *e*, while that obtained using HF/cc-pVQZ-DK3 is 0.03 *e*. This is still a smaller difference, however, than was observed for main-group diatomics, such as MgO which exhibited a charge difference of ~0.5 *e* depending on basis set used, and LiF which showed an even larger basis set dependence of ~1.25 *e*. The difference between the cc-pV*n*Z-DK3 and cc-pwCV*n*Z-DK3 basis sets is shown to be

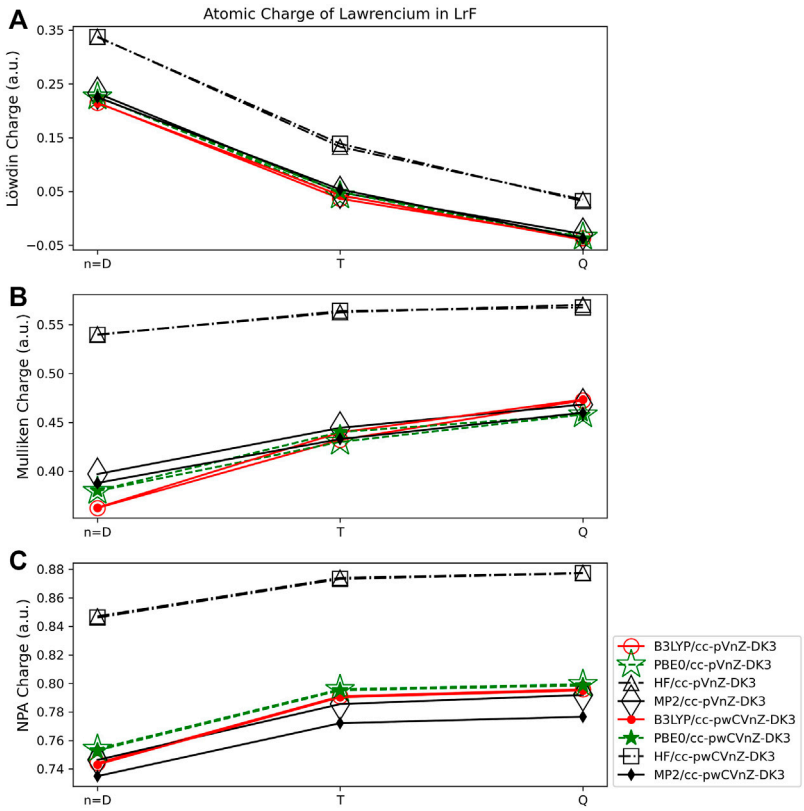


FIGURE 10
Atomic charge of lawrencium in LrF determined using a number of different theoretical methods, Dunning style basis sets, and wavefunction-based population analysis methods: **(A)** Löwdin, **(B)** Mulliken, and **(C)** NPA (*Note that scales vary from one analysis method to another.).

TABLE 3 Basis set and quantum method dependencies from wavefunction and volume based population analysis methods applied to main group, transition metal and heavy metal molecules.

Scheme type	Population method	Main group	Transition metal	Heavy metal
Wavefunction/ orbital based	Mulliken	large basis set sensitivity	similar as for main group	similar as for main group
Wavefunction/ orbital based	Löwdin	largest basis set sensitivity, non-physical charge assignment	basis set dependence less than observed for main group	more dependent on basis set when used for LrF than VO, but less basis set dependent than when used for main group
Wavefunction/ orbital based	NPA	least basis set dependent of the wavefunction based methods	least basis set dependent of the wavefunction based methods	least basis set dependent of the wavefunction based methods
Volume based	AIM	less dependent on basis set and method than wavefunction based methods	less dependent on basis set and method than wavefunction based methods	less dependent on basis set and method than wavefunction based methods
Volume based	Hirshfeld	least dependent on basis set/ quantum method of population schemes considered	least dependent on basis set/quantum method of population schemes considered	least dependent on basis set/quantum method of population schemes considered

very small for this and all other population methods, amounting to differences of charge of 0.001–0.01 *e* for basis sets with the same cardinal number (such as double-ζ). As was observed for VO, the Löwdin method results in negative charges for the Lr atom when some basis sets are used (cc-pVQZ-DK3 and cc-pwCVQZ-DK3). Regarding quantum method dependence, the Löwdin charges obtained using MP2, B3LYP, and PBE0 are all within 0.01 *e* of each other at any given basis set level. The HF method results in Löwdin charges that are ~0.10 *e* larger than those obtained using the other three methods.

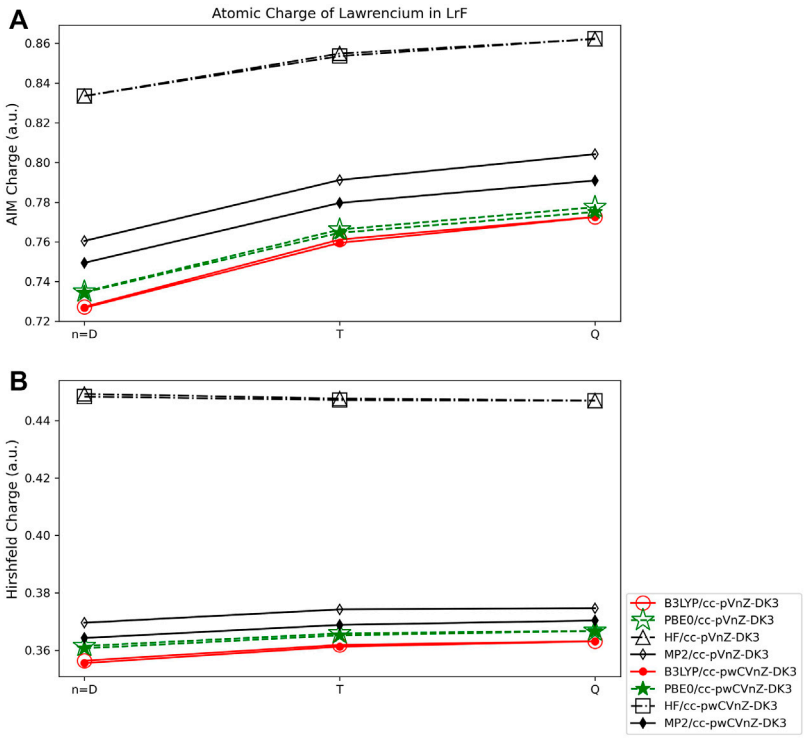


FIGURE 11
Atomic charge of lawrencium in LrF determined using a number of theoretical methods, Dunning style basis sets, and population analysis methods: **(A)** AIM, and **(B)** Hirshfeld (*Note that scales vary from one analysis method to another.).

TABLE 4 Basis set and quantum method dependencies from electrostatic potential population analysis methods applied to main group and transition metal molecules.

Scheme type	Population method	Main group	Transition metal
ESP	Chelp	not recommended: assigns non-physical charges	large dependence of quantum method
ESP	ChelpG	more dependent on quantum method and basis set than NPA, Hirshfeld, and AIM	more dependent on quantum method than NPA and Hirshfeld
ESP	Merz-Kollman	more dependent on quantum method and basis set than NPA, Hirshfeld, and AIM	more dependent on quantum method than NPA and Hirshfeld

For LrF, the Mulliken population method shows less basis set dependence than the Löwdin populations. The largest difference in Mulliken charges are those obtained using B3LYP, where the charge difference is still only 0.11 *e* (Figure 10B). This is similar as for VO and for main group diatomics. The Mulliken charges obtained for LrF exhibit similar quantum method dependence as for Lowdin charges, with MP2 and DFT results being consistent with each other, and HF charges larger; in this case, the difference between the charges obtained using the HF method and the other three quantum methods is slightly larger (~0.15 *e*).

Finally, the charges obtained using NPA for LrF (Figure 10C) are again the least basis set dependent on the wavefunction methods, with the largest difference being 0.06 *e* for the charges obtained using the cc-pVDZ-DK3 and cc-pVQZ-DK3 basis sets and B3LYP. The charges determined using NPA show similar quantum method dependence as for the Löwdin and Mulliken methods, with MP2 and both DFT methods yielding charges within ~0.01 *e* of one another at any given basis set level, and the HF charges being ~0.10 *e* larger than those obtained with the other three quantum methods.

3.3.2 Volume based population analysis

The volume-based population methods applied to LrF show limited basis set dependence, with charges obtained using the AIM method (Figure 11A) varying by 0.05 *e* at most, such as those obtained using the PBE0 functional and double-ζ and quadruple-ζ basis sets. The charges obtained using the Hirshfeld method (Figure 11B) are even less dependent on the basis set used, with charges varying by less than 0.01 *e* for any given quantum method.

The DFT and MP2 methods result in charges that are within 0.01 *e* of one another at any basis set level, with charges obtained using HF ~0.10 *e* larger than the other quantum methods.

4 Conclusion

In this work, the effect of basis set and quantum mechanical method choices on the prediction of atomic charges with eight different population analysis schemes was investigated. Tables 3, 4 summarize the data and conclusions drawn for each of the population analysis methods considered herein, for main group molecules, a transition metal molecule (VO), and heavy metal molecule (LrF). Wavefunction-based, volume-based, and ESP methods were utilized. Molecules including main group, transition metal, and heavy element species were considered. This is one of the first, if not the first time the cc-pV*n*Z-DK3 and cc-pwCV*n*Z-DK3 basis sets for an actinide molecule have been utilized in population analysis. The largest basis set dependence for the LrF molecule was observed when the Löwdin population analysis was used, with the HF method, where the charges varied by as much as 0.31 *e*, depending upon basis set chosen.

The effect of molecular polarity in the determination of atomic charge was evaluated. It was shown that for more polar molecules, basis set dependence becomes more significant, regardless of quantum method used, especially for the wavefunction based population analysis schemes.

Ideally, charge assignment schemes should be independent of basis set and method approach. The Hirshfeld population analysis atomic charges are the least sensitive to changes in basis set and quantum method as compared to those of the other population analysis methods investigated. However, the Hirshfeld method underestimates the charge on molecules such as LiF, where expected charges are ~+1 and ~-1 on the Li and F, respectively due to ionic bonding. AIM most often predicts charges that are expected from ionic bonding, followed closely by NPA. The largest variations in atomic charges occur for the Löwdin population analysis method. Löwdin and CHELP atomic charges can result in unphysical charges with the correlation consistent basis sets or large Pople style basis sets. For the VO molecule, the use of augmented correlation consistent basis sets was found to be important for obtaining physically meaningful charges when the Löwdin method was used.

Orbital-based methods are shown to have a much larger dependence on basis set than electrostatic potential and volume-based methods. Utilizing NPA reduces the basis set dependence compared to other orbital based methods such as Mulliken and Löwdin charges. Volume and potential based methods also typically show a reduction in basis set and quantum method dependency. Out of the volume-based schemes considered, the Hirshfeld method has the least dependence on basis set for the molecule set. Quantum method dependence is also important with maximum differences in charges from ~0.10 *e* to 0.50 *e* when within a particular basis set and population scheme, especially when smaller basis sets are used. Caution should be taken when using population analysis methods to assign charge as they are often shown to be both basis set and quantum method dependent.

Data availability statement

The original contributions presented in the study are included in the article/Supplementary Material, further inquiries can be directed to the corresponding author.

Author contributions

JP acquired molecular geometries from NIST. KJ acquired initial data and wrote initial draft of manuscript. SN and AW acquired more data and are responsible for the completed manuscript.

Acknowledgments

The Institute for Cyber-Enabled Research (ICER) at Michigan State University is acknowledged for the use of high-performance computing resources.

Conflict of interest

The authors declare that the research was conducted in the absence of any commercial or financial relationships that could be construed as a potential conflict of interest.

Publisher's note

All claims expressed in this article are solely those of the authors and do not necessarily represent those of their affiliated organizations, or those of the publisher, the editors and the reviewers. Any product that may be evaluated in this article, or claim that may be made by its manufacturer, is not guaranteed or endorsed by the publisher.

Supplementary material

The Supplementary Material for this article can be found online at: https://www.frontiersin.org/articles/10.3389/fchem.2023.1152500/full#supplementary-material

References

Adamo, C., and Barone, V. (1999). Toward reliable density functional methods without adjustable parameters: The PBE0 model. *J. Chem. Phys.* 110 (13), 6158–6170. doi:10.1063/1.478522

Allen, F. H., Kennard, O., Watson, D. G., Brammer, L., Orpen, A. G., and Taylor, R. (1987). Tables of bond lengths determined by X-ray and neutron diffraction. Part 1. Bond lengths in organic compounds. *J. Chem. Soc. Perkin Trans.* 2 (12), S1. doi:10.1039/p298700000s1

Bachrach, S. M. (1994). "Population analysis and electron densities from quantum Mechanics," in *Reviews in computational chemistry, volume V*. Editors K. B. Lipkowitz and D. B. Boyd (New York: VCH Publishers, Inc.), 171–227.

Bader, R. F. W. (1990). *Atoms in molecules: A quantum theory*. Oxford, United Kingdom: Clarendon Press, 438. International series of monographs on chemistry, xviii. doi:10.1002/0470845015.caa012

Bai, Z., Jiang, X. Z., and Luo, K. H. (2022). Effects of water on pyridine pyrolysis: A reactive force field molecular dynamics study. *Energy* 238, 121798. doi:10.1016/j.energy.2021.121798

Balabanov, N. B., and Peterson, K. A. (2006). Basis set limit electronic excitation energies, ionization potentials, and electron affinities for the 3d transition metal atoms: Coupled cluster and multireference methods. *J. Chem. Phys.* 125 (7), 074110. doi:10.1063/1.2335444

Balabanov, N. B., and Peterson, K. A. (2005). Systematically convergent basis sets for transition metals. I. All-electron correlation consistent basis sets for the 3d elements Sc-Zn. *J. Chem. Phys.* 123 (6), 064107. doi:10.1063/1.1998907

Bayly, C. I., Cieplak, P., Cornell, W., and Kollman, P. A. (1993). A well-behaved electrostatic potential based method using charge restraints for deriving atomic charges: The RESP model. *J. Phys. Chem.* 97 (40), 10269–10280. doi:10.1021/j100142a004

Besler, B. H., Merz, K. M., and Kollman, P. A. (1990). Atomic charges derived from semiempirical methods. *J. Comput. Chem.* 11 (4), 431–439. doi:10.1002/jcc.540110404

Binkley, J. S., and Pople, J. A. (1977). Self-consistent molecular orbital methods. XIX. Split-valence Gaussian-type basis sets for beryllium. *J. Chem. Phys.* 66 (2), 879–880. doi:10.1063/1.433929

Breneman, C. M., and Wiberg, K. B. (1990). Determining atom-centered monopoles from molecular electrostatic potentials. The need for high sampling density in formamide conformational analysis. *J. Comput. Chem.* 11 (3), 361–373. doi:10.1002/jcc.540110311

Bruhn, G., Davidson, E. R., Mayer, I., and Clark, A. E. (2006). Löwdin population analysis with and without rotational invariance. *Int. J. Quantum Chem.* 106 (9), 2065–2072. doi:10.1002/qua.20981

Bultinck, P., Van Alsenoy, C., Ayers, P. W., and Carbó-Dorca, R. (2007). Critical analysis and extension of the Hirshfeld atoms in molecules. *J. Chem. Phys.* 126 (14), 144111. doi:10.1063/1.2715563

Catone, D., Satta, M., Castrovilli, M. C., Bolognesi, P., Avaldi, L., and Cartoni, A. (2021). Photoionization of methanol: A molecular source for the prebiotic chemistry. *Chem. Phys. Lett.* 771, 138467. doi:10.1016/j.cplett.2021.138467

Chirlian, L. E., Franclt, M. M., and Francl, M. M. (1987). Atomic charges derived from electrostatic potentials: A detailed study. *J. Comput. Chem.* 8 (6), 894–905. doi:10.1002/jcc.540080616

Cho, M., Sylvetsky, N., Eshafi, S., Santra, G., Efremenko, I., and Martin, J. M. L. (2020). The atomic partial charges arboretum: Trying to see the forest for the trees. *ChemPhysChem* 21 (8), 688–696. doi:10.1002/cphc.202000040

Cramer, C. J. (2002). *Essentials of computational chemistry*. 2nd edn. New York: Wiley.

da Silva, T. U., Pougy, K. d. C., Albuquerque, M. G., da Silva Lima, C. H., and Machado, S. d. P. (2022). Development of parameters compatible with the CHARMM36 force field for [Fe4S4]2+ clusters and molecular dynamics simulations of adenosine-5'-phosphosulfate reductase in GROMACS 2019. *J. Biomol. Struct. Dyn.* 40 (8), 3481–3491. doi:10.1080/07391102.2020.1847687

Davidson, E. R., and Chakravorty, S. (1992). A test of the Hirshfeld definition of atomic charges and moments. *Theor. Chim. Acta* 83, 319–330. doi:10.1007/bf01113058

Davidson, E. R., and Clark, A. E. (2022). "A viewpoint on population analyses," in *International journal of quantum chemistry* (New York, United States: John Wiley and Sons Inc). doi:10.1002/qua.26860

Dill, J. D., and Pople, J. A. (1975). Self-consistent molecular orbital methods. XV. Extended Gaussian-type basis sets for lithium, beryllium, and boron. *J. Chem. Phys.* 62, 2921–2923. doi:10.1063/1.430801

Dunning, T. H., J., Peterson, K. A., and Wilson, A. K. (2001). Gaussian basis sets for use in correlated molecular calculations. X. The atoms aluminum through argon revisited. *J. Chem. Phys.* 114 (21), 9244–9253. doi:10.1063/1.1367373

Dunning, T. H. J. (1989). Gaussian basis sets for use in correlated molecular calculations. I. The atoms boron through neon and hydrogen. *J. Chem. Phys.* 90 (2), 1007–1023. doi:10.1063/1.456153

Feng, R., and Peterson, K. A. (2017). Correlation consistent basis sets for actinides. II. the atoms Ac and Np-Lr. *J. Chem. Phys.* 147 (8), 084108. doi:10.1063/1.4994725

Foster, J. P., and Weinhold, F. (1980). Natural hybrid orbitals. *J. Am. Chem. Soc.* 102 (22), 7211–7218. doi:10.1021/ja00544a007

Francl, M. M., Pietro, W. J., Hehre, W. J., Binkley, J. S., Gordon, M. S., DeFrees, D. J., et al. (1982). Self-consistent molecular orbital methods. XXIII. A polarization-type basis set for second-row elements. *J. Chem. Phys.* 77 (7), 3654–3665. doi:10.1063/1.444267

Frisch, M. J., Trucks, G. W., Schlegel, H. B., Scuseria, G. E., Robb, M. A., Cheeseman, J. R., et al. (2016). *Gaussian 16, revision C.01*. Wallingford, CT: Gaussian, Inc.

Gordon, S., Binkley, J. S., Pople, J. A., Pietro, W. J., and Hehre, W. J. (1982). Self-consistent molecular-orbital methods. 22. Small split-valence basis sets for second-row elements. *J. Am. Chem. Soc.* 104, 2797–2803. doi:10.1021/ja00374a017

Hariharan, P. C., and Pople, J. A. (1973). The influence of polarization functions on molecular orbital hydrogenation energies. *Theor. Chim. Acta* 28, 213–222. doi:10.1007/bf00533485

Hehre, W. J., Ditchfield, R., and Pople, J. A. (1972). Self - consistent molecular orbital methods. XII. Further extensions of Gaussian - type basis sets for use in molecular orbital studies of organic molecules. *J. Chem. Phys.* 56, 2257–2261. doi:10.1063/1.1677527

Heidar-Zadeh, F., Ayers, P. W., Verstraelen, T., Vinogradov, I., Vöhringer-Martinez, E., and Bultinck, P. (2018). Information-theoretic approaches to atoms-in-molecules: Hirshfeld family of partitioning schemes. *J. Phys. Chem. A* 122 (17), 4219–4245. doi:10.1021/acs.jpca.7b08966

Hirshfeld, F. L. (1977). Bonded-atom fragments for describing molecular charge densities. *Theor. Chim. Acta* 44 (2), 129–138. doi:10.1007/BF00549096

Jabłoński, M., and Palusiak, M. (2010). Basis set and method dependence in quantum theory of atoms in molecules calculations for covalent bonds. *J. Phys. Chem. A* 114 (47), 12498–12505. doi:10.1021/jp106740e

Jensen, F. (2007). *Introduction to computational chemistry*. 2nd Ed. Chichester: John Wiley & Sons, Ltd. doi:10.1007/s00214-013-1372-6

Johnson, R. D., III (2015). *NIST computational chemistry comparison and Benchmark Database., NIST standard reference, Database number 101.*

Kendall, R. A., Dunning, T. H., and Harrison, R. J. (1992). Electron affinities of the first-row atoms revisited. Systematic basis sets and wave functions. *J. Chem. Phys.* 96 (9), 6796–6806. doi:10.1063/1.462569

Kognole, A. A., Lee, J., Park, S., Jo, S., Chatterjee, P., Lemkul, J. A., et al. (2022). CHARMM-GUI Drude prepper for molecular dynamics simulation using the classical Drude polarizable force field. *J. Comput. Chem.* 43 (5), 359–375. doi:10.1002/jcc.26795

Laerdahl, J. K., Fægri, K., Visscher, L., and Saue, T. (1998). A fully relativistic Dirac – Hartree – Fock and second-order Möller – Plesset study of the lanthanide and actinide contraction. *J. Chem. Phys.* 109, 10806–10817. doi:10.1063/1.477686

Löwdin, P. O. (1970). On the nonorthogonality problem. *Adv. Quantum Chem.* 5 (C), 185–199. doi:10.1016/S0065-3276(08)60339-1

Martin, F., and Zipse, H. (2005). Charge distribution in the water molecule - a comparison of methods. *J. Comput. Chem.* 26 (1), 97–105. doi:10.1002/jcc.20157

Mayer, I. (2004). Löwdin population analysis is not rotationally invariant. *Chem. Phys. Lett.* 393 (1–3), 209–212. doi:10.1016/j.cplett.2004.06.031

McLean, A. D., and Chandler, G. S. (1980). Contracted Gaussian basis sets for molecular calculations. I. Second row atoms, Z=11-18. *J. Chem. Phys.* 72, 5639–5648. doi:10.1063/1.438980

Miliordos, E., and Mavridis, A. (2007). Electronic structure of vanadium oxide. Neutral and charged species, VO0,±. *J. Phys. Chem. A* 111 (10), 1953–1965. doi:10.1021/jp067451b

Mulliken, R. S. (1955). Electronic population analysis on LCAO–MO molecular wave functions. I. *J. Chem. Phys.* 23 (10), 1833–1840. doi:10.1063/1.1740588

Mulliken, R. S. (1971). Iodine revisited. *J. Chem. Phys.* 55 (1), 288–309. doi:10.1063/1.1675521

Noell, J. O. (1982). Modified electronic population analysis for transition-metal complexes. *Inorg. Chem.* 21, 11–14. doi:10.1021/ic00131a003

North, S. C., Almeida, N. M. S., Melin, T. R. L., and Wilson, A. K. (2023). Multireference wavefunction-based investigation of the ground and excited states of LrF and LrO. *J. Phys. Chem. A* 127, 107–121. doi:10.1021/acs.jpca.2c06968

Novir, S. B., and Aram, M. R. (2020). Quantum mechanical simulation of Chloroquine drug interaction with C60 fullerene for treatment of COVID-19. *Chem. Phys. Lett.* 757, 137869. doi:10.1016/j.cplett.2020.137869

Peterson, K. A. (2015). Correlation consistent basis sets for actinides. I. the Th and U atoms. *J. Chem. Phys.* 142 (7), 074105. doi:10.1063/1.4907596

Prascher, B. P., Woon, D. E., Peterson, K. A., Dunning, T. H., and Wilson, A. K. (2011). Gaussian basis sets for use in correlated molecular calculations. VII. Valence, core-valence, and scalar relativistic basis sets for Li, Be, Na, and Mg. *Theor. Chem. Accounts* 128 (1), 69–82. doi:10.1007/s00214-010-0764-0

Raghavachari, K., Binkley, J. S., Seeger, R., and Pople, J. A. (1980). Self-consistent molecular orbital methods. XX. A basis set for correlated wave functions. *J. Chem. Phys.* 72, 650–654. doi:10.1063/1.438955

Rangel-Galván, M., Castro, M. E., Perez-Aguilar, J. M., Caballero, N. A., Rangel-Huerta, A., and Melendez, F. J. (2022). Theoretical study of the structural stability, chemical reactivity, and protein interaction for NMP compounds as modulators of the endocannabinoid system. *Molecules* 27 (2), 414. doi:10.3390/molecules27020414

Reed, A. E., and Weinhold, F. (1983). Natural bond orbital analysis of near-Hartree-Fock water dimer. *J. Chem. Phys.* 78 (6), 4066–4073. doi:10.1063/1.445134

Reed, A. E., and Weinhold, F. (1985). Natural localized molecular orbitals. *J. Chem. Phys.* 83 (4), 1736–1740. doi:10.1063/1.449360

Reed, A. E., Weinstock, R. B., and Weinhold, F. (1985). Natural population analysis. *J. Chem. Phys.* 83 (2), 735–746. doi:10.1063/1.449486

Reiher, M., and Wolf, A. (2004). Exact decoupling of the Dirac Hamiltonian. I. General theory. *J. Chem. Phys.* 121 (5), 2037–2047. doi:10.1063/1.1768160

Ritchie, J. P., and Bachrach, S. M. (1987). Some methods and applications of electron density distribution analysis. *J. Comput. Chem.* 8 (4), 499–509. doi:10.1002/jcc.540080430

Ritchie, J. P. (1985). Electron density distribution analysis for nitromethane, nitromethide, and nitramide. *J. Am. Chem. Soc.* 107 (7), 1829–1837. doi:10.1021/ja00293a005

Saha, S., Roy, R. K., and Ayers, P. W. (2009). Are the Hirshfeld and mulliken population analysis schemes consistent with chemical intuition? *Int. J. Quantum Chem.* 109, 1790–1806. doi:10.1002/qua.21901

Sigfridsson, E., and Ryde, U. (1998). Comparison of methods for deriving atomic charges from the electrostatic potential and moments. *J. Comput. Chem.* 19 (4), 377–395. doi:10.1002/(SICI)1096-987X(199803)19:4<377:AID-JCC1>3.0.CO;2-P

Singh, U. C., and Kollman, P. A. (1984). An approach to computing electrostatic charges for molecules. *J. Comput. Chem.* 5 (2), 129–145. doi:10.1002/jcc.540050204

Teatum, E., Waber, J., and Gschneidner, K. A. (1960). "Compilation of calculated data useful in predicting metallurgical behavior of the elements in binary alloy systems, Laboratory., Los Alamos Scientific Commission," in *U S atomic energy* (United States: Los Alamos Scientific Laboratory of the University of California).

Uene, N., Mabuchi, T., Zaitsu, M., Yasuhara, S., and Tokumasu, T. (2022). Reactive force-field molecular dynamics simulation for the surface reaction of SiH (x = 2–4) species on Si(1 0 0)-(2 × 1):H surfaces in chemical vapor deposition processes. *Comput. Mater. Sci.* 204, 111193. doi:10.1016/j.commatsci.2022.111193

Wiberg, K. B., and Rablen, P. R. (2018). Atomic charges. *J. Org. Chem.* 83 (24), 15463–15469. doi:10.1021/acs.joc.8b02740

Wiberg, K. B., and Rablen, P. R. (1993). Comparison of atomic charges derived via different procedures. *J. Comput. Chem.* 14 (12), 1504–1518. doi:10.1002/jcc.540141213

Zhang, Y., Elfeghe, S., and Tang, Z. (2022). Mechanism study of Cd(II) ion adsorption onto resins with sulfonic/phosphonic groups using electronic structure methods. *J. Mol. Liq.* 358, 119199. doi:10.1016/j.molliq.2022.119199

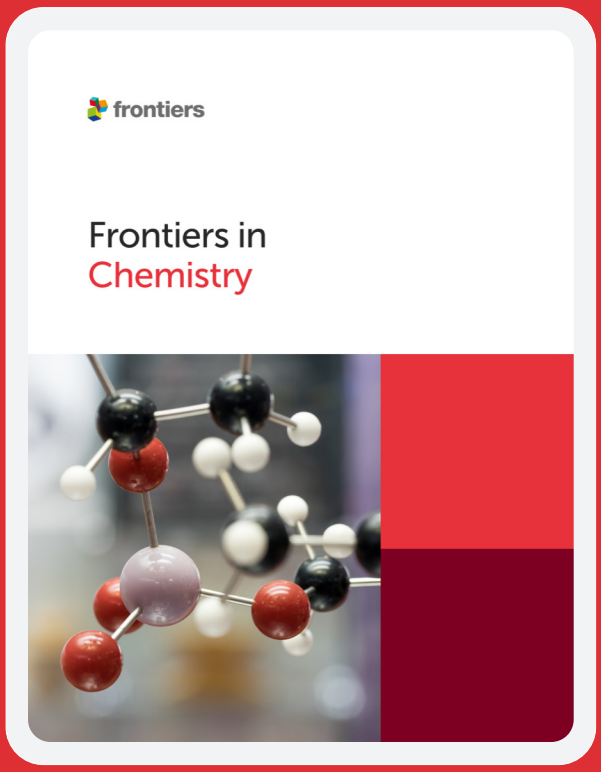
Frontiers in Chemistry

Explores all fields of chemical science across the periodic table

Advances our understanding of how atoms, ions, and molecules come together and come apart. It explores the role of chemistry in our everyday lives - from electronic devices to health and wellbeing.

Discover the latest Research Topics

See more →



Frontiers

Avenue du Tribunal-Fédéral 34
1005 Lausanne, Switzerland
frontiersin.org

Contact us

+41 (0)21 510 17 00
frontiersin.org/about/contact